MANY-BODY FERMION DENSITY MATRICES

VOLUME I

A Dissertation

Presented to the Faculty of the Graduate School

of Cornell University

in Partial Fulfillment of the Requirements for the Degree of

Doctor of Philosophy

by

Siew-Ann Cheong

May 2006

MANY-BODY FERMION DENSITY MATRICES

Siew-Ann Cheong, Ph.D.

Cornell University 2006

This four-part thesis is on the reduced many-body density matrices of systems of noninteracting and interacting spinless fermions, and the exact solution of ladder models of interacting spinless fermions. In the first part (Chapters 2 and 3), we derived an exact formula relating the density matrix and Green function for a cluster of sites within a system of noninteracting spinless fermions in any dimensions. Based on the thermodynamic form of the cluster density matrix in this exact formula, we proposed a truncation scheme in which the new Hilbert space is built from a truncated set of spinless fermion operators.

In the second part (Chapter 4), we studied various finite size effects in the cluster density-matrix spectra, and looked at how these can be reduced or eliminated using the method of twist boundary conditions averaging, for finite two-dimensional systems of noninteracting and interacting spinless fermions. We also checked the feasibility of the operator-based truncation scheme for interacting systems.

In the third part (Chapters 5, 6, and 8), we developed a systematic and unbiased machinery, based on the decomposition of the density matrix of two disjoint clusters a and b, into a sum of products of an operator on cluster a and an operator on cluster b, to extract the various quantum-mechanical correlations, from a numerical exact-diagonalization ground-state wave function. This machinery was applied to explore the ground-state phase diagram of the extended Hubbard ladder of spinless fermions with

correlated hops (which are next-nearest-neighbor hops that occur in the presence of occupied nearest neighbors).

In the fourth part (Chapter 7), we introduced three analytical maps which allow us to ultimately write the ground states, of the extended Hubbard ladder of spinless fermions in three limiting cases, in terms of the one-dimensional Fermi-sea ground state. We also introduced the technique of intervening-particle expansion, where a ladder correlation function is written as a sum over conditional expectations, each of which can be ultimately mapped to a one-dimensional Fermi-sea expectation, to calculate various correlation functions in the weak inter-leg, strong inter-leg, and strong correlated hopping limits.

BIOGRAPHICAL SKETCH

Cheong, Siew-Ann (张寿安) was born on November 4, 1969 to Cheong Ah Sang and Guh Ah Chu, the eldest of three sons born to them. His father Cheong Ah Sang was a vocational institute instructor specializing in metal welding until he retired in 2003. His mother Guh Ah Chu has had so many jobs that nobody in the family remembers every job that she has been in. She has been a housewife, a seamstress, and a canteen operator. As of mid-2005, she has worked as a coffeeshop assistant for ten years. Siew-Ann's two younger brothers, Siew Vim and Siew Kuan, are in the engineering and teaching profession respectively.

Growing up in the rural northwest of Singapore, Siew-Ann has always been fascinated by all manner of plants and animals, though he had never found the neighbors' irritable dogs endearing. On rare occasions, when he was not avoiding, or running for dear life, from these furry creatures, he would end up eating one of them, when a neighbor develop an irresistible craving for dog meat. At other times, he would unwittingly sample pythons, monitor lizards, terrapins, and other forms of wild birds and beasts which inhabit the swampy neighborhood. Gastronomical adventures aside, Siew-Ann also enjoyed scampering up the hills during the December monsoon seasons to fly his home-made kites, or make his way down to the streams to trudge in the foul-smelling mud, always hoping to catch a small fish or two. He would also lose track of time playing hide-and-seek in the vegetable plots with kids from the neighborhood, and come home after sunset to find his father or mother with a cane in the hand. Sometimes, when Siew-Ann was not being whipped for his pranks, his father would bring him on a trek around the neighborhood, or drive to the marshes and nature reserves in Singapore, or take week-long trips to various parts of peninsular Malaysia to collect butterfly specimens.

Siew-Ann never remembered much of what he learnt in Ama Keng Primary School, where he went for his elementary school education. Apart from the stern form teacher in Primary Two, who spanked him for fumbling on his multiplication tables, and thus left an indelible impression on the young boy, Siew-Ann can only remember playing marbles, tops, trading cards, five-stones, zero-point, Rubik cubes and other rural children games not designed to bankrupt working-class parents. He distinctly remembers feeling a sense of relief, after squatting down in the school field every Friday after recess, trying to brush his teeth with no toothpaste and a minimal amount of gargling water, to move on to the Chinese High School for his middle school education. He cannot remember very clearly what he learnt there as well, and did not really mind the fact that he was coming in near the end of the his class after every examination. He remembers vividly, however, a swarm of young school boys (him included) in white T-shirt and red shorts, pretending to run four kilometers every Saturday morning. When the head of the school's Physical Education Department decided that the students were not getting fitter, Siew-Ann and company trekked up Bukit Timah Nature Reserve every other Saturday morning. He was not quite sure he had gotten any fitter, but the monkeys calling Bukit Timah Nature Reserve home did not care, so long as the middle school students continued to generously hand out food.

After a four-year stint in the Chinese High School, Siew-Ann moved on to the Hwa Chong Junior College for his high school education. He has many strong memories in this period of his life. First he was infatuated with and spurned by (approximate order only) a girl in his class. Then he re-connected with badminton, which he picked up as an elementary school kid in his front yard, and which is the only sports he has ever played well at. And just as the hectic high-school life was beginning to settle into some semblance of monotony, the school buildings were declared structurally unsafe. Thence

he began a nomadic life along with the rest of his Class of 1986, attending lectures and tutorials, first at the Ngee Ann Polytechnic, and then at the newly-completed and yet-to-be-occupied Riverside Secondary School. He enjoyed the flux and uncertainty so much that it actually felt fun taking the Cambridge GCE 'A' Levels examination.

However, life was not always kind to him. A few weeks after graduating from Hwa Chong Junior College, Siew-Ann was enlisted for military service, mandatory for every able-bodied Singaporean male. The regimental life in the army was a shock to him, but he managed to complete his basic military training with limbs and sanity intact, before the powers-that-be decided that he had performed well enough to be sent to the infantry section leader course. After spending weeks after weeks after weeks in the jungle, combating a lack of sleep and jungle rot, as well as some fictitious enemies, Siew-Ann finally lost his marbles and decided that he like Army life. He signed some forms that he never looked at ever again, and was promptly put behind a desk as a contract soldier. His jungle rot improved, but his morale did not, and so he started writing songs to vent the frustrations of being chained to a desk, mindlessly shoving papers.

Music and songwriting opened a whole new world to Siew-Ann: one in which life's most enduring moments are documented in terms of ephemeral and transient notes; one of fleeting emotions which brush the heart and soul, and yet leave lasting scars; one of passion and disdain; and one of things we would see with our eyes, but missed with our hearts. In the quest for kindred spirits, Siew-Ann met a few songwriters who would become his best friends. Together, they set up a music publishing company, and strived to produce compilations of songs which they felt have soul and character. In those dizzying days and nights, Siew-Ann and friends camped in recording studios, became members of the Composers and Authors Society of Singapore (COMPASS), got swin-

dled of money, met with people in the business, whose highest points on their heads are the tips of their noses, and even appeared on television! Digusted with the lack of support and resources for budding songwriters, Siew-Ann joined the executive committee of the Young Songwriters Society (YSS) to work the underground songwriting scene in Singapore. He organized workshops, help produced concerts, and kept his mind active and adrenalin rushing, amidst an Army life that had morphed into something utterly mundane.

Another major transition in Siew-Ann's life came in 1993, when he broke his contract with the Army, and went on to tertiary education at the National University of Singapore (NUS). Siew-Ann found picking up books after laying them off for five years tough, and it took him quite a while before all the stuff he learned as a high-schooler, and was now relearning as a 24-year-old, came into focus once again. In this relearning process, Siew-Ann remembers feeling excited after a classmate showed him how to integrate $\int \sin^2\theta\, d\theta$ with the use of a trigonometric identity. Notwithstanding the fact that he was juggling the production of a music album with the production of a music concert, and also trying to make friends with geeks, he topped the Science faculty in his first year of study. It surprised him very much. He was also very flattered that the professors are treating him with a great deal of respect, and agreed to an invitation by his chemistry professor to work with her in the summer, which culminated in the publication [G. K. Chuah, S. Jaenicke, S. A. Cheong and K. S. Chan, "The Influence of Preparation Conditions on Surface Area of Zirconia", Applied Catalysis A: General, **15**, 267 (1996)]. He continued to do well in physics and chemistry in his second year, even though he was now seriously distracted courting one of his classmates. This classmate was to later become Mrs Cheong in January 2004.

While music and songwriting opened his eyes to the temporal world of love, hope,

and yearning, his stint as a Science student in NUS opened his eyes to yet another brave new world. This is the world of reason and intellect, where through various arcane rites of initiation (furiously copying down notes as the professors flashed transparencies after transparencies, for example) and intense study (mugging real hard to cram one semester's worth of information into the superficial areas of the brain real fast, so that these information can be regurgitated on demand within two-hour examinations), one acquires the ability — at least in principle — to see what had been, what is, and that which has yet to be. Weathering an initially rocky relationship, as all couples must, with his wife-to-be, Siew-Ann continued to do well, in his third and fourth years in NUS, to win several prestigious academic awards. By the end of his undergraduate studies, Siew-Ann was convinced a life in academia, a life in which the mind never rests, is right for him.

After a one-year accelerated M.Sc. program, earning stipend to pay off his tuition loan, Siew-Ann came to Cornell. Nominally to earn a Ph.D. in Physics, Siew-Ann's real aim was to soak in the excitement of doing science with the best minds in the world. He was not disappointed. Through tough homeworks and gruelling term papers, and then on to the never-ending calculations for his thesis projects, there were not many days in his seven-and-a-half years in Ithaca, where he had failed to learn something new. Especially memorable were the one- and two-loop calculations in PHYS 651 Relativistic Quantum Field Theory taught by Prof. Philip Argyres, who is now at the University of Cincinnati, the Bethe lattice renormalization-group calculations and his first term paper on cellular automaton models for traffic simulation in PHYS 653 Statistical Physics taught by his advisor Prof. Chris Henley, and the tight-binding calculations and plotting of two-dimensional dispersion relations in PHYS 635 Solid State Physics I taught by Prof. Dan Ralph. Siew-Ann also enjoyed, perhaps more than he should be allowed to,

the laboratory course PHYS 510 required by the department, receiving kind permission from Prof. Donald Hartill to continue working on the nonlinear oscillator experiment after the spring semester of 1999 officially ended. Siew-Ann then turned in a 78-page report for the experiment, far exceeding the usual 10-page length expected of PHYS 510 reports. In retrospect, this was a harbinger of the shape of things to come.

In the summer of 1999, Siew-Ann started working with Prof. James Sethna on the analytical study of dislocation dynamics. Having labored the first half of summer and making no progress whatsoever, Siew-Ann was shepherded into doing computational studies of dislocation dynamics instead. Unfortunately, he found the prospect of working for months on a huge C++ code base for molecular dynamics simulation, before it could be ready for actual runs, unappealing. Siew-Ann therefore switched to working with Prof. Chris Henley in his second summer, developing a numerical real-space renormalization-group scheme based on the many-body density matrix for interacting systems. Ironically, he ended up writing a sizeable Octave code base for these density-matrix computations. After making good progress initially, Siew-Ann found himself stuck, despite slogging long and hard hours hacking away at the problem. With immense determination and perseverance, and fighting frequent bouts of disillusion, Siew-Ann finally managed to push the calculations through, to obtain the exact formula (2.4.30) in Chapter 2. Steeled by the experience, Siew-Ann then found himself doing projects after projects, sometimes in parallel, that led further and further away from the original goal of a numerical renormalization-group scheme for interacting systems.

Before coming to Cornell, Siew-Ann had the naive notion that doing scientific research meant formulating a general outline of a workable research program, with primary and secondary goals, as well as the methods to use all thought out. He thought that all that was left to be done was to break the research program down into digestible and

tractable stages, and then work through these stages in sequential fashion, solving piecemeal problems along the way. Siew-Ann was surprised to learn here in Cornell that no physicist actually does things this way. Instead, doing research is very much like a man who finds himself lost in a forest, groping to find a way out. He would first follow what appears to be the most promising direction out of the woods, but be forced to reconsider his options when he gets mired down. Frequently, he would have to pick new, and more promising directions. This was true when Siew-Ann was working with Prof. James Sethna, but especially true of the research that he did under Prof. Chris Henley, explaining why his 1278-page thesis consists of a seemingly incongruent set of calculations, all connected in some ways, but not quite advancing an overall program of research. The 'forest' Siew-Ann found himself in is the 'forest' of "Many-Body Fermion Density Matrices", but sometimes he find that he has to make his way across structurally different 'vegetations', nested within the 'forest', of twist boundary conditions averaging, as well as the exact solution of interacting spinless fermions on ladders.

Through the many thesis research projects that he has carried through to completion, and many semi-completed mini research projects of his own, Siew-Ann — who became a proud first-time father in May 2005 — has learnt, though not yet mastered, the art of doing scientific research. From finding the right questions to ask, to identifying the right analytical and numerical tools to use, to scheduling parallel calculations to most efficiently tap his creative energies, to packaging results to present them in the best possible light, Siew-Ann is becoming increasingly confident that he would soon be able to set and pursue research programs of his own. In other words, Siew-Ann thinks he can make his way out of the woods, should he wake up one day to find himself lost...

To Karen and Ernest,

the number-one and number-two persons in my life

ACKNOWLEDGEMENTS

This thesis nearly tore our family apart emotionally, especially in the months of October and November of 2005, when the prospects of finishing seemed most bleak. I thank my wife, Karen Tan Sue Ling, and my son, Ernest Emmanuel Cheong Hao'en, for enduring my absence and the dire financial situation that we as a family have been in, as well as for forgiving my missing of all but a few of Ernest's milestones in life. Karen and I thank God for giving us the courage to enter into the Sacrament of Matrimony in January 2004, the strength to live through two years of poverty, and the inspiration needed to finish up this thesis. We are grateful to God that Karen and I were able to spend two weeks of quality time together before May 12, 2005, and we offer up our deepest gratitude to God for making us a family of three on that fateful day. We thank Mother Mary and Saint Gerard for their intercessions, constantly thank God for our son Ernest, the greatest gift of life. We pray that we will continue to learn how to see His Grace in the most trying of circumstances.

On behalf of Ernest, we thank the doctors and midwives, especially Dr James Fogel, of Ob/Gyn Associates of Ithaca, and also Dr Lawrence Dolkart, of the Health Center for Women, and Arnot-Ogden Medical Center in Elmira, New York for their pre-natal care of Karen, before she return to Singapore in December 2004. We thank Dr Catherine Yap for her skillful adminstration of the epidural anesthesia for Karen. We are indebted to Dr Yeoh Swee Choo, Karen's gynaecologist and obstetrician, for her pre- and post-natal care of Karen, and her prompt decision to perform episiotomy while delivering Ernest, when his heart stopped beating during the pushing stage. We thank Dr Lee Bee Wah, Ernest's pediatrician, for helping clear Ernest's lungs of amniotic fluid, so that he can take his first breath. We thank the midwives and nursing staff of Mount Elizabeth Hospital. We are especially grateful to lactation specialist Tan Guat Choo, for being

patient with Ernest, as Karen and him both learn the ropes of breast feeding. We thank Auntie Christina Kwek for her help and encouragement, without which Karen and I would probably have decided to give up breast feeding.

We thank Karen's parents, Tan Heng Gui ("Grandpa") and Rosalin Lim Mui Keng ("Grandma"), for their care and support of Karen in the months before Ernest was born, and especially for doting on Ernie boy after he was born. We thank them for giving this poor little family a roof over our heads, and all the delicious and nutritious food that far far surpasses mere sustenance. We thank them for all the clothes and toys they bought for Ernie boy. We thank Grandma for rocking Ernie boy to sleep every night while he was still a tiny little baby, and for organizing Ernie boy's one-month-old party. We thank Grandpa for giving Ernie boy the car rides he enjoys everyday, and being Ernie boy's favorite play buddy. We thank Auntie Lily for coming almost everyday to cook for the family, and help look after Ernie boy while Karen was still in 'confinement'. We thank her for continuing to come help take care of Ernie boy when Karen did a relief teaching stint from July to November 2005. We thank her for sharing her love with Ernie boy. We thank my parents, Cheong Ah Sang and Guh Ah Chu ("Po Po"), for being there for me when I was young, and for teaching me in their own silent ways, what a family meant. We thank Po Po for coming to visit Ernie boy and us, even when she is busy ekeing out a living. We also thank Miss Lim Oon Hua for visiting Karen and Ernest at the hospital, Mrs Yeo Shih Fong for visiting Karen and Ernest at the hospital and at home, and Mrs Lek Bee Hoon for making baby-sized pillows and bolsters and their cases, in addition to visiting Karen and Ernest at home. We thank the Kong family for various gifts and presents for Karen and Ernest, especially for the hand-sewn patchwork blanket for Ernie boy. We are very grateful to Joachim and Maria Sagaram for agreeing to be Ernie boy's godparents.

We thank Father Mose Yap, formerly of Saint Mary of the Angels Church in Bukit Batok, Singapore, and now ministering in Sabah, East Malaysia, for being our spiritual guide in Singapore before we got married. We thank the Cornell Catholic Community for being our spiritual pillar, for the year (2003) before we got married, the year (2004) when both of us were here in Ithaca, and for the year (2005) that we were separated by 20,000 kilometers. We thank Father Michael Mahler, now Pastor of Saint Catherine of Siena Church in Ithaca, Father Robert Smith and Father Daniel McMullin, for sharing their wisdom and reflections on the biblical readings, and their constant challenge and reminder to live an authentic Christian life. We thank the chaplains, Theresa Miller and Phil Fiadino for being the often overlooked threads that weave the community together. We especially thank Sister Donna Fannon, for preparing me for the Sacraments of Baptism, First Communion, and Confirmation, and organizing the various Catholic couple get-togethers. We thank Prof. Piet Brouwer for agreeing to be my godfather, and Piet, Gerburg and Benedict for inviting us to their home to play with Benedict, and to share fellowship and meals. We thank the Goettel's, Mike, Sara and Hans for their fellowship at Annabel Taylor and also at their cozy home. We thank the Henry's, Rob and Cassie, for taking up the unenviable task of organizing the Emmaus Bible discussion group, from which we have benefitted a great deal. We thank the Smallidge's, Pete, Kelly, Natalie and Adelaide, for inviting me to their log-cabin home for a late-summer gathering last year. We thank them all for their comforting presence every Sunday morning, when Karen and I were both here in Ithaca in 2004, and especially in 2005, when I was here all alone.

I thank all the past and present members of the Cornell Badminton Club, for the camaraderie and thrill I enjoyed on the courts of Helen Newman Hall (and occasionally in Barton Hall). I thank the old guards who are forever here, injuries notwithstanding:

Prof. Anil Netravali, faculty advisor to the club, Xiaoshi Jin, Cornell alumni and former president of the club, David Sagan, who has been here and playing badminton for as far back as anyone can remember, and David Post, for his good humor. I thank all the members who graciously invited me to join them, when I started playing with the club in 2000, and who has since left Cornell: George, who was president of the club for 1999/2000; Panarairat Srichaiyarat, president of the club for 2000/2001 and now an Assistant Professor at Chiang Mai University, Thailand; Wipas Wimonsate, now at the Thailand Environment Institute; Jinlin Peng, who used to drive all the way to Ithaca from Corning to play badminton every Saturday morning; Lidong Zhou, now with Microsoft Research, and wife; and Zhong Huang. I thank my sparring partners, who has given me many good games, before going where their careers led them: Martin Roth, who flew all the way to Singapore for my wedding; Rachel Zhang, former Johnson School Assistant Professor and now faculty at the Hong Kong University of Science and Technology, and her husband Paul Zhu; Dewi Novianty; Kimberley Mok, now in New York City; Jacky Cheung (no, not the Hong Kong Heavenly King, but no less charming to the ladies!); Betty Ka Bik Luk and Wallace Leung; Lincoln Yeh, the southpaw law student who transferred from Cornell to Columbia; Xianzheng Zhang, a former postdoctoral researcher in Cornell, whom I used to have a lot of trouble beating in singles games; Xiaochun Fan, now at Harvard Medical School as a postdoctoral researcher; Kiran Kannancheri; Roman Boltnev, who was here for a year as a NATO fellow working on low-temperature physics with Prof. David Lee, and who was here again for the summer of 2005; Ishan Sharma, now in the Department of Applied Mathematics and Theoretical Physics, Cambridge University as a postdoctoral researcher, and plays on the Cambridge University badminton team. Karen and I thank him for giving us his microwave for free before he left for Cambridge; Jonas Korlach, now in San Diego; Si-

mon Maddick, a British student who came to Cornell for a one-year exchange program last year; Radha Narayan; Arthur Chuan Lee; Jingfeng Zeng, now in Texas, whom I had many Saturday-afternoon singles games with; Yen Thi Hong Cu, now in Yale as a doctoral student; Ningxi Zhang; Clement Xiaofei Wang; and Linghao Zhong. I thank fellow Singaporeans in the club who has graduated from Cornell and returned to fulfill their promises to the people of Singapore, for conversing with me using the undecipherable 'Singlish': Peichin Lim; James, who diminuitive stature lures you into a false sense of security, until you get hit by his powerful smashes; and Yiliang 'Cannonball' Ho, now with the Republic of Singapore Airforce, who makes his statements with the 'sonic booms' of his smashes. Karen and I are indebted to Feng Zhao, now an Assistant Professor of Finance and Economics at Rutgers University, for giving us his 1991 Dodge Dynasty when he left Cornell in August 2004. Since then Karen and I were spared the 30-minute walk from Maplewood to Helen Newman every morning for Karen's aerobics classes. I thank all the present members who give me fast games: Archit Lal, Shengfeng Shen, Ram Narayan, Hengky Chandrahalim, Mike Hsu, Chula Watugala, Winson Lin, Mark Law, Daphne Ng, Zhongtao Fu, Sze Wei Ang, Yuping Zhou, Karen Lin, Seung Jin Oh, Peeyush Bhargava, Prof. David Strang, Charlie Wang and wife; as well those who give me slow but fun games: I-ho Chang, Ivan Han, Jeng-Huei Chen, Terence Tan, and Evelyn Choi. I like them to know that the adrenalin rushes kept me going, through the frustrating parts of the thesis research, and especially the five agonizing months spent writing this thesis.

I thank fellow doctoral students Lek Heng Lim, who came to Cornell as a Ph.D. student in Mathematics in the same year as me, was housemate with me for a year, and transferred to Stanford University a year after that; Hway Kiong Lim, who came to Cornell as a Ph.D. student in Mathematics one year after us, and was housemate with me

for three years; and Kelken Chang, who came to Cornell as a Ph.D. student in Physics in 2002. I thank them for having lunch or dinner with me daily, either at the Ivy Room and the Trillium on campus; Burger King, Subway and Ling Ling Garden restaurant in East Hill; the Hong Kong restaurant, the Little Thai House restaurant, the Vietnamese restaurant, and Sangam Indian restaurant in Collegetown, and understandingly hearing out my many grouses. I thank Lek Heng and Hway Kiong for frequently chiding me for the lack of mathematical rigor in my calculations, but yet always remain ready to extend helpful suggestions. I especially thank Hway Kiong, for his expert help setting up Linux on my computers, and also for taking so many fantastic badminton action photographs of me.

I thank Prof. Chris Henley for his guidance throughout my thesis work, writing letters of recommendation to the various positions and fellowships that I have applied to in the past year, and showing me glimpses of what goes on in a genius's mind. I thank Prof. James Sethna and Prof. Paul McEuen for agreeing to sit on my Special Committee, and Prof. Sethna for writing letters of recommendation for my various job and fellowship applications. While writing up the results in Chapter 3, which became Ref. 198, I have benefitted from discussions with Prof. James P. Sethna on numerical integration schemes and their expected dependence on the integration grid size. I thank Prof. Garnet Chan of the Cornell Chemistry Department, for illuminating me on how to numerically implement the fast trace-down algorithm used in Chapter 4. I thank Prof. N. David Mermin for helping clear a confusion of mine, while I was formulating the operator singular value decomposition of the correlation density matrix in Chapters 5 and 6. I thank Prof. Piet Brouwer for showing me how to do the contour integration in Figure 5.8. I also thank Ellen Hertz and Herman Rubin, for pointing out, on `sci.math.research`, references to the Lindeberg Theorem used in Chapter 3.

Karen and I thank Prof. Vinay Ambegaokar, who showed genuine concern for the long time I have spent on my doctoral studies. Though not on my Special Committee, he graciously agreed to help me write letters of recommendation, to the postdoctoral positions I have applied unsuccessfully for, to my application for the Agency for Science, Technology and Research (A*Star) Postdoctoral Fellowship, and to my application to join the faculty at the Nanyang Technological University.

Last, and certainly not the least, we thank all those who offer us hopes for a better tomorrow, in the form of gainful employment! We like to thank Chris Myers and Dave Schneider, for offering me a postdoctoral position at the Cornell Theory Center, after my own five-month search for a postdoctoral position has proven fruitless. We also thank Prof. Lee Soo Ying, Dean of the School of Physical and Mathematical Sciences, Nanyang Technological University, Singapore, and Prof. Alfred Huan Cheng Hon, Head of the Physics and Applied Physics Division there, for offering to take me on their faculty upon my return to Singapore.

The research done for this thesis was first supported by National Science Foundation grant DMR-9981744, and then by National Science Foundation grant DMR-0240953. I also made use of the computing facility of the Cornell Center for Materials Research (CCMR), with support from the National Science Foundation Materials Research Science and Engineering Centers (MRSEC) program (DMR-0079992).

TABLE OF CONTENTS

LIST OF TABLES

LIST OF FIGURES

CHAPTER 1

INTRODUCTION

1.1 Overview

A great deal can be learnt from exact solutions of quantum many-body problems (see for example, Refs. 1–4). However, we know only of a handful of exactly solvable models. These are typically one-dimensional, and are either simplified models of a few classes of real materials, or describe no real materials at all. To learn more about realistic and higher-dimensional models, we therefore resort to either approximate analytical methods or numerical solutions.

There are two chief approaches to approximate analytical calculations. The first, perturbation analysis, relies on us being able to write down convergent or asymptotic series expansions of the observables we are interested in, and therefore works only in restricted ranges of parameter values in the many-body Hamiltonian. The second, variational calculations[1], requires us to make a biased first guess as to what form the many-body wave function may take, thus closing the door to discovering unusual, and unexpected, behaviours in the many-body ground state.

The two traditional numerical approaches, applied to finite systems, are exact diagonalization and quantum Monte Carlo. These are exact, in the sense that no *a priori* assumptions are needed for the methods to work. However, for quantum lattice models of fermions, the former is constrained by the size of the Hilbert space, which grows exponentially with the number of sites, while the latter is plagued by the 'minus-sign problem'. For quantum lattice models of bosons, the Hilbert space is infinite-dimensional

[1] In practice, variational calculations is often very numerical and computational in nature, because when evaluating expectations, the high-dimensional integration involved must invariably be done using Monte Carlo integration. Monte Carlo-assisted variational calculations are described in greater detail in Section 1.2.2.3.

even for finite systems. In either case, because of the enormous computational complexity involved, there is no hope of getting directly to the thermodynamic limit of infinite system size. In view of these difficulties, one then hopes for the next best thing: approximate numerical solutions that capture the essence of the physics.

This is where renormalization group (RG) approaches come in [5–15]. We know from the renormalization group that in most many-body problems, only a few degrees of freedom, *viz.* those with low energies and long wavelengths, really matter. Hence, it should be possible in principle to discard the irrelevant parts of the Hilbert space, Indeed, in such approaches to the approximate solution of otherwise intractable problems, the size of the Hilbert space is kept in check by aggressive truncation, with the hope that the small number of states kept will reproduce the more important features of the physics. Whatever the RG scheme, ultimately its success will lie in how the truncation is done. Typically, the large-system ground-state wave function is calculated iteratively by adding one cluster of sites at a time to the numerical system to be exactly diagonalized. Since the quantum-mechanical state of a cluster of sites embedded in a larger system must in general be described by a density matrix, it is natural to use the density matrix to guide the truncations. This is done, for example, in the highly-successful Density-Matrix Renormalization Group (DMRG) method [14–17]. However, the method uses an algorithm that is inherently one-dimensional in nature, and therefore can only be successfully applied to study interacting quantum systems in one dimension, or to two-dimensional quantum systems that can be forced into one dimension as strips [18, 19]. Recently, the DMRG has been generalized to higher dimensions [20, 21], but its usefulness in solving higher-dimensional strongly-correlated many-body problems has yet to be convincingly demonstrated. The need for a real-space renormalization-group method for higher-dimensional, interacting lattice models that is accurate, efficient, and scalable,

remains.

Besides its central role in guiding renormalization-group truncations, the density matrix can also be used as a diagnostic tool. This is the role the density matrix plays in the Contractor Renormalization (CORE) method for numerical renormalization group in two dimensions [22–27]. Frequently, where numerical renormalization-group methods are lacking, exact diagonalization is used to gain insights into the physics of higher-dimensional models. The critical question then becomes how we can augment numerical exact diagonalization, which is only feasible on comparatively small systems, to extract the maximum information about the thermodynamic limit. The density matrix also forms the basis of a method to identify the order parameter related to a quasi-degeneracy of ground states [28].

To position the work done in this thesis, which is largely computational and numerical in nature, in relation to the larger body of existing literature, I will give a concise summary of the state of affairs surrounding the developments of exact numerical methods in Section 1.2 and renormalization-group methods in Section 1.3. In these two sections, as well as in subsequent chapters carrying literature reviews of their own, it is neither possible nor desirable to give an exhaustive list of published works. This is especially so when the topics reviewed have generated, or are still generating, intense interest. Therefore, if comprehensive monographs and texts exist and are well recognized, I will cite only these. Otherwise, if review articles exist, I will cite the pioneering papers, and then refer the reader to the review articles.

In Section 1.4, I will provide a road map to the various chapters in this thesis, highlighting the important results along the way. Apart from giving a *precis* of all the work that is reported in this thesis, the summary of important results contained in Section 1.4 is intended to equip readers with enough background information to go directly to any

chapter in the thesis, without having to read all preceding chapters.

1.2 Exact Numerical Methods for Finite Lattices

1.2.1 Exact and Lanczos Diagonalization

In the exact diagonalization of quantum lattice problems, one chooses an appropriate many-body basis $\{|\phi_i\rangle\}$, and construct the Hamiltonian matrix H by calculating the matrix elements $H_{ij} = \langle\phi_i|H|\phi_j\rangle$ explicitly. If the matrix H is dense, or when all the eigenvectors and eigenvalues are required, the exact diagonalization (ED) can be done using the algorithms described in Refs. 29 and 30. Efficient FORTRAN77 routines implementing these algorithms can be found in the Linear Algebra Package (LAPACK) [31, 32], as well as in LAPACK95, the FORTRAN95 interface to LAPACK [33, 34]. These LAPACK diagonalization routines are what Octave, which is the principal programming environment used in this thesis, calls.

Full diagonalization is not commonly used in physics, for two reasons: (i) the size of the Hilbert space, and hence the size of the Hamiltonian matrix, is typically too large to be stored in memory; and (ii) only the ground state and low-lying excited states of a quantum system are of interest to physicists. For these reasons, ED practitioners typically perform Lanczos or Jacobi-Davidson diagonalization to solve for a small number of eigenvectors and eigenvalues. Tutorials on the two methods can be found in Ref. 35, and Refs. 36 and 37 respectively, while a review of Lanczos diagonalization can be found in Refs. 38 and 39. Readers wishing only to get a flavor of exact diagonalization methods, particularly on basis representation, symmetry reduction of the size of the Hilbert space, and measurement of correlations and dynamics, can refer to the series of talks given during the ALPS User Workshop on Computational Methods for Strongly

Correlated Systems and Nanomagnetics, held in Lugano, Switzerland from September 26 to October 1, 2004 [40, 41].

It is difficult to trace the history of full diagonalization as applied to quantum many-body systems, because the name probably became popular only later. The earliest instances of full diagonalization that I am aware of are the works by Shiba and Pincus [42], and Shiba [43], and by Heinig and Monecke [44, 45], both on the Hubbard model. Full diagonalization caught on, judging from the rate of publications, in the computational physics community as a numerical technique complimentary to QMC in the later half of the 1980s [46–56]. The Lanczos algorithm for partial diagonalization was described in 1950 by Lanczos [57, 58], and first applied in physics by Bonner and Fisher [59] and Oitmaa and Betts [60] to study the Heisenberg model. This was followed shortly by Jullien and Martin, who used it to study the periodic Anderson model [61]. The Jacobi-Davidson algorithm for partial diagonalization is only starting to be tried out by the computational many-body community (see for example, Refs. 62 and 63). Whether performing full or partial ED, the goal of studying ever larger systems requires practitioner to apply symmetries to aggressively reduce the size of the Hilbert space. By restricting their exact diagonalization to fermion configurations of a particular spin, Cini *et al* managed to further reduce the rank of the matrices they handle to the square root of the rank of matrices built up from spinful bases [64].

Recently, de Raedt and coworkers introduced the method of stochastic diagonalization [65, 66]. The basic idea behind this method, also known as Monte Carlo diagonalization (to be distinguished from the method of Quantum Monte Carlo diagonalization in nuclear physics developed and used almost exclusively by Mizusaki and coworkers [67]), is that out of the D Hilbert space basis states chosen for a quantum many-body problem, the ground state has significant amplitudes only for a small number $D^* \ll D$

of the basis states. The stochastic diagonalization algorithm searches for these D^* basis states amongst the complete set of D basis states iteratively. At the nth iteration, the set of n basis states chosen at the $(n-1)$th iteration is used to construct a reduced Hamiltonian matrix $H^{(n)}$ by projecting the full Hamiltonian matrix H onto the space spanned by the n basis states. A modified Jacobi-Davidson algorithm is then used to partially diagonalize $H^{(n)}$ to the form

$$U^{(n)}H^{(n)}U^{(n)^\dagger} = \begin{bmatrix} E_1^{(n)} & \mathbf{0}^T \\ \mathbf{0} & \tilde{H}^{(n)} \end{bmatrix}, \tag{1.2.1}$$

where $U^{(n)}$ is an appropriate unitary transformation constructed using the modified Jacobi-Davidson algorithm, $E_1^{(n)}$ is the minimum eigenvalue of $H^{(n)}$, $\mathbf{0}$ is a $(n-1)\times 1$ null vector, and $\tilde{H}^{(n)}$ is the $(n-1)\times(n-1)$ undiagonalized remnant of $H^{(n)}$. A basis state is then randomly sampled from the unused set of $(D-n)$ basis states to augment the reduced Hamiltonian matrix. The unitary transformation $U^{(n)}$ is also augmented to act on this new basis state trivially. This new basis state is considered important if it produces a significant change (measured against some desired tolerance) to the minimum eigenvalue $E_1^{(n)}$, and the $(n+1)$th iteration is started with the new basis state included. Otherwise, a new basis state is sampled from the $(D-n)$ unused basis states, until an important basis state is found, or until the algorithm is deemed to have converged. Although the method has been demonstrated on matrices up to $10^{35}\times 10^{35}$ in size (!), it has not been used extensively [68–73]. The method is also known to suffer from convergence problems in some cases [74].

1.2.2 Quantum Monte Carlo

1.2.2.1 Comparison between QMC and ED

Compared to ED, Quantum Monte Carlo (QMC) as an exact numerical method is highly scalable in two ways. First of all, the method itself is not directly constrained by the size of the Hilbert space. For a given memory M (expressed in bits), ED can only work with fermionic systems with up to $N \sim \log M$ sites, whereas QMC is capable of going up to $N \sim M$ sites. This difference in scaling behaviour becomes more and more marked as the memory available for computation increases. QMC beats ED hands down for soft-core bosonic systems, because the latter method simply cannot handle the infinite-dimensional Hilbert space. The second advantage in scalability has to do with computation time. For ED, the typical computation time expended to solve for a ground-state wave function in a ($D \sim e^{\alpha N}$)-dimensional Hilbert space is D^3 multiplied by some $O(\log D)$ factor, which is indeterminable because of the iterative nature of the QR and Lanczos algorithms. This significant computational expenditure can be ameliorated by doing the matrix diagonalization on a vector machine, where the core matrix multiplications are vector-accelerated, or by doing block matrix diagonalization on a shared-memory symmetric-multiprocessor machine, where acceleration is achieved by adopting the divide-and-conquer strategy. Computation time for QMC, whose algorithm is inherently parallel to begin with, can be readily reduced through the use of distributed computing. If the QMC community finds a big problem that is important enough to warrant the effort, it is not hard to imagine a QMC@Home running as a screen saver on millions of desktop machines.

Lest the above description of QMC sounds like the prescription for a panacea to numerical solution of quantum many-body problems, let me make clear here that QMC

does have its limitations. Otherwise, nobody will be doing any ED, and we certainly would not be studying density matrices in this thesis. In Section 1.2.2.2, let me guide the reader through the history of the QMC method, before going further in Sections 1.2.2.3, 1.2.2.4 and 1.2.2.5 to describe the three methods that have come to be known collectively as QMC. Then in Section 1.2.2.6, I will discuss the 'minus sign' problem in QMC studies of many-fermion problems, and some recent efforts by the QMC practitioners to overcome or avoid this problem.

1.2.2.2 A Short History of QMC

To better appreciate the QMC method, it is important to first understand the basics of classical Monte Carlo, for which there are many good texts (see, for example, [75, 76]). The basic idea behind the Monte Carlo method is to have a population of random walkers perform a weighted random walk in some sampling space. The weighting and sampling algorithm must be so designed that the population of random walkers eventually converge onto the distribution function, which is the solution to the problem that the Monte Carlo method seeks to solve.

The first application of the Monte Carlo method to quantum systems was reported by Metropolis in 1954 [77], although he credited Ulam for the idea. In this semi-published work, the single-particle Schrödinger equation is discretized and casted into the form of a discrete diffusion equation, which is then solved by the usual random walk method (see, for example, [78]). This work generated little interest, apart from a series of papers by Anderson [79–81], because the technique described is not practical for many-body problems.

In present-day literature, we find three varieties of QMC methods being applied to quantum many-body problems. The first, which has since come to be known as

Variational Monte Carlo (VMC), is an extension of the variational approach to quantum many-body problems. It was first applied to a system of bosons by McMillan in 1965 [82], and to a system of fermions by Ceperley a few years later [83, 84]. The second variety of QMC found in the literature is known as *Green Function Monte Carlo* (GFMC). This method was first used in 1962 by Kalos in few-body nuclear physics problems [85], before he used it in 1970 to find the ground state of a fluid of bosons interacting via the Lennard-Jones potential [86]. This led on to a quick succession (by 1970 standards) of papers studying hard-sphere [87, 88], Lennard-Jones [89, 90], and Yukawa boson fluids [91, 92] using the method. An early review of the VMC and GFMC methods can be found in Ref. 93. The third variety of QMC goes by the name of Path-Integral Monte Carlo (PIMC) [94–98]. A modern review of all three methods can be found in Ref. 99.

1.2.2.3 Variational Monte Carlo

In this method, one writes down for Bose liquids the variational *Bijl wave function* of the form

$$\tilde{\psi}(\mathbf{r}) = \prod_{i<j} f(r_{ij}) = \exp\left[-\frac{1}{2}\sum_{i<j} u(r_{ij})\right], \tag{1.2.2}$$

which is a product of two-particle correlation functions $u(r_{ij})$, also called *pseudopotential functions*. Here $\mathbf{r} = (r_{1,1}, \ldots, r_{1,d}; \ldots; r_{P,1}, \ldots, r_{P,d})$ is a point in the configuration space of P particles in d dimensions. For Fermi liquids, the variational *Bijl-Dingle-Jastrow wave function* is of the form

$$\tilde{\psi}(\mathbf{r}) = D(\mathbf{r}) \exp\left[-\frac{1}{2}\sum_{i<j} u(r_{ij})\right], \tag{1.2.3}$$

where $D(\mathbf{r})$ is the ideal Fermi gas wave function, i.e. a determinant of plane waves. The variational parameters used by the method reside in the pseudopotentials $u(r_{ij})$.

The expectation

$$\langle A \rangle = \frac{\int d^{Pd}\mathbf{r}\, \tilde{\psi}^*(\mathbf{r}) A(\mathbf{r}) \tilde{\psi}(\mathbf{r})}{\int d^{Pd}\mathbf{r}\, |\tilde{\psi}(\mathbf{r})|^2}. \tag{1.2.4}$$

of a given observable $A(\mathbf{r})$ is then evaluated in the VMC method by drawing a set of m configuration space points $\{\mathbf{r}_i\}_{i=1}^m$ from the probability distribution

$$p(\mathbf{r}) = \frac{|\tilde{\psi}(\mathbf{r})|^2}{\int d^{Pd}\mathbf{r}\, |\tilde{\psi}(\mathbf{r})|^2}, \tag{1.2.5}$$

so that the expectation $\langle A \rangle$ is given by

$$\langle A \rangle = \lim_{m\to\infty} \frac{1}{m} \sum_{i=1}^{m} \tilde{\psi}^*(\mathbf{r}_i) A(\mathbf{r}_i) \tilde{\psi}(\mathbf{r}_i). \tag{1.2.6}$$

As we can see, this is not an exact numerical method, because of the use of variational wave functions. Rather, it is just a numerical method to evaluate expectations from a guessed ground-state wave function. Nonetheless, it is popular amongst theorists who want to learn something about many-body systems using variational means, and find that Monte Carlo integration is the only viable technique of integration when $Pd \gg 1$.

The state of the art in this method includes the introduction of three-body terms in the variational wave function [100–102], as well as means to incorporate backflow correlations [103–106]. For simulating quantum solids, Vitiello, Reatto and coworkers introduced pair-correlated variational wave functions, called *shadow wave functions*, with 'shadow' coordinates [107–110].

1.2.2.4 Green-Function Monte Carlo

In the original formulation of this method by Kalos [85,86,89], the Schrödinger equation

$$\Psi(\mathbf{r}, \tau + \Delta\tau) = \int d^{Pd}\mathbf{r}'\, G(\mathbf{r}, \mathbf{r}', \Delta\tau) \Psi(\mathbf{r}', \tau), \tag{1.2.7}$$

is written in integral form, in terms of the imaginary-time Green function

$$G(\mathbf{r}, \mathbf{r}', \tau) = \langle \mathbf{r}| \exp[-(H - \tilde{E})\tau] |\mathbf{r}'\rangle \tag{1.2.8}$$

where $|\mathbf{r}\rangle$ is a real space configuration state, and H is the Hamiltonian of the system. The energy $\tilde{E}$ that appears in $G(\mathbf{r}, \mathbf{r}', \tau)$ is a trial energy adjusted to keep the population of random walkers constant, and becomes equal to the ground-state energy when the random walkers attain the equilibrium (ground-state) distribution. For discrete imaginary time evolution on a computer, (1.2.7) can be written as

$$\Psi(\mathbf{r}, n+1) = \int d^{Pd}\mathbf{r}'\, G(\mathbf{r}, \mathbf{r}')\Psi(\mathbf{r}', n). \tag{1.2.9}$$

The reason why the population of random walkers converges onto the ground-state probability distribution was first explained by Trivedi and Ceperley in 1990 [111]. Essentially, what the method does is to take a *trial wave function* $\tilde{\Psi}$, also known as the *guiding wave function*, and apply the imaginary-time evolution operator $\exp[-(H-\tilde{E})\tau]$ to project out states orthogonal to the ground state. The trial wave function can be any function, but is typically chosen to be Hartree-Fock or Jastrow wave functions (both of these first suggested by Klein and Pickett in Ref. 112), or even a DMRG wave function (as was done by du Croo de Jongh *et al* in Ref. 113) to accelerate convergence. Once this was understood, GFMC practitioners started using the *filter operator*

$$F = \mathbb{1} - \tau(H - \tilde{E}), \tag{1.2.10}$$

which is the lowest-order term in the expansion of $\exp[-(H-\tilde{E})\tau]$, to project out states orthogonal to the ground state [114]. To ensure that the iterated wave function

$$\Psi^{(n)} = F^n\tilde{\Psi} \tag{1.2.11}$$

converges onto the ground-state wave function, the imaginary time step must be

$$\tau < \frac{2}{E_{\max} + E_0 - 2\tilde{E}}, \tag{1.2.12}$$

where $E_{\max}$ is the maximum energy of the system. Because of (1.2.11), this method is also called the *power projection method* [115–118].

To be able to treat (1.2.9) as defining a random walk in configuration space, so that it can be solved iteratively by Monte Carlo means, the ground-state wave function must be nodeless, in order that the Green function $G(\mathbf{r}, \mathbf{r}') \geq 0$ for all $\mathbf{r}$ and $\mathbf{r}'$. For bosons, this condition is satisfied, and the GFMC can be considered an exact numerical technique for computing various ground-state properties, since the only errors involved are statistical in nature, and therefore controllable by proper sampling. For fermions, on the other hand, the ground-state wave function vanishes on various nodal surfaces in configuration space. Thus the Green function $G(\mathbf{r}, \mathbf{r}')$ is not positive-definite, and cannot be directly interpreted as a transition probability.

This problem can be circumvented, if the hypothetical random walk (later GFMC simulations do not really maintain a population of random walkers) can be restricted to a region of configuration space for which $G(\mathbf{r}, \mathbf{r}')$ is positive, i.e. one of the configuration-space regions bounded by the nodal surfaces. For the purpose of calculating translationally-invariant local observables, for example the ground-state energy, having the ground-state wave function within such a region of configuration space is just as good as having the ground-state wave function over the entire configuration space. However, apart from problems with high symmetry, or few particles, these nodal surfaces are not known *a priori*. The possibility of working with a node-restricted region of configuration space was first suggested by Anderson in 1975 [79]. Klein and Pickett followed up on this suggestion in 1976, and even discussed the possibility of determining such surfaces *a posteriori*, but did not carry the program through [112]. So it was up to Ceperley and Alder in 1980 to first introduce the so called *fixed-node approximation* of GFMC [119] and apply it to a system of interacting fermions.

In the fixed-node GFMC method, a set of nodes is first imposed on the trial wave function. An effective imaginary-time evolution operator which fixes these nodes is then

constructed, and applied iteratively to the trial wave function. This is equivalent to seeking the ground-state wave function within a prescribed region where the ground-state wave function does not change sign. For an arbitrarily chosen set of nodes, the minimum energy eigenvalue so calculated will of course be higher than the true ground-state energy. Therefore, in the next, and most crucial *nodal relaxation* step of the method, the positions of the nodes are relaxed variationally until the calculated minimum energy eigenvalue takes on the lowest-possible value. However, this method involves Monte Carlo simulations (to sample the many-body wave function and construct the imaginary-time evolution operator) built upon Monte Carlo simulations (to variationally relax the nodes onto its ground-state nodal structure), and is very much more computationally expensive than an equivalent boson GFMC simulation. More importantly, the method calculates only an approximate ground-state wave function, since it uses an approximate fixed-node Green function $\exp(-\tau H_{\mathrm{FN}})$ instead of the exact imaginary-time Green function $\exp(-\tau H)$ to filter out the ground state from the best variational guess $|\tilde{\Psi}\rangle$. The effective fixed-node Hamiltonian H_{FN} depends on the trial wave function, and thus the fixed-node approximation becomes exact if the trial wave function chosen is the exact ground-state wave function.

For quantum lattices, the zero-temperature GFMC method was successfully applied to the two-dimensional antiferromagnetic Heisenberg model by Trivedi and Ceperley [111, 120]. For finite-temperature GFMC simulations on one-dimensional lattices, the Suzuki-Trotter decomposition formula is first used to map the one-dimensional quantum problem to a two-dimensional classical statistical mechanics problem. The second dimension in the classical problem is inverse temperature [121, 122]. This manner of QMC simulation was first done by Barker [123], not on a lattice, followed by Hirsch *et al* [124–126], on a lattice for the one-dimensional Hubbard model, and then

by Barnes *et al* [127] and Carlson [128] for the Heisenberg antiferromagnet. Through the use of various interpolation schemes, the fixed-node GFMC was extended to lattice fermions [114, 129, 130]. A recent review of GFMC for lattice fermions can be found in Ref. 131.

1.2.2.5 Path-Integral Monte Carlo

The PIMC method was first suggested by Brush in 1961, before it could be feasibly done on a computer [96]. The method, first implemented computationally in the early 1980s [132–134], is widely used by the quantum chemists for electronic structure calculations, and judging from the burgeoning citations, rapidly gained popularity within the QMC community in physics at the turn of the century.

In this finite-temperature method, we start out with the canonical density matrix

$$\rho(\mathbf{r}, \mathbf{r}'; \beta) = \sum_{\alpha} e^{-\beta E_\alpha} \phi_\alpha^*(\mathbf{r}) \phi_\alpha(\mathbf{r}'), \tag{1.2.13}$$

which is the sum of the energy eigenfunctions of the Hamiltonian, weighted by the Boltzmann factor. This density matrix satisfies the convolution identity,

$$\rho(\mathbf{r}, \mathbf{r}'; \beta) = \int \cdots \int d\mathbf{r}_1 \cdots d\mathbf{r}_{M-1}\, \rho(\mathbf{r}, \mathbf{r}_1; \tau) \cdots \rho(\mathbf{r}_{M-1}, \mathbf{r}'; \tau), \tag{1.2.14}$$

obtained from the Suzuki-Trotter decomposition formula [121, 122], where $\beta = 1/k_B T$ is the inverse temperature, and $\tau = \beta/M$ is the imaginary time step. As M is increased and τ approaches zero (the high-temperature limit), one can write down the semiclassical form

$$\rho(\mathbf{r}, \mathbf{r}'; \tau) = (4\pi\lambda\tau)^{-3N/2} \exp\left[-\frac{(\mathbf{r} - \mathbf{r}')^2}{4\lambda\tau} - \tau V(\mathbf{r}) \right], \tag{1.2.15}$$

for the high-temperature canonical density matrix, where $\lambda = \hbar^2/2m$. More accurate approximations for the high-temperature canonical density matrix $\rho(\mathbf{r}, \mathbf{r}', \tau)$ can also be

used. Substituting (1.2.15) into (1.2.14) reduces the problem of calculating the finite-temperature canonical density matrix $\rho(\mathbf{r}, \mathbf{r}'; \beta)$ into a problem of high-dimensional integration, which is ideally suited to the Monte Carlo technique.

In the high-dimensional Monte Carlo integration, sampling the intermediate configurations $\mathbf{r}_1, \ldots, \mathbf{r}_{M-1}$ is equivalent to sampling a path in configuration space. As such, this method is well suited to study quantum tunneling [135–141]. Depending on the potential $V(\mathbf{r})$ experienced by the quantum-mechanical particles, the sampled paths may also have more 'curvature' at some regions of configuration space, and less 'curvature' in other regions. This allows for multigrid adaptations to be carried out [142], where the intermediate configurations are not sampled uniformly, but adaptively. Despite these strengths, the PIMC method, which is reviewed in Ref. 143, also suffers from the 'minus sign' problem.

1.2.2.6 The 'Minus Sign' Problem

The origin of the 'minus sign' problem is Pauli's Exclusion Principle, which requires a change of sign upon interchange of fermions. As a result, when the ground-state energy or partition function of a Fermi system is calculated using GFMC or PIMC, one obtains contributions of different signs which tend to cancel. The 'minus sign' problem refers to the problem of subtracting large negative contributions from large positive contributions to the wave function, giving rise to a statistical average that is exponentially smaller than its statistical variance. This makes it generically difficult to obtain statistically accurate results for a many-fermion problem, except in one dimension [144], or when the fermion problem can be mapped to a boson problem [145, 146].

In one-dimensional fermion problems subject to fixed boundary conditions, Assaad *et al* observed that the 'minus sign' problem does not arise, even though fermion ex-

changes take place in the Monte Carlo sampling process [144]. When periodic boundary conditions are imposed, a factor of $(-1)^{P-1}$, where P is the total number of fermions in the simulation, is incurred whenever a Monte-Carlo-sampled fermionic world line crosses the boundary. For large systems, these boundary-crossing world lines occurs only rarely. Therefore, QMC practitioners simply ignore all histories of the whole system in which any world line has a net (signed) number of boundary crossings that is nonzero. This is known in the literature as the *zero-winding boundary conditions*. The results obtained with zero-winding boundary conditions are always approximate, but the accuracy improves with increasing system size, because the number of boundary-crossing paths decreases relative to the number of non-boundary-crossing paths with increasing system size.

For higher-dimensional many-fermion problems, approximations have to be introduced to circumvent the 'minus sign' problem. Various schemes have been proposed to control the 'minus sign' problem, the earliest being writing the non-positive-definite Green function as the difference between two positive-definite functions, each of which can treated as transition probabilities [147–149]. However, these two positive-definite functions do not evolve independently in imaginary time. GFMC practioners found that this interdependent time evolution of the two positive-definition functions makes the scheme computationally inefficient. Another scheme involves performing a Hubbard-Stratonovich transformation on the grand-canonical density matrix, and then integrating out the fermionic degrees of freedom to leave a bosonic PIMC problem in Slater-determinant space [150, 151]. However, this procedure introduces a determinant which is a sum of large positive and negative terms. The 'minus sign' problem therefore appears in a different guise in this scheme, and was not eliminated.

More recently, Sorella *et al* proposed a stochastic reconfiguration approach to con-

trolling the 'minus sign' problem in the GFMC [152, 153]. The key insight behind this scheme is that for GFMC simulations plagued by the 'minus sign' problem, the average sign $\langle s \rangle$ of the sampled configurations goes to zero exponentially in the number of iterations. When this happens, the iterated wave function stop converging towards the ground-state wave function after a small number of iterations. In the stochastic reconfiguration scheme, the sampled configurations are re-weighted to favor those configurations making positive contributions to the Green function. The average sign $\langle s \rangle$ now converges exponentially to a non-zero value, leaving the iterated wave function to continue converging towards the ground-state wave function with every new iteration.

At around the same time that the stochastic reconfiguration was proposed, Mak *et al* proposed a multilevel blocking algorithm to remedy the 'minus sign' problem in PIMC [154–157]. This has the same flavor as writing the Green function as the difference between two positive-definite functions, but executed with greater sophistication. The idea behind the scheme is to first cut up the imaginary time β into a small number of m time slices. The 'minus sign' problem is kept in check, because there are few fermion exchanges in the 'paths' $\{\mathbf{r}_1, \ldots, \mathbf{r}_{m-1}\}$ sampled and statistically averaged at this coarse level. The time slicing is then refined to include time slices between the coarse time slices. 'Paths' are then sampled and statistically averaged at this finer level, *using* information already available from the coarse time statistical average, so that we need to deal only with fermion exchanges occurring at the refined time slices. This process of making the imaginary-time slices finer and finer can be iterated, so that the overall 'minus sign' problem is handled one bite-sized chunk at a time.

While both recent schemes look promising, it is still too early to say whether they have solved the 'minus sign' problem once and for all. Of the two, the stochastic reconfiguration scheme has generated more interest, because it is very easy to imple-

ment (especially if one already has a GFMC code at hand), and runs just as quickly as the GFMC. However, apart from numerical examples of the scheme having found the 'correct' ground state, there is no deeper theoretical insight into how and why the reweighting works, or whether it might introduce other systematic errors. The multilevel blocking scheme, having a renormalization-group flavor, takes more human time to implement, and, because of the multiple level Monte Carlo simulations, is likely to take more computer time to run as well.

1.2.3 The ALPS Project

Exact numerical methods for solving quantum many-body problems came of age with the launch of the Algorithms and Libraries for Physics Simulations (ALPS) open source project [158,159] in March 2004. Apart from providing high-level simulation codes and C++ libraries for exact/Lanczos diagonalization and Quantum Monte Carlo, the ALPS collaboration is also working to add DMRG to the numerical suite targetted at studying strongly-correlated quantum systems. This is a far cry from the early days of exact numerical studies, where each research group maintains customized code bases where every little thing is done differently, and a new group hoping to break into the field faces the prospect of one to two years of unproductive coding before it can even attempt to look into any interesting physics.

The ALPS project gives established and new groups access to a common code base, with the hope that the free licensing scheme would:

1. encourage community-wide adoption in workhorse-type applications that would serve to:

   (a) produce refinements to the core algorithms to make them increasingly effi-

cient; and

(b) generate intense scrutiny on the correctness of the code, so that bugs get weeded out in a short amount of time.

2. encourages users to extend the code base that is already actively maintained by the ALPS collaboration.

To help popularize the project, the ALPS webpage at `http://alps.comp-phys.org` provides a series of easy-to-follow tutorials on how to write XML job and task files, which the ALPS scheduler system can pick up to start the actual simulations. The ALPS collaboration also organize user workshops to ease the transition into using the code base. Most importantly, Grzegorz Pawlowski made available in November 2004 a special "live-CD" Linux distribution with ALPS pre-installed. Called the cdALPS, this is a modified ClusterKnoppix distribution that is ready to use on clusters and single workstations.

1.3 Quantum Renormalization Group Methods

In this section, I will review the historical developments and modern advances in attempt to formulate quantum renormalization-group (QRG) methods for solving quantum many-body problems. Many books and reviews are available for the highly-successful DMRG and derivative methods, so I will refer the readers to these [160–166], and give a brief review on renormalization-group methods other than the DMRG, which I roughly classify into (i) block-spin type QRG; and (ii) QRG with no blocking scheme. These will be reviewed in Sections 1.3.1 and 1.3.2 respectively.

1.3.1 Block-Spin Type QRG

Block-spin type QRG are renormalization-group schemes modeled after Kadanoff's block-spin transformation in classical statistical mechanics, whereby a large system is cut up into small blocks, within which a fraction of the degrees of freedom are integrated out. The 'coarse-grained' blocks then play the role of atomic sites in the system, and are again grouped into blocks to iterate the process of state reduction. The earliest attempt at formulating a block-spin type QRG was by Drell *et al* in 1977 [167], where they applied the block-spin QRG transformation on a chain of harmonic oscillators with nearest-neighbor coupling and also to the Ising model in a transverse field. This was followed by Fields *et al*, who did a block-spin type QRG study on the spin-$\frac{1}{2}$ antiferromagnetic Heisenberg model in one dimension [168, 169], and Hirsch, who did a block-spin type QRG study on the Hubbard model in one, two, and three dimensions [170]. The results from these early studies indicate that, while it is possible to devise block-spin type QRG schemes that are accurate in one dimension (see also Refs. 171 and 172, who generalize Fields *et al*'s work to antiferromagnetic Heisenberg chains with higher spins), such schemes do not work well in higher dimensions (see also Refs. 173, 174, and 175).

The real-space QRG that we are have in mind, the *raison d'etre* for the work presented in Chapters 2, 3 and 4, is closest in spirit to that proposed by Klein *et al* [6, 7], and Malrieu and Guihéry [8]. In these works, the ground-state wave function, along with a sufficiently large set of low-lying energy eigenstates, of a finite system of N sites are obtained through ED. This finite system is then divided into N/N_C identical clusters, each containing N_C sites, which will play the role of *supersites* in the next RG iteration. In Malrieu and Guihéry's approach, we find that though they do not explicitly mention calculating the density matrix of the N_C-site cluster, this is effectively done when they computed the *overlap matrix*. The overlap matrix measures not only the overlap

between direct products of cluster states and the system ground state, but also between direct products of cluster states and the low-lying system excited states. The eigenvalues of the overlap matrix are then used to determine how closely the system Hilbert space can be written as a direct product of cluster Hilbert spaces, and guide the construct of the system Hamiltonian in the next RG step.

Recently, Degenhard proposed a more abstract approach to block-spin type QRG transformation [12]. He noted that the chief problem with block-spin type QRG transformation is that it is in general not possible to construct a truncated Hamiltonian (or any observable, for that matter) — from the truncated Hamiltonian within each block — which reproduces accurately the low-energy spectrum of the full Hamiltonian. To get around this problem, Degenhard proposes a solution in the spirit of supersymmetric techniques in condensed matter physics, i.e. to augment the original Hilbert space $\mathcal{H}$ by an *auxiliary space* $\mathcal{H}'$ to give the *superspace* $\mathcal{H}'' = \mathcal{H} \otimes \mathcal{H}'$. With the choice of an appropriate auxiliary space, one would *first* perform block truncation of the superspace observables, and *then* integrate out the auxiliary variables to get the accurate truncated physical observables. In this way, the interblock correlations captured by the auxiliary variables are built into the block-truncated observables. Unfortunately, Degenhard gave no prescription on how one goes about finding such an auxiliary space, and how one would integrate out the auxiliary variables, so the proposed technology remains a *gedanken* one.

1.3.2 QRG With No Blocking Scheme

The failure of all real-space QRG based on blocking schemes has been consensually blamed on long-range correlations in the strongly-correlated systems on which they have been applied. However, going to momentum-space to deal with the long-range corre-

lations is not a solution, because a momentum-space QRG scheme will likely miss the short-range correlations which carry much of the important physics, just as real-space QRG schemes miss the physics of long-range correlations. This 'damned-if-you-do-and-damned-if-you-don't' situation led Monthoux and Manousakis to devise a QRG scheme that does not involve blocking in real space [10]. In this QRG scheme, Monthoux and Manousakis first treat the short-range correlations by considering a finite system of N sites in real space. The Hamiltonian H of this finite system is then written as the sum of a mean-field part H_0, whose eigenvalue problem is solved (or easy to solve), and a quantum-fluctuation part $H_1 = H - H_0$, which correlates the states of H_0. The full Hamiltonian H is then diagonalized using an adaptively selected truncated basis of D_0^* eigenstates (out of a total of $D_0 \gg D_0^*$ eigenstates) of H_0, while the contributions of the $D_0 - D_0^*$ eigenstates not included in the truncated basis are treated perturbatively. This truncated basis, which is perturbatively optimized with respect to the ground state of H within the finite system, is then used to exactly diagonalize H to obtain a set of n lowest-lying excited states $\{|\Phi_i\rangle\}_{i=1}^n$.

In the second stage of their QRG scheme, a small set of m momentum-space observables $\{O_j(\mathbf{q})\}_{j=1}^m$ known to produce long-range correlations is chosen. A variational calculation is then carried out in the space spanned by

$$\{|\Phi_i\rangle\}_{i=1}^n, \quad \{O_1(\mathbf{q})\,|\Phi_i\rangle\}_{i=1}^n, \quad \ldots, \quad \{O_m(\mathbf{q})\,|\Phi_i\rangle\}_{i=1}^n, \tag{1.3.1}$$

for all wave vectors $\mathbf{q}$ in the FBZ. The motivation behind the design of this second step of Monthoux and Manousakis's QRG scheme is not explained, apart from the fact that it seemed like a reasonable thing to do. In fact, for the spin-$\frac{1}{2}$ antiferromagnetic Heisenberg chain on which the QRG scheme was tested, the two-stage algorithm performs poorly. Monthoux and Manousakis argued that the QRG scheme will fare better when applied to higher-dimensional systems, since quantum fluctuations are not as strong in

higher dimensions.

1.4 Road Map to Chapters and Results

In this section, we will provide an overview of the conceptual organization of the thesis in Section 1.4.1. We will then highlight the most important results in each of the main chapters in Sections 1.4.2 to 1.4.8. To help readers navigate quickly to where these important results occur in the main chapters, the equations in Sections 1.4.2 to 1.4.8 are duplicates of the same equations in the main chapters, bearing the equation number given them in the main chapters. Readers are warned here that, because the flow of our highlights of the main results are not necessarily the same as the flow of our presentation of these results in the main chapters, the equation numbering will be out of order in Sections 1.4.2 to 1.4.8. Finally, in Section 1.4.9, we give an overall summary of the appendices in this thesis.

1.4.1 Overview of the Chapters

Conceptually, the work that I have done for my thesis can be most conveniently divided into three major parts: (i) reduced density matrices of noninteracting spinless fermions (exclusively in Chapters 2 and 3, but calculations on noninteracting systems can also be found in Chapters 4, 5 and 6); (ii) reduced density matrices of interacting spinless fermions (the subject of detailed numerical study in Chapter 4, but also calculated numerically in Chapter 8); and (iii) the use of the correlation density matrix as a diagnostic tool (investigated in Chapter 8, with preparatory materials presented in Chapters 5, 6 and 7). Although the chief goal of my thesis research is to understand the behaviour of a system of strongly-interacting fermions through the use of the density matrix, a signifi-

cant fraction of my effort has been invested in elucidating the structure of the many-body density matrix (as opposed to the one-particle and two-particle density matrices that is more commonly found in the literature) of a system of noninteracting spinless fermions. This has proven instrumental in guiding our subsequent study of the structure of the many-body density matrix of a system of interacting spinless fermions. Analytical and numerical tools developed while studying noninteracting systems also turned out to be immensely helpful when we are figuring out how to best use the correlation density matrix as a diagnostic tool, and how we can extract the maximum amount of information from this beast.

The schematic diagram in Figure 1.1 shows the various chapters and their main results, as well as how subsequent chapters depend on the main results of earlier chapters. This can be used as a road map to navigate through this lengthy tome. Chapter 2, the first material chapter in this thesis, forms the basis to the remaining chapters. Two key ingredients are found in this chapter. The first is an exact formula, relating the cluster density matrix to the cluster Green-function matrix, used in Chapter 3 to study the scaling properties of the density-matrix spectrum of a one-dimensional chain. The structure of the cluster density matrix in the exact formula also forms the basis for a statistical mechanics analogy we put forth in Chapter 3, based on which we devise an operator-based truncation scheme. This exact formula is also used in Chapter 4 to calculate the density-matrix spectra of noninteracting spinless fermions in finite two-dimensional systems, and again in Chapter 5 to calculate the cluster and supercluster density-matrix eigenvalues. The second key ingredient is the formalism of referencing operators, which is used in Chapters 2 and 5 to calculate the cluster and correlation density matrices explicitly. In Chapter 6, this referencing operator formalism is put to good use when I describe the operator singular value decomposition. There is no real need to read this chapter, once

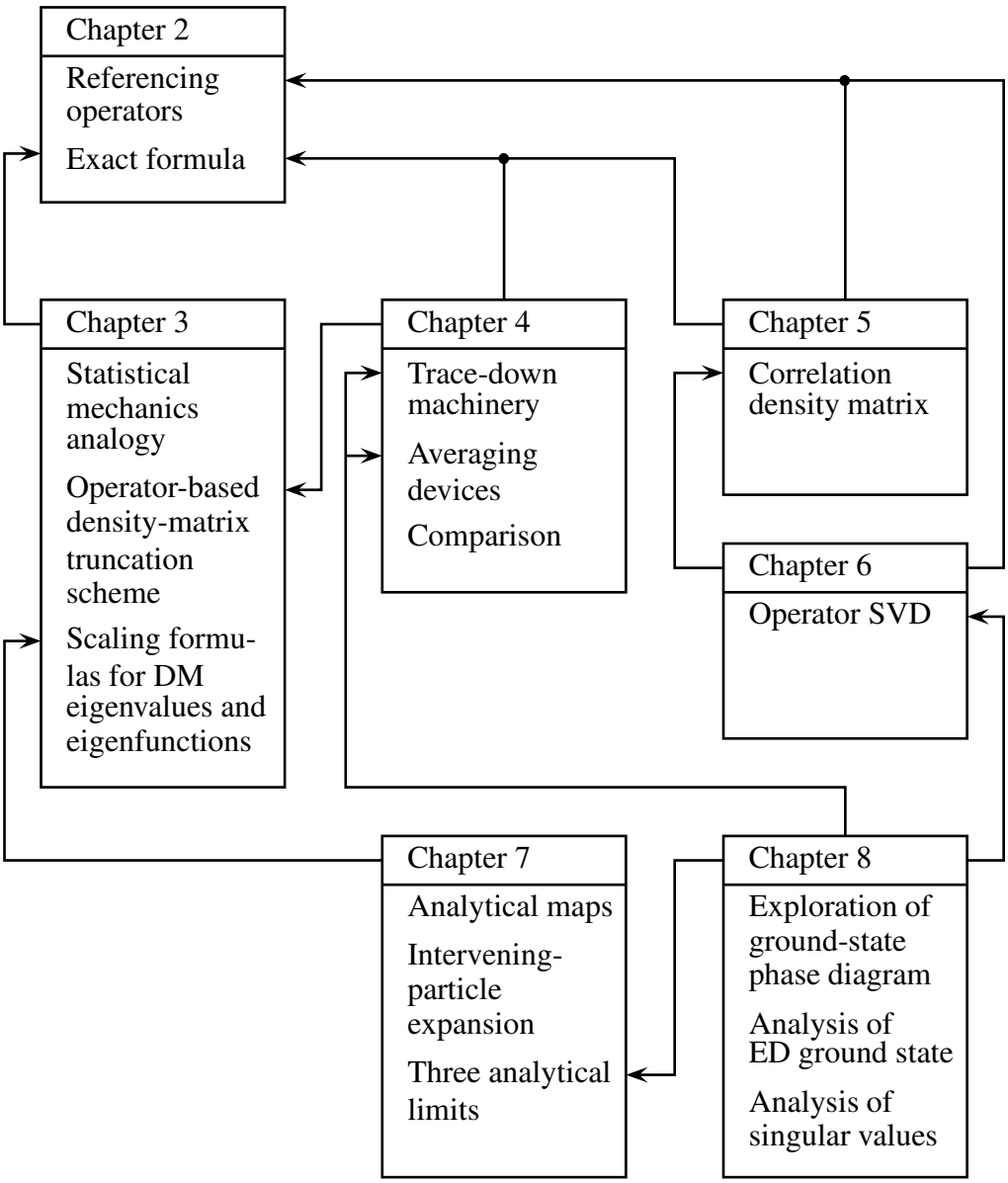

Figure 1.1: Schematic diagram showing the main results (boxed) in each chapter of the thesis. The arrows in the diagram point from a latter chapter to specific result(s) in previous chapter(s), that the latter chapter depends upon. The columns corresponds to the rough division of the work done in this thesis into studies of (i) reduced density matrices of noninteracting spinless fermions (left), (ii) reduced density matrices of interacting spinless fermions (middle), and (iii) use of the correlation density matrix as a diagnostic tool (right).

the reader knows where to find the exact formula, and which section to refer to for the formalism of referencing operators.

The main results contained in Chapter 3 are the statistical mechanics analogy relating the density-matrix eigenstates and eigenvalues to the many-body energy eigenstates and eigenvalues of a system of noninteracting spinless fermions, as suggested by the exact formula of Chapter 2, as well as the operator-based density-matrix truncation scheme developed based on this analogy. Part of the motivation behind comparing the cluster density-matrix spectra for noninteracting and strongly-interacting spinless fermions in Chapter 4 is to test this truncation scheme. Otherwise, the scaling formulas for the cluster density-matrix eigenvalues and eigenfunctions, which are numerical results supplementary to the operator-based density-matrix truncation scheme in the remainder of Chapter 3 form a fascinating little story. This part of Chapter 3 can be read as a standalone part of the thesis, since subsequent chapters do not depend critically on it (apart from the use of scaling formulas for the distribution of single-particle pseudo-energies in two parts of Chapter 7).

Chapter 4 represents a major shift in gear — not only are we moving on to study interacting systems, we also developed a large Octave code base to handle exact diagonalization and the trace-down calculation of cluster density matrices, as well as to implement various averaging devices. As a chapter, this is heavy reading, although the results reported herein are not that exciting. Readers intending to proceed further to later chapters should focus on getting through Section 4.3, where the trace-down machinery is formulated, and Section 4.6.3, where we discuss the performance of twist boundary conditions averaging in obtaining good approximations to the infinite-system cluster density-matrix spectrum. Both sections are pertinent to Chapter 8.

Chapter 5, 6, 7 and 8 represent yet another major shift in my thesis research direction.

Instead of aiming towards the development of truncation schemes for renormalization-group methods, we are now interested in using the cluster density matrix as a systematic and unbiased diagnostic tool to discover important correlations in a numerical ground-state wave function. Chapter 5, where we define the correlation density matrix, and Chapter 6, where we develop an operator singular value decomposition, constitute preparatory materials for Chapter 8, where we numerically singular value decompose the correlation density matrix for the extended Hubbard ladder of spinless fermions with correlated hops, and analyze the behaviours of the singular values and eigen-operators obtained. Readers are encouraged to skip to Chapter 7, once they have gone through the materials in Sections 5.2, 6.2 and 6.3.

In the largely independent (depending only on two small results in Chapter 3), and forbiddingly lengthy (248 pages!) Chapter 7, we developed a novel set of analytical tools that allows us to write down the ground-state wave function of the extended Hubbard ladder of spinless fermions with correlated hops, described by the Hamiltonian (7.3.2), and also calculate various ground-state correlations, in three very special limiting cases. Readers who are numerically inclined, and whose chief interest lies in getting to Chapter 8, will only need to know which points in Chapter 7 to find the analytical results that are used to guide our analysis of the singular values and eigen-operators coming out from the numerical operator singular value decomposition of the correlation density matrix. Readers who are analytically inclined, especially those who are condensed matter theorists in the field of Luttinger-liquid physics, might find the analytical results obtained in these three limiting cases, along with the analytical tools developed to arrive at them, an interesting standalone chapter to read.

Finally, in Chapter 8, the numerical machinery of operator singular value decomposition of the correlation density matrix is put to the test, and used to explore the ground-

state phase diagram of the extended Hubbard ladder of spinless fermions with correlated hops. For the purpose of making comparisons, we analyzed in Section 8.3 the structure of the ED ground state by looking out for qualitative features, in the many-body twisted energy band structure, as well as in the distribution of ground-state amplitudes. Readers can skip this lengthy section, and proceed directly to Section 8.4, where we operator singular value decompose the correlation density matrix of two (2×2) clusters within a two-legged ladder of length $L = 8$, and based on our analyses of the singular values and eigen-operators, mapped out the dominant quantum phase at various parameter points on the ground-state phase diagram.

1.4.2 Highlights of Chapter 2

In Chapter 2, we calculate the density matrix of a cluster of N_C sites cut out from a d-dimensional system of noninteracting spinless fermions, described by the nearest-neighbor hopping Hamiltonian

$$H_t = -t \sum_{\langle \mathbf{r},\mathbf{r}' \rangle} \left[c^\dagger_{\mathbf{r}} c_{\mathbf{r}'} + c^\dagger_{\mathbf{r}'} c_{\mathbf{r}} \right]. \tag{2.1.1}$$

We chose a trivial model as our starting point for two reasons. First, we have the benefit of being guided at every step of the way, by the facts that we know what the ground state looks like at *every* filling fraction $\bar{n}$, and we are able to calculate *all* ground-state correlations. Surprisingly, apart from the partial result obtained by Chung and Peschel in Ref. 176, no one has ever written down a formula for the cluster density matrix in such a system, even though everyone expected it to have a simple structure. Secondly, a renormalization-group method that is expected to discover that a strongly-interacting system is ultimately a Fermi liquid, must first be able to pass the test on a noninteracting Fermi liquid. We argue that to devise a density-matrix-based truncation scheme that gets

the Fermi liquid physics right, it is necessary to have a thorough understanding on the structure of the noninteracting cluster density matrix.

Prior to discovering the paper by Chung and Peschel, and adapting their method to noninteracting spinless fermions, we were developing an alternative formulation for the calculation of cluster density-matrix elements. Working in the many-body cluster occupation-number basis $\{|\mathbf{l}\rangle = |n_{l_1} n_{l_2} \cdots n_{l_{N_C}}\rangle\}$, where $l_1, l_2, \ldots, l_{N_C}$ are the N_C sites of the cluster, and $n_{l_1}, n_{l_2}, \ldots, n_{l_{P_C}}$ are their occupation numbers, we introduce a set of *referencing operators*

$$K_{\mathbf{l}} = \prod_{i=1}^{N_C} \left[n_{l_i} c_{l_i} + (1 - n_{l_i}) c_{l_i} c_{l_i}^\dagger \right], \tag{2.3.5}$$

such that

$$K_{\mathbf{l}} \, |\mathbf{l}'\rangle = \delta_{\mathbf{l},\mathbf{l}'} \, |0\rangle_C \,, \tag{2.3.6}$$

where $|0\rangle_C$ is the *reference state*, whereby the cluster is completely unoccupied. In terms of these referencing operators, we find that the cluster density-matrix elements can be written as

$$\langle \mathbf{l} | \rho_C | \mathbf{l}' \rangle = \langle \Psi | K_{\mathbf{l}}^\dagger K_{\mathbf{l}'} | \Psi \rangle \,, \tag{2.3.8}$$

where $|\Psi\rangle$ is the ground-state wave function. Early numerical experiments on small clusters in a one-dimensional system hinted at further structure in the density-matrix eigenvalues and eigenstates, that led us to conjecture (2.4.31). Beyond this first foray into the world of referencing operators, this formalism is not used again, until we rediscover its value in Chapter 6.

The above conjecture made us relook at the paper by Chung and Peschel [176], where they describe a partial trace technology based on fermionic coherent states. A fermionic coherent state

$$|\boldsymbol{\xi}\rangle = |\xi_1 \xi_2 \cdots \xi_N\rangle = \exp\left(- \textstyle\sum_{i=1}^N \xi_i c_i^\dagger \right) |0\rangle \tag{2.4.10}$$

is a wave packets defined in terms of anticommuting Grassmann variables $\xi_i\xi_j = -\xi_j\xi_i$, such that the combination $\xi_i c_i$ commutes with all other combinations $\xi_j c_j$. The matrix elements

$$\langle \boldsymbol{\xi}\boldsymbol{\eta}|\rho|\boldsymbol{\xi}'\boldsymbol{\eta}'\rangle = \mathscr{Q}^{-1} \exp\left[\begin{pmatrix}\boldsymbol{\xi}^* & \boldsymbol{\eta}^*\end{pmatrix} e^{\Gamma} \begin{pmatrix}\boldsymbol{\xi}' \\ \boldsymbol{\eta}'\end{pmatrix}\right] \tag{2.4.15}$$

of the grand-canonical density matrix

$$\begin{aligned} \rho &= \mathscr{Q}^{-1} \exp[-\beta(H-\mu F)] \\ &= \mathscr{Q}^{-1} \exp\left(\textstyle\sum_{i,j} \Gamma_{ij} c_i^\dagger c_j\right) \\ &= \mathscr{Q}^{-1} \exp\left(\textstyle\sum_k \tilde{\Gamma}_{kk} \tilde{c}_k^\dagger \tilde{c}_k\right) \end{aligned} \tag{2.4.1) \& (2.4.3}$$

are then calculated in the over-complete basis $\{|\boldsymbol{\xi}\boldsymbol{\eta}\rangle\}$. Here $\mathscr{Q}$, β and μ have their usual meanings, $F = \sum_i c_i^\dagger c_i = \sum_k \tilde{c}_k^\dagger \tilde{c}_k$ is the total number operator, while $\boldsymbol{\xi}$ and $\boldsymbol{\eta}$ are Grassmann variables corresponding to cluster and environment degrees of freedom respectively.

We then trace over environment degrees of freedom by performing simple Gaussian integrals over the environment Grassmann variables, perform block matrix computations in both real space and momentum space, and using the block matrix inversion formulas found in Appendix B to obtain the cluster density-matrix elements

$$\langle \boldsymbol{\xi}|\rho_C|\boldsymbol{\xi}'\rangle = \det(\mathbb{1} - G_C) \exp\left[\boldsymbol{\xi}^* G_C (\mathbb{1} - G_C)^{-1} \boldsymbol{\xi}'\right], \tag{2.4.29}$$

which can then be inverted to give the exact formula

$$\rho_C = \det(\mathbb{1} - G_C) \exp\left\{\sum_{ij} \left[\log G_C (\mathbb{1} - G_C)^{-1}\right]_{ij} c_i^\dagger c_j\right\} \tag{2.4.30}$$

relating the cluster density matrix ρ_C to the cluster Green-function matrix G_C.

The main point of (2.4.30), which is easy to generalize to spinfull fermions, is that the cluster density matrix ρ_C and the cluster Green-function matrix G_C are simultane-

ously diagonalizable. Thus, if $|\lambda_l\rangle = f_l^\dagger |0\rangle$ are the eigenstates of G_C with eigenvalues λ_l, where f_l are fermion operators satisfying the usual anticommutation relations $\{f_l, f_l^\dagger\} = \mathbb{1}$, then ρ_C can be written as

$$\rho_C = \left[\prod_l (1 - \lambda_l)\right] \exp\left\{-\varphi_l f_l^\dagger f_l\right\}. \tag{2.4.31}$$

If we call

$$\tilde{H} = \varphi_l f_l^\dagger f_l \tag{2.5.2}$$

the pseudo-Hamiltonian, and identify

$$\varphi_l = -\log \frac{\lambda_l}{1 - \lambda_l} \tag{2.5.3}$$

to be the single-particle pseudo-energy, the cluster density matrix can be written in the statistical-mechanical form

$$\rho_C = \mathcal{Q}^{-1} \exp\left[-\tilde{H}\right], \tag{2.5.1}$$

where the reciprocal of the normalization constant

$$\mathcal{Q} = \left[\prod_l (1 - \lambda_l)\right]^{-1} \tag{1.4.1}$$

can be thought of as the grand-canonical partition function.

1.4.3 Highlights of Chapter 3

In Chapter 3, we elaborated further on the statistical mechanics analogy implied by (2.5.1), identifying in Section 3.3.1 the one-to-one correspondence between the many-particle cluster density-matrix eigenstates

$$|w_L\rangle = \prod_{l \text{ occupied}} f_l^\dagger |0\rangle, \tag{3.3.1}$$

and eigenvalues

$$w_L = \mathcal{Q}^{-1} \exp\left[-\sum_{l=1}^{N_C} n_l \varphi_l\right], \tag{3.3.2}$$

where n_l is the pseudo-occupation number, and the many-particle energy eigenstate and Boltzmann weights of a system of noninteracting spinless fermions. Further more, the relation

$$\lambda_l = \frac{1}{\exp \varphi_l + 1} = \langle n_l \rangle \tag{3.3.7}$$

tells us that the eigenvalue λ_l of the cluster Green-function matrix G_C plays the role of the average pseudo-occupation number of the single-particle pseudo-energy level with pseudo-energy φ_l. We know therefore that cutting a cluster out from an infinite system produces a spectrum of eigenvalues λ_l of G_C that is smeared out compared to the zero-temperature Fermi-Dirac distribution. This is similar to the effect of finite temperature on the momentum distribution.

More importantly, this statistical mechanics analogy tells us that the cluster density-matrix eigenstate with the largest eigenvalue has the structure of a Fermi sea, in which single-particle pseudo-energy levels below the pseudo-Fermi level $\varphi_F = 0$ are filled, and those above are empty. In this picture, cluster density-matrix eigenstates with large weights then look like particle-, hole-, or particle-hole excitations about the Fermi sea ground state. Therefore, at temperatures lower than the pseudo-Fermi temperature $T_F = 1$, which is always satisfied for a cluster of any size $N_C > 1$, we know from the statistical mechanics analogy that the average pseudo-occupation number $\lambda_l = \langle n_l \rangle$ changes rapidly only in a narrow range of single-particle pseudo-energies about the pseudo-Fermi energy. This inspired us to devise an operator-based density-matrix truncation scheme in Section 3.3.3, in which we introduce a cutoff φ_*, and demand that all single-particle pseudo-energy levels with $\varphi_l < -\varphi_*$ be always occupied, and those with $\varphi_l > +\varphi_*$ be always empty. To build up a many-particle eigenstate of the cluster density matrix, we then let all of the pseudo-fermion operators f_l for $\varphi_l < -\varphi_*$, none of the pseudo-fermion operators f_l for $\varphi_l > +\varphi_*$, and some of the pseudo-fermion operators f_l

for $-\varphi_* < \varphi_l < +\varphi_*$ act on the vacuum. Exhausting all combinations of f_l for which $-\varphi_* < \varphi_l < +\varphi_*$, we then obtain a retained set of many-particle cluster density-matrix eigenstates in which the only degrees of freedom are the pseudo-energy levels within the cutoff φ_* from the pseudo-Fermi level φ_F.

Numerical studies showed that this truncation scheme has various advantages. These studies were: (i) calculations of the dispersion relation of a one-dimensional system of noninteracting spinless fermions in Sections 3.9 and 3.10, as well as (ii) scaling analysis based on the observed numerical scaling behaviour

$$\varphi(l, N_C, \bar{n}) \cong N_C f(\bar{n}, x), \tag{3.5.6}$$

where

$$x \equiv (l - l_F)/N_C, \quad l_F = \bar{n}N_C + \tfrac{1}{2}, \tag{3.5.7)\&(3.5.8}$$

is the scaling variable, and $f(\bar{n}, x)$ is the scaling function, of the single-particle pseudo-energies for cluster of different sizes N_C in Section 3.5.

1.4.4 Highlights of Chapter 4

In Chapter 4, we embark on comparative numerical studies of the cluster density matrix for spinless fermions on a two-dimensional square lattice, using the Octave code base described in Appendix C. In this chapter, we study both the noninteracting model given in (2.1.1) and the strongly-interacting model described by the Hamiltonian

$$H_{tV} = H_t + V \sum_{\langle \mathbf{r}, \mathbf{r}' \rangle} n_{\mathbf{r}} n_{\mathbf{r}'}, \tag{4.2.1}$$

in the limit of $V \to \infty$ so that there can be no nearest-neighbor occupation.

Since no exact formula for the cluster density matrix exists for the model of strongly-interacting spinless fermions given in (4.2.1), we have to resort to exactly diagonalizing

finite systems defined by the lattice vectors $\mathbf{R}_1$ and $\mathbf{R}_2$, and the periodic boundary conditions $\mathbf{r} + \mathbf{R}_1 = \mathbf{r}$ and $\mathbf{r} + \mathbf{R}_2 = \mathbf{r}$, to obtain the P-particle ground-state wave function $|\Psi\rangle$, and then proceed to trace this down to obtain the cluster density matrix. In Section 4.3, we show that it is indeed possible to give a definition for the cluster density matrix for a system of fermions that is consistent with (i) it being obtained by tracing the system density matrix $\rho = |\Psi\rangle\langle\Psi|$ over environment degrees of freedom,

$$\rho_C = \mathrm{Tr}_E\, \rho; \tag{1.4.2}$$

and (ii) it being able to reproduce the expectations of *any* observable A local to the cluster,

$$\langle\Psi|A|\Psi\rangle = \langle A\rangle = \mathrm{Tr}_C\, \rho_C A. \tag{1.4.3}$$

This is provided we define the matrix elements of ρ_C to be

$$\langle \mathbf{l}|\rho_C|\mathbf{l}'\rangle = \sum_{\mathbf{m}} \sum_{\mathbf{m}'} (-1)^{f(\mathbf{n};\mathbf{l},\mathbf{m})} (-1)^{f(\mathbf{n}';\mathbf{l}',\mathbf{m}')} \Psi_{\mathbf{l},\mathbf{m}} \Psi_{\mathbf{l}',\mathbf{m}'} \delta_{\mathbf{m},\mathbf{m}'}, \tag{4.3.39}$$

where $\mathbf{n}$, $\mathbf{n}'$ are configurations of the system, $\mathbf{l}$, $\mathbf{l}'$ are configurations of the cluster, $\mathbf{m}$, $\mathbf{m}'$ are configurations of the environment, and $(-1)^{f(\mathbf{n};\mathbf{l},\mathbf{m})}$ is the fermion sign incurred when reordering the operators associated with the system configuration $\mathbf{n}$, to one in which the operators associated with the cluster configuration $\mathbf{l}$ are all to the right of operators associated with the environment configuration $\mathbf{m}$.

Numerically exact diagonalization of small finite systems introduces finite size effects that depend on the number of sites in the system, the number of particles in the system, and the shape of the $\mathbf{R}_1 \times \mathbf{R}_2$ system. To do a meaningful comparison of the cluster density-matrix spectra of noninteracting and strongly-interacting spinless fermions on such systems, we perform, in addition to degeneracy- and orientation-averaging to restore full square lattice symmetry to the density matrix of our chosen five-site, cross-shaped cluster, twist boundary conditions averaging to reduce finite size effects in the

numerics. We tested the performance of twist boundary conditions averaging, the detailed formulation and technical aspects of which can be found in Appendix D, on finite noninteracting systems, and found that the method produces an averaged cluster density-matrix spectrum that is a good approximation to infinite-system limit. This gave us confidence in applying the method to interacting systems.

1.4.5 Highlights of Chapter 5

In the beginning of Chapter 5, we define the correlation density matrix to be

$$\rho^c = \rho^{ab} - \rho^a \otimes \rho^b, \tag{5.2.1}$$

where ρ^a and ρ^b are the cluster density matrices of the disjoint clusters a and b respectively, and ρ^{ab} is the supercluster density matrix of the supercluster ab. This is the only important ingredient in this chapter that we need for Chapter 6. The remainder of Chapter 5 are calculations of the correlation density matrix for the (1 + 1) and (2 + 2) superclusters in the one-dimensional Fermi sea, BCS and number-projected-BCS superconducting ground states. We need the matrix elements obtained from these lengthy calculations to push analytical examples of operator singular value decomposition through in Chapter 6, but otherwise the rest of Chapter 5 is not important enough to warrant careful reading. Readers interested in learning how we can use the correlation density matrix, and its operator singular value decomposition, to diagnose the important physics buried in a strongly-correlated many-body ground-state wave function should skip to Chapter 6 to pick up one final technical ingredient, followed by a cursory look at Chapter 7 (unless the reader's chief interest is in reading Chapter 7), before proceeding to Chapter 8.

1.4.6 Highlights of Chapter 6

The most significant result in Chapter 6 is the operator singular value decomposition described in Section 6.3. This is the last key technical ingredient that a reader needs to pick up before going on to Chapter 8. But in order for me to meaningfully describe the operator singular value decomposition, we must first grasp the geometrical picture presented in Section 6.2, of what happens in ordinary matrix singular value decomposition of a matrix M. If we think of the columns of M, $m_1, \ldots, m_N$ as column vectors, then we realize that matrix singular value decomposition is an orthogonalization procedure similar in spirit, but not in means, to Gram-Schmidt orthonormalization.

In Gram-Schmidt orthonormalization, we force the orthogonalized vector from each stage of the iterative procedure to have unit norm, and as such, the overall procedure cannot be expressed in terms of the action of unitary matrices on M. For matrix singular value decomposition, the column vectors m_i are orthogonalized at each stage through an appropriate unitary transformation, and thus the overall orthogonalization can be effected by a unitary matrix. However, if we choose the appropriate unitary matrix V such that it acts on M from the right, the column vectors collected in the matrix MV are mutually orthogonal, but not normalized. Denoting by σ_i the vector norm of the ith column, we can also write the matrix of orthogonalized column vectors as

$$MV = U\Sigma, \tag{6.2.4}$$

where U is a matrix of orthonormalized column vectors, and Σ is a diagonal matrix of the norms of column vectors in MV. This can then be written in the usual form

$$M = U\Sigma V^\dagger \tag{6.2.2}$$

for the matrix singular value decomposition of M.

Armed with this insight, I realized that to properly define an operator version of the singular value decomposition, I needed to copy two crucial ingredients from matrix singular value decomposition: (i) that I be able to tell that two operators are 'orthogonal' to each other; and (ii) for each operator, that I be able to 'normalize' it. This requires us to choose an appropriate operator inner product. In essence, we want to be able to think of the terms in an operator expansion as our 'column vectors', and yet each term is to retain its property as a matrix acting on a Hilbert space. The appropriate inner product for two operators X and X' is thus the Frobenius inner product

$$(X, X')_F = \mathrm{Tr}\, XX'^{\dagger}, \tag{1.4.4}$$

which becomes the usual vector inner product when the $D \times D$ matrices for X and X' are unravelled into $D^2 \times 1$ column vectors. Together with the Frobenius norm

$$||X||_F = \sqrt{\mathrm{Tr}\, XX^{\dagger}}, \tag{1.4.5}$$

we are now equipped to think of operator singular value decomposition as a series of unitary transformations, acting to orthogonalize one pair of operators at a time. Unlike Gram-Schmidt orthonormalization, each of these unitary transformations tend to mess up previously orthogonalized operators, which is why singular value decomposition has to been done iteratively. This is explained in greater detail in Section 6.3.

The notion of operator singular value decomposition arises naturally when dealing with the correlation density matrix, which can be thought of as the generalized order parameter between the disjoint clusters a and b. We want to think of the correlations between a and b as coming from independent quantum fluctuations, and so it is natural to demand that the order parameter associated with each independent quantum fluctuation be in some sense 'orthogonal' to each other, so that they can be cleanly separated out in the correlation density matrix. Also, to be able to compare the strengths of quantum

fluctuations associated with two 'orthogonal' order parameters in a given ground-state wave function, we need to have the means to tell that their quantum fluctuations are of equal strength. This requirement implies a common unit strength of quantum fluctuations that we can compare against leads naturally to the notion that order parameters must be normalizable. We find that, with the choice of the Frobenius inner product, the set of products of two referencing operators (one each for the initial and final configurations) forms a good orthonormal operator basis to begin with. The correlation density matrix is expanded in terms of these as

$$\rho^c = \sum_{\mathbf{n}=\mathbf{l}\cup\mathbf{m}} \sum_{\mathbf{n}'=\mathbf{l}'\cup\mathbf{m}'} \left[(-1)^{f(\mathbf{n},\mathbf{n}')} \langle \mathbf{n}|\rho^{ab}|\mathbf{n}'\rangle - \langle \mathbf{l}|\rho^{a}|\mathbf{l}'\rangle \langle \mathbf{m}|\rho^{b}|\mathbf{m}'\rangle\right] K_{\mathbf{l}}^{\dagger} K_{\mathbf{l}'} K_{\mathbf{m}}^{\dagger} K_{\mathbf{m}'}, \tag{6.3.18}$$

where $(-1)^{f(\mathbf{n},\mathbf{n}')}$ is the fermion sign incurred when reordering the referencing operator product $K_{\mathbf{n}}^{\dagger} K_{\mathbf{n}'}$ to get $K_{\mathbf{l}}^{\dagger} K_{\mathbf{l}'} K_{\mathbf{m}}^{\dagger} K_{\mathbf{m}'}$. Ordinary matrix singular value decomposition can then be performed numerically on the matrix of coefficients

$$K_{\lambda\mu} = \left[(-1)^{f(\mathbf{n},\mathbf{n}')} \langle \mathbf{n}|\rho^{ab}|\mathbf{n}'\rangle - \langle \mathbf{l}|\rho^{a}|\mathbf{l}'\rangle \langle \mathbf{m}|\rho^{b}|\mathbf{m}'\rangle\right], \tag{6.3.23}$$

which we call the correlation K matrix, which is indexed by the fused indices $\boldsymbol{\lambda} = \mathbf{l}\mathbf{l}'$ and $\boldsymbol{\mu} = \mathbf{m}\mathbf{m}'$.

The remainder of the chapter is another collection of lengthy calculations to analytically singular value decompose the (1 + 1) and (2 + 2) correlation density matrix for the one-dimensional Fermi sea, BCS, and number-projected BCS ground states. It is not necessary to wade through all these tedious calculations to get to the physics in Chapter 8. The only extra insight gleamed from these calculations is that in the operator singular value decomposition

$$\rho_C = \sum_l \sigma_l X_l Y_l^{\dagger}, \tag{6.3.1}$$

of the cluster density matrix ρ_C, the operators X_l and Y_l are not the order parameters O^a and O^b themselves, but are instead projection-like operators which single out their

corresponding order parameters. For example, if X_l and Y_l corresponds to the order parameter O_l, then

$$\mathrm{Tr}\, X_l Y_l^\dagger O_{l'}^{a\,\dagger} O_{l'}^b = \delta_{ll'}, \tag{6.4.19}$$

and consequently, the correlation of O_l in cluster a and cluster b is simply the lth singular value, i.e.

$$\langle O_l^{a\,\dagger} O_l^b \rangle = \sigma_l. \tag{6.4.20}$$

1.4.7 Highlights of Chapter 7

Chapter 7 is a lengthy excursion away from the main numerical theme in Chapters 5, 6 and 8, which was the correlation density matrix, and its operator singular value decomposition, as a systematic and unbiased tool for discovering quantum-mechanical ground-state correlations. In this chapter, we take a closer look at the extended Hubbard ladder of spinless fermions with correlated hops, described by the Hamiltonian

$$\begin{aligned} H_{t_\parallel t_\perp t' V} = & -t_\parallel \sum_i \sum_j \left(c_{i,j}^\dagger c_{i,j+1} + c_{i,j+1}^\dagger c_{i,j} \right) - t_\perp \sum_i \sum_j \left(c_{i,j}^\dagger c_{i+1,j} + c_{i+1,j}^\dagger c_{i,j} \right) \\ & - t' \sum_i \sum_j \left(c_{i,j}^\dagger n_{i+1,j+1} c_{i,j+2} + c_{i,j+2}^\dagger n_{i+1,j+1} c_{i,j} \right) \\ & - t' \sum_i \sum_j \left(c_{i+1,j}^\dagger n_{i,j+1} c_{i+1,j+2} + c_{i+1,j+2}^\dagger n_{i,j+1} c_{i+1,j} \right) \\ & + V \sum_i \sum_j n_{i,j} n_{i,j+1} + V \sum_i \sum_j n_{i,j} n_{i+1,j}, \end{aligned} \tag{7.3.2}$$

with $V \to \infty$ nearest-neighbor repulsion, absolute amplitudes $t_\parallel$ for nearest-neighbor hops along the legs $i = 1, 2$, $t_\perp$ for hops along the rungs $j = 1, \ldots, L$, and t' for next-nearest-neighbor correlated hops along the legs, of the ladder of length L. A next-nearest-neighbor correlated hop is one in which a spinless fermion hops from site $\mathbf{r}$ to a next-nearest-neighbor site $\mathbf{r}'$, if the site $\mathbf{r}''$, which is a nearest-neighbor site to both $\mathbf{r}$ and $\mathbf{r}'$, is occupied (see Figure 7.8).

To solve for the ground-state wave functions, and calculate ground-state correlations, for this extended Hubbard ladder of spinless fermions with correlated hops in three limiting cases: (i) the weak inter-leg hopping limit, $t_\perp \ll t_\parallel$, $t' = 0$; (ii) the strong inter-leg hopping limit, $t_\perp \gg t_\parallel$, $t' = 0$; and (iii) the strong correlated hopping limit, $t' \gg t_\parallel, t_\perp$, we developed in Section 7.4 a set of novel analytical tools, consisting of three maps, the notion of corresponding observables, and a method of writing the expectation of ladder observables in terms of an expansion over conditional expectations.

The three maps are:

(a) the right-exclusion configuration-to-configuration map,

$$A^\dagger_{j_1} A^\dagger_{j_2+1} \cdots A^\dagger_{j_P+P+1} |0\rangle \mapsto a^\dagger_{j_1} a^\dagger_{j_2} \cdots a^\dagger_{j_P} |0\rangle \,, \qquad (7.4.12)\&(7.4.13)$$

with $1 \le j_1 < j_2 < \cdots < j_P \le L' = L - P$. This maps between P-particle configurations on a periodic nearest-neighbor excluded chain of length L to P-particle configurations on a periodic nearest-neighbor included chain of length $L' = L - P$, where $a_j = b_j$ and $A_j = B_j$ if we are dealing with bosons, and $a_j = c_j$ and $A_j = C_j$ if we are dealing with spinless fermions, described in Section 7.4.3;

(b) the Bloch-state-to-Bloch-state map,

$$|j_1, j_2 + 1, \ldots, j_P + P - 1; q\rangle \mapsto |j_1, j_2, \ldots, j_P; q'\rangle \,. \qquad (7.4.65)$$

Here the period-l nearest-neighbor excluded and period-l' nearest-neighbor included Bloch states are defined, in terms of the period-l nearest-neighbor excluded P-particle configuration $A^\dagger_{j_1} A^\dagger_{j_2+1} \cdots A^\dagger_{j_P+P+1} |0\rangle$, and the period-$l'$ nearest-neighbor included P-particle configuration $a^\dagger_{j_1} a^\dagger_{j_2} \cdots a^\dagger_{j_P} |0\rangle$ respectively. Also, the translation operator T_r, which shifts all particles to the right by r sites, is

$$|j_1, j_2 + 1, \ldots, j_P + P - 1; q\rangle = \frac{1}{\sqrt{l}} \sum_r e^{-\mathrm{i}\, qr}\, T_r A^\dagger_{j_1} A^\dagger_{j_2+1} \cdots A^\dagger_{j_P+P-1} |0\rangle \qquad (7.4.16)$$

and

$$|j_1, j_2, \ldots, j_P; q'\rangle = \frac{1}{\sqrt{l'}} \sum_{r'} e^{-\mathrm{i}\, q' r'}\, T_{r'} a^\dagger_{j_1} a^\dagger_{j_2} \cdots a^\dagger_{j_P} |0\rangle \tag{7.4.15}$$

respectively, described in Section 7.4.4;and

(c) the wave-vector-to-wave-vector map,

$$q = \frac{2\pi m}{L} \mapsto q' = \frac{2\pi m}{L'}, \tag{7.4.61}$$

for all integers m, described in Section 7.4.5, which tells us how the wave vector q in an energy eigenstate $|\Psi(q)\rangle$ of the nearest-neighbor excluded chain is related to the wave vector q' in an energy eigenstate $|\Psi'(q')\rangle$ of the nearest-neighbor included chain.

These three maps help us write down the ground-state wave function of strongly-interacting ladder spinless fermions with infinite nearest-neighbor repulsion in the three limiting cases, in terms of the ground-state wave function of a chain of noninteracting spinless fermions.

We then introduce in Section 7.4.6 the notion of *corresponding observables* O and O', whose matrix elements between the respective $q = 0$, period-l_1 and period-l_2 nearest-neighbor excluded, and $q' = 0$, period-l'_1 and period-l'_2 nearest-neighbor included Bloch states are such that

$$\sqrt{l_1 l_2}\, \langle i_1, i_2 + 1, \ldots, i_P + P - 1; q = 0|O|j_1 = i_1, j_2 + 1, \ldots, j_P + P - 1; q = 0\rangle = \sqrt{l'_1 l'_2}\, \langle i_1, i_2, \ldots, i_P; q' = 0|O'|j_1 = i_1, j_2, \ldots, j_P; q' = 0\rangle\,, \tag{7.4.95}$$

so that the ground-state expectations $\langle O\rangle$ and $\langle O'\rangle$ are related by

$$\langle O\rangle = \frac{\bar{N}}{\bar{n}} \langle O'\rangle\,, \tag{7.4.97}$$

where $\bar{N}$ is the filling fraction in the nearest-neighbor excluded chain, and $\bar{n}$ is the filling fraction in the nearest-neighbor included chain.

Following this, we develop in Section 7.4.7 the method of intervening-particle expansion, where for two observables O_j and O_{j+r} separated by r sites on the nearest-neighbor excluded chain, we first write down an *intervening-particle expansion*

$$\langle O_j O_{j+r} \rangle = \sum_{\{p\}} \langle O_j O_p O_{j+r} \rangle \,, \tag{7.4.106}$$

of the correlation $\langle O_j O_{j+r} \rangle$ in terms of the condition expectations $\langle O_j O_p O_{j+r} \rangle$, where O_p is a product of p particle-occupation number operators N_j and $r - p$ hole-occupation number operators $(\mathbb{1} - N_j)$, and the sum is over all possible ways to have intervening particles between O_j and O_{j+r}. Then, we write down for each nearest-neighbor excluded term $\langle O_j O_p O_{j+r} \rangle$ in the expansion (7.4.106), a corresponding nearest-neighbor-included-chain expectation $\langle O'_j O'_p O'_{j+r-p} \rangle$ which we know how to evaluate, and sum over all corresponding nearest-neighbor-included-chain expectations, to write

$$\langle O_j O_{j+r} \rangle = \frac{\bar{N}}{\bar{n}} \sum_{\{p\}} \langle O'_j O'_p O'_{j+r-p} \rangle \,, \tag{7.4.109}$$

after making use of (7.4.97).

In the remainder of this chapter, we solve for the ground-state wave function, and calculate various ground-state correlations in the three limiting cases, the main results of which are summarized in Section 7.3. In Section 7.5, we look at the limit of infinitely strong correlated hops, $t' \gg t_\parallel, t_\perp$. In Section 7.5.1, we argue that the effective degrees of freedom are tightly bound pairs with immutable flavors. These flavors are determined by the specific arrangement of the two bound-pair particles, and are conserved by correlated hops. The two degenerate ladder ground states are thus effectively that of a chain of hard-core bosons with infinite nearest-neighbor repulsion. We checked this by numerical ED in Sections 7.5.2 and 7.5.3, before describing in Section 7.5.4 the long

sequence of maps from bound pairs on a ladder of length L to nearest-neighbor excluded hard-core bosons on a chain of length L to nearest-neighbor included hard-core bosons on a chain of length $L' = L - P$ to noninteracting spinless fermions on a chain of length L', with the help of the three analytical maps developed in Section 7.4. In Section 7.5.5, we discuss the general properties of ladder correlation functions which can be written as nearest-neighbor excluded hard-core boson correlations in this strongly correlated hopping limit, before going on to calculate, with the help of the intervening-particle expansion described in Section 7.4.7, the superconducting (SC) and charge-density-wave (CDW) correlations in Sections 7.5.6 and 7.5.7 respectively. By summing over the intervening-particle expansions numerically, we find numerically that both the SC and CDW correlations decay with distance as power laws. Performing nonlinear curve fits of the numerical correlations, we find that we could extract reliable estimates of the various leading SC and CDW correlation exponents. Finally, in Section 7.5.8, we use a restricted-probability argument to show that Fermi-liquid (FL) correlations decay exponentially with distance, governed by a filling-fraction-dependent correlation length, within the quantum-mechanical ground state in this strongly correlated hopping limit. We find, as expect from making the absolute correlated hopping amplitude t' large, that SC correlations dominate at large distances.

In Section 7.6, we look at the limit of vanishing inter-leg and correlated hoppings, $t_\perp \ll t_\parallel$, $t' = 0$. We argue, in Section 7.6.1, that there will be two degenerate ground states, one symmetric with respect to reflection about the ladder axis, and the other anti-symmetric, and that successive spinless fermions must be on alternate legs of the ladder in all ground-state configurations. We call these the *staggered ground states*, and write their wave functions (7.6.3) in terms of the Fermi sea ground-state wave function (7.6.2) with the help of a *staggered map* between ladder configurations and nearest-neighbor

included chain configurations. We then calculate various ground-state correlations in Sections 7.6.2, 7.6.3, and 7.6.4. In Section 7.6.2, we find, using a restricted-probability argument of the same flavor as that used in Section 7.5.8, that the non-vanishing FL correlations decay exponentially with distance, governed by a filling-fraction-dependent correlation length.

In Sections 7.6.3 and 7.6.4, we find analytically and numerically, through the use of the intervening-particle expansion, that the CDW and SC correlations decay with distance as power laws. The intervening-particle expansions of the CDW+ and SC+ correlations, which are symmetric with respect to reflections about the ladder axis, sum directly into simple noninteracting-spinless-fermion expectations, and thus we can read off straightaway the CDW+ and SC+ correlation exponents. The intervening-particle expansions of the CDW− and SC− correlations, which are antisymmetric with respect to reflections about the ladder axis, must be summed numerically. Reliable estimates of the leading CDW− and SC− correlation exponents are then obtained by nonlinear curve fitting the numerical correlations obtained. We find in this vanishing inter-leg hopping limit that the CDW− correlation dominates at large distances.

In Section 7.7, we look at the limit of very strong inter-leg hopping, $t_\perp \gg t_\parallel$, $t' = 0$. We argue in Section 7.7.1 that in this limit, each spinless fermion spends most of its time hopping back and forth along the rung it is on, and only very rarely hops along the legs to an adjacent rung. Therefore, each spinless fermion will be in a quantum state very close to the symmetric eigenstate of one rung, and we can think of the ladder of spinless fermions in this limit as essentially a one-dimensional chain of rung-fermions with infinite nearest-neighbor repulsion. The ground state (7.7.6) of such a one-dimensional chain of nearest-neighbor excluding rung-fermions can then be written in terms of the ground state (7.7.3) of a chain of noninteracting spinless fermions,

with the help of the three analytical maps described in Section 7.4. Within this picture of strongly-interacting rung-fermions, we also explain why quarter-filling on the ladder is special, as it gives rise to a 'dynamic solid' phase, in which rung-fermions occupy either all the even rungs, or all the odd rungs, and cannot hop along the legs to adjacent rungs because of the infinite nearest-neighbor repulsion between them. For ladder filling greater than a quarter, we describe how the system will phase separate into a high-density inert solid phase, in which spinless fermions cannot hop at all, and the lower-density 'dynamic solid' phase.

In Sections 7.7.2, 7.7.3 and 7.7.4, we calculate the FL, CDW, and SC ground-state correlations in this strong inter-leg hopping limit, and find that all of them decay with distance as power laws. Summing their intervening-particle expansions numerically, we find that of the three limiting cases studied, the asymptotic behaviours of the FL, CDW, and SC correlations are the most complicated in this strong inter-leg hopping limit. Performing very careful nonlinear curve fitting of the numerical correlations, we obtain reliable leading correlation exponents for the FL, CDW, and SC correlations, to conclude that the SC correlation dominates at very large distances.

1.4.8 Highlights of Chapter 8

As we emphasized time and again, the numerical work presented in Chapter 8 is the *raison d'être* for the numerical machinery developed in Chapters 5 and 6, as well as the analytical results obtained in Chapter 7 (although the analytical tools and the results they lead to are also interesting in their own right). The goal, through calculating (from an ED ground-state wave function) the correlation density matrix of two disjoint clusters separated by various distances, and the operator singular value decomposition of this object, is to obtain at each parameter point on the ground-state phase diagram (see Fig-

ure 8.1) of the quarter-filled ladder, a systematic and unbiased list of independent order parameters and their correlations, sorted according to their types and symmetries. To check that we are getting sensible results from the machinery of operator singular value decomposition of the correlation density matrix, we also perform a series of detailed analyses of the structures of the ED ground-state wave functions from which the correlation density matrices are calculated. This allows us to compare, at every parameter point, the qualitative conclusions about the dominant quantum phases we are drawing, from the analysis of the ED ground-state wave functions, as well as the from the analysis of the singular values of the correlation density matrix. We do the analysis of ED ground-state structures in Section 8.3, and the analysis of correlation density-matrix singular values in Section 8.4, after we discuss various technical intricacies, associated with the two forms of analysis, in Section 8.2.

In Section 8.3, we analyze the ED ground-state structure by looking out for distinguish qualitative features in the many-body twisted energy band structures and the distributions of ground-state amplitudes. This is done first in Section 8.3.1 for the reference states associated with the three analytical limits studied in Chapter 7, then in Section 8.3.2 for the ED ground states at three parameter points chosen to be close to where there is a 'phase transition' or 'crossover' from one reference state to another, and then finally in Section 8.3.3 for the ED ground state at a parameter point chosen to close to where the lines of 'phase transitions' or 'crossovers' meet. We find that, knowing the 'finger prints' of the reference states in the many-body twisted energy band structures and the distributions of ground-state amplitudes, and comparing the structures of the ED ground states at the other parameter points to these reference states, obtained through very laborious analyses of the distributions of ground-state amplitudes, we can build up a fairly accurate picture of the ground-state phase diagram.

Having derived this picture of the ground-state phase diagram of the quarter-filled ladder from our analysis of the ED ground-state structure, we proceed to analyze in Section 8.4 the singular values at each parameter point of the correlation density matrix of two disjoint (2×2) clusters. Singular-value analyses are done in Section 8.4.2 for the reference states associated with the three analytical limits studied in Chapter 7, in Section 8.4.3 for the ground states at the three parameter points chosen to be close to where there is a 'phase transition' or 'crossover' from one reference state to another, and then in Section 8.4.4 for the ground state at a parameter point close to where the lines of 'phase transitions' or 'crossovers' meet. Based on these analyses, we build up an independent picture of the ground-state phase diagram: we find that, with less effort expended on the analysis of singular values, we have essentially the same picture of the ground-state phase diagram as obtained after investing a great deal of effort on the analysis of ED ground-state structures. More importantly, through the method of operator singular value decomposition of the correlation density matrix, we also have sorted lists of order parameters and their correlations (the singular values) at the various numerically accessible separations. These sorted lists tell us, at least at small separations we can handle with numerical ED, what the dominant correlation types and symmetries are.

1.4.9 Highlights of the Appendices

This thesis also contains five appendices, two major and three minor. These appendices, which appear in the order they are referenced within the main chapters and other appendices, contain technical details which are of interest only to practioners keen on replicating or extending the results described in the main chapters. If the reader is only interested in gaining an appreciation of the materials presented in the chapters, there is

no need to read any of the appendices.

The two major appendices are Appendices C and D. Appendix C describes the organization of the Octave code base used in Chapters 4 and 7, important algorithms, and lists the code for all functions. The code base can be roughly grouped into four parts. The first of these four parts of the code base sets things up — including system definition, Hilbert space and Hamiltonian matrix generation, Bloch-partitioning of the Hilbert space and Bloch state generation — and then performs numerical ED. This part of the code base can be used independently of the rest, if one is interested only in studying the structure of an interacting ground state. The second part of the code base develops the trace-down calculation of the cluster density matrix, and therefore relies on having a wave function supplied by the ED part of the code. The third part of the code base then takes as input, cluster density matrices supplied by the second part of the code base to perform degeneracy, orientation, and twist boundary conditions averaging. The fourth part of the code base provides extra functionalities to handle the correlation density matrix calculation for disjoint clusters, and build up the correlation $\mathbf{K}$ matrix for numerical singular value decomposition.

Appendix D explains how the method of twist boundary conditions averaging works to reduce finite size effects in the numerical study of finite systems, using as example a system of noninteracting spinless fermions. Important concepts such as wave vector sampling and ground-state selection are introduced, and the effect of a choice of gauge on the performance of twist boundary conditions averaging is discussed. We also elucidate the helpful notion of a (single-particle or many-particle) Brillouin Zone (BZ) partition structure, and how we can use a twist surface to visualize the effect of an added phase twist on various observables in the ground state subject to twist boundary conditions. With the aid of BZ partition structures and twist surfaces, we explain when twist

boundary conditions averaging is effective, or ineffective, in approximating the infinite-system $2n$-point functions. We also explained in detail how to technically implement twist boundary conditions averaging through the use of the special-point and tetrahedron schemes for BZ integration, and discuss performance and convergence issues.

The three minor appendices are Appendices A, B, and E. Appendix A contains the key derivations and formulas, for the two-point function in a Fermi sea ground state, as well as the Wick factorization of higher $2n$-point functions, which allows us to expressed them as $n \times n$ determinants of two-point functions. We use formulas from Appendix A in our calculations within Chapters 2, 3, and 5. Appendix B contains the key formulas relating the blocks in a symmetric matrix $\mathscr{M}$ to the corresponding blocks in its inverse $\mathscr{M}^{-1}$. These formulas are used in Chapter 2 to derive the exact formula for the cluster density matrix ρ_C in terms of the cluster Green-function matrix G_C. The final minor appendix, Appendix E, describes the finite-element formulas used for tetrahedron integration in Appendix D.

CHAPTER 2

EXACT FORMULA

2.1 Introduction

To get more mileage out of density matrix-based renormalization group methods, surely we must develop a deep understanding of the structure of density matrices of the simplest possible systems, for which analytic results are available to guide us. Therefore, it is appropriate to begin by considering the ground state of a one-dimensional chain of noninteracting spinless fermions described by a nearest-neighbour hopping Hamiltonian

$$H_t = -t \sum_j \left[c_j^\dagger c_{j+1} + c_{j+1}^\dagger c_j \right], \tag{2.1.1}$$

where c_j and $c_j^\dagger$ are the spinless fermion annihilation and creation operators acting on site j. The Hamiltonian H_t is diagonal in momentum space, and can be written as

$$H = \sum_k \epsilon_k \tilde{c}_k^\dagger \tilde{c}_k, \tag{2.1.2}$$

where

$$\tilde{c}_k \equiv \frac{1}{\sqrt{N}} \sum_j c_j \, e^{\mathrm{i}kj}, \quad \tilde{c}_k^\dagger \equiv \frac{1}{\sqrt{N}} \sum_j c_j^\dagger \, e^{-\mathrm{i}kj} \tag{2.1.3}$$

are the momentum space annihilation and creation operators, and ϵ_k is the single-particle energy associated with wavevector k. The ground state is a Fermi sea

$$|\Psi_F\rangle = \prod_{k \text{ filled}} \tilde{c}_k^\dagger \, |0\rangle, \tag{2.1.4}$$

where $|0\rangle$ is the vacuum, and the product is over the wavevectors inside the Fermi surface.[1] A 'cluster' is then identified within this one-dimensional system by choosing N_C

[1] Here we observe that, in one dimension, one has the same Fermi sea ground state for a variety of translationally-invariant Hamiltonians with hoppings to further neighbors, provided their dispersion relation is monotonic so that the Fermi surface occurs at the same wave vector for a given filling.

sites that need not be contiguous, following which we can define the many-body density matrix ρ_C of the cluster starting from the zero-temperature many-body wave function and tracing out all sites outside the chosen cluster of N_C sites.

With the goal of understanding the structure and spectrum of the density matrix, and their implications on RG truncation schemes in mind, Peschel *et al* calculated exactly the half-chain density matrix for several models [176–178]. For a chain of coupled harmonic oscillators and a chain of spinless Bogoliubov fermions, they found that the half-chain density matrices

$$\rho_1 = \mathcal{Q}_B^{-1} \exp\left(-\tilde{H}_B\right), \quad \rho_1 = \mathcal{Q}_F^{-1} \exp\left(-\tilde{H}_F\right) \tag{2.1.5}$$

where $\mathcal{Q}_B^{-1}$ and $\mathcal{Q}_F^{-1}$ are normalization constants, so that $\mathrm{Tr}\,\rho_1 = 1$, can be expressed exactly as the exponential of the pseudo-Hamiltonians

$$\tilde{H}_B = \sum_{l=1} \varphi_l^B b_l^\dagger b_l, \quad \tilde{H}_F = \sum_{l=1} \varphi_l^F f_l^\dagger f_l \tag{2.1.6}$$

respectively. The spectra of these pseudo-Hamiltonians are generated by a set of independent bosonic and fermionic operators, b_l and f_l, associated with the single-particle pseudo-energies φ_l^B and φ_l^F respectively. Consequently, the many-particle density-matrix eigenstates can be built up from the set of single-particle creation operators and eigenvalues. This is quite analogous to the energy eigenstates of a noninteracting system of fermions.

In this chapter, we pursue their analysis further for a system of noninteracting spinless fermions. Just as for the case of the half-chain, the density matrix ρ_C of a cluster of N_C sites cut out from a larger overall d-dimensional system, the cluster density matrix

$$\rho_C = \mathcal{Q}^{-1} \exp(-\tilde{H}) \tag{2.1.7}$$

is the exponential of a *pseudo-Hamiltonian*

$$\tilde{H} = \sum_{l=1}^{N_C} \varphi_l f_l^\dagger f_l, \tag{2.1.8}$$

with N_C *pseudo-fermion operators* f_l, each associated with a *single-particle pseudo-energy spectrum* φ_l. The Fock-Hilbert space of the cluster is therefore spanned by all 2^{N_C} products of the pseudo-creation operators $f_l^\dagger$. Adapting the Grassmannian trace technology used in Ref. 176, we obtained a closed-form formula relating the cluster density matrix ρ_C and the cluster Green-function matrix G_C (to be defined in Section 2.3.4).

The organization of the chapter will be as follows: we will start in Section 2.2 by reviewing the density matrix formulation of quantum mechanics, and how the density matrix ρ_C of a subsystem can be obtained from the density matrix ρ of the overall system by performing a partial trace over environment degrees of freedom. Following this, we will describe in Section 2.3 an alternative approach to calculating the density matrix elements as expectations of referencing operators. We shall show that the real-space structure, and the strong signs that point to a closed-form expression for ρ_C, is most readily discerned within this alternative formulation. Then, in Section 2.4, we derive this closed-form expression for ρ_C in terms of the cluster Green-function matrix G_C by adapting the technique put forward by Chung and Peschel [176]. The existence of such a relation between ρ_C and G_C tells us that ρ_C is completely determined by its zero- and one-particle sectors. We discuss the implications of this in Section 2.5.3, where we illustrate how the eigenvectors and eigenvalues of the $(P_C > 1)$-sectors of ρ_C can be constructed out of the eigenvectors and eigenvalues of the one-particle sector. We also show how symmetries of the Hamiltonian that are realized in ρ_C affect the pattern of degeneracies in the eigenvalues of these sectors, an understanding of which is important in formulating an operator-based density-matrix truncation scheme.

2.2 Density-Matrix Formulation of Quantum Mechanics

2.2.1 Basic Properties

In quantum mechanics one distinguishes between *pure states*, which occur, for example, at $T = 0$ when the system is totally decoupled from the rest of the universe, and *mixed states*, which occur, for example, at $T > 0$ when the system is in thermodynamic equilibrium with the rest of the universe. A pure state can be described by a wave function $|\Psi\rangle$ in the usual formulation of quantum mechanics, whereas a mixed state cannot. Both type of states are treated on equal footing in the density-matrix formulation of quantum mechanics, in which the state of a system is described by a density matrix ρ (see, for example, Refs. 179–181), which is a positive-definite hermitian operator with unit trace,

$$\mathrm{Tr}\,\rho = 1. \tag{2.2.1}$$

As a result of being positive-definite and of unit trace, all eigenvalues

$$w_n \geq 0 \tag{2.2.2}$$

of ρ are nonnegative, and satisfy the sum rule

$$\sum_n w_n = 1. \tag{2.2.3}$$

A pure state described by the wave function $|\Psi\rangle$ is equivalently described by the density matrix

$$\rho = |\Psi\rangle\langle\Psi|, \tag{2.2.4}$$

which is a projection operator, i.e. $\rho^2 = \rho$ and thus $\mathrm{Tr}\,\rho^2 = \mathrm{Tr}\,\rho = 1$. For such a state, (2.2.2) and (2.2.3) together imply that one of the eigenvalues of ρ is one, while the rest are zero. A mixed state, which cannot be described a wave function, can be thought of

as a weighted sum of pure-state density matrices. We write the density matrix of such a state as

$$\rho = \sum_{\alpha} |\Psi_\alpha\rangle \, \omega_\alpha \, \langle\Psi_\alpha| \,, \tag{2.2.5}$$

where $\omega_\alpha < 1$ is the probability of finding the system in the pure state $|\Psi_\alpha\rangle$. Note that the probabilities ω_α are not necessarily the eigenvalues of ρ, because the pure states $|\Psi_\alpha\rangle$ need not be orthogonal to each other. For a mixed state, the density matrix $\rho \neq \rho^2$ is not a projection operator, and we find that $\mathrm{Tr}\,\rho^2 < 1$.

In the density-matrix formulation of quantum mechanics, the expectation of an observable A in a state described by ρ is given by

$$\langle A \rangle = \mathrm{Tr}(\rho A). \tag{2.2.6}$$

If the density matrix $\rho = |\Psi\rangle\langle\Psi|$ describes a pure state $|\Psi\rangle$, then we can evaluate the trace over a complete basis $\{|n\rangle\}$ to find that

$$\mathrm{Tr}\,\rho A = \sum_{n} \langle n|\Psi\rangle \, \langle\Psi|A|n\rangle = \sum_{n} \langle\Psi|A|n\rangle \, \langle n|\Psi\rangle = \langle\Psi|A|\Psi\rangle \,, \tag{2.2.7}$$

which agrees with the formula $\langle A \rangle = \langle\Psi|A|\Psi\rangle$ for the expectation of A in the usual formulation of quantum mechanics.

While we will not be concern with time evolution in this thesis, let us note, for completeness of the presentation of basic properties of density matrices, that the time evolution of a wave function $|\Psi(t)\rangle$ is governed by the Time-Dependent Schrödinger Equation

$$\mathrm{i}\,\hbar \frac{\partial}{\partial t} |\Psi\rangle = H \, |\Psi\rangle \,, \tag{2.2.8}$$

which can be formally integrated to give

$$|\Psi_\alpha(t)\rangle = U(t, t_0) \, |\Psi_\alpha(t_0)\rangle \,, \tag{2.2.9}$$

where

$$U(t,t_0) = \exp\left[-\frac{\mathrm{i}}{\hbar}H(t-t_0)\right] \tag{2.2.10}$$

is the time evolution operator.

If we write the density matrix $\rho(t)$ at each time t always as (2.2.5), then the time dependence of $\rho(t)$ must be

$$\begin{aligned}\rho(t) &= \sum_\alpha |\Psi_\alpha(t)\rangle\, w_\alpha\, \langle\Psi_\alpha(t)| \\ &= \sum_\alpha U(t,t_0)\,|\Psi_\alpha(t_0)\rangle\, w_\alpha\, \langle\Psi_\alpha(t_0)|\, U^\dagger(t,t_0) \\ &= U(t,t_0)\rho(t_0)U^\dagger(t,t_0),\end{aligned} \tag{2.2.11}$$

With such a time dependence, the time-dependent density matrix satisfies the *quantum Liouville equation*

$$\mathrm{i}\,\hbar\frac{d\rho}{dt} = [H,\rho]\,, \tag{2.2.12}$$

which is also called the *Schrödinger equation for the density matrix*. Note that since

$$\rho^2(t) = U(t,t_0)\rho(t_0)U^\dagger(t,t_0)U(t,t_0)\rho(t_0)U^\dagger(t,t_0) = U(t,t_0)\rho^2(t_0)U^\dagger(t,t_0), \tag{2.2.13}$$

if $\rho^2(t_0) = \rho(t_0)$, then $\rho^2(t) = \rho(t)$, i.e. a pure state remains a pure state under time evolution. Similarly, a mixed state remains a mixed state under time evolution.

2.2.2 Reduced Density Matrix of a Subsystem

In this chapter, we shall be mainly interested in a finite subsystem of N_C sites, which we call the *cluster*, embedded within a larger system of N sites, with periodic boundary conditions in d dimensions. The latter can then be taken to the thermodynamic limit of infinite number of sites, i.e. $N \to \infty$. The system minus the cluster is called the *environment* of the cluster. If the overall system is known to be in a pure state $|\Psi\rangle$, then

the quantum-mechanical state of the cluster is in general a mixed state, described by a cluster density matrix ρ_C.

To see that this is so, let us present the argument used in Ref. 179. If $\{|\phi_i\rangle\}$ is a basis for the cluster, and $\{|\theta_j\rangle\}$ is a basis for the environment, then the most general pure state of the system can be written as

$$|\Psi\rangle = \sum_{i,j} C_{ij} |\phi_i\rangle |\theta_j\rangle . \tag{2.2.14}$$

For an observable A acting only within the cluster, i.e.

$$A |\phi_i\rangle |\theta_j\rangle = (A |\phi_i\rangle) |\theta_j\rangle , \tag{2.2.15}$$

its expectation is given by

$$\begin{aligned}
\langle A\rangle = \langle\Psi|A|\Psi\rangle &= \sum_{i,j;i',j'} C^*_{ij} C_{i'j'} \langle\theta_j| \langle\phi_i| A |\phi_{i'}\rangle |\theta_{j'}\rangle \\
&= \sum_{i,j;i',j'} C^*_{ij} C_{i'j'} \langle\theta_j| (\langle\phi_i|A|\phi_{i'}\rangle) |\theta_{j'}\rangle \\
&= \sum_{i,j;i',j'} C^*_{ij} C_{i'j'} (\langle\phi_i|A|\phi_{i'}\rangle) \langle\theta_j|\theta_{j'}\rangle \\
&= \sum_{i,j;i',j'} C^*_{ij} C_{i'j'} \langle\phi_i|A|\phi_{i'}\rangle \delta_{jj'} \\
&= \sum_{i,j;i'} C^*_{ij} C_{i'j} \langle\phi_i|A|\phi_{i'}\rangle .
\end{aligned} \tag{2.2.16}$$

In general, an expectation of this form cannot be written as $\langle\phi|A|\phi\rangle$ for some pure state $|\phi\rangle$. Instead, we must define a cluster density matrix ρ_C, whose matrix elements in the $\{|\phi_i\rangle\}$ basis are

$$(\rho_C)_{i'i} = \langle\phi_{i'}|\rho_C|\phi_i\rangle = \sum_j C^*_{ij} C_{i'j}, \tag{2.2.17}$$

so that the expectation of A in (2.2.16) can be written as

$$\langle A\rangle = \sum_{i,i'} \langle\phi_{i'}|\rho_C|\phi_i\rangle \langle\phi_i|A|\phi_{i'}\rangle = \sum_{i'} \langle\phi_{i'}|\rho_C A|\phi_{i'}\rangle = \mathrm{Tr}\, \rho_C A, \tag{2.2.18}$$

where we have used the completeness of the basis $\{|\phi_i\rangle\}$. It is clear that ρ_C satisfies all the basis properties of a general density matrix described in Section 2.2.1. Moreover, the sum over j in (2.2.17) suggests that the matrix elements of ρ_C are themselves some sort of trace over the environment, whose degrees of freedom — the basis functions $\{|\theta_j\rangle\}$ — are indexed by j. We call ρ_C a *reduced density matrix* because it is obtained from a system wave function $|\Psi\rangle$, or equivalently, the pure-state density matrix $\rho = |\Psi\rangle\langle\Psi|$, by tracing over environmental degrees of freedom.

We can take

$$\langle A\rangle_C = \mathrm{Tr}\,\rho_C A = \mathrm{Tr}\,\rho A = \langle A\rangle\,, \tag{2.2.19}$$

for all observables A acting locally on the cluster, to be a defining property of the cluster density matrix ρ_C, and make this presentation more formal. Using the subscripts C and E respectively to indicate traces over degrees of freedom associated with the cluster and its environment, we rewrite (2.2.6) as

$$\langle A\rangle = \mathrm{Tr}(\rho A) = \mathrm{Tr}_{C,E}(\rho A). \tag{2.2.20}$$

For an observable A acting soley within the cluster, it is commonly assumed[2] that we can trivially trace over the environmental degrees of freedom to get

$$\langle A\rangle = \mathrm{Tr}_C\left\{\left[\mathrm{Tr}_E(\rho)\right]A\right\}. \tag{2.2.21}$$

Comparing this with (2.2.19), we find a consistent expectation for A whether it is taken over the entire system or just over the cluster, if the cluster density matrix is defined as

$$\rho_C = \mathrm{Tr}_E(\rho). \tag{2.2.22}$$

[2]We shall scrutinize this assumption in Chapter 4.

2.3 Density Matrix of a Finite Cluster

In this section, we develop the method of referencing operators to explicitly calculate the density matrix elements of a finite cluster of N_C sites embedded in a larger (finite or infinite) system of noninteracting spinless fermions. We will do this in Section 2.3.1, after formulating the cluster density-matrix elements as overlaps between the environmental states associated with two given cluster states. Then in Section 2.3.4, we will calculate the cluster density matrix for several finite one-dimensional chains of noninteracting spinless fermions, and by analyzing the index structure of the matrices involved, conjecture a closed-form expression for the one-particle cluster density matrix in terms of the cluster Green-function matrix. We will prove this conjecture in Section 2.4.

To begin with, let us note that any pure state of a large, possibly infinite, system can be written as

$$|\Psi\rangle = \sum_{\mathbf{l}} |\mathbf{l}\rangle\, |e_{\mathbf{l}}\rangle\,, \tag{2.3.1}$$

where $|\mathbf{l}\rangle$ is a complete orthonormal many-body basis for the cluster, and $|e_{\mathbf{l}}\rangle$ is the unnormalized state of the environment associated with the state $|\mathbf{l}\rangle$ on the cluster. Using this form for $|\Psi\rangle$ in (2.2.6), we find that

$$\langle A\rangle = \sum_{\mathbf{l},\mathbf{l}'} \langle e_{\mathbf{l}}|\, \langle \mathbf{l}|\, A\, |\mathbf{l}'\rangle\, |e_{\mathbf{l}'}\rangle = \mathrm{Tr}_C(\rho_C A) \tag{2.3.2}$$

if the cluster density matrix ρ_C is defined such that

$$(\rho_C)_{\mathbf{l}'\mathbf{l}} = \langle e_{\mathbf{l}}|e_{\mathbf{l}'}\rangle\,, \tag{2.3.3}$$

i.e. the matrix element of ρ_C between $|\mathbf{l}\rangle$ and $|\mathbf{l}'\rangle$ is none other than the overlap between their associated environmental states $|e_{\mathbf{l}}\rangle$ and $|e_{\mathbf{l}'}\rangle$.

2.3.1 Method of Referencing Operators

When dealing with a finite cluster and an infinite environment, it makes no sense to evaluate the environmental overlaps $\langle e_{\mathbf{l}}|e_{\mathbf{l}'}\rangle$ by first calculating $|e_{\mathbf{l}}\rangle$ and $|e_{\mathbf{l}'}\rangle$. Instead, we find that it possible to evaluate such environmental overlaps with the help of operator products that are defined entirely within the finite cluster. To do so, let us choose the many-body states $|\mathbf{l}\rangle$ on the cluster to be the occupation number basis states

$$|\mathbf{l}\rangle = |n_1^{\mathbf{l}} n_2^{\mathbf{l}} \cdots n_{N_C}^{\mathbf{l}}\rangle\,, \tag{2.3.4}$$

where $n_j^{\mathbf{l}} = 0$ or 1 depending on whether the site j in the cluster is empty or occupied in the state $|\mathbf{l}\rangle$. We then define the *referencing operators*

$$K_{\mathbf{l}} = \prod_{j=1}^{N_C} \left[n_j^{\mathbf{l}} c_j + (1 - n_j^{\mathbf{l}}) c_j c_j^\dagger \right], \tag{2.3.5}$$

such that the effect of $K_{\mathbf{l}}$ acting on a state $|\mathbf{l}'\rangle$ is

$$K_{\mathbf{l}}\,|\mathbf{l}'\rangle = \delta_{\mathbf{l}\mathbf{l}'}\,|0\rangle_C\,, \tag{2.3.6}$$

where $|0\rangle_C$ is the chosen *reference state*, for which all sites in the cluster are empty. Letting $K_{\mathbf{l}}$ act on the Fermi-sea ground state $|\Psi_F\rangle$ in (2.1.4), we obtain

$$K_{\mathbf{l}}\,|\Psi_F\rangle = \sum_{\mathbf{l}''} K_{\mathbf{l}}\,|\mathbf{l}''\rangle\,|e_{\mathbf{l}''}\rangle = |0\rangle_C\,|e_{\mathbf{l}}\rangle\,. \tag{2.3.7}$$

Hence, in terms of the operators $K_{\mathbf{l}}$ and their conjugates $K_{\mathbf{l}}^\dagger$, the cluster density-matrix elements are found to be

$$(\rho_C)_{\mathbf{l}'\mathbf{l}} = \langle e_{\mathbf{l}}|e_{\mathbf{l}'}\rangle = \left\langle \Psi_F \middle| K_{\mathbf{l}}^\dagger K_{\mathbf{l}'} \middle| \Psi_F \right\rangle = \langle K_{\mathbf{l}}^\dagger K_{\mathbf{l}'}\rangle. \tag{2.3.8}$$

From the way the operators $K_{\mathbf{l}}$ are defined, we know that the cluster density matrix ρ_C is real and symmetric. Furthermore, $(\rho_C)_{\mathbf{l}'\mathbf{l}}$ vanishes if the states $|\mathbf{l}\rangle$ and $|\mathbf{l}'\rangle$ do not contain the same number of fermions P_C. Consequently, the non-zero matrix elements

of ρ_C are found in a total of $(N_C + 1)$ diagonal blocks, corresponding to the various P-particle sectors, for $P_C = 0, 1, \ldots, N_C$. We shall call such submatrices ρ_{N_C,P_C}, and their eigenvalues the *P-particle density-matrix weights* $w_{N_C,P_C,l}$, where $l = 1, \ldots, \mathrm{rank}(\rho_{N_C,P_C})$.

2.3.2 Example Calculations for Finite Clusters

2.3.2.1 $N_C = 2$

For a cluster of $N_C = 2$ sites on an infinite chain, we have a total of $D_C = 2^2 = 4$ occupation-number cluster basis states. We write these as

$$|\mathbf{l}_1\rangle = |00\rangle\,, \quad |\mathbf{l}_2\rangle = |01\rangle\,, \quad |\mathbf{l}_3\rangle = |10\rangle\,, \quad |\mathbf{l}_4\rangle = |11\rangle\,, \tag{2.3.9}$$

where in $|n_{l_1} n_{l_2}\rangle$, $l_1 < l_2$ is the first site of the cluster, and l_2 is the second site of the cluster. Without loss of generality, we can always relabel the sites on our chain so that $l_1 = 1$, and $l_2 = 2$. The corresponding referencing operators are

$$\begin{aligned} K_{\mathbf{l}_1} &= (\mathbb{1} - n_1)(\mathbb{1} - n_2), \\ K_{\mathbf{l}_2} &= (\mathbb{1} - n_1)c_2, \quad K_{\mathbf{l}_3} = c_1(\mathbb{1} - n_2), \\ K_{\mathbf{l}_4} &= c_1 c_2, \end{aligned} \tag{2.3.10}$$

where $\mathbb{1}$ is the identity operator, and $n_j = c_j^\dagger c_j$ the occupation number operator at site j.

We observe that

$$\begin{aligned} &\langle K_{\mathbf{l}_1}^\dagger K_{\mathbf{l}_2}\rangle = \langle c_2^\dagger(\mathbb{1} - n_1)(\mathbb{1} - n_1)(\mathbb{1} - n_2)\rangle = \langle c_2^\dagger(\mathbb{1} - n_1)\rangle = 0, \\ &\langle K_{\mathbf{l}_1}^\dagger K_{\mathbf{l}_3}\rangle = \langle (\mathbb{1} - n_2)c_1^\dagger(\mathbb{1} - n_1)(\mathbb{1} - n_2)\rangle = \langle c_1^\dagger(\mathbb{1} - n_2)\rangle = 0, \\ &\langle K_{\mathbf{l}_1}^\dagger K_{\mathbf{l}_4}\rangle = \langle c_2^\dagger c_1^\dagger(\mathbb{1} - n_1)(\mathbb{1} - n_2)\rangle = \langle c_2^\dagger c_1^\dagger\rangle = 0, \\ &\langle K_{\mathbf{l}_2}^\dagger K_{\mathbf{l}_4}\rangle = \langle c_2^\dagger c_1^\dagger(\mathbb{1} - n_1)c_2\rangle = \langle c_2^\dagger c_1^\dagger c_2\rangle = 0, \\ &\langle K_{\mathbf{l}_3}^\dagger K_{\mathbf{l}_4}\rangle = \langle c_2^\dagger c_1^\dagger c_1(\mathbb{1} - n_2)\rangle = \langle c_2^\dagger c_1^\dagger c_1\rangle = 0, \end{aligned} \tag{2.3.11}$$

i.e. the cluster density matrix has no nonzero matrix elements between cluster states with different number of particles. We also observe that

$$\begin{aligned}\langle K_{\mathbf{l}_2}^\dagger K_{\mathbf{l}_3}\rangle &= \langle (\mathbb{1}-n_2)c_1^\dagger(\mathbb{1}-n_1)c_2\rangle = \langle c_2^\dagger c_1\rangle\,,\\ \langle K_{\mathbf{l}_3}^\dagger K_{\mathbf{l}_2}\rangle &= \langle c_2^\dagger(\mathbb{1}-n_1)c_1(\mathbb{1}-n_2)\rangle = \langle c_2^\dagger c_1\rangle\,,\end{aligned} \tag{2.3.12}$$

which are equal, since all Fermi-sea ground-state $2n$-point functions are real, and so the cluster density matrix is real and symmetric.

We calculate the cluster density matrix sector by sector. In the zero-particle sector, the cluster density-matrix element is

$$\begin{aligned}\rho_{C,0} = \langle \mathbf{l}_1|\rho_C|\mathbf{l}_1\rangle &= \langle K_{\mathbf{l}_1}^\dagger K_{\mathbf{l}_1}\rangle = \langle (\mathbb{1}-n_2)(\mathbb{1}-n_1)(\mathbb{1}-n_1)(\mathbb{1}-n_2)\rangle\\ &= \langle (\mathbb{1}-n_1)(\mathbb{1}-n_2)\rangle = 1-\langle n_1\rangle-\langle n_2\rangle+\langle n_1n_2\rangle\,.\end{aligned} \tag{2.3.13}$$

Using the results in Appendix A, we write this zero-particle cluster density-matrix element as

$$\rho_{C,0} = 1-2\bar{n}+\bar{n}^2\left[1-g^2(1)\right], \tag{2.3.14}$$

where $\bar{n}$ is the *average number of particles per site*, or the *filling fraction* of the chain, and

$$g(r) = \frac{\sin\bar{n}\pi r}{\bar{n}\pi r} \tag{2.3.15}$$

is the *reduced two-point function* of the one-dimensional Fermi sea.

In the one-particle sector, the cluster density-matrix elements are

$$\begin{aligned}\langle \mathbf{l}_2|\rho_C|\mathbf{l}_2\rangle &= \langle K_{\mathbf{l}_2}^\dagger K_{\mathbf{l}_2}\rangle = \langle c_2^\dagger(\mathbb{1}-n_1)(\mathbb{1}-n_1)c_2\rangle = \langle(\mathbb{1}-n_1)n_2\rangle\\ &= \langle n_2\rangle-\langle n_1n_2\rangle = \bar{n}-\bar{n}^2\left[1-g^2(1)\right],\\ \langle \mathbf{l}_2|\rho_C|\mathbf{l}_3\rangle &= \langle K_{\mathbf{l}_3}^\dagger K_{\mathbf{l}_2}\rangle = \langle(\mathbb{1}-n_2)c_1^\dagger(\mathbb{1}-n_1)c_2\rangle = \langle c_1^\dagger c_2\rangle = \bar{n}g(1),\\ \langle \mathbf{l}_3|\rho_C|\mathbf{l}_2\rangle &= \langle K_{\mathbf{l}_2}^\dagger K_{\mathbf{l}_3}\rangle = \langle c_2^\dagger(\mathbb{1}-n_1)c_1(\mathbb{1}-n_2)\rangle = \langle c_2^\dagger c_1\rangle = \bar{n}g(1),\\ \langle \mathbf{l}_3|\rho_C|\mathbf{l}_3\rangle &= \langle K_{\mathbf{l}_3}^\dagger K_{\mathbf{l}_3}\rangle = \langle(\mathbb{1}-n_2)c_1^\dagger c_1(\mathbb{1}-n_2)\rangle = \langle n_1(\mathbb{1}-n_2)\rangle\\ &= \langle n_1\rangle-\langle n_1n_2\rangle = \bar{n}-\bar{n}^2\left[1-g^2(1)\right],\end{aligned} \tag{2.3.16}$$

while in the two-particle sector, the cluster density-matrix element is

$$\rho_{C,2} = \langle \mathbf{l}_4 | \rho_C | \mathbf{l}_4 \rangle = \langle K_{\mathbf{l}_4}^\dagger K_{\mathbf{l}_4} \rangle = \langle c_2^\dagger c_1^\dagger c_1 c_2 \rangle = \langle n_1 n_2 \rangle = \bar{n}^2 \left[1 - g^2(1) \right]. \tag{2.3.17}$$

At half-filling, $\bar{n} = \frac{1}{2}$, $g(1) = \frac{2}{\pi}$, and we can write out the cluster density matrix, in the cluster occupation-number basis defined in (2.3.9), explicitly as

$$\rho_C = \begin{bmatrix} \frac{1}{4}\left(1 - \frac{4}{\pi^2}\right) & 0 & 0 & 0 \\ 0 & \frac{1}{2} - \frac{1}{4}\left(1 - \frac{4}{\pi^2}\right) & \frac{1}{\pi} & 0 \\ 0 & \frac{1}{\pi} & \frac{1}{2} - \frac{1}{4}\left(1 - \frac{4}{\pi^2}\right) & 0 \\ 0 & 0 & 0 & \frac{1}{4}\left(1 - \frac{4}{\pi^2}\right) \end{bmatrix}. \tag{2.3.18}$$

Diagonalizing this matrix, we get the cluster density-matrix weights

$$\begin{aligned} w_{2,0} &= \left(\frac{1}{2} - \frac{1}{\pi}\right)\left(\frac{1}{2} + \frac{1}{\pi}\right); \\ w_{2,1,1} = \left(\frac{1}{2} + \frac{1}{\pi}\right)^2, \quad w_{2,1,2} &= \left(\frac{1}{2} - \frac{1}{\pi}\right)^2; \\ w_{2,2} &= \left(\frac{1}{2} - \frac{1}{\pi}\right)\left(\frac{1}{2} + \frac{1}{\pi}\right). \end{aligned} \tag{2.3.19}$$

Here, we see that the degeneracy

$$w_{2,0} = w_{2,2} \tag{2.3.20}$$

expected from particle-hole symmetry at half-filling, and the relation

$$\frac{w_{2,1,1}}{w_{2,0}} = \frac{w_{2,0}}{w_{2,1,2}} \tag{2.3.21}$$

between the ratios of the one-particle cluster density-matrix weights to the zero-particle cluster density-matrix weight.

2.3.2.2 $N_C = 3$

For a cluster of $N_C = 3$ sites on an infinite chain, we have a total of $D_C = 2^3 = 8$ occupation-number cluster basis states. We write these as

$$\begin{gathered} |\mathbf{l}_1\rangle = |000\rangle\,; \\ |\mathbf{l}_2\rangle = |001\rangle\,, \quad |\mathbf{l}_3\rangle = |010\rangle\,, \quad |\mathbf{l}_4\rangle = |100\rangle\,; \\ |\mathbf{l}_5\rangle = |011\rangle\,, \quad |\mathbf{l}_6\rangle = |101\rangle\,, \quad |\mathbf{l}_7\rangle = |011\rangle\,; \\ |\mathbf{l}_8\rangle = |111\rangle\,, \end{gathered} \tag{2.3.22}$$

where, with relabeling of the sites on the chain, the occupation-number cluster basis states are $|n_1 n_2 n_3\rangle$. The corresponding referencing operators are

$$\begin{gathered} K_{\mathbf{l}_1} = (\mathbb{1} - n_1)(\mathbb{1} - n_2)(\mathbb{1} - n_3); \\ K_{\mathbf{l}_2} = (\mathbb{1} - n_1)(\mathbb{1} - n_2)c_3, \quad K_{\mathbf{l}_3} = (\mathbb{1} - n_1)c_2(\mathbb{1} - n_2), \quad K_{\mathbf{l}_4} = c_1(\mathbb{1} - n_2)(\mathbb{1} - n_3); \\ K_{\mathbf{l}_5} = (\mathbb{1} - n_1)c_2 c_3, \quad K_{\mathbf{l}_6} = c_1(\mathbb{1} - n_2)c_3, \quad K_{\mathbf{l}_7} = c_1 c_2(\mathbb{1} - n_3); \\ K_{\mathbf{l}_8} = c_1 c_2 c_3. \end{gathered} \tag{2.3.23}$$

We can easily check, in the same way that we have done for the case of $N_C = 2$, that the cluster density matrix is block-diagonal, with each diagonal block corresponding to the number of particles P_C within the cluster. We compute these P_C-particle sectors of ρ_C one at a time. The zero-particle and three-particle sectors of the cluster density matrix each contain one matrix element, which are also straightforward to calculate. These are

$$\begin{aligned} \rho_{C,0} &= \langle \mathbf{l}_1 | \rho_C | \mathbf{l}_1 \rangle = \langle K_{\mathbf{l}_1}^\dagger K_{\mathbf{l}_1} \rangle = \langle (\mathbb{1} - n_1)(\mathbb{1} - n_2)(\mathbb{1} - n_3) \rangle \\ &= \langle \mathbb{1} - n_1 - n_2 - n_3 + n_1 n_2 + n_2 n_3 + n_3 n_1 - n_1 n_2 n_3 \rangle \\ &= 1 - 3\bar{n} + \langle n_1 n_2 \rangle + \langle n_2 n_3 \rangle + \langle n_1 n_3 \rangle - \langle n_1 n_2 n_3 \rangle, \\ \rho_{C,3} &= \langle \mathbf{l}_8 | \rho_C | \mathbf{l}_8 \rangle = \langle K_{\mathbf{l}_8}^\dagger K_{\mathbf{l}_8} \rangle = \langle c_3^\dagger c_2^\dagger c_1^\dagger c_1 c_2 c_3 \rangle = \langle n_1 n_2 n_3 \rangle \,. \end{aligned} \tag{2.3.24}$$

Using the results in Appendix A, these matrix elements becomes

$$\begin{aligned}\rho_{C,0} &= 1 - 3\bar{n} + \bar{n}^2\left[3 - 2g^2(1) - g^2(2)\right] - \\ &\quad \bar{n}^3\left[1 - 2g^2(1) + 2g^2(1)g(2) - g^2(2)\right], \\ \rho_{C,3} &= \bar{n}^3\left[1 - 2g^2(1) + 2g^2(1)g(2) - g^2(2)\right].\end{aligned} \tag{2.3.25}$$

In the one-particle and two-particle cluster density-matrix sectors, there are nine matrix elements each. These matrix elements are not simply sums of products of occupation number operators, so we need to find a more systematic way to evaluate them. First of all, let us note that in the product $K_{\mathbf{l}}^\dagger K_{\mathbf{l}'}$ of referencing operators, we tend to end up with repeated operators within the product. The first order of business would therefore be to reduce the product $K_{\mathbf{l}}^\dagger K_{\mathbf{l}'}$ to a simpler operator product, in which each operator c_j or $c_j^\dagger$ appears only once, if at all. Next, we normal order this simplified operator product by bring all creation operators to the left, and all annihilation operators to the right. We then end up generically with a sum of normal-ordered operator products, each of which we can evaluate using the results in Appendix A.

In the one-particle sector, the cluster density-matrix elements are expectations of the products of referencing operators,

$$K_{\mathbf{l}_2}^\dagger K_{\mathbf{l}_2} = c_3^\dagger c_2 c_2^\dagger c_1 c_1^\dagger c_1 c_1^\dagger c_2 c_2^\dagger c_3, \tag{2.3.26a}$$

$$K_{\mathbf{l}_2}^\dagger K_{\mathbf{l}_3} = c_3^\dagger c_2 c_2^\dagger c_1 c_1^\dagger c_1 c_1^\dagger c_2 c_3 c_3^\dagger, \tag{2.3.26b}$$

$$K_{\mathbf{l}_2}^\dagger K_{\mathbf{l}_4} = c_3^\dagger c_2 c_2^\dagger c_1 c_1^\dagger c_1 c_2 c_2^\dagger c_3 c_3^\dagger; \tag{2.3.26c}$$

$$K_{\mathbf{l}_3}^\dagger K_{\mathbf{l}_2} = c_3 c_3^\dagger c_2^\dagger c_1 c_1^\dagger c_1 c_1^\dagger c_2 c_2^\dagger c_3, \tag{2.3.26d}$$

$$K_{\mathbf{l}_3}^\dagger K_{\mathbf{l}_3} = c_3 c_3^\dagger c_2^\dagger c_1 c_1^\dagger c_1 c_1^\dagger c_2 c_3 c_3^\dagger, \tag{2.3.26e}$$

$$K_{\mathbf{l}_3}^\dagger K_{\mathbf{l}_4} = c_3 c_3^\dagger c_2^\dagger c_1 c_1^\dagger c_1 c_2 c_2^\dagger c_3 c_3^\dagger; \tag{2.3.26f}$$

$$K_{\mathbf{l}_4}^\dagger K_{\mathbf{l}_2} = c_3 c_3^\dagger c_2 c_2^\dagger c_1^\dagger c_1 c_1^\dagger c_2 c_2^\dagger c_3, \tag{2.3.26g}$$

$$K_{\mathbf{l}_4}^\dagger K_{\mathbf{l}_3} = c_3 c_3^\dagger c_2 c_2^\dagger c_1^\dagger c_1 c_1^\dagger c_2 c_3 c_3^\dagger, \tag{2.3.26h}$$

$$K_{\mathbf{l}_4}^\dagger K_{\mathbf{l}_4} = c_3 c_3^\dagger c_2 c_2^\dagger c_1^\dagger c_1 c_2 c_2^\dagger c_3 c_3^\dagger. \tag{2.3.26i}$$

We simplify these products so that each fermion operator appears only once, if at all, and normal order them to obtain

$$K_{\mathbf{l}_2}^\dagger K_{\mathbf{l}_2} = c_3^\dagger c_2 c_2^\dagger c_1 c_1^\dagger c_3 = -c_1^\dagger c_2^\dagger c_3^\dagger c_1 c_2 c_3 + c_2^\dagger c_3^\dagger c_2 c_3 + c_1^\dagger c_3^\dagger c_1 c_3 + c_3^\dagger c_3, \tag{2.3.27a}$$

$$K_{\mathbf{l}_2}^\dagger K_{\mathbf{l}_3} = c_3^\dagger c_2 c_1 c_1^\dagger = c_3^\dagger c_2 + c_1^\dagger c_3^\dagger c_1 c_2, \tag{2.3.27b}$$

$$K_{\mathbf{l}_2}^\dagger K_{\mathbf{l}_4} = c_3^\dagger c_2 c_2^\dagger c_1 = c_3^\dagger c_1 - c_2^\dagger c_3^\dagger c_1 c_2; \tag{2.3.27c}$$

$$K_{\mathbf{l}_3}^\dagger K_{\mathbf{l}_2} = c_2^\dagger c_3 c_1 c_1^\dagger = c_2^\dagger c_3 + c_1^\dagger c_2^\dagger c_1 c_3, \tag{2.3.27d}$$

$$K_{\mathbf{l}_3}^\dagger K_{\mathbf{l}_3} = c_3 c_3^\dagger c_2^\dagger c_2 c_1 c_1^\dagger = c_2^\dagger c_2 + c_1^\dagger c_2^\dagger c_1 c_2 + c_2^\dagger c_3^\dagger c_2 c_3 - c_1^\dagger c_2^\dagger c_3^\dagger c_1 c_2 c_3, \tag{2.3.27e}$$

$$K_{\mathbf{l}_3}^\dagger K_{\mathbf{l}_4} = c_3 c_3^\dagger c_2^\dagger c_1 = c_2^\dagger c_1 + c_2^\dagger c_3^\dagger c_1 c_3; \tag{2.3.27f}$$

$$K_{\mathbf{l}_4}^\dagger K_{\mathbf{l}_2} = -c_3 c_2 c_2^\dagger c_1^\dagger = c_1^\dagger c_3 - c_1^\dagger c_2^\dagger c_2 c_3, \tag{2.3.27g}$$

$$K_{\mathbf{l}_4}^\dagger K_{\mathbf{l}_3} = -c_3 c_3^\dagger c_2 c_1^\dagger = c_1^\dagger c_2 + c_1^\dagger c_3^\dagger c_2 c_3, \tag{2.3.27h}$$

$$K_{\mathbf{l}_4}^\dagger K_{\mathbf{l}_4} = c_3 c_3^\dagger c_2 c_2^\dagger c_1^\dagger c_1 = c_1^\dagger c_1 + c_1^\dagger c_2^\dagger c_1 c_2 + c_1^\dagger c_3^\dagger c_1 c_3 - c_1^\dagger c_2^\dagger c_3^\dagger c_1 c_2 c_3. \tag{2.3.27i}$$

Using the results in Appendix A to evaluate the expectations of these sums of operator products, we then find the one-particle cluster density-matrix elements to be

$$\begin{aligned}\langle \mathbf{l}_2 | \rho_C | \mathbf{l}_2 \rangle = \bar{n} + \bar{n}^2 \left[g^2(1) + g^2(2) - 2 \right] + \\ \bar{n}^3 \left[1 - 2g^2(1) - g^2(2) + 2g^2(1) g(2) \right],\end{aligned} \tag{2.3.28a}$$

$$\langle \mathbf{l}_2 | \rho_C | \mathbf{l}_3 \rangle = \bar{n} g(1) - \bar{n}^2 g(1)[1 - g(2)], \tag{2.3.28b}$$

$$\langle \mathbf{l}_2 | \rho_C | \mathbf{l}_4 \rangle = \bar{n} g(2) + \bar{n}^2 [g^2(1) - g(2)]; \tag{2.3.28c}$$

$$\langle \mathbf{l}_3 | \rho_C | \mathbf{l}_2 \rangle = \bar{n} g(1) - \bar{n}^2 g(1)[1 - g(2)], \tag{2.3.28d}$$

$$\langle \mathbf{l}_3 | \rho_C | \mathbf{l}_3 \rangle = \bar{n} - 2\bar{n}^2 \left[1 - g^2(1) \right] + \bar{n}^3 \left[1 - 2g^2(1) - g^2(2) + 2g^2(1) g(2) \right], \tag{2.3.28e}$$

$$\langle \mathbf{l}_3 | \rho_C | \mathbf{l}_4 \rangle = \bar{n} g(1) - \bar{n}^2 g(1) \left[1 - g(2) \right]; \tag{2.3.28f}$$

$$\langle \mathbf{l}_4 | \rho_C | \mathbf{l}_2 \rangle = \bar{n} g(2) + \bar{n}^2 \left[g^2(1) - g(2) \right], \tag{2.3.28g}$$

$$\langle \mathbf{l}_4|\rho_C|\mathbf{l}_3\rangle = \bar{n}g(1) - \bar{n}^2 g(1)\left[1 - g(2)\right], \tag{2.3.28h}$$

$$\langle \mathbf{l}_4|\rho_C|\mathbf{l}_4\rangle = \bar{n} + \bar{n}^2\left[g^2(1) + g^2(2) - 2\right] + \bar{n}^3\left[1 - 2g^2(1) - g^2(2) + 2g^2(1)g(2)\right]. \tag{2.3.28i}$$

Doing the same for the two-particle sector, we would start from the products of referencing operators,

$$K_{\mathbf{l}_5}^\dagger K_{\mathbf{l}_5} = c_3^\dagger c_2^\dagger c_1 c_1^\dagger c_1 c_1^\dagger c_2 c_3, \tag{2.3.29a}$$

$$K_{\mathbf{l}_5}^\dagger K_{\mathbf{l}_6} = c_3^\dagger c_2^\dagger c_1 c_1^\dagger c_1 c_2 c_2^\dagger c_3, \tag{2.3.29b}$$

$$K_{\mathbf{l}_5}^\dagger K_{\mathbf{l}_7} = c_3^\dagger c_2^\dagger c_1 c_1^\dagger c_1 c_2 c_3 c_3^\dagger; \tag{2.3.29c}$$

$$K_{\mathbf{l}_6}^\dagger K_{\mathbf{l}_5} = c_3^\dagger c_2 c_2^\dagger c_1^\dagger c_1 c_1^\dagger c_2 c_3, \tag{2.3.29d}$$

$$K_{\mathbf{l}_6}^\dagger K_{\mathbf{l}_6} = c_3^\dagger c_2 c_2^\dagger c_1^\dagger c_1 c_2 c_2^\dagger c_3, \tag{2.3.29e}$$

$$K_{\mathbf{l}_6}^\dagger K_{\mathbf{l}_7} = c_3^\dagger c_2 c_2^\dagger c_1^\dagger c_1 c_2 c_3 c_3^\dagger; \tag{2.3.29f}$$

$$K_{\mathbf{l}_7}^\dagger K_{\mathbf{l}_5} = c_3 c_3^\dagger c_2^\dagger c_1^\dagger c_1 c_1^\dagger c_2 c_3, \tag{2.3.29g}$$

$$K_{\mathbf{l}_7}^\dagger K_{\mathbf{l}_6} = c_3 c_3^\dagger c_2^\dagger c_1^\dagger c_1 c_2 c_2^\dagger c_3, \tag{2.3.29h}$$

$$K_{\mathbf{l}_7}^\dagger K_{\mathbf{l}_7} = c_3 c_3^\dagger c_2^\dagger c_1^\dagger c_1 c_2 c_3 c_3^\dagger, \tag{2.3.29i}$$

simplify them so that each fermion operator occurs at most once, and normal order them to obtain

$$K_{\mathbf{l}_5}^\dagger K_{\mathbf{l}_5} = -c_2^\dagger c_3^\dagger c_2 c_3 + c_1^\dagger c_2^\dagger c_3^\dagger c_1 c_2 c_3, \tag{2.3.30a}$$

$$K_{\mathbf{l}_5}^\dagger K_{\mathbf{l}_6} = -c_2^\dagger c_3^\dagger c_1 c_3, \tag{2.3.30b}$$

$$K_{\mathbf{l}_5}^\dagger K_{\mathbf{l}_7} = -c_2^\dagger c_3^\dagger c_1 c_2; \tag{2.3.30c}$$

$$K_{\mathbf{l}_6}^\dagger K_{\mathbf{l}_5} = -c_1^\dagger c_3^\dagger c_2 c_3, \tag{2.3.30d}$$

$$K_{\mathbf{l}_6}^\dagger K_{\mathbf{l}_6} = -c_1^\dagger c_3^\dagger c_1 c_3 + c_1^\dagger c_2^\dagger c_3^\dagger c_1 c_2 c_3, \tag{2.3.30e}$$

$$K_{\mathbf{l}_6}^\dagger K_{\mathbf{l}_7} = -c_1^\dagger c_3^\dagger c_1 c_2; \tag{2.3.30f}$$

$$K_{\mathbf{l}_7}^\dagger K_{\mathbf{l}_5} = -c_1^\dagger c_2^\dagger c_2 c_3, \tag{2.3.30g}$$

$$K_{\mathbf{l}_7}^\dagger K_{\mathbf{l}_6} = -c_1^\dagger c_2^\dagger c_1 c_3, \tag{2.3.30h}$$

$$K_{\mathbf{l}_7}^\dagger K_{\mathbf{l}_7} = -c_1^\dagger c_2^\dagger c_1 c_2 + c_1^\dagger c_2^\dagger c_3^\dagger c_1 c_2 c_3. \tag{2.3.30i}$$

Taking the expectation of these normal-ordered operator products, we then find the two-particle cluster density-matrix elements to be

$$\langle \mathbf{l}_5|\rho_C|\mathbf{l}_5\rangle = \bar{n}^2\left[1 - g^2(1)\right] - \bar{n}^3\left[1 - 2g^2(1) + 2g^2(1)g(2) - g^2(2)\right], \tag{2.3.31a}$$

$$\langle \mathbf{l}_5|\rho_C|\mathbf{l}_6\rangle = \bar{n}^2 g(1)\left[1 - g(2)\right], \tag{2.3.31b}$$

$$\langle \mathbf{l}_5|\rho_C|\mathbf{l}_7\rangle = \bar{n}^2\left[g^2(1) - g(2)\right]; \tag{2.3.31c}$$

$$\langle \mathbf{l}_6|\rho_C|\mathbf{l}_5\rangle = \bar{n}^2 g(1)\left[1 - g(2)\right], \tag{2.3.31d}$$

$$\langle \mathbf{l}_6|\rho_C|\mathbf{l}_6\rangle = \bar{n}^2\left[1 - g^2(2)\right] - \bar{n}^3\left[1 - 2g^2(1) + 2g^2(1)g(2) - g^2(2)\right], \tag{2.3.31e}$$

$$\langle \mathbf{l}_6|\rho_C|\mathbf{l}_7\rangle = \bar{n}^2 g(1)\left[1 - g(2)\right]; \tag{2.3.31f}$$

$$\langle \mathbf{l}_7|\rho_C|\mathbf{l}_5\rangle = \bar{n}^2\left[g^2(1) - g(2)\right], \tag{2.3.31g}$$

$$\langle \mathbf{l}_7|\rho_C|\mathbf{l}_6\rangle = \bar{n}^2 g(1)\left[1 - g(2)\right], \tag{2.3.31h}$$

$$\langle \mathbf{l}_7|\rho_C|\mathbf{l}_7\rangle = \bar{n}^2\left[1 - g^2(1)\right] - \bar{n}^3\left[1 - 2g^2(1) + 2g^2(1)g(2) - g^2(2)\right]. \tag{2.3.31i}$$

At half-filling, $\bar{n} = \frac{1}{2}$, $g(1) = \frac{2}{\pi}$, $g(2) = 0$, so we can write out the cluster density-matrix elements explicitly as

$$\langle \mathbf{l}_1|\rho_C|\mathbf{l}_1\rangle = \frac{1}{8} - \frac{1}{\pi^2} = \langle \mathbf{l}_8|\rho_C|\mathbf{l}_8\rangle; \tag{2.3.32a}$$

in the zero-particle sector,

$$\langle \mathbf{l}_2|\rho_C|\mathbf{l}_2\rangle = \frac{1}{8}, \quad \langle \mathbf{l}_2|\rho_C|\mathbf{l}_3\rangle = \frac{1}{2\pi}, \quad \langle \mathbf{l}_2|\rho_C|\mathbf{l}_4\rangle = \frac{1}{\pi^2}; \tag{2.3.32b}$$

$$\langle \mathbf{l}_3|\rho_C|\mathbf{l}_2\rangle = \frac{1}{2\pi}, \quad \langle \mathbf{l}_3|\rho_C|\mathbf{l}_3\rangle = \frac{1}{8} + \frac{1}{\pi^2}, \quad \langle \mathbf{l}_3|\rho_C|\mathbf{l}_4\rangle = \frac{1}{2\pi}; \tag{2.3.32c}$$

$$\langle \mathbf{l}_4|\rho_C|\mathbf{l}_2\rangle = \frac{1}{\pi^2}, \quad \langle \mathbf{l}_4|\rho_C|\mathbf{l}_3\rangle = \frac{1}{2\pi}, \quad \langle \mathbf{l}_4|\rho_C|\mathbf{l}_4\rangle = \frac{1}{8}; \tag{2.3.32d}$$

in the one-particle sector,

$$\langle \mathbf{l}_5|\rho_C|\mathbf{l}_5\rangle = \frac{1}{8}, \quad \langle \mathbf{l}_5|\rho_C|\mathbf{l}_6\rangle = \frac{1}{2\pi}, \quad \langle \mathbf{l}_5|\rho_C|\mathbf{l}_7\rangle = \frac{1}{\pi^2}; \tag{2.3.32e}$$

$$\langle \mathbf{l}_6|\rho_C|\mathbf{l}_5\rangle = \frac{1}{2\pi}, \quad \langle \mathbf{l}_6|\rho_C|\mathbf{l}_6\rangle = \frac{1}{8} + \frac{1}{\pi^2}, \quad \langle \mathbf{l}_6|\rho_C|\mathbf{l}_7\rangle = \frac{1}{2\pi}; \tag{2.3.32f}$$

$$\langle \mathbf{l}_7|\rho_C|\mathbf{l}_5\rangle = \frac{1}{\pi^2}, \quad \langle \mathbf{l}_7|\rho_C|\mathbf{l}_6\rangle = \frac{1}{2\pi}, \quad \langle \mathbf{l}_7|\rho_C|\mathbf{l}_7\rangle = \frac{1}{8}; \tag{2.3.32g}$$

in the two-particle sector, and

$$\langle \mathbf{l}_8|\rho_C|\mathbf{l}_8\rangle = \frac{1}{8} - \frac{1}{\pi^2}, \tag{2.3.32h}$$

in the three-particle sector of ρ_C.

We can diagonalize the P_C-particle sectors of ρ_C separately. The zero-particle and three-particle cluster density-matrix weights can be read off as

$$w_{3,0} = \left(\frac{1}{2\sqrt{2}} - \frac{1}{\pi}\right)\left(\frac{1}{2\sqrt{2}} + \frac{1}{\pi}\right) = w_{3,3}. \tag{2.3.33}$$

The one-particle and two-particle cluster density-matrix weights can then be obtained using *Mathematica* as

$$\begin{aligned} w_{3,1,1} &= \left(\frac{1}{2\sqrt{2}} + \frac{1}{\pi}\right)^2, \\ w_{3,1,2} &= \left(\frac{1}{2\sqrt{2}} - \frac{1}{\pi}\right)\left(\frac{1}{2\sqrt{2}} + \frac{1}{\pi}\right), \\ w_{3,1,3} &= \left(\frac{1}{2\sqrt{2}} - \frac{1}{\pi}\right)^2; \end{aligned} \tag{2.3.34}$$

and

$$\begin{aligned} w_{3,2,1} &= \left(\frac{1}{2\sqrt{2}} + \frac{1}{\pi}\right)^2, \\ w_{3,2,2} &= \left(\frac{1}{2\sqrt{2}} - \frac{1}{\pi}\right)\left(\frac{1}{2\sqrt{2}} + \frac{1}{\pi}\right), \\ w_{3,2,3} &= \left(\frac{1}{2\sqrt{2}} - \frac{1}{\pi}\right)^2. \end{aligned} \tag{2.3.35}$$

As with the case of $N_C = 2$, we find degeneracies

$$\begin{aligned} w_{3,0} &= w_{3,1,2} = w_{3,2,2} = w_{3,3}, \\ w_{3,1,1} &= w_{3,2,1}, \quad w_{3,1,3} = w_{3,2,3}, \end{aligned} \tag{2.3.36}$$

and the relations between ratios

$$\frac{w_{3,1,1}}{w_{3,0}} = \frac{w_{3,0}}{w_{3,1,3}}, \quad \frac{w_{3,2,1}}{w_{3,0}} = \frac{w_{3,0}}{w_{3,2,3}}. \tag{2.3.37}$$

At this stage, these degeneracies and relations between ratios of cluster density-matrix weights are a mystery to us.

2.3.2.3 $N_C = 4$

For a cluster of $N_C = 4$ sites on an infinite chain, we write down the $D_C = 2^4 = 16$ referencing operators, calculate their products for the nonzero cluster density-matrix elements, simplify and normal order these products, before taking their expectations to write the matrix elements in terms of the filling fraction $\bar{n}$ and the reduced two-point functions $g(r)$, for $r = 1, 2, 3$. The nonzero matrix elements are too numerous and messy to write down, so we write them down only for the case of half-filling, $\bar{n} = \frac{1}{2}$, where $g(1) = \frac{2}{\pi}$, $g(2) = 0$ and $g(3) = -\frac{1}{3\pi}$.

The cluster density matrix ρ_C has a total of five diagonal blocks, corresponding to $P_C = 0, 1, 2, 3, 4$ spinless fermions within the cluster. These block-diagonal matrices have ranks 1, 4, 6, 4, and 1. For the zero-particle sector of ρ_C, we find the matrix element at half-filling to be

$$\langle 0000|\rho_C|0000\rangle = \frac{1}{16} - \frac{7}{9\pi^2} + \frac{16}{9\pi^4}. \tag{2.3.38}$$

This is also the zero-particle cluster density-matrix weight

$$w_{4,0} = \frac{1}{16} - \frac{7}{9\pi^2} + \frac{16}{9\pi^4} = 0.00194257\ldots. \tag{2.3.39}$$

For the one-particle sector of ρ_C, we find the $4{\times}4 = 16$ matrix elements at half-filling to be

$$\langle 1000|\rho_C|1000\rangle = \frac{1}{16} - \frac{2}{9\pi^2} - \frac{16}{9\pi^4}, \tag{2.3.40a}$$

$$\langle 1000|\rho_C|0100\rangle = \frac{1}{4\pi} - \frac{4}{3\pi^3}, \tag{2.3.40b}$$

$$\langle 1000|\rho_C|0010\rangle = \frac{1}{3\pi^2}, \tag{2.3.40c}$$

$$\langle 1000|\rho_C|0001\rangle = \frac{4}{3\pi^3} - \frac{1}{12\pi}; \tag{2.3.40d}$$

$$\langle 0100|\rho_C|1000\rangle = \frac{1}{4\pi} - \frac{4}{3\pi^3}, \tag{2.3.40e}$$

$$\langle 0100|\rho_C|0100\rangle = \frac{1}{16} + \frac{2}{9\pi^2} - \frac{16}{9\pi^4}, \tag{2.3.40f}$$

$$\langle 0100|\rho_C|0010\rangle = \frac{1}{4\pi} - \frac{4}{9\pi^3}, \tag{2.3.40g}$$

$$\langle 0100|\rho_C|0001\rangle = \frac{1}{3\pi^2}; \tag{2.3.40h}$$

$$\langle 0010|\rho_C|1000\rangle = \frac{1}{3\pi^2}, \tag{2.3.40i}$$

$$\langle 0010|\rho_C|0100\rangle = \frac{1}{4\pi} - \frac{4}{9\pi^3}, \tag{2.3.40j}$$

$$\langle 0010|\rho_C|0010\rangle = \frac{1}{16} + \frac{2}{9\pi^2} - \frac{16}{9\pi^4}, \tag{2.3.40k}$$

$$\langle 0010|\rho_C|0001\rangle = \frac{1}{4\pi} - \frac{4}{3\pi^3}; \tag{2.3.40l}$$

$$\langle 0001|\rho_C|1000\rangle = \frac{4}{3\pi^3} - \frac{1}{12\pi}, \tag{2.3.40m}$$

$$\langle 0001|\rho_C|0100\rangle = \frac{1}{3\pi^2}, \tag{2.3.40n}$$

$$\langle 0001|\rho_C|0010\rangle = \frac{1}{4\pi} - \frac{4}{3\pi^3}, \tag{2.3.40o}$$

$$\langle 0001|\rho_C|0001\rangle = \frac{1}{16} - \frac{2}{9\pi^2} - \frac{16}{9\pi^4}. \tag{2.3.40p}$$

Diagonalizing the diagonal-block matrix for this sector using *Mathematica*, we find the one-particle cluster density-matrix weights

$$w_{4,1,1} = \frac{A + C}{144\pi^8} = 0.169659\ldots, \tag{2.3.41a}$$

$$w_{4,1,2} = \frac{B + D}{144\pi^8} = 0.00675675\ldots, \tag{2.3.41b}$$

$$w_{4,1,3} = \frac{A - C}{144\pi^8} = 0.000560044\ldots, \tag{2.3.41c}$$

$$w_{4,1,4} = \frac{B - D}{144\pi^8} = 0.0000223041\ldots, \tag{2.3.41d}$$

where

$$\begin{aligned} A &= -256\pi^4 + 64\pi^5 + 12\pi^7 + 9\pi^8, \\ B &= -256\pi^4 - 64\pi^5 - 12\pi^7 + 9\pi^8, \\ C &= 4\sqrt{13(256\pi^{10} - 128\pi^{11} - 80\pi^{12} + 24\pi^{13} + 9\pi^{14})}, \\ D &= 4\sqrt{13(256\pi^{10} + 128\pi^{11} - 80\pi^{12} - 24\pi^{13} + 9\pi^{14})}. \end{aligned} \tag{2.3.42}$$

For the two-particle sector of ρ_C, we find the $6\times6 = 36$ matrix elements at half-filling to be

$$\langle 1100|\rho_C|1100\rangle = \frac{1}{16} - \frac{2}{9\pi^2} + \frac{16}{9\pi^4}, \tag{2.3.43a}$$

$$\langle 1100|\rho_C|1010\rangle = \langle 1010|\rho_C|1100\rangle = \frac{1}{4\pi} + \frac{4}{9\pi^3}, \tag{2.3.43b}$$

$$\langle 1100|\rho_C|1001\rangle = \langle 1001|\rho_C|1100\rangle = \frac{2}{3\pi^2}, \tag{2.3.43c}$$

$$\langle 1100|\rho_C|0110\rangle = \langle 0110|\rho_C|1100\rangle = \frac{2}{3\pi^2}, \tag{2.3.43d}$$

$$\langle 1100|\rho_C|0101\rangle = \langle 0101|\rho_C|1100\rangle = \frac{1}{12\pi} + \frac{4}{3\pi^3}, \tag{2.3.43e}$$

$$\langle 1100|\rho_C|0011\rangle = \langle 0011|\rho_C|1100\rangle = \frac{1}{3\pi^2}; \tag{2.3.43f}$$

$$\langle 1010|\rho_C|1010\rangle = \frac{1}{16} + \frac{7}{9\pi^2} + \frac{16}{9\pi^4}, \tag{2.3.43g}$$

$$\langle 1010|\rho_C|1001\rangle = \langle 1001|\rho_C|1010\rangle = \frac{1}{4\pi} + \frac{4}{3\pi^3}, \tag{2.3.43h}$$

$$\langle 1010|\rho_C|0110\rangle = \langle 0110|\rho_C|1010\rangle = \frac{1}{4\pi} + \frac{4}{3\pi^3}, \tag{2.3.43i}$$

$$\langle 1010|\rho_C|0101\rangle = \langle 0101|\rho_C|1010\rangle = \frac{4}{3\pi^2}, \tag{2.3.43j}$$

$$\langle 1010|\rho_C|0011\rangle = \langle 0011|\rho_C|1010\rangle = \frac{1}{12\pi} + \frac{4}{3\pi^3}; \tag{2.3.43k}$$

$$\langle 1001|\rho_C|1001\rangle = \frac{1}{16} + \frac{2}{9\pi^2} + \frac{16}{9\pi^4}, \tag{2.3.43l}$$

$$\langle 1001|\rho_C|0110\rangle = \langle 0110|\rho_C|1001\rangle = \frac{1}{\pi^2}, \tag{2.3.43m}$$

$$\langle 1001|\rho_C|0101\rangle = \langle 0101|\rho_C|1001\rangle = \frac{1}{4\pi} + \frac{4}{3\pi^3}, \tag{2.3.43n}$$

$$\langle 1001|\rho_C|0011\rangle = \langle 0011|\rho_C|1001\rangle = \frac{2}{3\pi^2}; \tag{2.3.43o}$$

$$\langle 0110|\rho_C|0110\rangle = \frac{1}{16} + \frac{2}{9\pi^2} + \frac{16}{9\pi^4}, \tag{2.3.43p}$$

$$\langle 0110|\rho_C|0101\rangle = \langle 0101|\rho_C|0110\rangle = \frac{1}{4\pi} + \frac{4}{3\pi^3}, \tag{2.3.43q}$$

$$\langle 0110|\rho_C|0011\rangle = \langle 0011|\rho_C|0110\rangle = \frac{2}{3\pi^2}; \tag{2.3.43r}$$

$$\langle 0101|\rho_C|0101\rangle = \frac{1}{16} + \frac{7}{9\pi^2} + \frac{16}{9\pi^4}, \tag{2.3.43s}$$

$$\langle 0101|\rho_C|0011\rangle = \langle 0011|\rho_C|0101\rangle = \frac{1}{4\pi} + \frac{4}{9\pi^3}; \tag{2.3.43t}$$

$$\langle 0011|\rho_C|0011\rangle = \frac{1}{16} - \frac{2}{9\pi^2} + \frac{16}{9\pi^4}. \tag{2.3.43u}$$

Diagonalizing the diagonal-block matrix for this sector using *Mathematica*, we find the two-particle cluster density-matrix weights to be

$$\begin{aligned} w_{4,2,1} &= \frac{256 + 304\pi^2 + 9\pi^4 + 8\sqrt{13}\,\pi(16 + 3\pi^2)}{144\pi^4} \\ &= 0.589295\ldots, \end{aligned} \tag{2.3.44a}$$

$$\begin{aligned} w_{4,2,2} &= \frac{256 - 128\pi - 80\pi^2 + 24\pi^3 + 9\pi^4}{144\pi^4} \\ &= 0.0488447\ldots, \end{aligned} \tag{2.3.44b}$$

$$\begin{aligned} w_{4,2,3} = w_{2,4} &= \frac{256 - 112\pi^2 + 9\pi^4}{144\pi^4} \\ &= 0.00194527\ldots, \end{aligned} \tag{2.3.44c}$$

$$\begin{aligned} w_{4,2,5} &= \frac{256 + 128\pi - 80\pi^2 - 24\pi^3 + 9\pi^4}{144\pi^4} \\ &= 0.0000774716\ldots, \end{aligned} \tag{2.3.44d}$$

$$\begin{aligned} w_{4,2,6} &= \frac{(256 - 112\pi^2 + 9\pi^4)^2}{144\pi^4(256 + 304\pi^2 + 9\pi^4 + 8\sqrt{13}\,\pi(16 + 3\pi^2))} \\ &= 6.42136\cdots\times 10^{-6}. \end{aligned} \tag{2.3.44e}$$

Because of particle-hole symmetry at half-filling, the three-particle cluster density matrix is identical to the one-particle cluster density matrix element-wise, while the four-particle cluster density-matrix element, which is also the four-particle cluster

density-matrix weight $w_{4,4}$, is identical to the zero-particle cluster density-matrix weight $w_{4,0}$. Apart from these expected degeneracies, we also find that

$$\frac{w_{4,1,1}}{w_{4,0}} = \frac{w_{4,0}}{w_{4,1,4}} \neq \frac{w_{4,1,2}}{w_{4,0}} = \frac{w_{4,0}}{w_{4,1,3}}, \tag{2.3.45}$$

and

$$\frac{w_{4,2,1}}{w_{4,0}} = \frac{w_{4,0}}{w_{4,2,6}} \neq \frac{w_{4,2,2}}{w_{4,0}} = \frac{w_{4,0}}{w_{4,2,5}} \neq \frac{w_{4,2,3}}{w_{4,0}} = \frac{w_{4,0}}{w_{4,2,4}} = 1. \tag{2.3.46}$$

We shall see in Section 2.5.2 that this is also the consequence of particle-hole symmetry.

2.3.3 Index Structure of the Cluster Density-Matrix Elements

In general, for a cluster of N_C sites, we see from Section 2.3.2 that we will need to write down a total of 2^{N_C} referencing operators to calculate the $\sim 2^{N_C}$ nonzero cluster density-matrix elements. For large clusters, this is extremely tedious and has to be automated, but for small clusters, containing $N_C = 3$ sites for example, we find that we can write down the cluster density-matrix elements out explicitly as

$$\langle 000|\rho_C|000\rangle = 1 - \left(G_{\overline{1}1} + G_{\overline{2}2} + G_{\overline{3}3}\right) - \left(G_{\overline{12}12} + G_{\overline{13}13} + G_{\overline{23}23}\right) - G_{\overline{123}123}; \tag{2.3.47a}$$

$$\langle 001|\rho_C|001\rangle = G_{\overline{3}3} + G_{\overline{13}13} + G_{\overline{23}23} - G_{\overline{123}123}, \tag{2.3.47b}$$

$$\langle 001|\rho_C|010\rangle = G_{\overline{3}2} + G_{\overline{13}12}, \tag{2.3.47c}$$

$$\langle 001|\rho_C|100\rangle = G_{\overline{3}1} - G_{\overline{23}12}, \tag{2.3.47d}$$

$$\langle 010|\rho_C|001\rangle = G_{\overline{3}2} + G_{\overline{13}12}, \tag{2.3.47e}$$

$$\langle 010|\rho_C|010\rangle = G_{\overline{2}2} + G_{\overline{12}12} + G_{\overline{23}23} - G_{\overline{123}123}, \tag{2.3.47f}$$

$$\langle 010|\rho_C|100\rangle = G_{\overline{2}1} + G_{\overline{23}13}, \tag{2.3.47g}$$

$$\langle 100|\rho_C|001\rangle = G_{\overline{1}3} - G_{\overline{12}23}, \tag{2.3.47h}$$

$$\langle 100|\rho_C|010\rangle = G_{\overline{1}2} + G_{\overline{13}23}, \tag{2.3.47i}$$

$$\langle 100|\rho_C|100\rangle = G_{\overline{1}1} + G_{\overline{12}12} + G_{\overline{13}13} - G_{\overline{123}123}; \tag{2.3.47j}$$

$$\langle 011|\rho_C|011\rangle = -G_{\overline{23}23} + G_{\overline{123}123}, \tag{2.3.47k}$$

$$\langle 011|\rho_C|101\rangle = -G_{\overline{23}13}, \tag{2.3.47l}$$

$$\langle 011|\rho_C|110\rangle = -G_{\overline{23}12}, \tag{2.3.47m}$$

$$\langle 101|\rho_C|011\rangle = -G_{\overline{13}23}, \tag{2.3.47n}$$

$$\langle 101|\rho_C|101\rangle = -G_{\overline{13}13} + G_{\overline{123}123}, \tag{2.3.47o}$$

$$\langle 101|\rho_C|110\rangle = -G_{\overline{13}12}, \tag{2.3.47p}$$

$$\langle 110|\rho_C|011\rangle = -G_{\overline{12}23}, \tag{2.3.47q}$$

$$\langle 110|\rho_C|101\rangle = -G_{\overline{12}13}, \tag{2.3.47r}$$

$$\langle 110|\rho_C|110\rangle = -G_{\overline{12}12} + G_{\overline{123}123}; \tag{2.3.47s}$$

$$\langle 111|\rho_C|111\rangle = -G_{\overline{123}123}, \tag{2.3.47t}$$

in terms of the two-point function

$$G_{\bar{i}j} = \langle c_i^\dagger c_j\rangle = \bar{n}g(|i-j|), \tag{2.3.48}$$

and the $2n$-point functions

$$G_{\overline{i_1 i_2} j_1 j_2} = (-1)^{\frac{2(2-1)}{2}} \begin{vmatrix} G_{\overline{i_1} j_1} & G_{\overline{i_1} j_2} \\ G_{\overline{i_2} j_1} & G_{\overline{i_2} j_2} \end{vmatrix}, \tag{2.3.49a}$$

$$G_{\overline{i_1 i_2 i_3} j_1 j_2 j_3} = (-1)^{\frac{3(3-1)}{2}} \begin{vmatrix} G_{\overline{i_1} j_1} & G_{\overline{i_1} j_2} & G_{\overline{i_1} j_3} \\ G_{\overline{i_2} j_1} & G_{\overline{i_2} j_2} & G_{\overline{i_2} j_3} \\ G_{\overline{i_3} j_1} & G_{\overline{i_3} j_2} & G_{\overline{i_3} j_3} \end{vmatrix}, \tag{2.3.49b}$$

of the infinite chain of noninteracting spinless fermions, where $\bar{n}$ is the filling fraction, $i, i_1, i_2, \ldots, j, j_1, j_2, \cdots = 1, \ldots, N_C$ are sites within the cluster, and $g(r)$ is the reduced two-point function defined in (2.3.15). As shown explicitly above, the $2n$-point functions $G_{\overline{i_1 \cdots i_n} j_1 \cdots j_n}$ Wick factorizes into sums of products of two-point functions $G_{\bar{i}j}$ for our noninteracting system, with an overall fermion factor of $(-1)^{n(n-1)/2}$.

At this point, let us note that since the two-point functions $G_{\bar{i}j}$ are labelled by two indices — the first the site on which the creation operator $c_i^\dagger$ acts, and the second the site on which the annihilation operator c_j acts — it is convenient to organize them into a *system Green-function matrix* $\mathscr{G}$ given by

$$\mathscr{G} = \begin{bmatrix} G_{\bar{1}1} & \cdots & G_{\bar{1}N_C} & G_{\bar{1}N_C+1} & \cdots & G_{\bar{1}N} \\ G_{\bar{2}1} & \cdots & G_{\bar{2}N_C} & G_{\bar{2}N_C+1} & \cdots & G_{\bar{2}N} \\ \vdots & \ddots & \vdots & \vdots & \ddots & \vdots \\ G_{\overline{N_C}1} & \cdots & G_{\overline{N_C}N_C} & G_{\overline{N_C}N_C+1} & \cdots & G_{\overline{N_C}N} \\ G_{\overline{N_C+1}1} & \cdots & G_{\overline{N_C+1}N_C} & G_{\overline{N_C+1}N_C+1} & \cdots & G_{\overline{N_C+1}N} \\ \vdots & \ddots & \vdots & \vdots & \ddots & \vdots \\ G_{\bar{N}1} & \cdots & G_{\bar{N}N_C} & G_{\bar{N}N_C+1} & \cdots & G_{\bar{N}N} \end{bmatrix}, \tag{2.3.50}$$

where $N \to \infty$ is the number of sites within the system. The matrix

$$G_C = \begin{bmatrix} G_{\bar{1}1} & G_{\bar{1}2} & \cdots & G_{\bar{1}N_C} \\ G_{\bar{2}1} & G_{\bar{2}2} & \cdots & G_{\bar{2}N_C} \\ \vdots & \vdots & \ddots & \vdots \\ G_{\overline{N_C}1} & G_{\overline{N_C}2} & \cdots & G_{\overline{N_C}N_C} \end{bmatrix} \tag{2.3.51}$$

is the *restriction of $\mathscr{G}$ to the cluster*, and we call G_C the *cluster Green-function matrix*. As a result of the translational invariance of the Hamiltonian H_t in (2.1.1), $\mathscr{G}$ is also translationally invariant. In real space, this means that its matrix elements $\mathscr{G}_{ij} = G_{\bar{i}j} = \langle c_i^\dagger c_j \rangle$ are functions only of $|i-j|$. When $\mathscr{G}$ is restricted to the cluster to give G_C, however, this translational invariance is lost, due to the fact that the presence of a cluster in the system allows an unambiguous definition of the origin.

From (2.3.5) and (2.3.8), we see on the one hand that the cluster density-matrix elements $\langle \mathbf{l}|\rho_C|\mathbf{l}'\rangle$ can all be written as sums of $2n$-point functions — which themselves factor into sums of products of two-point functions — and so we find that $\langle \mathbf{l}|\rho_C|\mathbf{l}'\rangle$ are

all functions of $G_{\overline{i'}j'}$. On the other hand, the one-particle sector of ρ_C contains matrix elements $\langle \mathbf{l}|\rho_C|\mathbf{l}'\rangle$ connecting the cluster occupation-number basis states $|\mathbf{l}\rangle$ and $|\mathbf{l}'\rangle$, which contain one particle each at sites, say, i and j respectively. Therefore, the matrix elements within the one-particle sector $\rho_{C,1}$ of the cluster density matrix may be indexed using i and j instead of $\mathbf{l}$ and $\mathbf{l}'$. Diligently writing down the polynomial expressions

$$\begin{aligned}(\rho_{C,1})_{ij} = &\sum_{i_1,j_1}^{N_C} \alpha^{(1)}_{ij;i_1j_1} G_{\overline{i}_1 j_1} + \sum_{\substack{i_1,i_2,\\ j_1,j_2}}^{N_C} \alpha^{(2)}_{ij;i_1i_2j_1j_2} G_{\overline{i}_1 j_1} G_{\overline{i}_2 j_2} + \cdots + \\ &\sum_{\substack{i_1,\ldots,i_{N_C},\\ j_1,\ldots,j_{N_C}}}^{N_C} \alpha^{(N_C)}_{ij;i_1\cdots i_{N_C}j_1\cdots j_{N_C}} G_{\overline{i}_1 j_1}\cdots G_{\overline{i_{N_C}} j_{N_C}},\end{aligned} \tag{2.3.52}$$

we find that: (a) the coefficients $\alpha^{(n)}_{ij;i_1\cdots i_n j_1\cdots j_n}$ are independent of i and j; and (b) indices other than i and j always appear in pairs, as if they are summed over.

2.3.3.1 $N_C = 2$

In the $2n$-point function $G_{\overline{i_1\cdots i_n} j_1\cdots j_n}$, the bar over the creation-operator indices $i_1,\ldots,i_n$ is used to distinguish them from the annihilation-operator indices $j_1,\ldots,j_n$. For the two-point function $G_{\bar{i}j}$, it is clear that the first index i refers to the creation operator, while the second index j refers to the annihilation operator. We therefore drop the bar over the creation-operator index, when dealing exclusively with two-point functions.

For a cluster of $N_C = 2$ sites on an infinite chain, we rewrite the one-particle cluster density-matrix elements using the index structure described above as

$$(\rho_{C,1})_{11} = G_{11} + G_{1212} = G_{11} - G_{11}G_{22} + G_{12}G_{21} = G_{11} - \det G_C, \tag{2.3.53a}$$

$$(\rho_{C,1})_{12} = G_{12}, \tag{2.3.53b}$$

$$(\rho_{C,1})_{21} = G_{21}, \tag{2.3.53c}$$

$$(\rho_{C,1})_{22} = G_{22} + G_{1212} = G_{22} - \det G_C. \tag{2.3.53d}$$

Looking at the matrix elements, we find that we can write a matrix relationship

$$\rho_{C,1} = G_C - \det G_C \, \mathbb{1} \tag{2.3.54}$$

between the one-particle cluster density matrix $\rho_{C,1}$ and the cluster Green-function matrix G_C.

A simple consequence of $\rho_{C,1}$ being the function (2.3.54) of G_C is that $\rho_{C,1}$ and G_C are simultaneously diagonalizable, and as such, the one-particle cluster density-matrix weights w_l must be given in terms of the cluster Green-function matrix eigenvalues λ_l as

$$w_l = \lambda_l - \prod_{l'} \lambda_{l'}. \tag{2.3.55}$$

We checked this relation between eigenvalues numerically for various filling fractions, and find it holding true in every case.

2.3.3.2 $N_C = 3$

For a cluster of $N_C = 3$ sites on an infinite chain, there are nine one-particle cluster density-matrix elements. Instead of listing all of them, as we have done for the case of $N_C = 2$, let us consider a *particular* one-particle cluster density-matrix element,

$$(\rho_{C,1})_{21} = G_{21} - G_{21}G_{33} + G_{23}G_{31}. \tag{2.3.56}$$

If, like the case of $N_C = 2$, a matrix relationship exists between $\rho_{C,1}$ and G_C, then (2.3.56) can be written as

$$(\rho_{C,1})_{21} = [f(G_C)]_{21}, \tag{2.3.57}$$

for some matrix function $f(G_C)$ of the cluster Green-function matrix G_C.

Clearly, the leading term G_{21} in (2.3.56) tells us that the leading term in $f(G_C)$ ought to be G_C, so we must now figure out what remaining terms in $f(G_C)$ would give $G_{21}G_{33}$ and $G_{23}G_{31}$. Now, the term $G_{23}G_{31}$ looks like it is part of $(G_C^2)_{21} = G_{21}G_{11} + G_{22}G_{21} +$

$G_{23}G_{31}$, except for the fact that $G_{21}G_{11} + G_{22}G_{21}$ do not appear in (2.3.56). We must therefore add and subtract them in (2.3.56), to get

$$\begin{aligned}(\rho_{C,1})_{21} &= G_{21} - G_{21}G_{33} + G_{23}G_{31} \\ &= G_{21} - G_{21}G_{11} - G_{21}G_{22} - G_{21}G_{33} + G_{21}G_{11} + G_{22}G_{21} + G_{23}G_{31}.\end{aligned} \tag{2.3.58}$$

We find then that the subtracted terms $-(G_{21}G_{11} + G_{21}G_{22})$ combine with $-G_{21}G_{33}$ to give $-G_{21}\,\mathrm{Tr}\,G_C$, and thus

$$(\rho_{C,1})_{21} = G_{21} - G_{21}\,\mathrm{Tr}\,G_C + (G_C^2)_{21}. \tag{2.3.59}$$

To see whether a formula of the same form as (2.3.59) holds for the other one-particle cluster density-matrix elements, we check another off-diagonal matrix element,

$$\begin{aligned}(\rho_{C,1})_{32} &= G_{32} - G_{32}G_{11} + G_{31}G_{12} \\ &= G_{32} - G_{32}(G_{11} + G_{22} + G_{33}) + G_{31}G_{12} + G_{32}G_{22} + G_{33}G_{32} \\ &= G_{32} - G_{32}\,\mathrm{Tr}\,G_C + (G_C^2)_{32},\end{aligned} \tag{2.3.60}$$

and more importantly, a digonal matrix element,

$$\begin{aligned}(\rho_{C,1})_{11} &= G_{11} - G_{11}G_{22} + G_{12}G_{12} - G_{11}G_{33} + G_{13}G_{13} + \begin{vmatrix} G_{11} & G_{12} & G_{13} \\ G_{21} & G_{22} & G_{23} \\ G_{31} & G_{32} & G_{33} \end{vmatrix} \\ &= G_{11} - G_{11}(G_{11} + G_{22} + G_{33}) + G_{11}G_{11} + G_{12}G_{12} + G_{13}G_{13} + \det G.\end{aligned} \tag{2.3.61}$$

Using the fact that the two-point functions are symmetric with respect to exchange of the indices i and j, i.e. $G_{ij} = G_{ji}$, we can write the diagonal matrix element as

$$\begin{aligned}(\rho_{C,1})_{11} &= G_{11} - G_{11}(G_{11} + G_{22} + G_{33}) + G_{11}G_{11} + G_{12}G_{12} + G_{13}G_{13} + \det G \\ &= G_{11} - G_{11}(G_{11} + G_{22} + G_{33}) + G_{11}G_{11} + G_{12}G_{21} + G_{13}G_{31} + \det G \\ &= G_{11} - G_{11}\,\mathrm{Tr}\,G_C + (G_C^2)_{11} + \det G_C.\end{aligned} \tag{2.3.62}$$

We find an extra term, $\det G_C$, for the diagonal one-particle cluster density-matrix elements as compared to the off-diagonal one-particle cluster density-matrix elements, but as we have seen for the case of $N_C = 2$, this is not a problem, and we can write down the matrix relationship

$$\rho_{C,1} = G_C - G_C \operatorname{Tr} G_C + G_C^2 + \det G_C \, \mathbb{1} \tag{2.3.63}$$

between the one-particle cluster density matrix $\rho_{C,1}$ and the cluster Green-function matrix G_C.

With $\rho_{C,1}$ being related to G_C by (2.3.54), we expect the one-particle cluster density-matrix weights w_l to be given in terms of the cluster Green-function matrix eigenvalues λ_l as

$$w_l = \lambda_l \left(1 - \sum_{l'} \lambda_{l'} \right) + \lambda_l^2 + \prod_{l'} \lambda_{l'}. \tag{2.3.64}$$

We checked this relation between eigenvalues numerically for various filling fractions, and find it holding true in every case.

2.3.3.3 $N_C = 4$

For a cluster of $N_C = 4$ sites on an infinite chain, four (out of sixteen) one-particle cluster density-matrix elements are

$$\begin{aligned}(\rho_{C,1})_{11} = {} & G_{11} + G_{\overline{14}14} + G_{\overline{13}13} + G_{\overline{12}12} - \\ & G_{\overline{134}134} - G_{\overline{124}124} - G_{\overline{123}123} - G_{\overline{1234}1234}, \end{aligned} \tag{2.3.65a}$$

$$(\rho_{C,1})_{12} = G_{12} + G_{\overline{14}24} + G_{\overline{13}23} - G_{\overline{134}234}, \tag{2.3.65b}$$

$$(\rho_{C,1})_{13} = G_{13} + G_{\overline{14}34} - G_{\overline{12}23} + G_{\overline{124}234}, \tag{2.3.65c}$$

$$(\rho_{C,1})_{14} = G_{14} - G_{\overline{13}34} - G_{\overline{12}24} - G_{\overline{123}234}. \tag{2.3.65d}$$

The off-diagonal matrix elements $(\rho_{C,1})_{12}$, $(\rho_{C,1})_{13}$, and $(\rho_{C,1})_{14}$ have the same structure, which is significantly simpler than that of the diagonal matrix element $(\rho_{C,1})_{11}$, so

we will start figuring out the relationship between $\rho_{C,1}$ and G_C from $(\rho_{C,1})_{12}$. First of all, we note that

$$\begin{aligned}(\rho_{C,1})_{12} &= G_{12} - G_{12}G_{44} + G_{14}G_{42} - G_{12}G_{33} + G_{13}G_{32} + \begin{vmatrix} G_{12} & G_{13} & G_{14} \\ G_{32} & G_{33} & G_{34} \\ G_{42} & G_{43} & G_{44} \end{vmatrix} \\ &= (\text{linear in } G_C) + (\text{quadratic in } G_C) + (\text{cubic in } G_C)\end{aligned} \tag{2.3.66}$$

is a polynomial function of G_C containing up to the third power of G_C. From (2.3.66), we see that the term linear in G_C is obvious: it is simply $(G_C)_{12} = G_{12}$. For the term quadratic in G_C, we find, by doing the same kind of adding and subtracting extra terms quadratic in G_C in the case of $N_C = 3$, that

$$\begin{aligned}&-G_{12}G_{44} + G_{14}G_{42} - G_{12}G_{33} + G_{13}G_{32} \\ &= -G_{12}(G_{11} + G_{22} + G_{33} + G_{44}) + G_{11}G_{12} + G_{12}G_{22} + G_{13}G_{32} + G_{14}G_{42} \\ &= -G_{12}\,\mathrm{Tr}\,G_C + (G_C^2)_{12}.\end{aligned} \tag{2.3.67}$$

This has exactly the same form as the quadratic terms for the case of $N_C = 3$.

To deduce the form of the cubic terms, let us organize all the possible cubic terms into products of G_C and its trace. These are

$$\begin{aligned}(G_C^3)_{12} = {} & G_{12}(G_{11}G_{11} + G_{12}G_{21} + G_{13}G_{31} + G_{14}G_{41}) + \\ & G_{22}(G_{11}G_{12} + G_{12}G_{22} + G_{13}G_{32} + G_{14}G_{42}) + \\ & G_{32}(G_{11}G_{13} + G_{12}G_{23} + G_{13}G_{33} + G_{14}G_{43}) + \\ & G_{42}(G_{11}G_{14} + G_{12}G_{24} + G_{13}G_{34} + G_{14}G_{44}),\end{aligned} \tag{2.3.68a}$$

$$\begin{aligned}(G_C^2)_{12}\,\mathrm{Tr}\,G_C = {} & G_{11}G_{11}G_{12} + 2G_{11}G_{12}G_{22} + G_{12}G_{22}G_{22} + \\ & G_{11}G_{13}G_{32} + G_{13}G_{22}G_{32} + G_{11}G_{12}G_{33} + \\ & G_{12}G_{22}G_{33} + G_{13}G_{32}G_{33} + G_{11}G_{14}G_{42} +\end{aligned}$$

$$G_{14}G_{22}G_{42} + G_{14}G_{33}G_{42} + G_{11}G_{12}G_{44} +$$
$$G_{12}G_{22}G_{44} + G_{13}G_{32}G_{44} + G_{14}G_{42}G_{44}, \tag{2.3.68b}$$

$$G_{12}\,\mathrm{Tr}\,G_C^2 = G_{11}G_{11}G_{12} + 2G_{12}G_{12}G_{21} + G_{12}G_{22}G_{22} +$$
$$2G_{12}G_{13}G_{31} + 2G_{12}G_{23}G_{32} + G_{12}G_{33}G_{33} +$$
$$2G_{12}G_{14}G_{41} + 2G_{12}G_{24}G_{42} + 2G_{12}G_{34}G_{43} + G_{12}G_{44}G_{44}, \tag{2.3.68c}$$

$$G_{12}(\mathrm{Tr}\,G_C)^2 = G_{11}G_{11}G_{12} + 2G_{11}G_{12}G_{22} + G_{12}G_{22}G_{22} +$$
$$2G_{11}G_{12}G_{33} + 2G_{12}G_{22}G_{33} + G_{12}G_{33}G_{33} +$$
$$2G_{11}G_{12}G_{44} + 2G_{12}G_{22}G_{44} + 2G_{12}G_{33}G_{44} + G_{12}G_{44}G_{44}. \tag{2.3.68d}$$

There are also the cubic functions $\mathrm{Tr}\,G_C^3$, $\mathrm{Tr}\,G_C\,\mathrm{Tr}\,G_C^2$ and $(\mathrm{Tr}\,G_C)^3$ of G_C, but as we have seen in the cases of $N_C = 2$ and $N_C = 3$, these index-free functions of G_C must be associated with the diagonal elements, and as such do not contribute to the matrix element $(\rho_{C,1})_{12}$.

Comparing these with the cubic group of terms

$$-G_{14}G_{33}G_{42} - G_{12}G_{34}G_{43} - G_{13}G_{32}G_{44} + G_{13}G_{34}G_{42} + G_{14}G_{32}G_{43} + G_{12}G_{33}G_{44} \tag{2.3.69}$$

in $(\rho_{C,1})_{12}$, we find that the cubic combination

$$(G_C^3)_{12} - (G_C^2)_{12}\,\mathrm{Tr}\,G_C = -G_{14}G_{33}G_{42} - G_{13}G_{32}G_{44} + G_{13}G_{34}G_{42} +$$
$$G_{14}G_{32}G_{43} + G_{12}G_{12}G_{21} - G_{11}G_{12}G_{22} +$$
$$G_{12}G_{13}G_{31} + G_{12}G_{23}G_{32} - G_{11}G_{12}G_{33} - \tag{2.3.70}$$
$$G_{12}G_{22}G_{33} + G_{12}G_{14}G_{41} + G_{12}G_{24}G_{42} -$$
$$G_{11}G_{12}G_{44} - G_{12}G_{22}G_{44}$$

contains terms which agrees with four out of six of the cubic terms of $(\rho_{C,1})_{12}$.

Also, we find that the cubic combination

$$\begin{aligned}\tfrac{1}{2}G_{12}[\operatorname{Tr}G_C^2-(\operatorname{Tr}G_C)^2] = {} & G_{12}G_{12}G_{21}-G_{11}G_{12}G_{22}+G_{12}G_{13}G_{31}+\\ & G_{12}G_{23}G_{32}-G_{11}G_{12}G_{33}-G_{12}G_{22}G_{33}+\\ & G_{12}G_{14}G_{41}+G_{12}G_{24}G_{42}+G_{12}G_{34}G_{43}-\\ & G_{11}G_{12}G_{44}-G_{12}G_{22}G_{44}-G_{12}G_{33}G_{44}\end{aligned} \tag{2.3.71}$$

looks similar to the extraneous terms in $G_C^3-G_C^2\operatorname{Tr}G_C$. Indeed, the cubic combination

$$\begin{aligned}\{G_C^3-G_C^2\operatorname{Tr}G_C-\tfrac{1}{2}G_C[\operatorname{Tr}G_C^2-(\operatorname{Tr}G_C)^2]\}_{12} = {} & -G_{14}G_{33}G_{42}+\\ & G_{13}G_{34}G_{42}+G_{14}G_{32}G_{43}-G_{12}G_{34}G_{43}-G_{13}G_{32}G_{44}+G_{12}G_{33}G_{44}\end{aligned} \tag{2.3.72}$$

gives precisely the cubic group of terms in $(\rho_{C,1})_{12}$.

We then checked that the cubic group of terms in $(\rho_{C,1})_{11}$ is also given by

$$\{G_C^3-G_C^2\operatorname{Tr}G_C-\tfrac{1}{2}G_C[\operatorname{Tr}G_C^2-(\operatorname{Tr}G_C)^2]\}_{11}. \tag{2.3.73}$$

Therefore, we need not introduce any further index-free cubic functions of G_C. The only index-free function of G_C is the quartic $\det G_C = G_{\overline{1234}1234}$, so that the matrix relationship between $\rho_{C,1}$ and G_C can be written as

$$\rho_{C,1} = G_C+G_C^2-G_C\operatorname{Tr}G_C+G_C^3-G_C^2\operatorname{Tr}G_C-\tfrac{1}{2}G_C\left[\operatorname{Tr}G_C^2-(\operatorname{Tr}G_C)^2\right]-\det G_C\,\mathbb{1}. \tag{2.3.74}$$

2.3.4 Conjecture Based on Index Structure

Comparing the matrix relationships (2.3.54), (2.3.63) and (2.3.74), we find that all the terms in (2.3.54) are contained in (2.3.63), and all the terms in (2.3.63) are in turn contained in (2.3.74). In fact, after laboring hard to find the matrix relationship between $\rho_{C,1}$ and G_C for a cluster of $N_C = 5$ sites on an infinite chain, we find that all the terms

in (2.3.74) are contained in the matrix relationship for $N_C = 5$. This led us to speculate that the series expansion relation

$$\begin{aligned}\rho_{C,1} = {} & G_C + G_C^2 - G_C \operatorname{Tr}(G_C) + \\ & G_C^3 - G_C^2 \operatorname{Tr}(G_C) - \tfrac{1}{2}\left\{\operatorname{Tr}(G_C^2) - [\operatorname{Tr}(G_C)]^2\right\} G_C + \\ & G_C^4 - G_C^3 \operatorname{Tr}(G_C) - \tfrac{1}{2}\left\{\operatorname{Tr}(G_C^2) - [\operatorname{Tr}(G_C)]^2\right\} G_C^2 - \\ & \left\{\tfrac{1}{3}\operatorname{Tr}(G_C^3) - \tfrac{1}{2}\operatorname{Tr}(G_C)\operatorname{Tr}(G_C^2) + \tfrac{1}{6}[\operatorname{Tr}(G_C)^3]\right\} G_C + \cdots\end{aligned} \tag{2.3.75}$$

between $\rho_{C,1}$ and G_C might be true for all N_C.

Of course, for $N_C = 2$, (2.3.5) and (2.3.8) tell us that $\rho_{C,1}$ can be at most $O(G_C^2)$, since its matrix elements never contain terms with more than two creation and two annihilation operators. Yet (2.3.75) is perfectly valid for $N_C = 2$, because terms that are higher order than $O(G_C^2)$ vanish automatically. For $N_C = 3$ and $N_C = 4$, we find similarly that terms higher order than $O(G_C^3)$ and $O(G_C^4)$ vanish, respectively. Therefore, if we conjecture that (2.3.75) gives the leading terms to an infinite series that holds true for all $N_C > 5$, we can factorize it into

$$\rho_{C,1} = (G_C + G_C^2 + G_C^3 + \cdots) \exp\left[-\operatorname{Tr}(G_C + \tfrac{1}{2}G_C^2 + \tfrac{1}{3}G_C^3 + \cdots)\right]. \tag{2.3.76}$$

Noting that the series inside the trace is just $-\log(\mathbb{1} - G_C)$, (2.3.76) can be compactly written as

$$\rho_{C,1} = G_C(\mathbb{1} - G_C)^{-1} \det(\mathbb{1} - G_C). \tag{2.3.77}$$

We shall prove this conjecture in Section 2.4.

2.4 Derivation of Closed-Form Formula

In passing from (2.3.75) to (2.3.77), a leap of faith was required, and it would appear forbiddingly difficult to actually prove (2.3.77) for arbitrary cluster sizes N_C, by the

algebraic manipulations used in Section 2.3.3. Fortunately, an alternate technique introduced by Chung and Peschel [176] can be adapted and extended for calculating the density matrix of a finite cluster, although it comes with its own set of technical difficulties. It turns out that if the whole system were in the Fermi sea ground state, the derivation would require the inversion of singular matrices. In the end, the singularities do cancel and give a well-defined answer, but a regularization is needed to avoid divergences in the intermediate steps. In Ref. 176, Chung and Peschel avoided the inversion of singular matrices, by working with a Hamiltonian with nonzero anomalous terms containing double creation or double annihilation operators. In our case, the most natural way to deal with the problem of inverting singular matrices would be to generalize our problem to nonzero temperature, in which case the limit $T \to 0$ then provides the needed regularization.

In essence, the calculation is just that of evaluating a Gaussian integral with the usual shift in integration variables. However, because we are dealing with fermions, whose creation and annihilation operators anticommute rather than commute, additional machinery is needed to accomplish the feat of Gaussian integration. After casting the system density matrix ρ as a Gaussian of the fermion operators, we introduce fermionic coherent states with the aid of anticommuting Grassmann variables. The matrix elements of ρ between such coherent states, obtained via a translation machinery, are similarly of Gaussian form, but are now easier to handle. A Gaussian integration over the environmental degrees of freedom then yields elements of the cluster density matrix ρ_C, following which reverse translation gives ρ_C proper.

2.4.1 Exponential Form for System Density Matrix

To get the calculations underway, we consider the grand-canonical $T > 0$ density matrix ρ of the overall system that the cluster is embedded in. As always, this is given by

$$\rho = \mathscr{Q}^{-1} \exp[-\beta(H - \mu F)] \tag{2.4.1}$$

where $\beta \equiv 1/k_B T$ is the inverse temperature, μ the chemical potential, and

$$F \equiv \sum_k \tilde{c}_k^\dagger \tilde{c}_k = \sum_i c_i^\dagger c_i \tag{2.4.2}$$

is the fermion number operator. The prefactor $\mathscr{Q}^{-1}$ in (2.4.1) is just the reciprocal of the grand partition function, to ensure that $\mathrm{Tr}(\rho) = 1$.

The notations can be made more compact if we introduce the matrices Γ and its Fourier transform $\tilde{\Gamma}$, such that

$$\rho = \mathscr{Q}^{-1} \exp\left(\sum_{i,j} \Gamma_{ij} c_i^\dagger c_j\right) = \mathscr{Q}^{-1} \exp\left(\sum_k \tilde{\Gamma}_{kk} \tilde{c}_k^\dagger \tilde{c}_k\right), \tag{2.4.3}$$

where we have made use of the fact that $H - \mu F$, and hence $\tilde{\Gamma}$, is diagonal in momentum space. The matrix elements of Γ can be read off from (2.1.1) as

$$\Gamma_{ij} = \begin{cases} \beta\mu, & \text{if } i = j; \\ \beta t, & \text{if } i \text{ and } j \text{ are nearest neighbors;} \\ 0, & \text{otherwise,} \end{cases} \tag{2.4.4}$$

while those of $\tilde{\Gamma}$ can be read off from (2.1.2) as

$$\tilde{\Gamma}_{kk} = -\beta E_k, \tag{2.4.5}$$

where $E_k \equiv \epsilon_k - \mu$ is the single-particle energy measured relative to μ.

In order to prove our conjecture (2.3.77), we need to somehow relate Γ to $\mathscr{G}$. To do this, let us note that since $\mathscr{G}$ is translationally invariant, its Fourier transform $\tilde{\mathscr{G}}$ is diagonal in momentum space, with matrix elements given in the grand-canonical ensemble

as

$$\tilde{\mathscr{G}}_{kk} = \langle \tilde{c}_k^\dagger \tilde{c}_k \rangle = \frac{1}{\exp \beta E_k + 1}, \tag{2.4.6}$$

observing which we find that

$$\tilde{\mathscr{G}}_{kk} = \exp(\tilde{\Gamma}_{kk}) \left[\exp(\tilde{\Gamma}_{kk}) + 1 \right]^{-1}. \tag{2.4.7}$$

But since both $\tilde{\mathscr{G}}$ and $\tilde{\Gamma}$ are diagonal matrices, we have the relation

$$e^{\tilde{\Gamma}} = \tilde{\mathscr{G}}(\mathbb{1} - \tilde{\mathscr{G}})^{-1}, \tag{2.4.8}$$

where $e^{\tilde{\Gamma}}$ is the matrix exponential of $\tilde{\Gamma}$.

Of course, $\mathscr{G}$ and $\tilde{\mathscr{G}}$ corresponds merely to the matrix of the same Hilbert space operator evaluated in two diferent bases, and the same is true of Γ and $\tilde{\Gamma}$. As such, the matrix relation (2.4.8) between $e^{\tilde{\Gamma}}$ and $\tilde{\mathscr{G}}$ holds true for e^{Γ} and $\mathscr{G}$ as well, i.e. we have

$$e^{\Gamma} = \mathscr{G}(\mathbb{1} - \mathscr{G})^{-1}. \tag{2.4.9}$$

2.4.2 Key Formulas Involving Grassmann Variables

In the next stage of our derivations, we need to make use of Grassmann variables. These are anticommuting c-numbers familiar in the context of field theory (see for example, Ref. 182). If ξ_i and ξ_j are Grassmann variables, where $i \neq j$, then we have $\xi_i \xi_j = -\xi_j \xi_i$ and $\xi_i^2 = 0 = \xi_j^2$. The purpose of introducing these is to define the fermionic coherent states

$$|\boldsymbol{\xi}\rangle = |\xi_1 \xi_2 \cdots \xi_N\rangle = \exp\left(- \textstyle\sum_{i=1}^N \xi_i c_i^\dagger \right) |0\rangle, \tag{2.4.10}$$

which are eigenstates of the fermion annihilation operators, i.e. $c_i |\boldsymbol{\xi}\rangle = -\xi_i |\boldsymbol{\xi}\rangle$. The value of coherent states in general is that one can replace the manipulation of non-commuting operators by the manipulation of c-number matrix elements. In the present

case of fermions, anticommuting operators may be made to commute by the insertion of Grassmann coefficients.

There are three key formulas involving Grassmann algebra that we need for the derivations in this section. The first involves the matrix element of an exponentiated bilinear operator $\exp\left(\sum_{i,j}\Gamma_{ij}c_i^\dagger c_j\right)$ between fermionic coherent states $|\boldsymbol{\xi}\rangle$ and $|\boldsymbol{\xi}'\rangle$, given by

$$\langle\boldsymbol{\xi}|\exp\left(\sum_{i,j}\Gamma_{ij}c_i^\dagger c_j\right)|\boldsymbol{\xi}'\rangle = \exp\left[\sum_{i,j}(e^\Gamma)_{ij}\xi_i^*\xi_j'\right], \tag{2.4.11}$$

where e^Γ is the exponential of the matrix Γ. The second formula expresses the trace of an operator A as a Grassmann integral over its coherent state matrix elements as

$$\mathrm{Tr}(A) = \int\prod_i d\xi_i^*\, d\xi_i\, e^{-\sum_i \xi_i^*\xi_i}\,\langle -\boldsymbol{\xi}|A|\boldsymbol{\xi}\rangle\,. \tag{2.4.12}$$

The third formula that we would need is the Gaussian integral over Grassmann variables,

$$\int\prod_i d\xi_i^*\, d\xi_i\, e^{\sum_{j,k}\xi_j^* A_{jk}\xi_k} = \det A. \tag{2.4.13}$$

The strategy then would be to evaluate the matrix elements of ρ in (2.4.3) using (2.4.11), follow the prescription in (2.2.22) where we trace over the environmental degrees of freedom using (2.4.12), and then use (2.4.11) in reverse to recover ρ_C from its coherent state matrix elements. Before we do so, let us first tidy up the notations by relabelling the coherent states as

$$|\boldsymbol{\xi\eta}\rangle = |\xi_1\cdots\xi_{N_C};\eta_1\cdots\eta_{N-N_C}\rangle = \exp\left(-\sum_{i=1}^{N_C}\xi_i c_i^\dagger - \sum_{j=1}^{N-N_C}\eta_j c_j^\dagger\right)|0\rangle\,, \tag{2.4.14}$$

where $\boldsymbol{\xi} = \{\xi_1,\ldots,\xi_{N_C}\}$ are Grassmann coordinates associated with sites within the cluster, and $\boldsymbol{\eta} = \{\eta_1,\ldots,\eta_{N-N_C}\}$ are Grassmann coordinates associated with sites in the environment.

2.4.3 Matrix Block Form

Seeing that ρ is written in (2.4.3) as the exponential of a quadratic form with coefficient matrix Γ, we make use of (2.4.11) to write down its matrix element between the fermionic coherent states $|\boldsymbol{\xi}\,\boldsymbol{\eta}\rangle$ and $|\boldsymbol{\xi}'\,\boldsymbol{\eta}'\rangle$ as a Gaussian in Grassmann variables:

$$\langle \boldsymbol{\xi}\,\boldsymbol{\eta}|\rho|\boldsymbol{\xi}'\,\boldsymbol{\eta}'\rangle = \mathcal{Q}^{-1} \exp\left[\begin{pmatrix}\boldsymbol{\xi}^* & \boldsymbol{\eta}^*\end{pmatrix} e^{\Gamma} \begin{pmatrix}\boldsymbol{\xi}' \\ \boldsymbol{\eta}'\end{pmatrix}\right]. \tag{2.4.15}$$

Our task now is to derive the matrix elements of ρ_C in the same Gaussian form, after tracing out the environment.

To find the matrix elements $\langle\boldsymbol{\xi}|\rho_C|\boldsymbol{\xi}'\rangle$ of the density matrix ρ_C for the cluster of N_C sites, we use (2.4.12) and perform a partial trace over the environment to give

$$\begin{aligned}
\langle\boldsymbol{\xi}|\rho_C|\boldsymbol{\xi}'\rangle &= \int d\boldsymbol{\eta}^* d\boldsymbol{\eta}\, e^{-\boldsymbol{\eta}^* \mathbb{1} \boldsymbol{\eta}}\, \langle \boldsymbol{\xi}\, -\boldsymbol{\eta}|\rho|\boldsymbol{\xi}'\,\boldsymbol{\eta}\rangle \\
&= \mathcal{Q}^{-1} \int d\boldsymbol{\eta}^* d\boldsymbol{\eta} \exp\left[\begin{pmatrix}\boldsymbol{\xi}^* & -\boldsymbol{\eta}^*\end{pmatrix}\begin{pmatrix}\mathbb{0} & \mathbb{0} \\ \mathbb{0} & \mathbb{1}\end{pmatrix}\begin{pmatrix}\boldsymbol{\xi}' \\ \boldsymbol{\eta}\end{pmatrix}\right] \exp\left[\begin{pmatrix}\boldsymbol{\xi}^* & -\boldsymbol{\eta}^*\end{pmatrix} e^{\Gamma} \begin{pmatrix}\boldsymbol{\xi}' \\ \boldsymbol{\eta}\end{pmatrix}\right] \\
&= \mathcal{Q}^{-1}\, e^{-\boldsymbol{\xi}^* \mathbb{1} \boldsymbol{\xi}'} \int d\boldsymbol{\eta}^* d\boldsymbol{\eta} \exp\left[\begin{pmatrix}\boldsymbol{\xi}^* & -\boldsymbol{\eta}^*\end{pmatrix}(\mathbb{1} + e^{\Gamma}) \begin{pmatrix}\boldsymbol{\xi}' \\ \boldsymbol{\eta}\end{pmatrix}\right].
\end{aligned} \tag{2.4.16}$$

Following this we must express these matrix elements in a form that would allow us to trace over the environment. To do so, let us first write $(\mathbb{1} + e^{\Gamma})$ in matrix block form as

$$\mathbb{1} + e^{\Gamma} = \begin{bmatrix} A & B \\ B^T & C \end{bmatrix} \tag{2.4.17}$$

where A is the $N_C \times N_C$ *cluster submatrix*, obtained by restricting the indices i and j of $(\mathbb{1} + e^{\Gamma})$ in coordinate space to range only over sites within the cluster, C is the $(N - N_C) \times (N - N_C)$ *environment submatrix*, obtained by restricting the indices i and j of $(\mathbb{1} + e^{\Gamma})$ to range only over sites in the environment, and B is the $N_C \times (N - N_C)$

decoherence submatrix of $(\mathbb{1} + e^{\Gamma})$, obtained by restricting the the row index to range only over sites within the cluster and the column index to range only over sites in the environment.

2.4.4 Tracing Down the System Density Matrix

With (2.4.16) and (2.4.17), the cluster density-matrix elements can then be written as

$$\langle \boldsymbol{\xi} | \rho_C | \boldsymbol{\xi}' \rangle = \mathscr{Q}^{-1} \, e^{\boldsymbol{\xi}^* (A - \mathbb{1}) \boldsymbol{\xi}'} \int d\boldsymbol{\eta}^* d\boldsymbol{\eta} \, e^{\boldsymbol{\xi}^* B \boldsymbol{\eta} - \boldsymbol{\eta}^* B^T \boldsymbol{\xi}' - \boldsymbol{\eta}^* C \boldsymbol{\eta}}. \tag{2.4.18}$$

Here we have made use of the fact that since the Grassmann variables occur quadratically in each term in the exponential, they commute with one another and we may thus factor the exponential as if it is an exponential of c-numbers.

By performing a shift of the integration variables $\boldsymbol{\eta}$ and $\boldsymbol{\eta}^*$, and then evaluating the Grassmann Gaussian integral using (2.4.13), we find that

$$\langle \boldsymbol{\xi} | \rho_C | \boldsymbol{\xi}' \rangle = \mathscr{Q}^{-1} \det C \, e^{\boldsymbol{\xi}^* [A - \mathbb{1} - B C^{-1} B^T] \boldsymbol{\xi}'}, \tag{2.4.19}$$

which parallels Eq. (14) in Ref. 176. From (2.4.19), we see that the expression for $\langle \boldsymbol{\xi} | \rho_C | \boldsymbol{\xi}' \rangle$ involves only the Grassman coordinates ξ_i and ξ_i' associated with sites within the cluster. This is good. But it also involve the decoherence submatrix B as well as the environment submatrix C, with the latter appearing both in the exponential as well as in the normalization constant. These matrices have indices that range over sites outside the cluster, which we are supposed to have traced out and gotten over with.

Indeed, this must have been successfully done, since $A - \mathbb{1} - BC^{-1}B^T$ is a $N_C \times N_C$ matrix whose indices range only over sites within the cluster. In fact, using (B.0.5) in Appendix B, we can express this matrix entirely in terms of submatrices within the cluster, and write (2.4.19) as

$$\langle \boldsymbol{\xi} | \rho_C | \boldsymbol{\xi}' \rangle = \mathscr{Q}^{-1} \det C \, e^{\boldsymbol{\xi}^* [D^{-1} - \mathbb{1}] \boldsymbol{\xi}'}, \tag{2.4.20}$$

where D is the cluster submatrix of $(\mathbb{1}+e^{\Gamma})^{-1}$, obtained by restricting its indices to range only over sites within the cluster. That leaves only the $\det C$ in the normalization that we have to deal with.

To express $\mathscr{Q}^{-1}\det C$ in terms of submatrices whose indices range only over sites within the cluster, we make use of the fact that

$$\begin{aligned}\mathrm{Tr}(\rho_C) = 1 &= \int d\boldsymbol{\xi}^* d\boldsymbol{\xi}\, e^{-\boldsymbol{\xi}^*\mathbb{1}\boldsymbol{\xi}}\,\langle -\boldsymbol{\xi}|\rho_C|\boldsymbol{\xi}\rangle \\ &= \mathscr{Q}^{-1}\det C \int d\boldsymbol{\xi}^* d\boldsymbol{\xi}\, e^{-\boldsymbol{\xi}^* D^{-1}\boldsymbol{\xi}} = \mathscr{Q}^{-1}\det C\,\det D^{-1},\end{aligned} \tag{2.4.21}$$

which means that

$$\mathscr{Q}^{-1}\det C = \det D. \tag{2.4.22}$$

With this we have succeeded in writing down a Gaussian form for the coherent state matrix elements of ρ_C involving only degrees of freedom within the cluster. Using the translation machinery provided by (2.4.11), we then establish the exponentiated form

$$\rho_C = \det D\,\exp\left\{\sum_{i,j}\left[\log(D^{-1}-\mathbb{1})\right]_{ij} c_i^\dagger c_j\right\} \tag{2.4.23}$$

of Chung and Peschel.

At this point, let us remark that the above formula for ρ_C is of no practical use, if to find the matrix D, we actually have to evaluate the matrix $(\mathbb{1}+e^{\Gamma})$, whose indices run over the entire system, take its inverse $(\mathbb{1}+e^{\Gamma})^{-1}$, and then from this identify the cluster submatrix D. This is essentially what was done in Ref. 176, where the matrix parallel to $D^{-1}-\mathbb{1}$ was computed numerically, for the case of an environment equal in size to the cluster. For our problem, identifying $A-BC^{-1}B^T$ as D^{-1} with the aid of our analytic relation (B.0.5) allows us to work with arbitrary, even infinite, environment sizes.

Furthermore, armed with the relationship (2.4.9) obtained in Section 2.4.1, we can find that the normalization and matrix of coefficients appearing in (2.4.20) in terms of

the cluster Green-function matrix G_C. From

$$\mathbb{1} + e^{\Gamma} = \mathbb{1} + \mathscr{G}(\mathbb{1} - \mathscr{G})^{-1} = (\mathbb{1} - \mathscr{G})^{-1}. \tag{2.4.24}$$

we see that D is just $(\mathbb{1} - \mathscr{G})$ restricted to the cluster, i.e.

$$D = \mathbb{1} - G_C, \tag{2.4.25}$$

and consequently,

$$D^{-1} = (\mathbb{1} - G_C)^{-1}. \tag{2.4.26}$$

With this, the normalization constant for ρ_C can be written as

$$\det D = \det(\mathbb{1} - G_C). \tag{2.4.27}$$

For the matrix of coefficients $(D^{-1} - \mathbb{1})$ in the exponential, we see that

$$D^{-1} - \mathbb{1} = (\mathbb{1} - G_C)^{-1} - \mathbb{1} = G_C(\mathbb{1} - G_C)^{-1}. \tag{2.4.28}$$

With this substitution, the matrix elements of ρ_C now reads as

$$\langle \boldsymbol{\xi} | \rho_C | \boldsymbol{\xi}' \rangle = \det(\mathbb{1} - G_C) \exp\left[\boldsymbol{\xi}^* G_C (\mathbb{1} - G_C)^{-1} \boldsymbol{\xi}' \right]. \tag{2.4.29}$$

so that, after using (2.4.11) in reverse translation, we can read off the operator form of ρ_C as

$$\rho_C = \det(\mathbb{1} - G_C) \, \exp\left\{ \sum_{ij} \left[\log G_C (\mathbb{1} - G_C)^{-1} \right]_{ij} c_i^\dagger c_j \right\}. \tag{2.4.30}$$

In a suitable basis diagonalizing $\log G_C(\mathbb{1} - G_C)^{-1}$, this becomes

$$\rho_C = \det(\mathbb{1} - G_C) \, \exp\left[- \textstyle\sum_l \varphi_l f_l^\dagger f_l \right], \tag{2.4.31}$$

where the f_l's are linear combinations of c_j's, and φ_l is the associated pseudo-energy (see (2.5.3) for definition). With (2.4.31), we see that to find ρ_C, we need only calculate the

$N_C \times N_C$ cluster Green-function matrix G_C from the ground state wavefunction with the aid of operators local to the cluster, and diagonalize it to determine f_l and subsequently φ_l. Peschel later re-derived (2.4.30) using a simpler approach [183].

To connect this with the results that we obtained in Section 2.3.4, let us evaluate the matrix elements for the zero- and one-particle sectors of ρ_C. Taylor expanding the exponential in (2.4.31) gives us

$$\rho_C = \det(\mathbb{1} - G_C) \prod_l \left[\mathbb{1} + (e^{-\varphi_l} - 1) f_l^\dagger f_l\right], \tag{2.4.32}$$

and so we see that the zero-particle sector is given by

$$\rho_{C,0} = {}_C\langle 0|\rho_C|0\rangle_C = \det(\mathbb{1} - G_C), \tag{2.4.33}$$

while in the basis diagonalizing ρ_C, the matrix elements in the one-particle sector are given by

$$\begin{aligned} {}_C\langle 0|f_l \rho_{C,1} f_l^\dagger|0\rangle_C &= \det(\mathbb{1} - G_C)\left[{}_C\langle 0|f_l \mathbb{1} f_l^\dagger|0\rangle_C + \sum_{l'} (e^{-\varphi_{l'}} - 1) {}_C\langle 0|f_l f_{l'}^\dagger f_{l'} f_l^\dagger|0\rangle_C\right] \\ &= \det(\mathbb{1} - G_C)\, e^{-\varphi_l} = \det(\mathbb{1} - G_C)\left[G_C(\mathbb{1} - G_C)^{-1}\right]_{ll}. \end{aligned} \tag{2.4.34}$$

This completes the proof of our conjecture at the end of Section 2.3 that as a matrix, $\rho_{C,1}$ is related to G_C by (2.3.77).

While we have used one-dimensional notations exclusively thus far, it is easy to see that nothing in our derviations depends explicitly on the dimensionality of the system of noninteracting spinless fermions. In fact, nothing in our derivations demands that the overall system be infinite either. In Chapter 4, we will apply (2.4.31) to calculate the cluster density-matrix spectra of clusters in finite two-dimensional systems of noninteracting spinless fermions.

2.4.5 Alternative Regularization

In our derivation of the exact formula (2.4.30), we started working with the grand-canonical system density matrix at finite temperature $T > 0$, and take the limit $T \to 0$ *after* we have completed the various matrix inversions, by noting implicitly that no particular step in the whole derivation depends on what value the temperature T takes. If we were fussy, we can always choose T to be infinitesimally small (but for all practical purposes, zero), so that all steps in our derivation carries through.

Alternatively, we can work directly at $T = 0$, using a different regularization. Realizing that we have definite occupation numbers, i.e. $\langle \tilde{c}_k^\dagger \tilde{c}_k \rangle = 0, 1$ at $T = 0$, the system density matrix ρ must be written as a product

$$\rho = \prod_{|k|<k_F} \tilde{c}_k^\dagger \tilde{c}_k \prod_{|k'|>k_F} \tilde{c}_{k'} \tilde{c}_{k'}^\dagger \tag{2.4.35}$$

of projection operators. This is possible only if

$$\tilde{\Gamma}_{kk} = \begin{cases} +\infty, & |k| < k_F; \\ -\infty, & |k| > k_F. \end{cases} \tag{2.4.36}$$

For the purpose of algebraic manipulations, this choice of $\tilde{\Gamma}_{kk}$ must be regularized, i.e. we write

$$\tilde{\Gamma}_{kk} = \Lambda \operatorname{sgn}(k_F - |k|), \tag{2.4.37}$$

and take $\Lambda \to \infty$ at the end of the calculations. With this choice of regularization, the coefficient matrix e^Γ we encounter in (2.4.15) can be written as

$$e^\Gamma = e^{-\Lambda} \mathbb{1} + (e^\Lambda - e^{-\Lambda}) \mathscr{G}, \tag{2.4.38}$$

where $\mathscr{G}$ is the zero-temperature system Green-function matrix, whose matrix elements

in momentum space are

$$\tilde{\mathscr{G}}_{kk} = \theta(k_F - |k|), \quad \theta(x) = \begin{cases} 0, & x < 0; \\ 1, & x > 0. \end{cases} \tag{2.4.39}$$

It is then easy to show that the inverse of the coefficient matrix $(\mathbb{1} + e^{\Gamma})$, which we need to determine the cluster submatrix D in (2.4.23), is

$$(\mathbb{1} + e^{\Gamma})^{-1} = (1 + e^{-\Lambda})^{-1}\mathbb{1} + [(1 + e^{\Lambda})^{-1} - (1 + e^{-\Lambda})^{-1}]\mathscr{G}, \tag{2.4.40}$$

which becomes $(\mathbb{1} - \mathscr{G})$ in the limit of $\Lambda \to \infty$, just as we have obtained in (2.4.25).

2.5 Structure and Properties of Cluster Density Matrix

In this section, we will discuss the implications of the exponentiated form (2.4.31) of the cluster density matrix ρ_C. In Section 2.5.1, we take advantage of the thermodynamic form of ρ_C to define a pseudo-Hamiltonian for a system of noninteracting spinless fermions. The pseudo-Hamiltonian is written in terms of a set of pseudo-fermion operators, and the dispersion relation is then given by a corresponding set of single-particle pseudo-energies. Following this, in Section 2.5.2 we look how particle-hole symmetry of a half-filled Fermi sea manifests itself in the pseudo-dispersion relation. Finally, in Section 2.5.3, we discuss how, knowing the set of pseudo-fermion operators and single-particle pseudo-energies, we can build up the entire spectrum of many-particle cluster density-matrix eigenstates and weights.

2.5.1 The Single-Particle Pseudo-Energies

In the closed-form formula (2.4.31) for the cluster density matrix ρ_C, the fermion operators f_l and coefficients φ_l, can all be determined by diagonalizing the cluster Green-

function matrix G_C. This tells us that the many-particle weights and eigenstates of ρ_C are determined completely by those in the zero- and one-particle sectors.

Noting that ρ_C can be written in the form

$$\rho_C = \det(\mathbb{1} - G_C) \exp\left[-\sum_l \varphi_l f_l^\dagger f_l\right] = \mathscr{Q}^{-1} \exp[-\tilde{H}] \tag{2.5.1}$$

which resembles the density matrix of a quantum canonical ensemble, we call

$$\tilde{H} = \sum_l \varphi_l f_l^\dagger f_l \tag{2.5.2}$$

the *pseudo-Hamiltonian*. Because $\tilde{H}$ consists only of bilinears of independent fermion operators f_l and $f_{l'}$ satisfying $\{f_l^\dagger, f_{l'}\} = \delta_{ll'}\,\mathbb{1}$, it describes a noninteracting system of spinless fermions, with *pseudo-fermion operators* f_l and $f_l^\dagger$, and a dispersion relation given by the corresponding set of *single-particle pseudo-energies*

$$\varphi_l = -(\log G_C(\mathbb{1} - G_C)^{-1})_{ll} = -\log \frac{\lambda_l}{1 - \lambda_l}, \tag{2.5.3}$$

for $l = 1, \ldots, N_C$. Here λ_l are the eigenvalues of the cluster Green-function matrix G_C. In terms of λ_l, the zero- and one-particle cluster density-matrix weights are given by

$$w_0 = \mathscr{Q}^{-1} = \det(\mathbb{1} - G_C) = \prod_l (1 - \lambda_l), \tag{2.5.4}$$

and

$$w_l = \mathscr{Q}^{-1} \exp(-\varphi_l) \tag{2.5.5}$$

respectively.

2.5.2 Particle-Hole Symmetry at Half-Filling

To complete our understanding of the structure and spectrum of ρ_C, we want to know how symmetries of the original problem are built into ρ_C. In particular, we will consider

particle-hole symmetry on a bipartite lattice, on which we define a 'charge-conjugation' operator $\mathscr{C}$, with $\mathscr{C}^2 = \mathbb{1}$. One possible form for the charge-conjugation operator is

$$\mathscr{C} = \prod_j \left[i^{j+1} c_j^\dagger + (-i)^{j+1} c_j \right], \tag{2.5.6}$$

where the product runs over all lattice sites. The action of $\mathscr{C}$ on the coordinate space fermion operators can be defined to be

$$\mathscr{C} c_i \mathscr{C} = -(-1)^i c_i^\dagger, \quad \mathscr{C} c_i^\dagger \mathscr{C} = -(-1)^i c_i, \tag{2.5.7}$$

where $(-1)^i$ is defined to be $+1$ (-1) whenever the site i belongs to the even (odd) sublattice. In a d-dimensional hypercubic lattice, where the site index is $i = \{i_1, i_2, \ldots, i_d\}$, the factor $(-1)^i$ is rightfully given by $(-1)^i = (-1)^{i_1 + i_2 + \cdots + i_d}$.

There are two conditions, one on the dispersion relation ϵ_k, and the other on the chemical potential μ, implied by particle-hole symmetry. To derive the first condition on the dispersion relation, we note from (2.5.7) that in momentum space — when the lattice is a Bravais lattice — that

$$\mathscr{C} \tilde{c}_k \mathscr{C} = -\tilde{c}^\dagger_{-k-Q}, \qquad \mathscr{C} \tilde{c}_k^\dagger \mathscr{C} = -\tilde{c}_{-k+Q}, \tag{2.5.8}$$

where the wavevector Q is defined by $e^{\mathrm{i}\, Q i} = (-1)^i$.[3] We can then check, with (2.1.2) and (2.5.8), that

$$\mathscr{C} H \mathscr{C} = \sum_k \epsilon_k \tilde{c}_{-k+Q} \tilde{c}^\dagger_{-k-Q} = \sum_{k'} \epsilon_{-k'-Q} \tilde{c}_{k'+2Q} \tilde{c}^\dagger_{k'}. \tag{2.5.9}$$

Now, from the definition of Q, it is clear that

$$\tilde{c}_{k'+2Q} = \frac{1}{\sqrt{N}} \sum_j e^{\mathrm{i}(k'+2Q)j} c_j = \frac{1}{\sqrt{N}} \sum_j e^{\mathrm{i}\, k' j} [(-1)^j]^2 c_j = \tilde{c}_{k'}, \tag{2.5.10}$$

[3] If the bipartite lattice is not a Bravais lattice, then whereever the wavevector k appears as an index, it must be replaced by the combination of k and a band index. All of the results — in particular those of Section 2.5.2 — still go through in this generalized case, provided that all lattice sites are symmetry equivalent.

and thus (dropping the prime on the dummy wavevector k' that is summed over)

$$\mathscr{C}H\mathscr{C} = \sum_k \epsilon_{-k-Q}\tilde{c}_k\tilde{c}_k^\dagger = \sum_k \epsilon_{-k-Q} + \sum_k -\epsilon_{-k-Q}\tilde{c}_k^\dagger\tilde{c}_k. \tag{2.5.11}$$

For time-reversal invariant systems, $\epsilon_{-k} = \epsilon_k$. Also, for our choice of Hamiltonian, $\sum_k \epsilon_{-k-Q} = \sum_{k'} \epsilon_{k'} = \mathrm{Tr}\, H = 0$. Thus (2.5.11) simplifies to

$$\mathscr{C}H\mathscr{C} = \sum_k -\epsilon_{k+Q}\tilde{c}_k^\dagger\tilde{c}_k. \tag{2.5.12}$$

Since it is clear from (2.1.1) and (2.5.7) that $\mathscr{C}H\mathscr{C} = H$, (2.5.12) tells us that the dispersion relation associated with the particle-hole symmetric Hamiltonian H must satisfy the condition

$$\epsilon_{k+Q} = -\epsilon_k. \tag{2.5.13}$$

Next, to understand how the second condition on the chemical potential comes about, let us note the trivial fact that, since ρ_C is a reduced density matrix of ρ, for there to be any sense in talking about the manifestation of particle-hole symmetry in ρ_C, ρ must first be particle-hole symmetric, i.e. $\mathscr{C}\rho\mathscr{C} = \rho$. When ρ is the density matrix of the ground state at $T = 0$, then it is particle-hole symmetric whenever the ground state $|\Psi_F\rangle$ is. For $|\Psi_F\rangle$ to be particle-hole symmetric, it must have the transformation property

$$\mathscr{C}\,|\Psi_F\rangle = \eta_{\mathscr{C}}\,|\Psi_F\rangle\,, \tag{2.5.14}$$

where $\eta_{\mathscr{C}} = \pm 1$ is a phase factor associated with $\mathscr{C}$. We know that this is satisfied only by the half-filled ground state. At finite temperature, when ρ is taken from the grand canonical ensemble and has the form given in (2.4.1), what, if any, extra conditions must be satisfied in order for ρ to be particle-hole symmetric?

Indeed, there appears to be cause for concern: unlike H, which is invariant under 'charge-conjugation', the fermion number operator F transforms under $\mathscr{C}$ as

$$\mathscr{C}F\mathscr{C} = \sum_i \mathscr{C}c_i^\dagger c_i\mathscr{C} = \sum_i c_i c_i^\dagger = N - F, \tag{2.5.15}$$

and so for ρ to be particle-hole symmetric, i.e.

$$\mathscr{C}\rho\mathscr{C} = \mathscr{Q}^{-1}\exp\beta[H-\mu(N-F)] = \rho, \tag{2.5.16}$$

we must have $\mu = 0$. For a dispersion relation satisfying (2.5.13), $\mu = 0$ corresponds to precisely the situation of half-filling. At least for the grand canonical ensemble, there appears to be no other conditions necessary for ρ to be particle-hole symmetric.

With these conditions in mind, we may now proceed to investigate how particle-hole symmetry shows up in the pseudo-energy spectrum (and hence the spectrum of the cluster density matrix ρ_C). But first, we must understand how the symmetry manifests itself in the Green function matrix $\mathscr{G}$, and its restriction to the cluster, G_C. Knowing from our arguments above that $\mu = 0$, we see that the matrix elements of $\tilde{\mathscr{G}}$ in momentum space simplifies to

$$\tilde{\mathscr{G}}_{kk} = \frac{1}{\exp\beta\epsilon_k + 1}. \tag{2.5.17}$$

Furthermore, using (2.5.13), we can relate $\tilde{\mathscr{G}}_{k+Q,k+Q}$ to $\tilde{\mathscr{G}}_{kk}$ by

$$\tilde{\mathscr{G}}_{k+Q,k+Q} = \frac{1}{\exp\beta\epsilon_{k+Q}+1} = \frac{1}{\exp(-\beta\epsilon_k)+1} = 1-\tilde{\mathscr{G}}_{kk}. \tag{2.5.18}$$

This gives rise to the condition

$$\mathscr{G}_{ij} = \delta_{ij} - (-1)^{(i-j)}\mathscr{G}_{ij} \tag{2.5.19}$$

that must be satisfied by the matrix elements of $\mathscr{G}$ in coordinate space.

This same result can be derived more transparently for the special case of $T = 0$: using the fact that $\mathscr{C}^2 = \mathbb{1}$, $\eta_{\mathscr{C}}^2 = 1$, as well as (2.5.7) and (2.5.14), we find that

$$\begin{aligned}\mathscr{G}_{ij} &= \langle\Psi_F|c_i^\dagger c_j|\Psi_F\rangle = \langle\Psi_F|\mathscr{C}(\mathscr{C}c_i^\dagger\mathscr{C})(\mathscr{C}c_j\mathscr{C})\mathscr{C}|\Psi_F\rangle \\ &= (-1)^{i+j}\langle\Psi_F|c_ic_j^\dagger|\Psi_F\rangle = (-1)^{i+j}\delta_{ij} - (-1)^{i+j}\langle\Psi_F|c_j^\dagger c_i|\Psi_F\rangle \\ &= \delta_{ij} - (-1)^{i+j}\mathscr{G}_{ij},\end{aligned} \tag{2.5.20}$$

where we have made use of the fact that $\mathscr{G}$ is symmetric, i.e. $\mathscr{G}_{ji} = \mathscr{G}_{ij}$.

Since (2.5.20) is a condition satisfied by the matrix elements of $\mathscr{G}$ individually, it holds just as well to those restricted to the cluster, i.e. G_{ij}. In particular, we note that (2.5.20) can actually be written as a matrix equation, which when restricted to the cluster reads as

$$G_C = \mathbb{1} - JG_CJ, \tag{2.5.21}$$

where $J = \mathrm{diag}(e^{\mathrm{i}\,Q_i}) = \mathrm{diag}(1, -1, 1, -1, \dots)$ in coordinate space, and $J^2 = \mathbb{1}$.

To appreciate the implications of (2.5.21), let us consider an eigenvector $|\lambda_l\rangle$ of G_C which corresponds to the eigenvalue λ_l, such that

$$G_C\,|\lambda_l\rangle = \lambda_l\,|\lambda_l\rangle\,. \tag{2.5.22}$$

From (2.4.30), we know that $|\lambda_l\rangle$ is also a one-particle eigenvector of ρ_C, with single-particle pseudo-energy

$$\varphi_l = -\log\lambda_l + \log(1-\lambda_l). \tag{2.5.23}$$

Using (2.5.21), we find that

$$\begin{aligned} G_CJ\,|\lambda_l\rangle &= (\mathbb{1} - JG_CJ)J\,|\lambda_l\rangle \\ &= J\,|\lambda_l\rangle - JG_CJ^2\,|\lambda_l\rangle \\ &= J\,|\lambda_l\rangle - JG_C\,|\lambda_l\rangle \\ &= J\,|\lambda_l\rangle - \lambda_lJ\,|\lambda_l\rangle \\ &= (1-\lambda_l)J\,|\lambda_l\rangle\,, \end{aligned} \tag{2.5.24}$$

i.e. the state $|\lambda_{l'}\rangle \equiv J\,|\lambda_l\rangle$ generated by particle-hole symmetry from $|\lambda_l\rangle$ is also an eigenvector of G, with eigenvalue $\lambda_{l'} = (1-\lambda_l)$. The pseudo-energy $\varphi_{l'}$ associated with $|\lambda_{l'}\rangle$ is then

$$\varphi_{l'} = -\log\lambda_{l'} + \log(1-\lambda_{l'}) = -\varphi_l. \tag{2.5.25}$$

It is interesting to note how the weights $w_{B,1,l}$, being exponentials of the pseudo-energies φ_l, hide this particular aspect of particle-hole symmetry.

2.5.3 The Many-Particle Cluster Density-Matrix Eigenstates

Finally, let us demonstrate how the many-particle cluster density-matrix eigenstates and eigenvalues can be constructed from the zero- and one-particle eigenstates and eigenvalues, using the half-filled one-dimensional infinite chain of noninteracting spinless fermions as an example.

For a cluster of $N_C = 3$ sites, we know from Section 2.3.2.2 that the zero-particle cluster density-matrix weight is

$$w_{3,0} = \left(\tfrac{1}{\sqrt{8}} - \tfrac{1}{\pi}\right)\left(\tfrac{1}{\sqrt{8}} + \tfrac{1}{\pi}\right) = \mathscr{Q}^{-1}, \tag{2.3.33}$$

while the one-particle cluster density-matrix weights are

$$\begin{aligned} w_{3,1,1} &= \left(\tfrac{1}{\sqrt{8}} + \tfrac{1}{\pi}\right)^2, \\ w_{3,1,2} &= \left(\tfrac{1}{\sqrt{8}} - \tfrac{1}{\pi}\right)\left(\tfrac{1}{\sqrt{8}} + \tfrac{1}{\pi}\right), \\ w_{3,1,3} &= \left(\tfrac{1}{\sqrt{8}} - \tfrac{1}{\pi}\right)^2. \end{aligned} \tag{2.3.34}$$

The single-particle pseudo-energies are therefore

$$\begin{aligned} \varphi_1 &= -\log\frac{w_{3,1,1}}{w_{3,0}} = -\log\frac{\frac{1}{\sqrt{8}} + \frac{1}{\pi}}{\frac{1}{\sqrt{8}} - \frac{1}{\pi}} = -2.94777\ldots, \\ \varphi_2 &= -\log\frac{w_{3,1,2}}{w_{3,0}} = -\log 1 = 0, \\ \varphi_3 &= -\log\frac{w_{3,1,3}}{w_{3,0}} = -\log\frac{\frac{1}{\sqrt{8}} - \frac{1}{\pi}}{\frac{1}{\sqrt{8}} + \frac{1}{\pi}} = +2.94777\ldots. \end{aligned} \tag{2.5.26}$$

We call $\varphi_1 = -\varphi_3$ a *particle-hole conjugate pair* of pseudo-energies, and say that φ_3 is the particle-hole conjugate of φ_1. The one-particle cluster density-matrix eigenstates are

created by the pseudo-fermion operators

$$\begin{aligned} f_1^\dagger &= \tfrac{1}{2}c_1^\dagger + \tfrac{1}{\sqrt{2}}c_2^\dagger + \tfrac{1}{2}c_3^\dagger, \\ f_2^\dagger &= \tfrac{1}{\sqrt{2}}c_1^\dagger - \tfrac{1}{\sqrt{2}}c_3^\dagger, \\ f_3^\dagger &= \tfrac{1}{2}c_1^\dagger - \tfrac{1}{\sqrt{2}}c_2^\dagger + \tfrac{1}{2}c_3^\dagger, \end{aligned} \tag{2.5.27}$$

corresponding to single-particle pseudo-energies φ_1, φ_2 and φ_3 respectively.

We can easily check that the $f_l^\dagger$'s obey the same anticommutator relation as the $c_i^\dagger$'s. This means that the many-particle cluster density-matrix eigenstates have the structure of noninteracting spinless pseudo-fermions occupying single-particle pseudo-energy levels subject to Pauli's Exclusion Principle. We can therefore write down the two-particle cluster density-matrix eigenstates as being created by the non-repeating products

$$\begin{aligned} f_1^\dagger f_2^\dagger &= -\tfrac{1}{2}c_2^\dagger c_3^\dagger - \tfrac{1}{\sqrt{2}}c_1^\dagger c_3^\dagger - \tfrac{1}{2}c_1^\dagger c_2^\dagger, \\ f_1^\dagger f_3^\dagger &= \tfrac{1}{\sqrt{2}}c_2^\dagger c_3^\dagger - \tfrac{1}{\sqrt{2}}c_1^\dagger c_2^\dagger, \\ f_2^\dagger f_3^\dagger &= -\tfrac{1}{2}c_2^\dagger c_3^\dagger + \tfrac{1}{\sqrt{2}}c_1^\dagger c_3^\dagger - \tfrac{1}{2}c_1^\dagger c_2^\dagger, \end{aligned} \tag{2.5.28}$$

of pseudo-fermion operators. These two-particle cluster density-matrix eigenstates are associated with the two-particle pseudo-energies $\varphi_1 + \varphi_2 = \varphi_1$, $\varphi_1 + \varphi_3 = 0 = \varphi_2$ and $\varphi_2 + \varphi_3 = \varphi_3$ respectively. Here we see that because of the particle-hole symmetry in the ground-state wavefunction, the two-particle pseudo-energies are identical to the one-particle pseudo-energies, which implies thus that the two-particle cluster density-matrix weights are identical to the one-particle cluster density-matrix weights. This is indeed what we observed in Section 2.3.2.2.

Similarly, the one and only three-particle cluster density-matrix eigenstate is created by the unique (up to anticommutations) product

$$f_1^\dagger f_2^\dagger f_3^\dagger = c_1^\dagger c_2^\dagger c_3^\dagger, \tag{2.5.29}$$

of pseudo-fermion operators. The three-particle pseudo-energy associated with this eigenstate is $\varphi_1 + \varphi_2 + \varphi_3 = 0$, and we find that $w_{3,3} = w_{3,0}$. For larger clusters at various filling fractions, we verified numerically all the many-particle eigenstates and eigenvalues of the cluster density matrix can be constructed in this manner from the zero-particle and one-particle eigenstates and weights.

Another manifestation of particle-hole symmetry is a queer degeneracy between cluster density-matrix weights in the P_C- and $(P_C + 2)$-particle sectors. This we understand as follows: if $\varphi_{l_1} + \cdots + \varphi_{l_{P_C}}$ is a cluster density-matrix weight in the P_C-particle sector, then in general, when the cluster size is large, we can find weights $(\varphi_{l_1} + \cdots + \varphi_{l_{P_C}}) + \varphi_{l_{P_C+1}} + \varphi_{l_{P_C+2}} = (\varphi_{l_1} + \cdots + \varphi_{l_{P_C}})$ in the $(P_C + 2)$-particle sector, where $\varphi_{l_{P_C+1}}$ and $\varphi_{l_{P_C+2}}$ are particle-hole conjugates of each other.

In fact, from the construction outlined above, we also know the pattern of degeneracy. For example, for a cluster with $N_C = 4$ sites on a half-filled infinite chain, the one-particle pseudo-energies are

$$\begin{aligned}
\varphi_1 &= -\log \frac{w_{4,1,1}}{w_{4,0}} = -4.46839\ldots, \\
\varphi_2 &= -\log \frac{w_{4,1,2}}{w_{4,0}} = -1.24514\ldots, \\
\varphi_3 &= -\log \frac{w_{4,1,3}}{w_{4,0}} = +1.24514\cdots = -\varphi_2, \\
\varphi_4 &= -\log \frac{w_{4,1,4}}{w_{4,0}} = +4.46839\cdots = -\varphi_1.
\end{aligned} \tag{2.5.30}$$

Since there are only two particle-hole conjugate pairs of single-particle pseudo-energies, we know that the three-particle pseudo-energies, which are sums of three distinct single-particle pseudo-energies, will always contain one particle-hole conjugate pair. The value of the three-particle pseudo-energies are thus determined solely by the unpaired single-particle pseudo-energy in the sum. There are four ways this can happen, and they correspond to having φ_1, φ_2, φ_3, and φ_4 being unpaired in the sum. Therefore, the three-

particle pseudo-energies are identical to the one-particle pseudo-energies, and there are no degeneracies. There are two degenerate two-particle pseudo-energies, corresponding to $\varphi_1 + \varphi_4 = 0$, and $\varphi_2 + \varphi_3 = 0$.

For a cluster of $N_C = 6$ sites on a half-filled infinite chain, the one-particle pseudo-energies are of the form $-\varphi_a < -\varphi_b < -\varphi_c < \varphi_c < \varphi_b < \varphi_a$. In the three-particle sector of the cluster density matrix, we find the pattern of three-particle pseudo-energies to be

$$
\begin{gathered}
\varphi_c + \varphi_b + \varphi_a; \\
-\varphi_c + \varphi_b + \varphi_a; \\
-\varphi_b + \varphi_b + \varphi_a, \quad -\varphi_c + \varphi_c + \varphi_a; \\
-\varphi_b + \varphi_c + \varphi_a; \\
-\varphi_a + \varphi_b + \varphi_a, \quad -\varphi_c + \varphi_c + \varphi_b; \\
-\varphi_a + \varphi_c + \varphi_b; \\
-\varphi_a + \varphi_c + \varphi_a, \quad -\varphi_b + \varphi_c + \varphi_b; \\
-\varphi_a - \varphi_c + \varphi_a, \quad -\varphi_b - \varphi_c + \varphi_b; \\
-\varphi_b - \varphi_c + \varphi_a; \\
-\varphi_a - \varphi_b + \varphi_a, \quad -\varphi_b - \varphi_c + \varphi_c; \\
-\varphi_a - \varphi_c + \varphi_b; \\
-\varphi_a - \varphi_b + \varphi_b, \quad -\varphi_a - \varphi_c + \varphi_c; \\
-\varphi_a - \varphi_b + \varphi_c; \\
-\varphi_a - \varphi_b - \varphi_c,
\end{gathered}
\tag{2.5.31}
$$

where the three-particle pseudo-energies are ranked in descending order.

CHAPTER 3

OPERATOR-BASED DM TRUNCATION SCHEME

3.1 A Quick Guide to Chapter 3

In this chapter, we apply the exact formula (2.4.31) derived in Chapter 2 for a system of noninteracting spinless fermions to: (i) develop a statistical mechanics analogy between the many-particle cluster density-matrix eigenstates and the many-particle energy eigenstates of a system of noninteracting spinless fermions; (ii) devise an Operator-Based Density-Matrix Truncation Scheme based on this statistical mechanics analogy; and (iii) study the scaling properties of the cluster density-matrix weights with cluster size, specifically for the case of one dimension.

After listing the specific questions we seek to answer in Section 3.2, we move on to study (i) and (ii) in Section 3.3. The statistical mechanics analogy is fleshed out in Sections 3.3.1 and 3.3.2, before we describe the Operator-Based Density-Matrix Truncation Scheme in Section 3.3.3. In preparation for a study of the performance of such a truncation scheme in Sections 3.6.4 and 3.9, we investigate how the cluster density-matrix weights of a one-dimensional system of noninteracting spinless fermions scale with cluster size in Section 3.5. By performing numerical scaling collapses, we find universal scaling laws (3.5.6) at each filling fraction, which we then used to derive the asymptotic behaviours of the largest cluster density-matrix weights in the limit of very large clusters in Sections 3.6.1 and 3.6.3, as well as the influence of a single-particle energy gap on the scaling properties of the noninteracting cluster density-matrix weights in Section 3.6.2.

We used (3.5.6) to calculate the weight discarded by the Operator-Based Density-Matrix Truncation Scheme in Section 3.6.4, before moving on to Section 3.9, where

we calculate the single-particle dispersion relation of one-dimensional noninteracting spinless fermions within the truncation scheme. We checked the spurious energy gap appearing at the Fermi level in Section 3.9.1, and the deviation in the Fermi velocity in Section 3.9.2, due to truncation, and found that the approximate dispersion relation calculated in the Operator-Based Density-Matrix Truncation Scheme agrees with the true dispersion relation better than one would expected based on the discarded weight. We also compare the performance of the Operator-Based Density-Matrix Truncation Scheme with an Operator-Based Plane-Wave Truncation Scheme in Section 3.10, and found that the former scheme offers better control over the numerical errors in various observables calculated.

3.2 Introduction

In Chapter 2, we extended the results of Chung and Peschel [176] to derive an exact formula for the many-body density matrix ρ_C of a cluster of N_C sites cut out from an infinite system of noninteracting (spinless or spinfull) fermions, and found that the many-particle eigenvalues and eigenstates of ρ_C can all be constructed out of the one-particle eigenvalues and one-particle eigenstates respectively [184]. In Section 3.3.1, we exploit this simple factorized nature of ρ_C and its eigenfunctions for a system of noninteracting fermions (and by implication for any Fermi liquid), which follows from (2.1.7) and (2.1.8), to developed a statistical-mechanical analogy between the density matrix eigenstates and the many-body states of a system of noninteracting fermions. Each density-matrix eigenstate corresponds to a particular set of occupation of single-particle pseudo-energy levels, and the density matrix eigenstate with the largest weight, having the structure of a Fermi sea ground state, unambiguously defines pseudo-Fermi level.

After summarizing in Section 3.3.2 the important results we obtain in Chapter 2, which gives the exact relations between the cluster density matrix ρ_C, the cluster Green-function matrix G_C, as well as their eigenstates and eigenvalues, we outline in Section 3.3.3 the main ideas behind an operator-based truncation of the density matrix eigenstates, where single-particle pseudo-energy levels far away from the pseudo-Fermi level are removed as degrees of freedom, based on the statistical-mechanical analogy described in Section 3.3.1. We devote this chapter entirely to noninteracting fermions, because the analytic results of Ref. 184 permit many calculations that could not be done by numerical brute force in an interacting case, or can be carried out only by quite different methods (such as Monte Carlo). Furthermore, our hypothetical renormalization or projection algorithm using density-matrix truncation would first be applied to a well-understood system in which the low-energy excitations behave as noninteracting quasiparticles (as in a Fermi liquid or a d-wave superconducting phase). Our imagined numerical method in such a system would extract renormalized pseudo-creation operators $\tilde{f}_l^\dagger$ which are related to the single-particle operators $\{f_l^\dagger\}$ in the same way that quasiparticle creation operators are related to bare fermion creation operators. The pseudo-dispersion relation for the renormalized $\{\tilde{f}_l^\dagger\}$ is thus expected to scale in the same fashion as the pseudo-dispersion φ_l encoded in (2.1.8) of the noninteracting fermions.

The relation between the single-particle density matrix eigenstates and single-particle energy eigenstates of a system of noninteracting spinless fermions also suggests how the distribution of single-particle pseudo-energies φ_l is expected to scale with the cluster size N_C. Numerically, a scaling relationship between φ_l and N_C was found indeed, for the overall chain at various fillings $\bar{n}$. Our analytical results from Ref. 184 shed light on this eigenvalue scaling in two ways. Firstly, as in Ref. 176, they allow numerical study of the density matrix for system sizes so large that they would be inaccessible to any

other techniques. Secondly, the exact connection of the cluster density matrix ρ_C to the cluster Green-function matrix G_C gives hints about the eigenvalue distribution, which we discuss further in Section 3.5. These scaling relations tell us that the cluster size N_C plays the role of an inverse temperature in the statistical-mechanical description of the density-matrix eigenstates and eigenvalues.

The implications of the scaling behaviour of the single-particle pseudo-energies are discussed in Section 3.6, where we derived the asymptotic behaviour, in the limit of infinite cluster sizes, of the largest density-matrix weight and the truncated weight W_t, which is the sum of weights of the density matrix eigenstates retained in the operator-based DM truncation scheme. Through the calculations in this chapter, we aim to understand the analytic structure of ρ_C, and to begin to understand the quantitative errors due to truncation. This includes the question: what is the proper measure of error? The most familiar measure, the retained fraction of total density matrix weight, does not seem to be the best measure of error. Compared to the traditional density-matrix truncation scheme used in the DMRG, our operator-based density-matrix truncation scheme gives for the same number of density matrix eigenstates retained a slightly larger discarded weight $\epsilon = 1 - W_t$ (see Figure 3.10 in Section 3.6.4). This quantity gives a $O(\epsilon)$ estimate as an upper bound — a worst case scenario — for the error incurred when computing the expectation of a most general observable. As with examples in numerical integration, the performance of an algorithm in integrating some classes of functions may be much better than that expected from the straightforward error analysis, as evidenced by the small errors obtained in Section 3.9 for the calculations of the dispersion relation. The results are highly encouraging: the dispersion relation calculated in the operator-based density-matrix truncation scheme differ from the true dispersion relation by an amount much smaller than what is suggested by the discarded weight ϵ.

Besides quasiparticle dispersion relations, real-space correlation functions are also interesting quantities to calculate, and these invariably depend on the real-space structure of the many-body ground state wave function. Since this wave function is to be written in terms of the one-particle density matrix eigenfunctions, it is important to understand the real space structure of these as well. The one-particle density matrix eigenfunctions kept in our operator-based density-matrix truncation scheme have spatial structures that are very similar to each other. In Section 3.8 we look into a representative one-particle density matrix eigenfunction, the pseudo-Fermi eigenfunction, for each cluster size N_C, and found that they also obey a universal scaling relation. This brings us to another question that we need to address when formulating a truncation scheme, which is whether — when we are severely truncating the Hilbert space, and attempting only to obtain the low-energy excitations — the density matrix eigenstates are the optimal basis. There are two parts to this question, the first being how well our truncated basis can approximate the ground-state wave function, and the second being how well we can approximate ground-state expectations performing calculations within the truncated basis. In Section 3.9.3, we address the first part of the question, and check how well such a truncated basis of one-particle density-matrix eigenfunctions can approximate the true single-particle wave function at the Fermi level, which is a plane wave with wavevector k_F. We find the approximation to be good even when less than one quarter of the one-particle density-matrix eigenfunctions are kept. This is impressive, considering the fact that in the operator-based density-matrix truncation scheme, the number of many-particle density matrix eigenstates thus represented by the one-particle density matrix eigenstates retained constitutes a miniscule fraction of the total number of density-matrix eigenstates.

Finally, for systems where we know that the true single-particle wavefunctions are

plane waves, it seems *a priori* plausible that a plane wave-based operator-based truncation scheme might outperform the operator-based density matrix truncation scheme. We look into this possibility in Section 3.10, and find that while there are a few aspects in calculating the dispersion relation where the *operator-based plane wave (PW) truncation scheme* outperforms the operator-based DM truncation scheme, the overall performance of the PW scheme is inferior to the DM scheme.

3.3 Operator-Based Density Matrix Truncation

3.3.1 Structure of Density-Matrix Eigenvalues and Eigenstates

Because the Hamiltonian in (2.1.1) conserves particle number, the eigenstates of ρ_C have definite particle number, and may be grouped into various P_C-particle sectors, where $P_C = 0, 1, \ldots, N_C$. A consequence of our fundamental formulas (2.1.7) and (2.1.8) is that every eigenstate of ρ_C has the form

$$|\chi_L\rangle = \prod_{p=1}^{P_C} f_{l_p}^\dagger |0\rangle \,. \tag{3.3.1}$$

Each eigenstate is specified by a list of *pseudo-occupation numbers* $\{n_l\}$, where $n_{l_p} = 1$ for the factors contained in (3.3.1), and is zero otherwise. Furthermore, the corresponding eigenvalue, the *cluster density-matrix weight*, is simply given by

$$w_L = \mathscr{Q}^{-1} \exp\left[-\sum_{l=1}^{N_C} n_l \varphi_l\right], \tag{3.3.2}$$

where the quantity

$$\Phi = \sum_l n_l \varphi_l \tag{3.3.3}$$

appearing in the exponent is the *total pseudo-energy*. In terms of the single-particle pseudo-energies $\{\varphi_l\}$, the normalization constant of the cluster density matrix in (2.1.7)

can be written as

$$\mathscr{Q} \equiv \sum_{\{n_l\}} \exp\left[-\sum_l n_l \varphi_l\right], \tag{3.3.4}$$

where the summation is over all 2^{N_C} combinations of occupations.

It is immediately clear from (3.3.2) that the cluster density-matrix eigenstate of maximum weight corresponds to the minimum total pseudo-energy. This is obtained by setting $n_l = 1$ for $\varphi_l < 0$ and $n_l = 0$ for $\varphi_l > 0$. In complete analogy to the real energy of a noninteracting system of fermions, we simply fill up the *single-particle pseudo-energy levels (PELs)* from the lowest up to a *pseudo-Fermi level*. The maximum density-matrix weight always turns out to occur with the cluster fractional filling that is closest to the bulk filling of the Fermi sea ground state. More generally, the maximum-weight state in the P_C-particle sector is obtained by filling the states with the P_C lowest single-particle pseudo-energies. Finally, it is clear that the next-highest weights, or equivalently the next-lowest total pseudo-energies in the P_C-particle sector, are obtained by making particle-hole excitations involving the PELs near to the last one filled.

The above analogy may be extended to note that (2.1.7) is exactly the density matrix that would be obtained (see for example, Ref. 185) at temperature $T = 1$ if $\tilde{H}$ were the Hamiltonian. The reciprocal of the normalization constant $\mathscr{Q}$ of ρ_C in (3.3.4) just corresponds to the grand partition function for the cluster of N_C sites. Among other things, this implies that $\langle n_l \rangle$, the average particle number in a particular PEL, has the functional form of the Fermi-Dirac distribution. We will actually apply this idea in a slightly different way, so as to relate the single-particle pseudo-energies φ_l for different cluster sizes. If we were dealing with an actual Hamiltonian, the dispersion relation would imply a density of states which would be multiplied by the system size to obtain the actual distribution of states. Our numerical scaling results in Section 3.5.1 confirm

that pseudo-energies behave similarly to real energies.

3.3.2 Pseudo-Energies and Cluster Green-Function Matrix

In Chapter 2 we obtain an exact formula

$$\tilde{H} = -\sum_{ij} \left[\log G_C(\mathbb{1} - G_C)^{-1}\right]_{ij} c_i^\dagger c_j, \tag{3.3.5}$$

which, with (2.1.7), relates ρ_C to the cluster Green-function matrix G_C, whose matrix elements are $G_C(i, j) = \langle c_i^\dagger c_j \rangle$ with i and j restricted to sites within the cluster. Clearly (3.3.5) becomes (2.1.7) when the pseudo-Hamiltonian is diagonalized. Also, (3.3.5) tells us that the quadratic form of $\tilde{H}$ in (3.3.5) and G_C are simultaneously diagonalizable. If we denote by

$$|\chi_l\rangle = f_l^\dagger |0\rangle = \sum_{j=1}^{N_C} \chi_l(j) c_j^\dagger |0\rangle , \tag{3.3.6}$$

the single-particle eigenstate of $\tilde{H}$ with eigenvalue φ_l, then $\{\chi_l(j)\}$ is the eigenvector of G_C with eigenvalue λ_l. The single-particle pseudo-energies are related to the eigenvalues of G_C by (2.5.3), or equivalently,

$$\lambda_l = \frac{1}{\exp \varphi_l + 1}, \tag{3.3.7}$$

i.e. the eigenvalues of G_C are the average pseudo-occupation numbers $\langle n_l \rangle$. Note that we sometimes write φ_l as $\varphi(l, N_C)$ to make explicit the dependence on cluster size N_C. We will assume that φ_l are ordered from the most negative to the most positive values.

Another notable result that was derived in Chapter 2 is that

$$\mathscr{Q}^{-1} = \det(\mathbb{1} - G_C) = \prod_{l=1}^{N_C} (1 - \lambda_l). \tag{3.3.8}$$

Along with (3.3.5) and (2.5.3), (3.3.8) comprises the final ingredients that allow numerical computation of the density matrix even in very large clusters. Aside from the

possibilities of truncation, (3.3.1) through (3.3.8) have completely reduced a $2^{N_C} \times 2^{N_C}$ diagonalization problem into a $N_C \times N_C$ problem, a computational shortcut which allows numerical studies of large clusters.

3.3.3 Recipe for Operator-Based Truncation

The analytical structure of (2.1.8) hints at the proper design of a truncation scheme. The retained Hilbert space of a cluster *should not* be the span of those density-matrix eigenstates whose weight exceeds a cutoff. Instead, we should implement a 'consistent' truncation, such that the truncated Hilbert space consists of exactly $2^{l_{\max}}$ states, built from all combinations of $l_{\max}$ pseudo-creation operators $f_1^\dagger, \ldots, f_{l_{\max}}^\dagger$, acting on a cluster 'vacuum state' $|0\rangle_C$, and satisfying fermion anticommutation relations.

In the traditional density-matrix-based truncation scheme used in DMRG, the recipe for truncation is to sort all density-matrix weights in descending order, and then retain only the eigenstates associated with the weights that exceed a certain cut off. Let us refer to this as the *weight-ranked DM truncation scheme*. In light of our understanding of the structure of the many-body density matrix, we can see that the weight-ranked DM truncation scheme will certainly retain the eigenstate with maximum weight, the pseudo-Fermi sea described in Section 3.3.1, along with eigenstates that are 'particle excitations', 'hole excitations' and 'particle-hole excitations' from the pseudo-Fermi sea. If we arrange the entire collection of many-particle density-matrix eigenstates into a state graph — where the nodes are the many-particle density-matrix eigenstates, and an edge will be drawn between two nodes, if the many-body density-matrix eigenstates they represent are connected by the action of the pseudo-fermion operators f_l or $f_l^\dagger$ — then the state graph looks like a N_C-dimensional hypercubic lattice near the pseudo-Fermi sea. What the weight-ranked DM truncation does in this state graph picture is

to remove nodes, and in effect cut bonds, out from this hypercubic lattice, producing a subgraph that is much less connected and containing tenuous links. Because of this, when the Hamiltonian is projected onto the weight-ranked DM truncated basis, spurious interactions are introduced.

We can apply the pseudo-energy analogy in choosing how to truncate, given the form of the density matrix. It is familiar, in the truncation used in Fourier-space-based quantum renormalization groups, to discard all single-particle degrees of freedom except for a shell around the Fermi surface. In the same way, let us discard all operators f_l as degrees of freedom, except those for which $|\varphi_l|$ is less than some threshold φ_*. For all other f_l, we 'freeze' n_l by setting n_l to its ground-state value

$$n_l = \begin{cases} 1, & \text{for } \varphi_l < -\varphi_*; \\ 0, & \text{for } \varphi_l > \varphi_*. \end{cases} \tag{3.3.9}$$

This choice gives the maximum density matrix weight, among the eigenstates having any particular set of n_l for the retained single-particle pseudo-energy levels. The spirit of this truncation scheme is similar to that used in quantum chemistry [186–188], except that the notion of a Fermi surface is more fuzzy in atoms and molecules. The idea that truncation consists of decreasing the thickness of a shell of wavevectors around the Fermi surface appeared in the original renormalization group for a quantum-mechanical solid-state problem (Anderson's poor man's RG for the Kondo problem [189]). This obvious notion — that the action is around the Fermi surface — necessarily appears in every effective form of truncation intended for a metal (see for example, Ref. 190 and Ref. 191, among others). However, to our knowledge all such schemes used a basis of plane waves or of energy eigenstates. Our variation uses PELs in analogy to the use of energy eigenstates in these previous problems. Deriving from the density matrix, it makes sense only in procedures that involving cutting a real-space cluster out of a larger

system.

Within this *operator-based density matrix (DM) truncation scheme*, we can define an effective Hamiltonian for the truncated Hilbert space, just by taking the matrix elements of the true Hamiltonian between all the retained states. Using an operator-based truncation, this will have a particularly clean form: first replace each creation operator $c_j^\dagger$ by the equivalent combination of all $\{f_l^\dagger\}$; then replace $f_l^\dagger f_l \to 1$ for each single-particle pseudo-energy $\varphi_l < -\varphi_*$ (these are frozen to be always occupied), and otherwise remove all terms involving the operators that are truncated. Thus, if the original Hamiltonian has at most $l_{\max}$-fermion terms, the same will be true for the truncated Hamiltonian. This prescription shows that such a truncation is possible for general models, once one knows the appropriate density matrix, but we shall apply it only to noninteracting models in this chapter.

3.4 Asymptotics of Eigenvalue Distribution

Before going on to study the scaling behaviours of the single-particle cluster density-matrix pseudo-energies and eigenfunctions in Sections 3.5 and 3.8 respectively, let us look at the distribution of many-particle cluster density-matrix weights, or equivalently, the cluster density-matrix total pseudo-energies, since the details of this distribution affect the performance of the weight-ranked density-matrix truncation scheme used in the DMRG.

In the literature, this distribution has been studied by mapping by one-dimensional quantum-mechanical systems to two-dimensional classical statistical systems. The half-chain density matrix ρ_1 of the one-dimensional quantum-mechanical system can then be calculated from a product of corner transfer matrices of the two-dimensional classical statistical system. For integrable two-dimensional classical statistical systems, the

corner transfer matrix is given by a single infinite tensor product, and its asymptotic eigenvalue distribution is well understood [1]. Consequently, the distinct eigenvalues of ρ_1 are, up to the choice of normalization for ρ_1, given by z^l, where $0 < z < 1$ and l is a non-negative integer.[1] The distinct eigenvalues $w_l = z^l = \exp(-l \log |z|)$ therefore exhibits an exponential decay as a function of the ordinal number l of distinct eigenvalues.

Of course, when the eigenvalues are ordered using the usual ordinal number L that disregards degeneracy between eigenvalues, the decay of w_L with L will no longer be exponential. Through the use of some clever substitutions, Okunishi *et al* found that this decay is on the average given by [193]

$$w_L \sim \exp[-\alpha(\log L)^2], \tag{3.4.1}$$

where α is a constant that can be calculated exactly for integrable systems. This asymptotic decay law (which looks nearly exponential on a semilog plot over not too large a range of L) appears to be universal for both integrable and nonintegrable one-dimensional quantum systems, as verified numerically in their own work [193], as well as the work of Peschel *et al* [176–178]. Peschel *et al* also investigated the density matrix eigenvalue distribution for two-dimensional quantum systems [176, 194], and found a much slower decay.

In this section, we describe an alternative universal asymptotic eigenvalue distribution based on (3.3.2) and (3.3.3) that may be numerically indistinguishable from the one proposed by Okunishi *et al* near the lower tail of the distribution. To derive this universal asymptotic distribution, let us consider how the total pseudo-energy Φ behaves as a function of the ordinal number L, which ranks Φ in ascending order. We observe first that if $p(\Phi)\, d\Phi$ is the probability, when picking a total pseudo-energy at random,

[1] This result is rederived from a field theory perspective for a chain of coupled oscillators in Ref. 192, in contrast to the more traditional approach in Ref. 178.

to find it within the interval $(\Phi, \Phi + d\Phi)$, and if $\mathcal{N} = 2^{N_C}$ is the grand total number of total pseudo-energies that we can form from $\{\varphi_1, \varphi_2, \ldots, \varphi_{N_C}\}$, then $\mathcal{N} p(\Phi)\, d\Phi$ is the number of total pseudo-energies found in the interval. Clearly this must be equal to dL, the difference in ordinal numbers of Φ and $\Phi + d\Phi$, i.e.

$$dL = \mathcal{N} p(\Phi)\, d\Phi, \tag{3.4.2}$$

so that

$$L(\Phi) = \mathcal{N} \int^{\Phi} p(\Phi')\, d\Phi'. \tag{3.4.3}$$

Therefore, to find $L(\Phi)$, and thereafter invert it to get $\Phi(L)$, we should first figure out what $p(\Phi)$ is.

For a system of noninteracting fermions, the Pauli Exclusion Principle requires that the P_C single-particle pseudo-energies adding up to Φ must be distinct, though their order in the sum is not important. We can write this sum, very generally, as

$$\Phi = 0 \cdot \varphi_1 + \cdots + 1 \cdot \varphi_{l_1} + \cdots + 1 \cdot \varphi_{l_{P_C}} + 0 \cdot \varphi_{l_{P_C}+1} + \cdots = \sum_{l=1}^{N_C} n_l \varphi_l, \tag{3.4.4}$$

where $n_l = 0$ or 1, and N_C is the total number of single-particle pseudo-energies (also the number of sites within the cluster). With this, we see that different Φ's corresponds to different combinations of n_l's, i.e. the n_l's can be interpreted as independent identical binomial random variables. In the asymptotic limit of very large cluster sizes, $\Phi = \sum_{l=1}^{N_C} n_l \varphi_l$ is the sum of a large number of uniformly-bounded random variables, and therefore it follows from the Lindeberg-Feller Central Limit Theorem (a generalized version of the usual Central Limit Theorem) that the asymptotic distribution of Φ is normal [195,196]. Such a distribution is universal, in the sense that the details of the distribution of $\{\varphi_l\}$ themselves are absorbed into the mean $\bar{\Phi} = \frac{1}{2}\sum_l \varphi_l$ and standard deviation $\sigma = (\frac{1}{4}\sum_l \varphi_l^2)^{1/2}$ of the total pseudo-energy distribution. Different pseudo-energy

distributions giving the same $\bar{\Phi}$ and σ thus produce total pseudo-energy distributions that differ only in their tails.

With $p(\Phi) \sim \left(\sqrt{2\pi\sigma^2}\right)^{-1} \exp[-(\Phi - \bar{\Phi})^2/\sigma^2]$ known, we can determine the asymptotic behaviour of $L(\Phi)$, in the limit of $L \gg 1$ and $L \ll \mathcal{N}$, as

$$\begin{aligned} L(\Phi) &\sim \frac{1}{\sqrt{2\pi\sigma^2}} \int_{-\infty}^{\Phi} \exp\left[-\frac{(\Phi' - \bar{\Phi})^2}{\sigma^2}\right] d\Phi' \\ &\sim 1 + \mathrm{erf}((\Phi - \bar{\Phi})/\sigma). \end{aligned} \tag{3.4.5}$$

where $\mathrm{erf}(z)$ is the error function. We checked this analysis numerically with a 'fake' single-particle pseudo-energy spectrum $\{\varphi_l\}$ by taking N_C random numbers uniformly distributed between zero and one. With this 'fake' single-particle pseudo-energy spectrum, we then generated the entire spectrum of $\mathcal{N} = 2^{N_C}$ total pseudo-energies. The total pseudo-energy distributed generated by a 'fake' spectrum of six single-particle pseudo-energies is shown in Figure 3.1. When the N_C random single-particle pseudo-energies are sampled from other uniformly-bounded statistical distributions, the same distribution is obtained, after shifting by the respective means $\bar{\Phi}$ and rescaling by the respective standard deviations σ, verifying that such an asymptotic distribution is indeed universal. There are, of course, non-universal deviations from this asymptotic behaviour at the tails of the distribution. We will need to worry about these tails when we get to Sec. 3.6.4, when we look into truncation errors.

For a set of N_C pseudo-energies φ_l, there are a total of $\mathcal{N} = 2^{N_C}$ total pseudo-energies Φ. Clearly, it is not possible to exhaust the entire spectrum of Φ if N_C is large. If, as was done by Okunishi *et al* [193] and Peschel *et al* [176–178], we calculate only the largest density-matrix eigenvalues (i.e. the smallest total pseudo-energies), then we are in effect exploring only the part of the distribution for which $\Phi < \bar{\Phi}$. In Figure 3.2 we show a magnified view of this region of the distribution, with Φ plotted against $(\log L)^2$. Here we see that the asymptotic formula (3.4.1) derived by Okunishi *et al* for integrable

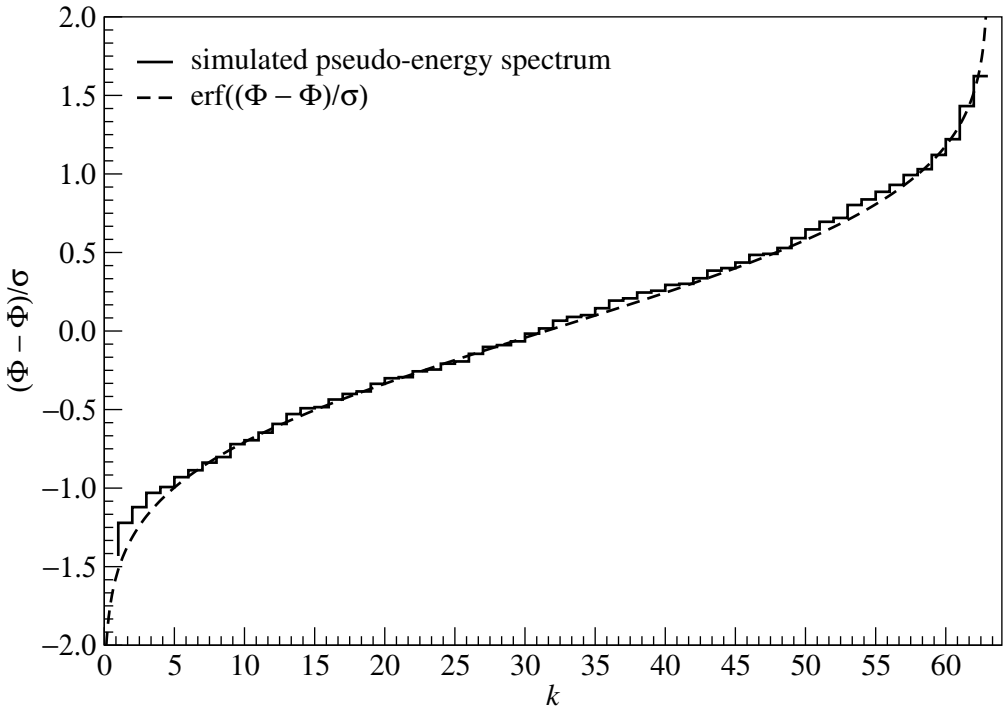

Figure 3.1: 'Faked' distribution of total pseudo-energy Φ as a function of the ordinal number L, after shifting by $\bar{\Phi}$ and scaling by the standard deviation σ. These 'faked' total pseudo-energies are generated from 6 random number uniformly distributed between 0 and 1. Also shown is $\mathrm{erf}((\Phi - \bar{\Phi})/\sigma)$.

quantum systems appears to fit this region of our 'fake' total pseudo-energy spectrum even better than the asymptotic behaviour (3.4.5) that we derived, even though it is not right for our problem. In view of this, one must be careful in interpreting numerical fits elsewhere as providing evidence for universality of the $(\log L)^2$ asymptotic behaviour.

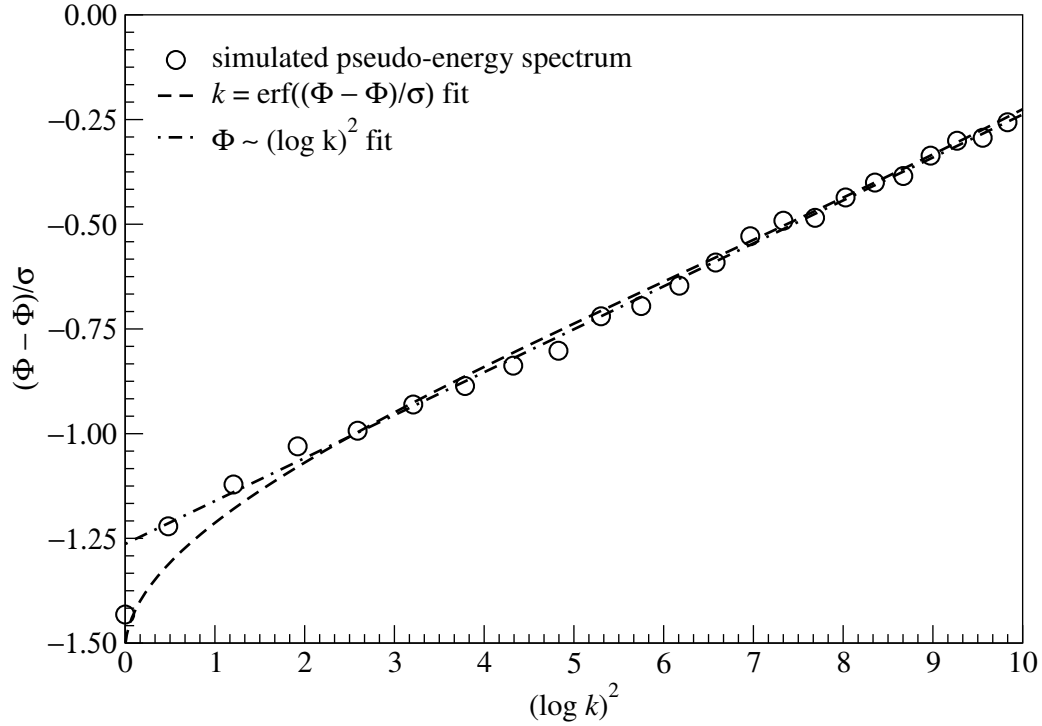

Figure 3.2: 'Faked' distribution of total pseudo-energy Φ plotted against $(\log L)^2$, for $\Phi < \bar{\Phi}$, along with a fit using Okunishi *et al*'s asymptotic formula (3.4.1).

3.5 Scaling Behaviour of Eigenvalue Distribution

Since the many-particle density matrix eigenvalues are built, according to (3.3.2), from the single-particle pseudo-energies, the latter are the focus of our numerical investigations in this section. For our numerical work in the remainder of this chapter, we will specialize to the one-dimensional system of noninteracting spinless fermions. If our entire system consists only of the cluster in a pure state at $T = 0$, then every eigen-

value λ_l of the cluster Green-function matrix G_C, being the average pseudo-occupation number $\langle n_l \rangle$ of a PEL, would either be zero or one. At $T > 0$, λ_l follow a Fermi-Dirac distribution. We will see later that cutting out a finite cluster from a $T = 0$ system, by tracing over the environment of the cluster, has a similar effect on the eigenvalues of G_C as would taking $T > 0$ when the cluster is the whole system.

In a translationally invariant system with filling $\bar{n}$ (at $T = 0$), a fraction $\bar{n}$ of the eigenvalues of G_C are one, while the rest are zero. Cutting out a cluster of length N_C must smooth out this step (much as having $T > 0$ makes it into a Fermi-Dirac distribution), and we expect the transition from one to zero to occur over a fraction $\sim 1/N_C$. This guess was inspired by the analogy of pseudo-energy φ_l in (2.1.8) to the real energy, which near the Fermi level scales linearly with wavevector $\sim 1/N_C$. This ${N_C}^{-1}$ scaling suggests the conjecture of a scaling form for the single-particle pseudo-energy like $\varphi_l \approx N_C f(l/N_C)$, and indeed we find below just such a scaling form.

3.5.1 Pseudo-Energies and Pseudo-Occupation Numbers

In this subsection we calculate numerically the eigenvalues λ_l of the cluster Green-function matrix G_C, and use (2.5.3) to compute the single-particle pseudo-energies φ_l. For a chain of noninteracting spinless fermions in its ground state, the matrix elements of the cluster Green-function matrix G_C are

$$G_C(i, j) = \frac{\sin \pi \bar{n} |i - j|}{\pi |i - j|}, \tag{3.5.1}$$

where $\bar{n}$ is the filling fraction. Figure 3.3 shows how λ_l, the eigenvalues of G_C, are distributed for different filling fractions $\bar{n}$ and different cluster sizes N_C.

At half-filling $\bar{n} = \frac{1}{2}$, our numerical studies suggest a scaling relationship of the form

$$\varphi(l, N_C) \cong N_C f(x), \tag{3.5.2}$$

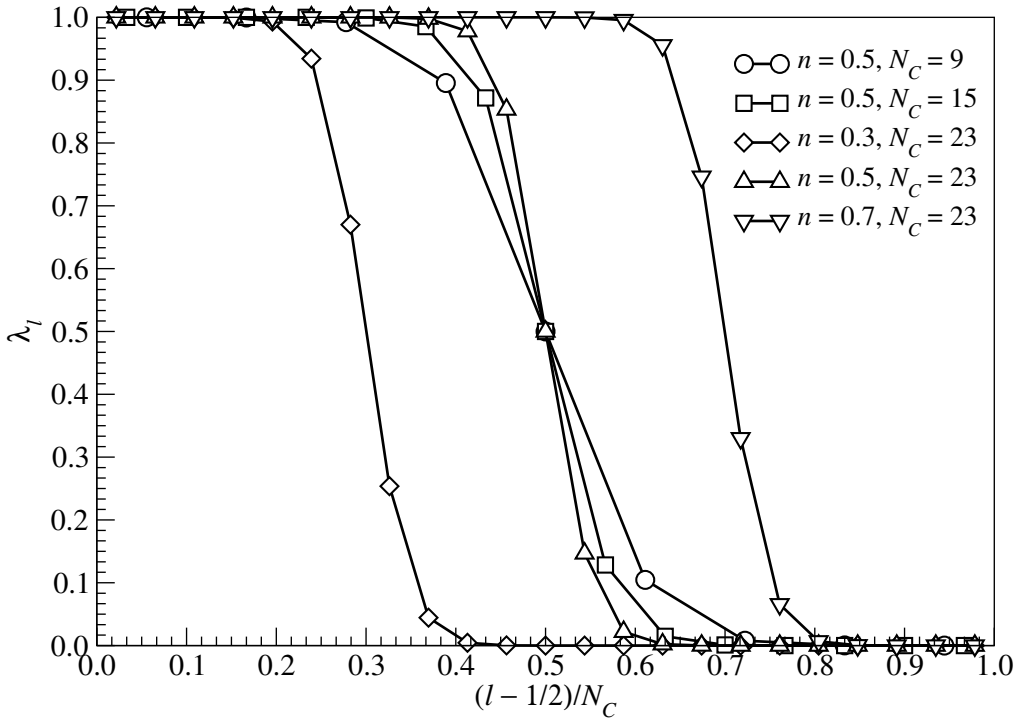

Figure 3.3: Distribution of λ_l for different filling fractions and cluster sizes. In order to compare λ_l for different cluster sizes, the interval $l \in [1, N_C]$ is rescaled such that $(l - \frac{1}{2})/N_C \in (0, 1)$. With this rescaling, $\lambda = \frac{1}{2}$ always occur at $[(l - \frac{1}{2})/N_C] = \bar{n}$.

where $x \equiv [(l-\frac{1}{2})/N_C]-\frac{1}{2}$, as shown in Figure 3.4. There are two observations on Figure 3.4 we would like to make. First of all, with our choice of the scaling variable x, the scaling function $f(x)$ always passes through the origin, i.e.

$$f(0) = 0. \tag{3.5.3}$$

Secondly, from Figure 3.4, we see that $f(x)$ is an odd function, i.e.

$$f(-x) = -f(x), \tag{3.5.4}$$

which is what we would expect from particle-hole symmetry when the overall system is at half-filling, and $f(x)$ has a finite positive slope at $x = 0$, i.e.

$$f'(0) > 0. \tag{3.5.5}$$

Similar scaling behaviours of the form

$$\varphi(l, N_C, \bar{n}) \cong N_C f(\bar{n}, x) \tag{3.5.6}$$

are found for all $\bar{n}$, with the generic scaling variable

$$x \equiv (l - l_F)/N_C, \tag{3.5.7}$$

where

$$l_F = \bar{n}N_C + \tfrac{1}{2} \tag{3.5.8}$$

plays the role of a Fermi wavevector, and a filling fraction-dependent scaling function $f(\bar{n}, x)$, as shown in FIG. 3.5. The scaling functions continue to satisfy

$$f(\bar{n}, 0) = 0, \tag{3.5.9}$$

and

$$f'(\bar{n}, 0) > 0, \tag{3.5.10}$$

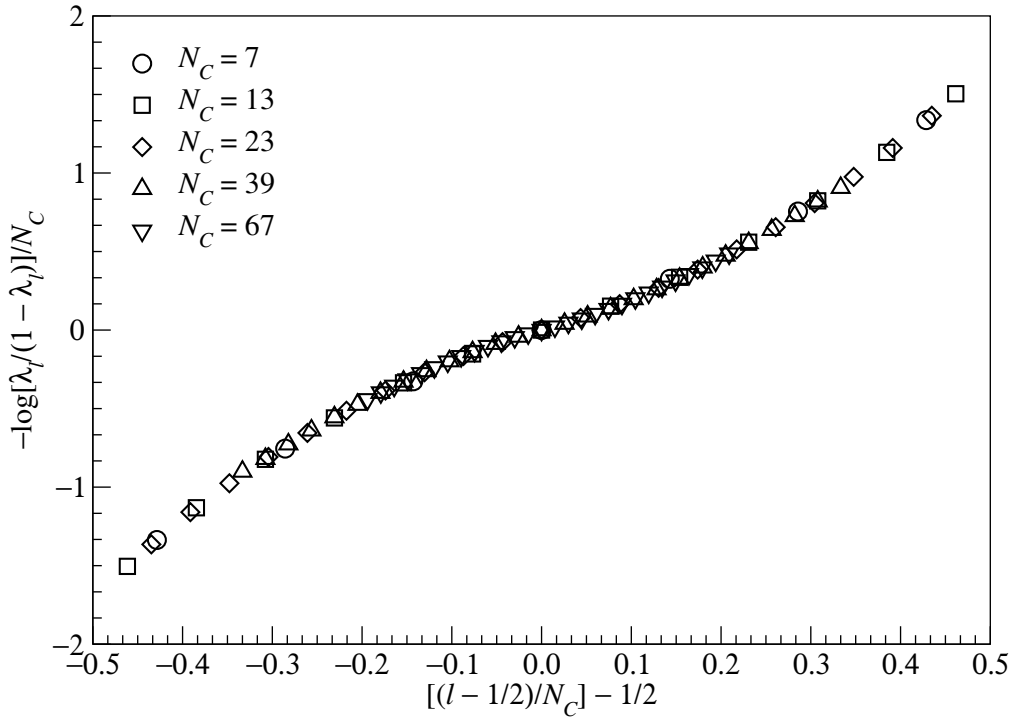

Figure 3.4: Plot of $-{N_C}^{-1}\log[\lambda_l/(1-\lambda_l)]$ as a function of the scaling variable $x \equiv [(l-\frac{1}{2})/N_C] - 1/2$ for various cluster sizes at half-filling, showing a scaling collapse onto the scaling function $f(x)$. For $N_C > 23$, the largest and smallest pseudo-energies are severely affected by numerical truncation errors in the diagonalization routines, and thus not shown.

but $f(\bar{n}, x)$ is no longer an odd function of x for $\bar{n} \neq \frac{1}{2}$. Instead, the particle-hole symmetry inherent in our model is manifested as

$$f(\bar{n}, -x) = -f(1 - \bar{n}, x). \tag{3.5.11}$$

From (3.3.7) and (3.5.6), we can write λ_l as

$$\lambda_l = \frac{1}{\exp(N_C f) + 1}, \tag{3.5.12}$$

which tells us that $f(\bar{n}, x)$ plays the role of a dispersion relation $\epsilon(k)$, while N_C plays the role of the inverse temperature β. This confirms our suspicion that the effect of cutting a cluster out of an overall system in its ground state at $T = 0$ is to ascribe to the cluster an effective temperature. As expected, this effective temperature approaches zero as the cluster size is increased, since we are keeping more and more information about the overall system, which we know to be at $T = 0$.

3.5.2 Normalization Constant

Having understood that λ_l is related to the scaling function $f(\bar{n}, x)$ as in (3.5.12), we are now ready to investigate the scaling behaviour of the normalization constant $\mathscr{Q}^{-1}$, which is related to λ_l by (3.3.8). We do this first at half-filling. As can be seen from Figure 3.3, at half-filling roughly half of the λ_l are approximately one, whereas the other half are approximately zero. The product $\prod_l (1 - \lambda_l)$ is therefore determined primarily by the $\sim N_C/2$ λ_l's that are nearly one. For these eigenvalues, $\exp[N_C f(x)] \ll 1$ and thus $1 - \lambda_l \approx \exp[N_C f(x)]$ (when it is clear what the filling fraction is, we will drop the argument $\bar{n}$ in $f(\bar{n}, x)$ to keep the notations neat). With this, we find that

$$\begin{aligned} \mathscr{Q}^{-1} &= \prod_{l=1}^{N_C} (1 - \lambda_l) \approx \prod_{l=1}^{N_C/2} \exp[N_C f(x)] \\ &\approx \exp\left\{ N_C \int_{-1/2}^{0} f(x)\, dx \right\} = \exp\left\{ -N_C \int_{0}^{1/2} f(x)\, dx \right\}, \end{aligned} \tag{3.5.13}$$

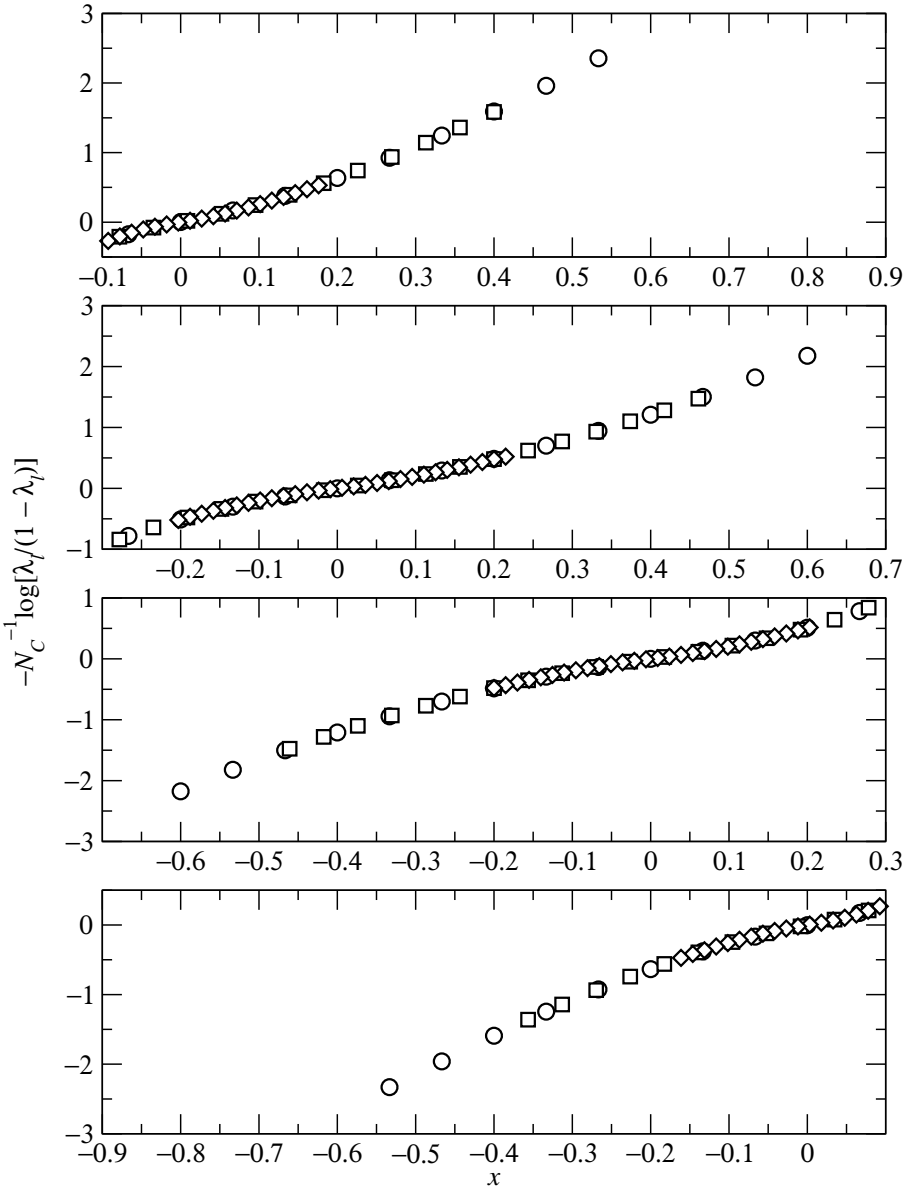

Figure 3.5: Scaling collapses for (from top to bottom) $\bar{n} = 0.1$, 0.3, 0.7 and 0.9, plotted against the scaling variable $x \equiv (l - \frac{1}{2})/N_C - \bar{n}$, for three different cluster sizes: $N_C = 15$ ($\circ$), $N_C = 23$ ($\square$) and $N_C = 67$ ($\diamond$).

where we made used the observed odd symmetry of the scaling function in (3.5.4) when the overall system is at half-filling, so that the integral within the exponent is positive. From (3.5.13), we see that $\mathscr{Q}^{-1}$ decreases exponentially with cluster size N_C.

In general, for $\bar{n}$ not too close to zero, where the argument that those λ_l's that are near one makes the dominant contribution holds, we find that

$$\begin{aligned}\mathscr{Q}^{-1} &\approx \exp\left\{N_C \int_{-\bar{n}}^{0} f(\bar{n}, x)\, dx\right\} \\ &= \exp\left\{-N_C \int_{0}^{\bar{n}} f(1-\bar{n}, x)\, dx\right\},\end{aligned} \tag{3.5.14}$$

where we made use of (3.5.11). For $\bar{n}$ very close to zero, there are a handful of λ_l's of $O(1)$, and the rest are all nearly zero, behaving like $\lambda_l \approx \exp[-N_C f(\bar{n}, x)]$. Ignoring these handful of $O(1)$ λ_l's, we find that the contribution to $\mathscr{Q}^{-1}$ from those $\lambda_l \ll 1$ is proportional to the product $\prod_l (1-\lambda_l) \approx 1 - \sum_l \lambda_l$, and so

$$\mathscr{Q}^{-1} \propto \left[1 - \int_0^{1-\bar{n}} e^{-N_C f(\bar{n},x)}\, dx\right]. \tag{3.5.15}$$

The integral can be evaluated as a cumulant expansion, but we can already see that for large N_C, the integral will not be important, and thus $\mathscr{Q}^{-1}$ derives most of its value from the few $O(1)$ λ_l's. In contrast, when $\bar{n}$ is very close to 1, then most of the eigenvalues λ_l of G are close to 1, and these continue to dominate the product $\prod_l (1-\lambda_l)$, and the asymptotic formula derived in (3.5.13) continues to be valid.

3.6 Density-Matrix Weights: Implications of Eigenvalue Scaling

With our understanding of the structure of the many-particle density-matrix eigenvalues and eigenstates developed in Section 3.3.1, and on the scaling behaviour of the single-particle pseudo-energy found in Section 3.5, we want to now address the question of how much of the Hilbert space we can truncate. Clearly, the answer to this question depends

on what measure of error we intend to use as our criteria for judging how well the truncated Hilbert space describes the physics associated with the parent model. In this section we look at the most common measure of error, used in the DMRG [14, 15] and quantum chemistry calculations [186–188]: for a properly-normalized density matrix, the density-matrix weights w_L satisfy the sum rule

$$\sum_L w_L = 1. \tag{3.6.1}$$

If the ordinal numbers L are chosen such that w_L is ranked in decreasing order, and a total of $L_{\max}$ density matrix eigenstates are retained, then the truncated weight

$$W_t = \sum_{L \leq L_{\max}} w_L \leq 1, \tag{3.6.2}$$

and the discarded weight

$$\epsilon = 1 - W_t \tag{3.6.3}$$

are frequently used as figures of merit for the truncation scheme, since for a bounded operator A, the truncation error in $\langle A \rangle$ is $O(\epsilon)$.

3.6.1 The Gapless Chain of Noninteracting Spinless Fermions

Instead of diving in to look at W_t or ϵ, let us consider first a related question: how large is the maximum weight for a cluster of N_C sites embedded within an overall system of gapless noninteracting spinless fermions? For our discussions, we will consider the half-filled case; it will be straightforward to extend the arguments presented below to $\bar{n} \neq \frac{1}{2}$. For convenience, let us take N_C to be even.[2] Let us denote by $|F\rangle$, where $F = N_C/2$, the many-particle density-matrix eigenstate having the largest weight. This state is always kept in the operator-based truncation scheme. Recall from Section 3.3

[2]The same conclusion holds for the case of N_C odd, apart from the technical annoyance that there are *two* many-particle density-matrix eigenstates with the largest weight.

that, as shown in Figure 3.6(b), this is the analog among density matrix eigenstates of the Fermi sea ground state among energy eigenstates. In this $N_C/2$-particle state, the single-particle pseudo-energy is filled up to just before $x = 0$, which we shall call the *pseudo-Fermi level*. The many-particle density-matrix eigenstates of the cluster having the next largest weights, of which there are two, will be called $|F-1\rangle$ (Figure 3.6(a)) and $|F+1\rangle$ (Figure 3.6(c)), having respectively one less or one more particle.

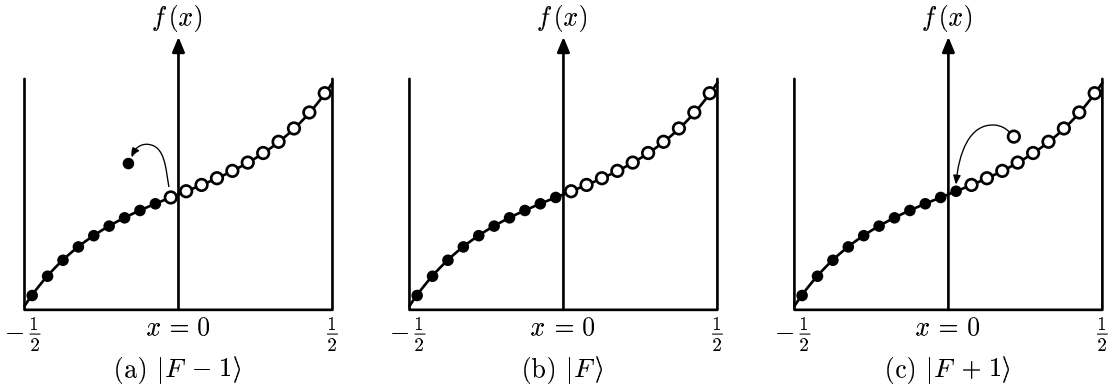

(a) $|F-1\rangle$ (b) $|F\rangle$ (c) $|F+1\rangle$

Figure 3.6: Schematic diagram showing the three many-particle density-matrix eigenstates, (a) $|F-1\rangle$, (b) $|F\rangle$ and (c) $|F+1\rangle$, with the largest weights, for a cluster of N_C (N_C even) sites within a overall system that is half-filled.

We can understand the weight ratio w_{F-1}/w_F or w_{F+1}/w_F as follows. By (3.3.2), $|F\rangle$ is the state with $n_l = 1$ for $l = 1, \ldots, N_C/2$ and $n_l = 0$ for $l = N_C/2+1, \ldots, N_C$. The state $|F+1\rangle$ differs only in having $n_{N_C/2+1} = 1$, while $|F-1\rangle$ differs only in having $n_{N_C/2} = 0$. Near the pseudo-Fermi level, the scaling function has a slope of $f'(0)$, while the spacing between adjacent pseudo-energies on the rescaled l/N_C axis is $1/N_C$. Thus $\varphi_{N_C/2+1} - \varphi_{N_C/2} \approx f'(0)$. But when the actual filling is $\bar{n} = \frac{1}{2}$, we know by particle-hole symmetry that $\varphi_{N_C/2+1} = -\varphi_{N_C/2}$, so $\varphi_{N_C/2} \approx -f'(0)/2$ and $\varphi_{N_C/2+1} \approx f'(0)/2$. It follows from (3.3.2), that

$$\frac{w_{F+1}}{w_F} = \frac{w_{F-1}}{w_F} \approx \exp(-f'(0)). \tag{3.6.4}$$

For $\bar{n} \neq \frac{1}{2}$, (3.5.6) would tell us that these ratios are approximately $\exp(-f'(\bar{n}, 0))$.

This is quite different from what would happen when the cluster contains half of the entire system, as considered in the standard DMRG algorithm, or in Ref. 176. If the fraction (N_C/N) in the cluster approached one, the state $|F\rangle$ must become the Fermi sea ground state of the overall system, and consequently contains all the weight. If the cluster is merely a finite fraction of the system, we still expect a much larger ratio than (3.6.4). It would be interesting to check the behaviour of the ratios in (3.6.4) for the case $N_C, N \to \infty$ with $N_C/N = 1/2$, but we have not investigated this.

3.6.2 The Gapped Chain of Noninteracting Spinless Fermions

For the purpose of understanding the pseudo-energy spectrum of non-interacting systems better, we also considered the dimerized tight-binding Hamiltonian

$$\begin{aligned} H &= -t \sum_{j=1}^{N} \left[1 + (-1)^j \delta\right] \left(c_j^\dagger c_{j+1} + c_{j+1}^\dagger c_j\right) \\ &= \sum_k \epsilon_k \left[\tilde{c}_k^\dagger \tilde{c}_k - \tilde{c}_{k+\frac{\pi}{a}}^\dagger \tilde{c}_{k+\frac{\pi}{a}}\right] - \mathrm{i}\, \Delta_k \left[\tilde{c}_{k+\frac{\pi}{a}}^\dagger \tilde{c}_k - \tilde{c}_k^\dagger \tilde{c}_{k+\frac{\pi}{a}}\right], \end{aligned} \tag{3.6.5}$$

where

$$\epsilon_k = -2t \cos ka, \quad \Delta_k = 2t\delta \sin ka. \tag{3.6.6}$$

In this model, the hopping integral t modulated by the $(-1)^j\delta$ term to produce an energy gap. Henceforth let us choose the scale of energy to be such that $t = 1$. The Hamiltonian in (3.6.5) can be diagonalized in terms of second-quantized operators (see, for example, Ref. 197), to be written as

$$H = \sum_{|k| < \frac{\pi}{2a}} E(k) \left(a_{k,+}^\dagger a_{k,+} - a_{k,-}^\dagger a_{k,-}\right), \tag{3.6.7}$$

with

$$E(k) = \sqrt{\epsilon^2(k) + \Delta^2(k)}. \tag{3.6.8}$$

In terms of $\Delta(k)$ and $\epsilon(k)$, we can define an angle ϕ_k such that

$$\tan 2\phi_k = \Delta(k)/\epsilon(k), \tag{3.6.9}$$

and whose sine and cosine we denote as

$$\alpha_k = \cos\phi_k, \quad \beta_k = \sin\phi_k. \tag{3.6.10}$$

In terms of these, the operators $a_{k,+}$ and $a_{k,-}$ for the upper and lower bands are given by

$$\begin{aligned} a_{k,-} &= \alpha_k \tilde{c}_k + \mathrm{i}\,\beta_k \tilde{c}_{k+\pi}, \\ a_{k,+} &= -\beta_k \tilde{c}_k + \mathrm{i}\,\alpha_k \tilde{c}_{k+\pi} \end{aligned} \tag{3.6.11}$$

respectively.

At half-filling, the lower band is completely filled while the upper band is completely empty, and the ground state can written simply as

$$|\Psi\rangle = \prod_{|k|<\frac{\pi}{2}} a^\dagger_{k,-} |0\rangle\,. \tag{3.6.12}$$

For this ground state, the two-point function is given by

$$G(i,j) = \frac{1}{2\pi} \int_{-\frac{\pi}{2}}^{\frac{\pi}{2}} dk\, e^{\mathrm{i}\,k(i-j)}\, \frac{\cos k - \mathrm{i}(-1)^i \delta \sin k}{\sqrt{\cos^2 k + \delta^2 \sin^2 k}}, \tag{3.6.13}$$

using which we can construct the cluster Green-function matrix G_C, and hence, using (2.5.3), the pseudoenergies which correspond to the density-matrix eigenvalues. For a fixed cluster size of $N_C = 23$, the pseudo-energy spectra for different hopping modulation δ is shown in Figure 3.7, compared to that of the gapless case. Scaling behaviour of the single-particle pseudo-energies was found for all δ, each governed by a different scaling function $f(\bar{n}, \delta, x)$. The scaling collapse plot for $\delta = 0.5$ is shown in Figure 3.8, compared to the scaling function $f(\bar{n}, \delta = 0, x)$ for the gapless case.

Analyzing the three density-matrix eigenstates with the largest weights, we find again that the ratios of density matrix weights w_{F+1}/w_F and w_{F-1}/w_F to be independent of cluster size N_C when the overall system is at half-filling. However, these ratios

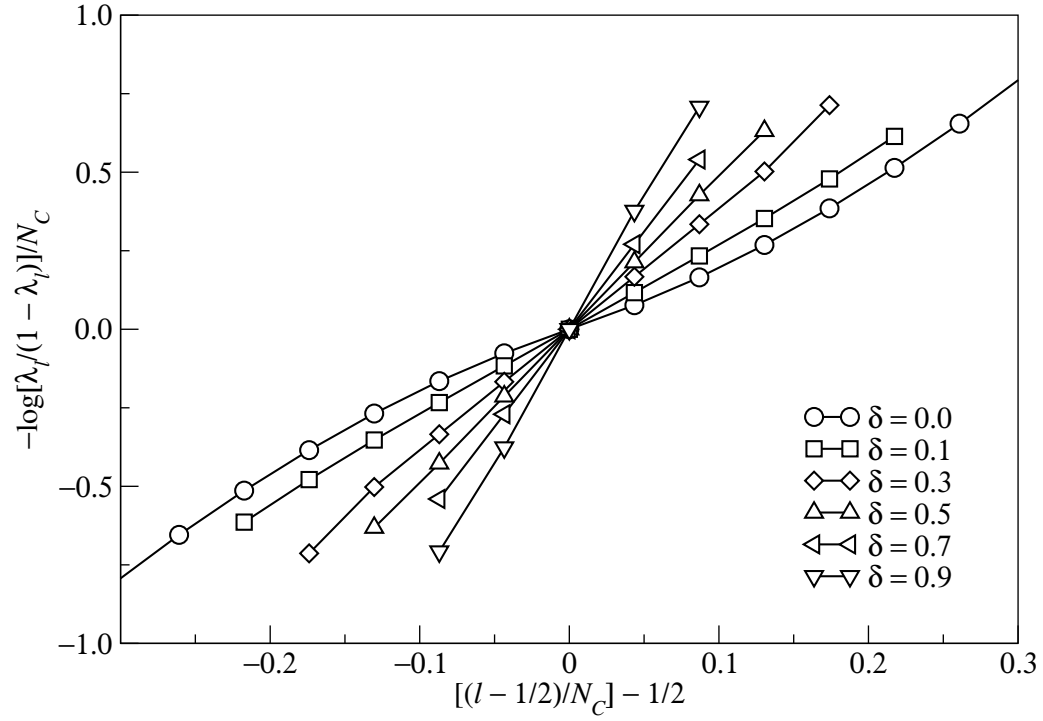

Figure 3.7: Plot of $-{N_C}^{-1}\log[\lambda_l/(1-\lambda_l)]$ as a function of the scaling variable $x = (l-\frac{1}{2})/N_C - \frac{1}{2}$, for a cluster of size $N_C = 23$, with different hopping modulations $\delta = 0.1, 0.3, 0.5, 0.7, 0.9$. Pseudo-energies for $|x| > 0.2$ for $\delta > 0$ are not shown because these are severely affected by numerical errors incurred in the numerical integration and diagonalization routines. The various sets of straight line segments are intended to guide the eye in visualizing the data.

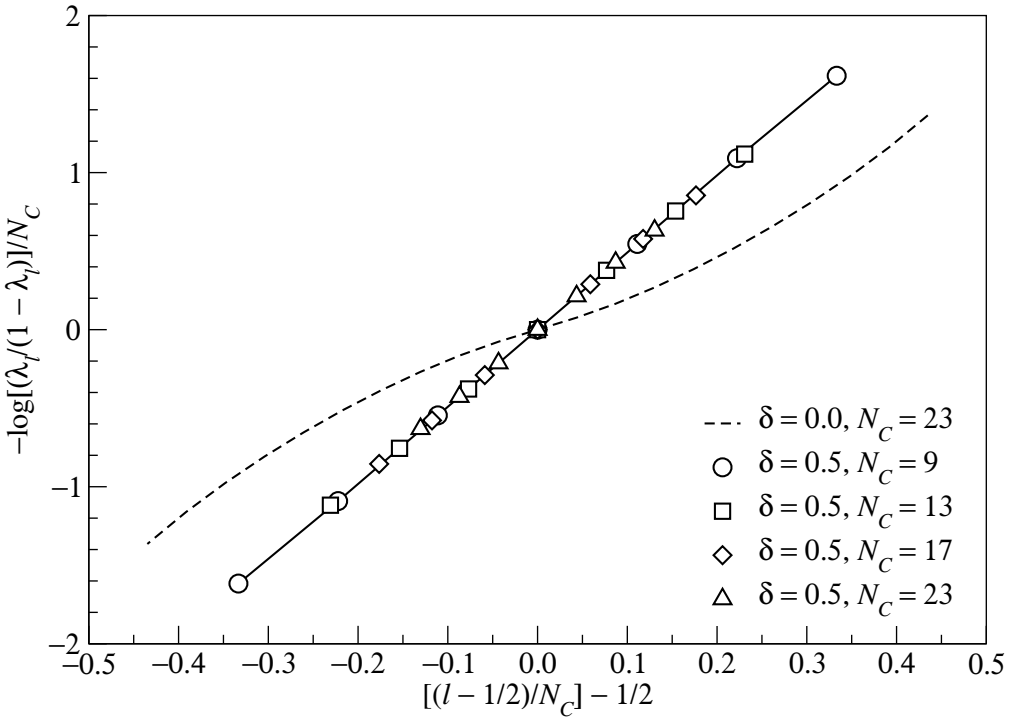

Figure 3.8: Plot of $-{N_C}^{-1} \log[\lambda_l/(1-\lambda_l)]$ as a function of the scaling variable $x = (l - \frac{1}{2})/N_C - \frac{1}{2}$, for hopping modulation $\delta = 0.5$ and different cluster sizes $B = 9, 13, 17, 23$. The pseudo-energies for $|x| > 0.3$ are not shown as these are severely affected by numerical errors in the numerical integration and diagonalization routines. Also shown, is an approximate dashed curve for the scaling function $f(x)$ for $\bar{n} = \frac{1}{2}$ and $\delta = 0$, obtained from the data for $N_C = 23$. The straight line segments are intended to guide the eye in visualizing the data.

depend strongly on the hopping modulation δ. As we can see from Figure 3.7, the slope of the scaling curve at $x = 0$ is steeper for larger δ. This indicates that — everything else being equal for finite N_C — a smaller fraction of density-matrix states is needed to capture the same total weight if the system is gapped.

We have not investigated the case $N_C/N \to 1/2$, as in the standard DMRG algorithm, but we naturally expect the ratios $w_F/w_{F\pm1}$ to increase in a gapped system. Thus $|F\rangle$ would be a better approximation to the ground state in a gapped system than in a gapless system, which is known as an empirical fact in the DMRG context. Our approach, if extended to the case $N_C/N > 0$, would give an analytic justification for this common observation.

3.6.3 Largest Density-Matrix Weight

For even N_C clusters on a gapless chain of noninteracting spinless fermions described the Hamiltonian (2.1.1), the largest density-matrix weight w_F can be numerically computed reliably till $N_C \approx 20$, and its dependence on N_C is shown in Figure 3.9. Also shown in Figure 3.9 is a fit of the numerical data to

$$w_F(N_C) = w_{F,\infty} + \Delta w_F \, \exp(-N_C/N_{C,0}), \tag{3.6.14}$$

where $w_{F,\infty}$, Δw_F and $N_{C,0}$ are curve-fitting parameters. Here the exponentially decaying term is merely chosen to produce a good curve fit — we believe the N_C-dependence may be more complex — but what is interesting is the fact that w_F tends to a constant, $w_{F,\infty}$, in the limit of $N_C \to \infty$. We find that we can understand this in terms of the scaling formulas developed so far.

From Section 3.3 we saw that the largest many-particle density-matrix weight w_F corresponds to the situation for which all PELs below the pseudo-Fermi level $\varphi_F = 0$

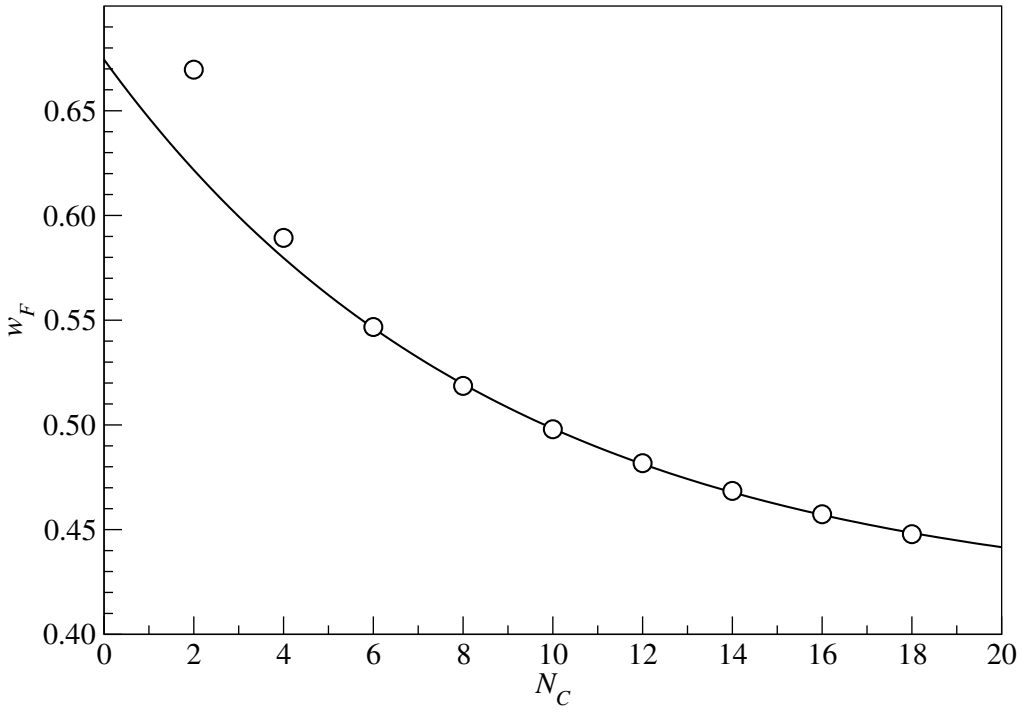

Figure 3.9: Plot of the largest density-matrix weight w_F as a function of the cluster size N_C for N_C even. The solid curve shown is a fit of the form $w_F = w_{F,\infty} + \Delta w_F \exp(-N_C/N_{C,0})$. The best fit to this small data set is obtained by neglecting the data points for $N_C = 2$ and $N_C = 4$, for which we get $w_{F,\infty} = 0.41$, $\Delta w_F = 0.26$ and $N_{C,0} = 0.11$.

are occupied, and all those above are empty. This means that

$$w_F = \mathscr{Q}^{-1} \prod_{l<l_F} e^{-\varphi_l}. \tag{3.6.15}$$

Using the fact that $\mathscr{Q}$ can be written explicitly as

$$\mathscr{Q} = \prod_l (1 + e^{-\varphi_l}), \tag{3.6.16}$$

we then find that

$$w_F = \prod_{l<l_F} \frac{e^{-\varphi_l}}{1 + e^{-\varphi_l}} \prod_{l>l_F} \frac{1}{1 + e^{-\varphi_l}} = \prod_l \frac{1}{1 + e^{-|\varphi_l|}}. \tag{3.6.17}$$

To evaluate w_F, we evaluate first its logarithm, which is

$$-\log w_F = \sum_l \log\left(1 + e^{-|\varphi_l|}\right). \tag{3.6.18}$$

Here we make two approximations. Firstly, because of (3.5.6), we know that $\varphi_l \propto N_C$, and so except for a handful of single-particle pseudo-energies φ_l very near φ_F, all the exponentials are very small numbers. Using the approximation $\log(1+x) \approx x$ for $x \ll 1$, we write (3.6.18) as

$$-\log w_F \approx \sum_l e^{-|\varphi_l|}. \tag{3.6.19}$$

Secondly, we note that because of (3.5.6), single-particle pseudo-energies far away from $\varphi_F = 0$ will contribute negligibly to the above sum. For N_C sufficiently large, those single-particle pseudo-energies making significant contribution in (3.6.18) will lie within a small interval about l_F where a linear approximation of the form

$$\varphi_l \approx N_C f'(0) \frac{l - l_F}{N_C} = f'(0)(l - l_F) \tag{3.6.20}$$

adequately describes the pseudo-dispersion relation. Substituting (3.6.20) into (3.6.19), we find then that

$$-\log w_F \approx \sum_{l=1}^{N_C} e^{-f'(0)|l-l_F|} \approx 2 \sum_{l>l_F}^{\infty} e^{-f'(0)(l-l_F)}. \tag{3.6.21}$$

This is a geometric series which we can readily sum to give

$$-\log w_F = \frac{2}{1-\exp(-f'(0))}, \tag{3.6.22}$$

i.e. the largest density-matrix weight w_F is found to approach a constant value of

$$w_F = \exp\left[-\frac{2}{1-\exp(-f'(0))}\right] \tag{3.6.23}$$

as $N_C \to \infty$. From Figure 3.4 and Figure 3.5, we see that $f'(0) \approx 5$, and so we predict the asymptotic value of w_F to be aproximately 0.13. This is smaller than the $w_{F,\infty} = 0.41$ found numerically.

3.6.4 Discarded Weight

Now that we understand more about the scaling behaviour of the largest density matrix weight w_F, let us analyze the discarded weight incurred by the operator-based DM truncation scheme. We compute numerically the discarded weight incurred by the operator-based DM truncation scheme and that incurred by the weight-ranked DM truncation scheme, and show them in Figure 3.10 as a function of the number of many-body states kept as a comparison. As we can see, the discarded weight incurred by the operator-based DM truncation scheme is larger compared to the weight-ranked DM truncation scheme, for the same number of many-particle eigenstates kept. This is expected, since the weight-ranked DM truncation scheme is by definition the most efficient scheme in exhausting the sum rule given in (3.6.1). In spite of this seemingly poorer 'convergence' property, we believe that the operator-based truncation scheme has advantages that cannot be reproduced by the weight-ranked truncation scheme, to be argued in detail in Section 3.9.

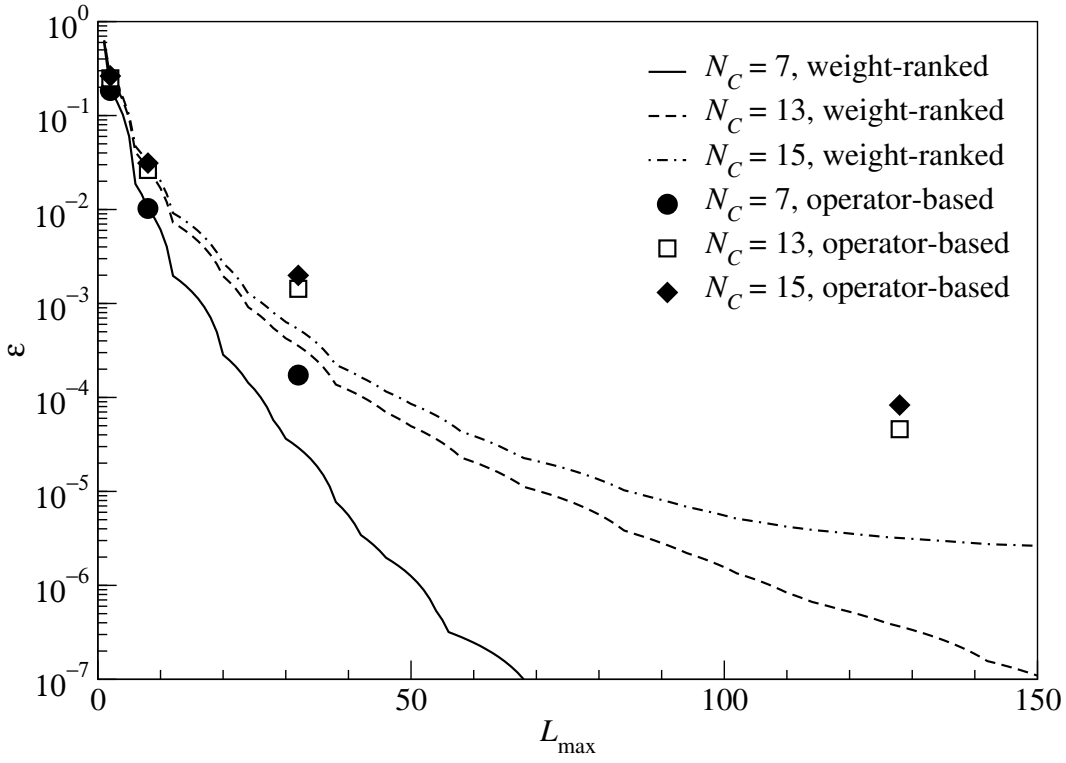

Figure 3.10: Discarded weight ϵ as a function of the number of states kept: weight-ranked (as done in the DMRG), and operator-based.

Writing the total density matrix weight explicitly as

$$W = \mathscr{Q}^{-1} \prod_{\text{kept}} (1 + e^{-\varphi_l}) \prod_{\text{below}} (1 + e^{-\varphi_l}) \prod_{\text{above}} (1 + e^{-\varphi_l}), \tag{3.6.24}$$

where the subscript 'kept', 'below' and 'above' refer to PELs retained, approximated as always occupied and approximated as always empty in the operator-based truncation scheme respectively. The truncated weight W_t calculated from the operator-based truncation scheme is

$$W_t = \mathscr{Q}^{-1} \prod_{\text{kept}} (1 + e^{-\varphi_l}) \prod_{\text{below}} e^{-\varphi_l} \prod_{\text{above}} 1. \tag{3.6.25}$$

Since $W = 1$, the ratio $W_t/W = W_t$ can be written as

$$W_t = \prod_{\text{below}} \frac{e^{-\varphi_l}}{1 + e^{-\varphi_l}} \prod_{\text{above}} \frac{1}{1 + e^{-\varphi_l}} = \prod_{\text{below}} \frac{1}{1 + e^{\varphi_l}} \prod_{\text{above}} \frac{1}{1 + e^{-\varphi_l}}. \tag{3.6.26}$$

This expression has a simple interpretation in terms of the pseudo-occupation numbers $\{\lambda_l\}$. Using (3.3.7), we find that we can write W_t as

$$W_t = \prod_{\text{below}} \lambda_l \prod_{\text{above}} (1 - \lambda_l), \tag{3.6.27}$$

i.e. the truncated weight W_t is given by the product of pseudo-occupation numbers λ_l of those PELs we insist are always occupied, together with the product of the single-hole pseudo-occupation numbers $(1 - \lambda_l)$ of those PELs we insist are always empty. From Figure 3.3 we see that λ_l changes fairly rapidly from $\lambda_l \lesssim 1$ to $\lambda_l \gtrsim 0$, over a small range of PELs. Therefore, it appears that there is a fairly large range of l's for which λ_l is very close to one or very close to zero. However, this does not mean that we should perform an operator-based truncation scheme keeping only the small number of PELs whose λ_l's are significantly different from one or zero. This is because W_t is bounded from above by

$$W_t \leq \prod_{\text{below}} \lambda_{\max} \prod_{\text{above}} (1 - \lambda_{\min}) \leq (\lambda^*)^{(1-\gamma)N_C}, \tag{3.6.28}$$

where γ is the fraction of PELs retained in the operator-based truncation scheme, and

$$\lambda^* = \max(\lambda_{\max}, 1 - \lambda_{\min}). \tag{3.6.29}$$

Because the exponent is $O(N_C)$, this number can still be very small.

This brings us to the question we posed in the beginning of this section: how much of the Hilbert space do we truncate? If W_t is the only criterion then we see that a compromise is necessary. For a small cluster, the number of PELs with λ_l significantly different from one or zero is a sizeable fraction of the total number of PELs, but this number is manageable. For a large cluster, the number of PELs with λ_l significantly different from one or zero is a tiny fraction of the total number of PELs, but we still need γ to be reasonably large for W_t to be appreciable in magnitude. This of course means that an unmanageably large number of PELs has to be retained.

To make the above discussions more water-tight, let us make use of the scaling relations obtained thus far to find a formula relating the truncated weight W_t to both the cluster size N_C and the fraction γ of PELs retained. Taking the logarithm of (3.6.26) we find, using the fact that $\exp(-|\varphi_l|) \ll 1$ for l far below l_F, and $\exp(-\varphi_l) \ll 1$ for l far above l_F, that

$$\begin{aligned}
-\log W_t &= \sum_{\text{below}} \log(1 + e^{\varphi_l}) + \sum_{\text{above}} \log(1 + e^{-\varphi_l}) \\
&\approx \sum_{\text{below}} e^{\varphi_l} + \sum_{\text{above}} e^{-\varphi_l} \\
&= \sum_{l<l_F} e^{\varphi_l} - \sum_{l=l_F-\gamma N_C/2}^{l_F} e^{\varphi_l} + \sum_{l>l_F} e^{-\varphi_l} - \sum_{l_F}^{l_F+\gamma N_C/2} e^{-\varphi_l} \\
&= \Phi^* - \sum_{l=l_F-\gamma N_C/2}^{l_F} e^{\varphi_l} - \sum_{l_F}^{l_F+\gamma N_C/2} e^{-\varphi_l},
\end{aligned} \tag{3.6.30}$$

where Φ^* is a constant.

If N_C is large and γ small, then the linear approximation (3.6.20) for φ_l is valid, in

which case the two sums in (3.6.30) are equal, and given by

$$\sum_{l_F}^{l_F+\gamma N_C/2} e^{-\varphi_l} \approx \sum_{l_F}^{l_F+\gamma N_C/2} e^{-f'(0)(l-l_F)} = \frac{1-\exp(-\gamma N_C f'(0)/2)}{1-\exp(-f'(0))}. \tag{3.6.31}$$

With this, we can write W_t as

$$W_t \approx W^* \exp\left[\frac{2}{1-e^{-f'(0)}}\left(1-e^{-\gamma N_C f'(0)/2}\right)\right], \tag{3.6.32}$$

where $W^* = \exp(-\Phi^*)$. We can find W^* by taking the limit $\gamma \to 0$, in which case we retain no degree of freedom in the PELs. Within the operator-based truncation scheme, this means that we insist all PELs below φ_F to be always occupied and all those above φ_F to be always empty, i.e. only the density matrix eigenstate with the largest weight is retained, and we should have

$$W_t = w_F = W^*, \tag{3.6.33}$$

and so

$$W_t \approx w_F \exp\left[\frac{2}{1-e^{-f'(0)}}\left(1-e^{-\gamma N_C f'(0)/2}\right)\right]. \tag{3.6.34}$$

This can be simplified further, using (3.6.23) to get

$$W_t \approx \exp\left[-\frac{2}{1-e^{-f'(0)}} e^{-\gamma N_C f'(0)/2}\right]. \tag{3.6.35}$$

In the limit of $\gamma \to 1$, we see from the above expression that W_t does not tend to one, but we understand that this is because the linear approximation (3.6.20) is only valid for a small range of PELs about φ_F, i.e. only for small γ. In this regime, we may further approximate W_t as

$$W_t \approx \exp\left[-\frac{2}{1-e^{-f'(0)}}\left(1-\frac{f'(0)\gamma N_C}{2}\right)\right] \approx w_F \exp\left(\frac{f'(0)}{1-e^{-f'(0)}}\, l_{\max}\right), \tag{3.6.36}$$

where

$$l_{\max} = \gamma N_C \tag{3.6.37}$$

is the number of PELs retained. As we can see, for small γ, the truncated weight W_t increases exponentially with $l_{\max}$. Also, whenever (3.6.36) is valid, we get approximately the same truncated weight W_t whether we use $N_C = 100$ and $\gamma = 0.2$ or $N_C = 200$ and $\gamma = 0.1$. We will see in Section 3.9 that whenever the retained γN_C PELs lies within the regime where the pseudo-dispersion relation is linear, the truncation errors are essentially determined by $l_{\max} = \gamma N_C$.

3.7 Entanglement Entropy

After the bulk of the numerical studies in this Chapter was submitted as a manuscript to Ref. 198, we were alerted in an email communication with Peschel to a recent result in the field of quantum computing, where Vidal *et al* computed the entanglement entropy

$$S = -\operatorname{Tr} \rho_C \log_2 \rho_C, \tag{3.7.1}$$

of a cluster of N_C spins in the one-dimensional XX (Ising) and XY spin chains [199,200]. Their main results, obtained using conformal field theory arguments, and which are also verified by Jin and Korepin [201], is that at the quantum critical points, the entanglement entropy scales as

$$\begin{aligned} S_{XX} &\approx \frac{1}{3} \left(\log_2 N_C + \pi \right), \\ S_{XY} &\approx \frac{1}{6} \left(\log_2 N_C + \pi \right). \end{aligned} \tag{3.7.2}$$

Peschel had checked that the scaling form for the single-particle pseudo-energy $\varphi(l, N_C)$ we presented in Ref. 198 would not imply an entanglement entropy of the form $S \sim \log N_C$, which is expected of noninteracting spinless fermions, since it can be mapped to the critical Ising spin chain. We rechecked the scaling form for $\varphi(l, N_C)$, and derive in this subsection an improved scaling form which does give rise to a $S \sim \log N_C$ entanglement entropy for the cluster of N_C sites in a one-dimensional chain of noninter-

acting spinless fermions.

3.7.1 Relation to Green-Function Matrix Eigenvalues

Because we write our density-matrix eigenvalues as $w = e^{-\Phi}/\mathcal{Q}$, it is more convenient for us to use the definition

$$S = -\operatorname{Tr}\rho_C \log \rho_C \tag{3.7.3}$$

for the entanglement entropy. It is easy to see that this entanglement entropy, defined in terms of the natural logarithm, differs from the one defined by Vidal *et al* (in terms of the base-2 logarithm) by a constant multiplier, i.e.

$$S_2 = -\sum_L w_L \log_2 w_L = -\sum_L w_L \frac{\log w_L}{\log 2} = \frac{S_e}{\log 2}. \tag{3.7.4}$$

Therefore, the results of Vidal *et al*, in terms of the natural logarithm, would look like

$$\begin{aligned} S_{XX,e} &= \log 2\, S_{XX,2} \approx \frac{1}{3}\left(\log N_C + \pi \log 2\right), \\ S_{XY,e} &= \log 2\, S_{XY,2} \approx \frac{1}{6}\left(\log N_C + \pi \log 2\right). \end{aligned} \tag{3.7.5}$$

Using the notations in Section 3.3.1 to denote by Φ_L the Lth total pseudoenergy of the cluster density matrix ρ_C, we can write the entanglement entropy as

$$S = -\sum_L \frac{e^{-\Phi_L}}{\mathcal{Q}} \log \frac{e^{-\Phi_L}}{\mathcal{Q}}, \tag{3.7.6}$$

where $\mathcal{Q}$ is the grand partition function defined in (3.3.4). Using the statistical-mechanical analogies

$$\mathcal{Q} = \sum_L e^{-\Phi_L}, \qquad \langle\Phi\rangle = \frac{\sum_L \Phi_L\, e^{-\Phi_L}}{\sum_L e^{-\Phi_L}}, \tag{3.7.7}$$

we can then simplify (3.7.6) to obtain

$$\begin{aligned} S &= -\frac{1}{\mathcal{Q}} \sum_L e^{-\Phi_L} \left(-\Phi_L - \log \mathcal{Q}\right) \\ &= \frac{1}{\mathcal{Q}} \sum_L \Phi_L\, e^{-\Phi_L} + \frac{\log \mathcal{Q}}{\mathcal{Q}} \sum_L e^{-\Phi_L} \\ &= \langle\Phi\rangle + \log \mathcal{Q}. \end{aligned} \tag{3.7.8}$$

This is the analog of $F = E - TS$, where F is the Helmholtz free energy, E is the internal energy, T is the temperature, and S the entropy.

To simplify (3.7.8) further, we note from (2.5.1) and (2.4.31) that the zero-particle eigenvalue of ρ_C is

$$e^{-\varphi_0} = \det(\mathbb{1} - G) = \mathscr{Q}^{-1}. \tag{3.7.9}$$

This tells us that

$$\log \mathscr{Q} = \varphi_0 = -\log \prod_l (1 - \lambda_l) = -\sum_l \log(1 - \lambda_l). \tag{3.7.10}$$

Then, using the fact that the total pseudo-energy Φ can be written in terms of the single-particle pseudo-energies φ_l in (3.3.3), we find that

$$\langle \Phi \rangle = \sum_l \langle n_l \rangle \varphi_l = \sum_l \lambda_l \varphi_l, \tag{3.7.11}$$

where we made use of (3.3.7).

Combining (3.7.10) and (3.7.11), and also (2.5.3), we obtain a highly suggestive form

$$\begin{aligned} S &= \sum_l \lambda_l \varphi_l - \sum_l \log(1 - \lambda_l) \\ &= \sum_l \left[-\lambda_l \log \lambda_l + \lambda_l \log(1 - \lambda_l) \right] - \sum_l \log(1 - \lambda_l) \\ &= -\sum_l \lambda_l \log \lambda_l - \sum_l (1 - \lambda_l) \log(1 - \lambda_l) \end{aligned} \tag{3.7.12}$$

for the entanglement entropy. Using semiconductor physics terminology, we can therefore think of the entanglement entropy S as being the sum of a particle-occupation entropy ($-\sum_l n_l \log n_l$) and a hole-occupation entropy ($-\sum_l p_l \log p_l$). From (3.7.12), we also realized that those eigenvalues λ_l very close to being zero or being one contributes negligibly to S, and the dominant contribution to S comes from a small interval around $\lambda = \frac{1}{2}$.

3.7.2 Numerical Evaluation of the Entanglement Entropy

To understand how S scales with the cluster size N_C, let us first take a look at the generic behaviour of the function

$$f(\lambda) = -\lambda \log \lambda - (1-\lambda)\log(1-\lambda) \tag{3.7.13}$$

for the eigenvalues λ_l of G. At half-filling and for cluster size $N_C = 15$, we find that $f(\lambda_l)$ has the behaviour shown in Figure 3.11. The cumulative sum of $f(\lambda_l)$ is shown in Figure 3.12. As expected, λ_l's close to being zero or one makes negligible contribution to the entanglement entropy S. The dominant contribution to S comes from $\lambda_l \sim \frac{1}{2}$. Therefore, if we express S in terms of the pseudo-energies φ_l instead, then this is equivalent to saying that the dominant contributions to S comes from those φ_l's near the pseudo-Fermi level.

This is an important result to us, if we are interested in numerically evaluating the entanglement entropy S for very large clusters. Because of the finite precision of the IEEE floating point numbers, it is numerically impossible to evaluate those λ_l's very close to zero or one reliably, and so naively we might think that it would not be possible to evaluate S reliably for large clusters as well. However, with the above observation, we realize that all we need is to be able to evaluate those eigenvalues λ_l of the cluster Green-function matrix G_C that are close to $\frac{1}{2}$ reliably. Based on our experience diagonalizing G_C for large cluster sizes, these intermediate eigenvalues appear to be reliable, even when those eigenvalues close to zero and one are affected by numerical truncation errors of about the magnitude of the machine epsilon.

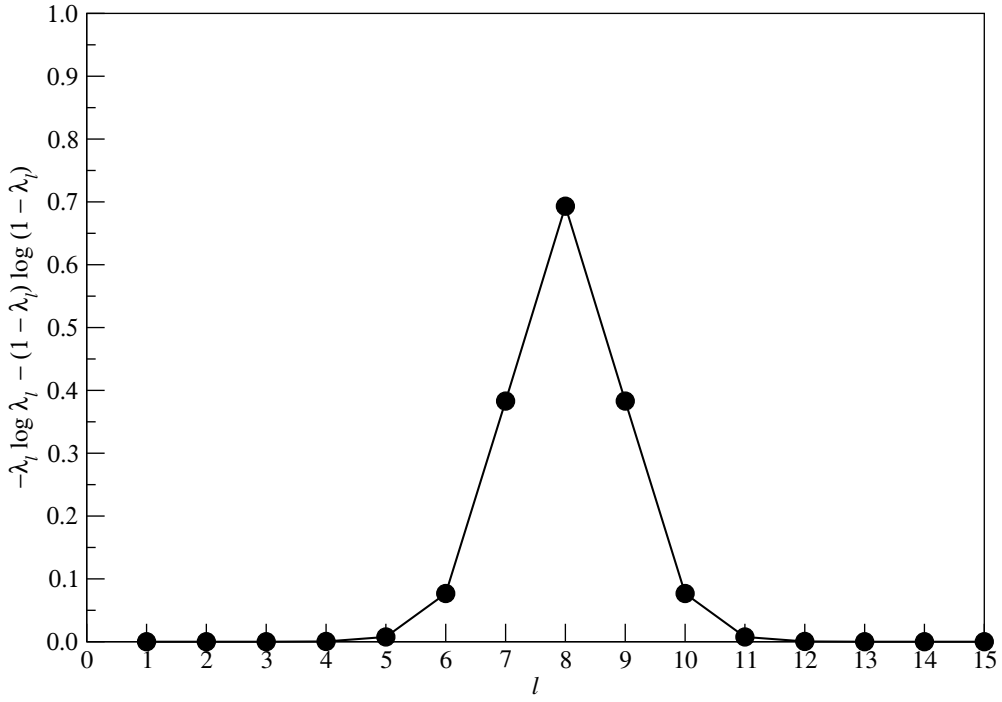

Figure 3.11: Plot of the function $f(\lambda) = -\lambda \log \lambda - (1-\lambda)\log(1-\lambda)$ against the ordinal number l of the eigenvalues λ_l of the cluster Green-function matrix G_C of a cluster of $N_C = 15$ sites within a one-dimensional chain of noninteracting spinless fermions at half-filling.

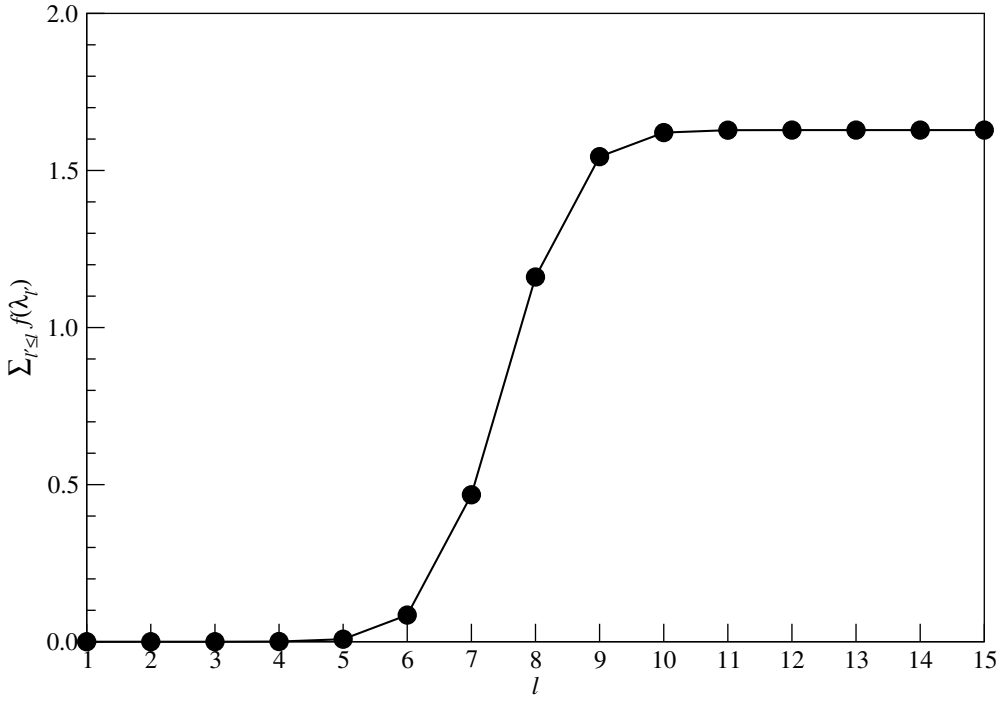

Figure 3.12: Plot of the cumulative sum $\sum_{l' \le l} f(\lambda_{l'})$, where $f(\lambda) = -\lambda \log \lambda - (1 - \lambda) \log(1 - \lambda)$, against the ordinal number l of the eigenvalues λ_l of the cluster Green-function matrix G_C, for a cluster of $N_C = 15$ sites within a half-filled one-dimensional chain of noninteracting spinless fermions.

3.7.3 Entanglement Entropy for Even- and Odd-Sized Clusters

Computing the entanglement entropy S using (3.7.12), we find that S is indeed logarithmic in the cluster size N_C. In fact, we find that there are two logarithmic behaviours for S, one for even cluster sizes, and another for odd cluster sizes, as shown in Figure 3.13. We fit the numerical data for even and odd cluster sizes separately to an equation of the form $S = a \log N_C + b$, as shown in Figure 3.14, to find for odd N_C,

$$S_{\text{odd}} = 0.33744 \log N_C + 1.4052, \tag{3.7.14}$$

whereas for even N_C,

$$S_{\text{even}} = 0.3346 \log N_C + 0.72163. \tag{3.7.15}$$

Comparing these two fits to (3.7.5) for the Ising spin chain, we find that the slopes obtained are both close enough to $1/3$. The fitted intercept for even N_C, 0.72163, is also close to the expected intercept $\pi \log 2/3 = 0.72586\ldots$ for the Ising spin chain. Further, we note that the difference between the intercepts for odd N_C and even N_C, $1.4502 - 0.72163 = 0.68357$, is closed to being $\log 2 = 0.69315\ldots$. From these observations, we believe that

$$\begin{aligned} S_{\text{odd}} &= \frac{1}{3} \log N_C + \frac{\pi \log 2}{3} + \log 2, \\ S_{\text{even}} &= \frac{1}{3} \log N_C + \frac{\pi \log 2}{3}. \end{aligned} \tag{3.7.16}$$

3.7.4 Calculating S From Our Scaling Form

As discussed in Section 3.7.1, only thoses λ_l's in a small interval about $\lambda = \frac{1}{2}$ contribute significantly to S. We know from Section 3.5 that these correspond to those φ_l's near $\varphi_F = 0$. According to the scaling form in (3.5.6), near the pseudo-Fermi level, the pseudo-dispersion relation is well approximated by (3.6.20). Substituting (3.6.20) into

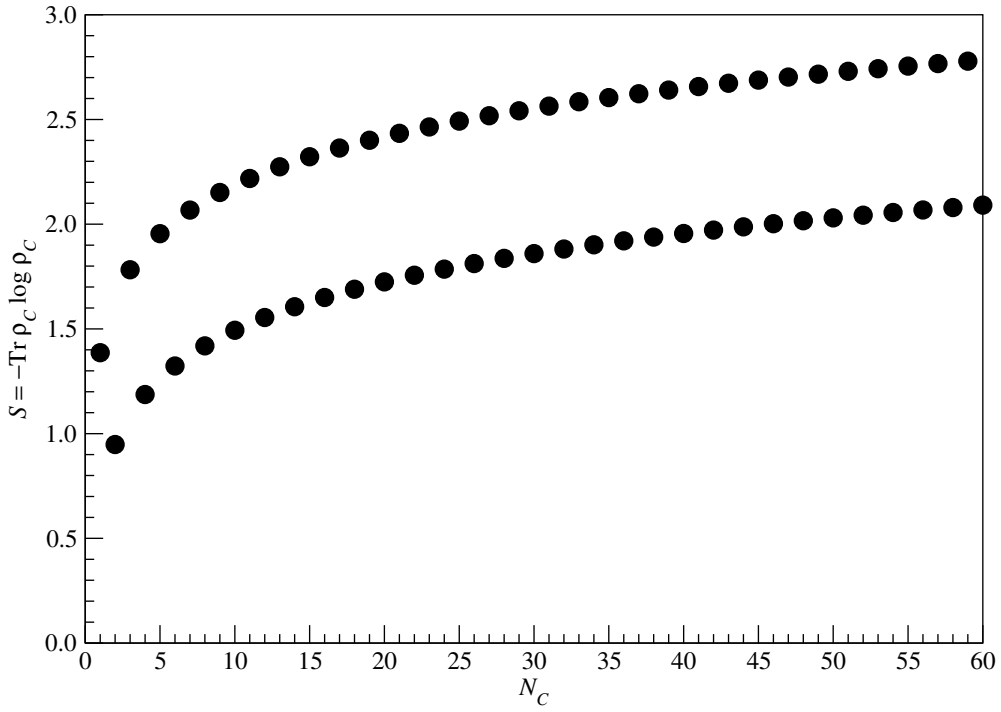

Figure 3.13: Entanglement entropy $S = \mathrm{Tr}\,\rho_C \log \rho_C$ for clusters of N_C sites in a one-dimensional system of noninteracting spinless fermions. The entanglement entropy appears to increase without bound following one logarithmic behaviour for even N_C, and another logarithmic behaviour for odd N_C.

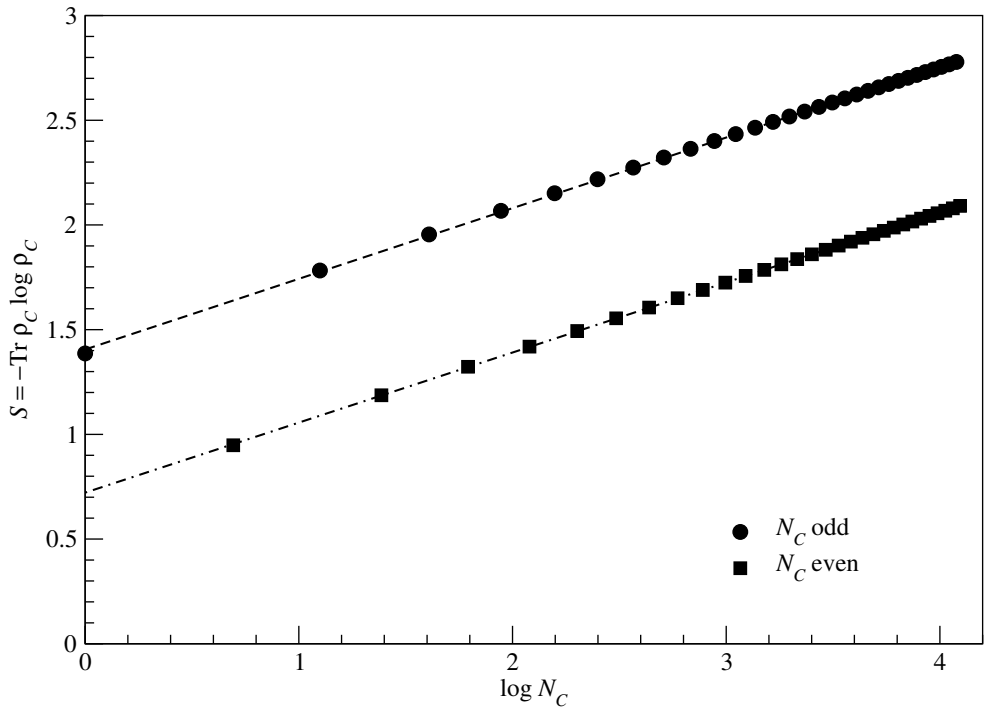

Figure 3.14: Fits of the entanglement entropy $S = \mathrm{Tr}\,\rho_C \log \rho_C$ of a one-dimensional system of noninteracting spinless fermions to the form $S = a \log N_C + b$. For odd cluster sizes, we find that $a = 0.33744$ and $b = 1.4052$, whereas for even cluster sizes, we find that $a = 0.3346$ and $b = 0.72163$.

(3.3.7) and then into (3.7.12), we get

$$S \approx \sum_l \frac{\log\left[1 + e^{f'(0)(l-l_F)}\right]}{1 + e^{f'(0)(l-l_F)}} + \sum_l \frac{\log\left[1 + e^{-f'(0)(l-l_F)}\right]}{1 + e^{-f'(0)(l-l_F)}}. \tag{3.7.17}$$

In the limit of $N_C \to \infty$, more and more pseudo-energy levels can be found in the quasilinear regime near the pseudo-Fermi level, and therefore it is justified to convert the sums into integrals, as

$$S \approx \int_{-\infty}^{+\infty} dl\, \frac{\log\left[1 + e^{f'(0)(l-l_F)}\right]}{1 + e^{f'(0)(l-l_F)}} + \int_{-\infty}^{+\infty} dl\, \frac{\log\left[1 + e^{-f'(0)(l-l_F)}\right]}{1 + e^{-f'(0)(l-l_F)}}, \tag{3.7.18}$$

where the limits of integration have been extended to $\pm\infty$, even though pseudoenergies far from φ_F are not in the quasilinear regime. However, these pseudo-energies contribute negligibly to S anyway, and we do not incur too much error in extending the lower and upper limits of integration.

With a change of integration variable

$$\xi = f'(0)(l - l_F), \tag{3.7.19}$$

we can rewrite the expression for the entanglement entropy as

$$S \approx \frac{1}{f'(0)} \int_{-\infty}^{+\infty} d\xi\, \frac{\log(1 + e^{\xi})}{1 + e^{\xi}} + \frac{1}{f'(0)} \int_{-\infty}^{+\infty} d\xi\, \frac{\log(1 + e^{-\xi})}{1 + e^{-\xi}}, \tag{3.7.20}$$

which can be further simplified to

$$S \approx \frac{2}{f'(0)} \int_{-\infty}^{\infty} d\xi\, \frac{\log(1 + e^{\xi})}{1 + e^{\xi}}. \tag{3.7.21}$$

A second change of variable

$$y = 1 + e^{\xi}, \qquad dy = e^{\xi}\, d\xi = (y - 1)\, d\xi, \tag{3.7.22}$$

then allows us to write the entanglement entropy as

$$S \approx \frac{2}{f'(0)} \int_{1}^{\infty} dy\, \frac{\log y}{y(y - 1)}. \tag{3.7.23}$$

Using *Mathematica*, we evaluate the integral as

$$\int_1^\infty dy \, \frac{\log y}{y(y-1)} = \frac{\pi^2}{6}, \tag{3.7.24}$$

so based on the scaling form in (3.5.6), we should obtain an entanglement entropy

$$S \approx \frac{\pi^2}{3f'(0)} \tag{3.7.25}$$

that does not depend on the cluster size.

Clearly, this does not agree with the logarithmic behaviour of S observed in Figure 3.13, which we have checked numerically up to a cluster size of $N_C = 60$, nor with Vidal *et al*, who checked the logarithmic behaviour numerically up to a cluster size of $N_C = 100$. The eigenvalues λ_l of the cluster Green function matrix cannot be obtained reliably from numerical exact diagonalization for large cluster sizes, but we understand from Section 3.7.2 that we need only obtain the eigenvalues within a small interval of $\lambda = \frac{1}{2}$ reliably. With this observation, we further compute the entanglement entropy S for clusters with up to $N_C = 500$ sites. At a cluster size of $N_C = 500$, it is possible to reliably compute about one-tenth of the eigenvalues of the cluster Green-function matrix G_C. We find that S continues to grow logarithmically with N_C up to these large cluster sizes, as shown in Figure 3.15 for even N_C. In Figure 3.15, we show the logarithmic fit $S = a \log N_C + b$ obtained using the numerical data for up to $N_C = 60$. As we can see, this fit continues to be good for even cluster sizes, up to $N_C = 500$. We need therefore to find a way to salvage our scaling form in (3.5.6), so that we obtain an entanglement entropy that agrees with the conformal-field-theoretic predictions of $S \sim \log N_C$ as $N_C \to \infty$.

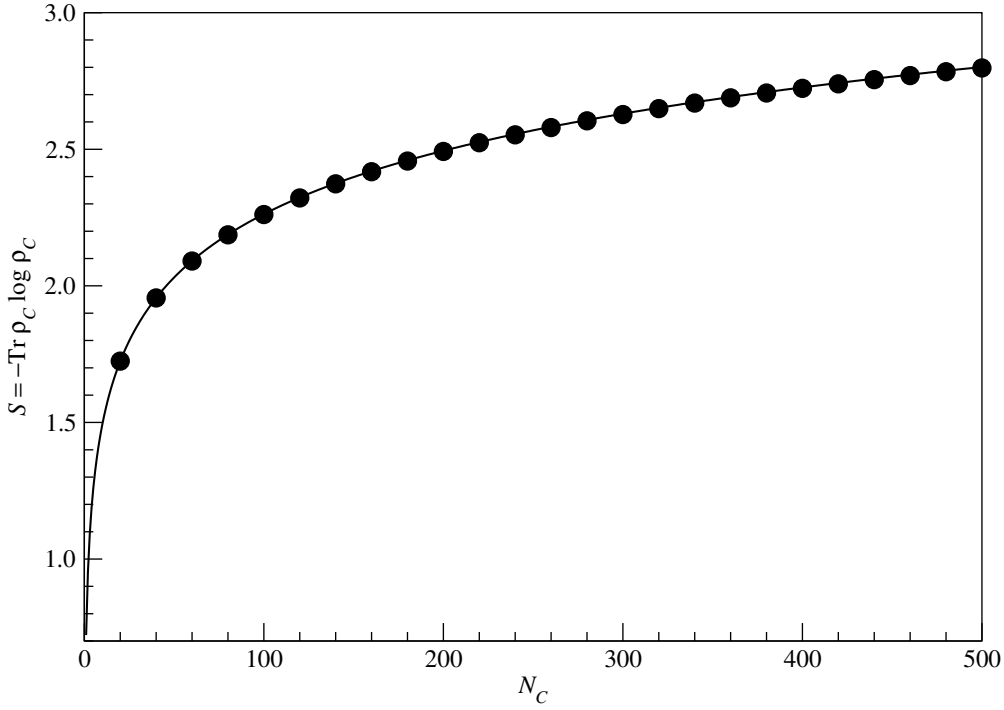

Figure 3.15: Entanglement entropy $S = -\mathrm{Tr}\,\rho_C \log \rho_C$ for clusters of up to $N_C = 500$ sites in a one-dimensional system of noninteracting spinless fermions. Also shown is the logarithmic fit $S = 0.3346 \log N_C + 0.72163$ obtained for even N_C up to $N_C = 60$.

3.7.5 Improved Scaling Form for Pseudo-Energy

If, instead of a universal linear scaling near the pseudo-Fermi level, the pseudo-dispersion relation scales non-universally with cluster size N_C as

$$\varphi_l \approx \frac{\alpha}{\kappa + \log N_C}(l - l_F), \tag{3.7.26}$$

where α and κ are some yet-to-be-determined constants, then we can repeat the calculations in the previous subsubsection to find that

$$S \approx \frac{\pi^2}{3\alpha}\log N_C + \frac{\kappa\pi^2}{3\alpha}. \tag{3.7.27}$$

Comparing this with (3.7.16), we find that we need the constants α and κ to be

$$\alpha = \pi^2, \quad \kappa_{\text{even}} = \pi\log 2, \quad \kappa_{\text{odd}} = (\pi + 3)\log 2. \tag{3.7.28}$$

Two questions therefore come to mind: (1) do we see numerically the non-universal scaling (3.7.26) near the pseudo-Fermi level; and (2) how is it that we missed this behaviour the first time round?

To answer the first question, we compute the pseudo-energies $\varphi(l, N_C)$ for even cluster sizes between $8 \leq N_C \leq 30$. Then, we performed a least-square-cubic fit with the eight $\varphi(l, N_C)$ closest to $\varphi_F = 0$, and differentiate the resulting cubic curve to obtain a numerical value for the slope $\varphi'(l_F, N_C) = d\varphi(l_F, N_C)/dl$ at the pseudo-Fermi level. If (3.7.26) is correct, then the slope should be equal to $\alpha/(\kappa + \log N_C)$. Indeed, plotting $1/\varphi'(l_F, N_C)$ against $\log N_C$, as shown in Figure 3.16, we find a pretty decent fit given by

$$\frac{1}{\varphi'(l_F, N_C)} = 0.23209 + 0.10564\log N_C, \tag{3.7.29}$$

or, writing in the same form as (3.7.26),

$$\varphi'(l_F, B) = \frac{9.4661}{2.1970 + \log B}. \tag{3.7.30}$$

The numerical values $\alpha = 9.4661$ and $\kappa = 2.1970$ agree well with the values $\alpha = \pi^2 = 9.8696\ldots$ and $\kappa = \pi \log 2 = 2.1776\ldots$ deduced in (3.7.28). Thus a scaling of the form (3.7.26) is indeed present.

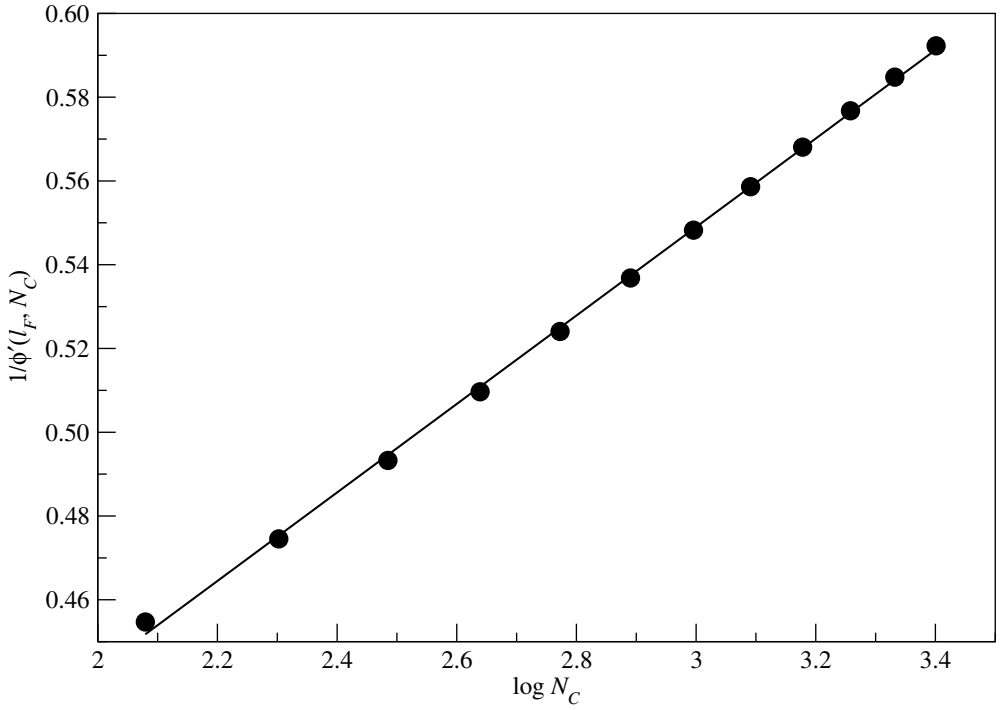

Figure 3.16: Plot of the reciprocal of the slope of the pseudo-dispersion relation, $1/\varphi'(l_F, N_C)$, as a function of the cluster size N_C, for a one-dimensional system of non-interacting spinless fermions. Also shown is the linear fit $1/\varphi'(l_F, N_C) = 0.23209 + 0.10564 \log N_C$.

To answer the second question, let us note that, in the quasilinear region about the pseudo-Fermi level, we can write (3.7.26) in terms of the scaling variable $x = (l - l_F)/N_C$ introduced in Section 3.5.1 as

$$\varphi(l, N_C) \approx \frac{\alpha}{\kappa + \log N_C} \cdot N_C x. \tag{3.7.31}$$

In Section 3.5.1, we define the scaling function $f(x)$ such that $\varphi(l, N_C) \approx N_C f(x)$, but

there is no harm in writing this scaling relation as

$$\varphi(l, N_C) \approx cN_C \tilde{f}(x), \tag{3.7.32}$$

such that $\tilde{f}(x)$ has unit slope at $x = 0$. The assertion we made in Section 3.5.1 about the universal scaling of $\varphi(l, N_C)$ is that the factor c is independent of cluster size N_C.

In terms of the 'normalized' scaling function $\tilde{f}(x)$, (3.7.26) then implies a scaling relation of the form

$$\varphi(l, N_C) \approx \frac{\alpha N_C}{\kappa + \log N_C} \tilde{f}(x). \tag{3.7.33}$$

We may then proceed to ask: how different are the functions $\alpha N_C/(\kappa + \log N_C)$ and cN_C, if we are allowed to choose whichever c that is best for our purpose? In Section 3.5.1, we worked with a range of cluster sizes from $N_C = 7$ to $N_C = 67$. For this range of cluster sizes, we find that a decent linear fit of the form $cN_C + d$ can be applied to the logarithmic function $\alpha N_C/(\kappa + \log N_C)$, as shown in Figure 3.17. In fact, if we go to larger and larger cluster sizes, the function $\alpha N_C/(\kappa + \log N_C)$ looks more and more linear, even though a linear fit of the form $cN_C + d$ would produce a slope c that decreases as the range of N_C included increases. This is why we missed this extra logarithmic dependence on cluster size in the scaling analysis performed in Section 3.5.1.

3.8 Single-Particle Density-Matrix Eigenfunctions

3.8.1 *A Priori* Expectations

As noted already in Section 3.3.3, in the many-body eigenstates with largest weights, all the very negative PELs will be occupied and all the very positive PELs will be empty. The only PELs with significant varying occupancy are those near the pseudo-Fermi level.

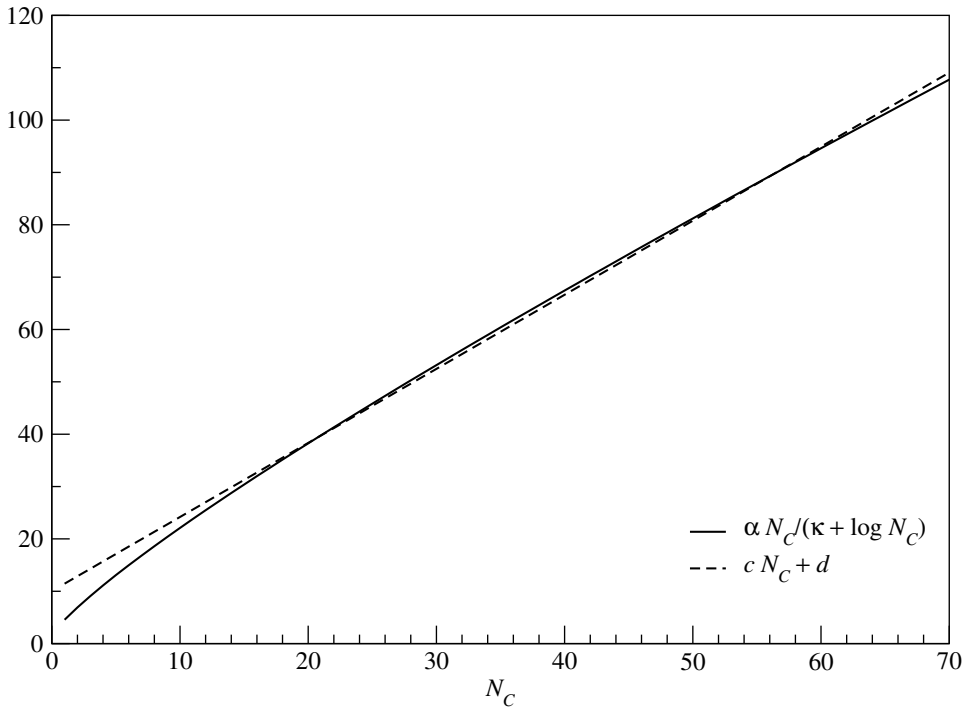

Figure 3.17: Linear fit of the form $cN_C + d$ applied to the function $\alpha N_C/(\kappa + \log N_C)$ for cluster sizes up to $N_C = 70$.

By construction, the many-body density-matrix eigenstates with large weights constitute the likely configurations of the cluster. The difference between the large-weight eigenstates of the P_C-particle and $(P_C + 1)$-particle sectors of the density matrix is in the application of a creation operator $f_l^\dagger$ such that the pseudo-energy $|\varphi_l|$ is close to $\varphi_F = 0$. In real space, it is likeliest that we can add a particle near the ends of the N_C-site cluster, for one can imagine that, in the first configuration, this particle was just past the end in an adjacent cluster, and we merely hopped it a short distance across the boundary to create the state of $(P_C + 1)$ particles on the cluster in question. It follows that the single-particle eigenfunctions with single-particle pseudo-energies near the pseudo-Fermi level have their greatest amplitude near the cluster's boundaries. In other words, it is the sites near the end that are most correlated with the environmental degrees of freedom that we discarded.

3.8.2 General Features

As noted earlier, the eigenstates of ρ_C are all built up from the eigenstates $|\chi_l\rangle$ of G, which are simultaneously the one-particle eigenstates of ρ_C. As such, the effects of basis truncation, particularly in obtaining a truncated expansion of the target state $|\Psi\rangle$, must be understood in terms of the features of these one-particle eigenstates. The real-space features of $|\chi_l\rangle$ can most easily be understood in terms of the corresponding eigenfunctions $\chi_l(j)$, where $j = 1, \ldots, N_C$ are sites on the cluster. At half-filling, the probability densities $|\chi_l(j)|^2$ exhibit particle-hole symmetry, as is shown in Figure 3.18 for the example of $N_C = 9$. In general, by node counting, we see that the sequence of N_C single-particle eigenfunctions are in one-to-one correspondence with the sequence of N_C plane-wave states on the cluster, where the ordinal number l of the single-particle eigenfunctions is

related to the wave vector k of the plane-wave states on the cluster by

$$k = \frac{2\pi(l-1)}{N_C}, \qquad l = 1, \ldots, N_C. \tag{3.8.1}$$

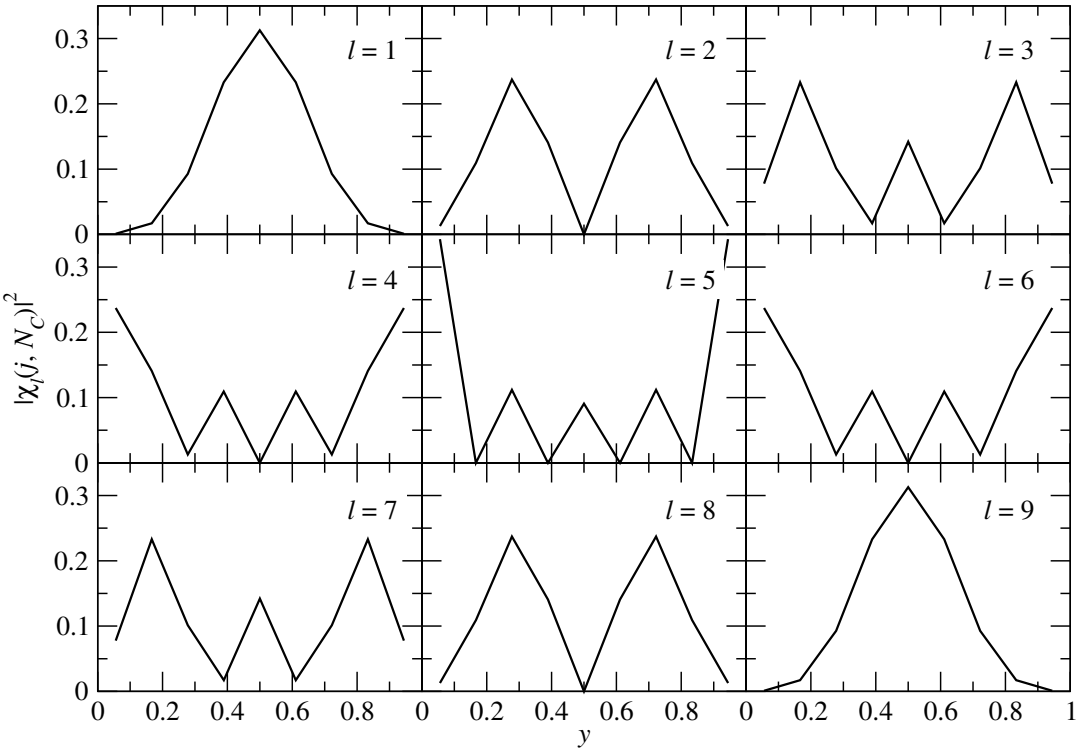

Figure 3.18: Probability density of the normalized one-particle eigenfunctions $\chi_l(j)$ (plotted against the scaling variable $y = (j - \frac{1}{2})/N_C$) of ρ_C on a cluster of $N_C = 9$ sites at half-filling, showing the particle-hole symmetry of the overall system. The subplots are arranged in order of increasing pseudo-energy.

3.8.3 Scaling Behaviour

For odd N_C, the pseudo-energy $\varphi_{(N_C+1)/2}$ sits at the pseudo-Fermi level, and we may call the corresponding eigenfunction $\chi_F(j) \equiv \chi_{(N_C+1)/2}(j)$ the *pseudo-Fermi eigenfunction*. The probability density associated with $\chi_F(j)$ has nodes at every even j, as shown in in Figure 3.19 for the case of $N_C = 23$. The most prominent feature of the pseudo-Fermi

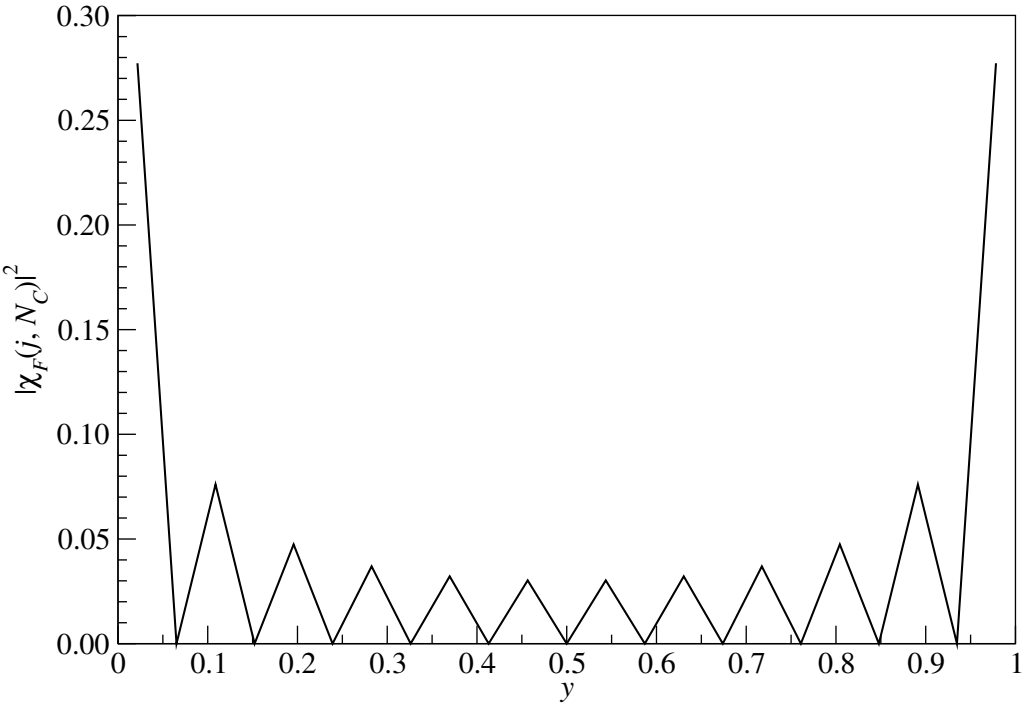

Figure 3.19: Probability density function $|\chi_F(j, N_C)|^2$ of the pseudo-Fermi eigenfunction for $N_C = 23$, plotted against the scaled variable $(j - \frac{1}{2})/N_C$.

eigenfunction, i.e. the amplitude being strongest near the boundaries of the cluster, was first observed by White [15]. This appears to be a generic feature that occurs in both integrable and nonintegrable 1-dimensional systems. Using the example of a chain of coupled harmonic oscillators, Gaite explained this "concentration of resolution of quantum states near the boundaries" as a simple consequence of angular quantization of the density matrix [192].

To analyze $|\chi_F(j, N_C)|^2$ (where we write the N_C dependence of $\chi_F(j)$ more explicitly) more carefully, we first rescale the eigenvectors obtained from Octave [202] such that

$$|\chi_F((N_C + 1)/2, N_C)|^2 = 1 \tag{3.8.2}$$

for $N_C = 4p + 1$, $p = 1, 2, \ldots$. For $N_C = 4p + 3$, $|\chi_F((N_C + 1)/2, N_C)|^2 = 0$ and the rescaling cannot be carried out as unambiguously as for the $N_C = 4p + 1$ series. This rescaling is harmless, since eigenvectors are only defined up to an arbitrary normalization. After this trivial rescaling, we find that the pseudo-Fermi probability density can be put into a scaling form

$$|\chi_F(j, N_C)|^2 \cong N(N_C) g(y) \frac{\frac{1}{2}[1 - (-1)^j]}{\sin^2 \pi y}, \tag{3.8.3}$$

where

$$y \equiv (j - \frac{1}{2})/N_C \tag{3.8.4}$$

is the rescaled coordinate on the cluster, and $g(y)$ is the scaling function shown in Figure 3.20.

In (3.8.3), $N(N_C)$ is a N_C-dependent normalization factor, chosen to ensure that the pseudo-Fermi wavefunction given is properly normalized in the limit of $N_C \to \infty$, i.e.

$$\lim_{N_C \to \infty} \sum_{j=1}^{N_C} |\chi_F(j, N_C)|^2 = 1. \tag{3.8.5}$$

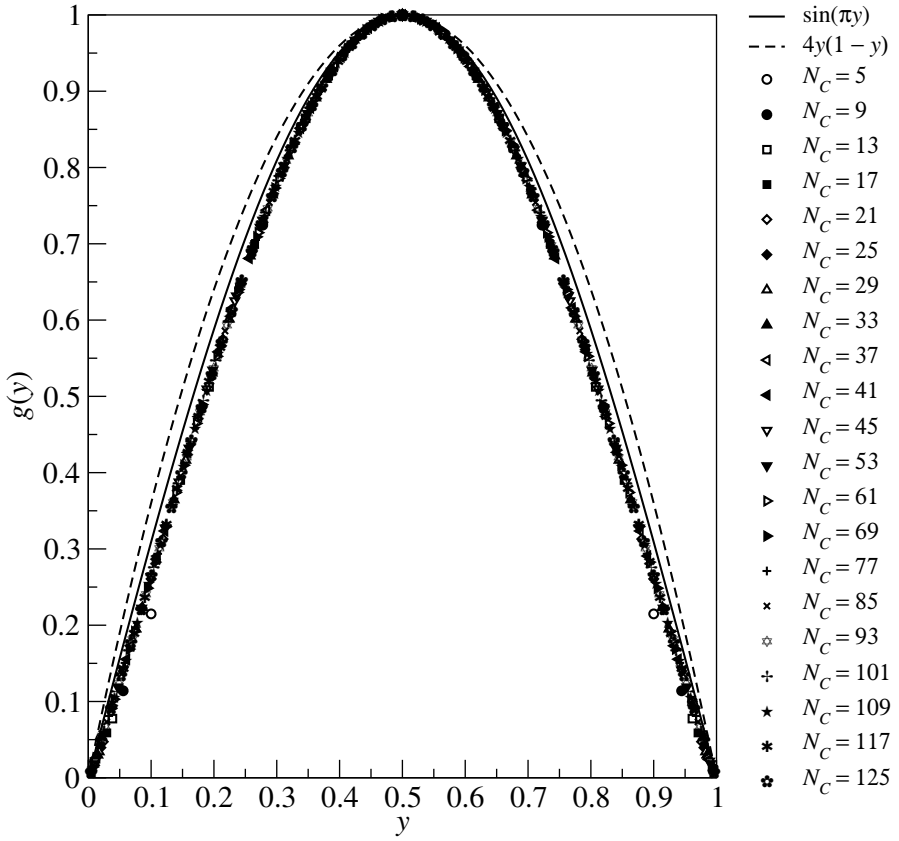

Figure 3.20: Plot of the rescaled envelope function $g(y)$ for various cluster sizes $N_C = 4p + 1$, $p = 1, 2, \ldots$, compared against $\sin \pi y$ and $4y(1 - y)$, where $y = (j - \frac{1}{2})/N_C$ is the rescaled coordinate on the cluster.

Although we cannot compute $N(N_C)$ analytically, we venture a guess to its dependence on N_C by noting that the functions $g(y)$ and $\sin \pi y$ are not very different from the function $4y(1-y)$, and so we expect

$$\begin{aligned}\sum_{j=1}^{N_C} g(y)\frac{\frac{1}{2}[1-(-1)^j]}{\sin^2 \pi y} &\sim \sum_{j=1}^{N_C} 4y(1-y)\frac{\frac{1}{2}[1-(-1)^j]}{[4y(1-y)]^2} \\ &= \frac{1}{4}\sum_{j\ \text{odd}}^{N_C}\left[\frac{1}{y}+\frac{1}{1-y}\right],\end{aligned} \tag{3.8.6}$$

which we can easily work out to have the form

$$\sum_{j=1}^{N_C} g(y)\frac{\frac{1}{2}[1-(-1)^j]}{\sin^2 \pi y} \sim N_C\left(\log N_C + C\right), \tag{3.8.7}$$

where C is a constant. Numerically, the best fit for $N(N_C)$ in the range of cluster sizes $N_C = 33$ to $N_C = 125$ is obtained with

$$N^{-1}(N_C) = 0.249 N_C \log N_C + 0.668 N_C. \tag{3.8.8}$$

Working in the continuum limit of $N_C \gg 1$, Peschel later derived [203] an scaling form of

$$|\chi_F(y)|^2 \propto \frac{1}{y(1-y)}. \tag{3.8.9}$$

Because of the enhanced amplitude near the edge of the cluster exhibited in the real-space structure of density-matrix eigenfunctions with single-particle pseudo-energies close to the pseudo-Fermi level, and conversely, enhanced amplitude near the center of the cluster exhibited in the real-space structure of density-matrix eigenfunctions with single-particle pseudo-energies far away from the pseudo-Fermi level, we worry that these eigenfunctions might not be a good basis to use for expanding spatially uniform plane waves, which are the true single-particle energy eigenstates in our model. We address this concern in Section 3.9.3.

3.9 Operator-Based Density-Matrix Truncation Calculation of Dispersion Relation

In a gapless system, we conjecture that low-lying excitations *above* the ground state are built from the same operators as the long-wavelength fluctuations *within* the ground state. This supposition is certainly validated if the system has a continuous symmetry and the long-wavelength modes are Goldstone modes. In general it is justified by the relationships between correlation functions (for the ground-state fluctuations) and response functions (for low-energy excitations).

Despite its poor convergence properties as far as exhausting the sum rule (3.6.1) is concerned, the operator-based truncation would still get the salient features of the physics right. We check this by projecting the Hamiltonian in (2.1.1) onto the truncated set of fermion operators f_l, and calculate the dispersion relation therefrom. There are two physical quantities of interest here: (a) for odd number of sites N_C, the middle band crosses the Fermi level, and we can ask how the Fermi velocity, given by the slope of the dispersion relation at the Fermi level, scales with N_C and the fraction γ of fermion operators kept; or (b) for even N_C, a band gap develops as a result of truncation at the Fermi level, and we can ask how the size of this band gap depends on N_C and γ.

3.9.1 Energy Gap at Fermi Level

In Figure 3.21, we show the general features of the dispersion relation $\epsilon(k)$ calculated within the operator-based truncation scheme, using the example of a cluster of $N_C = 8$ sites. Apart from the energy gap ΔE that opens up at the Fermi level $\epsilon_F = 0$, we see that there is a one-to-one correspondence between the PEL truncated and the energy band absent from the dispersion relation. More precisely, if we order the energy bands and

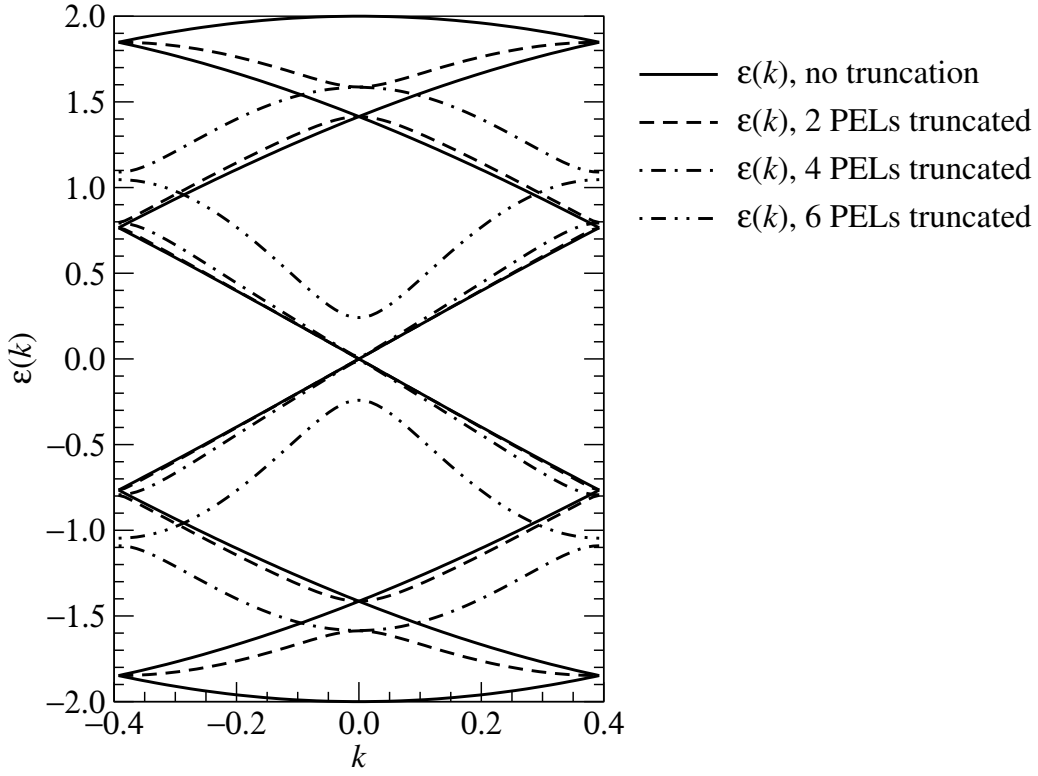

Figure 3.21: Dispersion relation $\epsilon(k)$ for a cluster of $N_C = 8$ sites, where the effects of truncating 2, 4 and 6 PELs are shown. For this cluster size, truncating 2, 4 and 6 PELs corresponds to fractions $\gamma = 0.75$, 0.50 and 0.25 of PELs retained. For $\gamma = 0.75$, the energy bands (dashed curves) just below and above the Fermi level $\epsilon_F = 0$ agree with the true dispersion relation (solid curve) so well that the difference is not discernible at the scales presented in the figure.

the PELs from the lowest to the highest as $\{\epsilon_1(k), \ldots, \epsilon_{N_C}(k)\}$ and $\{\varphi_1, \ldots, \varphi_{N_C}\}$, then if we truncate PEL φ_l, the energy band $\epsilon_l(k)$ will also be removed from the numerically calculated dispersion relation. For fixed γ, the gap ΔE decays exponentially with cluster size N_C, as is shown in Figure 3.22, i.e. we have

$$\Delta E = \Delta E_0 \exp(-\kappa(\gamma) N_C), \tag{3.9.1}$$

where $\kappa(\gamma)$ is an attenuation coefficient whose γ-dependence is shown in Figure 3.23. Here we see also that $\Delta E(N_C, \gamma)$ for different γ appears to converge onto a common limit $\Delta E_0 \equiv \Delta E(N_C = 0)$. Of course, there is no physical sense in talking about a cluster of zero size, but it is nevertheless a useful number to keep in mind when studying the scaling behaviour of $\Delta E(N_C, \gamma)$ as γ varies. ΔE_0 is approximately four, which is the bandwidth of the exact dispersion relation, in all cases.

In particular, in the limit of $\gamma \to 1$, where all PELs are retained, the gap is exactly zero for all nonzero clusters sizes N_C. In this limit, if we start out at a 'gap' of ΔE_0 at a 'cluster size' of $N_C = 0$, then to have $\Delta E = 0$ at $N_C = 1$, we need the attenuation coefficient κ to be infinite, i.e. we expect the limiting behaviour $\lim_{\gamma \to 1} \kappa(\gamma) = \infty$. On the other hand, in the limit of $\gamma \to 0$, where we retain none of the PELs, it is again physically meaningless to talk of a dispersion relation. Nevertheless, if we pretend that we are able to calculate a 'dispersion relation' in this limit, then it is reasonable, following the trend observed in Figure 3.22, that the gap never closes, i.e. we expect the limiting behaviour $\lim_{\gamma \to 0} \kappa(\gamma) = 0$. These limiting behaviours appear to be borne out in the trend observed in Figure 3.23.

Another notable feature in Figure 3.23 is the fact that $\kappa(\gamma) \approx \gamma$ for $\gamma \ll 1$, which is the regime we are most interested to apply the operator-based truncation scheme in. To appreciate the relevance of this observation, let us first note from Figure 3.21 the general feature that the smaller the gap ΔE, the better the truncated dispersion relation

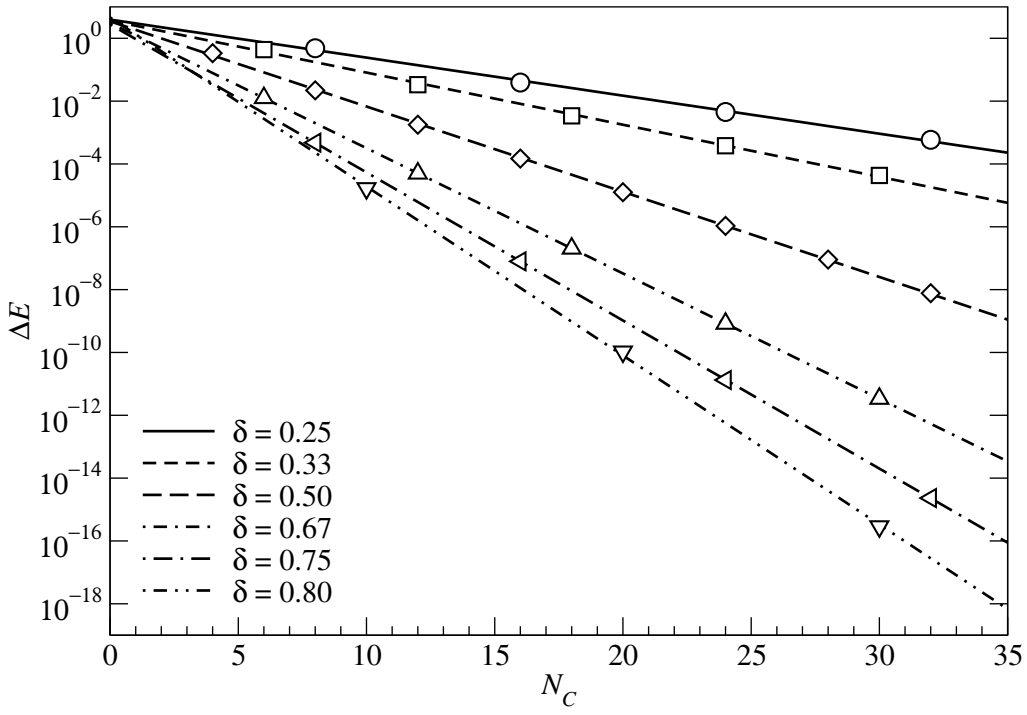

Figure 3.22: Plot of the gap ΔE as a function of cluster size N_C for various constant fractions $\gamma = 1/4, 1/3, 1/2, 2/3, 3/4, 4/5$ of PELs retained. Also shown are fits to the data points for various γ to $\Delta E(\gamma, N_C) = \Delta E_0 \exp(-\kappa(\gamma) N_C)$.

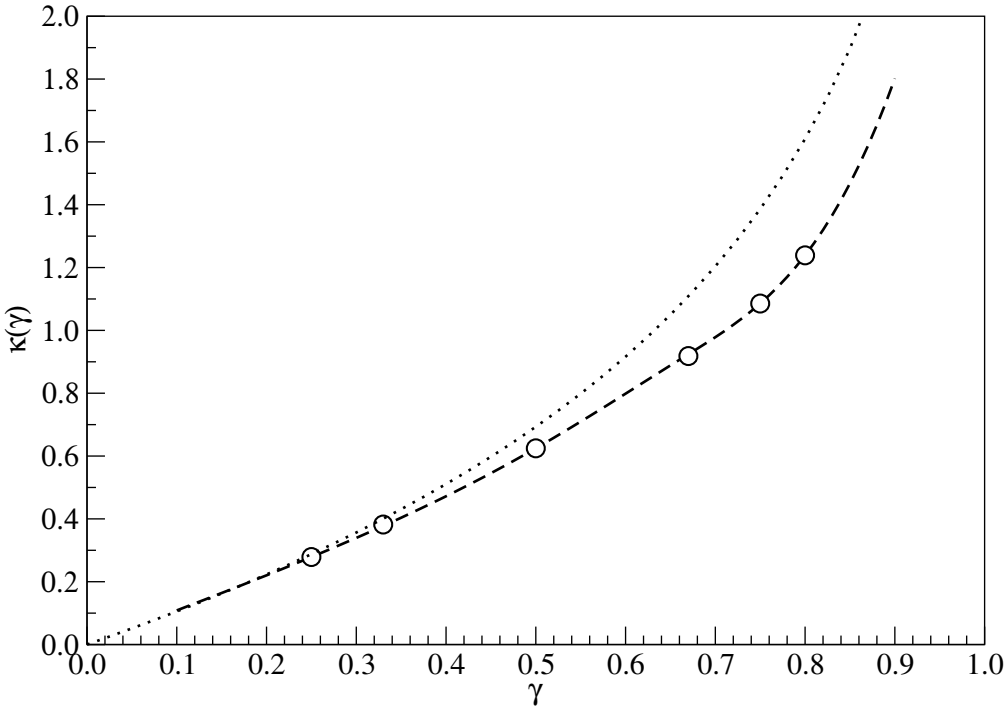

Figure 3.23: Plot of the attenuation coefficient $\kappa(\gamma)$ with which the spurious gap ΔE decays, as a function of the fraction γ of PELs retained. A cubic spline curve (dashed curve) is superimposed on the data points to aid visualization. Also shown (dotted curve) is $-\log(1-\gamma)$.

matches the true dispersion relation about the Fermi level. From (3.6.36) we saw that the truncated weight W_t depends only on the combination $l_{\max} = \gamma N_C$ in this regime, and as far as W_t is concerned, there is no difference whether we choose to keep 10 out of 100 PELs ($\gamma = 0.1$) or 10 out of 200 PELs ($\gamma = 0.05$). Here we see a similar exponential dependence on $l_{\max}$ for the spurious gap ΔE that arises due to truncation: if we write $\kappa \approx \gamma$ in this regime, then $\Delta E \approx \Delta E_0 \exp(-N_C\gamma) = \Delta E_0 \exp(-l_{\max})$. Such an exponential behaviour implies that we have very good control over the numerical accuracy of the dispersion relations — in particular near the Fermi level —- calculated in the operator-based DM truncation scheme.

3.9.2 Fermi Velocity

When the cluster size N_C is odd, the central energy band crosses the Fermi level, and the quantity of interest becomes the Fermi velocity v_F. This can be determined from the truncated dispersion relation by taking the numerical central derivative of the central energy band at $k = \pm\bar{n}\pi/N_C$. At half-filling, $\epsilon(k = \pm\pi/2N_C) = 0$ exactly because of particle-hole symmetry. This feature of the dispersion relation was found to be preserved in the numerical dispersion relations computed within the operator-based DM truncation scheme. On the global scale, we find numerically that the shifts in the central energy band at the Brillouin zone center and Brillouin zone edge are such that $v_F > 2$ always. However, when N_C is large, the numerical diagonalization routine introduces artefacts on the energy scale of 10^{-13}, resulting in the locally evaluated v_F coming out to be very slightly less than 2. As such, we analyze the behaviour of v_F as a function of N_C and γ only for $N_C < 150$, as shown in Figure 3.24.

As can be seen from Figure 3.24, the difference $(v_F - 2)$ decays more or less expo-

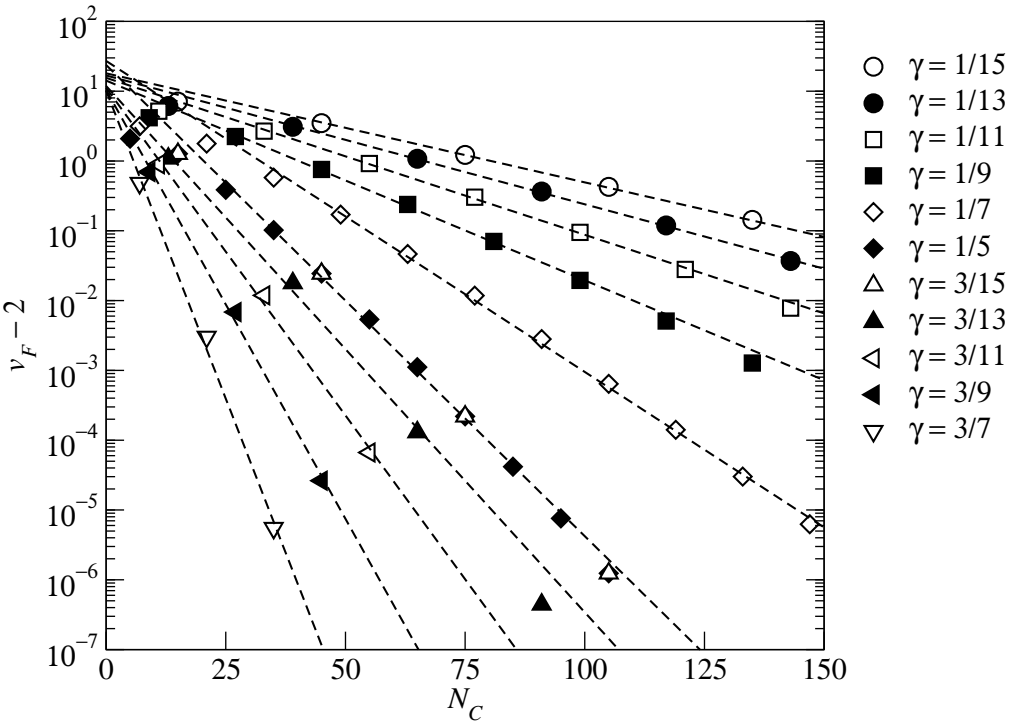

Figure 3.24: Plot of Fermi velocity deviation ($v_F - 2$) calculated from the truncated dispersion relation, as a function of the cluster size N_C, for various fractions $\gamma = 1/15, 1/13, 1/11, 1/9, 1/7, 1/5, 3/15, 3/13, 3/11, 3/9, 3/7$ of PELs retained. Fits to average exponential decays are also shown.

nentially with N_C for various γ, i.e.

$$(v_F - 2) \cong \exp(-\xi(\gamma)N_C), \tag{3.9.2}$$

where $\xi(\gamma)$ is the γ-dependent attenuation coefficient for the average exponential decay. The γ-dependence of $\xi(\gamma)$ is shown in Figure 3.25.

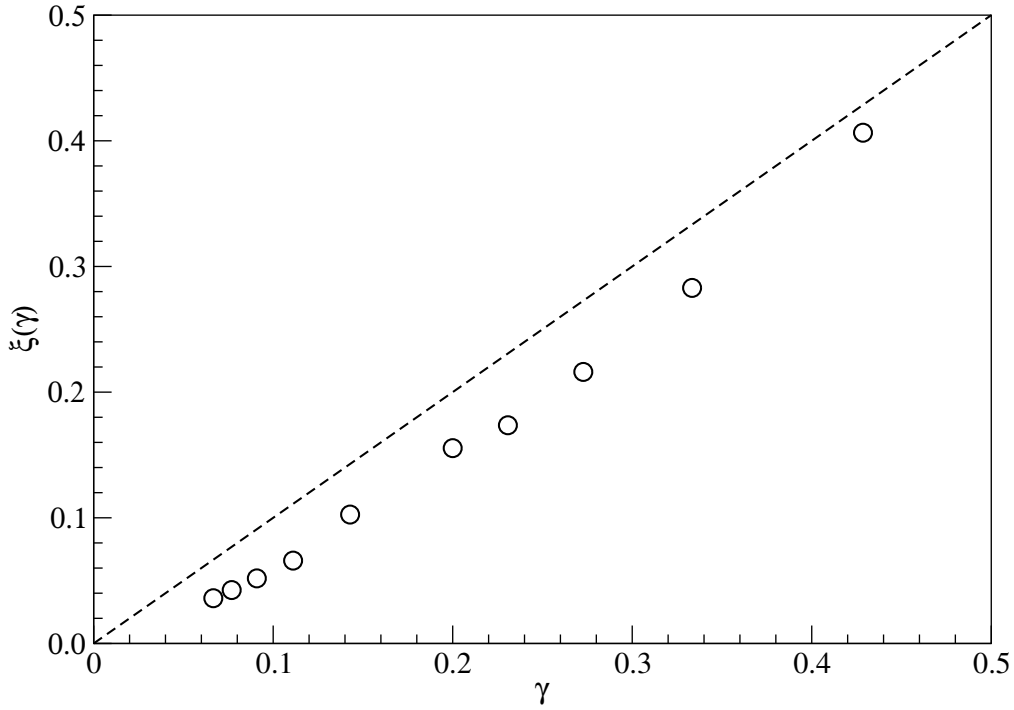

Figure 3.25: Plot of the attenuation coefficient $\xi(\gamma)$ as a function of the fraction γ of PELs retained. Also shown (dashed line) is the expected behaviour $\xi(\gamma) = \gamma$.

3.9.3 Real-Space Structure of Eigenfunctions of Truncated Hamiltonian

The eigenfunctions of the untruncated Hamiltonian (2.1.1) are spatially uniform plane waves, with amplitude $\exp(\mathrm{i}\,kj)/\sqrt{N_C}$ on site j of the cluster of N_C sites. These can be expanded in terms of the density-matrix eigenfunctions $\chi_l(j, N_C)$. Naively, we expect that if we drop those $\chi_l(j, N_C)$ associated with pseudo-energies $\varphi(l, B)$ far from the

pseudo-Fermi level φ_F, as we would in our operator-based truncation scheme which removes these single-particle pseudo-energy levels as degrees of freedom, the remaining terms, all having enhanced amplitudes at the edge of the cluster, would sum to a function with enhanced amplitude at the edge of the cluster. It would therefore seem like we are attempting to approximate a spatially-uniform plane wave with a function with the wrong real-space structure.

However, the key insight we gain from our study of cluster density matrices is that while the system-wide density matrix ρ_0 commutes with H in (2.1.1), the cluster density matrix ρ_C obtained by tracing down ρ_0 does not commute with $H(k)$, for all k. Therefore, after operator-based truncation $H(k) \rightarrow \tilde{H}(k)$, we would need to diagonalize $\tilde{H}(k)$ to find the truncated dispersion relation $\epsilon_l(k)$. Thus, the function that would approximate the plane wave is not the latter's truncated expansion in terms of the eigenfunction of the one-particle cluster density matrix, but rather, a particular eigenfunction of $\tilde{H}(k)$, which is an appropriate linear combination of the $\chi_l(j, N_C)$ retained in the operator-based truncation scheme. We show in Figure 3.26 the spatial structure of such a function, for various numbers of density-matrix eigenfunctions retained. As we can see, for a cluster of $N_C = 23$ sites, keeping seven density-matrix eigenfunctions with pseudo-energies around φ_F would produce a decent approximation to the plane wave with $k = \pi/2N_C$.

3.9.4 Discussion

We speculate that the fact that the operator-based density-matrix truncation scheme succeeds so well suggests that appropriate linear combinations of the density-matrix eigenfunctions can closely approximate a plane wave with wavevector $\pm k_F$. This is only possible by taking the difference of two eigenfunctions so as to cancel the enhancements of the envelope function seen at the ends of the cluster (see Section 3.8). Indeed,

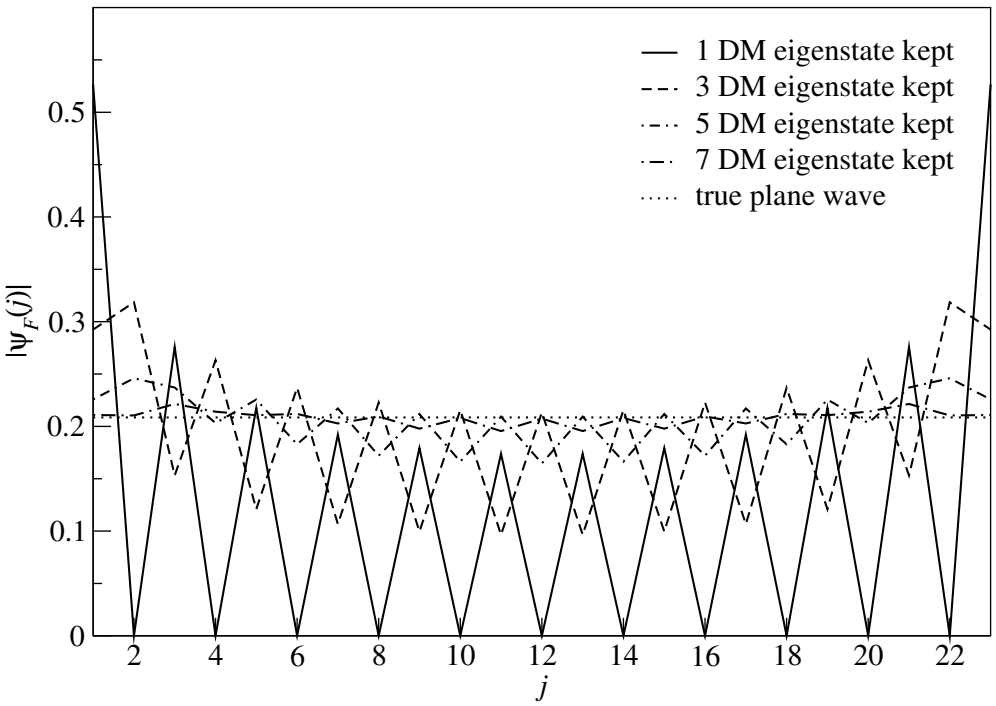

Figure 3.26: Amplitudes of eigenfunctions of the truncated Hamiltonian $\tilde{H}(k_F)$ for different numbers of PELs retained, for a cluster of $N_C = 23$ sites at half-filling.

the fact that we get the correct slope v_F of the dispersion near k_F suggests that by taking different weights, a continuously varying effective wave vector can be approximated.

The fact that the goodness of approximation depends only on the number of eigenfunctions kept, means that we approximate the wavefunction about as well in two successive clusters of N_C sites, as we do in one big cluster of $2N_C$ sites. One could speculate that there might exist some sort of approximate composition formula, analogous to Clebsch-Gordan formulas for combining angular momenta, that provides the $2N_C$-site eigenfunctions in terms of the direct product of the N_C-site eigenfunctions.

3.10 Operator-Based Plane-Wave Truncation Scheme

As we saw in Section 3.8, eigenstates of the density matrix ρ_C are approximately plane waves (with wave vector q determined by the boundary conditions on the cluster of N_C sites) modified by some envelope function. Apart from the effects of the envelope functions, the operator-based truncation scheme described above is likened to truncating wavevectors q far away from the Fermi wavevector k_F. It is therefore natural to investigate how a operator-based truncation scheme based on plane waves would fare against that based on the density-matrix eigenstates.

3.10.1 Exact Dispersion at Zone Center

Compared to the *operator-based DM truncation scheme* developed above, the most striking feature of the *operator-based plane wave (PW) truncation scheme* is that it gets the dispersion exactly right at the zone center, as shown for the case of $N_C = 8$ in Figure 3.27, and for the case of $N_C = 10$ in Figure 3.28. We understand this as follows.

To evaluate the dispersion relation in a cluster description, we start by defining the

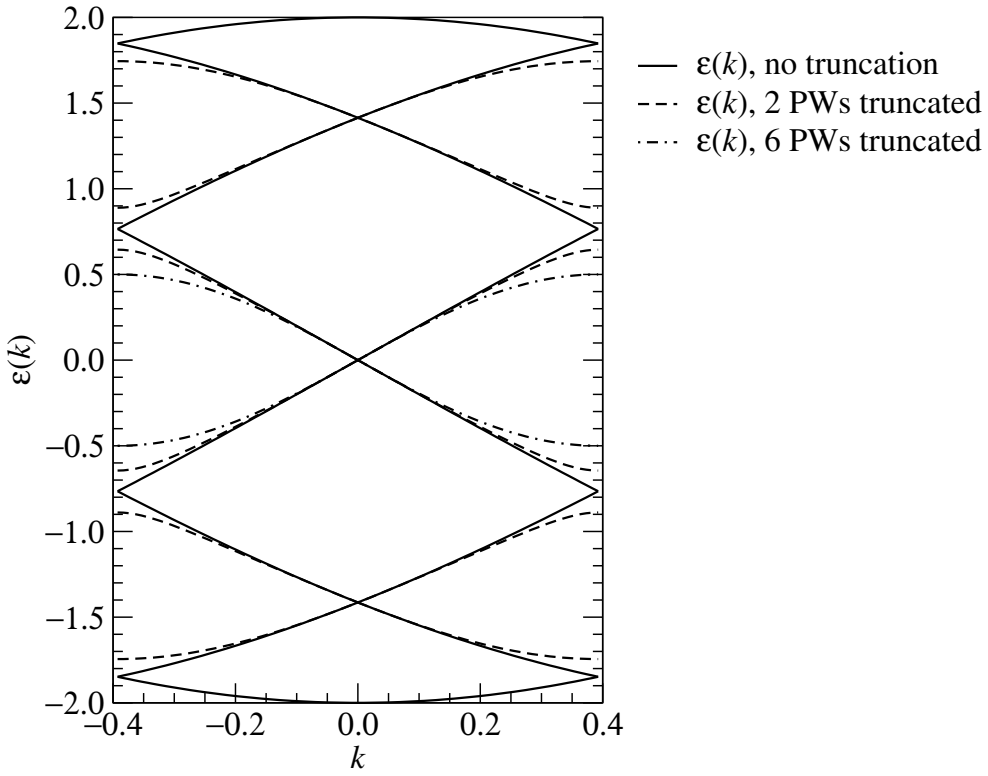

Figure 3.27: Dispersion relation $\epsilon(k)$ for a cluster of $N_C = 8$ sites, where the effect of truncating 2 and 6 plane waves (PWs) are shown. For $N_C = 4n$, the Fermi level is located at the zone center, and $\epsilon(k)$ is always gapless here regardless of the number of plane waves truncated.

direct Bloch basis states

$$|j,k\rangle = \frac{1}{\sqrt{N/N_C}} \sum_J e^{\mathrm{i}\,kJN_C} \,|j,J\rangle\,, \quad j = 1,\ldots,N_C, \tag{3.10.1}$$

where $|j,J\rangle = c^\dagger_{j+JN_C}|0\rangle$ is the single-particle occupation number basis state at site $j + JN_C$ along the chain. In this basis, the Hamiltonian (2.1.1) for a chain of N non-interacting spinless fermions takes on a block-diagonal form. Diagonalizing the $N_C \times N_C$ diagonal block

$$H(k) = \begin{bmatrix} 0 & -1 & 0 & \cdots & -e^{-\mathrm{i}\,kJN_C} \\ -1 & 0 & -1 & \cdots & 0 \\ 0 & -1 & 0 & \cdots & 0 \\ \vdots & & & \ddots & \vdots \\ -e^{\mathrm{i}\,kJN_C} & 0 & 0 & \cdots & 0 \end{bmatrix} \tag{3.10.2}$$

for $-\pi/N_C \le k < \pi/N_C$ then gives the dispersion relation within the reduced zone scheme.

For the operator-based PW truncation scheme, we need to work with the plane wave states $|q,J\rangle$ on each cluster of N_C sites, where the wavevector q is determined by periodic boundary condition, i.e. $\exp(\mathrm{i}\,qN_C) = 1$. These plane wave states are related to the single-particle occupation number basis states by

$$|q,J\rangle = \frac{1}{\sqrt{N_C}} \sum_{j=1}^{N_C} e^{\mathrm{i}\,qj} \,|j,J\rangle\,. \tag{3.10.3}$$

A Bloch basis state parallel to (3.10.1) can be defined as

$$|q,k\rangle = \frac{1}{\sqrt{N/N_C}} \sum_J e^{\mathrm{i}\,kJN_C} \,|q,J\rangle\,, \tag{3.10.4}$$

where $qN_C/2\pi = 0,\ldots,N_C - 1$. From (3.10.3) and (3.10.4), it is easy to see that

$$|q,k\rangle = \frac{1}{\sqrt{N_C}} \sum_{j=1}^{N_C} e^{\mathrm{i}\,qj} \,|j,k\rangle\,. \tag{3.10.5}$$

At the zone center, $k = 0$, and the $N_C \times N_C$ Hamiltonian matrix in the $|j, k\rangle$ basis that we need to diagonalize becomes

$$H(0) = \begin{bmatrix} 0 & -1 & 0 & \cdots & -1 \\ -1 & 0 & -1 & \cdots & 0 \\ 0 & -1 & 0 & \cdots & 0 \\ \vdots & \vdots & \vdots & \ddots & \vdots \\ -1 & 0 & 0 & \cdots & 0 \end{bmatrix}. \tag{3.10.6}$$

It is trivial to check that the eigenstates of this Hamiltonian matrix are precisely the plane waves $|Q, 0\rangle$ on the cluster. Therefore, in the $|q, k\rangle$ basis, $H(k)$ is diagonal at $k = 0$, and so truncating some plane waves from the Hilbert space produces no effect on the dispersion here.

To be more precise, in performing truncation, a linear subspace of the Hilbert space is chosen, and the Hamiltonian projected onto this subspace. If $|\psi\rangle$ is an eigenstate of the full Hamiltonian, and if $|\psi\rangle$ is retained in the truncated Hilbert space, then it will continue to be an eigenstate of the truncated Hamiltonian, with the same eigenvalue.

3.10.2 Energy Gap at Zone Boundary

For even cluster sizes with $N_C = 4n$, the Fermi level is located at the zone center in the reduced zone scheme, and so there is no energy gap to speak of. On the other hand, for even cluster sizes with $N_C = 4n + 2$, the Fermi level is located at the zone boundary. At the zone boundary, operator-based PW truncation introduces an energy gap ΔE at the Fermi level, as shown in Figure 3.28 for $N_C = 10$.

As in the case for the operator-based DM truncation scheme, we investigate the behaviour of the energy gap ΔE as a function of the cluster size N_C for a fixed fraction $(1 - \gamma)$ of cluster states truncated. However, for the operator-based PW truncation

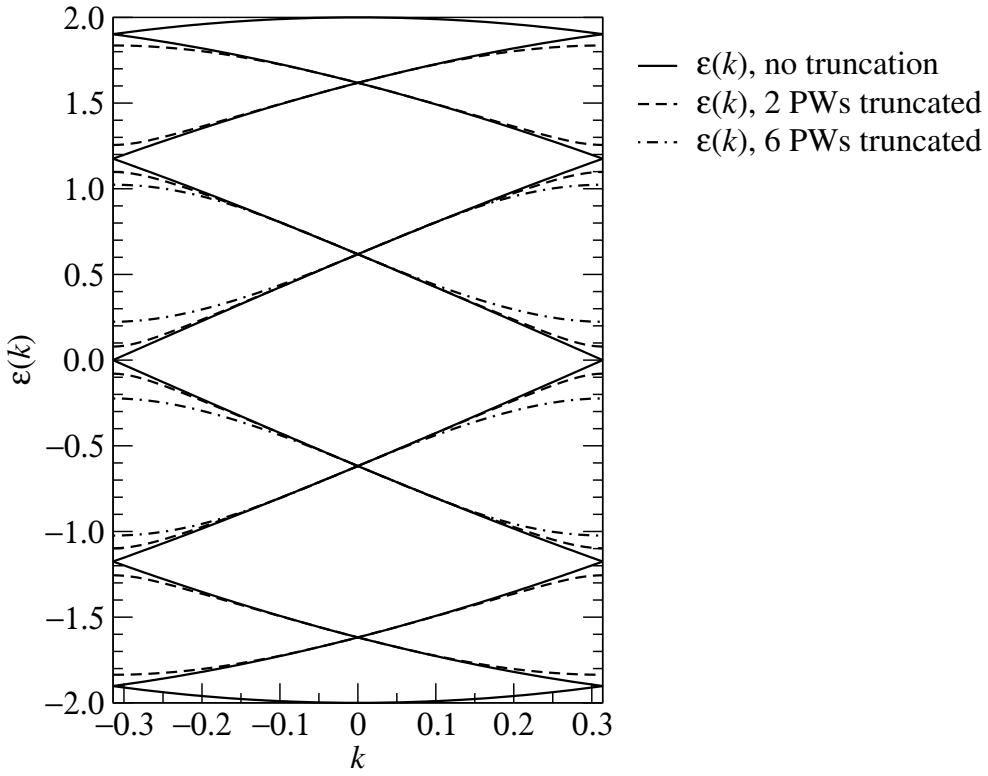

Figure 3.28: Dispersion relation $\epsilon(k)$ for a cluster of $N_C = 10$ sites, where the effect of truncating 2 and 6 plane waves (PWs) are shown. For $N_C = 4n + 2$, the Fermi level is located at the zone boundary, and the operator-based plane wave truncation scheme introduces an energy gap ΔE here.

scheme, the number of plane wave states that can be truncated, if N_C is even, is $4m + 2$, $m = 0, 1, 2, \ldots$. Thus the only realizable series of cluster sizes N_C on which we can perform fixed $(1 - \gamma)$ truncation are of the form $N_C = r(4m + 2)$, $r = 2, 3, \ldots$. The fraction γ of cluster plane wave states retained is related to the series index r by

$$\gamma = 1 - \frac{1}{r}. \tag{3.10.7}$$

Half of these realizable series have cluster sizes that are multiples of four, for which the Fermi level is at the Brillouin zone center where the dispersion relation we have shown in the previous subsection to be gapless. In this subsection we are interested in those cluster sizes for which r is an odd integer, since for these cluster sizes the Fermi level is at the Brillouin zone boundary, where a gap develops in the dispersion relation as a result of truncation. The behaviour of ΔE as a function of N_C for three series of r is shown in Figure 3.29.

As can be seen from Figure 3.29, the gap depends on cluster size as an inverse power law

$$\Delta E(N_C, \gamma) = \frac{\Delta E_1(\gamma)}{N_C}, \tag{3.10.8}$$

where $\Delta E_1(\gamma)$ is a γ-dependent prefactor. This is in stark contrast to the exponential dependence (3.9.1) found for the case of the operator-based density-matrix truncation scheme.

3.10.3 Fermi Velocity

For odd N_C, we again investigate the behaviour of v_F as a function of N_C for the operator-based plane-wave truncation scheme. The number of cluster plane waves that can be truncated is $4m + 3$, $m = 0, 1, 2, \ldots$ and the series of realizable cluster sizes are $N_C = r(4m + 3)$, $r = 3, 5, \ldots$. Unlike in the operator-based DM truncation scheme, there

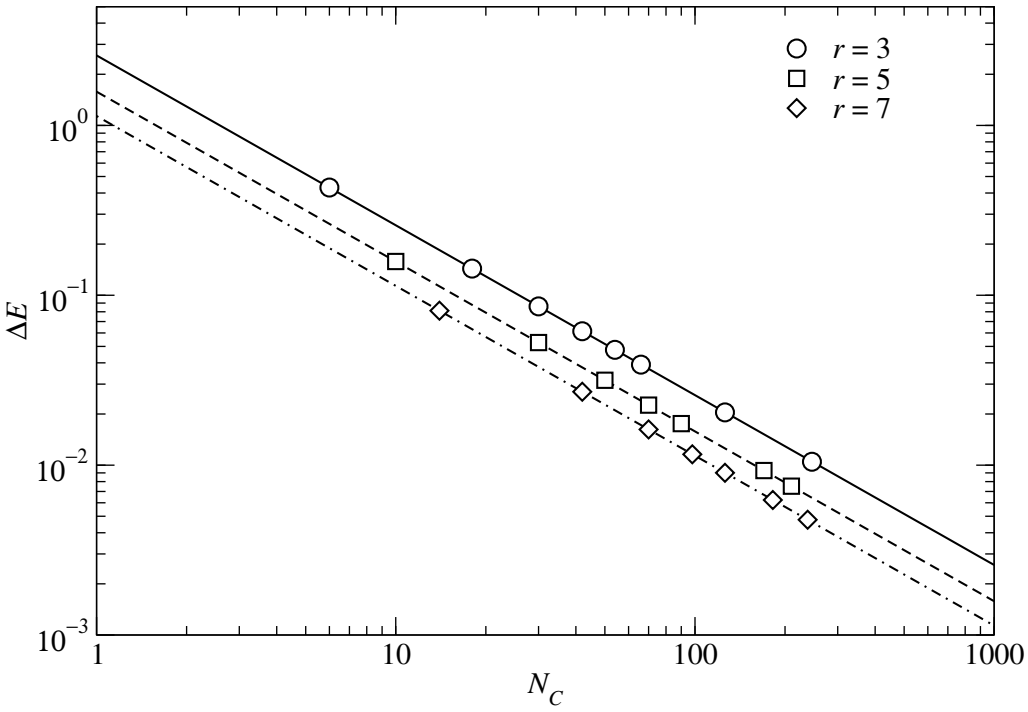

Figure 3.29: Plot of ΔE as a function of cluster size N_C for $r = 3, 5$ and 9, corresponding to the fractions $\gamma = 2/3, 4/5, 6/7$ of cluster plane wave states retained. Also shown are the fits of the data points to the formula $\Delta E(N_C, \gamma) = \Delta E_1(\gamma)/N_C$. From the fits, we have $\Delta E_1 = 2.58263$ for $\gamma = 2/3$, $\Delta E_1 = 1.57991$ for $\gamma = 4/5$ and $\Delta E_1 = 1.13532$ for $\gamma = 6/7$.

appears to be two different systematic behaviours for $v_F(N_C, \gamma)$, one for $r = 4p - 1$ and another for $r = 4p + 1$ ($p = 1, 2, \ldots$). We find that the Fermi velocity can be fitted very well to the formula

$$v_F = \begin{cases} \bar{v}_F(\gamma) + c_+(\gamma)/N_C, & r = 4p - 1; \\ \bar{v}_F(\gamma) - c_-(\gamma)/N_C, & r = 4p + 1. \end{cases} \tag{3.10.9}$$

The plots of $\bar{v}_F(\gamma)$ and $c_\pm(\gamma)$ as a function of γ are shown in Figure 3.30 and Figure 3.31 respectively.

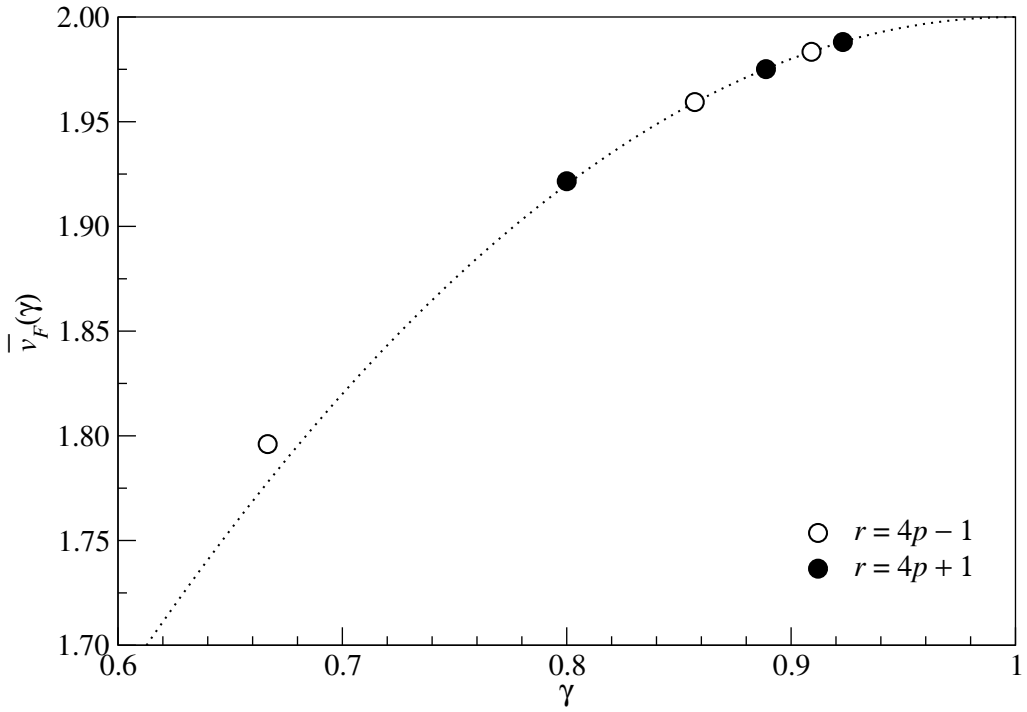

Figure 3.30: Plot of $\bar{v}_F$ as a function of γ in the operator-based PW truncation scheme for both the $r = 4p - 1$ series and $r = 4p + 1$ series. Also shown as the dashed curve is $2[1 - (1 - \gamma)^2]$, which appears to fit the data points well near $\gamma = 1$.

As can be seen from Figure 3.30, the exact value of the Fermi velocity is obtained only in the double limit of $N_C \to \infty$ and $\gamma \to 1$. Compared to the operator-based DM truncation scheme, where we manage to achieve the exact Fermi velocity for any

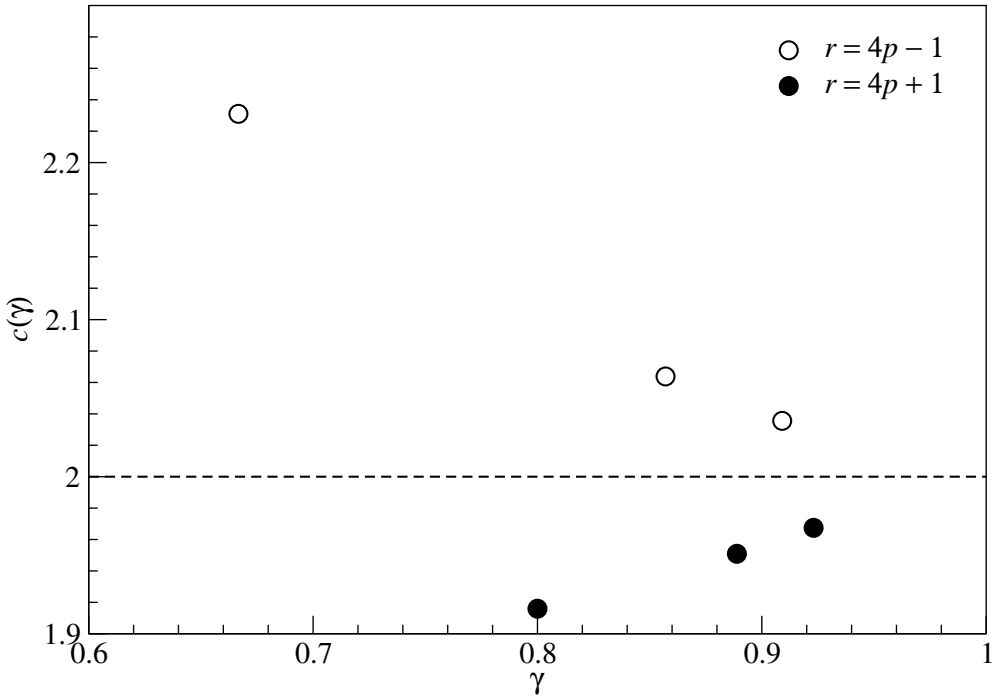

Figure 3.31: Plot of $c_{\pm}$ as a function of γ in the operator-based PW truncation scheme for both the $r = 4p - 1$ series ($c_+(\gamma)$) and $r = 4p + 1$ ($c_-(\gamma)$) series. Both $c_+(\gamma)$ and $c_-(\gamma)$ appears to be converging towards 2. In fact, from the graph we find that $|c_{\pm}(\gamma) - 2| \approx 0.43(1 - \gamma)$.

γ, this is clearly undesirable. Furthermore, even very close to $\gamma = 1$, the computed Fermi velocity approaches the limiting value $\bar{v}_F(\gamma)$ as N_C^{-1}. This is much slower than the exponential convergence of $\exp(-\xi(\gamma)N_C)$ found for the operator-based DM truncation scheme.

CHAPTER 4

CLUSTER DENSITY MATRICES FOR TWO-DIMENSIONAL SYSTEMS

4.1 A Quick Guide to Chapter 4

In this chapter, I calculate the cluster density matrices for two-dimensional systems of spinless fermions. As explained in Section 4.2, our chief motivations are to check whether: (i) the density matrices of the same cluster in a noninteracting and interacting Fermi-sea ground state have the same structure (they do not); (ii) the exact formula (2.4.31) for the noninteracting cluster density matrix can be as readily applied in two dimensions as compared to one dimension (we can); and (iii) it is possible and practical to compute the interacting cluster density matrix numerically (it is).

I address motivation (iii) in Section 4.3, where we show that it is possible to define a reduced many-fermion density matrix that is consistent with two properties expected of a reduced density matrix of a cluster of sites: (a) that it be obtainable from the system density matrix by tracing over environment degrees of freedom; and (b) that it be able to reproduce the expectations of observables local to cluster. I find that, in all but the most bizarre quantum many-body ground states, the cluster density matrix as defined by (4.3.38) satisfies both requirements. At the end of Section 4.3, we also describe how to numerically calculate the matrix elements of the fermion cluster density matrix efficiently using (4.3.39).

To address motivation (i), we compare the cluster density matrices for a system of noninteracting spinless fermions and a system of strongly-interacting spinless fermions with infinite nearest-neighbor repulsion. For the comparison to be meaningful, the non-interacting and interacting cluster density matrices have to be evaluated for the *same* cluster, from the ground states of the *same* finite systems. We present technicalities re-

lating to the cluster and the finite systems chosen for numerical studies in Sections 4.4 and 4.5 respectively. We then calculate the noninteracting and interacting cluster density matrices in Section 4.6 and 4.7 respectively.

In Section 4.6, which is substantially longer than Section 4.7, we address motivation (ii), and at the same time use noninteracting spinless fermions as a testbed in Section 4.6.1 for investigating the influence of various finite size effects on the raw numerics, and the application of the method of twist boundary conditions averaging in Section 4.6.3 to reduce such finite size effects. In Sections 4.7.2, 4.7.3 and 4.7.4, we present the twist-boundary-conditions-averaged zero-, one-, and two-particle cluster density-matrix weights of strongly-interacting spinless fermions with infinite nearest-neighbor repulsion in finite systems with between $N = 11$ to $N = 20$ sites. The behaviours of these as a function of the filling fraction are found expectedly to be significantly different from the corresponding weights of noninteracting spinless fermions.

4.2 Introduction

In Chapter 2, we extended the results of Chung and Peschel [176] to write the density matrix of a cluster of N_C sites cut out from a system of noninteracting spinless fermions in d dimensions as the exponential of a quadratic operator [184], called the pseudo-Hamiltonian, as it resembles the Hamiltonian of a noninteracting system. We then applied this result in Chapter 3 on the numerical studies of noninteracting spinless fermions in one dimension, to better understand how the distribution of cluster density-matrix eigenvalues scale with N_C, and to explore the possibility of designing truncation schemes based on the pseudo-Hamiltonian [198]. We believe truncation schemes such as that described in Ref. 198 will be helpful to the choice of basis states in renormalization groups such as CORE.

Thus, some questions motivating the studies presented in this chapter were: (i) does the density matrix of an interacting Fermi-liquid system resembles that of a noninteracting one? (ii) can we apply our exact result in Ref. 184 to two dimensions as well as for one dimension? (iii) is it numerically practical to compute this sort of density matrix in a fermion system. To answer these questions, we investigate a spinless analog of the extended Hubbard model, given by the Hamiltonian

$$H_{tV} = -t \sum_{\langle \mathbf{r},\mathbf{r}' \rangle} \left[c^\dagger_{\mathbf{r}} c_{\mathbf{r}'} + c^\dagger_{\mathbf{r}'} c_{\mathbf{r}} \right] + V \sum_{\langle \mathbf{r},\mathbf{r}' \rangle} n_{\mathbf{r}} n_{\mathbf{r}'}, \tag{4.2.1}$$

in the limit of $V \to \infty$, so that fermions are not allowed to be nearest neighbors of each other. This model is chosen because it has a rich zero-temperature phase diagram [204–206], where we find practically free fermions in the limit $\bar{n} \ll 1$, and an inert solid at half-filling $\bar{n} = \frac{1}{2}$. As the filling fraction approaches quarter-filling from below, $\bar{n} \to \frac{1}{4}^-$, the system becomes congested, highly correlated, but is nonetheless a Fermi liquid, perhaps with additional orders that are not clear in small systems. Slightly above quarter-filling, the dense fluid coexists with an array of stripes, the latter behaving like an inert solid when the stripes are far apart. When we go to slightly below half-filling, the system is expected to support stable arrays of stripes.

To probe this rich variety of structures in the ground state at different filling fraction $\bar{n}$, we describe in Section 4.3 how the reduced density matrix of a small cluster, with the appropriate symmetry properties, can be calculated from a finite non-square system subject to twist boundary conditions. Then in Section 4.6, we investigate in great detail the cluster density-matrix spectra of the noninteracting system, particularly on how to handle finite size effects in the numerics, for comparison with the cluster density-matrix spectra of a strongly-interacting system, presented in Section 4.7. We also discuss in Section 4.7 the prospects of designing an Operator-Based Density-Matrix Truncation Scheme for interacting systems, at some, if not at all, filling fractions.

4.3 Formulation

As far as I am aware of in the quantum mechanics literature, it is implicitly assumed that we can *always* calculate a reduced density matrix starting from a given many-body wave function, whether we are dealing with bosons or fermions. By considering a lattice model of spinless fermions, we will show that this is indeed the case, furnishing a simple proof in the process. We find that there are subtle fermion signs to worry about, before we arrive at a definition for the density matrix of a cluster of sites, that is consistent with it being obtained by tracing out the degrees of freedom outside the cluster, and it carrying all quantum information local to the cluster.

This section is organized as follows: in Section 4.3.1, we introduce the notations (see also Appendix C) used to denote the many-fermion basis states of the system, cluster, and the environment of the cluster. Then in Section 4.3.2, we look at two alternative definitions of the cluster density matrix, the first derived from partially tracing over the environment in Section 4.3.2.2, and the second derived by demanding that the cluster density matrix recovers the correct expectation for an arbitrary observable local to the cluster in Section 4.3.2.3. In Section 4.3.2.4, we discuss the general applicability of the cluster density-matrix formula, and when it might fail. We also explain how the formula derived for the fermionic cluster density matrix will also apply for the bosonic cluster density matrix, by trivially assigning all 'fermion' signs that occur in the bosonic cluster density-matrix elements to +1. Finally, in Section 4.3.3, we discuss two computational implementations to calculate the cluster density-matrix elements, in particular on how the computational costs are expected to scale with the size of the system Hilbert space, the size of the cluster Hilbert space and the size of the environment Hilbert space.

4.3.1 Occupation Number Basis States

Since a cluster is a collection of sites identified in real space, it is natural to choose as a many-body basis the real-space configurations. The derivation in Section 4.3.2 does not depend on dimensionality, but we shall assume a two-dimensional lattice for the sake of concreteness.

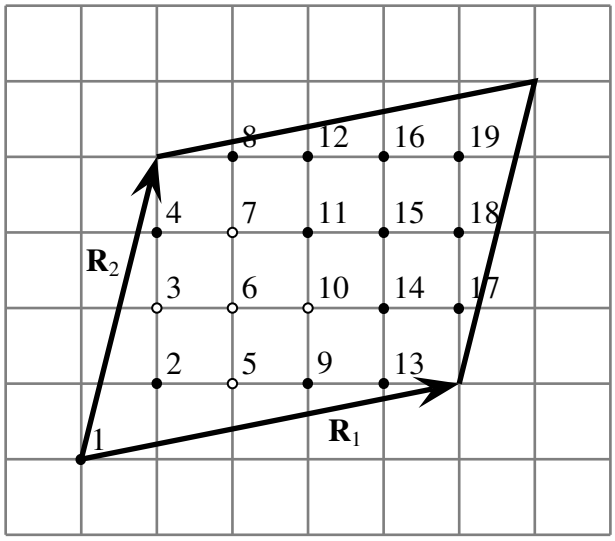

Figure 4.1: Indexing the sites of the $\mathbf{R}_1 \times \mathbf{R}_2$ system, where we start from the leftmost, bottommost site, working our way upwards and then rightwards. In the example $(5,1) \times (1,4)$ shown, there are a total of $N = 19$ sites, numbered from the first, at $(0,0)$, to the nineteenth, at $(5,4)$. The sites $\{3,5,6,7,10\}$ belonging to our five-site, cross-shaped cluster are marked as open circles, while the rest of the sites, which constitutes the environment of the cluster, are marked as filled circles.

For the finite $\mathbf{R}_1 \times \mathbf{R}_2$ system with $N = R_{1x}R_{2y} - R_{2x}R_{1y}$ sites, we label the sites $j = 1$ through $j = N$, so that for any pair of sites (x_{j_1}, y_{j_1}) and (x_{j_2}, y_{j_2}), we have $x_{j_1} \leq x_{j_2}$ and $y_{j_1} < y_{j_2}$ if $j_1 < j_2$. This is shown in Figure 4.1. We then distinguish between sites

within the cluster, of which there are N_C of them, $(x_{j_1^C}, y_{j_1^C})$, $(x_{j_2^C}, y_{j_2^C})$, ..., $(x_{j_{N_C}^C}, y_{j_{N_C}^C})$, and sites outside of the cluster, of which there are $N_E = N - N_C$ of them, $(x_{j_1^E}, y_{j_1^E})$, $(x_{j_2^E}, y_{j_2^E})$, ..., $(x_{j_{N_E}^E}, y_{j_{N_E}^E})$. We think of the N_E sites outside the cluster as constituting the *environment* to the cluster.

We work with the occupation number basis states, which we shall write as

$$|\mathbf{n}\rangle \equiv |n_1 n_2 \dots n_N\rangle \equiv |j_1 j_2 \cdots j_P\rangle \equiv c_{j_1}^\dagger c_{j_2}^\dagger \cdots c_{j_P}^\dagger |0\rangle\,, \tag{4.3.1}$$

where $n_1, n_2, \dots, n_N$ are the occupation numbers of the N system sites, and $j_1 < \cdots < j_P$ are the P occupied sites in the system (see also Appendix C.3.1). These can be thought of as a direct product of the occupation number basis states of the cluster

$$|\mathbf{l}\rangle \equiv |n_1^C n_2^C \dots n_{N_C}^C\rangle \equiv |l_1 l_2 \cdots l_{P_C}\rangle \equiv c_{l_1}^\dagger c_{l_2}^\dagger \cdots c_{l_{P_C}}^\dagger |0\rangle\,, \tag{4.3.2}$$

where $n_1^C, n_2^C, \dots, n_{N_C}^C$ are the occupation numbers of the N_C cluster sites, and $l_1 < \cdots < l_{P_C}$ are the P_C occupied sites within the cluster, and the occupation number basis states of the environment

$$|\mathbf{m}\rangle \equiv |n_1^E n_2^E \dots n_{N_E}^E\rangle \equiv |m_1 m_2 \cdots m_{P_E}\rangle \equiv c_{m_1}^\dagger c_{m_2}^\dagger \cdots c_{m_{P_E}}^\dagger |0\rangle\,, \tag{4.3.3}$$

where n_1^E, n_2^E, ..., $n_{N_E}^E$ are the occupation numbers of the $N_E = N - N_C$ environment sites, and $m_1 < \cdots < m_{P_E}$ are the $P_E = P - P_C$ occupied sites in the environment. We shall also be using the notation $\mathbf{n} = \{j_1, j_2, \dots, j_P\}$, $\mathbf{l} = \{l_1, l_2, \dots, l_{P_C}\}$ and $\mathbf{m} = \{m_1, m_2, \dots, m_{P_E}\}$ to denote the list of occupied sites in the system, the cluster, and the environment respectively.

To write the system occupation number basis state $|\mathbf{n}\rangle$ as a direct product of the cluster occupation number basis state $|\mathbf{l}\rangle$ and the environment occupation number basis states $|\mathbf{m}\rangle$, where the occupied sites

$$\{j_1, \dots, j_P\} = \{l_1, \dots, l_{P_C}\} \cup \{m_1, \dots, m_{P_E}\} \tag{4.3.4}$$

in $|\mathbf{n}\rangle$ is the union of the occupied sites in $|\mathbf{l}\rangle$ and $|\mathbf{m}\rangle$, with the site indices l and m resorted in ascending order to give the site indices j, we must reorder the operators in

$$|\mathbf{n}\rangle = c^\dagger_{j_1} \cdots c^\dagger_{j_P} |0\rangle = (-1)^{f(\mathbf{n};\mathbf{l},\mathbf{m})} \left(c^\dagger_{m_1} \cdots c^\dagger_{m_{P_E}}\right)\left(c^\dagger_{l_1} \cdots c^\dagger_{l_{P_C}}\right) |0\rangle\,, \tag{4.3.5}$$

so that the environment operators are to the left of the cluster operators, incurring a fermion sign $(-1)^{f(\mathbf{n};\mathbf{l},\mathbf{m})}$.

4.3.2 Cluster Density-Matrix Elements

The density matrix ρ_C of a cluster cut out from a larger system is a density operator which gives the expectation

$$\langle\Psi|A|\Psi\rangle = \langle A\rangle = \mathrm{Tr}_C\, \rho_C A \tag{4.3.6}$$

for any observable A local to the cluster, when the larger system is in its ground state $|\Psi\rangle$. In the quantum mechanics literature, it is commonly, and implicitly, stated without proof that the cluster density matrix ρ_C can be calculated from the ground-state density matrix

$$\rho = |\Psi\rangle\langle\Psi| \tag{4.3.7}$$

of the system, by tracing out degrees of freedom outside of the cluster. We write this as

$$\rho_C = \mathrm{Tr}_E\, \rho, \tag{4.3.8}$$

where the subscript E denotes a trace over environmental degrees of freedom. In the following subsections, we shall show that it is possible to define an object ρ_C, for both *bosons* and *fermions*, which is consistent with both (4.3.6) and (4.3.8).

4.3.2.1 Ground-State Density Matrix

To do this, let us first write the P-particle ground-state wave function of the system as

$$|\Psi\rangle = \sum_{\mathbf{n}} \Psi_{\mathbf{n}} |\mathbf{n}\rangle = \sum_{\mathbf{n}} \Psi_{\mathbf{n}} c^{\dagger}_{j_1} \cdots c^{\dagger}_{j_P} |0\rangle , \tag{4.3.9}$$

in terms of the many-fermion occupation number basis states defined in (4.3.1), where $\Psi_{\mathbf{n}}$ is the amplitude associated with configuration $|\mathbf{n}\rangle$, and c_j, $c^{\dagger}_j$ are fermion annihilation and creation operators acting on the site (x_j, y_j). Alternatively, we can write $|\Psi\rangle$ as

$$\begin{aligned} |\Psi\rangle &= \sum_{\mathbf{l}} \sum_{\mathbf{m}} (-1)^{f(\mathbf{n};\mathbf{l},\mathbf{m})} \Psi_{\mathbf{l},\mathbf{m}} |\mathbf{l}\rangle |\mathbf{m}\rangle \\ &= \sum_{\mathbf{l}} \sum_{\mathbf{m}} (-1)^{f(\mathbf{n};\mathbf{l},\mathbf{m})} \Psi_{\mathbf{l},\mathbf{m}} c^{\dagger}_{m_1} \cdots c^{\dagger}_{m_{P_E}} c^{\dagger}_{l_1} \cdots c^{\dagger}_{l_{P_C}} |0\rangle , \end{aligned} \tag{4.3.10}$$

in terms of the direct product of configuration bases of the cluster and the environment, where c_l and $c^{\dagger}_l$ are fermion annihilation and creation operators acting on site (x_l, y_l) within the cluster, and c_m and $c^{\dagger}_m$ are fermion annihilation and creation operators acting on site (x_m, y_m) within the environment. In (4.3.10), the amplitude $\Psi_{\mathbf{l},\mathbf{m}} = \Psi_{\mathbf{n}}$ is taken directly from the expansion in (4.3.9), while the factor $(-1)^{f(\mathbf{n};\mathbf{l},\mathbf{m})}$ comes from the reordering of the operator product $c^{\dagger}_{j_1} \cdots c^{\dagger}_{j_P}$ to get the operator product $c^{\dagger}_{m_1} \cdots c^{\dagger}_{m_{P_E}} c^{\dagger}_{l_1} \cdots c^{\dagger}_{l_{P_C}}$ in (4.3.5).

Similarly, the ground-state density matrix in (4.3.7) can be written as

$$\rho = \sum_{\mathbf{n}} \sum_{\mathbf{n}'} \Psi_{\mathbf{n}} \Psi^{*}_{\mathbf{n}'} c^{\dagger}_{j_1} \cdots c^{\dagger}_{j_P} |0\rangle \langle 0| c_{j'_P} \cdots c_{j'_1}, \tag{4.3.11}$$

using the system basis, or as

$$\begin{aligned} \rho = \sum_{\mathbf{l},\mathbf{m}} \sum_{\mathbf{l}',\mathbf{m}'} (-1)^{f(\mathbf{n};\mathbf{l},\mathbf{m}) + f(\mathbf{n}';\mathbf{l}',\mathbf{m}')} \Psi_{\mathbf{l},\mathbf{m}} \Psi^{*}_{\mathbf{l}',\mathbf{m}'} \times \\ c^{\dagger}_{m_1} \cdots c^{\dagger}_{m_{P_E}} c^{\dagger}_{l_1} \cdots c^{\dagger}_{l_{P_C}} |0\rangle \langle 0| c_{l'_{P'_C}} \cdots c_{l'_1} c_{m'_{P'_E}} \cdots c_{m'_1}, \end{aligned} \tag{4.3.12}$$

using the direct-product basis between cluster configurations and environment configurations.

4.3.2.2 Tracing Over the Environment

Now, let us learn more about the trace-down machinery that would allow us to obtain the cluster density matrix ρ_C from the ground-state density matrix ρ. Our goal is to understand whether there could be subtleties involved in this trace-down that depend on whether we are working with bosons or fermions. We work first with more definite examples, and then generalize. Since we incur no sign changes when exchanging boson operators, let us work through the fermionic case, and return to the bosonic case after we have understood how ρ_C relates to ρ.

Trace formula involving referencing operators. As a first example, let us we consider a system with three sites, and a cluster of one site, namely, site $j = 1$. The trace of ρ over all states, which can be thought of as the ground-state expectation of the simplest observable, i.e. the identity operator $\mathbb{1}$, is then given by

$$\begin{aligned}\mathrm{Tr}_{1,2,3}\,\rho = \langle 0|\rho|0\rangle + \langle 0|c_1\rho c_1^\dagger|0\rangle + \langle 0|c_2\rho c_2^\dagger|0\rangle + \langle 0|c_3\rho c_3^\dagger|0\rangle + \\ \langle 0|c_2c_1\rho c_1^\dagger c_2^\dagger|0\rangle + \langle 0|c_3c_1\rho c_1^\dagger c_3^\dagger|0\rangle + \langle 0|c_3c_2\rho c_2^\dagger c_3^\dagger|0\rangle + \\ \langle 0|c_3c_2c_1\rho c_1^\dagger c_2^\dagger c_3^\dagger|0\rangle = 1.\end{aligned} \tag{4.3.13}$$

If ρ_1 is the cluster density matrix obtained by tracing ρ over sites $j = 2$ and $j = 3$, then the trace of ρ_1 over all states on site $j = 1$ must also be one, i.e.

$$\mathrm{Tr}_1\,\rho_1 = \langle 0|\rho_1|0\rangle + \langle 0|c_1\rho_1 c_1^\dagger|0\rangle = 1. \tag{4.3.14}$$

Writing (4.3.13) as

$$\begin{aligned}\mathrm{Tr}_{1,2,3}\,\rho = \langle 0|[\rho + c_2\rho c_2^\dagger + c_3\rho c_3^\dagger + c_3c_2\rho c_2^\dagger c_3^\dagger]|0\rangle + \\ \langle 0|c_1[\rho + c_2\rho c_2^\dagger + c_3\rho c_3^\dagger + c_3c_2\rho c_2^\dagger c_3^\dagger]c_1^\dagger|0\rangle = 1,\end{aligned} \tag{4.3.15}$$

we find that the normalization condition (4.3.14) can be satisfied if we define ρ_1 to be

$$\rho_1 = \rho + c_2\rho c_2^\dagger + c_3\rho c_3^\dagger + c_3c_2\rho c_2^\dagger c_3^\dagger. \tag{4.3.16}$$

Staring at (4.3.16), we find that ρ_1 is the sum of a series of terms, each of which can be written as

$$[(1-n_3)\mathbb{1}+n_3c_3]\,[(1-n_2)\mathbb{1}+n_2c_3]\,\rho\left[(1-n_2)\mathbb{1}+n_2c_2^\dagger\right]\left[(1-n_3)\mathbb{1}+n_3c_3^\dagger\right], \quad (4.3.17)$$

for $n_2, n_3 = 0, 1$. The products of operators pre- and post-multiplying ρ are none other than the referencing operators introduced in Chapter 2. In Chapter 2, and also in Ref. 184, we had introduced referencing operators $K_{\mathbf{l}}$ associated with the cluster occupation number basis states $|\mathbf{l}\rangle$ to calculate the cluster density matrix elements. Here we find referencing operators $K_{\mathbf{m}}$ associated with the environment occupation number basis states $|\mathbf{m}\rangle$ instead, in terms of which we can rewrite (4.3.17) as a diagonal sum

$$\rho_1 = \sum_{\mathbf{m}} K_{\mathbf{m}}\rho K_{\mathbf{m}}^\dagger. \quad (4.3.18)$$

Fermion signs in matrix elements. To understand where fermion signs might creep in when we trace out the environment, let us look at a more complex example: a system of eight sites, within which we define a cluster of three sites, namely, the sites $\{1, 2, 5\}$. Suppose the ground state $|\Psi\rangle$ that we are handed contains a total of $P = 5$ fermions, then we might imagine that one possible term in the ground-state density matrix ρ with nonzero matrix element looking like

$$c_2^\dagger c_3^\dagger c_5^\dagger c_7^\dagger c_8^\dagger\,|0\rangle\langle 0|\,c_8c_6c_5c_4c_1. \quad (4.3.19)$$

Based on what we have written down in (4.3.16), it would appear at first that this expression contributes a multitude of terms to ρ_C. However, on a second look, we find that a lot of these terms vanish. For example, the term

$$c_4\left(c_2^\dagger c_3^\dagger c_5^\dagger c_7^\dagger c_8^\dagger\,|0\rangle\langle 0|\,c_8c_6c_5c_4c_1\right)c_4^\dagger \quad (4.3.20)$$

coming from $c_4\rho c_4^\dagger$ vanishes, because the annihilation operator c_4 can be anticommuted all the way through the string of creation operators to annihilate the vacuum $|0\rangle$ from

the left. Similarly, the creation operator $c_4^\dagger$ can be anticommuted all the way through the string of annihilation operators to annihilate the vacuum $\langle 0|$ from the right.

For the term given in (4.3.19), we see that the only only combination of operators, which does not annihilate $|0\rangle$ when acting on ρ from the left, is $c_8 c_7 c_3$. However, the corresponding combination of operators, $c_3^\dagger c_7^\dagger c_8^\dagger$, when acting on ρ from the right, will annihilate $\langle 0|$ from the right. The only combination of operators which does not annihilate $\langle 0|$ when acting on ρ from the right is $c_4^\dagger c_6^\dagger c_8^\dagger$, but the corresponding combination of operators, $c_8 c_6 c_4$, when acting on ρ from the left, will annihilate $|0\rangle$. Hence the term given in (4.3.19) will not contribute at all to ρ_C, because the environment of the configuration $[2, 3, 5, 7, 8]$ does not match the environment of the configuration $[1, 4, 5, 6, 8]$. On the other hand, the diagonal term

$$c_2^\dagger c_3^\dagger c_5^\dagger c_6^\dagger c_8^\dagger \, |0\rangle \langle 0| \, c_8 c_6 c_5 c_3 c_2, \tag{4.3.21}$$

in ρ, which has a matching environment $[3, 6, 8]$, does contribute to ρ_C. Tracing over the environment, we find the contribution from this term to be

$$c_8 c_6 c_3 \left(c_2^\dagger c_3^\dagger c_5^\dagger c_6^\dagger c_8^\dagger \, |0\rangle \langle 0| \, c_8 c_6 c_5 c_3 c_2 \right) c_3^\dagger c_6^\dagger c_8^\dagger = (-1)^{2+3} c_2^\dagger c_5^\dagger \, |0\rangle \langle 0| \, c_5 c_2 (-1)^{2+3}, \tag{4.3.22}$$

where the first $(-1)^{2+3}$ is the fermion sign incurred when anticommuting $c_5^\dagger$ through $c_6^\dagger c_8^\dagger$ (two anticommutations) and subsequently $c_2^\dagger$ through $c_3^\dagger c_6^\dagger c_8^\dagger$ (three anticommutations), while the second $(-1)^{2+3}$ is the fermion signs incurred when anticommuting c_5 through $c_8 c_6$ (two anticommutations) and subsequently c_2 through $c_8 c_6 c_3$ (three anticommutations). The fermion signs incurred from the two sides cancel each other, and so for diagonal terms like (4.3.21) in ρ, there is no distinction between the boson case and the fermion case.

To illustrate how non-trivial fermion signs enter into the components of our fermion

cluster density matrix, consider the off-diagonal term

$$c_2^\dagger c_3^\dagger c_5^\dagger c_6^\dagger c_8^\dagger \left|0\right\rangle \left\langle 0\right| c_8 c_6 c_3 c_2 c_1 \tag{4.3.23}$$

in ρ. When tracing this term over the environment, the only surviving piece is

$$c_8 c_6 c_3 \left(c_2^\dagger c_3^\dagger c_5^\dagger c_6^\dagger c_8^\dagger \left|0\right\rangle \left\langle 0\right| c_8 c_6 c_3 c_2 c_1\right) c_3^\dagger c_6^\dagger c_8^\dagger = (-1)^{2+3} c_2^\dagger c_5^\dagger \left|0\right\rangle \left\langle 0\right| c_2 c_1 (-1)^{3+3}, \tag{4.3.24}$$

which carries an overall fermion sign

$$(-1)^{2+3+3+3} = -1 \tag{4.3.25}$$

which distinguishes the fermion case from the boson case.

Finally, let us consider the term

$$c_2^\dagger c_4^\dagger c_5^\dagger c_6^\dagger c_8^\dagger \left|0\right\rangle \left\langle 0\right| c_8 c_6 c_4 c_2 c_1, \tag{4.3.26}$$

which has a matching environment [4, 6, 8]. After tracing this term over the environment, we obtain

$$c_8 c_6 c_4 \left(c_2^\dagger c_4^\dagger c_5^\dagger c_6^\dagger c_8^\dagger \left|0\right\rangle \left\langle 0\right| c_8 c_6 c_4 c_2 c_1\right) c_4^\dagger c_6^\dagger c_8^\dagger = (-1)^{2+3} c_2^\dagger c_5^\dagger \left|0\right\rangle \left\langle 0\right| c_2 c_1 (-1)^{3+3}, \tag{4.3.27}$$

i.e. the term $c_2^\dagger c_5^\dagger \left|0\right\rangle \left\langle 0\right| c_2 c_1$ in ρ_C picks up contributions from (4.3.23) and (4.3.26). In fact, all terms in ρ containing $c_2^\dagger c_5^\dagger \left|0\right\rangle \left\langle 0\right| c_2 c_1$ and a common environment contributes to the $c_2^\dagger c_5^\dagger \left|0\right\rangle \left\langle 0\right| c_2 c_1$ term in ρ_C.

From these example calculations, we make several observations. Firstly, each term

$$\left|\mathbf{n}\right\rangle \left\langle \mathbf{n}'\right| = c_{j_1}^\dagger \cdots c_{j_P}^\dagger \left|0\right\rangle \left\langle 0\right| c_{j'_P} \cdots c_{j'_1} \tag{4.3.28}$$

in ρ contributes to only one term, say

$$c_{m_{P_E}} \cdots c_{m_1} \left(c_{j_1}^\dagger \cdots c_{j_P}^\dagger \left|0\right\rangle \left\langle 0\right| c_{j'_P} \cdots c_{j'_1}\right) c_{m_1}^\dagger \cdots c_{m_{P_E}}^\dagger, \tag{4.3.29}$$

in ρ_C after the trace over over environmental sites, where $c_{m_1}, \ldots, c_{m_{P_E}}$ are the P_E operators acting on sites in the environment. Secondly, (4.3.29) vanishes unless the environmental sites $\{m_1, \ldots, m_{P_E}\}$ are occupied in the configurations $[j_1, \ldots, j_P]$ and $[j'_1, \ldots, j'_P]$, i.e. only those system occupation number basis states $|\mathbf{n}\rangle$ and $|\mathbf{n}'\rangle$ with the same environment will contribute to ρ_C. Finally, to get the cluster density matrix element $\langle \mathbf{l}|\rho_C|\mathbf{l}'\rangle$, we sum over all pairs of $|\mathbf{n}\rangle = (-1)^{f(\mathbf{n};\mathbf{l},\mathbf{m})}\,|\mathbf{l}\rangle\,|\mathbf{m}\rangle$ and $|\mathbf{n}'\rangle = (-1)^{f(\mathbf{n}';\mathbf{l}',\mathbf{m})}\,|\mathbf{l}'\rangle\,|\mathbf{m}\rangle$ with common environment $|\mathbf{m}\rangle$.

For bosonic systems, the same derivation for the cluster density-matrix elements satisfying (4.3.8) goes through, except that we incur no sign change with the exchange of boson operators. Therefore, all we need to do is to set

$$(-1)^{f(\mathbf{n};\mathbf{l},\mathbf{m})} = 1 \tag{4.3.30}$$

for all $|\mathbf{n}\rangle = (-1)^{f(\mathbf{n};\mathbf{l},\mathbf{m})}\,|\mathbf{l}\rangle\,|\mathbf{m}\rangle$. However, at the implementational level, we distinguish between two cases: (i) the maximum number of bosons at each site is finite; and (ii) there is no limit to how many bosons can occupy each site. In case (i), the Fock-Hilbert space of the bosonic system is ultimately finite, whether or not the bosonic Hamiltonian conserves total particle number. All we have to do is to write down a finite set of generalized referencing operators $K_{\mathbf{m}}$ which maps environment configurations with multiply occupied sites to the empty reference environment state, before applying (4.3.18) to effect the trace over the environment. For example, for a system with $N = 5$ sites and $P = 7$ bosons, and a maximum of three bosons at each site, the referencing operator for the configuration $[1, 2, 2, 4, 4, 4, 5]$ is

$$K_{[1,2,2,4,4,4,5]} = a_1 (a_2)^2 a_3 a_3^\dagger (a_4)^3 a_5. \tag{4.3.31}$$

In case (ii), the Fock-Hilbert space is infinite, and so is the set of generalized referencing operators for the environment. If we are dealing with a fixed-particle-number

state, which comes, for example, as the energy eigenstate of a particle-number-conserving bosonic Hamiltonian, we need only deal with a finite Hilbert space and a finite set of generalized referencing operators. This presents no technical difficulties. Otherwise, if we deal with bosonic states with indefinite-particle-number, for example, a BCS-like superposition of states with different total particle numbers, we will very likely be dealing with a system density matrix ρ which expands into an infinite series of terms. In addition, we would also be required to sum an infinite number of $K_{\mathbf{m}}\rho K_{\mathbf{m}}^{\dagger}$ terms in (4.3.18) to trace down the system density matrix ρ. We cannot possibly hope to implement these infinite sums on a computer, apart from exceptional cases where the system ground state can be very well approximated by the superposition over a finite number of many-boson configurations.

Necessary but insufficient. Two points of caution must be made here before we proceed further. First, ρ is an operator acting on the system Hilbert space, while ρ_1 is by definition an operator acting on the cluster Fock-Hilbert space. The way ρ_1 is written as the sum of products of operators acting on the system Hilbert space in (4.3.18) obscures the fact that ρ_1 actually contains no operator acting outside of the cluster, and thus acts effectively only on the cluster Fock-Hilbert space.

Second, every positive-definite observable (see Section 2.2.1) local to the cluster can be made to have a cluster trace (over site $j = 1$) of unity, if we multiply it by the right constant. The positive-definite observable ρ_1 defined in (4.3.16) is, in a sense, special, because it is related to the ground-state density matrix ρ by a sum of projection transformations effected by the referencing operators $K_{\mathbf{m}}$. However, ρ_1 as defined in (4.3.16) is not unique in this sense, because we can define alternative sets of referencing

operators

$$K_{\mathbf{m}}(\mathbf{m}_0)\,|\mathbf{m}'\rangle = e^{\mathrm{i}\,\phi(\mathbf{m}',\mathbf{m}_0)}\delta_{\mathbf{m},\mathbf{m}'}\,|\mathbf{m}_0\rangle\,, \tag{4.3.32}$$

mapping to a non-empty reference configuration $|\mathbf{m}_0\rangle$, incurring a phase of $e^{\mathrm{i}\,\phi(\mathbf{m},\mathbf{m}_0)}$ for the configuration $\mathbf{m}$. The observable $\rho_1(\mathbf{m}_0)$ obtained by replacing $K_{\mathbf{m}}$ by $K_{\mathbf{m}}(\mathbf{m}_0)$ in (4.3.18), is isospectral with ρ_1, and thus positive-definite with unit cluster trace.

Nevertheless, for an arbitrary local observable A, $\mathrm{Tr}_C\,\rho_1 A$ and $\mathrm{Tr}_C\,\rho_1(\mathbf{m}_0)A$ will not agree in general. In fact, only those sets of referencing operators for which $\rho_1(\mathbf{m}_0) = \rho_1$, will the cluster trace with A give

$$\mathrm{Tr}_C\,\rho_1(\mathbf{m}_0)A = \mathrm{Tr}_C\,\rho_1 A = \langle\Psi|A|\Psi\rangle\,. \tag{4.3.6}$$

Therefore, the requirements that the cluster density matrix to have unit cluster trace, and be obtainable from the ground-state density matrix by tracing over the environment, constitutes necessary but insufficient conditions for the density operator ρ_1 to be cluster density matrix. Ultimately, ρ_1 must satisfy (4.3.6), in order to qualify as the density matrix describing the quantum-mechanical state of the cluster.

4.3.2.3 Evaluating Cluster Expectations

How will we know that the candidate cluster density matrix (4.3.18) derived in Section 4.3.2.2 also satisfy (4.3.6)? Perhaps the condition (4.3.6) will require us to define a different density operator? To check this, we evaluate the ground-state expectation $\langle A\rangle = \mathrm{Tr}\,\rho A$ of an observable A using (4.3.12), to obtain

$$\begin{aligned}
&\sum_{\mathbf{l}'',\mathbf{m}''}\sum_{\mathbf{l},\mathbf{m}}\sum_{\mathbf{l}',\mathbf{m}'}(-1)^{f_{\mathbf{j}}+f_{\mathbf{j}'}}\Psi_{\mathbf{l},\mathbf{m}}\Psi^*_{\mathbf{l}',\mathbf{m}'}\times\\
&\langle 0|\,c_{l''_{P''_C}}\cdots c_{l''_1}c_{m''_{P''_E}}\cdots c_{m''_1}c^\dagger_{m_1}\cdots c^\dagger_{m_{P_E}}c^\dagger_{l_1}\cdots c^\dagger_{l_{P_C}}\,|0\rangle\times\\
&\langle 0|\,c_{l'_{P'_C}}\cdots c_{l'_1}c_{m'_{P'_E}}\cdots c_{m'_1}Ac^\dagger_{m''_1}\cdots c^\dagger_{m''_{P''_E}}c^\dagger_{l''_1}\cdots c^\dagger_{l''_{P''_C}}\,|0\rangle\,,
\end{aligned} \tag{4.3.33}$$

which is a sum of products of two expectations.

In the first expectation

$$\langle 0|c_{l''_{P''_C}} \cdots c_{l''_1} c_{m''_{P''_E}} \cdots c_{m''_1} c^\dagger_{m_1} \cdots c^\dagger_{m_{P_E}} c^\dagger_{l_1} \cdots c^\dagger_{l_{P_C}} |0\rangle \,, \tag{4.3.34}$$

if $\mathbf{m}'' \neq \mathbf{m}$ because $P''_E \neq P_E$, then we would have one or more unbalanced annihilation operators which can be pushed right all the way through to annihilate $|0\rangle$, or one or more unbalanced creation operator which can be pushed left all the way through to annihilate $\langle 0|$. Alternatively, we have may have $P''_E = P_E$ but $\mathbf{m}'' \neq \mathbf{m}$, in which case the creation operators in $\mathbf{m}$ do not match up with the annihilation operators in $\mathbf{m}''$. Only when $\mathbf{m}'' = \mathbf{m}$ is this expectation nonzero, which can therefore be simplified as

$$\langle 0|c_{l''_{P''_C}} \cdots c_{l''_1} c^\dagger_{l_1} \cdots c^\dagger_{l_{P_C}} |0\rangle \, \delta_{\mathbf{m},\mathbf{m}''}. \tag{4.3.35}$$

In the second expectation

$$\langle 0|c_{l'_{P'_C}} \cdots c_{l'_1} c_{m'_{P'_E}} \cdots c_{m'_1} A c^\dagger_{m''_1} \cdots c^\dagger_{m''_{P''_E}} c^\dagger_{l''_1} \cdots c^\dagger_{l''_{P''_C}} |0\rangle \,, \tag{4.3.36}$$

we note that if A is an observable acting only within the cluster, it can be written as a sum of products of creation and annihilation operators within the cluster. Whatever the fermion sign we incur when anticommuting $c^\dagger_{m''_1} \cdots c^\dagger_{m''_{P''_E}}$ through A, this expectation will vanish unless $\mathbf{m}'' = \mathbf{m}'$. Consequently, we have $P''_E = P'_E$, and hence $P''_C = P'_C$ in a ground state with a fixed ($= P$) number of particles. The only terms in the operator expansion of A that contribute nontrivially to the expectation are those containing a balanced product of creation and annihilation operators. Therefore, in computing the expectation of A, we can simply bring $c^\dagger_{m''_1} \cdots c^\dagger_{m''_{P''_E}}$ across A as if they commute with one another, giving us

$$\langle 0|c_{l'_{P'_C}} \cdots c_{l'_1} A c^\dagger_{l''_1} \cdots c^\dagger_{l''_{P''_C}} |0\rangle \, \delta_{\mathbf{m}',\mathbf{m}''}. \tag{4.3.37}$$

With these two observations, we realized that the expectation of an observable A local to the cluster can be written as (4.3.6), provided we define the fermion cluster density matrix ρ_C to be

$$\rho_C = \sum_{\mathbf{l},\mathbf{l}'} \sum_{\mathbf{m},\mathbf{m}'} (-1)^{f(\mathbf{n};\mathbf{l},\mathbf{m})+f(\mathbf{n}';\mathbf{l}',\mathbf{m}')} \Psi_{\mathbf{l},\mathbf{m}} \Psi^*_{\mathbf{l}',\mathbf{m}'} \delta_{\mathbf{m},\mathbf{m}'} c^\dagger_{l_1} \cdots c^\dagger_{l_{P_C}} |0\rangle \langle 0| c_{l'_{P'_C}} \cdots c_{l'_1}, \quad (4.3.38)$$

whose matrix elements are

$$\langle \mathbf{l}|\rho_C|\mathbf{l}'\rangle = \sum_{\mathbf{m}} \sum_{\mathbf{m}'} (-1)^{f(\mathbf{n};\mathbf{l},\mathbf{m})+f(\mathbf{n}';\mathbf{l}',\mathbf{m}')} \Psi_{\mathbf{l},\mathbf{m}} \Psi^*_{\mathbf{l}',\mathbf{m}'} \delta_{\mathbf{m},\mathbf{m}'}. \quad (4.3.39)$$

This agrees with the cluster density matrix elements we derived in Section 4.3.2.2 by partially tracing the ground-state density matrix ρ over the environment.

4.3.2.4 Consistency Between Definitions of Cluster Density Matrix

For bosonic systems, there is no nontrivial 'fermion' sign to complicate matters, so (4.3.18) and (4.3.38) give the same cluster density matrix. For fermionic systems, we note that to get from (4.3.36) to (4.3.37), and thus furnish the definition in (4.3.38) for the cluster density matrix that is consistent with both (4.3.6) and (4.3.8), we need to be able to commute all products of environment operators through the observable A, so that our definition for ρ_C in (4.3.38) does not depend on which observable A we are looking into. For this, we need to address two questions: (i) are there non-trivial local observables A with $\langle A\rangle \neq 0$ for which we cannot commute *all* products of environment operators through? and (ii) are there trivial local observables A with $\langle A\rangle = 0$ for which we would end up calculating a non-zero expectation?

We find that these two conditions are satisfied for all physical fermionic ground states that we can think of[1]. For fermionic ground states with definite particle number,

[1]We run into problem, if the ground-state wave function is a superposition of terms containing both even and odd number of particles. For these ground states, there will

which is what we would get from exact diagonalization, these two conditions are certainly satisfied. These two conditions are also true for a BCS ground state, which has indefinite particle number. For all non-trivial observables, we would still receive contributions to their expectations only from configurations for which $\mathbf{m}'' = \mathbf{m}'$, i.e. $P''_E = P'_E$. However, because the wave function consists of a linear superposition of terms with an even number of fermions, it is possible to receive nonzero contributions from those cluster configurations $\mathbf{l}''$ and $\mathbf{l}'$ such that $P''_C - P'_C$ is a nonnegative even number. For example, the anomalous local observable $A = c^\dagger_{j_1^C} c^\dagger_{j_2^C}$ will receive non-zero contributions from those cluster configurations $\mathbf{l}''$ and $\mathbf{l}'$ with $P'_C - P''_C = 2$. In any case, anomalous local observables A must still consists of a sum of products of an even number of fermion operators, though not necessarily all balanced, and we can therefore commute all products $c^\dagger_{m''_1} \cdots c^\dagger_{m''_{P''_E}}$ of environment operators through A to arrive at (4.3.37).

4.3.3 Computational Implementation

In this section, we will discuss the computational complexity of implement two algorithms to calculate the cluster density-matrix elements using (4.3.39). Details on the actual algorithm and coding can be found mostly in Appendix C, which describes system definition, basis state generation, calculating the Hamiltonian matrix elements, exact diagonalization, and trace-down calculation of the cluster density-matrix elements from the ground-state wave function. Appendix C also describes two averaging apparatus used in the numerical study of the cluster density matrices, but twist boundary

be *some* anomalous local observables A containing products of odd numbers of fermion operators, which has non-zero ground-state expectation. In such cases, the cluster density matrix is not a physically meaningful description of the quantum-mechanical state of the cluster, because if we calculate its matrix elements using (4.3.39), we would end up with the wrong expectations for many anomalous observables. Fortunately, ground states of this nature are not know to occur at all in physically meaningful models, so we do not need to be unduly worried about this scenario.

conditions averaging, the most important averaging machinery needed in Section 4.7.1 to extract infinite-system properties from the cluster density-matrix spectra, is described at length in Appendix D.

To determine the computational complexity involved in calculating the cluster density matrix numerically, let us denote by $D(P)$ the size of the system Hilbert space with P particles, $D_C(P_C)$ the size of the cluster Hilbert space with P_C particles, and $D_E(P_E) = D_E(P - P_C)$ the size of the environment Hilbert space with $P_E = P - P_C$ particles. Noting that there can be no matrix elements between cluster configurations with different number of particles, we calculate each P_C sector of the cluster density matrix separately. To keep our notations compact, let us drop the P and P_C dependences in $D(P)$, and $D_{C,E}(P, P_C)$ respectively from this point onwards, and reinstate these dependences only when necessary.

The naive way to compute the cluster density-matrix elements, after looking at the formula (4.3.39), would be to immediately start nested "for" loops in $\mathbf{l}$ and $\mathbf{l}'$, each running over D_C indices. For each pair of cluster configurations $|\mathbf{l}\rangle$ and $|\mathbf{l}'\rangle$, one would need to then determine which of the P-particle configurations $|\mathbf{n}\rangle$ contain the two cluster configurations. This involves running through the D configurations in the system Hilbert space, and for each configuration, comparing the P occupied sites with the P_C occupied sites in the cluster configurations $|\mathbf{l}\rangle$ and $|\mathbf{l}'\rangle$. The computational effort incurred for this matching is thus $O(DP)$. Two vectors of indices, $\mathbf{i}$, whose entries are the indices of system configurations $|\mathbf{n}\rangle$ giving cluster configuration $|\mathbf{l}\rangle$, and $\mathbf{i}'$, whose entries are the indices of system configurations $|\mathbf{n}'\rangle$ giving cluster configuration $|\mathbf{l}'\rangle$, are obtained. The lengths of these index vectors vary, but are of $O(D_E)$. One can then compare the two index vectors, at a computational cost of $O(D_E^2)$, to find which pairs of system configurations giving cluster configurations $|\mathbf{l}\rangle$ and $|\mathbf{l}'\rangle$ share the same environment configuration.

Following this, one can sum over the amplitude of such pairs, at a computational cost of $O(D_E)$, to obtain the cluster density-matrix element $\langle \mathbf{l}|\rho_C|\mathbf{l}'\rangle$. For this naive algorithm, the net computational effort is on the order of $D_C^2(DP + D_E^2 + D_E) \sim D_C^2(DP + D_E^2)$.

Alternatively, we can note that the formula (4.3.39) for the matrix element $\langle \mathbf{l}|\rho_C|\mathbf{l}'\rangle$ of the cluster density matrix looks like an inner product between two vectors, and pre-sort the ground-state wave function. Running through the D system configurations, we determine, at a computational cost of P for each system configuration $|\mathbf{n}\rangle$, what cluster configuration $|\mathbf{l}\rangle$ and environment configuration $|\mathbf{m}\rangle$ it contains. We must then search through the cluster and environment Hilbert spaces to determine what the indices of $|\mathbf{l}\rangle$ and $|\mathbf{m}\rangle$ are in their corresponding Hilbert spaces. This incurs a computational effort on the order of $D_C P_C$ and $D_E P_E$ respectively. Once these indices are determined, the amplitudes in the ground-state wave function can be organized into a $D_C \times D_E$ matrix. The net computational expenditure is thus on the order of $D(P + D_C P_C + D_E P_E) \sim D(D_C P_C + D_E P_E)$. After sorting the ground-state wave function, we can then start nested "for" loops in $\mathbf{l}$ and $\mathbf{l}'$, each running over D_C indices, to evaluate the matrix element $\langle \mathbf{l}|\rho_C|\mathbf{l}'\rangle$ as the inner product between two vectors of length D_E. This trace-down stage incurs a computational cost of $O(D_C^2 D_E)$. Overall, the computational cost is on the order of $D(D_C P_C + D_E P_E) + D_C^2 D_E$.

For models allowing nearest-neighbor occupation, the system Hilbert space is the direct product of the cluster Hilbert space and the environment Hilbert space, i.e. $D = D_C D_E$. Since the number P of particles is small in any reasonable exact diagonalization, we can treat it as a $O(1)$ constant. For small clusters, the size D_C of the cluster Hilbert space will also be small, so that the size D_E of the environment Hilbert space will be comparable in magnitude to D. With these considerations, we find that the computational cost for the naive algorithm is $O(DD_C^2 + D_C^2 D_E^2) \sim O(D^2)$, while the computational

cost for the inner-product algorithm with pre-sorting is $O(D + DD_E + D_E) \sim O(D^2)$. The efficiency of the two algorithms therefore depend on the prefactors.

For a model such as (4.2.1), where nearest-neighbor occupation is forbidden, the system Hilbert space can be significantly smaller than the direct product of the cluster Hilbert space and the environment Hilbert space, i.e. $D < D_C D_E$. Given again that P and D_C are small numbers, the computational cost for the two algorithms are essentially determined by the ratio $D_C D_E / D$. This ratio is strongly dependent on the dimensionality of the problem: the superfluous configurations generated by the direct product of the cluster Hilbert space and the environment Hilbert space are invalid because they contain nearest-neighbor sites, right at the boundary between the cluster and its environment, which are occupied. In one dimension, the number of superfluous configurations is small, because the boundary between the cluster and its environment consists only of two bonds, whatever the size N_C of the cluster. In two dimensions, the boundary between the cluster and its environment is a line cutting roughly $\sqrt{N_C}$ bonds. The number of superfluous configurations is then proportional to $\exp(\alpha_2 \sqrt{N_C})$, where α_2 is a constant prefactor which depends on the shape of the cluster. In d dimensions, the number of boundary bonds is on the order of $N_C^{(d-1)/d}$, and the number of superfluous states is proportional to $\exp(\alpha_d N_C^{(d-1)/d})$. Therefore, in dimensions greater than one, $D_C D_E$ become increasingly larger than D as N_C is increased, and the inner-product algorithm with pre-sorting, which involves only one power of $D_C D_E$, is more efficient than the naive algorithm, which involves $(D_C D_E)^2$. We use the pre-sorting algorithm for all our calculations on interacting spinless fermions with infinite nearest-neighbor repulsion in this chapter.

4.4 The Five-Site, Cross-Shaped Cluster

4.4.1 Symmetries and Irreducible Representations

The five-site, cross-shaped cluster shown in Figure 4.2 has the full point group symmetry of the square lattice. This point symmetry group, which is the dihedral group D_4, has eight elements: the identity, a C_4 rotation, a C_2 rotation, a plane σ_x of reflection symmetry along the x-axis, a plane σ_y of reflection symmetry along the y-axis, a plane σ_{y-x} of reflection symmetry along the line $y - x = 0$, a plane σ_{y+x} of reflection symmetry along the line $y + x = 0$, and an inversion i about the central site [207–209]. This point symmetry group can be generated by σ_x, σ_y, σ_{y-x} and σ_{y+x}, and has five irreducible representations A_1, A_2, B_1, B_2 and E.

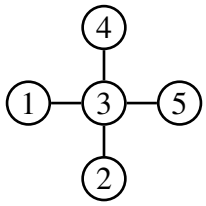

Figure 4.2: The five-site, cross-shaped cluster whose cluster density matrix we are interested in calculating for both a system of noninteracting, as well as strongly-interacting spinless fermions.

4.4.2 One-Particle Cluster States

There is a one-to-one correspondence between the five irreducible representations and the one-particle cluster states. But instead of labeling the one-particle cluster states as

$|A_1\rangle$, $|A_2\rangle$, $|B_1\rangle$, $|B_2\rangle$ and $|E\rangle$, we adopt an angular-momentum-like notation,

$$\begin{aligned}
|s_+\rangle = |A_1\rangle &= \tfrac{1}{\sqrt{5}}\left(c_1^\dagger + c_2^\dagger + c_3^\dagger + c_4^\dagger + c_5^\dagger\right)|0\rangle\,, \\
|s_-\rangle = |A_2\rangle &= \tfrac{1}{\sqrt{5}}\left(c_1^\dagger + c_2^\dagger - c_3^\dagger + c_4^\dagger + c_5^\dagger\right)|0\rangle\,, \\
|p_x\rangle = |B_1\rangle &= \tfrac{1}{\sqrt{2}}\left(c_1^\dagger - c_5^\dagger\right)|0\rangle\,, \\
|p_y\rangle = |B_2\rangle &= \tfrac{1}{\sqrt{2}}\left(c_2^\dagger - c_4^\dagger\right)|0\rangle\,, \\
|d\rangle = |E\rangle &= \tfrac{1}{2}\left(c_1^\dagger - c_2^\dagger - c_4 + c_5^\dagger\right)|0\rangle\,,
\end{aligned} \tag{4.4.1}$$

that would make the structure of these one-particle cluster states more obvious.

In terms of the one-particle configurational basis states

$$\begin{aligned}
|1,1\rangle = c_1^\dagger|0\rangle\,, \quad |1,2\rangle = c_2^\dagger|0\rangle\,, \quad |1,3\rangle = c_3^\dagger|0\rangle\,, \\
|1,4\rangle = c_4^\dagger|0\rangle\,, \quad |1,5\rangle = c_5^\dagger|0\rangle\,,
\end{aligned} \tag{4.4.2}$$

we can write these one-particle cluster states as

$$\begin{aligned}
|s_+\rangle = |A_1\rangle &= \tfrac{1}{\sqrt{5}}(1,1,1,1,1), \\
|s_-\rangle = |A_2\rangle &= \tfrac{1}{\sqrt{5}}(1,1,-1,1,1), \\
|p_x\rangle = |B_1\rangle &= \tfrac{1}{\sqrt{2}}(1,0,0,0,-1), \\
|p_y\rangle = |B_2\rangle &= \tfrac{1}{\sqrt{2}}(0,1,0,-1,0), \\
|d\rangle = |E\rangle &= \tfrac{1}{2}(1,-1,0,-1,1).
\end{aligned} \tag{4.4.3}$$

For the purpose of calculating the one-particle cluster density-matrix eigenstates and eigenvalues, we find it more convenient to work with the one-particle cluster states

$$\begin{aligned}
|s\rangle &= \tfrac{1}{\sqrt{2}}|s_+\rangle + \tfrac{1}{\sqrt{2}}|s_-\rangle = \tfrac{1}{2}(1,1,0,1,1), \\
|\bar{s}\rangle &= (0,0,1,0,0), \\
|p_+\rangle &= \tfrac{1}{\sqrt{2}}|p_x\rangle + \tfrac{\mathrm{i}}{\sqrt{2}}|p_y\rangle = \tfrac{1}{2}(1,\mathrm{i},0,-\mathrm{i},-1), \\
|p_-\rangle &= \tfrac{1}{\sqrt{2}}|p_x\rangle - \tfrac{\mathrm{i}}{\sqrt{2}}|p_y\rangle = \tfrac{1}{2}(1,-\mathrm{i},0,\mathrm{i},-1).
\end{aligned} \tag{4.4.4}$$

For a cluster density matrix ρ_C possessing the full point group symmetry of the square lattice, the one-particle state $|d\rangle$ is constrained by symmetry to always be an eigenstate of ρ_C. We call its weight w_d. Furthermore, the one-particle states $|p_x\rangle$ and $|p_y\rangle$ are also equivalent under the square lattice symmetry, and hence their weights w_{p_x} and w_{p_y} are equal. We call this doubly-degenerate one-particle weight w_p. On the other hand, the s-symmetry one-particle eigenstates of ρ_C are in general not $|s_+\rangle$, $|s_-\rangle$ or $|s\rangle$, $|\bar{s}\rangle$, but some admixture of the form

$$\begin{aligned} |s_1\rangle &= \cos\theta\,|s\rangle + \sin\theta\,|\bar{s}\rangle\,, \\ |s_2\rangle &= -\sin\theta\,|s\rangle + \cos\theta\,|\bar{s}\rangle\,. \end{aligned} \tag{4.4.5}$$

We call their corresponding weights w_{s_1} and w_{s_2} respectively.

4.4.3 Two-Particle Cluster States

This angular-momentum-like notation can be extended to multi-particle states of the cluster. Though the quantum numbers used to label the one-particle states are, strictly speaking, not angular momentum quantum numbers, we apply the rules of angular momenta addition as if they were to write down the angular-momentum-like quantum numbers for the multi-particle states. In particular, for the two-particle states of the cluster, we have

$$\begin{gathered} |S\,\rangle = |p_+p_-\rangle\,, \quad |S'\rangle = |s\bar{s}\rangle\,, \\ |P_+\rangle = |sp_+\rangle\,, \quad |P'_+\rangle = |\bar{s}p_+\rangle\,, \quad |P''_+\rangle = |p_-d\rangle\,, \\ |P_-\rangle = |sp_-\rangle\,, \quad |P'_-\rangle = |\bar{s}p_-\rangle\,, \quad |P''_-\rangle = |p_+d\rangle\,, \\ |D\rangle = |sd\rangle\,, \quad |D'\rangle = |\bar{s}d\rangle\,. \end{gathered} \tag{4.4.6}$$

In the system of strongly-interacting spinless fermions with infinite nearest-neighbor repulsion, only six out of these ten two-particle cluster states are allowed. These six allowed two-particle cluster states, which have vanishing amplitudes for configurations

where site 3 is occupied, are

$$
\begin{aligned}
|S\rangle = |p_+p_-\rangle &= \tfrac{1}{\sqrt{6}}\left(-\mathrm{i}\,c_1^\dagger c_2^\dagger + \mathrm{i}\,c_1^\dagger c_4^\dagger - c_1^\dagger c_5^\dagger + c_2^\dagger c_4^\dagger + \mathrm{i}\,c_2^\dagger c_5^\dagger - \mathrm{i}\,c_4^\dagger c_5^\dagger\right)|0\rangle\,, \\
|P_+\rangle = |sp_+\rangle &= \tfrac{1}{\sqrt{12}}\Big[-(1-\mathrm{i})c_1^\dagger c_2^\dagger - (1+\mathrm{i})c_1^\dagger c_4^\dagger - 2c_1^\dagger c_5^\dagger - 2\,\mathrm{i}\,c_2^\dagger c_4^\dagger \\
&\qquad - (1+\mathrm{i})c_2^\dagger c_5^\dagger - (1-\mathrm{i})c_4^\dagger c_5^\dagger\Big]|0\rangle\,, \\
|P_-\rangle = |sp_-\rangle &= \tfrac{1}{\sqrt{12}}\Big[-(1+\mathrm{i})c_1^\dagger c_2^\dagger - (1-\mathrm{i})c_1^\dagger c_4^\dagger - 2c_1^\dagger c_5^\dagger + 2\,\mathrm{i}\,c_2^\dagger c_4^\dagger \\
&\qquad - (1-\mathrm{i})c_2^\dagger c_5^\dagger - (1+\mathrm{i})c_4^\dagger c_5^\dagger\Big]|0\rangle\,, \\
|P'_+\rangle = |p_-d\rangle &= \tfrac{1}{\sqrt{12}}\Big[-(1-\mathrm{i})c_1^\dagger c_2^\dagger - (1+\mathrm{i})c_1^\dagger c_4^\dagger + 2c_1^\dagger c_5^\dagger + 2\,\mathrm{i}\,c_2^\dagger c_4^\dagger \\
&\qquad - (1+\mathrm{i})c_2^\dagger c_5^\dagger - (1-\mathrm{i})c_4^\dagger c_5^\dagger\Big]|0\rangle\,, \\
|P'_-\rangle = |p_+d\rangle &= \tfrac{1}{\sqrt{12}}\Big[-(1+\mathrm{i})c_1^\dagger c_2^\dagger - (1-\mathrm{i})c_1^\dagger c_4^\dagger + 2c_1^\dagger c_5^\dagger - 2\,\mathrm{i}\,c_2^\dagger c_4^\dagger \\
&\qquad - (1-\mathrm{i})c_2^\dagger c_5^\dagger - (1+\mathrm{i})c_4^\dagger c_5^\dagger\Big]|0\rangle\,, \\
|D\rangle = |sd\rangle &= -\tfrac{1}{2}\left(c_1^\dagger c_2^\dagger + c_1^\dagger c_4^\dagger - c_2^\dagger c_5^\dagger - c_4^\dagger c_5^\dagger\right)|0\rangle\,.
\end{aligned}
\tag{4.4.7}
$$

In terms of the two-particle configurational basis states

$$
\begin{aligned}
|2,1\rangle = c_1^\dagger c_2^\dagger|0\rangle\,, \quad |2,2\rangle = c_1^\dagger c_4^\dagger|0\rangle\,, \quad |2,3\rangle = c_1^\dagger c_5^\dagger|0\rangle\,, \\
|2,4\rangle = c_2^\dagger c_4^\dagger|0\rangle\,, \quad |2,5\rangle = c_2^\dagger c_5^\dagger|0\rangle\,, \quad |2,6\rangle = c_4^\dagger c_5^\dagger|0\rangle\,,
\end{aligned}
\tag{4.4.8}
$$

we can write the allowed two-particle cluster states as

$$
\begin{aligned}
|S\rangle &= \tfrac{1}{\sqrt{6}}(-\mathrm{i},\mathrm{i},-1,1,\mathrm{i},-\mathrm{i}), \\
|P_+\rangle &= -\tfrac{1}{\sqrt{12}}(1-\mathrm{i},1+\mathrm{i},2,2\,\mathrm{i},1+\mathrm{i},1-\mathrm{i}), \\
|P'_+\rangle &= -\tfrac{1}{\sqrt{12}}(1-\mathrm{i},1+\mathrm{i},-2,-2\,\mathrm{i},1+\mathrm{i},1-\mathrm{i}), \\
|P_-\rangle &= -\tfrac{1}{\sqrt{12}}(1+\mathrm{i},1-\mathrm{i},2,-2\,\mathrm{i},1-\mathrm{i},1+\mathrm{i}), \\
|P'_-\rangle &= -\tfrac{1}{\sqrt{12}}(1+\mathrm{i},1-\mathrm{i},-2,2\,\mathrm{i},1-\mathrm{i},1+\mathrm{i}), \\
|D\rangle &= -\tfrac{1}{2}(1,1,0,0,-1,-1).
\end{aligned}
\tag{4.4.9}
$$

As we can see from (4.4.9), there is only one allowed two-particle cluster state each of S- and D-symmetry. Therefore, $|S\rangle$ and $|D\rangle$ are constrained by symmetry to be two-

particle eigenstates of the strongly-interacting cluster density matrix, and we call their weights w_S and w_D respectively. In the P-symmetry sector, mixing is expected between $|P_+\rangle$ and $|P'_+\rangle$, as well as between $|P_-\rangle$ and $|P'_-\rangle$, to give the two-particle eigenstates

$$\begin{aligned} |P_{1,\pm}\rangle &= \alpha_\pm |P_\pm\rangle + \beta_\pm |P'_\pm\rangle , \\ |P_{2,\pm}\rangle &= -\beta_\pm |P_\pm\rangle + \alpha_\pm |P'_\pm\rangle . \end{aligned} \tag{4.4.10}$$

We expect the weights of these pairs of two-particle eigenstates to be

$$w_{P_1} = w_{P_{1,+}} = w_{P_{1,-}} \neq w_{P_2} = w_{P_{2,+}} = w_{P_{2,-}}. \tag{4.4.11}$$

4.4.4 Symmetry Transformations on the Cluster States

For the purpose of orientation averaging the density matrix ρ_C of the cross-shaped cluster, we need to evaluate the unitary transformation $U_g \rho_C U_g^\dagger$ on ρ_C induced by the symmetry transformation $g \in \mathscr{G}$, where $\mathscr{G}$ is the full point symmetry group of the square lattice. However, because $\mathscr{G}$ is generated by the symmetry operations σ_x, σ_y, σ_{y-x} and σ_{y+x}, we need only the unitary transformations induced by these four generators.

In the one-particle sector, the unitary transformations induced by the four generators

are, in the basis of the one-particle cluster states defined in (4.4.2),

$$
\begin{aligned}
U_{1,x} &= \begin{bmatrix} 1 & 0 & 0 & 0 & 0 \\ 0 & 0 & 0 & 1 & 0 \\ 0 & 0 & 1 & 0 & 0 \\ 0 & 1 & 0 & 0 & 0 \\ 0 & 0 & 0 & 0 & 1 \end{bmatrix}, \quad U_{1,y} = \begin{bmatrix} 0 & 0 & 0 & 0 & 1 \\ 0 & 1 & 0 & 0 & 0 \\ 0 & 0 & 1 & 0 & 0 \\ 0 & 0 & 0 & 1 & 0 \\ 1 & 0 & 0 & 0 & 0 \end{bmatrix}, \\
U_{1,y-x} &= \begin{bmatrix} 0 & 1 & 0 & 0 & 0 \\ 1 & 0 & 0 & 0 & 0 \\ 0 & 0 & 1 & 0 & 0 \\ 0 & 0 & 0 & 0 & 1 \\ 0 & 0 & 0 & 1 & 0 \end{bmatrix}, \quad U_{1,y+x} = \begin{bmatrix} 0 & 0 & 0 & 1 & 0 \\ 0 & 0 & 0 & 0 & 1 \\ 0 & 0 & 1 & 0 & 0 \\ 1 & 0 & 0 & 0 & 0 \\ 0 & 1 & 0 & 0 & 0 \end{bmatrix}.
\end{aligned} \tag{4.4.12}
$$

In the ($P \geq 2$)-particle sectors, one has to be careful about the fermion signs. For the two-particle cluster states defined in (4.4.6), we find the action of σ_x is such that

$$
\begin{aligned}
U_{2,x} c_1^\dagger c_2^\dagger |0\rangle &= c_1^\dagger c_4^\dagger |0\rangle , \\
U_{2,x} c_1^\dagger c_4^\dagger |0\rangle &= c_1^\dagger c_2^\dagger |0\rangle , \\
U_{2,x} c_1^\dagger c_5^\dagger |0\rangle &= c_1^\dagger c_5^\dagger |0\rangle , \\
U_{2,x} c_2^\dagger c_4^\dagger |0\rangle &= c_4^\dagger c_2^\dagger |0\rangle = -c_2^\dagger c_4^\dagger |0\rangle , \\
U_{2,x} c_2^\dagger c_5^\dagger |0\rangle &= c_4^\dagger c_5^\dagger |0\rangle , \\
U_{2,x} c_4^\dagger c_5^\dagger |0\rangle &= c_2^\dagger c_5^\dagger |0\rangle .
\end{aligned} \tag{4.4.13}
$$

Therefore, the transformation matrix associated with σ_x in the two-particle sector is

$$U_{2x} = \begin{bmatrix} 0 & 1 & 0 & 0 & 0 & 0 \\ 1 & 0 & 0 & 0 & 0 & 0 \\ 0 & 0 & 1 & 0 & 0 & 0 \\ 0 & 0 & 0 & -1 & 0 & 0 \\ 0 & 0 & 0 & 0 & 0 & 1 \\ 0 & 0 & 0 & 0 & 1 & 0 \end{bmatrix}. \tag{4.4.14}$$

Similarly, going through the action of σ_y, σ_{y-x} and σ_{y+x} on the two-particle cluster states, we find their associated transformation matrices to be

$$U_{2,y} = \begin{bmatrix} 0 & 0 & 0 & 0 & -1 & 0 \\ 0 & 0 & 0 & 0 & 0 & -1 \\ 0 & 0 & -1 & 0 & 0 & 0 \\ 0 & 0 & 0 & 1 & 0 & 0 \\ -1 & 0 & 0 & 0 & 0 & 0 \\ 0 & -1 & 0 & 0 & 0 & 0 \end{bmatrix}, \tag{4.4.15a}$$

$$U_{2,y-x} = \begin{bmatrix} -1 & 0 & 0 & 0 & 0 & 0 \\ 0 & 0 & 0 & 0 & 1 & 0 \\ 0 & 0 & 0 & 1 & 0 & 0 \\ 0 & 0 & 1 & 0 & 0 & 0 \\ 0 & 1 & 0 & 0 & 0 & 0 \\ 0 & 0 & 0 & 0 & 0 & -1 \end{bmatrix}, \tag{4.4.15b}$$

$$U_{2,y+x} = \begin{bmatrix} 0 & 0 & 0 & 0 & 0 & 1 \\ 0 & -1 & 0 & 0 & 0 & 0 \\ 0 & 0 & 0 & -1 & 0 & 0 \\ 0 & 0 & -1 & 0 & 0 & 0 \\ 0 & 0 & 0 & 0 & -1 & 0 \\ 1 & 0 & 0 & 0 & 0 & 0 \end{bmatrix}. \tag{4.4.15c}$$

In the three-particle sector, we have the configurational basis states

$$\begin{aligned} |3,1\rangle &= c_1^\dagger c_2^\dagger c_4^\dagger |0\rangle, \quad |3,2\rangle = c_1^\dagger c_2^\dagger c_5^\dagger |0\rangle, \\ |3,3\rangle &= c_1^\dagger c_4^\dagger c_5^\dagger |0\rangle, \quad |3,4\rangle = c_2^\dagger c_4^\dagger c_5^\dagger |0\rangle. \end{aligned} \tag{4.4.16}$$

Letting the symmetry operations act on these configurational basis states, we find their associated transformation matrices to be

$$\begin{aligned} U_{3,x} &= \begin{bmatrix} -1 & 0 & 0 & 0 \\ 0 & 0 & 1 & 0 \\ 0 & 1 & 0 & 0 \\ 0 & 0 & 0 & -1 \end{bmatrix}, \quad U_{3,y} = \begin{bmatrix} 0 & 0 & 0 & 1 \\ 0 & -1 & 0 & 0 \\ 0 & 0 & -1 & 0 \\ 1 & 0 & 0 & 0 \end{bmatrix}, \\ U_{3,y-x} &= \begin{bmatrix} 0 & -1 & 0 & 0 \\ -1 & 0 & 0 & 0 \\ 0 & 0 & 0 & -1 \\ 0 & 0 & -1 & 0 \end{bmatrix}, \quad U_{3,y+x} = \begin{bmatrix} 0 & 0 & 1 & 0 \\ 0 & 0 & 0 & 1 \\ 1 & 0 & 0 & 0 \\ 0 & 1 & 0 & 0 \end{bmatrix}. \end{aligned} \tag{4.4.17}$$

In the four-particle sector, there is only one allowed cluster state, i.e.

$$|4,1\rangle = c_1^\dagger c_2^\dagger c_4^\dagger c_5^\dagger |0\rangle. \tag{4.4.18}$$

Under the action of σ_x, this state becomes

$$U_x |4,1\rangle = c_1^\dagger c_4^\dagger c_2^\dagger c_5^\dagger |0\rangle = -c_1^\dagger c_2^\dagger c_4^\dagger c_5^\dagger |0\rangle, \tag{4.4.19}$$

and so

$$U_{4,x} = -1. \tag{4.4.20}$$

Similarly, based on the action of σ_y, σ_{y-x} and σ_{y+x} on the four-particle cluster state, we deduce that

$$U_{4,y} = -1, \quad U_{4,y-x} = +1, \quad U_{4,y+x} = +1. \tag{4.4.21}$$

These transformation matrices are stored in a Octave data file, which is loaded when necessary to facilitate orientation averaging.

4.5 System Shapes and Sizes

To be able to do exact diagonalization on desktop computers with a single Pentium-4-class processor using up to 1 GB of RAM, we cannot work with very large system sizes. If we keep the entire, sparse, Hamiltonian matrix in memory, the $(5, 1) \times (1, 5)$ system is about the largest we can work with. Memory considerations aside, the computational time needed to diagonalize the Bloch-reduced Hamiltonians for each and every Bloch state to seek out the ground state also becomes prohibitively long if we increase the system size to beyond 20 sites, because of the need to twist-boundary-conditions average over a few hundred twist vectors $\boldsymbol{\phi}$ restricted to the FBZ.

Furthermore, we cannot work with highly-elongated systems, because our cross-shaped cluster would be contorted beyond recognition by the periodic boundary conditions imposed. Therefore, we are restricted by these two considerations to just a small number of finite systems that we *can* work with. A non-exhaustive list is shown in Table 4.1, and we work with a few of them with between $N = 11$ to $N = 20$ sites.

Table 4.1: List of finite $\mathbf{R}_1 \times \mathbf{R}_2$ systems that can exactly diagonalized on Pentium-4-class machines with up to 1 GB of RAM, within a reasonable amount of time, with twist boundary conditions averaging. The number of sites N within the system, the size D of the $P = 4$ particle Hilbert space, the orientation of the system relative to the underlying square lattice, and the sites of the chosen cluster relative to the system, are also shown.

system	$\mathbf{R}_1$	$\mathbf{R}_2$	N	D
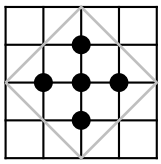	$(2, -2)$	$(2, 2)$	8	2
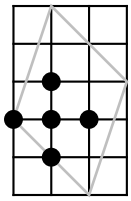	$(2, -2)$	$(1, 3)$	8	2
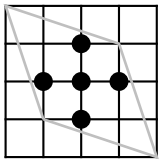	$(3, -1)$	$(-1, 3)$	8	2
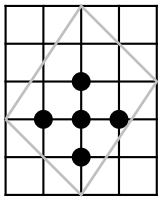	$(2, -2)$	$(3, 2)$	10	5
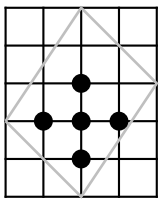	$(2, -2)$	$(1, 4)$	10	5

(continued on next page)

Table 4.1: (continued)

system	$\mathbf{R}_1$	$\mathbf{R}_2$	N	D
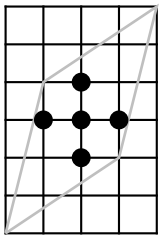	$(3, 2)$	$(1, 4)$	10	5
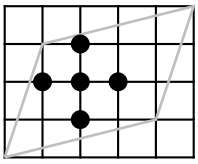	$(4, 1)$	$(1, 3)$	11	11
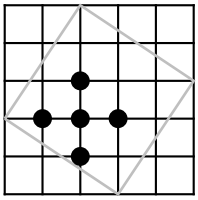	$(3, -2)$	$(2, 3)$	13	39
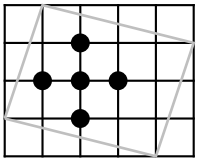	$(4, -1)$	$(1, 3)$	13	52
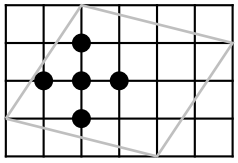	$(4, -1)$	$(2, 3)$	14	77

(continued on next page)

Table 4.1: (continued)

system	$\mathbf{R}_1$	$\mathbf{R}_2$	N	D
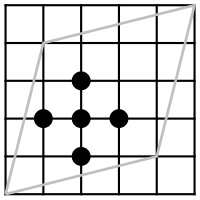	$(4, 1)$	$(1, 4)$	15	135
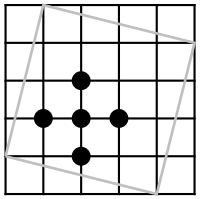	$(4, -1)$	$(1, 4)$	17	340
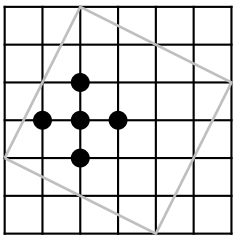	$(4, -2)$	$(2, 4)$	20	1005
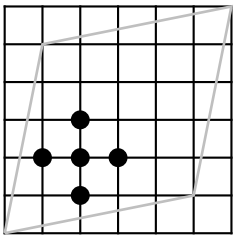	$(5, 1)$	$(1, 5)$	24	3042

4.6 Noninteracting Spinless Fermions

We argued in Chapters 2 and 3 that it is important to first understand the structure of cluster density matrices of noninteracting systems before moving on to interacting systems. In these two chapters, we undertook an exhaustive study on the structure of the noninteracting cluster density matrix in one dimension. In this section, we investigate the structure of the cluster density matrix in a two-dimensional system of noninteracting spinless fermions, before moving on to study the cluster density matrix of a two-dimensional system of strongly-interacting spinless fermions with infinite nearest-neighbor repulsion.

Our starting point is the exact formula (2.4.31) for noninteracting spinless fermions in d dimensions. This relates the cluster density matrix ρ_C to the cluster Green-function matrix G_C, whose matrix elements are

$$G_C(\mathbf{r}, \mathbf{r}') = \langle \Psi | c_{\mathbf{r}}^\dagger c_{\mathbf{r}'} | \Psi \rangle \,, \tag{4.6.1}$$

where $c_{\mathbf{r}}$ and $c_{\mathbf{r}'}$ are annihilation operators acting on the cluster sites $\mathbf{r}$ and $\mathbf{r}'$ respectively. Using the relation

$$c_{\mathbf{r}} = \frac{1}{\sqrt{N}} \sum_{\mathbf{k} \in \mathrm{FBZ}} e^{-\mathrm{i}\,\mathbf{k}\cdot\mathbf{r}}\, \tilde{c}_{\mathbf{k}} \tag{4.6.2}$$

between the real-space fermion operators $c_{\mathbf{r}}$ and the momentum-space fermion operators $\tilde{c}_{\mathbf{k}}$, we find that the cluster Green-function matrix elements can be written as

$$\begin{aligned} G_C(\mathbf{r}, \mathbf{r}') &= \frac{1}{N} \sum_{\mathbf{k}} \sum_{\mathbf{k}'} e^{\mathrm{i}\,\mathbf{k}\cdot\mathbf{r}}\, e^{-\mathrm{i}\,\mathbf{k}'\cdot\mathbf{r}'}\ \langle \Psi | \tilde{c}_{\mathbf{k}}^\dagger \tilde{c}_{\mathbf{k}'} | \Psi \rangle \\ &= \frac{1}{N} \sum_{\mathbf{k}} \sum_{\mathbf{k}'} e^{\mathrm{i}\,\mathbf{k}\cdot\mathbf{r}}\, e^{-\mathrm{i}\,\mathbf{k}'\cdot\mathbf{r}'} \begin{cases} \delta_{\mathbf{k},\mathbf{k}'}, & \text{if } \mathbf{k} \text{ and } \mathbf{k}' \text{ are filled;} \\ 0, & \text{if one or more of them empty,} \end{cases} \\ &= \frac{1}{N} \sum_{\mathbf{k} \text{ filled}} e^{\mathrm{i}\,\mathbf{k}\cdot(\mathbf{r}-\mathbf{r}')}. \end{aligned} \tag{4.6.3}$$

The corollary of (2.4.31) is that, if λ_l is an eigenvalue of the cluster Green-function

matrix G_C, the corresponding one-particle weight of ρ_C is

$$w_l = \lambda_l \prod_{l' \neq l} (1 - \lambda_{l'}). \tag{4.6.4}$$

If we so wish, we can calculate the Green-function matrix for a cluster in an infinite system, by converting the sum in (4.6.3) into an integral over $\mathbf{k}$. However, to better understand how we can tease information regarding the infinite system out of finite systems, and also to make the comparison between noninteracting and strongly-interacting systems more meaningful (as we can only treat small systems in the latter case), we do not do this. Instead, for a finite $\mathbf{R}_1 \times \mathbf{R}_2$ system with N sites and P noninteracting particles, we determine the set of wave vectors $\{\mathbf{k}_n\}_{n=1}^{P}$ with the lowest single-particle energies

$$\epsilon_{\mathbf{k}_n} = -(\cos k_{n,x} + \cos k_{n,y}), \tag{4.6.5}$$

and evaluate the finite-system cluster Green-function matrix elements by summing over these occupied wave vectors.

This gives rise to cluster density-matrix spectra contaminated by various finite size effects. In Section 4.6.1, we look into these finite size effects, which will presumably also arise when we exactly diagonalize finite systems of interacting fermions. We will see that finite size effects become less and less important as expected, as the size of the system is increased. Nevertheless, noninteracting system sizes of a few hundred sites are still necessary to get a decent approximation of the infinite-system cluster density-matrix spectra. Such sizes are not practical for exactly diagonalizing the strongly-interacting system, and so we look into the method of twist boundary conditions averaging in Section 4.6.3. This allows us to calculate the cluster density-matrix spectra for an ensemble of small finite systems, and therefrom extract the infinite system limit. We found the performance of this averaging apparatus to satisfactorily approximate the infinite-system limit cluster density-matrix spectra for noninteracting systems.

4.6.1 Finite Size Effects and the Infinite-System Limit

The finite systems chosen for our numerical study of the cluster density-matrix spectra of noninteracting spinless fermions and strongly-interacting spinless fermions with infinite nearest-neighbor repulsion are the $(4,1)\times(1,3)$ system ($N = 11$ sites), $(3,-2)\times(2,3)$ system ($N = 13$ sites), $(4,1)\times(1,4)$ system ($N = 15$ sites), $(4,-1)\times(1,4)$ system ($N = 17$ sites) and $(4,-2)\times(2,4)$ system ($N = 20$ sites).

The organization of this subsection is as follows: in Sections 4.6.1.1 and 4.6.1.2, we will look at how the finite size effects show up in the zero- and one-particle weights of the noninteracting cluster density matrix. Then in Section 4.6.1.3, we look at how the density-matrix spectra changes as the system size is increased for a sequence of systems $(4n,-n)\times(n,4n)$. From this sequence of systems, we realized that the infinite-system limits for the cluster density-matrix weights are achieved numerically for system with a few hundred sites. In Sections 4.6.1.4 and 4.6.1.5, we take a more detailed look at the residual shell and shape effects that linger in the numerical spectra.

4.6.1.1 Tables of Weights

The zero- and one-particle cluster density-matrix weights, as well as the mixing angle θ between $|s\rangle$ and $|\bar{s}\rangle$, are calculated for various particle numbers P in the $(4,1)\times(1,3)$, $(3,-2)\times(2,3)$, $(4,1)\times(1,4)$, $(4,-1)\times(1,4)$, and $(4,-2)\times(2,4)$ systems subject only to periodic boundary conditions, and shown in Tables 4.2, 4.3, 4.4, 4.5, and 4.6.

The dependence of the zero- and one-particle weights on the filling fraction $\bar{n}$ will become apparent only when we graph them. This we do in the next subsubsection. From the tabulated values of $\sin\theta$, however, it is quite clear that

$$\lim_{\bar{n}\to 0}\sin\theta = \frac{1}{\sqrt{5}}, \quad \lim_{\bar{n}\to\frac{1}{2}}\sin\theta = \frac{1}{\sqrt{2}}. \tag{4.6.6}$$

Table 4.2: The zero- and one-particle cluster density-matrix weights, and the sine of the mixing angle θ, of the $(4,1)\times(1,3)$ system with $N = 11$ sites and $P = 1,2,3,4,5$ noninteracting spinless fermions subject to periodic boundary conditions.

P	$\bar{n}$	w_0	w_{s_1}	w_{s_2}	$w_{p_\pm}$	w_d	$\sin\theta$
1	0.0909	0.54545	0.45455	0	0	0	0.44721
2	0.1818	0.30253	0.39312	0.00768	0.03956	0.02917	0.53913
3	0.2727	0.14746	0.31962	0.00629	0.04436	0.03147	0.60027
4	0.3636	0.06767	0.20147	0.00543	0.04429	0.01736	0.65506
5	0.4545	0.02419	0.10938	0.00274	0.03077	0.00733	0.70143

Table 4.3: The zero- and one-particle cluster density-matrix weights, and the sine of the mixing angle θ, of the $(3,-2)\times(2,3)$ system with $N = 13$ sites and $P = 1,2,3,4,5,6$ noninteracting spinless fermions subject to periodic boundary conditions.

P	$\bar{n}$	w_0	w_{s_1}	w_{s_2}	$w_{p_\pm}$	w_d	$\sin\theta$
1	0.0769	0.61538	0.38462	0	0	0	0.44721
2	0.1538	0.38352	0.34932	0.00837	0.05625	0.00600	0.53935
3	0.2308	0.21950	0.29829	0.00804	0.07545	0.00698	0.60118
4	0.3077	0.11075	0.23524	0.00521	0.06895	0.00537	0.64330
5	0.3846	0.04532	0.16691	0.00247	0.04748	0.00298	0.67310
6	0.4615	0.02135	0.10770	0.00191	0.02740	0.00778	0.71016

Table 4.4: The zero- and one-particle cluster density-matrix weights, and the sine of the mixing angle θ, of the $(4,1)\times(1,4)$ system with $N = 15$ sites and $P = 1,2,3,4,5,6,7$ noninteracting spinless fermions subject to periodic boundary conditions.

P	$\bar{n}$	w_0	w_{s_1}	w_{s_2}	$w_{p_\pm}$	w_d	$\sin\theta$
1	0.0667	0.66667	0.33333	0	0	0	0.44721
2	0.1333	0.44626	0.33520	0.00666	0.03721	0.03313	0.53516
3	0.2000	0.28296	0.31927	0.00689	0.05148	0.04537	0.58992
4	0.2667	0.16631	0.28861	0.00511	0.04993	0.04349	0.62590
5	0.3333	0.08690	0.24894	0.00306	0.03865	0.03319	0.65089
6	0.4000	0.03964	0.18689	0.00172	0.02971	0.01514	0.67635
7	0.4667	0.01246	0.12765	0.00062	0.01517	0.00476	0.69660

The first limit is easy to understand: in the limit of $\bar{n} \to 0$, all sites in the cluster are equally likely to be occupied, so the uniform one-particle cluster state

$$|s_+\rangle = \frac{1}{\sqrt{5}}(1,1,1,1,1) = \frac{1}{2}(1,1,0,1,1)\cdot\frac{2}{\sqrt{5}} + (0,0,1,0,0)\cdot\frac{1}{\sqrt{5}} \tag{4.6.7}$$

must be a one-particle eigenstate of the cluster density matrix, i.e. the eigenstate $|s_1\rangle = |s_+\rangle$ comes with a mixing angle of $\sin\theta = \frac{1}{\sqrt{5}} = 0.4472\ldots$.

Also, at half-filling $\bar{n} = \frac{1}{2}$, the Fermi surface is a square rotated by $\pi/4$ in momentum space. Because of its simple shape, it becomes possible for us to evaluate the infinite-

Table 4.5: The zero- and one-particle cluster density-matrix weights, and the sine of the mixing angle θ, of the $(4,-1)\times(1,4)$ system with $N = 17$ sites and $P = 1, 2, 3, 4, 5, 6, 7, 8$ noninteracting spinless fermions subject to periodic boundary conditions.

P	$\bar{n}$	w_0	w_{s_1}	w_{s_2}	$w_{p_\pm}$	w_d	$\sin\theta$
1	0.0588	0.70588	0.29412	0	0	0	0.44721
2	0.1176	0.49213	0.33723	0.00402	0.03478	0.02132	0.52431
3	0.1765	0.32558	0.35657	0.00415	0.04951	0.02949	0.56679
4	0.2353	0.19932	0.35508	0.00312	0.04921	0.02836	0.59310
5	0.2941	0.10691	0.33698	0.00189	0.03835	0.02130	0.61083
6	0.3529	0.06395	0.24528	0.00293	0.03685	0.01564	0.64224
7	0.4118	0.03486	0.16973	0.00254	0.03055	0.01024	0.67183
8	0.4706	0.01656	0.10918	0.00164	0.02183	0.00574	0.69934

Table 4.6: The zero- and one-particle cluster density-matrix weights, and the sine of the mixing angle θ, of the $(4,-2)\times(2,4)$ system with $N = 20$ sites and $P = 1,2,3,4,5,6,7,8,9,10$ noninteracting spinless fermions subject to periodic boundary conditions.

P	$\bar{n}$	w_0	w_{s_1}	w_{s_2}	$w_{p_\pm}$	w_d	$\sin\theta$
1	0.0500	0.75000	0.25000	0	0	0	0.44721
2	0.1000	0.55499	0.30821	0.00304	0.03700	0.00703	0.51857
3	0.1500	0.39481	0.34546	0.00332	0.05640	0.01012	0.55596
4	0.2000	0.26581	0.36317	0.00271	0.06134	0.01036	0.57857
5	0.2500	0.16447	0.36387	0.00188	0.05482	0.00866	0.59362
6	0.3000	0.10685	0.30286	0.00255	0.04857	0.01354	0.62170
7	0.3500	0.06499	0.24641	0.00227	0.03899	0.01379	0.64614
8	0.4000	0.03585	0.19509	0.00160	0.02789	0.01117	0.66742
9	0.4500	0.01672	0.14941	0.00089	0.01672	0.00717	0.68596
10	0.5000	0.00882	0.10663	0.00073	0.00882	0.00882	0.70711

system cluster Green-function matrix as

$$G_C = \begin{bmatrix} \frac{1}{2} & 0 & \frac{2}{\pi^2} & 0 & 0 \\ 0 & \frac{1}{2} & \frac{2}{\pi^2} & 0 & 0 \\ \frac{2}{\pi^2} & \frac{2}{\pi^2} & \frac{1}{2} & \frac{2}{\pi^2} & \frac{2}{\pi^2} \\ 0 & 0 & \frac{2}{\pi^2} & \frac{1}{2} & 0 \\ 0 & 0 & \frac{2}{\pi^2} & 0 & \frac{1}{2} \end{bmatrix}. \tag{4.6.8}$$

The s sector of this matrix is

$$\begin{bmatrix} \langle s|G|s\rangle & \langle s|G|\bar{s}\rangle \\ \langle \bar{s}|G|s\rangle & \langle \bar{s}|G|\bar{s}\rangle \end{bmatrix} = \begin{bmatrix} \frac{1}{2} & \frac{4}{\pi^2} \\ \frac{4}{\pi^2} & \frac{1}{2} \end{bmatrix}, \tag{4.6.9}$$

and so the s eigenvalues and eigenvalues are

$$\lambda_{s_1} = \frac{1}{2} + \frac{4}{\pi^2}, \quad |\lambda_{s_1}\rangle = \frac{1}{\sqrt{2}}|s\rangle + \frac{1}{\sqrt{2}}|\bar{s}\rangle\,; \tag{4.6.10}$$

$$\lambda_{s_2} = \frac{1}{2} - \frac{4}{\pi^2}, \quad |\lambda_{s_2}\rangle = \frac{1}{\sqrt{2}}|s\rangle - \frac{1}{\sqrt{2}}|\bar{s}\rangle\,. \tag{4.6.11}$$

So indeed, we know analytically that $\sin\theta = 1/\sqrt{2}$ when $\bar{n} = \frac{1}{2}$.

A corollary of $\theta = \frac{\pi}{4}$ at $\bar{n} = \frac{1}{2}$ is that the dominant one-particle eigenstate of the cluster density matrix is

$$|s_1\rangle = \frac{1}{2}(1,1,0,1,1)\cdot\frac{1}{\sqrt{2}} + (0,0,1,0,0)\cdot\frac{1}{\sqrt{2}} = \frac{1}{2\sqrt{2}}(1,1,2,1,1). \tag{4.6.12}$$

In this one-particle cluster density-matrix eigenstate, it is therefore four times more likely to find the central site occupied than the peripheral sites occupied. This is a consequence of the Fermi-Dirac statistics of the spinless fermion, which gives rise to a many-body ground-state wave function which vanishes on various nodal hypersurfaces in configuration space. A many-fermion configuration where the particles are more uniformly distributed is further away from such nodal hypersurfaces compared to a many-fermion configuration where the particles are more clustered. As a result,

the more uniformly-distributed many-fermion configuration will have a larger absolute amplitude compared to the more clustered many-fermion configuration. This argument holds for all $\bar{n} > 0$, which means that when there is only one particle within the cluster, it will always be more likely to find the particle at the center of the cluster, rather than on the peripheral sites.

4.6.1.2 Graphs of Weights

To visualize the structures in the zero- and one-particle weights of the cluster density matrix, we graph them as a function of the filling fraction $\bar{n}$. For noninteracting spinless fermions, it is possible to calculate the cluster density-matrix weights for $\bar{n} > \frac{1}{2}$, but we do not do so, because these filling fractions are inaccessible in systems of strongly-interacting spinless fermions with infinite nearest-neighbor repulsion, and therefore no meaningful comparison can be made between the two models for $\bar{n} > \frac{1}{2}$.

The zero-particle weight as a function of $\bar{n}$ for the various systems studied is shown in Figure 4.3, while the one-particle weights as functions of $\bar{n}$ for the various systems studied are shown in Figure 4.4. In Figure 4.3, we see that the zero-particle weight data points coming from different systems appear to fall onto a smooth curve. This is encouraging, because we believe that there ought to be a unique infinite-system zero-particle cluster density-matrix weight $w_0(\bar{n})$ which is a smooth function of the filling fraction $\bar{n}$, and the finite-system data points seem to collapsing onto this function. Unfortunately, we also see in Figure 4.4 severe scatter in the one-particle weight data points coming from different systems. This scatter is due to the fact that we are exact-diagonalizing small finite systems, and as such the numerical cluster density-matrix spectra deviates from the infinite-system cluster density-matrix spectrum.

We refer to these systematic deviations collectively as *finite size effects*, and identify

three primary sources of finite size effects as (i) finite domain effect, which has to do with the fact that the small set of discrete wave vectors allowed are not adequately representative of the continuous set of wave vectors on the infinite square lattice; (ii) shell effect, which has to do with the fact that the set of discrete wave vectors allowed are organized by symmetry into shells in reciprocal space, each of which can be partially or fully filled in the many-body ground state; and (iii) shape effect, which has to do with the detailed shape of the non-square system we introduced. Together, these finite size effects make it impossible to say anything meaningful about the cluster density-matrix spectrum as a function of the filling fraction $\bar{n} = P/N$.

4.6.1.3 The $(4, -1) \times (1, 4)$ Sequence of Systems

Seeing the infinite-system limit $w_0(\bar{n})$ invitingly suggested by the numerical data for the zero-particle cluster density-matrix weight, we would like to believe that there are unique infinite-system limits $w_{s_1}(\bar{n})$, $w_p(\bar{n})$, $w_d(\bar{n})$ and $w_{s_2}(\bar{n})$ for the one-particle cluster density-matrix weights. The data shown in Figure 4.4 certainly do not suggest this, so are we misguided in confessing such a belief?

One good thing about dealing with noninteracting systems is that, with the help of (2.4.31), we can study the cluster density-matrix for very large, but nonetheless finite, systems. Let us therefore examine the cluster density-matrix spectra for a sequence $(4n, -n) \times (n, 4n)$ of systems based on the same prototypical lattice vectors, $\mathbf{R}_1 = (4, -1)$ and $\mathbf{R}_2 = (1, 4)$. These systems have the same shape, but different system sizes. The zero- and one-particle cluster density-matrix weights for the $(4, -1) \times (1, 4)$, $(8, 2) \times (2, 8)$ and $(32, -8) \times (8, 32)$ systems are shown in Figure 4.5.

As the system size is increased, we find that the cluster density-matrix spectrum do indeed approach an infinite system limit. For this series of systems, the infinite-system

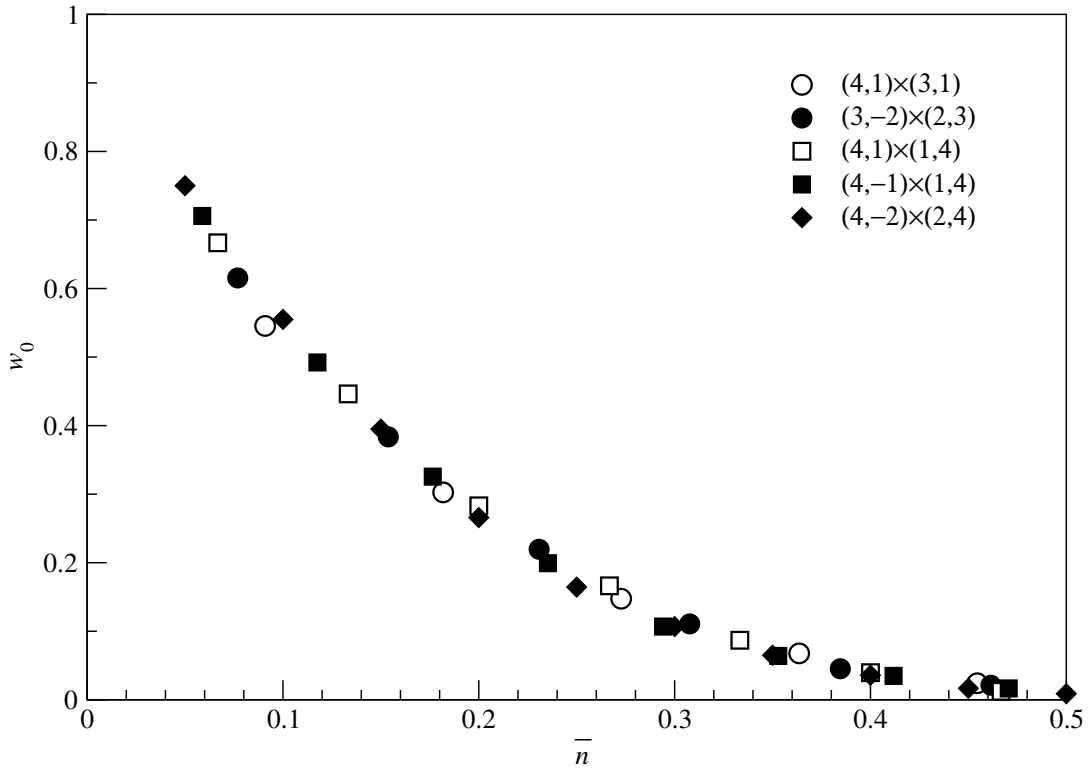

Figure 4.3: The zero-particle weight of the cluster density matrix of a five-site, cross-shaped cluster for systems of noninteracting spinless fermions subject to periodic boundary conditions. The data points coming from the $(3, -2) \times (2, 3)$ (●), $(4, 1) \times (1, 3)$ (○), $(4, 1) \times (1, 4)$ (□), $(4, -1) \times (1, 4)$ (■) and $(4, -2) \times (2, 4)$ (♦) systems appear to fall onto a smooth curve.

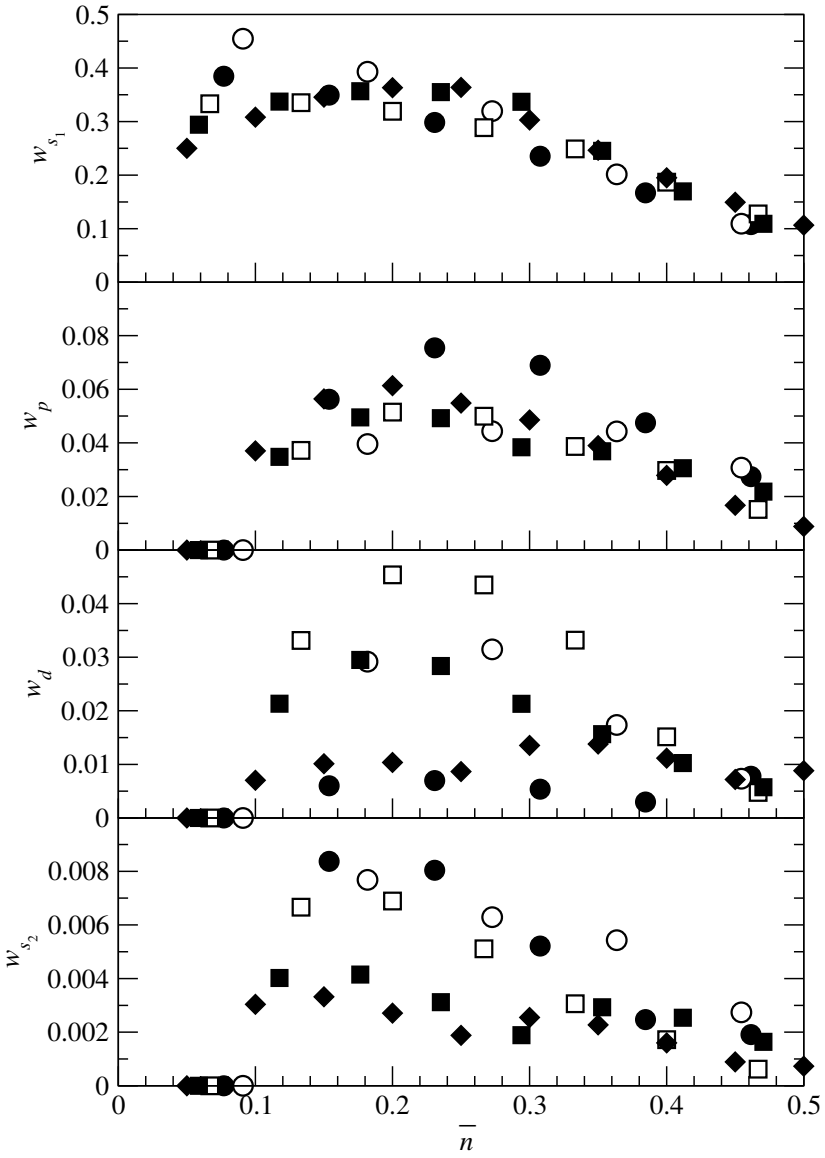

Figure 4.4: The one-particle weights of the cluster density matrix of a five-site, cross-shaped cluster for the $(3,-2)\times(2,3)$ (●), $(4,1)\times(1,3)$ (○), $(4,1)\times(1,4)$ (□), $(4,-1)\times(1,4)$ (■) and $(4,-2)\times(2,4)$ (♦) systems of noninteracting spinless fermions, with periodic boundary conditions imposed.

limit is more or less reached by the time we get to the $(16, -4) \times (4, 16)$ system, with $N = 272$, judging from the convergence of the one-particle weights shown in Figure 4.6. We find also that the shell effect affects weights of different symmetry differently: w_{s_1} is almost unaffected, while w_d is the most severely affected. Shell effect persists in w_d even up to a system size of $N = 1088$ sites for the $(32, -8) \times (8, 32)$ system.

From Figure 4.6, we also see what appears to be a linear rise of the one-particle cluster density-matrix weight w_{s_1} with the filling fraction $\bar{n}$, i.e. $w_{s_1} \sim \bar{n}$ for small $\bar{n}$, and what looks like a quadratic rise of the one-particle cluster density-matrix weights w_p, w_d, and w_{s_2} with $\bar{n}$, i.e. $w_p, w_d, w_{s_2} \sim \bar{n}^2$ for small $\bar{n}$. We will check these asymptotic behaviours as $\bar{n} \to 0$ in Section 4.6.2.

For the $(8, -2) \times (2, 8)$, $(16, -4) \times (4, 16)$ and $(32, -8) \times (8, 32)$ systems, we also show the sine of the mixing angle $\sin\theta$ as a function of the filling fraction $\bar{n}$ in Figure 4.7. From Figure 4.7, it appears that $\sin\theta$ is a linear function of $\bar{n}$. This is surprising, because if the linear behaviour extends beyond $\bar{n} = 0.5$, then by $\bar{n} = 1$, we would have $\sin\theta = \frac{1}{\sqrt{2}} + (\frac{1}{\sqrt{2}} - \frac{1}{\sqrt{5}}) = 0.967\ldots$. This is a little surprising, because at $\bar{n} = 1$, the cluster Green-function matrix is the identity matrix, and is not expected to favour any particular linear combination of $|s\rangle$ and $|\bar{s}\rangle$.

4.6.1.4 More on the Shell Effect

Before moving on to Section 4.6.2 to learn more about the asymptotic behaviour of the one-particle cluster density-matrix weights as $\bar{n} \to 0$, let us look more carefully at the shell effect exhibited in the filling dependence of the one-particle cluster density-matrix weights. For the d-symmetry one-particle cluster density-matrix weight w_d for the $(16, -4) \times (4, 16)$ and $(32, -8) \times (8, 32)$ systems, we show the 'shells' in Figures 4.8 and 4.9 respectively.

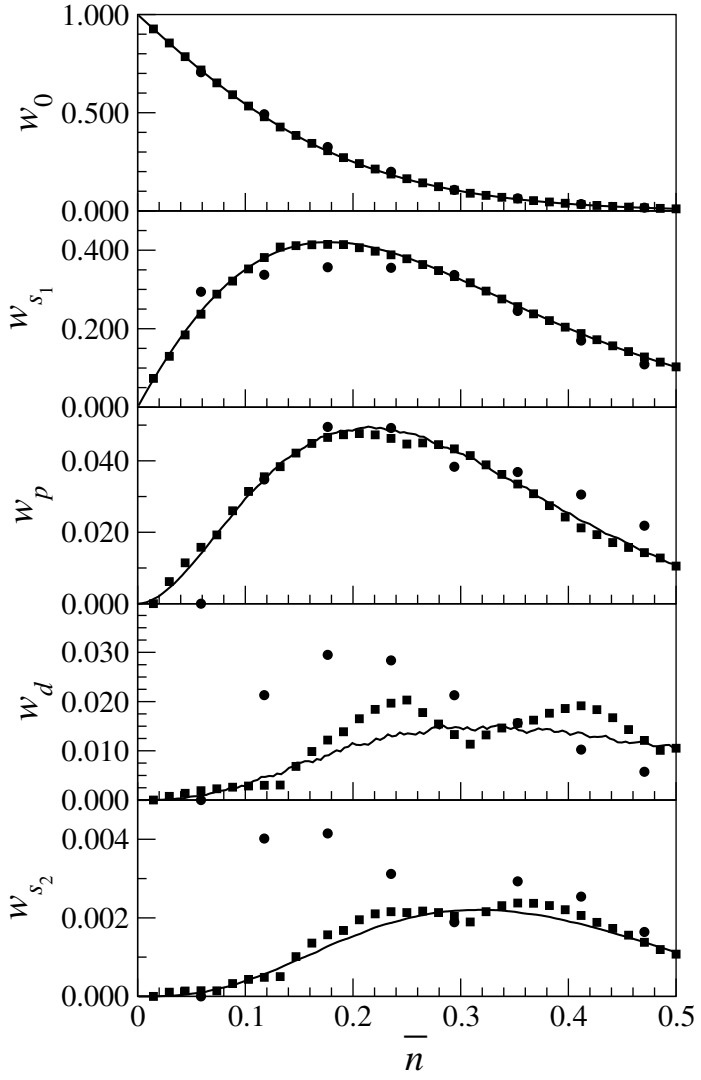

Figure 4.5: Zero- and one-particle weights of the cluster density matrix of a five-site, cross-shaped cluster for finite systems of noninteracting spinless fermions with periodic boundary conditions imposed. The systems, $(32,-8)\times(8,32)$ (solid line), $(4,-1)\times(1,4)$ (●), and $(8,-2)\times(2,8)$ (■) have the same shape but different sizes. For w_{s_1}, we see the finite domain effect deviations for the $(4,-1)\times(1,4)$ system is practically gone by the time we get to the $(8,-2)\times(2,8)$ system. For the rest of the one-particle weights, the finite domain effect is largely removed in the $(8,-2)\times(2,8)$ system, but shell effect persists. In fact, shell effect is still visible in the $(32,-8)\times(8,32)$ system.

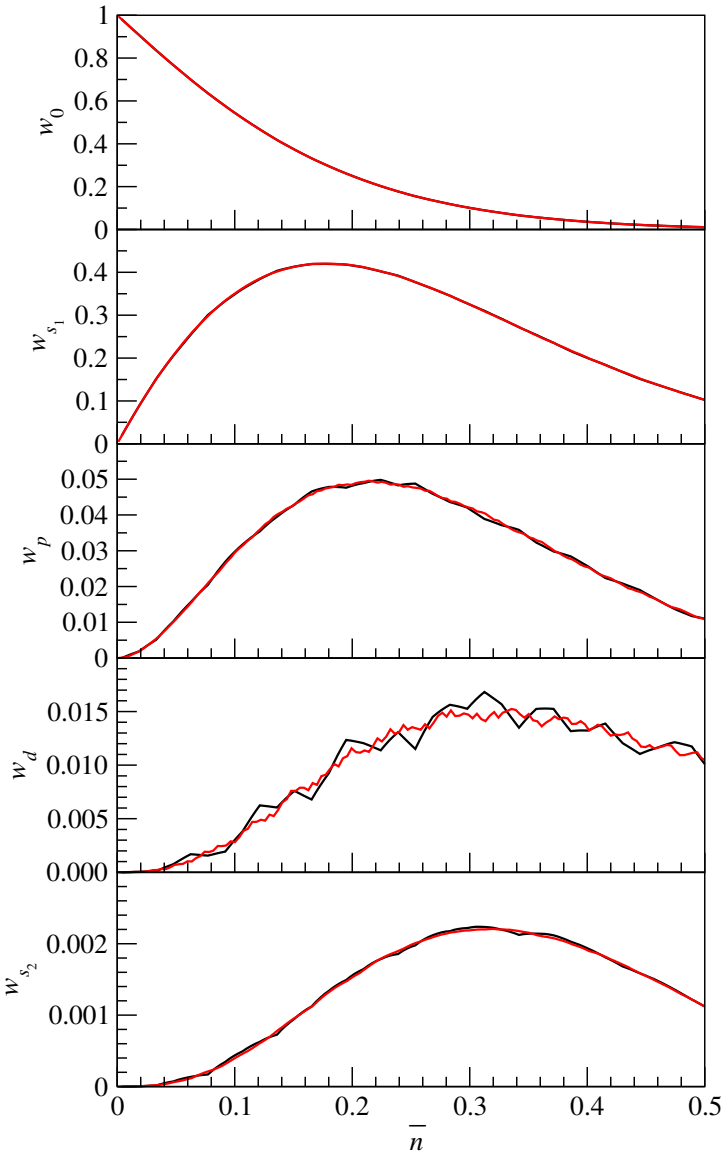

Figure 4.6: Zero- and one-particle weights of the cluster density matrix of a five-site, cross-shaped cluster for the $(16, -4) \times (4, 16)$ (black solid curve) and $(32, -8) \times (8, 32)$ (red solid curve) systems of noninteracting spinless fermions with periodic boundary conditions imposed. Ignoring the persistent shell effect remaining, we see that the cluster density-matrix spectra of the two systems agree, and thus the infinite-system limit is for practical purposes achieved in the $(16, -4) \times (4, 16)$ system.

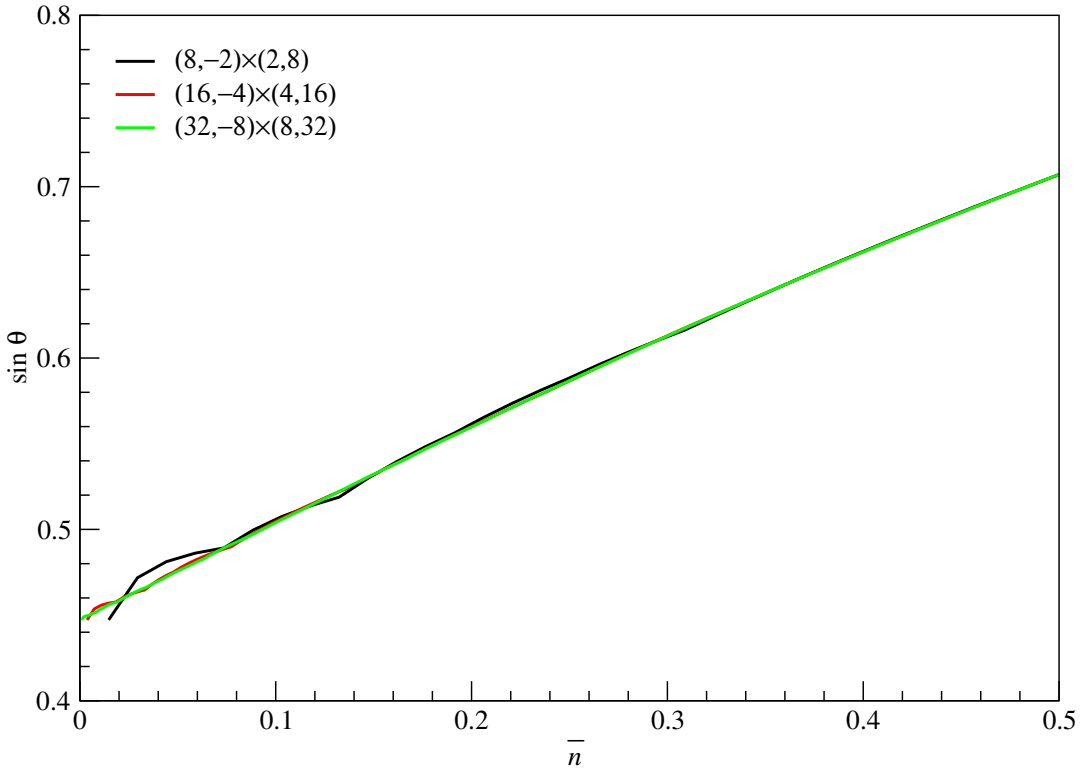

Figure 4.7: Sine of the mixing angle θ, between the one-particle cluster states $|s\rangle$ and $|\bar{s}\rangle$ in the one-particle cluster density-matrix eigenstates of s-symmetry, as a function of the filling fraction $\bar{n}$.

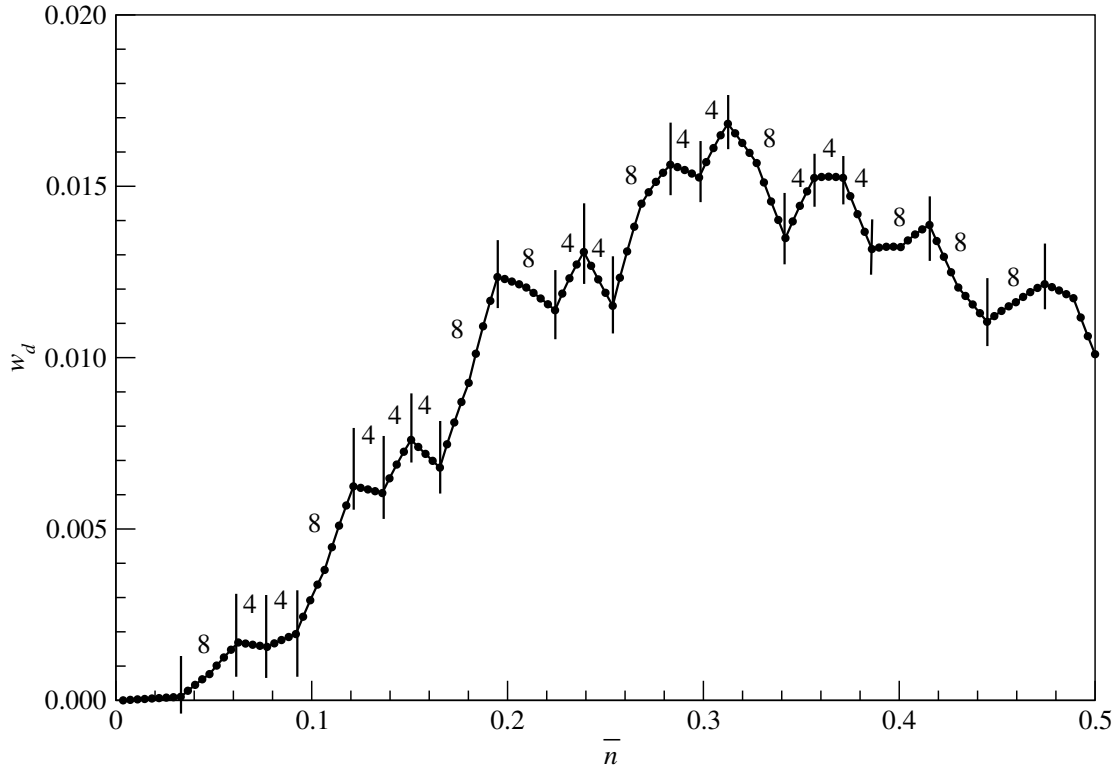

Figure 4.8: Shell effect in the one-particle cluster density-matrix weight w_d of the $(16, -4) \times (4, 16)$ system of noninteracting spinless fermions.

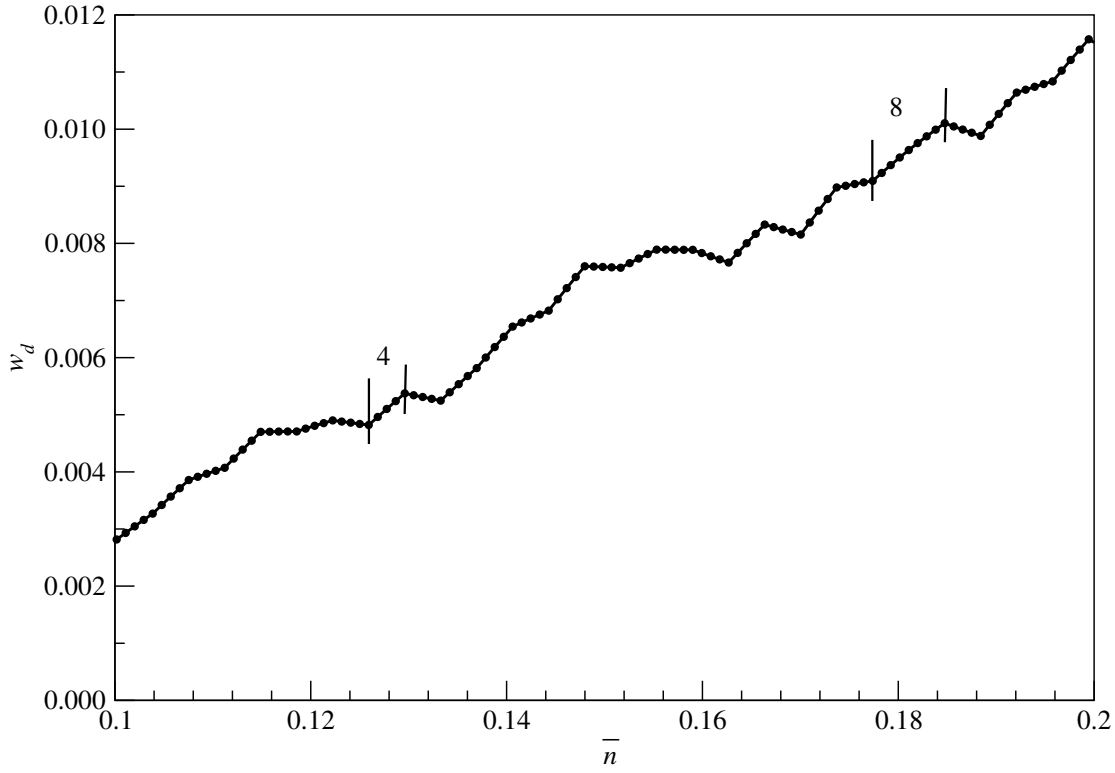

Figure 4.9: Shell effect in the one-particle cluster density-matrix weight w_d of the $(32, -8) \times (8, 32)$ system of noninteracting spinless fermions.

As expected, the shell structure corresponds to every four or eight particles put into the finite system. We identify a 'shell' of four or eight particles as those occupation numbers for which w_d is monotonically increasing or decreasing. If we adopt a stricter definition of a 'shell' as one in which w_d changes smoothly with occupation number, then all the shells of eight particles must be broken down into two shells of four particles each, as there is a rather obvious kink in w_d after the fourth particle in each eight-particle shell.

4.6.1.5 More on the Shape Effect

Next we look at the shape effect, which is the most subtle of the finite size effects, and hardest of them all to remove. To study this effect, we choose to look at the one-particle cluster density-matrix weights for several systems with between 200 to 300 sites of different shapes. For systems of these sizes, the finite domain effect and shell effect are negligible, but we nevertheless find, as shown in Figure 4.10, small deviations between w_{s_1} from systems of different shapes. This is despite that fact that for each system shape, the cluster density-matrix spectra will not improve very much with further increase in system size. We attribute these deviations to the shape effect, and expect that they will go away eventually with increasing system size to give a shape-independent infinite-system limit. In the course of our numerical studies, we discover that shape effect deviations in the cluster density-matrix spectra cannot be removed by the the combination of degeneracy, orientation, and twist boundary conditions averaging. Fortunately, these deviations are always small.

Therefore, as a little summary, we find of the finite size effects that, working without twist boundary conditions averaging, the finite domain effect is the first to go away (at about 200 sites), followed by the shell effect (there is still some residual effects at 4000+

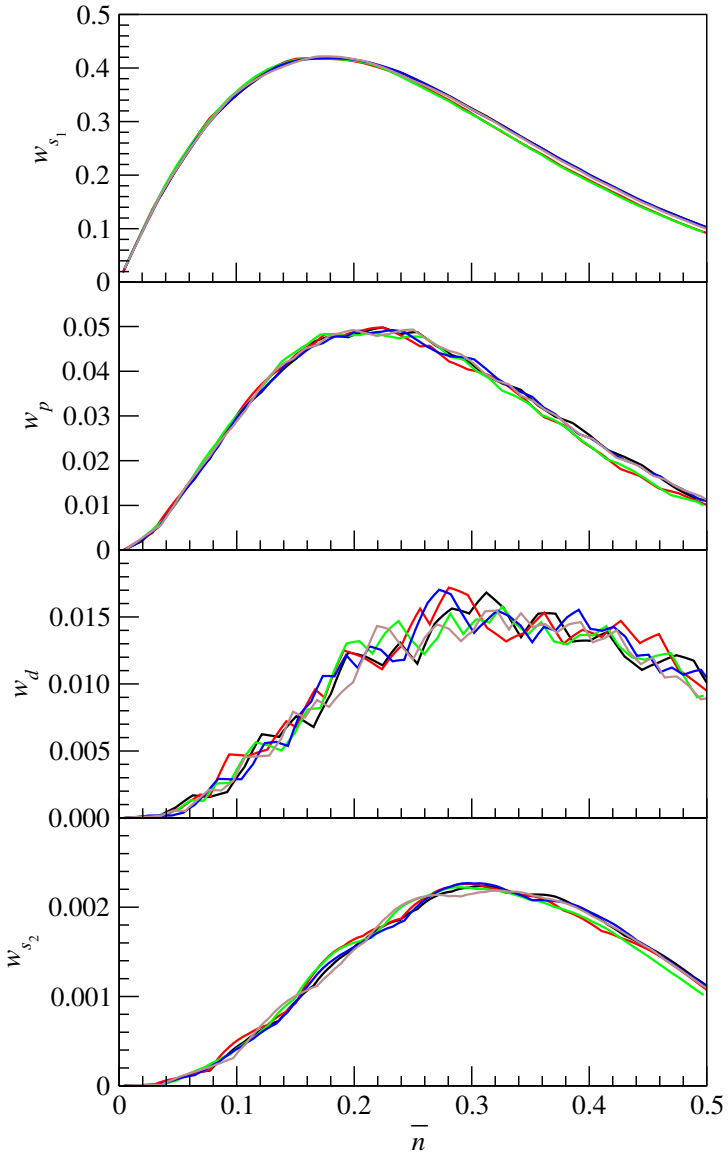

Figure 4.10: One-particle weights of the cluster density matrix of a five-site, cross-shaped cluster for the $(16, -4) \times (4, 16)$ (black), $(16, 4) \times (4, 16)$ (red), $(16, 4) \times (4, 12)$ (green), $(16, 3) \times (2, 13)$ (blue), and $(15, -5) \times (3, 14)$ (brown) systems of noninteracting spinless fermions subject to periodic boundary conditions.

sites, so presumably this effect goes away at about 10,000 sites, which is more than 100 times the maximum system size that we can exactly diagonalize), and then finally the shape effect (from Figure 4.10, it looks like this goes away extremely slowly).

4.6.2 One-Particle Weights at Small Filling Fractions

4.6.2.1 Numerical Asymptotics

In Section 4.6.1.3, we noticed the asymptotic linear rise of the one-particle cluster density-matrix weight w_{s_1} and quadratic rise of the one-particle cluster density-matrix weights w_p, w_d and w_{s_2} with small filling fractions $\bar{n} \to 0$. In this section, let us look at these asymptotic behaviours more carefully.

For the $(64, -16) \times (16, 64)$ system with $N = 4352$ sites, I calculated the one-particle cluster density-matrix weights for $1 \leq P \leq 200$ (corresponding to $0.00022 \leq \bar{n} \leq 0.04413$) noninteracting spinless fermions. This series of calculations took about 9.5 days on a Pentium-4-class processor. I then fitted power laws of the form

$$w = A\,\bar{n}^{\beta}, \tag{4.6.13}$$

for $\bar{n} \ll 1$, to the four one-particle weights. Because of shell effects, which persists for w_d and w_{s_2} even at this large system size, these power-law fits have to be done with care, and at the expense of ignoring the data points for the lowest filling fractions. The power-law fits to the one-particle weights are shown in Table 4.7, and the closeness-of-fit shown in Figures 4.11, 4.12, 4.13 and 4.14. A similar power-law fit was applied to the $(32, -8) \times (8, 32)$ system at low filling fractions, and the exponents obtained are

$$\beta_{s_1} = 0.98276, \quad \beta_p = 1.80759, \quad \beta_d = 2.55199, \quad \beta_{s_2} = 3.02898. \tag{4.6.14}$$

The numerical exponents obtained suggest that the asymptotic rise of the one-particle

cluster density-matrix weights are $w_{s_1} \sim \bar{n}$, $w_p \sim \bar{n}^2$, and $w_d, w_{s_2} \sim \bar{n}^3$. We verify this behaviour analytically in the next subsubsection.

Table 4.7: Power-law fits of the one-particle cluster density-matrix weights to $w = A\,\bar{n}^{\beta}$, for the $(64, -16) \times (16, 64)$ system of $1 \leq P \leq 200$ noninteracting spinless fermions subject to periodic boundary conditions.

	A	β	data points used
w_{s_1}	4.0318	0.96329	all 200
	4.8433	0.99593	first 20
w_p	3.1364	1.8669	exclude first 10
	2.0853	1.74876	exclude first 100
	3.5014	1.8908	exclude first 10 and last 50
w_d	2.7245	2.8034	exclude first
	2.4219	2.76748	exclude first 99
w_{s_2}	0.39149	2.89084	exclude first 8
	0.31948	2.8316	exclude first 99

4.6.2.2 Analytical Asymptotics

In the limit of $\bar{n} \to 0$, the Fermi surface is a circle, and we can compute the two-point functions $G(\mathbf{r}, \mathbf{r}')$ for an infinite system easily as

$$\begin{aligned} G(\mathbf{r}, \mathbf{r}') &= \frac{1}{4\pi^2} \int_0^{k_F} k\,dk \int_0^{2\pi} e^{ik|\mathbf{r}-\mathbf{r}'|\cos\theta}\,d\theta = \frac{1}{2\pi} \int_0^{k_F} k\,J_0(k|\mathbf{r}-\mathbf{r}'|)\,dk \\ &= \frac{1}{2\pi|\mathbf{r}-\mathbf{r}'|^2} \int_0^{k_F|\mathbf{r}-\mathbf{r}'|} \xi\,J_0(\xi)\,d\xi = \frac{k_F|\mathbf{r}-\mathbf{r}'|\,J_1(k_F|\mathbf{r}-\mathbf{r}'|)}{2\pi|\mathbf{r}-\mathbf{r}'|^2} \\ &= \frac{k_F}{2\pi|\mathbf{r}-\mathbf{r}'|}\,J_1(k_F|\mathbf{r}-\mathbf{r}'|), \end{aligned} \tag{4.6.15}$$

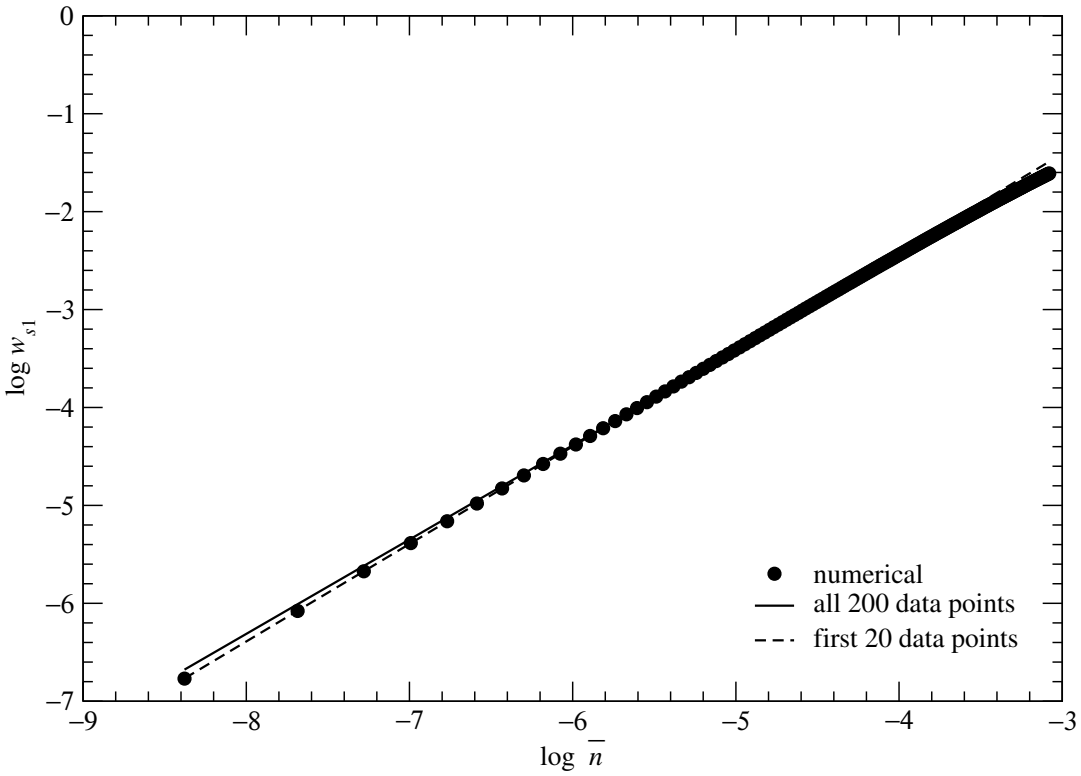

Figure 4.11: Power-law fits of the form $w_{s_1} = A_{s_1}\,\bar{n}^{\beta_{s_1}}$. Using all 200 data points, we have $w_{s_1} = 4.0318\,\bar{n}^{0.96329}$, whereas if the first 20 data points are used, we have $w_{s_1} = 4.8433\,\bar{n}^{0.99593}$. The first fit agrees better with the data for larger $\bar{n}$, whereas the latter fit agrees better with the data for smaller $\bar{n}$. The exponents from the fits are both close to one.

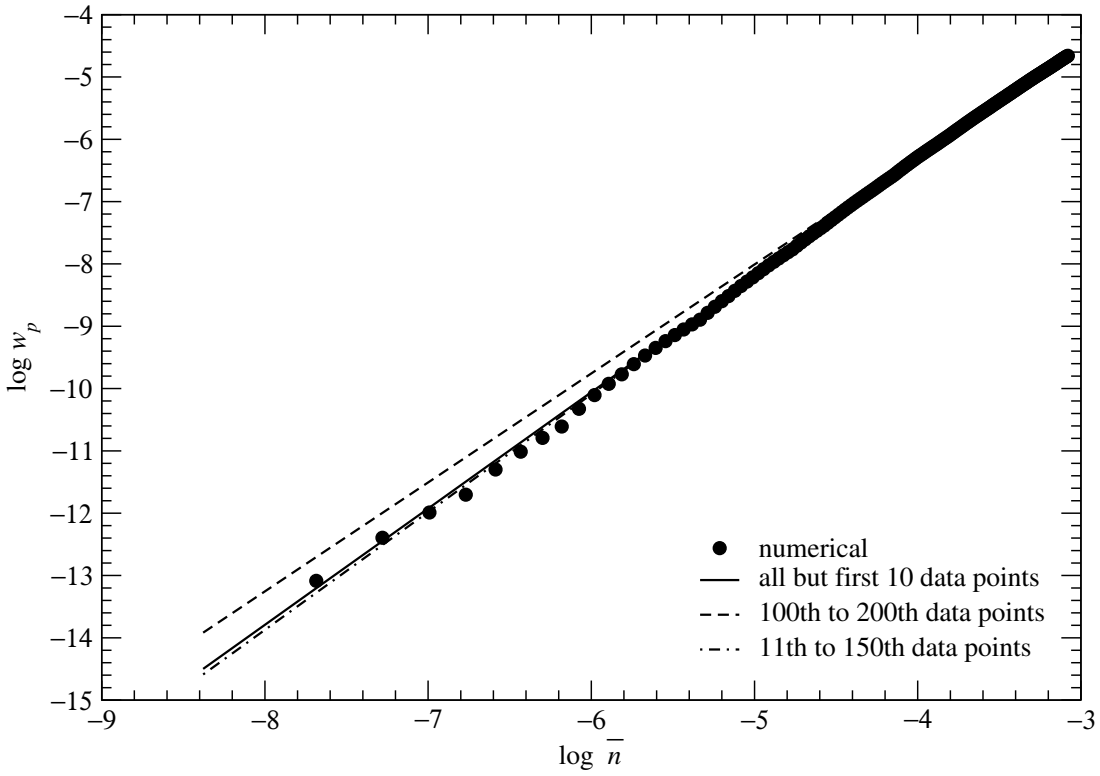

Figure 4.12: Power-law fits of the form $w_p = A_p\,\bar{n}^{\beta_p}$. A muted shell effect shows up on the log-log plot at very low filling fractions, and we use all but the first ten of the 200 data points to fit a power law of $w_p = 3.1364\,\bar{n}^{1.8669}$. If we exclude the first 100 data points, the power-law fit is then $w_p = 2.0853\,\bar{n}^{1.74876}$, whereas if we exclude the first ten and the last 50 data points, we get a power-law fit of $w_p = 3.5014\,\bar{n}^{1.8908}$.

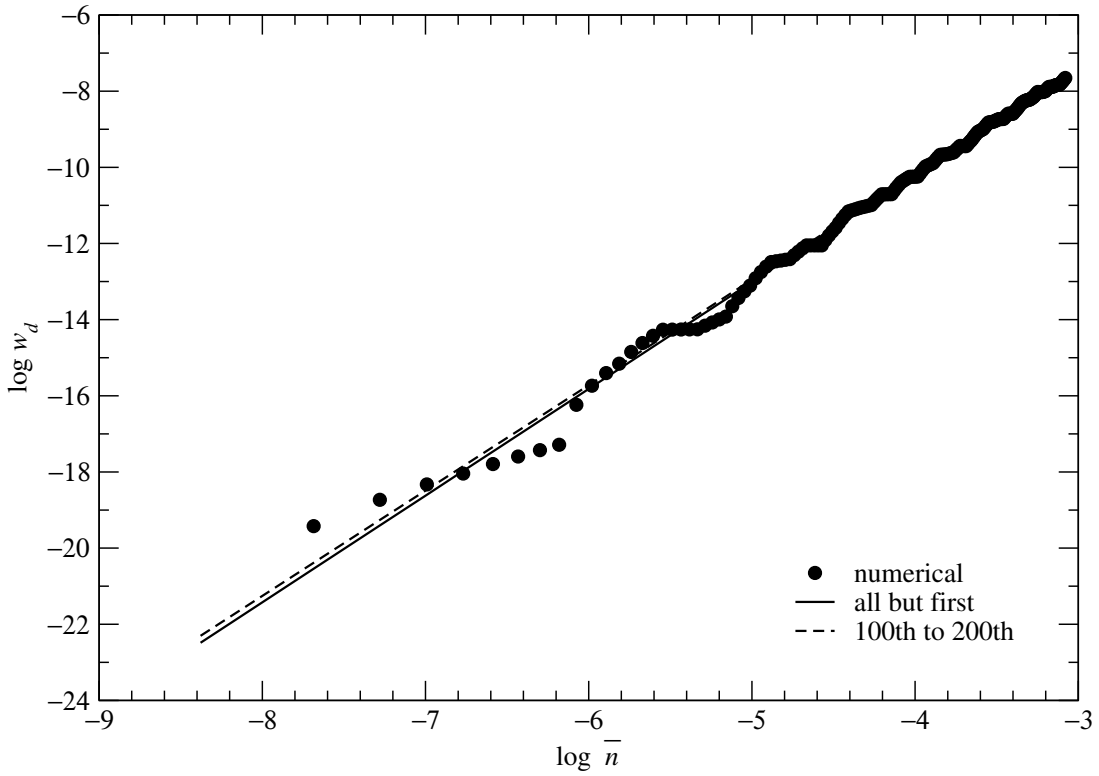

Figure 4.13: Power-law fits of the form $w_d = A_d\,\bar{n}^{\beta_d}$. For this one-particle weight, shell effects are pronounced, and there does not appear to be any less noisy region to do the power-law fit. Using all but the first of the 200 data points, we obtain a power-law fit of $w_d = 2.7245\,\bar{n}^{2.8034}$. If we exclude the first 99 data points, the power-law fit becomes $w_d = 2.4219\,\bar{n}^{2.76748}$. For lower filling fractions, both power laws do not agree well with the data points.

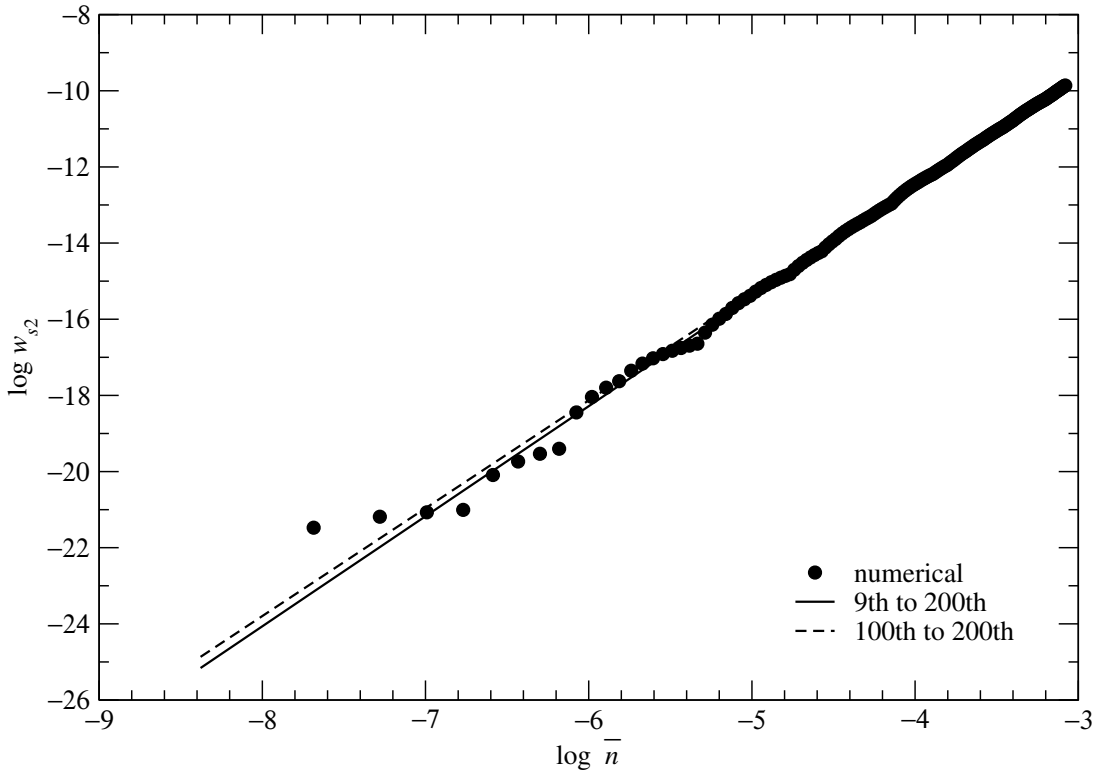

Figure 4.14: Power-law fits of the form $w_{s_2} = A_{s_2}\,\bar{n}^{\beta_{s_2}}$. For this one-particle weight, shell effects are less pronouced than in w_d, but are still severe at low filling fractions. Using all but the first eight of the 200 data points, we obtain a power-law fit $w_{s_2} = 0.39149\,\bar{n}^{2.89084}$. If we exclude the first 99 data points, the power-law fit becomes $w_{s_2} = 0.31948\,\bar{n}^{2.8316}$. Again, both power laws do not agree well with the data points at lower filling fractions.

where $J_0(\xi)$ and $J_1(\xi)$ are the zeroth and first order Bessel functions of the first kind [210].

Furthermore, using the fact that

$$\frac{\pi k_F^2}{4\pi^2} = \bar{n}, \quad k_F = \sqrt{4\pi\bar{n}}, \tag{4.6.16}$$

we can write the infinite-system two-point function in terms of the filling fraction $\bar{n}$ as

$$G(\mathbf{r}, \mathbf{r}'; \bar{n}) = \frac{\sqrt{\bar{n}}}{\sqrt{\pi}|\mathbf{r} - \mathbf{r}'|} J_1(\sqrt{4\pi\bar{n}}|\mathbf{r} - \mathbf{r}'|). \tag{4.6.17}$$

To derive the asymptotic behaviour of $G(\mathbf{r}, \mathbf{r}')$, and hence the cluster density-matrix elements, as $\bar{n} \to 0$, we series expand $J_1(\xi)$ about $\xi = 0$, to get

$$J_1(\xi) = \frac{\xi}{2} - \frac{\xi^3}{16} + \frac{\xi^5}{384} + \cdots . \tag{4.6.18}$$

If we neglect terms higher than linear order in ξ, we find that

$$G(\mathbf{r}, \mathbf{r}'; \bar{n}) \approx \frac{\sqrt{\bar{n}}}{\sqrt{\pi}|\mathbf{r} - \mathbf{r}'|} \frac{\sqrt{4\pi\bar{n}}|\mathbf{r} - \mathbf{r}'|}{2} = \bar{n}, \tag{4.6.19}$$

which means that we have thrown out the baby with the bathwater. In fact, if we keep terms up to third order in ξ, the d-symmetry eigenvalue of the cluster Green-function matrix will vanish. Therefore, we keep terms up to fifth order in ξ, to obtain

$$\begin{aligned} G(\mathbf{r}, \mathbf{r}'; \bar{n}) &= \frac{\sqrt{\bar{n}}}{\sqrt{\pi}|\mathbf{r} - \mathbf{r}'|} \left[\frac{\sqrt{4\pi\bar{n}}|\mathbf{r} - \mathbf{r}'|}{2} - \frac{\sqrt{4\pi\bar{n}}(4\pi\bar{n})|\mathbf{r} - \mathbf{r}'|^3}{16} + \frac{\sqrt{4\pi\bar{n}}(4\pi\bar{n})^2|\mathbf{r} - \mathbf{r}'|^5}{384} \right] \\ &= \bar{n}\left[1 - \frac{\bar{n}\pi}{2}|\mathbf{r} - \mathbf{r}'|^2 + \frac{\bar{n}^2\pi^2}{12}|\mathbf{r} - \mathbf{r}'|^4 \right], \end{aligned} \tag{4.6.20}$$

Noting that if we write G as

$$G = \bar{n}\mathsf{g} = \bar{n} \begin{bmatrix} 1 & \mathsf{a} & \mathsf{b} & \mathsf{a} & \mathsf{c} \\ \mathsf{a} & 1 & \mathsf{b} & \mathsf{c} & \mathsf{a} \\ \mathsf{b} & \mathsf{b} & 1 & \mathsf{b} & \mathsf{b} \\ \mathsf{a} & \mathsf{c} & \mathsf{b} & 1 & \mathsf{a} \\ \mathsf{c} & \mathsf{a} & \mathsf{b} & \mathsf{a} & 1 \end{bmatrix}, \tag{4.6.21}$$

then the eigenvalues are always

$$\begin{aligned}
\lambda_{s_1} &= \bar{n}\left[1 + \mathsf{a} + \tfrac{1}{2}\mathsf{c} + \tfrac{1}{2}\sqrt{4\mathsf{a}^2 + 16\mathsf{b}^2 + 4\mathsf{ac} + \mathsf{c}^2}\right], \\
\lambda_{p} &= \bar{n}\left[1 - \mathsf{c}\right], \\
\lambda_{d} &= \bar{n}\left[1 - 2\mathsf{a} + \mathsf{c}\right], \\
\lambda_{s_2} &= \bar{n}\left[1 + \mathsf{a} + \tfrac{1}{2}\mathsf{c} - \tfrac{1}{2}\sqrt{4\mathsf{a}^2 + 16\mathsf{b}^2 + 4\mathsf{ac} + \mathsf{c}^2}\right].
\end{aligned} \tag{4.6.22}$$

Here, the coefficients a, b, c are to fifth order in ξ, and thus second order in $\bar{n}$,

$$\mathsf{a} \approx 1 - \bar{n}\pi + \frac{1}{3}\bar{n}^2\pi^2, \tag{4.6.23a}$$

$$\mathsf{b} \approx 1 - \frac{1}{2}\bar{n}\pi + \frac{1}{12}\bar{n}^2\pi^2, \tag{4.6.23b}$$

$$\mathsf{c} \approx 1 - 2\bar{n}\pi + \frac{4}{3}\bar{n}^2\pi^2, \tag{4.6.23c}$$

such that, to $O(\bar{n}^2)$, we have

$$\sqrt{4\mathsf{a}^2 + 16\mathsf{b}^2 + 4\mathsf{ac} + \mathsf{c}^2} = 5 - 4\bar{n}\pi + \frac{28}{15}\bar{n}^2\pi^2. \tag{4.6.24}$$

With (4.6.23) and (4.6.24), we then find the cluster Green-function matrix eigenvalues in (4.6.22) to be, up to $O(\bar{n}^2)$,

$$\lambda_{s_1} = \bar{n}\left[5 - 4\pi\bar{n} + \frac{29}{15}\pi^2\bar{n}^2\right], \tag{4.6.25a}$$

$$\lambda_{p} = \bar{n}^2\left[2\pi - \frac{4}{3}\pi^2\bar{n}\right], \tag{4.6.25b}$$

$$\lambda_{d} = \frac{2}{3}\pi^2\bar{n}^3, \tag{4.6.25c}$$

$$\lambda_{s_2} = \frac{1}{15}\pi^2\bar{n}^3. \tag{4.6.25d}$$

Having these eigenvalues, we can then work out to $O(\bar{n}^2)$, the zero-particle cluster density-matrix weight

$$w_0 = (1 - \lambda_{s_1})(1 - \lambda_p)^2(1 - \lambda_d)(1 - \lambda_{s_2}) \approx 1 - 5\bar{n} + 20\pi\bar{n}^3, \tag{4.6.26}$$

and the one-particle cluster density-matrix weights

$$w_{s_1} = \lambda_{s_1}(1-\lambda_p)^2(1-\lambda_d)(1-\lambda_{s_2}) \approx \bar{n}\left[5 - 4\pi\bar{n} + \left(\frac{29\pi^2}{15} - 20\pi\right)\bar{n}^2\right], \tag{4.6.27a}$$

$$w_p = (1-\lambda_{s_1})\lambda_p(1-\lambda_p)(1-\lambda_d)(1-\lambda_{s_2}) \approx \bar{n}^2\left[2\pi - \left(10\pi + \frac{4}{3}\pi^2\right)\bar{n}\right], \tag{4.6.27b}$$

$$w_d = (1-\lambda_{s_1})(1-\lambda_p)^2\lambda_d(1-\lambda_{s_2}) \approx \frac{2\pi^2}{3}\bar{n}^3, \tag{4.6.27c}$$

$$w_{s_2} = (1-\lambda_{s_1})(1-\lambda_p)^2(1-\lambda_d)\lambda_{s_2} \approx \frac{\pi^2}{15}\bar{n}^3. \tag{4.6.27d}$$

This confirms our numerical observations in Section 4.6.2.1, that $w_{s_1} \sim \bar{n}$, $w_p \sim \bar{n}^2$, $w_d, w_{s_2} \sim \bar{n}^3$ to leading order in $\bar{n}$.

In Figure 4.15, we compare this $O(\bar{n}^3)$ analysis with the numerical data from the $(32, -4) \times (4, 32)$ system. The agreement at small $\bar{n}$ is very good, considering that there is no free parameter in the $O(\bar{n}^3)$ analysis. We can do analyses of higher and higher order in $\bar{n}$, but we must not expect better agreement, before we account for the fact that at higher $\bar{n}$, the Fermi surface would no longer be a circle.

4.6.3 Twist Boundary Conditions Averaging

When an analytical formula is available, as is the case for a system of noninteracting spinless fermions, there is always the option of going to very large system sizes to determine the infinite-system limit for the spectrum of the cluster density matrix ρ_C. For a system of strongly-interacting spinless fermions, this option is not available, and twist boundary conditions averaging is the best that we can do. In this subsection, we demonstrate, using the noninteracting system as a test case, that the method of twist boundary conditions averaging, described at length in Appendix D, is a reliable technique to reduce the finite domain and shell effects, using an ensemble of finite-system spectra.

For the noninteracting system, the cluster density matrix ρ_C can be calculated from the cluster Green-function matrix G_C with the aid of (2.4.31). When I started out imple-

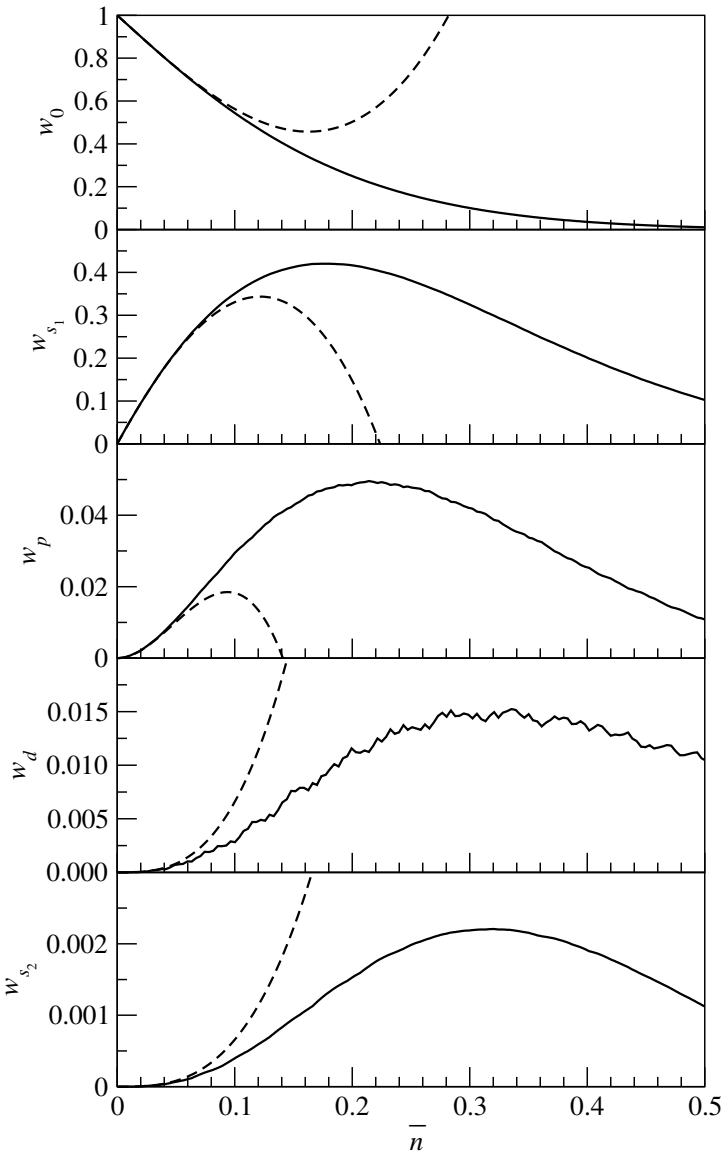

Figure 4.15: Zero- and one-particle weights (solid curves) of the cluster density matrix of a five-site, cross-shaped cluster for the $(32, -8) \times (8, 32)$ system of noninteracting spinless fermions with periodic boundary conditions imposed, compared against their $O(\bar{n}^3)$ analytical values (dashed curves) within an infinite system at low filling fraction $\bar{n} \to 0$. Agreement between the approximate analytical and numerical weights are very good for $\bar{n} < 0.04$, beyond which we will need to (i) go to higher orders in $\bar{n}$; and (ii) treat the shape of the Fermi surface more carefully, to get better agreement.

menting twist boundary conditions averaging for such a system, I was tempted to twist-boundary-conditions average G_C, and then calculate ρ_C from the averaged G_C. However, the relation (2.4.31) is nonlinear, so ρ_C of the averaged G_C is in general not the same as ρ_C averaged over G_C at different twist vectors (although we expect $\overline{\rho_C(G_C)} = \rho_C(\overline{G_C})$ for noninteracting spinless fermions, if the method of twist boundary conditions averaging is successful in eliminating all finite size effects). Since ρ_C is the observable we are interested in calculating for both the noninteracting and interacting cases, we perform twist boundary conditions averaging on ρ_C only.

4.6.3.1 The $(4, -1) \times (1, 4)$ Sequence of Noninteracting Systems Revisited

First, let us look at the $(4n, -n) \times (n, 4n)$ sequence of noninteracting systems again, this time with twist boundary conditions averaging. Integration over the twist angle domain is done with the special-point integration scheme described in Appendix D.6.2. From our detailed study in Appendix D of the twist surface $\langle\Psi(\phi_x, \phi_y)|O|\Psi(\phi_x, \phi_y)\rangle$ of a generic observable O, where $|\Psi(\phi_x, \phi_y)\rangle$ is the many-body ground state, in the boundary gauge (see Sections D.2.1.2, D.2.1.3 and D.2.3.2, most importantly the gauge transformation (D.2.56)), of a finite system of N sites subject to twist boundary conditions with twist vector $\boldsymbol{\phi} = (\phi_x, \phi_y)$, we know that there are cusps and cuts on the twist surface. For non-square systems, these cusps and cuts demarcate features with a hierarchy of sizes on the twist surface. The 'typical' twist surface feature has a linear dimension of $2\pi/\sqrt{N}$. These are decorated by fine structures with linear dimension $2\pi/N$, which are in turn decorated by hyperfine structures with linear dimensions $2\pi/N^2$. The number of integration points we choose to use is therefore determined by what feature size we want to integrate faithfully.

For the purpose of this study, we decided to integrate the fine structure on the twist

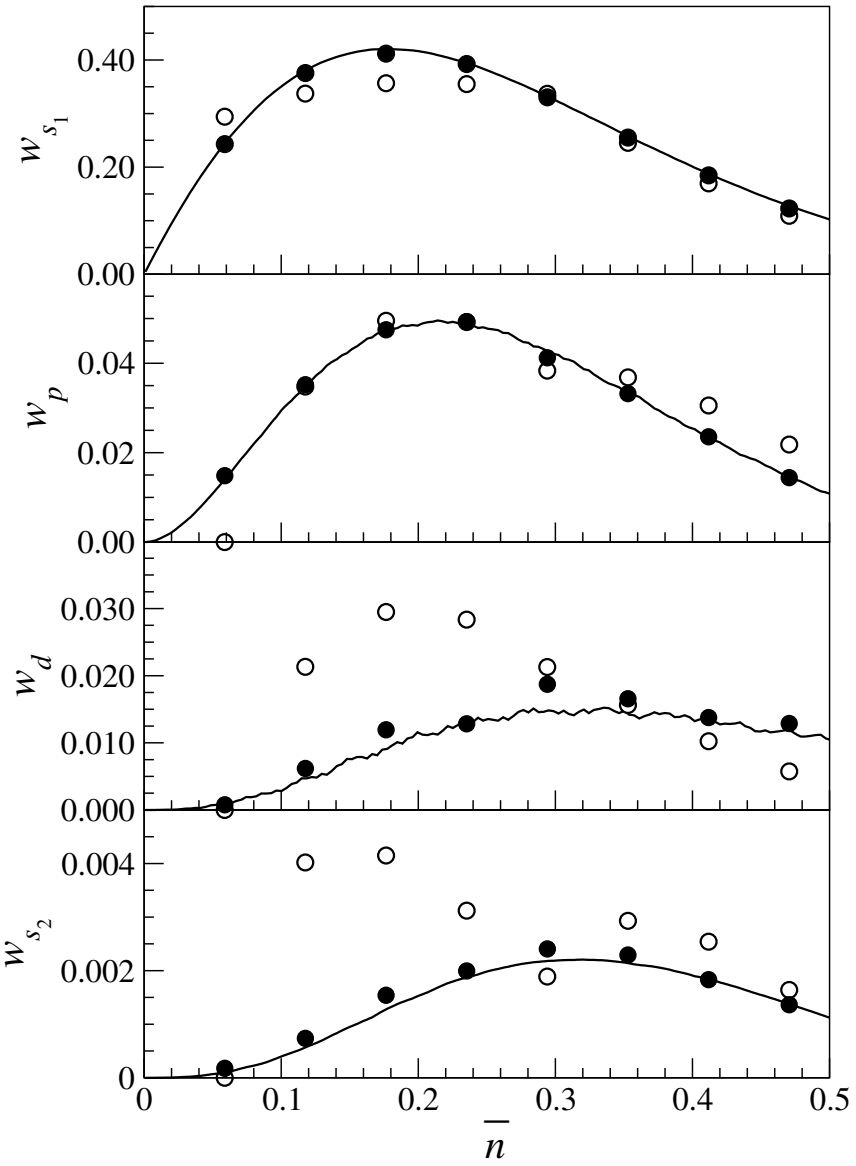

Figure 4.16: One-particle weights of the cluster density matrix of a five-site, cross-shaped cluster within systems of noninteracting spinless fermions. The performance of twist boundary conditions averaging, using $q = 16$ Monkhorst-Pack special-point integration over the unrestricted twist angle domain, in reducing finite size effects for the $(4, -1)\times(1, 4)$ system (●) is checked against the $(4, -1)\times(1, 4)$ (○) and the $(32, -8)\times(8, 32)$ (solid line) systems with periodic boundary conditions imposed.

surface faithfully. Therefore, we chose to average the spectrum of ρ_C over a $q = 16$ Monkhorst-Pack grid (which consists of 256 integration points in the First Brillouin Zone) for the $(4, -1) \times (1, 4)$ system with $N = 17$ sites, and the $(8, -2) \times (2, 8)$ system with $N = 68$ sites. We find that twist boundary conditions averaging does indeed result in an averaged spectrum which approximates the infinite-system limit well (see Figures 4.16 and 4.17). As we can see, twist boundary conditions averaging works better on a larger system, since the finite size effects in larger systems are smaller to begin with. In fact, the twist-boundary-conditions averaged w_d in the $(8, -2) \times (2, 8)$ system appears to be 'smoother' than w_d from the $(32, -4) \times (4, 32)$ system.

Finally, we checked the performance of Monkhorst-Pack special-point integration of the twist boundary conditions for various orders q. In Figure 4.18, we see that the one-particle cluster density-matrix weight w_d is smoothed out beyond $q = 7$. However, compared the smoothed spectra for $q = 7$, $q = 8$ and $q = 16$, we find that there are small, but discernible differences between them. Based on our understanding of the structure of twist surfaces, we understand why these are so. The gross structure of the twist surface of w_d can be properly integrated over with only a small Monkhorst-Pack order, which is why we have a rapid convergence, manifested as a smoothing, of the spectra from $q = 2$ to $q = 7$. The fine structures of the w_d twist surface, however, requires a minimum order of $q \sim N$, to properly integrate over, which is why we see the convergence slowing down from $q = 7$ to $q = 16$. In Figure 4.19, we present this convergence behaviour in a different way, by plotting the difference between the Monkhorst-Pack q-integrated spectra of the one-particle cluster density-matrix weight w_{s_1} from the $(8, -2) \times (2, 8)$ system, and the unaveraged w_{s_1} from the $(32, -8) \times (8, 32)$ system subject to periodic boundary conditions. On this 'magnified' scale, the remnant shell effects after twist boundary conditions averaging becomes very obvious.

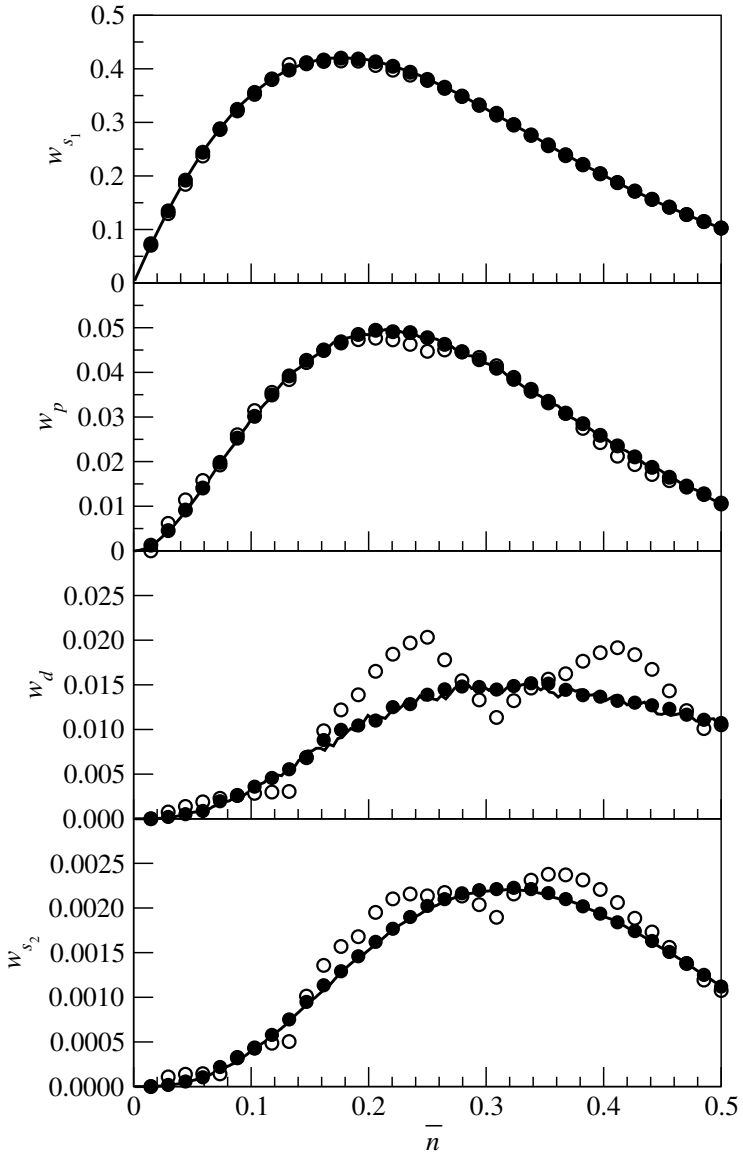

Figure 4.17: One-particle weights of the cluster density matrix of a five-site, cross-shaped cluster within systems of noninteracting spinless fermions. The performance of twist boundary conditions averaging, using $q = 16$ Monkhorst-Pack special-point integration over the unrestricted twist angle domain, in reducing finite size effects for the $(8, -2)\times(2, 8)$ system (●) is checked against the $(8, -2)\times(2, 8)$ (○) and the $(32, -8)\times(8, 32)$ (solid line) systems with periodic boundary conditions imposed.

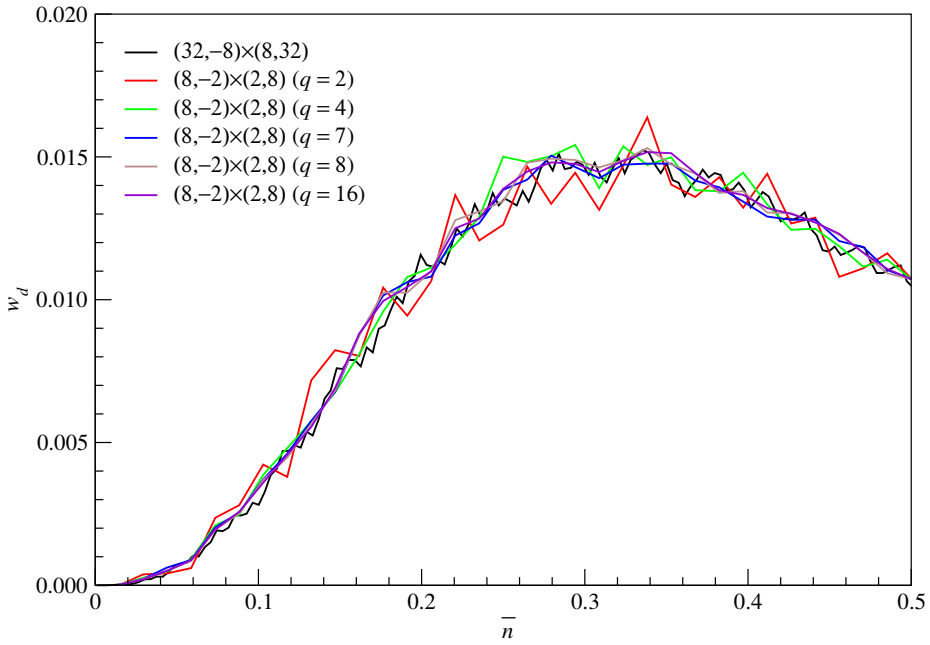

Figure 4.18: The Monkhorst-Pack special-point integration of the twist boundary conditions of the one-particle cluster density-matrix weight w_d for the $(8, -2) \times (2, 8)$ system of noninteracting spinless fermions, with orders $q = 2, 4, 7, 8, 16$ over the unrestricted twist angle domain.

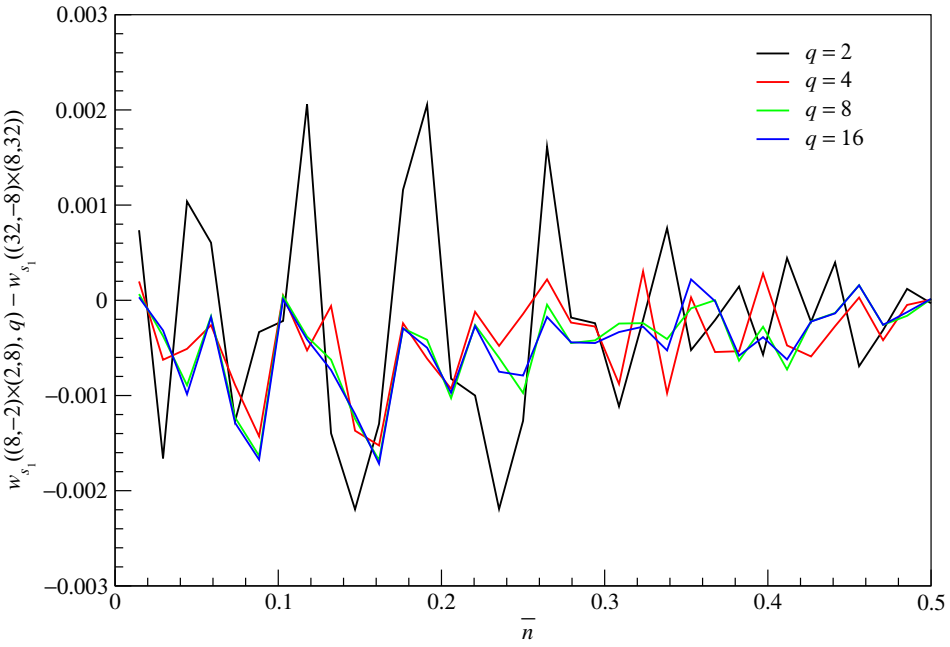

Figure 4.19: Difference between the one-particle cluster density-matrix weight w_{s_1} averaged over twist boundary conditions using Monkhorst-Pack special-point integration of order q over the unrestricted twist angle domain, for the $(8,-2)\times(2,8)$ system, and the unaveraged w_{s_1} from the $(32,-8)\times(8,32)$ system subject to periodic boundary conditions.

4.6.3.2 Twist-Boundary-Conditions Averaging Systems of Different Shapes

From the previous subsubsection, we saw that twist boundary conditions averaging does not completely eliminate shell effects, and that averaging a larger system gives rise to smaller remnant shell effects, thus producing averaged spectra that are closer to the infinite-system limit. However, when we ultimately use twist boundary conditions averaging on interacting systems, the largest system size we can go to is about 32 sites, where we will likely incur a memory cost of roughly 2 GB, and run times of the order of a month for each twist vector. Therefore, to obtain results in any reasonable amount of time, we would be constrained to work with systems with no more than 20 sites.

To reduce the bias associated with any one particular choice of finite system, and build up a sense of how the infinite-system cluster density-matrix spectrum looks like as a function of $\bar{n}$, we superimpose the twist-boundary-conditions averaged weights obtained from various finite systems. We saw in Figure 4.4 how bad this looks with twist boundary conditions averaging. After twist boundary conditions averaging, we see in Figure 4.20 that the data points coming from different systems, with sizes ranging from $N = 11$ sites to $N = 24$ sites, now fall much closer to, if not on, the infinite-system limit. Had we not been able to calculate a better approximation to the infinite-system cluster density-matrix spectrum, which will be the case for interacting systems, the superposed twist-boundary-conditions averaged data points for different system gives us a far better sense of how the infinite-system spectrum would look like. This gives us more confidence that the comparison of the numerical results of the strongly-interacting system against that of the noninteracting system will be meaningful.

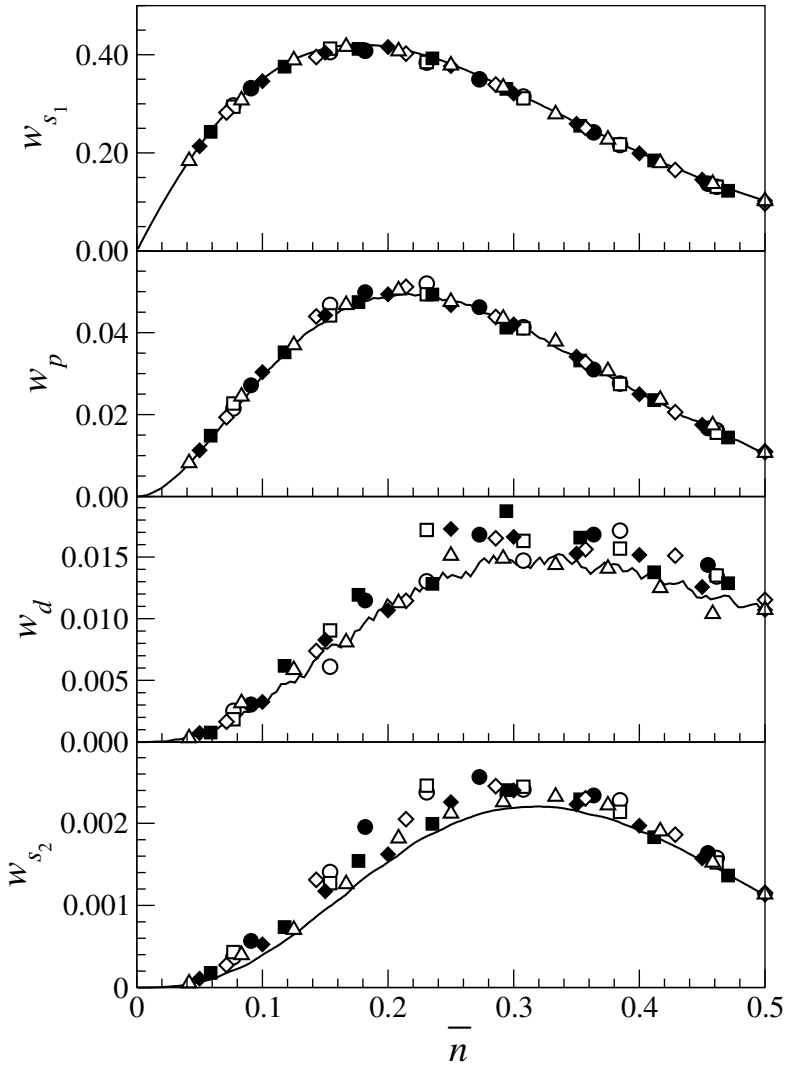

Figure 4.20: One-particle weights of the cluster density matrix of a five-site, cross-shaped cluster, for the $(3,-2)\times(2,3)$ (●), $(4,1)\times(1,3)$ (○), $(4,-1)\times(1,3)$ (□), $(4,-1)\times(1,4)$ (■), $(4,-1)\times(2,3)$ (◊), $(4,-2)\times(2,4)$ (♦) and $(5,1)\times(1,5)$ (△) systems of noninteracting spinless fermions subject to twist boundary conditions averaging, using $q = 16$ Monkhorst-Pack special-point integration over the unrestricted twist angle domain. Also shown is the $(32,-8)\times(8,32)$ (solid line) system subject to periodic boundary conditions.

4.7 Strongly-Interacting Spinless Fermions

As explained in Ref. 211, our interest in studying the strongly-interacting model (4.2.1) of spinless fermions with infinite nearest-neighbor repulsion is to check whether its expected Fermi-liquid behaviour will be manifest in the structure of its cluster density matrix. Based on our exact result in Ref. 184 for noninteracting fermions, the cluster density matrix for a Fermi liquid should be the exponential of a noninteracting pseudo-Hamiltonian. For a cluster density matrix with such a structure, the multi-particle eigenstates and multi-particle weights are all products of the one-particle eigenstates and one-particle weights respectively.

While we do not expect the zero-particle, one-particle and two-particle cluster density-matrix weights of the strongly-interacting system, presented in Sections 4.7.2, 4.7.3 and 4.7.4 respectively, to have the same dependence on the filling fraction $\bar{n}$ as those of a noninteracting system, we checked whether it is possible to: (i) write the two-particle eigenstates as the product of one-particle eigenstates; and (ii) predict the relative ordering of the two-particle weights based on the relative ordering of the one-particle weights. These two criteria, when met, forms the basis of an Operator-Based Density-Matrix Truncation Scheme described in Ref. 198. Based on the results in Section 4.7.3 and Section 4.7.4, we discuss the prospect of designing such a truncation scheme for the strongly-interacting system, at some or all filling fraction $\bar{n}$.

4.7.1 Twist Boundary Conditions Averaging

4.7.1.1 Before Averaging

We saw in Figure 4.4 how difficult it is to make sense of the finite-system cluster density-matrix spectra, because of finite size effects, for a noninteracting system. Just so we

have a sense of the magnitude of finite size effects we are dealing with in an interacting system, we show in Figure 4.21 the zero- and one-particle cluster density-matrix weights for the $(4,1)\times(1,3)$, $(3,-2)\times(2,3)$ and $(4,1)\times(1,4)$ system subject only to periodic boundary conditions.

As expected, the scatter of the data points for the one-particle cluster density-matrix weight w_d is bad. But even for those weights for which the scatter seems small, we know from the comparison of Figures 4.4 and 4.20 that finite-system spectra that are in close agreement with one another need not necessarily agree closely with the infinite-system spectra, or with the twist boundary conditions averaged approximation to the infinite-system spectra.

4.7.1.2 Twist Surfaces

In Appendix D.4, we showed the twist surfaces of the one-particle cluster density-matrix weights of the $(4,1)\times(1,3)$ system of strongly-interacting spinless fermions with infinite nearest-neighbor repulsion. However, in performing twist boundary conditions averaging of the cluster density matrix ρ_C, we do not actually integrate over the twist surfaces of the one-particle weights w_{s_1} and w_{s_2}. Instead, we integrate over the twist surfaces of the cluster density-matrix elements $\langle s|\rho_C|s\rangle$, $\langle s|\rho_C|\bar{s}\rangle = \langle \bar{s}|\rho_C|s\rangle$ and $\langle \bar{s}|\rho_C|\bar{s}\rangle$, two of which are shown in Figure 4.22, before we diagonalize the twist-boundary-conditions averaged cluster density matrix to obtain the one-particle weights.

Not shown in Figure 4.22 is the matrix element $\langle \bar{s}|\rho_c|\bar{s}\rangle$, which turns out not to depend on the phase twist in the boundary conditions. From the twist surfaces of $\langle s|\rho_C|\bar{s}\rangle$ and $\langle \bar{s}|\rho_C|\bar{s}\rangle$, we can discern gross features of linear dimension $\frac{\pi}{4} \approx \frac{\pi}{\sqrt{N}}$, and fine structures of linear dimension $\frac{\pi}{16} \approx \frac{\pi}{N}$. These fine structures are even more obvious on the twist surfaces of $\langle p_+|\rho_C|p_+\rangle = w_p$, and $\langle d|\rho_C|d\rangle = w_d$, which are shown in Figure 4.23.

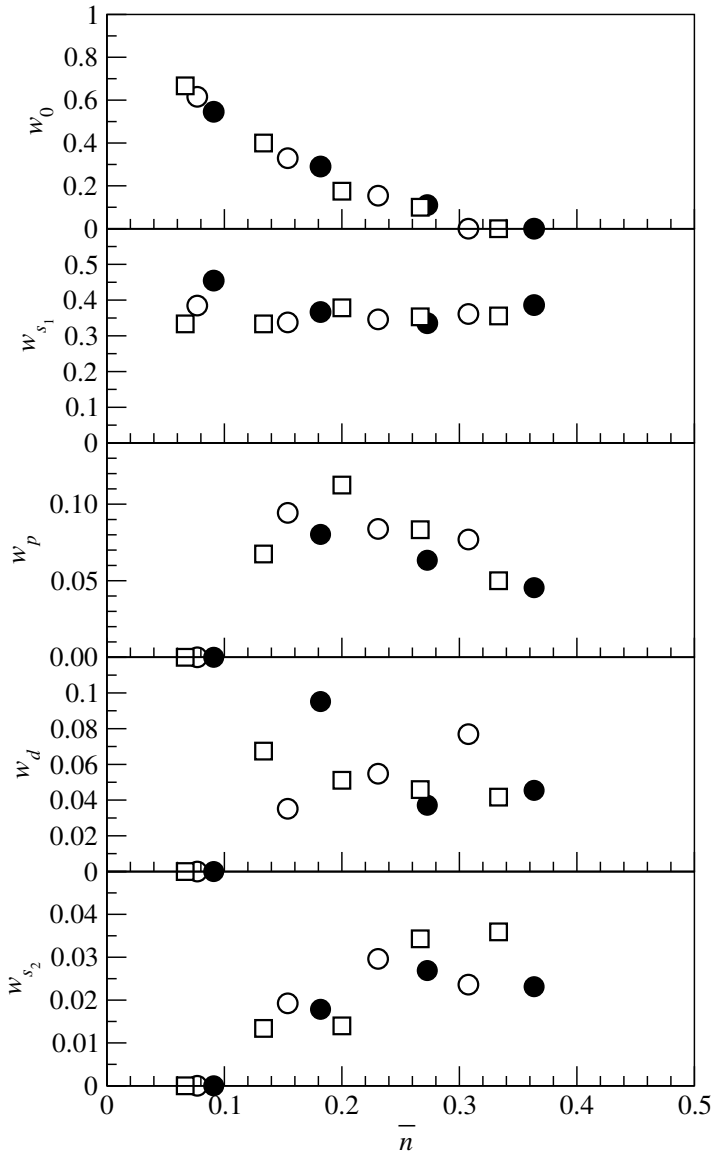

Figure 4.21: The zero- and one-particle weights of the cluster density matrix of a five-site, cross-shaped cluster for the $(3,-2)\times(2,3)$ (○), $(4,1)\times(1,3)$ (●), and $(4,1)\times(1,4)$ (□) systems of strongly-interacting spinless fermions with infinite nearest-neighbor repulsion, subject to periodic boundary conditions.

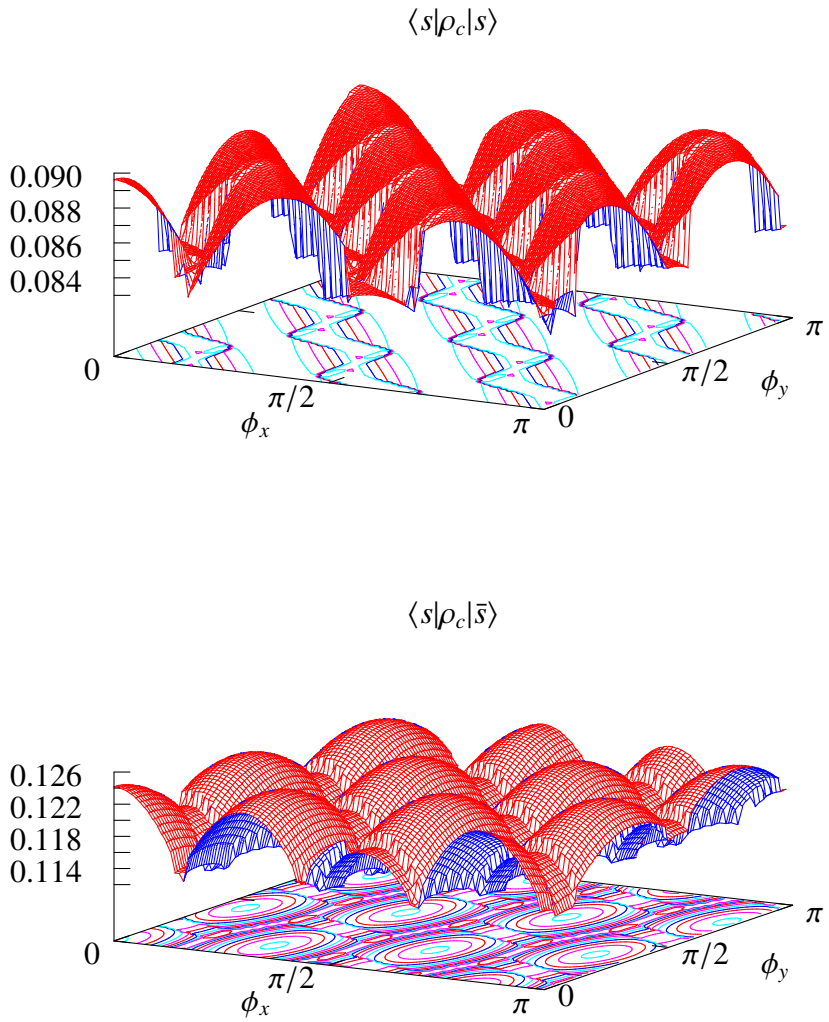

Figure 4.22: Twist surfaces for the matrix elements $\langle s|\rho_C|\bar{s}\rangle$ and $\langle \bar{s}|\rho_C|\bar{s}\rangle$ of the density matrix ρ_C for a five-site, cross-shaped cluster within a $(4,1)\times(1,3)$ system with $P = 3$ strongly-interacting spinless fermions with infinite nearest-neighbor repulsion, subject to twist boundary conditions.

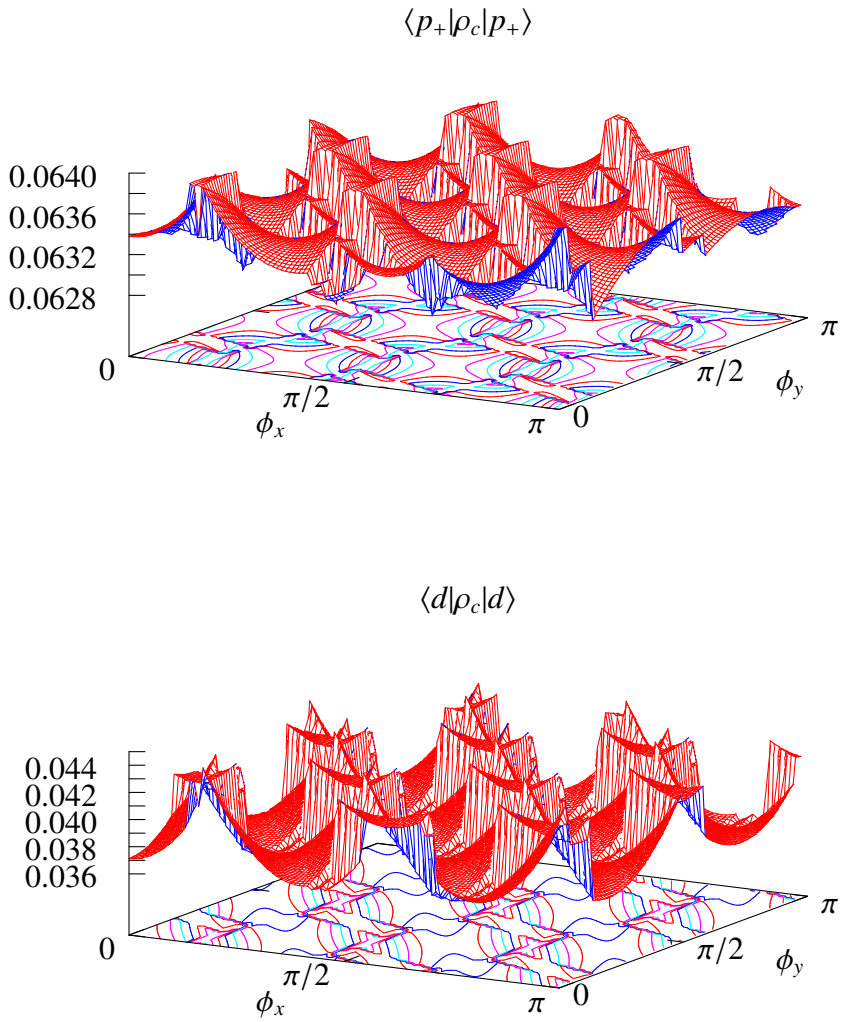

Figure 4.23: Twist surfaces for the matrix elements $\langle p_+|\rho_C|p_+\rangle = w_p$, and $\langle d|\rho_C|d\rangle = w_d$ of the cluster density matrix ρ_C for a five-site, cross-shaped cluster within a $(4,1)\times(1,3)$ system with $P = 3$ strongly-interacting spinless fermions with infinite nearest-neighbor repulsion, subject to twist boundary conditions.

As we can see, there is a spread in value of about 4% for $\langle s|\rho_c|s\rangle$, 6% for $\langle s|\rho_c|\bar{s}\rangle$, 2% for $\langle p_+|\rho_c|p_+\rangle$ and 22% for $\langle d|\rho_c|d\rangle$. This is why it is important to integrate properly the fine structures for the d-symmetry one-particle cluster density-matrix weight w_d.

4.7.1.3 Performance of Twist Boundary Conditions Averaging

For the strongly-interacting system, we are constrained by the computational time expenditure to do only $q = 8$ Monkhorst-Pack special-point integration over twist boundary conditions. As we have argued in the previous subsubsection, this is not quite enough to properly integrate over the twist surface fine structures of finite systems with between $N = 11$ to $N = 20$ sites. However, we have also seen in Figure 4.18 that we may still be able to reduce shell effects significantly with a integration order of $q \approx \sqrt{N}$. Our choice of $q = 8$ is therefore intermediate between orders properly integrating over the gross features and properly integrating over the fine structures.

In Figure 4.24, we see that twist boundary conditions averaging with $q = 8$ Monkhorst-Pack special-point integration gives us one-particle cluster density-matrix weights that are more sensible at low filling fractions — without twist boundary conditions averaging, the one-particle cluster density-matrix weights w_p, w_d and w_{s_2} are always zero at the lowest filling fraction accessible to each system. Scatter in the data points is reduced, to varying extents, in all one-particle weights, but most successfully in the s-symmetry weights.

4.7.1.4 Half-Filling

For a system of strongly-interacting spinless fermions with infinite nearest-neighbor repulsion, the ground-state at half-filling consists of a checker-board pattern of occupation. There are two such checker-board patterns: one with the even sites occupied, and

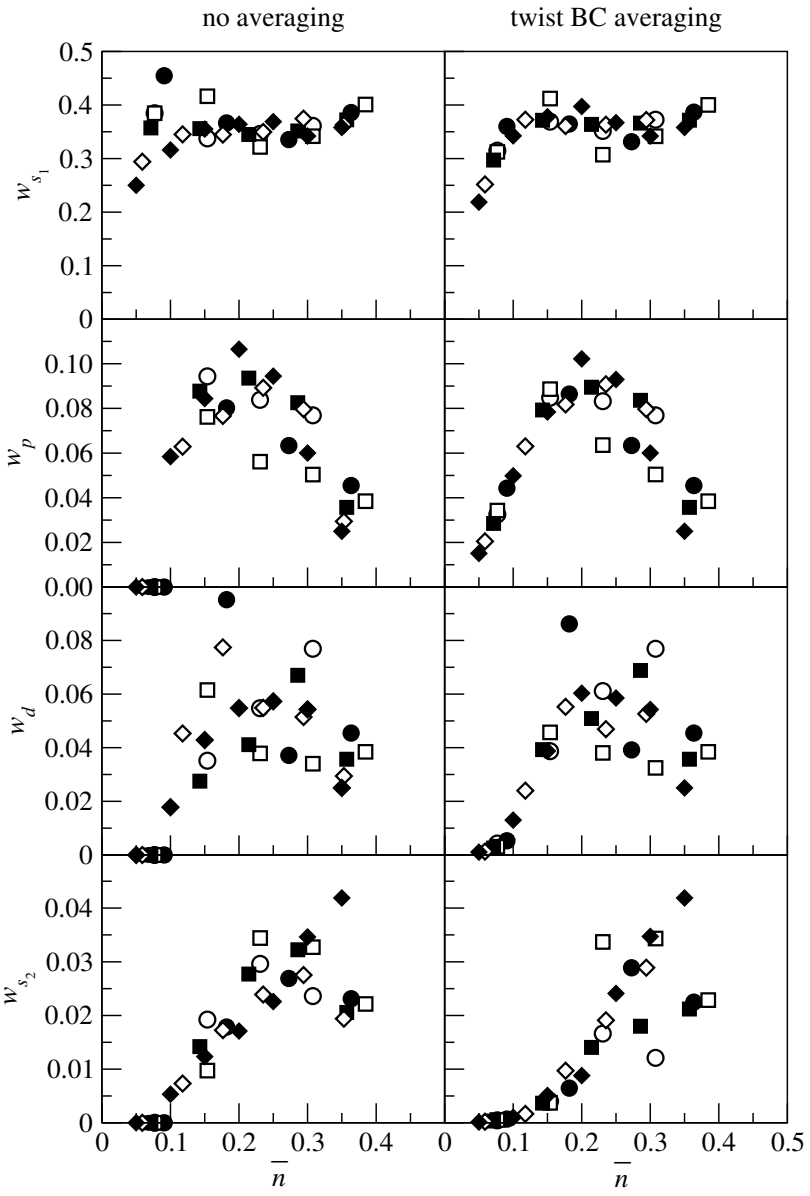

Figure 4.24: The one-particle weights of the cluster density matrix of a five-site, cross-shaped cluster, for the $(3,-2)\times(2,3)$ (○), $(4,1)\times(1,3)$ (●), $(4,-1)\times(1,3)$ (□), $(4,-1)\times(1,4)$ (■), $(4,-1)\times(2,3)$ (◊) and $(4,-2)\times(2,4)$ (♦) systems of strongly-interacting spinless fermions with infinite nearest-neighbor repulsion, subject to periodic boundary conditions (left) and twist boundary conditions averaging (right).

the other with the odd sites occupied. For these ground states, which are not affected at all by twist boundary conditions, we can work out the cluster density matrix exactly, by noting that the configuration of the five-site cluster can look like

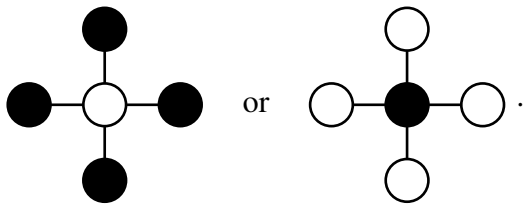 or . (4.7.1)

This means that the one-particle sector of ρ_C has no nonzero matrix elements for the configuration on the left, and looks like

$$\rho_{C,1} = \begin{bmatrix} 0 & 0 & 0 & 0 & 0 \\ 0 & 0 & 0 & 0 & 0 \\ 0 & 0 & 1 & 0 & 0 \\ 0 & 0 & 0 & 0 & 0 \\ 0 & 0 & 0 & 0 & 0 \end{bmatrix} \tag{4.7.2}$$

for the configuration on the right. Since the two configurations are equally likely to occur at half-filling, the one-particle sector of ρ_C therefore looks like

$$\bar{\rho}_{C,1} = \begin{bmatrix} 0 & 0 & 0 & 0 & 0 \\ 0 & 0 & 0 & 0 & 0 \\ 0 & 0 & \frac{1}{2} & 0 & 0 \\ 0 & 0 & 0 & 0 & 0 \\ 0 & 0 & 0 & 0 & 0 \end{bmatrix} \tag{4.7.3}$$

after degeneracy averaging.

For $\rho_{C,1}$ given in (4.7.3), the s-sector consists of the independent matrix elements

$$\langle s|\rho_{C,1}|s\rangle = 0, \quad \langle s|\rho_{C,1}|\bar{s}\rangle = 0, \quad \langle \bar{s}|\rho_{C,1}|\bar{s}\rangle = \tfrac{1}{2}, \tag{4.7.4}$$

which tells us that

$$w_{s_1}(\bar{n} = \tfrac{1}{2}) = \tfrac{1}{2}, \quad w_{s_2}(\bar{n} = \tfrac{1}{2}) = 0. \tag{4.7.5}$$

We also find the p- and d-sectors of $\rho_{C,1}$ to have matrix elements

$$\langle p_+|\rho_{c,1}|p_+\rangle = \langle p_-|\rho_{c,1}|p_-\rangle = 0, \quad \langle d|\rho_{c,1}|d\rangle = 0, \tag{4.7.6}$$

which tells us therefore that

$$w_{p_+} = w_{p_-} = w_d = 0. \tag{4.7.7}$$

From (4.7.1), it is easy to see that all of the two-particle cluster density-matrix weights w_S, w_{P_1}, w_{P_2}, and w_D are zero when the system is at half-filling.

4.7.2 Zero-Particle Sector of Cluster Density Matrix

The zero-particle cluster density-matrix weight calculated for various finite strongly-interacting systems is shown in Figure 4.25. Also shown in the figure is the zero-particle cluster density-matrix weight of the noninteracting $(32, -8) \times (8, 32)$ system. As we can see, the zero-particle weights of the respective systems only start differing significantly from each other for $\bar{n} > 0.1$. With repulsive interactions between spinless fermions, it is more difficult in a congested system ($\bar{n} > 0.2$) to form an empty cluster of sites from quantum fluctuations. As a result, the strongly-interacting w_0 falls below the noninteracting w_0. However, this fact alone does not tell us anything more about the correlations in the strongly-interacting ground state, and so we move on to consider the one-particle cluster density-matrix weights.

4.7.3 One-Particle Sector of Cluster Density Matrix

As explained in the beginning of this section, we calculate the spectra of the cluster density matrix for the strongly-interacting system to examine how much of the Operator-

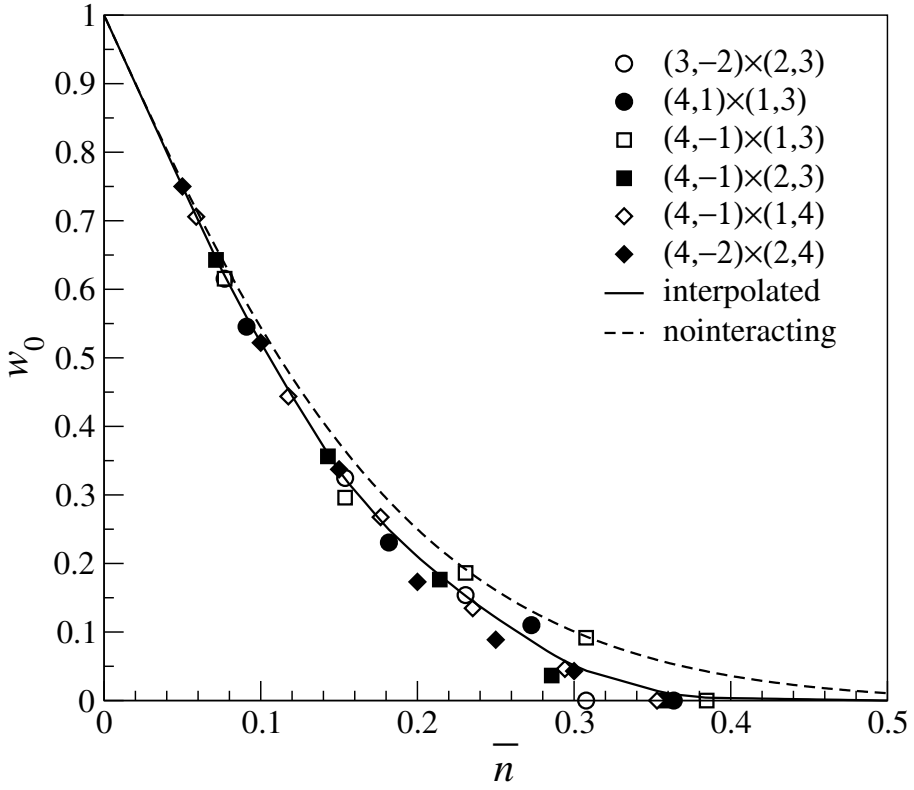

Figure 4.25: Zero-particle weight of the cluster density matrix of a five-site, cross-shaped cluster, for the $(3,-2)\times(2,3)$ (○), $(4,1)\times(1,3)$ (●), $(4,-1)\times(1,3)$ (□), $(4,-1)\times(1,4)$ (■), $(4,-1)\times(2,3)$ (◊) and $(4,-2)\times(2,4)$ (♦) systems of strongly-interacting spinless fermions subject to twist boundary conditions averaging, using $q = 8$ Monkhorst-Pack special-point integration. At $\bar{n} = 0$ and $\bar{n} = \frac{1}{2}$, we know analytically that $w_0 = 1$ and $w_0 = 0$ respectively, and the solid 'curve' interpolates between these two known limits and the equally weighted data points at finite filling fractions $0 < \bar{n} < \frac{1}{2}$. Also shown as the dashed curve is the zero-particle weight of the $(32,-8)\times(8,32)$ (solid line) system of noninteracting spinless fermions with periodic boundary conditions imposed.

Based Density-Matrix Truncation Scheme, developed in Ref. 198 for a noninteracting system, can be applied to a strongly-interacting one. In this section, we present results for a series of calculations to determine the infinite-system limit of the one-particle cluster density-matrix spectra for our strongly-interacting system as a function of filling fraction $\bar{n}$, before going on to discuss the applicability of the Operator-Based Density-Matrix Truncation Scheme.

Though we really do need to worry about the evolution of the structure of $|s_1\rangle$ and $|s_2\rangle$ as a function of $\bar{n}$ in both the noninteracting and strongly-interacting systems, the one-particle weights are ordered by their magnitudes as $w_{s_1} > w_p > w_d > w_{s_2}$ for both systems. But while the noninteracting one-particle weights go down by roughly one order of magnitude as we go through the sequence $w_{s_1} \rightarrow w_p \rightarrow w_d \rightarrow w_{s_2}$, we see from Figure 4.26 that the interacting one-particle weights decay more slowly along this same sequence.

We studied the finite $(3,-2)\times(2,3)$ (●), $(4,1)\times(1,3)$ (○), $(4,-1)\times(1,3)$ (□), $(4,-1)\times(1,4)$ (■), $(4,-1)\times(2,3)$ (◊) and $(4,-2)\times(2,4)$ (⧫) systems subject to twist boundary conditions averaging, using $q = 8$ Monkhorst-Pack special-point integration. At a filling fraction of $\bar{n} = 0$, the system approaches the noninteracting limit, and thus all the one-particle weights are zero. At half-filling, we know from Section 4.7.1.4 that $w_{s_1} = \frac{1}{2}$ and $w_p = w_d = w_{s_2} = 0$. The solid 'curves' in Figure 4.26 interpolate between these two known limits and the equally weighted data points at finite filling fractions $0 < \bar{n} < \frac{1}{2}$. Also shown in Figure 4.26 as the dashed curves are the one-particle weights of the noninteracting $(32,-8)\times(8,32)$ (solid line) system subject to periodic boundary conditions.

In an Operator-Based Density-Matrix Truncation Scheme, we discard one-particle cluster density-matrix eigenstates with very small weights, and keep only the many-

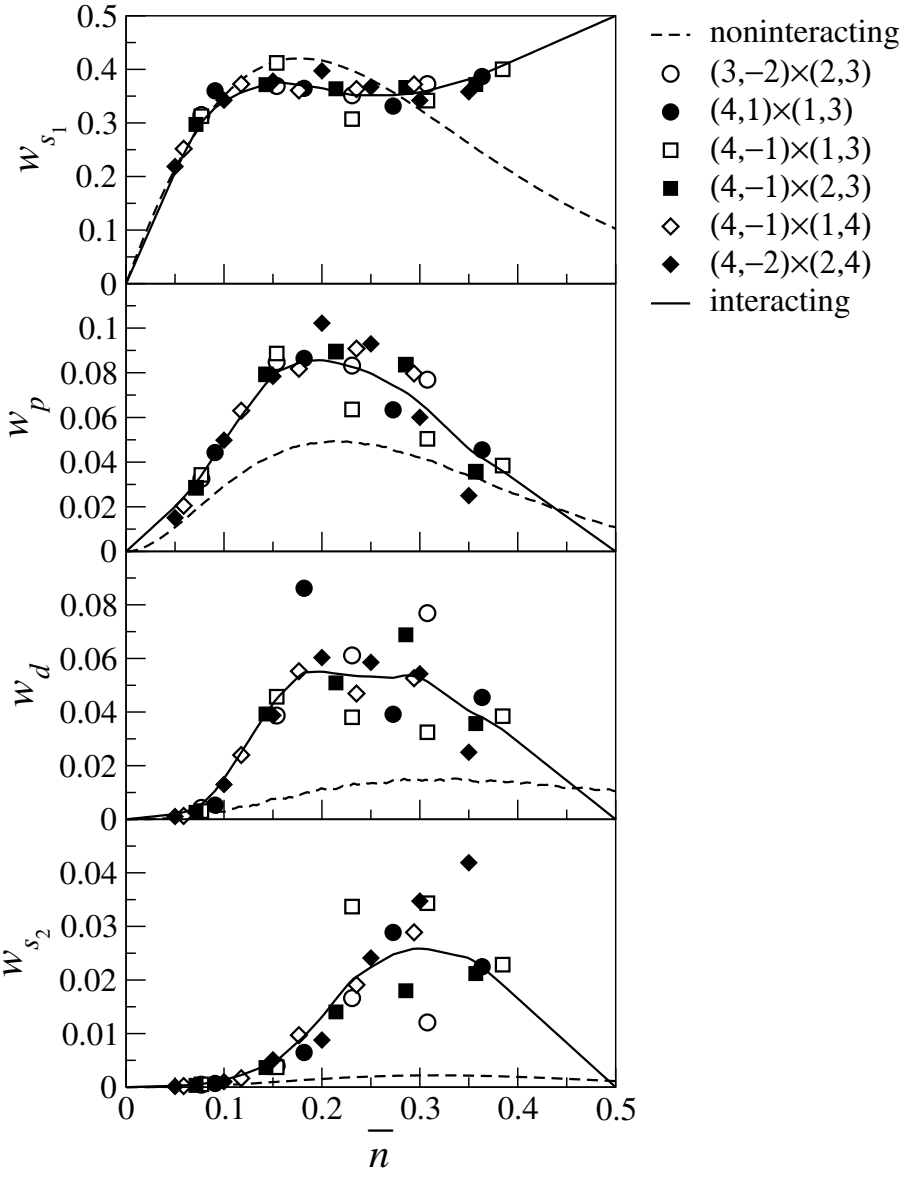

Figure 4.26: One-particle weights of the cluster density matrix of a five-site, cross-shaped cluster, for the $(3,-2)\times(2,3)$ (○), $(4,1)\times(1,3)$ (●), $(4,-1)\times(1,3)$ (□), $(4,-1)\times(1,4)$ (■), $(4,-1)\times(2,3)$ (◊) and $(4,-2)\times(2,4)$ (⧫) systems of strongly-interacting spinless fermions subject to twist boundary conditions averaging, using $q = 8$ Monkhorst-Pack special-point integration.

particle cluster density-matrix eigenstates built from the retained one-particle eigenstates. The sum of weights of the truncated set of cluster density-matrix eigenstates will then be very nearly one, *if* the discarded one-particle weights are all very small compared to the maximum one-particle weight. As we can see from Figure 4.26, the ratio of the largest one-particle weight, w_{s_1}, to the smallest one-particle weight, w_{s_2}, is not large enough for us to justify keeping $|s_1\rangle$ and discarding $|s_2\rangle$, except when the system is very close to half-filled. This calls into question the validity, or value, of the truncation scheme.

4.7.4 Two-Particle Sector of Cluster Density Matrix

Of the two-particle states listed in (4.4.6), the only states which are allowed by the no-nearest-neighbor constraint to appear in the cluster Hilbert space are $|S\rangle$, $|P_\pm\rangle$, $|P''_\pm\rangle$ and $|D\rangle$. We know therefore that the two-particle sector of ρ_C comprises a 1×1 S-diagonal block (with weight w_S), a 1×1 D-diagonal block (with weight w_D), and two degenerate 2×2 P-diagonal blocks (with weights w_{P_1} and w_{P_2}). The two-particle weights are shown as a function of filling $\bar{n}$ in Figure 4.27.

For the finite $(3,-2)\times(2,3)$ (●), $(4,1)\times(1,3)$ (○), $(4,-1)\times(1,3)$ (□), $(4,-1)\times(1,4)$ (■), $(4,-1)\times(2,3)$ (◊) and $(4,-2)\times(2,4)$ (⧫) systems studied, subject to twist boundary conditions averaging, using $q = 8$ Monkhorst-Pack special-point integration, all the two-particle weights are zero at $\bar{n} = 0$ as the systems approach the noninteracting limit. At half-filling $\bar{n} = \frac{1}{2}$, we know from Section 4.7.1.4 that all the two-particle weights are zero. In Figure 4.27, the solid 'curves' interpolates between these two known limits and the equally weighted data points at finite filling fractions $0 < \bar{n} < \frac{1}{2}$.

There are significantly fewer nontrivial two-particle eigenstates of ρ_C than predicted by the combination of one-particle eigenstates. This poses no problem to our Operator-

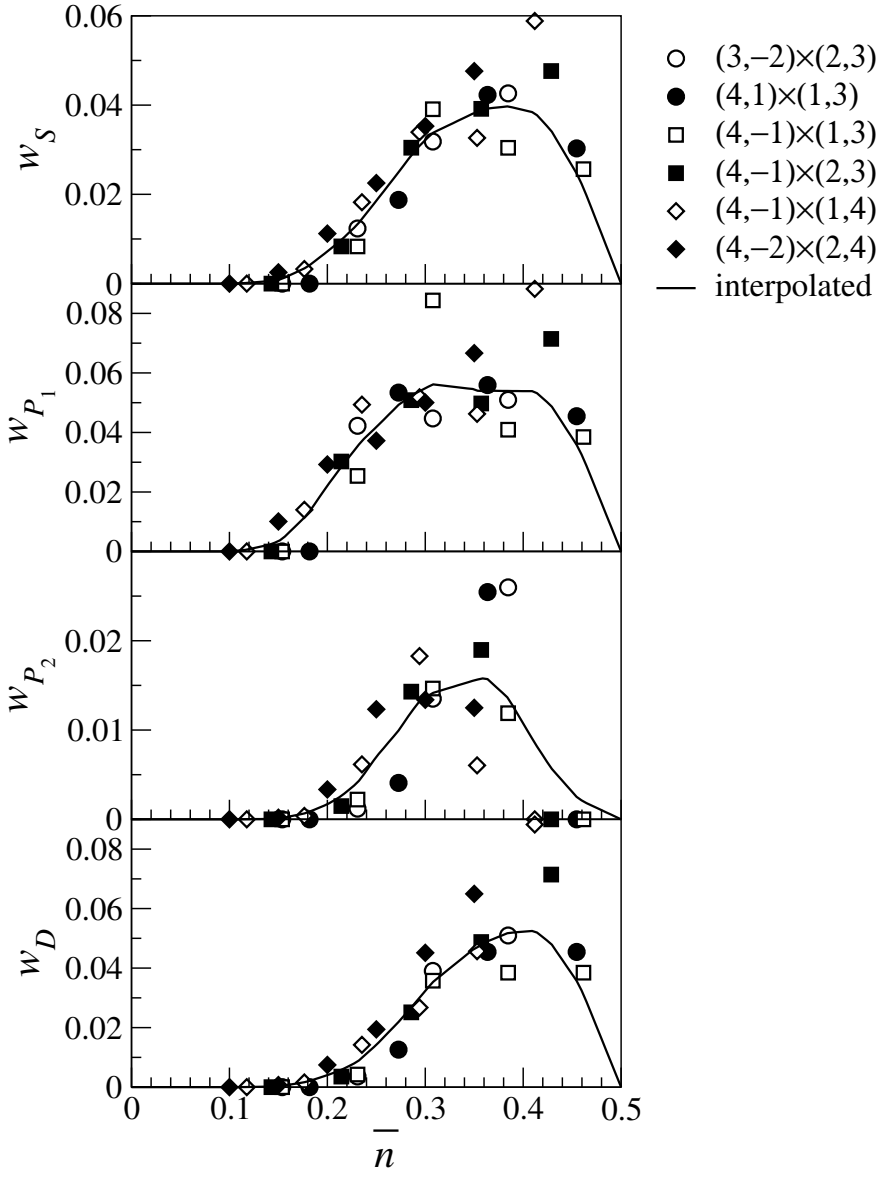

Figure 4.27: Two-particle weights of the cluster density matrix of a five-site, cross-shaped cluster, for the $(3,-2)\times(2,3)$ (○), $(4,1)\times(1,3)$ (●), $(4,-1)\times(1,3)$ (□), $(4,-1)\times(1,4)$ (■), $(4,-1)\times(2,3)$ (◊) and $(4,-2)\times(2,4)$ (⧫) systems of strongly-interacting spinless fermions subject to twist boundary conditions averaging, using $q = 8$ Monkhorst-Pack special-point integration.

Based Density-Matrix Truncation Scheme, if the non-occurring two-particle states are predicted to have small enough weights that they will be excluded by the truncation scheme. However, we find that this is not the case. For example, the two-particle state $|S'\rangle$, which does not occur, is predicted by simple combination of the one-particle states $|s\rangle$ and $|\bar{s}\rangle$ to have a weight comparable to that of the two-particle state $|S\rangle$, which does occur. This means that if we are to push the Operator-Based Density-Matrix Truncation Scheme through, we cannot do so naively.

Of the two-particle weights that are allowed by the no-nearest-neighbor constraint, we expect their weights to follow the sequence $w_{P_1} \gtrsim w_D > w_S$, if they can indeed to thought of products of one-particle states. From Figure 4.27, we indeed observe this sequence of two-particle weights, even though their actual magnitudes (calculated as the product of one-particle weights divided by the zero-particle weight) do not come out right.

CHAPTER 5

CORRELATION DENSITY MATRIX

5.1 A Quick Guide to Chapter 5

As mentioned in the road-map Section 1.4 in Chapter 1, Chapters 5, 6 and 7 constitute the preparatory materials for Chapter 8, where we illustrate a systematic method of extracting various long-range correlations from a many-body ground-state wave function, by performing numerical singular value decomposition on the correlation density matrix. In Section 5.2, we define the correlation density matrix for disjoint clusters separated by a distance r, and give reasons why we think this is the appropriate object to study to systematically determine the order parameters present in a ground-state wave function. I then present example calculations of the correlation density matrix for a one-dimensional Fermi-sea ground state and a one-dimensional superconducting ground state in Sections 5.3 and 5.4 respectively. These calculations are supplementary in nature, and readers whose goal is to get to the interesting physics in Chapter 8 can proceed to Chapter 6 after finishing Section 5.2.

5.2 Motivation

One of the applications of cluster density matrices is as a diagnostic tool for discovering any long range order in a given state of a quantum-mechanical system (spin, boson, fermion), and the associated order parameter. In ED or QMC studies, one typically makes a first guess as to what the order parameter might be, before computing its expectation in the given state. The choice of which expectations to calculate is clearly biased by our perception of what order parameters might be important in the given state. If we start, however, from the cluster density matrix, which contains all operators local to the

cluster, including the order parameters, then no input is required *a priori*, apart from specification of the cluster. As far as order parameters compatible with the choice of the cluster is concerned, this approach is unbiased.

To discover the order parameters in a quantum-mechanical ground state, consider two disjoint clusters a and b, and the combined supercluster ab. In terms of their cluster density matrices ρ^a, ρ^b and ρ^{ab} respectively, we define the correlation density matrix to be

$$\rho^c = \rho^{ab} - \rho^a \otimes \rho^b, \tag{5.2.1}$$

where $\rho^a \otimes \rho^b$ is the direct product of ρ^a and ρ^b. The direct product of $\rho^a : V^a \to V^a$ and $\rho^b : V^b \to V^b$, where V^a is the Fock-Hilbert space of cluster a and V^b is the Fock-Hilbert space of cluster b, is defined such that a state $|x\rangle \otimes |y\rangle \in V^a \otimes V^b$, with $|x\rangle \in V^a$ and $|y\rangle \in V^b$, is mapped to

$$(\rho^a \otimes \rho^b)\,|x\rangle \otimes |y\rangle = (\rho^a\,|x\rangle) \otimes (\rho^b\,|y\rangle). \tag{5.2.2}$$

The matrix element of $\rho^a \otimes \rho^b$ between $|x\rangle \otimes |y\rangle$ and $|x'\rangle \otimes |y'\rangle$ is thus

$$\langle y'| \otimes \langle x'|\,(\rho^a \otimes \rho^b)\,|x\rangle \otimes |y\rangle = \langle x'|\rho^a|x\rangle\,\langle y'|\rho^b|y\rangle\,. \tag{5.2.3}$$

In the case where the cluster a is uncorrelated with the cluster b, the supercluster density matrix ρ^{ab} would simply be $\rho^a \otimes \rho^b$, and ρ^c would be a null matrix. Therefore, the correlation density matrix captures long-range correlations present in ρ^{ab} but not in $\rho^a \otimes \rho^b$. We think of such long-range correlations as a consequence of the independent actions of operators X acting on cluster a, accompanied by the *simultaneous* actions of operators Y acting on cluster b. The structure of these operators is determined by the order parameter they are associated with, and we can determine what they are numerically by performing a singular value decomposition on ρ^c. I will postpone the discussion on

the singular value decomposition to Chapter 6 and Chapter 7. In this chapter, I will only show calculations for the correlation density matrix.

5.3 One-Dimensional Noninteracting Spinless Fermions

In line with our research philosophy of looking at the simplest possible case, before moving on to tackle more complex systems, we look at the one-dimensional noninteracting spinless fermions with nearest-neighbor hopping. For this system, we derived in Chapter 2 a formula (2.4.30) for the cluster density matrix in terms of the cluster Green-function matrix. Whenever helpful, we will compute the cluster and supercluster Green-function matrices, and make use of (2.4.30) to calculate the cluster and supercluster density matrices. This is done in Sections 5.3.1 and 5.3.2 for the (1 + 1) and (2 + 2) superclusters.

However, we find it difficult to extract the asymptotic behaviours of the correlation density matrices for the larger (2 + 2) supercluster as the intercluster separation $r \to \infty$ using the exact formula (2.4.30) between the cluster/supercluster Green-function matrices and the cluster/supercluster density matrices. Therefore, in Section 5.3.3, we calculate the (2 + 2) supercluster density matrix using the method of referencing operators developed in Section 2.3.1, before going on to calculate the (2 + 2) correlation density matrix in Section 5.3.4.

5.3.1 Two Clusters with One Site Each

In this subsection, we calculate the correlation density matrix of the the simplest possible supercluster consisting of two disjoint clusters separated by a distance r, using the exact formula (2.4.30) relating the cluster/supercluster density matrices to the clus-

ter/supercluster Green-function matrices. This simplest (1 + 1) supercluster consists of the sites $j = 0$ (cluster a) and $j = r$ (cluster b), i.e. two clusters of one site each. The occupation number basis states on this (1 + 1) supercluster are written in the form $|\mathbf{n}_a\rangle|\mathbf{n}_b\rangle = |\mathbf{n}_a\mathbf{n}_b\rangle = |n_0 n_r\rangle$, where n_0 is the occupation number of cluster a, and n_r is the occupation number of cluster b.

5.3.1.1 Supercluster Density Matrix

For this (1 + 1) supercluster, the supercluster Green-function matrix is

$$G^{ab} = \begin{bmatrix} \langle c_0^\dagger c_0\rangle & \langle c_0^\dagger c_r\rangle \\ \langle c_r^\dagger c_0\rangle & \langle c_r^\dagger c_r\rangle \end{bmatrix} = \bar{n}\begin{bmatrix} 1 & g(r) \\ g(r) & 1 \end{bmatrix}, \tag{5.3.1}$$

whose eigenvectors

$$|\lambda_+^{ab}\rangle = \tfrac{1}{\sqrt{2}}(1,1), \quad |\lambda_-^{ab}\rangle = \tfrac{1}{\sqrt{2}}(1,-1), \tag{5.3.2}$$

are associated with the eigenvalues

$$\lambda_\pm^{ab} = \bar{n}(1 \pm g(r)). \tag{5.3.3}$$

To compute the supercluster density matrix ρ^{ab}, we need to first evaluate the zero-particle supercluster density-matrix weight

$$w_0^{ab} = \det(\mathbb{1} - G^{ab}) = [1 - \bar{n}(1 + g(r))][1 - \bar{n}(1 - g(r))]. \tag{5.3.4}$$

Following this, we evaluate the one-particle supercluster density-matrix weight

$$w_\pm^{ab} = \bar{n}(1 \pm g(r))[1 - \bar{n}(1 \mp g(r))], \tag{5.3.5}$$

and the single-particle pseudo-energies

$$\varphi_\pm^{ab} = -\log\frac{\lambda_\pm^{ab}}{1 - \lambda_\pm^{ab}} = -\log\frac{\bar{n}(1 \pm g(r))}{1 - \bar{n}(1 \pm g(r))}. \tag{5.3.6}$$

With the eigenvectors given in (5.3.2), we can then write the one-particle sector of ρ^{ab} as

$$\rho_1^{ab} = |\lambda_+^{ab}\rangle\, w_+^{ab}\, \langle\lambda_+^{ab}| + |\lambda_-^{ab}\rangle\, w_-^{ab}\, \langle\lambda_-^{ab}| = \begin{bmatrix} \bar{n} - \bar{n}^2(1 - g^2(r)) & \bar{n}\, g(r) \\ \bar{n}\, g(r) & \bar{n} - \bar{n}^2(1 - g^2(r)) \end{bmatrix}. \quad (5.3.7)$$

For this choice of supercluster, there is only one two-particle supercluster density-matrix eigenstate, with two-particle pseudo-energy

$$\begin{aligned} \Phi_2^{ab} &= \varphi_+^{ab} + \varphi_-^{ab} = -\log \frac{\bar{n}(1 + g(r))}{1 - \bar{n}(1 + g(r))} - \log \frac{\bar{n}(1 - g(r))}{1 - \bar{n}(1 - g(r))} \\ &= -\log \frac{\bar{n}^2(1 - g^2(r))}{\det(\mathbb{1} - G^{ab})}, \end{aligned} \quad (5.3.8)$$

and so the two-particle supercluster density-matrix weight is

$$w_2^{ab} = \det(\mathbb{1} - G^{ab})\, e^{-\Phi_2^{ab}} = \bar{n}^2(1 - g^2(r)). \quad (5.3.9)$$

5.3.1.2 Direct Product Density Matrix

Next, we calculate the cluster density matrices ρ^a and ρ^b, starting from the Green function matrices

$$G^a = \langle c_0^\dagger c_0\rangle = \bar{n} = \langle c_r^\dagger c_r\rangle = G^b. \quad (5.3.10)$$

The zero-particle weights of ρ^a and ρ^b are thus

$$\det(\mathbb{1} - G^a) = 1 - \bar{n} = \det(1 - G^b), \quad (5.3.11)$$

whereas the one-particle sectors of ρ^a and ρ^b are

$$\rho_1^{a,b} = \det(\mathbb{1} - G^{a,b})\, G^{a,b}(\mathbb{1} - G^{a,b})^{-1} = \bar{n}. \quad (5.3.12)$$

Using the above results and (5.2.3), we then find the zero-particle sector of $\rho^a \otimes \rho^b$ to be

$$\langle 00|(\rho^a \otimes \rho^b)|00\rangle = \rho_0^a \rho_0^b = (1 - \bar{n})^2. \quad (5.3.13)$$

For the one-particle sector, we have

$$\langle 10|(\rho^a \otimes \rho^b)|10\rangle = \langle 1|\rho^a|1\rangle \langle 0|\rho^b|0\rangle = \bar{n}(1-\bar{n}); \tag{5.3.14a}$$

$$\langle 10|(\rho^a \otimes \rho^b)|01\rangle = \langle 1|\rho^a|0\rangle \langle 0|\rho^b|1\rangle = 0; \tag{5.3.14b}$$

$$\langle 01|(\rho^a \otimes \rho^b)|10\rangle = \langle 0|\rho^a|1\rangle \langle 1|\rho^b|0\rangle = 0; \tag{5.3.14c}$$

$$\langle 01|(\rho^a \otimes \rho^b)|01\rangle = \langle 0|\rho^a|0\rangle \langle 1|\rho^b|1\rangle = \bar{n}(1-\bar{n}), \tag{5.3.14d}$$

and thus

$$(\rho^a \otimes \rho^b)_1 = \begin{bmatrix} \bar{n}(1-\bar{n}) & 0 \\ 0 & \bar{n}(1-\bar{n}) \end{bmatrix}. \tag{5.3.15}$$

For the two-particle sector, we have

$$\langle 11|(\rho^a \otimes \rho^b)|11\rangle = \langle 1|\rho^a|1\rangle \langle 1|\rho^b|1\rangle = \bar{n}^2. \tag{5.3.16}$$

5.3.1.3 Correlation Density Matrix

Combining (5.3.4), (5.3.7), (5.3.9), (5.3.13), (5.3.15), and (5.3.16), we then calculate the correlation density matrix to be

$$\rho^c = \begin{bmatrix} -\bar{n}^2\, g^2(r) & 0 & 0 & 0 \\ 0 & \bar{n}^2\, g^2(r) & \bar{n}\, g(r) & 0 \\ 0 & \bar{n}\, g(r) & \bar{n}^2\, g^2(r) & 0 \\ 0 & 0 & 0 & -\bar{n}^2\, g^2(r) \end{bmatrix}. \tag{5.3.17}$$

As we can see, this correlation density matrix is traceless, which is theoretically necessary, since $\mathrm{Tr}\,\rho^{ab} = 1$ and $\mathrm{Tr}\,\rho^a \otimes \rho^b = 1$. Also, because $\bar{n} \leq 1$ and $|g(r)| \leq 1$, we find in the one-particle sector that the off-diagonal matrix element has a larger magnitude than the diagonal matrix element. In fact, from the r-dependence of $g(r)$, we see that the off-diagonal matrix element decays as r^{-1}, while the diagonal matrix element decays as r^{-2}.

In addition, because ρ_1^{ab} and $(\rho^a \otimes \rho^b)_1$ are simultaneously diagonalizable, the eigenvectors of ρ_1^c are just those of ρ_1^{ab}, and its eigenvalues are

$$\delta w_+ = \bar{n}\, g(r)(1 + \bar{n}\, g(r)) \quad \text{and} \quad \delta w_- = -\bar{n}\, g(r)(1 - \bar{n}\, g(r)). \tag{5.3.18}$$

5.3.2 Two Clusters with Two Sites Each

In this subsection, we attempt to calculate the correlation density matrix of the the next simplest supercluster, consisting of two symmetric disjoint clusters of two sites each, separated by a distance r, using the exact formula (2.4.30) relating the cluster/supercluster density matrices to the cluster/supercluster Green-function matrices. This (2 + 2) supercluster consists of the sites $j = 0, 1, r, r + 1$, and for the clusters $a = \{0, 1\}$ and $b = \{r, r + 1\}$, we write the occupation number basis states as $|\mathbf{n}_a\rangle\,|\mathbf{n}_b\rangle = |\mathbf{n}_a\mathbf{n}_b\rangle = |n_0 n_1 n_r n_{r+1}\rangle$, where n_0 and n_1 are the occupation numbers on cluster a, and n_r and n_{r+1} are the occupation numbers on cluster b.

In Section 5.3.2.1, we calculate the direct product density matrix of the (2 + 2) supercluster, and proceed to calculate the eigenvalues and eigenstates of the supercluster Green-function matrix in Section 5.3.2.2. Using the analytical formulas for the supercluster Green-function matrix, we then analyze graphically the behaviours of the zero-particle and one-particle supercluster density-matrix weights in Sections 5.3.2.3 and 5.3.2.4. At this point, we realized that investing time manipulating the highly cumbersome algebraic expressions in Section 5.3.2.2 is not profitable, and gave up deriving expressions for the supercluster and correlation density matrices, starting from analytical formulas for the eigenvalues and eigenstates of the supercluster Green-function matrix.

5.3.2.1 Direct Product Density Matrix

For the (2 + 2) supercluster, the cluster Green-function matrices are

$$G^a = \bar{n}\begin{bmatrix} 1 & g(1) \\ g(1) & 1 \end{bmatrix} = G^b, \tag{5.3.19}$$

with eigenvectors

$$|\lambda_{j,+}\rangle = \tfrac{1}{\sqrt{2}}(c_j^\dagger|0\rangle + c_{j+1}^\dagger|0\rangle) \quad \text{and} \quad |\lambda_{j,-}\rangle = \tfrac{1}{\sqrt{2}}(c_j^\dagger|0\rangle - c_{j+1}^\dagger|0\rangle), \tag{5.3.20}$$

corresponding to the eigenvalues

$$\lambda_{j,\pm} = \bar{n}(1 \pm g(1)), \tag{5.3.21}$$

where $j = 0$ for cluster a and $j = r$ for cluster b.

Using the shorthand notation

$$\begin{gathered} g \equiv g(1), \quad p \equiv 1 - g(1), \quad q \equiv 1 + g(1); \\ \mathsf{a} \equiv g(1), \quad \mathsf{b} \equiv g(r), \quad \mathsf{c} \equiv g(r+1), \quad \mathsf{d} \equiv g(r-1), \end{gathered} \tag{5.3.22}$$

we can write the zero-particle weights for ρ^a and ρ^b as

$$\rho_0^a = \det(\mathbb{1} - G^a) = (1 - \bar{n}p)(1 - \bar{n}q) = \det(\mathbb{1} - G^b) = \rho_0^b, \tag{5.3.23}$$

and the one-particle density-matrix weights of ρ^a and ρ^b as

$$\begin{aligned} w_+^a &= \det(\mathbb{1} - G^a)\frac{\lambda_+^a}{1 - \lambda_+^a} = \det(\mathbb{1} - G^a)\frac{\bar{n}(1 + g(1))}{1 - \bar{n}(1 + g(1))} = \bar{n}q(1 - \bar{n}p), \\ w_-^a &= \det(\mathbb{1} - G^a)\frac{\lambda_-^a}{1 - \lambda_-^a} = \det(\mathbb{1} - G^a)\frac{\bar{n}(1 - g(1))}{1 - \bar{n}(1 - g(1))} = \bar{n}p(1 - \bar{n}q), \\ w_+^b &= \det(\mathbb{1} - G^b)\frac{\lambda_+^b}{1 - \lambda_+^b} = \det(\mathbb{1} - G^b)\frac{\bar{n}(1 + g(1))}{1 - \bar{n}(1 + g(1))} = \bar{n}q(1 - \bar{n}p), \\ w_-^b &= \det(\mathbb{1} - G^b)\frac{\lambda_-^b}{1 - \lambda_-^b} = \det(\mathbb{1} - G^b)\frac{\bar{n}(1 - g(1))}{1 - \bar{n}(1 - g(1))} = \bar{n}p(1 - \bar{n}q), \end{aligned} \tag{5.3.24}$$

corresponding to the single-particle pseudo-energies

$$\begin{aligned}\phi^a_+ &= -\log\frac{\bar{n}q}{1-\bar{n}q},\\ \phi^a_- &= -\log\frac{\bar{n}p}{1-\bar{n}p},\\ \phi^b_+ &= -\log\frac{\bar{n}q}{1-\bar{n}q},\\ \phi^b_- &= -\log\frac{\bar{n}p}{1-\bar{n}p}.\end{aligned} \tag{5.3.25}$$

With (5.3.20) and (5.3.24), we write the one-particle sectors of ρ^a and ρ^b out as

$$\rho^a_1 = \begin{bmatrix}\langle 10|\rho^a|10\rangle & \langle 10|\rho^a|01\rangle\\ \langle 01|\rho^a|10\rangle & \langle 01|\rho^a|01\rangle\end{bmatrix} = \begin{bmatrix}\bar{n}(1-\bar{n}pq) & \bar{n}\,g\\ \bar{n}\,g & \bar{n}(1-\bar{n}pq)\end{bmatrix} \tag{5.3.26}$$

and

$$\rho^b_1 = \begin{bmatrix}\langle 10|\rho^b|10\rangle & \langle 10|\rho^b|01\rangle\\ \langle 01|\rho^b|10\rangle & \langle 01|\rho^b|01\rangle\end{bmatrix} = \begin{bmatrix}\bar{n}(1-\bar{n}pq) & \bar{n}\,g\\ \bar{n}\,g & \bar{n}(1-\bar{n}pq)\end{bmatrix} \tag{5.3.27}$$

respectively.

Finally, we find first the two-particle pseudo-energies

$$\begin{aligned}\Phi^a_2 = \varphi^a_+ + \varphi^a_- &= -\log\frac{\bar{n}^2pq}{\det(\mathbb{1}-G^a)},\\ \Phi^b_2 = \varphi^b_+ + \varphi^b_- &= -\log\frac{\bar{n}^2pq}{\det(\mathbb{1}-G^b)},\end{aligned} \tag{5.3.28}$$

using which we write the two-particle density-matrix weights as

$$w^a_2 = \bar{n}^2pq = w^b_2. \tag{5.3.29}$$

Now, we work out the tensor product of ρ^a and ρ^b. In the zero-particle sector, we have

$$\begin{aligned}\langle 0000|(\rho^a\otimes\rho^b)|0000\rangle &= \langle 00|\rho^a|00\rangle\,\langle 00|\rho^b|00\rangle\\ &= (1-\bar{n}p)^2(1-\bar{n}q)^2\\ &= 1-4\bar{n}+2\bar{n}^2(3-\mathsf{a}^2)\\ &\quad -4\bar{n}^3(1-\mathsf{a}^2)+\bar{n}^4(1-2\mathsf{a}^2+\mathsf{a}^4),\end{aligned} \tag{5.3.30}$$

when expanded out in terms of a, b, c and d. For the other sectors of $(\rho^a \otimes \rho^b)$, particle number conservation between the initial state $|\mathbf{n}\rangle$ and final state $|\mathbf{n}'\rangle$ implies the condition

$$n_0 + n_1 = n_0' + n_1', \quad n_r + n_{r+1} = n_r' + n_{r+1}', \tag{5.3.31}$$

and so the only nonzero matrix elements in the one-particle sector are

$$\langle 1000|(\rho^a \otimes \rho^b)|1000\rangle = \langle 10|\rho^a|10\rangle \langle 00|\rho^b|00\rangle = \bar{w}, \tag{5.3.32a}$$

$$\langle 1000|(\rho^a \otimes \rho^b)|0100\rangle = \langle 10|\rho^a|01\rangle \langle 00|\rho^b|00\rangle = \frac{\epsilon}{2}, \tag{5.3.32b}$$

$$\langle 0100|(\rho^a \otimes \rho^b)|1000\rangle = \langle 01|\rho^a|10\rangle \langle 00|\rho^b|00\rangle = \frac{\epsilon}{2}, \tag{5.3.32c}$$

$$\langle 0100|(\rho^a \otimes \rho^b)|0100\rangle = \langle 01|\rho^a|01\rangle \langle 00|\rho^b|00\rangle = \bar{w}, \tag{5.3.32d}$$

$$\langle 0010|(\rho^a \otimes \rho^b)|0010\rangle = \langle 00|\rho^a|00\rangle \langle 10|\rho^b|10\rangle = \bar{w}, \tag{5.3.32e}$$

$$\langle 0010|(\rho^a \otimes \rho^b)|0001\rangle = \langle 00|\rho^a|00\rangle \langle 10|\rho^b|01\rangle = \frac{\epsilon}{2}, \tag{5.3.32f}$$

$$\langle 0001|(\rho^a \otimes \rho^b)|0010\rangle = \langle 00|\rho^a|00\rangle \langle 01|\rho^b|10\rangle = \frac{\epsilon}{2}, \tag{5.3.32g}$$

$$\langle 0001|(\rho^a \otimes \rho^b)|0001\rangle = \langle 00|\rho^a|00\rangle \langle 01|\rho^b|01\rangle = \bar{w}, \tag{5.3.32h}$$

where

$$\begin{aligned} w_- &= \bar{n}p(1-\bar{n}p)(1-\bar{n}q)^2, \quad w_+ = (1-\bar{n}p)^2\bar{n}q(1-\bar{n}q), \\ \bar{w} &= \frac{1}{2}(w_+ + w_-) = \bar{n}(1-\bar{n}pq)(1-\bar{n}p)(1-\bar{n}q), \\ \epsilon &= w_+ - w_- = 2\bar{n}g(1-\bar{n}p)(1-\bar{n}q). \end{aligned} \tag{5.3.33}$$

Again, we can expand the matrix elements with the one-particle sector of the direct product density matrix, in terms of a, b, c and d, by noting that

$$\begin{aligned} \bar{w} &= \bar{n} - \bar{n}^2(3-\mathsf{a}^2) + 3\bar{n}^3(1-\mathsf{a}^2) - \bar{n}^4(1-2\mathsf{a}^2+\mathsf{a}^4), \\ \frac{\epsilon}{2} &= \bar{n}\mathsf{a} - 2\bar{n}^2\mathsf{a} + \bar{n}^3(\mathsf{a}-\mathsf{a}^3). \end{aligned} \tag{5.3.34}$$

In the two-particle sector, the nonzero matrix elements are

$$\langle 1100|(\rho^a \otimes \rho^b)|1100\rangle = \langle 11|\rho^a|11\rangle \langle 00|\rho^b|00\rangle = w_{21}, \tag{5.3.35a}$$

$$\langle 1010|(\rho^a \otimes \rho^b)|1010\rangle = \langle 10|\rho^a|10\rangle \langle 10|\rho^b|10\rangle = w_{22}, \tag{5.3.35b}$$

$$\langle 1010|(\rho^a \otimes \rho^b)|0110\rangle = \langle 10|\rho^a|01\rangle \langle 10|\rho^b|10\rangle = w_{23}, \tag{5.3.35c}$$

$$\langle 1010|(\rho^a \otimes \rho^b)|1001\rangle = \langle 10|\rho^a|10\rangle \langle 10|\rho^b|01\rangle = w_{23}, \tag{5.3.35d}$$

$$\langle 1010|(\rho^a \otimes \rho^b)|0101\rangle = \langle 10|\rho^a|01\rangle \langle 10|\rho^b|01\rangle = w_{24}, \tag{5.3.35e}$$

$$\langle 1001|(\rho^a \otimes \rho^b)|1010\rangle = \langle 10|\rho^a|10\rangle \langle 01|\rho^b|10\rangle = w_{23}, \tag{5.3.35f}$$

$$\langle 1001|(\rho^a \otimes \rho^b)|1001\rangle = \langle 10|\rho^a|10\rangle \langle 01|\rho^b|01\rangle = w_{22}, \tag{5.3.35g}$$

$$\langle 1001|(\rho^a \otimes \rho^b)|0110\rangle = \langle 10|\rho^a|01\rangle \langle 01|\rho^b|10\rangle = w_{24}, \tag{5.3.35h}$$

$$\langle 1001|(\rho^a \otimes \rho^b)|0101\rangle = \langle 10|\rho^a|01\rangle \langle 01|\rho^b|01\rangle = w_{23}, \tag{5.3.35i}$$

$$\langle 0110|(\rho^a \otimes \rho^b)|1010\rangle = \langle 01|\rho^a|10\rangle \langle 10|\rho^b|10\rangle = w_{23}, \tag{5.3.35j}$$

$$\langle 0110|(\rho^a \otimes \rho^b)|1001\rangle = \langle 01|\rho^a|10\rangle \langle 10|\rho^b|01\rangle = w_{24}, \tag{5.3.35k}$$

$$\langle 0110|(\rho^a \otimes \rho^b)|0110\rangle = \langle 01|\rho^a|01\rangle \langle 10|\rho^b|10\rangle = w_{22}, \tag{5.3.35l}$$

$$\langle 0110|(\rho^a \otimes \rho^b)|0101\rangle = \langle 01|\rho^a|01\rangle \langle 10|\rho^b|01\rangle = w_{23}, \tag{5.3.35m}$$

$$\langle 0101|(\rho^a \otimes \rho^b)|1010\rangle = \langle 01|\rho^a|10\rangle \langle 01|\rho^b|10\rangle = w_{24}, \tag{5.3.35n}$$

$$\langle 0101|(\rho^a \otimes \rho^b)|1001\rangle = \langle 01|\rho^a|10\rangle \langle 01|\rho^b|01\rangle = w_{23}, \tag{5.3.35o}$$

$$\langle 0101|(\rho^a \otimes \rho^b)|0110\rangle = \langle 01|\rho^a|01\rangle \langle 01|\rho^b|10\rangle = w_{23}, \tag{5.3.35p}$$

$$\langle 0101|(\rho^a \otimes \rho^b)|0101\rangle = \langle 01|\rho^a|01\rangle \langle 01|\rho^b|01\rangle = w_{22}, \tag{5.3.35q}$$

$$\langle 0011|(\rho^a \otimes \rho^b)|0011\rangle = \langle 00|\rho^a|00\rangle \langle 11|\rho^b|11\rangle = w_{21}, \tag{5.3.35r}$$

where the four independent matrix elements are

$$\begin{aligned}
w_{21} &= \bar{n}^2 pq(1-\bar{n}p)(1-\bar{n}q) = \bar{n}^2(1-\mathsf{a}^2) - 2\bar{n}^3(1-\mathsf{a}^2) + \bar{n}^4(1-\mathsf{a}^2)^2, \\
w_{22} &= \bar{n}^2(1-\bar{n}pq)^2 = \bar{n}^2 - 2\bar{n}^3(1-\mathsf{a}^2) + \bar{n}^4(1-\mathsf{a}^2)^2, \\
w_{23} &= \bar{n}^2 g(1-\bar{n}pq) = \bar{n}^2\mathsf{a} - \bar{n}^3\mathsf{a}(1-\mathsf{a}^2), \\
w_{24} &= \bar{n}^2 g^2 = \bar{n}^2\mathsf{a}^2.
\end{aligned} \tag{5.3.36}$$

In the three-particle sector, the nonzero matrix elements are

$$\langle 1110|(\rho^a \otimes \rho^b)|1110\rangle = \langle 11|\rho^a|11\rangle \langle 10|\rho^b|10\rangle = w_{31}, \tag{5.3.37a}$$

$$\langle 1110|(\rho^a \otimes \rho^b)|1101\rangle = \langle 11|\rho^a|11\rangle \langle 10|\rho^b|01\rangle = w_{32}, \tag{5.3.37b}$$

$$\langle 1101|(\rho^a \otimes \rho^b)|1110\rangle = \langle 11|\rho^a|11\rangle \langle 01|\rho^b|10\rangle = w_{32}, \tag{5.3.37c}$$

$$\langle 1101|(\rho^a \otimes \rho^b)|1101\rangle = \langle 11|\rho^a|11\rangle \langle 01|\rho^b|01\rangle = w_{31}, \tag{5.3.37d}$$

$$\langle 1011|(\rho^a \otimes \rho^b)|1011\rangle = \langle 10|\rho^a|10\rangle \langle 11|\rho^b|11\rangle = w_{31}, \tag{5.3.37e}$$

$$\langle 1011|(\rho^a \otimes \rho^b)|0111\rangle = \langle 10|\rho^a|01\rangle \langle 11|\rho^b|11\rangle = w_{32}, \tag{5.3.37f}$$

$$\langle 0111|(\rho^a \otimes \rho^b)|1011\rangle = \langle 01|\rho^a|10\rangle \langle 11|\rho^b|11\rangle = w_{32}, \tag{5.3.37g}$$

$$\langle 0111|(\rho^a \otimes \rho^b)|0111\rangle = \langle 01|\rho^a|01\rangle \langle 11|\rho^b|11\rangle = w_{31}, \tag{5.3.37h}$$

where the two independent matrix elements are

$$\begin{aligned} w_{31} &= \bar{n}^3 pq(1 - \bar{n}pq) = \bar{n}^3(1 - \mathsf{a}^2) - \bar{n}^4(1 - 2\mathsf{a}^2 + \mathsf{a}^4), \\ w_{32} &= \bar{n}^3 gpq = \bar{n}^3(\mathsf{a} - \mathsf{a}^3). \end{aligned} \tag{5.3.38}$$

Finally, the four-particle sector is given by

$$\langle 1111|(\rho^a \otimes \rho^b)|1111\rangle = \langle 11|\rho^a|11\rangle \langle 11|\rho^b|11\rangle = \bar{n}^4 p^2 q^2 \bar{n}^4(1 - 2\mathsf{a}^2 + \mathsf{a}^4). \tag{5.3.39}$$

5.3.2.2 Eigenvalues and Eigenvectors of the Supercluster Green-Function Matrix

For the supercluster ab, the Green-function matrix is given by

$$G^{ab} = \bar{n} \begin{bmatrix} 1 & g(1) & g(r) & g(r+1) \\ g(1) & 1 & g(r-1) & g(r) \\ g(r) & g(r-1) & 1 & g(1) \\ g(r+1) & g(r) & g(1) & 1 \end{bmatrix} = \bar{n} \begin{bmatrix} 1 & \mathsf{a} & \mathsf{b} & \mathsf{c} \\ \mathsf{a} & 1 & \mathsf{d} & \mathsf{b} \\ \mathsf{b} & \mathsf{d} & 1 & \mathsf{a} \\ \mathsf{c} & \mathsf{b} & \mathsf{a} & 1 \end{bmatrix}, \tag{5.3.40}$$

whose eigenvalues are

$$\lambda_1^{ab} = \frac{\bar{n}}{2}\left\{2 + (\mathsf{c}+\mathsf{d}) - \sqrt{4(\mathsf{a}+\mathsf{b})^2 + (\mathsf{d}-\mathsf{c})^2}\right\}, \tag{5.3.41a}$$

$$\lambda_2^{ab} = \frac{\bar{n}}{2}\left\{2 - (\mathsf{c}+\mathsf{d}) - \sqrt{4(\mathsf{a}-\mathsf{b})^2 + (\mathsf{d}-\mathsf{c})^2}\right\}, \tag{5.3.41b}$$

$$\lambda_3^{ab} = \frac{\bar{n}}{2}\left\{2 - (\mathsf{c}+\mathsf{d}) + \sqrt{4(\mathsf{a}-\mathsf{b})^2 + (\mathsf{d}-\mathsf{c})^2}\right\}, \tag{5.3.41c}$$

$$\lambda_4^{ab} = \frac{\bar{n}}{2}\left\{2 + (\mathsf{c}+\mathsf{d}) + \sqrt{4(\mathsf{a}+\mathsf{b})^2 + (\mathsf{d}-\mathsf{c})^2}\right\}. \tag{5.3.41d}$$

These can be written as

$$\lambda_1^{ab} = \frac{\bar{n}}{2}\left\{2 + D - \sqrt{4A^2 + C^2}\right\}, \tag{5.3.42a}$$

$$\lambda_2^{ab} = \frac{\bar{n}}{2}\left\{2 - D - \sqrt{4B^2 + C^2}\right\}, \tag{5.3.42b}$$

$$\lambda_3^{ab} = \frac{\bar{n}}{2}\left\{2 - D + \sqrt{4B^2 + C^2}\right\}, \tag{5.3.42c}$$

$$\lambda_4^{ab} = \frac{\bar{n}}{2}\left\{2 + D + \sqrt{4A^2 + C^2}\right\}, \tag{5.3.42d}$$

if we note that the matrix elements a, b, c and d only appear in the combinations

$$A = \mathsf{a} + \mathsf{b}, \quad B = \mathsf{a} - \mathsf{b}, \quad C = \mathsf{d} - \mathsf{c}, \quad D = \mathsf{d} + \mathsf{c}. \tag{5.3.43}$$

In terms of A, B, C and D, the corresponding unnormalized eigenvectors produced by *Mathematica* are

$$|\tilde{\lambda}_1^{ab}\rangle = \left(1, \frac{C - \sqrt{4A^2 + C^2}}{2A}, \frac{C - \sqrt{4A^2 + C^2}}{2A}, 1\right), \tag{5.3.44a}$$

$$|\tilde{\lambda}_2^{ab}\rangle = \left(1, -\frac{C + \sqrt{4B^2 + C^2}}{2B}, \frac{C + \sqrt{4B^2 + C^2}}{2B}, -1\right), \tag{5.3.44b}$$

$$|\tilde{\lambda}_3^{ab}\rangle = \left(1, -\frac{C - \sqrt{4B^2 + C^2}}{2B}, \frac{C - \sqrt{4B^2 + C^2}}{2B}. - 1\right), \tag{5.3.44c}$$

$$|\tilde{\lambda}_4^{ab}\rangle = \left(1, \frac{C + \sqrt{4A^2 + C^2}}{2A}, \frac{C + \sqrt{4A^2 + C^2}}{2A}, 1\right). \tag{5.3.44d}$$

To construct the one-particle sector of ρ^{ab}, we need these eigenvectors to be normalized.

Computing the norms

$$\langle\tilde{\lambda}_1^{ab}|\tilde{\lambda}_1^{ab}\rangle = \frac{(4A^2+C^2) - C\sqrt{4A^2+C^2}}{A^2} = \frac{E^2-CE}{A^2} = \frac{E(E-C)}{A^2}, \tag{5.3.45a}$$

$$\langle\tilde{\lambda}_2^{ab}|\tilde{\lambda}_2^{ab}\rangle = \frac{(4B^2+C^2) + C\sqrt{4B^2+C^2}}{B^2} = \frac{F^2+CF}{B^2} = \frac{F(F+C)}{B^2}, \tag{5.3.45b}$$

$$\langle\tilde{\lambda}_3^{ab}|\tilde{\lambda}_3^{ab}\rangle = \frac{(4B^2+C^2) - C\sqrt{4B^2+C^2}}{B^2} = \frac{F^2-CF}{B^2} = \frac{F(F-C)}{B^2}, \tag{5.3.45c}$$

$$\langle\tilde{\lambda}_4^{ab}|\tilde{\lambda}_4^{ab}\rangle = \frac{(4A^2+C^2) + C\sqrt{4A^2+C^2}}{A^2} = \frac{E^2+CE}{A^2} = \frac{E(E+C)}{A^2}, \tag{5.3.45d}$$

where

$$E = \sqrt{4A^2+C^2}, \quad F = \sqrt{4B^2+C^2}, \tag{5.3.46}$$

we then obtain the normalized eigenvectors

$$|\lambda_1^{ab}\rangle = \left(\frac{A}{\sqrt{E(E-C)}}, -\frac{\sqrt{E-C}}{2\sqrt{E}}, -\frac{\sqrt{E-C}}{2\sqrt{E}}, \frac{A}{\sqrt{E(E-C)}}\right), \tag{5.3.47a}$$

$$|\lambda_2^{ab}\rangle = \left(\frac{B}{\sqrt{F(F+C)}}, -\frac{\sqrt{F+C}}{2\sqrt{F}}, \frac{\sqrt{F+C}}{2\sqrt{F}}, -\frac{B}{\sqrt{F(F+C)}}\right), \tag{5.3.47b}$$

$$|\lambda_3^{ab}\rangle = \left(\frac{B}{\sqrt{F(F-C)}}, \frac{\sqrt{F-C}}{2\sqrt{F}}, -\frac{\sqrt{F-C}}{2\sqrt{F}}, -\frac{B}{\sqrt{F(F-C)}}\right), \tag{5.3.47c}$$

$$|\lambda_4^{ab}\rangle = \left(\frac{A}{\sqrt{E(E+C)}}, \frac{\sqrt{E+C}}{2\sqrt{E}}, \frac{\sqrt{E+C}}{2\sqrt{E}}, \frac{A}{\sqrt{E(E+C)}}\right), \tag{5.3.47d}$$

whose exterior products are

$$|\lambda_1^{ab}\rangle\langle\lambda_1^{ab}| = \begin{bmatrix} \frac{A^2}{E(E-C)} & -\frac{A}{2E} & -\frac{A}{2E} & \frac{A^2}{E(E-C)} \\ -\frac{A}{2E} & \frac{E-C}{4E} & \frac{E-C}{4E} & -\frac{A}{2E} \\ -\frac{A}{2E} & \frac{E-C}{4E} & \frac{E-C}{4E} & -\frac{A}{2E} \\ \frac{A^2}{E(E-C)} & -\frac{A}{2E} & -\frac{A}{2E} & \frac{A^2}{E(E-C)} \end{bmatrix}, \tag{5.3.48a}$$

$$|\lambda_2^{ab}\rangle\langle\lambda_2^{ab}| = \begin{bmatrix} \frac{B^2}{F(F+C)} & -\frac{B}{2F} & \frac{B}{2F} & -\frac{B^2}{F(F+C)} \\ -\frac{B}{2F} & \frac{F+C}{4F} & -\frac{F+C}{4F} & \frac{B}{2F} \\ \frac{B}{2F} & -\frac{F+C}{4F} & \frac{F+C}{4F} & -\frac{B}{2F} \\ -\frac{B^2}{F(F+C)} & \frac{B}{2F} & -\frac{B}{2F} & \frac{B^2}{F(F+C)} \end{bmatrix}, \tag{5.3.48b}$$

$$|\lambda_3^{ab}\rangle\langle\lambda_3^{ab}| = \begin{bmatrix} \frac{B^2}{F(F-C)} & \frac{B}{2F} & -\frac{B}{2F} & -\frac{B^2}{F(F-C)} \\ \frac{B}{2F} & \frac{F-C}{4F} & -\frac{F-C}{4F} & -\frac{B}{2F} \\ -\frac{B}{2F} & -\frac{F-C}{4F} & \frac{F-C}{4F} & \frac{B}{2F} \\ -\frac{B^2}{F(F-C)} & -\frac{B}{2F} & \frac{B}{2F} & \frac{B^2}{F(F-C)} \end{bmatrix}, \tag{5.3.48c}$$

$$|\lambda_4^{ab}\rangle\langle\lambda_4^{ab}| = \begin{bmatrix} \frac{A^2}{E(E+C)} & \frac{A}{2E} & \frac{A}{2E} & \frac{A^2}{E(E+C)} \\ \frac{A}{2E} & \frac{E+C}{4E} & \frac{E+C}{4E} & \frac{A}{2E} \\ \frac{A}{2E} & \frac{E+C}{4E} & \frac{E+C}{4E} & \frac{A}{2E} \\ \frac{A^2}{E(E+C)} & \frac{A}{2E} & \frac{A}{2E} & \frac{A^2}{E(E+C)} \end{bmatrix}. \tag{5.3.48d}$$

Our intention is to use these to evaluate the full supercluster density matrix, and thence the correlation density matrix.

5.3.2.3 Graphical Analysis of Zero-Particle Supercluster Density-Matrix Weight

Unlike the case of the (1 + 1) supercluster, the analytical expressions for the (2 + 2) supercluster density-matrix weights are messy. Although we understand completely the asymptotic behaviour of the reduced two-point function $g(r)$, and hence what asymptotic behaviours to expect for each of the supercluster density-matrix eigenvalues, it would still take a forbidding amount of work to see for ourselves where in the forest of algebraic expressions these asymptotic behaviours come from. However, it does not take us very long to write an Octave script to compute the supercluster Green-function matrix eigenvalues λ^{ab} as a function of filling fraction $\bar{n}$ and cluster separation r, and therefrom the supercluster density-matrix weights. Therefore, we graph them, either as functions of $\bar{n}$, or of r, and see how our expectations about their asymptotic behaviours are realized.

We begin by looking at the zero-particle weight w_0^{ab} of ρ^{ab}, which is given by

$$w_0^{ab} = \det(\mathbb{1} - G^{ab}) = (1 - \lambda_1^{ab})(1 - \lambda_2^{ab})(1 - \lambda_3^{ab})(1 - \lambda_4^{ab}). \tag{5.3.49}$$

We plot the zero-particle weight w_0^{ab} as a function of the separation r between clusters (Figure 5.1), for various filling fractions, and as a function of the filling fraction (Figure 5.2), for various cluster separations.

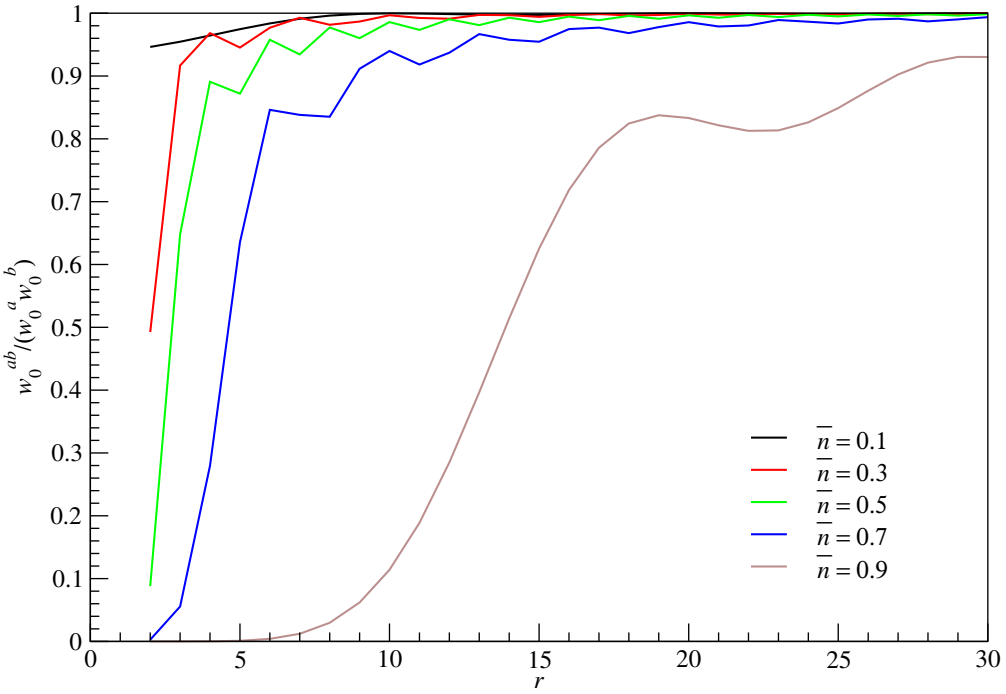

Figure 5.1: Plot of the ratio $w_0^{ab}/(w_0^a w_0^b)$ of a $(2+2)$ supercluster, as a function of cluster separation $r \geq 2$, for various filling fractions in a one-dimensional system of noninteracting spinless fermions.

5.3.2.4 Graphical Analysis of One-Particle Supercluster Density-Matrix Weights

The one-particle weights of the supercluster density matrix ρ^{ab} are given by

$$w_1^{ab} = \lambda_1^{ab}(1-\lambda_2^{ab})(1-\lambda_3^{ab})(1-\lambda_4^{ab}), \tag{5.3.50a}$$

$$w_2^{ab} = (1-\lambda_1^{ab})\lambda_2^{ab}(1-\lambda_3^{ab})(1-\lambda_4^{ab}), \tag{5.3.50b}$$

$$w_3^{ab} = (1-\lambda_1^{ab})(1-\lambda_2^{ab})\lambda_3^{ab}(1-\lambda_4^{ab}), \tag{5.3.50c}$$

$$w_4^{ab} = (1-\lambda_1^{ab})(1-\lambda_2^{ab})(1-\lambda_3^{ab})\lambda_4^{ab}. \tag{5.3.50d}$$

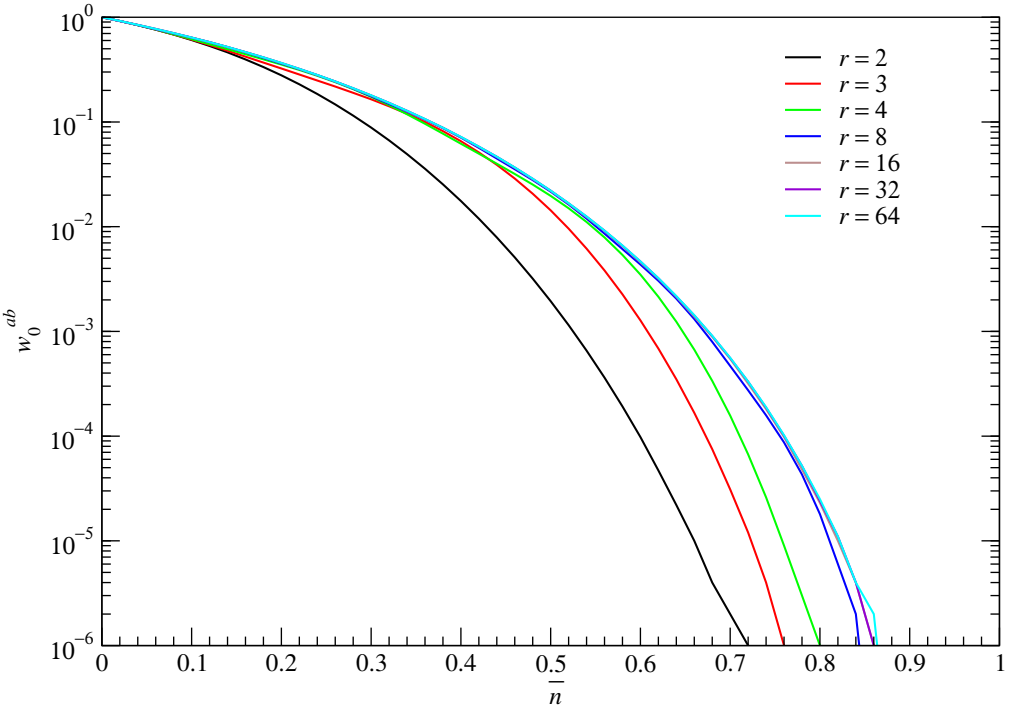

Figure 5.2: Plot of the zero-particle weight w_0^{ab} of the density matrix of a (2 + 2) supercluster, as a function of filling fraction $\bar{n}$, for various cluster separations $2 \leq r \leq 64$ in a one-dimensional system of noninteracting spinless fermions.

Because of their algebraic structures in (5.3.42), two of these weights (w_1^{ab} and w_2^{ab}, shown in Figure 5.3 for $\bar{n} = \frac{1}{2}$) are small, and the other two (w_3^{ab} and w_4^{ab}, shown in Figure 5.4 for $\bar{n} = \frac{1}{2}$) are large.

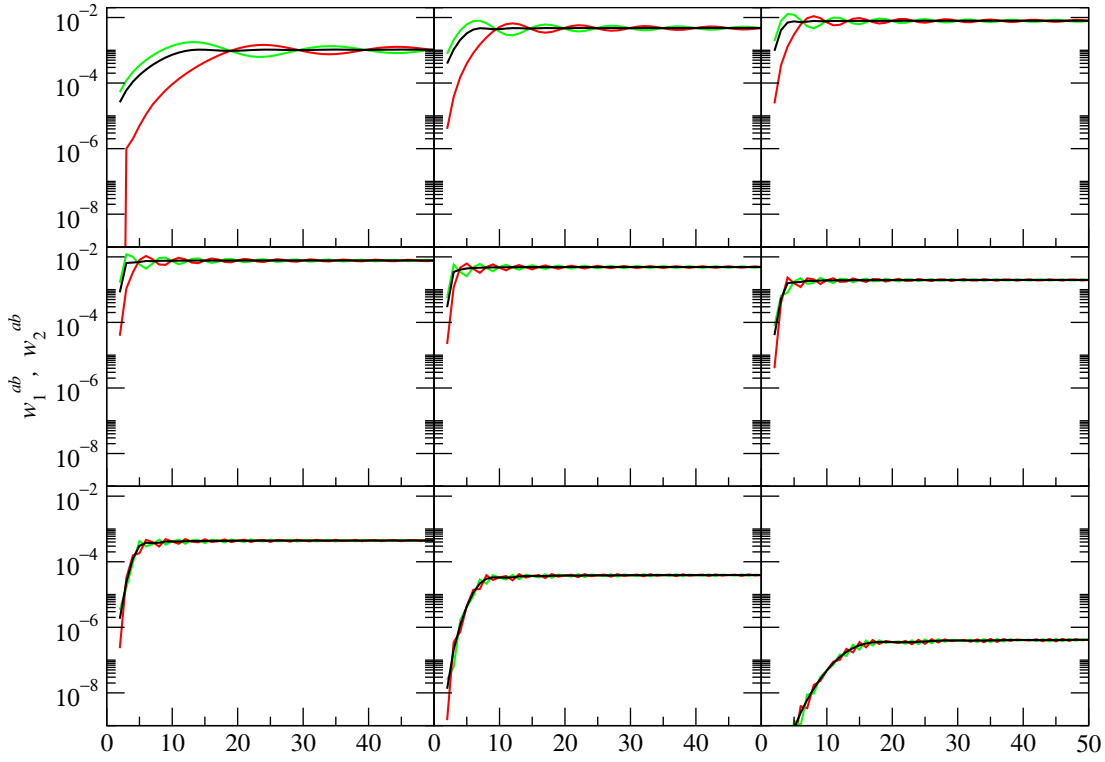

Figure 5.3: Plot of the two small one-particle weights w_1^{ab} (red curve) and w_2^{ab} (green curve), as functions of the cluster separation r, of the supercluster density matrix ρ^{ab} of the $(2+2)$ supercluster in a one-dimensional system of noninteracting spinless fermions at half-filling. Also shown, as the black curve, is the average of the two one-particle weights. The filling fractions are (top row, left to right) $\bar{n} = 0.1, 0.2, 0.3$, (middle row, left to right) $\bar{n} = 0.4, 0.5, 0.6$, and (bottom row, left to right) $\bar{n} = 0.7, 0.8, 0.9$.

In Section 2.5.2, we learned that the particle-hole symmetry of the half-filled chain of noninteracting spinless fermions manifests itself as the pairing between all one-particle weights of the density matrix of a contiguous cluster, such that for every one-particle weight w_1 we find in the spectrum of the cluster density matrix, we can find another

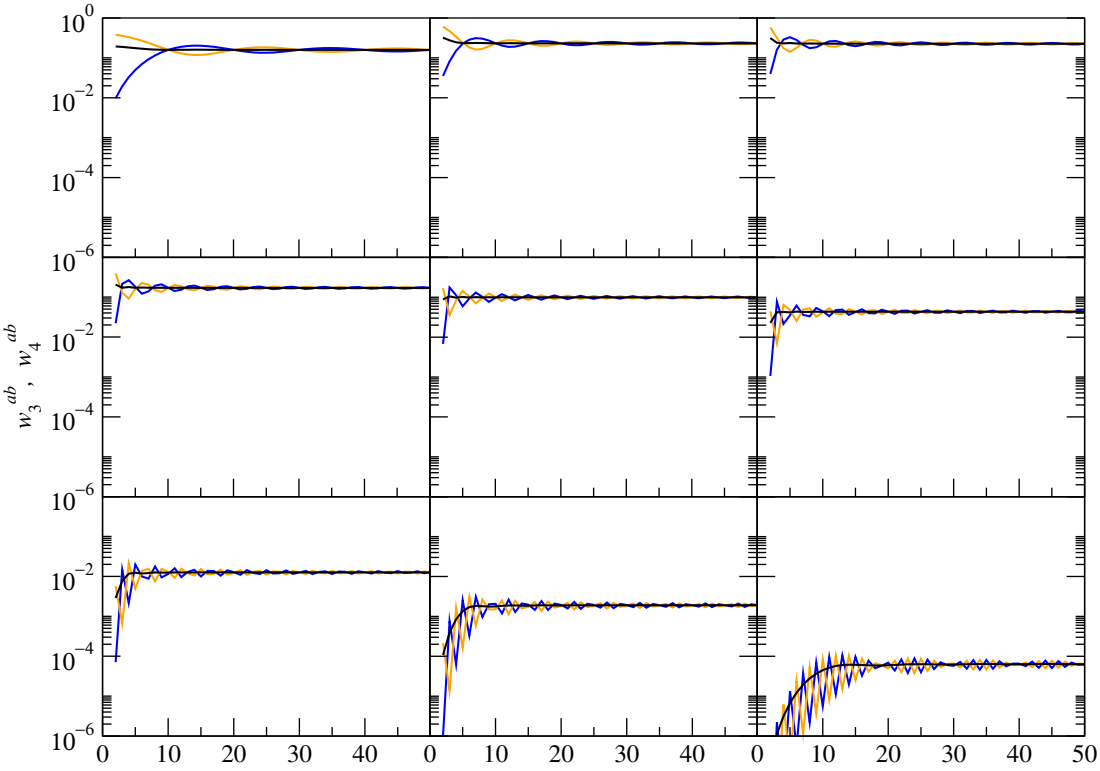

Figure 5.4: Plot of the two large one-particle weights w_3^{ab} (blue curve) and w_4^{ab} (orange curve), as functions of the cluster separation r, of the supercluster density matrix ρ^{ab} of the $(2+2)$ supercluster in a one-dimensional system of noninteracting spinless fermions at half-filling. Also shown, as the black curve, is the average of the two one-particle weights. The filling fractions are (top row, left to right) $\bar{n} = 0.1, 0.2, 0.3$, (middle row, left to right) $\bar{n} = 0.4, 0.5, 0.6$, and (bottom row, left to right) $\bar{n} = 0.7, 0.8, 0.9$.

one-particle weight w_1^*, with the property that

$$w_1 w_1^* = \mathscr{Q}^{-2}, \tag{5.3.51}$$

where $\mathscr{Q}^{-1}$ is the normalization constant of the cluster density matrix.

For the (2 + 2) cluster in a half-filled chain, the normalization constant $\mathscr{Q}^{-1}$ of the supercluster density matrix exhibits Friedel oscillations, when plotted as a function of the cluster separation r. Worried that this Friedel oscillation might be so strong that it obscures any particle-hole symmetry between the one-particle supercluster density-matrix weights, we calculate instead the ratio $\omega = (w_1^{ab} + w_2^{ab})/(w_3^{ab} + w_4^{ab})$ of average weights, with the hope that this quantity, which we plot in Figure 5.5, is less severely affected by Friedel oscillations. From the figure, we find that $\omega(1 - \bar{n}) \approx \omega(\bar{n})$, with better and better agreement as r increases.

There are two possibilities here: (1) $(w_1 + w_2)$ and $(w_3 + w_4)$ are separately particle-hole symmetric; or (2) neither are particle-hole symmetric, but the ratio is nonetheless. It turns out, as we start looking at the structure of w_l^{ab}, $l = 1, 2, 3, 4$, as functions of the filling fraction $\bar{n}$ (Figure 5.6), that the second case is true. What this means is that, unlike in a contiguous cluster of four sites in a half-filled chain, where the four one-particle cluster density-matrix weights $w_1 > w_2 > w_3 > w_4$ satisfy the particle-hole symmetry relation

$$w_1 w_4 = w_2 w_3 = \mathscr{Q}^{-2}, \tag{5.3.52}$$

for two disjoint clusters in a half-filled chain, with one-particle weights $w_1 > w_2 > w_3 > w_4$, we cannot identity w_4 as the particle-hole conjugate of w_1, and w_3 as the particle-hole conjugate of w_2.

From Figure 5.6, we also see that for small r, the four one-particle weights are spaced out more or less logarithmically, but as r gets larger, the four one-particle weights

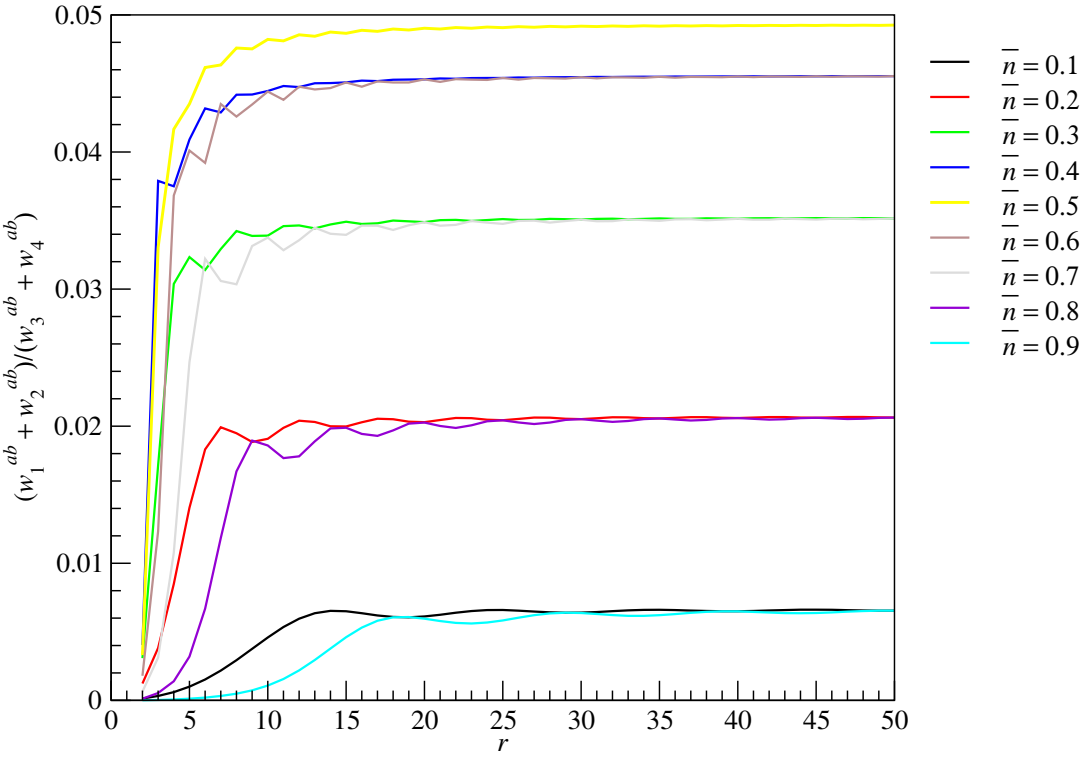

Figure 5.5: Plot of the ratio $\omega = (w_1^{ab} + w_2^{ab})/(w_3^{ab} + w_4^{ab})$ of average weights for the (2 + 2) supercluster density matrix in a one-dimensional system of noninteracting spinless fermions.

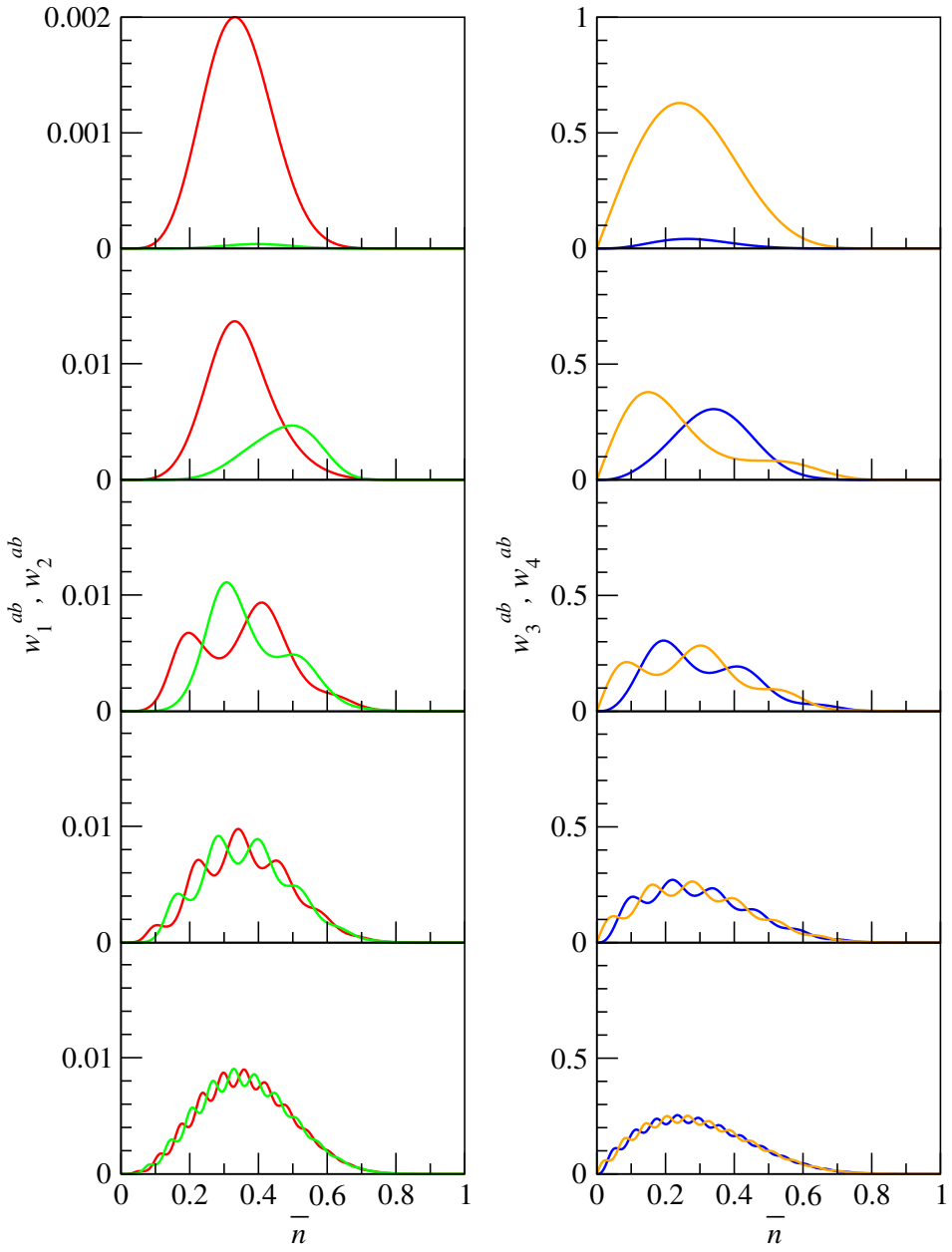

Figure 5.6: Plot of the small (left column) one-particle weights w_1^{ab} (red curves), w_2^{ab} (green curves), and the large (right column) one-particle weights w_3^{ab} (blue curves), w_4^{ab} (orange curves), of the (2 + 2) supercluster density matrix in a one-dimensional system of noninteracting spinless fermions, as functions of the filling fraction $\bar{n}$. The cluster separations are, from the top row down, $r = 2, 4, 8, 16, 32$.

become grouped into two pairs. As we can see, for large r, the relative order of the weights in each pair alternates as a result of Friedel oscillations, and we find it more informative to look at the average weights of each pair, as shown in Figure 5.7.

As we can see from Figure 5.7, the dependence of the average weights on $\bar{n}$ approaches a limiting form as $r \to \infty$, and for this system, this limit is more or less reached between $r = 8$ and $r = 16$. We can also see that the two average weights are not peaked at the same filling fraction: the larger average weight peaks at $\bar{n} \sim 0.25$, whereas the smaller average weight peaks at $\bar{n} \sim 0.34$.

5.3.3 The (2 + 2) Supercluster Density Matrix

With the exact expressions in (5.3.42) and (5.3.47) for the eigenvalues λ_l^{ab} and the eigenvectors $|\lambda_l^{ab}\rangle$ respectively for the supercluster Green-function matrix, it is in principle possible to write down exact expressions for the matrix elements of ρ^c, in the same way that we have done for the (1 + 1) supercluster. However, it is an algebraic nightmare to work with these exact expressions and compute

$$\rho^{ab} = \sum_l |\lambda_l^{ab}\rangle \, w_l^{ab}(\lambda_l^{ab}) \, \langle \lambda_l^{ab}| \, . \tag{5.3.53}$$

Approximate treatment by expanding λ_l^{ab} and $|\lambda_l^{ab}\rangle$ in powers of $\bar{n}$ and r^{-1} is also treacherously tedious. We therefore resort to calculating ρ^c exactly using the method of referencing operators introduced in Chapter 2, and then perform approximate analysis for the matrix elements.

Performing this referencing-operator calculation one sector at a time, we find the

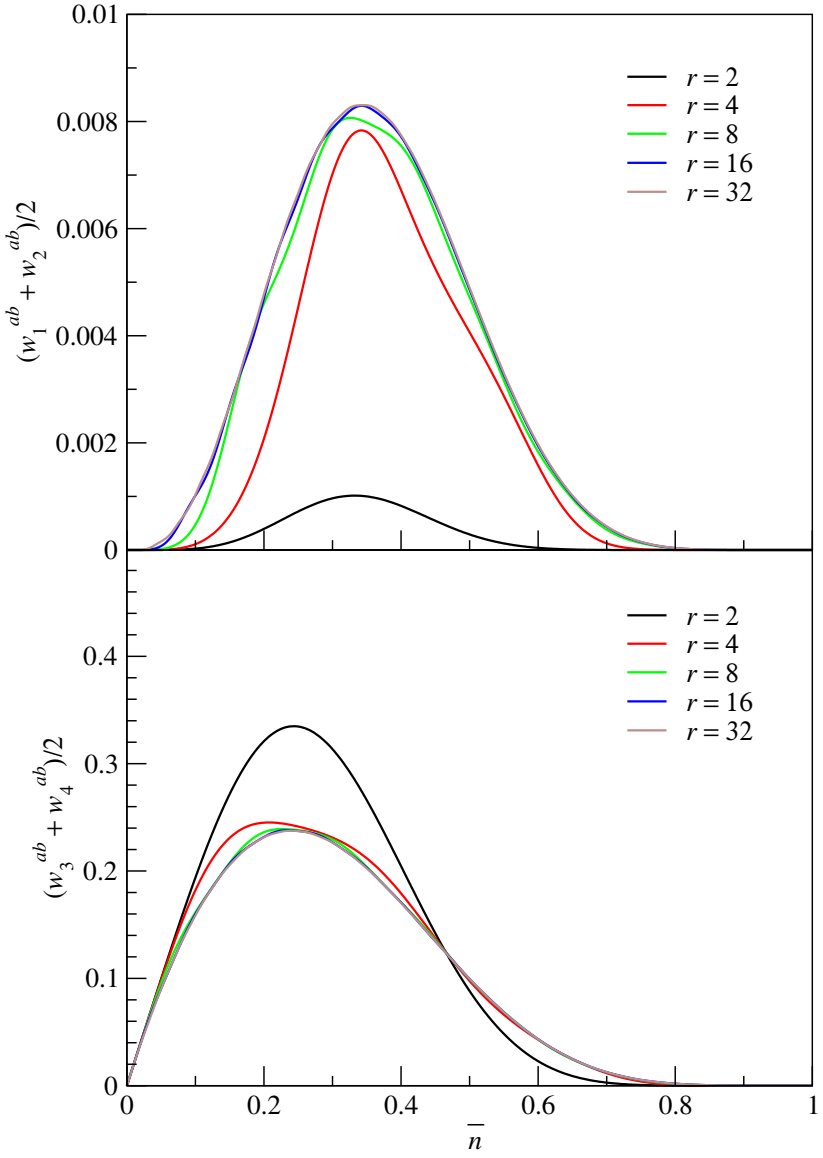

Figure 5.7: Plot of the averaged one-particle weights $\frac{1}{2}(w_1^{ab} + w_2^{ab})$ and $\frac{1}{2}(w_3^{ab} + w_4^{ab})$ of the (2 + 2) supercluster density matrix in a one-dimensional system of noninteracting spinless fermions, as a function of the filling fraction $\bar{n}$, for various cluster separations.

zero-particle sector of the supercluster density matrix ρ^{ab} to be

$$\begin{aligned}\langle 0000|\rho^{ab}|0000\rangle = 1 &- 4\bar{n} + \bar{n}^2(6 - 2a^2 - 2b^2 - c^2 - d^2) \\ &- 2\bar{n}^3(2 - 2a^2 - 2b^2 - c^2 - d^2 + 2abc + 2abd) \\ &+ \bar{n}^4(1 - 2a^2 - 2b^2 - c^2 - d^2 + 4abc + 4abd) \\ &+ \bar{n}^4(a^4 + b^4 - 2a^2b^2 - 2a^2cd - 2b^2cd + c^2d^2).\end{aligned} \tag{5.3.54}$$

The one-particle sector of ρ^{ab}, calculated using the method of referencing operators, has matrix elements

$$\begin{aligned}\langle 1000|\rho^{ab}|1000\rangle = \bar{n} &- \bar{n}^2(3 - a^2 - b^2 - c^2) \\ &+ \bar{n}^3(3 - 3a^2 - 3b^2 - 2c^2 - d^2 + 4abc + 2abd) \\ &- \bar{n}^4(1 - 2a^2 - 2b^2 - c^2 - d^2 + 4abc + 4abd) \\ &- \bar{n}^4(a^4 + b^4 - 2a^2b^2 - 2a^2cd - 2b^2cd + c^2d^2),\end{aligned} \tag{5.3.55a}$$

$$\begin{aligned}\langle 1000|\rho^{ab}|0100\rangle = \bar{n}a &- \bar{n}^2(2a - bc - bd) \\ &+ \bar{n}^3(a - a^3 + ab^2 - bc - bd + acd),\end{aligned} \tag{5.3.55b}$$

$$\begin{aligned}\langle 1000|\rho^{ab}|0010\rangle = \bar{n}b &- \bar{n}^2(2b - ac - ad) \\ &+ \bar{n}^3(b - b^3 + a^2b - ac - ad + bcd),\end{aligned} \tag{5.3.55c}$$

$$\begin{aligned}\langle 1000|\rho^{ab}|0001\rangle = \bar{n}c &- 2\bar{n}^2(c - ab) \\ &+ \bar{n}^3(-2ab + c + a^2d + b^2d - cd^2),\end{aligned} \tag{5.3.55d}$$

$$\begin{aligned}\langle 0100|\rho^{ab}|0100\rangle = \bar{n} &- \bar{n}^2(3 - a^2 - b^2 - d^2) \\ &+ \bar{n}^3(3 - 3a^2 - 3b^2 - c^2 - 2d^2 + 2abc + 4abd) \\ &- \bar{n}^4(1 - 2a^2 - 2b^2 - c^2 - d^2 + 4abc + 4abd) \\ &- \bar{n}^4(a^4 + b^4 - 2a^2b^2 - 2a^2cd - 2b^2cd + c^2d^2),\end{aligned} \tag{5.3.55e}$$

$$\begin{aligned}\langle 0100|\rho^{ab}|0010\rangle = \bar{n}d &- 2\bar{n}^2(d - ab) \\ &+ \bar{n}^3(-2ab + a^2c + b^2c + d - c^2d),\end{aligned} \tag{5.3.55f}$$

$$\langle 0100|\rho^{ab}|0001\rangle = \bar{n}b - \bar{n}^2 a(d-c) + \bar{n}^3(b - b^3 + a^2 b - ac - ad + bcd), \tag{5.3.55g}$$

$$\langle 0010|\rho^{ab}|0010\rangle = \bar{n} - \bar{n}^2(3 - a^2 - b^2 - d^2) + \bar{n}^3(3 - 3a^2 - 3b^2 - c^2 - 2d^2 + 2abc + 4abd) - \bar{n}^4(1 - 2a^2 - 2b^2 - c^2 - d^2 + 4abc + 4abd) - \bar{n}^4(a^4 + b^4 - 2a^2b^2 - 2a^2cd - 2b^2cd + c^2d^2), \tag{5.3.55h}$$

$$\langle 0010|\rho^{ab}|0001\rangle = \bar{n}a - \bar{n}^2(2a - bc - bd) + \bar{n}^3(a - a^3 + ab^2 - bc - bd + acd), \tag{5.3.55i}$$

$$\langle 0001|\rho^{ab}|0001\rangle = \bar{n} - \bar{n}^2(3 - a^2 - b^2 - c^2) + \bar{n}^3(3 - 3a^2 - 3b^2 - 2c^2 - d^2 + 4abc + 2abd) - \bar{n}^4(1 - 2a^2 - 2b^2 - c^2 - d^2 + 4abc + 4abd) - \bar{n}^4(a^4 + b^4 - 2a^2b^2 - 2a^2cd - 2b^2cd + c^2d^2). \tag{5.3.55j}$$

The two-particle sector of ρ^{ab}, calculated using the method of referencing operators, has matrix elements

$$\langle 1100|\rho^{ab}|1100\rangle = \bar{n}^2(1 - a^2) - \bar{n}^3(2 - 2a^2 - 2b^2 - c^2 - d^2 + 2abc + 2abd) + \bar{n}^4(1 - 2a^2 - 2b^2 - c^2 - d^2 + 4abc + 4abd) + \bar{n}^4(a^4 + b^4 - 2a^2b^2 - 2a^2cd - 2b^2cd + c^2d^2), \tag{5.3.56a}$$

$$\langle 1100|\rho^{ab}|1010\rangle = \bar{n}^2(-ab + d) - \bar{n}^3(-2ab + a^2c + b^2c + d - c^2d), \tag{5.3.56b}$$

$$\langle 1100|\rho^{ab}|1001\rangle = \bar{n}^2(b - ac) + \bar{n}^3(-b - a^2b + b^3 + ac + ad - bcd), \tag{5.3.56c}$$

$$\langle 1100|\rho^{ab}|0110\rangle = \bar{n}^2(-b + ad) - \bar{n}^3(-b - a^2b + b^3 + ac + ad - bcd), \tag{5.3.56d}$$

$$\langle 1100|\rho^{ab}|0101\rangle = \bar{n}^2(ab - c) + \bar{n}^3(-2ab + c + a^2d + b^2d - cd^2), \tag{5.3.56e}$$

$$\langle 1100|\rho^{ab}|0011\rangle = \bar{n}^2(b^2 - cd), \tag{5.3.56f}$$

$$\begin{aligned}\langle 1010|\rho^{ab}|1010\rangle = {} & \bar{n}^2(1 - b^2) \\ & - \bar{n}^3(2 - 2a^2 - 2b^2 - c^2 - d^2 + 2abc + 2abd) \\ & + \bar{n}^4(1 - 2a^2 - 2b^2 - c^2 - d^2 + 4abc + 4abd) \\ & + \bar{n}^4(a^4 + b^4 - 2a^2b^2 - 2a^2cd - 2b^2cd + c^2d^2),\end{aligned} \tag{5.3.56g}$$

$$\langle 1010|\rho^{ab}|1001\rangle = \bar{n}^2(a - bc) - \bar{n}^3(a - a^3 + ab^2 - bc - bd + acd), \tag{5.3.56h}$$

$$\langle 1010|\rho^{ab}|0110\rangle = \bar{n}^2(a - bd) - \bar{n}^3(a - a^3 + ab^2 - bc - bd + acd), \tag{5.3.56i}$$

$$\langle 1010|\rho^{ab}|0101\rangle = \bar{n}^2(a^2 - cd), \tag{5.3.56j}$$

$$\langle 1010|\rho^{ab}|0011\rangle = \bar{n}^2(ab - c) + \bar{n}^3(-2ab + c + a^2d + b^2d - cd^2), \tag{5.3.56k}$$

$$\begin{aligned}\langle 1001|\rho^{ab}|1001\rangle = {} & \bar{n}^2(1 - c^2) \\ & - 2\bar{n}^3(1 - a^2 - b^2 - c^2 + 2abc) \\ & + \bar{n}^4(1 - 2a^2 - 2b^2 - c^2 - d^2 + 4abc + 4abd) \\ & + \bar{n}^4(a^4 + b^4 - 2a^2b^2 - 2a^2cd - 2b^2cd + c^2d^2),\end{aligned} \tag{5.3.56l}$$

$$\langle 1001|\rho^{ab}|0110\rangle = \bar{n}^2(a^2 - b^2), \tag{5.3.56m}$$

$$\langle 1001|\rho^{ab}|0101\rangle = \bar{n}^2(a - bc) - \bar{n}^3(a - a^3 + ab^2 - bc - bd + acd), \tag{5.3.56n}$$

$$\langle 1001|\rho^{ab}|0011\rangle = \bar{n}^2(b - ac) + \bar{n}^3(-b - a^2b + b^3 + ac + ad - bcd), \tag{5.3.56o}$$

$$\begin{aligned}\langle 0110|\rho^{ab}|0110\rangle = {} & \bar{n}^2(1 - d^2) \\ & - 2\bar{n}^3(1 - a^2 - b^2 - d^2 + 2abd) \\ & + \bar{n}^4(1 - 2a^2 - 2b^2 - c^2 - d^2 + 4abc + 4abd) \\ & + \bar{n}^4(a^4 + b^4 - 2a^2b^2 - 2a^2cd - 2b^2cd + c^2d^2),\end{aligned} \tag{5.3.56p}$$

$$\langle 0110|\rho^{ab}|0101\rangle = \bar{n}^2(a - bd) - \bar{n}^3(a - a^3 + ab^2 - bc - bd + acd), \tag{5.3.56q}$$

$$\langle 0110|\rho^{ab}|0011\rangle = \bar{n}^2(ad - b) - \bar{n}^3(-b - a^2b + b^3 + ac + ad - bcd), \tag{5.3.56r}$$

$$\langle 0101|\rho^{ab}|0101\rangle = \bar{n}^2(1-b^2) - \bar{n}^3(2-2a^2-2b^2-c^2-d^2+2abc+2abd) + \bar{n}^4(1-2a^2-2b^2-c^2-d^2+4abc+4abd) + \bar{n}^2(a^4+b^4-2a^2b^2-2a^2cd-2b^2cd+c^2d^2), \quad (5.3.56s)$$

$$\langle 0101|\rho^{ab}|0011\rangle = \bar{n}^2(d-ab) - \bar{n}^3(-2ab+a^2c+b^2c+d-c^2d), \quad (5.3.56t)$$

$$\langle 0011|\rho^{ab}|0011\rangle = \bar{n}^2(1-a^2) - \bar{n}^3(2-2a^2-2b^2-c^2-d^2+2abc+2abd) + \bar{n}^4(1-2a^2-2b^2-c^2-d^2+4abc+4abd) + \bar{n}^4(a^4+b^4-2a^2b^2-2a^2cd-2b^2cd+c^2d^2). \quad (5.3.56u)$$

The three-particle sector of ρ^{ab}, calculated using the method of referencing operators, has matrix elements

$$\langle 1110|\rho^{ab}|1110\rangle = \bar{n}^3(1-a^2-b^2-d^2+2abd) - \bar{n}^4(1-2a^2-2b^2-c^2-d^2+4abc+4abd) - \bar{n}^4(a^4+b^4-2a^2b^2-2a^2cd-2b^2cd+c^2d^2), \quad (5.3.57a)$$

$$\langle 1110|\rho^{ab}|1101\rangle = \bar{n}^3(a-a^3+ab^2-bc-bd+acd), \quad (5.3.57b)$$

$$\langle 1110|\rho^{ab}|1011\rangle = -\bar{n}^3(b-b^3+a^2b-ac-ad+bcd), \quad (5.3.57c)$$

$$\langle 1110|\rho^{ab}|0111\rangle = \bar{n}^3(-2ab+c+a^2d+b^2d-cd^2), \quad (5.3.57d)$$

$$\langle 1101|\rho^{ab}|1101\rangle = \bar{n}^3(1-a^2-b^2-c^2+2abc) - \bar{n}^4(1-2a^2-2b^2-c^2-d^2+4abc+4abd) - \bar{n}^4(a^4+b^4-2a^2b^2-2a^2cd-2b^2cd+c^2d^2), \quad (5.3.57e)$$

$$\langle 1101|\rho^{ab}|1011\rangle = \bar{n}^3(-2ab+a^2c+b^2c+d-cd^2), \quad (5.3.57f)$$

$$\langle 1101|\rho^{ab}|0111\rangle = -\bar{n}^3(b-b^3+a^2b-ac-ad+bcd), \quad (5.3.57g)$$

$$\begin{aligned}\langle 1011|\rho^{ab}|1011\rangle &= \bar{n}^3(1 - a^2 - b^2 - c^2 + 2abc) \\ &\quad - \bar{n}^4(1 - 2a^2 - 2b^2 - c^2 - d^2 + 4abc + 4abd) \\ &\quad - \bar{n}^4(a^4 + b^4 - 2a^2b^2 - 2a^2cd - 2b^2cd + c^2d^2), \qquad (5.3.57h)\end{aligned}$$

$$\langle 1011|\rho^{ab}|0111\rangle = \bar{n}^3(a - a^3 + ab^2 - bc - bd + acd), \qquad (5.3.57i)$$

$$\begin{aligned}\langle 0111|\rho^{ab}|0111\rangle &= \bar{n}^3(1 - a^2 - b^2 - d^2 + 2abd) \\ &\quad + \bar{n}^4(1 - 2a^2 - 2b^2 - c^2 - d^2 + 4abc + 4abd) \\ &\quad + \bar{n}^4(a^4 + b^4 - 2a^2b^2 - 2a^2cd - 2b^2cd + c^2d^2). \qquad (5.3.57j)\end{aligned}$$

Finally, the four-particle sector of ρ^{ab}, calculated using the method of referencing operators, is

$$\begin{aligned}\langle 1111|\rho^{ab}|1111\rangle &= \bar{n}^4(1 - 2a^2 - 2b^2 - c^2 - d^2 + 4abc + 4abd) \\ &\quad + \bar{n}^4(a^4 + b^4 - 2a^2b^2 - 2a^2cd - 2b^2cd + c^2d^2).\end{aligned} \qquad (5.3.58)$$

5.3.4 The (2 + 2) Correlation Density Matrix

Gathering the pieces in (5.3.30), (5.3.32), (5.3.35), (5.3.37), (5.3.39), and (5.3.54), (5.3.55), (5.3.56), (5.3.57), (5.3.58) together, we can write down the nonzero matrix elements of the correlation density matrix ρ^c. The zero-particle sector of ρ^c is

$$\begin{aligned}\langle 0000|\rho^c|0000\rangle &= -\bar{n}^2(2b^2 + c^2 + d^2) \\ &\quad + 2\bar{n}^3(2b^2 + c^2 + d^2 - 2abc - 2abd) \\ &\quad + \bar{n}^4(-2b^2 - c^2 - d^2 + 4abc + 4abd) \\ &\quad + \bar{n}^4(b^4 - 2a^2b^2 - 2a^2cd - 2b^2cd + c^2d^2).\end{aligned} \qquad (5.3.59)$$

The one-particle sector of ρ^c has matrix elements

$$\begin{aligned}\langle 1000|\rho^c|1000\rangle &= \bar{n}^2(b^2 + c^2) \\ &\quad - \bar{n}^3(3b^2 + 2c^2 + d^2 - 4abc - 2abd)\end{aligned}$$

$$+ \bar{n}^4(2b^2 + c^2 + d^2 - 4abc - 4abd - b^4)$$

$$+ \bar{n}^4(2a^2b^2 + 2a^2cd + 2b^2cd - c^2d^2), \tag{5.3.60a}$$

$$\langle 1000|\rho^c|0100\rangle = \bar{n}^2(bc + bd) + \bar{n}^3(ab^2 - bc - bd + acd), \tag{5.3.60b}$$

$$\langle 1000|\rho^c|0010\rangle = \bar{n}b - \bar{n}^2(2b - ac - ad)$$

$$+ \bar{n}^3(b - b^3 + a^2b - ac - ad + bcd), \tag{5.3.60c}$$

$$\langle 1000|\rho^c|0001\rangle = \bar{n}c - 2\bar{n}^2(c - ab)$$

$$+ \bar{n}^3(-2ab + c + a^2d + b^2d - cd^2), \tag{5.3.60d}$$

$$\langle 0100|\rho^c|0100\rangle = \bar{n}^2(b^2 + d^2)$$

$$- \bar{n}^3(3b^2 + c^2 + 2d^2 - 2abc - 4abd)$$

$$+ \bar{n}^4(2b^2 + c^2 + d^2 - 4abc - 4abd - b^4)$$

$$+ \bar{n}^4(2a^2b^2 + 2a^2cd + 2b^2cd - c^2d^2), \tag{5.3.60e}$$

$$\langle 0100|\rho^c|0010\rangle = \bar{n}d - 2\bar{n}^2(d - ab)$$

$$+ \bar{n}^3(-2ab + a^2c + b^2c + d - c^2d), \tag{5.3.60f}$$

$$\langle 0100|\rho^c|0001\rangle = -\bar{n}^3(b - b^3 + a^2b - ac - ad + bcd), \tag{5.3.60g}$$

$$\langle 0010|\rho^c|0010\rangle = \bar{n}^2(b^2 + d^2)$$

$$- \bar{n}^3(3b^2 + c^2 + 2d^2 - 2abc - 4abd)$$

$$+ \bar{n}^4(2b^2 + c^2 + d^2 - 4abc - 4abd - b^4)$$

$$+ \bar{n}^4(2a^2b^2 + 2a^2cd + 2b^2cd - c^2d^2), \tag{5.3.60h}$$

$$\langle 0010|\rho^c|0001\rangle = \bar{n}^2(bc + bd) + \bar{n}^3(ab^2 - bc - bd + acd), \tag{5.3.60i}$$

$$\langle 0001|\rho^c|0001\rangle = \bar{n}^2(b^2 + c^2)$$

$$- \bar{n}^3(3b^2 + 2c^2 + d^2 - 4abc - 2abd)$$

$$+ \bar{n}^4(2b^2 + c^2 + d^2 - 4abc - 4abd - b^4)$$

$$+ \bar{n}^4(2a^2b^2 + 2a^2cd + 2b^2cd - c^2d^2). \tag{5.3.60j}$$

The two-particle sector of ρ^c has matrix elements

$$\begin{aligned}\langle 1100|\rho^c|1100\rangle &= \bar{n}^3(2b^2 + c^2 + d^2 - 2abc - 2abd) \\ &\quad + \bar{n}^4(-2b^2 - c^2 - d^2 + 4abc + 4abd) \\ &\quad + \bar{n}^4(b^4 - 2a^2b^2 - 2a^2cd - 2b^2cd + c^2d^2),\end{aligned} \tag{5.3.61a}$$

$$\langle 1100|\rho^c|1010\rangle = \bar{n}^2(d - ab) - \bar{n}^3(-2ab + a^2c + b^2c + d - c^2d), \tag{5.3.61b}$$

$$\langle 1100|\rho^c|1001\rangle = \bar{n}^2(b - ac) + \bar{n}^3(-b - a^2b + b^3 + ac + ad - bcd), \tag{5.3.61c}$$

$$\langle 1100|\rho^c|0110\rangle = \bar{n}^2(-b + ad) - \bar{n}^3(-b - a^2b + b^3 + ac + ad - bcd), \tag{5.3.61d}$$

$$\langle 1100|\rho^c|0101\rangle = \bar{n}^2(ab - c) + \bar{n}^3(-2ab + c + a^2d + b^2d - cd^2), \tag{5.3.61e}$$

$$\langle 1100|\rho^c|0011\rangle = \bar{n}^2(b^2 - cd), \tag{5.3.61f}$$

$$\begin{aligned}\langle 1010|\rho^c|1010\rangle &= -\bar{n}^2b^2 + \bar{n}^3(2b^2 + c^2 + d^2 - 2abc - 2abd) \\ &\quad + \bar{n}^4(-2b^2 - c^2 - d^2 + 4abc + 4abd) \\ &\quad + \bar{n}^4(b^4 - 2a^2b^2 - 2a^2cd - 2b^2cd + c^2d^2),\end{aligned} \tag{5.3.61g}$$

$$\langle 1010|\rho^c|1001\rangle = -\bar{n}^2bc - \bar{n}^3(ab^2 - bc - bd + acd), \tag{5.3.61h}$$

$$\langle 1010|\rho^c|0110\rangle = -\bar{n}^2bd - \bar{n}^3(ab^2 - bc - bd + acd), \tag{5.3.61i}$$

$$\langle 1010|\rho^c|0101\rangle = -\bar{n}^2cd, \tag{5.3.61j}$$

$$\langle 1010|\rho^c|0011\rangle = \bar{n}^2(ab - c) + \bar{n}^3(-2ab + c + a^2d + b^2d - cd^2), \tag{5.3.61k}$$

$$\begin{aligned}\langle 1001|\rho^c|1001\rangle &= -\bar{n}^2c^2 + \bar{n}^3(2b^2 + c^2 + d^2 - 2abc - 2abd) \\ &\quad + \bar{n}^4(-2b^2 - c^2 - d^2 + 4abc + 4abd) \\ &\quad + \bar{n}^4(b^4 - 2a^2b^2 - 2a^2cd - 2b^2cd + c^2d^2),\end{aligned} \tag{5.3.61l}$$

$$\langle 1001|\rho^c|0110\rangle = -\bar{n}^2b^2, \tag{5.3.61m}$$

$$\langle 1001|\rho^c|0101\rangle = -\bar{n}^2bc - \bar{n}^3(ab^2 - bc - bd + acd), \tag{5.3.61n}$$

$$\langle 1001|\rho^c|0011\rangle = \bar{n}^2(b - ac) + \bar{n}^3(-b - a^2b + b^3 + ac + ad - bcd), \tag{5.3.61o}$$

$$\begin{aligned}\langle 0110|\rho^c|0110\rangle = &-\bar{n}^2d^2 + \bar{n}^3(2b^2 + c^2 + d^2 - 2abc - 2abd) \\ &+ \bar{n}^4(-2b^2 - c^2 - d^2 + 4abc + 4abd) \\ &+ \bar{n}^4(b^4 - 2a^2b^2 - 2a^2cd - 2b^2cd + c^2d^2),\end{aligned} \tag{5.3.61p}$$

$$\langle 0110|\rho^c|0101\rangle = -\bar{n}^2bd - \bar{n}^3(ab^2 - bc - bd + acd), \tag{5.3.61q}$$

$$\langle 0110|\rho^c|0011\rangle = \bar{n}^2(-b + ad) - \bar{n}^3(-b - a^2b + b^3 + ac + ad - bcd), \tag{5.3.61r}$$

$$\begin{aligned}\langle 0101|\rho^c|0101\rangle = &-\bar{n}^2b^2 + \bar{n}^3(2b^2 + c^2 + d^2 - 2abc - 2abd) \\ &+ \bar{n}^4(-2b^2 - c^2 - d^2 + 4abc + 4abd) \\ &+ \bar{n}^4(b^4 - 2a^2b^2 - 2a^2cd - 2b^2cd + c^2d^2),\end{aligned} \tag{5.3.61s}$$

$$\langle 0101|\rho^c|0011\rangle = \bar{n}^2(d - ab) - \bar{n}^3(-2ab + a^2c + b^2c + d - c^2d), \tag{5.3.61t}$$

$$\begin{aligned}\langle 0011|\rho^c|0011\rangle = &\bar{n}^3(2b^2 + c^2 + d^2 - 2abc - 2abd) \\ &+ \bar{n}^4(-2b^2 - c^2 - d^2 + 4abc + 4abd) \\ &+ \bar{n}^4(b^4 - 2a^2b^2 - 2a^2cd - 2b^2cd + c^2d^2).\end{aligned} \tag{5.3.61u}$$

The three-particle sector of ρ^c has matrix elements

$$\begin{aligned}\langle 1110|\rho^c|1110\rangle = &-\bar{n}^3(b^2 + d^2 - 2abd) \\ &+ \bar{n}^4(2b^2 + c^2 + d^2 - 4abc - 4abd - b^4) \\ &+ \bar{n}^4(2a^2b^2 + 2a^2cd + 2b^2cd - c^2d^2),\end{aligned} \tag{5.3.62a}$$

$$\langle 1110|\rho^c|1101\rangle = \bar{n}^3(ab^2 - bc - bd + acd), \tag{5.3.62b}$$

$$\langle 1110|\rho^c|1011\rangle = -\bar{n}^3(b - b^3 + a^2b - ac - ad + bcd), \tag{5.3.62c}$$

$$\langle 1110|\rho^c|0111\rangle = \bar{n}^3(-2ab + c + a^2d + b^2d - cd^2), \tag{5.3.62d}$$

$$\begin{aligned}\langle 1101|\rho^c|1101\rangle = &-\bar{n}^3(b^2 + c^2 - 2abc) \\ &+ \bar{n}^4(2b^2 + c^2 + d^2 - 4abc - 4abd - b^4)\end{aligned}$$

$$+ \bar{n}^4(2a^2b^2 + 2a^2cd + 2b^2cd - c^2d^2), \tag{5.3.62e}$$

$$\langle 1101|\rho^c|1011\rangle = \bar{n}^3(-2ab + a^2c + b^2c + d - cd^2), \tag{5.3.62f}$$

$$\langle 1101|\rho^c|0111\rangle = -\bar{n}^3(b - b^3 + a^2b - ac - ad + bcd), \tag{5.3.62g}$$

$$\begin{aligned}\langle 1011|\rho^c|1011\rangle = &-\bar{n}^3(b^2 + c^2 - 2abc)\\ &+ \bar{n}^4(2b^2 + c^2 + d^2 - 4abc - 4abd - b^4)\\ &+ \bar{n}^4(2a^2b^2 + 2a^2cd + 2b^2cd - c^2d^2),\end{aligned} \tag{5.3.62h}$$

$$\langle 1011|\rho^c|0111\rangle = \bar{n}^3(ab^2 - bc - bd + acd), \tag{5.3.62i}$$

$$\begin{aligned}\langle 0111|\rho^c|0111\rangle = &-\bar{n}^3(b^2 + d^2 - 2abd)\\ &+ \bar{n}^4(2b^2 + c^2 + d^2 - 4abc - 4abd - b^4)\\ &+ \bar{n}^4(2a^2b^2 + 2a^2cd + 2b^2cd - c^2d^2).\end{aligned} \tag{5.3.62j}$$

Finally, the four-particle sector of ρ^c is

$$\begin{aligned}\langle 1111|\rho^c|1111\rangle = &-\bar{n}^4(2b^2 + c^2 + d^2 - 4abc - 4abd - b^4)\\ &- \bar{n}^4(2a^2b^2 + 2a^2cd + 2b^2cd - c^2d^2).\end{aligned} \tag{5.3.63}$$

From this messy list of matrix elements, we find that those which are of $O(r^{-1})$ are

$$\langle 1000|\rho^c|0010\rangle \approx \bar{n}b - \bar{n}^2(2b - ac - ad) + \bar{n}^3(b + a^2b - ac - ad), \tag{5.3.64a}$$

$$\langle 1000|\rho^c|0001\rangle \approx \bar{n}c - 2\bar{n}^2(c - ab) + \bar{n}^3(-2ab + c + a^2d), \tag{5.3.64b}$$

$$\langle 0100|\rho^c|0010\rangle \approx \bar{n}^3(-2ab + a^2c + d), \tag{5.3.64c}$$

$$\langle 0100|\rho^c|0001\rangle \approx -\bar{n}^3(b + a^2b - ac - ad), \tag{5.3.64d}$$

$$\langle 1100|\rho^c|1010\rangle \approx \bar{n}^2(d - ab) - \bar{n}^3(-2ab + a^2c + d), \tag{5.3.64e}$$

$$\langle 1100|\rho^c|1001\rangle \approx \bar{n}^2(b - ac) + \bar{n}^3(-b - a^2b + ac + ad), \tag{5.3.64f}$$

$$\langle 1100|\rho^c|0110\rangle \approx \bar{n}^2(-b + ad) - \bar{n}^3(-b - a^2b + ac + ad), \tag{5.3.64g}$$

$$\langle 1100|\rho^c|0101\rangle \approx \bar{n}^2(ab - c) + \bar{n}^3(-2ab + c + a^2d), \tag{5.3.64h}$$

$$\langle 1010|\rho^c|0011\rangle \approx \bar{n}^2(\mathsf{ab}-\mathsf{c})+\bar{n}^3(-2\mathsf{ab}+\mathsf{c}+\mathsf{a}^2\mathsf{d}), \tag{5.3.64i}$$

$$\langle 1001|\rho^c|0011\rangle \approx \bar{n}^2(\mathsf{b}-\mathsf{ac})+\bar{n}^3(-\mathsf{b}-\mathsf{a}^2\mathsf{b}+\mathsf{ac}+\mathsf{ad}), \tag{5.3.64j}$$

$$\langle 0110|\rho^c|0011\rangle \approx \bar{n}^2(-\mathsf{b}+\mathsf{ad})-\bar{n}^3(-\mathsf{b}-\mathsf{a}^2\mathsf{b}+\mathsf{ac}+\mathsf{ad}), \tag{5.3.64k}$$

$$\langle 0101|\rho^c|0011\rangle \approx \bar{n}^2(\mathsf{d}-\mathsf{ab})-\bar{n}^3(-2\mathsf{ab}+\mathsf{a}^2\mathsf{c}+\mathsf{d}), \tag{5.3.64l}$$

$$\langle 1110|\rho^c|1011\rangle \approx -\bar{n}^3(\mathsf{b}+\mathsf{a}^2\mathsf{b}-\mathsf{ac}-\mathsf{ad}), \tag{5.3.64m}$$

$$\langle 1110|\rho^c|0111\rangle \approx \bar{n}^3(-2\mathsf{ab}+\mathsf{c}+\mathsf{a}^2\mathsf{d}), \tag{5.3.64n}$$

$$\langle 1101|\rho^c|1011\rangle \approx \bar{n}^3(-2\mathsf{ab}+\mathsf{a}^2\mathsf{c}+\mathsf{d}), \tag{5.3.64o}$$

$$\langle 1101|\rho^c|0111\rangle \approx -\bar{n}^3(\mathsf{b}+\mathsf{a}^2\mathsf{b}-\mathsf{ac}-\mathsf{ad}). \tag{5.3.64p}$$

These $O(r^{-1})$ matrix elements will come in handy when we singular value decompose the (2 + 2) correlation density matrix analytically in Chapter 6.

5.4 One-Dimensional Superconducting Ground State

In preparation for our numerical operator singular value decomposition of the correlation density matrix in Chapter 8 for the spinless extended Hubbard ladder described by the Hamiltonian (7.3.2), we want to understand not only how the operator singular value decomposition pulls out the correct Fermi-liquid order parameters, but also to understand how the superconducting order parameters emerge from the operator singular value decomposition as well. For the rest of this chapter, let me work out analytically the correlation density matrices of the $(1+1)$ and $(2+2)$ superclusters in a one-dimensional superconductor, and then proceed to singular value decompose them in Chapter 6.

5.4.1 BCS Ground State

The simplest example of a one-dimensional superconducting is a BCS s-wave superconductor. For spinfull fermions, the ground-state wave function is well known to be

$$|\Psi_{\mathrm{BCS}}\rangle = \prod_{\mathbf{k}} \left(u_{\mathbf{k}} + v_{\mathbf{k}} \tilde{c}^{\dagger}_{\mathbf{k},\uparrow} \tilde{c}^{\dagger}_{-\mathbf{k},\downarrow}\right) |0\rangle \,, \tag{5.4.1}$$

where the normalized coefficients $u_{\mathbf{k}}$ and $v_{\mathbf{k}}$ are given by

$$u^2_{\mathbf{k}} = \frac{1}{2}\left(1 + \frac{\xi_{\mathbf{k}}}{E_{\mathbf{k}}}\right), \quad v^2_{\mathbf{k}} = \frac{1}{2}\left(1 - \frac{\xi_{\mathbf{k}}}{E_{\mathbf{k}}}\right), \quad 2u_{\mathbf{k}} v_{\mathbf{k}} = \frac{\Delta_{\mathbf{k}}}{E_{\mathbf{k}}}. \tag{5.4.2}$$

The energy quantities $\xi_{\mathbf{k}}$ and $E_{\mathbf{k}}$ are related to the dispersion relation $\epsilon_{\mathbf{k}}$ of the uncondensed fermion system by

$$\xi_{\mathbf{k}} = \epsilon_{\mathbf{k}} - \mu, \quad E_{\mathbf{k}} = \sqrt{\xi^2_{\mathbf{k}} + \Delta^2_{\mathbf{k}}}, \tag{5.4.3}$$

where μ is the chemical potential, and $\Delta_{\mathbf{k}}$ is the superconducting gap.

But of course we are dealing with spinless fermions here, so we drop the spin index, and define the spinless BCS ground state to be

$$|\Psi_{\mathrm{BCS}}\rangle = \prod_{\mathbf{k}} \left(u_{\mathbf{k}} + v_{\mathbf{k}} \tilde{c}^{\dagger}_{\mathbf{k}} \tilde{c}^{\dagger}_{-\mathbf{k}}\right) |0\rangle \,. \tag{5.4.4}$$

In this spinless BCS ground state, we find an anomalous expectation

$$\begin{aligned}
&\langle \Psi_{\mathrm{BCS}} | \tilde{c}^{\dagger}_{\mathbf{k}} \tilde{c}^{\dagger}_{-\mathbf{k}} | \Psi_{\mathrm{BCS}} \rangle \\
&= \langle 0 | (\cdots)(u_{\mathbf{k}} + v_{\mathbf{k}} \tilde{c}_{-\mathbf{k}} \tilde{c}_{\mathbf{k}}) \tilde{c}^{\dagger}_{\mathbf{k}} \tilde{c}^{\dagger}_{-\mathbf{k}} (u_{\mathbf{k}} + v_{\mathbf{k}} \tilde{c}^{\dagger}_{\mathbf{k}} \tilde{c}^{\dagger}_{-\mathbf{k}}) (\cdots) | 0 \rangle \\
&= \langle 0 | (\cdots)[u^2_{\mathbf{k}} \tilde{c}^{\dagger}_{\mathbf{k}} \tilde{c}^{\dagger}_{-\mathbf{k}} + u_{\mathbf{k}} v_{\mathbf{k}} \tilde{c}^{\dagger}_{\mathbf{k}} \tilde{c}^{\dagger}_{-\mathbf{k}} \tilde{c}^{\dagger}_{\mathbf{k}} \tilde{c}^{\dagger}_{-\mathbf{k}} + v_{\mathbf{k}} u \mathbf{k} \tilde{c}_{-\mathbf{k}} \tilde{c}_{\mathbf{k}} \tilde{c}^{\dagger}_{\mathbf{k}} \tilde{c}^{\dagger}_{-\mathbf{k}} + v^2_{\mathbf{k}} \tilde{c}_{-\mathbf{k}} \tilde{c}_{\mathbf{k}} \tilde{c}^{\dagger}_{\mathbf{k}} \tilde{c}^{\dagger}_{-\mathbf{k}} \tilde{c}^{\dagger}_{\mathbf{k}} \tilde{c}^{\dagger}_{-\mathbf{k}}](\cdots) | 0 \rangle \\
&= v_{\mathbf{k}} u_{\mathbf{k}},
\end{aligned} \tag{5.4.5}$$

just as we would have in a BCS ground state of spinfull fermions. Here,

$$(\cdots) = \prod_{\mathbf{k}' \neq \mathbf{k}} \left(u_{\mathbf{k}'} + v_{\mathbf{k}'} \tilde{c}^{\dagger}_{\mathbf{k}'} \tilde{c}^{\dagger}_{-\mathbf{k}'}\right) \tag{5.4.6}$$

is a shorthand for the product of operators with all the occupied wave vectors, except for the wave vector **k**. From this point on, we will not use the vectorial **k** index, since we are dealing with a one-dimensional system.

5.4.1.1 Bogoliubov Quasiparticles

In Section 5.4.1.2, we will calculate various expectations in the spinless BCS ground state. For this, we need to first write the spinless BCS ground state (5.4.4) as being created from the vacuum by a product of independent Bogoliubov-Valatin operators.

To motivate the definition of these Bogoliubov-Valatin operators, we examine what happens when we let the spinless fermion creation and annhilation operators act on the spinless BCS ground state $|\Psi_{\mathrm{BCS}}\rangle$. First, letting $\tilde{c}_k^\dagger$ act on $|\Psi_{\mathrm{BCS}}\rangle$, we find

$$\tilde{c}_k^\dagger |\Psi_{\mathrm{BCS}}\rangle = \tilde{c}_k^\dagger (u_k + v_k \tilde{c}_k^\dagger \tilde{c}_{-k}^\dagger)(\cdots)|0\rangle = u_k \tilde{c}_k^\dagger (\cdots)|0\rangle \,. \tag{5.4.7}$$

If we define

$$|k\rangle = \tilde{c}_k^\dagger (\cdots)|0\rangle \,, \tag{5.4.8}$$

we can write the action of $\tilde{c}_k^\dagger$ on $|\Psi_{\mathrm{BCS}}\rangle$ as

$$\tilde{c}_k^\dagger |\Psi_{\mathrm{BCS}}\rangle = u_k |k\rangle \,, \tag{5.4.9}$$

where $|k\rangle$ is the state with a quasiparticle excitation with wave vector k about the BCS ground state. Similarly, letting $\tilde{c}_{-k}^\dagger$ act on $|\Psi_{\mathrm{BCS}}\rangle$, we get

$$\tilde{c}_{-k}^\dagger |\Psi_{\mathrm{BCS}}\rangle = u_k |-k\rangle \,, \tag{5.4.10}$$

where

$$|-k\rangle = \tilde{c}_{-k}^\dagger (\cdots)|0\rangle \tag{5.4.11}$$

is the state with a quasiparticle excitation with wave vector $-k$ about the BCS ground state.

Next, we let the annihilation operators act on the spinless BCS ground state. Letting $\tilde{c}_k$ act on $|\Psi_{\text{BCS}}\rangle$, we find that

$$\tilde{c}_k |\Psi_{\text{BCS}}\rangle = v_k \tilde{c}_k \tilde{c}_k^\dagger \tilde{c}_{-k}^\dagger (\cdots) |0\rangle = v_k \tilde{c}_{-k}^\dagger (\cdots) |0\rangle = v_k |-k\rangle , \tag{5.4.12}$$

whereas letting $\tilde{c}_{-k}$ act on $|\Psi_{\text{BCS}}\rangle$, we find that

$$\tilde{c}_{-k} |\Psi_{\text{BCS}}\rangle = v_k \tilde{c}_{-k} \tilde{c}_k^\dagger \tilde{c}_{-k}^\dagger (\cdots) |0\rangle = -v_k \tilde{c}_k^\dagger (\cdots) |0\rangle = -v_k |k\rangle . \tag{5.4.13}$$

This tells us that if we define the Bogoliubov-Valatin operators

$$\begin{aligned} \gamma_k^\dagger &= u_k \tilde{c}_k^\dagger - v_k \tilde{c}_{-k}, \quad \gamma_k = u_k \tilde{c}_k - v_k \tilde{c}_{-k}^\dagger, \\ \gamma_{-k}^\dagger &= u_k \tilde{c}_{-k}^\dagger + v_k \tilde{c}_k, \quad \gamma_{-k} = u_k \tilde{c}_{-k} + v_k \tilde{c}_k^\dagger, \end{aligned} \tag{5.4.14}$$

we would have the properties that

$$\begin{aligned} \gamma_k^\dagger |\Psi_{\text{BCS}}\rangle &= |k\rangle , \qquad \gamma_k |\Psi_{\text{BCS}}\rangle = 0; \\ \gamma_{-k}^\dagger |\Psi_{\text{BCS}}\rangle &= |-k\rangle , \quad \gamma_{-k} |\Psi_{\text{BCS}}\rangle = 0. \end{aligned} \tag{5.4.15}$$

From (5.4.14), we also know that

$$u_{-k} = u_k, \quad v_{-k} = -v_k. \tag{5.4.16}$$

Since this symmetry property (5.4.16) is independent of the detailed functional form of the dispersion relation ϵ_k and the superconducting gap Δ_k, and since $E_k = E_{-k}$ is an even function of the wave vector k, we know that the superconducting gap Δ_k must be an odd function of k, i.e.

$$\Delta_k = -\Delta_{-k}. \tag{5.4.17}$$

The simplest superconducting gap satisfying this symmetry property is

$$\Delta_k = \begin{cases} -\Delta, & k < 0; \\ \\ +\Delta, & k > 0. \end{cases} \tag{5.4.18}$$

5.4.1.2 Expectations in the BCS Ground State

Since the single-quasiparticle excited states are orthogonal to each other, we have then

$$\langle \Psi_{\mathrm{BCS}} | \gamma_k \gamma_{k'}^\dagger | \Psi_{\mathrm{BCS}} \rangle = \delta_{kk'}, \quad \langle \Psi_{\mathrm{BCS}} | \gamma_k^\dagger \gamma_{k'} | \Psi_{\mathrm{BCS}} \rangle = 0. \tag{5.4.19}$$

This allows us to compute the expectation of products of $\tilde{c}_k^\dagger$ and $\tilde{c}_k$. First, let us note that any product of an odd number of $\tilde{c}_k^\dagger$ and $\tilde{c}_k$ will yield a sum of terms, each containing an odd number of the Bogoliubov-Valatin operators $\gamma_k^\dagger$ and γ_k. The expectation of such terms vanish, and hence the expansion of the product of an odd number of $\tilde{c}_k^\dagger$ and $\tilde{c}_k$ is also zero. For a product of an even number of $\tilde{c}_k^\dagger$ and $\tilde{c}_k$, we find that for two-operator terms,

$$\begin{aligned}
\langle \Psi_{\mathrm{BCS}} | \tilde{c}_{k_1} \tilde{c}_{k_2} | \Psi_{\mathrm{BCS}} \rangle &= \langle \Psi_{\mathrm{BCS}} | (u_{k_1} \gamma_{k_1} + v_{k_1} \gamma_{-k_1}^\dagger)(u_{k_2} \gamma_{k_2} + v_{k_2} \gamma_{-k_2}^\dagger) | \Psi_{\mathrm{BCS}} \rangle \\
&= u_{k_1} v_{k_2} \langle \Psi_{\mathrm{BCS}} | \gamma_{k_1} \gamma_{-k_2}^\dagger | \Psi_{\mathrm{BCS}} \rangle \\
&= u_{k_1} v_{k_2} \delta_{k_1, -k_2}, \qquad (5.4.20) \\
\langle \Psi_{\mathrm{BCS}} | \tilde{c}_{k_1} \tilde{c}_{k_2}^\dagger | \Psi_{\mathrm{BCS}} \rangle &= \langle \Psi_{\mathrm{BCS}} | (u_{k_1} \gamma_{k_1} + v_{k_1} \gamma_{-k_1}^\dagger)(u_{k_2} \gamma_{k_2}^\dagger + v_{k_2} \gamma_{-k_2}) | \Psi_{\mathrm{BCS}} \rangle \\
&= u_{k_1} u_{k_2} \langle \Psi_{\mathrm{BCS}} | \gamma_{k_1} \gamma_{k_2}^\dagger | \Psi_{\mathrm{BCS}} \rangle \\
&= u_{k_1} u_{k_2} \delta_{k_1, k_2}, \qquad (5.4.21) \\
\langle \Psi_{\mathrm{BCS}} | \tilde{c}_{k_1}^\dagger \tilde{c}_{k_2} | \Psi_{\mathrm{BCS}} \rangle &= \langle \Psi_{\mathrm{BCS}} | (u_{k_1} \gamma_{k_1}^\dagger + v_{k_1} \gamma_{-k_1})(u_{k_2} \gamma_{k_2} + v_{k_2} \gamma_{-k_2}^\dagger) | \Psi_{\mathrm{BCS}} \rangle \\
&= v_{k_1} v_{k_2} \langle \Psi_{\mathrm{BCS}} | \gamma_{-k_1} \gamma_{-k_2}^\dagger | \Psi_{\mathrm{BCS}} \rangle \\
&= v_{k_1} v_{k_2} \delta_{k_1, k_2}, \qquad (5.4.22) \\
\langle \Psi_{\mathrm{BCS}} | \tilde{c}_{k_1}^\dagger \tilde{c}_{k_2}^\dagger | \Psi_{\mathrm{BCS}} \rangle &= \langle \Psi_{\mathrm{BCS}} | (u_{k_1} \gamma_{k_1}^\dagger + v_{k_1} \gamma_{-k_1})(u_{k_2} \gamma_{k_2}^\dagger + v_{k_2} \gamma_{-k_2}) | \Psi_{\mathrm{BCS}} \rangle \\
&= v_{k_1} u_{k_2} \langle \Psi_{\mathrm{BCS}} | \gamma_{-k_1} \gamma_{k_2}^\dagger | \Psi_{\mathrm{BCS}} \rangle \\
&= v_{k_1} u_{k_2} \delta_{k_1, -k_2}. \qquad (5.4.23)
\end{aligned}$$

For the four-operator terms, we need to be more careful. First let us look at

$$\begin{aligned}\langle\Psi_{\mathrm{BCS}}|\tilde{c}_{k_1}\tilde{c}_{k_2}\tilde{c}_{k_3}\tilde{c}_{k_4}|\Psi_{\mathrm{BCS}}\rangle &= \langle\Psi_{\mathrm{BCS}}|(u_{k_1}\gamma_{k_1}+v_{k_1}\gamma^{\dagger}_{-k_1})(u_{k_2}\gamma_{k_2}+v_{k_2}\gamma^{\dagger}_{-k_2})\times \\ &\qquad (u_{k_3}\gamma_{k_3}+v_{k_3}\gamma^{\dagger}_{-k_3})(u_{k_4}\gamma_{k_4}+v_{k_4}\gamma^{\dagger}_{-k_4})|\Psi_{\mathrm{BCS}}\rangle \\ &= u_{k_1}u_{k_2}v_{k_3}v_{k_4}\,\langle\Psi_{\mathrm{BCS}}|\gamma_{k_1}\gamma_{k_2}\gamma^{\dagger}_{-k_3}\gamma^{\dagger}_{-k_4}|\Psi_{\mathrm{BCS}}\rangle \\ &\quad + u_{k_1}v_{k_2}u_{k_3}v_{k_4}\,\langle\Psi_{\mathrm{BCS}}|\gamma_{k_1}\gamma^{\dagger}_{-k_2}\gamma_{k_3}\gamma^{\dagger}_{-k_4}|\Psi_{\mathrm{BCS}}\rangle\,, \end{aligned} \tag{5.4.24}$$

which gives a sum of two possibly nonzero terms. In the first term, the action of $\gamma^{\dagger}_{-k_3}\gamma^{\dagger}_{-k_4}$ produces two independent quasiparticle excitations: first a quasiparticle excitation with wave vector $-k_4$, followed by a quasiparticle excitation with wave vector $-k_3$. For the expectation to be nonzero, these two quasiparticle excitations must be annihilated by γ_{k_1} and γ_{k_2}. If we annihilate the quasiparticles in the order they were created, the expectation value is $+1$, whereas if we were to annihilate the quasiparticles in reverse order, this would be the same as anticommuting γ_{k_1} and γ_{k_2} and then annihilating in the correct order, in which case the expectation value is -1.

In the second term, we have the sequence $\gamma_{k_1}\gamma^{\dagger}_{-k_2}\gamma_{k_3}\gamma^{\dagger}_{-k_4}$ acting on $|\Psi_{\mathrm{BCS}}\rangle$, where $\gamma^{\dagger}_{-k_4}$ first creates a quasiparticle with wave vector $-k_4$. If $k_3 = -k_4$, then this quasiparticle is immediately annihilated, before $\gamma^{\dagger}_{-k_2}$ acts to create another quasiparticle of wave vector $-k_2$. For the expectation to be nonzero, we then need $k_1 = -k_2$ so this second quasiparticle is annihilated. However, unlike in the first term, we cannot get a nonzero expectation value if $k_3 = -k_2$, because this would mean physically that we annihilate a quasiparticle with wave vector $-k_2$ before it is created. Therefore, the expectation of this four-operator term evaluates to

$$\begin{aligned}\langle\Psi_{\mathrm{BCS}}|\tilde{c}_{k_1}\tilde{c}_{k_2}\tilde{c}_{k_3}\tilde{c}_{k_4}|\Psi_{\mathrm{BCS}}\rangle = \;& + u_{k_1}u_{k_2}v_{k_3}v_{k_4}\delta_{k_1,-k_4}\delta_{k_2,-k_3} \\ & - u_{k_1}u_{k_2}v_{k_3}v_{k_4}\delta_{k_1,-k_3}\delta_{k_2,-k_4} \\ & + u_{k_1}v_{k_2}u_{k_3}v_{k_4}\delta_{k_1,-k_2}\delta_{k_3,-k_4}. \end{aligned} \tag{5.4.25}$$

Similarly,

$$\begin{aligned}
\langle\Psi_{\rm BCS}|\tilde{c}_{k_1}\tilde{c}_{k_2}\tilde{c}_{k_3}\tilde{c}^\dagger_{k_4}|\Psi_{\rm BCS}\rangle &= \langle\Psi_{\rm BCS}|(u_{k_1}\gamma_{k_1}+v_{k_1}\gamma^\dagger_{-k_1})(u_{k_2}\gamma_{k_2}+v_{k_2}\gamma^\dagger_{-k_2})\times \\
&\qquad (u_{k_3}\gamma_{k_3}+v_{k_3}\gamma^\dagger_{-k_3})(u_{k_4}\gamma^\dagger_{k_4}+v_{k_4}\gamma_{-k_4})|\Psi_{\rm BCS}\rangle \\
&= u_{k_1}u_{k_2}v_{k_3}u_{k_4}\,\langle\Psi_{\rm BCS}|\gamma_{k_1}\gamma_{k_2}\gamma^\dagger_{-k_3}\gamma^\dagger_{k_4}|\Psi_{\rm BCS}\rangle \\
&\quad + u_{k_1}v_{-k_2}u_{k_3}u_{k_4}\,\langle\Psi_{\rm BCS}|\gamma_{k_1}\gamma^\dagger_{-k_2}\gamma_{k_3}\gamma^\dagger_{k_4}|\Psi_{\rm BCS}\rangle \\
&= \ + u_{k_1}u_{k_2}v_{k_3}u_{k_4}\delta_{k_1,k_4}\delta_{k_2,-k_3} \\
&\quad - u_{k_1}u_{k_2}v_{k_3}u_{k_4}\delta_{k_1,-k_3}\delta_{k_2,k_4} \\
&\quad + u_{k_1}v_{-k_2}u_{k_3}u_{k_4}\delta_{k_1,-k_2}\delta_{k_3,k_4}, \qquad (5.4.26)
\end{aligned}$$

$$\begin{aligned}
\langle\Psi_{\rm BCS}|\tilde{c}_{k_1}\tilde{c}_{k_2}\tilde{c}^\dagger_{k_3}\tilde{c}^\dagger_{k_4}|\Psi_{\rm BCS}\rangle &= \langle\Psi_{\rm BCS}|(u_{k_1}\gamma_{k_1}+v_{k_1}\gamma^\dagger_{-k_1})(u_{k_2}\gamma_{k_2}+v_{k_2}\gamma^\dagger_{-k_2})\times \\
&\qquad (u_{k_3}\gamma^\dagger_{k_3}+v_{k_3}\gamma_{-k_3})(u_{k_4}\gamma^\dagger_{k_4}+v_{k_4}\gamma_{-k_4})|\Psi_{\rm BCS}\rangle \\
&= u_{k_1}u_{k_2}u_{k_3}u_{k_4}\,\langle\Psi_{\rm BCS}|\gamma_{k_1}\gamma_{k_2}\gamma^\dagger_{k_3}\gamma^\dagger_{k_4}|\Psi_{\rm BCS}\rangle \\
&\quad + u_{k_1}v_{k_2}v_{k_3}u_{k_4}\,\langle\Psi_{\rm BCS}|\gamma_{k_1}\gamma^\dagger_{-k_2}\gamma_{-k_3}\gamma^\dagger_{k_4}|\Psi_{\rm BCS}\rangle \\
&= \ + u_{k_1}u_{k_2}u_{k_3}u_{k_4}\delta_{k_1,k_4}\delta_{k_2,k_3} \\
&\quad - u_{k_1}u_{k_2}u_{k_3}u_{k_4}\delta_{k_1,k_3}\delta_{k_2,k_4} \\
&\quad + u_{k_1}v_{k_2}v_{k_3}u_{k_4}\delta_{k_1,-k_2}\delta_{k_3,-k_4}, \qquad (5.4.27)
\end{aligned}$$

$$\begin{aligned}
\langle\Psi_{\rm BCS}|\tilde{c}_{k_1}\tilde{c}^\dagger_{k_2}\tilde{c}^\dagger_{k_3}\tilde{c}^\dagger_{k_4}|\Psi_{\rm BCS}\rangle &= \langle\Psi_{\rm BCS}|(u_{k_1}\gamma_{k_1}+v_{k_1}\gamma^\dagger_{-k_1})(u_{k_2}\gamma^\dagger_{k_2}+v_{k_2}\gamma_{-k_2})\times \\
&\qquad (u_{k_3}\gamma^\dagger_{k_3}+v_{k_3}\gamma_{-k_3})(u_{k_4}\gamma^\dagger_{k_4}+v_{k_4}\gamma_{-k_4})|\Psi_{\rm BCS}\rangle \\
&= u_{k_1}v_{k_2}u_{k_3}u_{k_4}\,\langle\Psi_{\rm BCS}|\gamma_{k_1}\gamma_{-k_2}\gamma^\dagger_{k_3}\gamma^\dagger_{k_4}|\Psi_{\rm BCS}\rangle \\
&\quad + u_{k_1}u_{k_2}v_{k_3}u_{k_4}\,\langle\Psi_{\rm BCS}|\gamma_{k_1}\gamma^\dagger_{k_2}\gamma_{-k_3}\gamma^\dagger_{k_4}|\Psi_{\rm BCS}\rangle \\
&= \ + u_{k_1}v_{k_2}u_{k_3}u_{k_4}\delta_{k_1,k_4}\delta_{k_2,-k_3} \\
&\quad - u_{k_1}v_{k_2}u_{k_3}u_{k_4}\delta_{k_1,k_3}\delta_{k_2,-k_4} \\
&\quad + u_{k_1}u_{k_2}v_{k_3}u_{k_4}\delta_{k_1,k_2}\delta_{k_3,-k_4}, \qquad (5.4.28)
\end{aligned}$$

$$\begin{aligned}
\langle\Psi_{\mathrm{BCS}}|\tilde{c}^{\dagger}_{k_1}\tilde{c}^{\dagger}_{k_2}\tilde{c}^{\dagger}_{k_3}\tilde{c}^{\dagger}_{k_4}|\Psi_{\mathrm{BCS}}\rangle &= \langle\Psi_{\mathrm{BCS}}|(u_{k_1}\gamma^{\dagger}_{k_1} + v_{k_1}\gamma_{-k_1})(u_{k_2}\gamma^{\dagger}_{k_2} + v_{k_2}\gamma_{-k_2})\times \\
&\qquad (u_{k_3}\gamma^{\dagger}_{k_3} + v_{k_3}\gamma_{-k_3})(u_{k_4}\gamma^{\dagger}_{k_4} + v_{k_4}\gamma_{-k_4})|\Psi_{\mathrm{BCS}}\rangle \\
&= v_{k_1}v_{k_2}u_{k_3}u_{k_4}\,\langle\Psi_{\mathrm{BCS}}|\gamma_{-k_1}\gamma_{-k_2}\gamma^{\dagger}_{k_3}\gamma^{\dagger}_{k_4}|\Psi_{\mathrm{BCS}}\rangle \\
&\quad + v_{k_1}u_{k_2}v_{k_3}u_{k_4}\,\langle\Psi_{\mathrm{BCS}}|\gamma_{-k_1}\gamma^{\dagger}_{k_2}\gamma_{-k_3}\gamma^{\dagger}_{k_4}|\Psi_{\mathrm{BCS}}\rangle \\
&= + v_{k_1}v_{k_2}u_{k_3}u_{k_4}\delta_{k_1,-k_4}\delta_{k_2,-k_3} \\
&\quad - v_{k_1}v_{k_2}u_{k_3}u_{k_4}\delta_{k_1,-k_3}\delta_{k_2,-k_4} \\
&\quad + v_{k_1}u_{k_2}v_{k_3}u_{k_4}\delta_{k_1,-k_2}\delta_{k_3,-k_4}. \qquad (5.4.29)
\end{aligned}$$

5.4.1.3 Wick Factorization

From (5.4.20), (5.4.21), (5.4.22), (5.4.23) and (5.4.25), we see that

$$\begin{aligned}
\langle\Psi_{\mathrm{BCS}}|\tilde{c}_{k_1}\tilde{c}_{k_2}\tilde{c}_{k_3}\tilde{c}_{k_4}|\Psi_{\mathrm{BCS}}\rangle = &+ (u_{k_1}v_{k_4}\delta_{k_1,-k_4})\,(u_{k_2}v_{k_3}\delta_{k_2,-k_3}) \\
&- (u_{k_1}v_{k_3}\delta_{k_1,-k_3})\,(u_{k_2}v_{k_4}\delta_{k_2,-k_4}) \qquad (5.4.30) \\
&+ (u_{k_1}v_{k_2}\delta_{k_1,-k_2})\,(u_{k_3}v_{k_4}\delta_{k_3,-k_4})\,,
\end{aligned}$$

which can then be written as

$$\begin{aligned}
\langle\Psi_{\mathrm{BCS}}|\tilde{c}_{k_1}\tilde{c}_{k_2}\tilde{c}_{k_3}\tilde{c}_{k_4}|\Psi_{\mathrm{BCS}}\rangle = &+ \langle\Psi_{\mathrm{BCS}}|\tilde{c}_{k_1}\tilde{c}_{k_4}|\Psi_{\mathrm{BCS}}\rangle\,\langle\Psi_{\mathrm{BCS}}|\tilde{c}_{k_2}\tilde{c}_{k_3}|\Psi_{\mathrm{BCS}}\rangle \\
&- \langle\Psi_{\mathrm{BCS}}|\tilde{c}_{k_1}\tilde{c}_{k_3}|\Psi_{\mathrm{BCS}}\rangle\,\langle\Psi_{\mathrm{BCS}}|\tilde{c}_{k_2}\tilde{c}_{k_4}|\Psi_{\mathrm{BCS}}\rangle \qquad (5.4.31) \\
&+ \langle\Psi_{\mathrm{BCS}}|\tilde{c}_{k_1}\tilde{c}_{k_2}|\Psi_{\mathrm{BCS}}\rangle\,\langle\Psi_{\mathrm{BCS}}|\tilde{c}_{k_3}\tilde{c}_{k_4}|\Psi_{\mathrm{BCS}}\rangle\,,
\end{aligned}$$

i.e. the four-operator expectation Wick factorizes into a sum of products of two-operator expectations. We can check that this Wick factorization holds for the other four-operator expectations, and it is also true for higher-order expectations.

For higher-order expectations, Wick factorization will produce a huge number of terms (over 100 for eight-operator expectations which we will encounter for the (2 + 2) supercluster), and so it is necessary to develop an expedient means of bookkeeping

to make sure that we have all the terms. The bookkeeping algorithm employed is as follows:

1. Keep the order of the operators fixed;
2. Start Wick contracting from the leftmost uncontracted operator,
   (a) connect to the rightmost uncontracted operator; or
   (b) if such a contraction has already been employed, move to the next operator on the left.
3. Repeat the first two steps until all operators have been contracted;
4. Determine the sign of the Wick-contracted term by reordering the operators, so that contracted operators occur in pairs.

Using the above four-annihilation-operator expectation as an example, we have

$$\begin{aligned}
\langle\Psi_{\mathrm{BCS}}|\tilde{c}_{k_1}\tilde{c}_{k_2}\tilde{c}_{k_3}\tilde{c}_{k_4}|\Psi_{\mathrm{BCS}}\rangle = &+ \langle\Psi_{\mathrm{BCS}}|\overbrace{\tilde{c}_{k_1}\tilde{c}_{k_2}\tilde{c}_{k_3}\tilde{c}_{k_4}}|\Psi_{\mathrm{BCS}}\rangle \\
&+ \langle\Psi_{\mathrm{BCS}}|\overbrace{\tilde{c}_{k_1}\tilde{c}_{k_2}\tilde{c}_{k_3}\tilde{c}_{k_4}}|\Psi_{\mathrm{BCS}}\rangle \\
&+ \langle\Psi_{\mathrm{BCS}}|\overbrace{\tilde{c}_{k_1}\tilde{c}_{k_2}}\overbrace{\tilde{c}_{k_3}\tilde{c}_{k_4}}|\Psi_{\mathrm{BCS}}\rangle \\
= &+ \langle\Psi_{\mathrm{BCS}}|\overbrace{\tilde{c}_{k_1}\tilde{c}_{k_4}}\overbrace{\tilde{c}_{k_2}\tilde{c}_{k_3}}|\Psi_{\mathrm{BCS}}\rangle \\
&- \langle\Psi_{\mathrm{BCS}}|\overbrace{\tilde{c}_{k_1}\tilde{c}_{k_3}}\overbrace{\tilde{c}_{k_2}\tilde{c}_{k_4}}|\Psi_{\mathrm{BCS}}\rangle \\
&+ \langle\Psi_{\mathrm{BCS}}|\overbrace{\tilde{c}_{k_1}\tilde{c}_{k_2}}\overbrace{\tilde{c}_{k_3}\tilde{c}_{k_4}}|\Psi_{\mathrm{BCS}}\rangle\,.
\end{aligned} \tag{5.4.32}$$

Now, using the relation

$$c_j = \frac{1}{\sqrt{N}}\sum_k e^{-\mathrm{i}kj}\,\tilde{c}_k \tag{5.4.33}$$

between the real-space fermion operators and the momentum-space fermion operators,

we find that the four-operator expectation

$$
\begin{aligned}
&\langle\Psi_{\mathrm{BCS}}|c_{j_1}c_{j_2}c_{j_3}c_{j_4}|\Psi_{\mathrm{BCS}}\rangle \\
&= \frac{1}{N^2}\sum_{k_1}\sum_{k_2}\sum_{k_3}\sum_{k_4} e^{-\mathrm{i}k_1 j_1}\, e^{-\mathrm{i}k_2 j_2}\, e^{-\mathrm{i}k_3 j_3}\, e^{-\mathrm{i}k_4 j_4}\, \langle\Psi_{\mathrm{BCS}}|\tilde{c}_{k_1}\tilde{c}_{k_2}\tilde{c}_{k_3}\tilde{c}_{k_4}|\Psi_{\mathrm{BCS}}\rangle \\
&= +\frac{1}{N^2}\sum_{k_1}\sum_{k_2}\sum_{k_3}\sum_{k_4} e^{-\mathrm{i}k_1 j_1}\, e^{-\mathrm{i}k_2 j_2}\, e^{-\mathrm{i}k_3 j_3}\, e^{-\mathrm{i}k_4 j_4} \times \\
&\qquad\qquad \langle\Psi_{\mathrm{BCS}}|\tilde{c}_{k_1}\tilde{c}_{k_4}|\Psi_{\mathrm{BCS}}\rangle\, \langle\Psi_{\mathrm{BCS}}|\tilde{c}_{k_2}\tilde{c}_{k_3}|\Psi_{\mathrm{BCS}}\rangle \\
&\quad -\frac{1}{N^2}\sum_{k_1}\sum_{k_2}\sum_{k_3}\sum_{k_4} e^{-\mathrm{i}k_1 j_1}\, e^{-\mathrm{i}k_2 j_2}\, e^{-\mathrm{i}k_3 j_3}\, e^{-\mathrm{i}k_4 j_4} \times \\
&\qquad\qquad \langle\Psi_{\mathrm{BCS}}|\tilde{c}_{k_1}\tilde{c}_{k_3}|\Psi_{\mathrm{BCS}}\rangle\, \langle\Psi_{\mathrm{BCS}}|\tilde{c}_{k_2}\tilde{c}_{k_4}|\Psi_{\mathrm{BCS}}\rangle \\
&\quad +\frac{1}{N^2}\sum_{k_1}\sum_{k_2}\sum_{k_3}\sum_{k_4} e^{-\mathrm{i}k_1 j_1}\, e^{-\mathrm{i}k_2 j_2}\, e^{-\mathrm{i}k_3 j_3}\, e^{-\mathrm{i}k_4 j_4} \times \\
&\qquad\qquad \langle\Psi_{\mathrm{BCS}}|\tilde{c}_{k_1}\tilde{c}_{k_2}|\Psi_{\mathrm{BCS}}\rangle\, \langle\Psi_{\mathrm{BCS}}|\tilde{c}_{k_3}\tilde{c}_{k_4}|\Psi_{\mathrm{BCS}}\rangle \\
&= +\left(\frac{1}{N}\sum_{k_1}\sum_{k_4} e^{-\mathrm{i}k_1 j_1}\, e^{-\mathrm{i}k_4 j_4}\, \langle\Psi_{\mathrm{BCS}}|\tilde{c}_{k_1}\tilde{c}_{k_4}|\Psi_{\mathrm{BCS}}\rangle\right)\times \\
&\qquad\qquad \left(\frac{1}{N}\sum_{k_2}\sum_{k_3} e^{-\mathrm{i}k_2 j_2}\, e^{-\mathrm{i}k_3 j_3}\, \langle\Psi_{\mathrm{BCS}}|\tilde{c}_{k_2}\tilde{c}_{k_3}|\Psi_{\mathrm{BCS}}\rangle\right) \\
&\quad -\left(\frac{1}{N}\sum_{k_1}\sum_{k_3} e^{-\mathrm{i}k_1 j_1}\, e^{-\mathrm{i}k_3 j_3}\, \langle\Psi_{\mathrm{BCS}}|\tilde{c}_{k_1}\tilde{c}_{k_3}|\Psi_{\mathrm{BCS}}\rangle\right)\times \\
&\qquad\qquad \left(\frac{1}{N}\sum_{k_2}\sum_{k_4} e^{-\mathrm{i}k_2 j_2}\, e^{-\mathrm{i}k_4 j_4}\, \langle\Psi_{\mathrm{BCS}}|\tilde{c}_{k_2}\tilde{c}_{k_4}|\Psi_{\mathrm{BCS}}\rangle\right) \\
&\quad +\left(\frac{1}{N}\sum_{k_1}\sum_{k_2} e^{-\mathrm{i}k_1 j_1}\, e^{-\mathrm{i}k_2 j_2}\, \langle\Psi_{\mathrm{BCS}}|\tilde{c}_{k_1}\tilde{c}_{k_2}|\Psi_{\mathrm{BCS}}\rangle\right)\times \\
&\qquad\qquad \left(\frac{1}{N}\sum_{k_3}\sum_{k_4} e^{-\mathrm{i}k_3 j_3}\, e^{-\mathrm{i}k_4 j_4}\, \langle\Psi_{\mathrm{BCS}}|\tilde{c}_{k_3}\tilde{c}_{k_4}|\Psi_{\mathrm{BCS}}\rangle\right) \\
&= +\langle\Psi_{\mathrm{BCS}}|c_{j_1}c_{j_4}|\Psi_{\mathrm{BCS}}\rangle\, \langle\Psi_{\mathrm{BCS}}|c_{j_2}c_{j_3}|\Psi_{\mathrm{BCS}}\rangle \\
&\quad -\langle\Psi_{\mathrm{BCS}}|c_{j_1}c_{j_3}|\Psi_{\mathrm{BCS}}\rangle\, \langle\Psi_{\mathrm{BCS}}|c_{j_2}c_{j_4}|\Psi_{\mathrm{BCS}}\rangle \\
&\quad +\langle\Psi_{\mathrm{BCS}}|c_{j_1}c_{j_2}|\Psi_{\mathrm{BCS}}\rangle\, \langle\Psi_{\mathrm{BCS}}|c_{j_3}c_{j_4}|\Psi_{\mathrm{BCS}}\rangle
\end{aligned}
\tag{5.4.34}
$$

Wick factorizes as well. This makes life simple for us, since we need to evaluate real-

space expectations instead of momentum-space expectations when calculating the cluster and supercluster density matrices using the method of referencing operators.

5.4.1.4 Asymptotic Behaviour of Two-Point Functions

Before we use the results in Section 5.4.1.3, and go ahead evaluating real-space expectations that will be used in calculating the (2 + 2) supercluster density matrix, let us note that certain terms will occur over and over again in the expressions for the matrix elements. It is therefore worthwhile introducing the shorthand notations

$$\begin{aligned} f_u &= \frac{1}{N}\sum_k u_k^2, \quad f_v = \frac{1}{N}\sum_k v_k^2, \\ g_u(r) &= \frac{1}{N}\sum_k e^{\mathrm{i}kr} u_k^2, \quad g_v(r) = \frac{1}{N}\sum_k e^{\mathrm{i}kr} v_k^2, \\ h(r) &= \frac{1}{N}\sum_k e^{\mathrm{i}kr} u_k v_k, \end{aligned} \tag{5.4.35}$$

where the functions f, g and h are two-point functions of the superconducting ground state. Using the fact that $u_{-k} = u_k$ and $v_{-k} = -v_k$, we know that g_u and g_v are purely real, while h is purely imaginary.

Since the two-point functions $g_u(r)$, $g_v(r)$ and $h(r)$ will eventually appear in the supercluster density-matrix elements in various combinations, it would also be good to have a feel of what their asymptotic behaviours are like. For generic dispersion relations ϵ_k and superconducting gaps Δ_k, u_k^2 will be very nearly zero for $|k| < k_F$, and very nearly one for $|k| > k_F$, where $v_k^2 = 1 - u_k^2$ will be very nearly one for $|k| < k_F$ and very nearly zero for $|k| > k_F$, where the Fermi wave vector is such that $\epsilon_{k_F} = \mu$, with μ being the chemical potential. The values of u_k^2 and v_k^2 will change smoothly from zero to one, and one to zero respectively over very small intervals of wave vectors $(\pm k_F - \delta k, \pm k_F + \delta k)$ around the two Fermi wave vectors $\pm k_F$, for some $\delta k \ll k_F$. Meanwhile, the product $u_k v_k$, whose values at the two Fermi points $\pm k_F$ are ± 1, will drop off very rapidly away

from $\pm k_F$, so that outside these two very small intervals $(\pm k_F - \delta k, \pm k_F + \delta k)$, its value would be very nearly zero.

This tells us that in $h(r)$, the dominant contributions in the sum over wave vectors k comes from the two very small intervals $(\pm k_F - \delta k, \pm k_F + \delta k)$. We can therefore write

$$h(r) \approx \frac{1}{N} \sum_{k \approx -k_F} e^{\mathrm{i}\, kr} u_k v_k + \frac{1}{N} \sum_{k \approx +k_F} e^{\mathrm{i}\, kr} u_k v_k. \tag{5.4.36}$$

Over these two small intervals of wave vectors $(\pm k_F - \delta k, \pm k_F + \delta k)$, a generic superconducting gap Δ_k will not change appreciably, so we can replace Δ_k by its values $\pm \Delta_{k_F}$ at the two Fermi points $\pm k_F$. Over these two small intervals of wave vectors $(\pm k_F - \delta k, \pm k_F + \delta k)$, we can also linearize the dispersion relation, to write

$$\epsilon_k - \mu = \pm \hbar v_F (k \mp k_F), \tag{5.4.37}$$

where v_F is the Fermi velocity.

Converting the sums over k to integrals over k in the usual way, we can then write (5.4.36) as

$$h(r) \approx \int_{-k_F - \delta k}^{-k_F + \delta k} \frac{dk}{2\pi} \frac{-\Delta_{k_F}\, e^{\mathrm{i}\, kr}}{\sqrt{\hbar^2 v_F^2 (k + k_F)^2 + \Delta_{k_F}^2}} + \int_{k_F - \delta k}^{k_F + \delta k} \frac{dk}{2\pi} \frac{\Delta_{k_F}\, e^{\mathrm{i}\, kr}}{\sqrt{\hbar^2 v_F^2 (k - k_F)^2 + \Delta_{k_F}^2}}. \tag{5.4.38}$$

Making the change of integration variable from $k \to k' = k + k_F$ in the integral over $(-k_F - \delta k, -k_F + \delta k)$, and the change of integration variable from $k \to k' = k - k_F$ in the integral over $(k_F - \delta k, k_F + \delta k)$, we then obtain

$$\begin{aligned} h(r) &\approx -\frac{\Delta_{k_F}}{2\pi\hbar v_F}\, e^{-\mathrm{i}\, k_F r} \int_{-\delta k}^{+\delta k} dk' \, \frac{e^{\mathrm{i}\, k' r}}{\sqrt{k'^2 + \kappa^2}} + \frac{\Delta_{k_F}}{2\pi\hbar v_F}\, e^{\mathrm{i}\, k_F r} \int_{-\delta k}^{+\delta k} dk' \, \frac{e^{\mathrm{i}\, k' r}}{\sqrt{k'^2 + \kappa^2}} \\ &= \frac{\mathrm{i}\, \Delta_{k_F}}{\pi\hbar v_F} \sin k_F r \int_{-\delta k}^{+\delta k} dk' \, \frac{e^{\mathrm{i}\, k' r}}{\sqrt{k'^2 + \kappa^2}}, \end{aligned} \tag{5.4.39}$$

where

$$\kappa = \frac{\Delta_{k_F}}{\hbar v_F} \tag{5.4.40}$$

is the reciprocal of the superconducting correlation length ξ.

Strictly speaking, the $(k'^2 + \kappa^2)^{-1/2}$ term in the integrand does not fall off with k' rapidly enough for its integral over $-\infty < k' < +\infty$ to converge absolutely. Fortunately, the integral of the overall integrand $e^{\mathrm{i}\,k'r}(k'^2+\kappa^2)^{-1/2}$ does converge when integrated over $-\infty < k' < +\infty$, when r is much larger than the superconducting correlation length ξ. This is because $e^{\mathrm{i}\,k'r}$ oscillates very rapidly at large k', and thus the integral of $e^{\mathrm{i}\,k'r}(k'^2 + \kappa^2)^{-1/2}$ over one half-period of $e^{\mathrm{i}\,k'r}$ tends to cancel the integral over the next half-period. By simple scaling arguments, we know, therefore, that the integral of $e^{\mathrm{i}\,k'r}(k'^2 + \kappa^2)^{-1/2}$ over $-\infty < k' < +\infty$ receives its dominant contribution from the interval $-r^{-1} < k' < +r^{-1}$, and so we can, to a very good approximation, extend the range of integration in (5.4.39) to $-\infty < k' < \infty$, and write

$$h(r) \approx \frac{\mathrm{i}\,\Delta_{k_F}}{\pi\hbar v_F} \sin k_F r \int_{-\infty}^{+\infty} dk' \, \frac{e^{\mathrm{i}\,k'r}}{\sqrt{k'^2 + \kappa^2}}. \tag{5.4.41}$$

We can evaluate the integral over k' using contour integration. The integrand $e^{\mathrm{i}\,k'r}$ $(k'^2 + \kappa^2)^{-1/2}$ has two branch cuts, so we pick the closed contour $C = \mathrm{I} + \mathrm{II} + \mathrm{III} + \mathrm{IV} + \mathrm{V}$ on the complex k' plane, as shown in Figure 5.8. Since $e^{\mathrm{i}\,k'r}(k'^2 + \kappa^2)^{-1/2}$ is analytic in the region of complex k'-plane bounded by the closed contour C, we know that

$$\oint_C dk' \, \frac{e^{\mathrm{i}\,k'r}}{\sqrt{k'^2 + \kappa^2}} = 0 = \int_{\mathrm{I}} + \int_{\mathrm{II}} + \int_{\mathrm{III}} + \int_{\mathrm{IV}} + \int_{\mathrm{V}}, \tag{5.4.42}$$

where $\int_{C_i}$ is a shorthand for

$$\int_{C_i} dk' \, \frac{e^{\mathrm{i}\,k'r}}{\sqrt{k'^2 + \kappa^2}}. \tag{5.4.43}$$

Because the integrand vanishes along parts I and V of the closed contour, we also know that

$$\int_{\mathrm{I}} = 0 \int_{\mathrm{V}}. \tag{5.4.44}$$

This tells us that

$$\int_{\mathrm{I}} = -\int_{\mathrm{III}} - \int_{\mathrm{IV}}, \tag{5.4.45}$$

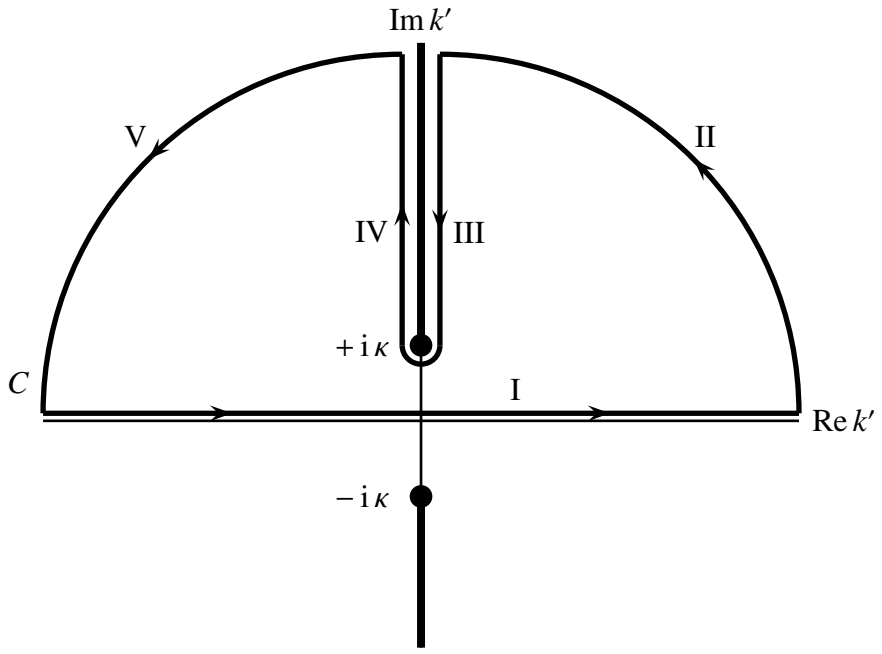

Figure 5.8: Integration of the function $e^{\mathrm{i}k'r}(k'^2+\kappa^2)^{-1/2}$ over the closed path $C = \mathrm{I} + \mathrm{II} + \mathrm{III} + \mathrm{IV} + \mathrm{IV}$ in the complex k'-plane.

where

$$\int_{\mathrm{I}} = \int_{-\infty}^{+\infty} dk' \, \frac{e^{\mathrm{i}k'r}}{\sqrt{k'^2+\kappa^2}} \tag{5.4.46}$$

is the integral we wished to evaluate, and

$$\int_{\mathrm{III}} = \int_{+\mathrm{i}\infty}^{+\mathrm{i}\kappa} dk' \, \frac{e^{\mathrm{i}k'r}}{\sqrt{k'^2+\kappa^2}}, \tag{5.4.47}$$

$$\int_{\mathrm{IV}} = \int_{+\mathrm{i}\kappa}^{+\mathrm{i}\infty} dk' \, \frac{e^{\mathrm{i}k'r}}{\sqrt{k'^2+\kappa^2}}. \tag{5.4.48}$$

By changing integration variables to $k' = \mathrm{i}k''$, we then find that

$$\int_{\mathrm{III}} = \int_{+\infty}^{+\kappa} \mathrm{i}\, dk'' \, \frac{e^{-k''r}}{+\mathrm{i}\sqrt{k''^2-\kappa^2}} = -\int_{+\kappa}^{+\infty} dk'' \, \frac{e^{-k''r}}{\sqrt{k''^2-\kappa^2}}, \tag{5.4.49}$$

$$\int_{\mathrm{IV}} = \int_{+\kappa}^{+\infty} \mathrm{i}\, dk'' \, \frac{e^{-k''r}}{-\mathrm{i}\sqrt{k''^2-\kappa^2}} = -\int_{+\kappa}^{+\infty} dk'' \, \frac{e^{-k''r}}{\sqrt{k''^2-\kappa^2}}, \tag{5.4.50}$$

where we pick $\sqrt{-1} = \pm\mathrm{i}$ on the positive and negative sides of the branch cut. We thus

have $\int_{\mathrm{III}} = \int_{\mathrm{IV}}$, and

$$\int_{-\infty}^{+\infty} dk' \, \frac{e^{\mathrm{i}\,k'r}}{\sqrt{k'^2 + \kappa^2}} = 2 \int_{+\kappa}^{+\infty} dk'' \, \frac{e^{-k''r}}{\sqrt{k''^2 - \kappa^2}}, \tag{5.4.51}$$

which we find, using *Mathematica*, to be

$$\int_{-\infty}^{+\infty} dk' \, \frac{e^{\mathrm{i}\,k'r}}{\sqrt{k'^2 + \kappa^2}} = 2K_0(\kappa r), \tag{5.4.52}$$

where $K_n(x)$ is the nth-order modified Bessel function of the second kind. From Ref. 210 and Ref. 212, we know that for fixed n, and $x \gg n$,

$$K_n(x) \approx \sqrt{\frac{\pi}{2}} \, \frac{e^{-x}}{\sqrt{x}}. \tag{5.4.53}$$

Combining the results in (5.4.41), (5.4.52), and (5.4.53), we then obtain the asymptotic behaviour

$$h(r) \approx \mathrm{i}\,\kappa \, \sqrt{\frac{2}{\pi}} \, \frac{e^{-\kappa r}}{\sqrt{\kappa r}} \, \sin k_F r \tag{5.4.54}$$

for the anomalous two-point function $h(r)$.

Now, let us turn our attention to $g_u(r)$ and $g_v(r)$. Writing them as integrals over $-\pi \leq k \leq +\pi$,

$$g_u(r) = \int_{-\pi}^{+\pi} \frac{dk}{2\pi} \, e^{\mathrm{i}\,kr} \, u_k^2, \tag{5.4.55}$$

$$g_v(r) = \int_{-\pi}^{+\pi} \frac{dk}{2\pi} \, e^{\mathrm{i}\,kr} \, v_k^2, \tag{5.4.56}$$

and integrating by parts,

$$g_u(r) = \left[\frac{e^{\mathrm{i}\,kr} u_k^2}{\mathrm{i}\,r} \right]_{-\pi}^{+\pi} - \frac{1}{\mathrm{i}\,r} \int_{-\pi}^{+\pi} \frac{dk}{2\pi} \, e^{\mathrm{i}\,kr} \, \frac{du_k^2}{dk}, \tag{5.4.57}$$

$$g_v(r) = \left[\frac{e^{\mathrm{i}\,kr} v_k^2}{\mathrm{i}\,r} \right]_{-\pi}^{+\pi} - \frac{1}{\mathrm{i}\,r} \int_{-\pi}^{+\pi} \frac{dk}{2\pi} \, e^{\mathrm{i}\,kr} \, \frac{dv_k^2}{dk}, \tag{5.4.58}$$

we make two observations: (i) because $u_{-k}^2 = u_k^2$, $v_{-k}^2 = v_k^2$, and $e^{-\mathrm{i}\,\pi} = e^{+\mathrm{i}\,\pi}$, the boundary terms vanish, and we are left with $\mathrm{i}\,/r$ multiplied by the Fourier transforms of du_k^2/dk and dv_k^2/dk.

Since u_k^2 and v_k^2 are very nearly zero and one at most values of k, apart from the small intervals $(\pm k_F - \delta k, \pm k_F + \delta k)$, we can again break the integral over $-\pi \leq k \leq +\pi$ into two pieces, one centered about each Fermi point $\pm k_F$. Linearizing the dispersion relation and fixing the value of the superconducting gap, as we have done when evaluating the Fourier transform of $u_k v_k$, we find that within the small intervals $(\pm k_F - \delta k, \pm k_F + \delta k)$ about the Fermi points $\pm k_F$,

$$u_k^2 = \frac{1}{2}\left(1 \pm \frac{\hbar v_F(k \mp k_F)}{\sqrt{\hbar^2 v_F^2 (k \mp k_F)^2 + \Delta_{k_F}^2}}\right), \tag{5.4.59}$$

$$v_k^2 = \frac{1}{2}\left(1 \mp \frac{\hbar v_F(k \mp k_F)}{\sqrt{\hbar^2 v_F^2 (k \mp k_F)^2 + \Delta_{k_F}^2}}\right). \tag{5.4.60}$$

With the change of variables from $k \rightarrow k' = k \pm k_F$, we then find the derivatives of u_k^2 and v_k^2 within the two small intervals $(\pm k_F - \delta k, \pm k_F + \delta k)$ to be

$$\frac{du_{k'}^2}{dk'} = \pm \frac{\kappa^2}{2(k'^2 + \kappa^2)^{3/2}}, \tag{5.4.61}$$

$$\frac{dv_{k'}^2}{dk'} = \mp \frac{\kappa^2}{2(k'^2 + \kappa^2)^{3/2}}, \tag{5.4.62}$$

respectively.

Just as we did when evaluating $h(r)$, let us extend the limits of the integrals about both Fermi points, to write

$$\begin{aligned} g_u(r) &\approx -\frac{\mathrm{i}\,\kappa^2}{2\pi r}\, e^{-\mathrm{i}\,k_F r} \int_{-\infty}^{+\infty} dk'\, \frac{e^{\mathrm{i}\,k' r}}{(k'^2 + \kappa^2)^{3/2}} + \frac{\mathrm{i}\,\kappa^2}{2\pi r}\, e^{\mathrm{i}\,k_F r} \int_{-\infty}^{+\infty} dk'\, \frac{e^{\mathrm{i}\,k' r}}{(k'^2 + \kappa^2)^{3/2}} \\ &= -\frac{\kappa^2}{\pi r}\, \sin k_F r \int_{-\infty}^{+\infty} dk'\, \frac{e^{\mathrm{i}\,k' r}}{(k'^2 + \kappa^2)^{3/2}}, \end{aligned} \tag{5.4.63}$$

$$g_v(r) \approx \frac{\kappa^2}{\pi r}\, \sin k_F r \int_{-\infty}^{+\infty} dk'\, \frac{e^{\mathrm{i}\,k' r}}{(k'^2 + \kappa^2)^{3/2}}. \tag{5.4.64}$$

Unlike the integral for $h(r)$, *Mathematica* could evaluate the integral for $g_u(r)$ and $g_v(r)$, giving it to be

$$\int_{-\infty}^{+\infty} dk'\, \frac{e^{\mathrm{i}\,k' r}}{(k'^2 + \kappa^2)^{3/2}} = \frac{2r}{\kappa}\, K_1(\kappa r), \tag{5.4.65}$$

where $K_1(x)$ is the first-order modified Bessel function of the second kind. The asymptotic behaviour of $K_1(x)$ as x becomes large is given in (5.4.53). Combining the results in (5.4.63), (5.4.64), (5.4.65) and (5.4.53), we find the asymptotic behaviours

$$g_u(r) \approx -\kappa \sqrt{\frac{2}{\pi}} \frac{e^{-\kappa r}}{\sqrt{\kappa r}} \sin k_F r, \tag{5.4.66a}$$

$$g_v(r) \approx \kappa \sqrt{\frac{2}{\pi}} \frac{e^{-\kappa r}}{\sqrt{\kappa r}} \sin k_F r, \tag{5.4.66b}$$

for the usual two-point functions.

5.4.1.5 List of Two-Point Functions

Now, we already know from Section 5.4.1 that the expectation of the product of an odd number of fermion operators vanishes, so the only nonzero expectations which we need to compute are products of an even number of fermion operators, which can all be Wick factorized into sums of products of two-operator expectations. For the (2 + 2) supercluster, which consists of the sites $j = 0, 1, r, r + 1$, the two-operator expectations are

$$\begin{aligned}
\langle \Psi_{\mathrm{BCS}} | c_0 c_1 | \Psi_{\mathrm{BCS}} \rangle &= \frac{1}{N} \sum_{k_1} \sum_{k_2} e^{-\mathrm{i}\, k_2} \langle \Psi_{\mathrm{BCS}} | \tilde{c}_{k_1} \tilde{c}_{k_2} | \Psi_{\mathrm{BCS}} \rangle \\
&= \frac{1}{N} \sum_{k_1} \sum_{k_2} e^{-\mathrm{i}\, k_2} u_{k_1} v_{k_2} \delta_{k_1, -k_2} \\
&= \frac{1}{N} \sum_{k_1} e^{\mathrm{i}\, k_1} u_{k_1} v_{-k_1} \\
&= \frac{1}{N} \sum_{k_1} e^{-\mathrm{i}\, k_1} u_{k_1} v_{k_1} = h^*(1), \qquad (5.4.67) \\
\langle \Psi_{\mathrm{BCS}} | c_0 c_r | \Psi_{\mathrm{BCS}} \rangle &= \frac{1}{N} \sum_{k_1} \sum_{k_2} e^{-\mathrm{i}\, k_2 r} \langle \Psi_{\mathrm{BCS}} | \tilde{c}_{k_1} \tilde{c}_{k_2} | \Psi_{\mathrm{BCS}} \rangle \\
&= \frac{1}{N} \sum_{k_1} \sum_{k_2} e^{-\mathrm{i}\, k_2 r} u_{k_1} v_{k_2} \delta_{k_1, -k_2} \\
&= \frac{1}{N} \sum_{k_1} e^{\mathrm{i}\, k_1 r} u_{k_1} v_{-k_1}
\end{aligned}$$

$$= \frac{1}{N}\sum_{k_1} e^{-\mathrm{i}\,k_1 r} u_{k_1} v_{k_1} = h^*(r), \tag{5.4.68}$$

$$\begin{aligned}
\langle \Psi_{\mathrm{BCS}} | c_0 c_{r+1} | \Psi_{\mathrm{BCS}} \rangle &= \frac{1}{N}\sum_{k_1}\sum_{k_2} e^{-\mathrm{i}\,k_2(r+1)} \langle \Psi_{\mathrm{BCS}} | \tilde{c}_{k_1} \tilde{c}_{k_2} | \Psi_{\mathrm{BCS}} \rangle \\
&= \frac{1}{N}\sum_{k_1}\sum_{k_2} e^{-\mathrm{i}\,k_2(r+1)} u_{k_1} v_{k_2} \delta_{k_1,-k_2} \\
&= \frac{1}{N}\sum_{k_1} e^{\mathrm{i}\,k_1(r+1)} u_{k_1} v_{-k_1} \\
&= \frac{1}{N}\sum_{k_1} e^{-\mathrm{i}\,k_1(r+1)} u_{k_1} v_{k_1} = h^*(r+1),
\end{aligned} \tag{5.4.69}$$

$$\begin{aligned}
\langle \Psi_{\mathrm{BCS}} | c_0 c_0^\dagger | \Psi_{\mathrm{BCS}} \rangle &= \frac{1}{N}\sum_{k_1}\sum_{k_2} \langle \Psi_{\mathrm{BCS}} | \tilde{c}_{k_1} \tilde{c}_{k_2}^\dagger | \Psi_{\mathrm{BCS}} \rangle \\
&= \frac{1}{N}\sum_{k_1}\sum_{k_2} u_{k_1} u_{k_2} \delta_{k_1,k_2} \\
&= \frac{1}{N}\sum_{k_1} u_{k_1}^2 = f_u,
\end{aligned} \tag{5.4.70}$$

$$\begin{aligned}
\langle \Psi_{\mathrm{BCS}} | c_0 c_1^\dagger | \Psi_{\mathrm{BCS}} \rangle &= \frac{1}{N}\sum_{k_1}\sum_{k_2} e^{\mathrm{i}\,k_2} \langle \Psi_{\mathrm{BCS}} | \tilde{c}_{k_1} \tilde{c}_{k_2}^\dagger | \Psi_{\mathrm{BCS}} \rangle \\
&= \frac{1}{N}\sum_{k_1}\sum_{k_2} e^{\mathrm{i}\,k_2} u_{k_1} u_{k_2} \delta_{k_1,k_2} \\
&= \frac{1}{N}\sum_{k_1} e^{\mathrm{i}\,k_1}\, u_{k_1}^2 = g_u(1),
\end{aligned} \tag{5.4.71}$$

$$\begin{aligned}
\langle \Psi_{\mathrm{BCS}} | c_0 c_r^\dagger | \Psi_{\mathrm{BCS}} \rangle &= \frac{1}{N}\sum_{k_1}\sum_{k_2} e^{\mathrm{i}\,k_2 r} \langle \Psi_{\mathrm{BCS}} | \tilde{c}_{k_1} \tilde{c}_{k_2}^\dagger | \Psi_{\mathrm{BCS}} \rangle \\
&= \frac{1}{N}\sum_{k_1}\sum_{k_2} e^{\mathrm{i}\,k_2 r} u_{k_1} u_{k_2} \delta_{k_1,k_2} \\
&= \frac{1}{N}\sum_{k_1} e^{\mathrm{i}\,k_1 r}\, u_{k_1}^2 = g_u(r),
\end{aligned} \tag{5.4.72}$$

$$\begin{aligned}
\langle \Psi_{\mathrm{BCS}} | c_0 c_{r+1}^\dagger | \Psi_{\mathrm{BCS}} \rangle &= \frac{1}{N}\sum_{k_1}\sum_{k_2} e^{\mathrm{i}\,k_2(r+1)} \langle \Psi_{\mathrm{BCS}} | \tilde{c}_{k_1} \tilde{c}_{k_2}^\dagger | \Psi_{\mathrm{BCS}} \rangle \\
&= \frac{1}{N}\sum_{k_1}\sum_{k_2} e^{\mathrm{i}\,k_2(r+1)} u_{k_1} u_{k_2} \delta_{k_1,k_2}
\end{aligned}$$

$$= \frac{1}{N}\sum_{k_1} e^{\mathrm{i}k_1(r+1)}\, u_{k_1}^2 = g_u(r+1), \tag{5.4.73}$$

$$\begin{aligned}
\langle\Psi_{\mathrm{BCS}}|c_1 c_r|\Psi_{\mathrm{BCS}}\rangle &= \frac{1}{N}\sum_{k_1}\sum_{k_2} e^{-\mathrm{i}k_1}\, e^{-\mathrm{i}k_2 r}\,\langle\Psi_{\mathrm{BCS}}|\tilde{c}_{k_1}\tilde{c}_{k_2}|\Psi_{\mathrm{BCS}}\rangle \\
&= \frac{1}{N}\sum_{k_1}\sum_{k_2} e^{-\mathrm{i}k_1}\, e^{-\mathrm{i}k_2 r} u_{k_1} v_{k_2}\delta_{k_1,-k_2} \\
&= \frac{1}{N}\sum_{k_1} e^{\mathrm{i}k_1(r-1)}\, u_{k_1} v_{-k_1} \\
&= \frac{1}{N}\sum_{k_1} e^{-\mathrm{i}k_1(r-1)}\, u_{k_1} v_{k_1} = h^*(r-1),
\end{aligned} \tag{5.4.74}$$

$$\begin{aligned}
\langle\Psi_{\mathrm{BCS}}|c_1 c_{r+1}|\Psi_{\mathrm{BCS}}\rangle &= \frac{1}{N}\sum_{k_1}\sum_{k_2} e^{-\mathrm{i}k_1}\, e^{-\mathrm{i}k_2(r+1)}\,\langle\Psi_{\mathrm{BCS}}|\tilde{c}_{k_1}\tilde{c}_{k_2}|\Psi_{\mathrm{BCS}}\rangle \\
&= \frac{1}{N}\sum_{k_1}\sum_{k_2} e^{-\mathrm{i}k_1}\, e^{-\mathrm{i}k_2(r+1)} u_{k_1} v_{k_2}\delta_{k_1,-k_2} \\
&= \frac{1}{N}\sum_{k_1} e^{\mathrm{i}k_1 r}\, u_{k_1} v_{-k_1} \\
&= \frac{1}{N}\sum_{k_1} e^{-\mathrm{i}k_1 r}\, u_{k_1} v_{k_1} = h^*(r),
\end{aligned} \tag{5.4.75}$$

$$\begin{aligned}
\langle\Psi_{\mathrm{BCS}}|c_1 c_0^\dagger|\Psi_{\mathrm{BCS}}\rangle &= \frac{1}{N}\sum_{k_1}\sum_{k_2} e^{-\mathrm{i}k_1}\,\langle\Psi_{\mathrm{BCS}}|\tilde{c}_{k_1}\tilde{c}_{k_2}|\Psi_{\mathrm{BCS}}\rangle \\
&= \frac{1}{N}\sum_{k_1}\sum_{k_2} e^{-\mathrm{i}k_1} u_{k_1} u_{k_2}\delta_{k_1,k_2} \\
&= \frac{1}{N}\sum_{k_1} e^{-\mathrm{i}k_1}\, u_{k_1}^2 = g_u(1),
\end{aligned} \tag{5.4.76}$$

$$\begin{aligned}
\langle\Psi_{\mathrm{BCS}}|c_1 c_1^\dagger|\Psi_{\mathrm{BCS}}\rangle &= \frac{1}{N}\sum_{k_1}\sum_{k_2} e^{-\mathrm{i}k_1}\, e^{\mathrm{i}k_2}\,\langle\Psi_{\mathrm{BCS}}|\tilde{c}_{k_1}\tilde{c}_{k_2}|\Psi_{\mathrm{BCS}}\rangle \\
&= \frac{1}{N}\sum_{k_1}\sum_{k_2} e^{-\mathrm{i}k_1}\, e^{\mathrm{i}k_2} u_{k_1} u_{k_2}\delta_{k_1,k_2} \\
&= \frac{1}{N}\sum_{k_1} u_{k_1}^2 = f_u,
\end{aligned} \tag{5.4.77}$$

$$\langle\Psi_{\mathrm{BCS}}|c_1 c_r^\dagger|\Psi_{\mathrm{BCS}}\rangle = \frac{1}{N}\sum_{k_1}\sum_{k_2} e^{-\mathrm{i}k_1}\, e^{\mathrm{i}k_2 r}\,\langle\Psi_{\mathrm{BCS}}|\tilde{c}_{k_1}\tilde{c}_{k_2}|\Psi_{\mathrm{BCS}}\rangle$$

$$= \frac{1}{N}\sum_{k_1}\sum_{k_2} e^{-\mathrm{i}k_1}\, e^{\mathrm{i}k_2 r} u_{k_1} u_{k_2} \delta_{k_1,k_2}$$

$$= \frac{1}{N}\sum_{k_1} e^{\mathrm{i}k_1(r-1)} u_{k_1}^2 = g_u(r-1), \tag{5.4.78}$$

$$\langle \Psi_{\mathrm{BCS}} | c_1 c_{r+1}^\dagger | \Psi_{\mathrm{BCS}} \rangle = \frac{1}{N}\sum_{k_1}\sum_{k_2} e^{-\mathrm{i}k_1}\, e^{\mathrm{i}k_2(r+1)} \langle \Psi_{\mathrm{BCS}} | \tilde{c}_{k_1} \tilde{c}_{k_2} | \Psi_{\mathrm{BCS}} \rangle$$

$$= \frac{1}{N}\sum_{k_1}\sum_{k_2} e^{-\mathrm{i}k_1}\, e^{\mathrm{i}k_2(r+1)} u_{k_1} u_{k_2} \delta_{k_1,k_2}$$

$$= \frac{1}{N}\sum_{k_1} e^{\mathrm{i}k_1 r} u_{k_1}^2 = g_u(r), \tag{5.4.79}$$

$$\langle \Psi_{\mathrm{BCS}} | c_r c_{r+1} | \Psi_{\mathrm{BCS}} \rangle = \frac{1}{N}\sum_{k_1}\sum_{k_2} e^{-\mathrm{i}k_1 r}\, e^{-\mathrm{i}k_2(r+1)} \langle \Psi_{\mathrm{BCS}} | \tilde{c}_{k_1} \tilde{c}_{k_2} | \Psi_{\mathrm{BCS}} \rangle$$

$$= \frac{1}{N}\sum_{k_1}\sum_{k_2} e^{-\mathrm{i}k_1 r}\, e^{-\mathrm{i}k_2(r+1)} u_{k_1} v_{k_2} \delta_{k_1,-k_2}$$

$$= \frac{1}{N}\sum_{k_1} e^{\mathrm{i}k_1}\, u_{k_1} v_{-k_1}$$

$$= \frac{1}{N}\sum_{k_1} e^{-\mathrm{i}k_1}\, u_{k_1} v_{k_1} = h^*(1), \tag{5.4.80}$$

$$\langle \Psi_{\mathrm{BCS}} | c_r c_0^\dagger | \Psi_{\mathrm{BCS}} \rangle = \frac{1}{N}\sum_{k_1}\sum_{k_2} e^{-\mathrm{i}k_1 r} \langle \Psi_{\mathrm{BCS}} | \tilde{c}_{k_1} \tilde{c}_{k_2} | \Psi_{\mathrm{BCS}} \rangle$$

$$= \frac{1}{N}\sum_{k_1}\sum_{k_2} e^{-\mathrm{i}k_1 r} u_{k_1} u_{k_2} \delta_{k_1,k_2}$$

$$= \frac{1}{N}\sum_{k_1} e^{-\mathrm{i}k_1 r}\, u_{k_1}^2 = g_u(r), \tag{5.4.81}$$

$$\langle \Psi_{\mathrm{BCS}} | c_r c_1^\dagger | \Psi_{\mathrm{BCS}} \rangle = \frac{1}{N}\sum_{k_1}\sum_{k_2} e^{-\mathrm{i}k_1 r}\, e^{\mathrm{i}k_2} \langle \Psi_{\mathrm{BCS}} | \tilde{c}_{k_1} \tilde{c}_{k_2} | \Psi_{\mathrm{BCS}} \rangle$$

$$= \frac{1}{N}\sum_{k_1}\sum_{k_2} e^{-\mathrm{i}k_1 r}\, e^{\mathrm{i}k_2} u_{k_1} u_{k_2} \delta_{k_1,k_2}$$

$$= \frac{1}{N}\sum_{k_1} e^{-\mathrm{i}k_1(r-1)}\, u_{k_1}^2 = g_u(r-1), \tag{5.4.82}$$

$$\langle \Psi_{\mathrm{BCS}} | c_r c_r^\dagger | \Psi_{\mathrm{BCS}} \rangle = \frac{1}{N}\sum_{k_1}\sum_{k_2} e^{-\mathrm{i}k_1 r}\, e^{\mathrm{i}k_2 r} \langle \Psi_{\mathrm{BCS}} | \tilde{c}_{k_1} \tilde{c}_{k_2} | \Psi_{\mathrm{BCS}} \rangle$$

$$= \frac{1}{N}\sum_{k_1}\sum_{k_2} e^{-\mathrm{i}k_1 r}\, e^{\mathrm{i}k_2 r} u_{k_1} u_{k_2} \delta_{k_1,k_2}$$

$$= \frac{1}{N}\sum_{k_1} u_{k_1}^2 = f_u, \tag{5.4.83}$$

$$\langle \Psi_{\mathrm{BCS}} | c_r c_{r+1}^\dagger | \Psi_{\mathrm{BCS}} \rangle = \frac{1}{N}\sum_{k_1}\sum_{k_2} e^{-\mathrm{i}k_1 r}\, e^{\mathrm{i}k_2 (r+1)} \langle \Psi_{\mathrm{BCS}} | \tilde{c}_{k_1} \tilde{c}_{k_2} | \Psi_{\mathrm{BCS}} \rangle$$

$$= \frac{1}{N}\sum_{k_1}\sum_{k_2} e^{-\mathrm{i}k_1 r}\, e^{\mathrm{i}k_2 (r+1)} u_{k_1} u_{k_2} \delta_{k_1,k_2}$$

$$= \frac{1}{N}\sum_{k_1} e^{\mathrm{i}k_1}\, u_{k_1}^2 = g_u(1), \tag{5.4.84}$$

$$\langle \Psi_{\mathrm{BCS}} | c_{r+1} c_0^\dagger | \Psi_{\mathrm{BCS}} \rangle = \frac{1}{N}\sum_{k_1}\sum_{k_2} e^{-\mathrm{i}k_1 (r+1)} \langle \Psi_{\mathrm{BCS}} | \tilde{c}_{k_1} \tilde{c}_{k_2} | \Psi_{\mathrm{BCS}} \rangle$$

$$= \frac{1}{N}\sum_{k_1}\sum_{k_2} e^{-\mathrm{i}k_1 (r+1)} u_{k_1} u_{k_2} \delta_{k_1,k_2}$$

$$= \frac{1}{N}\sum_{k_1} e^{-\mathrm{i}k_1 (r+1)}\, u_{k_1}^2 = g_u(r+1), \tag{5.4.85}$$

$$\langle \Psi_{\mathrm{BCS}} | c_{r+1} c_1^\dagger | \Psi_{\mathrm{BCS}} \rangle = \frac{1}{N}\sum_{k_1}\sum_{k_2} e^{-\mathrm{i}k_1 (r+1)}\, e^{\mathrm{i}k_2} \langle \Psi_{\mathrm{BCS}} | \tilde{c}_{k_1} \tilde{c}_{k_2} | \Psi_{\mathrm{BCS}} \rangle$$

$$= \frac{1}{N}\sum_{k_1}\sum_{k_2} e^{-\mathrm{i}k_1 (r+1)}\, e^{\mathrm{i}k_2} u_{k_1} u_{k_2} \delta_{k_1,k_2}$$

$$= \frac{1}{N}\sum_{k_1} e^{-\mathrm{i}k_1 r}\, u_{k_1}^2 = g_u(r), \tag{5.4.86}$$

$$\langle \Psi_{\mathrm{BCS}} | c_{r+1} c_r^\dagger | \Psi_{\mathrm{BCS}} \rangle = \frac{1}{N}\sum_{k_1}\sum_{k_2} e^{-\mathrm{i}k_1 (r+1)}\, e^{\mathrm{i}k_2 r} \langle \Psi_{\mathrm{BCS}} | \tilde{c}_{k_1} \tilde{c}_{k_2} | \Psi_{\mathrm{BCS}} \rangle$$

$$= \frac{1}{N}\sum_{k_1}\sum_{k_2} e^{-\mathrm{i}k_1 (r+1)}\, e^{\mathrm{i}k_2 r} u_{k_1} u_{k_2} \delta_{k_1,k_2}$$

$$= \frac{1}{N}\sum_{k_1} e^{-\mathrm{i}k_1}\, u_{k_1}^2 = g_u(1), \tag{5.4.87}$$

$$\langle \Psi_{\mathrm{BCS}} | c_{r+1} c_{r+1}^\dagger | \Psi_{\mathrm{BCS}} \rangle = \frac{1}{N}\sum_{k_1}\sum_{k_2} e^{-\mathrm{i}k_1 (r+1)}\, e^{\mathrm{i}k_2 (r+1)} \langle \Psi_{\mathrm{BCS}} | \tilde{c}_{k_1} \tilde{c}_{k_2} | \Psi_{\mathrm{BCS}} \rangle$$

$$= \frac{1}{N}\sum_{k_1}\sum_{k_2} e^{-\mathrm{i}k_1 (r+1)}\, e^{\mathrm{i}k_2 (r+1)} u_{k_1} u_{k_2} \delta_{k_1,k_2}$$

$$= \frac{1}{N}\sum_{k_1} u_{k_1}^2 = f_u, \tag{5.4.88}$$

$$\langle \Psi_{\mathrm{BCS}}|c_0^\dagger c_1^\dagger|\Psi_{\mathrm{BCS}}\rangle = \frac{1}{N}\sum_{k_1}\sum_{k_2} e^{\mathrm{i}\,k_2}\,\langle \Psi_{\mathrm{BCS}}|\tilde{c}_{k_1}\tilde{c}_{k_2}|\Psi_{\mathrm{BCS}}\rangle$$

$$= \frac{1}{N}\sum_{k_1}\sum_{k_2} e^{\mathrm{i}\,k_2} v_{k_1} u_{k_2}\delta_{k_1,-k_2}$$

$$= \frac{1}{N}\sum_{k_1} e^{-\mathrm{i}\,k_1} u_{k_1} v_{k_1} = h^*(1), \tag{5.4.89}$$

$$\langle \Psi_{\mathrm{BCS}}|c_0^\dagger c_r^\dagger|\Psi_{\mathrm{BCS}}\rangle = \frac{1}{N}\sum_{k_1}\sum_{k_2} e^{\mathrm{i}\,k_2 r}\,\langle \Psi_{\mathrm{BCS}}|\tilde{c}_{k_1}\tilde{c}_{k_2}|\Psi_{\mathrm{BCS}}\rangle$$

$$= \frac{1}{N}\sum_{k_1}\sum_{k_2} e^{\mathrm{i}\,k_2 r} v_{k_1} u_{k_2}\delta_{k_1,-k_2}$$

$$= \frac{1}{N}\sum_{k_1} e^{-\mathrm{i}\,k_1 r} u_{k_1} v_{k_1} = h^*(r), \tag{5.4.90}$$

$$\langle \Psi_{\mathrm{BCS}}|c_0^\dagger c_{r+1}^\dagger|\Psi_{\mathrm{BCS}}\rangle = \frac{1}{N}\sum_{k_1}\sum_{k_2} e^{\mathrm{i}\,k_2(r+1)}\,\langle \Psi_{\mathrm{BCS}}|\tilde{c}_{k_1}\tilde{c}_{k_2}|\Psi_{\mathrm{BCS}}\rangle$$

$$= \frac{1}{N}\sum_{k_1}\sum_{k_2} e^{\mathrm{i}\,k_2(r+1)} v_{k_1} u_{k_2}\delta_{k_1,-k_2}$$

$$= \frac{1}{N}\sum_{k_1} e^{-\mathrm{i}\,k_1(r+1)} u_{k_1} v_{k_1} = h^*(r+1), \tag{5.4.91}$$

$$\langle \Psi_{\mathrm{BCS}}|c_1^\dagger c_r^\dagger|\Psi_{\mathrm{BCS}}\rangle = \frac{1}{N}\sum_{k_1}\sum_{k_2} e^{\mathrm{i}\,k_1}\, e^{\mathrm{i}\,k_2 r}\,\langle \Psi_{\mathrm{BCS}}|\tilde{c}_{k_1}\tilde{c}_{k_2}|\Psi_{\mathrm{BCS}}\rangle$$

$$= \frac{1}{N}\sum_{k_1}\sum_{k_2} e^{\mathrm{i}\,k_1}\, e^{\mathrm{i}\,k_2 r} v_{k_1} u_{k_2}\delta_{k_1,-k_2}$$

$$= \frac{1}{N}\sum_{k_1} e^{-\mathrm{i}\,k_1(r-1)} u_{k_1} v_{k_1} = h^*(r-1), \tag{5.4.92}$$

$$\langle \Psi_{\mathrm{BCS}}|c_1^\dagger c_{r+1}^\dagger|\Psi_{\mathrm{BCS}}\rangle = \frac{1}{N}\sum_{k_1}\sum_{k_2} e^{\mathrm{i}\,k_1}\, e^{\mathrm{i}\,k_2(r+1)}\,\langle \Psi_{\mathrm{BCS}}|\tilde{c}_{k_1}\tilde{c}_{k_2}|\Psi_{\mathrm{BCS}}\rangle$$

$$= \frac{1}{N}\sum_{k_1}\sum_{k_2} e^{\mathrm{i}\,k_1}\, e^{\mathrm{i}\,k_2(r+1)} v_{k_1} u_{k_2}\delta_{k_1,-k_2}$$

$$= \frac{1}{N}\sum_{k_1} e^{-\mathrm{i}\,k_1 r} u_{k_1} v_{k_1} = h^*(r), \tag{5.4.93}$$

$$\begin{aligned}\langle\Psi_{\rm BCS}|c_r^\dagger c_{r+1}^\dagger|\Psi_{\rm BCS}\rangle &= \frac{1}{N}\sum_{k_1}\sum_{k_2} e^{{\rm i}\,k_1 r}\, e^{{\rm i}\,k_2(r+1)}\,\langle\Psi_{\rm BCS}|\tilde{c}_{k_1}\tilde{c}_{k_2}|\Psi_{\rm BCS}\rangle \\ &= \frac{1}{N}\sum_{k_1}\sum_{k_2} e^{{\rm i}\,k_1 r}\, e^{{\rm i}\,k_2(r+1)} v_{k_1}u_{k_2}\delta_{k_1,-k_2} \\ &= \frac{1}{N}\sum_{k_1} e^{-{\rm i}\,k_1}u_{k_1}v_{k_1} = h^*(1). \end{aligned} \tag{5.4.94}$$

Using the two-operator expectations calculated above, we also compute a few of the four-operator expectations, which arise very frequently in our calculations for the (2+2) correlation density matrix. We have

$$\begin{aligned}\langle\Psi_{\rm BCS}|c_0c_0^\dagger c_1c_1^\dagger|\Psi_{\rm BCS}\rangle &= \ +\langle\Psi_{\rm BCS}|c_0c_1^\dagger|\Psi_{\rm BCS}\rangle\langle\Psi_{\rm BCS}|c_0^\dagger c_1|\Psi_{\rm BCS}\rangle \\ &\quad -\langle\Psi_{\rm BCS}|c_0c_1|\Psi_{\rm BCS}\rangle\langle\Psi_{\rm BCS}|c_0^\dagger c_1^\dagger|\Psi_{\rm BCS}\rangle \\ &\quad +\langle\Psi_{\rm BCS}|c_0c_0^\dagger|\Psi_{\rm BCS}\rangle\langle\Psi_{\rm BCS}|c_1c_1^\dagger|\Psi_{\rm BCS}\rangle \\ &= f_u^2 - g_u^2(1) + |h(1)|^2, \end{aligned} \tag{5.4.95}$$

$$\begin{aligned}\langle\Psi_{\rm BCS}|c_0^\dagger c_0c_1c_1^\dagger|\Psi_{\rm BCS}\rangle &= \langle\Psi_{\rm BCS}|c_1c_1^\dagger|\Psi_{\rm BCS}\rangle - \langle\Psi_{\rm BCS}|c_0c_0^\dagger c_1c_1^\dagger|\Psi_{\rm BCS}\rangle \\ &= f_u - f_u^2 + g_u^2(1) - |h(1)|^2 \\ &= f_u(1-f_u) + g_u^2(1) - |h(1)|^2, \end{aligned} \tag{5.4.96}$$

$$\begin{aligned}\langle\Psi_{\rm BCS}|c_0c_0^\dagger c_1^\dagger c_1|\Psi_{\rm BCS}\rangle &= \langle\Psi_{\rm BCS}|c_0c_0^\dagger|\Psi_{\rm BCS}\rangle - \langle\Psi_{\rm BCS}|c_0c_0^\dagger c_1c_1^\dagger|\Psi_{\rm BCS}\rangle \\ &= f_u - f_u^2 + g_u^2(1) - |h(1)|^2 \\ &= f_u(1-f_u) + g_u^2(1) - |h(1)|^2, \end{aligned} \tag{5.4.97}$$

$$\begin{aligned}\langle\Psi_{\rm BCS}|c_rc_r^\dagger c_{r+1}c_{r+1}^\dagger|\Psi_{\rm BCS}\rangle &= \ +\langle\Psi_{\rm BCS}|c_rc_{r+1}^\dagger|\Psi_{\rm BCS}\rangle\langle\Psi_{\rm BCS}|c_r^\dagger c_{r+1}|\Psi_{\rm BCS}\rangle \\ &\quad -\langle\Psi_{\rm BCS}|c_rc_{r+1}|\Psi_{\rm BCS}\rangle\langle\Psi_{\rm BCS}|c_r^\dagger c_{r+1}^\dagger|\Psi_{\rm BCS}\rangle \\ &\quad +\langle\Psi_{\rm BCS}|c_rc_r^\dagger|\Psi_{\rm BCS}\rangle\langle\Psi_{\rm BCS}|c_{r+1}c_{r+1}^\dagger|\Psi_{\rm BCS}\rangle \\ &= f_u^2 - g_u^2(1) + |h(1)|^2, \end{aligned} \tag{5.4.98}$$

$$\begin{aligned}\langle\Psi_{\rm BCS}|c_r^\dagger c_rc_{r+1}c_{r+1}^\dagger|\Psi_{\rm BCS}\rangle &= \langle\Psi_{\rm BCS}|c_{r+1}c_{r+1}^\dagger|\Psi_{\rm BCS}\rangle - \langle\Psi_{\rm BCS}|c_rc_r^\dagger c_{r+1}c_{r+1}^\dagger|\Psi_{\rm BCS}\rangle \\ &= f_u - f_u^2 + g_u^2(1) - |h(1)|^2 \end{aligned}$$

$$= f_u(1 - f_u) + g_u^2(1) - |h(1)|^2, \tag{5.4.99}$$

$$\begin{aligned}\langle \Psi_{\mathrm{BCS}}|c_r c_r^\dagger c_{r+1}^\dagger c_{r+1}|\Psi_{\mathrm{BCS}}\rangle &= \langle \Psi_{\mathrm{BCS}}|c_r c_r^\dagger|\Psi_{\mathrm{BCS}}\rangle - \langle \Psi_{\mathrm{BCS}}|c_r c_r^\dagger c_{r+1} c_{r+1}^\dagger|\Psi_{\mathrm{BCS}}\rangle \\ &= f_u - f_u^2 + g_u^2(1) - |h(1)|^2 \\ &= f_u(1 - f_u) + g_u^2(1) - |h(1)|^2, \end{aligned} \tag{5.4.100}$$

where we make use of the fact that $h(r)$ is purely imaginary, so that $h^*(r) = -h(r)$.

5.4.2 The (1 + 1) Supercluster

Cluster density matrices. For the (1 + 1) supercluster, we start by computing the cluster density matrices ρ^a and ρ^b. The matrix elements of ρ^a are

$$\begin{aligned}\langle 0|\rho^a|0\rangle &= \langle \Psi_{\mathrm{BCS}}|c_0 c_0^\dagger|\Psi_{\mathrm{BCS}}\rangle = \frac{1}{N}\sum_{k_1}\sum_{k_2}\langle \Psi_{\mathrm{BCS}}|\tilde{c}_{k_1}\tilde{c}_{k_2}^\dagger|\Psi_{\mathrm{BCS}}\rangle \\ &= \frac{1}{N}\sum_{k_1}\sum_{k_2} u_{k_1}u_{k_2}\delta_{k_1,k_2} = \frac{1}{N}\sum_{k_1} u_{k_1}^2 = f_u, \end{aligned} \tag{5.4.101a}$$

$$\langle 0|\rho^a|1\rangle = 0, \tag{5.4.101b}$$

$$\langle 1|\rho^a|0\rangle = 0, \tag{5.4.101c}$$

$$\begin{aligned}\langle 1|\rho^a|1\rangle &= \langle \Psi_{\mathrm{BCS}}|c_0^\dagger c_0|\Psi_{\mathrm{BCS}}\rangle = \frac{1}{N}\sum_{k_1}\sum_{k_2}\langle \Psi_{\mathrm{BCS}}|\tilde{c}_{k_1}^\dagger\tilde{c}_{k_2}|\Psi_{\mathrm{BCS}}\rangle \\ &= \frac{1}{N}\sum_{k_1}\sum_{k_2} v_{k_1}v_{k_2}\delta_{k_1,k_2} = \frac{1}{N}\sum_{k_1} v_{k_1}^2 = f_v. \end{aligned} \tag{5.4.101d}$$

The matrix elements of ρ^b are similar.

Direct product density matrix. The direct product density matrix $\rho^a \otimes \rho^b$ has matrix elements

$$\langle 00|(\rho^a \otimes \rho^b)|00\rangle = \langle 0|\rho^a|0\rangle\langle 0|\rho^b|0\rangle = f_u^2, \tag{5.4.102a}$$

$$\langle 00|(\rho^a \otimes \rho^b)|10\rangle = \langle 0|\rho^a|1\rangle\langle 0|\rho^b|0\rangle = 0, \tag{5.4.102b}$$

$$\langle 00|(\rho^a \otimes \rho^b)|01\rangle = \langle 0|\rho^a|0\rangle\langle 0|\rho^b|1\rangle = 0, \tag{5.4.102c}$$

$$\langle 00|(\rho^a \otimes \rho^b)|11\rangle = \langle 0|\rho^a|1\rangle\langle 0|\rho^b|1\rangle = 0, \tag{5.4.102d}$$

$$\langle 10|(\rho^a \otimes \rho^b)|10\rangle = \langle 1|\rho^a|1\rangle\langle 0|\rho^b|0\rangle = f_u f_v, \tag{5.4.102e}$$

$$\langle 10|(\rho^a \otimes \rho^b)|01\rangle = \langle 1|\rho^a|0\rangle\langle 0|\rho^b|1\rangle = 0, \tag{5.4.102f}$$

$$\langle 10|(\rho^a \otimes \rho^b)|11\rangle = \langle 1|\rho^a|1\rangle\langle 0|\rho^b|1\rangle = 0, \tag{5.4.102g}$$

$$\langle 01|(\rho^a \otimes \rho^b)|01\rangle = \langle 0|\rho^a|0\rangle\langle 1|\rho^b|1\rangle = f_u f_v, \tag{5.4.102h}$$

$$\langle 01|(\rho^a \otimes \rho^b)|11\rangle = \langle 0|\rho^a|1\rangle\langle 1|\rho^b|1\rangle = 0, \tag{5.4.102i}$$

$$\langle 11|(\rho^a \otimes \rho^b)|11\rangle = \langle 1|\rho^a|1\rangle\langle 1|\rho^b|1\rangle = f_v^2. \tag{5.4.102j}$$

Supercluster density matrix. The supercluster density matrix has matrix elements

$$\langle 00|\rho^{ab}|00\rangle = f_u^2 - g_u^2(r) + |h(r)|^2, \tag{5.4.103a}$$

$$\langle 00|\rho^{ab}|10\rangle = 0, \tag{5.4.103b}$$

$$\langle 00|\rho^{ab}|01\rangle = 0, \tag{5.4.103c}$$

$$\langle 00|\rho^{ab}|11\rangle = h(r), \tag{5.4.103d}$$

$$\langle 10|\rho^{ab}|10\rangle = f_u(1 - f_u) + g_u^2(r) - |h(r)|^2, \tag{5.4.103e}$$

$$\langle 10|\rho^{ab}|01\rangle = g_v(r), \tag{5.4.103f}$$

$$\langle 10|\rho^{ab}|11\rangle = 0, \tag{5.4.103g}$$

$$\langle 01|\rho^{ab}|01\rangle = f_u(1 - f_u) + g_u^2(r) - |h(r)|^2, \tag{5.4.103h}$$

$$\langle 01|\rho^{ab}|11\rangle = 0, \tag{5.4.103i}$$

$$\langle 11|\rho^{ab}|11\rangle = (1 - f_u)^2 - g_u^2(r) + |h(r)|^2. \tag{5.4.103j}$$

It is trivial, once we write the matrix elements this way, to check that $\mathrm{Tr}\,\rho^{ab} = 1$.

Correlation density matrix. With all matrix elements expressed in terms of the two-point functions f, g and h, we can now write out the correlation density matrix explicitly as

$$\rho^c = \rho^{ab} - \rho^a \otimes \rho^b = \begin{bmatrix} -g_u^2 + |h|^2 & 0 & 0 & h \\ 0 & g_u^2 - |h|^2 & g_v & 0 \\ 0 & g_v & g_u^2 - |h|^2 & 0 \\ h^* & 0 & 0 & -g_u^2 + |h|^2 \end{bmatrix} \tag{5.4.104}$$

where we have also made use of the normalization condition $u_k^2 + v_k^2 = 1$, which thus leads to $f_u + f_v = 1$. Compared to the correlation density matrix of the Fermi sea ground state in (5.3.17), we find superficially, they have very similar structure, except that for the superconducting ground state, there is an extra off-diagonal correlation density matrix element $h(r)$.

Of course, we need to check the asymptotic behaviours of the matrix elements in order to compare the BCS correlation density matrix in (5.4.104) to the noninteracting Fermi-liquid correlation density matrix in (5.3.17). Using (5.4.54) and (5.4.66) obtained in Section 5.4.1.4, we see that the diagonal elements of ρ^c vanish identically, leaving only the non-zero off-diagonal matrix elements, which decay as $\exp(-\kappa r)/\sqrt{r}$. We can write the asymptotic form of the (1 + 1) correlation density matrix in the BCS ground state as

$$\rho^c = \kappa \sqrt{\frac{2}{\pi}} \frac{e^{-\kappa r}}{\sqrt{\kappa r}} \sin k_F r \begin{bmatrix} 0 & 0 & 0 & \mathrm{i} \\ 0 & 0 & 1 & 0 \\ 0 & 1 & 0 & 0 \\ -\mathrm{i} & 0 & 0 & 0 \end{bmatrix}. \tag{5.4.105}$$

We see how that the asymptotic form between the BCS correlation density matrix and the noninteracting Fermi-liquid correlation density matrix differs both in the leading

asymptotic dependence on the separation r, in the pattern of non-zero matrix elements, and also in the relative phase between matrix elements.

5.4.3 The (2 + 2) Supercluster

Cluster density matrices. For the (2 + 2) supercluster, the cluster density matrices ρ^a and ρ^b can be obtained from the (1 + 1) case in (5.4.103) by setting $r = 1$. The matrix elements are therefore

$$\langle 00|\rho^{a,b}|00\rangle = f_u^2 - g_u^2(1) + |h(1)|^2, \tag{5.4.106a}$$

$$\langle 00|\rho^{a,b}|10\rangle = 0, \tag{5.4.106b}$$

$$\langle 00|\rho^{a,b}|01\rangle = 0, \tag{5.4.106c}$$

$$\langle 00|\rho^{a,b}|11\rangle = h(1), \tag{5.4.106d}$$

$$\langle 10|\rho^{a,b}|10\rangle = f_u(1 - f_u) + g_u^2(1) - |h(1)|^2, \tag{5.4.106e}$$

$$\langle 10|\rho^{a,b}|01\rangle = -g_u(1), \tag{5.4.106f}$$

$$\langle 10|\rho^{a,b}|11\rangle = 0, \tag{5.4.106g}$$

$$\langle 01|\rho^{a,b}|01\rangle = f_u(1 - f_u) + g_u^2(1) - |h(1)|^2, \tag{5.4.106h}$$

$$\langle 01|\rho^{a,b}|11\rangle = 0, \tag{5.4.106i}$$

$$\langle 11|\rho^{a,b}|11\rangle = (1 - f_u)^2 - g_u^2(1) + |h(1)|^2, \tag{5.4.106j}$$

where we observe that

$$g_v(1) = \frac{1}{N}\sum_k e^{\mathrm{i}\,k} v_k^2 = \frac{1}{N}\sum_k e^{\mathrm{i}\,k}(1 - u_k^2) = -\frac{1}{N}\sum_k e^{\mathrm{i}\,k} u_k^2 = -g_u(1), \tag{5.4.107}$$

since $\frac{1}{N}\sum_k e^{\mathrm{i}\,k} \to \int_{-\pi}^{+\pi} dk\, e^{\mathrm{i}\,k} = 0$.

Direct product density matrix. The nonzero matrix elements of the direct product density matrix $\rho^a \otimes \rho^b$ are

$$\langle 0000|(\rho^a \otimes \rho^b)|0000\rangle = \left[f_u^2 - g_u^2(1) + |h(1)|^2\right]^2, \tag{5.4.108}$$

$$\langle 0000|(\rho^a \otimes \rho^b)|1100\rangle = h(1)\left[f_u^2 - g_u^2(1) + |h(1)|^2\right], \tag{5.4.109}$$

$$\langle 0000|(\rho^a \otimes \rho^b)|0011\rangle = h(1)\left[f_u^2 - g_u^2(1) + |h(1)|^2\right], \tag{5.4.110}$$

$$\langle 0000|(\rho^a \otimes \rho^b)|1111\rangle = h^2(1), \tag{5.4.111}$$

$$\langle 1000|(\rho^a \otimes \rho^b)|1000\rangle = \left[f_u(1-f_u) + g_u^2(1) - |h(1)|^2\right]\left[f_u^2 - g_u^2(1) + |h(1)|^2\right], \tag{5.4.112}$$

$$\langle 1000|(\rho^a \otimes \rho^b)|0100\rangle = -g_u(1)\left[f_u^2 - g_u^2(1) + |h(1)|^2\right], \tag{5.4.113}$$

$$\langle 1000|(\rho^a \otimes \rho^b)|1011\rangle = \left[f_u(1-f_u) + g_u^2(1) - |h(1)|^2\right]h(1), \tag{5.4.114}$$

$$\langle 1000|(\rho^a \otimes \rho^b)|0111\rangle = -g_u(1)h(1), \tag{5.4.115}$$

$$\langle 0100|(\rho^a \otimes \rho^b)|0100\rangle = \left[f_u(1-f_u) + g_u^2(1) - |h(1)|^2\right]\left[f_u^2 - g_u^2(1) + |h(1)|^2\right], \tag{5.4.116}$$

$$\langle 0100|(\rho^a \otimes \rho^b)|1011\rangle = -g_u(1)h(1), \tag{5.4.117}$$

$$\langle 0100|(\rho^a \otimes \rho^b)|0111\rangle = \left[f_u(1-f_u) + g_u^2(1) - |h(1)|^2\right]h(1), \tag{5.4.118}$$

$$\langle 0010|(\rho^a \otimes \rho^b)|0010\rangle = \left[f_u(1-f_u) + g_u^2(1) - |h(1)|^2\right]\left[f_u^2 - g_u^2(1) + |h(1)|^2\right], \tag{5.4.119}$$

$$\langle 0010|(\rho^a \otimes \rho^b)|0001\rangle = -g_u(1)\left[f_u^2 - g_u^2(1) + |h(1)|^2\right], \tag{5.4.120}$$

$$\langle 0010|(\rho^a \otimes \rho^b)|1110\rangle = h(1)\left[f_u(1-f_u) + g_u^2(1) - |h(1)|^2\right], \tag{5.4.121}$$

$$\langle 0010|(\rho^a \otimes \rho^b)|1101\rangle = -g_u(1)h(1), \tag{5.4.122}$$

$$\langle 0001|(\rho^a \otimes \rho^b)|0001\rangle = \left[f_u(1-f_u) + g_u^2(1) - |h(1)|^2\right]\left[f_u^2 - g_u^2(1) + |h(1)|^2\right], \tag{5.4.123}$$

$$\langle 0001|(\rho^a \otimes \rho^b)|1110\rangle = -g_u(1)h(1), \tag{5.4.124}$$

$$\langle 0001|(\rho^a \otimes \rho^b)|1101\rangle = h(1)\left[f_u(1-f_u) + g_u^2(1) - |h(1)|^2\right], \tag{5.4.125}$$

$$\langle 1100|(\rho^a \otimes \rho^b)|1100\rangle = \left[(1-f_u)^2 - g_u^2(1) + |h(1)|^2\right]\left[f_u^2 - g_u^2(1) + |h(1)|^2\right], \tag{5.4.126}$$

$$\langle 1100|(\rho^a \otimes \rho^b)|0011\rangle = |h(1)|^2, \tag{5.4.127}$$

$$\langle 1100|(\rho^a \otimes \rho^b)|1111\rangle = h(1)\left[(1-f_u)^2 - g_u^2(1) + |h(1)|^2\right], \tag{5.4.128}$$

$$\langle 1010|(\rho^a \otimes \rho^b)|1010\rangle = \left[f_u(1-f_u) + g_u^2(1) - |h(1)|^2\right]^2, \tag{5.4.129}$$

$$\langle 1010|(\rho^a \otimes \rho^b)|1001\rangle = -g_u(1)\left[f_u(1-f_u) + g_u^2(1) - |h(1)|^2\right], \tag{5.4.130}$$

$$\langle 1010|(\rho^a \otimes \rho^b)|0110\rangle = -g_u(1)\left[f_u(1-f_u) + g_u^2(1) - |h(1)|^2\right], \tag{5.4.131}$$

$$\langle 1010|(\rho^a \otimes \rho^b)|0101\rangle = g_u^2(1), \tag{5.4.132}$$

$$\langle 1001|(\rho^a \otimes \rho^b)|1001\rangle = \left[f_u(1-f_u) + g_u^2(1) - |h(1)|^2\right]^2, \tag{5.4.133}$$

$$\langle 1001|(\rho^a \otimes \rho^b)|0110\rangle = g_u^2(1), \tag{5.4.134}$$

$$\langle 1001|(\rho^a \otimes \rho^b)|0101\rangle = -g_u(1)\left[f_u(1-f_u) + g_u^2(1) - |h(1)|^2\right], \tag{5.4.135}$$

$$\langle 0110|(\rho^a \otimes \rho^b)|0110\rangle = \left[f_u(1-f_u) + g_u^2(1) - |h(1)|^2\right]^2, \tag{5.4.136}$$

$$\langle 0110|(\rho^a \otimes \rho^b)|0101\rangle = -g_u(1)\left[f_u(1-f_u) + g_u^2(1) - |h(1)|^2\right], \tag{5.4.137}$$

$$\langle 0101|(\rho^a \otimes \rho^b)|0101\rangle = \left[f_u(1-f_u) + g_u^2(1) - |h(1)|^2\right]^2, \tag{5.4.138}$$

$$\langle 0011|(\rho^a \otimes \rho^b)|0011\rangle = \left[f_u^2 - g_u^2(1) + |h(1)|^2\right]\left[(1-f_u)^2 - g_u^2(1) + |h(1)|^2\right], \tag{5.4.139}$$

$$\langle 0011|(\rho^a \otimes \rho^b)|1111\rangle = h(1)\left[(1-f_u)^2 - g_u^2(1) + |h(1)|^2\right], \tag{5.4.140}$$

$$\langle 1110|(\rho^a \otimes \rho^b)|1110\rangle = \left[f_u(1-f_u) + g_u^2(1) - |h(1)|^2\right]\left[(1-f_u)^2 - g_u^2(1) + |h(1)|^2\right], \tag{5.4.141}$$

$$\langle 1110|(\rho^a \otimes \rho^b)|1101\rangle = -g_u(1)\left[(1-f_u)^2 - g_u^2(1) + |h(1)|^2\right], \tag{5.4.142}$$

$$\langle 1101|(\rho^a \otimes \rho^b)|1101\rangle = \left[f_u(1-f_u) + g_u^2(1) - |h(1)|^2\right]\left[(1-f_u)^2 - g_u^2(1) + |h(1)|^2\right], \tag{5.4.143}$$

$$\langle 1011|(\rho^a \otimes \rho^b)|1011\rangle = \left[f_u(1-f_u) + g_u^2(1) - |h(1)|^2\right]\left[(1-f_u)^2 - g_u^2(1) + |h(1)|^2\right], \tag{5.4.144}$$

$$\langle 1011|(\rho^a \otimes \rho^b)|0111\rangle = -g_u(1)\left[(1-f_u)^2 - g_u^2(1) + |h(1)|^2\right], \tag{5.4.145}$$

$$\langle 0111|(\rho^a \otimes \rho^b)|0111\rangle = \left[f_u(1-f_u) + g_u^2(1) - |h(1)|^2\right]\left[(1-f_u)^2 - g_u^2(1) + |h(1)|^2\right], \tag{5.4.146}$$

$$\langle 1111|(\rho^a \otimes \rho^b)|1111\rangle = \left[(1 - f_u)^2 - g_u^2(1) + |h(1)|^2\right]^2 . \tag{5.4.147}$$

***O*(1) Supercluster density matrix elements.** Even with the help of Wick factorization, it would still take me forever to write down all the nonzero matrix elements of ρ^{ab}. However, if we believe that in a superconducting ground state, the dominant correlation does not decay with distance, then the only important matrix elements will be those which are $O(1)$. If these are the only matrix elements that we want to calculate, then there is an additional computational shortcut we can take to avoid doing unnecessary calculations: the only $O(1)$ matrix elements are those for which the corresponding expectation consists of an *even* number of operators from cluster a, and an *even* number of operators from cluster b. Should we have an *odd* number of operators from cluster a in the expectation, then after Wick factorization, we would end up with a sum of products of two-operator expectations, in which we cannot avoid involving one operator from cluster a and another operator from cluster b. Such a two-operator expectation is certain to introduce r-dependence into the overall expectation value. On the other hand, if the number of operators from cluster a is even, then some of these Wick factorized terms will involve cluster a operators Wick contracted with cluster a operators, and cluster b operators Wick contracted with cluster b operators only. These make $O(1)$ contributions to the overall expectation.

From this observation, we can also see how to speed up our calculation of the ex-

pectation: Wick factorize the a and b operators separately. For example,

$$\begin{aligned}
&\langle\Psi_{\rm BCS}|c_0c_0^\dagger c_1c_1^\dagger c_r^\dagger c_{r+1}^\dagger|\Psi_{\rm BCS}\rangle \\
\approx\ &\langle\Psi_{\rm BCS}|c_0c_0^\dagger c_1c_1^\dagger|\Psi_{\rm BCS}\rangle\,\langle\Psi_{\rm BCS}|c_r^\dagger c_{r+1}^\dagger|\Psi_{\rm BCS}\rangle \\
=\ &+\langle\Psi_{\rm BCS}|c_0c_1^\dagger|\Psi_{\rm BCS}\rangle\,\langle\Psi_{\rm BCS}|c_0^\dagger c_1|\Psi_{\rm BCS}\rangle\,\langle\Psi_{\rm BCS}|c_r^\dagger c_{r+1}^\dagger|\Psi_{\rm BCS}\rangle \\
&-\langle\Psi_{\rm BCS}|c_0c_1|\Psi_{\rm BCS}\rangle\,\langle\Psi_{\rm BCS}|c_0^\dagger c_1^\dagger|\Psi_{\rm BCS}\rangle\,\langle\Psi_{\rm BCS}|c_r^\dagger c_{r+1}^\dagger|\Psi_{\rm BCS}\rangle \\
&+\langle\Psi_{\rm BCS}|c_0c_0^\dagger|\Psi_{\rm BCS}\rangle\,\langle\Psi_{\rm BCS}|c_1c_1^\dagger|\Psi_{\rm BCS}\rangle\,\langle\Psi_{\rm BCS}|c_r^\dagger c_{r+1}^\dagger|\Psi_{\rm BCS}\rangle\,,
\end{aligned} \tag{5.4.148}$$

where the remaining slew of terms would be $O(r^{-1/2}\exp(-\kappa r))$. To further speed up the calculation, let us note that the only $O(1)$ matrix elements of ρ^{ab} are those between states n^an^b and m^am^b satisfying the *selection rule*

$$m^a - n^a = 0, \pm 2; \quad m^b - n^b = 0, \pm 2. \tag{5.4.149}$$

With the aid of this selection rule, we should be able to gloss over a huge number of the matrix elements, and only expend a small effort in computing the rest.

The $O(1)$ matrix elements of ρ^{ab} are then found to be

$$\langle 0000|\rho^{ab}|0000\rangle = \left[f_u^2 - g_u^2(1) + |h(1)|^2\right]^2, \tag{5.4.150}$$

$$\langle 0000|\rho^{ab}|1100\rangle = h(1)\left[f_u^2 - g_u^2(1) + |h(1)|^2\right], \tag{5.4.151}$$

$$\langle 0000|\rho^{ab}|0011\rangle = h(1)\left[f_u^2 - g_u^2(1) + |h(1)|^2\right], \tag{5.4.152}$$

$$\langle 0000|\rho^{ab}|1111\rangle = -|h(1)|^2, \tag{5.4.153}$$

$$\langle 1000|\rho^{ab}|1000\rangle = \left[f_u(1-f_u) + g_u^2(1) - |h(1)|^2\right]\left[f_u^2 - g_u^2(1) + |h(1)|^2\right], \tag{5.4.154}$$

$$\vdots$$

Without computing all the $O(1)$ matrix elements of ρ^{ab}, we can already see that these would be identical to the matrix elements of $\rho^a \otimes \rho^b$. This means that $\rho^c = 0$ identically at the $O(1)$ level. Of course, I was being silly: the true long-range superconducting order

is contained in ρ^{ab} but not ρ^{c}, just like the constant asymptote at large separations of the density-density correlation appears in the unsubtracted expectation $\langle n_j n_{j+r}\rangle$, but not the subtracted expectation $\langle n_j n_{j+r}\rangle - \langle n_j\rangle\langle n_{j+r}\rangle$. Therefore, we ought to look for signatures of the superconducting order in the one-dimensional spinless BCS ground state within ρ^{c} at the next highest level, which we have seen in Section 5.4.1.4, is $O(r^{-1/2}\exp(-\kappa r))$. As expected from our understanding that superconductivity emerges as an off-diagonal long-range order, this $O(r^{-1/2}\exp(-\kappa r))$ search will find us looking out for those off-diagonal matrix elements containing a single power of $h(r)$.

From what we understand about the Wick factorization of the BCS $2n$-point functions, and knowing the general form of the supercluster density-matrix elements in terms of expectations of products of referencing operators, we know which matrix elements will contain terms proportional to $h(r)$. These matrix elements occur between initial and final supercluster configurations both containing two spinless fermions, such that the initial configuration contains one spinless fermion in cluster a and one spinless fermion in cluster b, and both spinless fermions are in cluster a or cluster b in the final configuration, and vice versa. For example, the supercluster density-matrix element between $|1010\rangle$ and $|1100\rangle$, where the configurations are written as $|n_0 n_1 n_r n_{r+1}\rangle$, with sites $j = 0, 1$ in cluster a, and sites $j = r, r+1$ in cluster b, will contain a term proportional to $h(r)$. Similarly, the supercluster density-matrix element between $|1001\rangle$ and $|0011\rangle$ will also contain a term proportional to $h(r)$.

At this point, I have decided not to pursue this calculation any further. The $O(h(r))$ correlation density-matrix elements are not difficult to identify and calculate, but we have a more serious problem to deal with: the BCS ground state given in (5.4.4) defines a state with indefinite particle number. This is acceptable theoretically for an infinite chain, in a grand-canonical sense, but for numerical ground states obtained through

exact diagonalization, we always deal with ground states with fixed particle numbers. If one such numerical ground state exhibits superconducting quasi-long-range order, how will this order be captured by our correlation density matrix?

5.4.4 Particle-Number-Projected BCS Wave Function

To answer this question, we must discard the usual BCS wave function

$$|\Psi_{\mathrm{BCS}}\rangle = \prod_k (u_k + v_k \tilde{c}_k^\dagger \tilde{c}_{-k}^\dagger)\,|0\rangle\,, \tag{5.4.155}$$

which does not have a definite particle number, and work with the particle-number-projected BCS wave function

$$|\Psi_p\rangle = \left[\sum_k \varphi_k \tilde{c}_k^\dagger \tilde{c}_{-k}^\dagger\right]^p |0\rangle\,, \tag{5.4.156}$$

where p is the number of Cooper pairs, and $\varphi_k = v_k/u_k$. An important distinction between $|\Psi_p\rangle$ and $|\Psi_{\mathrm{BCS}}\rangle$ is that $|\Psi_p\rangle$ has no anomalous expectations, i.e.

$$\langle\Psi_p|\tilde{c}_k^\dagger \tilde{c}_{k'}^\dagger|\Psi_p\rangle = 0 = \langle\Psi_p|\tilde{c}_k \tilde{c}_{k'}|\Psi_p\rangle\,. \tag{5.4.157}$$

However, expectations are difficult to calculate using $|\Psi_p\rangle$, and people usually start from a BCS wave function of the form

$$|\Psi_{\mathrm{BCS}}(\phi)\rangle = \prod_k (u_k + v_k\, e^{\mathrm{i}\,\phi} \tilde{c}_k^\dagger \tilde{c}_{-k}^\dagger)\,|0\rangle\,, \tag{5.4.158}$$

which is just as good as the usual BCS wave function, where the phase ϕ has been arbitrarily chosen to be zero anyway. The particle-number-projected BCS wave function is then written as

$$|\Psi_p\rangle = C \int_0^{2\pi} d\phi\, e^{-\mathrm{i}\,p\phi}\,|\Psi_{\mathrm{BCS}}(\phi)\rangle\,, \tag{5.4.159}$$

where C is a normalization constant, to be determined in the calculations. The desired expectations are then calculated using this wave function. The factor of $e^{-\mathrm{i}\,p\phi}$ ensures

that only the contribution from the component of $|\Psi_{\rm BCS}\rangle$ containing p pairs is picked out in the integration over ϕ. This was first done by Bayman in 1960 [213]. The reason why Bayman's number projection method works, i.e. the integration over ϕ picking out the desired number of particles, was pointed out by Dietrich *et al* in their 1963 paper [214]. Since then, this was the method of choice in dealing with particle number projection, both in early studies of the effect of pair correlations in nuclei [215–220], as well as more recent studies of superconducting quantum dots [221–224].

When this method of particle number projection is used, one generally end up with Fowler-Darwin type integrals, called *residue integrals* by Dietrich *et al*, [214] which had to be evaluated numerically, or analytically under certain approximations. Dietrich *et al* [214], and Ma and Rasmussen [217] introduced recurrence relations to aid in evaluating the residue integrals.

5.4.4.1 Direct Evaluation of Expectation Values

Knowing nothing of the Bayman method of particle-number projection before doing the literature search, I grope for means to directly evaluate the expectation of various operator products within the p-pair superconducting ground state described by (5.4.156). I tried emulating the procedure of calculating expectation values within the usual BCS ground state, but is always hampered by a proliferation of terms in trying to construct Bogoliubov-Valatin like operators. After many false starts, I stumbled upon a set of recurrence relations, very much in the spirit of Dietrich *et al*, and Ma and Rasmussen, which would allow me to express most operator product expectation values in a compact form.

Action of annihilation operators. For the usual BCS wave function in (5.4.155), the action of an annihilation operator $\tilde{c}_k$ and creation operator $\tilde{c}_k^\dagger$ produces elementary excitations which can be massaged into a uniform form, allowing for the definition of γ_k in terms of $\tilde{c}_k$ and $\tilde{c}_{-k}^\dagger$. For the particle-number-projected BCS wave function in (5.4.156), the action of an annihilation operator looks very different from the action of a creation operator, so there is no easy way to define Bogoliubov-Valatin-like operator.

However, the action of the annihilation operator $\tilde{c}_k$ on $|\Psi_p\rangle$ forms the basis of the recurrence relations that I stumbled upon. To begin with, using the anticommutation relation $\tilde{c}_k\tilde{c}_k^\dagger = 1 - \tilde{c}_k^\dagger\tilde{c}_k$ we can show easily that

$$\begin{aligned}
\tilde{c}_k(\cdots + \varphi_k\tilde{c}_k^\dagger\tilde{c}_{-k}^\dagger + \cdots) &= (\cdots + \varphi_k\tilde{c}_k^\dagger\tilde{c}_{-k}^\dagger + \cdots)\tilde{c}_k + \varphi_k\tilde{c}_{-k}^\dagger, \\
\tilde{c}_{-k}(\cdots + \varphi_k\tilde{c}_k^\dagger\tilde{c}_{-k}^\dagger + \cdots) &= (\cdots + \varphi_k\tilde{c}_k^\dagger\tilde{c}_{-k}^\dagger + \cdots)\tilde{c}_k - \varphi_k\tilde{c}_k^\dagger,
\end{aligned} \tag{5.4.160}$$

where we choose to highlight the wave vector k in the sum

$$(\cdots + \varphi_k\tilde{c}_k^\dagger\tilde{c}_{-k}^\dagger + \cdots) = \sum_{k'} \varphi_{k'}\tilde{c}_{k'}^\dagger\tilde{c}_{-k'}^\dagger. \tag{5.4.161}$$

Using these relations, it is then straightforward to check that

$$\begin{aligned}
\tilde{c}_k(\cdots + \varphi_k\tilde{c}_k^\dagger\tilde{c}_{-k}^\dagger + \cdots)^2 &= (\cdots + \varphi_k\tilde{c}_k^\dagger\tilde{c}_{-k}^\dagger + \cdots)^2\tilde{c}_k \\
&\quad + 2\varphi_k\tilde{c}_{-k}^\dagger(\cdots + \varphi_k\tilde{c}_k^\dagger\tilde{c}_{-k}^\dagger + \cdots), \\
\tilde{c}_{-k}(\cdots + \varphi_k\tilde{c}_k^\dagger\tilde{c}_{-k}^\dagger + \cdots)^2 &= (\cdots + \varphi_k\tilde{c}_k^\dagger\tilde{c}_{-k}^\dagger + \cdots)^2\tilde{c}_{-k} \\
&\quad - 2\varphi_k\tilde{c}_k^\dagger(\cdots + \varphi_k\tilde{c}_k^\dagger\tilde{c}_{-k}^\dagger + \cdots).
\end{aligned} \tag{5.4.162}$$

Using mathematical induction, we can then show that

$$\begin{aligned}
\tilde{c}_k(\cdots + \varphi_k\tilde{c}_k^\dagger\tilde{c}_{-k}^\dagger + \cdots)^p &= (\cdots + \varphi_k\tilde{c}_k^\dagger\tilde{c}_{-k}^\dagger + \cdots)^p\tilde{c}_k \\
&\quad + p\varphi_k\tilde{c}_{-k}^\dagger(\cdots + \varphi_k\tilde{c}_k^\dagger\tilde{c}_{-k}^\dagger + \cdots)^{p-1}, \\
\tilde{c}_{-k}(\cdots + \varphi_k\tilde{c}_k^\dagger\tilde{c}_{-k}^\dagger + \cdots)^p &= (\cdots + \varphi_k\tilde{c}_k^\dagger\tilde{c}_{-k}^\dagger + \cdots)^p\tilde{c}_{-k} \\
&\quad - p\varphi_k\tilde{c}_k^\dagger(\cdots + \varphi_k\tilde{c}_k^\dagger\tilde{c}_{-k}^\dagger + \cdots)^{p-1}.
\end{aligned} \tag{5.4.163}$$

This tells us that

$$\begin{aligned} \tilde{c}_k \left|\Psi_p\right\rangle &= p\varphi_k \tilde{c}^\dagger_{-k} \left|\Psi_{p-1}\right\rangle , \\ \tilde{c}_{-k} \left|\Psi_p\right\rangle &= -p\varphi_k \tilde{c}^\dagger_{k} \left|\Psi_{p-1}\right\rangle . \end{aligned} \tag{5.4.164}$$

Expectation of annihilation-annihilation operators. Consider the expectation of the two-operator term $\tilde{c}_{k_1}\tilde{c}_{k_2}$. If $k_2 = k_1$, then the expectation vanishes automatically. If $k_2 = -k_1$, then we find that

$$\begin{aligned} \langle\Psi_p|\tilde{c}_k\tilde{c}_{-k}|\Psi_p\rangle &= -p\varphi_k \langle\Psi_p|\tilde{c}_k\tilde{c}^\dagger_k|\Psi_{p-1}\rangle \\ &= -p\varphi_k \langle\Psi_p|\Psi_{p-1}\rangle + p\varphi_k \langle\Psi_p|\tilde{c}^\dagger_k\tilde{c}_k|\Psi_{p-1}\rangle . \end{aligned} \tag{5.4.165}$$

Now if we expand out $|\Psi_p\rangle$ in its full gory details, each term in the expansion consists of $2p$ creation operators, whereas each term in the expansion of $|\Psi_{p-1}\rangle$ consists of $2(p-1)$ creation operators. It should therefore be clear that $|\Psi_p\rangle$ and $|\Psi_{p'}\rangle$ are orthogonal to each other for $p \neq p'$. With this, we find that

$$\begin{aligned} \langle\Psi_p|\tilde{c}_k\tilde{c}_{-k}|\Psi_p\rangle &= p\varphi_k \langle\Psi_p|\tilde{c}^\dagger_k\tilde{c}_k|\Psi_{p-1}\rangle \\ &= p^2\varphi_k^2 \langle\Psi_{p-1}|\tilde{c}_{-k}\tilde{c}_k|\Psi_{p-1}\rangle \\ &= -p^2\varphi_k^2 \langle\Psi_{p-1}|\tilde{c}_k\tilde{c}_{-k}|\Psi_{p-1}\rangle , \end{aligned} \tag{5.4.166}$$

which is a recurrence formula relating $\langle\Psi_p|\tilde{c}_{-k}\tilde{c}_k|\Psi_p\rangle$ to $\langle\Psi_{p-1}|\tilde{c}_{-k}\tilde{c}_k|\Psi_{p-1}\rangle$.

We can use this recurrence formula recursively, to obtain

$$\begin{aligned} \langle\Psi_p|\tilde{c}_k\tilde{c}_{-k}|\Psi_p\rangle &= -p^2\varphi_k^2 \langle\Psi_{p-1}|\tilde{c}_k\tilde{c}_{-k}|\Psi_{p-1}\rangle \\ &= (-1)^2[p(p-1)\varphi_k^2]^2 \langle\Psi_{p-2}|\tilde{c}_k\tilde{c}_{-k}|\Psi_{p-2}\rangle \\ &= \dots \\ &= (-1)^p[p!\varphi_k^p]^2 \langle\Psi_0|\tilde{c}_k\tilde{c}_{-k}|\Psi_0\rangle . \end{aligned} \tag{5.4.167}$$

But since $|\Psi_0\rangle = |0\rangle$ is the true vacuum, the final expectation is zero, which tells us that $\langle\Psi_p|\tilde{c}_k\tilde{c}_{-k}|\Psi_p\rangle = 0$ for all p.

Finally, for $k_2 \neq \pm k_1$, we find that

$$\begin{aligned}
\langle \Psi_p | \tilde{c}_{k_1} \tilde{c}_{k_2} | \Psi_p \rangle &= p\varphi_{k_2} \langle \Psi_p | \tilde{c}_{k_1} \tilde{c}^\dagger_{-k_2} | \Psi_{p-1} \rangle \\
&= -p\varphi_{k_2} \langle \Psi_p | \tilde{c}^\dagger_{-k_2} \tilde{c}_{k_1} | \Psi_{p-1} \rangle \\
&= p^2 \varphi^2_{k_2} \langle \Psi_{p-1} | \tilde{c}_{k_2} \tilde{c}_{k_1} | \Psi_{p-1} \rangle \\
&= -p^2 \varphi^2_{k_2} \langle \Psi_{p-1} | \tilde{c}_{k_1} \tilde{c}_{k_2} | \Psi_{p-1} \rangle ,
\end{aligned} \tag{5.4.168}$$

which we can use recursively to show that

$$\langle \Psi_p | \tilde{c}_{k_1} \tilde{c}_{k_2} | \Psi_p \rangle = 0, \quad k_2 \neq \pm k_1. \tag{5.4.169}$$

Combining all three results, we then have

$$\langle \Psi_p | \tilde{c}_{k_1} \tilde{c}_{k_2} | \Psi_p \rangle = 0, \tag{5.4.170}$$

for all k_1 and k_2. From the simple fact that $|\Psi_p\rangle$ contains $2p$ particles, and $\tilde{c}_{k_1} \tilde{c}_{k_2} |\Psi_p\rangle$ contains $2(p-1)$ particles, we know that their overlap must strictly be zero. It is therefore reassuring that our recurrence formula gets this right.

Expectation of creation-creation operators. Next we consider the expectation of the two-operator term $\tilde{c}^\dagger_{k_1} \tilde{c}^\dagger_{k_2}$. Again, if $k_2 = k_1$, the expectation vanishes automatically. For the case of $k_2 = -k_1$, we have

$$\begin{aligned}
\langle \Psi_p | \tilde{c}^\dagger_k \tilde{c}^\dagger_{-k} | \Psi_p \rangle &= p\varphi_k \langle \Psi_{p-1} | \tilde{c}_{-k} \tilde{c}^\dagger_{-k} | \Psi_p \rangle \\
&= p\varphi_k \langle \Psi_{p-1} | \Psi_p \rangle - p\varphi_k \langle \Psi_{p-1} | \tilde{c}^\dagger_{-k} \tilde{c}_{-k} | \Psi_p \rangle \\
&= p^2 \varphi^2_k \langle \Psi_{p-1} | \tilde{c}^\dagger_{-k} \tilde{c}^\dagger_k | \Psi_{p-1} \rangle \\
&= -p^2 \varphi^2_k \langle \Psi_{p-1} | \tilde{c}^\dagger_k \tilde{c}^\dagger_{-k} | \Psi_{p-1} \rangle .
\end{aligned} \tag{5.4.171}$$

We arrive at this same recursion formula for $k_2 \neq \pm k_1$. Using this recursion formula recursively, we find that

$$\langle \Psi_p | \tilde{c}^\dagger_{k_1} \tilde{c}^\dagger_{k_2} | \Psi_p \rangle = 0, \tag{5.4.172}$$

for all k_1 and k_2. Again, our recurrence formula arrives correctly at the vanishing overlap between $|\Psi_p\rangle$, which contains $2p$ particles, and $\tilde{c}^\dagger_{k_1}\tilde{c}^\dagger_{k_2}|\Psi_p\rangle$, which contains $2(p+1)$ particles.

Expectation of creation-annihilation operators. Finally, we consider the expectation of the two-operator term $\tilde{c}^\dagger_{k_1}\tilde{c}_{k_2}$. If $k_2 = k_1$, we have

$$\begin{aligned}
\langle\Psi_p|\tilde{c}^\dagger_k\tilde{c}_k|\Psi_p\rangle &= p^2\varphi_k^2\,\langle\Psi_{p-1}|\tilde{c}_{-k}\tilde{c}^\dagger_{-k}|\Psi_{p-1}\rangle \\
&= p^2\varphi_k^2\,\langle\Psi_{p-1}|\Psi_{p-1}\rangle - p^2\varphi_k^2\,\langle\Psi_{p-1}|\tilde{c}^\dagger_{-k}\tilde{c}_{-k}|\Psi_{p-1}\rangle \\
&= p^2\varphi_k^2\,\langle\Psi_{p-1}|\Psi_{p-1}\rangle - p^2(p-1)^2\varphi_k^4\,\langle\Psi_{p-2}|\tilde{c}_k\tilde{c}^\dagger_k|\Psi_{p-2}\rangle \\
&= p^2\varphi_k^2\,\langle\Psi_{p-1}|\Psi_{p-1}\rangle - p^2(p-1)^2\varphi_k^4\,\langle\Psi_{p-2}|\Psi_{p-2}\rangle \\
&\quad + p^2(p-1)^2\varphi_k^4\,\langle\Psi_{p-2}|\tilde{c}^\dagger_k\tilde{c}_k|\Psi_{p-2}\rangle\,.
\end{aligned} \tag{5.4.173}$$

If p is even, then we can apply this recursion formula recursively to get

$$\begin{aligned}
\langle\Psi_p|\tilde{c}^\dagger_k\tilde{c}_k|\Psi_p\rangle = &+ p^2\varphi_k^2\,\langle\Psi_{p-1}|\Psi_{p-1}\rangle - p^2(p-1)^2\varphi_k^4\,\langle\Psi_{p-2}|\Psi_{p-2}\rangle \\
&+ p^2(p-1)^2(p-2)^2\varphi_k^6\,\langle\Psi_{p-3}|\Psi_{p-3}\rangle \\
&- p^2(p-1)^2(p-2)^2(p-3)^2\varphi_k^8\,\langle\Psi_{p-4}|\Psi_{p-4}\rangle \\
&+ p^2(p-1)^2(p-2)^2(p-3)^2\varphi_k^8\,\langle\Psi_{p-4}|\tilde{c}^\dagger_k\tilde{c}_k|\Psi_{p-4}\rangle \\
= &\ \ldots \\
= &-\sum_{r=1}^{p}(-1)^r\left[\frac{p!}{(p-r)!}\varphi_k^r\right]^2\langle\Psi_{p-r}|\Psi_{p-r}\rangle + (p!)^2\varphi_k^{2p}\,\langle 0|\tilde{c}^\dagger_k\tilde{c}_k|0\rangle \\
= &-\sum_{r=1}^{p}(-1)^r\left[\frac{p!}{(p-r)!}\varphi_k^r\right]^2\langle\Psi_{p-r}|\Psi_{p-r}\rangle = \tilde{F}(p,k),
\end{aligned} \tag{5.4.174}$$

where we assume that

$$\langle\Psi_{p-p}|\Psi_{p-p}\rangle = \langle\Psi_0|\Psi_0\rangle = \langle 0|0\rangle = 1, \tag{5.4.175}$$

i.e. the vacuum $|0\rangle$ is normalized. Here we note that because of the way that $|\Psi_p\rangle$ is defined in (5.4.156), it is not normalized.

If p is odd, then we will not be able to get down to $|\Psi_0\rangle = |0\rangle$ using the recursion formula, but will instead end up with an expression like

$$\begin{aligned}\langle\Psi_p|\tilde{c}_k^\dagger\tilde{c}_k|\Psi_p\rangle = &-\sum_{r=1}^{p-1}(-1)^r\left[\frac{p!}{(p-r)!}\varphi_k^r\right]^2\langle\Psi_{p-r}|\Psi_{p-r}\rangle \\ &+ (p!)^2\varphi_k^{2(p-1)}\langle\Psi_1|\tilde{c}_k^\dagger\tilde{c}_k|\Psi_1\rangle\,.\end{aligned} \tag{5.4.176}$$

However, we know that $\tilde{c}_k|\Psi_1\rangle = \varphi_k\tilde{c}_{-k}^\dagger|0\rangle$, and so

$$\langle\Psi_1|\tilde{c}_k^\dagger\tilde{c}_k|\Psi_1\rangle = \varphi_k^2\langle 0|\tilde{c}_{-k}\tilde{c}_{-k}^\dagger|0\rangle = \varphi_k^2. \tag{5.4.177}$$

This means that

$$\begin{aligned}\langle\Psi_p|\tilde{c}_k^\dagger\tilde{c}_k|\Psi_p\rangle &= -\sum_{r=1}^{p-1}(-1)^r\left[\frac{p!}{(p-r)!}\varphi_k^r\right]^2\langle\Psi_{p-r}|\Psi_{p-r}\rangle + (p!)^2\varphi_k^{2p} \\ &= -\sum_{r=1}^{p}(-1)^r\left[\frac{p!}{(p-r)!}\varphi_k^r\right]^2\langle\Psi_{p-r}|\Psi_{p-r}\rangle = \tilde{F}(p,k),\end{aligned} \tag{5.4.178}$$

i.e. we have the same result for even and odd p.

For the case of $k_2 = -k_1$, we find that

$$\langle\Psi_p|\tilde{c}_k^\dagger\tilde{c}_{-k}|\Psi_p\rangle = -p^2\varphi_k^2\langle\Psi_{p-1}|\tilde{c}_{-k}\tilde{c}_k^\dagger|\Psi_{p-1}\rangle = p^2\varphi_k^2\langle\Psi_{p-1}|\tilde{c}_k^\dagger\tilde{c}_{-k}|\Psi_{p-1}\rangle\,. \tag{5.4.179}$$

Using this recurrence formula recursively, we then find that

$$\langle\Psi_p|\tilde{c}_k^\dagger\tilde{c}_{-k}|\Psi_p\rangle = (p!)^2\varphi_k^{2p}\langle 0|\tilde{c}_k^\dagger\tilde{c}_{-k}|0\rangle = 0. \tag{5.4.180}$$

Similarly, for the case of $k_2 \neq \pm k_1$, we find that

$$\begin{aligned}\langle\Psi_p|\tilde{c}_{k_1}^\dagger\tilde{c}_{k_2}|\Psi_p\rangle &= p^2\varphi_{k_1}\varphi_{k_2}\langle\Psi_{p-1}|\tilde{c}_{-k_1}\tilde{c}_{-k_2}^\dagger|\Psi_{p-1}\rangle \\ &= -p^2\varphi_{k_1}\varphi_{k_2}\langle\Psi_{p-1}|\tilde{c}_{-k_2}^\dagger\tilde{c}_{-k_1}|\Psi_{p-1}\rangle \\ &= -p^2(p-1)^2\varphi_{k_1}^2\varphi_{k_2}^2\langle\Psi_{p-2}|\tilde{c}_{k_2}\tilde{c}_{k_1}^\dagger|\Psi_{p-2}\rangle \\ &= p^2(p-1)^2\varphi_{k_1}^2\varphi_{k_2}^2\langle\Psi_{p-2}|\tilde{c}_{k_1}^\dagger\tilde{c}_{k_2}|\Psi_{p-2}\rangle\,.\end{aligned} \tag{5.4.181}$$

Using this formula recursively, we find that

$$\langle \Psi_p | \tilde{c}^\dagger_{k_1} \tilde{c}_{k_2} | \Psi_p \rangle = (p!)^2 \varphi^p_{k_1} \varphi^p_{k_2} \langle 0 | \tilde{c}^\dagger_{k_1} \tilde{c}_{k_2} | 0 \rangle = 0 \tag{5.4.182}$$

for even p, and

$$\begin{aligned} \langle \Psi_p | \tilde{c}^\dagger_{k_1} \tilde{c}_{k_2} | \Psi_p \rangle &= (p!)^2 \varphi^{p-1}_{k_1} \varphi^{p-1}_{k_2} \langle \Psi_1 | \tilde{c}^\dagger_{k_1} \tilde{c}_{k_2} | \Psi_1 \rangle \\ &= (p!)^2 \varphi^p_{k_1} \varphi^p_{k_2} \langle 0 | \tilde{c}_{-k_1} \tilde{c}^\dagger_{-k_2} | 0 \rangle = 0 \end{aligned} \tag{5.4.183}$$

for odd p. Therefore, summarizing all the cases, we have

$$\langle \Psi_p | \tilde{c}^\dagger_{k_1} \tilde{c}_{k_2} | \Psi_p \rangle = \tilde{F}(p, k_1) \, \delta_{k_1, k_2}. \tag{5.4.184}$$

Three-operator expectations. These always vanishes in $|\Psi_p\rangle$, which has a definite number of particles, or in the BCS ground state, which is a superposition of states with an even number of particles. The only kind of quantum-mechanical state we can construct for which three-operator expectations can be nonzero are those which consists of a superposition of states with mixed even and odd number of particles. However, we have argued in Section 4.3.2.4 that such states are not physically meaningful, as they cannot be the eigenstates of any reasonably Hamiltonian for a system of fermions.

Four-operator expectations. Balanced four-operator products are those of the form $\tilde{c}^\dagger_{k_1} \tilde{c}^\dagger_{k_2} \tilde{c}_{k_3} \tilde{c}_{k_4}$, $\tilde{c}_{k_1} \tilde{c}_{k_2} \tilde{c}^\dagger_{k_3} \tilde{c}^\dagger_{k_4}$, ... Since all such operator products can be manipulated into the form $\tilde{c}^\dagger_{k_1} \tilde{c}^\dagger_{k_2} \tilde{c}_{k_3} \tilde{c}_{k_4}$, we will focus on calculating the expectation of this term. Again, our goal is to obtain a recurrence formula, if it is not already possible to express the expectation in terms of sums of products of zero- and two-operator expectations. However, compared to two-operator expectations, there are now vastly more possibilities to consider. While these possibilities can still be enumerated with a reasonable amount of effort, when we get to six-operator expectations, directly enumerating all the possible combinations of the wave vectors would become combinatorially prohibitive.

As such, we want to understand more about when an expectation is nonzero, so that we can quickly zero in (pardon the pun) on these expectations, and not bother with those which we know, without performing any calculations, will turn out to be zero. To do this, let us re-examine the two-operator expectation $\langle\Psi_p|\tilde{c}^\dagger_{k_1}\tilde{c}_{k_2}|\Psi_p\rangle$, which we know is nonzero only when $k_1 = k_2$. In Section 5.4.4.1, we found that

$$\tilde{c}_k\,|\Psi_p\rangle = \tilde{c}_k\Big[\sum_{k'}\varphi_{k'}\tilde{c}^\dagger_{k'}\tilde{c}^\dagger_{-k'}\Big]^p|0\rangle = p\varphi_k\tilde{c}^\dagger_{-k}\Big[\sum_{k'}\varphi_{k'}\tilde{c}^\dagger_{k'}\tilde{c}^\dagger_{-k'}\Big]^{p-1}|0\rangle\,. \tag{5.4.185}$$

Because $\tilde{c}^\dagger_{-k}$ kills all the $\tilde{c}^\dagger_k\tilde{c}^\dagger_{-k}$ terms in the product, a more illuminating way to write the action of $\tilde{c}_k$ on $|\Psi_p\rangle$ is

$$\tilde{c}_k\,|\Psi_p\rangle = p\varphi_k\tilde{c}^\dagger_{-k}\Big[\sum_{k'\neq k}\varphi_{k'}\tilde{c}^\dagger_{k'}\tilde{c}^\dagger_{-k'}\Big]^{p-1}|0\rangle\,. \tag{5.4.186}$$

With this in mind, we check that

$$\langle\Psi_p|\tilde{c}^\dagger_{k_1}\tilde{c}_{k_2}|\Psi_p\rangle = p\varphi_{k_2}\,\langle 0|\Big(\sum_k\varphi_k\tilde{c}_{-k}\tilde{c}_k\Big)^p\tilde{c}^\dagger_{k_1}\tilde{c}^\dagger_{-k_2}\Big(\sum_{k'\neq k_2}\varphi_{k'}\tilde{c}^\dagger_{k'}\tilde{c}^\dagger_{-k'}\Big)^{p-1}|0\rangle\,, \tag{5.4.187}$$

which vanishes if $k_2 = -k_1$. If $k_2 \neq -k_1$, we can anticommute the two operators, and let $\tilde{c}^\dagger_{-k_2}$ act to the left as

$$\begin{aligned}\langle\Psi_p|\tilde{c}^\dagger_{k_1}\tilde{c}_{k_2}|\Psi_p\rangle &= -p\varphi_{k_2}\,\langle 0|\Big(\sum_k\varphi_k\tilde{c}_{-k}\tilde{c}_k\Big)^p\tilde{c}^\dagger_{-k_2}\tilde{c}^\dagger_{k_1}\Big(\sum_{k'\neq k_2}\varphi_{k'}\tilde{c}^\dagger_{k'}\tilde{c}^\dagger_{-k'}\Big)^{p-1}|0\rangle \\ &= p^2\varphi^2_{k_2}\,\langle 0|\Big(\sum_{k\neq k_2}\varphi_k\tilde{c}_{-k}\tilde{c}_k\Big)^{p-1}\tilde{c}_{k_2}\tilde{c}^\dagger_{k_1}\Big(\sum_{k'\neq k_2}\varphi_{k'}\tilde{c}^\dagger_{k'}\tilde{c}^\dagger_{-k'}\Big)^{p-1}|0\rangle\,.\end{aligned} \tag{5.4.188}$$

Here is the key step in our reasoning: if $k_2 \neq k_1$, then we can just anticommute the two operators to get

$$\langle\Psi_p|\tilde{c}^\dagger_{k_1}\tilde{c}_{k_2}|\Psi_p\rangle = p^2\varphi^2_{k_2}\,\langle 0|\Big(\sum_{k\neq k_2}\varphi_k\tilde{c}_{-k}\tilde{c}_k\Big)^{p-1}\tilde{c}^\dagger_{k_1}\tilde{c}_{k_2}\Big(\sum_{k'\neq k_2}\varphi_{k'}\tilde{c}^\dagger_{k'}\tilde{c}^\dagger_{-k'}\Big)^{p-1}|0\rangle\,. \tag{5.4.189}$$

But since $\tilde{c}^\dagger_{k_2}$ has been excluded from the product of sum $\left(\sum_{k'\neq k_2}\varphi_{k'}\tilde{c}^\dagger_{k'}\tilde{c}^\dagger_{-k'}\right)^{p-1}$, $\tilde{c}_{k_2}$ will just push right through this term to annihilate the vacuum $|0\rangle$, giving us a zero expectation value. On the other hand, if $k_2 = k_1$, then apart from the term in (5.4.189), which

we know goes to zero, we also get a zero-operator term,

$$\langle\Psi_p|\tilde{c}^\dagger_{k_1}\tilde{c}_{k_2}|\Psi_p\rangle = p^2\varphi^2_{k_2}\,\langle 0|\Big(\sum_{k\neq k_2}\varphi_k\tilde{c}_{-k}\tilde{c}_k\Big)^{p-1}\Big(\sum_{k'\neq k_2}\varphi_{k'}\tilde{c}^\dagger_{k'}\tilde{c}^\dagger_{-k'}\Big)^{p-1}|0\rangle\,, \tag{5.4.190}$$

which gives us an expectation that is nonzero in general.

Having understood this 'zipper'-like machinery which tells us which expectations are zero, we now consider the four-operator expectation $\langle\Psi_p|\tilde{c}^\dagger_{k_1}\tilde{c}^\dagger_{k_2}\tilde{c}_{k_3}\tilde{c}_{k_4}|\Psi_p\rangle$. As with the two-operator expectation, we 'zipper' only one operator, $\tilde{c}_{k_4}$, back and forth to decide whether the given expectation vanishes. Starting with

$$\langle\Psi_p|\tilde{c}^\dagger_{k_1}\tilde{c}^\dagger_{k_2}\tilde{c}_{k_3}\tilde{c}_{k_4}|\Psi_p\rangle = p\varphi_{k_4}\,\langle 0|\Big(\sum_{k}\varphi_k\tilde{c}_{-k}\tilde{c}_k\Big)^{p}\tilde{c}^\dagger_{k_1}\tilde{c}^\dagger_{k_2}\tilde{c}_{k_3}\tilde{c}^\dagger_{-k_4}\Big(\sum_{k'\neq k_4}\varphi_{k'}\tilde{c}^\dagger_{k'}\tilde{c}^\dagger_{-k'}\Big)^{p-1}|0\rangle\,, \tag{5.4.191}$$

we note the following possibilities:

1. $k_3 = k_4$: for this case, the operator product $\tilde{c}_{k_3}\tilde{c}_{k_4}$ is zero, and hence the expectation vanishes;

2. $k_3 = -k_4$: for this case, we find, after using the anticommutation relation between $\tilde{c}_{k_3}$ and $\tilde{c}^\dagger_{-k_4}$,

$$\begin{aligned}
&\langle 0|\Big(\sum_{k}\varphi_k\tilde{c}_{-k}\tilde{c}_k\Big)^{p}\tilde{c}^\dagger_{k_1}\tilde{c}^\dagger_{k_2}\tilde{c}_{k_3}\tilde{c}^\dagger_{-k_4}\Big(\sum_{k'\neq k_4}\varphi_{k'}\tilde{c}^\dagger_{k'}\tilde{c}^\dagger_{-k'}\Big)^{p-1}|0\rangle\\
=\;&+\langle 0|\Big(\sum_{k}\varphi_k\tilde{c}_{-k}\tilde{c}_k\Big)^{p}\tilde{c}^\dagger_{k_1}\tilde{c}^\dagger_{k_2}\Big(\sum_{k'\neq k_4}\varphi_{k'}\tilde{c}^\dagger_{k'}\tilde{c}^\dagger_{-k'}\Big)^{p-1}|0\rangle\\
&-\langle 0|\Big(\sum_{k}\varphi_k\tilde{c}_{-k}\tilde{c}_k\Big)^{p}\tilde{c}^\dagger_{k_1}\tilde{c}^\dagger_{k_2}\tilde{c}^\dagger_{-k_4}\tilde{c}_{k_3}\Big(\sum_{k'\neq k_4}\varphi_{k'}\tilde{c}^\dagger_{k'}\tilde{c}^\dagger_{-k'}\Big)^{p-1}|0\rangle\,.
\end{aligned} \tag{5.4.192}$$

Noting that the exclusion of $\tilde{c}^\dagger_{k_4}$ also imply the exclusion of $\tilde{c}^\dagger_{-k_4} = \tilde{c}^\dagger_{k_3}$, we see that $\tilde{c}_{k_3}$ can be pushed all the way through $\left(\sum_{k'\neq k_4}\varphi_{k'}\tilde{c}^\dagger_{k'}\tilde{c}^\dagger_{-k'}\right)^{p-1}$ to annihilate the

vacuum. This means that

$$\begin{aligned}
&\langle 0|\Big(\sum_{k}\varphi_k\tilde{c}_{-k}\tilde{c}_k\Big)^p\tilde{c}^\dagger_{k_1}\tilde{c}^\dagger_{k_2}\tilde{c}_{k_3}\tilde{c}^\dagger_{-k_4}\Big(\sum_{k'\neq k_4}\varphi_{k'}\tilde{c}^\dagger_{k'}\tilde{c}^\dagger_{-k'}\Big)^{p-1}|0\rangle \\
&= \langle 0|\Big(\sum_{k}\varphi_k\tilde{c}_{-k}\tilde{c}_k\Big)^p\tilde{c}^\dagger_{k_1}\tilde{c}^\dagger_{k_2}\Big(\sum_{k'\neq k_4}\varphi_{k'}\tilde{c}^\dagger_{k'}\tilde{c}^\dagger_{-k'}\Big)^{p-1}|0\rangle \\
&= p\varphi_{k_1}\,\langle 0|\Big(\sum_{k\neq k_1}\varphi_k\tilde{c}_{-k}\tilde{c}_k\Big)^{p-1}\tilde{c}_{-k_1}\tilde{c}^\dagger_{k_2}\Big(\sum_{k'\neq k_4}\varphi_{k'}\tilde{c}^\dagger_{k'}\tilde{c}^\dagger_{-k'}\Big)^{p-1}|0\rangle\,.
\end{aligned} \tag{5.4.193}$$

Left with the two operators $\tilde{c}_{-k_1}$ and $\tilde{c}^\dagger_{k_2}$, we consider the subcases:

(a) $k_2 = k_1$: for this subcase, the operator product $\tilde{c}^\dagger_{k_1}\tilde{c}^\dagger_{k_2}$ is zero, and we know the expectation vanishes, without having to fuss with the above expression any further.

(b) $k_2 = -k_1$: for this subcase, we use the anticommutation relation between $\tilde{c}_{-k_1}$ and $\tilde{c}^\dagger_{k_2}$ to get

$$\begin{aligned}
&p\varphi_{k_1}\,\langle 0|\Big(\sum_{k\neq k_1}\varphi_k\tilde{c}_{-k}\tilde{c}_k\Big)^{p-1}\tilde{c}_{-k_1}\tilde{c}^\dagger_{k_2}\Big(\sum_{k'\neq k_4}\varphi_{k'}\tilde{c}^\dagger_{k'}\tilde{c}^\dagger_{-k'}\Big)^{p-1}|0\rangle \\
&= +\,p\varphi_{k_1}\,\langle 0|\Big(\sum_{k\neq k_1}\varphi_k\tilde{c}_{-k}\tilde{c}_k\Big)^{p-1}\Big(\sum_{k'\neq k_4}\varphi_{k'}\tilde{c}^\dagger_{k'}\tilde{c}^\dagger_{-k'}\Big)^{p-1}|0\rangle \\
&\quad -\,p\varphi_{k_1}\,\langle 0|\Big(\sum_{k\neq k_1}\varphi_k\tilde{c}_{-k}\tilde{c}_k\Big)^{p-1}\tilde{c}^\dagger_{k_2}\tilde{c}_{-k_1}\Big(\sum_{k'\neq k_4}\varphi_{k'}\tilde{c}^\dagger_{k'}\tilde{c}^\dagger_{-k'}\Big)^{p-1}|0\rangle\,.
\end{aligned} \tag{5.4.194}$$

Again, we find that the second term in the above expression vanishes, because the exclusion of $\tilde{c}_{k_1}$ also imply the exclusion of $\tilde{c}_{-k_1} = \tilde{c}_{k_2}$, and so $\tilde{c}^\dagger_{k_2}$ can be pushed all the way through $\left(\sum_{k\neq k_1}\varphi_k\tilde{c}_{-k}\tilde{c}_k\right)^{p-1}$ to annihilate the vacuum from the right. As for the first term, we find that the many-particle state $\left(\sum_{k\neq k_1}\varphi_k\tilde{c}^\dagger_k\tilde{c}^\dagger_{-k}\right)^{p-1}$ consists of a sum of terms, each containing $2(p-1)$ particles, in which the single-particle states with wave vector $\pm k_1$ are empty, whereas the many-particle state $\left(\sum_{k\neq k_4}\varphi_k\tilde{c}^\dagger_k\tilde{c}^\dagger_{-k}\right)^{p-1}$ consists of a sum of terms, each containing $2(p-1)$ particles, in which the single-particle states with wave vector $\pm k_4$ are empty. Therefore,

i. if $k_1 \neq k_4$, we find that because the overlap between each term from $\left(\sum_{k\neq k_1} \varphi_k \tilde{c}_k^\dagger \tilde{c}_{-k}^\dagger\right)^{p-1}$ and any term from $\left(\sum_{k\neq k_4} \varphi_k \tilde{c}_k^\dagger \tilde{c}_{-k}^\dagger\right)^{p-1}$ is zero, the overall overlap between $\left(\sum_{k\neq k_1} \varphi_k \tilde{c}_k^\dagger \tilde{c}_{-k}^\dagger\right)^{p-1}$ and $\left(\sum_{k\neq k_4} \varphi_k \tilde{c}_k^\dagger \tilde{c}_{-k}^\dagger\right)^{p-1}$ must also be zero;

ii. if $k_1 = k_4$, then $\left(\sum_{k\neq k_1} \varphi_k \tilde{c}_k^\dagger \tilde{c}_{-k}^\dagger\right)^{p-1}$ and $\left(\sum_{k\neq k_4} \varphi_k \tilde{c}_k^\dagger \tilde{c}_{-k}^\dagger\right)^{p-1}$ are the same state, and the overlap is nonzero.

(c) $k_2 \neq \pm k_1$: for this subcase, we have

$$\begin{aligned} & p\varphi_{k_1} \langle 0| \left(\sum_{k\neq k_1} \varphi_k \tilde{c}_{-k}\tilde{c}_k\right)^{p-1} \tilde{c}_{-k_1} \tilde{c}_{k_2}^\dagger \left(\sum_{k'\neq k_4} \varphi_{k'} \tilde{c}_{k'}^\dagger \tilde{c}_{-k'}^\dagger\right)^{p-1} |0\rangle \\ = & -p\varphi_{k_1} \langle 0| \left(\sum_{k\neq k_1} \varphi_k \tilde{c}_{-k}\tilde{c}_k\right)^{p-1} \tilde{c}_{k_2}^\dagger \tilde{c}_{-k_1} \left(\sum_{k'\neq k_4} \varphi_{k'} \tilde{c}_{k'}^\dagger \tilde{c}_{-k'}^\dagger\right)^{p-1} |0\rangle . \end{aligned} \tag{5.4.195}$$

We see then that:

i. if $k_1 = \pm k_4$, then $\tilde{c}_{-k_1}$ would push right through $\left(\sum_{k'\neq k_4} \varphi_{k'} \tilde{c}_{k'}^\dagger \tilde{c}_{-k'}^\dagger\right)^{p-1}$ to annihilate the vacuum, making the expectation zero.

ii. if $k_1 \neq \pm k_4$, then we have

$$\begin{aligned} & p\varphi_{k_1} \langle 0| \left(\sum_{k\neq k_1} \varphi_k \tilde{c}_{-k}\tilde{c}_k\right)^{p-1} \tilde{c}_{-k_1} \tilde{c}_{k_2}^\dagger \left(\sum_{k'\neq k_4} \varphi_{k'} \tilde{c}_{k'}^\dagger \tilde{c}_{-k'}^\dagger\right)^{p-1} |0\rangle \\ = & -p\varphi_{k_1} \langle 0| \left(\sum_{k\neq k_1} \varphi_k \tilde{c}_{-k}\tilde{c}_k\right)^{p-1} \tilde{c}_{k_2}^\dagger \tilde{c}_{-k_1} \left(\sum_{k'\neq k_4} \varphi_{k'} \tilde{c}_{k'}^\dagger \tilde{c}_{-k'}^\dagger\right)^{p-1} |0\rangle \\ = & p^2\varphi_{k_1}^2 \langle 0| \left(\sum_{k\neq k_1} \varphi_k \tilde{c}_{-k}\tilde{c}_k\right)^{p-1} \tilde{c}_{k_2}^\dagger \tilde{c}_{k_1}^\dagger \left(\sum_{k'\neq k_1,k_4} \varphi_{k'} \tilde{c}_{k'}^\dagger \tilde{c}_{-k'}^\dagger\right)^{p-2} |0\rangle \\ = & -p^2\varphi_{k_1}^2 \langle 0| \left(\sum_{k\neq k_1} \varphi_k \tilde{c}_{-k}\tilde{c}_k\right)^{p-1} \tilde{c}_{k_1}^\dagger \tilde{c}_{k_2}^\dagger \left(\sum_{k'\neq k_1,k_4} \varphi_{k'} \tilde{c}_{k'}^\dagger \tilde{c}_{-k'}^\dagger\right)^{p-2} |0\rangle , \end{aligned} \tag{5.4.196}$$

and so we see that $\tilde{c}_{k_1}^\dagger$ pushes all the way through $\left(\sum_{k\neq k_1} \varphi_k \tilde{c}_{-k}\tilde{c}_k\right)^{p-1}$ to annihilate the vacuum from the right, i.e. the expectation vanishes.

3. $k_3 \neq \pm k_4$: in this case, we have

$$\begin{aligned}\langle\Psi_p|\tilde{c}^\dagger_{k_1}\tilde{c}^\dagger_{k_2}\tilde{c}_{k_3}\tilde{c}_{k_4}|\Psi_p\rangle &= p\varphi_{k_4}\langle 0|\Big(\sum_k \varphi_k \tilde{c}_{-k}\tilde{c}_k\Big)^p \tilde{c}^\dagger_{k_1}\tilde{c}^\dagger_{k_2}\tilde{c}_{k_3}\tilde{c}^\dagger_{-k_4}\Big(\sum_{k'\neq k_4}\varphi_{k'}\tilde{c}^\dagger_{k'}\tilde{c}^\dagger_{-k'}\Big)^{p-1}|0\rangle \\ &= -p\varphi_{k_4}\langle 0|\Big(\sum_k \varphi_k \tilde{c}_{-k}\tilde{c}_k\Big)^p \tilde{c}^\dagger_{k_1}\tilde{c}^\dagger_{k_2}\tilde{c}^\dagger_{-k_4}\tilde{c}_{k_3}\Big(\sum_{k'\neq k_4}\varphi_{k'}\tilde{c}^\dagger_{k'}\tilde{c}^\dagger_{-k'}\Big)^{p-1}|0\rangle\,.\end{aligned} \tag{5.4.197}$$

The subcases are:

(a) if $k_4 = -k_2$ or $k_4 = -k_1$, the expectation vanishes;

(b) if $k_4 \neq -k_1$ and $k_4 \neq -k_2$, we can anticommute $\tilde{c}^\dagger_{-k_4}$ through $\tilde{c}^\dagger_{k_1}$ and $\tilde{c}^\dagger_{k_2}$ to give

$$\begin{aligned}&\langle\Psi_p|\tilde{c}^\dagger_{k_1}\tilde{c}^\dagger_{k_2}\tilde{c}_{k_3}\tilde{c}_{k_4}|\Psi_p\rangle \\ &= p\varphi_{k_4}\langle 0|\Big(\sum_k \varphi_k \tilde{c}_{-k}\tilde{c}_k\Big)^p \tilde{c}^\dagger_{k_1}\tilde{c}^\dagger_{k_2}\tilde{c}_{k_3}\tilde{c}^\dagger_{-k_4}\Big(\sum_{k'\neq k_4}\varphi_{k'}\tilde{c}^\dagger_{k'}\tilde{c}^\dagger_{-k'}\Big)^{p-1}|0\rangle \\ &= -p\varphi_{k_4}\langle 0|\Big(\sum_k \varphi_k \tilde{c}_{-k}\tilde{c}_k\Big)^p \tilde{c}^\dagger_{k_1}\tilde{c}^\dagger_{k_2}\tilde{c}^\dagger_{-k_4}\tilde{c}_{k_3}\Big(\sum_{k'\neq k_4}\varphi_{k'}\tilde{c}^\dagger_{k'}\tilde{c}^\dagger_{-k'}\Big)^{p-1}|0\rangle \\ &= p^2\varphi^2_{k_4}\langle 0|\Big(\sum_{k\neq k_4} \varphi_k \tilde{c}_{-k}\tilde{c}_k\Big)^{p-1} \tilde{c}_{k_4}\tilde{c}^\dagger_{k_1}\tilde{c}^\dagger_{k_2}\tilde{c}_{k_3}\Big(\sum_{k'\neq k_4}\varphi_{k'}\tilde{c}^\dagger_{k'}\tilde{c}^\dagger_{-k'}\Big)^{p-1}|0\rangle\,.\end{aligned} \tag{5.4.198}$$

From this point on, the only thing stopping $\tilde{c}_{k_4}$ pushing right all the way through to annihilate the vacuum from the left is $\tilde{c}^\dagger_{k_1}$ and $\tilde{c}^\dagger_{k_2}$, and

i. if $k_4 = k_1$, we end up with

$$\begin{aligned}&\langle\Psi_p|\tilde{c}^\dagger_{k_1}\tilde{c}^\dagger_{k_2}\tilde{c}_{k_3}\tilde{c}_{k_4}|\Psi_p\rangle \\ &= p^2\varphi^2_{k_4}\langle 0|\Big(\sum_{k\neq k_4} \varphi_k \tilde{c}_{-k}\tilde{c}_k\Big)^{p-1} \tilde{c}^\dagger_{k_2}\tilde{c}_{k_3}\Big(\sum_{k'\neq k_4}\varphi_{k'}\tilde{c}^\dagger_{k'}\tilde{c}^\dagger_{-k'}\Big)^{p-1}|0\rangle\,,\end{aligned} \tag{5.4.199}$$

which we see, from an earlier argument, is nonzero only when $k_2 = k_3$;

ii. if $k_4 = k_2$, we end up with

$$\begin{aligned}&\langle\Psi_p|\tilde{c}^\dagger_{k_1}\tilde{c}^\dagger_{k_2}\tilde{c}_{k_3}\tilde{c}_{k_4}|\Psi_p\rangle \\ &= -p^2\varphi^2_{k_4}\langle 0|\Big(\sum_{k\neq k_4} \varphi_k \tilde{c}_{-k}\tilde{c}_k\Big)^{p-1} \tilde{c}^\dagger_{k_1}\tilde{c}_{k_3}\Big(\sum_{k'\neq k_4}\varphi_{k'}\tilde{c}^\dagger_{k'}\tilde{c}^\dagger_{-k'}\Big)^{p-1}|0\rangle\,,\end{aligned} \tag{5.4.200}$$

which we again know is nonzero only when $k_1 = k_3$; otherwise,

iii. if $k_4 \neq k_1, k_2$, the expectation is zero.

In summary, we find that the expectation of the operator product $\tilde{c}^\dagger_{k_1}\tilde{c}^\dagger_{k_2}\tilde{c}_{k_3}\tilde{c}_{k_4}$ is nonzero only when

1. $k_3 = -k_4$, $k_2 = -k_1$ and $k_1 = k_4$;

2. $k_3 \neq \pm k_4$, $k_4 = k_1$ and $k_2 = k_3$; and

3. $k_3 \neq \pm k_4$, $k_4 = k_2$ and $k_1 = k_3$.

If we think of the first case as a special case of the second case, then the expectation can be written as

$$\begin{aligned}\langle\Psi_p|\tilde{c}^\dagger_{k_1}\tilde{c}^\dagger_{k_2}\tilde{c}_{k_3}\tilde{c}_{k_4}|\Psi_p\rangle = \langle\Psi_p|\tilde{c}^\dagger_{k_1}\tilde{c}^\dagger_{k_2}\tilde{c}_{k_2}\tilde{c}_{k_1}|\Psi_p\rangle\,\delta_{k_1,k_4}\delta_{k_2,k_3} \\ + \langle\Psi_p|\tilde{c}^\dagger_{k_1}\tilde{c}^\dagger_{k_2}\tilde{c}_{k_1}\tilde{c}_{k_2}|\Psi_p\rangle\,\delta_{k_1,k_3}\delta_{k_2,k_4},\end{aligned} \tag{5.4.201}$$

which is in fact, a Wick factorization.

However, this Wick factorization does not allow us to write the four-operator expectations in terms of products of two-operator expectations. To see this, let us evaluate the first nonzero expectation, which takes the form

$$\begin{aligned}\langle\Psi_p|\tilde{c}^\dagger_k\tilde{c}^\dagger_{-k}\tilde{c}_{-k}\tilde{c}_k|\Psi_p\rangle &= p\varphi_k\,\langle\Psi_p|\tilde{c}^\dagger_k\tilde{c}^\dagger_{-k}\tilde{c}_{-k}\tilde{c}^\dagger_{-k}|\Psi_{p-1}\rangle \\ &= p\varphi_k\,\langle\Psi_p|\tilde{c}^\dagger_k\tilde{c}^\dagger_{-k}|\Psi_{p-1}\rangle - p\varphi_k\,\langle\Psi_p|\tilde{c}^\dagger_k\tilde{c}^\dagger_{-k}\tilde{c}^\dagger_{-k}\tilde{c}_{-k}|\Psi_{p-1}\rangle \\ &= p^2\varphi_k^2\,\langle\Psi_{p-1}|\tilde{c}_{-k}\tilde{c}^\dagger_{-k}|\Psi_{p-1}\rangle \\ &= p^2\varphi_k^2\,\langle\Psi_{p-1}|\Psi_{p-1}\rangle - p^2\varphi_k^2\,\langle\Psi_{p-1}|\tilde{c}^\dagger_{-k}\tilde{c}_{-k}|\Psi_{p-1}\rangle \\ &= p^2\varphi_k^2\,\langle\Psi_{p-1}|\Psi_{p-1}\rangle - p^2\varphi_k^2\tilde{F}(p-1,-k).\end{aligned} \tag{5.4.202}$$

From the definition of $\tilde{F}(p,k)$ in (5.4.174), we see that

$$\begin{aligned}\tilde{F}(p,-k) &= -\sum_{r=1}^{p}(-1)^r\left[\frac{p!}{(p-r)!}\varphi_{-k}\right]^2\langle\Psi_{p-r}|\Psi_{p-r}\rangle \\ &= -\sum_{r=1}^{p}(-1)^r\left[-\frac{p!}{(p-r)!}\varphi_k\right]^2\langle\Psi_{p-r}|\Psi_{p-r}\rangle = \tilde{F}(p,k).\end{aligned} \tag{5.4.203}$$

Also, writing out the terms of $\tilde{F}(p,k)$ and $\tilde{F}(p-1,k)$ explicitly, we have

$$\begin{aligned}\tilde{F}(p,k) &= p^2\varphi_k^2\,\langle\Psi_{p-1}|\Psi_{p-1}\rangle - p^2(p-1)^2\varphi_k^4\,\langle\Psi_{p-2}|\Psi_{p-2}\rangle + \cdots\,,\\ \tilde{F}(p-1,k) &= (p-1)^2\varphi_k^2\,\langle\Psi_{p-2}|\Psi_{p-2}\rangle - \cdots\,,\end{aligned} \tag{5.4.204}$$

which gives us a joint recurrence relation

$$\tilde{F}(p,k) + p^2\varphi_k^2\tilde{F}(p-1,k) = p^2\varphi_k^2\,\langle\Psi_{p-1}|\Psi_{p-1}\rangle \tag{5.4.205}$$

satisfied by $\tilde{F}(p,k)$ and $\langle\Psi_p|\Psi_p\rangle$.

Substituting (5.4.204) and (5.4.205) into (5.4.202), we find that

$$\langle\Psi_p|\tilde{c}_k^\dagger\tilde{c}_{-k}^\dagger\tilde{c}_{-k}\tilde{c}_k|\Psi_p\rangle = \tilde{F}(p,k) + p^2\varphi_k^2\tilde{F}(p-1,k) - p^2\varphi_k^2\tilde{F}(p-1,k) = \tilde{F}(p,k). \tag{5.4.206}$$

Observe that

$$\langle\Psi_p|\tilde{c}_k^\dagger\tilde{c}_{-k}^\dagger\tilde{c}_{-k}\tilde{c}_k|\Psi_p\rangle = \tilde{F}(p,k) = \langle\Psi_p|\tilde{c}_k^\dagger\tilde{c}_k|\Psi_p\rangle\,, \tag{5.4.207}$$

and not the product between $\tilde{F}(p,k) = \langle\Psi_p|\tilde{c}_k^\dagger\tilde{c}_k|\Psi_p\rangle$ and $\tilde{F}(p,-k) = \langle\Psi_p|\tilde{c}_{-k}^\dagger\tilde{c}_{-k}|\Psi_p\rangle$. Similarly, after writing $\langle\Psi_p|\tilde{c}_k^\dagger\tilde{c}_{-k}^\dagger\tilde{c}_k\tilde{c}_{-k}|\Psi_p\rangle = -\langle\Psi_p|\tilde{c}_k^\dagger\tilde{c}_{-k}^\dagger\tilde{c}_{-k}\tilde{c}_k|\Psi_p\rangle$, we have the second, 'bidiagonal', expectation

$$\langle\Psi_p|\tilde{c}_k^\dagger\tilde{c}_{-k}^\dagger\tilde{c}_k\tilde{c}_{-k}|\Psi_p\rangle = -\tilde{F}(p,k). \tag{5.4.208}$$

These are, of course, special cases of the four-operator expectations $\langle\Psi_p|\tilde{c}_{k_1}^\dagger\tilde{c}_{k_2}^\dagger\tilde{c}_{k_2}\tilde{c}_{k_1}|\Psi_p\rangle$ and $\langle\Psi_p|\tilde{c}_{k_1}^\dagger\tilde{c}_{k_2}^\dagger\tilde{c}_{k_1}\tilde{c}_{k_2}|\Psi_p\rangle$.

For the case where $k_2 \neq -k_1$, we find that

$$\begin{aligned}\langle\Psi_p|\tilde{c}_{k_1}^\dagger\tilde{c}_{k_2}^\dagger\tilde{c}_{k_2}\tilde{c}_{k_1}|\Psi_p\rangle &= p\varphi_{k_1}\,\langle\Psi_p|\tilde{c}_{k_1}^\dagger\tilde{c}_{k_2}^\dagger\tilde{c}_{k_2}\tilde{c}_{-k_1}^\dagger|\Psi_{p-1}\rangle\\ &= -p\varphi_{k_1}\,\langle\Psi_p|\tilde{c}_{-k_1}^\dagger\tilde{c}_{k_1}^\dagger\tilde{c}_{k_2}^\dagger\tilde{c}_{k_2}|\Psi_{p-1}\rangle\\ &= p^2\varphi_{k_1}^2\,\langle\Psi_{p-1}|\tilde{c}_{k_1}\tilde{c}_{k_1}^\dagger\tilde{c}_{k_2}^\dagger\tilde{c}_{k_2}|\Psi_{p-1}\rangle\\ &= p^2\varphi_{k_1}^2\,\langle\Psi_{p-1}|\tilde{c}_{k_2}^\dagger\tilde{c}_{k_2}|\Psi_{p-1}\rangle\\ &\quad - p^2\varphi_{k_1}^2\,\langle\Psi_{p-1}|\tilde{c}_{k_1}^\dagger\tilde{c}_{k_2}^\dagger\tilde{c}_{k_2}\tilde{c}_{k_1}|\Psi_{p-1}\rangle\\ &= p^2\varphi_{k_1}^2\tilde{F}(p-1,k_2) - p^2\varphi_{k_1}^2\,\langle\Psi_{p-1}|\tilde{c}_{k_1}^\dagger\tilde{c}_{k_2}^\dagger\tilde{c}_{k_2}\tilde{c}_{k_1}|\Psi_{p-1}\rangle\,,\end{aligned} \tag{5.4.209}$$

which looks quite different from the case where $k_2 = -k_1$. In any case, we can use (5.4.209) recursively to obtain

$$\begin{aligned}
\langle\Psi_p|\tilde{c}^\dagger_{k_1}\tilde{c}^\dagger_{k_2}\tilde{c}_{k_2}\tilde{c}_{k_1}|\Psi_p\rangle &= p^2\varphi^2_{k_1}\tilde{F}(p-1,k_2) - p^2\varphi^2_{k_1}\,\langle\Psi_{p-1}|\tilde{c}^\dagger_{k_1}\tilde{c}^\dagger_{k_2}\tilde{c}_{k_2}\tilde{c}_{k_1}|\Psi_{p-1}\rangle \\
&= +p^2\varphi^2_{k_1}\tilde{F}(p-1,k_2) - p^2(p-1)^2\varphi^4_{k_1}\tilde{F}(p-2,k_2) \\
&\quad + p^2(p-1)^2\varphi^4_{k_1}\,\langle\Psi_{p-2}|\tilde{c}^\dagger_{k_1}\tilde{c}^\dagger_{k_2}\tilde{c}_{k_2}\tilde{c}_{k_1}|\Psi_{p-2}\rangle \\
&= \ldots \\
&= -\sum_{r=1}^{p}(-1)^r\left[\frac{p!}{(p-r)!}\varphi^r_{k_1}\right]^2\tilde{F}(p-r,k_2) \\
&\quad + (-1)^p\,\langle 0|\tilde{c}^\dagger_{k_1}\tilde{c}^\dagger_{k_2}\tilde{c}_{k_2}\tilde{c}_{k_1}|0\rangle \\
&= -\sum_{r=1}^{p}(-1)^r\left[\frac{p!}{(p-r)!}\varphi^r_{k_1}\right]^2\tilde{F}(p-r,k_2) = \tilde{G}(p,k_1,k_2).
\end{aligned} \tag{5.4.210}$$

Now, because $\langle\Psi_p|\tilde{c}^\dagger_{k_1}\tilde{c}^\dagger_{k_2}\tilde{c}_{k_2}\tilde{c}_{k_1}|\Psi_p\rangle = \langle\Psi_p|\tilde{c}^\dagger_{k_2}\tilde{c}^\dagger_{k_1}\tilde{c}_{k_1}\tilde{c}_{k_2}|\Psi_p\rangle$, we have the symmetry property

$$\tilde{G}(p,k_1,k_2) = \tilde{G}(p,k_2,k_1), \tag{5.4.211}$$

even though it does not look manifestly so in the definition of $\tilde{G}(p,k_1,k_2)$ above,

The *p*-pair norms. We can continue evaluating the expectations of five-operator, six-operator, ..., n-operator terms in terms of the p-pair norms $\langle\Psi_p|\Psi_p\rangle$ and codify the results in terms of $\tilde{F}(p,k)$, $\tilde{G}(p,k_1,k_2)$, $\tilde{H}(p,k_1,k_2,k_3)$, and so on, but with the four-operator expectations at hand, we are ready to work out what the p-pair norms are themselves. Realistically speaking, we might eventually not be able to write these p-pair norms down explicitly as compact sums, but at the very least, we should have a recurrence formula that relates $\langle\Psi_p|\Psi_p\rangle$ to lower-order norms.

To do this, let us write

$$\begin{aligned}\langle\Psi_p|\Psi_p\rangle &= \langle\Psi_{p-1}|\Big(\sum_k \varphi_k \tilde{c}_{-k}\tilde{c}_k\Big)\Big(\sum_{k'} \varphi_{k'}\tilde{c}^\dagger_{k'}\tilde{c}^\dagger_{-k'}\Big)|\Psi_{p-1}\rangle \\ &= \sum_k\sum_{k'}\varphi_k\varphi_{k'}\,\langle\Psi_{p-1}|\tilde{c}_{-k}\tilde{c}_k\tilde{c}^\dagger_{k'}\tilde{c}^\dagger_{-k'}|\Psi_{p-1}\rangle\,.\end{aligned} \tag{5.4.212}$$

As discussed earlier, we see that if $k' \neq \pm k$, we would be able to push $\tilde{c}^\dagger_{k'}$ left through $\tilde{c}_{-k}\tilde{c}_k$, act on $\langle\Psi_{p-1}|$ to yield a product not involving k, and become $\tilde{c}_{-k'}$. We can then push $\tilde{c}_{-k'}$ right through $\tilde{c}_{-k}\tilde{c}_k$, anticommute with $\tilde{c}^\dagger_{-k'}$, and end up with two terms,

$$\begin{aligned}&(p-1)\varphi_{k'}\,\langle 0|\Big(\sum_{k''\neq k'}\varphi_{k''}\tilde{c}_{-k''}\tilde{c}_{k''}\Big)^{p-2}\tilde{c}_{-k}\tilde{c}_k\Big(\sum_{k'''}\varphi_{k'''}\tilde{c}^\dagger_{k'''}\tilde{c}^\dagger_{-k'''}\Big)^{p-1}|0\rangle \\ &= (p-1)^2\varphi_k\varphi_{k'}\,\langle 0|\Big(\sum_{k''\neq k'}\varphi_{k''}\tilde{c}_{-k''}\tilde{c}_{k''}\Big)^{p-2}\tilde{c}_{-k}\tilde{c}^\dagger_{-k}\Big(\sum_{k'''\neq k}\varphi_{k'''}\tilde{c}^\dagger_{k'''}\tilde{c}^\dagger_{-k'''}\Big)^{p-2}|0\rangle\,,\end{aligned} \tag{5.4.213}$$

and

$$-(p-1)\varphi_{k'}\,\langle 0|\Big(\sum_{k''\neq k'}\varphi_{k''}\tilde{c}_{-k''}\tilde{c}_{k''}\Big)^{p-2}\tilde{c}_{-k}\tilde{c}_k\tilde{c}^\dagger_{-k'}\tilde{c}_{-k'}\Big(\sum_{k'''}\varphi_{k'''}\tilde{c}^\dagger_{k'''}\tilde{c}^\dagger_{-k'''}\Big)^{p-1}|0\rangle\,, \tag{5.4.214}$$

The first term (5.4.213) will itself yield two terms upon anticommutation of $\tilde{c}_{-k}$ and $\tilde{c}^\dagger_{-k}$. The first of these is an overlap between the states in which $(k', -k')$ and $(k, -k)$ are missing respectively, and hence vanishes. The second of these contains $\tilde{c}_{-k}$ to the right of $\tilde{c}^\dagger_{-k}$, and thus $\tilde{c}_{-k}$ can be pushed all the way through the product term to annihilate the vacuum from the left. For the second term (5.4.214), we simply push $\tilde{c}^\dagger_{-k'}$ left through $\tilde{c}_{-k}\tilde{c}_k$, and then through the product term, which does not contain $\tilde{c}_{-k'}$, because this has been eliminated by the action of $\tilde{c}^\dagger_{k'}$ earlier, to subsequently annihilate the vacuum from the right. This second term therefore vanishes as well, and thus the expectation $\langle\Psi_p|\tilde{c}_{-k}\tilde{c}_k\tilde{c}^\dagger_{k'}\tilde{c}^\dagger_{-k'}|\Psi_p\rangle$ is zero unless $k' = \pm k$, and we would write this expectation as

$$\langle\Psi_p|\tilde{c}_{-k}\tilde{c}_k\tilde{c}^\dagger_{k'}\tilde{c}^\dagger_{-k'}|\Psi_p\rangle = \langle\Psi_p|\tilde{c}_{-k}\tilde{c}_k\tilde{c}^\dagger_k\tilde{c}^\dagger_{-k}|\Psi_p\rangle\,(\delta_{k,k'} - \delta_{k,-k'})\,. \tag{5.4.215}$$

We can further simplify this result, by noting that the sum over k' in (5.4.212) is restricted to the positive half of the First Brillouin Zone (because we are summing wave

vectors pairwise), we pick up only the $k' = k$ term after summing over k', i.e.

$$\langle \Psi_p | \Psi_p \rangle = \sum_k \varphi_k^2 \, \langle \Psi_{p-1} | \tilde{c}_{-k} \tilde{c}_k \tilde{c}_k^\dagger \tilde{c}_{-k}^\dagger | \Psi_{p-1} \rangle \, . \tag{5.4.216}$$

Writing the expectation in (5.4.216) in terms of expectations we already know, we find that

$$\begin{aligned} \langle \Psi_{p-1} | \tilde{c}_{-k} \tilde{c}_k \tilde{c}_k^\dagger \tilde{c}_{-k}^\dagger | \Psi_{p-1} \rangle &= \langle \Psi_{p-1} | \Psi_{p-1} \rangle - \langle \Psi_{p-1} | \tilde{c}_k^\dagger \tilde{c}_k | \Psi_{p-1} \rangle \\ &\quad - \langle \Psi_{p-1} | \tilde{c}_{-k}^\dagger \tilde{c}_{-k} | \Psi_{p-1} \rangle + \langle \Psi_{p-1} | \tilde{c}_k^\dagger \tilde{c}_{-k}^\dagger \tilde{c}_{-k} \tilde{c}_k | \Psi_{p-1} \rangle \\ &= \langle \Psi_{p-1} | \Psi_{p-1} \rangle - \tilde{F}(p-1, k) \\ &\quad - \tilde{F}(p-1, -k) + \tilde{F}(p-1, k) \\ &= \langle \Psi_{p-1} | \Psi_{p-1} \rangle - \tilde{F}(p-1, k). \end{aligned} \tag{5.4.217}$$

Substituting (5.4.217) into (5.4.216), we then obtain the recurrence formula

$$\langle \Psi_p | \Psi_p \rangle = \sum_k \varphi_k^2 \, \langle \Psi_{p-1} | \Psi_{p-1} \rangle - \sum_k \varphi_k^2 \tilde{F}(p-1, k). \tag{5.4.218}$$

On its own, (5.4.218) is not very useful for computing $\langle \Psi_p | \Psi_p \rangle$ explicitly, because the recurrence formula also involves $\tilde{F}(p-1, k)$, which is itself a complicated sum of norms. But we can simplify it further by rewriting (5.4.205) as

$$\frac{1}{p^2} \tilde{F}(p, k) = \varphi_k^2 \Big[\langle \Psi_{p-1} | \Psi_{p-1} \rangle - \tilde{F}(p-1, k) \Big], \tag{5.4.219}$$

to write $\langle \Psi_p | \Psi_p \rangle$ as

$$\langle \Psi_p | \Psi_p \rangle = \frac{1}{p^2} \sum_k \tilde{F}(p, k). \tag{5.4.220}$$

This is a compact way of writing a pth order recurrence formula relating $\langle \Psi_p | \Psi_{p-1} \rangle$ to $\langle \Psi_{p-1} | \Psi_{p-1} \rangle$, $\langle \Psi_{p-2} | \Psi_{p-2} \rangle$, …, $\langle \Psi_1 | \Psi_1 \rangle$, and $\langle \Psi_0 | \Psi_0 \rangle = \langle 0 | 0 \rangle = 1$.

Using (5.4.220), (5.4.174) and (5.4.205), we can then work out the p-pair norms from the ground up. We find that,

$$\langle \Psi_0 | \Psi_0 \rangle = 1; \tag{5.4.221a}$$

$$\tilde{F}(1,k) = \left(\frac{1!}{0!}\varphi_k\right)^2 \langle\Psi_0|\Psi_0\rangle = \varphi_k^2, \tag{5.4.221b}$$

$$\langle\Psi_1|\Psi_1\rangle = \frac{1}{1^2}\sum_k \tilde{F}(1,k) = \sum_k \varphi_k^2; \tag{5.4.221c}$$

$$\begin{aligned}\tilde{F}(2,k) &= \left(\frac{2!}{1!}\varphi_k\right)^2 \langle\Psi_1|\Psi_1\rangle - \left(\frac{2!}{0!}\varphi_k^2\right)^2 \langle\Psi_0|\Psi_0\rangle \\ &= 4\left(\varphi_k^2 \sum_{k'} \varphi_{k'}^2 - \varphi_k^4\right),\end{aligned} \tag{5.4.221d}$$

$$\langle\Psi_2|\Psi_2\rangle = \frac{1}{2^2}\sum_k \tilde{F}(2,k) = \left(\sum_k \varphi_k^2\right)^2 - \sum_k \varphi_k^4; \tag{5.4.221e}$$

$$\begin{aligned}\tilde{F}(3,k) &= 3^2\varphi_k^2 \langle\Psi_2|\Psi_2\rangle - 3^2\varphi_k^2\tilde{F}(2,k) \\ &= 9\varphi_k^2\left(\sum_{k'} \varphi_{k'}\right)^2 - 9\varphi_k^2 \sum_{k'} \varphi_{k'}^4 - 36\varphi_k^4 \sum_{k'} \varphi_{k'}^2 + 36\varphi_k^6,\end{aligned} \tag{5.4.221f}$$

$$\langle\Psi_3|\Psi_3\rangle = \frac{1}{3^2}\sum_k \tilde{F}(3,k) = \left(\sum_k \varphi_k^2\right)^3 - 5\left(\sum_k \varphi_k^2\right)\left(\sum_k \varphi_k^4\right) - 4\sum_k \varphi_k^6, \tag{5.4.221g}$$

and so on and so forth. In any case, it appears that our recurrence formula for computing $\langle\Psi_p|\Psi_p\rangle$ is not practical if p is a large number. Of course, if p is large, we would use the usual BCS wave function instead. If the chemical potential μ is tuned such that the average number of pairs in the BCS ground state is p, the particle number fluctuation would be on the order of p^{-1}. Therefore, for most of the supercluster density-matrix elements, we should not be able to tell whether we have evaluated them from the definite- or indefinite-particle-number BCS ground states. For those supercluster density-matrix elements which are explicitly zero in the definite-particle-number BCS ground state, we then expect to find small nonzero values, proportional to the variance of the particle-number fluctuation, for such matrix elements in the indefinite-particle-number BCS ground state.

5.4.5 The (1 + 1) Supercluster

Cluster density matrices. For the (1 + 1) supercluster, we again start by computing the cluster density matrices ρ^a and ρ^b. The matrix elements of the unnormalized ρ^a are

$$\begin{aligned}\langle 0|\rho^a|0\rangle &= \langle \Psi_p|c_0 c_0^\dagger|\Psi_p\rangle = \frac{1}{N}\sum_{k_1}\sum_{k_2}\langle \Psi_p|\tilde{c}_{k_1}\tilde{c}_{k_2}^\dagger|\Psi_p\rangle \\ &= \frac{1}{N}\sum_{k_1}\sum_{k_2}\langle \Psi_p|\Psi_p\rangle\,\delta_{k_1,k_2} - \frac{1}{N}\sum_{k_1}\sum_{k_2}\langle \Psi_p|\tilde{c}_{k_2}^\dagger\tilde{c}_{k_1}|\Psi_p\rangle\,\delta_{k_1,k_2} \\ &= \frac{1}{N}\sum_{k_1}\langle \Psi_p|\Psi_p\rangle - \frac{1}{N}\sum_{k_1}\tilde{F}(p,k_1) = \frac{1}{N}\sum_{k_1}\frac{\tilde{F}(p+1,k)}{p^2\varphi_k^2}, \end{aligned} \tag{5.4.222a}$$

$$\langle 0|\rho^a|1\rangle = 0, \tag{5.4.222b}$$

$$\langle 1|\rho^a|0\rangle = 0, \tag{5.4.222c}$$

$$\begin{aligned}\langle 1|\rho^a|1\rangle &= \langle \Psi_p|c_0^\dagger c_0|\Psi_p\rangle = \frac{1}{N}\sum_{k_1}\sum_{k_2}\langle \Psi_p|\tilde{c}_{k_1}^\dagger\tilde{c}_{k_2}|\Psi_p\rangle \\ &= \frac{1}{N}\sum_{k_1}\sum_{k_2}\tilde{F}(p,k_1)\delta_{k_1,k_2} = \frac{1}{N}\sum_{k_1}\tilde{F}(p,k_1). \end{aligned} \tag{5.4.222d}$$

The matrix elements of ρ^b are similar.

Unlike with the usual BCS wave function $|\Psi_{\text{BCS}}\rangle$, we cannot use ρ^a and ρ^b directly as calculated, because $|\Psi_p\rangle$ is not normalized. Before we proceed to compute the direct product density matrix, we need to normalize ρ^a and ρ^b. This can be done by demanding that $\operatorname{Tr}\rho^a = 1 = \operatorname{Tr}\rho^b$. From (5.4.222), we see that the trace of ρ^a is just $\langle \Psi_p|\Psi_p\rangle$, so the matrix elements of the properly normalized block density matrices would be

$$\langle 0|\rho^a|0\rangle = 1 - f(p,0), \tag{5.4.223a}$$

$$\langle 0|\rho^a|1\rangle = 0, \tag{5.4.223b}$$

$$\langle 1|\rho^a|0\rangle = 0, \tag{5.4.223c}$$

$$\langle 1|\rho^a|1\rangle = f(p,0), \tag{5.4.223d}$$

where we define

$$f(p,0) = \frac{1}{N}\sum_k \frac{\tilde{F}(p,k)}{\langle\Psi_p|\Psi_p\rangle}. \tag{5.4.224}$$

Direct product density matrix. The direct product density matrix $\rho^a \otimes \rho^b$ has nonzero matrix elements

$$\langle 00|(\rho^a \otimes \rho^b)|00\rangle = (1 - f(p,0))^2, \tag{5.4.225a}$$

$$\langle 10|(\rho^a \otimes \rho^b)|10\rangle = f(p,0)(1 - f(p,0)), \tag{5.4.225b}$$

$$\langle 01|(\rho^a \otimes \rho^b)|01\rangle = f(p,0)(1 - f(p,0)), \tag{5.4.225c}$$

$$\langle 11|(\rho^a \otimes \rho^b)|11\rangle = f^2(p,0). \tag{5.4.225d}$$

Supercluster density matrix. The unnormalized supercluster density matrix has nonzero matrix elements

$$\langle 00|\rho^{ab}|00\rangle = \langle\Psi_p|\Psi_p\rangle\left[1 - 2f(p,0) + \frac{f(p,0)}{N} + g(p,0) - \frac{f(p,2r)}{N} - g(p,r)\right], \tag{5.4.226a}$$

$$\langle 10|\rho^{ab}|10\rangle = \langle\Psi_p|\Psi_p\rangle\left[f(p,0) - \frac{f(p,0)}{N} - g(p,0) + \frac{f(p,2r)}{N} + g(p,r)\right], \tag{5.4.226b}$$

$$\langle 10|\rho^{ab}|01\rangle = \langle\Psi_p|\Psi_p\rangle\, f(p,r), \tag{5.4.226c}$$

$$\langle 01|\rho^{ab}|01\rangle = \langle\Psi_p|\Psi_p\rangle\left[f(p,0) - \frac{f(p,0)}{N} - g(p,0) + \frac{f(p,2r)}{N} + g(p,r)\right], \tag{5.4.226d}$$

$$\langle 11|\rho^{ab}|11\rangle = \langle\Psi_p|\Psi_p\rangle\left[\frac{f(p,0)}{N} + g(p,0) - \frac{f(p,2r)}{N} - g(p,r)\right], \tag{5.4.226e}$$

where we define

$$f(p,r) = \frac{1}{N}\sum_k e^{\mathrm{i}kr}\frac{\tilde{F}(p,k)}{\langle\Psi_p|\Psi_p\rangle}, \quad g(p,r) = \frac{1}{N^2}\sum_k\sum_{k'\neq k} e^{\mathrm{i}(k-k')r}\frac{\tilde{G}(p,k,k')}{\langle\Psi_p|\Psi_p\rangle}. \tag{5.4.227}$$

Taking the trace, we again find that $\mathrm{Tr}\,\rho^{ab} = \langle\Psi_p|\Psi_p\rangle$, and so the normalized nonzero matrix elements are

$$\langle 00|\rho^{ab}|00\rangle = \left[1 - 2f(p,0) + \frac{f(p,0)}{N} + g(p,0) - \frac{f(p,2r)}{N} - g(p,r)\right], \tag{5.4.228a}$$

$$\langle 10|\rho^{ab}|10\rangle = \left[f(p,0) - \frac{f(p,0)}{N} - g(p,0) + \frac{f(p,2r)}{N} + g(p,r)\right], \tag{5.4.228b}$$

$$\langle 10|\rho^{ab}|01\rangle = f(p,r), \tag{5.4.228c}$$

$$\langle 01|\rho^{ab}|01\rangle = \left[f(p,0) - \frac{f(p,0)}{N} - g(p,0) + \frac{f(p,2r)}{N} + g(p,r)\right], \tag{5.4.228d}$$

$$\langle 11|\rho^{ab}|11\rangle = \left[\frac{f(p,0)}{N} + g(p,0) - \frac{f(p,2r)}{N} - g(p,r)\right]. \tag{5.4.228e}$$

Correlation density matrix. Using (5.4.225) and (5.4.228), we then find the nonzero matrix elements of ρ^c to be

$$\langle 00|\rho^c|00\rangle = \frac{f(p,0)}{N} + g(p,0) - \frac{f(p,2r)}{N} - g(p,r) - f^2(p,0), \tag{5.4.229a}$$

$$\langle 10|\rho^c|10\rangle = -\frac{f(p,0)}{N} - g(p,0) + \frac{f(p,2r)}{N} + g(p,r) + f^2(p,0), \tag{5.4.229b}$$

$$\langle 10|\rho^c|01\rangle = f(p,r), \tag{5.4.229c}$$

$$\langle 01|\rho^c|01\rangle = -\frac{f(p,0)}{N} - g(p,0) + \frac{f(p,2r)}{N} + g(p,r) + f^2(p,0), \tag{5.4.229d}$$

$$\langle 11|\rho^c|11\rangle = \frac{f(p,0)}{N} + g(p,0) - \frac{f(p,2r)}{N} - g(p,r) - f^2(p,0). \tag{5.4.229e}$$

The correlation density matrix thus have the structure

$$\rho^c = \begin{bmatrix} A & 0 & 0 & 0 \\ 0 & -A & B & 0 \\ 0 & B^* & -A & 0 \\ 0 & 0 & 0 & A \end{bmatrix}, \tag{5.4.230}$$

where

$$A = \frac{f(p,0)}{N} + g(p,0) - \frac{f(p,2r)}{N} - g(p,r) - f^2(p,0), \quad B = f(p,r). \tag{5.4.231}$$

This structure is entirely analogous to the $(1+1)$ correlation density matrix of a chain of noninteracting spinless fermions. The only difference between the two ground states are the different singular values. This is not surprising, since we already expected that

the superconducting ground state cannot be distinguished from the Fermi sea ground state at the (1 + 1) supercluster level. We also expect that they *will* be distinguishable at the (2 + 2) supercluster level. To verify this, we will need to calculate the supercluster density matrix of the (2 + 2) supercluster, which requires us to work out six- and eight-operator expectations in the particle-number projected BCS ground state. As it turned out, I never had the time to return to do this in the course of my thesis work.

MANY-BODY FERMION DENSITY MATRICES

VOLUME II

A Dissertation

Presented to the Faculty of the Graduate School

of Cornell University

in Partial Fulfillment of the Requirements for the Degree of

Doctor of Philosophy

by

Siew-Ann Cheong

May 2006

CHAPTER 6

SINGULAR VALUE DECOMPOSITION

6.1 A Quick Guide to Chapter 6

As mentioned in the road-map Section 1.4 in Chapter 1, Chapter 6 provides the second-to-last key ingredient — the operator singular value decomposition (6.3.1) of the correlation density matrix starting from an operator expansion (6.3.18) in terms of products of referencing operators — needed to appreciate the numerical results presented in Chapter 8. To arrive at these key formulas, I revisit ordinary matrix singular value decomposition in Section 6.2, to develop a geometrical picture in which the columns of the matrix to be singular value decomposed, viewed as vectors, are iteratively orthogonalized through successive unitary transformations.

This key insight, not found in any numerical analysis texts describing matrix singular value decomposition, allows me to identify in Section 6.3 the two key ingredients, i.e. that (i) we have the means to tell that two operators are 'orthogonal' to each other; and (ii) we have the means to 'normalize' an operator, to properly define an operator singular value decomposition. I discuss how a suitable Frobenius-orthonormalization of operators can be done in Section 6.3.1, and then proceed to expand the correlation density matrix in terms of a Frobenius-orthonormal basis of operators in Section 6.3.2. We will find that each operator in the Frobenius-orthonormal basis is a product of two of the referencing operators introduced in Chapter 2.

In Sections 6.4 and 6.5, the correlation density matrices calculated, respectively, from the one-dimensional Fermi-sea and superconducting ground states are operator singular value decomposed manually. I am very proud that I was able to push the operator singular value decomposition through by hand for the most tedious case of a

half-filled Fermi-sea ground state. However, this feat has very little impact on the numerical calculations done in Chapter 8, because (6.3.18) spares us of these long and tedious calculations altogether! Instead, we simply construct a coefficient matrix, called the correlation-**K** matrix, and let a computer do the numerical matrix singular value decomposition to yield the operator singular value decomposition (6.3.1) of the correlation density matrix. Readers wishing to proceed to the physics of the extended Hubbard ladder of spinless fermions in Chapter 7 can also go ahead to that chapter after reading Sections 6.2 and 6.3, and be spared from the pages and pages of calculations in the remainder of Chapter 6.

6.2 Matrix Singular Value Decomposition

In the singular value decomposition of a given real $N \times N$ matrix M, the goal is to write M as

$$M = u_1 \, \sigma_1 \, v_1^T + u_2 \, \sigma_2 \, v_2^T + + \cdots + u_N \, \sigma_N \, v_N^T, \tag{6.2.1}$$

where $\sigma_1 \geq \sigma_2 \geq \cdots \geq \sigma_N \geq 0$ are the *singular values*, and the sets of orthonormal vectors $\{u_i\}$ and $\{v_i\}$ are the *left eigenvectors* and *right eigenvectors* of M. This decomposition of the matrix M can be written in the matrix form

$$M = U \Sigma V^T, \tag{6.2.2}$$

where U and V are orthogonal matrices, and Σ is a diagonal matrix of singular values. When written as

$$U = \begin{pmatrix} u_1 & u_2 & \cdots & u_N \end{pmatrix}, \quad V = \begin{pmatrix} v_1 & v_2 & \cdots & v_N \end{pmatrix}, \tag{6.2.3}$$

the columns of U and V are the left and right eigenvectors u_i and v_i of M respectively. Because the sequence of singular values σ_i can be ordered such that they are strictly

nonincreasing, the singular value decomposition of M can be used as a means of approximating M, by keeping only a small number of terms in the expansion (6.2.1). This is the aspect of singular value decomposition that we are most interested in.

Rewriting (6.2.2) as

$$U\Sigma = \tilde{U} = \begin{pmatrix} \tilde{u}_1 & \tilde{u}_2 & \cdots & \tilde{u}_N \end{pmatrix} = \begin{pmatrix} m_1 & m_2 & \cdots & m_N \end{pmatrix} V = MV, \tag{6.2.4}$$

where the column vectors $\tilde{u}_i$ making up $\tilde{U}$ are mutually orthogonal but not normalized, while the column vectors m_i making up M are neither mutually orthogonal nor normalized, we can develop a simple geometric picture of what happens in singular value decomposition. Performing the matrix multiplication $\tilde{U} = MV$, we find that in the first column of $\tilde{U}$,

$$\tilde{U} = \begin{pmatrix} \tilde{u}_{1,1} & \cdots \\ \tilde{u}_{1,2} & \cdots \\ \vdots & \ddots \\ \tilde{u}_{1,N} & \cdots \end{pmatrix}, \tag{6.2.5}$$

the matrix element $\tilde{u}_{1,i}$ is obtained by multiplying the ith row in U with the first column in V^T. Therefore, the column vector $\tilde{u}_1$ can be thought of as a linear combination of $u_1, u_2, \ldots, u_N$. Going through this same argument, we realized that $\tilde{u}_2, \ldots, \tilde{u}_N$ are all linear combinations of $u_1, u_2, \ldots, u_N$. Therefore, we see that the orthogonal set of vectors $\tilde{u}_i$ are obtained by taking the appropriate linear combinations of the non-orthogonal set of vectors m_i.

To have a better appreciation of how this orthogonalization is achieved, let us consider a simple example. Suppose we are given the 2×2 matrix

$$M = \begin{pmatrix} 1 & 2 \\ 3 & 4 \end{pmatrix}, \tag{6.2.6}$$

whose column vectors

$$m_1 = \begin{pmatrix} 1 \\ 3 \end{pmatrix}, \quad m_2 = \begin{pmatrix} 2 \\ 4 \end{pmatrix} \tag{6.2.7}$$

are certainly not normalized nor orthogonal. To obtain the orthogonal set of vectors $\tilde{u}_1$ and $\tilde{u}_2$ from m_1 and m_2, we post-multiplying M by the 2×2 orthogonal matrix

$$V = \begin{pmatrix} \cos\theta & -\sin\theta \\ \sin\theta & \cos\theta \end{pmatrix}, \tag{6.2.8}$$

for some mixing angle θ that we need to determine.

Performing the matrix multiplication, we read off the vectors $\tilde{u}_1$ and $\tilde{u}_2$ as

$$\tilde{u}_1 = \cos\theta\, m_1 + \sin\theta\, m_2, \quad \tilde{u}_2 = -\sin\theta\, m_1 + \cos\theta\, m_2. \tag{6.2.9}$$

Demanding that $\tilde{u}_1$ and $\tilde{u}_2$ to be orthogonal to each other, i.e. $\tilde{u}_1^T \tilde{u}_2 = 0$, we find that

$$-\cos\theta\sin\theta\, m_1^T m_1 - \sin^2\theta\, m_2^T m_1 + \cos^2\theta\, m_1^T m_2 + \cos\theta\sin\theta\, m_2^T m_2 = 0, \tag{6.2.10}$$

which simplifies to

$$\tan 2\theta = \frac{2 m_1^T m_2}{m_1^T m_1 - m_2^T m_2}, \tag{6.2.11}$$

which we can solve for the mixing angle θ.

For the above example, we have

$$m_1^T m_1 = 10, \quad m_2^T m_2 = 20, \quad m_1^T m_2 = m_2^T m_1 = 14, \tag{6.2.12}$$

and we find two solutions,

$$\begin{gathered} V = \begin{pmatrix} \frac{1}{\sqrt{2}}\left[1 + \frac{5}{\sqrt{221}}\right]^{\frac{1}{2}} & \frac{1}{\sqrt{2}}\left[1 - \frac{5}{\sqrt{221}}\right]^{\frac{1}{2}} \\ -\frac{1}{\sqrt{2}}\left[1 - \frac{5}{\sqrt{221}}\right]^{\frac{1}{2}} & \frac{1}{\sqrt{2}}\left[1 + \frac{5}{\sqrt{221}}\right]^{\frac{1}{2}} \end{pmatrix} = \begin{pmatrix} 0.81742 & 0.57605 \\ -0.57605 & 0.81742 \end{pmatrix}, \\ \tilde{u}_1 = \begin{pmatrix} -0.33468 \\ 0.14805 \end{pmatrix}, \quad \tilde{u}_2 = \begin{pmatrix} 2.21088 \\ 4.99781 \end{pmatrix}, \end{gathered} \tag{6.2.13}$$

and

$$V = \begin{pmatrix} \frac{1}{\sqrt{2}}\left[1 - \frac{5}{\sqrt{221}}\right]^{\frac{1}{2}} & -\frac{1}{\sqrt{2}}\left[1 + \frac{5}{\sqrt{221}}\right]^{\frac{1}{2}} \\ \frac{1}{\sqrt{2}}\left[1 + \frac{5}{\sqrt{221}}\right]^{\frac{1}{2}} & \frac{1}{\sqrt{2}}\left[1 - \frac{5}{\sqrt{221}}\right]^{\frac{1}{2}} \end{pmatrix} = \begin{pmatrix} 0.57605 & -0.81742 \\ 0.81742 & 0.57605 \end{pmatrix},$$
$$\tilde{u}_1 = \begin{pmatrix} 2.21088 \\ 4.99781 \end{pmatrix}, \quad \tilde{u}_2 = \begin{pmatrix} 0.33468 \\ -0.14805 \end{pmatrix}, \tag{6.2.14}$$

which are equivalent to one another. The singular values are just the norm of $\tilde{u}_1$ and $\tilde{u}_2$, and if we choose the solution which ranks the singular values in decreasing order, are

$$\sigma_1 = ||\tilde{u}_1|| = 5.46499, \quad \sigma_2 = ||\tilde{u}_2|| = 0.36597. \tag{6.2.15}$$

For larger matrices M with $N > 2$, instead of just one orthogonality condition (6.2.11) we need to solve to obtain the matrix $\tilde{U}$ whose columns are orthogonal vectors, we would need to solve $N(N-1)/2$ orthogonality conditions for $N(N-1)/2$ mixing angles to ensure that the column vectors $\tilde{u}_i$ are mutually orthogonal. These $N(N-1)/2$ orthogonality conditions take the form of coupled transcendental equations, and so cannot in general be solved in one fell swoop, as I have demonstrated in the example above. Indeed, numerical singular value decomposition is almost always done iteratively. But now that we understand that singular value decomposition merely involves taking the appropriate linear combinations of the columns of the matrix M to form columns of the matrix $\tilde{U}$ which are mutually orthogonal, we know how to proceed to perform singular value decomposition analytically in very simple cases where this can be done.

6.3 Operator Singular Value Decomposition

The correlation density matrix defined in (5.2.1) contains all possible correlations between two disjoint clusters a and b, over and above those which can be deduced from correlations local to a and b. We imagine that these correlations arise as a result of

the sum of a collection of *independent*, simultaneous ground-state quantum fluctuation of some *order parameters* X_l on cluster a and Y_l on cluster b. Based on this intuitive picture, we expect that the correlation density matrix can be written as

$$\rho^c = \sigma_1 X_1 Y_1^\dagger + \sigma_2 X_2 Y_2^\dagger + \cdots + \sigma_m X_m Y_m^\dagger, \tag{6.3.1}$$

where $m \leq \min(N_a, N_b)$ is the number of nontrivial order parameters that contribute to the correlation between clusters a and b. Here N_a is the dimension of the operator algebra on cluster a and N_b is the dimension of the operator algebra on cluster b.

However, the matrix elements of the correlation density matrix are typically calculated in some convenient basis of operators A_i and B_j, acting on the clusters a and b respectively, so that the operator expansion we start with looks like

$$\rho^c = \rho^c_{11} A_1 B_1^\dagger + \rho^c_{12} A_1 B_2^\dagger + \cdots + \rho^c_{N_a N_b} A_{N_a} B_{N_b}^\dagger. \tag{6.3.2}$$

To get from (6.3.2) to (6.3.1), an operator singular value decomposition is required. To be able to do this, we need to know what it means mathematically for two operators X_l and $X_{l'}$ to represent independent quantum fluctuations. Drawing from our understanding of matrix singular value decomposition, we say that X_l and $X_{l'}$ are independent as operators if they are orthogonal with respect to some operator inner product. This same operator inner product will also allow us to 'normalize' the set of orthogonal operators $X_1, X_2, \ldots, X_m$ (and also $Y_1, Y_2, \ldots, Y_m$). We think of normalized operators as acting on the cluster Fock-Hilbert space with equal 'strength', so that a comparison of the singular values σ_l is then a meaningful way to determine which inter-cluster correlations are stronger in the quantum-mechanical ground state of the system. As always, we need to be careful about the fermion signs that arise from the exchange of fermion operators.

Another important point to note is that different order parameters in a quantum-mechanical ground state are frequently distinguished by their symmetries, and what

conserved quantities they are associated with. Order parameters O_l and $O_{l'}$ with different symmetries, and conserving different quantities are orthogonal in the sense that they produce quantum fluctuations $O_l |\Psi\rangle$ and $O_{l'} |\Psi\rangle$ of the ground state $|\Psi\rangle$ that necessarily have no overlap with one another. However, in operator singular value decomposition ρ^c into products $X_l Y_l$, where the set $\{X_l\}$ form an orthogonal set of operators, and the set $\{Y_l\}$ form another orthogonal set of operators, our method of operator singular value decomposition will mix order parameters of different symmetries, in the exceptional situation where these order parameters have the same absolute singular value. When this happens, it is usually easy to form appropriate linear combinations of the mixed eigen-operators, to recover the definite-symmetry order parameters.

6.3.1 Frobenius Operator Orthonormalization

But what kind of inner product should we be using for our basis of operators A_i and B_j? From our understanding of matrix singular value decomposition, we know that we will be taking linear combinations of the sets of operators $\{A_i\}$ and $\{B_j\}$ which are not mutually orthogonal to form the sets of of operators $\{X_l\}$ and $\{Y_l\}$ are mutually orthogonal, so we will be thinking of the operators $\{A_i\}$ and $\{B_j\}$ as vectors. On the other hand, if we think of the action of $\{A_i\}$ and $\{B_j\}$ on the Fock-Hilbert spaces of clusters a and b respectively, then we are thinking of $\{A_i\}$ and $\{B_j\}$ as matrices.

For an $N \times N$ matrix M acting on a given linear space V, its *Frobenius norm*

$$\|M\|_F = \left[\sum_{i,j} |M_{ij}|^2\right]^{1/2} = \left[\mathrm{Tr}\, MM^\dagger\right]^{1/2} = \left[\mathrm{Tr}\, M^\dagger M\right]^{1/2} \geq 0, \tag{6.3.3}$$

where $M^\dagger$ is the hermitian adjoint of M, is a basis-independent measure of the action of M on the linear space V. This norm allows us to think of M both as a matrix effecting a linear transformation on V, as well as a vector of length N^2, since it is 'linear' with

respect to multiplication by a scalar, i.e.

$$\|\alpha M\|_F = |\alpha| \|M\|_F. \tag{6.3.4}$$

Also, if M_1 and M_2 are matrices acting on V, so is $\alpha_1 M_1 + \alpha_2 M_2$, whose Frobenius norm is

$$\begin{aligned} \|\alpha_1 M_1 + \alpha_2 M_2\|_F^2 &= \mathrm{Tr}(\alpha_1 M_1 + \alpha_2 M_2)(\alpha_1^* M_1^\dagger + \alpha_2^* M_2^\dagger) \\ &= |\alpha_1|^2 \|M_1\|_F^2 + \alpha_1 \alpha_2^* \,\mathrm{Tr}\, M_1 M_2^\dagger + \\ &\quad \alpha_2 \alpha_1^* \,\mathrm{Tr}\, M_2 M_1^\dagger + |\alpha_2|^2 \|M_2\|_F^2. \end{aligned} \tag{6.3.5}$$

Comparing this with the norm of a linear combination $\alpha_1 u_1 + \alpha_2 u_2$ of vectors u_1 and u_2,

$$\|\alpha_1 u_1 + \alpha_2 u_2\|^2 = |\alpha_1|^2 \|u_1\|^2 + \alpha_1 \alpha_2^* \, u_1 \cdot u_2 + \alpha_2 \alpha_1^* \, u_2 \cdot u_1 + |\alpha_2|^2 \|u_2\|^2, \tag{6.3.6}$$

we realized that

$$\mathrm{Tr}\, M_1 M_2^\dagger = \sum_{i,j} M_{1,ij} M_{2,ij}^* \tag{6.3.7}$$

plays the role of an inner product of matrices. We can then use this inner product to decide whether two operators are orthogonal. In particular, a set of operators $\{A_i\}$ is said to be *Frobenius-orthonormal*, or just *orthonormal*, if

$$\mathrm{Tr}\, A_i A_j^\dagger = \delta_{ij}, \tag{6.3.8}$$

for all pairs of operators A_i and A_j.

6.3.2 Operator Expansion of Correlation Density Matrix

The cluster and supercluster density matrix elements are calculated within the occupation number bases of the clusters and the supercluster. Let us denote by $\{|\mathbf{l}\rangle\}$ the occupation number basis on cluster a, $\{|\mathbf{m}\rangle\}$ the occupation number basis on cluster b,

and $\{|\mathbf{n}\rangle\}$ the occupation number basis on the supercluster ab. From Chapter 2, we know that the matrix element $\langle \mathbf{l}|\rho^a|\mathbf{l}'\rangle$ can be computed from the ground-state wave function as the expectation of a product of referencing operators,

$$\rho^a_{ll'} = \langle \mathbf{l}|\rho^a|\mathbf{l}'\rangle = \langle \Psi|K^\dagger_{\mathbf{l}} K_{\mathbf{l}'}|\Psi\rangle\,, \tag{6.3.9}$$

where $K_{\mathbf{l}}$ and $K_{\mathbf{l}'}$ are referencing operators which acts on their designated configurations $|\mathbf{l}\rangle$ and $|\mathbf{l}'\rangle$ of cluster a respectively to yield the completely empty configuration $|0\rangle_a$ of cluster a, and annihilates all other configurations, i.e.

$$K_{\mathbf{l}}\,|\mathbf{l}''\rangle = \delta_{\mathbf{l}\mathbf{l}''}\,|0\rangle_a\,, \quad K_{\mathbf{l}'}\,|\mathbf{l}'''\rangle = \delta_{\mathbf{l}'\mathbf{l}'''}\,|0\rangle_a\,. \tag{6.3.10}$$

It follows from (6.3.10) that

$$\langle \mathbf{l}''|K^\dagger_{\mathbf{l}} K_{\mathbf{l}'}|\mathbf{l}'''\rangle = \delta_{\mathbf{l}\mathbf{l}''}\delta_{\mathbf{l}'\mathbf{l}'''}{}_a\langle 0|0\rangle_a = \delta_{\mathbf{l}\mathbf{l}''}\delta_{\mathbf{l}'\mathbf{l}'''}, \tag{6.3.11}$$

i.e. the operator product $K^\dagger_{\mathbf{l}} K_{\mathbf{l}'}$ has non-zero matrix elements only between the initial and final states $|\mathbf{l}'\rangle$ and $|\mathbf{l}\rangle$.

With (6.3.11) in mind, the natural operator expansion of ρ^a involving its matrix elements $\rho^a_{ll'}$ in the occupation number basis can then be written as

$$\rho^a = \sum_{l,l'} \rho^a_{ll'} K^\dagger_{\mathbf{l}} K_{\mathbf{l}'}\,. \tag{6.3.12}$$

Similarly, we can write the operator expansion of the cluster density matrix ρ^b as

$$\rho^b = \sum_{m,m'} \rho^b_{mm'} K^\dagger_{\mathbf{m}} K_{\mathbf{m}'}\,, \tag{6.3.13}$$

and that of the supercluster density matrix ρ^{ab} as

$$\rho^{ab} = \sum_{n,n'} \rho^{ab}_{nn'} K^\dagger_{\mathbf{n}} K_{\mathbf{n}'}\,. \tag{6.3.14}$$

Using (6.3.12) and (6.3.13), we can write down the operator expansion of the direct product density matrix $\rho^a \otimes \rho^b$ simply as

$$\rho^a \otimes \rho^b = \sum_{l,l'} \sum_{m,m'} \rho^a_{ll'} \rho^b_{mm'} K^\dagger_{\mathbf{l}} K_{\mathbf{l}'} K^\dagger_{\mathbf{m}} K_{\mathbf{m}'}. \tag{6.3.15}$$

We must now subtract $\rho^a \otimes \rho^b$ from ρ^{ab} to obtain the correlation density matrix ρ^c. To do this, we make use of the fact that for disconnected clusters a and b, if we number all the sites in a before numbering the sites in b, then in the referencing operator $K_{\mathbf{n}}$ for any occupation number basis state $|\mathbf{n}\rangle$ on the supercluster ab, all operators acting on cluster a appear before operators acting on cluster b. Furthermore, if we write the occupation number basis state $|\mathbf{n}\rangle = |\mathbf{l}\rangle |\mathbf{m}\rangle$, where $|\mathbf{l}\rangle$ is the configuration on cluster a, and $|\mathbf{m}\rangle$ is the configuration on cluster b, then $K_{\mathbf{n}} = K_{\mathbf{l}} K_{\mathbf{m}}$, where $K_{\mathbf{l}}$ is the referencing operator associated with configuration $|\mathbf{l}\rangle$ on cluster a, and $K_{\mathbf{m}}$ is the referencing operator associated with configuration $|\mathbf{m}\rangle$ on cluster b.

With this in mind, we can write the operator expansion of ρ^{ab} as

$$\rho^{ab} = \sum_{n,n'} \rho^{ab}_{nn'} K^\dagger_{\mathbf{n}} K_{\mathbf{n}'} = \sum_{n,n'} \rho^{ab}_{nn'} K^\dagger_{\mathbf{m}} K^\dagger_{\mathbf{l}} K_{\mathbf{l}'} K_{\mathbf{m}'}. \tag{6.3.16}$$

Moving $K^\dagger_{\mathbf{m}}$ past $K^\dagger_{\mathbf{l}} K_{\mathbf{l}'}$, so that all the referencing operators on cluster a are to the left of referencing operators on cluster b, we have

$$\rho^{ab} = \sum_{n,n'} (-1)^{f_{nn'}} \rho^{ab}_{nn'} K^\dagger_{\mathbf{l}} K_{\mathbf{l}'} K^\dagger_{\mathbf{m}} K_{\mathbf{m}'}, \tag{6.3.17}$$

where $(-1)^{f_{nn'}}$ is the fermion sign incurred when moving $K^\dagger_{\mathbf{m}}$ past $K^\dagger_{\mathbf{l}} K_{\mathbf{l}'}$. The operator expansion of ρ^c is thus

$$\rho^c = \sum_{n,n'} \left[(-1)^{f_{nn'}} \rho^{ab}_{nn'} - \rho^a_{ll'} \rho^b_{mm'} \right] K^\dagger_{\mathbf{l}} K_{\mathbf{l}'} K^\dagger_{\mathbf{m}} K_{\mathbf{m}'}. \tag{6.3.18}$$

The neatest property of this operator expansion for ρ^c is that the product of referencing operators

$$X_{\mathbf{l}\mathbf{l}'} = K^\dagger_{\mathbf{l}} K_{\mathbf{l}'}, \quad Y_{\mathbf{m}\mathbf{m}'} = K^\dagger_{\mathbf{m}} K_{\mathbf{m}'}, \tag{6.3.19}$$

already constitute Frobenius-orthonormal initial bases of operators, i.e.

$$\mathrm{Tr}\, X_{\mathbf{ll'}} X^{\dagger}_{\mathbf{l''l'''}} = \delta_{\mathbf{ll'},\mathbf{l''l'''}}, \quad \mathrm{Tr}\, Y_{\mathbf{mm'}} Y^{\dagger}_{\mathbf{m''m'''}} = \delta_{\mathbf{mm'},\mathbf{m''m'''}}. \tag{6.3.20}$$

Since we want to treat $X_{\mathbf{ll'}}$ and $Y_{\mathbf{mm'}}$ as the basis vectors in a linear space of operators, we work with the fused indices $\lambda = ll'$, which runs from $\lambda = 1$ to $\lambda = (D^a)^2$, where D^a is the dimension of the Fock-Hilbert space of cluster a, and $\mu = mm'$, which runs from $\mu = 1$ to $\mu = (D^b)^2$, where D^b is the dimension of the Fock-Hilbert space of cluster b. We then write (6.3.18) as

$$\rho^c = \mathbf{X}^T \mathbf{K} \mathbf{Y}, \tag{6.3.21}$$

where

$$\mathbf{X} = \begin{bmatrix} X_1 \\ X_2 \\ \vdots \\ X_{(D^a)^2} \end{bmatrix}, \quad \mathbf{Y} = \begin{bmatrix} Y_1 \\ Y_2 \\ \vdots \\ Y_{(D^b)^2} \end{bmatrix}, \tag{6.3.22}$$

and $\mathbf{K}$ is the $(D^a)^2 \times (D^b)^2$ *correlation-*$\mathbf{K}$ *matrix*, whose matrix elements are

$$K_{\lambda\mu} = \left[(-1)^{f_{nn'}} \rho^{ab}_{nn'} - \rho^a_{ll'} \rho^b_{mm'} \right]. \tag{6.3.23}$$

The correlation-$\mathbf{K}$ matrix is just an ordinary matrix of complex numbers, so we can perform a numerical matrix singular value decomposition on it to obtain

$$\mathbf{K} = U \Sigma V^{\dagger}, \tag{6.3.24}$$

where U and V are unitary matrices, and $\Sigma = \mathrm{diag}(\sigma_1, \sigma_2, \ldots, \sigma_{\min[(D^a)^2,(D^b)^2]})$ is a diagonal matrix of singular values.

Treating U and V as unitary transformations on the linear space of operators X_λ and

Y_μ respectively, we then find

$$\rho^c = \begin{bmatrix} X_1 & X_2 & \cdots & X_{(D^a)^2} \end{bmatrix} U \Sigma V^T \begin{bmatrix} Y_1 \\ Y_2 \\ \vdots \\ Y_{(D^b)^2} \end{bmatrix} = \begin{bmatrix} X'_1 & X'_2 & \cdots & X'_{(D^a)^2} \end{bmatrix} \Sigma \begin{bmatrix} Y'_1 \\ Y'_2 \\ \vdots \\ Y'_{(D^b)^2} \end{bmatrix}. \quad (6.3.25)$$

We can check that the transformed operators $X'_{\lambda'}$ and $Y'_{\mu'}$, which are linear combinations of X_λ and Y_μ respectively, are again Frobenius-orthonormal. Therefore, the sum

$$\rho^c = \sigma_1 X'_1 Y'_1 + \sigma_2 X'_2 Y'_2 + \cdots + \sigma_{\min[(D^a)^2,(D^b)^2]} X'_{\min[(D^a)^2,(D^b)^2]} Y'_{\min[(D^a)^2,(D^b)^2]}, \quad (6.3.26)$$

which can be written in the form (6.3.1), and which has been obtained from the numerical matrix singular value decomposition of the correlation-**K** matrix, is the proper operator singular value decomposition of the correlation density matrix.

6.4 One-Dimensional Noninteracting Spinless Fermions

In the remainder of this chapter, let us apply the operator singular value decomposition machinery developed above on a one-dimensional system of noninteracting spinless fermions in this section, and a one-dimensional system with a BCS ground state in the next section, before going on to investigate what the singular value decomposition of ρ^c yields in strongly interacting quasi-one-dimensional systems.

6.4.1 The (1 + 1) Supercluster

For the (1 + 1) supercluster, the clusters are $a = \{j = 0\}$ and $b = \{j = r\}$. In terms of the supercluster occupation number basis states $|n_0 n_r\rangle$, where n_0 is the occupation number of the site $j = 0$ in cluster a, and n_r is the occupation number of the site $j = r$ in cluster

b, the nonzero correlation density matrix elements are, according to (5.3.17),

$$\begin{aligned}
\langle 00|\rho^c|00\rangle &= \langle 11|\rho^c|11\rangle = -\bar{n}^2 g^2, \\
\langle 10|\rho^c|10\rangle &= \langle 01|\rho^c|01\rangle = \bar{n}^2 g^2, \\
\langle 10|\rho^c|01\rangle &= \langle 01|\rho^c|10\rangle = \bar{n} g,
\end{aligned} \tag{6.4.1}$$

where $g \equiv g(r)$ is the reduced Green function defined in (2.3.15). The product of referencing operators associated with these matrix elements are, after simplification,

$$\begin{aligned}
(00, 00) &\mapsto c_0 c_0^\dagger c_r c_r^\dagger, \\
(10, 10) &\mapsto c_0^\dagger c_0 c_r c_r^\dagger, \\
(10, 01) &\mapsto c_0^\dagger c_r, \\
(01, 10) &\mapsto c_r^\dagger c_0, \\
(01, 01) &\mapsto c_0 c_0^\dagger c_r^\dagger c_r, \\
(11, 11) &\mapsto c_0^\dagger c_0 c_r^\dagger c_r,
\end{aligned} \tag{6.4.2}$$

and so the operator expansion of ρ^c is

$$\begin{aligned}
\rho^c &= -\bar{n}^2 g^2 c_0 c_0^\dagger c_r c_r^\dagger + \bar{n}^2 g^2 c_0^\dagger c_0 c_r c_r^\dagger + \bar{n} g c_0^\dagger c_r + \\
&\quad \bar{n} g c_r^\dagger c_0 + \bar{n}^2 g^2 c_0 c_0^\dagger c_r^\dagger c_r - \bar{n}^2 g^2 c_0^\dagger c_0 c_r^\dagger c_r \\
&= \bar{n} g (c_0^\dagger c_r + c_r^\dagger c_0) + \bar{n}^2 g^2 (-c_0 c_0^\dagger c_r c_r^\dagger + c_0^\dagger c_0 c_r c_r^\dagger + c_0 c_0^\dagger c_r^\dagger c_r - c_0^\dagger c_0 c_r^\dagger c_r) \\
&= \bar{n} g (c_0^\dagger c_r + c_r^\dagger c_0) + \bar{n}^2 g^2 (-\mathbb{1} + 2 c_0^\dagger c_0 + 2 c_r^\dagger c_r - 4 c_0^\dagger c_0 c_r^\dagger c_r) \\
&= \bar{n} g (c_0^\dagger c_r + c_r^\dagger c_0) - \bar{n}^2 g^2 (\mathbb{1} - 2 c_0^\dagger c_0)(\mathbb{1} - 2 c_r^\dagger c_r) \\
&= \bar{n} g (c_0^\dagger c_r + c_r^\dagger c_0) - \bar{n}^2 g^2 (c_0 c_0^\dagger - c_0^\dagger c_0)(c_r c_r^\dagger - c_r^\dagger c_r).
\end{aligned} \tag{6.4.3}$$

Without constructing the correlation-$\mathbf{K}$ matrix and performing numerical matrix singular value decomposition, we find that the operator singular value decomposition

$$\rho^c = \sigma_1 X_1 Y_1^\dagger + \sigma_2 X_2 Y_2^\dagger + \sigma_3 X_3 Y_3^\dagger, \tag{6.4.4}$$

has already been achieved, simply by writing down and simplifying (6.4.3). The singular values, left and right eigen-operators can be read off as

$$\begin{aligned}
&\sigma_1 = +\bar{n}g, && X_1 = c_0^\dagger, && Y_1 = c_r^\dagger, \\
&\sigma_2 = -\bar{n}g, && X_2 = c_0, && Y_2 = c_r, \\
&\sigma_3 = -2\bar{n}^2 g^2, && X_3 = \tfrac{1}{\sqrt{2}}(c_0 c_0^\dagger - c_0^\dagger c_0), && Y_3 = \tfrac{1}{\sqrt{2}}(c_r c_r^\dagger - c_r^\dagger c_r).
\end{aligned} \tag{6.4.5}$$

We can check that the set of left eigen-operators $\{X_1, X_2, X_3\}$ are indeed Frobenius-orthonormal, i.e. they are normalized with respect to the Frobenius norm,

$$\begin{aligned}
\operatorname{Tr} X_1 X_1^\dagger &= \operatorname{Tr} c_0^\dagger c_0 = \operatorname{Tr} n_0 = \langle 0|n_0|0\rangle + \langle 1|n_0|1\rangle = 0 + 1 = 1, \\
\operatorname{Tr} X_2 X_2^\dagger &= \operatorname{Tr} c_0 c_0^\dagger = \operatorname{Tr}(\mathbb{1} - n_0) = \langle 0|\mathbb{1} - n_0|0\rangle + \langle 1|\mathbb{1} - n_0|1\rangle = 1 + 0 = 1, \\
\operatorname{Tr} X_3 X_3^\dagger &= \tfrac{1}{2}\operatorname{Tr}(c_0 c_0^\dagger - c_0^\dagger c_0)(c_0 c_0^\dagger - c_0^\dagger c_0) \\
&= \tfrac{1}{2}\operatorname{Tr}(c_0 c_0^\dagger c_0 c_0^\dagger - c_0 c_0^\dagger c_0^\dagger c_0 - c_0^\dagger c_0 c_0 c_0^\dagger + c_0^\dagger c_0 c_0^\dagger c_0) \\
&= \tfrac{1}{2}\operatorname{Tr}(c_0 c_0^\dagger + c_0^\dagger c_0) = \tfrac{1}{2}\operatorname{Tr}\mathbb{1} = 1,
\end{aligned} \tag{6.4.6}$$

and also mutually orthogonal with respect to the Frobenius inner product,

$$\begin{aligned}
\operatorname{Tr} X_1 X_2^\dagger &= \operatorname{Tr} c_0^\dagger c_0^\dagger = 0, \\
\operatorname{Tr} X_1 X_3^\dagger &= \tfrac{1}{\sqrt{2}}\operatorname{Tr} c_0^\dagger (c_0 c_0^\dagger - c_0^\dagger c_0) = \tfrac{1}{\sqrt{2}}\operatorname{Tr} c_0^\dagger = 0, \\
\operatorname{Tr} X_2 X_3^\dagger &= \tfrac{1}{\sqrt{2}}\operatorname{Tr} c_0 (c_0 c_0^\dagger - c_0^\dagger c_0) = \tfrac{1}{\sqrt{2}}\operatorname{Tr} c_0 = 0.
\end{aligned} \tag{6.4.7}$$

Similar calculations will show that the set of right eigen-operators $\{Y_1, Y_2, Y_3\}$ are also Frobenius-orthonormal. Hence we have obtained the operator singular value decomposition of ρ^c for the $(1+1)$ supercluster after very little additional work, after ρ^c has been calculated in Section 5.3.1!

But does this operator singular value decomposition tell us what we already know about the Fermi sea ground state of a one-dimensional system of noninteracting spinless fermions? For a Fermi sea ground state, we know that the dominant correlations

are of the form $\langle c_j^\dagger c_{j+r}\rangle$, and that these decay with a power law r^{-1} in the separation r. Density-density correlations $\langle c_j^\dagger c_j c_{j+r}^\dagger c_{j+r}\rangle$, which do not constitute independent quantum fluctuations for a Fermi sea, are also known to decay faster with separation r as power law r^{-2}. From the operator singular value decomposition, we see that indeed, the singular values $\sigma_1 = -\sigma_2 = \bar{n}g$ associated with $X_1 Y_1^\dagger = c_0^\dagger c_r$ and $X_2 Y_2^\dagger = c_0 c_r^\dagger$ decays as $g \sim r^{-1}$ with separation r, while the singular value $\sigma_3 = -2\bar{n}^2 g^2$ associated with $X_3 Y_3^\dagger = \frac{1}{2}(c_0 c_0^\dagger - c_0^\dagger c_0)(c_r c_r^\dagger - c_r^\dagger c_r)$ decays as $g^2 \sim r^{-2}$ with separation r. This gives us confidence that our operator singular value decomposition is doing the right thing in breaking up the correlation density matrix into the various order parameters.

6.4.2 The (2 + 2) Supercluster

For the (2 + 2) supercluster, the correlation density matrix ρ^c has a more complicated structure as compared to the (1 + 1) supercluster, and there is no hope to analytically singular value decompose ρ^c in the most general case. Therefore, even though we have the exact expressions for all matrix elements, we will only consider those which are $O(r^{-1})$, as listed in (5.3.64). Writing out the operator expansion of ρ^c in terms of the product of referencing operators explicitly at this level of approximation, we find that

$$\begin{aligned}
\rho^c \approx & - \langle 1000|\rho^c|0010\rangle\, c_0 c_1 c_1^\dagger c_r^\dagger c_{r+1} c_{r+1}^\dagger - \langle 1000|\rho^c|0001\rangle\, c_0 c_1 c_1^\dagger c_r c_r^\dagger c_{r+1}^\dagger \\
& - \langle 0100|\rho^c|0010\rangle\, c_0 c_0^\dagger c_1 c_r^\dagger c_{r+1} c_{r+1}^\dagger - \langle 0100|\rho^c|0001\rangle\, c_0 c_0^\dagger c_1 c_r c_r^\dagger c_{r+1}^\dagger \\
& - \langle 1100|\rho^c|1010\rangle\, c_0^\dagger c_0 c_1 c_r^\dagger c_{r+1} c_{r+1}^\dagger - \langle 1100|\rho^c|1001\rangle\, c_0^\dagger c_0 c_1 c_r c_r^\dagger c_{r+1}^\dagger \\
& + \langle 1100|\rho^c|0110\rangle\, c_0 c_1^\dagger c_1 c_r^\dagger c_{r+1} c_{r+1}^\dagger + \langle 1100|\rho^c|0101\rangle\, c_0 c_1^\dagger c_1 c_r c_r^\dagger c_{r+1}^\dagger \\
& + \langle 1010|\rho^c|0011\rangle\, c_0 c_1 c_1^\dagger c_r^\dagger c_r c_{r+1}^\dagger - \langle 1001|\rho^c|0011\rangle\, c_0 c_1 c_1^\dagger c_r^\dagger c_{r+1}^\dagger c_{r+1} \\
& + \langle 0110|\rho^c|0011\rangle\, c_0 c_0^\dagger c_1 c_r^\dagger c_r c_{r+1}^\dagger - \langle 0101|\rho^c|0011\rangle\, c_0 c_0^\dagger c_1 c_r^\dagger c_{r+1}^\dagger c_{r+1} \\
& + \langle 1110|\rho^c|1011\rangle\, c_0^\dagger c_0 c_1 c_r^\dagger c_r c_{r+1}^\dagger - \langle 1110|\rho^c|0111\rangle\, c_0 c_1^\dagger c_1 c_r^\dagger c_r c_{r+1}^\dagger
\end{aligned} \tag{6.4.8}$$

$$
\begin{aligned}
&- \langle 1101|\rho^c|1011\rangle\, c_0^\dagger c_0 c_1 c_r^\dagger c_{r+1}^\dagger c_{r+1} + \langle 1101|\rho^c|0111\rangle\, c_0 c_1^\dagger c_1 c_r^\dagger c_{r+1}^\dagger c_{r+1} \\
&+ \text{h.c.}
\end{aligned}
$$

Expanding these operator products, regrouping and reordering the operators so that within the product of operators acting on cluster a or cluster b, all creation operators are to the left of annihilation operators, and that both creation and annihilation operators are further ordered according to the sites, we obtain

$$
\begin{aligned}
\rho^c \approx & - \langle 1000|\rho^c|0010\rangle\, c_0 c_r^\dagger - \langle 1000|\rho^c|0001\rangle\, c_0 c_{r+1}^\dagger - \langle 0100|\rho^c|0010\rangle\, c_1 c_r^\dagger \\
& - \langle 0100|\rho^c|0001\rangle\, c_1 c_{r+1}^\dagger + (\langle 0100|\rho^c|0010\rangle - \langle 1100|\rho^c|1010\rangle)\, c_0^\dagger c_0 c_1 c_r^\dagger \\
& + (\langle 0100|\rho^c|0001\rangle - \langle 1100|\rho^c|1001\rangle)\, c_0^\dagger c_0 c_1 c_{r+1}^\dagger \\
& - (\langle 1000|\rho^c|0010\rangle + \langle 1100|\rho^c|0110\rangle)\, c_1^\dagger c_0 c_1 c_r^\dagger \\
& - (\langle 1000|\rho^c|0001\rangle + \langle 1100|\rho^c|0101\rangle)\, c_1^\dagger c_0 c_1 c_{r+1}^\dagger \\
& - (\langle 1000|\rho^c|0001\rangle + \langle 1010|\rho^c|0011\rangle)\, c_0 c_r^\dagger c_{r+1}^\dagger c_r \\
& + (\langle 1000|\rho^c|0010\rangle - \langle 1001|\rho^c|0011\rangle)\, c_0 c_r^\dagger c_{r+1}^\dagger c_{r+1} \\
& - (\langle 0100|\rho^c|0001\rangle + \langle 0110|\rho^c|0011\rangle)\, c_1 c_r^\dagger c_{r+1}^\dagger c_r \\
& + (\langle 0100|\rho^c|0010\rangle - \langle 0101|\rho^c|0011\rangle)\, c_1 c_r^\dagger c_{r+1}^\dagger c_{r+1} \\
& + (\langle 0100|\rho^c|0001\rangle - \langle 1100|\rho^c|1001\rangle \\
& + \langle 0110|\rho^c|0011\rangle - \langle 1110|\rho^c|1011\rangle) c_0^\dagger c_0 c_1 c_r^\dagger c_{r+1}^\dagger c_r \\
& + (- \langle 0100|\rho^c|0010\rangle + \langle 1100|\rho^c|1010\rangle \\
& + \langle 0101|\rho^c|0011\rangle - \langle 1101|\rho^c|1011\rangle) c_0^\dagger c_0 c_1 c_r^\dagger c_{r+1}^\dagger c_{r+1} \\
& - (\langle 1000|\rho^c|0001\rangle + \langle 1100|\rho^c|0101\rangle \\
& + \langle 1010|\rho^c|0011\rangle + \langle 1110|\rho^c|0111\rangle) c_1^\dagger c_0 c_1 c_r^\dagger c_{r+1}^\dagger c_r \\
& + (\langle 1000|\rho^c|0010\rangle + \langle 1100|\rho^c|0110\rangle \\
& - \langle 1001|\rho^c|0011\rangle - \langle 1101|\rho^c|0111\rangle) c_1^\dagger c_0 c_1 c_r^\dagger c_{r+1}^\dagger c_{r+1} + \text{h.c.}
\end{aligned}
\tag{6.4.9}
$$

Even with the simplified expansion (6.4.9) of ρ^c, where all matrix elements are of $O(r^{-1})$ — matrix elements of ρ^c of order higher than $O(r^{-2})$ have been discarded — it is not possible to singular value decompose ρ^c by hand for arbitrary filling $\bar{n}$ and separation r between the two clusters. The cases of (i) the limit of $\bar{n} \to 0$ (Section 6.4.3) and (ii) the half-filling regime $\bar{n} = \frac{1}{2}$ (Sections 6.4.4 and 6.4.5) are the only two special regimes where I have succeeded, with a significant amount of trial and error, in doing the singular value decomposition of ρ^c can be done by hand.

6.4.3 Approximate Decomposition in the $\bar{n} \to 0$ Limit

In this limit of a very dilute system of free spinless fermions, the most significant matrix elements in ρ^c are those which are $O(r^{-1})$ as well as $O(\bar{n})$. These matrix elements, which occur only in the one-particle sector of ρ^c, and their corresponding operator expansion terms, are

$$\begin{aligned}
\langle 1000|\rho^c|0010\rangle &= \bar{n}\mathsf{b}, \qquad K^\dagger_{10,a} K_{00,a} K^\dagger_{00,b} K_{10,b} = +c_0^\dagger c_1 c_1^\dagger c_r c_{r+1} c_{r+1}^\dagger; \\
\langle 1000|\rho^c|0001\rangle &= \bar{n}\mathsf{c}, \qquad K^\dagger_{10,a} K_{00,a} K^\dagger_{00,b} K_{01,b} = +c_0^\dagger c_1 c_1^\dagger c_r c_r^\dagger c_{r+1}; \\
\langle 0100|\rho^c|0010\rangle &= \bar{n}\mathsf{d}, \qquad K^\dagger_{01,a} K_{00,a} K^\dagger_{00,b} K_{10,b} = +c_0 c_0^\dagger c_1^\dagger c_r c_{r+1} c_{r+1}^\dagger; \\
\langle 0100|\rho^c|0001\rangle &= \bar{n}\mathsf{b}, \qquad K^\dagger_{01,a} K_{00,a} K^\dagger_{00,b} K_{01,b} = +c_0 c_0^\dagger c_1^\dagger c_r c_r^\dagger c_{r+1}; \\
\langle 0010|\rho^c|1000\rangle &= \bar{n}\mathsf{b}, \qquad K^\dagger_{00,a} K_{10,a} K^\dagger_{10,b} K_{00,b} = -c_0 c_1 c_1^\dagger c_r^\dagger c_{r+1} c_{r+1}^\dagger; \\
\langle 0010|\rho^c|0100\rangle &= \bar{n}\mathsf{d}, \qquad K^\dagger_{00,a} K_{01,a} K^\dagger_{10,b} K_{00,b} = -c_0 c_0^\dagger c_1 c_r^\dagger c_{r+1} c_{r+1}^\dagger; \\
\langle 0001|\rho^c|1000\rangle &= \bar{n}\mathsf{c}, \qquad K^\dagger_{00,a} K_{10,a} K^\dagger_{01,b} K_{00,b} = -c_0 c_1 c_1^\dagger c_r c_r^\dagger c_{r+1}^\dagger; \\
\langle 0001|\rho^c|0100\rangle &= \bar{n}\mathsf{b}, \qquad K^\dagger_{00,a} K_{01,a} K^\dagger_{01,b} K_{00,b} = -c_0 c_0^\dagger c_1 c_r c_r^\dagger c_{r+1}^\dagger,
\end{aligned} \tag{6.4.10}$$

where $K_{n_0 n_1, a}$ is the referencing operator associated with the occupation number basis state $|n_0 n_1\rangle$ of cluster a, $K_{n_r n_{r+1}, b}$ is the referencing operator associated with the occupation number basis state $|n_r n_{r+1}\rangle$ of cluster b, and a, b, c and d are the reduced two-point

functions defined in (5.3.22).

In the limit of $\bar{n} \to 0$, the Friedel oscillations have very long wavelengths, so that $\mathsf{c} = \sin\pi\bar{n}(r+1)/\pi\bar{n}(r+1)$ and $\mathsf{d} = \sin\pi\bar{n}(r-1)/\pi\bar{n}(r-1)$ differ only slightly from $\mathsf{b} = \sin\pi\bar{n}r/\pi\bar{n}r$. Therefore, we can make the approximation $\mathsf{b} \approx \mathsf{c} \approx \mathsf{d}$, in which case we write the correlation density matrix as

$$\begin{aligned}\rho^c \approx \bar{n}\mathsf{b}\Big[&c_0^\dagger c_1 c_1^\dagger c_r c_{r+1} c_{r+1}^\dagger - c_0 c_1 c_1^\dagger c_r^\dagger c_{r+1} c_{r+1}^\dagger + c_0^\dagger c_1 c_1^\dagger c_r c_r^\dagger c_{r+1} \\ &- c_0 c_1 c_1^\dagger c_r c_r c_r^\dagger c_{r+1}^\dagger + c_0 c_0^\dagger c_1^\dagger c_r c_{r+1} c_{r+1}^\dagger - c_0 c_0^\dagger c_1 c_r^\dagger c_{r+1} c_{r+1}^\dagger \\ &+ c_0 c_0^\dagger c_1^\dagger c_r c_r^\dagger c_{r+1} - c_0 c_0^\dagger c_1 c_r c_r^\dagger c_{r+1}^\dagger\Big].\end{aligned} \tag{6.4.11}$$

We can start singular value decomposing ρ^c by first noting that (6.4.11) can be written as

$$\begin{aligned}\rho^c &= \bar{n}\mathsf{b}(c_0^\dagger c_1 c_1^\dagger + c_0 c_0^\dagger c_1^\dagger) c_r c_{r+1} c_{r+1}^\dagger + \bar{n}\mathsf{b}(c_0^\dagger c_1 c_1^\dagger + c_0 c_0^\dagger c_1^\dagger) c_r c_r^\dagger c_{r+1} + \text{h.c.} \\ &= \bar{n}\mathsf{b}(c_0^\dagger c_1 c_1^\dagger + c_0 c_0^\dagger c_1^\dagger)(c_r c_{r+1} c_{r+1}^\dagger + c_r c_r^\dagger c_{r+1}) + \text{h.c.}.\end{aligned} \tag{6.4.12}$$

Based on the form of the operator terms in (6.4.12), let us define the operators

$$\begin{aligned}X_1 &= \frac{1}{\sqrt{2}}(c_0^\dagger c_1 c_1^\dagger + c_0 c_0^\dagger c_1^\dagger), \\ Y_1 &= \frac{1}{\sqrt{2}}(c_r^\dagger c_{r+1} c_{r+1}^\dagger + c_r c_r^\dagger c_{r+1}^\dagger); \\ X_2 &= \frac{1}{\sqrt{2}}(c_0 c_1 c_1^\dagger + c_0 c_0^\dagger c_1) = X_1^\dagger, \\ Y_2 &= \frac{1}{\sqrt{2}}(c_r c_{r+1} c_{r+1}^\dagger + c_r c_r^\dagger c_{r+1}) = Y_1^\dagger.\end{aligned} \tag{6.4.13}$$

In order for

$$\rho^c = 2\bar{n}\mathsf{b}\, X_1 Y_1^\dagger + \text{h.c.} \tag{6.4.14}$$

to be the proper operator singular value decomposition of ρ^c, we need the sets of operators $\{X_1, X_2 = X_1^\dagger\}$ and $\{Y_1, Y_2 = Y_1^\dagger\}$ to be separately Frobenius-orthonormal. Checking this, we find that

$$\operatorname{Tr} X_1 X_1^\dagger = \frac{1}{2}\operatorname{Tr}(c_0^\dagger c_1 c_1^\dagger + c_0 c_0^\dagger c_1^\dagger)(c_0 c_1 c_1^\dagger + c_0 c_0^\dagger c_1)$$

$$= \frac{1}{2}\operatorname{Tr}(c_0^\dagger c_0 c_1 c_1^\dagger + c_0^\dagger c_1 + c_1^\dagger c_0 + c_0 c_0^\dagger c_1^\dagger c_1)$$
$$= \frac{1}{2}(1 + 0 + 0 + 1) = 1, \tag{6.4.15a}$$
$$\operatorname{Tr} X_2 X_2^\dagger = \frac{1}{2}\operatorname{Tr}(c_0 c_1 c_1^\dagger + c_0 c_0^\dagger c_1)(c_0^\dagger c_1 c_1^\dagger + c_0 c_0^\dagger c_1^\dagger)$$
$$= \frac{1}{2}\operatorname{Tr}(c_0 c_0^\dagger c_1 c_1^\dagger + c_0 c_0^\dagger c_1 c_1^\dagger)$$
$$= \frac{1}{2}(1 + 1) = 1, \tag{6.4.15b}$$
$$\operatorname{Tr} X_1 X_2^\dagger = \frac{1}{2}\operatorname{Tr}(c_0^\dagger c_1 c_1^\dagger + c_0 c_0^\dagger c_1^\dagger)(c_0^\dagger c_1 c_1^\dagger + c_0 c_0^\dagger c_1^\dagger) = 0, \tag{6.4.15c}$$

i.e. X_1 and X_2 are indeed Frobenius-orthonormal operators. Similarly, we can check that Y_1 and Y_2 are Frobenius-orthonormal operators. Thus, by regrouping operators as we have done in (6.4.12), we have trivially singular value decomposed ρ^c in the dilute limit.

Now, are the operators X_1, X_2, Y_1 and Y_2 that emerged from the operator singular value decomposition of ρ^c the order parameters we expect from a Fermi sea ground state? Naively, from our discussions at the beginning of Section 6.3, we had expected the operators X_1 and X_2 emerging from the operator singular value decomposition to be *the* Fermi-liquid order parameters, which are linear combinations of the bare operators $c_0^\dagger$ and $c_1^\dagger$. We find, instead, operators like

$$X_1 = \frac{1}{\sqrt{2}}[c_0^\dagger(\mathbb{1} - n_1) + c_1^\dagger(\mathbb{1} - n_0)]. \tag{6.4.16}$$

Thinking about the forms of X_1 and X_2 more carefully, we understand why these operators must take the form that they do.

If $O_l(r)$ is a proper order parameter of the quantum-mechanical ground state, then its subtracted correlation $\langle O_l^\dagger(0) O_l(r)\rangle - \langle O_l^\dagger(0)\rangle \langle O_l(r)\rangle$ can also be computed from the correlation density matrix as

$$\langle O_l^\dagger(0) O_l(r)\rangle - \langle O_l^\dagger(0)\rangle \langle O_l(r)\rangle = \operatorname{Tr} \rho^c O_l^\dagger(0) O_l(r), \tag{6.4.17}$$

provided the clusters chosen have operator algebras which are large enough to represent O_l. If we are confident that the operator singular value decomposition

$$\rho^c = \sum_l \sigma_l X_l Y_l^\dagger \tag{6.4.18}$$

breaks the correlation density matrix up into terms corresponding to different order parameters O_l, then the eigen-operators X_l and Y_l must be such that

$$\mathrm{Tr}\, X_{l'} Y_{l'}^\dagger O_l^\dagger(0) O_l(r) = \delta_{ll'}, \tag{6.4.19}$$

i.e. each operator product term in the singular value decomposition of ρ^c picks out *one and only one* of the proper ground-state order parameters. A corollary of this is that

$$\langle O_l^\dagger(0) O_l(r)\rangle = \sigma_l. \tag{6.4.20}$$

For $X_1 = \frac{1}{\sqrt{2}}[c_0^\dagger(\mathbb{1} - n_1) + c_1^\dagger(\mathbb{1} - n_0)]$, the order parameter which it picks out is $O_1 = \frac{1}{\sqrt{2}}(c_0 + c_1)$, which is indeed a Fermi-liquid order parameter.

6.4.4 Approximate Decomposition at Half-Filling: Even Cluster Separation

In the half-filling regime $\bar{n} = \frac{1}{2}$, we look first at the case of even cluster separation. In this case, $\mathsf{b} = 0$, and for large cluster separations $r \to \infty$,

$$\begin{aligned} \mathsf{c} &\approx \frac{\sin\pi\bar{n}(r+1)}{\pi\bar{n}r} = \frac{\sin\pi\bar{n}r\cos\pi\bar{n}}{\pi\bar{n}r} + \frac{\cos\pi\bar{n}r\sin\pi\bar{n}}{\pi\bar{n}r} = \frac{2}{\pi r}(-1)^{r/2}, \\ \mathsf{d} &\approx \frac{\sin\pi\bar{n}(r-1)}{\pi\bar{n}r} = \frac{\sin\pi\bar{n}r\cos\pi\bar{n}}{\pi\bar{n}r} - \frac{\cos\pi\bar{n}r\sin\pi\bar{n}}{\pi\bar{n}r} = -\frac{2}{\pi r}(-1)^{r/2} = -\mathsf{c}. \end{aligned} \tag{6.4.21}$$

Unlike in the dilute limit, the $O(r^{-1})$ matrix elements in the two- and three-particle sectors of ρ_c are not small compared to the $O(r^{-1})$ matrix elements in the one-particle sector of ρ^c. There being no $O(r^{-1})$ matrix elements in the zero- and four-particle sector of ρ^c, we must therefore consider all the $O(r^{-1})$ matrix elements in the one-, two-, and three-particle sectors of ρ^c.

6.4.4.1 $O(r^{-1})$ Correlation Density-Matrix Elements

In the one-particle sector, we find that to $O(r^{-1})$, the matrix elements of ρ^c (and the corresponding product of referencing operators, written out only for nonzero matrix elements) are

$$\langle 1000|\rho^c|0010\rangle = 0; \tag{6.4.22a}$$

$$\langle 1000|\rho^c|0001\rangle = +\frac{1}{8}(1-\mathsf{a}^2)\mathsf{c}, \qquad K^\dagger_{10,a}K_{00,a}K^\dagger_{00,b}K_{01,b} = +c^\dagger_0 c_1 c^\dagger_1 c_r c^\dagger_r c_{r+1}; \tag{6.4.22b}$$

$$\langle 0100|\rho^c|0010\rangle = -\frac{1}{8}(1-\mathsf{a}^2)\mathsf{c}, \qquad K^\dagger_{01,a}K_{00,a}K^\dagger_{00,b}K_{10,b} = +c_0 c^\dagger_0 c^\dagger_1 c_r c_{r+1} c^\dagger_{r+1}; \tag{6.4.22c}$$

$$\langle 0100|\rho^c|0001\rangle = 0; \tag{6.4.22d}$$

$$\langle 0010|\rho^c|1000\rangle = 0; \tag{6.4.22e}$$

$$\langle 0010|\rho^c|0100\rangle = -\frac{1}{8}(1-\mathsf{a}^2)\mathsf{c}, \qquad K^\dagger_{00,a}K_{01,a}K^\dagger_{10,b}K_{00,b} = -c_0 c^\dagger_0 c_1 c^\dagger_r c_{r+1} c^\dagger_{r+1}; \tag{6.4.22f}$$

$$\langle 0001|\rho^c|1000\rangle = +\frac{1}{8}(1-\mathsf{a}^2)\mathsf{c}, \qquad K^\dagger_{00,a}K_{10,a}K^\dagger_{01,b}K_{00,b} = -c_0 c_1 c^\dagger_1 c_r c^\dagger_r c^\dagger_{r+1}; \tag{6.4.22g}$$

$$\langle 0001|\rho^c|0100\rangle = 0, \tag{6.4.22h}$$

where $K_{n_0 n_1,a}$ is the referencing operator associated with the occupation number basis state $|n_0 n_1\rangle$ of cluster a, $K_{n_r n_{r+1},b}$ is the referencing operator associated with the occupation number basis state $|n_r n_{r+1}\rangle$ of cluster b, and a, b, c and d are the reduced two-point functions defined in (5.3.22).

In the two-particle sector, we find that

$$\langle 1100|\rho^c|1010\rangle = -\left[\frac{1}{4}-\frac{1}{8}(1-\mathsf{a}^2)\right]\mathsf{c}, \qquad K^\dagger_{11,a}K_{10,a}K^\dagger_{00,b}K_{10,b} = +c^\dagger_0 c_0 c^\dagger_1 c_r c_{r+1} c^\dagger_{r+1}; \tag{6.4.23a}$$

$$\langle 1100|\rho^c|1001\rangle = -\frac{1}{4}\mathsf{ac}, \qquad K^\dagger_{11,a}K_{10,a}K^\dagger_{00,b}K_{01,b} = +c^\dagger_0 c_0 c^\dagger_1 c_r c^\dagger_r c_{r+1}; \tag{6.4.23b}$$

$$\langle 1100|\rho^c|0110\rangle = -\frac{1}{4}\mathsf{ac}, \qquad K^\dagger_{11,a}K_{01,a}K^\dagger_{00,b}K_{10,b} = -c_0^\dagger c_1^\dagger c_1 c_r c_{r+1} c_{r+1}^\dagger; \tag{6.4.23c}$$

$$\langle 1100|\rho^c|0101\rangle = -\left[\frac{1}{4} - \frac{1}{8}(1-\mathsf{a}^2)\right]\mathsf{c}, \qquad K^\dagger_{11,a}K_{01,a}K^\dagger_{00,b}K_{01,b} = -c_0^\dagger c_1^\dagger c_1 c_r c_r^\dagger c_{r+1}; \tag{6.4.23d}$$

$$\langle 1010|\rho^c|1100\rangle = -\left[\frac{1}{4} - \frac{1}{8}(1-\mathsf{a}^2)\right]\mathsf{c}, \qquad K^\dagger_{10,a}K_{11,a}K^\dagger_{10,b}K_{00,b} = -c_0^\dagger c_0 c_1 c_r^\dagger c_{r+1} c_{r+1}^\dagger; \tag{6.4.23e}$$

$$\langle 1010|\rho^c|0011\rangle = -\left[\frac{1}{4} - \frac{1}{8}(1-\mathsf{a}^2)\right]\mathsf{c}, \qquad K^\dagger_{10,a}K_{00,a}K^\dagger_{10,b}K_{11,b} = -c_0^\dagger c_1 c_1^\dagger c_r^\dagger c_r c_{r+1}; \tag{6.4.23f}$$

$$\langle 1001|\rho^c|1100\rangle = -\frac{1}{4}\mathsf{ac}, \qquad K^\dagger_{10,a}K_{11,a}K^\dagger_{01,b}K_{00,b} = -c_0^\dagger c_0 c_1 c_r c_r^\dagger c_{r+1}^\dagger; \tag{6.4.23g}$$

$$\langle 1001|\rho^c|0011\rangle = -\frac{1}{4}\mathsf{ac}, \qquad K^\dagger_{10,a}K_{00,a}K^\dagger_{01,b}K_{11,b} = +c_0^\dagger c_1 c_1^\dagger c_r c_{r+1}^\dagger c_{r+1}; \tag{6.4.23h}$$

$$\langle 0110|\rho^c|1100\rangle = -\frac{1}{4}\mathsf{ac}, \qquad K^\dagger_{01,a}K_{11,a}K^\dagger_{10,b}K_{00,b} = +c_0 c_1^\dagger c_1 c_r^\dagger c_{r+1} c_{r+1}^\dagger; \tag{6.4.23i}$$

$$\langle 0110|\rho^c|0011\rangle = -\frac{1}{4}\mathsf{ac}, \qquad K^\dagger_{01,a}K_{00,a}K^\dagger_{10,b}K_{11,b} = -c_0 c_0^\dagger c_1^\dagger c_r^\dagger c_r c_{r+1}; \tag{6.4.23j}$$

$$\langle 0101|\rho^c|1100\rangle = -\left[\frac{1}{4} - \frac{1}{8}(1-\mathsf{a}^2)\right]\mathsf{c}, \qquad K^\dagger_{01,a}K_{11,a}K^\dagger_{01,b}K_{00,b} = +c_0 c_1^\dagger c_1 c_r c_r^\dagger c_{r+1}^\dagger; \tag{6.4.23k}$$

$$\langle 0101|\rho^c|0011\rangle = -\left[\frac{1}{4} - \frac{1}{8}(1-\mathsf{a}^2)\right]\mathsf{c}, \qquad K^\dagger_{01,a}K_{00,a}K^\dagger_{01,b}K_{11,b} = +c_0 c_0^\dagger c_1^\dagger c_r c_{r+1}^\dagger c_{r+1}; \tag{6.4.23l}$$

$$\langle 0011|\rho^c|1010\rangle = -\left[\frac{1}{4} - \frac{1}{8}(1-\mathsf{a}^2)\right]\mathsf{c}, \qquad K^\dagger_{00,a}K_{10,a}K^\dagger_{11,b}K_{10,b} = +c_0 c_1 c_1^\dagger c_r^\dagger c_r c_{r+1}^\dagger; \tag{6.4.23m}$$

$$\langle 0011|\rho^c|1001\rangle = -\frac{1}{4}\mathsf{ac}, \qquad K^\dagger_{00,a}K_{10,a}K^\dagger_{11,b}K_{01,b} = -c_0c_1c_1^\dagger c_r^\dagger c_{r+1}^\dagger c_{r+1}; \tag{6.4.23n}$$

$$\langle 0011|\rho^c|0110\rangle = -\frac{1}{4}\mathsf{ac}, \qquad K^\dagger_{00,a}K_{01,a}K^\dagger_{11,b}K_{10,b} = +c_0c_0^\dagger c_1c_r^\dagger c_rc_{r+1}^\dagger; \tag{6.4.23o}$$

$$\langle 0011|\rho^c|0101\rangle = -\left[\frac{1}{4} - \frac{1}{8}(1-\mathsf{a}^2)\right]\mathsf{c}, \qquad K^\dagger_{00,a}K_{01,a}K^\dagger_{11,b}K_{01,b} - c_0c_0^\dagger c_1c_r^\dagger c_{r+1}^\dagger c_{r+1}. \tag{6.4.23p}$$

In the 3-particle sector, we find that

$$\langle 1110|\rho^c|1011\rangle = 0; \tag{6.4.24a}$$

$$\langle 1110|\rho^c|0111\rangle = +\frac{1}{8}(1-\mathsf{a}^2)\mathsf{c}, \qquad K^\dagger_{11,a}K_{01,a}K^\dagger_{10,b}K_{11,b} = +c_0^\dagger c_1^\dagger c_1c_r^\dagger c_rc_{r+1}; \tag{6.4.24b}$$

$$\langle 1101|\rho^c|1011\rangle = -\frac{1}{8}(1-\mathsf{a}^2)\mathsf{c}, \qquad K^\dagger_{11,a}K_{10,a}K^\dagger_{01,b}K_{11,b} = +c_0^\dagger c_0c_1^\dagger c_rc_{r+1}^\dagger c_{r+1}; \tag{6.4.24c}$$

$$\langle 1101|\rho^c|0111\rangle = 0; \tag{6.4.24d}$$

$$\langle 1011|\rho^c|1110\rangle = 0; \tag{6.4.24e}$$

$$\langle 1011|\rho^c|1101\rangle = -\frac{1}{8}(1-\mathsf{a}^2)\mathsf{c}, \qquad K^\dagger_{10,a}K_{11,a}K^\dagger_{11,b}K_{01,b} = -c_0^\dagger c_0c_1c_r^\dagger c_{r+1}^\dagger c_{r+1}; \tag{6.4.24f}$$

$$\langle 0111|\rho^c|1110\rangle = +\frac{1}{8}(1-\mathsf{a}^2)\mathsf{c}, \qquad K^\dagger_{01,a}K_{11,a}K^\dagger_{11,b}K_{10,b} = -c_0c_1^\dagger c_1c_r^\dagger c_rc_{r+1}^\dagger; \tag{6.4.24g}$$

$$\langle 0111|\rho^c|1101\rangle = 0. \tag{6.4.24h}$$

6.4.4.2 Grouping of Operator Expansion Terms

Grouping operator expansion terms with the same coefficients, we then write down the (2 + 2) correlation density matrix as

$$\rho^c = \rho^c_A + \rho^c_B + \rho^c_C, \tag{6.4.25}$$

where

$$\rho^c_A = A\Big[-c_0^\dagger c_0c_1^\dagger c_rc_r^\dagger c_{r+1} + c_0^\dagger c_1^\dagger c_1c_rc_{r+1}c_{r+1}^\dagger + c_0^\dagger c_0c_1c_rc_r^\dagger c_{r+1}^\dagger - c_0^\dagger c_1c_1^\dagger c_rc_{r+1}^\dagger c_{r+1}$$

$$- c_0 c_1^\dagger c_1 c_r^\dagger c_{r+1} c_{r+1}^\dagger + c_0 c_0^\dagger c_1^\dagger c_r^\dagger c_r c_{r+1} + c_0 c_1 c_1^\dagger c_r^\dagger c_{r+1}^\dagger c_{r+1} - c_0 c_0^\dagger c_1 c_r^\dagger c_r c_{r+1}^\dagger \Big], \tag{6.4.26a}$$

$$\rho_B^c = B\Big[+c_0^\dagger c_1 c_1^\dagger c_r c_r^\dagger c_{r+1} - c_0 c_0^\dagger c_1^\dagger c_r c_{r+1} c_{r+1}^\dagger + c_0 c_0^\dagger c_1 c_r^\dagger c_{r+1} c_{r+1}^\dagger - c_0 c_1 c_1^\dagger c_r c_r^\dagger c_{r+1}^\dagger$$
$$+ c_0^\dagger c_1^\dagger c_1 c_r^\dagger c_r c_{r+1} - c_0^\dagger c_0 c_1^\dagger c_r c_{r+1}^\dagger c_{r+1} + c_0^\dagger c_0 c_1 c_r^\dagger c_{r+1}^\dagger c_{r+1} - c_0 c_1^\dagger c_1 c_r^\dagger c_r c_{r+1}^\dagger \Big], \tag{6.4.26b}$$

$$\rho_C^c = -C\Big[+c_0^\dagger c_0 c_1^\dagger c_r c_{r+1} c_{r+1}^\dagger - c_0^\dagger c_1^\dagger c_1 c_r c_r^\dagger c_{r+1} - c_0^\dagger c_0 c_1 c_r^\dagger c_{r+1} c_{r+1}^\dagger - c_0^\dagger c_1 c_1^\dagger c_r^\dagger c_r c_{r+1}$$
$$+ c_0 c_1^\dagger c_1 c_r c_r^\dagger c_{r+1}^\dagger + c_0 c_0^\dagger c_1^\dagger c_r c_{r+1}^\dagger c_{r+1} + c_0 c_1 c_1^\dagger c_r^\dagger c_r c_{r+1}^\dagger - c_0 c_0^\dagger c_1 c_r^\dagger c_{r+1}^\dagger c_{r+1} \Big], \tag{6.4.26c}$$

with coefficients

$$A = \frac{1}{4}\mathsf{ac}, \quad B = \frac{1}{8}(1-\mathsf{a}^2)\mathsf{c}, \quad C = \left[\frac{1}{4} - \frac{1}{8}(1-\mathsf{a}^2)\right]\mathsf{c}. \tag{6.4.27}$$

Because the two clusters are symmetrical, the correlation density matrix ought to be invariant under an inversion operation, which maps the sites

$$0 \leftrightarrow r+1, \quad 1 \leftrightarrow r. \tag{6.4.28}$$

We then checked that the terms ρ_A^c, ρ_B^c and ρ_C^c defined in (6.4.26) are independently invariant under the inversion.

We can simplify the expressions for ρ_A^c, ρ_B^c and ρ_C^c by writing parts of the operator expansion terms in term of the occupation number operators n_0, n_1, n_r, and n_{r+1}. After this has been done, we find that

$$\rho_A^c = A\Big\{ + (c_0^\dagger c_r - c_0 c_r^\dagger)(n_1 - n_{r+1}) - (c_1^\dagger c_{r+1} - c_1 c_{r+1}^\dagger)(n_0 - n_r)\Big\}, \tag{6.4.29a}$$

$$\rho_B^C = B\Big\{ + (c_0^\dagger c_{r+1} - c_0 c_{r+1}^\dagger)[(\mathbb{1} - n_1)(\mathbb{1} - n_r) + n_1 n_r]$$
$$- (c_1^\dagger c_r - c_1 c_r^\dagger)[(\mathbb{1} - n_0)(\mathbb{1} - n_{r+1}) + n_0 n_{R+1}]\Big\}, \tag{6.4.29b}$$

$$\rho_C^c = C\Big\{ + (c_0^\dagger c_{r+1} - c_0 c_{r+1}^\dagger)[n_1(\mathbb{1} - n_r) + (\mathbb{1} - n_1)n_r]$$
$$- (c_1^\dagger c_r - c_1 c_r^\dagger)[n_0(\mathbb{1} - n_{r+1}) + (\mathbb{1} - n_0)n_{R+1}]\Big\}. \tag{6.4.29c}$$

6.4.4.3 Baby Operator Singular Value Decomposition of ρ^c_A

Since ρ^c is a sum of three terms, the best scenario we can hope for is for us to be able to operator singular value decompose the three sums separately. For this to be true, we must have

$$\rho^c_A = \sum_l \sigma_{l,A} X_{l,A} Y_{l,A}, \quad \rho^c_B = \sum_l \sigma_{l,B} X_{l,B} Y_{l,B}, \quad \rho^c_C = \sum_l \sigma_{l,C} X_{l,C} Y_{l,C}, \tag{6.4.30}$$

such that

$$\mathrm{Tr}\, X_{l,\alpha} X_{l',\beta} = \delta_{l,l'}\delta_{\alpha,\beta}, \quad \mathrm{Tr}\, Y_{l,\alpha} Y_{l',\beta} = \delta_{l,l'}\delta_{\alpha,\beta}, \tag{6.4.31}$$

for all combinations of l, l', and $\alpha,\beta = A, B, C$. In other words, the operators $X_{l,A}$ must not only be Frobenius-orthonormal to other others $X_{l',A}$ coming from the operator singular value decomposition of ρ^c_A, but also those operators $X_{l'',B}$ and $X_{l''',C}$ coming from the operator singular value decomposition of ρ^c_B and ρ^c_C respectively. This Frobenius-orthonormality must also be true of the combined set of operators $\{Y_{l,A}, Y_{l',B}, Y_{l'',C}\}$.

We do not know that this breaking up of the operator singular value decomposition of ρ^c into separate operator singular value decompositions of ρ^c_A, ρ^c_B and ρ^c_C will indeed be the case *a priori*. But with no other plausible simplification of the problem of operator singular value decomposing ρ^c, let us work with the assumption that this is the case. If we find later that this is not possible, we can think of a way out then. We will start with ρ^c_A, since it looks the simplest, in terms of its operator content.

Looking at the eight operator terms in ρ^c_A, one might naively conclude that (6.4.29a) is already *the* operator singular value decomposition. If we were correct in making this claim, then the left and right eigen-operators, along with the singular values, would be

$$X_1 = c_0^\dagger n_1, \qquad Y_1 = c_r^\dagger, \qquad \sigma_1 = +A = +\frac{1}{4}\mathsf{ac}, \tag{6.4.32a}$$

$$X_2 = c_0^\dagger, \qquad Y_2 = c_r^\dagger n_{r+1}, \qquad \sigma_2 = -A = -\frac{1}{4}\mathsf{ac}, \tag{6.4.32b}$$

$$X_3 = c_0 n_1, \qquad Y_3 = c_r, \qquad \sigma_3 = -A = -\frac{1}{4}\mathsf{ac}, \tag{6.4.32c}$$

$$X_4 = c_0, \qquad Y_4 = c_r n_{r+1}, \qquad \sigma_4 = +A = +\frac{1}{4}\mathsf{ac}. \tag{6.4.32d}$$

However, checking the Frobenius norms

$$\operatorname{Tr} X_1 X_1^\dagger = \operatorname{Tr} c_0^\dagger n_1 n_1 c_0 = \operatorname{Tr} n_0 n_1 = 1, \tag{6.4.33a}$$

$$\operatorname{Tr} X_2 X_2^\dagger = \operatorname{Tr} c_0^\dagger c_0 = \operatorname{Tr} n_0 = 2, \tag{6.4.33b}$$

$$\operatorname{Tr} X_3 X_3^\dagger = \operatorname{Tr} c_0 n_1 n_1 c_0^\dagger = \operatorname{Tr}(\mathbb{1} - n_0) n_1 = \operatorname{Tr} n_1 - \operatorname{Tr} n_0 n_1 = 2 - 1 = 1, \tag{6.4.33c}$$

$$\operatorname{Tr} X_4 X_4^\dagger = \operatorname{Tr} c_0 c_0^\dagger = \operatorname{Tr}(\mathbb{1} - n_0) = \operatorname{Tr} \mathbb{1} - \operatorname{Tr} n_0 = 4 - 2 = 2, \tag{6.4.33d}$$

and Frobenius inner products

$$\operatorname{Tr} X_1 X_2^\dagger = \operatorname{Tr} c_0^\dagger n_1 c_0 = \operatorname{Tr} n_0 n_1 = 1, \tag{6.4.34a}$$

$$\operatorname{Tr} X_1 X_3^\dagger = \operatorname{Tr} c_0^\dagger n_1 n_1 c_0^\dagger = 0, \tag{6.4.34b}$$

$$\operatorname{Tr} X_1 X_4^\dagger = \operatorname{Tr} c_0^\dagger n_1 c_0^\dagger = 0, \tag{6.4.34c}$$

$$\operatorname{Tr} X_2 X_3^\dagger = \operatorname{Tr} c_0^\dagger n_1 c_0^\dagger = 0, \tag{6.4.34d}$$

$$\operatorname{Tr} X_2 X_4^\dagger = \operatorname{Tr} c_0^\dagger c_0^\dagger = 0, \tag{6.4.34e}$$

$$\operatorname{Tr} X_3 X_4^\dagger = \operatorname{Tr} c_0 n_1 c_0^\dagger = \operatorname{Tr}(\mathbb{1} - n_0) n_1 = \operatorname{Tr} n_1 - \operatorname{Tr} n_0 n_1 = 2 - 1 = 1, \tag{6.4.34f}$$

we find that X_1 is not orthogonal to X_2, X_3 is not orthogonal to X_4, while X_2 and X_4 are not normalized.

Since X_2 is neither normalized nor orthogonal to X_1, we can think of it as some linear combination

$$X_2 = \alpha X_1 + \beta \tilde{X}_2 \tag{6.4.35}$$

of X_1, and a Frobenius-normalized operator $\tilde{X}_2$ which is orthogonal to X_1. Writing X_2 as

$$X_2 = c_0^\dagger = c_0^\dagger n_1 + c_0^\dagger (\mathbb{1} - n_1), \tag{6.4.36}$$

where the first term is just X_1, we can identify the second term as our Frobenius-orthonormalized operator

$$\tilde{X}_2 = c_0^\dagger(\mathbb{1} - n_1). \tag{6.4.37}$$

We check that

$$\operatorname{Tr}\tilde{X}_2\tilde{X}_2^\dagger = \operatorname{Tr} c_0^\dagger(\mathbb{1}-n_1)(\mathbb{1}-n_1)c_0 = \operatorname{Tr} n_0(\mathbb{1}-n_1) = \operatorname{Tr} n_0 - \operatorname{Tr} n_0 n_1 = 2-1 = 1, \tag{6.4.38}$$

and

$$\operatorname{Tr} X_1\tilde{X}_2 = \operatorname{Tr} c_0^\dagger n_1(\mathbb{1} - n_1)c_0 = \operatorname{Tr} n_0(n_1 - n_1^2) = \operatorname{Tr} n_0(n_1 - n_1) = 0, \tag{6.4.39}$$

which tells us that $\tilde{X}_2$ so identified is indeed normalized and orthogonal to X_1. Similarly, the operator

$$\tilde{X}_4 = c_0(1 - n_1) \tag{6.4.40}$$

is normalized and orthogonal to X_1, $\tilde{X}_2$, and X_3.

With this set of Frobenius-orthonormal X_l operators, and a corresponding set of Y_l operators, we can then write the proper singular value decomposition of ρ_A^c as

$$\begin{aligned}
\rho_A^c = &+ c_0^\dagger n_1 \cdot [c_r n_{r+1} + c_r(\mathbb{1} - n_{R+1})] \cdot \left(+\frac{1}{4}\mathsf{ac}\right) \\
&+ [c_0^\dagger n_1 + c_0^\dagger(\mathbb{1} - n_1)] \cdot c_r n_{r+1} \cdot \left(-\frac{1}{4}\mathsf{ac}\right) \\
&+ c_1^\dagger n_0 \cdot [c_{r+1}^\dagger n_r + c_{r+1}^\dagger(\mathbb{1} - n_r)] \cdot \left(-\frac{1}{4}\mathsf{ac}\right) \\
&+ [c_1 n_0 + c_1(\mathbb{1} - n_0)] \cdot c_{r+1} n_r \cdot \left(+\frac{1}{4}\mathsf{ac}\right) + \text{h.c.} \\
= &+ c_0^\dagger n_1 \cdot c_r(\mathbb{1} - n_{r+1}) \cdot \left(+\frac{1}{4}\mathsf{ac}\right) + c_0^\dagger(\mathbb{1} - n_1) \cdot c_r n_{r+1} \cdot \left(-\frac{1}{4}\mathsf{ac}\right) \\
&+ c_1^\dagger n_0 \cdot c_{r+1}(\mathbb{1} - n_r) \cdot \left(-\frac{1}{4}\mathsf{ac}\right) + c_1^\dagger(\mathbb{1} - n_0) \cdot c_{r+1}^\dagger n_r \cdot \left(+\frac{1}{4}\mathsf{ac}\right) + \text{h.c.},
\end{aligned} \tag{6.4.41}$$

where, renaming $\tilde{X}_2$ as X_2 and $\tilde{X}_4$ as X_4,

$$X_1 = c_0^\dagger n_1, \qquad Y_1 = c_r^\dagger(\mathbb{1} - n_{r+1}), \qquad \sigma_1 = +\frac{1}{4}\mathsf{ac}, \tag{6.4.42a}$$

$$X_2 = c_0^\dagger(\mathbb{1} - n_1), \qquad Y_2 = c_r^\dagger n_{r+1}, \qquad \sigma_2 = -\frac{1}{4}\mathsf{ac}, \tag{6.4.42b}$$

$$X_3 = c_1^\dagger n_0, \qquad Y_3 = c_{r+1}^\dagger(\mathbb{1} - n_r), \qquad \sigma_3 = -\frac{1}{4}\mathsf{ac}, \tag{6.4.42c}$$

$$X_4 = c_1^\dagger(\mathbb{1} - n_0), \qquad Y_4 = c_{r+1}^\dagger n_r, \qquad \sigma_4 = +\frac{1}{4}\mathsf{ac}. \tag{6.4.42d}$$

The hermitian conjugate terms can be obtained trivially. Here, we find that the absolute singular values are degenerate, and thus the eigen-operators so defined in (6.4.42) are not unique. If we encounter absolute singular value degeneracies in our operator singular value decomposition of ρ^c, we must be careful in choosing our eigen-operators. But here, we are doing only a baby operator singular value decomposition of ρ_A^c, where our chief interest is to discover the tools needed to operator singular value decompose ρ^c, so we will pursue this absolute-singular-value degeneracy no further.

6.4.4.4 Partial Operator Singular Value Decomposition of $\boldsymbol{\rho_A^c + \rho_C^c}$

Moving on from our baby operator singular value decomposition of ρ_A^c, we consider ρ_B^c and ρ_C^c. In these two terms, we find the same set of operators X_l and Y_l, but they occur in different combinations. To perform an overall singular value decomposition of ρ^c, we therefore need to first introduce notation that is consistent across all three terms. To this end, we define the operators

$$\begin{aligned} X_1 &= c_0^\dagger n_1, & Y_1 &= c_{r+1}^\dagger n_r, \\ X_2 &= c_0^\dagger(\mathbb{1} - n_1), & Y_2 &= c_{r+1}^\dagger(\mathbb{1} - n_r), \\ X_3 &= c_1^\dagger n_0, & Y_3 &= c_r^\dagger n_{r+1}, \\ X_4 &= c_1^\dagger(\mathbb{1} - n_0), & Y_4 &= c_r^\dagger(\mathbb{1} - n_{r+1}), \end{aligned} \tag{6.4.43}$$

in terms of the bare operators c_0, c_1, c_r, c_{r+1}, as well as their hermitian conjugates.

In terms of the operators defined in (6.4.43), ρ^c can be written as

$$\begin{aligned}\rho^c = A &\left[X_1 Y_4^\dagger - X_2 Y_3^\dagger - X_3 Y_2^\dagger + X_4 Y_1^\dagger + \text{h.c.}\right] \\ + B &\left[+X_1 Y_1^\dagger + X_2 Y_2^\dagger + X_3 Y_3^\dagger + X_4 Y_4^\dagger + \text{h.c.}\right] \\ + C &\left[X_1 Y_2^\dagger + X_2 Y_1^\dagger - X_3 Y_4^\dagger - X_4 Y_3^\dagger + \text{h.c.}\right].\end{aligned} \tag{6.4.44}$$

As a result of our choice for the X_l and Y_l operators, the operator expansion of ρ_B^c has the structure of an inner product $\mathbf{X}^T\mathbf{Y}$ of the vectors of operators

$$\mathbf{X} = \begin{bmatrix} X_1 & X_2 & X_3 & X_4 \end{bmatrix}^T, \quad \mathbf{Y} = \begin{bmatrix} Y_1 & Y_2 & Y_3 & Y_4 \end{bmatrix}. \tag{6.4.45}$$

This inner product structure is invariant under arbitrary unitary transformations of the operator bases $\{X_1, X_2, X_3, X_4\}$ and $\{Y_1, Y_2, Y_3, Y_4\}$, i.e. if we perform unitary rotations of the Frobenius-orthonormal operator bases $\{X_1, X_2, X_3, X_4\}$ and $\{Y_1, Y_2, Y_3, Y_4\}$ to get the new Frobenius-orthonormal operator bases $\{X_1', X_2', X_3', X_4'\}$ and $\{Y_1', Y_2', Y_3', Y_4'\}$, we will find ρ_B^c to be

$$\rho_B^c = B\left[X_1' Y_1'^\dagger + X_2' Y_2'^\dagger + X_3' Y_3'^\dagger + X_4' Y_4'^\dagger + \text{h.c.}\right] \tag{6.4.46}$$

in terms of the new bases of operators. Therefore, we can leave ρ_B^c alone, and focus on obtaining an operator singular value decomposition of $\rho_A^c + \rho_C^c$.

To do so, let us first note that in ρ_A^c and ρ_C^c, the odd X_l's always come with the even $Y_{l'}$'s, while the even X_l's always come with the odd $Y_{l'}$'s. Taking advantage of this, let us restrict our attention to those terms in ρ_A^c and ρ_C^c involving odd X_l's, which are

$$AX_1 Y_4^\dagger - AX_3 Y_2^\dagger + CX_1 Y_2^\dagger - CX_3 Y_4^\dagger + \text{h.c.} \tag{6.4.47}$$

If we do not worry about the hermitian conjugate terms, there are four operator terms in $\rho_A^c + \rho_C^c$ with X_l odd. Our goal is to find a rotated operator basis, with

$$\begin{aligned} X_1' &= \alpha X_1 + \beta X_3, \\ X_3' &= -\beta X_1 + \alpha X_3, \end{aligned} \tag{6.4.48}$$

or equivalently,

$$\begin{aligned} X_1 &= \alpha X_1' - \beta X_3', \\ X_3 &= \beta X_1' + \alpha X_3', \end{aligned} \tag{6.4.49}$$

and some rotated operator basis for $Y_{l'}$, so that the operator expansion contains fewer terms. Substituting (6.4.49) into (6.4.47), we find that

$$\begin{aligned} &A(\alpha X_1' - \beta X_3')Y_4^\dagger - A(\beta X_1' + \alpha X_3')Y_2^\dagger + C(\alpha X_1' - \beta X_3')Y_2^\dagger - C(\beta X_1' + \alpha X_3')Y_4^\dagger \\ &= X_1'[-(A\beta - C\alpha)Y_2^\dagger + (A\alpha - C\beta)Y_4^\dagger] - X_3'[(A\alpha + C\beta)Y_2^\dagger + (A\beta + C\alpha)Y_4^\dagger]. \end{aligned} \tag{6.4.50}$$

We can massage this into the form

$$A' X_1' Y_2'^\dagger + B' X_3' Y_4'^\dagger, \tag{6.4.51}$$

provided the rotated basis of Y_2' and Y_4' is related to the original basis of Y_2 and Y_4 by

$$\begin{aligned} A' Y_2'^\dagger &= -(A\beta - C\alpha)Y_2^\dagger + (A\alpha - C\beta)Y_4^\dagger, \\ B' Y_4'^\dagger &= -(A\alpha + C\beta)Y_2^\dagger - (A\beta + C\alpha)Y_4^\dagger. \end{aligned} \tag{6.4.52}$$

To find what α and β must be for this to be true, we demand that $Y_2'^\dagger$ and $Y_4'^\dagger$ be orthogonal. This gives us

$$\begin{aligned} A'B' \operatorname{Tr} Y_2' Y_4'^\dagger &= (A\beta - C\alpha)(A\alpha + C\beta) \operatorname{Tr} Y_2 Y_2^\dagger \\ &\quad + (A\beta - C\alpha)(A\beta + C\alpha) \operatorname{Tr} Y_2 Y_4^\dagger \\ &\quad - (A\alpha - C\beta)(A\alpha + C\beta) \operatorname{Tr} Y_4 Y_2^\dagger \\ &\quad - (A\alpha - C\beta)(A\beta + C\alpha) \operatorname{Tr} Y_4 Y_4^\dagger \\ &= \cancel{A^2\alpha\beta} + AC\beta^2 - AC\alpha^2 - \cancel{C^2\alpha\beta} \\ &\quad - \cancel{A^2\alpha\beta} - AC\alpha^2 + AC\beta^2 + \cancel{C^2\alpha\beta} \\ &= 2AC(\beta^2 - \alpha^2) = 0, \end{aligned} \tag{6.4.53}$$

which then tells us that $\alpha^2 = \beta^2$. Since $\alpha^2 + \beta^2 = 1$ for X_1' and X_3' to be normalized, we must therefore have

$$\alpha = \frac{1}{\sqrt{2}}, \quad \beta = \pm\frac{1}{\sqrt{2}}. \tag{6.4.54}$$

Whichever β we choose, we get (up to a minus sign) the same X_1' and X_3', so let us pick $\beta = +\frac{1}{\sqrt{2}}$, to obtain

$$\begin{aligned} X_1' &= \frac{1}{\sqrt{2}}(X_1 + X_3), \quad X_3' = -\frac{1}{\sqrt{2}}(X_1 - X_3), \\ Y_2' &= -\frac{1}{\sqrt{2}}(Y_2 - Y_4), \quad Y_4' = -\frac{1}{\sqrt{2}}(Y_2 + Y_4). \end{aligned} \tag{6.4.55}$$

In terms of the operators X_1', X_3', Y_2' and Y_4', we can then write the terms in $\rho_A^c + \rho_C^c$ involving odd X_l's as

$$(A - C)X_1'Y_2'^{\dagger} + (A + C)X_3'Y_4'^{\dagger} + \text{h.c.}. \tag{6.4.56}$$

Having reached this stage of the singular value decomposition, we see that we can tidy up the notations a little. First we can pull all the negative signs in front of X_3', Y_2' and Y_4' out, and stick any remaining negative sign to the singular values. As a matter of consistency, let me also swap the indices of X_1' and X_3', so that the partial singular value decomposition for odd X_l-terms in $\rho_A^c + \rho_C^c$ can be written as

$$(A + C)X_1'Y_4'^{\dagger} - (A - C)X_3'Y_2'^{\dagger} + \text{h.c.}. \tag{6.4.57}$$

The reason for this swapping of indices is so that we can define neatly the rotated operators

$$\begin{aligned} X_1' &= \frac{1}{\sqrt{2}}(X_1 - X_3), \quad Y_1' = \frac{1}{\sqrt{2}}(Y_1 - Y_3), \\ X_2' &= \frac{1}{\sqrt{2}}(X_2 - X_4), \quad Y_2' = \frac{1}{\sqrt{2}}(Y_2 - Y_4), \\ X_3' &= \frac{1}{\sqrt{2}}(X_1 + X_3), \quad Y_3' = \frac{1}{\sqrt{2}}(Y_1 + Y_3), \\ X_4' &= \frac{1}{\sqrt{2}}(X_2 + X_4), \quad Y_4' = \frac{1}{\sqrt{2}}(Y_2 + Y_4), \end{aligned} \tag{6.4.58}$$

consistently between the X_l and $Y_{l'}$ operators. With this operator basis, the remaining terms in $\rho_A^c + \rho_C^c$, involving even X_l's, then singular value decompose to

$$(A + C)X_4'Y_1'^{\dagger} - (A - C)X_2'Y_3'^{\dagger} + \text{h.c.}. \tag{6.4.59}$$

The complete singular value decomposition of $\rho_A^c + \rho_C^c$ is then

$$\rho_A^c + \rho_C^c = (A+C)X_1' Y_4'^\dagger - (A-C)X_2' Y_3'^\dagger - (A-C)X_3' Y_2'^\dagger + (A+C)X_4' Y_1'^\dagger + \text{h.c.} \quad (6.4.60)$$

6.4.4.5 Full Operator Singular Value Decomposition of ρ^c

We are now ready to complete the singular value decomposition of ρ^c. To do this, let us write ρ_B^c in terms of the primed operators as

$$\rho_B^c = B\left[+X_1' Y_1'^\dagger + X_2' Y_2'^\dagger + X_3' Y_3'^\dagger + X_4' Y_4'^\dagger + \text{h.c.}\right], \quad (6.4.61)$$

so that ρ^c becomes

$$\begin{aligned} \rho^c = &+ A' X_1' Y_4'^\dagger \quad + A' X_4' Y_1'^\dagger \\ &+ B' X_1' Y_1'^\dagger \quad + B' X_3' Y_3'^\dagger \\ &+ B' X_2' Y_2'^\dagger \quad + B' X_4' Y_4'^\dagger \\ &- C' X_2' Y_3'^\dagger \quad - C' X_3' Y_2'^\dagger + \text{h.c.}, \end{aligned} \quad (6.4.62)$$

where

$$A' = A + C, \quad B' = B, \quad C' = A - C. \quad (6.4.63)$$

Staring at (6.4.62) very intently, we see that X_1' goes only with Y_1' and Y_4', while Y_1' goes only with X_1' and X_4'. Similarly, we find that X_2' goes only with Y_2' and Y_3', while Y_2' goes only with X_2' and X_3'. Therefore, ρ^c comprises two groups of operators, whose indices $\{1,4\}$ and $\{2,3\}$ do not mix. We can then singular value decompose each group independently.

The first of these two indicial groups is

$$\rho_{\{1,4\}}^c = A' X_1' Y_4'^\dagger + B' X_1' Y_1'^\dagger + B' X_4' Y_4'^\dagger + A' X_4' Y_1'^\dagger. \quad (6.4.64)$$

If we define the rotated double-primed operator basis

$$\begin{aligned} X_1'' &= \alpha' X_1' - \beta' X_4', \\ X_4'' &= \beta' X_1' + \alpha' X_4'; \\ Y_1'' &= \gamma' Y_1' - \delta' Y_4', \\ Y_4'' &= \delta' Y_1' + \gamma' Y_4' \end{aligned} \tag{6.4.65}$$

in terms of the primed operator basis, or, equivalently,

$$\begin{aligned} X_1' &= \alpha' X_1'' + \beta' X_4'', \\ X_4' &= -\beta' X_1'' + \alpha' X_4''; \\ Y_1' &= \gamma' Y_1'' + \delta' Y_4'', \\ Y_4' &= -\delta' Y_1'' + \gamma' Y_4'', \end{aligned} \tag{6.4.66}$$

we find that (6.4.64) becomes

$$\begin{aligned} \rho^c_{\{1,4\}} = &+ A'(\alpha' X_1'' + \beta' X_4'')(-\delta' {Y_1''}^\dagger + \gamma' {Y_4''}^\dagger) \\ &+ B'(\alpha' X_1'' + \beta' X_4'')(\gamma' {Y_1''}^\dagger + \delta' {Y_4''}^\dagger) \\ &+ B'(-\beta' X_1'' + \alpha' X_4'')(-\delta' {Y_1''}^\dagger + \gamma' {Y_4''}^\dagger) \\ &+ A'(-\beta' X_1'' + \alpha' X_4'')(\gamma' {Y_1''}^\dagger + \delta' {Y_4''}^\dagger) \\ = &+ (-A'\alpha'\delta' + B'\alpha'\gamma' + B'\beta'\delta' - A'\beta'\gamma') X_1'' {Y_1''}^\dagger \\ &+ (+A'\alpha'\gamma' + B'\alpha'\delta' - B'\beta'\gamma' - A'\beta'\delta') X_1'' {Y_4''}^\dagger \\ &+ (-A'\beta'\delta' + B'\beta'\gamma' - B'\alpha'\delta' + A'\alpha'\gamma') X_4'' {Y_1''}^\dagger \\ &+ (+A'\beta'\gamma' + B'\beta'\delta' + B'\alpha'\gamma' + A'\alpha'\delta') X_4'' {Y_4''}^\dagger. \end{aligned} \tag{6.4.67}$$

Out of these four terms, we can demand that any one of the X_1'' term and any one of the X_4'' term remains, as long as their associated Y'' operators are different. Let us demand then that the coefficients of the $X_1'' {Y_4''}^\dagger$ and $X_4'' {Y_1''}^\dagger$ terms be zero. Then we get

$$A'\alpha'\gamma' + B'\alpha'\delta' - B'\beta'\gamma' - A'\beta'\delta' = 0, \tag{6.4.68a}$$

$$-A'\beta'\delta' + B'\beta'\gamma' - B'\alpha'\delta' + A'\alpha'\gamma' = 0, \tag{6.4.68b}$$

which is a set of two equations for four unknowns α', β', γ' and δ'. Of course we know that $\alpha'^2 + \beta'^2 = 1$ and $\gamma'^2 + \delta'^2 = 1$ so that the double-primed operators are normalized, but we can always normalize α', β', γ' and δ' after solving (6.4.68). We make use of this freedom to choose $\alpha' = 1 = \gamma'$, to obtain

$$A' + B'\delta' - B'\beta' - A'\beta'\delta' = 0, \tag{6.4.69a}$$

$$-A'\beta'\delta' + B'\beta' - B'\delta' + A' = 0, \tag{6.4.69b}$$

Equating (6.4.69a) and (6.4.69b) and noting cancellations, we then find $\beta' = \delta'$. Substituting this result back into (6.4.69a), we find that $\beta^2 = 1$, or $\beta = \pm 1$. After normalization, we then have $\alpha' = \frac{1}{\sqrt{2}}$, $\beta' = \pm\frac{1}{\sqrt{2}}$ and $\gamma' = \frac{1}{\sqrt{2}}$, $\delta' = \pm\frac{1}{\sqrt{2}}$. Up to a minus sign, $\beta' = \pm\frac{1}{\sqrt{2}}$ gives the same set of double-primed operators, so we can choose $\beta' = \frac{1}{\sqrt{2}}$, giving us the double-primed operators and singular values

$$\begin{aligned} X_1'' &= \frac{1}{\sqrt{2}}(X_1' - X_4'), \qquad Y_1'' = \frac{1}{\sqrt{2}}(Y_1' - Y_4'), \qquad \sigma_1'' = B' - A', \\ X_4'' &= \frac{1}{\sqrt{2}}(X_1' + X_4'), \qquad Y_4'' = \frac{1}{\sqrt{2}}(Y_1' + Y_4'), \qquad \sigma_4'' = B' + A'. \end{aligned} \tag{6.4.70}$$

The second indicial group is

$$\rho^c_{\{2,3\}} = B'X_2'Y_2'^\dagger - C'X_2'Y_3'^\dagger - C'X_3'Y_2'^\dagger + B'X_3'Y_3'^\dagger. \tag{6.4.71}$$

Again, if we define the rotated double-primed operator basis

$$\begin{aligned} X_2'' &= \bar{\alpha}'X_2' - \bar{\beta}'X_3', \\ X_3'' &= \bar{\beta}'X_2' + \bar{\alpha}'X_3'; \\ Y_2'' &= \bar{\gamma}'Y_2' - \bar{\delta}'Y_3', \\ Y_3'' &= \bar{\delta}'Y_2' + \bar{\gamma}'Y_3' \end{aligned} \tag{6.4.72}$$

in terms of the primed operator basis, or, equivalently,

$$\begin{aligned} X_2' &= \bar{\alpha}' X_2'' + \bar{\beta}' X_3'', \\ X_3' &= -\bar{\beta}' X_2'' + \bar{\alpha}' X_3''; \\ Y_2' &= \bar{\gamma}' Y_2'' + \bar{\delta}' Y_3'', \\ Y_3' &= -\bar{\delta}' Y_2'' + \bar{\gamma}' Y_3'', \end{aligned} \tag{6.4.73}$$

we find that (6.4.71) becomes

$$\begin{aligned} \rho^c_{\{2,3\}} = &+ B'(\bar{\alpha}' X_2'' + \bar{\beta}' X_3'')(\bar{\gamma}' {Y_2''}^\dagger + \bar{\delta}' {Y_3''}^\dagger) \\ &- C'(\bar{\alpha}' X_2'' + \bar{\beta}' X_3'')(-\bar{\delta}' {Y_2''}^\dagger + \bar{\gamma}' {Y_3''}^\dagger) \\ &- C'(-\bar{\beta}' X_2'' + \bar{\alpha}' X_3'')(\bar{\gamma}' {Y_2''}^\dagger + \bar{\delta}' {Y_3''}^\dagger) \\ &+ B'(-\bar{\beta}' X_2'' + \bar{\alpha}' X_3'')(-\bar{\delta}' {Y_2''}^\dagger + \bar{\gamma}' {Y_3''}^\dagger) \\ = &+ (+B'\bar{\alpha}'\bar{\gamma}' + C'\bar{\alpha}'\bar{\delta}' + C'\bar{\beta}'\bar{\gamma}' + B'\bar{\beta}'\bar{\delta}') X_2'' {Y_2''}^\dagger \\ &+ (+B'\bar{\alpha}'\bar{\delta}' - C'\bar{\alpha}'\bar{\gamma}' + C'\bar{\beta}'\bar{\delta}' - B'\bar{\beta}'\bar{\gamma}') X_2'' {Y_3''}^\dagger \\ &+ (+B'\bar{\beta}'\bar{\gamma}' + C'\bar{\beta}'\bar{\delta}' - C'\bar{\alpha}'\bar{\gamma}' - B'\bar{\alpha}'\bar{\delta}') X_3'' {Y_2''}^\dagger \\ &+ (+B'\bar{\beta}'\bar{\delta}' - C'\bar{\beta}'\bar{\gamma}' - C'\bar{\alpha}'\bar{\delta}' + B'\bar{\alpha}'\bar{\gamma}') X_3'' {Y_3''}^\dagger. \end{aligned} \tag{6.4.74}$$

Demanding that the coefficients of $X_2'' {Y_3''}^\dagger$ and $X_3'' {Y_2''}^\dagger$ vanish, we have

$$\begin{aligned} B'\bar{\alpha}'\bar{\delta}' - C'\bar{\alpha}'\bar{\gamma}' + C'\bar{\beta}'\bar{\delta}' - B'\bar{\beta}'\bar{\gamma}' = 0, \\ B'\bar{\beta}'\bar{\gamma}' + C'\bar{\beta}'\bar{\delta}' - C'\bar{\alpha}'\bar{\gamma}' - B'\bar{\alpha}'\bar{\delta}' = 0. \end{aligned} \tag{6.4.75}$$

It is easy to see that just as for (6.4.68), solving this system of equations will give

$$\bar{\alpha}' = \bar{\beta}' = \frac{1}{\sqrt{2}} = \bar{\gamma}' = \bar{\delta}'. \tag{6.4.76}$$

The double-primed operators and singular values are then

$$\begin{aligned} X_2'' &= \frac{1}{\sqrt{2}}(X_2' - X_3'), \qquad Y_2'' = \frac{1}{\sqrt{2}}(Y_2' - Y_3'), \qquad \sigma_2'' = B' + C', \\ X_3'' &= \frac{1}{\sqrt{2}}(X_2' + X_3'), \qquad Y_3'' = \frac{1}{\sqrt{2}}(Y_2' + Y_3'), \qquad \sigma_3'' = B' - C'. \end{aligned} \tag{6.4.77}$$

Pulling all our calculations together, we can write down the complete singular value decomposition of ρ^c, for a half-filled chain of noninteracting spinless fermions, at the $O(r^{-1})$ level as

$$\rho^c = \sum_l \sigma_l'' X_l'' Y_l''^{\dagger} + \text{h.c.}, \tag{6.4.78}$$

where, in terms of the reduced two-point functions a and c, and the unprimed set of operators,

$$\begin{aligned}
X_1'' &= \frac{1}{4}(X_1 - X_2 - X_3 - X_4), & Y_1'' &= \frac{1}{4}(Y_1 - Y_2 - Y_3 - Y_4), & \sigma_1'' &= -\frac{1}{4}\mathsf{a}(1+\mathsf{a})\mathsf{c},\\
X_2'' &= \frac{1}{4}(-X_1 + X_2 - X_3 - X_4), & Y_2'' &= \frac{1}{4}(-Y_1 + Y_2 - Y_3 - Y_4), & \sigma_2'' &= \frac{1}{4}\mathsf{a}(1-\mathsf{a})\mathsf{c},\\
X_3'' &= \frac{1}{4}(X_1 + X_2 + X_3 - X_4), & Y_3'' &= \frac{1}{4}(Y_1 + Y_2 + Y_3 - Y_4), & \sigma_3'' &= \frac{1}{4}(1-\mathsf{a})\mathsf{c},\\
X_4'' &= \frac{1}{4}(X_1 + X_2 - X_3 + X_4), & Y_4'' &= \frac{1}{4}(Y_1 + Y_2 - Y_3 + Y_4), & \sigma_4'' &= \frac{1}{4}(1+\mathsf{a})\mathsf{c}.
\end{aligned} \tag{6.4.79}$$

6.4.5 Approximate Decomposition at Half-Filling: Odd Cluster Separation

In the half-filling regime $\bar{n} = \frac{1}{2}$, $\mathsf{c} = 0 = \mathsf{d}$ when r is odd, while

$$\mathsf{b} = \frac{\sin \pi \bar{n} r}{\pi \bar{n} r} = \frac{2}{\pi r}(-1)^{(r-1)/2}. \tag{6.4.80}$$

Keeping only the matrix elements to $O(r^{-1})$, we find that in the one-particle sector of ρ^c, the matrix elements (and their corresponding product of referencing operators) are

$$\langle 1000|\rho^c|0010\rangle = +\frac{1}{8}(1+\mathsf{a}^2)\mathsf{b}, \qquad K^\dagger_{10,a} K_{00,a} K^\dagger_{00,b} K_{10,b} = +c_0^\dagger c_1 c_1^\dagger c_r c_{r+1} c_{r+1}^\dagger; \tag{6.4.81a}$$

$$\langle 1000|\rho^c|0001\rangle = +\frac{1}{4}\mathsf{a}\mathsf{b}, \qquad K^\dagger_{10,a} K_{00,a} K^\dagger_{00,b} K_{01,b} = +c_0^\dagger c_1 c_1^\dagger c_r c_r^\dagger c_{r+1}; \tag{6.4.81b}$$

$$\langle 0100|\rho^c|0010\rangle = +\frac{1}{4}\mathsf{a}\mathsf{b}, \qquad K^\dagger_{01,a} K_{00,a} K^\dagger_{00,b} K_{10,b} = +c_0 c_0^\dagger c_1^\dagger c_r c_{r+1} c_{r+1}^\dagger; \tag{6.4.81c}$$

$$\langle 0100|\rho^c|0001\rangle = +\frac{1}{8}(1+\mathsf{a}^2)\mathsf{b}, \qquad K^\dagger_{01,a} K_{00,a} K^\dagger_{00,b} K_{01,b} = +c_0 c_0^\dagger c_1^\dagger c_r c_r^\dagger c_{r+1}; \tag{6.4.81d}$$

$$\langle 0010|\rho^c|1000\rangle = +\frac{1}{8}(1+\mathsf{a}^2)\mathsf{b}, \qquad K^\dagger_{00,a}K_{10,a}K^\dagger_{10,b}K_{00,b} = -c_0c_1c_1^\dagger c_r^\dagger c_{r+1}c_{r+1}^\dagger; \quad (6.4.81e)$$

$$\langle 0010|\rho^c|0100\rangle = +\frac{1}{4}\mathsf{ab}, \qquad K^\dagger_{00,a}K_{01,a}K^\dagger_{10,b}K_{00,b} = -c_0c_0^\dagger c_1c_r^\dagger c_{r+1}c_{r+1}^\dagger; \quad (6.4.81f)$$

$$\langle 0001|\rho^c|1000\rangle = +\frac{1}{4}\mathsf{ab}, \qquad K^\dagger_{00,a}K_{10,a}K^\dagger_{01,b}K_{00,b} = -c_0c_1c_1^\dagger c_rc_r^\dagger c_{r+1}^\dagger; \quad (6.4.81g)$$

$$\langle 0001|\rho^c|0100\rangle = +\frac{1}{8}(1+\mathsf{a}^2)\mathsf{b}, \qquad K^\dagger_{00,a}K_{01,a}K^\dagger_{01,b}K_{00,b} = -c_0c_0^\dagger c_1c_rc_r^\dagger c_{r+1}^\dagger, \quad (6.4.81h)$$

where $K_{n_0n_1,a}$ is the referencing operator associated with the occupation number basis state $|n_0n_1\rangle$ of cluster a, $K_{n_rn_{r+1},b}$ is the referencing operator associated with the occupation number basis state $|n_rn_{r+1}\rangle$ of cluster b, and a, b, c and d are the reduced two-point functions defined in (5.3.22).

In the two-particle sector, we find that

$$\langle 1100|\rho^c|1001\rangle = +\left[\frac{1}{4}-\frac{1}{8}(1+\mathsf{a}^2)\right]\mathsf{b}, \qquad K^\dagger_{11,a}K_{10,a}K^\dagger_{00,b}K_{01,b} = +c_0^\dagger c_0c_1^\dagger c_rc_r^\dagger c_{r+1}; \quad (6.4.82a)$$

$$\langle 1100|\rho^c|0110\rangle = -\left[\frac{1}{4}-\frac{1}{8}(1+\mathsf{a}^2)\right]\mathsf{b}, \qquad K^\dagger_{11,a}K_{01,a}K^\dagger_{00,b}K_{10,b} = -c_0^\dagger c_1^\dagger c_1c_rc_{r+1}c_{r+1}^\dagger; \quad (6.4.82b)$$

$$\langle 1001|\rho^c|1100\rangle = +\left[\frac{1}{4}-\frac{1}{8}(1+\mathsf{a}^2)\right]\mathsf{b}, \qquad K^\dagger_{10,a}K_{11,a}K^\dagger_{01,b}K_{00,b} = -c_0^\dagger c_0c_1c_rc_r^\dagger c_{r+1}^\dagger; \quad (6.4.82c)$$

$$\langle 1001|\rho^c|0011\rangle = +\left[\frac{1}{4}-\frac{1}{8}(1+\mathsf{a}^2)\right]\mathsf{b}, \qquad K^\dagger_{10,a}K_{00,a}K^\dagger_{01,b}K_{11,b} = +c_0^\dagger c_1c_1^\dagger c_rc_{r+1}^\dagger c_{r+1}; \quad (6.4.82d)$$

$$\langle 0110|\rho^c|1100\rangle = -\left[\frac{1}{4}-\frac{1}{8}(1+\mathsf{a}^2)\right]\mathsf{b}, \qquad K^\dagger_{01,a}K_{11,a}K^\dagger_{11,b}K_{00,b} = +c_0c_1^\dagger c_1c_r^\dagger c_{r+1}c_{r+1}^\dagger; \quad (6.4.82e)$$

$$\langle 0110|\rho^c|0011\rangle = -\left[\frac{1}{4}-\frac{1}{8}(1+\mathsf{a}^2)\right]\mathsf{b}, \qquad K^\dagger_{01,a}K_{00,a}K^\dagger_{10,b}K_{11,b} = -c_0c_0^\dagger c_1^\dagger c_r^\dagger c_rc_{r+1}; \quad (6.4.82f)$$

$$\langle 0011|\rho^c|1001\rangle = +\left[\frac{1}{4} - \frac{1}{8}(1+\mathsf{a}^2)\right]\mathsf{b}, \qquad K^\dagger_{00,a}K_{10,a}K^\dagger_{11,b}K_{01,b} = -c_0c_1c_1^\dagger c_r^\dagger c_{r+1}^\dagger c_{r+1}; \tag{6.4.82g}$$

$$\langle 0011|\rho^c|0110\rangle = -\left[\frac{1}{4} - \frac{1}{8}(1+\mathsf{a}^2)\right]\mathsf{b}, \qquad K^\dagger_{00,a}K_{01,a}K^\dagger_{11,b}K_{10,b} = +c_0c_0^\dagger c_1c_r^\dagger c_rc_{r+1}^\dagger. \tag{6.4.82h}$$

We suspect that the absolute $O(r^{-1})$ matrix elements in the two-particle sector of ρ^c are the same as a queer consequence of particle-hole symmetry in the half-filled chain of noninteracting spinless fermions.

In the three-particle sector, we find that

$$\langle 1110|\rho^c|1011\rangle = -\frac{1}{8}(1+\mathsf{a}^2)\mathsf{b}, \qquad K^\dagger_{11,a}K_{10,a}K^\dagger_{10,b}K_{11,b} = -c_0^\dagger c_0c_1^\dagger c_r^\dagger c_rc_{r+1}; \tag{6.4.83a}$$

$$\langle 1110|\rho^c|0111\rangle = -\frac{1}{4}\mathsf{ab}, \qquad K^\dagger_{11,a}K_{01,a}K^\dagger_{10,b}K_{11,b} = +c_0^\dagger c_1^\dagger c_1c_r^\dagger c_rc_{r+1}; \tag{6.4.83b}$$

$$\langle 1101|\rho^c|1011\rangle = -\frac{1}{4}\mathsf{ab}, \qquad K^\dagger_{11,a}K_{10,a}K^\dagger_{01,b}K_{11,b} = +c_0^\dagger c_0c_1^\dagger c_rc_{r+1}^\dagger c_{r+1}; \tag{6.4.83c}$$

$$\langle 1101|\rho^c|0111\rangle = -\frac{1}{8}(1+\mathsf{a}^2)\mathsf{b}, \qquad K^\dagger_{11,a}K_{01,a}K^\dagger_{01,b}K_{11,b} = -c_0^\dagger c_1^\dagger c_1c_rc_{r+1}^\dagger c_{r+1}; \tag{6.4.83d}$$

$$\langle 1011|\rho^c|1110\rangle = -\frac{1}{8}(1+\mathsf{a}^2)\mathsf{b}, \qquad K^\dagger_{10,a}K_{11,a}K^\dagger_{11,b}K_{10,b} = +c_0^\dagger c_0c_1c_r^\dagger c_rc_{r+1}^\dagger; \tag{6.4.83e}$$

$$\langle 1011|\rho^c|1101\rangle = -\frac{1}{4}\mathsf{ab}, \qquad K^\dagger_{10,a}K_{11,a}K^\dagger_{11,b}K_{01,b} = -c_0^\dagger c_0c_1c_r^\dagger c_{r+1}^\dagger c_{r+1}; \tag{6.4.83f}$$

$$\langle 0111|\rho^c|1110\rangle = -\frac{1}{4}\mathsf{ab}, \qquad K^\dagger_{01,a}K_{11,a}K^\dagger_{11,b}K_{10,b} = -c_0c_1^\dagger c_1c_r^\dagger c_rc_{r+1}^\dagger; \tag{6.4.83g}$$

$$\langle 0111|\rho^c|1101\rangle = -\frac{1}{8}(1+\mathsf{a}^2)\mathsf{b}, \qquad K^\dagger_{01,a}K_{11,a}K^\dagger_{11,b}K_{01,b} = +c_0c_1^\dagger c_1c_r^\dagger c_{r+1}^\dagger c_{r+1}. \tag{6.4.83h}$$

6.4.5.1 Grouping of Operator Expansion Terms

Redefining our three distinct matrix elements A, B and C in (6.4.27) to be

$$A = \frac{1}{4}\mathsf{ab}, \quad B = \frac{1}{8}(1+\mathsf{a}^2)\mathsf{b}, \quad C = \left[\frac{1}{4} - \frac{1}{8}(1+\mathsf{a}^2)\right]\mathsf{b}, \tag{6.4.84}$$

we write the correlation density matrix as

$$\begin{aligned}
\rho^c = \; &+ A \quad \Big[+ (c_0^\dagger c_{r+1} - c_0 c_{r+1}^\dagger)[(\mathbb{1} - n_1)(\mathbb{1} - n_r) - n_1 n_r] \\
&\qquad + (c_1^\dagger c_r - c_1 c_r^\dagger)[(\mathbb{1} - n_0)(\mathbb{1} - n_{r+1}) - n_0 n_{R+1}]\Big] \\
&+ B \quad \Big[+ (c_0^\dagger c_r - c_0 c_r^\dagger)[(\mathbb{1} - n_1)(\mathbb{1} - n_{r+1}) + n_1 n_{R+1}] \\
&\qquad + (c_1^\dagger c_{r+1} - c_1 c_{r+1}^\dagger)[(\mathbb{1} - n_0)(\mathbb{1} - n_r) + n_0 n_r]\Big] \\
&+ C \quad \Big[+ (c_0^\dagger c_r - c_0 c_r^\dagger)[n_1(\mathbb{1} - n_{r+1}) + (\mathbb{1} - n_1) n_{R+1}] \\
&\qquad + (c_1^\dagger c_{r+1} - c_1 c_{r+1}^\dagger)[n_0(\mathbb{1} - n_r) + (\mathbb{1} - n_0) n_r]\Big].
\end{aligned} \tag{6.4.85}$$

In terms of the operators introduced in (6.4.43), we find that this can be written as

$$\begin{aligned}
\rho^c = \; &+ A\Big[+ X_2 Y_2^\dagger - X_1 Y_1^\dagger + X_4 Y_4^\dagger - X_3 Y_3^\dagger\Big] \\
&+ B\Big[+ X_2 Y_4^\dagger + X_1 Y_3^\dagger + X_4 Y_2^\dagger + X_3 Y_1^\dagger\Big] \\
&+ C\Big[+ X_1 Y_4^\dagger + X_2 Y_3^\dagger + X_3 Y_2^\dagger + X_4 Y_1^\dagger\Big] + \text{h.c.} \\
= \; &\rho_A^c + \rho_B^c + \rho_C^c.
\end{aligned} \tag{6.4.86}$$

6.4.5.2 Partial Operator Singular Value Decomposition of $\rho_B^c + \rho_C^c$

When the intercluster separation is even, we found ρ_B^c looking like an inner product $\mathbf{X}^T\mathbf{Y}$, and so we left it alone while performing a partial singular value decomposition of $\rho_A^c + \rho_C^c$. Here, when the intercluster separation is odd, it is ρ_A^c that looks closest to being an inner product, even though the signs of the terms alternate. We leave it alone, and partial singular value decompose $\rho_B^c + \rho_C^c$, which is

$$\begin{aligned}
&+ BX_1 Y_3^\dagger \quad + BX_3 Y_1^\dagger \\
&+ CX_1 Y_4^\dagger \quad + CX_3 Y_2^\dagger \\
&+ CX_2 Y_3^\dagger \quad + CX_4 Y_1^\dagger \\
&+ BX_2 Y_4^\dagger \quad + BX_4 Y_2^\dagger + \text{h.c.},
\end{aligned} \tag{6.4.87}$$

instead. From the way we write $\rho_B^c + \rho_C^c$ in (6.4.87), we realized that there are two independent subgroups of terms, within which the indices $(1,2)$ and $(3,4)$ are mixed independently. To singular value decompose the first subgroup of operators, let us introduce the rotated operators

$$\begin{aligned} X_1' &= \alpha_1 X_1 - \beta_1 X_2, \quad Y_3' = \gamma_1 Y_3 - \delta_1 Y_4, \\ X_2' &= \beta_1 X_1 + \alpha_1 X_2, \quad Y_4' = \delta_1 Y_3 + \gamma_1 Y_4, \end{aligned} \tag{6.4.88}$$

or equivalently,

$$\begin{aligned} X_1 &= \alpha_1 X_1' + \beta_1 X_2', \quad Y_3 = \gamma_1 Y_3' + \delta_1 Y_4', \\ X_2 &= -\beta_1 X_1' + \alpha_1 X_2', \quad Y_4 = -\delta_1 Y_3' + \gamma_1 Y_4', \end{aligned} \tag{6.4.89}$$

so that

$$\begin{aligned} BX_1Y_3^\dagger + CX_1Y_4^\dagger + CX_2Y_3^\dagger + BX_2Y_4^\dagger = \; & + B(\alpha_1 X_1' + \beta_1 X_2')(\gamma_1 {Y_3'}^\dagger + \delta_1 {Y_4'}^\dagger) \\ & + B(-\beta_1 X_1' + \alpha_1 X_2')(-\delta_1 {Y_3'}^\dagger + \gamma_1 {Y_4'}^\dagger) \\ & + C(\alpha_1 X_1' + \beta_1 X_2')(-\delta_1 {Y_3'}^\dagger + \gamma_1 {Y_4'}^\dagger) \\ & + C(-\beta_1 X_1' + \alpha_1 X_2')(\gamma_1 {Y_3'}^\dagger + \delta_1 {Y_4'}^\dagger). \end{aligned} \tag{6.4.90}$$

If we demand that the coefficients of $X_1' {Y_3'}^\dagger$ and $X_2' {Y_4'}^\dagger$ both vanish, then we obtain

$$+ B\alpha_1\gamma_1 + B\beta_1\delta_1 - C\alpha_1\delta_1 - C\beta_1\gamma_1 = 0, \tag{6.4.91a}$$

$$+ B\beta_1\delta_1 + B\alpha_1\gamma_1 + C\beta_1\gamma_1 + C\alpha_1\delta_1 = 0. \tag{6.4.91b}$$

Again, by postponing normalization of the coefficients until the end, we can choose $\alpha_1 = 1 = \gamma_1$, to obtain the simplified system of equations

$$+ B + B\beta_1\delta_1 - C\delta_1 - C\beta_1 = 0, \tag{6.4.92a}$$

$$+ B\beta_1\delta_1 + B + C\beta_1 + C\delta_1 = 0. \tag{6.4.92b}$$

Subtracting the two equations, we find that

$$\beta_1 = \pm 1 = -\delta_1. \tag{6.4.93}$$

We can choose $\beta_1 = 1$, because choosing $\beta_1 = -1$ will give us an equivalent set of eigenvectors, and the same singular value. The normalized coefficients are therefore

$$\alpha_1 = \frac{1}{\sqrt{2}}, \quad \beta_1 = \frac{1}{\sqrt{2}}, \quad \gamma_1 = \frac{1}{\sqrt{2}}, \quad \delta_1 = -\frac{1}{\sqrt{2}}, \tag{6.4.94}$$

and the eigen-operators and their corresponding singular values are

$$\begin{aligned} X_1' &= \frac{1}{\sqrt{2}}(X_1 - X_2), \quad Y_4' = \frac{1}{\sqrt{2}}(-Y_3 + Y_4), \quad \sigma_1' = C - B, \\ X_2' &= \frac{1}{\sqrt{2}}(X_1 + X_2), \quad Y_3' = \frac{1}{\sqrt{2}}(Y_3 + Y_4), \quad \sigma_2' = C + B. \end{aligned} \tag{6.4.95}$$

Similarly, defining the rotated basis of operators

$$\begin{aligned} X_3' &= \alpha_3 X_3 - \beta_3 X_4, \quad Y_1' = \gamma_3 Y_1 - \delta_3 Y_2, \\ X_4' &= \beta_3 X_3 + \alpha_3 X_4, \quad Y_2' = \delta_3 Y_1 + \gamma_3 Y_2, \end{aligned} \tag{6.4.96}$$

or equivalently,

$$\begin{aligned} X_3 &= \alpha_3 X_3' + \beta_3 X_4', \quad Y_1 = \gamma_3 Y_1' + \delta_3 Y_2', \\ X_4 &= -\beta_3 X_3' + \alpha_3 X_4', \quad Y_2 = -\delta_3 Y_1' + \gamma_3 Y_2', \end{aligned} \tag{6.4.97}$$

and performing partial singular value decomposition on the second subgroup of operators, we find the eigen-operators and singular values

$$\begin{aligned} X_3' &= \frac{1}{\sqrt{2}}(X_3 - X_4), \quad Y_2' = \frac{1}{\sqrt{2}}(-Y_1 + Y_2), \quad \sigma_3' = C - B, \\ X_4' &= \frac{1}{\sqrt{2}}(X_3 + X_4), \quad Y_1' = \frac{1}{\sqrt{2}}(Y_1 + Y_2), \quad \sigma_4' = C + B. \end{aligned} \tag{6.4.98}$$

We can then check that under the basis transformation

$$\begin{aligned} X_1 &= \frac{1}{\sqrt{2}}(X_1' + X_2'), \quad Y_1 = \frac{1}{\sqrt{2}}(Y_1' - Y_2'), \\ X_2 &= \frac{1}{\sqrt{2}}(-X_1' + X_2'), \quad Y_2 = \frac{1}{\sqrt{2}}(Y_1' + Y_2'), \\ X_3 &= \frac{1}{\sqrt{2}}(X_3' + X_4'), \quad Y_3 = \frac{1}{\sqrt{2}}(-Y_3' + Y_4'), \\ X_4 &= \frac{1}{\sqrt{2}}(-X_3' + X_4'), \quad Y_4 = \frac{1}{\sqrt{2}}(Y_3' + Y_4'), \end{aligned} \tag{6.4.99}$$

the ρ_A^c has an invariant structure, i.e.

$$A(-X_1Y_1^\dagger + X_2Y_2^\dagger - X_3Y_3^\dagger + X_4Y_4^\dagger) = A(-X_1'Y_1'^\dagger + X_2'Y_2'^\dagger - X_3'Y_3'^\dagger + X_4'Y_4'^\dagger). \quad (6.4.100)$$

With this, we rewrite ρ^c as

$$\begin{aligned} \rho^c = \; & + A' \quad \left[- X_1'Y_1'^\dagger + X_2'Y_2'^\dagger - X_3'Y_3'^\dagger + X_4'Y_4'^\dagger \right] \\ & + B' \quad \left[+ X_3'Y_2'^\dagger + X_1'Y_4'^\dagger \right] \\ & + C \quad \left[+ X_2'Y_3'^\dagger + X_4'Y_1'^\dagger \right] + \text{h.c.}, \end{aligned} \quad (6.4.101)$$

where

$$A' = A, \quad B' = C - B, \quad C' = C + B. \quad (6.4.102)$$

6.4.5.3 Full Operator Singular Value Decomposition of ρ^c

To complete the operator singular value decomposition, we regroup the terms in ρ^c as

$$\begin{aligned} \rho^c = & - A'X_1'Y_1'^\dagger \quad + A'X_2'Y_2'^\dagger \\ & + B'X_1'Y_4'^\dagger \quad + C'X_2'Y_3'^\dagger \\ & + C'X_4'Y_1'^\dagger \quad + B'X_3'Y_2'^\dagger \\ & + A'X_4'Y_4'^\dagger \quad - A'X_3'Y_3'^\dagger + \text{h.c.}, \end{aligned} \quad (6.4.103)$$

making clear the two indicial groups which do not mix.

Looking at the first indicial group

$$- A'X_1'Y_1'^\dagger + B'X_1'Y_4'^\dagger + C'X_4'Y_1'^\dagger + A'X_4'Y_4'^\dagger, \quad (6.4.104)$$

we find that if we define the rotated double-primed operator basis

$$\begin{aligned} X_1'' &= \alpha_1'X_1' - \beta_1'X_4', \\ X_4'' &= \beta_1'X_1' + \alpha_1'X_4'; \\ Y_1'' &= \gamma_1'Y_1' - \delta_1'Y_4', \\ Y_4'' &= \delta_1'Y_1' + \gamma_1'Y_4' \end{aligned} \quad (6.4.105)$$

in terms of the primed operator basis, or, equivalently,

$$\begin{aligned} X_1' &= \alpha_1' X_1'' + \beta_1' X_4'', \\ X_4' &= -\beta_1' X_1'' + \alpha_1' X_4''; \\ Y_1' &= \gamma_1' Y_1'' + \delta_1' Y_4'', \\ Y_4' &= -\delta_1' Y_1'' + \gamma_1' Y_4'', \end{aligned} \tag{6.4.106}$$

then (6.4.104) becomes

$$\begin{aligned} &- A'(\alpha_1' X_1'' + \beta_1' X_4'')(\gamma_1' {Y_1''}^\dagger + \delta_1' {Y_4''}^\dagger) \\ &+ B'(\alpha_1' X_1'' + \beta_1' X_4'')(-\delta_1' {Y_1''}^\dagger + \gamma_1' {Y_4''}^\dagger) \\ &+ C'(-\beta_1' X_1'' + \alpha_1' X_4'')(\gamma_1' {Y_1''}^\dagger + \delta_1' {Y_4''}^\dagger) \\ &+ A'(-\beta_1' X_1'' + \alpha_1' X_4'')(-\delta_1' {Y_1''}^\dagger + \gamma_1' {Y_4''}^\dagger) \\ = &+ (-A'\alpha_1'\gamma_1' - B'\alpha_1'\delta_1' - C'\beta_1'\gamma_1' + A'\beta_1'\delta_1') X_1'' {Y_1''}^\dagger \\ &+ (-A'\alpha_1'\delta_1' + B'\alpha_1'\gamma_1' - C'\beta_1'\delta_1' - A'\beta_1'\gamma_1') X_1'' {Y_4''}^\dagger \\ &+ (-A'\beta_1'\gamma_1' - B'\beta_1'\delta_1' + C'\alpha_1'\gamma_1' - A'\alpha_1'\delta_1') X_4'' {Y_1''}^\dagger \\ &+ (-A'\beta_1'\delta_1' + B'\beta_1'\gamma_1' + C'\alpha_1'\delta_1' + A'\alpha_1'\gamma_1') X_4'' {Y_4''}^\dagger. \end{aligned} \tag{6.4.107}$$

Demanding that the coefficients of $X_1'' {Y_4''}^\dagger$ and $X_4'' {Y_1''}^\dagger$ both be zero, and choosing $\alpha_1' = 1 = \gamma_1'$ (where we will normalize $\alpha_1', \beta_1', \gamma_1'$ and δ_1' at the end), we obtain

$$-A'\delta_1' + B' - C'\beta_1'\delta_1' - A'\beta_1' = 0, \tag{6.4.108a}$$

$$-A'\beta_1' - B'\beta_1'\delta_1' + C' - A'\delta_1' = 0. \tag{6.4.108b}$$

Subtracting (6.4.108b) from (6.4.108a), we then find that

$$\beta_1'\delta_1' = -1. \tag{6.4.109}$$

Substituting (6.4.109) back into (6.4.108a), we find that

$$\beta_1' + \delta_1' = \frac{B' + C'}{A'}. \tag{6.4.110}$$

We can then combine (6.4.109) and (6.4.110) to obtain a quadratic equation

$$\beta_1'^2 - \frac{B' + C'}{A'}\beta_1' - 1 = 0 \tag{6.4.111}$$

for β_1', which we can solve to get

$$\beta_1' = \frac{B' + C'}{2A'} \pm \frac{1}{2}\sqrt{\left(\frac{B' + C'}{A'}\right)^2 + 4}. \tag{6.4.112}$$

Using (6.4.84) and (6.4.102), we find that

$$\frac{B' + C'}{A'} = \frac{1 - \mathsf{a}^2}{\mathsf{a}}, \tag{6.4.113}$$

and hence

$$\beta_1' = \frac{1 - \mathsf{a}^2}{2\mathsf{a}} \pm \frac{1 + \mathsf{a}^2}{2\mathsf{a}} = \frac{1}{\mathsf{a}}, -\mathsf{a}. \tag{6.4.114}$$

After normalization, we then find two sets of coefficients

$$\alpha_1' = \frac{\mathsf{a}}{\sqrt{1 + \mathsf{a}^2}}, \quad \beta_1' = \frac{1}{\sqrt{1 + \mathsf{a}^2}}, \quad \gamma_1' = \frac{1}{\sqrt{1 + \mathsf{a}^2}}, \quad \delta_1' = -\frac{\mathsf{a}}{\sqrt{1 + \mathsf{a}^2}}, \tag{6.4.115}$$

and

$$\alpha_1' = \frac{1}{\sqrt{1 + \mathsf{a}^2}}, \quad \beta_1' = -\frac{\mathsf{a}}{\sqrt{1 + \mathsf{a}^2}}, \quad \gamma_1' = \frac{\mathsf{a}}{\sqrt{1 + \mathsf{a}^2}}, \quad \delta_1' = \frac{1}{\sqrt{1 + \mathsf{a}^2}}. \tag{6.4.116}$$

For the first set of coefficients, we have the eigen-operators and singular values

$$\begin{aligned} X_1'' &= \frac{\mathsf{a}}{\sqrt{1 + \mathsf{a}^2}} X_1' - \frac{1}{\sqrt{1 + \mathsf{a}^2}} X_4', \\ Y_1'' &= \frac{1}{\sqrt{1 + \mathsf{a}^2}} Y_1' + \frac{\mathsf{a}}{\sqrt{1 + \mathsf{a}^2}} Y_4', \\ \sigma_1'' &= -\frac{1}{4}(1 + \mathsf{a}^2)\mathsf{b}; \end{aligned} \tag{6.4.117a}$$

$$\begin{aligned} X_4'' &= \frac{1}{\sqrt{1 + \mathsf{a}^2}} X_1' + \frac{\mathsf{a}}{\sqrt{1 + \mathsf{a}^2}} X_4', \\ Y_4'' &= -\frac{\mathsf{a}}{\sqrt{1 + \mathsf{a}^2}} Y_1' + \frac{1}{\sqrt{1 + \mathsf{a}^2}} Y_4', \\ \sigma_4'' &= 0, \end{aligned} \tag{6.4.117b}$$

whereas for the second set of coefficients, we have the eigen-operators and singular values

$$\begin{aligned} X_1'' &= \frac{1}{\sqrt{1+\mathsf{a}^2}}\, X_1' + \frac{\mathsf{a}}{\sqrt{1+\mathsf{a}^2}}\, X_4', \\ Y_1'' &= \frac{\mathsf{a}}{\sqrt{1+\mathsf{a}^2}}\, Y_1' - \frac{1}{\sqrt{1+\mathsf{a}^2}}\, Y_4', \end{aligned} \tag{6.4.118a}$$

$$\sigma_1'' = 0,$$

$$\begin{aligned} X_4'' &= -\frac{\mathsf{a}}{\sqrt{1+\mathsf{a}^2}}\, X_1' + \frac{1}{\sqrt{1+\mathsf{a}^2}}\, X_4', \\ Y_4'' &= \frac{1}{\sqrt{1+\mathsf{a}^2}}\, Y_1' + \frac{\mathsf{a}}{\sqrt{1+\mathsf{a}^2}}\, Y_4', \end{aligned} \tag{6.4.118b}$$

$$\sigma_4'' = \frac{1}{4}(1+\mathsf{a}^2)\mathsf{b}.$$

Up to a relabelling, we see that the eigen-operators and singular values for the two sets of coefficients are the same.

Turning our attention to the second indicial group, we see that we can make it look like the first indicial group if we identify the indicial correspondence

$$3 \leftrightarrow 1, \quad 2 \leftrightarrow 4. \tag{6.4.119}$$

Here let us remind the reader that the indices $\{1, 2, 3, 4\}$ are arbitrarily chosen labels for the four linearly-independent (with respect to the Frobenius inner product) operators which we can construct on cluster a (for $\{X_1, X_2, X_3, X_4\}$) and on cluster b (for $\{Y_1, Y_2, Y_3, Y_4\}$). These indices are not related in any way to the four sites within the (2 + 2) supercluster. In any case, with (6.4.119), we find that there is no need to go through the tedious calculations again for the indicial group $\{2, 3\}$. Based on what we have learnt for the $\{1, 4\}$ indicial group, we can simply write down the eigen-operators and singular values for the $\{2, 3\}$ indicial group as

$$X_3'' = \frac{\mathsf{a}}{\sqrt{1+\mathsf{a}^2}}\, X_3' - \frac{1}{\sqrt{1+\mathsf{a}^2}}\, X_2',$$

$$Y_3'' = \frac{1}{\sqrt{1+\mathsf{a}^2}}\, Y_3' + \frac{\mathsf{a}}{\sqrt{1+\mathsf{a}^2}}\, Y_2', \tag{6.4.120a}$$

$$\sigma_3'' = -\frac{1}{4}(1+\mathsf{a}^2)\mathsf{b};$$

$$X_2'' = \frac{1}{\sqrt{1+\mathsf{a}^2}}\, X_3' + \frac{\mathsf{a}}{\sqrt{1+\mathsf{a}^2}}\, X_2',$$

$$Y_2'' = -\frac{\mathsf{a}}{\sqrt{1+\mathsf{a}^2}}\, Y_3' + \frac{1}{\sqrt{1+\mathsf{a}^2}}\, Y_2', \tag{6.4.120b}$$

$$\sigma_2'' = 0,$$

Collecting the results from our calculations, we find then that the correlation density matrix for a half-filled chain of noninteracting fermions, for $(2+2)$ clusters at large odd separations, has a particularly simple structure. The only two nonzero singular values are degenerate, with value $-\frac{1}{4}(1+\mathsf{a}^2)\mathsf{b}$, and eigen-operators

$$\begin{aligned}
X_1'' &= \frac{1}{\sqrt{2(1+\mathsf{a}^2)}}\left[\mathsf{a}X_1 - \mathsf{a}X_2 - X_3 - X_4\right], \\
Y_1'' &= \frac{1}{\sqrt{2(1+\mathsf{a}^2)}}\left[Y_1 + Y_2 - \mathsf{a}Y_3 + \mathsf{a}Y_4\right]; \\
X_3'' &= \frac{1}{\sqrt{2(1+\mathsf{a}^2)}}\left[-X_1 - X_2 + \mathsf{a}X_3 - \mathsf{a}X_4\right], \\
Y_3'' &= \frac{1}{\sqrt{2(1+\mathsf{a}^2)}}\left[-\mathsf{a}Y_1 + \mathsf{a}Y_2 + Y_3 + Y_4\right],
\end{aligned} \tag{6.4.121}$$

or any linear combination between the double-primed indices 1 and 3.

As we have noted in the discussion right after (6.4.42), the eigen-operators X_1'', X_3'', Y_1'', Y_3'' are not unique when their singular values are degenerate. In this regime of a half-filled chain with odd intercluster separation, the overriding symmetry that we should make manifest is particle-hole symmetry. Therefore, we must form the appropriate linear combinations X_1''' and X_3''' of X_1'' and X_3'', and Y_1''' and Y_1''' of Y_1'' and Y_3'', so that the triple-primed operators transform as

$$X_1''' \to X_1'''^{\dagger}, \quad X_3''' \to -X_3'''^{\dagger}; \quad Y_1''' \to Y_1'''^{\dagger}, \quad Y_3''' \to -Y_3'''^{\dagger}, \tag{6.4.122}$$

under charge conjugation.

6.5 One-Dimensional Superconducting Ground State

6.5.1 BCS Ground State

6.5.1.1 The (1 + 1) Supercluster

For the (1 + 1) supercluster, we can write out the operator expansion of ρ^c of a one-dimensional BCS ground state as

$$\rho^c = -A(c_0c_0^\dagger - c_0^\dagger c_0)(c_rc_r^\dagger - c_r^\dagger c_r) + Bc_0^\dagger c_r - Bc_0c_r^\dagger - iCc_0^\dagger c_r^\dagger - iCc_0c_r, \tag{6.5.1}$$

where, recycling notations used for the noninteracting spinless fermions, the independent matrix elements are

$$A = |g_u|^2 - |h|^2, \quad B = g_v, \quad iC = h. \tag{6.5.2}$$

As with the case of the Fermi sea ground state, the A group of operators are already properly singular value decomposed. We need only focus on the B and C group of operators. It is easy to check that

$$\begin{aligned} &\frac{C-B}{2i}(c_0^\dagger + ic_0)(c_r^\dagger - ic_r) + \frac{C+B}{2i}(c_0^\dagger - ic_0)(c_r^\dagger + ic_r) \\ &= \frac{C-B}{2i}(c_0^\dagger c_r^\dagger - ic_0^\dagger c_r + ic_0c_r^\dagger + c_0c_r) + \frac{C+B}{2i}(c_0^\dagger c_r^\dagger + ic_0^\dagger c_r - ic_0c_r^\dagger + c_0c_r) \\ &= -iCc_0^\dagger c_r^\dagger + Bc_0^\dagger c_r - Bc_0c_r^\dagger - iCc_0c_r. \end{aligned} \tag{6.5.3}$$

Therefore, the proper singular value decomposition of ρ^c is

$$\rho^c = \sigma_1 X_1 Y_1^\dagger + \sigma_2 X_2 Y_2^\dagger + \sigma_3 X_3 Y_3^\dagger, \tag{6.5.4}$$

where the eigen-operators and singular values are

$$\begin{aligned} X_1 &= \frac{1}{\sqrt{2}}(c_0^\dagger - ic_0), & Y_1 &= \frac{1}{\sqrt{2}}(c_r^\dagger + ic_r), & \sigma_1 &= B + C; \\ X_2 &= \frac{1}{\sqrt{2}}(c_0^\dagger + ic_0), & Y_2 &= \frac{1}{\sqrt{2}}(c_r^\dagger - ic_r), & \sigma_2 &= B - C; \\ X_3 &= \frac{1}{\sqrt{2}}(c_0c_0^\dagger - c_0^\dagger c_0), & Y_3 &= \frac{1}{\sqrt{2}}(c_rc_r^\dagger - c_r^\dagger c_r), & \sigma_3 &= -2A. \end{aligned} \tag{6.5.5}$$

It is straightforward to check that the X_l's are orthogonal to each other and the $Y_{l'}$'s are orthogonal to each other. In contrast to the Fermi sea ground state, the operators X_1 and X_2 arising from the singular value decomposition are not bare operators, but Bogoliubov-Valatin operators.

More importantly, from our results in Section 5.4.1.4, we know that

$$g_u(r) \sim \frac{\exp(-\kappa r)}{\sqrt{r}}, \quad g_v(r) \sim \frac{\exp(-\kappa r)}{\sqrt{r}}, \quad h(r) \sim \frac{\exp(-\kappa r)}{\sqrt{r}}, \tag{6.5.6}$$

and thus at large separations $r \to \infty$, the asymptotic behaviours of the singular values are

$$\sigma_1 \sim \frac{\exp(-\kappa r)}{\sqrt{r}}, \quad \sigma_2 \sim \frac{\exp(-\kappa r)}{\sqrt{r}}, \tag{6.5.7}$$

while σ_3 decays with r faster than $\exp(-2\kappa r)/r$. This tells us that the Bogoliubov-Valatin-type order parameters X_1, X_2 and Y_1, Y_2 are the most important at large separations.

6.5.1.2 The (2 + 2) Supercluster

I did not have time then to complete this calculation, and it looks like I will never have the time to do so while trying to complete this thesis. Someone interested in doing analytical singular value decomposition will have to do this calculation, as well as that for the particle-number-projected BCS ground state.

CHAPTER 7

LONG-RANGE ORDERS IN A LUTTINGER LIQUID

7.1 A Quick Guide to Chapter 7

Chapter 7 is interesting in two ways: (i) as preparatory material for Chapter 8, where we analyze the order parameters coming out from the ground-state correlation density matrix for an interacting model of spinless fermions; and (ii) in its own right, as a chapter on the exact solution of strongly-interacting spinless fermions on ladder systems, by mapping them to noninteracting spinless fermions in one dimension. We imagine that the readers of this chapter will be divided along similar lines, where we have a first group interested in seeing the method of operator singular value decomposition of the correlation density matrix put into practice numerically, and a second group interested in the analytical tools developed, as well as the analytical results obtained, in this Chapter.

For the first group of readers, Chapter 7 carries on from where Chapters 5 and 6 left off, where we supply further theoretical background, in particular, on the various order parameters known to be important in the ground state of interacting one-dimensional chains and ladder systems, for the numerical studies in Chapter 8. As we will be working exclusively with two-legged ladder systems, which are quasi-one-dimensional, it is important to first have a sense of the Luttinger-liquid physics of one-dimensional interacting systems. I review this in Section 7.2, so that we understand what order parameters to expect from our exactly-diagonalized interacting ground states. Readers familiar with the physics of Tomonaga-Luttinger and Luther-Emery liquids, in particular those from the second group, should skip the extensive review in Section 7.2 and proceed to Section 7.3, where I describe the extended Hubbard model (7.3.1) of strongly-interacting spinless fermions, augmented to incorporate correlated hops. Correlated hops favor-

ing superconducting correlations are introduced, so that, apart from the filling fraction $\bar{n}$ and the anisotropy t_y/t_x of nearest-neighbor hops, we have another tunable parameter, the ratio t'/t_x of correlated-hopping to nearest-neighbor-hopping matrix elements, to play with.

In Section 7.3, I will also briefly review three limiting cases for the model given in (7.3.1), for which we have good analytical understanding. This serves as a road map to Sections 7.5, 7.6 and 7.7 in this chapter for both group of readers, which we imagine will part company at this point in the chapter. Readers from the first group, whose chief interest is getting to the numerical results in Chapter 8, is expected to gain enough information from Section 7.3.2 to go directly to Chapter 8, without having the need to first go through the lengthy Sections 7.5, 7.6 and 7.7, where these three limiting cases are elucidated at length. Readers from the second group, whose chief interest is in learning how the analytical results in Sections 7.5, 7.6 and 7.7 are obtained, are invited to read through these sections leisurely, and thereafter move on to Chapter 8 if they are also interested in the numerical results there.

7.2 The Physics of Tomonaga-Luttinger and Luther-Emery Liquids

Interacting one-dimensional spinfull fermion systems fall into two universality classes. When the relevant interactions are repulsive in nature, the long-wavelength, low-energy behaviour are those of the Tomonaga-Luttinger liquid [225,226], whereas if the relevant interactions are attractive in nature, the interacting fermion system behaves like a Luther-Emery liquid [227,228]. In both cases, there is separation of the charge and spin degrees of freedom. The charge excitations, called *holons*, are gapless in both the Tomonaga-Luttinger and Luther-Emery liquids, whereas the spin excitations, called *spinons*, are gapless in the former and gapped in the latter.

In the Tomonaga-Luttinger and Luther-Emery liquid ground states, various theoretical approaches (see review by Sólyom [229]) tell us that the $2k_F$ and $4k_F$ charge density waves (CDW), $2k_F$ spin density wave (SDW), singlet superconductivity (SSC) and triplet superconductivity (TSC) are the most important long-range correlations. In a Tomonaga-Luttinger liquid, all these correlations decay as power laws, whereas in a Luther-Emery liquid, the CDW and SSC correlations decay as power laws while the SDW and TSC correlations decay exponentially, as a result of the gapped spinon spectrum.

These asymptotic power laws, where they occur, are written for the charge density $n(r)$, the spin density $\boldsymbol{\sigma}(r)$, the singlet pairing operator $\Delta_{0,0}(r)$, and the triplet pairing operator $\Delta_{1,m=0,\pm1}(r)$, as [229–231]

$$\langle n(0)n(r)\rangle = \frac{K_\rho}{\pi^2 r^2} + A_2 r^{-K_\rho - K_\sigma}\cos 2k_F r + A_4 r^{-4K_\rho}\cos 4k_F r, \tag{7.2.1a}$$

$$\langle \sigma_x(0)\sigma_x(r)\rangle = \langle \sigma_y(0)\sigma_y(r)\rangle = \frac{B_{0,xy}}{r^2} + B_{2,xy} r^{-K_\rho - K_\sigma^{-1}}\cos 2k_F r, \tag{7.2.1b}$$

$$\langle \sigma_z(0)\sigma_z(r)\rangle = \frac{B_{0,z}}{r^2} + B_{2,z} r^{-K_\rho - K_\sigma}\cos 2k_F r, \tag{7.2.1c}$$

$$\langle \Delta^\dagger_{0,0}(0)\Delta_{0,0}(r)\rangle = \langle \Delta^\dagger_{1,0}(0)\Delta_{1,0}(r)\rangle = D_0 r^{-K_\rho^{-1} - K_\sigma}, \tag{7.2.1d}$$

$$\langle \Delta^\dagger_{1,\pm1}(0)\Delta_{1,\pm1}(r)\rangle = D_0' r^{-K_\rho^{-1} - K_\sigma^{-1}} \tag{7.2.1e}$$

in terms of the density and spin stiffness constants K_ρ and K_σ respectively. Equivalently, the correlation exponents can be written in terms of the exponents

$$\begin{aligned} \gamma_\rho &= \tfrac{1}{8}(K_\rho + K_\rho^{-1} - 2), \\ \gamma_\sigma &= \tfrac{1}{8}(K_\sigma + K_\sigma^{-1} - 2) \end{aligned} \tag{7.2.2}$$

appearing in the quantum-mechanical propagator. The equal-time quantum-mechanical propagator, also called the (equal-time) two-point function, thus have a power-law decay of the form $G(r) \sim r^{-\nu}$, where

$$\nu = 1 + 2\sum_{\lambda=\rho,\sigma} \gamma_\lambda, \tag{7.2.3}$$

i.e.

$$G(r) \sim r^{-\frac{1}{4}\left[(K_\rho + K_\rho^{-1}) + (K_\sigma + K_\sigma^{-1})\right]}. \tag{7.2.4}$$

The parameters K_ρ and K_σ (or γ_ρ and γ_σ, equivalently) depends generically on the filling fraction and the interaction strength, and thus the correlation exponents are non-universal.

For spinless fermions, there is only one independent stiffness constant $K_\rho = K_\sigma = K$ [231, 232], so that the spinfull power laws which have proper spinless analogs simplify to

$$G(r) = C_1 r^{-\frac{1}{2}\left(K + K^{-1}\right)} \cos k_F r, \tag{7.2.5a}$$

$$\langle n(0)n(r)\rangle = \frac{K}{\pi r^2} + A_2 r^{-2K} \cos 2k_F r + A_4 r^{-4K} \cos 4k_F r. \tag{7.2.5b}$$

Another simplification to the form of the power laws occurs when the chain of interacting spinfull fermions is spin-rotation invariant. This happens, for example, when the chain is not subjected to an external magnetic field. When spin-rotation symmetry is present, the spin stiffness constant must be $K_\sigma = 1$, and the ground-state properties become completely determined by the single nontrivial Luttinger parameter K_ρ. The spinfull power laws thus become

$$G(r) = C_1 r^{-\frac{1}{4}\left(K_\rho + K_\rho^{-1} + 2\right)} \cos k_F r, \tag{7.2.6a}$$

$$\langle n(0)n(r)\rangle = \frac{K_\rho}{\pi r^2} + A_2 r^{-K_\rho - 1} \cos 2k_F r + A_4 r^{-4K_\rho} \cos 4k_F r, \tag{7.2.6b}$$

$$\langle \boldsymbol{\sigma}(0) \cdot \boldsymbol{\sigma}(r)\rangle = \frac{1}{\pi r^2} + B_2 r^{-K_\rho - 1} \cos 2k_F r, \tag{7.2.6c}$$

$$\langle \Delta_0^\dagger(0)\Delta_0(r)\rangle = \langle \Delta_1^\dagger(0)\Delta_1(r)\rangle = A r^{-K_\rho^{-1} - 1}. \tag{7.2.6d}$$

For a Fermi liquid, which is a special case, we have $K_\rho = 1$, so that the two-point function decays as r^{-1}, while both the CDW and SC correlations decay as r^{-2}. Through more detailed analysis of the RG equations, the CDW and SDW correlations are found

to contain logarithmic corrections [233, 234]

$$\langle n(0)n(r)\rangle = \frac{K_\rho}{\pi r^2} + A_2 r^{-K_\rho - 1} \log^{-\frac{3}{2}} r \cos 2k_F r + A_4 r^{-4K_\rho} \cos 4k_F r, \tag{7.2.7a}$$

$$\langle \boldsymbol{\sigma}(0) \cdot \boldsymbol{\sigma}(r)\rangle = \frac{1}{\pi r^2} + B_2 r^{-K_\rho - 1} \log^{\frac{1}{2}} r \cos 2k_F r. \tag{7.2.7b}$$

7.2.1 The One-Dimensional Hubbard Model

The one-dimensional Hubbard model, described by the Hamiltonian

$$H_{tU} = -t \sum_{i,\sigma} \left(c^\dagger_{i,\sigma} c_{i+1,\sigma} + c^\dagger_{i+1,\sigma} c_{i,\sigma} \right) + U \sum_i n_{i,\uparrow} n_{i,\downarrow}, \quad n_{i,\sigma} = c^\dagger_{i,\sigma} c_{i,\sigma}, \tag{7.2.8}$$

was solved exactly for all filling fractions $\bar{n}$ and scaled parameters U/t [235–237]. Spin-charge separation is manifest in the structure of the exact analytical ground-state wave function. At half-filling, $\bar{n} = 1$, the holon spectrum is gapped, and the ground state is an insulating antiferromagnet. Away from half-filling, renormalization-group and bosonization analysis [228, 229, 234, 238, 239] tells us that the ground state is a Tomonaga-Luttinger liquid for repulsive on-site interactions ($U > 0$), and is a Luther-Emery liquid for attractive on-site interactions ($U < 0$). Numerical calculations using Quantum Monte Carlo [240–242] and exact diagonalization [240, 243] provide further evidence to the non-Fermi liquid ground-state behaviour of the one-dimensional Hubbard model, when $|U| \neq 0$.

To flesh out the phase diagram of the one-dimensional Hubbard model, one need to determine the quantum phase of the ground state for any given value of $\bar{n}$ and U/t. This is not a straightforward matter, because it is generally difficult to evaluate correlation functions directly from the exact analytical ground-state wave function, and hence decide which order parameter has the most dominant correlations. The theory of conformal invariance tells us that the universality class of a conformal-invariant quantum

system is completely determined by the central charge of its underlying Virasoro algebra [244]. Consequently, the asymptotic behaviour of ground-state correlation functions and the finite-size corrections to the ground-state energy are related [245, 246]. Therefore, by calculating (analytically or numerically) the ground-state energy of a sequence of finite systems, and looking at how it scales with system size, one can calculate the correlation exponents without evaluating a single correlation function.

It turns out that the method of finite-size scaling depends only upon the structure of the Hilbert space, not on the conformal invariance of the model it is applied to, and thus can also be applied to non-conformal-invariant models. Therefore, the method of finite-size scaling can be used on the one-dimensional Hubbard model, which is not conformal-invariant, because the holon Fermi velocity v_c and the spinon Fermi velocity v_s are different, but has the same Hilbert space structure as a conformal field theory with $v_c = v_s$ [247]. Using the method of finite-size scaling [248–251] or otherwise [234, 238, 241, 242, 252, 253], the correlation exponents are calculated analytically and numerically over the entire phase diagram of the one-dimensional Hubbard model.

A related model exhibiting Tomonaga-Luttinger/Luther-Emery liquid physics, the one-dimensional extended Hubbard model, described by the Hamiltonian

$$\begin{aligned} H_{tUV} &= -t \sum_{i,\sigma} \left(c^\dagger_{i,\sigma} c_{i+1,\sigma} + c^\dagger_{i+1,\sigma} c_{i,\sigma} \right) + U \sum_i n_{i,\uparrow} n_{i,\downarrow} + V \sum_i n_i n_{i+1} \\ &= H_{tU} + V \sum_i n_i n_{i+1}, \end{aligned} \tag{7.2.9}$$

where $n_{i,\sigma} = c^\dagger_{i,\sigma} c_{i,\sigma}$, and $n_i = \sum_\sigma n_{i,\sigma}$, and its spinless analog, are not integrable, except in the strong-coupling limit of $U/t \to \infty$, and when $U = -2V < 0$. In the strong-coupling limit, we can use the Jordan-Wigner transformation to map the model to the spin-$\frac{1}{2}$ XXZ spin chain, which was solved by Luther and Peschel [232]. When $U = -2V < 0$, the model can be mapped to the exactly solvable two-flavor Gross-Neveu

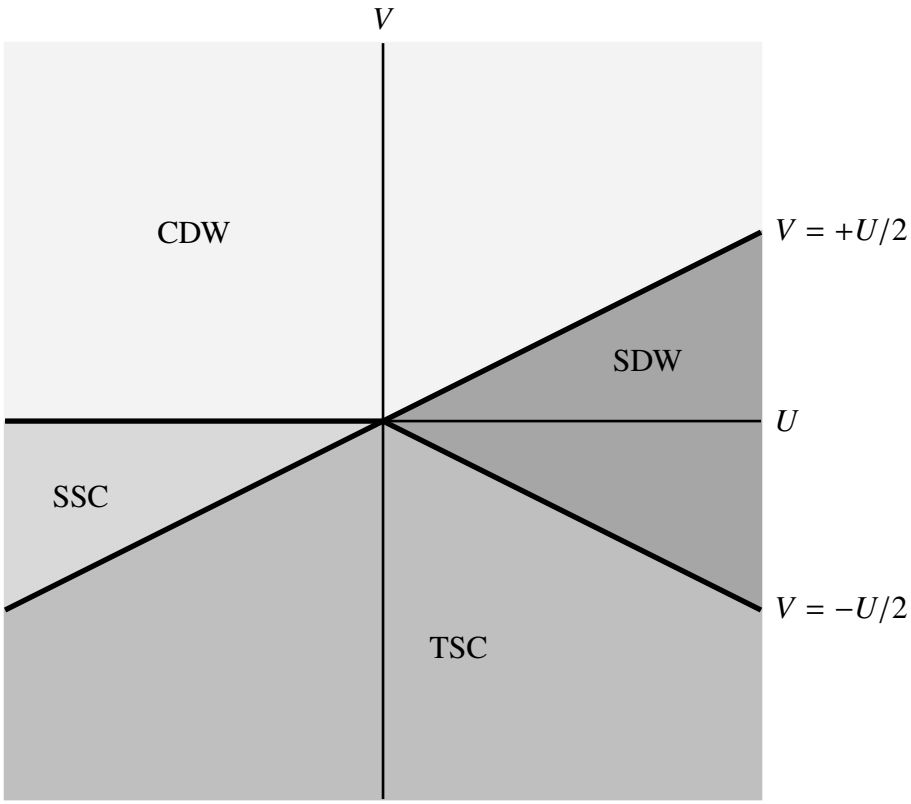

Figure 7.1: Ground-state phase diagram of the one-dimensional extended Hubbard model, obtained using weak-coupling renormalization-group analysis. Phase separation is believed to occur for very negative V.

model. Away from these two limits, numerical calculation of response functions [124–126, 254–256] and perturbation theory and bosonization calculations [234, 257] helped determine the phase diagram shown in Figure 7.1.

7.2.2 The One-Dimensional *t*-*J* Model

The one-dimensional *t*-*J* model, is described by the Hamiltonian,

$$H_{tJ} = -t \sum_{i,\sigma} \left(\breve{c}^{\dagger}_{i,\sigma} \breve{c}_{i+1,\sigma} + \breve{c}^{\dagger}_{i+1,\sigma} \breve{c}_{i,\sigma} \right) + J \sum_{i} \left(\mathbf{S}_i \cdot \mathbf{S}_{i+1} - \tfrac{1}{4} n_i n_{i+1} \right), \tag{7.2.10}$$

where

$$\breve{c}_{i,\sigma} = c_{i,\sigma}(1 - n_{i,-\sigma}), \quad \mathbf{S}_i = c^{\dagger}_{i,\alpha} \, (\boldsymbol{\sigma}/2)_{\alpha\beta} \, c_{i,\beta}, \quad n_i = c^{\dagger}_{i,\uparrow} c_{i,\uparrow} + c^{\dagger}_{i,\downarrow} c_{i,\downarrow} \tag{7.2.11}$$

are the projected electron operator, spin-$\frac{1}{2}$ operator, and electron number at site i, respectively. This model is exactly solvable only in the supersymmetric limit $J = 2t$ [258–263], and the ground state was found to be a Tomonaga-Luttinger liquid. The ground state is also a Tomonaga-Luttinger liquid in the limit of $J/t \to 0$, because the *t*-*J* model is equivalent to the $U/t \to \infty$ Hubbard model to first order in perturbation theory [241].

In the $J/t \to 0$ limit, the correlation exponents of the one-dimensional *t*-*J* model are those of the $U/t \to \infty$ one-dimensional Hubbard model, whereas in the $J/t = 2$ supersymmetric limit, the correlation exponents can be found from the exact Bethe ansatz solutions using the method of finite-size scaling [264–267], from which we know that the SDW correlations is dominant. Elsewhere on the phase diagram, the nature of the ground state and correlation functions have to be determined numerically. Through the use of exact diagonalization, Quantum Monte Carlo and DMRG [117, 118, 144, 240, 268–279], as well as variational calculations [280–283], the ground state of the one-dimensional *t*-*J* model was found to be a Tomonaga-Luttinger liquid,

with SDW correlations dominant at long distances, in most parts of the phase diagram shown in Figure 7.2.

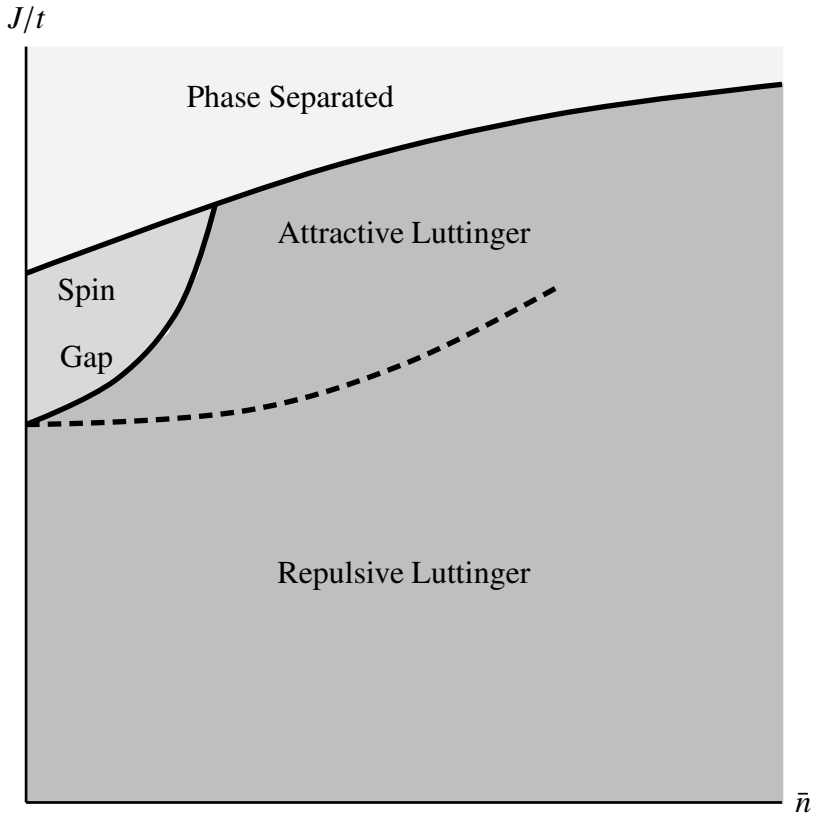

Figure 7.2: Ground-state phase diagram of the one-dimensional t-J model, obtained from variational calculations.

At large J/t, phase separation into an electron-rich phase and a hole-rich phase occurs, and superconducting order is enhanced in the vicinity of the phase-separation line, within a narrow spin-gapped Luther-Emery liquid phase at low filling fractions [117, 144, 240, 270, 271, 273, 280, 283–285]. SSC and TSC correlations are also enhanced by hole doping the one-dimensional t-J model away from half-filling, though they never become more dominant than the $2k_F$ CDW [264, 265, 268]. Using the two-dimensional argument presented by Emery, Kivelson and Lin [286,287], it is argued that phase separation occurs generically for t-J-like models. Indeed, phase separation also

occur in the t-J-J' model [288], the t-J-V model [277, 289] and the t-t_3-J model with three-site correlated hopping term (which occurs if the t-J model is derived from the Hubbard model) [278]. The picture that emerges from these studies on one-dimensional systems is that as the interaction range becomes larger, either by direct coupling between distant sites, or by allowing long-range hoppings, the phase separation line shifts to higher and higher J/t, and in some cases disappears altogether, giving a phase diagram like that of the one-dimensional Hubbard model. The spin-gapped Luther-Emery liquid phase with enhanced superconducting correlations was also found in the vicinity of the phase separation line in the t-J-V model, at finite $V > 0$ [277, 289].

7.2.3 The Hubbard and t-J Ladders

7.2.3.1 Coupled Luttinger Chains

After the Tomonaga-Luttinger/Luther-Emery liquid behaviour of one-dimensional models of spinless and spin-$\frac{1}{2}$ fermions become well understood, the question naturally arises of whether spin-charge separation occurs if the fermion is endowed with more internal degrees of freedom [290]. This is relevant to the study of ladder systems, for example, as a spin-$\frac{N}{2}$ chain can always be written as a spin-$\frac{1}{2}$ N-legged ladder with the appropriate interactions. This soon led to the study of coupled Luttinger chains of spinless and spinfull fermions [291–300]. The growing interest in understanding the behaviour of coupled chains of itinerant interacting fermions is due in part to the discovery that the ground state of an odd number of coupled spin-$\frac{1}{2}$ Heisenberg chains is gapless, while that of an even number of coupled spin-$\frac{1}{2}$ Heisenberg chains is gapped [301–313] (see Ref. 314 for a review), which is borne out experimentally [315, 316]. When the spin excitations are gapless, we expect to end up with a Tomonaga-Luttinger liquid ground state, where CDW correlations dominate SC correlations at large distances. When the

spin excitations are gapped, then singlet-to-triplet excitations are suppressed, and the fermions are more likely to stay bound as singlet pairs. This pairing tendency is expected to enhance SC correlations relative to CDW correlations [298], and thus a thorough understanding of the possible mechanisms of superconductivity in itinerant ladder systems (which are experimentally realizable [317–320]) might provide the insight needed to solve the outstanding problem of high-temperature superconductivity.

From bosonization and renormalization-group analysis, the low-energy behaviour of two weakly-coupled Tomonaga-Luttinger liquids with only forward scattering is characterized by two gapless modes and two gapped modes, one of which is critical and Ising-like, and whose correlations decay as a power law instead of exponentially [300]. For repulsive density-density interactions, the two gapless modes are identified as the out-of-phase CDW and SDW, whereas the in-phase CDW decays exponentially. In this regime, both singlet and triplet pairing correlations were found to be decay as power laws at large distances, with exponents more negative than those for the out-of-phase CDW and SDW. For attractive density-density interactions, the SSC correlation dominates at large distances, while the orbital antiferromagnetic and spin nematic correlations also decay with power laws with more negative exponents. When backscattering is introduced, all spin excitations develop a gap, and SC correlations dominate at large distances even for purely repulsive interactions.

7.2.3.2 Hubbard Ladders

Ladders are chains that are coupled spatially in a very specific way. As shown in Figure 7.3, the one-dimensional chains are called the *legs* of the ladder, whereas the links between the legs are called the *rungs*. When putting the Hubbard model on such ladder systems, we can have different hopping amplitudes $t_{\parallel}$ along the legs and $t_{\perp}$ along the

rungs. The nearest neighbor interactions $V_{\parallel} n_{i,j} n_{i,j\pm1}$ within a leg and $V_{\perp} n_{i,j} n_{i\pm1,j}$ across a rung can also be different in the extended Hubbard model. For the t-J model on a ladder system, the exchange interaction $J_{\parallel} \mathbf{S}_{i,j} \cdot \mathbf{S}_{i,j\pm1}$ along a leg need not be the same as $J_{\perp} \mathbf{S}_{i,j} \cdot \mathbf{S}_{i\pm1,j}$ across a rung.

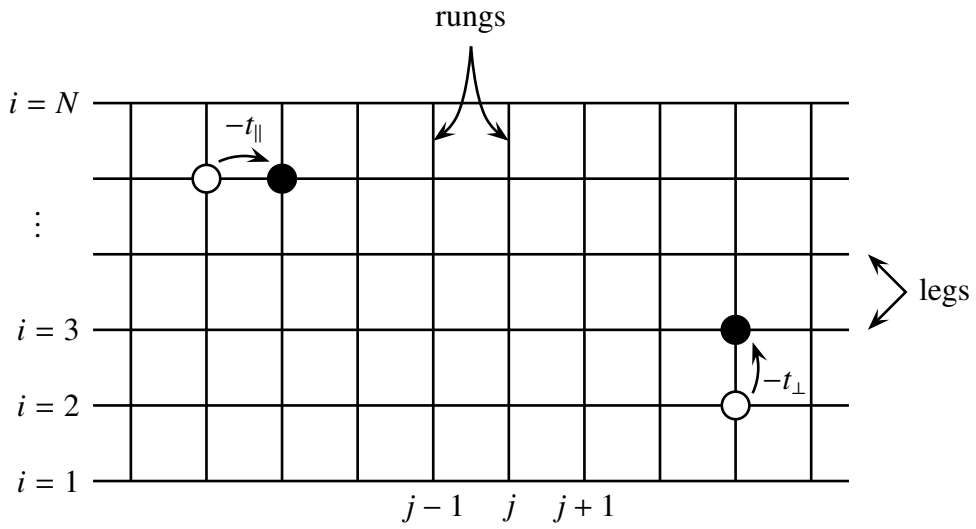

Figure 7.3: An N-legged ladder. In this diagram, we also show the matrix elements $-t_{\parallel}$ and $-t_{\perp}$ of nearest-neighbor hops along the legs and rungs of the ladder respectively.

With the aid of bosonization and renormalization-group analysis, the weak-coupling phase diagram of N-legged Hubbard ladders were determined. For the purpose of labeling the quantum phases, Balents and Fisher introduced the notation CxSy, where x and y are the number of gapless charge and gapless spin modes respectively [321]. In this notation, a one-band Tomonaga-Luttinger liquid is C1S1 and a two-band Tomonaga-Luttinger liquid is C2S2. For weak coupling $U \to 0^+$, it is physically meaningful to talk about N Tomonaga-Luttinger liquid bands. For large $t_{\perp} > N t_{\parallel}$, all the bands are well separated, and the ground state is a C0S0 insulator whenever the filling fraction is such that some of the bands are completely filled and the rest completely empty. When

the system is hole-doped away from these special filling fractions, the system becomes a one-band Tomonaga-Luttinger liquid, C1S1. For $t_\perp < Nt_\parallel$, the bands overlap over some range of energies, and when the Fermi energy lies within this range, the situation becomes more complicated. From renormalization-group analysis aided by numerical integration of the flow equations, the phase diagrams of the two-, three- and four-legged Hubbard ladders are obtained [293, 321–330]. These are shown in Figure 7.4, Figure 7.5, and Figure 7.6 respectively.

In the quantum phases with gapless charge excitations, the dominant superconducting correlations is found to be d-wave-like [321, 326, 327, 329]. This d-wave character of the superconducting correlations were also observed numerically [331–336]. More interestingly, from various analytical and numerical studies, the spin gap, expected to be present [337] for even-legged, half-filled Hubbard ladders from the study of Heisenberg spin ladders, persists under light doping [300, 312, 321–324, 329, 333, 334, 338–345]. Unlike for Heisenberg spin ladders, gapless and gapped spin excitations were found to co-exist in odd-legged Hubbard ladders [325, 328, 346]. From numerical studies at finite U, it was found that superconducting correlations are subdominant in the spin-gapped phase, and are the strongest where the spin gap is at its maximum [331, 332, 345, 347–350].

More recently, the phase diagram of the spinless and spinfull two-legged extended Hubbard ladder was studied [323, 351–356]. The spinless model can be mapped onto a spin-$\frac{1}{2}$ chain, where $t_\perp$ plays the role of a magnetic field, and its phase diagram determined and understood therefrom. The spinfull model can also be mapped onto a spin-$\frac{1}{2}$ chain with two flavors of fermions. At quarter-filling $\bar{n} = \frac{1}{2}$, it was found that both charge and spin excitations are gapped. Away from the special fillings, the weak-coupling phase diagram consists of four phases. In the limit of large on-site repulsion U, we have Phase

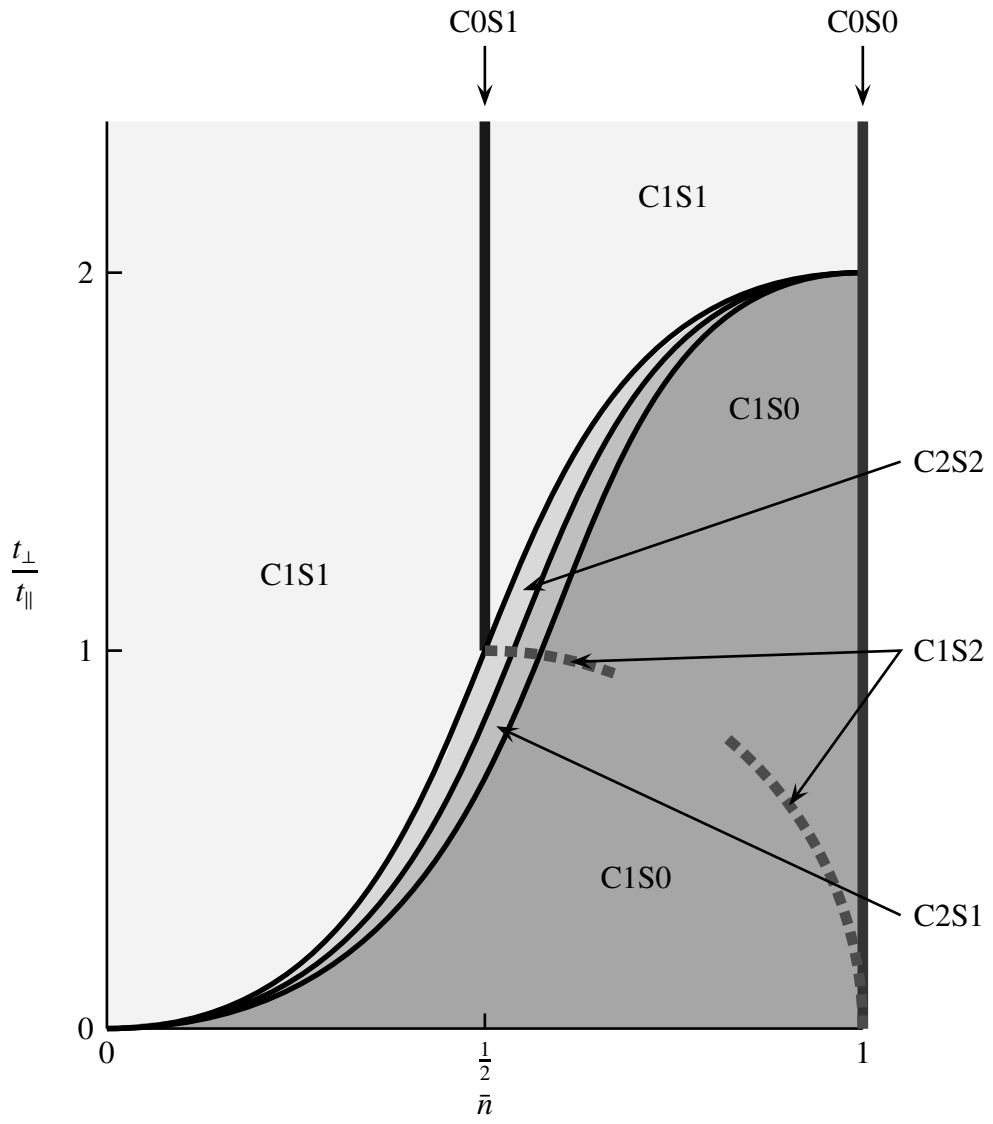

Figure 7.4: Ground-state phase diagram of the two-legged Hubbard ladder, obtained using weak-coupling renormalization-group analysis. Out of the nine possible quantum phases ($x = 0, 1, 2$ and $y = 0, 1, 2$), seven are realized in this model.

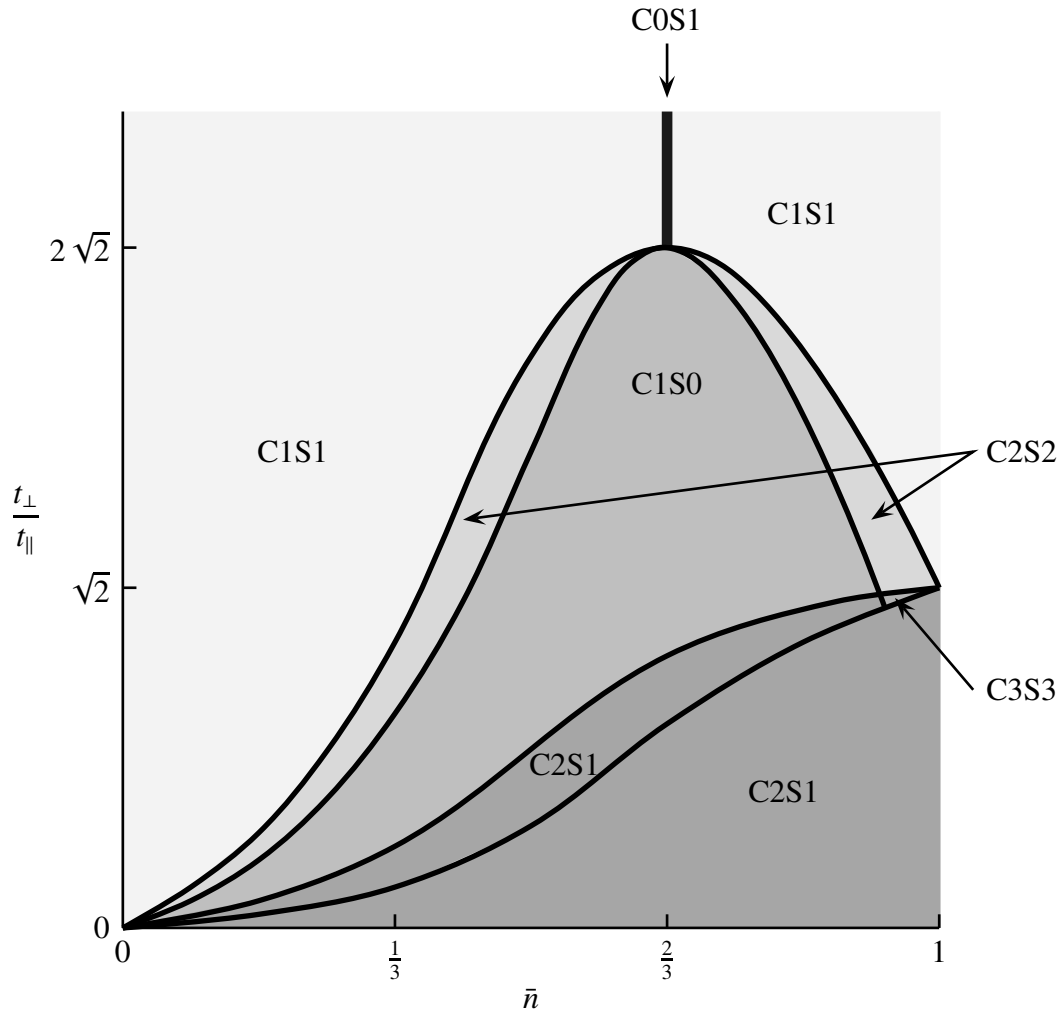

Figure 7.5: Ground-state phase diagram of the three-legged Hubbard ladder, obtained using weak-coupling renormalization-group analysis.

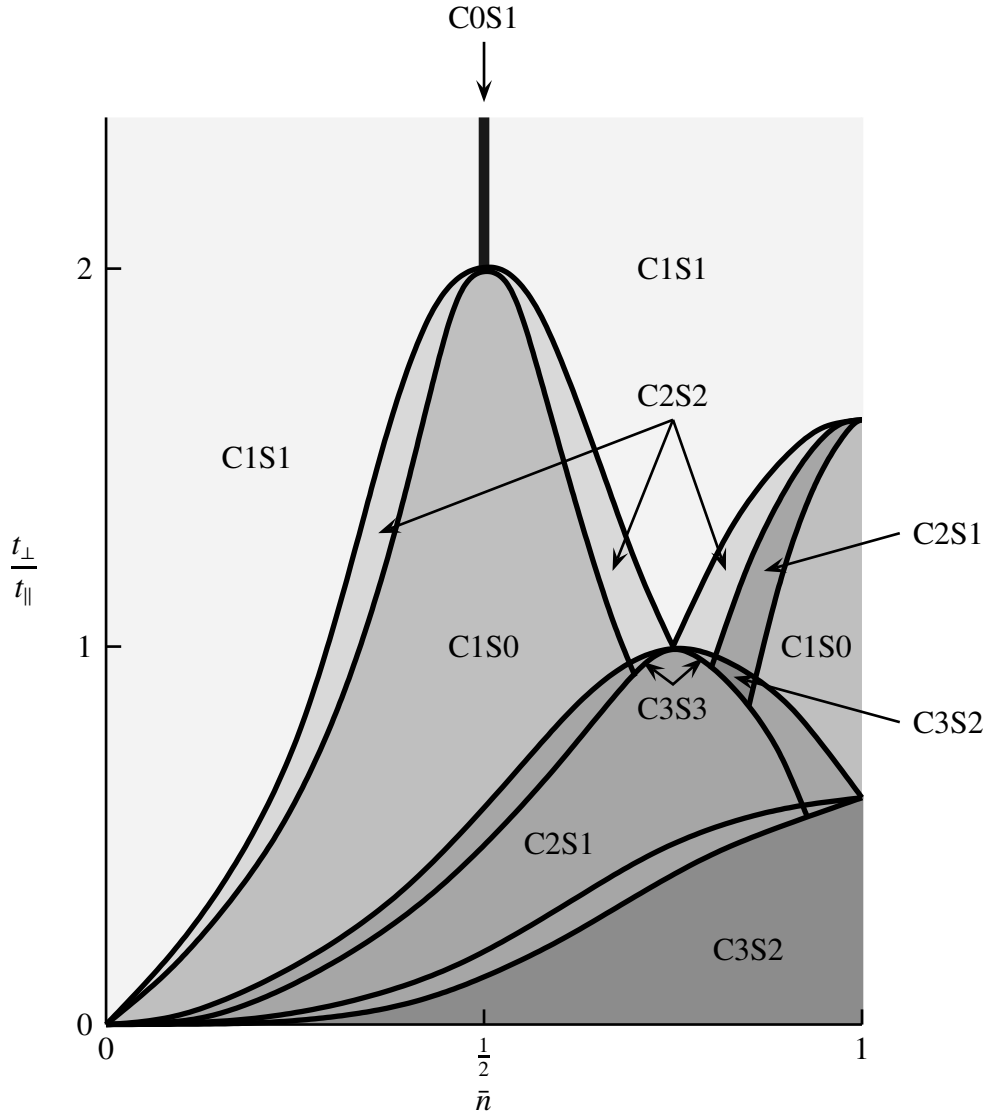

Figure 7.6: Ground-state phase diagram of the four-legged Hubbard ladder, obtained using weak-coupling renormalization-group analysis.

I, where the out-of-phase (π, π)-CDW dominates at large distances, while the in-phase $(\pi, 0)$-CDW decay exponentially and spin excitations are gapped. Phase II, which occurs in the limit of large interchain hopping, is dominated by the in-phase $(\pi, 0)$-CDW. There is a spin singlet on each rung, but the spin excitations are gapless. Between these two limits, we find Phase III, which is dominated by the in-phase $(\pi, 0)$-CDW, and where some spin excitations are gapped. The transition between Phase II and Phase III was found to be a commensurate-incommensurate transition. Finally, Phase IV consists of two essentially uncoupled Tomonaga-Luttinger liquids. In the strong-coupling limit, the quarter-filled insulating ground state was found to be ferromagnetic in nature.

7.2.3.3 *t-J* Ladders

The N-legged t-J ladder was also intensively studied. Analytical [357–359] and numerical studies [274, 335, 360] showed the even-odd effect in the half-filled insulating ground state with short-range antiferromagnetic correlations, and a spin gap that persists upon light doping, for various finite degrees of anisotropy $t_\perp/t_\parallel > 0$. In the spin-gapped Luther-Emery liquid phase, d-wave SC correlations were found to be enhanced [270, 274, 288, 361–365], and the low-energy properties are described by bound hole pairs [366]. Elsewhere on the phase diagram, the ground state is a Tomonaga-Luttinger liquid with gapless charge and spin excitations.

7.3 Analytical Limits of Interacting Spinless Fermions on a Ladder

In this section we will introduce the various limits of a ladder model of interacting spinless fermions for which we have analytical understanding of its ground-state structure and properties. We will start in Section 7.3.1 by motivating the inclusion of a correlated hopping term in the extended Hubbard model of spinless fermions, and go on to describe

briefly in Section 7.3.2 three limiting cases, for which we understand analytically what to expect in the ground state. The brief description in Section 7.3.2 is intended as a road map to guide readers through the detailed discussions of these three limiting cases in Sections 7.5, 7.6, and 7.7.

7.3.1 Correlated Hops and Superconductivity

For the purpose of studying the cluster density matrix of a system of strongly-interacting spinless fermions in Chapter 4, our numerical machinery has been geared towards the spinless extended Hubbard model (4.2.1) with $V \to \infty$, which excludes the possibility of occupation of pairs of sites which are nearest neighbors of each other. We chose to work with this model because it reduces the size of the Hilbert space, so that we have the option of exactly diagonalizing systems that are larger than what we could have handled if we allow all sites to be occupied.

However, the interactions in this $V \to \infty$ limit might be too strong for the emergence of more exotic phases in the ground state. We seek therefore to 'soften' the interaction while retaining the option of working with the smaller nearest-neighbor-excluded Hilbert space. If V had been very large but not infinite, then the sequence of hops shown in Figure 7.7(a) would have been possible.

We can incorporate such hops into the nearest-neighbor-excluded Hilbert space by eliminating the intermediate states using second-order perturbation theory, as shown in Figure 7.7(b), in the same way that the t-J model with $J/t \ll 1$ can be derived from the Hubbard model. Because the resulting next-next-nearest neighbor hops have nonzero amplitude $t' \sim t^2/V$ only when the next-nearest neighbor of the hopping particle is occupied, we call such transitions *correlated hops*. For the rest of our investigations, we shall treat the correlated hopping amplitude t' as being an independent parameter of our

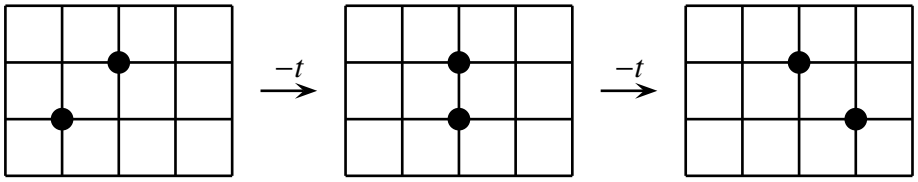

(a)

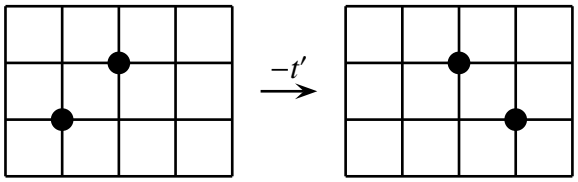

(b)

Figure 7.7: Sequence of (a) nearest-neighbor hops with amplitude t for very large but finite V, with an intermediate state with nearest-neighbor occupation, mapped onto a (b) next-next-nearest-neighbor hops with amplitude t', with no nearest-neighbor occupation, using second-order perturbation theory.

augmented model, described by the Hamiltonian[1]

$$\begin{aligned} H_{t_x t_y t' V} = &-t_x \sum_i \sum_j \left(c^\dagger_{i,j} c_{i,j+1} + c^\dagger_{i,j+1} c_{i,j} \right) - t_y \sum_i \sum_j \left(c^\dagger_{i,j} c_{i+1,j} + c^\dagger_{i+1,j} c_{i,j} \right) \\ &- t' \sum_i \sum_j \left(c^\dagger_{i,j} n_{i+1,j+1} c_{i,j+2} + c^\dagger_{i,j+2} n_{i+1,j+1} c_{i,j} \right) \\ &- t' \sum_i \sum_j \left(c^\dagger_{i+1,j} n_{i,j+1} c_{i+1,j+2} + c^\dagger_{i+1,j+2} n_{i,j+1} c_{i+1,j} \right) \\ &+ V \sum_i \sum_j n_{i,j} n_{i,j+1} + V \sum_i \sum_j n_{i,j} n_{i+1,j}, \end{aligned} \tag{7.3.1}$$

with infinite nearest-neighbor repulsion, $V \to \infty$. Here we incorporate possible anisotropy in the nearest-neighbor hops, by allowing t_x and t_y to be different. We shall also adopt the matrix elements shown in Figure 7.8. In Figure 7.8(iv), the hopping matrix element should be $-t'/2$ according to second-order perturbation theory, but we will adopt a matrix element of $-2t'$, which follows from (7.3.1). We choose this matrix elements, one to favor the formation of tightly-bound pairs, which we hope would be able to condense into a superconducting ground state, and two, because a Hamiltonian incorporating correlated hops with a matrix element of $-t'/2$ for Figure 7.8(iv) would be more complicated than that given in (7.3.1).

When the model (7.3.1) is placed on a two-legged ladder, we write the model as

$$\begin{aligned} H_{t_\parallel t_\perp t' V} = &-t_\parallel \sum_i \sum_j \left(c^\dagger_{i,j} c_{i,j+1} + c^\dagger_{i,j+1} c_{i,j} \right) - t_\perp \sum_i \sum_j \left(c^\dagger_{i,j} c_{i+1,j} + c^\dagger_{i+1,j} c_{i,j} \right) \\ &- t' \sum_i \sum_j \left(c^\dagger_{i,j} n_{i+1,j+1} c_{i,j+2} + c^\dagger_{i,j+2} n_{i+1,j+1} c_{i,j} \right) \\ &- t' \sum_i \sum_j \left(c^\dagger_{i+1,j} n_{i,j+1} c_{i+1,j+2} + c^\dagger_{i+1,j+2} n_{i,j+1} c_{i+1,j} \right) \\ &+ V \sum_i \sum_j n_{i,j} n_{i,j+1} + V \sum_i \sum_j n_{i,j} n_{i+1,j}, \end{aligned} \tag{7.3.2}$$

[1]This model was first suggested by Zhang and Henley in Ref. 204, but never before studied.

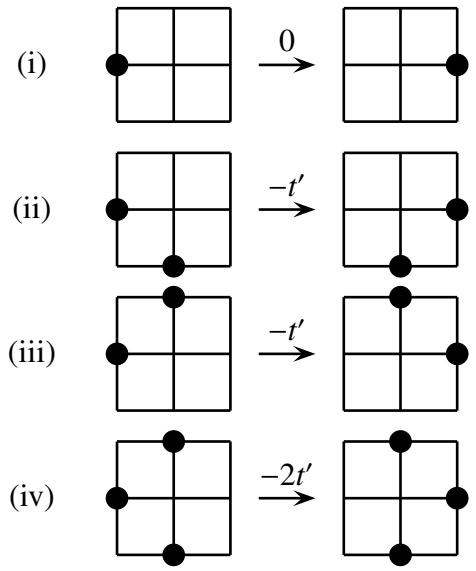

Figure 7.8: Correlated hopping matrix elements when none ((i)), one ((ii) and (iii)), and both ((iv)) of the next-nearest neighbors flanking the next-next-nearest-neighbor hop are occupied.

with $V \to \infty$ nearest-neighbor repulsion, adopting the convention $t_x \to t_\parallel$ for hops along the legs of the ladder, and $t_y \to t_\perp$ for hops along the rungs of the ladder.

7.3.2 The Three Limiting Cases: An Overview

For the model described by (7.3.1) with $V \to \infty$ on a ladder, the ground state is determined by the two independent model parameters, $t_\perp/t_\parallel$ and $t'/t_\parallel$, and the filling fraction $\bar{n}$. For fixed $\bar{n}$, the two-dimensional region in the ground-state phase diagram is bounded by three limiting cases,

(i) $t' \gg t_\parallel, t_\perp$, which we will discuss in detail in Section 7.5. In this limit, we find SC correlations dominating over the inevitable hard-core boson CDW correlations at large distances. Based on our numerical studies in Section 7.5, the leading SC correlation exponent appears to be universal, with a value of $\beta = \frac{1}{2}$, while the

leading CDW correlation exponent α appears to be nonuniversal. In this limit, FL correlations are found to decay exponentially;

(ii) $t_\perp \ll t_\parallel$, $t' = 0$, which we will discuss in detail in Section 7.6. In this limit, the two legs of the ladder are coupled only by infinite nearest-neighbor repulsion. The dominant correlations at large distances are those of a power-law CDW, for which we find numerically to have what appears to be an universal correlation exponent of $\alpha = \frac{1}{2}$. In this limit, the leading SC correlation exponent was found analytically to be $\beta = 2$, while FL correlations are found to decay exponentially;

(iii) $t_\perp \gg t_\parallel$, $t' = 0$, which we will discuss in detail in Section 7.7. In this limit, the particles are effectively localized onto the rungs of the ladder. When the ladder is quarter-filled, a true long-range CDW emerges in the two-fold degenerate ground state. Below quarter-filling, we find numerically that the SC power-law correlation dominate at large distances, with a leading universal correlation exponent $\beta = \frac{1}{8}$. The leading FL and CDW correlation exponents were also found numerically to take on the universal values $\nu = \frac{1}{4}$, and $\alpha = \frac{1}{2}$ respectively.

We summarize these leading correlation exponents, along with the wave vector of the oscillatory function modulating the leading correlations, in Table 7.1.

To zeroth order (i.e. without plunging into first-order perturbation theory calculations), the ground-state phase diagram can be obtained by interpolating between these three limiting cases. There will be three lines of quantum phase transitions or cross-overs, which at quarter-filling, separate the long-range CDW (LR-CDW), power-law CDW (PL-CDW), and SC phases. At quarter-filling, we can give hand-waving arguments as to where these three lines of critical points or cross-overs might be:

1. Suppose we start from the quarter-filled ladder with $t_\perp/t_\parallel \to \infty$, $t' = 0$. The ground

Table 7.1: A summary of the leading correlation exponents of various correlation functions that decay as power laws in the (i) $t' \gg t_{\parallel}, t_{\perp}$ (strong correlated hopping) limit; (ii) $t_{\perp} \ll t_{\parallel}$, $t' = 0$ (weak inter-leg hopping) limit; and (iii) $t_{\perp} \gg t_{\parallel}$, $t' = 0$ (strong inter-leg hopping limit. The wave vector k of the oscillatory function modulating the leading terms in the correlation functions are reported in terms of $k_F = \pi \bar{N}_1$, where $0 \leq \bar{N}_1 \leq \frac{1}{2}$ is the nearest-neighbor excluded chain filling fraction.

limit	correlation function	correlation exponent	wave vector
$t' \gg t_{\parallel}, t_{\perp}$	CDW-π	$\frac{1}{2} + \frac{5}{2}\left(\frac{1}{2} - \bar{N}_1\right)$	$2k_F$
		2	0
	SC	$\frac{1}{2}$	0
		$\frac{3}{2} \rightarrow \frac{1}{2}$	$2k_F$
$t_{\perp} \ll t_{\parallel}$, $t' = 0$	CDW+	2	0
		2	$2k_F$
	CDW$-$	$\frac{1}{2}$	$2k_F$
		2	0
	SC+	2	0
		2	$2k_F$
	SC$-$	$\frac{5}{2}$	$2k_F$
		4	0

(continued on next page)

Table 7.1: (continued)

limit	correlation function	correlation exponent	wave vector
$t_\perp \gg t_\parallel, t' = 0$	FL	$\frac{1}{4}$	k_F
		1	k_F
	CDW	$\frac{1}{2}$	$2k_F$
		2	0
		2	$2k_F$
	SC	$\frac{1}{8}$	0
		$\frac{1}{4}$	$2k_F$
		2	0
		2	$2k_F$

state, as described in Section 7.7, will be one in which the spinless fermions occupy every other rung, hopping back and forth along the rungs they are on. When $t' = 0$, a spinless fermion on rung j cannot hop along the leg to an adjacent rung $j+1$, even if $t_\parallel > 0$, because then the spinless fermion on rung $j+1$ would prohibit the spinless fermion on rung $j + 2$ from hopping back and forth, and vice versa, i.e. for a miniscule kinetic energy gain of $t_\parallel$, the chain incurs a huge kinetic energy penalty of $2t_\perp$, as shown in Figure 7.9.

When t' becomes large, however, these two 'jammed' spinless fermions can perform correlated hop, so that the kinetic energy gain is now $t' + t_\parallel \approx t'$. If $t' < 2t_\perp$, the kinetic energy gain is still insufficient to make up for the kinetic energy loss, whereas if $t' > 2t_\perp$, spinless fermions on the ladder would give up interleg hopping altogether, and perform correlated hops instead to minimize the ground-state

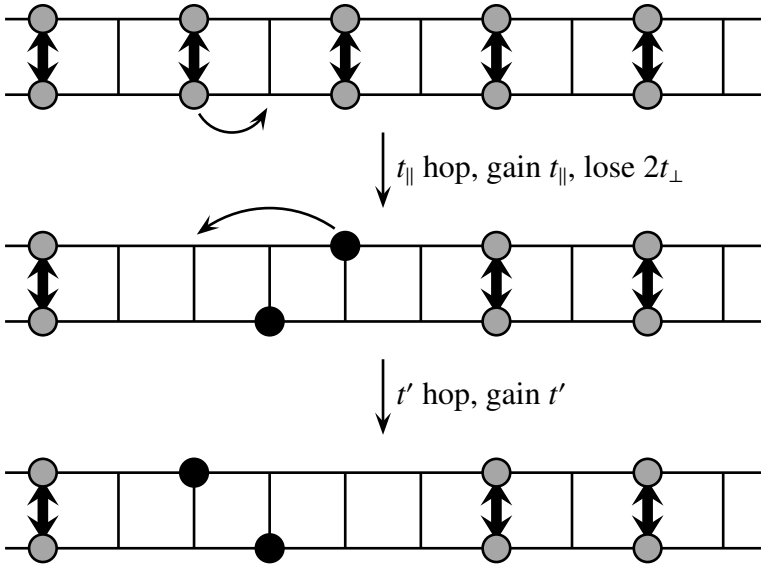

Figure 7.9: Kinetic energy gain by forming a correlated hopping bound pair versus kinetic energy loss from intra-rung hopping.

energy. Therefore, to zeroth order, we expect a quantum phase transition or crossover at $t' = 2t_\perp$.

2. Suppose we start from the quarter-filled ladder with $t_\perp/t_\parallel \to 0$, $t' = 0$. The ground state, as described in Section 7.6, will be one in which successive spinless fermions live on alternate legs of the ladder. The average spacing between two successive spinless fermions is therefore two lattice spacings, and each spinless fermion is free to hop one step, to the right or to the left, along the leg that it is on.

   When we increase $t_\perp$, keeping $t_\parallel$ fixed, we will find each spinless fermion hopping across the rung more and more frequently, as shown in Figure 7.10. However, once it does so, it will no longer be able to hop along the new leg that it has gotten onto, because of the infinite nearest-neigbhor repulsion it experiences. The kinetic energy gain by hopping across the rung is $t_\perp$, while the kinetic energy loss after hopping across the rung is $2t_\parallel$. Therefore, to zeroth order, we expect a quantum

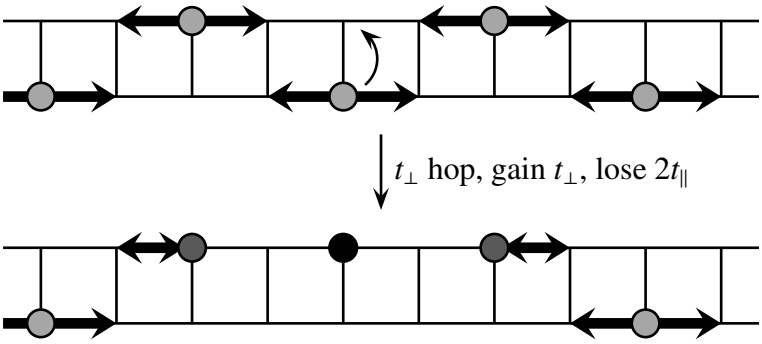

Figure 7.10: Kinetic energy gain from hopping across a rung, versus kinetic energy loss due to the elimination of two possible hops along the legs of the ladder.

phase transition or cross-over at $t_\perp/t_\parallel = 2$.

3. Finally, let us suppose we start from the quarter-filled ladder with $t'/t_\parallel \to \infty$. The ground state, as described in Section 7.5, consists of tightly-bound pairs, with an average pair-to-pair separation of four lattice spacing. The infinite nearest-neighbor repulsion constrains each bound-pair to hop only one lattice spacing to the right or to the left.

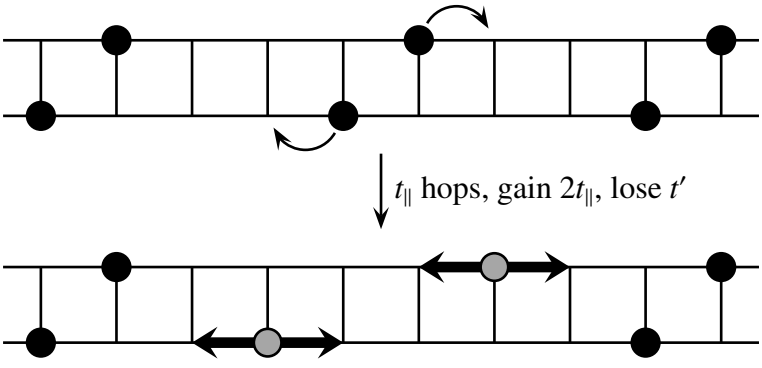

Figure 7.11: Kinetic energy gain from the dissociation of a bound pair into two spinless fermions hopping along the legs of the ladder, versus kinetic energy loss from the dissociation of a correlated-hopping bound pair.

When we keep $t_\parallel$ fixed, and make t' smaller, it becomes energetically favorable to

break one of the bound pairs to get two spinless fermions free to hop along the legs, as shown in Figure 7.11. The kinetic energy gain in doing so is $2t_{\|}$, while the kinetic energy loss for breaking a correlated-hopping pair is t'. Therefore, to zeroth order, we expect a quantum phase transition or cross-over at $t'/t_{\|} = 2$.

Since we are not expecting any new phases at the interior of the phase diagram, these three lines of critical points or cross-overs must meet at a point on the phase diagram. If we have three lines of true critical points, this point would be a quantum tricritical point. We therefore end up with a ground-state phase diagram which looks like that shown in Figure 7.12.

7.4 Analytical Machinery

In analyzing the three limiting cases summarized in Section 7.3.2, apart from using the well-known Jordan-Wigner transformation from one-dimensional hard-core bosons to one-dimensional noninteracting spinless fermions, we also developed two analytical techniques, one of which is novel and not found in the literature. The Jordan-Wigner transformation is used in Section 7.5 to calculate the SC and CDW correlations in the limit of $t' \gg t_{\perp}, t_{\|}$, while the two novel techniques, the nearest-neighbor exclusion map and the intervening-particle expansion, are used in all three limiting cases. It is therefore appropriate to develop the formalisms for the two novel techniques here in this section, along with a quick review of the Jordan-Wigner map, before these are used in Sections 7.5, 7.6 and 7.7. The Jordan-Wigner transformation is reviewed in Section 7.4.1, while the formalisms for the nearest-neighbor exclusion map and the intervening-particle expansion are developed in Sections 7.4.2 and 7.4.7 respectively.

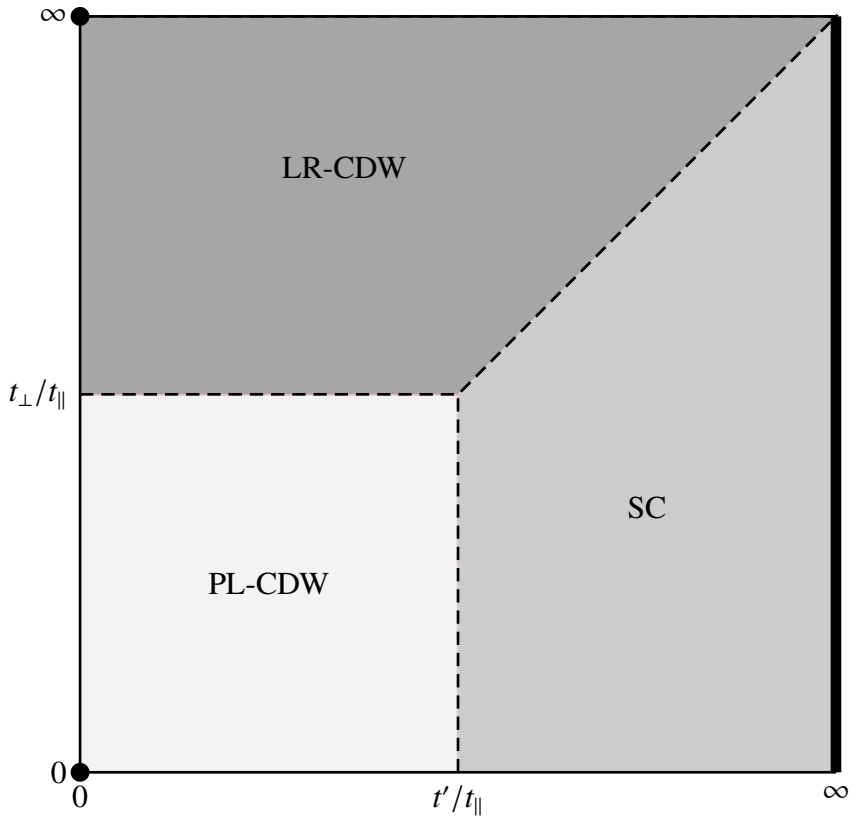

Figure 7.12: The zeroth-order ground-state phase diagram of the quarter-filled extended Hubbard model of spinless fermions with correlated hops described by (7.3.2). The three limiting cases for which we have analytical understanding are shown as the two dots (cases (ii), power-law CDW (PL-CDW) and (iii), long-range CDW (LR-CDW)), and the thick solid line (case (i), SC).

7.4.1 Jordan-Wigner Transformation

In Appendix C we mentioned that there is a one-to-one correspondence between the many-hard-core-boson and many-spinless-fermion configurations, and thus the two Hilbert spaces are identical in structure. On a one-dimensional chain, hard-core bosons cannot move past each other, as one boson must first hop on top of the other — a move explicitly forbidden by the hard-core condition — for this to happen. For a different reason (the Pauli Exclusion Principle), but to the same effect, noninteracting spinless fermions on a one-dimensional chain cannot exchange positions. Therefore, in one dimension, the hard-core-boson and noninteracting-spinless-fermion Hamiltonians are also identical in structure, and thus the ground state of a chain of hard-core bosons is related to the Fermi-sea ground state of a chain of noninteracting spinless fermions in a simple way. A translation machinery exists to map back and forth between these two ground states. This is the Jordan-Wigner transformation [367]

$$b_i = \prod_{j<i}(\mathbb{1} - 2c_j^\dagger c_j)\, c_i, \quad b_i^\dagger = c_i^\dagger \prod_{j<i}(\mathbb{1} - 2c_j^\dagger c_j), \tag{7.4.1}$$

which maps hard-core bosons to spinless fermions, where the product

$$\prod_{j<i}(\mathbb{1} - 2c_j^\dagger c_j) = \prod_{j<i}(\mathbb{1} - 2n_j) = \prod_{j<i}(-1)^{n_j} \tag{7.4.2}$$

is called the *Jordan-Wigner string*.

Later in Section 7.5 we will see how the pairs bound by correlated hops in the limit $t' \gg t_\perp, t_\parallel$ can be mapped to extended hard-core bosons (which are hard-core bosons with infinite nearest-neighbor repulsion), and then to hard-core bosons using the nearest-neighbor exclusion map described in Section 7.4.2, and then finally to noninteracting spinless fermions. In Section 7.4.2 we will show how extended-hard-core-boson expectations are related to appropriately chosen hard-core-boson expectations. This relation between extended-hard-core-boson expectations and hard-core-boson expectations will

typically involve an intervening-particle expansion, described in Section 7.4.7, and as such, we will encounter hard-core-boson expectations of the form

$$\langle b_i^\dagger (\mathbb{1} - n_{i+1}) \cdots n_{i+l_1} \cdots n_{i+l_p} \cdots (\mathbb{1} - n_{i+r'-1}) b_{i+r'} \rangle \,, \tag{7.4.3}$$

a lot, where there are p hard-core-boson occupation number operators n_{i+l}, at sites $i + l$, and $r' - p - 1$ hard-core-boson operators $(\mathbb{1} - n_{i+l'})$, at sites $i + l'$, between the hard-core boson operators $b_i^\dagger$ at site i and $b_{i+r'}$ at site $i + r'$.

To evaluate these expectations, we first invoke the Jordan-Wigner transformation (7.4.1) to replace all the hard-core-boson occupation number operators $n_j = b_j^\dagger b_j$ by spinless-fermion occupation number operators $n_j = c_j^\dagger c_j$ in (7.4.3). Then, to account for the two unpaired hard-core-boson operators at the ends of the hard-core-boson operator product, we write (7.4.3) as the spinless-fermion expectation

$$\langle c_i^\dagger \prod_{j<i} (\mathbb{1} - 2n_j)(\mathbb{1} - n_{i+1}) \cdots n_{i+l_1} \cdots n_{i+l_p} \cdots (\mathbb{1} - n_{i+r'-1}) \times \prod_{j<i} (\mathbb{1} - 2n_j) \prod_{i \le j < i+r'} (\mathbb{1} - 2n_j)\, c_{i+r'} \rangle. \tag{7.4.4}$$

Noting that all Jordan-Wigner string operators $(\mathbb{1} - 2n_j)$ commutes with $n_{j'}$ and $(\mathbb{1} - n_{j'})$, for $j < i$ and $i < j' < i + r'$, and that

$$(\mathbb{1} - 2n_j)(\mathbb{1} - 2n_j) = \mathbb{1}, \tag{7.4.5}$$

we can bring the Jordan-Wigner string $\prod_{j<i}(\mathbb{1} - 2n_j)$ associated with the annihilation operator $c_{i+r'}$ through the intervening spinless-fermion operators to obtain

$$\langle c_i^\dagger (\mathbb{1} - n_{i+1}) \cdots n_{i+l_1} \cdots n_{i+l_p} \cdots (\mathbb{1} - n_{i+r'-1}) \prod_{i \le j < i+r'} (\mathbb{1} - 2n_j) c_{i+r'} \rangle. \tag{7.4.6}$$

Then, using the fact that

$$c_i^\dagger (\mathbb{1} - 2n_i) = c_i^\dagger, \quad n_j(\mathbb{1} - 2n_j) = -n_j, \quad (\mathbb{1} - n_j)(\mathbb{1} - 2n_j) = (\mathbb{1} - n_j), \tag{7.4.7}$$

we can finally write the hard-core-boson expectation

$$\langle b_i^\dagger \prod_{\text{empty}} (\mathbb{1} - n_j) \prod_{\text{filled}} n_j \, b_{i+r'} \rangle = (-1)^p \, \langle c_i^\dagger \prod_{\text{empty}} (\mathbb{1} - n_j) \prod_{\text{filled}} n_j \, c_{i+r'} \rangle \tag{7.4.8}$$

as a spinless-fermion expectation, where p is the number of occupied sites between i and $i + r'$. The suffixes 'empty' or 'filled' in the products in (7.4.8) refer to the sites between i and $i + r$ which are empty or filled respectively.

7.4.2 Nearest-Neighbor Exclusion Map

In the limits of $t' \gg t_\perp, t_\parallel$ (Section 7.5), and $t_\perp \gg t_\parallel$, $t' = 0$ (Section 7.7), we will be dealing with one-dimensional quantum-mechanical particles (hard-core bosons in Section 7.5 and spinless fermions in Section 7.7) with infinite nearest-neighbor repulsion. We can solve for the ground states of such systems exactly, using a nearest-neighbor exclusion map to be elucidated in this section. This nearest-neighbor exclusion map, first used by Fendley to map a supersymmetric chain of spinless fermions to the XXZ chain [368], maps a chain of spinless fermions with infinite nearest-neighbor repulsion to a chain of noninteracting spinless fermions, and a chain of hard-core bosons with infinite nearest-neighbor repulsion to a chain of hard-core bosons, which can in turn to mapped to a chain of noninteracting spinless fermions using the Jordan-Wigner transformation briefly reviewed in Section 7.4.1.

There are three essential ingredients in the nearest-neighbor exclusion map. The first is a configuration-to-configuration mapping, described in Section 7.4.3, relating nearest-neighbor-excluded configurations to nearest-neighbor-included configurations. The second is a Bloch-state-to-Bloch-state mapping, described in Section 7.4.4, relating Bloch states formed from translationally-equivalent nearest-neighbor-excluded configurations to Bloch states formed from the corresponding translationally-equivalent

nearest-neighbor-included configurations. The third is a wave-vector-to-wave-vector mapping, described in Section 7.4.5, which relates the nearest-neighbor excluded wave vector to the nearest-neighbor included wave vector. We will explain in Sections 7.4.4 and 7.4.5 how the amplitudes of the nearest-neighbor-excluded Bloch states are identical to those of the nearest-neighbor-included Bloch states, and then in Section 7.4.6, explain how we can calculate the expectation $\langle O \rangle$ of an observable O in the ground state of a chain of spinless fermions with infinite nearest-neighbor repulsion, by calculating the expectation $\langle O' \rangle$ in the ground state of a chain of noninteracting spinless fermions, for an appropriately chosen observable O'.

7.4.3 Configuration-to-Configuration Mapping

To begin with, let us write the Hamiltonians for a chain of hard-core bosons, and a chain of spinless fermions, both with infinite nearest-neighbor repulsion, as

$$\begin{aligned} H_B &= -t \sum_j \left[B_j^\dagger B_{j+1} + B_{j+1}^\dagger B_j \right] + U \sum_j N_j(\mathbb{1} - N_j) + V \sum_j N_j N_{j+1}, \\ H_C &= -t \sum_j \left[C_j^\dagger C_{j+1} + C_{j+1}^\dagger C_j \right] + V \sum_j N_j N_{j+1}, \end{aligned} \tag{7.4.9}$$

respectively, where B_j and $B_j^\dagger$ are the extended hard-core boson annihilation and creation operators, C_j and $C_j^\dagger$ are the extended-core spinless fermion annihilation and creation operators, and $N_j = B_j^\dagger B_j$ or $N_j = C_j^\dagger C_j$ are the extended hard-core boson or extended-core spinless fermion occupation number operator, depending on the context. In the limit of $V \to \infty$, configurations with nearest-neighbor sites being occupied are not permitted for both the bosonic and fermionic cases, while in the limit of $U \to \infty$, each site on the chain can be occupied by no more than one boson. Let us call configurations in which there is at most one particle per site, and with no nearest-neighbor sites being occupied, *nearest-neighbor excluded configurations*.

In contrast, in the configurations of a chain of hard-core bosons, and a chain of noninteracting spinless fermions, with Hamiltonians

$$\begin{aligned} H_b &= -t \sum_j \left[b_j^\dagger b_{j+1} + b_{j+1}^\dagger b_j \right] + U \sum_j n_j (\mathbb{1} - n_j), \\ H_c &= -t \sum_j \left[c_j^\dagger c_{j+1} + c_{j+1}^\dagger c_j \right], \end{aligned} \tag{7.4.10}$$

where b_j and $b_j^\dagger$ are hard-core boson annihilation and creation operators, c_j and $c_j^\dagger$ are spinless fermion annihilation and creation operators, and $n_j = b_j^\dagger b_j$ or $n_j = c_j^\dagger c_j$ are the hard-core boson or spinless fermion occupation number operator, depending on the context, nearest-neighbor sites are allowed to be occupied. Again, in the limit of $U \to \infty$, each site on the chain can be occupied by no more than one boson. Let us call configurations in which there is at most one particle per site, and allowing nearest-neighbor occupation, *nearest-neighbor included configurations*.

There are several ways to construct a mapping between the nearest-neighbor excluded configurations and the nearest-neighbor included configurations: we can either exclude the site to the right of every particle, or exclude the site to the left of every particle, or exclude the site to the right of every particle to the right of a reference particle, exclude the site to the left of every particle to the left of the reference particle, and exclude both sites left and right of the reference particle. These maps are shown in Figure 7.13. For the rest of this thesis, we will adopt the *right-exclusion map*, in which the site to the right of every particle is excluded.

To write the right-exclusion map out explicitly, let us assume that there are P particles on a nearest-neighbor excluded chain of length L, which we wish to map to P particles on a nearest-neighbor included chain of length L'. Since the right-exclusion map excludes one to the right of every particle on the nearest-neighbor excluded chain, it is clear that the lengths L and L' of the nearest-neighbor excluded and nearest-neighbor

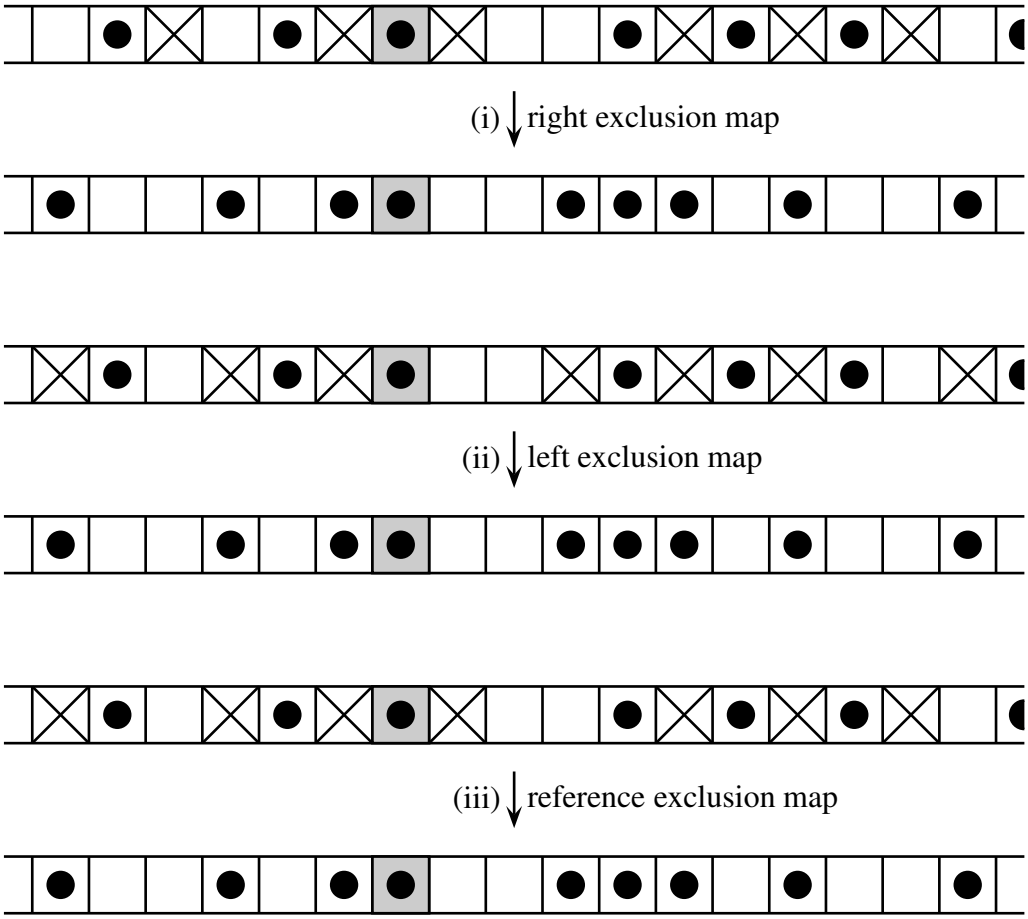

Figure 7.13: Three mappings between nearest-neighbor excluded configurations and nearest-neighbor included configurations: (i) the right-exclusion map (top); (ii) the left exclusion map (middle); and (iii) the reference exclusion map. The reference particle is the one in the shaded plaquette.

included chains are related by

$$L' = L - P. \tag{7.4.11}$$

Eventually, we will let $P, L, L' \to \infty$, keeping the ratio $\bar{n} = P/L$ (and hence the ratio $\bar{n}' = P/L'$) fixed, but for the rest of this section, we will work with finite chains.

For the purpose of writing down nearest-neighbor excluded and nearest-neighbor included configurations related by the right-exclusion map, we find it more convenient to construct the 'inverse' mapping, the *right-inclusion map*, which maps the nearest-neighbor included configuration

$$a^\dagger_{j_1} a^\dagger_{j_2} \cdots a^\dagger_{j_P} |0\rangle\,, \quad 1 \le j_1 < j_2 < \cdots < j_P \le L', \tag{7.4.12}$$

to the nearest-neighbor excluded configuration

$$A^\dagger_{j_1} A^\dagger_{j_2+1} \cdots A^\dagger_{j_P+P+1} |0\rangle\,, \tag{7.4.13}$$

where $a_j = b_j$ and $A_j = B_j$ if we are dealing with bosons, and $a_j = c_j$ and $A_j = C_j$ if we are dealing with spinless fermions. The most important result that follows from the right inclusion map is that, if $|a\rangle$ and $|b\rangle$ are P-particle nearest-neighbor included configurations, mapping to the P-particle nearest-neighbor excluded configurations $|A\rangle$ and $|B\rangle$, then

$$\langle a|H_b|b\rangle = \langle A|H_B|B\rangle\,, \quad \text{or} \quad \langle a|H_c|b\rangle = \langle A|H_C|B\rangle\,, \tag{7.4.14}$$

depending on whether we are dealing with bosons or fermions.

This is a necessary ingredient that would allow us to solve for the ground state of the chain of particles with infinite nearest-neighbor repulsion. Unfortunately, it is insufficient, because the right-exclusion map is not one-to-one, and thus the Hamiltonian matrices for the nearest-neighbor excluded and nearest-neighbor included chains are not identical in structure. The ground-state amplitude for a given nearest-neighbor excluded

infinite-chain configuration is therefore not given by the ground-state amplitude of the corresponding nearest-neighbor included infinite-chain configuration.

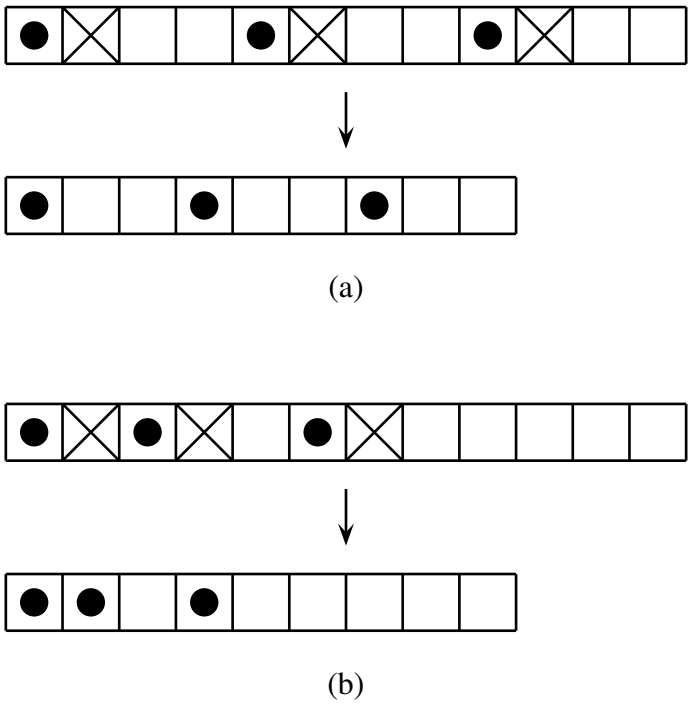

(a)

(b)

Figure 7.14: Two three-particle configurations on a nearest-neighbor excluded chain of length $L = 12$, which are mapped by the right-exclusion map to two corresponding three-particle configurations on a nearest-neighbor included chain of length $L' = 9$.

To see why the right-exclusion map is not one-to-one, consider a nearest-neighbor excluded chain of length $L = 12$ with $P = 3$ particles. This will be mapped by the right-exclusion map to a nearest-neighbor included chain of length $L = 9$. Performing repeated unit translations to the right on the nearest-neighbor excluded configuration (a) shown in Figure 7.14, we obtain a total of four translationally-related configurations, whereas doing the same to the nearest-neighbor included configuration (a), we end up with only three translationally-related configurations. Similarly, performing repeated unit translations to the right on the nearest-neighbor excluded configuration (b) in Figure 7.14, we obtain a total of 12 translationally-related configurations, whereas doing

the same to the nearest-neighbor included configuration (b), we end up with only nine translationally-related configurations. We call the nearest-neighbor excluded configurations (a) and (b) period-4 and period-12 configurations, because they are recovered after four and 12 unit translations to the right on the nearest-neighbor excluded chain respectively. Similarly, we call the nearest-neighbor included configurations (a) and (b) period-3 and period-9 configurations, because they are recovered after three and nine unit translations to right on the nearest-neighbor included chain respectively. What all this means, is that our right-exclusion map must map the four period-4 configurations generated from the nearest-neighbor excluded configuration (a) to the three period-3 configurations generated from the nearest-neighbor included configuration (a), and similarly, map the 12 period-12 configurations generated from the nearest-neighbor excluded configuration (b) to the nine period-9 configurations generated from the nearest-neighbor included configuration (b).

7.4.4 Bloch-State-to-Bloch-State Mapping

Fortunately, the many-to-one nature of the problem in the configuration-to-configuration right-exclusion map suggests its own solution. We start by partitioning the nearest-neighbor included Hilbert space and nearest-neighbor excluded Hilbert space into equivalence classes of translationally-related configurations. Two P-particle configurations, $\{i_1, i_2, \ldots, i_P\}$ and $\{j_1, j_2, \ldots, j_P\}$, on a periodic chain of length L, belong to the same translation-equivalence class, if and only if, after adding some integer r to the site indices j_1, j_2, $\ldots$, j_P modulo L, and reordering the resulting site indices in ascending order, we end up with the ordered list of site indices $i_1, i_2, \ldots, i_P$. When this is true, we say that $\{j_1, j_2, \ldots, j_P\}$ is related to $\{i_1, i_2, \ldots, i_P\}$ by a translation to the right by r sites. For a given equivalence class of translationally-related nearest-neighbor included

configurations, we can construct a corresponding equivalence class of translationally-related nearest-neighbor excluded configurations. We do so by picking a configuration from the nearest-neighbor included equivalence class, let the right inclusion map act on this nearest-neighbor included configuration, and then applying all possible translations to the resulting nearest-neighbor excluded configuration. The two equivalence classes, the first consisting of nearest-neighbor included configurations, and the second consisting of nearest-neighbor excluded configurations, do not contain the same total number of configurations, as we have argued in the previous subsection. However, we can see from the above construction that the nearest-neighbor included translational-equivalence classes are in one-to-one correspondence to the nearest-neighbor excluded translational-equivalence classes.

This suggests that, instead of the configurations themselves, we should use as basis states the nearest-neighbor included Bloch states

$$|j_1, j_2, \ldots, j_P; q'\rangle = \frac{\sum_{r'} e^{-\mathrm{i}q'r'} T_{r'} a^\dagger_{j_1} a^\dagger_{j_2} \cdots a^\dagger_{j_P} |0\rangle}{\sqrt{\mathcal{N}'(j_1, j_2, \ldots, j_P; q')}}, \tag{7.4.15}$$

and the nearest-neighbor excluded Bloch states

$$|j_1, j_2 + 1, \ldots, j_P + P - 1; q\rangle = \frac{\sum_{r} e^{-\mathrm{i}qr} T_r A^\dagger_{j_1} A^\dagger_{j_2+1} \cdots A^\dagger_{j_P+P-1} |0\rangle}{\sqrt{\mathcal{N}(j_1, j_2 + 1, \ldots, j_P + P - 1; q)}}. \tag{7.4.16}$$

Here T_r is the translation operator, whose actions on the creation operators are

$$T_r a^\dagger_j T_r^{-1} = a^\dagger_{j+r}, \quad T_r A^\dagger_j T_r^{-1} = A^\dagger_{j+r}, \tag{7.4.17}$$

while

$$\mathcal{N}'(j_1, \ldots, j_P; q') = \sum_{r'} \sum_{s'} e^{\mathrm{i}q'(r'-s')} \langle 0 | a_{j_P} \cdots a_{j_1} T^{-1}_{r'} T_{s'} a^\dagger_{j_1} \cdots a^\dagger_{j_P} | 0 \rangle \tag{7.4.18}$$

and

$$\mathcal{N}(j_1,\ldots,j_P+P-1;q)=\sum_r\sum_s e^{\mathrm{i}\,q(r-s)}\times$$
$$\langle 0|A_{j_P+P-1}\cdots A_{j_1}T_r^{-1}T_sA_{j_1}^\dagger\cdots A_{j_P+P-1}^\dagger|0\rangle \quad (7.4.19)$$

are the norms of the unnormalized Bloch states

$$\sum_{r'} e^{-\mathrm{i}\,q'r'}\,T_{r'}a_{j_1}^\dagger a_{j_2}^\dagger\cdots a_{j_P}^\dagger|0\rangle \quad (7.4.20)$$

and

$$\sum_{r} e^{-\mathrm{i}\,qr}\,T_rA_{j_1}^\dagger A_{j_2+1}^\dagger\cdots A_{j_P+P-1}^\dagger|0\rangle \quad (7.4.21)$$

respectively.

In the bases formed by the nearest-neighbor included, and nearest-neighbor excluded Bloch states defined in (7.4.15) and (7.4.16), the translationally-invariant Hamiltonians H_a and H_A, where $a=b,c$ and $A=B,C$, depending on whether we are dealing with bosons or fermions, are block-diagonal. These diagonal blocks, $H_a(q')$ and $H_A(q)$, of H_a and H_A, are characterized by the total momenta $\hbar q'$ and $\hbar q$ respectively. In this subsection, our goal is to show the matrices $H_a(q')$ and $H_A(q)$ have identical matrix elements for at least some pairs of wave vectors q' and q, and as such, their eigenstates $|\Psi_a(q')\rangle$ and $|\Psi_A(q)\rangle$ share the same set of Bloch-state amplitudes.

To do this, we need to work out the block-diagonal Hamiltonian matrix elements

$$\langle i_1,\ldots,i_P;q'|H_a|j_1,\ldots,j_P;q'\rangle \quad (7.4.22)$$

and

$$\langle i_1,\ldots,i_P+P-1;q|H_A|j_1,\ldots,j_P+P-1;q\rangle\,, \quad (7.4.23)$$

and norms $\mathcal{N}'(j_1,\ldots,j_P;q')$ and $\mathcal{N}(j_1,\ldots,j_P+P-1;q)$ for a nearest-neighbor excluded chain of length L mapping to a nearest-neighbor included chain of length $L'=L-P$, and show that $H_a(q')$ and $H_A(q)$ have identical matrix elements. We start with the simplest

possible case, considering the block-diagonal Hamiltonian matrices in the $q' = 0 = q$ Bloch sectors for the two chains.

In general, when constructing the Bloch states for periodic finite chains, we need to worry about the fermion signs that arise as spinless fermions are translated across the periodic boundary. Since we will ultimately take L and L' to infinity, where the specifics of the boundary conditions are expected to be unimportant, let us choose to work with closed shell boundary conditions. Closed shell boundary conditions are equivalent to the usual periodic boundary conditions when we impose it onto a finite chain with an odd number of fermions, and equivalent to antiperiodic boundary conditions when we impose it onto a finite chain with an even number of fermions. With this choice of boundary conditions, no sign change is incurred when we perform translation operations on any many-fermion configuration. Therefore, to deduce the normalization factors and Bloch Hamiltonian matrix elements, for both hard-core bosons and spinless fermions, a generic discussion based on hard-core bosons will suffice. In addition, we argue that there is nothing particularly special about having an odd or even number of particles on a nearest-neighbor excluded chain of odd or even length as we take $L, L' \to \infty$, so without loss of generality we can choose to work with an even number of particles on chains of even lengths.

Let us start by considering a nearest-neighbor excluded chain of length $L = 12$ with $P = 4$ particles. For the configuration

$$|0, 2, 5, 9\rangle \equiv A_0^\dagger A_2^\dagger A_5^\dagger A_9^\dagger |0\rangle \,, \tag{7.4.24}$$

we obtain a total of $L = 12$ translationally-equivalent nearest-neighbor excluded configurations as we apply unit translations to the right repeatedly, as shown in Figure 7.15.

Constructing the $q = 0$ Bloch state

$$|0, 2, 5, 9; q = 0\rangle = \frac{1}{\sqrt{12}} \sum_{r=0}^{11} T_r A_0^\dagger A_2^\dagger A_5^\dagger A_9^\dagger |0\rangle \tag{7.4.25}$$

for this translation-equivalence class of nearest-neighbor excluded configurations, we find the appropriate normalization factor to be $1/\sqrt{L}$.

On the other hand, for a period-l nearest-neighbor excluded configuration, such as the period-6 configuration

$$|0, 2, 6, 8\rangle \equiv A_0^\dagger A_2^\dagger A_6^\dagger A_8^\dagger |0\rangle \tag{7.4.26}$$

shown in Figure 7.16, we obtain l configurations after applying unit translations to the right repeatedly. We can then construct the $q = 0$ Bloch state very simply as

$$|0, 2, 6, 8; q = 0\rangle = \frac{1}{\sqrt{6}} \sum_{r=0}^{5} T_r A_0^\dagger A_2^\dagger A_6^\dagger A_8^\dagger |0\rangle \tag{7.4.27}$$

for this translation-equivalence class of nearest-neighbor excluded configurations, and find that the appropriate normalization factor is $1/\sqrt{l}$. Similarly, for the period-3 configuration

$$|0, 3, 6, 9\rangle \equiv A_0^\dagger A_3^\dagger A_6^\dagger A_9^\dagger |0\rangle \tag{7.4.28}$$

shown in Figure 7.17, we obtain only $l = 3$ configurations after applying unit translations to the right repeatedly. The $q = 0$ Bloch state is thus

$$|0, 3, 6, 9; q = 0\rangle = \frac{1}{\sqrt{3}} \sum_{r=0}^{2} T_r A_0^\dagger A_3^\dagger A_6^\dagger A_9^\dagger |0\rangle \tag{7.4.29}$$

for the translation-equivalence class of nearest-neighbor excluded configurations generated by $|0, 3, 6, 9\rangle$. The appropriate normalization factor, we find, is again $1/\sqrt{l}$. If we think of $|0, 2, 5, 9\rangle$ as a period-12 configuration, then the appropriate normalization factor for any configuration on the nearest-neighbor excluded chain of length $L = 12$ is always $1/\sqrt{l}$, where l, a divisor of L, is the period of the given configuration.

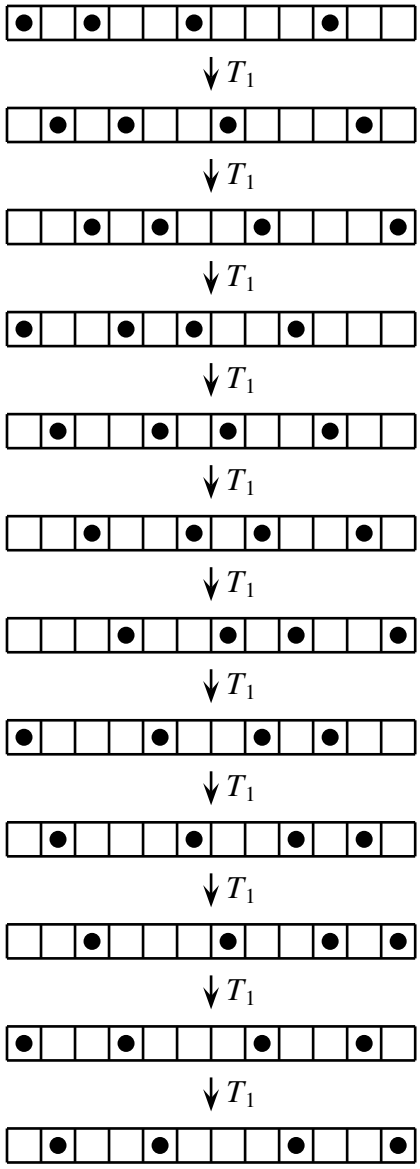

Figure 7.15: Twelve configurations are obtained by repeated application of unit translation to the right, to the generating configuration $|0, 2, 5, 9\rangle$ on a nearest-neighbor excluded chain of length $L = 12$ subject to closed shell boundary conditions.

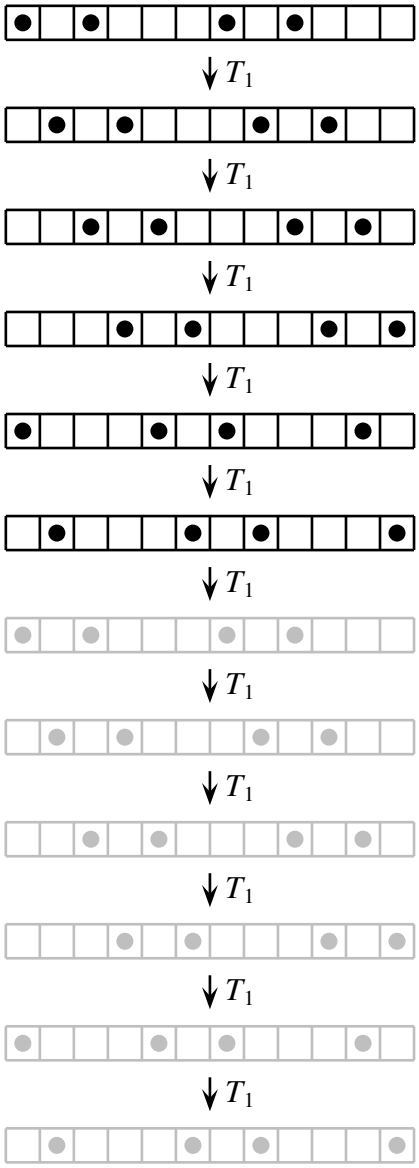

Figure 7.16: Six period-6 configurations are obtained by repeated application of unit translation to the right, to a generating period-6 configuration on a nearest-neighbor excluded chain of length $L = 12$ subject to closed shell boundary conditions. These six period-6 configurations are obtained after the first six unit translations to the right. Extra copies of these six period-6 configurations obtained for the next six unit translations to the right are grayed out.

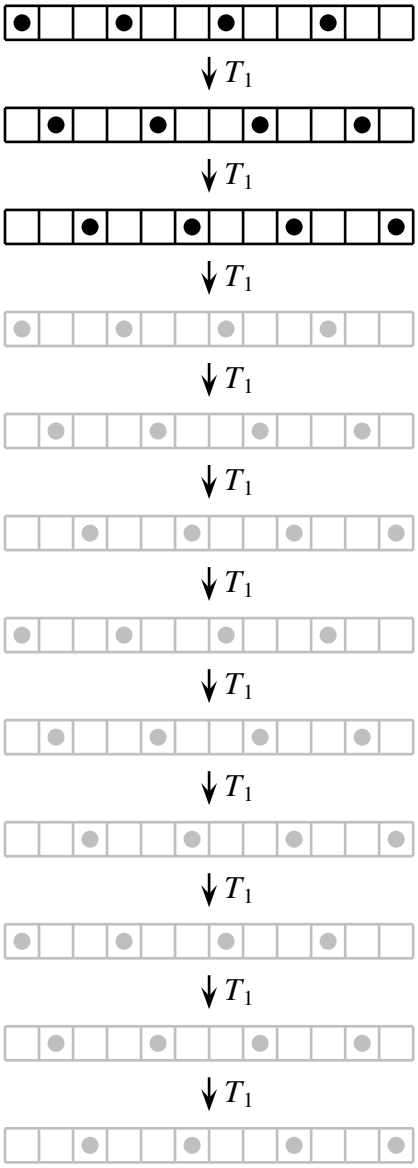

Figure 7.17: Three period-3 configurations are obtained by repeated application of unit translation to the right, to a generating period-3 configuration on a nearest-neighbor excluded chain of length $L = 12$ subject to closed shell boundary conditions. These three period-3 configurations are obtained after the first three unit translations to the right. Extra copies of these three period-3 configurations obtained for the next nine unit translations to the right are grayed out.

Using the right-exclusion map described in Section 7.4.3, we find the nearest-neighbor excluded chain of length $L = 12$ mapping to a nearest-neighbor included chain of length $L' = 8$. The period-12, period-6, and period-3 nearest-neighbor excluded configurations shown in Figures 7.15, 7.16 and 7.17 then map to period-8, period-4, and period-2 nearest-neighbor included configurations. In general, a period-l nearest-neighbor excluded configuration maps to a period-l' nearest-neighbor included configuration, where $l' = l - p$, and $m = p'$ is the number of particles within one period of the nearest-neighbor excluded and nearest-neighbor included chains. As with the nearest-neighbor excluded chain, applying unit translations to the right repeatedly to a period-l' nearest-neighbor included configuration yields l' configurations, and so the appropriate Bloch-state normalization factor is $1/\sqrt{l'}$.

With these normalization factors at hand, let us move on to calculate the matrix elements of the block-diagonal Hamiltonian matrices $H_a(0)$ and $H_A(0)$ between their respective $q = 0 = q'$ Bloch states. First of all, let us note that if we let the respective Hamiltonians act on periodic nearest-neighbor excluded, and nearest-neighbor included configurations, the resulting configurations will have the largest period, $l = L$ and $l' = L'$, since hopping one particle out of a periodic array of particles must necessarily destroy the periodicity of the initial configuration. Therefore, for both H_a, acting on nearest-neighbor included configurations, and H_A, acting on nearest-neighbor excluded configurations, the only nonzero block-diagonal Hamiltonian matrix elements occur between (i) configurations both with the largest period; and (ii) a low-period configuration and a largest-period configuration.

Figure 7.18 shows two Bloch states of period-12 nearest-neighbor excluded configurations between which the block-diagonal Hamiltonian matrix element is nonzero. Looking at the configuration $A_0^\dagger A_2^\dagger A_5^\dagger A_9^\dagger |0\rangle$ on the left of Figure 7.18, we find that it is

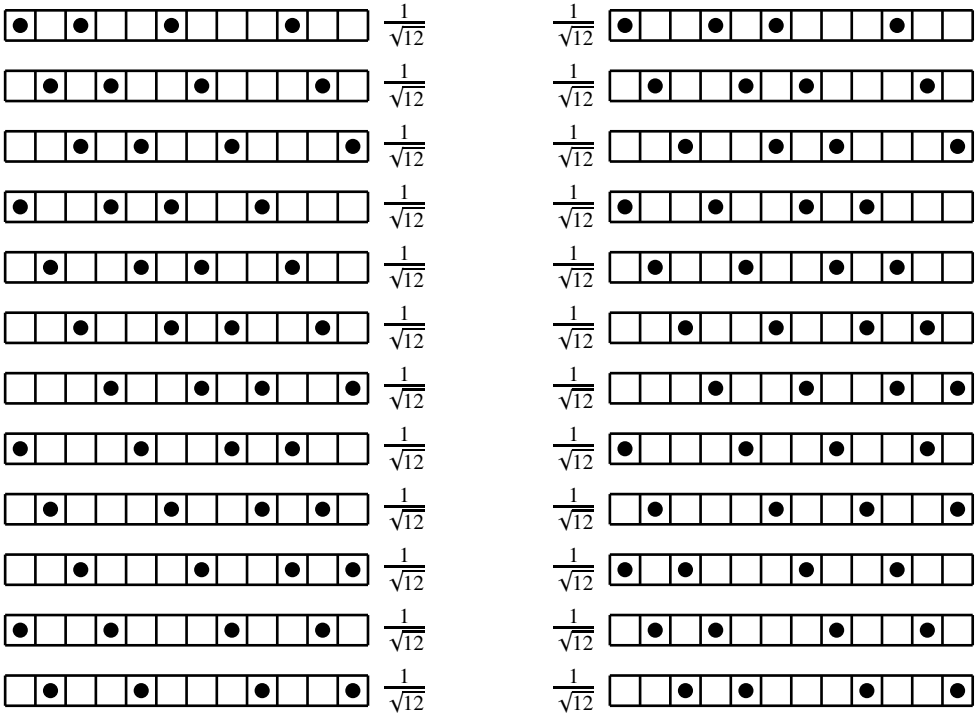

Figure 7.18: The normalized amplitudes of nearest-neighbor excluded configurations in the $q = 0$ Bloch state $|0, 2, 5, 9; q = 0\rangle$ (left) and the $q = 0$ Bloch state $|0, 3, 5, 9; q = 0\rangle$ (right), both consisting of period-12 configurations.

connected to the configurations $A_0^\dagger A_3^\dagger A_5^\dagger A_9^\dagger |0\rangle$ and $A_0^\dagger A_2^\dagger A_6^\dagger A_9^\dagger |0\rangle$ on the right of Figure 7.18 by a single-particle hop to the right. By translational symmetry, $T_r A_0^\dagger A_2^\dagger A_5^\dagger A_9^\dagger |0\rangle$ will then be connected to $T_r A_0^\dagger A_3^\dagger A_5^\dagger A_9^\dagger |0\rangle$ and $T_r A_0^\dagger A_2^\dagger A_6^\dagger A_9^\dagger |0\rangle$ by a single-particle hop to the right, for all translations r. Therefore, the Bloch Hamiltonian matrix element $\langle 0,2,5,9;q=0|H_a|0,3,5,9;q=0\rangle$ between these two Bloch states is

$$\underbrace{-t}_{\substack{\text{hopping}\\ \text{matrix}\\ \text{element}}} \times \underbrace{\frac{1}{\sqrt{L}}}_{\substack{\text{period-}L\\ \text{normalization}}} \times \underbrace{\frac{1}{\sqrt{L}}}_{\substack{\text{period-}L\\ \text{normalization}}} \times \underbrace{L}_{\substack{\text{number of}\\ \text{configurations}\\ \text{in Bloch state}}} \times \underbrace{s}_{\substack{\text{number of}\\ \text{single-particle}\\ \text{hops}}} = -st. \tag{7.4.30}$$

For this particular Bloch Hamiltonian matrix element, the number of configurations in the nearest-neighbor excluded Bloch state $|0,3,5,9;q=0\rangle$ connected to each configuration in the nearest-neighbor excluded Bloch state $|0,2,5,9;q=0\rangle$ by a single-particle hop, abbreviated as "*number of single-particle hops*" in (7.4.30), is $s=2$. We can see this from the fact that the generating configuration $A_0^\dagger A_2^\dagger A_5^\dagger A_9^\dagger |0\rangle$ in the nearest-neighbor excluded Bloch state $|0,2,5,9;q=0\rangle$ is connected to two configurations, $A_0^\dagger A_3^\dagger A_5^\dagger A_9^\dagger |0\rangle$ and $A_0^\dagger A_2^\dagger A_6^\dagger A_9^\dagger |0\rangle$, in the nearest-neighbor excluded Bloch state $|0,3,5,9;q=0\rangle$, by single-particle hops.

Mapping the $L=12$ nearest-neighbor excluded configurations in Figure 7.18 to the $L'=8$ nearest-neighbor included configurations in Figure 7.19, we find, using (7.4.14), the Bloch Hamiltonian matrix element between the two resulting $q'=0$ nearest-neighbor included Bloch states, $|0,1,3,6;q'=0\rangle$ and $|0,2,3,6;q'=0\rangle$, to be

$$\underbrace{-t}_{\substack{\text{hopping}\\ \text{matrix}\\ \text{element}}} \times \underbrace{\frac{1}{\sqrt{L'}}}_{\substack{\text{period-}L'\\ \text{normalization}}} \times \underbrace{\frac{1}{\sqrt{L'}}}_{\substack{\text{period-}L'\\ \text{normalization}}} \times \underbrace{L'}_{\substack{\text{number of}\\ \text{configurations}\\ \text{in Bloch state}}} \times \underbrace{s}_{\substack{\text{number of}\\ \text{single-particle}\\ \text{hops}}} = -st. \tag{7.4.31}$$

Here, we find that the number of configurations in the nearest-neighbor included Bloch state $|0,2,3,6;q'=0\rangle$ connected to each configuration in the nearest-neighbor included Bloch state $|0,1,3,6;q'=0\rangle$ is $s'=s=2$, since the right-exclusion map has the

matrix-element preserving property (7.4.14). This tells us that, if we have two period-L' nearest-neighbor included configurations $|a\rangle$ and $|b\rangle$ which maps to the period-L nearest-neighbor excluded configurations $|A\rangle$ and $|B\rangle$, their associated $q = 0 = q'$ Bloch Hamiltonian matrix elements are equal, i.e.

$$\langle a; q' = 0|H_a|b; q' = 0\rangle = \langle A; q = 0|H_A|B; q = 0\rangle \,. \tag{7.4.32}$$

At this point, let us note that the matrix element $-st$ found actually reflects the influence of finite size effects. In the example above, the period-L generating configurations $|0, 2, 5, 9\rangle$ and $|0, 3, 5, 9\rangle$ were chosen because we can get the latter from the former, by hopping the second particle in $|0, 2, 5, 9\rangle$ one step to the right, from site $j = 2$ to site $j = 3$. However, we also find in the list of translationally-equivalent configurations generated by $|0, 3, 5, 9\rangle$, the configuration $|0, 2, 6, 9\rangle$, which can be obtained by hopping the third particle in $|0, 2, 5, 9\rangle$ one step to the right, from site $j = 5$ to site $j = 6$. This is an unintended, and one may say 'accidental', consequence of imposing periodic boundary conditions on a finite chain, where the list of occupied sites $[0, 3, 5, 9]$, after translation to the right by nine steps, becomes $[0 \mapsto 9, 3 \mapsto 0, 5 \mapsto 2, 9 \mapsto 6] \equiv [0, 2, 6, 9]$. For different pairs of nearest-neighbor excluded Bloch states with nonzero Bloch Hamiltonian matrix elements, this "number of single-particle hops" s will be different, and because it receives in part contributions from the 'accidental' overlaps described above, s is always small, but larger for a larger number of particles, and smaller for a smaller number of particles, on a periodic chain of fixed length.

As we make the periodic chain longer and longer, these 'accidental' overlaps become more and more rare, because it gets harder and harder to find matches modulo a single-particle hop, between one generating configuration, and the list of configurations translationally-equivalent to another generating configuration. Therefore, in the limit of $L, L' \to \infty$, each period-L (period-L') nearest-neighbor excluded (included)

configuration within a given Bloch state will be connected to at most one other period-L (period-L') nearest-neighbor excluded (included) configuration within another given Bloch state. Therefore, the nonzero Bloch Hamiltonian matrix element between two $q = 0 = q'$ Bloch states of maximum-period configurations should properly be $-t$ in the infinite-chain limit, with $L, L', P \to \infty$, with $P/L = \bar{n}$ and $P/L' = \bar{n}'$ held fixed. With this, we conclude that (7.4.32) holds true for all maximum-period Bloch states in the infinite-chain limit.

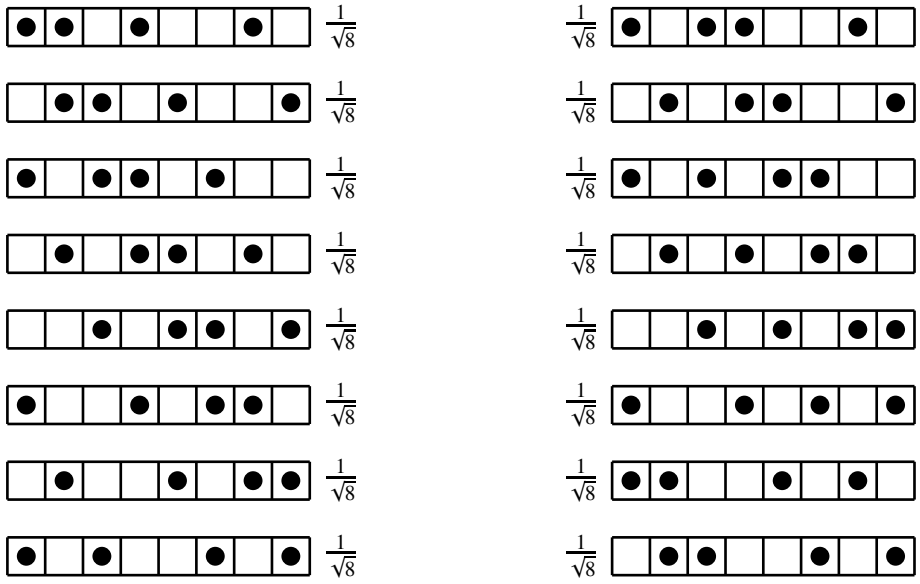

Figure 7.19: The normalized amplitudes of nearest-neighbor included configurations in the $q' = 0$ Bloch state $|0, 1, 3, 6; q' = 0\rangle$ (left) and the $q' = 0$ Bloch state $|0, 2, 3, 6; q' = 0\rangle$ (right). Both Bloch states consist of period-8 configurations.

Now let us work out the nonzero block-diagonal Hamiltonian matrix element between a $q = 0$ period-l nearest-neighbor excluded Bloch state and a $q = 0$ period-L nearest-neighbor excluded Bloch state. An example of two such nearest-neighbor excluded Bloch states for which the Bloch Hamiltonian matrix element is nonzero, is shown in Figure 7.20. Looking at the configuration $A_0^\dagger A_2^\dagger A_6^\dagger A_8^\dagger |0\rangle$ on the left of Figure

7.20, we find that it is connected to the configurations $A_0^\dagger A_3^\dagger A_6^\dagger A_8^\dagger |0\rangle$ and $A_0^\dagger A_2^\dagger A_6^\dagger A_9^\dagger |0\rangle$ by a single-particle hop to the right. By translational symmetry, $T_r A_0^\dagger A_2^\dagger A_6^\dagger A_8^\dagger |0\rangle$ will be connected to the configurations $T_r A_0^\dagger A_3^\dagger A_6^\dagger A_8^\dagger |0\rangle$ and $T_r A_0^\dagger A_2^\dagger A_6^\dagger A_9^\dagger |0\rangle$ by a single-particle hop to the right. Therefore, the block-diagonal Hamiltonian matrix element $\langle 0,2,6,8;q=0|H_a|0,3,6,8;q=0\rangle$ between these two Bloch states is

$$\underbrace{-t}_{\substack{\text{hopping}\\ \text{matrix}\\ \text{element}}} \times \underbrace{\frac{1}{\sqrt{l}}}_{\substack{\text{period-}l\\ \text{normalization}}} \times \underbrace{\frac{1}{\sqrt{L}}}_{\substack{\text{period-}L\\ \text{normalization}}} \times \underbrace{l}_{\substack{\text{number of}\\ \text{period-}l\\ \text{configurations}\\ \text{in Bloch state}}} \times \underbrace{s}_{\substack{\text{number of}\\ \text{single-particle}\\ \text{hops}}} = -st\sqrt{\frac{l}{L}}. \tag{7.4.33}$$

For this particular Bloch Hamiltonian matrix element, the "number of single-particle hops" is $s = 2$.

Mapping the $L = 12$ nearest-neighbor excluded configurations shown in Figure 7.20 to the $L' = 8$ nearest-neighbor included configurations shown in Figure 7.21, and using the relation (7.4.14), we find the block-diagonal Hamiltonian matrix element $\langle 0,1,4,5;q'=0|H_a|0,2,4,5;q'=0\rangle$ between the two resulting $q' = 0$ nearest-neighbor included Bloch states to be

$$\underbrace{-t}_{\substack{\text{hopping}\\ \text{matrix}\\ \text{element}}} \times \underbrace{\frac{1}{\sqrt{l'}}}_{\substack{\text{period-}l'\\ \text{normalization}}} \times \underbrace{\frac{1}{\sqrt{L'}}}_{\substack{\text{period-}L'\\ \text{normalization}}} \times \underbrace{l'}_{\substack{\text{number of}\\ \text{period-}l'\\ \text{configurations}\\ \text{in Bloch state}}} \times \underbrace{s'}_{\substack{\text{number of}\\ \text{single-particle}\\ \text{hops}}} = -s't\sqrt{\frac{l'}{L'}}, \tag{7.4.34}$$

where the "number of single-particle hops" is $s' = 2$. These same expressions (7.4.33) and (7.4.34) hold for the nearest-neighbor excluded, and neighbor-neighbor included, Bloch Hamiltonian matrix elements, between the period-3 and period-12 nearest-neighbor excluded Bloch states shown in Figure 7.22, and between the the period-2 and period-8 nearest-neighbor included Bloch states shown in Figure 7.23 respectively.

In the limit of $L, L' \to \infty$, the number of maximum-period nearest-neighbor excluded Bloch state configurations connected to each period-l nearest-neighbor excluded Bloch state configuration by a single-particle hop is $s = L/l$. Therefore, the nonzero

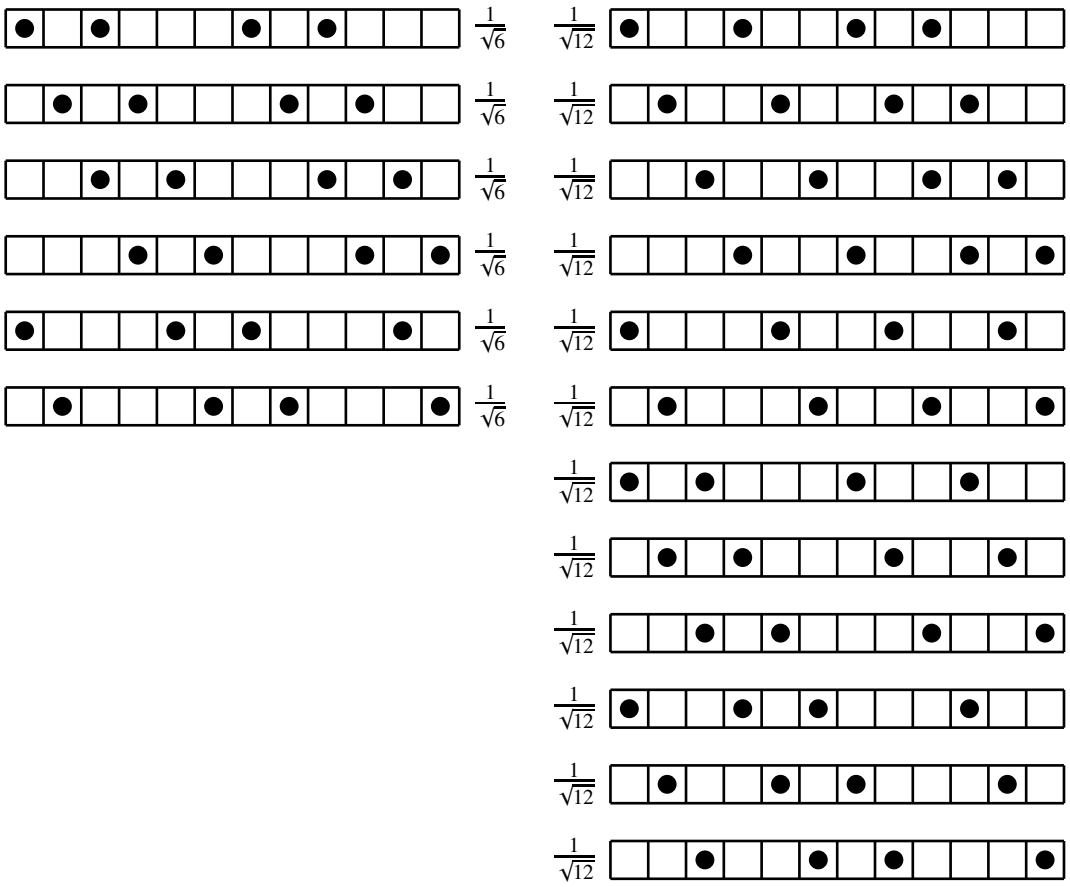

Figure 7.20: The normalized amplitudes of nearest-neighbor excluded configurations in the period-6 $q = 0$ Bloch state $|0, 2, 6, 8; q = 0\rangle$ (left) and the period-12 $q = 0$ Bloch state $|0, 3, 6, 8; q = 0\rangle$ (right).

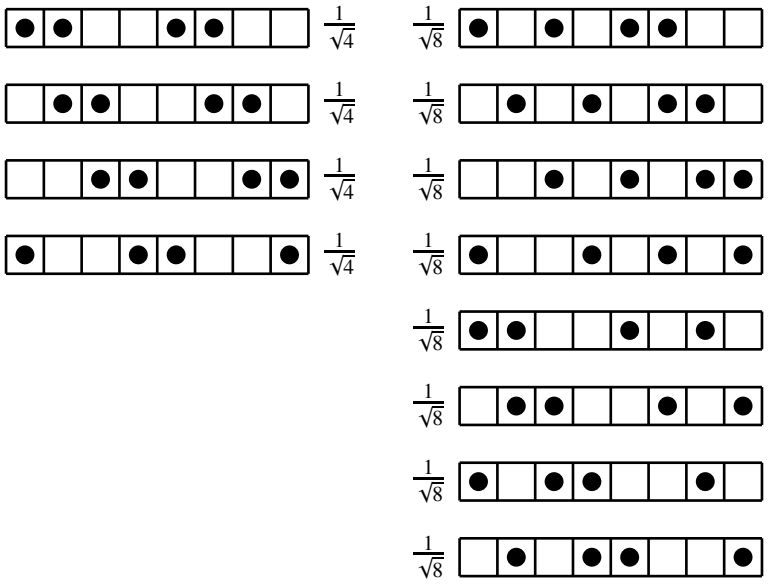

Figure 7.21: The normalized amplitudes of nearest-neighbor included configurations in the period-4 $q' = 0$ Bloch state $|0, 1, 4, 5; q' = 0\rangle$ (left) and the period-8 $q' = 0$ Bloch state $|0, 2, 4, 5; q' = 0\rangle$ (right).

Bloch Hamiltonian matrix element between a period-l nearest-neighbor excluded Bloch state and an period-L nearest-neighbor excluded Bloch state is

$$-t\frac{L}{l}\sqrt{\frac{l}{L}} = -t\sqrt{\frac{L}{l}}. \tag{7.4.35}$$

By a similar argument, we know that the nonzero Bloch Hamiltonian matrix element between a period-l' nearest-neighbor included Bloch state and an period-L' nearest-neighbor included Bloch state is

$$-t\sqrt{\frac{L'}{l'}}. \tag{7.4.36}$$

For the nearest-neighbor excluded $q = 0$ Bloch Hamiltonian matrix to be identical in structure to the nearest-neighbor included $q' = 0$ Bloch Hamiltonian matrix, we therefore need

$$\frac{L}{l} = \frac{L'}{l'}, \tag{7.4.37}$$

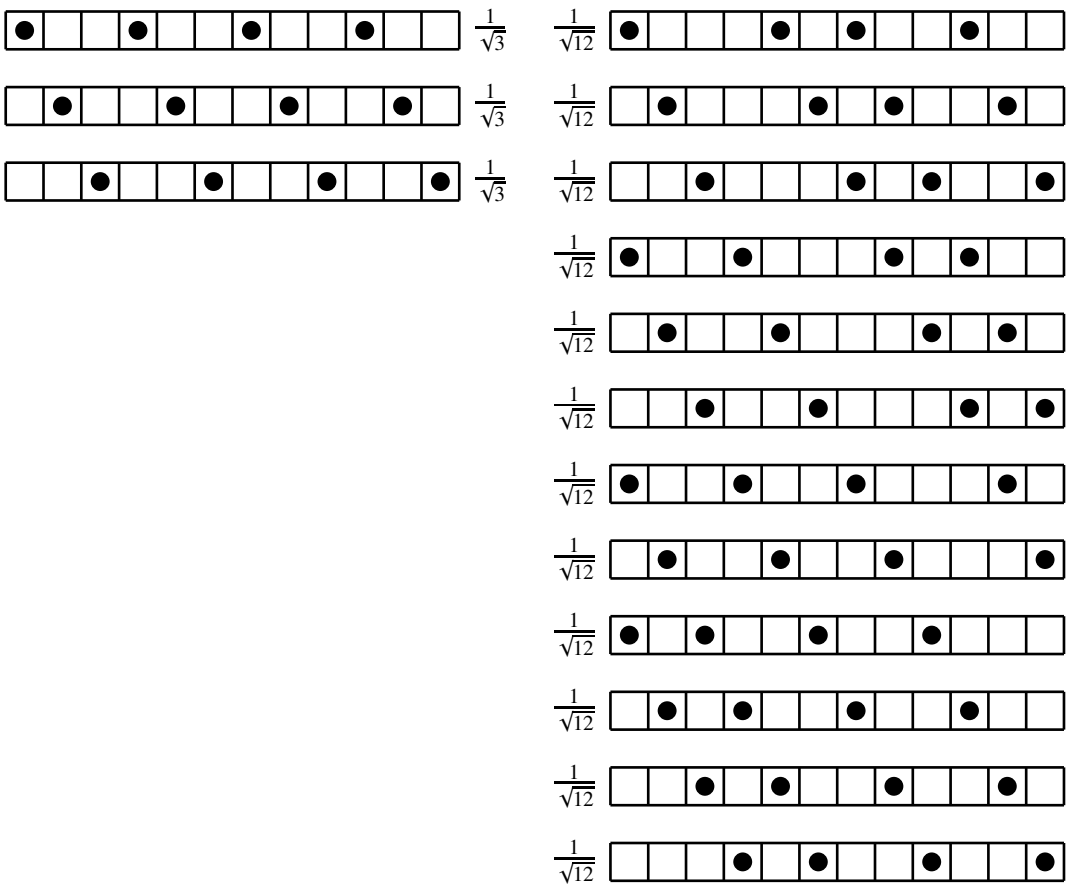

Figure 7.22: The normalized amplitudes of nearest-neighbor excluded configurations in the period-3 $q = 0$ Bloch state $|0, 3, 6, 9; q = 0\rangle$ (left) and the period-12 $q = 0$ Bloch state $|0, 4, 6, 9; q = 0\rangle$ (right).

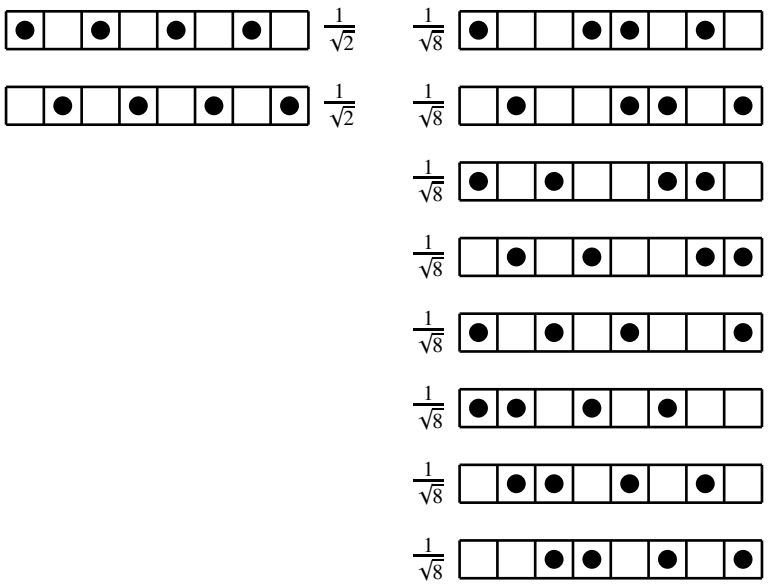

Figure 7.23: The normalized amplitudes of nearest-neighbor included configurations in the period-2 $q' = 0$ Bloch state $|0, 2, 4, 6; q' = 0\rangle$ (left) and the period-8 $q' = 0$ Bloch state $|0, 3, 4, 6; q' = 0\rangle$ (right).

as L and L' are taken to infinity, with $L' = L - P$, and keeping $\bar{n} = P/L$ fixed. Physically, the ratio L/l is the number of repeating period-l units in a chain of length L. By construction, the right-exclusion map preserves this number as a nearest-neighbor excluded configuration of period l on a chain of length L is mapped to a nearest-neighbor included configuration of period l' on a chain of length L'. Therefore, the nonzero $q = 0$ Bloch Hamiltonian matrix element $\langle A; q = 0|H_A|B; q = 0\rangle$ between a period-l nearest-neighbor excluded Bloch state $|A; q = 0\rangle$ and a period-L nearest-neighbor excluded Bloch state $|B; q = 0\rangle$ is indeed equal to the nonzero $q' = 0$ Bloch Hamiltonian matrix element $\langle a; q' = 0|H_a|b; q' = 0\rangle$ between a period-l' nearest-neighbor included Bloch state $|a; q' = 0\rangle$ and a period-L' nearest-neighbor included Bloch state $|b; q' = 0\rangle$, i.e.

$$\langle a; q' = 0|H_a|b; q' = 0\rangle = \langle A; q = 0|H_A|B; q = 0\rangle\,, \tag{7.4.38}$$

if the nearest-neighbor excluded configurations $|A\rangle$ and $|B\rangle$ are map to the nearest-neighbor included configurations $|a\rangle$ and $|b\rangle$ respectively.

Since we have covered all possible cases,

$$\langle a; q' = 0|H_a|b; q' = 0\rangle = \langle A; q = 0|H_A|B; q = 0\rangle\,, \tag{7.4.39}$$

must be true for all configurations $|A\rangle \mapsto |a\rangle$ and $|B\rangle \mapsto |b\rangle$. The $q = 0$ nearest-neighbor excluded Bloch Hamiltonian matrix $H_A(0)$ is therefore identical to the nearest-neighbor included $q' = 0$ Bloch Hamiltonian matrix $H_a(0)$. They have the same energy eigenvalues $E_n(q = 0) = E'_{n'}(q' = 0)$ and the same set of eigenvectors. Consequently, the $q = 0$ and $q' = 0$ eigenstates $|\Psi_n(q = 0)\rangle$ and $|\Psi'_{n'}(q' = 0)\rangle$ corresponding to the same energy eigenvalue $E_n(q = 0) = E'_{n'}(q' = 0)$ have the same Bloch-state amplitudes. In particular, if the nearest-neighbor included ground state is

$$|\Psi'_0(q' = 0)\rangle = \sum_{\{\mathbf{j}'\}} \Psi'_0(\mathbf{j}')\,|\mathbf{j}'; q' = 0\rangle\,, \tag{7.4.40}$$

where $\mathbf{j}' = \{j_1, j_2, \ldots, j_P\}$ and $\{\mathbf{j}'\}$ is the translation-equivalence class generated by $\mathbf{j}'$, the nearest-neighbor excluded ground state will be

$$|\Psi_0(q = 0)\rangle = \sum_{\{\mathbf{j}\}} \Psi_0(\mathbf{j})\,|\mathbf{j}; q = 0\rangle\,, \quad \Psi_0(\mathbf{j}) = \Psi'_0(\mathbf{j}'), \tag{7.4.41}$$

where $\mathbf{j} = \{j_1, j_2 + 1, \ldots, j_P + P - 1\}$ and $\{\mathbf{j}\}$ is the translation-equivalence class generated by $\mathbf{j}$.

7.4.5 Wave-Vector-to-Wave-Vector Map

Although our chief interest in developing the Bloch-state-to-Bloch-state mapping is to solve for the nearest-neighbor excluded ground state, which usually occurs in the $q = 0$ Bloch sector, by writing it in terms of the nearest-neighbor included ground state, which usually occurs in the $q' = 0$ Bloch sector, it is also of interest to check whether

the Bloch-state-to-Bloch-state map will allow us to solve for nearest-neighbor excluded states with $q \neq 0$ exactly as well. This is especially important if we encounter ground states occuring in Bloch sectors with $q, q' \neq 0$. We do this using the same example configurations as for $q = 0 = q'$.

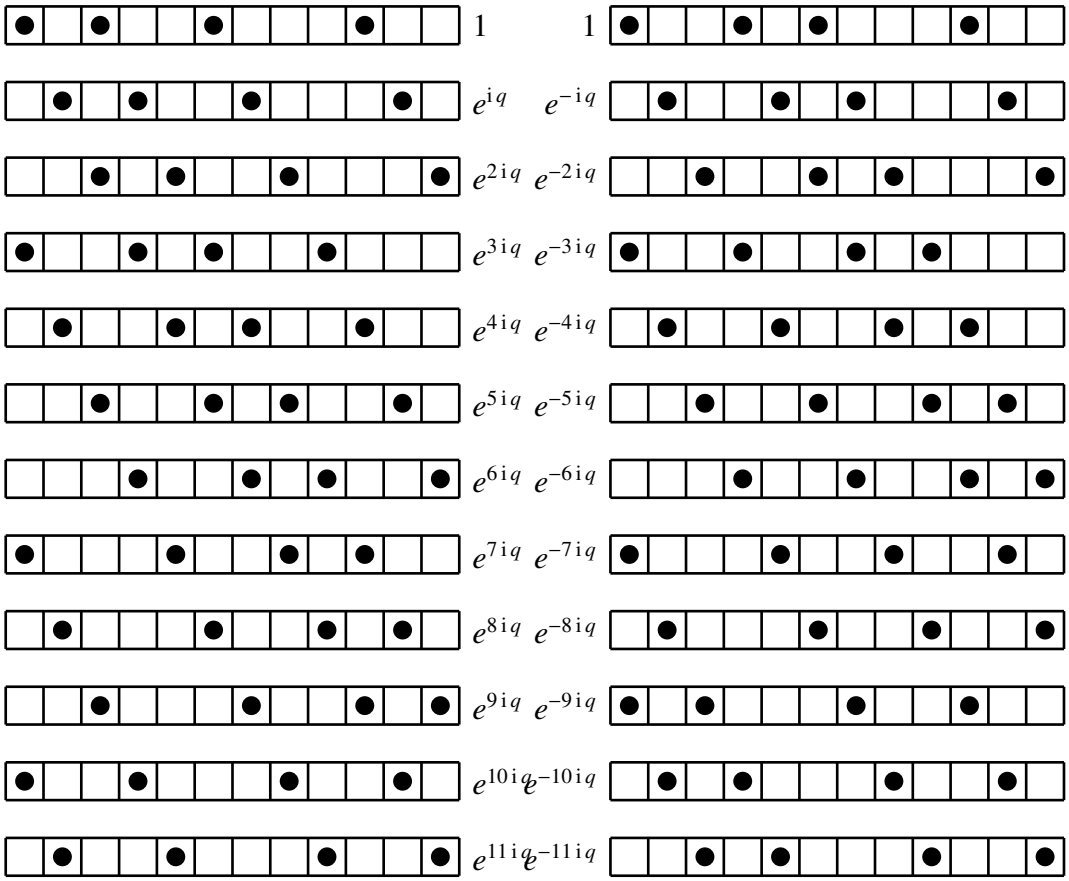

Figure 7.24: The phases of each nearest-neighbor excluded configurations in the $q \neq 0$ Bloch states $|0, 2, 5, 9; q\rangle$ (left) and $|0, 3, 5, 9; q\rangle$ (right), both consisting of period-12 configurations.

For the nonzero Bloch Hamiltonian matrix element $\langle 0, 2, 5, 9; q|H_A|0, 3, 5, 9; q\rangle$ between the maximum-period nearest-neighbor excluded Bloch states $|0, 2, 5, 9; q\rangle$ and $|0, 3, 5, 9; q\rangle$, we find from the lists of phases in Figure 7.24 that this matrix element

now becomes

$$\underbrace{-t}_{\substack{\text{hopping}\\ \text{matrix}\\ \text{element}}} \times \underbrace{\frac{1}{\sqrt{L}}}_{\substack{\text{period-}L\\ \text{normalization}}} \times \underbrace{\frac{1}{\sqrt{L}}}_{\substack{\text{period-}L\\ \text{normalization}}} \times \underbrace{L}_{\substack{\text{number of}\\ \text{configurations}\\ \text{in Bloch state}}} \times \left(1 + e^{-9\,\mathrm{i}\,q}\right) = -t\left(1 + e^{-9\,\mathrm{i}\,q}\right). \qquad (7.4.42)$$

Mapping the maximum-period nearest-neighbor excluded configurations in Figure 7.24 to the maximum-period nearest-neighbor included configurations in Figure 7.25, we find from the list of phases in Figure 7.25 that the nonzero Bloch Hamiltonian matrix element $\langle 0, 1, 3, 6; q'|H_a|0, 2, 3, 6; q'\rangle$ between the maximum-period nearest-neighbor included Bloch states $|0, 1, 3, 6; q'\rangle$ and $|0, 2, 3, 6; q'\rangle$ is

$$\underbrace{-t}_{\substack{\text{hopping}\\ \text{matrix}\\ \text{element}}} \times \underbrace{\frac{1}{\sqrt{L'}}}_{\substack{\text{period-}L'\\ \text{normalization}}} \times \underbrace{\frac{1}{\sqrt{L'}}}_{\substack{\text{period-}L'\\ \text{normalization}}} \times \underbrace{L'}_{\substack{\text{number of}\\ \text{configurations}\\ \text{in Bloch state}}} \times \left(1 + e^{-6\,\mathrm{i}\,q'}\right) = -t\left(1 + e^{-6\,\mathrm{i}\,q'}\right). \qquad (7.4.43)$$

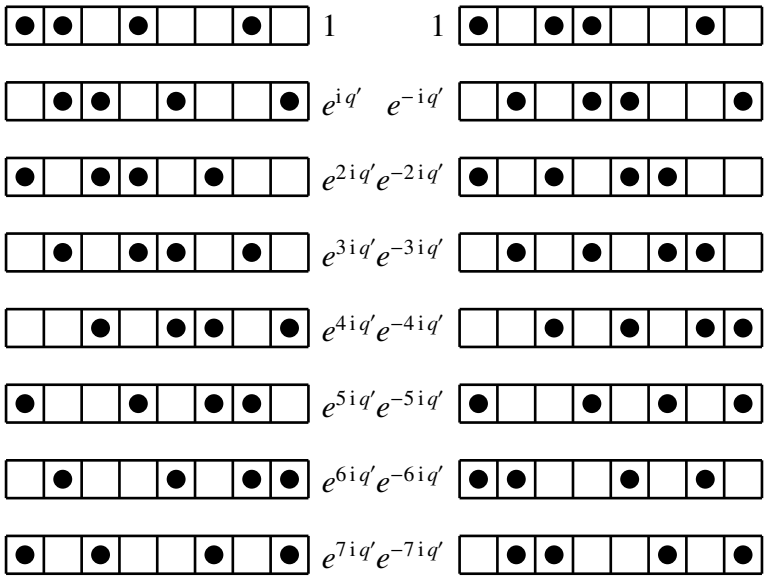

Figure 7.25: The phases of each nearest-neighbor included configurations in the $q' \neq 0$ Bloch states $|0, 1, 3, 6; q'\rangle$ (left) and $|0, 2, 3, 6; q'\rangle$ (right), both consisting of period-8 configurations.

We can make $\langle 0, 1, 3, 6; q'|H_a|0, 2, 3, 6; q'\rangle = \langle 0, 2, 5, 9; q|H_A|0, 3, 5, 9; q\rangle$ if we insist that $6q' = 9q$, but there is nothing really magical about the phases $e^{-6\,\mathrm{i}\,q'}$ and $e^{-9\,\mathrm{i}\,q}$.

As we have explained earlier, these represent finite size errors, since each maximum-period configuration will be related at most one maximum-period configuration in a given Bloch state as we take $L, L \to \infty$. In this infinite-chain limit, the nonzero Hamiltonian matrix element between two maximum-period Bloch states should properly be $-t$. This same matrix element is obtained whether we have nearest-neighbor excluded or nearest-neighbor included configurations on the infinite chain, so long as they have the maximum possible period.

For a Bloch state of period-l configurations connected to a Bloch state of period-L configurations by a single-particle hop, a systematic sum of phases appears in the Bloch Hamiltonian matrix element. For example, for the nearest-neighbor excluded configurations shown in Figure 7.26, a period-6 configuration in the left column of nearest-neighbor excluded configurations has an amplitude proportional to

$$e^{-\mathrm{i}\,q j_1}\,(1 + e^{-6\,\mathrm{i}\,q}), \tag{7.4.44}$$

where j_1 is the position of the reference particle. Since there are six period-6 configurations, we need to divide the amplitude in (7.4.44) by

$$\sqrt{6}\left|1 + e^{-6\,\mathrm{i}\,q}\right|^{1/2} \tag{7.4.45}$$

to properly normalize it.

In general, for a period-l configuration on a chain of length L subject to closed shell boundary conditions, its amplitude within a Bloch state with wave vector q would be proportional to

$$1 + e^{-\mathrm{i}\,lq} + \cdots + e^{-\mathrm{i}(L/l-1)q} = \sum_{s=1}^{L/l} e^{-\mathrm{i}(s-1)lq} = \frac{1 - e^{-\mathrm{i}\,Lq}}{1 - e^{-\mathrm{i}\,lq}} = e^{-\frac{\mathrm{i}}{2}(L-l)q}\,A(q), \tag{7.4.46}$$

where the amplitude function is

$$A(q) = \frac{\sin\frac{1}{2}Lq}{\sin\frac{1}{2}lq}. \tag{7.4.47}$$

Similarly, the amplitude of a period-l' nearest-neighbor included configuration on a chain of length L' would be proportional to $e^{-\frac{i}{2}(L'-l')q'}\,A(q')$, where the amplitude function is

$$A(q') = \frac{\sin\frac{1}{2}L'q'}{\sin\frac{1}{2}l'q'}. \tag{7.4.48}$$

In the context of N-slit interference in elementary optics, we learnt of a similar amplitude function

$$A(\beta) = \frac{\sin\frac{1}{2}N\beta}{\sin\frac{1}{2}\beta}, \tag{7.4.49}$$

which becomes zero at all the zeros of $\sin\frac{1}{2}N\beta$, except those which are simultaneously zeros of $\sin\frac{1}{2}\beta$. Our amplitude functions $A(q)$ and $A(q')$ would have similar behaviours. For an even number of particles on a nearest-neighbor excluded, or nearest-neighbor included chain of even length L, or L', subject to closed shell boundary conditions, however, the allowed wave vectors are integer multiples of $2\pi/L$, or $2\pi/L'$, and we can write them as

$$q = \frac{2\pi m}{L}, \quad q' = \frac{2\pi m'}{L'}. \tag{7.4.50}$$

Clearly, for the Bloch Hamiltonian matrix elements to agree, we need $A(q')$ to be zero, if $A(q)$ is zero, and $A(q')$ to be nonzero, if $A(q)$ is nonzero. Since $\sin\frac{1}{2}Lq$ is always zero, we find that $A(q)$ is only zero when $\sin\frac{1}{2}lq = 0$, when the product lm is a multiple of L, and in which case we have

$$A(q) = \lim_{q\to\frac{2\pi m}{L}} \frac{\sin\frac{1}{2}Lq}{\sin\frac{1}{2}lq} = \lim_{q\to\frac{2\pi m}{L}} \frac{L}{l}\frac{\cos\frac{1}{2}Lq}{\cos\frac{1}{2}lq} = \pm\frac{L}{l}. \tag{7.4.51}$$

Similarly, $\sin\frac{1}{2}L'q'$ is always zero, so $A(q')$ is nonzero only when $\sin\frac{1}{2}l'q' = 0$, when the product $l'm'$ is a multiple of L', and in which case we find that

$$A(q') = \lim_{q'\to\frac{2\pi m'}{L'}} \frac{\sin\frac{1}{2}L'q'}{\sin\frac{1}{2}l'q'} = \lim_{q'\to\frac{2\pi m'}{L'}} \frac{L'}{l'}\frac{\cos\frac{1}{2}L'q'}{\cos\frac{1}{2}l'q'} = \pm\frac{L'}{l'}. \tag{7.4.52}$$

To properly normalize the non-null period-l nearest-neighbor excluded Bloch states, and the non-null period-l' nearest-neighbor included Bloch states, we would need to divide them by

$$|A(q)| = \left|\frac{\sin\frac{1}{2}Lq}{\sin\frac{1}{2}lq}\right| = \frac{L}{l}, \quad |A(q')| = \left|\frac{\sin\frac{1}{2}L'q'}{\sin\frac{1}{2}l'q'}\right| = \frac{L'}{l'} \tag{7.4.53}$$

respectively. But as move on to calculate the Bloch Hamiltonian matrix elements between the non-null Bloch states in the rest of this subsection, let us also keep in mind the null Bloch states.

Inspecting Figure 7.26, we find that the first period-6 nearest-neighbor excluded configuration, counting from the top of the left column of configurations, is connected to the first and seventh period-12 nearest-neighbor excluded configurations, counting from the top of the right column of configurations, by a single-particle hop to the right. The second period-6 nearest-neighbor excluded configuration is then connected to the second and eighth period-12 nearest-neighbor excluded configurations by a single-particle hop to the right, and so on and so forth. In general, when the nearest-neighbor excluded Bloch state is non-null, the generating period-l configuration, which has conjugated amplitude

$$\frac{1}{\sqrt{l}}\left|\frac{\sin\frac{1}{2}lq}{\sin\frac{1}{2}Lq}\right|\sum_{s=1}^{L/l} e^{+\,\mathrm{i}(s-1)lq}, \tag{7.4.54}$$

will pick up a hopping matrix element of $-t$ from L/l period-L configurations. Each of these hopping matrix elements will be multiplied by the phase of the period-L configuration, and so the contribution of the generating period-l configuration to the Bloch Hamiltonian matrix element is

$$-t \times \frac{1}{\sqrt{L}} \times \frac{1}{\sqrt{l}}\left|\frac{\sin\frac{1}{2}lq}{\sin\frac{1}{2}Lq}\right|\sum_{s=1}^{L/l} e^{+\,\mathrm{i}(s-1)lq} \times \sum_{s=1}^{L/l} e^{-\,\mathrm{i}(s-1)lq}. \tag{7.4.55}$$

Here we see that the two sums are complex conjugates of each other, and so using

(7.4.46), we can write this contribution as

$$-\frac{t}{\sqrt{Ll}}\left|\frac{\sin\frac{1}{2}lq}{\sin\frac{1}{2}Lq}\right|\frac{\sin^2\frac{1}{2}Lq}{\sin^2\frac{1}{2}lq}=-\frac{t}{\sqrt{Ll}}\left|\frac{\sin\frac{1}{2}Lq}{\sin\frac{1}{2}lq}\right|=-\frac{t}{l}\sqrt{\frac{L}{l}}. \tag{7.4.56}$$

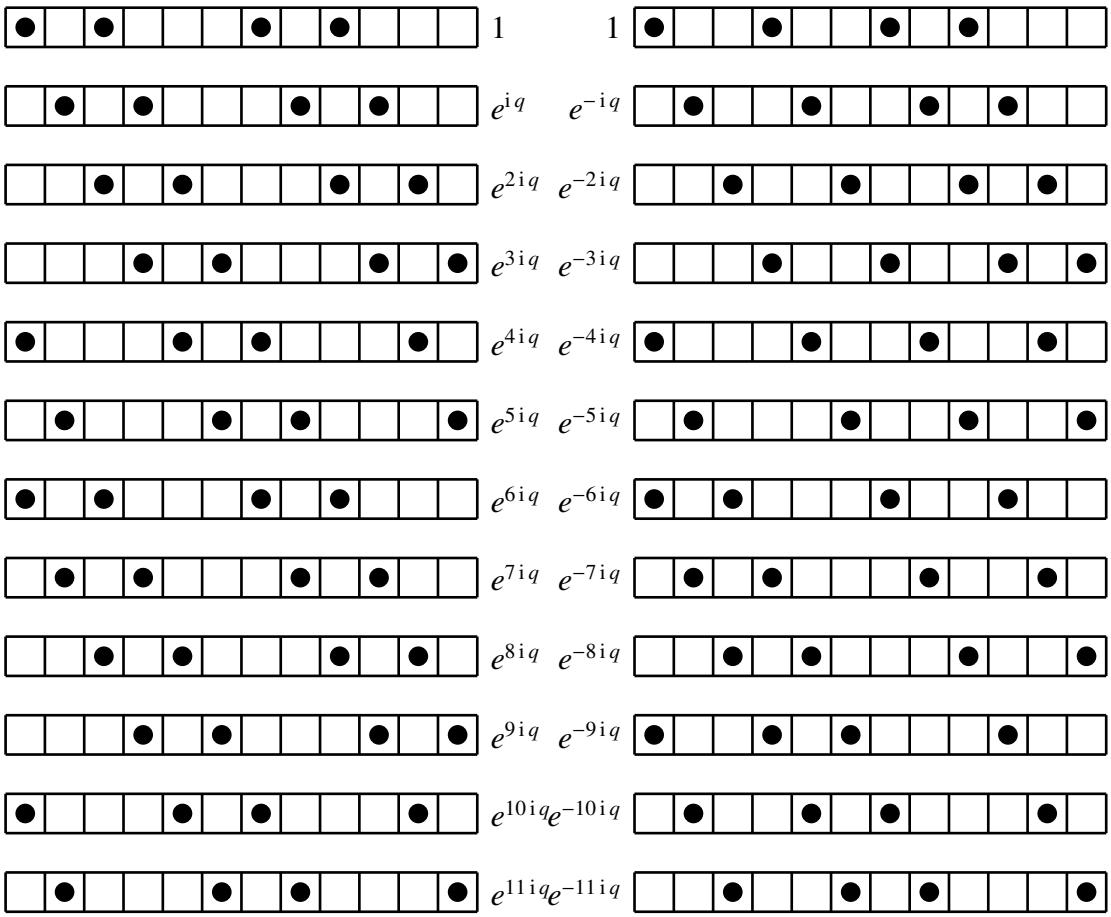

Figure 7.26: The phases of each nearest-neighbor excluded configurations in the period-6 $q \neq 0$ Bloch state $|0,2,6,8;q\rangle$ (left) and the period-12 $q \neq 0$ Bloch state $|0,3,6,8;q\rangle$ (right).

The second period-l configuration has conjugated amplitude

$$\frac{1}{\sqrt{l}}\left|\frac{\sin\frac{1}{2}lq}{\sin\frac{1}{2}Lq}\right|e^{+iq}\sum_{s=1}^{L/l}e^{+i(s-1)lq}, \tag{7.4.57}$$

and picks up a hopping matrix element of $-t$ from the period-L configurations with phases e^{-iq}, $e^{-i(l+1)q}$, ..., $e^{-i(L/l+1)q}$. Therefore, its contribution to the Bloch Hamiltonian

matrix element between the two Bloch states is

$$-t \times \frac{1}{\sqrt{L}} \times \frac{1}{\sqrt{l}} \left| \frac{\sin \frac{1}{2} lq}{\sin \frac{1}{2} Lq} \right| e^{+\mathrm{i}\, q} \sum_{s=1}^{L/l} e^{+\mathrm{i}(s-1) lq} \times e^{-\mathrm{i}\, q} \sum_{s=1}^{L/l} e^{-\mathrm{i}(s-1) lq}, \tag{7.4.58}$$

which is the same as that contributed by the generating period-l configuration. This agrees with our expectation that all translationally-equivalent period-l configurations make identical contributions to the Bloch Hamiltonian matrix element. Therefore, the nearest-neighbor excluded Bloch Hamiltonian matrix element is

$$-\frac{t}{l} \sqrt{\frac{L}{l}} \times l = -t \sqrt{\frac{L}{l}}, \tag{7.4.59}$$

which is the same as that for the $q = 0$ Bloch states. By similar arguments, we know that the Bloch Hamiltonian matrix element between the two nearest-neighbor included Bloch states will be

$$-t \sqrt{\frac{L'}{l'}}. \tag{7.4.60}$$

Knowing that the right-exclusion map preserves the ratio L/l, i.e. a period-l nearest-neighbor excluded configuration on a chain of length L is mapped to a period-l' nearest-neighbor included configuration on a chain of length L', such that $L/l = L'/l'$, we now lack just one final ingredient to conclude that $H_a(q') = H_A(q)$: a map between q and q' such that $\sin \frac{1}{2} l' q' = 0$ whenever $\sin \frac{1}{2} lq = 0$, and $\sin \frac{1}{2} l' q' \neq 0$ whenever $\sin \frac{1}{2} lq \neq 0$. If we choose the one-to-one map

$$q = \frac{2\pi m}{L} \mapsto q' = \frac{2\pi m}{L'}, \tag{7.4.61}$$

i.e. with $m' = m$ in (7.4.50), it then becomes clear that whenever the period-l nearest-neighbor excluded Bloch state with wave vector q is null, the period-l' nearest-neighbor included Bloch state with wave vector q' that it is mapped to by the right-exclusion and Bloch-state-to-Bloch-state maps will be null, and whenever the period-l nearest-neighbor excluded Bloch state with wave vector q is non-null, the period-l' nearest-

neighbor included Bloch state with wave vector q' that it is mapped to by the right-exclusion and Bloch-state-to-Bloch-state maps will also be non-null.

To summarize, we find that the combination of the right-exclusion map

$$A^\dagger_{j_1} A^\dagger_{j_2+1} \cdots A^\dagger_{j_P+P-1} |0\rangle \mapsto a^\dagger_{j_1} a^\dagger_{j_2} \cdots a^\dagger_{j_P} |0\rangle \tag{7.4.62}$$

relating the nearest-neighbor excluded configurations

$$|j_1, \ldots, j_P + P - 1\rangle = A^\dagger_{j_1} \cdots A^\dagger_{j_P+P-1} |0\rangle \tag{7.4.63}$$

to the nearest-neighbor included configurations

$$|j_1, \ldots, j_P\rangle = a^\dagger_{j_1} \cdots a^\dagger_{j_P} |0\rangle , \tag{7.4.64}$$

the Bloch-state-to-Bloch-state map

$$|j_1, \ldots, j_P + P - 1; q\rangle \mapsto |j_1, \ldots, j_P; q'\rangle \tag{7.4.65}$$

relating the nearest-neighbor excluded Bloch states

$$|j_1, j_2 + 1, \ldots, j_P + P - 1; q\rangle = \frac{\sum_r e^{-\mathrm{i}qr} T_r A^\dagger_{j_1} A^\dagger_{j_2+1} \cdots A^\dagger_{j_P+P-1} |0\rangle}{\sqrt{\mathcal{N}(j_1, j_2 + 1, \ldots, j_P + P - 1; q)}} \tag{7.4.16}$$

to the nearest-neighbor included Bloch states

$$|j_1, j_2, \ldots, j_P; q'\rangle = \frac{\sum_{r'} e^{-\mathrm{i}q'r'} T_{r'} a^\dagger_{j_1} a^\dagger_{j_2} \cdots a^\dagger_{j_P} |0\rangle}{\sqrt{\mathcal{N}'(j_1, j_2, \ldots, j_P; q')}}, \tag{7.4.15}$$

and the wave-vector-to-wave-vector map

$$q = \frac{2\pi m}{L} \mapsto q' = \frac{2\pi m}{L'} \tag{7.4.61}$$

relating the nearest-neighbor excluded wave vector q to the nearest-neighbor included wave vector q', ensures that the infinite-chain nearest-neighbor excluded, and nearest-neighbor included Bloch Hamiltonian matrices $H_A(q)$ and $H_a(q')$ have identical matrix elements.

Therefore, the entire many-particle energy spectrum of the nearest-neighbor excluded chain coincides with the many-particle energy spectrum of the nearest-neighbor included chain. There is also a one-to-one correspondence between the many-particle eigenstates for the two chains: even though the amplitudes of configurations related by the right-exclusion map are not the same (because the right-exclusion map is not one-to-one), the amplitudes of Bloch states related by the Bloch-state-to-Bloch-state map are (because the Bloch-state-to-Bloch-state map is one-to-one). This result, which continues to hold true as we take $L, L', P \to \infty$ with P/L (and hence P/L') held fixed, is very powerful, because of its implications to the finite-temperature thermodynamic properties of the two chains, but for the rest of this thesis, we will only need the relation between the ground states of the infinite nearest-neighbor excluded, and nearest-neighbor included chains.

7.4.6 Relation Between Expectations

From Section 7.4.4, we have seen that the ground state of the nearest-neighbor excluded chain can be obtained from the ground state

$$|\Psi'_0(q'=0)\rangle = \sum_{\{\mathbf{j}'\}} \Psi'_0(\mathbf{j}';q'=0)\,|\mathbf{j}';q'=0\rangle \tag{7.4.66}$$

of the nearest-neighbor included chain (where $\mathbf{j}' = \{j_1, j_2, \ldots, j_P\}$ and $\{\mathbf{j}'\}$ is the translation-equivalence class generated by $\mathbf{j}'$), by replacing $\mathbf{j}'$ with $\mathbf{j} = \{j_1, j_2+1, \ldots, j_P+P-1\}$, $q' = 0$ by $q = 0$, the normalized nearest-neighbor included Bloch states $|\mathbf{j}';q'=0\rangle$ by the normalized nearest-neighbor excluded Bloch states $|\mathbf{j};q=0\rangle$, and using the same Bloch state amplitudes

$$\Psi_0(\mathbf{j};q=0) = \Psi'_0(\mathbf{j}';q'=0). \tag{7.4.67}$$

For a nearest-neighbor excluded ground state with zero total momentum mapping to a nearest-neighbor included ground state with zero total momentum, it is understood that $q = 0 = q'$. Therefore, we will drop the wave vectors from the ground state wave functions to make the notations more compact, but leave them in the Bloch states, so that they would not be confused with their generating configurations.

Since the nearest-neighbor included hard-core boson ground state can be obtained from the noninteracting spinless fermion ground state by a Jordan-Wigner transformation, let us specialize our discussions to spinless fermions in this subsection, and work out the relationship between expectations on the nearest-neighbor excluded chain, and some corresponding expectations on the nearest-neighbor included chain.

To begin with, let us write the Fermi-sea ground state of noninteracting spinless fermions in terms of the Bloch states as

$$|\Psi_0'\rangle = \sum_{r_2>0} \cdots \sum_{r_P>0} \Psi_F(k_1, \ldots, k_P; r_2, \ldots, r_P) \, |q' = 0; r_2, \ldots, r_P\rangle \,, \tag{7.4.68}$$

where $k_1, \ldots, k_P$ are the P occupied single-particle wave vectors, with $k_1 + \cdots + k_P = q' = 0$, and

$$|q' = 0; r_2, \ldots, r_P\rangle = \frac{1}{\sqrt{l'}} \sum_{j_1} c_{j_1}^\dagger c_{j_1+r_2}^\dagger \cdots c_{j_1+r_2+\cdots+r_P}^\dagger \, |0\rangle \tag{7.4.69}$$

is the period-l' Bloch state associated with the generating nearest-neighbor included configuration $\{0, r_2, \ldots, r_2 + \cdots + r_P\}$. Applying the right-inclusion and the Bloch-state-to-Bloch-state maps, the nearest-neighbor included Bloch state associated with the period-l' generating configuration $\{0, r_2, \ldots, r_2 + \cdots + r_P\}$ is mapped to the period-l nearest-neighbor excluded Bloch state

$$|q = 0; r_2 + 1, \ldots, r_P + 1\rangle = \frac{1}{\sqrt{l}} \sum_{j_1} C_{j_1}^\dagger C_{j_1+r_2+1}^\dagger \cdots C_{j_1+r_2+\cdots+r_P+P-1}^\dagger \, |0\rangle \,. \tag{7.4.70}$$

Let us consider the expectation of the simplest nontrivial observable, the occupation number operator $N_j = C_j^\dagger C_j$ on the nearest-neighbor excluded chain, and $n_j = c_j^\dagger c_j$ on

the nearest-neighbor included chain. Clearly, these observables — which are diagonal in their respective configuration bases — measure the same physical property on the two chains, and we would like to consider them as a *corresponding pair of observables*. But how would we relate their expectations? Let us start answering this important question by calculating their expectations, and identify the key ingredients in these calculations that would allow to properly relate their expectations.

The expectation of n_j in a given $q' = 0$ period-l nearest-neighbor included Bloch state is

$$\langle q'=0; r_2, \ldots, r_P | n_j | q'=0; r_2, \ldots, r_P \rangle = \frac{1}{l'} \sum_{j_1} \langle 0 | c_{j_1+r_2+\cdots+r_P} \cdots c_{j_1} n_j c^\dagger_{j_1} \cdots c^\dagger_{j_1+r_2+\cdots+r_P} | 0 \rangle \,. \quad (7.4.71)$$

For a maximum-period Bloch state, $l' = L$, and there are L' nearest-neighbor included configurations in the sum over j_1. Thus as j_1 is varied, successive particles in the configuration moves past site j, and in this way, every particle 'registers' with n_j, telling us that

$$\sum_{j_1} \langle 0 | c_{j_1+r_2+\cdots+r_P} \cdots c_{j_1} n_j c^\dagger_{j_1} \cdots c^\dagger_{j_1+r_2+\cdots+r_P} | 0 \rangle = P, \quad (7.4.72)$$

the total number of particles in the chain. The expectation of n_j in a maximum-period nearest-neighbor included Bloch state is therefore

$$\langle q'=0; r_2, \ldots, r_P | n_j | q'=0; r_2, \ldots, r_P \rangle = \frac{P}{L'} = \bar{n}, \quad (7.4.73)$$

the average number of particles per site on the nearest-neighbor included chain.

For a period-l' nearest-neighbor included Bloch state, where $l' < L'$, there are l' configurations in the sum over j_1, and thus as j_1 is varied, all the particles within one period of the chain registers with n_j, giving us

$$\sum_{j_1} \langle 0 | c_{j_1+r_2+\cdots+r_P} \cdots c_{j_1} n_j c^\dagger_{j_1} \cdots c^\dagger_{j_1+r_2+\cdots+r_P} | 0 \rangle = p, \quad (7.4.74)$$

the total number of particles within one period of the chain. The expectation of n_j in a period-l' nearest-neighbor included Bloch state is therefore

$$\langle q' = 0; r_2, \ldots, r_P | n_j | q' = 0; r_2, \ldots, r_P \rangle = \frac{p}{l'}. \tag{7.4.75}$$

Since all configurations within this period-l' Bloch state have period l', the average number of particles per site within one period of the chain must be equal to the average number of particles per site over the entire chain. With all periodicities covered, we therefore have

$$\langle q' = 0; r_2, \ldots, r_P | n_j | q' = 0; r_2, \ldots, r_P \rangle = \bar{n} \tag{7.4.76}$$

for all $q' = 0$ nearest-neighbor included Bloch states $|q' = 0; r_2, \ldots, r_P\rangle$.

Consequently, the expectation of n_j in the nearest-neighbor included chain ground state is

$$\begin{aligned} \langle n_j \rangle &= \langle \Psi'_0 | n_j | \Psi'_0 \rangle \\ &= \sum_{r_2>0} \cdots \sum_{r_P>0} |\Psi_F(k_1, \ldots, k_P; r_2, \ldots, r_P)|^2 \times \\ &\qquad \langle q' = 0; r_2, \ldots, r_P | n_j | q' = 0; r_2, \ldots, r_P \rangle \\ &= \bar{n} \sum_{r_2>0} \cdots \sum_{r_P>0} |\Psi_F(k_1, \ldots, k_P; r_2, \ldots, r_P)|^2 . \end{aligned} \tag{7.4.77}$$

If the ground state is normalized, we must have

$$\sum_{r_2>0} \cdots \sum_{r_P>0} |\Psi_F(k_1, \ldots, k_P; r_2, \ldots, r_P)|^2 = 1, \tag{7.4.78}$$

and thus

$$\langle n_j \rangle = \bar{n}, \tag{7.4.79}$$

just as we had expected.

For the nearest-neighbor excluded chain, the expectation

$$\langle q = 0; r_2 + 1, \ldots, r_P + 1 | N_j | q = 0; r_2 + 1, \ldots, r_P + 1 \rangle$$

of N_j in the period-l Bloch state $|q = 0; r_2 + 1, \ldots, r_P + 1\rangle$ is

$$\frac{1}{\sqrt{l}} \sum_{j_1} \langle 0 | C_{j_1 + r_2 + \cdots + r_P + P - 1} \cdots C_{j_1} N_j C^\dagger_{j_1} \cdots C^\dagger_{j_1 + r_2 + \cdots + r_P + P - 1} | 0 \rangle \,. \tag{7.4.80}$$

By arguments similar to those use for the nearest-neigbhor included chain, we know that

$$\langle q = 0; r_2 + 1, \ldots, r_P + 1 | N_j | q = 0; r_2 + 1, \ldots, r_P + 1 \rangle = \bar{N} \tag{7.4.81}$$

for all $q = 0$ nearest-neighbor excluded Bloch states $|q = 0; r_2 + 1, \ldots, r_P + 1\rangle$, where $\bar{N}$ is the average number of particles per site for the nearest-neighbor excluded chain. Hence,

$$\begin{aligned} \langle N_j \rangle &= \langle \Psi_0 | N_j | \Psi_0 \rangle \\ &= \sum_{r_2 > 0} \cdots \sum_{r_P > 0} |\Psi_F(k_1, \ldots, k_P; r_2, \ldots, r_P)|^2 \times \\ &\qquad \langle q = 0; r_2 + 1, \ldots, r_P + 1 | N_j | q = 0; r_2 + 1, \ldots, r_P + 1 \rangle \\ &= \bar{N} \sum_{r_2 > 0} \cdots \sum_{r_P > 0} |\Psi_F(k_1, \ldots, k_P; r_2, \ldots, r_P)|^2 = \bar{N}. \end{aligned} \tag{7.4.82}$$

Having gone through the calculations for these two expectations, let us understand the key ingredients, of which there are two, that would allow us to properly relate them. The first is the fact that

$$\begin{aligned} \sum_{j_1} \langle 0 | C_{j_1 + r_2 + \cdots + r_P + P - 1} \cdots C_{j_1} N_j C^\dagger_{j_1} \cdots C^\dagger_{j_1 + r_2 + \cdots + r_P + P - 1} | 0 \rangle = \\ \sum_{j_1} \langle 0 | c_{j_1 + r_2 + \cdots + r_P} \cdots c_{j_1} n_j c^\dagger_{j_1} \cdots c^\dagger_{j_1 + r_2 + \cdots + r_P} | 0 \rangle \,, \end{aligned} \tag{7.4.83}$$

which is equal to either P or p, depending on whether the nearest-neighbor excluded, and nearest-neighbor included Bloch states have the maximum period, or a less-than-maximum period. The second is the fact that the nearest-neighbor excluded, and nearest-neighbor included Bloch states $|q = 0; r_2 + 1, \ldots, r_P + 1\rangle$ and $|q' = 0; r_2, \ldots, r_P\rangle$ have different normalization factors. Noting that

$$l\langle q=0;r_2+1,\ldots,r_P+1|N_j|q=0;r_2+1,\ldots,r_P+1\rangle =$$
$$\sum_{j_1}\langle 0|C_{j_1+r_2+\cdots+r_P+P-1}\cdots C_{j_1}N_jC^\dagger_{j_1}\cdots C^\dagger_{j_1+r_2+\cdots+r_P+P-1}|0\rangle\,, \quad (7.4.84)$$

and

$$l'\langle q'=0;r_2,\ldots,r_P|n_j|q'=0;r_2,\ldots,r_P\rangle =$$
$$\sum_{j_1}\langle 0|c_{j_1+r_2+\cdots+r_P}\cdots c_{j_1}n_jc^\dagger_{j_1}\cdots c^\dagger_{j_1+r_2+\cdots+r_P}|0\rangle\,, \quad (7.4.85)$$

we therefore find the relation

$$l\langle q=0;r_2+1,\ldots,r_P+1|N_j|q=0;r_2+1,\ldots,r_P+1\rangle =$$
$$l'\langle q'=0;r_2,\ldots,r_P|n_j|q'=0;r_2,\ldots,r_P\rangle\,. \quad (7.4.86)$$

For a maximum-period nearest-neighbor excluded Bloch state

$$|q=0;r_2+1,\ldots,r_P+1\rangle \quad (7.4.87)$$

which maps to a maximum-period nearest-neighbor included Bloch state

$$|q'=0;r_2,\ldots,r_P\rangle\,, \quad (7.4.88)$$

$l=L$ and $l'=L'$, and thus

$$\langle q=0;r_2+1,\ldots,r_P+1|N_j|q=0;r_2+1,\ldots,r_P+1\rangle =$$
$$\frac{L'}{L}\langle q'=0;r_2,\ldots,r_P|n_j|q'=0;r_2,\ldots,r_P\rangle\,. \quad (7.4.89)$$

The proportionality constant can be rewritten as

$$\frac{L'}{L}=\frac{L'/P}{L/P}=\frac{1/\bar{n}}{1/\bar{N}}=\frac{\bar{N}}{\bar{n}}, \quad (7.4.90)$$

in terms of the intensive chain parameters $\bar{N}$ and $\bar{n}$, so that we get a sensible proportionality constant as we take the limit $L,L'\to\infty$. For a period-l nearest-neighbor excluded Bloch state $|q=0;r_2+1,\ldots,r_P+1\rangle$ which maps to a period-l' nearest-neighbor included Bloch state $|q'=0;r_2,\ldots,r_P\rangle$, we have

$$\langle q = 0; r_2 + 1, \ldots, r_P + 1 | N_j | q = 0; r_2 + 1, \ldots, r_P + 1 \rangle = \frac{l'}{l} \langle q' = 0; r_2, \ldots, r_P | n_j | q' = 0; r_2, \ldots, r_P \rangle . \quad (7.4.91)$$

The proportionality constant can again be rewritten as

$$\frac{l'}{l} = \frac{l'/p}{l/p} = \frac{1/\bar{n}}{1/\bar{N}} = \frac{\bar{N}}{\bar{n}}, \quad (7.4.92)$$

which continues to be valid even when we are talking about periodic configurations with $l, l' \to \infty$.

Now, the ground-state expectation $\langle N_j \rangle$ can be written as a weighted sum over $\langle q = 0; r_2 + 1, \ldots, r_P + 1 | N_j | q = 0; r_2 + 1, \ldots, r_P + 1 \rangle$ within each nearest-neighbor excluded Bloch state $|q = 0; r_2 + 1, \ldots, r_P + 1\rangle$, while $\langle n_j \rangle$ can be written as the *same* weighted sum over the expectations $\langle q' = 0; r_2, \ldots, r_P | n_j | q' = 0; r_2, \ldots, r_P \rangle$ within each nearest-neighbor included Bloch state $|q' = 0; r_2, \ldots, r_P\rangle$. This is the consequence of the two ground states sharing the same Bloch-state amplitudes. Since the proportionality constants between the Bloch-state expectations are the same, term by term, we therefore have the relation

$$\langle N_j \rangle = \frac{\bar{N}}{\bar{n}} \langle n_j \rangle , \quad (7.4.93)$$

between the two ground-state expectations.

In general, for a given nearest-neighbor excluded chain observable O, we can in principle calculate its ground-state expectation by first determining all the amplitudes $\Psi_0(r_2 + 1, \ldots, r_P + 1)$ from the Fermi-sea ground state of the nearest-neighbor included chain, and then use these to calculate $\langle O \rangle$. However, this is extremely tedious, and for an arbitrary chain observable O, may not even be doable analytically. Instead, if it is possible, we want to find a corresponding nearest-neighbor included chain observable O', which need not have the same form as O, such that

$$\sum_{j_1} \langle 0|C_{j_1+r_2+\cdots+r_P+P-1} \cdots C_{j_1} O C^\dagger_{j_1} \cdots C^\dagger_{j_1+r_2+\cdots+r_P+P-1}|0\rangle =$$

$$\sum_{j_1} \langle 0|c_{j_1+r_2+\cdots+r_P} \cdots c_{j_1} O' c^\dagger_{j_1} \cdots c^\dagger_{j_1+r_2+\cdots+r_P}|0\rangle\,, \quad (7.4.94)$$

Again, by doing a term-by-term comparison of the Bloch-state expectations,

$$l\,\langle q=0; r_2+1,\ldots,r_P+1|O|q=0; r_2+1,\ldots,r_P+1\rangle =$$

$$l'\,\langle q'=0; r_2,\ldots,r_P|O'|q'=0; r_2,\ldots,r_P\rangle\,, \quad (7.4.95)$$

and noting that

$$\frac{l'}{l} = \frac{\bar{N}}{\bar{n}} \quad (7.4.96)$$

always, we have the relation

$$\langle O\rangle = \frac{\bar{N}}{\bar{n}}\,\langle O'\rangle \quad (7.4.97)$$

between the expectations of the corresponding pair of observables, O on the nearest-neighbor excluded chain, and O' on the nearest-neighbor included chain.

7.4.7 Intervening-Particle Expansion

Having derived the relation (7.4.97) between the ground-state expectations of a corresponding pair of observables O and O' on nearest-neighbor excluded, and nearest-neighbor included chains respectively, we will in this subsection describe how to properly construct the observable O' corresponding to a given observable O. For an observable O that is the product of local operators separated by r sites, we must first write its ground-state expectation as a sum over conditional ground-state expectations involving O. In each conditional ground-state expectation, the occupation numbers of the r sites between the two local operators making up O are *fixed*, and so the sum is over different ways to fix these occupation numbers. The reason for this encumbrance is

that two sites with separation r on the nearest-neighbor excluded chain are mapped by the right-exclusion map to two sites with varying separations on the nearest-neighbor included chain, depending on how many particles are found between the two sites in question. Therefore, it is necessary to fix the occupation numbers of the intervening sites to ensure that the conditional ground-state nearest-neighbor-excluded-chain expectation and ground-state nearest-neighbor-included-chain expectation satisfy the correspondence condition (7.4.94). In view of this, we call the technology that we will develop in this subsection the *intervening-particle expansion*.

To illustrate the machinery associated with the intervening-particle expansion, let us return to the generic notations of A_j and $A_j^\dagger$ for particle annihilation and creation operators on the nearest-neighbor excluded chain, and a_j and $a_j^\dagger$ for particle annihilation and creation operators on the nearest-neighbor included chain. We begin with the simplest observable, the two-point function $\langle A_i^\dagger A_{i+r}\rangle$, that is a product of two separated local operators $A_i^\dagger$ and A_{i+r}. First, let us write down the identity

$$\langle A_i^\dagger A_{i+r}\rangle = \langle A_i^\dagger [N_{i+1} + (\mathbb{1} - N_{i+1})] \cdots [N_{i+r-1} + (\mathbb{1} - N_{i+r-1})] A_{i+r}\rangle\,, \tag{7.4.98}$$

where $N_j = A_j^\dagger A_j$ is the occupation number operator at intervening site j. We then expand the product in (7.4.98) into a sum of terms,

$$\begin{aligned}
\langle A_i^\dagger A_{i+r}\rangle = {} & \langle A_i^\dagger (\mathbb{1} - N_{i+1}) \cdots (\mathbb{1} - N_{i+r-1}) A_{i+r}\rangle + \\
& \langle A_i^\dagger N_{i+1} \cdots (\mathbb{1} - N_{i+r-1}) A_{i+r}\rangle + \cdots + \\
& \langle A_i^\dagger (\mathbb{1} - N_{i+1}) \cdots N_{i+r-1} A_{i+r}\rangle + \\
& \langle A_i^\dagger N_{i+1} N_{i+2} \cdots (\mathbb{1} - N_{i+r-1}) A_{i+r}\rangle + \cdots + \\
& \langle A_i^\dagger (\mathbb{1} - N_{i+1}) \cdots N_{i+r-2} N_{i+r-1} A_{i+r}\rangle + \cdots + \\
& \langle A_i^\dagger N_{i+1} N_{i+2} \cdots N_{i+r-1} A_{i+r}\rangle\,,
\end{aligned} \tag{7.4.99}$$

each of which contains intervening particles at fixed sites. We call terms in the ex-

pansion with p intervening N_j's the p-intervening-particle expectations. Because of nearest-neighbor exclusion, most of the terms in (7.4.99) vanish. More importantly, all partial configurations between sites i and $i + r$ allowed by nearest-neighbor exclusion are included in (7.4.99).

Next, we construct a sum of corresponding nearest-neighbor included expectations, one for each nearest-neighbor excluded term in the expansion (7.4.99). The rules for this construction is simple:

1. **Nearest-neighbor exclusion.** To ensure that we do not generate partial configurations violating nearest-neighbor exclusion, we make the assignment

$$A_j^\dagger A_{j+1}^\dagger = 0 = A_j A_{j+1}. \tag{7.4.100}$$

   Note that this is not intended to be a statement on the operator algebra, but as a mere bookkeeping device for use only in evaluating expectations. The assignment

$$A_j^\dagger N_{j+1} = 0 = N_j A_{j+1} \tag{7.4.101}$$

   follows from (7.4.100).

2. **Right-exclusion map.** The right-exclusion map described in Section 7.4.3 then manifests itself by the substitution

$$A_j^\dagger(\mathbb{1} - N_{j+1}) \mapsto a_j^\dagger. \tag{7.4.102}$$

   The assignment

$$N_j(\mathbb{1} - N_{j+1}) = n_j \tag{7.4.103}$$

   follows from (7.4.102).

3. **Re-indexing.** Because the right-exclusion map, as effected by the assignment (7.4.102), merges the occupied site j and the empty site $j+1$ to its right, operators

to the right of site $j+1$ must be re-indexed. For example,

$$N_j(\mathbb{1} - N_{j+1})N_{j+2} \mapsto n_j n_{j+1}, \tag{7.4.104}$$

where the index $j+2$ on the nearest-neighbor excluded chain becomes $j+1$ on the nearest-neighbor included chain, and

$$N_j(\mathbb{1} - N_{j+1})(\mathbb{1} - N_{j+2})N_{j+3}(\mathbb{1} - N_{j+4})N_{j+5} \mapsto n_j(\mathbb{1} - n_{j+1})n_{j+2}n_{j+3}, \tag{7.4.105}$$

where the index $j+3$ on the nearest-neighbor excluded chain becomes $j+2$ on the nearest-neighbor included chain, and the index $j+5$ on the nearest-neighbor excluded chain becomes $j+3$ on the nearest-neighbor included chain.

In general, the index j on the nearest-neighbor excluded chain becomes $j-p$ if there are p particles to its left, including the left-most site in the expectation. This also means that, if in the original p-intervening-particle expectation on the nearest-neighbor excluded chain, the two ending operators are r sites apart, they will be $r-p$ sites apart in the corresponding p-intervening-particle expectation on the nearest-neighbor included chain.

To summarize, we can then calculate the expectation $\langle O_j O_{j+r}\rangle$ separated by r sites on the nearest-neighbor excluded chain, by first writing it as an intervening-particle expansion

$$\langle O_j O_{j+r}\rangle = \sum_{\{p\}} \langle O_j O_p O_{j+r}\rangle\,, \tag{7.4.106}$$

where O_p is a product of p particle-occupation number operators N_j and $r-p$ hole-occupation number operators $(\mathbb{1} - N_j)$, and the sum is over all possible ways to have intervening particles between O_j and O_{j+r}. Then, using the rules described above, we can write down for each term

$$\langle O_j O_p O_{j+r}\rangle \tag{7.4.107}$$

in the nearest-neighbor-excluded-chain expansion, a corresponding nearest-neighbor-included-chain expectation

$$\langle O'_j O'_p O'_{j+r-p} \rangle \tag{7.4.108}$$

which we know how to evaluate. Finally, we sum over all corresponding nearest-neighbor-included-chain expectations, to write

$$\langle O_j O_{j+r} \rangle = \frac{\bar{N}}{\bar{n}} \sum_{\{p\}} \langle O'_j O'_p O'_{j+r-p} \rangle \,, \tag{7.4.109}$$

after making use of (7.4.97) to relate nearest-neighbor-excluded-chain expectations to nearest-neighbor-included-chain expectations. Once we reach the point of writing down (7.4.109), we can take the limit of $L, L', P \to \infty$ with P/L fixed, to evaluate the expectation $\langle O_j O_{j+r} \rangle$ in the infinite-chain limit.

7.5 Infinitely-Strong Correlated Hops

In this section, we investigate the limit where the correlated-hopping matrix element becomes infinitely larger than the nearest-neighbor-hopping matrix element, so that the Hamiltonian in (7.3.2) simplifies to

$$\begin{aligned} H_{t'V} = & -t' \sum_i \sum_j \left(c^\dagger_{i,j} n_{i+1,j+1} c_{i,j+2} + c^\dagger_{i,j+2} n_{i+1,j+1} c_{i,j} \right) \\ & - t' \sum_i \sum_j \left(c^\dagger_{i+1,j} n_{i,j+1} c_{i+1,j+2} + c^\dagger_{i+1,j+2} n_{i,j+1} c_{i+1,j} \right) \\ & + V \sum_i \sum_j n_{i,j} n_{i,j+1} + V \sum_i \sum_j n_{i,j} n_{i+1,j}. \end{aligned} \tag{7.5.1}$$

We explain in Section 7.5.1 how pairs of spinless fermions are bound by correlated hops in this limit, and the degrees of freedom in the system become mobile bound pairs with infinite nearest-neighbor repulsion. We develop further analytical intuitions in Sections 7.5.2 and 7.5.3, where we deduce, with the aid of numerical ED calculations, the ground-state wave functions and ground-state energies for a single bound pair and two bound

pairs in a ladder of length L respectively. We find in both cases, the bound pairs behaving like hard-core bosons on a chain with shorter effective length L'.

In Section 7.5.4, we show how one can obtain the exact ground-state wave function and energies for $P/2$ bound pairs in a ladder of length L, by constructing a sequence of maps from bound pairs to extended hard-core bosons (hard-core bosons with infinite nearest-neighbor repulsion) to hard-core bosons to noninteracting spinless fermions. In Section 7.5.5, we discuss some general properties of ladder correlation functions in this strong correlated hopping limit which follows from this sequence of maps, before going on in Sections 7.5.6, 7.5.7 and 7.5.8 to calculate, numerically where necessary, various correlation functions for the ground state of an infinitely-long ladder, to aid our numerical studies of the operator singular value decomposition of the correlation density-matrix in Section 8.4.

7.5.1 Bound Pairs as Effective Degrees of Freedom

When t' become large compared to $t_{\parallel}$ and $t_{\perp}$, we expect the interacting spinless fermions on the two-legged ladder to form well-defined pairs, which are effectively bosons, and thereafter condense into a superconducting ground state. When $t_{\parallel}/t', t_{\perp}/t' > 0$, the size of these bound pairs fluctuate, as shown in Figure 7.27, and the core of the bound pairs get smeared out. This complicates the structure of the many-bound-pair ground state unnecessarily, so we look at the case of infinitely-strong correlated hops $t'/t_{\parallel}, t'/t_{\perp} \to \infty$, where the bound pairs are sharply-defined, and the ground state become significantly simpler in structure.

In this limit of $t'/t_{\parallel}, t'/t_{\perp} \to \infty$, nearest-neighbor hops drop out from the Hamiltonian in (7.3.2), and we find that each bound pair maintains a fixed 'flavor' as it correlated-hops about in the system, as shown in Figure 7.28. We say that a bound pair has an

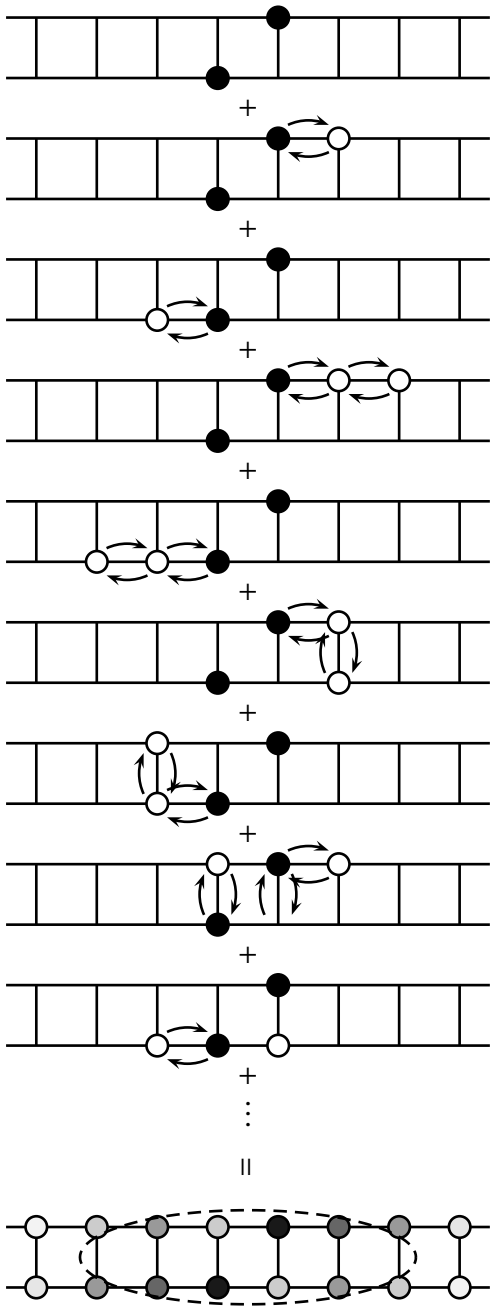

Figure 7.27: Quantum fluctuations of a bound pair of spinless fermions with infinite nearest-neighbor repulsion on a two-legged ladder, for finite nearest-neighbor hopping amplitudes $t_{\parallel}/t', t_{\perp}/t' > 0$.

even configuration, or that it has an *even flavor*, if the two particle coordinates are *even* (explained in caption of Figure 7.28), and *odd configuration* or *odd flavor*, if the two particle coordinates are *odd*. For illustration purposes, we will consistently color the plaquette occupied by an even bound pair red, and color the plaquette occupied by an odd bound pair green.

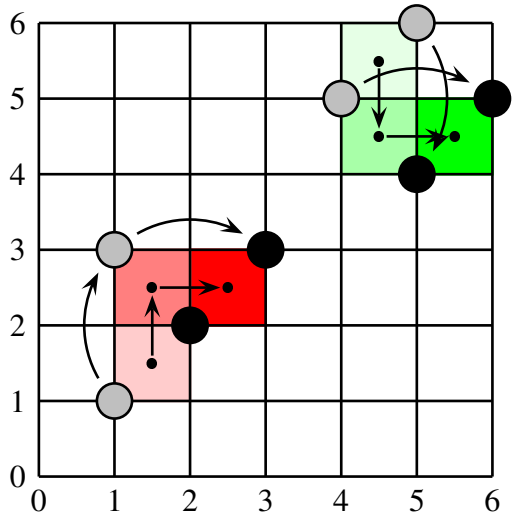

Figure 7.28: The conserved 'flavor' of bound pairs of spinless fermions which can only perform correlated hops on a square lattice. A particle coordinate (x, y) is said to be *even* if x and y are of the same parity, and odd otherwise. A bound pair of spinless fermions is then said to be in an *even configuration* (or having an *even flavor*) if the two particle coordinates are even, and in an *odd configuration* (or having an *odd flavor*) if the two particle coordinates are odd. In the square lattice shown above, the lower-left bound pair is in an even configuration (colored red), because the two particles started off at $(1, 1)$ and $(2, 2)$, before a correlated hop brings them to $(1, 3)$ and $(2, 2)$, and finally to $(2, 2)$ and $(3, 3)$. The upper-right bound pair, on the other hand, is in an odd configuration (colored green), because the two particles started off at $(4, 5)$ and $(5, 6)$, before a correlated hop brings them to $(4, 5)$ and $(5, 4)$, and then finally to $(5, 4)$ and $(6, 5)$.

7.5.2 Ground-State Wave Functions For a Single Bound Pair

In this section and the next, we deduce the ground-state wave function and ground-state energies by looking at the ED results of (7.3.2) for $P = 2$ (a single pair) and $P = 4$ particles (two pairs) respectively, on ladders of increasing length L. The ladder sites are indexed, by the Octave code described in Appendix C, in the manner shown in Figure 7.29. To perform ED using the occupation-number basis described in Appendix C.3.1, we set the nearest-neighbor-hopping matrix element to $t = 0$, and the correlated-hopping matrix element to $t' = 1$, so that we access the limit of $t'/t \to \infty$. With this choice of t and t', the scale of the energy eigenvalues obtained from exact diagonalization is set by $t' = 1$.

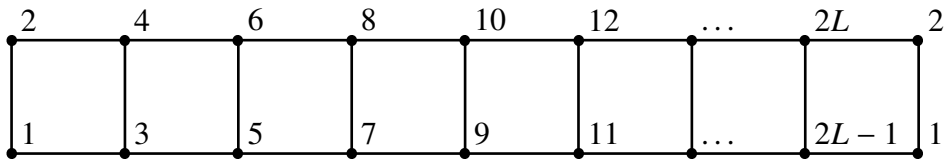

Figure 7.29: Indexing of sites on a two-legged ladder of length L.

As we expect from having two flavors of bound pairs, the single-bound-pair ground state is two-fold degenerate for ladders of even length L subject to periodic boundary conditions. For ladders of odd length L subject to periodic boundary conditions, the flavor of the bound pair changes as it goes around the boundary of the ladder, and so the conserved quantum numbers are not the even and odd flavors, but are instead the symmetric and antisymmetric combinations of the two flavors. This mixing between even and odd flavors lifts the ground-state degeneracy, giving a nondegenerate single-bound-pair ground state whose quantum number is the antisymmetric combination of flavors. From here on we consider only ladders of even length L, because we want to work with ground states containing bound pairs with a definite flavor.

For these ladders, the ground states always occur at wave vectors $\mathbf{q} = (\pi, 0)$ and $\mathbf{q} = (0, \pi)$, and the ground-state energy is always $E/t' = -2$, whatever the length L of the ladder. These ED ground states are translationally invariant both along the ladder axis, and perpendicular to the ladder axis (we imposed periodic boundary condition along this direction as well for the numerical ED). Both of these ED ground states therefore have definite total momentum, but indefinite flavor. We can always construct symmetric and antisymmetric linear combinations of these to obtain ground states with definite flavor, but indefinite total momentum. The two definite-flavor ground states both map to the ground state of a single hard-core boson on a ring.

Now, let us look at the structure of the ground-state wave functions more carefully. For example, on a ladder of length $L = 6$, the two definite-momentum ED ground-state wave functions are[2]

$$|\Psi(\pi,0)\rangle = \frac{1}{\sqrt{12}}$$

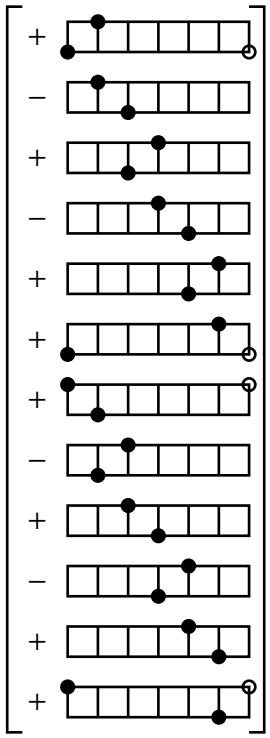

$$, \quad |\Psi(0,\pi)\rangle = \frac{1}{\sqrt{12}}$$

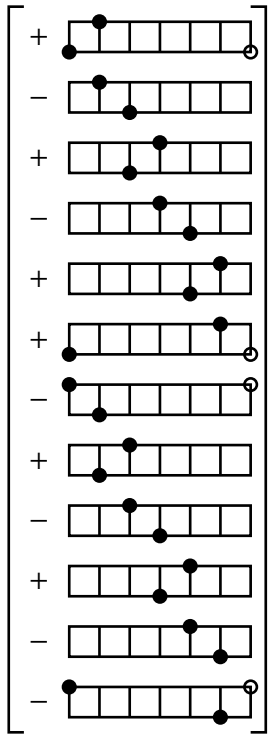

$$,$$

[2]The filled circles denote the sites where the two particles in the bound pair are on, while the open circle, on the right end, and the filled circle, on the the left end, of the same leg of the ladder, are equivalent sites by periodic boundary conditions.

which are the symmetric and antisymmetric combinations of the two definite-flavor ground-state wave functions. The same is true for the ED ground-state wave functions for a ladder of length $L = 8$. For $L = 6$ and $L = 8$, the definite-flavor ground-state wave functions are

$$|\Psi_{6,+}\rangle = \frac{1}{\sqrt{6}}$$

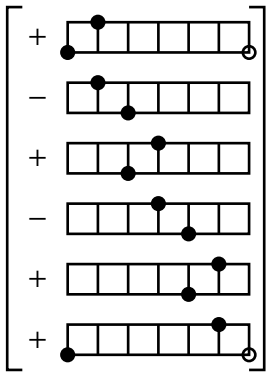

$$, \quad |\Psi_{6,-}\rangle = \frac{1}{\sqrt{12}}$$

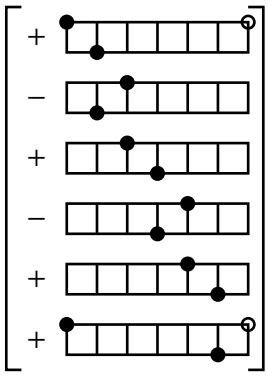

;

and

$$|\Psi_{8,+}\rangle = \frac{1}{\sqrt{8}}$$

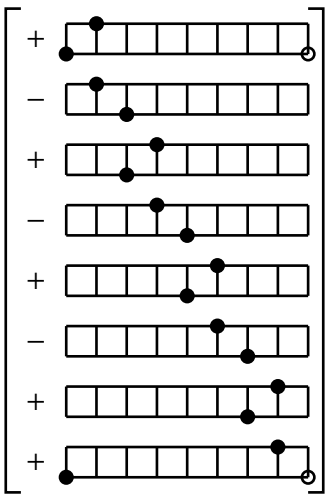

$$, \quad |\Psi_{8,-}\rangle = \frac{1}{\sqrt{8}}$$

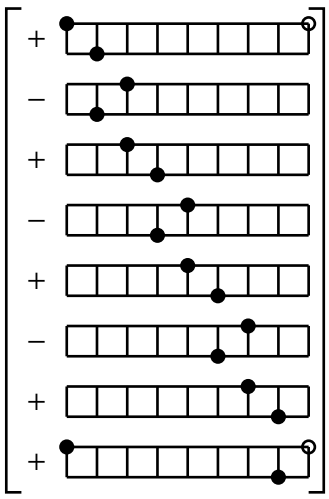

respectively.

Staring at these definite-flavor ground-state wave functions, we find that we can map the single even bound pair, whose particles sit on lattice sites in a plaquette, to an even hard-core boson at the center of the plaquette, to write $|\Psi_{6,+}\rangle$ as

$$|\Psi_{6,+}\rangle = \frac{1}{\sqrt{6}} \left[\begin{array}{l} + \\ - \\ + \\ - \\ + \\ + \end{array} \right. \quad \left. \begin{array}{l} \\ \\ \\ \\ \\ \\ \end{array} \right] = \frac{1}{\sqrt{6}} \sum_{j=1}^{6} B^{\dagger}_{j,+} |0\rangle \,.$$

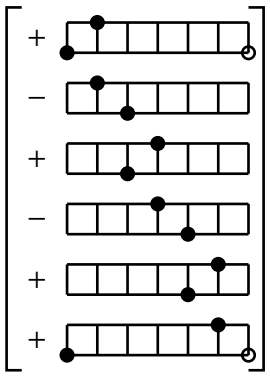

This is the $k = 0$ wave function of a single hard-core boson. Here, the hard-core boson operators are written in terms of the spinless fermion operators as

$$B^{\dagger}_{j,+} = \begin{cases} c^{\dagger}_{1,j} c^{\dagger}_{2,j+1}, & j \text{ odd;} \\ c^{\dagger}_{1,j+1} c^{\dagger}_{2,j}, & j \text{ even,} \end{cases} \tag{7.5.2}$$

i.e. ordered first with respect to the leg index, and then with respect to the rung index of of the ladder. Similarly, we can write the odd hard-core boson operators as

$$B^{\dagger}_{j,-} = \begin{cases} c^{\dagger}_{1,j+1} c^{\dagger}_{2,j}, & j \text{ odd;} \\ c^{\dagger}_{1,j} c^{\dagger}_{2,j+1}, & j \text{ even.} \end{cases} \tag{7.5.3}$$

At this point, let us warn that the bosons that the bound pairs map onto have extended hard cores, i.e. they exclude on-site and nearest-neighbor occupation. However, for a single bound pair on the ladder, this extended hard-core constrain is irrelevant, and we can use the mappings (7.5.2) and (7.5.3) to write down the single-bound-pair ground-state wave functions for ladders of even length L explicitly as

$$|\Psi_{\pm}\rangle = \tilde{B}^{\dagger}_{k=0,\pm} |0\rangle \,, \tag{7.5.4}$$

in terms of the momentum-space boson operators

$$\tilde{B}_{k,\pm} = \frac{1}{\sqrt{L}} \sum_{j=1}^{L} e^{-\mathrm{i}\, k j} \, B^{\dagger}_{j,\pm}. \tag{7.5.5}$$

7.5.3 Ground State For Two Bound Pairs

7.5.3.1 Flavors of Bound Pairs

With $P = 4$ particles on the ladder, we expect two well-defined bound pairs to form in the ground state. These bound pairs are also expected to interact strongly because of the extended hard-core constraint. Nevertheless, we can always write the ground-state wave function as a product of the center-of-mass wave function and the relative-separation wave function. Physically, what this means is that in the center-of-mass frame, we can think of the problem as one extended hard-core boson moving in a finite chain with fixed boundary conditions imposed by the other extended hard-core boson. However, we have two distinct flavors of bound pairs in our problem, which maps to two distinct flavors of extended hard-core bosons. It is important to understand how having two flavors of extended hard-core bosons will affect the structure of the two-bound-pair ground state.

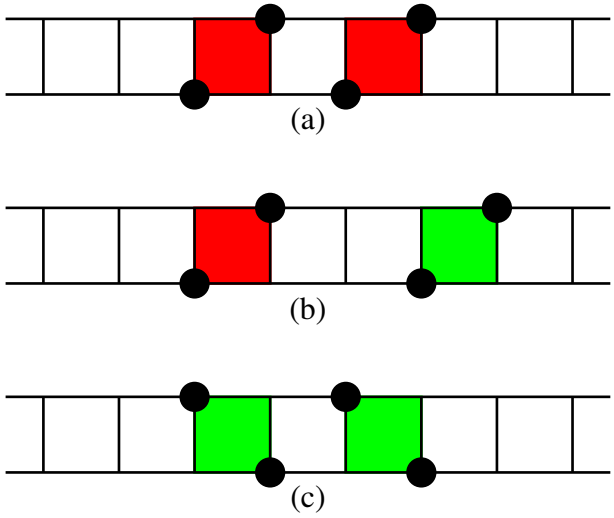

Figure 7.30: The closest approach two bound pairs can make to each other, if (a) they both have even flavors; (b) they have opposite flavors; and (c) they both have odd flavors.

As shown in Figure 7.30, two bound pairs with the same flavor can get within a separation $r = 2$ of each other, whereas two bound pairs with different flavors can only

achieve a closest approach with separation $r = 3$. Therefore, in the center-of-mass frame, we can map the problem of two bound pairs to the problem of a particle in a box of width $L' = L - 2$, if the two bound pairs have the same flavor, or to the problem of a particle in a box of width $L' = L - 4$, if the two bound pairs have different flavors. Since the ground-state energy of a particle in a box of width $L' = L - 2$ is lower than that of a particle in a box of width $L' = L - 4$, it is clear then, from this one-particle-in-a-box picture of the two-bound-pair problem, that the two-bound-pair ground state must consists of configurations in which the two bound pairs have the same flavor.

7.5.3.2 ED Ground-State Wave Functions

Exactly diagonalizing various ladders of even length L, we find that the ground state is two-fold degenerate, and always occur at $\mathbf{q} = (0, 0)$ and $\mathbf{q} = (\pi, \pi)$. This two-fold degeneracy is expected, because the two-even-bound-pair and two-odd-bound-pair problems can both be mapped to the same problem of a particle in a box of width $L' = L - 2$. Again, the ED ground states have definite total momentum, but not definite flavor. The definite-flavor ground states, which are symmetric and antisymmetric combinations of the ED ground states, are

$$|\Psi_{6,+}\rangle = \frac{1}{\sqrt{12}}$$

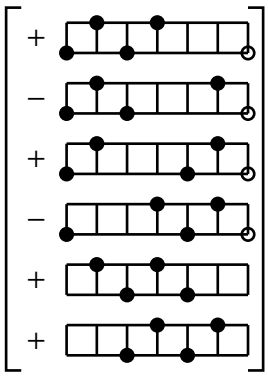

$$+ \frac{1}{\sqrt{6}}$$

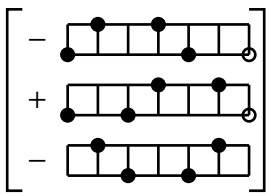

and

$$|\Psi_{6,-}\rangle = \frac{1}{\sqrt{12}}$$

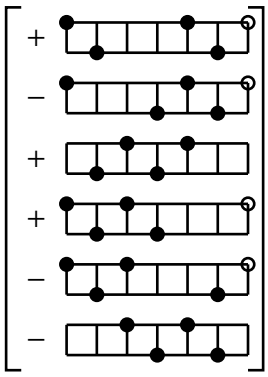

$$+ \frac{1}{\sqrt{6}}$$

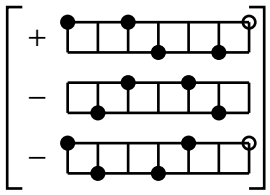

for $L = 6$, and

$$|\Psi_{8,+}\rangle = \tfrac{1}{\sqrt{48}}$$

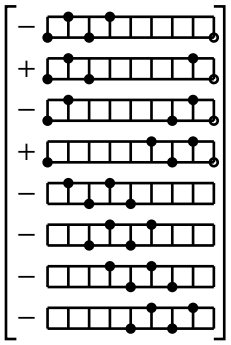

$$+\tfrac{1}{\sqrt{16}}$$

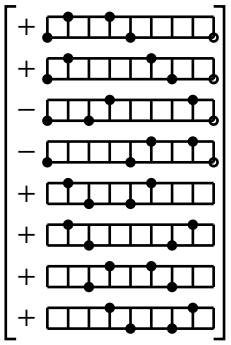

$$+\tfrac{1}{\sqrt{12}}$$

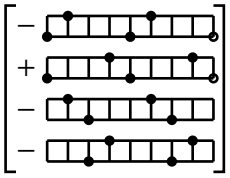

and

$$|\Psi_{8,-}\rangle = \tfrac{1}{\sqrt{48}}$$

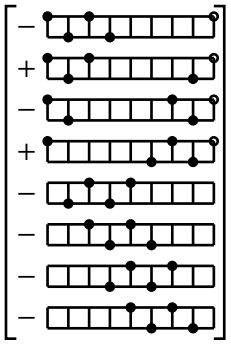

$$+\tfrac{1}{\sqrt{16}}$$

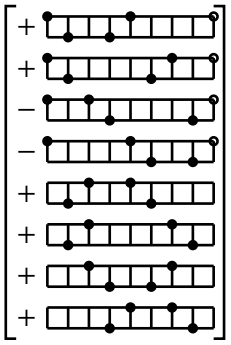

$$+\tfrac{1}{\sqrt{12}}$$

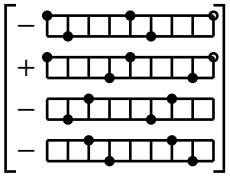

for $L = 8$.

As we can see from the ground-state wave functions for $L = 6$ and $L = 8$, there are very few independent amplitudes. For $|\Psi_{6,\pm}\rangle$, the group of configurations associated with the first absolute amplitude of $1/\sqrt{12}$ corresponds to bound pairs whose relative separations are $r = 2$ (which is as close as they can get to each other, see Figure 7.31 for

one such configuration) and $r = 4$ (measured relative to the left bound pair), while the group of configurations associated with the second absolute amplitude of $1/\sqrt{6}$ corresponds to bound pairs whose relative separations are $r = 3$ (see Figure 7.31 for one such configuration).

Figure 7.31: Configurations of two bound pairs with the same flavor on a two-legged ladder of length $L = 6$, with relative separations $r = 2$ (left) and $r = 3$ (right). The filled circles are the positions of the particles, while the dots indicate the centers of the plaquettes occupied by the bound pairs.

Similarly, for $|\Psi_{8,\pm}\rangle$, we find that the group of configurations associated with the absolute amplitude $1/\sqrt{48}$ corresponds to bound pairs whose separations are $r = 2$ (see Figure 7.32 for one such configuration) and $r = 6$, the group of configurations associated with the absolute amplitude $1/\sqrt{16}$ corresponds to bound pairs whose separations are $r = 3$ (see Figure 7.32 for one such configuration) and $r = 5$, and the group of configurations associated with the absolute amplitude $1/\sqrt{12}$ corresponds to configurations whose separations are $r = 4$ (see Figure 7.32 for one such configuration).

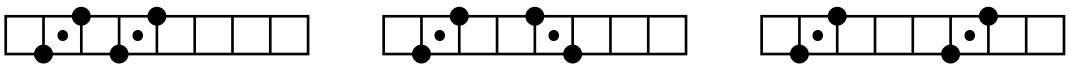

Figure 7.32: Configurations of two bound pairs of the same flavor on a two-legged ladder of length $L = 8$, with separations $r = 2$ (left), $r = 3$ (center), and $r = 4$ (right). The filled circles are the positions of the particles, while the dots indicate the centers of the plaquettes occupied by the bound pairs.

7.5.3.3 Particle-in-a-Box Wave Function

We understand these amplitudes as follows. For $L = 6$, the center-of-mass problem is that of a particle in a box of width $L' = 4$, whose position in the box is $r' = r-1$. Because of fixed boundary conditions, the amplitudes for separations $r' = 0$ and $r' = 4$ must vanish. Of the three non-zero amplitudes, $\Psi(r' = 1)$, $\Psi(r' = 2)$ and $\Psi(r' = 3)$, we have $\Psi(r' = 1) = \Psi(r' = 3)$ because of left-right symmetry, and thus only two independent absolute amplitudes. For $L = 8$, the center-of-mass problem is that of a particle moving in a box of width $L' = 6$, with three independent amplitudes $\Psi(r' = 1) = \Psi(r' = 5)$, $\Psi(r' = 2) = \Psi(r' = 4)$ and $\Psi(r' = 3)$.

Furthermore, we know what the relative separation wave function ought to be. For a particle in a box of width L', the ground-state wave function is

$$\psi(r') = \sqrt{\frac{2}{L'}} \sin \frac{\pi r'}{L'}. \tag{7.5.6}$$

Multiplying $\psi(r')$ by the $k = 0$ center-of-mass wave function

$$\phi(R) = \sqrt{\frac{1}{L}}, \tag{7.5.7}$$

where $R = 1, \ldots, L$ is the center-of-mass coordinate, we obtain the two-bound-pair ground-state wave function

$$\Psi(R, r') = \sqrt{\frac{2}{LL'}} \sin \frac{\pi r'}{L'} = \sqrt{\frac{2}{L(L-2)}} \sin \frac{\pi(r-1)}{L-2}. \tag{7.5.8}$$

Later at the end of Section 7.5.4.3, we shall argue that (7.5.8) should be more appropriately written as

$$\Psi(R, r') = \sqrt{\frac{2}{L(L-2)}} \left| \sin \frac{\pi(r-1)}{L-2} \right|, \tag{7.5.9}$$

since this is the wave function of a pair of bosons. Writing the relative coordinate dependence as the absolute value of a sine instead of a sine poses no difficulty, since

$\sin \frac{\pi(r-1)}{L-2}$ is always positive for $2 \leq r \leq L-2$. We checked that either (7.5.8) or (7.5.9) yields the correct amplitudes for the indefinite-flavor, definite-momentum two-bound-pair ground states on ladders of length up to $L = 16$.

7.5.3.4 Ground-State Energies

For the $L = 6$ to $L = 16$ ladders studied, the ground-state energies obtained from ED are tabulated in Table 7.2, along with closed-form expressions for the ground-state energies obtained using the Inverse Symbolic Calculator [369]. For two noninteracting fermions in a chain of length L', the ground-state energy is

$$E_0 = \epsilon(k = 0) + \epsilon(k = \pm\tfrac{2\pi}{L'}) = -4\cos^2\frac{\pi}{L'}, \tag{7.5.10}$$

if the chain is subjected to periodic boundary conditions, and

$$E_0 = \epsilon(k = -\tfrac{\pi}{L'}) + \epsilon(k = +\tfrac{\pi}{L'}) = -4\cos\frac{\pi}{L'}, \tag{7.5.11}$$

if the chain is subjected to antiperiodic boundary conditions. Here $\epsilon(k) = -2\cos k$ is the single-particle energy on such a chain. For our two-bound-pair problem, the ground-state energy obtained from ED, checked for even ladders with lengths up to $L = 18$, was found to be given by

$$E(L) = -4\cos\frac{\pi}{L-2}, \tag{7.5.12}$$

which corresponds to the ground-state energy of two noninteracting spinless fermions subject to antiperiodic boundary conditions. We shall understand how this *closed shell boundary condition* emerges as we map from bound pairs to extended hard-core bosons to hard-core bosons to noninteracting spinless fermions in the next subsection.

Table 7.2: Ground-state energies of two bound pairs in ladders of even length from $L = 6$ to $L = 16$.

L	E	closed form
6	−2.82842712474619	$-2\sqrt{2}$
8	−3.46410161513775	$-2\sqrt{3}$
10	−3.69551813004515	$-2\sqrt{2+\sqrt{2}}$
12	−3.80422606518062	$-\sqrt{10+\sqrt{20}}$
14	−3.86370330515628	$-2\sqrt{2+\sqrt{3}}$
16	−3.89971164872729	$-4\sin\frac{3\pi}{7}$

7.5.4 Mapping Bound Pairs to Hardcore Bosons

7.5.4.1 Preliminary Considerations

From the review in Section 7.2, we know that the low-energy physics of a quasi-one-dimensional system of spinless or spinfull fermions with weak attractive interactions is found, using perturbative RG analysis, to be that of a Luther-Emery liquid. In the Hamiltonian given by (7.3.2), there are no attractive interactions between particles, although we can imagine writing down an effective attractive interaction between particles that mimics the bound-pair formation effected by the correlated hops. However, for $t'/t_{\|} \to \infty$, this effective attractive interaction will have to be strong, and therefore perturbative RG analysis does not apply. A problem of strongly-bound spinfull fermions on a one-dimensional chain, which has a flavor very similar to our problem of strongly-bound spinless fermions on a two-legged ladder in the limit of $t'/t_{\|} \to \infty$, was solved by Efetov and Larkin [366].

By mapping the bound pairs to hard-core bosons and then subsequently, with the use of the Jordan-Wigner transformation, to noninteracting spinless fermions, Efetov and Larkin found that SC correlations dominate at large distances, decaying as a power law with correlation exponent $-\frac{1}{2}$. Because our problem of bound pairs on the two-legged ladder is so similar, we suspected that it might be possible to obtain an exact analytical solution through a similar, or extended sequence of maps, incorporating the triplet of maps described in Sections 7.4.3, 7.4.4 and 7.4.5. At first, it would appear that we have the added complication of having two flavors of extended hard-core bosons. Indeed, since the bound pairs have immutable flavors as they correlated-hop around, and also because they cannot move past each other, the P-bound-pair Hilbert space essentially breaks up into many independent sectors, each with a fixed sequence of flavors. The P-bound-pair problem in one sector is therefore an independent problem from that of another P-bound-pair sector. For example, on an even-length ladder subject to periodic boundary conditions, the six-bound-pair configuration $|RRGRRG\rangle$, where R (red) denotes an even bound pair, and G (green) denotes an odd bound pair, lies in the same sector as the configuration $|RGRRGR\rangle$, but not with the configuration $|RRRGGG\rangle$, for the obvious reason that the numbers of even and odd bound pairs are different, and also not with the configuration $|RRRGGR\rangle$, because they do not belong the same translation-equivalence class of immutable flavor sequences.

We do not expect to be able to solve the many-bound-pair problem in *all* fixed-flavor-sequence sectors with the help of the sequence of maps described in Sections 7.4.3, 7.4.4 and 7.4.5. We do, however, expect to be able to solve the many-bound-pair problem in *some* sectors with very special fixed flavor sequences, using the triplet of maps. In particular, we saw in Figure 7.30 having P bound pairs of mixed flavors on a finite ladder of length L means that some bound pairs will, on average, have a shorter interval

on the ladder between its two nearest neighbor bound pairs to hop around. The total kinetic energy of these $P/2$ mixed-flavor bound pairs would therefore be higher than the total kinetic energy of P bound pairs of the same flavor (all even or all odd), since each bound pair in this latter case will, on average, have the longest possible interval on the ladder between its two nearest neighbor bound pairs to hop around. This kinetic energy argument is valid for all L, and because there are no other parameters in the limit of $t'/t_{\parallel}, t'/t_{\perp} \to \infty$ and $V \to \infty$, we expect the ground state of an infinitely-long ladder to consist of bound pairs of a single flavor, at all filling fractions. We expect to be able to solve the many-bound-pair problem in this very special fixed-flavor-sequence sector, using the sequence of maps described in the next subsubsection.

7.5.4.2 Overview of Sequence of Maps

To begin with, let us consider the two-bound-pair ground-state wave function in (7.5.8), which applies to both mixed-flavor ground states. Since the definite-flavor ground states can be obtained by taking symmetric and antisymmetric combinations of the two mixed-flavor ground states, let us not worry about the normalization constant associated with the amplitudes, and just look at their spatial structures, which we find to be

$$\Psi(R, r) \propto \left| e^{\mathrm{i}\pi(r-1)/(L-2)} - e^{-\mathrm{i}\pi(r-1)/(L-2)} \right| . \tag{7.5.13}$$

Notwithstanding the fact that $\Psi(R, r)$ is ensured to be positive by the absolute value function, we can think of this amplitude as an antisymmetrized plane wave with $k = \pi/(L-2)$ for two noninteracting spinless fermions separated by a distance $r-1$. Indeed, after mapping bound pairs to extended hard-core bosons, we can then invoke the Bloch-state-to-Bloch-state mapping described in Section 7.4.4 to map the two-extended-hard-core-boson ground state to the two-hard-core-boson ground state, and thereafter mapped to the two-particle Fermi-sea ground state using the Jordan-Wigner transformation.

The proper sequence of maps therefore involve first mapping the bound pairs to extended hard-core bosons, and then to hard-core bosons, and finally to noninteracting spinless fermions. The bound pairs to extended hard-core bosons to hard-core bosons sequence of maps are shown in Figure 7.33, using $L = 6$ as an example. Our goal, in Sections 7.5.4.4 and 7.5.4.3, is to understand this sequence of maps thoroughly, by working with finite chains subject to periodic boundary condition, before proceeding to work out the infinite-chain correlation functions in Section 7.5.5.

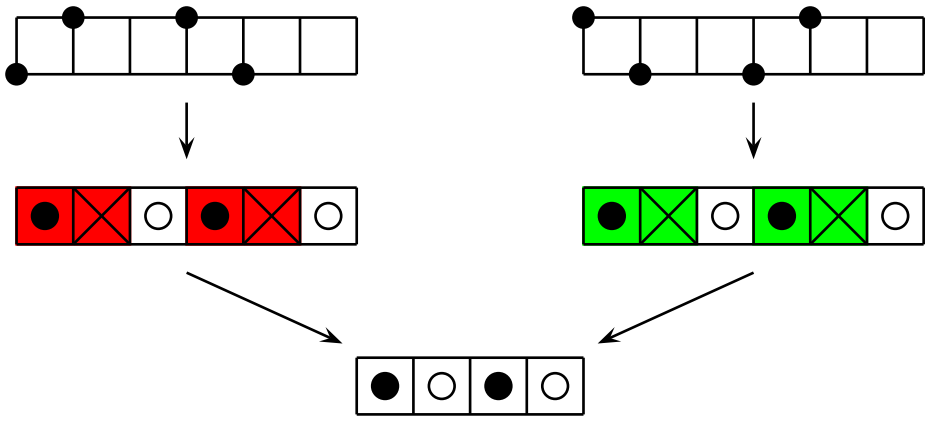

Figure 7.33: Mapping a two-bound-pair configuration on a ladder of length $L = 6$ to an extended hard-core boson configuration on a chain of length $L = 6$ to a hard-core boson configuration on a chain of length $L' = 4$. For consistency, we always exclude the plaquette on the right of the plaquette occupied by a bound pair. As shown above, a two-even-bound-pair configuration (whose extended hard-core boson configuration is colored red) and a two-odd-bound-pair configuration (whose extended hard-core boson configuration is colored green) are both mapped to the same hard-core boson configuration.

7.5.4.3 Hard-Core Bosons to Noninteracting Spinless Fermions

The first map, from bound pairs to extended hard-core bosons, is very simply given by (7.5.2) and (7.5.3), and poses no difficulty. The second map, from extended hard-core bosons to hard-core bosons, is the most difficult technically, and we will devote Section 7.5.4.4 to explore the technical intricacies associated with this map. But before we do this, let us explore the third map, from hard-core bosons to noninteracting spinless fermions, in this subsubsection, to get some important results under our belts. These results will be useful when we discuss the map from extended hard-core bosons to hard-core bosons.

We start with the example of $P' = 2$ noninteracting spinless fermions on a chain of length $L' = 4$, as shown in Figure 7.33. The two-noninteracting-spinless-fermion ground state can be written explicitly as

$$|\Psi_F\rangle = \tilde{c}^\dagger_{k_1} \tilde{c}^\dagger_{k_2} |0\rangle \,, \tag{7.5.14}$$

where k_1 and k_2 are the two occupied wave vectors (and whose values are determined by the boundary conditions imposed). Using the fact that

$$\tilde{c}^\dagger_k = \frac{1}{\sqrt{L'}} \sum_j e^{-\mathrm{i}kj} c^\dagger_j, \tag{7.5.15}$$

we can write the two-noninteracting-spinless-fermion ground state as

$$|\Psi_F\rangle = \sum_{j_1<j_2} A(k_1, k_2; j_1, j_2)\, c^\dagger_{j_1} c^\dagger_{j_2} |0\rangle \,, \tag{7.5.16}$$

in the ED basis of $\{c^\dagger_{j_1} c^\dagger_{j_2} |0\rangle\}_{j_1<j_2}$. The amplitude

$$A(k_1, k_2; j_1, j_2) = \frac{1}{L'} \left[e^{-\mathrm{i}(k_1 j_1 + k_2 j_2)} - e^{-\mathrm{i}(k_1 j_2 + k_2 j_1)} \right] \tag{7.5.17}$$

of the configuration $c^\dagger_{j_1} c^\dagger_{j_2} |0\rangle$, with $j_1 < j_2$, is obtained after we antisymmetrize the amplitudes of $c^\dagger_{j_1} c^\dagger_{j_2} |0\rangle$ and $c^\dagger_{j_2} c^\dagger_{j_1} |0\rangle$.

When we say that the two-hard-core boson ground state has the same structure as the two-noninteracting-spinless-fermion Fermi-sea ground state, we mean that the hard-core boson ground state is

$$|\Psi_B\rangle = \sum_{j_1<j_2} A(k_1, k_2; j_1, j_2)\, b^\dagger_{j_1} b^\dagger_{j_2} |0\rangle \tag{7.5.18}$$

in the ED basis of $\{b^\dagger_{j_1} b^\dagger_{j_2} |0\rangle\}_{j_1<j_2}$. This follows from the fact that the hard-core boson Hamiltonian is identical, matrix element by matrix element, to the noninteracting spinless fermion Hamiltonian. Naively, we might think that the hard-core boson ground state is

$$|\Psi_B\rangle = \tilde{b}^\dagger_{k_1} \tilde{b}^\dagger_{k_2} |0\rangle\,, \quad \tilde{b}^\dagger_k = \frac{1}{\sqrt{L'}} \sum_j e^{-\mathrm{i}kj} b^\dagger_j. \tag{7.5.19}$$

but we can check that we cannot arrive at (7.5.18) starting from (7.5.19), because the hard-core boson operators commute instead of anticommute.

For this same reason of the hard-core boson operators commuting with one another, the amplitude $A(k_1, k_2; j_1, j_2)$ looks worrying: if we exchange j_1 and j_2, we have $A(k_1, k_2; j_2, j_1) = -A(k_1, k_2; j_1, j_2)$. When this amplitude appears in the ground-state wave function of noninteracting spinless fermions, the anticommutation of $c^\dagger_{j_1}$ and $c^\dagger_{j_2}$ produces a minus sign that would cancel that coming from the amplitude, giving us back the same ground-state wave function. For hard-core bosons, $b^\dagger_{j_1}$ and $b^\dagger_{j_2}$ commute, and so it appears that we end up with a different wave function! To understand what is going on, let us single out a pair of sites $j'_1 < j'_2$, and imagine doing two EDs, one with the basis $\{b^\dagger_{j_1} b^\dagger_{j_2} |0\rangle\}_{j_1<j_2}$, and one with the basis $\{b^\dagger_{j_1} b^\dagger_{j_2} |0\rangle\}_{j_1<j_2;(j_1,j_2)\neq(j'_1,j'_2)} \cup \{b^\dagger_{j'_2} b^\dagger_{j'_1} |0\rangle\}$. Computing the matrix elements of the hard-core boson Hamiltonian, we find that the matrices in the two bases are identical, and thus have identical ground-state amplitudes. For this to be true of the basis states $b^\dagger_{j'_1} b^\dagger_{j'_2} |0\rangle$ and $b^\dagger_{j'_2} b^\dagger_{j'_1} |0\rangle$, the amplitude of the latter must be $-A(k_1, k_2; j'_2, j'_1) = A(k_1, k_2; j'_1, j'_2)$. For this reason, the hard-core boson ground

state is usually given in the literature [370, 371] as

$$|\Psi_B\rangle = \sum_{j_1<j_2<\cdots<j_P} |A(k_1, k_2, \ldots, k_P; j_1, j_2, \ldots, j_P)|\, b^\dagger_{j_1} b^\dagger_{j_2} \cdots b^\dagger_{j_P} |0\rangle \tag{7.5.20}$$

for P particles on a chain.

Later in Section 7.5.4.4, we will invoke the Bloch-state-to-Bloch-state map introduced in Section 7.4.4 between extended hard-core bosons to hard-core bosons. In this map, the amplitudes of interest are those of Bloch states, and not those of configurations. Therefore, let us rewrite $|\Psi_F\rangle$ as an expansion over the Bloch states. To make our discussions more general, we work with $P' = 3$ noninteracting spinless fermions on a chain of length L'. The steps involved can then be generalized to any number of noninteracting spinless fermions. We begin by writing down the properly-normalized three-fermion ground state, with single-particle wave vectors k_1, k_2 and k_3 occupied, as

$$|\Psi_F\rangle = \frac{1}{\sqrt{L'}}\frac{1}{\sqrt{L'}}\frac{1}{\sqrt{L'}} \sum_{j_1}\sum_{j_2}\sum_{j_3} e^{-\mathrm{i}k_1 j_1}\, e^{-\mathrm{i}k_2 j_2}\, e^{-\mathrm{i}k_3 j_3}\, c^\dagger_{j_1} c^\dagger_{j_2} c^\dagger_{j_3} |0\rangle\,. \tag{7.5.21}$$

To write (7.5.21) as a sum over Bloch states, we need to first identify and group configurations related by translational symmetry. This we do by breaking the sum in (7.5.21) up into six terms,

$$\begin{aligned}
|\Psi_F\rangle = {} & \frac{1}{\sqrt{L'}}\frac{1}{\sqrt{L'}}\frac{1}{\sqrt{L'}} \sum_{j_1<j_2<j_3} e^{-\mathrm{i}k_1 j_1}\, e^{-\mathrm{i}k_2 j_2}\, e^{-\mathrm{i}k_3 j_3}\, c^\dagger_{j_1} c^\dagger_{j_2} c^\dagger_{j_3} |0\rangle + \\
& \frac{1}{\sqrt{L'}}\frac{1}{\sqrt{L'}}\frac{1}{\sqrt{L'}} \sum_{j_1<j_3<j_2} e^{-\mathrm{i}k_1 j_1}\, e^{-\mathrm{i}k_2 j_2}\, e^{-\mathrm{i}k_3 j_3}\, c^\dagger_{j_1} c^\dagger_{j_2} c^\dagger_{j_3} |0\rangle + \\
& \frac{1}{\sqrt{L'}}\frac{1}{\sqrt{L'}}\frac{1}{\sqrt{L'}} \sum_{j_2<j_1<j_3} e^{-\mathrm{i}k_1 j_1}\, e^{-\mathrm{i}k_2 j_2}\, e^{-\mathrm{i}k_3 j_3}\, c^\dagger_{j_1} c^\dagger_{j_2} c^\dagger_{j_3} |0\rangle + \\
& \frac{1}{\sqrt{L'}}\frac{1}{\sqrt{L'}}\frac{1}{\sqrt{L'}} \sum_{j_2<j_3<j_1} e^{-\mathrm{i}k_1 j_1}\, e^{-\mathrm{i}k_2 j_2}\, e^{-\mathrm{i}k_3 j_3}\, c^\dagger_{j_1} c^\dagger_{j_2} c^\dagger_{j_3} |0\rangle + \\
& \frac{1}{\sqrt{L'}}\frac{1}{\sqrt{L'}}\frac{1}{\sqrt{L'}} \sum_{j_3<j_1<j_2} e^{-\mathrm{i}k_1 j_1}\, e^{-\mathrm{i}k_2 j_2}\, e^{-\mathrm{i}k_3 j_3}\, c^\dagger_{j_1} c^\dagger_{j_2} c^\dagger_{j_3} |0\rangle + \\
& \frac{1}{\sqrt{L'}}\frac{1}{\sqrt{L'}}\frac{1}{\sqrt{L'}} \sum_{j_3<j_2<j_1} e^{-\mathrm{i}k_1 j_1}\, e^{-\mathrm{i}k_2 j_2}\, e^{-\mathrm{i}k_3 j_3}\, c^\dagger_{j_1} c^\dagger_{j_2} c^\dagger_{j_3} |0\rangle\,,
\end{aligned} \tag{7.5.22}$$

and in each term rearrange the fermion operators in ascending order, so that the fermion operator with the smallest site index appears first, followed by the fermion operator with the next smallest site index, followed by the fermion operator with the largest site index. We then relabel the dummy indices j_1, j_2, j_3, so that j_1 always refers to the smallest site index, and j_3 always refers to the largest site index, before writing $j_2 = j_1 + r_2$ and $j_3 = j_1 + r_2 + r_3$, where $r_2 > 0$ and $r_3 > 0$ are the separations between the second particle and the first, and between the third particle and the second, respectively.

Finally, we reorder the sums, to sum over j_1 before summing over r_2 and r_3, to write the ground state for three noninteracting spinless fermions

$$|\Psi_F\rangle = \sum_{r_2>0} \sum_{r_3>0} \Psi_F(k_1, k_2, k_3; r_2, r_3) \frac{1}{\sqrt{L'}} \sum_{j_1} e^{-\mathrm{i}\, q j_1}\, c^\dagger_{j_1} c^\dagger_{j_1+r_2} c^\dagger_{j_1+r_2+r_3} |0\rangle \tag{7.5.23}$$

in terms of the normalized Bloch states

$$\frac{1}{\sqrt{L'}} \sum_{j} e^{-\mathrm{i}\, q j}\, c^\dagger_{j} c^\dagger_{j+r_2} c^\dagger_{j+r_2+r_3} |0\rangle\,. \tag{7.5.24}$$

Here

$$q = k_1 + k_2 + k_3 \tag{7.5.25}$$

is the total momentum wave vector, and

$$\begin{aligned}\Psi_F(k_1, k_2, k_3; r_2, r_3) = \frac{1}{\sqrt{L'}} \frac{1}{\sqrt{L'}} \Big[&+ e^{-\mathrm{i}[k_1 r_2 + k_2 (r_2+r_3)]} + e^{-\mathrm{i}[k_2 r_2 + k_3 (r_2+r_3)]} \\ &+ e^{-\mathrm{i}[k_3 r_2 + k_1 (r_2+r_3)]} - e^{-\mathrm{i}[k_1 (r_2+r_3) + k_2 r_2]} \\ &- e^{-\mathrm{i}[k_2 (r_2+r_3) + k_3 r_2]} - e^{-\mathrm{i}[k_3 (r_2+r_3) + k_1 r_2]} \Big]\end{aligned} \tag{7.5.26}$$

is the antisymmetrized amplitude of the Bloch state generated by the configuration $|0, r_2, r_2 + r_3\rangle$. From our discussions in Sections 7.4.6 and 7.5.4.3, and the fact that each configuration that appears in (7.5.18) occurs only once in a single Bloch state, the P-hard-core boson ground state $|\Psi_B\rangle$ can be obtained very simply from the P-noninteracting-spinless-fermion ground state $|\Psi_F\rangle$, by taking the absolute values of all

the fermionic amplitudes, i.e.

$$|\Psi_B\rangle = \sum_{r_2>0} \cdots \sum_{r_P>0} |\Psi_F(k_1, \ldots, k_P; r_2, \ldots, r_P)| \times \frac{1}{\sqrt{l'}} \sum_j e^{-\mathrm{i}\, qj}\, b_j^\dagger b_{j+r_2}^\dagger \cdots b_{j+r_2+\cdots+r_P}^\dagger |0\rangle\,, \quad (7.5.27)$$

where l' is the period of the Bloch state generated by $b_j^\dagger b_{j+r_2}^\dagger \cdots b_{j+r_2+\cdots+r_P}^\dagger |0\rangle$.

It is important to note that the wave vectors k_1, k_2, and k_3 appearing in the amplitudes $\Psi_F(k_1, k_2, k_3; r_2, r_3)$ are those of noninteracting spinless fermions that our bound pairs eventually map onto, and thus are allowed wave vectors for a chain of length L' (not L!) subject to the appropriate boundary conditions. For a translation-invariant system, the many-particle ground state always occurs with total momentum $q = 0$. Therefore, if we have an even number P of bound pairs on a ladder of length L subject to periodic boundary conditions, the ground-state problem eventually maps onto the ground-state problem of an even number of noninteracting spinless fermions on a chain of length $L' = L - P$ subject to *antiperiodic boundary conditions*, with allowed wave vectors $k_n = \pm\frac{(2n+1)\pi}{L'}$ and $q = \sum_{k_n \text{ occupied}} k_n = 0$. On the other hand, if we have an odd number P of bound pairs on a ladder of length L subject to periodic boundary conditions, the ground-state problem eventually maps onto the ground-state problem of an odd number of noninteracting spinless fermions on a chain of length $L' = L - P$ subject to *periodic boundary conditions*, with allowed wave vectors $k_n = \pm\frac{2n\pi}{L'}$, and $q = \sum_{k_n \text{ occupied}} k_n = 0$. In the literature, this manner of alternating boundary conditions for even and odd number of particles in the chain is called *closed shell boundary conditions*.

7.5.4.4 Extended Hard-Core Bosons to Hard-Core Bosons

Returning to the second map from extended hard-core bosons to hard-core bosons, let us consider the example of $P = 4$ spinless fermions with infinite nearest-neighbor repulsion

on a two-legged ladder of length $L = 6$ subject to periodic boundary conditions. For this problem, we expect, through the sequence of maps, the ground state to be mapped eventually onto $P' = 2$ noninteracting spinless fermions on a chain of length $L' = 4$ subject to antiperiodic boundary conditions. For antiperiodic boundary conditions on the $L' = 4$ chain, the allowed wave vectors are

$$k = -\frac{3\pi}{4}, -\frac{\pi}{4}, +\frac{\pi}{4}, +\frac{3\pi}{4}, \tag{7.5.28}$$

and the two occupied wave vectors are $k_1 = -\frac{\pi}{4}$ and $k_2 = +\frac{\pi}{4}$. We find thus the antisymmetrized two-fermion amplitudes, and the symmetrized two-hard-core-boson amplitudes, tabulated in Table 7.3.

Table 7.3: Antisymmetrized two-fermion and symmetrized two-hard-core-boson amplitudes on a chain of length $L' = 4$, for $k_1 = -\frac{\pi}{4}$ and $k_2 = +\frac{\pi}{4}$.

j_1	j_2	$A(k_1, k_2; j_1, j_2)$	$\lvert A(k_1, k_2; j_1, j_2)\rvert$
1	2	$-\mathrm{i}/2\sqrt{2}$	$1/2\sqrt{2}$
1	3	$-\mathrm{i}/2$	$1/2$
1	4	$-\mathrm{i}/2\sqrt{2}$	$1/2\sqrt{2}$
2	3	$-\mathrm{i}/2\sqrt{2}$	$1/2\sqrt{2}$
2	4	$-\mathrm{i}/2$	$1/2$
3	4	$-\mathrm{i}/2\sqrt{2}$	$1/2\sqrt{2}$

In Table 7.3, we find two independent amplitudes, which agrees with the number of independent amplitudes found in the ED ground states. The ratio of these two amplitudes are also correct. However, the numerical values of the amplitudes are not what we would expect naively: we have $\frac{1}{2}$ instead of $\frac{1}{\sqrt{6}}$, and $\frac{1}{2\sqrt{2}}$ instead of $\frac{1}{\sqrt{12}}$. We saw in Section 7.4.3 that the reason for this has to do with the many-to-one nature of the

right-exclusion map. Here we find a total of nine distinct even configurations for the finite ladder of length $L = 6$, which must map to six distinct configurations on the finite chain of length $L' = 4$. The solution we then saw in Section 7.4.4 is to map ladder Bloch states to chain Bloch states.

For $P' = 2$ hard-core bosons on a chain of length $L' = 4$, there are only two independent Bloch states, each associated with one of the two independent absolute amplitudes. We can write these as

$$\begin{aligned} |\alpha', q'\rangle &= \frac{1}{\sqrt{L'}} \sum_{r'=0}^{L'-1} e^{-iq'r'} \, T_{r'} \, |1, 2\rangle \,, \\ |\beta', q'\rangle &= \frac{1}{\sqrt{L'}} \sum_{r'=0}^{L'-1} e^{-iq'r'} \, T_{r'} \, |1, 3\rangle \,, \end{aligned} \tag{7.5.29}$$

where $|j_1, j_2\rangle = b^\dagger_{j_1} b^\dagger_{j_2} |0\rangle$, and $T_{r'}$ is the translation operator which translates each particle to the right by r'. Similarly, for two even bound pairs on a ladder of length $L = 6$, there are only two independent Bloch states associated with the two independent absolute amplitudes. We can write these as

$$|\alpha, q\rangle = \frac{1}{\sqrt{L}} \sum_{r=0}^{L-1} e^{-iqr} \, T_r \, \Big| \quad \Big\rangle \,,$$

$$|\beta, q\rangle = \frac{1}{\sqrt{L}} \sum_{r=0}^{L-1} e^{-iqr} \, T_r \, \Big| \quad \Big\rangle \,. \tag{7.5.30}$$

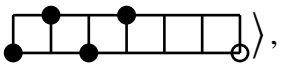

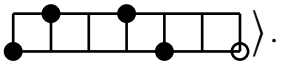

The hard-core-boson Hamiltonian H_b in (7.4.10) is block-diagonal in the basis formed by the Bloch states in (7.5.29), while the infinitely-strong correlated-hop Hamiltonian $H_{t'V}$ in (7.5.1) is block-diagonal in the basis formed by the Bloch states in (7.5.30). We then explained in Section 7.4.5 that the 2×2 diagonal block matrices $H_{\rm hb}(q')$ is identical to $H_{t'V}(q)$ if q' and q are related by (7.4.61). This condition is satisfied for the two-hard-core-boson and two-bound-pair ground states, where $q' = 0 = q$, in which case we find

that we can write the two ground states as

$$\begin{aligned} |\Psi'\rangle &= \Psi'_{\alpha',0}\,|\alpha',0\rangle + \Psi'_{\beta',0}\,|\beta',0\rangle\,, \\ |\Psi\rangle &= \Psi_{\alpha,0}\,|\alpha,0\rangle + \Psi_{\beta,0}\,|\beta,0\rangle\,, \end{aligned} \tag{7.5.31}$$

where we have identical amplitudes

$$\Psi'_{\alpha',0} = \Psi_{\alpha,0}, \quad \Psi'_{\beta',0} = \Psi_{\beta,0}. \tag{7.5.32}$$

In general, for P bound pairs mapping to P hard-core bosons, the P-bound-pair ground state, which occurs, say, with $q = q_0$, is

$$|\Psi\rangle = \sum_{\alpha} \Psi_{\alpha,q_0}\,|\alpha,q_0\rangle\,, \tag{7.5.33}$$

where the amplitudes $\Psi_{\alpha,q_0} = \Psi'_{\alpha',q'_0=q_0}$ can be obtained from the P-hard-core-boson ground state (7.5.27), which can in turn be obtained from the P-noninteracting-spinless-fermion ground state, given in (7.4.68) and (7.4.69), as shown at the end of Section 7.5.4.3. Because there are two flavors of bound pairs, and hence two flavors of hard-core bosons, we have two degenerate ground states, given by

$$|\Psi_\pm\rangle = \sum_{r_2>0} \cdots \sum_{r_P>0} |\Psi_F(k_1,\ldots,k_P;r_2,\ldots,r_P)|\,|q=0;r_2,\ldots,r_P\rangle_\pm\,, \tag{7.5.34}$$

where $\Psi_F(k_1,\ldots,k_P;r_2,\ldots,r_P)$ are the Bloch-state amplitudes of the P-noninteracting-spinless-fermion ground state (7.4.68), and

$$|q;r_2,\ldots,r_P\rangle_\pm \propto \sum_{j_1} e^{-\mathrm{i}\,q j_1}\, B^\dagger_{j_1,\pm} B^\dagger_{j_1+r_2+1,\pm} \cdots B^\dagger_{j_1+r_2+\cdots+r_P+P-1,\pm}\,|0\rangle \tag{7.5.35}$$

are the normalized Bloch states of the nearest-neighbor excluded chain of hard-core bosons.

7.5.5 General Properties of Ladder Correlation Functions

Having the full sequence of maps from bound pairs to extended hard-core bosons to hard-core bosons to noninteracting spinless fermions at our disposal, we want to take

advantage of our knowledge of the amplitudes $\Psi_F(k_1, \ldots, k_P; r_2, \ldots, r_P)$ to calculate various ladder correlation functions. Let us start by identifying the ladder correlations that take on the simplest forms in the extended hard-core boson picture. These would be the extended hard-core boson two-point functions

$$\langle B_i^\dagger B_{i+r} \rangle \,, \tag{7.5.36}$$

and the extended hard-core boson four-point functions

$$\langle B_i^\dagger B_i B_{i+r}^\dagger B_{i+r} \rangle \,, \tag{7.5.37}$$

which corresponds to SC correlations and plaquette-plaquette density correlations.

We note here that in order for the Bloch-state-to-Bloch-state mapping to work, we cannot restrict ourselves to definite-flavor states, but must work with definite-momentum states, which we saw in Sections 7.5.2 and 7.5.3 are symmetric and antisymmetric combinations

$$|\Psi_g\rangle = \tfrac{1}{\sqrt{2}}(|\Psi_+\rangle + |\Psi_-\rangle \,, \quad |\Psi_u\rangle = \tfrac{1}{\sqrt{2}}(|\Psi_+\rangle - |\Psi_-\rangle \,, \tag{7.5.38}$$

of the definite-flavor states. In either of these definite-momentum ground states, the expectations $\langle B_{i,+}^\dagger B_{j,-} \rangle$ and $\langle B_{i,-}^\dagger B_{j,+} \rangle$ vanishes, because the combination of hard-core boson operators will annihilate a hard-core boson of one flavor, and create one of another flavor, giving a state that has no overlap with the chosen ground state.

Because of this vanishing cross-correlation between the hard-core boson operators $B_{i,+}$ and $B_{i,-}$ defined in (7.5.2) and (7.5.3), we can choose to work instead with the symmetric and antisymmetric combinations

$$B_{i,g} = \tfrac{1}{\sqrt{2}} \left(B_{i,+} + B_{i,-} \right) , \quad B_{i,u} = \tfrac{1}{\sqrt{2}} \left(B_{i,+} - B_{i,-} \right) , \tag{7.5.39}$$

of $B_{i,+}$ and $B_{i,-}$. Furthermore, we know before evaluating any correlations, that for every expectation of a product strictly of $B_{i,g}$, we will find an identical expectation coming

from the corresponding product strictly of $B_{i,u}$. We say therefore that correlations which can be written in terms of expectations of extended hard-core boson operators are *two-fold degenerate*.

In addition, we also note that, when we write these expectations out as intervening-particle expansions of the form found in (7.4.99), the nature of the sum is different for even r and odd r. For even r, we sum over all intervening bound-pair configurations up till the one in which all free plaquettes are exhausted. For odd r, the sum over all intervening bound-pair configurations is up till configurations leaving just one plaquette free, which is then too 'small' to fit another bound pair. This gives rise to an even-odd modulation in *all* extended-hard-core-boson correlations, which is a shell-like effect having nothing to do with Fermi-liquid-type Friedel oscillations governed by the filling fraction $\bar{n}$.

7.5.6 Superconducting Correlations

As we have mentioned, the ladder SC correlations can be written as the extended hard-core boson two-point functions $\langle B_i^\dagger B_{i+r}\rangle$. We drop the *gerade* and *ungerade* indices g and u associated with the extended-hard-core-boson operators defined in (7.5.39) to make the notations more compact, bearing in mind $\langle B_{i,g}^\dagger B_{i+r,g}\rangle = \langle B_{i,u}^\dagger B_{i+r,u}\rangle$. Because $\langle B_i^\dagger B_{i+r}\rangle$ is the sum of various fixed-intervening-configuration terms of various effective separations in (7.4.99), there is no simple asymptotic formula for $\langle B_i^\dagger B_{i+r}\rangle$ in the limit of separation $r \to \infty$. However, it is possible to devise an algorithm to compute the numerical value of the infinite-ladder SC correlations $\langle \Delta_{j,g}^\dagger \Delta_{j+r,g}\rangle$ and $\langle \Delta_{i,u}^\dagger \Delta_{i+r,u}\rangle$, where

$$\begin{aligned}
\Delta_{i,g}^\dagger &= \tfrac{1}{\sqrt{2}}(c_{1,i}^\dagger c_{2,i+1}^\dagger + c_{1,i+1}^\dagger c_{2,i}^\dagger),\\
\Delta_{i,u}^\dagger &= \tfrac{1}{\sqrt{2}}(-1)^i\,(c_{1,i}^\dagger c_{2,i+1}^\dagger - c_{1,i+1}^\dagger c_{2,i}^\dagger),
\end{aligned} \tag{7.5.40}$$

for any separation and any ladder filling fraction. Since these two SC correlations are degenerate, we shall drop the indices g and u from here on.

7.5.6.1 Numerical Evaluation of Intervening-Particle Expansion

To motivate the algorithm, let us work out what $\langle \Delta_i^\dagger \Delta_{i+r} \rangle$ is for a few small separations r, and then generalize the expression to larger separations by induction. First, we note that the expectations $\langle B_i^\dagger B_{i+2} \rangle$ and $\langle B_i^\dagger B_{i+3} \rangle$ shown in Figures 7.34 and 7.35 respectively, have particularly simple structures, because the two extended hard-core boson operators are too close together for an intervening extended hard-core boson to fit between them. Using results from Sections 7.4.1, 7.4.6 and 7.4.7, we find that for $r = 2$,

$$\langle B_i^\dagger B_{i+2} \rangle = \langle B_i^\dagger (\mathbb{1} - N_{i+1}) B_{i+2} \rangle + \langle B_i^\dagger N_{i+1} B_{i+2} \rangle = \frac{\bar{N}_1}{\bar{n}_1} \langle b_i^\dagger b_{i+1} \rangle = \frac{\bar{N}_1}{\bar{n}_1} \langle c_i^\dagger c_{i+1} \rangle , \quad (7.5.41)$$

where $\bar{N}_1$ is the nearest-neighbor excluded chain filling fraction, and $\bar{n}_1$ is the nearest-neighbor included chain filling fraction. For the rest of this thesis, we will use $\bar{N}$ to denote nearest-neighbor excluded filling fractions, and $\bar{n}$ to denote nearest-neighbor included filling fractions, and the subscripts 1 and 2 to indicate whether these are of chains (which can be thought of as one-legged ladders), or of two-legged ladders. Similarly, we find for $r = 3$ that

$$\begin{aligned} \langle B_i^\dagger B_{i+3} \rangle = {} & \langle B_i^\dagger (\mathbb{1} - N_{i+1})(\mathbb{1} - N_{i+2}) B_{i+3} \rangle + \langle B_i^\dagger N_{i+1} (\mathbb{1} - N_{i+2}) B_{i+3} \rangle + \\ & \langle B_i^\dagger (\mathbb{1} - N_{i+1}) N_{i+2} B_{i+3} \rangle + \langle B_i^\dagger N_{i+1} N_{i+2} B_{i+3} \rangle \\ = {} & \frac{\bar{N}_1}{\bar{n}_1} \langle b_i^\dagger (\mathbb{1} - n_{i+1}) b_{i+2} \rangle = \frac{\bar{N}_1}{\bar{n}_1} \langle c_i^\dagger (\mathbb{1} - n_{i+1}) c_{i+2} \rangle , \end{aligned} \quad (7.5.42)$$

since the last three terms in the intervening-particle expansion vanish because of nearest-neighbor exclusion.

The infinite-ladder SC correlations, as shown in Figures 7.36 and 7.37, get more interesting for $r = 4$ and $r = 5$. From Figures 7.36 and 7.37, we see that for $r = 4$ and

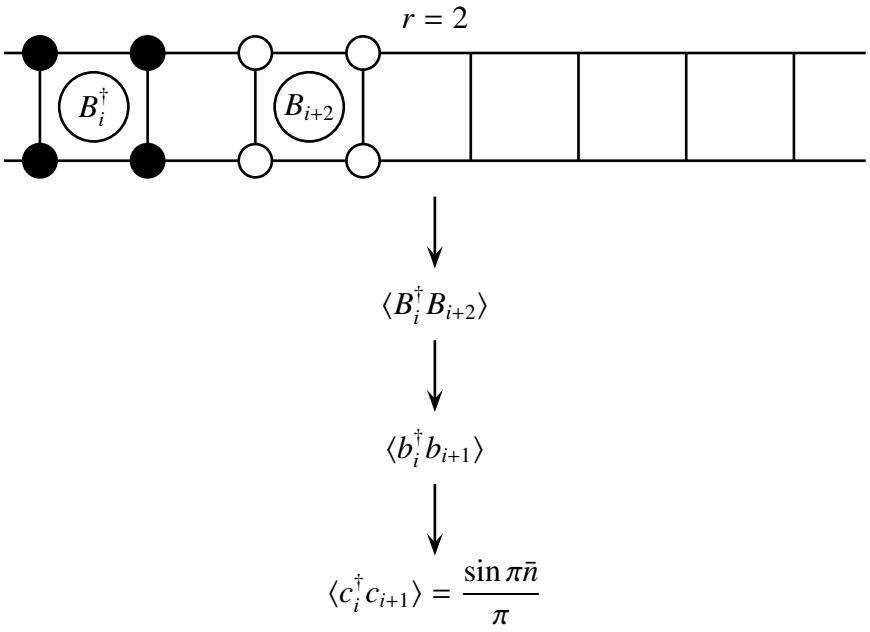

Figure 7.34: The infinite-ladder SC correlations for $r = 2$, expressed in terms of noninteracting spinless fermion expectations. The filled circles are the ladder sites on which spinless fermions are to be created by $B_i^\dagger$, while the open circles are the ladder sites on which spinless fermions are to be annihilated by B_{i+2}.

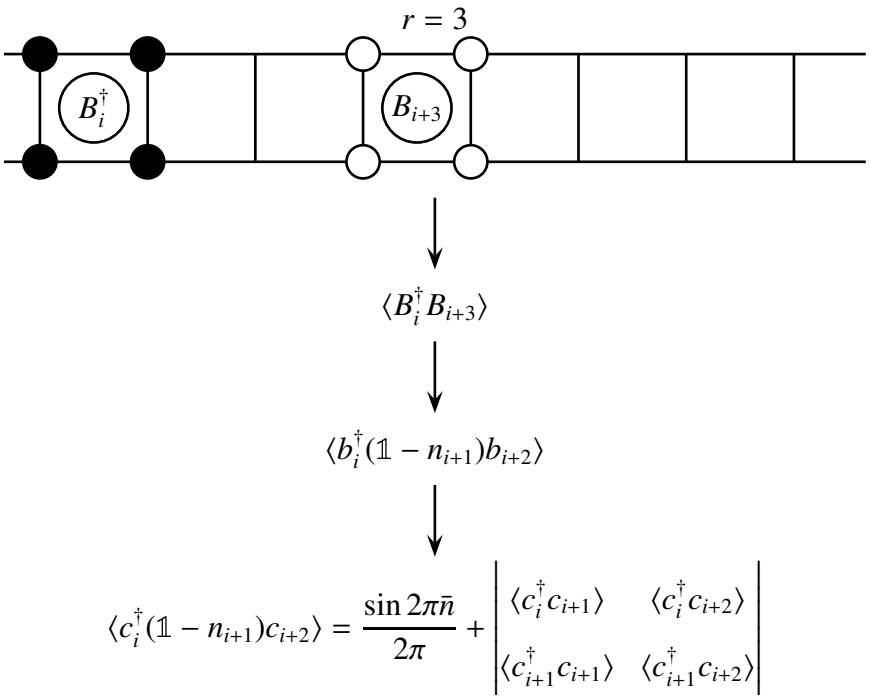

Figure 7.35: The infinite-ladder SC correlations for $r = 3$, expressed in terms of noninteracting spinless fermion expectations. The filled circles are the ladder sites on which spinless fermions are to be created by $B_i^\dagger$, while the open circles are the ladder sites on which spinless fermions are to be annihilated by B_{i+3}.

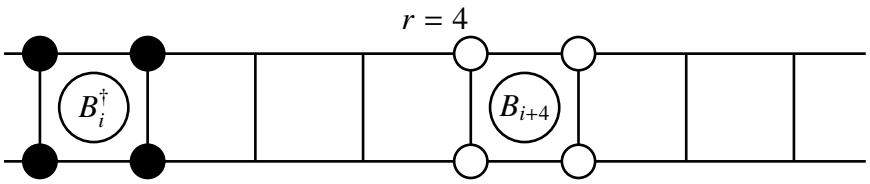

$$\downarrow$$

$$\langle B_i^\dagger B_{i+4}\rangle$$

$$\downarrow$$

$$\langle b_i^\dagger(\mathbb{1}-n_{i+1})(\mathbb{1}-n_{i+2})b_{i+3}\rangle + \langle b_i^\dagger n_{i+1} b_{i+2}\rangle$$

$$\downarrow$$

$$\langle c_i^\dagger(\mathbb{1}-n_{i+1})(\mathbb{1}-n_{i+2})c_{i+3}\rangle - \langle c_i^\dagger n_{i+1} c_{i+2}\rangle$$

$$\shortparallel$$

$$\bar{n}\,\mathsf{g}(3) + \bar{n}^2\begin{vmatrix}\mathsf{g}(1) & \mathsf{g}(3)\\ 1 & \mathsf{g}(2)\end{vmatrix} + \bar{n}^2\begin{vmatrix}\mathsf{g}(2) & \mathsf{g}(3)\\ 1 & \mathsf{g}(1)\end{vmatrix} + \bar{n}^3\begin{vmatrix}\mathsf{g}(1) & \mathsf{g}(2) & \mathsf{g}(3)\\ 1 & \mathsf{g}(1) & \mathsf{g}(2)\\ \mathsf{g}(1) & 1 & \mathsf{g}(1)\end{vmatrix} + \bar{n}^2\begin{vmatrix}\mathsf{g}(1) & \mathsf{g}(2)\\ 1 & \mathsf{g}(1)\end{vmatrix}$$

Figure 7.36: The infinite-ladder SC correlations for $r = 4$, expressed in terms of noninteracting spinless fermion expectations. The filled circles are the ladder sites on which spinless fermions are to be created by $B_i^\dagger$, while the open circles are the ladder sites on which spinless fermions are to be annihilated by B_{i+4}. Here $\mathsf{g}(r) = g(r)$ are the values of the reduced two-point function defined in (2.3.15).

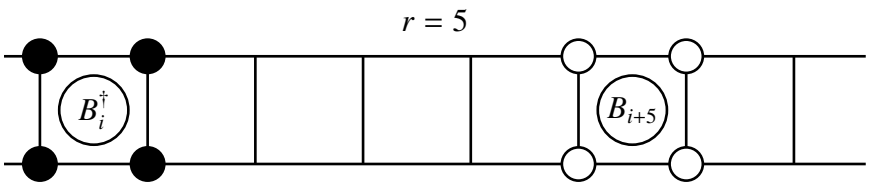

$$\downarrow$$

$$\langle B_i^\dagger B_{i+5}\rangle$$

$$\downarrow$$

$$\langle b_i^\dagger(\mathbb{1}-n_{i+1})(\mathbb{1}-n_{i+2})(\mathbb{1}-n_{i+3})b_{i+4}\rangle + \langle b_i^\dagger n_{i+1}(\mathbb{1}-n_{i+2})b_{i+3}\rangle + \langle b_i^\dagger(\mathbb{1}-n_{i+1})n_{i+2}b_{i+3}\rangle$$

$$\downarrow$$

$$\langle c_i^\dagger(\mathbb{1}-n_{i+1})(\mathbb{1}-n_{i+2})(\mathbb{1}-n_{i+3})c_{i+4}\rangle - \langle c_i^\dagger n_{i+1}(\mathbb{1}-n_{i+2})c_{i+3}\rangle - \langle c_i^\dagger(\mathbb{1}-n_{i+1})n_{i+2}c_{i+3}\rangle$$

$$=$$

$$\bar{n}\,\mathsf{g}(4) + \bar{n}^2\begin{vmatrix}\mathsf{g}(1) & \mathsf{g}(4)\\ 1 & \mathsf{g}(3)\end{vmatrix} + \bar{n}^2\begin{vmatrix}\mathsf{g}(2) & \mathsf{g}(4)\\ 1 & \mathsf{g}(2)\end{vmatrix} + \bar{n}^2\begin{vmatrix}\mathsf{g}(3) & \mathsf{g}(4)\\ 1 & \mathsf{g}(1)\end{vmatrix} +$$

$$\bar{n}^3\begin{vmatrix}\mathsf{g}(1) & \mathsf{g}(2) & \mathsf{g}(4)\\ 1 & \mathsf{g}(1) & \mathsf{g}(3)\\ \mathsf{g}(1) & 1 & \mathsf{g}(2)\end{vmatrix} + \bar{n}^3\begin{vmatrix}\mathsf{g}(1) & \mathsf{g}(3) & \mathsf{g}(4)\\ 1 & \mathsf{g}(2) & \mathsf{g}(3)\\ \mathsf{g}(2) & 1 & \mathsf{g}(1)\end{vmatrix} + \bar{n}^3\begin{vmatrix}\mathsf{g}(2) & \mathsf{g}(3) & \mathsf{g}(4)\\ 1 & \mathsf{g}(1) & \mathsf{g}(2)\\ \mathsf{g}(1) & 1 & \mathsf{g}(1)\end{vmatrix} +$$

$$\bar{n}^4\begin{vmatrix}\mathsf{g}(1) & \mathsf{g}(2) & \mathsf{g}(3) & \mathsf{g}(4)\\ 1 & \mathsf{g}(1) & \mathsf{g}(2) & \mathsf{g}(3)\\ \mathsf{g}(1) & 1 & \mathsf{g}(1) & \mathsf{g}(2)\\ \mathsf{g}(2) & \mathsf{g}(1) & 1 & \mathsf{g}(1)\end{vmatrix}$$

Figure 7.37: The infinite-ladder SC correlations for $r = 5$, expressed in terms of noninteracting spinless fermion expectations. The filled circles are the ladder sites on which spinless fermions are to be created by $B_i^\dagger$, while the open circles are the ladder sites on which spinless fermions are to be annihilated by B_{i+5}. Here $\mathsf{g}(r) = g(r)$ are the values of the reduced two-point function defined in (2.3.15).

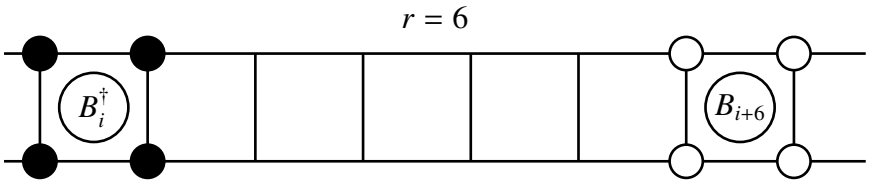

$$\downarrow$$

$$\langle B_i^\dagger B_{i+6} \rangle$$

$$\downarrow$$

$$\langle b_i^\dagger (\mathbb{1} - n_{i+1})(\mathbb{1} - n_{i+2})(\mathbb{1} - n_{i+3})(\mathbb{1} - n_{i+4}) b_{i+5} \rangle + \langle b_i^\dagger n_{i+1} (\mathbb{1} - n_{i+2})(\mathbb{1} - n_{i+3}) b_{i+4} \rangle +$$
$$\langle b_i^\dagger (\mathbb{1} - n_{i+1}) n_{i+2} (\mathbb{1} - n_{i+3}) b_{i+4} \rangle + \langle b_i^\dagger (\mathbb{1} - n_{i+1})(\mathbb{1} - n_{i+2}) n_{i+3} b_{i+4} \rangle +$$
$$\langle b_i^\dagger n_{i+1} n_{i+2} b_{i+3} \rangle$$

$$\downarrow$$

$$\langle c_i^\dagger (\mathbb{1} - n_{i+1})(\mathbb{1} - n_{i+2})(\mathbb{1} - n_{i+3})(\mathbb{1} - n_{i+4}) c_{i+5} \rangle - \langle c_i^\dagger n_{i+1} (\mathbb{1} - n_{i+2})(\mathbb{1} - n_{i+3} c_{i+4} \rangle -$$
$$\langle c_i^\dagger (\mathbb{1} - n_{i+1}) n_{i+2} (\mathbb{1} - n_{i+3}) c_{i+4} \rangle - \langle c_i^\dagger (\mathbb{1} - n_{i+1})(\mathbb{1} - n_{i+2}) n_{i+3} c_{i+4} \rangle +$$
$$\langle c_i^\dagger n_{i+1} n_{i+2} c_{i+3} \rangle$$

$$=$$

(see text)

Figure 7.38: The infinite-ladder SC correlations for $r = 6$, expressed in terms of noninteracting spinless fermion expectations. The filled circles are the ladder sites on which spinless fermions are to be created by $B_i^\dagger$, while the open circles are the ladder sites on which spinless fermions are to be annihilated by B_{i+6}.

$r = 5$, the infinite-ladder SC correlations are positive sums of the minors of the matrices

$$\mathbf{G}(4) = \bar{n} \begin{bmatrix} 1 & \mathsf{g}(1) & \mathsf{g}(2) & \mathsf{g}(3) \\ \mathsf{g}(1) & 1 & \mathsf{g}(1) & \mathsf{g}(2) \\ \mathsf{g}(2) & \mathsf{g}(1) & 1 & \mathsf{g}(1) \\ \mathsf{g}(3) & \mathsf{g}(2) & \mathsf{g}(1) & 1 \end{bmatrix} \tag{7.5.43}$$

for $r = 4$ and

$$\mathbf{G}(5) = \bar{n} \begin{bmatrix} 1 & \mathsf{g}(1) & \mathsf{g}(2) & \mathsf{g}(3) & \mathsf{g}(4) \\ \mathsf{g}(1) & 1 & \mathsf{g}(1) & \mathsf{g}(2) & \mathsf{g}(3) \\ \mathsf{g}(2) & \mathsf{g}(1) & 1 & \mathsf{g}(1) & \mathsf{g}(2) \\ \mathsf{g}(3) & \mathsf{g}(2) & \mathsf{g}(1) & 1 & \mathsf{g}(1) \\ \mathsf{g}(4) & \mathsf{g}(3) & \mathsf{g}(2) & \mathsf{g}(1) & 1 \end{bmatrix} \tag{7.5.44}$$

for $r = 5$. Here $\mathsf{g}(r) = g(r)$ are the values of the reduced noninteracting-spinless-fermion two-point function defined in (2.3.15).

Checking for $r = 6$, shown in Figure 7.38, we find that the infinite-ladder SC correlation is again the sum of minors of the matrix

$$\mathbf{G}(6) = \bar{n} \begin{bmatrix} 1 & \mathsf{g}(1) & \mathsf{g}(2) & \mathsf{g}(3) & \mathsf{g}(4) & \mathsf{g}(5) \\ \mathsf{g}(1) & 1 & \mathsf{g}(1) & \mathsf{g}(2) & \mathsf{g}(3) & \mathsf{g}(4) \\ \mathsf{g}(2) & \mathsf{g}(1) & 1 & \mathsf{g}(1) & \mathsf{g}(2) & \mathsf{g}(3) \\ \mathsf{g}(3) & \mathsf{g}(2) & \mathsf{g}(1) & 1 & \mathsf{g}(1) & \mathsf{g}(2) \\ \mathsf{g}(4) & \mathsf{g}(3) & \mathsf{g}(2) & \mathsf{g}(1) & 1 & \mathsf{g}(1) \\ \mathsf{g}(5) & \mathsf{g}(4) & \mathsf{g}(3) & \mathsf{g}(2) & \mathsf{g}(1) & 1 \end{bmatrix}. \tag{7.5.45}$$

Using the notation

$$\mathsf{G}^{r_1 \cdots r_m}_{c_1 \cdots c_m} \tag{7.5.46}$$

to denote the mth-order minor formed by the $1 \le r_1, \ldots, r_m \le r$ rows, and $1 \le c_1, \ldots, c_m \le r$ columns of $\mathbf{G}$, we then write the $r = 6$ infinite-ladder SC correlations as

$$\mathsf{G}^{1}_{6}+\mathsf{G}^{12}_{26}+\mathsf{G}^{13}_{36}+\mathsf{G}^{14}_{46}+\mathsf{G}^{15}_{56}+\mathsf{G}^{12}_{25}+\mathsf{G}^{13}_{35}+\mathsf{G}^{14}_{45}+$$
$$\mathsf{G}^{123}_{236}+\mathsf{G}^{124}_{246}+\mathsf{G}^{125}_{256}+\mathsf{G}^{134}_{346}+\mathsf{G}^{135}_{356}+\mathsf{G}^{145}_{456}+2\mathsf{G}^{123}_{235}+2\mathsf{G}^{124}_{245}+2\mathsf{G}^{134}_{345}+\mathsf{G}^{123}_{234}+$$
$$\mathsf{G}^{1234}_{2346}+\mathsf{G}^{1235}_{2356}+\mathsf{G}^{1245}_{2456}+\mathsf{G}^{1345}_{3456}+3\mathsf{G}^{1234}_{2345}+\mathsf{G}^{12345}_{23456}. \quad (7.5.47)$$

These minors are contributed by the five expectations shown in Figure 7.38, which corresponds to $p = 0$, 1 and 2 intervening pairs. For two extended-hard-core-boson operators separated by a distance r, the maximum number of intervening pairs that can fit between them is

$$p_{\max} = \left\lfloor \frac{r-2}{2} \right\rfloor, \quad (7.5.48)$$

where $\lfloor z \rfloor$ is the greatest integer less than z. In the p-intervening-pair expectations, the maximum separation that can appear in all the minors it contributes is

$$r_{\max} = r - p, \quad (7.5.49)$$

while the order of the minors goes from $m = p + 1$ to $m = r_{\max} - 1$, m being the number of rows and columns in a minor. For a given p and a given m, we can work out all the minors combinatorially.

Having clarified the steps to be taken, we use the following algorithm to compute the infinite-ladder SC correlation $\langle \Delta_i^\dagger \Delta_{i+r} \rangle$:

1. For each $(0 \le p \le p_{\max})$-intervening-pair expectation, we calculate the maximum separation $r_{\max} = r - p$ that can occur in the expectation, and sum over the minors it contribute order by order.

2. For each order $p + 1 \le m \le r_{\max} - 1$, we run over all possible indices $1 < j_1 < j_2 < \cdots < j_{m-1} < r_{\max}$, and construct the minors

$$\mathsf{G}^{1\, j_1\, j_2 \cdots j_{m-1}}_{j_1\, j_2 \cdots j_{m-1}\, r_{\max}}. \quad (7.5.50)$$

3. The contribution of $\mathsf{G}^{1\,j_1\,j_2\cdots\,j_{m-1}}_{j_1\,j_2\cdots\,j_{m-1}\,r_{\max}}$ to $\langle\Delta_i^\dagger\Delta_{i+r}\rangle$ is

$$\binom{m-1}{p}\mathsf{G}^{1\,j_1\,j_2\cdots\,j_{m-1}}_{j_1\,j_2\cdots\,j_{m-1}\,r_{\max}}. \tag{7.5.51}$$

The binomial coefficient $\binom{m-1}{p}$ gives the number of times the minor $\mathsf{G}^{1\,j_1\,j_2\cdots\,j_{m-1}}_{j_1\,j_2\cdots\,j_{m-1}\,r_{\max}}$ appears when we sum over all minors of order m from all p-intervening-pair expectations. For example, for $r = 6$ and $p = 1$, the order-3 minor G^{123}_{235} arises from both

$$\langle c_1^\dagger n_2(\mathbb{1}-n_3)(\mathbb{1}-n_4)c_5\rangle \quad \text{and} \quad \langle c_1^\dagger(\mathbb{1}-n_2)n_3(\mathbb{1}-n_4)c_5\rangle\,, \tag{7.5.52}$$

but not from

$$\langle c_1^\dagger(\mathbb{1}-n_3)(\mathbb{1}-n_3)n_4c_5\rangle\,. \tag{7.5.53}$$

Therefore, the multiplicity of G^{123}_{235} is the number of ways to place one intervening pair at either $j = 2$ or $j = 3$. For an order-3 minor, there are $3 - 1 = 2$ creation operator indices j apart from i, but only $p = 1$ of them can correspond to an intervening pair. The multiplicity of G^{123}_{235} is therefore

$$\binom{2}{1} = 2. \tag{7.5.54}$$

Another example is the case $r = 6$ and $p = 1$, where we find the order-4 minor G^{1234}_{2345} being contributed by all three expectations

$$\begin{aligned}
&\langle c_1^\dagger n_2(\mathbb{1}-n_3)(\mathbb{1}-n_4)c_5\rangle\,,\\
&\langle c_1^\dagger(\mathbb{1}-n_2)n_3(\mathbb{1}-n_4)c_5\rangle\,,\\
&\langle c_1^\dagger(\mathbb{1}-n_3)(\mathbb{1}-n_3)n_4c_5\rangle\,.
\end{aligned} \tag{7.5.55}$$

The predicted multiplicity of

$$\binom{4-1}{1} = \binom{3}{1} = 3 \tag{7.5.56}$$

agrees with this observation.

We note here that the formula for the multiplicity depends on the structure of the observable whose correlation we are evaluating. It is $\binom{m-1}{p}$ for the SC order parameters $\Delta_{i,g}$ and $\Delta_{i,u}$ defined in (7.5.40), but will typically be something else for some other observables. For a generic observable, we know of no quick way to write down the multiplicity formula. In all of the expectations calculated in this manner, we arrived at the multiplicity formula by working through a few simple cases, and from the observed patterns deduce a formula for arbitrary m and p.

4. The final ingredient that we need to get right to compute the infinite-ladder SC correlations is the nearest-neighbor included filling fraction $\bar{n}_1$. For $2P$ particles on a finite ladder of length L, forming P bound pairs, the nearest-neighbor excluded filling fraction is $\bar{N}_1 = P/L$. In the ground state, these P bound pairs map to P extended hard-core bosons on a chain of length L, which then maps to P hard-core bosons on a chain of length $L' = L - P$. Finally, this maps to P noninteracting spinless fermions on a chain of length $L' = L - P$. The nearest-neighbor included filling fraction is therefore

$$\bar{n}_1 = \frac{P}{L'} = \frac{P}{L-P} = \frac{\bar{N}_1}{1-\bar{N}_1}. \tag{7.5.57}$$

As $L \to \infty$ with $\bar{N}_1 = P/L$ fixed, we shall take $\bar{n}_1$ in (7.5.57) to be the value of $\bar{n}$ to stick into the calculations for the infinite-ladder SC correlations. After summing over the intervening-particle expansion, we must then multiply the nearest-neighbor included chain result by $\bar{N}_1/\bar{n}_1$ to get the correct numerical value for $\langle \Delta_i^\dagger \Delta_{i+r} \rangle$.

The algorithm described above is workable, but because it sums over a large number of minors generated on the fly, it is certainly not the most efficient. Using the above

algorithm as a basic outline, we can think of two approaches to accelerate the calculations. In the first approach, we note that minors of higher and higher orders make smaller and smaller contributions to the overall expectation, and so the most straightforward acceleration we can implement is to generate and sum only those minors making contributions upwards of the desired precision we wish to calculate the expectations to. We do this by first deciding on a cut off, and then for each p, stop summing higher-order minors when the current order m of minors have absolute values which are all smaller than the cut off. If we so desire, this cut off can be set at machine precision, but we can make significant savings in computation time if we sacrifice some precision. This is desirable, since we do not really require the numerical correlations to be accurate to double precision for the nonlinear curve fits we are about to perform, and we certainly do not need such precision just to graph the correlations.

The second approach to accelerating the calculations, in principle at least, is to note that many of the low-order minors are themselves minors of the high-order minors. Therefore, if we can write high-order minors as sums of products of low-order minors, we can perform a lookup on their existing values stored in memory to calculate the high-order minors. Of course, we might occasionally need to calculate those we do not yet have, but the hope that this would be infrequent enough that the calculations using looked-up values become faster and faster. However, there are many technical issues that we need to tackle in order to implement this acceleration scheme, the first of which would be to set up a rather elaborate data structure storing the minors as we calculate them. In case we do not have all the subminors need to compute the value of a particular minor, we would also need to implement a subroutine that would figure out from the data structure which subminors are needed, which of these already exist, and which of these do not, and thus have to be computed. When we consider implementing such

an acceleration scheme in Octave, we must therefore balance the theoretical speedup possible with the practical overhead incurred.

Figure 7.39 shows the infinite-ladder SC correlations $\langle \Delta_j^\dagger \Delta_{j+r} \rangle$ for separations $r = 2$ to $r = 17$ as functions of the nearest-neighbor excluded chain filling fraction $0 \leq \bar{N}_1 \leq \frac{1}{2}$. We make the following observations from Figure 7.39:

1. the infinite-ladder SC correlations $\langle \Delta_j^\dagger \Delta_{j+r} \rangle$ is always positive;

2. $\langle \Delta_j^\dagger \Delta_{j+r} \rangle$ rises linearly with small $\bar{N}_1$ for all r;

3. for small $\bar{N}_1$, $\langle \Delta_j^\dagger \Delta_{j+r} \rangle$ has an approximate scaling form depending on $\bar{N}_1 r$. In particular, $\langle \Delta_j^\dagger \Delta_{j+r} \rangle / \bar{N}_1 r \approx 0.5$ when $\bar{N}_1 r \approx 0.83$;

4. the even-odd modulation in $\langle \Delta_j^\dagger \Delta_{j+r} \rangle$ is most pronounced for $\bar{N}_1$ just below $\frac{1}{2}$, and

   (a) all $\langle \Delta_j^\dagger \Delta_{j+r} \rangle$ with even r vanishes with the same finite slope as $\bar{N}_1 \to \frac{1}{2}^-$;

   (b) all $\langle \Delta_j^\dagger \Delta_{j+r} \rangle$ with odd r vanishes with zero slope as $\bar{N}_1 \to \frac{1}{2}^-$.

For comparison with the numerical SC correlations obtained from finite ladders, we ought to plot $\langle \Delta_j \Delta_{j+r} \rangle$ as a function of r. For $P = 4$ and $P = 6$ on $L = 10$ ladders, and $P = 6$ on $L = 12$ ladders, the nearest-neighbor excluded chain filling fractions accessed by the numerical calculations are $\bar{N}_1 = 4/20 = 0.20$, $\bar{N}_1 = 6/20 = 0.30$ and $\bar{N}_1 = 6/24 = 0.25$ respectively. For this purpose, we really only need to compute the infinite-ladder SC correlations for separations up to $r = 6$. But since the algorithm described above allows us in principle to calculate numerically the infinite-ladder SC correlations for *any* separation, we want to take advantage of this analytical inroad that we have made to calculate $\langle \Delta_j \Delta_{j+r} \rangle$ for even larger separations. In this respect, we are limited by the number of minors we have to construct from a $r \times r$ Green-function matrix $\mathbf{G}(r)$. This number grows exponentially with r, so we have a rapidly diminishing return on the

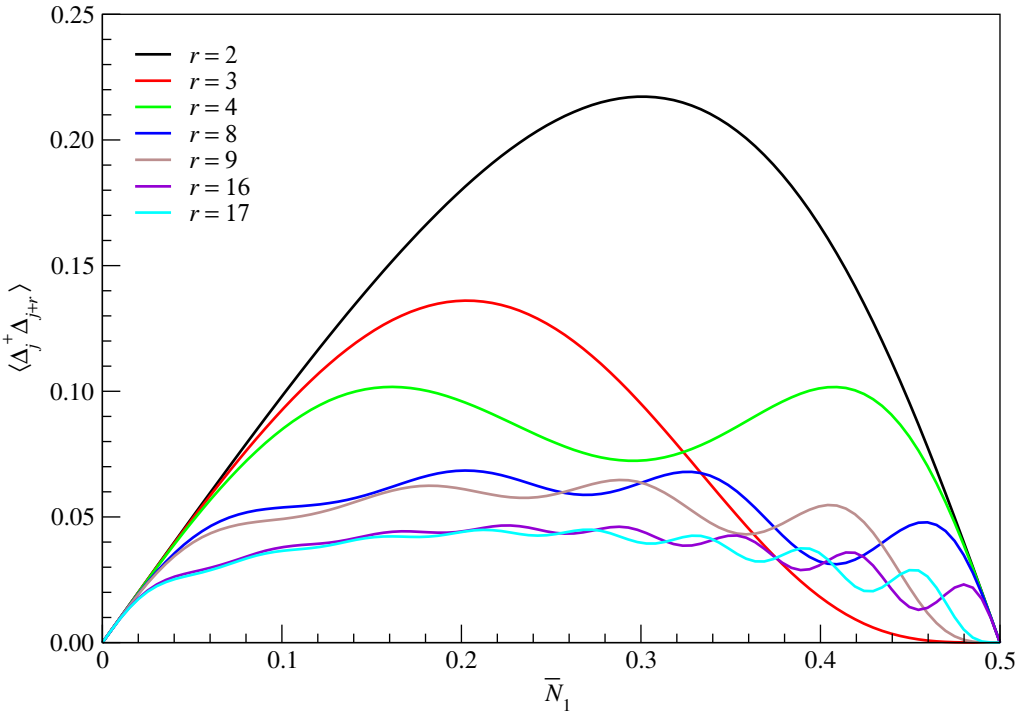

Figure 7.39: The infinite-ladder SC correlation $\langle \Delta_j^\dagger \Delta_{j+r} \rangle$, in the limit of $t' \gg t_\parallel, t_\perp$, as a function of the nearest-neighbor excluded chain filling fraction $\bar{N}_1$, for $r = 2$ to $r = 17$.

computational effort we incur to calculate $\langle \Delta_j \Delta_{j+r} \rangle$ as r increases. We choose therefore to evaluate the infinite-ladder SC correlations, for various nearest-neighbor excluded chain filling fractions $\bar{N}_1$, from a minimum separation of $r = 2$, up to a maximum separation of $r = 17$. For each $\bar{N}_1$, this numerical Octave calculation takes about twenty minutes on a single-processor, Pentium-4 class, 2.0-GHz machine.

7.5.6.2 Nonlinear Curve Fitting the Numerical Correlations

With sixteen data points for each series of infinite-ladder SC correlations versus separation at fixed nearest-neighbor excluded chain filling fractions, it is possible to learn more about the behaviour of such parameters as the correlation exponents as a function of the nearest-neighbor excluded chain filling fraction, by performing nonlinear curve fits on $\langle \Delta_j \Delta_{j+r} \rangle$. We use the nonlinear curve fitting function in xmgrace [372], which uses the Levenberg-Marquardt algorithm [373], to do these curve fits. We expect the asymptotic behaviour

$$\langle \Delta_j \Delta_{j+r} \rangle \sim A r^{-\beta} + B r^{-\gamma} \cos(kr + \phi) \tag{7.5.58}$$

for the infinite-ladder SC correlations, but find that fitting the numerical data to this asymptotic form doing a six-parameter fit (A, β, B, γ, k and ϕ) in xmgrace is both numerically inaccurate and unstable. First of all, the Levenberg-Marquardt algorithm gives equal weight to all data points, and so for rapidly decaying correlations, it might get the long-range tail wrong while reporting a good numerical fit. Secondly, the nonlinear curve fit of the sum of two power laws with comparable exponents, and independent amplitudes, tends frequently to be unstable, with pair(s) of exponent and amplitude running away to absurd values.

To remedy the first problem of inaccuracy in fitting rapidly decaying power laws, we note that if we multiply $\langle \Delta_j \Delta_{j+r} \rangle$ by r^β, then $r^\beta \langle \Delta_j \Delta_{j+r} \rangle \sim A + B r^{-(\gamma-\beta)} \cos(kr + \phi)$. By

curve fitting this modified asymptotic form, we can obtain the amplitude A more reliably. Furthermore, the nonlinear curve fit is observed to be numerically more stable when we fit the data to only one power law, because the parameter space is one dimension smaller. However, to reduce the dimensionality of the parameter space in this way, we would need to know what β is *a priori*. Since this information is not available, we tried multiplying $\langle \Delta_j^\dagger \Delta_{j+r} \rangle$ by various simple powers of r, and eyeball the resulting numerical data. We find, as shown in Figure 7.40, that $r^2 \langle \Delta_j^\dagger \Delta_{j+r} \rangle$ and $r \langle \Delta_j^\dagger \Delta_{j+r} \rangle$ are both increasing functions of r, and thus the correlation exponent must be $\beta < 1$.

Guided by Efetov and Larkin's result of a universal correlation exponent of $\beta = \frac{1}{2}$ for a chain of tightly-bound spinless-fermion pairs, we multiply $\langle \Delta_j^\dagger \Delta_{j+r} \rangle$ by $r^{1/2}$, and found visually that $r^{1/2} \langle \Delta_j^\dagger \Delta_{j+r} \rangle$ for various nearest-neighbor excluded chain filling fractions appear to be functions which oscillate about fixed means, with amplitudes that decay with increasing separation. This suggests that we fit the numerical data to the asymptotic form

$$r^{1/2} \langle \Delta_j^\dagger \Delta_{j+r} \rangle = A + B r^{-(\gamma - 1/2)} \cos(kr + \phi). \tag{7.5.59}$$

The fitted parameters are shown in Table 7.4. We also show, in Figure 7.41, $r^{1/2} \langle \Delta_j^\dagger \Delta_{j+r} \rangle$ for the nearest-neighbor excluded chain filling fractions $\bar{N}_1 = 0.20$, 0.25, and 0.30 that will be accessed in the numerical studies described in Chapter 8.

Figure 7.42 shows the effective wave vector k obtained from the nonlinear curve fits as a function of the nearest-neighbor excluded chain filling fraction $\bar{N}_1$. We find the effective wave vector to be $k = 2\pi \bar{N}_1$, even though terms in the intervening-particle expansion are expectations of the nearest-neighbor chain of hard-core bosons at filling fraction $\bar{n}_1$. We believe this to be a manifestation of Luttinger's theorem, which states that the volume of the reciprocal space bounded by the noninteracting Fermi surface is invariant quantity not affected by interactions, and applies in both Fermi and non-Fermi

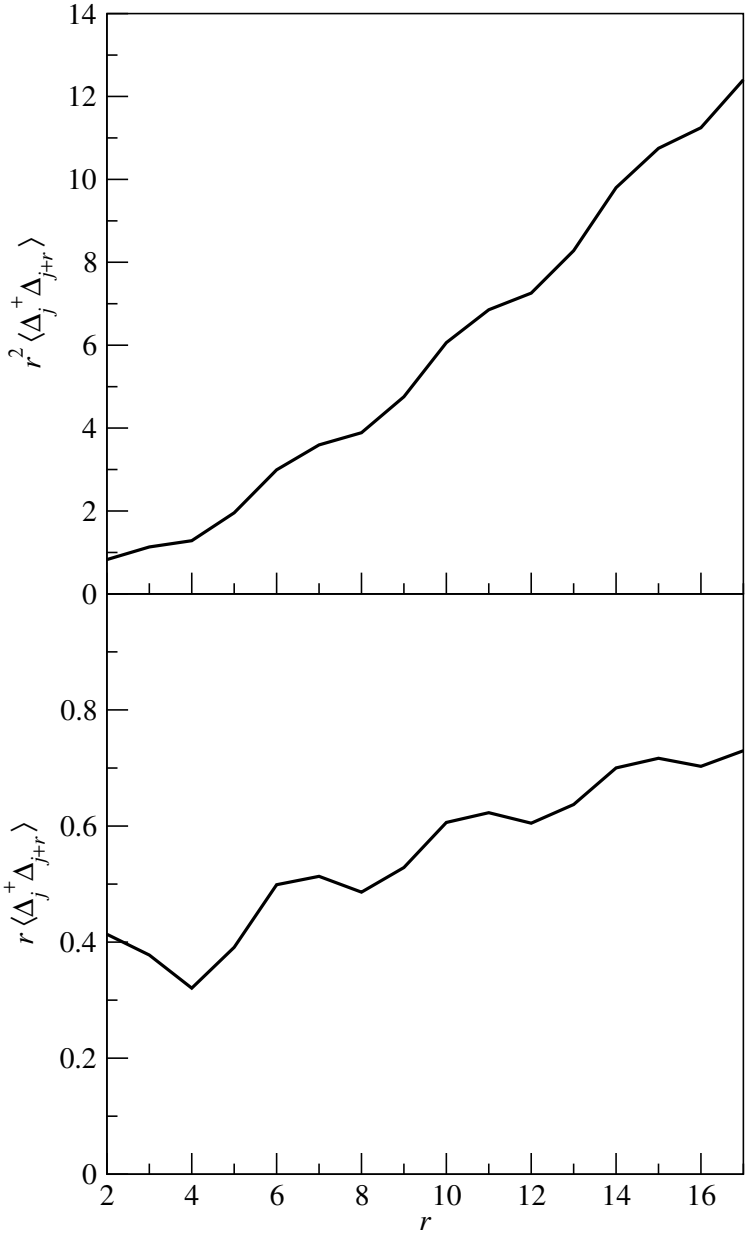

Figure 7.40: Multiplying the infinite-ladder SC correlation $\langle \Delta_j^\dagger \Delta_{j+r} \rangle$, for a nearest-neighbor excluded chain filling fraction of $\bar{N}_1 = 0.25$, by r^2 and r both lead to functions $r^2 \langle \Delta_j^\dagger \Delta_{j+r} \rangle$ (top) and $r \langle \Delta_j^\dagger \Delta_{j+r} \rangle$ (bottom) which increase with increasing r.

Table 7.4: Fitted parameters for a nonlinear curve fit of the infinite-ladder pure-correlated-hopping SC correlation $r^{1/2}\,\langle\Delta_j^\dagger\Delta_{j+r}\rangle$ to an asymptotic form $A + Br^{-(\gamma-1/2)}\cos(kr+\phi)$, for nearest-neighbor excluded chain filling fractions $0.05 \le \bar{N}_1 \le 0.45$, using separations $r \ge 4$.

$\bar{N}_1$	A	B	$\gamma - 1/2$	k	ϕ
0.05	0.113180	0.132597	1.31591	0.361277	2.34477
0.10	0.150285	0.722973	2.15222	0.609875	2.81640
0.15	0.171651	0.473746	1.98500	0.982064	2.33245
0.20	0.182088	0.113649	1.16919	1.28215	2.38606
0.25	0.182976	0.094231	0.908691	1.54751	2.79887
0.30	0.175071	0.172014	1.01765	1.85750	2.67414
0.35	0.157973	0.260783	1.04451	2.18007	2.40865
0.40	0.130627	0.278861	0.915458	2.50581	2.08360
0.45	0.089672	0.235307	0.701777	2.82241	1.85548

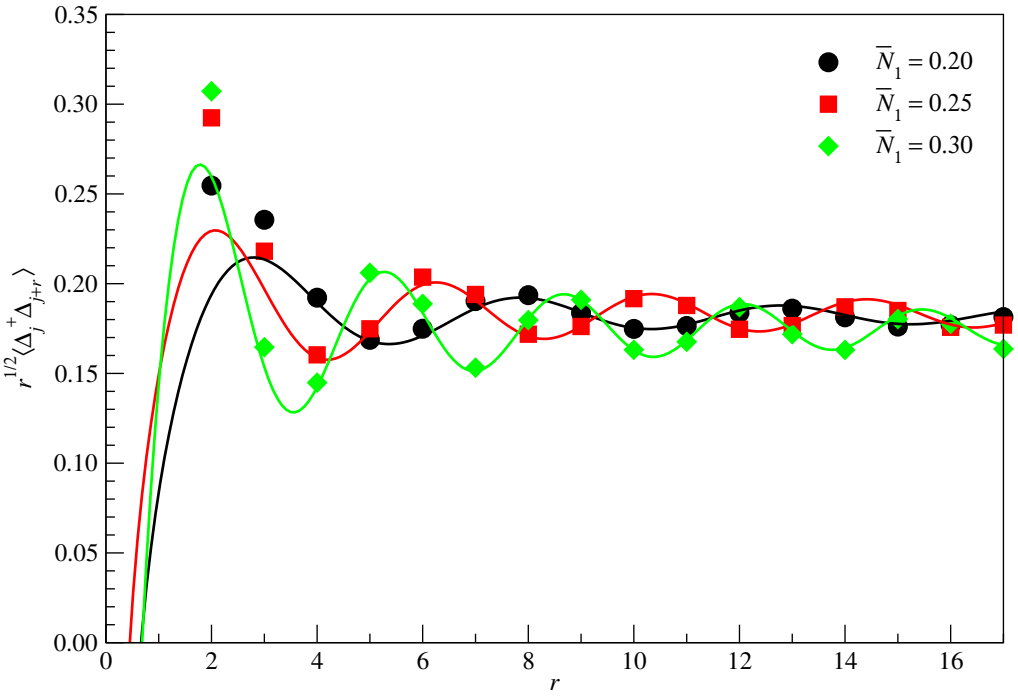

Figure 7.41: The infinite-ladder SC correlation $r^{1/2}\,\langle\Delta_j^\dagger\Delta_{j+r}\rangle$ as a function of the separation $2 \le r \le 17$ for nearest-neighbor excluded chain filling fractions $\bar{N}_1 = 0.20$ (black circles), 0.25 (red squares) and 0.30 (green diamonds). These are fitted to the asymptotic form $r^{1/2}\,\langle\Delta_j^\dagger\Delta_{j+r}\rangle = A + Br^{-(\gamma-1/2)}\cos(kr+\phi)$, to obtain $A = 0.182088$, $B = 0.113649$, $\gamma - 1/2 = 1.16919$, $k = 1.28215$ and $\phi = 2.38606$ for $\bar{N}_1 = 0.20$ (black curve), $A = 0.182976$, $B = 0.094231$, $\gamma - 1/2 = 0.908691$, $k = 1.54751$ and $\phi = 2.79887$ for $\bar{N}_1 = 0.25$ (red curve), and $A = 0.175071$, $B = 0.172014$, $\gamma - 2 = 1.01765$, $k = 1.85750$ and $\phi = 2.67414$ for $\bar{N}_1 = 0.30$ (green curve).

liquids [226, 374–379].

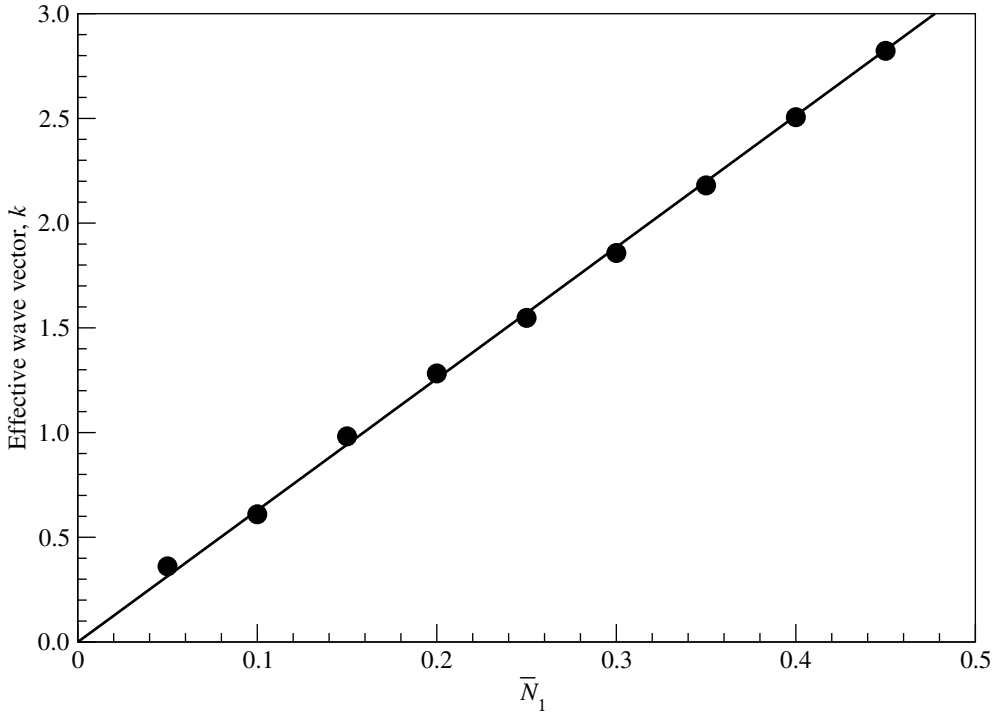

Figure 7.42: The effective wave vector k (filled circles) of the infinite-ladder SC correlations $\langle \Delta_j^\dagger \Delta_{j+r} \rangle$, in the limit $t' \gg t_\parallel, t_\perp$, as a function of the nearest-neighbor excluded chain filling fraction $\bar{N}_1$. Also shown as the solid line is the wave vector $k = 2\pi\bar{N}_1 = 2k_F$. The data points plotted here are from the five-parameter, $(A, B, \gamma - \frac{1}{2}, k, \phi)$, fit to (7.5.59), shown in Table 7.4.

Figure 7.43 shows the fitted amplitudes A and B as functions of the nearest-neighbor excluded chain filling fraction $\bar{N}_1$, while the fitted correlation exponent γ is shown as a function of $\bar{N}_1$ in Figure 7.44. While the fitted amplitude B is not as reliable as the fitted amplitude A, we find from Figure 7.43 that A is maximum when the ladder is quarter-filled, $\bar{N}_1 = \frac{1}{4}$, while B is minimum when $\bar{N}_1 = \frac{1}{4}$. The qualitative behaviour of the fitted correlation exponent γ as a function of $\bar{N}_1$ is harder to nail down, because we believe, based on our observations curve fitting $r^{1/2} \langle \Delta_j^\dagger \Delta_{j+r} \rangle$, that γ is fitted reliably probably in

a narrow range of filling fractions around $\bar{N}_1 = \frac{1}{4}$.

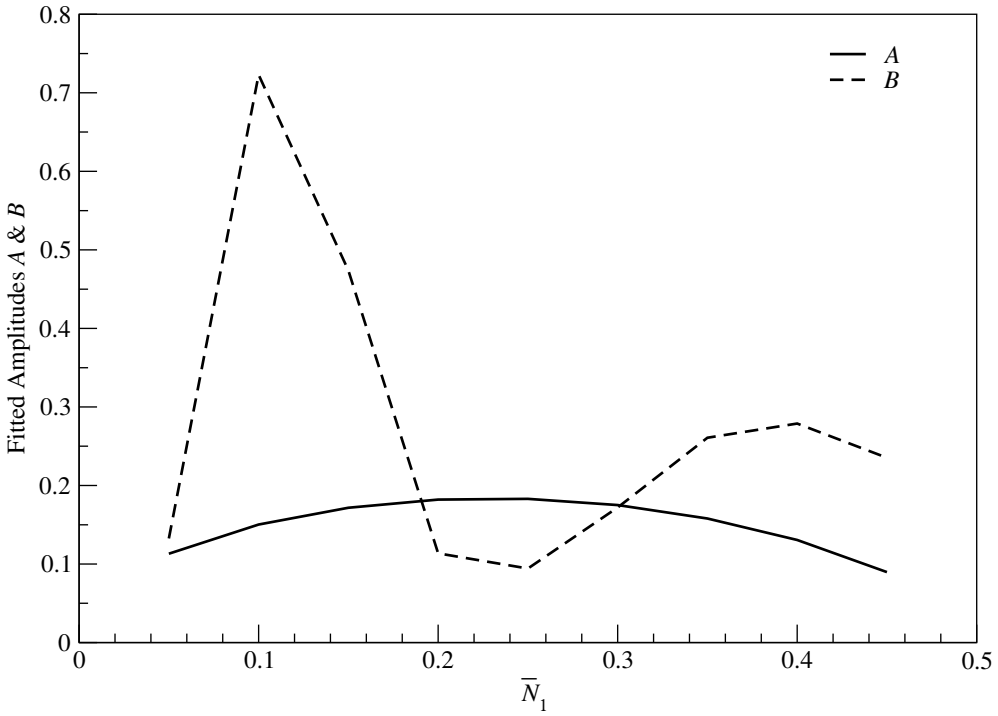

Figure 7.43: The fitted amplitudes A (solid line) and B (dashed line) of the infinite-ladder SC correlations $\langle \Delta_j^\dagger \Delta_{j+r} \rangle$, in the limit $t' \gg t_\parallel, t_\perp$, as a function of the nearest-neighbor excluded chain filling fraction $\bar{N}_1$. The data points plotted here are from the five-parameter, $(A, B, \gamma - \frac{1}{2}, k, \phi)$, fit to (7.5.59), shown in Table 7.4.

From Table 7.4 we find that the phase shift ϕ varies haphazardly, seemingly about an average value of $\frac{3\pi}{4}$, with the nearest-neighbor excluded chain filling fraction $\bar{N}_1$, and that some of the places where the fitted values of ϕ go 'wild' appears to be where the fitted values of B and γ go against the trends, too. To see whether we can say something more conclusive about the behaviours of these three parameters, we perform another three series of nonlinear curve fits, all of which having $k = 2\pi\bar{N}_1$ fixed. In the first of this series of nonlinear curve fits, which are to the asymptotic form

$$r^{1/2} \langle \Delta_j^\dagger \Delta_{j+r} \rangle = A r^{-(\beta - 1/2)} + B r^{-(\gamma - 1/2)} \cos(2\pi\bar{N}_1 r + \phi), \tag{7.5.60}$$

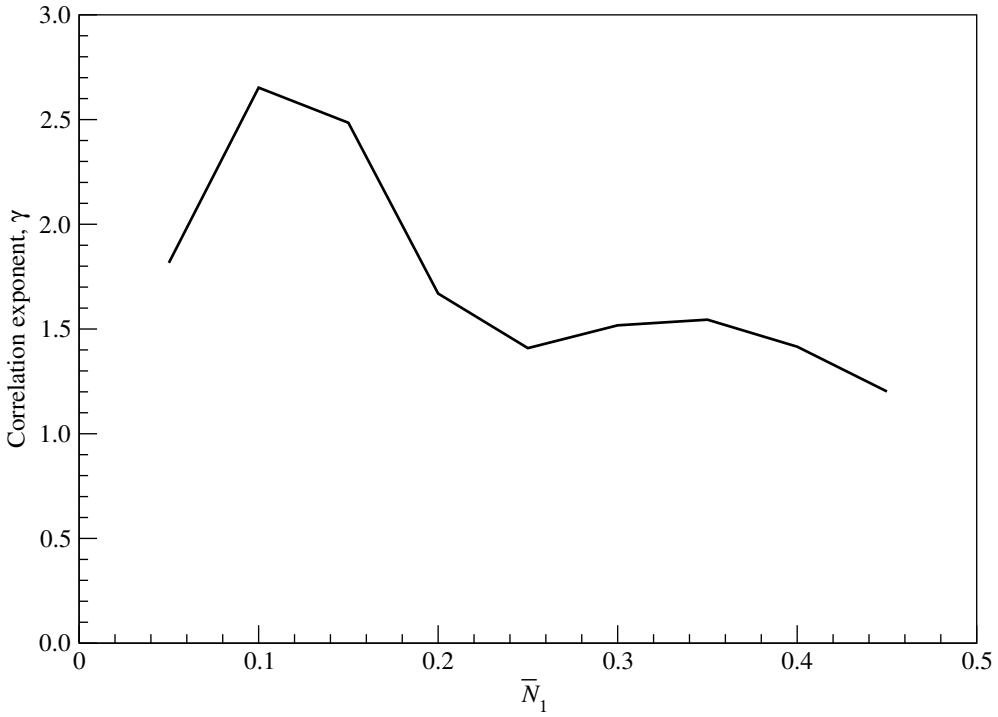

Figure 7.44: The fitted correlation exponent γ of the infinite-ladder SC correlations $\langle \Delta_j^\dagger \Delta_{j+r} \rangle$, in the limit $t' \gg t_\parallel, t_\perp$, as a function of the nearest-neighbor excluded chain filling fraction $\bar{N}_1$. The data points plotted here are from the five-parameter, $(A, B, \gamma - \frac{1}{2}, k, \phi)$, fit to (7.5.59), shown in Table 7.4.

we fix $\beta = \frac{1}{2}$ and $\phi = \frac{3\pi}{4}$, and relax these constraints one at a time to obtain Table 7.5.

7.5.6.3 Pitfalls of Nonlinear Curve Fitting

Looking at Table 7.5, we find that the full five-parameter fit, where it is successful, gives rise to the smoothest varying fitted parameters. We plot these as functions of $\bar{N}_1$ in Figure 7.45. While the fitted parameters now look smoother as functions of $\bar{N}_1$ (apart from the 'blip' at $\bar{N}_1 = 0.10$), they can in no way be regarded as the last word on the analytical asymptotic behaviour of the SC correlations. In fact, we find that the newly-fitted correlation exponent β is only very slightly larger than $\beta = \frac{1}{2}$. Because the difference is so small, we would like to believe that we are seeing the exponent that Efetov and Larkin calculated in Ref. 366, even though a fixed $\beta = \frac{1}{2}$ do not produce better fits numerically.

In performing nonlinear curve fits like that which we have done for $\langle \Delta_j^\dagger \Delta_{j+r} \rangle$, we should always worry about the numerical data receiving contributions from a sum of terms, some of which might be faster decaying power laws, while others might be decaying exponentials, but all of which becoming unimportant in the limit of large separations. We suspect that the small difference between the fitted and expected values of β might be a consequence of the faster decaying terms not having quite dropped out yet, and we end up with the annoying situation where an asymptotic form with slightly wrong exponents produce a better fit to the numerical data than an asymptotic form with the correct exponents. To obtain a deeper awareness of the pitfalls we would encounter while nonlinear curve fitting 'contaminated' numerical data to simple asymptotic forms, we perform a series of numerical experiments, where we generate the simulated data for a decaying, modulated, power law with known amplitude, correlation exponent, wave vector and phase shift, 'contaminated' by faster decaying power laws, as well as decaying expo-

Table 7.5: Fitted parameters for three series of nonlinear curve fit of the infinite-ladder pure-correlated-hopping SC correlation $r^{1/2}\,\langle\Delta_j^\dagger\Delta_{j+r}\rangle$ to an asymptotic form $Ar^{-(\beta-1/2)} + Br^{-(\gamma-1/2)}\cos(2\pi\bar{N}_1 r + \phi)$, for nearest-neighbor excluded chain filling fractions $0.05 \leq \bar{N}_1 \leq 0.45$, using separations $r \geq 4$. The full five-parameter fit cannot be done for $\bar{N}_1 = 0.05$ and $\bar{N}_1 = 0.10$ because the iterations would run away. The visual assessments of the quality of fits for each fit in the three series are also reported, with a qualitative scale going from perfect (cannot discern any differences between the data points and the fit), very good (can discern small differences between the data points and the fit), good (can discern small systematic deviations between data points and fit), not good (systematic deviations between data points and fit become worrying, but fit is generally acceptable), poor (systematic deviations too large for fit to be acceptable), to very poor (systematic deviations very large).

$\bar{N}_1$	A	$\beta - \frac{1}{2}$	B	$\gamma - \frac{1}{2}$	ϕ	visual
0.05	0.114449	0	0.245121	1.78432	$\frac{3\pi}{4}$	poor
	0.111919	0	0.142509	1.26401	2.75494	good
0.10	0.149881	0	70.3845	4.731	$\frac{3\pi}{4}$	very poor
	0.150279	0	0.81508	2.21348	2.71122	not good
0.15	0.171449	0	0.576677	2.12421	$\frac{3\pi}{4}$	poor
	0.171817	0	0.465178	1.97047	2.58825	not good
	0.184656	0.0302721	0.23747	1.59685	2.757	good

Table 7.5: (continued)

$\bar{N}_1$	A	$\beta - \frac{1}{2}$	B	$\gamma - \frac{1}{2}$	ϕ	visual
0.20	0.182002	0	0.0962155	1.10626	$\frac{3\pi}{4}$	very poor
	0.182256	0	0.110407	1.15024	2.54811	very poor
	0.196427	0.0324884	0.17195	1.34545	2.67789	good
0.25	0.183085	0	0.121574	1.03594	$\frac{3\pi}{4}$	poor
	0.183006	0	0.099698	0.933412	2.61709	poor
	0.197189	0.0322755	0.174021	1.19932	2.58779	good
0.30	0.175437	0	0.141567	0.929044	$\frac{3\pi}{4}$	not good
	0.175321	0	0.155362	0.971518	2.46308	not good
	0.189665	0.0344664	0.185405	1.05991	2.41725	good
0.35	0.158067	0	0.279228	1.08285	$\frac{3\pi}{4}$	not good
	0.15823	0	0.259947	1.04677	2.28532	not good
	0.171488	0.0351631	0.212002	0.953887	2.25036	good
0.40	0.131257	0	0.212586	0.827961	$\frac{3\pi}{4}$	very poor
	0.130625	0	0.289438	0.931033	2.02335	good
	0.137853	0.0235052	0.265719	0.891008	2.0272	good
0.45	0.0906443	0	1.12783	1.49903	$\frac{3\pi}{4}$	very poor
	0.0895991	0	0.228539	0.687774	1.80676	very good
	0.0884759	−0.0055429	0.229737	0.690272	1.80586	very good

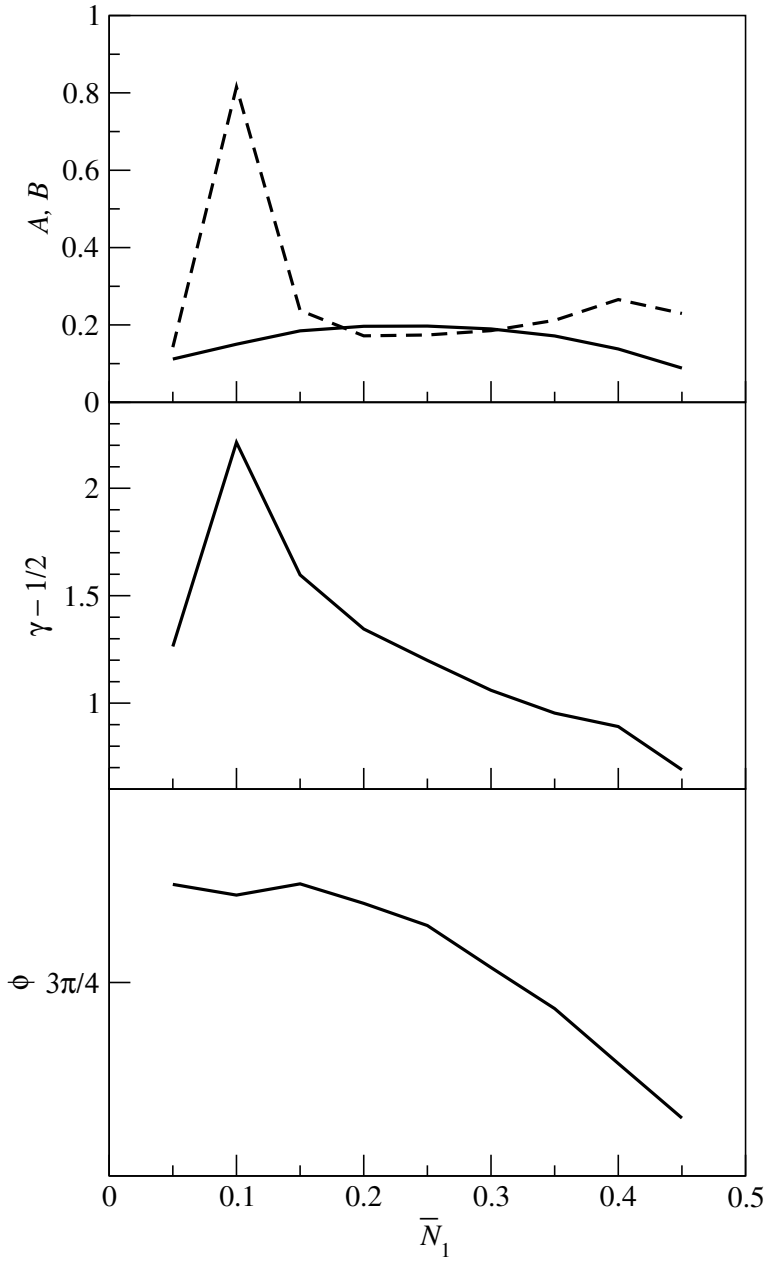

Figure 7.45: The fitted amplitudes A (top, solid) and B (top, dashed), correlation exponent γ (middle), and phase shift ϕ (bottom) of the infinite-ladder SC correlations $\langle \Delta_j^\dagger \Delta_{j+r} \rangle$, in the limit $t' \gg t_\parallel, t_\perp$, as a function of the nearest-neighbor excluded chain filling fraction $\bar{N}_1$. The data points plotted here are a composite of those from the four-parameter, $(A, B, \gamma - \frac{1}{2}, \phi)$, and five-parameter $(A, \beta - \frac{1}{2}, B, \gamma - \frac{1}{2}, \phi)$ fits to (7.5.60), shown in Table 7.5.

nentials, and see what errors we get in the fitted amplitude, correlation exponent, wave vector and phase shift.

To begin with, we fitted the numerical data generated from

$$C(r) = \left[\frac{1}{r} + \frac{1}{r^3}\right]\cos 2\pi\bar{n}r, \quad C(r) = \left[\frac{1}{r} + \frac{1}{r^5}\right]\cos 2\pi\bar{n}r \tag{7.5.61}$$

for $\bar{n} = 0.30$ ($k = 1.884955\ldots$) at integer values of $4 \leq r \leq 16$ to a single power law of the form

$$Ar^{-\nu}\cos(kr + \phi), \tag{7.5.62}$$

i.e. we assume that the leading power-law correction is modulated by the same oscillatory function. Visually, we judged both fits to be very good, with the fitted parameters being

$$\begin{aligned} &\nu' = 3, \quad A = 1.10393, \quad \nu = 1.03786, \quad k = 1.88556, \quad \phi = -0.00604242; \\ &\nu' = 5, \quad A = 1.00464, \quad \nu = 1.00193, \quad k = 1.88503, \quad \phi = -0.000788865. \end{aligned} \tag{7.5.63}$$

As expected, the faster the leading power law correction decays, the better the fitted parameters agree with the true parameters. More importantly, we note that for a power-law correction of the form introduced in (7.5.61), the errors incurred in fitting k and ϕ are small, less than one part in a hundred, when the $\nu' = 3$ power law correction has the same amplitude as the 'asymptotic' $\nu = 1$ power law we are trying to fit. On the other hand, the errors incurred in fitting A and ν are larger, at about 10% and 4% respectively.

Introducing a π phase shift to the $\nu' = 3$ power law correction, to generate numerical data from

$$C(r) = \left[\frac{1}{r} - \frac{1}{r^3}\right]\cos 2\pi\bar{n}r \tag{7.5.64}$$

for $\bar{n} = 0.30$ ($k = 1.884955\ldots$) at integer values of $4 \leq r \leq 16$, we find the fitted parameters

$$\nu' = 3,\ A = 0.902506,\ \nu = 0.96068,\ k = 1.8843,\ \phi = 0.00666531, \tag{7.5.65}$$

after obtaining a very good fit of the data to (7.5.62). Comparing (7.5.65) with (7.5.63), we find a change of sign in the errors incurred for the parameters. The magnitudes of the errors, however, remain more or less the same. For this same $2k_F$ power-law correction (7.5.64), we generated numerical data for $\bar{n} = 0.10$ ($k = 0.628318\ldots$), and find the fitted parameters

$$\nu' = 3,\ A = 0.8935,\ \nu = 0.956814,\ k = 0.630162,\ \phi = -0.0188769, \tag{7.5.66}$$

after obtained a very good visual fit of the data to (7.5.62). Apart from the sign change in the fitted value of ϕ (and the expected change in the fitted value of k), we find very similar errors in all fitted parameters. From this little analysis, we conclude that for $2k_F$ power-law corrections, the absolute magnitudes of the errors in the fitted parameters of the 'asymptotic' power law are most sensitive to how close the exponent ν' of the leading power law correction is to the exponent ν of the 'asymptotic' power law, and not very sensitive to amplitude and phase shift of the leading power-law correction, or even the filling fraction $\bar{n}$.

Next, we generated numerical data from

$$\begin{aligned} C(r) &= \left[\frac{1}{r} + \exp(-r)\right]\cos 2\pi\bar{n}r, \\ C(r) &= \left[\frac{1}{r} - \exp(-r)\right]\cos 2\pi\bar{n}r, \\ C(r) &= \left[\frac{1}{r} + \exp(-r/2)\right]\cos 2\pi\bar{n}r, \\ C(r) &= \left[\frac{1}{r^2} + \exp(-r)\right]\cos 2\pi\bar{n}r \end{aligned} \tag{7.5.67}$$

for $\bar{n} = 0.30$, for a decaying exponential correction. Fitting the numerical data to the

'asymptotic' power law (7.5.62), we find the fitted parameters

$$\begin{aligned} &A = 1.1013, \quad \nu = 1.04084, \quad k = 1.88624, \quad \phi = -0.013071, \\ &A = 0.906513, \quad \nu = 0.958588, \quad k = 1.8836, \quad \phi = 0.014021, \\ &A = 2.51283, \quad \nu = 1.36361, \quad k = 1.88611, \quad \phi = -0.00910245, \\ &A = 1.68912, \quad \nu = 2.23088, \quad k = 1.88895, \quad \phi = -0.0328451 \end{aligned} \tag{7.5.68}$$

respectively.

Comparing the fitted parameters in (7.5.68) with those in (7.5.63) and (7.5.65), we find that the parameters k and ϕ are still fitted quite reliably, i.e. incurring small absolute errors, but the parameters A and ν literally goes wild, when the correlation length ξ' of the decaying exponential correction is changed from $\xi' = 1$ to $\xi' = 2$. This is considering the fact that the contribution to $C(r)$ from the decaying exponential correction is one or more orders of magnitude smaller than the 'asymptotic' power law for practically the whole range of separations r the nonlinear curve fit is carried out. We therefore find the correlation exponent ν, which we obtained from nonlinear curve fits of numerical data to an 'asymptotic' power law, to be more sensitive to changes in the correlation length ξ' of a decaying exponential correction, than to changes in the correlation exponent ν' of a power-law correction.

Moving on, we consider $4k_F$ power-law corrections by generating numerical data from

$$C(r) = \frac{\cos 2\pi\bar{n}r}{r} + \frac{\cos 4\pi\bar{n}r}{r^3}, \tag{7.5.69}$$

for $\bar{n} = 0.10$ and $\bar{n} = 0.30$, at integer values of $4 \leq r \leq 16$. Performing nonlinear curve fitting of the data to the 'asymptotic' power law (7.5.62), we find the fitted parameters

$$\begin{aligned} &A = 0.933098, \quad \nu = 0.971548, \quad k = 0.628516, \quad \phi = -0.0058732, \\ &A = 0.864671, \quad \nu = 0.936453, \quad k = 1.88101, \quad \phi = 0.0371766, \end{aligned} \tag{7.5.70}$$

respectively. Again, as with the $2k_F$ power-law corrections, we find the amplitude A and correlation exponent ν more severely affected (on the order of 10% and 5% errors, respectively) than the wave vector k and phase shift ϕ (on the order of less than 1% error for both). We find that the fitted correlation exponent ν does not vary much with filling fraction $\bar{n}$.

However, when we generated numerical data from

$$\begin{aligned} C(r) &= \frac{\cos 2\pi\bar{n}r}{r} + \exp(-r)\,\cos 4\pi\bar{n}r, \\ C(r) &= \frac{\cos 2\pi\bar{n}r}{r^2} + \exp(-r)\,\cos 4\pi\bar{n}r, \\ C(r) &= \frac{\cos 2\pi\bar{n}r}{r} + \exp(-0.70r)\,\cos 4\pi\bar{n}r, \end{aligned} \tag{7.5.71}$$

for $\bar{n} = 0.30$, at integer values of $4 \leq r \leq 16$, and performing nonlinear curve fitting of the data to (7.5.62), we find the fitted parameters

$$\begin{aligned} &A = 0.883221, \quad \nu = 0.946152, \quad k = 1.87958, \quad \phi = 0.0551543, \\ &A = 0.523638, \quad \nu = 1.71363, \quad k = 1.84266, \quad \phi = 0.358212, \\ &A = 0.589631, \quad \nu = 0.773848, \quad k = 1.86794, \quad \phi = 0.17126, \end{aligned} \tag{7.5.72}$$

respectively. For these numerical data, which simulates 'contamination' by $4k_F$ decaying exponentials, we find a significantly poorer fit when the leading correlation exponent is larger, or when the correlation length of the decaying exponential is larger. When the fit becomes poor, the fitted correlation exponent ν and fitted phase shift ϕ naturally become significantly different from their true values. The other point to note is that the fitted phase shift ϕ now suffers from a large error, even though the fitted value of k still agrees reasonably well with its true value.

Given these deviations, which tends to be more serious when the 'contamination' is by decaying exponentials as opposed to power laws decaying faster than the 'asymptotic' power law which we seek, the natural question to ask is whether the accuracy of

the fit would improve if we have data for larger distances. For the numerical data up to $r = 32$, generated by

$$C(r) = \frac{\cos 2\pi\bar{n}r}{r} + \exp(-0.70r)\,\cos 4\pi\bar{n}r, \tag{7.5.73}$$

for $\bar{n} = 0.30$, we find the fitted parameters to be

$$A = 0.694656,\ \nu = 0.865171,\ k = 1.87822,\ \phi = 0.110604. \tag{7.5.74}$$

The deviation of the fitted correlation exponent from its true value is still significant, but as expected, it is now closer to the true value. However, for the correlations calculated numerically in this chapter, we frequently do not have the option to calculate the correlations for separations much larger than the $r = 16$ to $r = 18$ that we are currently working with.

To briefly summarize our little numerical experiment with simulated correlations, we have gained confidence in interpreting the fitted parameter values, if the dominant power-law correlation, with exponent ν, is 'contaminated' by subdominant power laws with larger exponents, with leading exponent ν'. As a crude estimate gleaned from the numerics, the error in the fitted leading correlation exponent ν is on the order of $r_{\max}^{(\nu'-\nu)/2}$. Based on the two forms of power-law corrections considered in our little numerical experiment, this error does not appear to depend on the filling fraction $\bar{n}$ at all. On the other hand, we find that if the dominant power-law correlation is 'contaminated' by decaying exponentials, the error in the fitted value ν may become large, depending on what the correlation length ξ' of the leading decaying exponential is. In Section 7.5.8 we shall see that exponential decays, which frequently arise from the correlation in question receiving contributions from restricted classes of ground-state amplitudes, have correlation lengths that depend generically on the filling fraction $\bar{n}$.

In undertaking this little numerical experiment, our goal was to assess, as best as

we can, how much of the fitted exponent γ we can trust, when we know that β is 'contaminated' to a level of about 5%. We also want to have a sense of whether the 'contamination' is by a decaying power law, which results in filling-fraction-independent deviations, or by a decaying exponential, which results in filling-fraction-dependent deviations. Looking once again at Table 7.5, and using the crude indicators coming out of our little numerical experiment, we would venture to guess that the deviation of γ from its true analytical value would be on the order of 10–20%, regardless of whether the 'contamination' was by decaying power laws or decaying exponentials. In fact, judging from the deviations in β, we can argue that if the 'contamination' is by a decaying exponential, it is by one whose correlation length ξ' depends very weakly on the filling fraction $\bar{N}_1$. In other words, the deviations of γ should also be more or less independent of $\bar{N}_1$, making it rather unlikely that γ is a filling-fraction-independent universal exponent. By a similar argument, the $\bar{N}_1$-dependence of the phase shift ϕ is also likely to be real, and not the artefact of our nonlinear curve fits.

7.5.7 Charge-Density-Wave Correlations

The simplest CDW correlations on the two-legged ladder are the four-point functions $\langle c^\dagger_{1,j} c_{1,j} c^\dagger_{1,j+r} c_{1,j+r} \rangle$, $\langle c^\dagger_{1,j} c_{1,j} c^\dagger_{2,j+r} c_{2,j+r} \rangle$, $\langle c^\dagger_{2,j} c_{2,j} c^\dagger_{1,j+r} c_{1,j+r} \rangle$, and $\langle c^\dagger_{2,j} c_{2,j} c^\dagger_{2,j+r} c_{2,j+r} \rangle$, which we call the CDW-$\sigma$ correlations. These are not easy to calculate within the pure-bound-pair ground state, because they cannot be written in terms of the expectations of extended hard-core boson operators, like we did for SC correlations in Section 7.5.6. We would need to apply constraint arguments more complex than what we shall do in Section 7.5.8 for the FL correlations, to narrow the expectations down to simple classes of probabilities.

In contrast, we can evaluate the CDW-π correlations

$$\langle B_j^\dagger B_j B_{j+r}^\dagger B_{j+r}\rangle = \langle N_j N_{j+r}\rangle \tag{7.5.75}$$

by writing them as the intervening-particle expansions

$$\begin{aligned}
\langle N_j N_{j+r}\rangle = {} & \langle N_j(\mathbb{1}-N_{j+1})\cdots(\mathbb{1}-N_{j+r-1})N_{j+r}\rangle + \\
& \langle N_j N_{j+1}(\mathbb{1}-N_{j+2})\cdots(\mathbb{1}-N_{j+r-1})N_{j+r}\rangle + \cdots + \\
& \langle N_j(\mathbb{1}-N_{j+1})\cdots(\mathbb{1}-N_{j+r-2})N_{j+r-1}N_{j+r}\rangle + \\
& \langle N_j N_{j+1}N_{j+2}(\mathbb{1}-N_{j+3})\cdots(\mathbb{1}-N_{j+r-1})N_{j+r}\rangle + \cdots + \\
& \langle N_j(\mathbb{1}-N_{j+1})\cdots(\mathbb{1}-N_{j+r-3})N_{j+r-2}N_{j+r-1}N_{j+r}\rangle + \cdots + \\
& \langle N_j N_{j+1}\cdots N_{j+r-1}N_{j+r}\rangle\,,
\end{aligned} \tag{7.5.76}$$

of the same form as (7.4.99). Here, let us note that we cannot write $\langle B_j^\dagger B_j B_{j+r}^\dagger B_{j+r}\rangle$ as simple linear combinations of the eight-point functions

$$\begin{aligned}
&\langle c_{2,j+1}^\dagger c_{1,j}^\dagger c_{1,j} c_{2,j+1} c_{2,j+r+1}^\dagger c_{1,j+r}^\dagger c_{1,j+r} c_{j+r+1}\rangle\,, \\
&\langle c_{2,j+1}^\dagger c_{1,j}^\dagger c_{1,j} c_{2,j+1} c_{2,j+r}^\dagger c_{1,j+r+1}^\dagger c_{1,j+r+1} c_{2,j+r}\rangle\,, \\
&\langle c_{2,j}^\dagger c_{1,j+1}^\dagger c_{1,j+1} c_{2,j} c_{2,j+r+1}^\dagger c_{1,j+r}^\dagger c_{1,j+r} c_{2,j+r+1}\rangle\,, \\
&\langle c_{2,j}^\dagger c_{1,j+1}^\dagger c_{1,j+1} c_{2,j} c_{2,j+r}^\dagger c_{1,j+r+1}^\dagger c_{1,j+r+1} c_{2,j+r}\rangle\,.
\end{aligned} \tag{7.5.77}$$

The reason for this is subtle: for example, a term like

$$\langle c_{2,j}^\dagger c_{1,j+1}^\dagger c_{1,j+1} c_{2,j} c_{2,j+r+1}^\dagger c_{1,j+r}^\dagger c_{1,j+r} c_{2,j+r+1}\rangle \tag{7.5.78}$$

will pick up contributions from the two configurations shown in Figure 7.46, while $\langle B_j^\dagger B_j B_{j+r}^\dagger B_{j+r}\rangle$ will only pick up a contribution from the top configuration shown in Figure 7.46. To write $\langle B_j^\dagger B_j B_{j+r}^\dagger B_{j+r}\rangle$ in terms of the ladder-spinless-fermion operators, we need to project out configurations in which the sites $(1,\, j-1)$ and $(2,\, j+2)$ are occupied, unless the spinless fermions occupying these sites are part of a bound pair. This tells

us that $\langle B_j^\dagger B_j B_{j+r}^\dagger B_{j+r}\rangle$ is some messy linear combination of eight-point, twelve-point, sixteen-point, ..., $4n$-point functions — too cumbersome for us to write out explicitly.

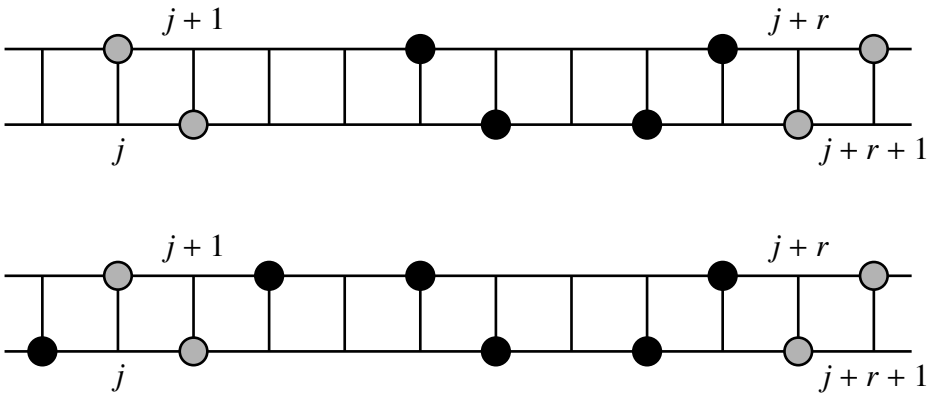

Figure 7.46: Two bound-pair configurations making contributions to the eight-point function $\langle c_{2,j}^\dagger c_{1,j+1}^\dagger c_{1,j+1} c_{2,j} c_{2,j+r+1}^\dagger c_{1,j+r}^\dagger c_{1,j+r} c_{2,j+r+1}\rangle$. Only the top configuration contributes to $\langle B_j^\dagger B_j B_{j+r}^\dagger B_{j+r}\rangle$.

We then write the CDW-π correlations as a sum of hard-core-boson expectations,

$$\begin{aligned}\frac{\bar{n}_1}{\bar{N}_1}\langle N_j N_{j+r}\rangle = {} & \langle n_j(\mathbb{1}-n_{j+1})\cdots(\mathbb{1}-n_{j+r-2})n_{j+r-1}\rangle + \\ & \langle n_j n_{j+1}(\mathbb{1}-n_{j+2})\cdots(\mathbb{1}-n_{j+r-3})n_{j+r-2}\rangle + \cdots + \\ & \langle n_j(\mathbb{1}-n_{j+1})\cdots(\mathbb{1}-n_{j+r-3})n_{j+r-2}\rangle + \cdots + \\ & \langle n_j n_{j+1}\cdots n_{j+r-p_{\max}-2}n_{j+r-p_{\max}-1}\rangle\,,\end{aligned} \tag{7.5.79}$$

using the rules and relations described in Sections 7.4.6 and 7.4.7. Here $p_{\max} = \lfloor (r-2)/2\rfloor$ is the number of intervening pairs that can fit between rungs j and $j+r$. The final step involves mapping this sum of hard-core-boson expectations to a sum of noninteracting-spinless-fermion expectations using the Jordan-Wigner transformation described in Section 7.4.1. However, where we had to account for the action of nontrivial Jordan-Wigner strings in calculating $\langle B_j^\dagger B_{j+r}\rangle$, there are no Jordan-Wigner strings to account for in any of the terms in (7.5.79). All hard-core-boson expectations in (7.5.79) are therefore identical to the corresponding noninteracting-spinless-fermion expectations.

7.5.7.1 Numerical Evaluation of Intervening-Particle Expansion

To calculate these infinite-ladder CDW-π correlations numerically, I used an algorithm modified from the one described in Section 7.5.6:

1. For each $(0 \leq p \leq p_{\max})$-intervening-pair expectation, we calculate the maximum separation $r_{\max} = r - p$ that can occur in the expectation, and sum over the minors it contribute order by order.

2. For each order $p + 2 \leq m \leq r_{\max}$, we run over all possible indices $1 < j_1 < j_2 < \cdots < j_{m-2} < r_{\max}$, and construct the minors

$$\mathsf{G}^{1\, j_1\, j_2 \cdots j_{m-2}\, r_{\max}}_{1\, j_1\, j_2 \cdots j_{m-2}\, r_{\max}}. \tag{7.5.80}$$

3. The contribution of $\mathsf{G}^{1\, j_1\, j_2 \cdots j_{m-2}\, r_{\max}}_{1\, j_1\, j_2 \cdots j_{m-2}\, r_{\max}}$ to $\langle N_j N_{j+r} \rangle - \langle N_j \rangle \langle N_{j+r} \rangle$ is

$$(-1)^{m+p} \binom{m-2}{p} \mathsf{G}^{1\, j_1\, j_2 \cdots j_{m-2}\, r_{\max}}_{1\, j_1\, j_2 \cdots j_{m-2}\, r_{\max}}, \tag{7.5.81}$$

   where the factor $(-1)^{m+p}$ accounts for the sign with which the properly-ordered expectation being summed appears in the expansion (7.5.79), the binomial coefficient $\binom{m-2}{p}$ accounts for how many times the minor $\mathsf{G}^{1\, j_1\, j_2 \cdots j_{m-2}\, r_{\max}}_{1\, j_1\, j_2 \cdots j_{m-2}\, r_{\max}}$ appears when we sum over all properly-ordered expectations with p intervening pairs.

4. After summing over the intervening-particle expansion, we multiply the nearest-neighbor included chain result by $\bar{N}_1/\bar{n}_1$ to get the correct numerical value for $\langle N_j N_{j+r} \rangle$.

Just as for noninteracting spinless fermions, where the CDW correlations

$$\langle n_j n_{j+r} \rangle - \langle n_j \rangle \langle n_{j+r} \rangle \tag{7.5.82}$$

are measured relative to the uncorrelated product of densities, we are interested in the infinite-ladder subtracted CDW-π correlations

$$\langle N_j N_{j+r} \rangle - \langle N_j \rangle \langle N_{j+r} \rangle . \tag{7.5.83}$$

For a Fermi-sea ground state, the subtracted CDW-σ correlations decay as r^{-2}. The subtracted CDW-π correlations,

$$\langle n_j n_{j+1} n_{j+r} n_{j+r+1} \rangle - \langle n_j n_{j+1} \rangle \langle n_{j+r} n_{j+r+1} \rangle , \tag{7.5.84}$$

which we can calculate readily as being equal to

$$\begin{aligned} \bar{n}^4 \Big[& -\mathsf{g}^2(r-1) - 2\mathsf{g}^2(r) - \mathsf{g}^2(r+1) + 4\mathsf{g}(1)\mathsf{g}(r-1)\mathsf{g}(r) + \\ & \mathsf{g}(1)\mathsf{g}(r-1)\mathsf{g}(r+1) + 2\mathsf{g}(1)\mathsf{g}(r)\mathsf{g}(r+1) + \mathsf{g}(1)\mathsf{g}^2(r+1) + \\ & \mathsf{g}^4(r) + \mathsf{g}^2(r-1)\mathsf{g}^2(r+1) - 2\mathsf{g}^2(1)\mathsf{g}(r-1)\mathsf{g}(r+1) - \\ & 2\mathsf{g}^2(r)\mathsf{g}(r-1)\mathsf{g}(r+1) - 2\mathsf{g}^2(1)\mathsf{g}^2(r) \Big], \end{aligned} \tag{7.5.85}$$

also decay as r^{-2}. For our extended Hubbard ladder of spinless fermions (7.5.1) in the limit of $t' \gg t_{\parallel}, t_{\perp}$, we have no clear idea how fast the CDW-σ correlations decay, or whether they decay faster or slower than the SC and CDW-π correlations. Therefore, we cannot readily conclude that SC correlations dominate at large distances, even though we expected this to be the case. We do the next best thing: extract the leading correlation exponent for the subtracted CDW-π correlations, and compare it to the leading SC correlation exponent of $\beta = \frac{1}{2}$.

7.5.7.2 Nonlinear Curve Fitting the Numerical Correlations

We initially fit the subtracted CDW-π correlations, obtained numerically for various nearest-neighbor excluded chain filling fractions, to the asymptotic form

$$A r^{-\alpha} \cos(kr + \phi), \tag{7.5.86}$$

but the fits at low filling fractions were poor, so we end up fitting the numerical correlations to the asymptotic form

$$Ar^{-\alpha}\cos(kr+\phi)+Br^{-\alpha'}, \tag{7.5.87}$$

which contains two power laws. To improve the accuracy and stability of the nonlinear curve fits, we should multiply $\langle N_j N_{j+r}\rangle - \langle N_j\rangle\langle N_{j+r}\rangle$ by an appropriate power of r prior to curve fitting, just like what we did for the SC correlations. However, it appears that the leading CDW-π correlation exponent is small enough that its power-law decay does not pose a serious problem to the nonlinear curve fitting. The fitted parameters obtained are shown in Table 7.6. We also show in Figure 7.47 plots of the subtracted CDW-π correlations as functions of the separation for the nearest-neighbor excluded chain filling fractions $\bar{N}_1 = 0.20$, 0.25, and 0.30 that will be accessed in the numerical studies in Chapter 8.

Comparing Table 7.6 with Table 7.4, we find that the CDW-π effective wave vectors k obtained from the curve fits are very close to fitted SC effective wave vectors. These oscillatory parts of the infinite-ladder SC, and infinite-ladder subtracted CDW-π correlations are the $2k_F$-oscillations frequently mentioned in the Luttinger-liquid literature. Figure 7.48 shows the fitted amplitudes A and B as functions of the nearest-neighbor excluded chain filling fraction $\bar{N}_1$. Just below half-filling, we can think of the nearly-half-filled hard-core boson ground state as a low-density ground state of holes. We should therefore be able to write the subtracted CDW correlation of a nearly-half-filled chain of hard-core bosons as

$$\langle n_j n_{j+r}\rangle - \langle n_j\rangle\langle n_{j+r}\rangle = +\bar{h}^2\frac{\sin^2\pi\bar{h}r}{\pi^2\bar{h}^2r^2}, \tag{7.5.88}$$

in terms of the hole filling fraction $\bar{h}$. This decays as a power law, with exponent -2, just as it does for all hard-core boson filling fractions, but the length scale over which

Table 7.6: Fitted parameters for a nonlinear curve fit of the infinite-ladder pure-correlated-hopping subtracted CDW-π correlation $\langle N_j N_{j+r}\rangle - \langle N_j\rangle\langle N_{j+r}\rangle$ to an asymptotic form $Ar^{-\alpha}\cos(kr+\phi) + Br^{-\alpha'}$, for nearest-neighbor excluded chain filling fractions $0.05 \le \bar{N}_1 \le 0.45$, for $r \ge 4$.

$\bar{N}_1$	A	α	k	ϕ	B	α'
0.05	0.0279578	1.64765	0.301952	0.398017	−0.0244789	1.74081
0.10	0.0358588	1.54516	0.615452	0.370872	−0.0407260	2.01936
0.15	0.0458263	1.40903	0.925821	0.403042	−0.0227397	1.80245
0.20	0.0574998	1.25173	1.23644	0.424936	−0.0170868	1.69780
0.25	0.0764329	1.11852	1.55540	0.355490	−0.0397412	2.15208
0.30	0.0948054	0.955024	1.87017	0.326109	−0.154549	2.99285
0.35	0.133010	0.844039	2.18557	0.290757	−0.0168631	1.92970
0.40	0.168151	0.684079	2.50131	0.259713	−0.000682455	0.636177
0.45	0.291234	0.630648	2.81602	0.269303	−0.265702	3.39895

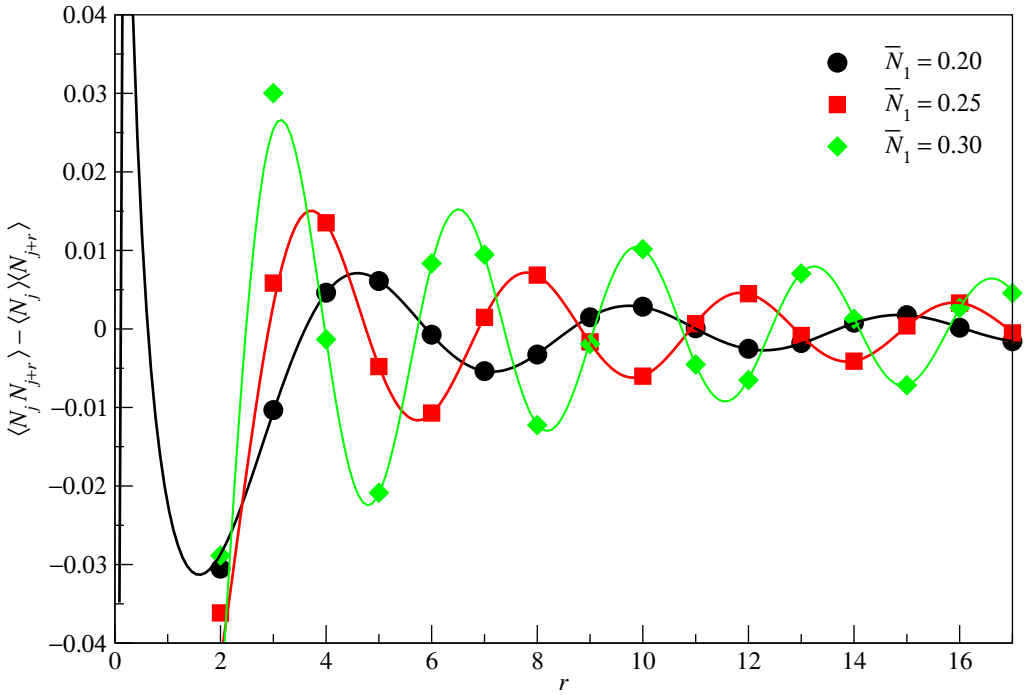

Figure 7.47: The subtracted CDW-π correlations $\langle N_j N_{j+r}\rangle - \langle N_j\rangle\langle N_{j+r}\rangle$ of an infinite ladder, as a function of the separation $2 \le r \le 17$ for nearest-neighbor excluded chain filling fractions $\bar{N}_1 = 0.20$ (black circles), 0.25 (red squares) and 0.30 (green diamonds). These are fitted to the asymptotic form $\langle N_j N_{j+r}\rangle - \langle N_j\rangle\langle N_{j+r}\rangle = Ar^{-\alpha}\cos(kr+\phi) + Br^{-\alpha'}$, to obtain $A = 0.0574998$, $\alpha = 1.25173$, $k = 1.23644$, $\phi = 0.424936$, $B = -0.0170868$ and $\alpha' = 1.69780$ for $\bar{N}_1 = 0.20$ (black curve), $A = 0.0764329$, $\alpha = 1.11852$, $k = 1.55540$, $\phi = 0.355490$, $B = -0.0397412$ and $\alpha' = 2.15208$ for $\bar{N}_1 = 0.25$ (red curve), and $A = 0.0948054$, $\alpha = 0.955024$, $k = 1.87017$, $\phi = 0.326109$, $B = -0.154549$ and $\alpha' = 2.99285$ for $\bar{N}_3 = 0.30$ (green curve).

this power law is manifest is $\xi = \bar{h}^{-1}$, which diverges as $\bar{h} \to 0$. Meanwhile, as $\bar{h} \to 0$, we expect from (7.5.88) that the amplitude $\bar{h}^2$ of the subtracted CDW correlation goes to zero. This does not seem to be happening in Figure 7.48, where we see both absolute amplitudes, $|A|$ and $|B|$, becoming large as $\bar{N}_1 \to \frac{1}{2}$, when they should instead both go to zero. We need not read too much into this behaviour, since we know from performing the nonlinear curve fit that the fits are not very reliable for nearest-neighbor excluded chain filling fractions close to $\bar{N}_1 = \frac{1}{2}$.

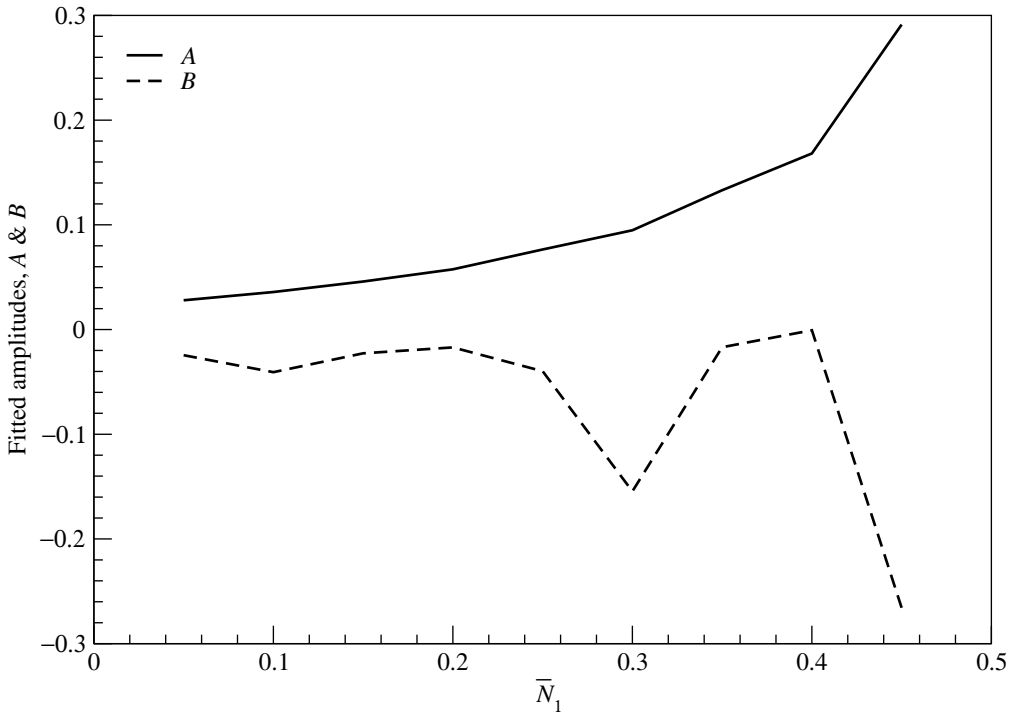

Figure 7.48: The fitted amplitudes A (solid line) and B (dashed line) of the infinite-ladder subtracted CDW-π correlations $\langle N_j N_{j+r} \rangle - \langle N_j \rangle \langle N_{j+r} \rangle$, in the limit $t' \gg t_{\|}, t_{\perp}$, as a function of the nearest-neighbor excluded chain filling fraction $\bar{N}_1$. The data points plotted here are from the six-parameter, $(A, \alpha, k, \phi, B, \alpha')$, fit to (7.5.87), shown in Table 7.6.

Figure 7.49 shows the fitted correlation exponents α and α' as functions of the

nearest-neighbor excluded chain filling fraction $\bar{N}_1$. The fit for α' is not very reliable, but it appears from Figure 7.49 that unlike the leading SC correlation exponent $\beta = \frac{1}{2}$, the leading CDW-π correlation exponent α is non-universal. Looking through all the values of α in Table 7.6, we find that $\alpha > \beta$ for all $\bar{N}_1$. For $\bar{N}_1$ close to $\frac{1}{2}$, the fitted values of α appear to be approaching $\beta = \frac{1}{2}$, but unfortunately, this is the filling-fraction regime where the nonlinear curve fits are least reliable. Therefore, it is difficult to say, based on the numerical results, where α will become smaller than β at some nearest-neighbor excluded chain filling fraction $\bar{N}_1 < \frac{1}{2}$. Perhaps even more worrying to us is the fact that α is not very big, or whether the leading CDW-σ correlation exponent will be smaller or larger than the leading CDW-π correlation exponent. It is possible that the leading CDW-σ correlation exponent might become smaller than $\beta = \frac{1}{2}$ above some critical nearest-neighbor excluded chain filling fraction $\bar{N}_{1,c}$, which we have no means of calculating.

Just as we have done for the SC correlations, we can try fitting the subtracted CDW-π correlations again, with the wave vector $k = 2\pi\bar{N}_1$ fixed, and see whether we can make the nonlinear curve fits more reliable. We have earlier noted, while k is unconstrained, that a fit to the simple asymptotic form (7.5.86) does not produce good fits. We do not expect the fits to this asymptotic form to become better with $k = 2\pi\bar{N}_1$ fixed, but we do it nonetheless to use the series of fitted parameters, which are shown in Table 7.7, as a crude bench mark. The main thing to note here is the haphazard behaviour of the fitted parameters as functions of the nearest-neighbor excluded chain filling fraction $\bar{N}_1$. We take this to mean that a leading-order correction must be included in (7.5.86), for the nonlinear curve fits to produce more reliable values for the fitted parameters. Recalling that we have obtained better-looking nonlinear curve fits of the numerical CDW-π correlation to (7.5.87), we try a leading-order correction that is of the form

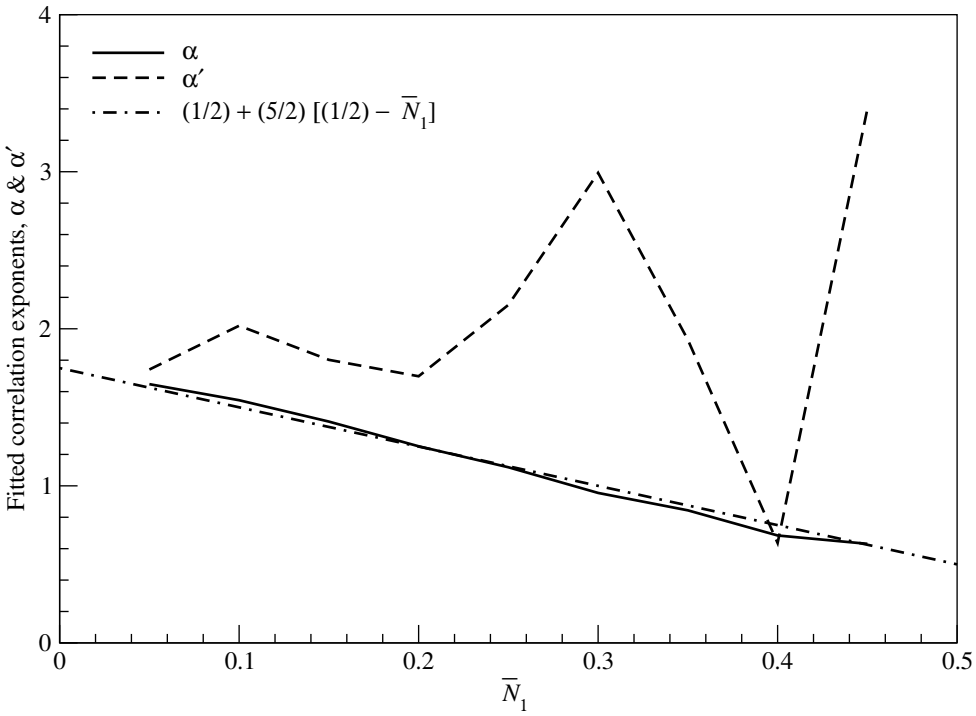

Figure 7.49: The fitted correlation exponents α (solid line) and α' (dashed line) of the infinite-ladder subtracted CDW-π correlations $\langle N_j N_{j+r}\rangle - \langle N_j\rangle\langle N_{j+r}\rangle$, in the limit $t' \gg t_\parallel, t_\perp$, as a function of the nearest-neighbor excluded chain filling fraction $\bar{N}_1$. Also shown as the dotted-dashed line is the linear function $\frac{1}{2} + \frac{5}{2}\left(\frac{1}{2} - \bar{N}_1\right)$, which α follows rather closely. The data points plotted here are from the six-parameter, $(A, \alpha, k, \phi, B, \alpha')$, fit to (7.5.87), shown in Table 7.6.

$Br^{-\alpha'}$.

Table 7.7: Fitted parameters for a nonlinear curve fit of the infinite-ladder pure-correlated-hopping subtracted CDW-π correlation $\langle N_j N_{j+r}\rangle - \langle N_j\rangle\langle N_{j+r}\rangle$ to an asymptotic form $Ar^{-\alpha}\cos(2\pi\bar{N}_1 r + \phi)$, for nearest-neighbor excluded chain filling fractions $0.05 \leq \bar{N}_1 \leq 0.45$, for $r \geq 4$.

$\bar{N}_1$	A	α	ϕ	visual
0.05	0.18281	2.3273	0.582934	very poor
0.10	0.287045	2.57121	−0.0345962	poor
0.15	0.0651428	1.61575	0.0994923	poor
0.20	0.0362065	1.04854	0.288858	poor
0.25	0.0599225	1.00758	0.277636	poor
0.30	0.103522	0.993297	0.2648	not good
0.35	0.147571	0.889726	0.1813	good
0.40	0.160796	0.666732	0.152614	good
0.45	0.328957	0.685923	0.17562	not good

This brings us back to Table 7.6, where we see that α' seems to be 'randomly' scattered around a mean value of $\alpha' = 2$. Though it does not appear as convincingly so as the leading correlation exponent $\beta = \frac{1}{2}$ in the SC correlations, we suspect that the subdominant CDW correlation exponent might also be universal. Therefore, apart from fixing $k = 2\pi\bar{N}_1$, we will also constrain $\alpha' = 2$ in one series of our curve fit to the asymptotic form (7.5.87), and relax this constraint in the other series. The fitted parameters for this two series of nonlinear curve fits are shown in Table 7.8. We find, in the process of nonlinear curve fitting the series with fixed $\alpha' = 2$, that the fits are good

visually. By comparing the constrained and unconstrained series of fitted parameters, we can very roughly gauge the nature of the leading correction. Judging from the strong dependence of α' on $\bar{N}_1$, it appears that the leading correction is a decaying exponential with a strongly-$\bar{N}_1$-dependent correlation length. Therefore, we need to exercise caution when interpreting the rest of the fitted parameters.

From Figure 7.49, we find that the fitted leading CDW correlation exponent α appears to follow the linear function

$$\alpha = \tfrac{1}{2} + \tfrac{5}{2}\left(\tfrac{1}{2} - \bar{N}_1\right) \tag{7.5.89}$$

rather closely. However, the leading CDW correlation exponents α for both the four-parameter, (A, α, ϕ, B), as well as the five-parameter, $(A, \alpha, \phi, B, \alpha')$, fits shown in Table 7.8, do not fall onto a smooth curve when plotted against $\bar{N}_1$. This led us to suspect that we might have fitted the leading CDW correlation exponent α 'correctly' the first time round, but are messing up α in our nonlinear curve fits with $\alpha' = 2$ fixed. Performing yet another series of nonlinear curve fit, this time with α constrained to the form in (7.5.89), we find that we obtain good fits over almost the entire range of nearest-neighbor excluded chain filling fractions $\bar{N}_1$ (except for $\bar{N}_1 = 0.45$). The fitted parameters are shown in Table 7.9.

Finally, having claimed earlier that the leading correction to our asymptotic form (7.5.86) might be a decaying exponential, it is only sensible to perform a series of nonlinear curve fits to the exponential-corrected asymptotic form

$$Ar^{-\alpha}\cos(2\pi\bar{N}_1 r + \phi) + B\exp(-r/\xi'). \tag{7.5.90}$$

We find good or acceptable fits over the entire range of $\bar{N}_1$, and the fitted parameters are shown in Table 7.10. In this series of curve fits, we allow the leading CDW correlation exponent α to freely vary, but we suspect that fixing α to the functional form in (7.5.89)

Table 7.8: Fitted parameters for two series of nonlinear curve fits of the infinite-ladder pure-correlated-hopping subtracted CDW-π correlation $\langle N_j N_{j+r}\rangle - \langle N_j\rangle\langle N_{j+r}\rangle$ to an asymptotic form $Ar^{-\alpha}\cos(2\pi\bar{N}_1 r+\phi)+Br^{-\alpha'}$, for nearest-neighbor excluded chain filling fractions $0.05 \le \bar{N}_1 \le 0.45$, for $r \ge 4$. For $\bar{N}_1 = 0.40$, the full five-parameter fit cannot be done because the iterations would run away.

$\bar{N}_1$	A	α	ϕ	B	α'	visual
0.05	0.040878	1.82412	0.162776	−0.0445519	2	very good
	0.0449925	1.86281	0.136836	−0.0501875	2.0584	very good
0.10	0.0402042	1.60067	0.267028	−0.0378689	2	good
	0.0316311	1.49397	0.272161	−0.0571974	2.19227	good
0.15	0.0409107	1.3584	0.291311	−0.0291461	2	good
	0.0456305	1.4112	0.267376	−0.013628	1.57786	good
0.20	0.0664881	1.32204	0.295907	−0.028582	2	good
	0.0607463	1.28178	0.287578	−0.0117856	1.51734	good
0.25	0.0762532	1.11894	0.234929	−0.0351995	2	good
	0.0823278	1.15394	0.228647	−0.116694	2.70344	good
0.30	0.0881624	0.921612	0.224257	−0.0416915	2	good
	0.0950603	0.955763	0.183688	−201.934	7.71059	good
0.35	0.140907	0.86933	0.183335	−0.0153533	2	good
	0.142457	0.873968	0.183194	−0.00410886	1.24539	good
0.40	0.16195	0.669848	0.150633	0.0103589	2	good
0.45	0.344937	0.706268	0.176753	−0.0305623	2	not good
	0.328957	0.685923	0.17562	−0.0305623	38.0137	not good

Table 7.9: Fitted parameters for a nonlinear curve fit of the infinite-ladder pure-correlated-hopping subtracted CDW-π correlation $\langle N_j N_{j+r}\rangle - \langle N_j\rangle\langle N_{j+r}\rangle$ to an asymptotic form $Ar^{-\alpha(\bar{N}_1)}\cos(2\pi\bar{N}_1 r + \phi) + Br^{-2}$, where $\alpha(\bar{N}_1) = \frac{1}{2} + \frac{5}{2}(\frac{1}{2} - \bar{N}_1)$, for nearest-neighbor excluded chain filling fractions $0.05 \leq \bar{N}_1 \leq 0.45$, for $r \geq 4$.

$\bar{N}_1$	A	ϕ	B	visual
0.05	0.0276053	0.190112	−0.0429842	good
0.10	0.033098	0.28957	−0.0404817	good
0.15	0.0421811	0.292405	−0.0290258	good
0.20	0.0577351	0.299305	−0.0256662	good
0.25	0.0770911	0.234901	−0.0354981	good
0.30	0.103083	0.230898	−0.0388471	good
0.35	0.142498	0.182805	−0.0144078	good
0.40	0.189303	0.161565	0.018315	good
0.45	0.287925	0.178943	−0.00311366	not good

will probably produce good fits as well. We also see from Table 7.10 that the ftted amplitude B and correlation length ξ' do not vary smoothly with $\bar{N}_1$. The fit also fails at $\bar{N}_1 = 0.35$ and $\bar{N} = 0.40$. With this new numerical evidence, we now weigh it more likely for the leading order correction to be a power law.

Table 7.10: Fitted parameters for a nonlinear curve fit of the infinite-ladder pure-correlated-hopping subtracted CDW-π correlation $\langle N_j N_{j+r}\rangle - \langle N_j\rangle \langle N_{j+r}\rangle$ to an asymptotic form $Ar^{-\alpha}\cos(2\pi\bar{N}_1 r + \phi) + B\exp(-r/\xi')$, for nearest-neighbor excluded chain filling fractions $0.05 \le \bar{N}_1 \le 0.45$, for $r \ge 4$. For $\bar{N}_1 = 0.35$ and $\bar{N}_1 = 0.40$, the full five-parameter fit cannot be done because the iterations would run away.

$\bar{N}_1$	A	α	ϕ	B	ξ'	visual
0.05	0.00364461	0.953849	0.61515	−0.00395607	5.87165	very good
0.10	0.104143	2.03204	0.196947	−0.00115268	9.44686	good
0.15	0.0503399	1.45318	0.250451	−0.00273516	5.16493	very good
0.20	0.0595762	1.27344	0.280019	−0.00302503	4.73924	good
0.25	0.0789765	1.13617	0.228861	−0.0148788	2.22452	good
0.30	0.0960752	0.960458	0.181741	−9.00983	0.528804	good
0.35	0.125695	0.820843	0.176424	-	-	good
0.40	0.17453	0.701496	0.139351	-	-	good
0.45	0.328957	0.685923	0.17562	0.220589	0.0691916	not good

Taken altogether, the various series of curve fits are consistent with a nonuniversal leading CDW correlation exponent α of the form given by (7.5.89), whether we believe the leading order correction is a power law with universal exponent $\alpha' = 2$, or a exponential with $\bar{N}_1$-dependent correlation length ξ'. Comparing Tables 7.6, 7.7, 7.8, 7.9,

and 7.10, we now have a more reliable picture, shown in Figure 7.50, of what the amplitude A and phase shift ϕ might be as functions of $\bar{N}_1$. Figure 7.50 provides convincing numerical evidence for a strongly-$\bar{N}_1$-dependent amplitude A. The phase shift ϕ, on the other hand, is such a weak function of $\bar{N}_1$ that it might be conceivable that its value is universal and equal to $\frac{\pi}{16}$.

7.5.8 Fermi-Liquid Correlations

Unlike the SC and CDW-π correlations, the infinite-ladder FL correlations cannot be as easily calculated using the sequence of maps described in Section 7.5.4. This is because, just like the case for CDW-σ correlations, the operators involved are not paired, and therefore cannot be written in terms of the extended hard-core-boson operators B_i. Nevertheless, because of the simple structure of the ground state, we can still develop considerable analytical insights into this correlation.

The key to understanding the behaviour of the FL correlation in this limiting case of $t'/t_{\parallel}, t'/t_{\perp} \to \infty$ is to realize that the ground state consists exclusively of a superposition of bound pair configurations. A configuration containing unpaired fermions, like the one shown in Figure 7.51 for example, cannot occur in the ground state. This exclusively bound-pair nature of the ground state configurations severely limits which FL correlations $\langle c^{\dagger}_{i,j} c_{i',j'} \rangle$ can be nonzero. Our first observation is that a bound pair always contains one particle on leg $i = 1$, and the other particle on leg $i = 2$. Therefore, if we annihilate a spinless fermion at site (i', j'), i.e. a particle on leg i', the spinless fermion that we create at site (i, j) must also be on the same leg, so that we can start from a bound-pair configuration, and end on a bound-pair configuration. This tells us that the only nonzero FL correlations are of the form $\langle c^{\dagger}_{i,j} c_{i,j'} \rangle$.

Secondly, because the bound pairs come in two flavors, even or odd, which is con-

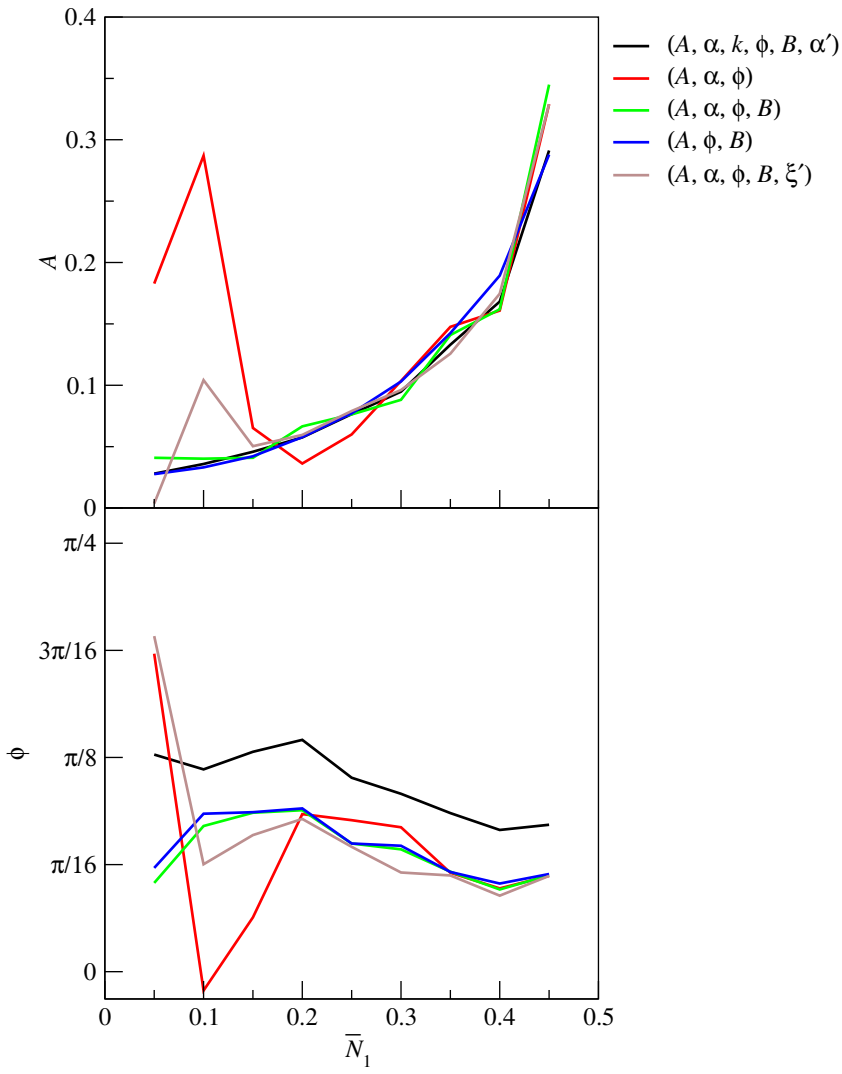

Figure 7.50: The fitted amplitude A (top) and phase shift ϕ (bottom) of the infinite-ladder subtracted CDW-π correlations $\langle N_j N_{j+r}\rangle - \langle N_j\rangle\langle N_{j+r}\rangle$, in the limit $t' \gg t_\parallel, t_\perp$, as a function of the nearest-neighbor excluded chain filling fraction $\bar{N}_1$, for nonlinear curve fits to the same asymptotic form (7.5.86), but different leading order corrections, with and without constraints. The parameters enclosed within each parenthesis are those allowed to vary in that particular nonlinear curve fit.

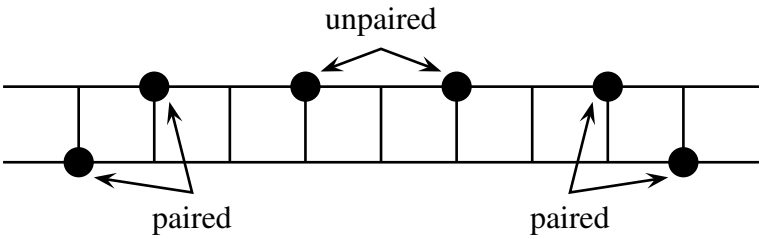

Figure 7.51: A configuration, of spinless fermions with infinite nearest-neighbor repulsion on a two-legged ladder, containing unpaired spinless fermions. This configuration does not occur in the ground state of the Hamiltonian in (7.3.2), in the limit of $t'/t_{\parallel}, t'/t_{\perp} \to \infty$.

served in correlated hops, we have two degenerate ground states. These ground states $|\Psi_+\rangle$ and $|\Psi_-\rangle$ have definite flavor, but indefinite-momentum, so we take their symmetric and antisymmetric combinations to obtain two definite-momentum ground states

$$\begin{aligned} |\Psi(\pi,0)\rangle &= \tfrac{1}{\sqrt{2}}\,|\Psi_+\rangle - \tfrac{1}{\sqrt{2}}\,|\Psi_-\rangle\,, \\ |\Psi(0,\pi)\rangle &= \tfrac{1}{\sqrt{2}}\,|\Psi_+\rangle + \tfrac{1}{\sqrt{2}}\,|\Psi_-\rangle\,. \end{aligned} \tag{7.5.91}$$

Unless we wish to make a distinction, we will use $|\Psi(\mathbf{q})\rangle$ to refer to both of these definite-momentum ground states, where $\mathbf{q} = (\pi, 0)$ or $\mathbf{q} = (0, \pi)$.

Now, for a FL correlation $\langle c^\dagger_{i,j} c_{i,j'}\rangle$ which is nonzero in $|\Psi(\mathbf{q})\rangle$, we find that the contributing matrix elements are all from one of the definite-flavor ground states. Therefore, we have

$$\langle\Psi(\mathbf{q})|c^\dagger_{i,j}c_{i,j'}|\Psi(\mathbf{q})\rangle = \tfrac{1}{2}\,\langle\Psi_\pm|c^\dagger_{i,j}c_{i,j'}|\Psi_\pm\rangle\,. \tag{7.5.92}$$

Furthermore, we note that if $c^\dagger_{1,j}c_{1,j'}$ has nonzero expectation in $|\Psi_+\rangle$, then $c^\dagger_{2,j}c_{2,j'}$ will have the same nonzero expectation in $|\Psi_-\rangle$, and vice versa. This tells us that

$$\langle\Psi_\pm|c^\dagger_{1,j}c_{1,j'}|\Psi_\pm\rangle = \langle\Psi_\mp|c^\dagger_{2,j}c_{2,j'}|\Psi_\mp\rangle\,, \tag{7.5.93}$$

and thus

$$\langle\Psi(\mathbf{q})|c^\dagger_{1,j}c_{1,j'}|\Psi(\mathbf{q})\rangle = \langle\Psi(\mathbf{q})|c^\dagger_{2,j}c_{2,j'}|\Psi(\mathbf{q})\rangle\,. \tag{7.5.94}$$

Taking the symmetric and antisymmetric combinations

$$c_{\pm,j} = \tfrac{1}{\sqrt{2}}(c_{1,j} \pm c_{2,j}) \tag{7.5.95}$$

of the spinless fermion operators on the same rung, we then find that

$$\langle \Psi(\mathbf{q}) | c^\dagger_{+,j} c_{+,j'} | \Psi(\mathbf{q}) \rangle = \langle \Psi(\mathbf{q}) | c^\dagger_{-,j} c_{-,j'} | \Psi(\mathbf{q}) \rangle > 0, \tag{7.5.96}$$

if $\langle \Psi(\mathbf{q}) | c^\dagger_{i,j} c_{i,j'} | \Psi(\mathbf{q}) \rangle > 0$, and

$$\langle \Psi(\mathbf{q}) | c^\dagger_{\pm,j} c_{\mp,j'} | \Psi(\mathbf{q}) \rangle = 0 \tag{7.5.97}$$

always.

For j even, $\langle c^\dagger_{1,j} c_{1,j+r} \rangle$ receives contributions only from $|\Psi_+\rangle$. In this even-flavor ground state, the odd sites $j = 2s + 1$ on leg $i = 1$ are never occupied. Therefore, $\langle c^\dagger_{1,j} c_{1,j+r} \rangle > 0$ if r is even, and $\langle c^\dagger_{1,j} c_{1,j+r} \rangle = 0$ if r is odd. For j odd, $\langle c^\dagger_{1,j} c_{1,j+r} \rangle$ receives contributions only from $|\Psi_-\rangle$, in which the even sites $j = 2s$ on leg $i = 1$ are never occupied. Thus we have a similarly extreme even-odd modulation $\langle c^\dagger_{1,j} c_{1,j+r} \rangle > 0$ if r is even, and $\langle c^\dagger_{1,j} c_{1,j+r} \rangle = 0$ if r is odd, and also, $\langle c^\dagger_{2,j} c_{2,j+r} \rangle > 0$ if r is even, with contributions from $|\Psi_-\rangle$ when j is even and from $|\Psi_+\rangle$ when j is odd, and $\langle c^\dagger_{2,j} c_{2,j+r} \rangle = 0$ if r is odd. This extreme even-odd modulation is softened in the expectations $\langle c^\dagger_{1a,j} c_{1a,j+r} \rangle$ and $\langle c^\dagger_{2a,j} c_{2a,j+r} \rangle$, where

$$\begin{aligned} c_{1a,j} &= \tfrac{1}{\sqrt{2}}(c_{1,j} + c_{1,j+1}), \\ c_{2a,j} &= \tfrac{1}{\sqrt{2}}(c_{2,j} + c_{2,j+1}), \end{aligned} \tag{7.5.98}$$

and accentuated in the expectations $\langle c^\dagger_{1b,j} c_{1b,j+r} \rangle$ and $\langle c^\dagger_{2b,j} c_{2b,j+r} \rangle$, where

$$\begin{aligned} c_{1b,j} &= \tfrac{1}{\sqrt{2}}(c_{1,j} - c_{1,j+1}), \\ c_{2b,j} &= \tfrac{1}{\sqrt{2}}(c_{2,j} - c_{2,j+1}). \end{aligned} \tag{7.5.99}$$

To derive the asymptotic behaviour of $\langle c^\dagger_{i,j} c_{i,j+r} \rangle$ as $r \to \infty$, let us note that for even $r = 2p$, the only nonzero contributions to $\langle c^\dagger_{i,j} c_{i,j+r} \rangle$ comes from the creation and annihilation of spinless fermions on the ends of a compact cluster of p bound pairs, as shown in Figure 7.52. The pair of initial and final configurations shown in Figure 7.52 makes a contribution $\Psi^*_f \Psi_i$ to the expectation $\langle c^\dagger_{i,j} c_{i,j+2p} \rangle$, so that

$$\langle c^\dagger_{i,j} c_{i,j+2p} \rangle = \sum_{(i,f)} \Psi^*_f \Psi_i \tag{7.5.100}$$

for all configurations with a compact p-bound-pair cluster between the rungs j and $j + 2p$. Clearly, these products of amplitudes will depend on where the other bound pairs are on the ladder. However, if the ladder filling fraction $\bar{n}_2$ is not too close to $\bar{n}_2 = \frac{1}{2}$, we expect

$$|\Psi_f| \approx |\Psi_i|, \quad \arg(\Psi_f) \approx \arg(\Psi_i), \tag{7.5.101}$$

so that on a infinitely-long ladder, $\langle c^\dagger_{i,j} c_{i,j+2p} \rangle$ is very nearly the probability of finding a compact p-bound-pair cluster between the rungs j and $j + 2p$. For our translationally-invariant system, this is the same as the probability of finding a compact p-bound-pair cluster *anywhere* on the ladder.[3]

We know how to calculate such a probability, which is none other than

$$\langle N_j N_{j+2} \cdots N_{j+2p} \rangle = \frac{\bar{N}_1}{\bar{n}_1} \langle n_j n_{j+1} \cdots n_{j+p} \rangle = \frac{\bar{N}_1}{\bar{n}_1} \det G_C(p), \tag{7.5.102}$$

after using the relation (7.4.109) between nearest-neighbor excluded and nearest-neighbor included expectations. Here $\det G_C(p)$ is the determinant of the noninteracting-

[3]Technically, the correct thing to do is to compute the p-particle sector of the cluster density matrix of a $(p + 1)$-site cluster, and look at the matrix element between a configuration with an empty site at the left end of the cluster and a configuration with an empty site at the right end of the cluster. However, the relevant cluster density matrix is that of a system of hard-core bosons. While this hard-core-boson cluster density matrix should be simply related to the noninteracting-spinless-fermion cluster density matrix, this relation has not been worked out, for use on this problem of finding FL correlations at large r for the bound-pair ground states on a two-legged ladder.

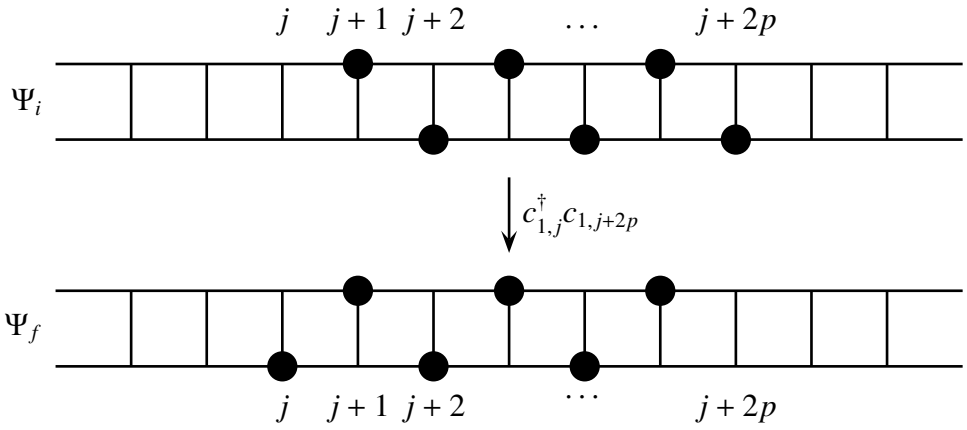

Figure 7.52: Compact p-bound-pair cluster configurations which contribute to the nonzero expectation of the FL operator product $c^{\dagger}_{1,j}c_{1,j+2p}$, which annihilates a spinless fermion on the right end of the compact p-bound-pair cluster, and creates a spinless fermion on the left end of the compact p-bound-pair cluster. Ψ_i and Ψ_f are the ground-state amplitudes of the initial and final configurations respectively.

spinless-fermion cluster Green-function matrix $G_C(p)$ for a cluster of p sites. Using the notation introduced in Chapter 3, we can write this determinant as

$$\det G_C(p) = \prod_{l=1}^{p} \lambda_l = \prod_{l=1}^{p} \frac{1}{e^{\varphi_l} + 1}, \tag{7.5.103}$$

where λ_l are the eigenvalues of the cluster Green-function matrix $G_C(p)$, and φ_l are the single-particle pseudo-energies of the cluster density matrix ρ_C, for the cluster of p sites in an infinite chain of noninteracting spinless fermions.

For very large clusters, $p \gg 1$, we know from Chapter 3 that $G_C(p)$ has approximately $\bar{n}_1 p$ eigenvalues which are almost one, and approximately $(1 - \bar{n}_1)p$ eigenvalues which are almost zero. The determinant of $G_C(p)$ is thus determined predominantly by the approximately $(1 - \bar{n}_1)p$ eigenvalues which are almost zero. For these λ_l, $e^{\varphi_l} \gg 1$, and thus

$$\det G_C(p) \approx \prod_{\lambda_l \sim 0} e^{-\varphi_l} = \exp\left(- \sum_{l_F}^{l_F + (1-\bar{n}_1)p} \varphi_l \right). \tag{7.5.104}$$

Using the approximate scaling formula (3.5.6), and converting the sum into an integral, we find that

$$\det G_C(p) \approx \exp\left(-p \int_0^{1-\bar{n}_1} f(\bar{n}_1, x)\, dx\right), \tag{7.5.105}$$

i.e. the probability of finding a compact p-bound-pair cluster decays exponentially with p in the limit of $p \gg 1$.

With the help of our sequence of maps from bound pairs on a two-legged ladder to extended hard-core bosons to hard-core bosons to noninteracting spinless fermions, the latter three all on one-dimensional chains, and this simple compact cluster argument, we conclude that the FL correlation $\langle c^\dagger_{i,j} c_{i,j+r} \rangle$ decays exponentially with separation r as

$$\langle c^\dagger_{i,j} c_{i,j+r} \rangle \sim \exp\left[-r/\xi(\bar{n}_2)\right], \tag{7.5.106}$$

with a filling-fraction-dependent correlation length

$$\xi(\bar{n}_2) = \frac{2}{\int_0^{1-\bar{n}_1(\bar{n}_2)} f(\bar{n}_1(\bar{n}_2), x)\, dx}. \tag{7.5.107}$$

From Section 3.5 we know that the scaling function $f(\bar{n}, x)$ depends only very weakly on $\bar{n}$, and thus, at very low ladder fillings $\bar{n}_2 \to 0$, the correlation length $\xi(\bar{n}_2)$ attains its minimum value of

$$\xi(0) = \frac{2}{\int_0^1 f(0, x)\, dx}, \tag{7.5.108}$$

and the FL correlation $\langle c^\dagger_{i,j} c_{i,j+r} \rangle$ decays most rapidly in this regime of $\bar{n}_2 \to 0$. This is expected physically, since a long cluster of occupied sites is very unlikely to occur at very low filling fractions, with or without quantum correlations.

In the regime of $\bar{n}_2 \to \frac{1}{2}$, we find that $\bar{n}_1 \to 1$, and thus the correlation length $\xi(\bar{n}_2)$ diverges according to (7.5.107). Of course, this diverging correlation length tells us nothing about the amplitude of the FL correlation. Indeed, when the ladder becomes half-filled, the two degenerate ground states are inert bound-pair solids. Each of the half-filled-ladder ground-state wave functions consists of a single configuration whereby all

available plaquettes are occupied by a bound pair, and it is not possible to annihilate a spinless fermion at the $(j + r)$th rung and create another at the jth rung. The FL correlation $\langle c^{\dagger}_{i,j} c_{i,j+r} \rangle$ is thus strictly zero in this half-filled-ladder limit.

7.6 Zero Inter-Leg Hopping

In this section, we will look into the structure of the ground state in the limit $t_{\perp}/t_{\parallel} \to 0$, $t' = 0$ in Section 7.6.1, where we will provide a kinetic-energy argument for the staggered nature of the ground state. We will also describe a map between staggered ladder spinless fermion configurations and noninteracting spinless fermion configurations, that allows us to write down the amplitudes of all staggered ground-state configurations. With the aid of this map of ladder ground states to noninteracting spinless fermions on a chain, and a general understanding of the staggered nature of the ladder ground-state configurations, we calculate the various correlation functions in Sections 7.6.2, 7.6.3 and 7.6.4. Finally, in Section 7.6.5, we summarize and discuss the asymptotic behaviours of the various correlation functions.

7.6.1 Structure of Ground State

In the limit of $t_{\perp} \to 0$, each spinless fermion on the two-legged ladder carries a permanent leg index, and thus the number of spinless fermions P_i on leg i are good quantum numbers. Obviously, two successive spinless fermions along the same leg of the ladder cannot move past each other. Because of the infinite nearest-neighbor repulsion, which acts across a rung, two successive spinless fermions on different legs of the ladder also cannot move past each other. Therefore, the Hilbert space of the P-spinless-fermion problem breaks up into many independent sectors, each with a fixed sequence of leg

indices. The P-spinless-fermion problem in one such sector is therefore an independent problem from that of another P-spinless-fermion sector. For example, the six-spinless-fermion configuration $|112112\rangle$, where the first particle is on leg $i = 1$, the second on leg $i = 1, \ldots$, and the sixth particle is on leg $i = 2$, lies in the same sector as the configuration $|121121\rangle$, but not with the configuration $|111222\rangle$, for the obvious reason that the numbers of leg-1 and leg-2 spinless fermions are different, and also not with the configuration $|111221\rangle$, because they do not belong to the same translation-equivalence class of immutable leg-index sequence.

Again, as with the P-bound-pair problem described in Section 7.5.4.1, we expect to be able to solve the P-spinless-fermion problem in *some* of the fixed-leg-index-sequence sectors, with the help of the triplet of maps described in Sections 7.4.3, 7.4.4 and 7.4.5. For example, we certainly can solve the P-spinless-fermion problem in the sector with fixed leg-index sequences $\{\cdots iiiiii \cdots\}$. We also expect to be be able to solve the P-spinless-fermion problem in the sector with fixed leg-index sequences $\{\cdots 11112222 \cdots\}$ or $\{\cdots 22221111 \cdots\}$, where there is a single domain wall in the ladder. In general, we are optimistic that we can solve P-spinless-fermion problem in fixed-leg-index-sequence sectors in which such domain walls occur periodically in the leg-index sequence. Our hope then is that the P-spinless-fermion ground state occurs in a fixed leg-index sequence sector which we can solve exactly with the help of the triplet of maps.

Now, if we look at the local segments

$$\{\cdots 111222 \cdots\}, \quad \{\cdots 112122 \cdots\}, \tag{7.6.1}$$

in two leg-index sequences, we will find that on average, the third and fourth particles in the local segment $\{\cdots 112122 \cdots\}$ will each have a longer interval on the ladder to hop around, compared to their counterparts in the local segment $\{\cdots 111222\}$, as shown

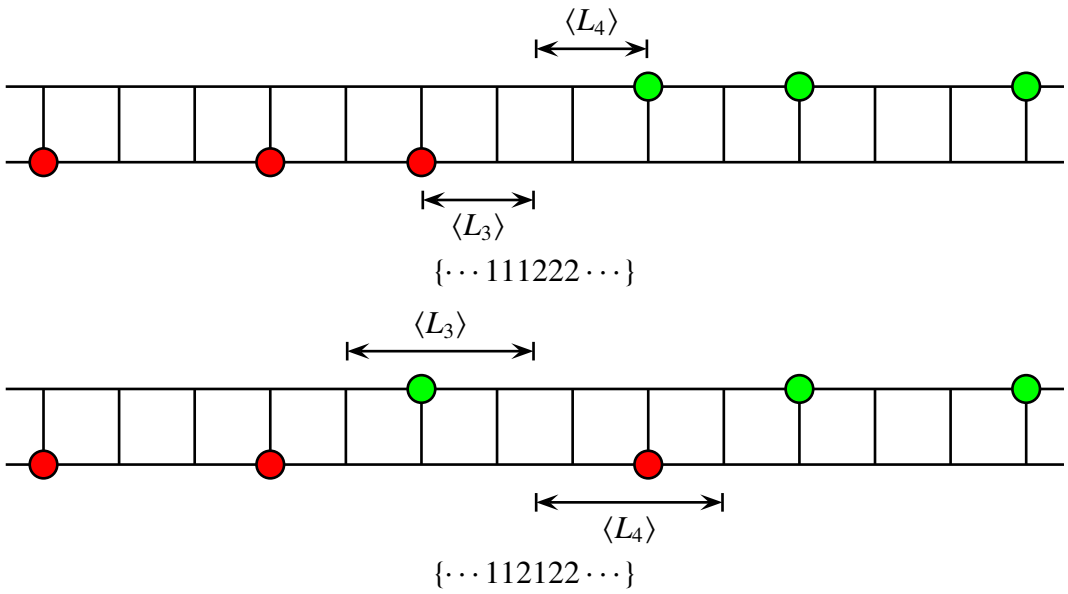

Figure 7.53: The average free chain lengths $\langle L_3 \rangle$ and $\langle L_4 \rangle$ available to the third and fourth spinless fermions in two local segments of six spinless fermions, $\{\cdots 111222 \cdots\}$ (top), and $\{\cdots 112122 \cdots\}$. In this figure, spinless fermions on leg $i = 1$ are colored red, while spinless fermions on leg $i = 2$ are colored green.

in Figure 7.53. This means that all else being the same, a leg-index sequence with the local segment $\{\cdots 112122\cdots\}$, which incorporates two domain walls, will have lower total kinetic energy than one with the local segment $\{\cdots 111222\cdots\}$, which incorporates one domain wall. In general, we will find that the lowest-energy state in a leg-index sequence with a larger number of domain walls to have lower total energy than the lowest-energy state in a leg-index sequence with a smaller number of domain walls. The P-spinless-fermion ground state, which has the the lowest possible total energy, must therefore have the largest number of domain walls, i.e. the P-spinless-fermion ground state must occur in the staggered sector, with leg-index sequence $\{\cdots 121212\ldots\}$, where successive spinless fermions occupy alternate legs. We call such a many-body ground state a *staggered ground state*.

In a staggered ground state, the configurations can be organized into pairs related by a reflection about the ladder axis, for example, the two configurations shown in Figure 7.54. If we demand that the staggered ground state must have definite symmetry with respect to reflection about the ladder axis, then the staggered ground state is two-fold degenerate. In the staggered ground state $|\Psi_+\rangle$, which is symmetric with respect to reflection about the ladder axis, the amplitudes of the symmetry-related pair of configurations must be equal. On the other hand, in the staggered ground state $|\Psi_-\rangle$, which is antisymmetric with respect to reflection about the ladder axis, the amplitudes of symmetry-related pair of configurations must be the negative of each other.

In the staggered sector, each spinless fermion on leg i will never directly feel the influence of the two leg-i particles nearest to it, so we can map each symmetry-related pair of staggered configurations for the spinless fermions with infinite nearest-neighbor repulsion on the two-legged ladder to a corresponding configuration for noninteracting spinless fermions on a chain, as shown in Figure 7.55. With this mapping, we can obtain

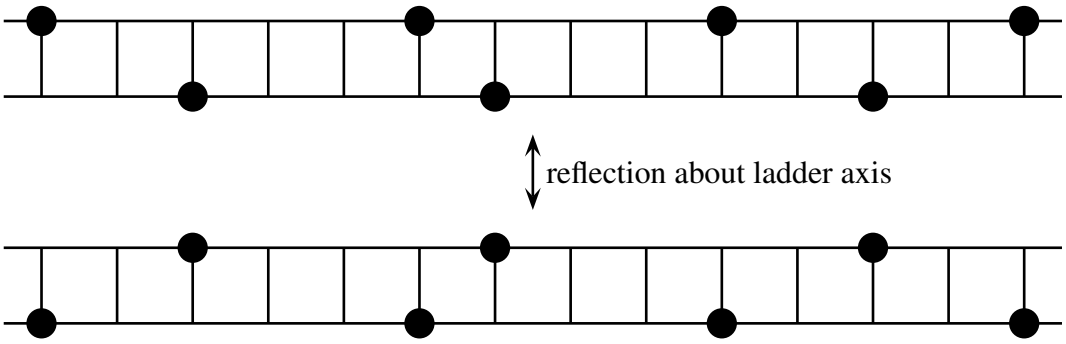

Figure 7.54: Two staggered configurations of spinless fermions with infinite nearest-neighbor repulsion on a two-legged ladder that are related by a reflection about the ladder axis.

the two degenerate ground-state wave functions in this limit of zero inter-leg hopping, $t_\perp \to 0$, from the Fermi sea ground-state wave function

$$|\Psi_F\rangle = \sum_{j_1} \cdots \sum_{j_P} A(k_1, \ldots, k_P; j_1, \ldots, j_P)\, c^\dagger_{j_1} c^\dagger_{j_2} \cdots c^\dagger_{j_{P-1}} c^\dagger_{j_P} |0\rangle\,, \tag{7.6.2}$$

assuming without too much loss of generality that P is even, as

$$|\Psi_\pm\rangle = \sum_{j_1} \cdots \sum_{j_P} A(k_1, \ldots, k_P; j_1, \ldots, j_P) \times \frac{1}{\sqrt{2}} \left(c^\dagger_{1,j_1} c^\dagger_{2,j_2} \cdots c^\dagger_{1,j_{P-1}} c^\dagger_{2,j_P} \pm c^\dagger_{2,j_1} c^\dagger_{1,j_2} \cdots c^\dagger_{2,j_{P-1}} c^\dagger_{1,j_P} \right) |0\rangle\,. \tag{7.6.3}$$

Note that in this map, a ladder with filling fraction $\bar{n}_2$ maps onto a chain of filling fraction $\bar{n}_1 = 2\bar{n}_2$.

In addition, when we use the ladder-fermion-to-chain-fermion map shown in (7.6.3) and Figure 7.55 to relate the expectations of interacting ladder spinless fermions to the expectations of noninteracting chain spinless fermions, for a ladder observable O_{ladder} which is mapped to the chain observable O_{chain},

$$\langle O_{\text{ladder}} \rangle_{\text{ladder}} = \tfrac{1}{2} \langle O_{\text{chain}} \rangle_{\text{chain}}\,, \tag{7.6.4}$$

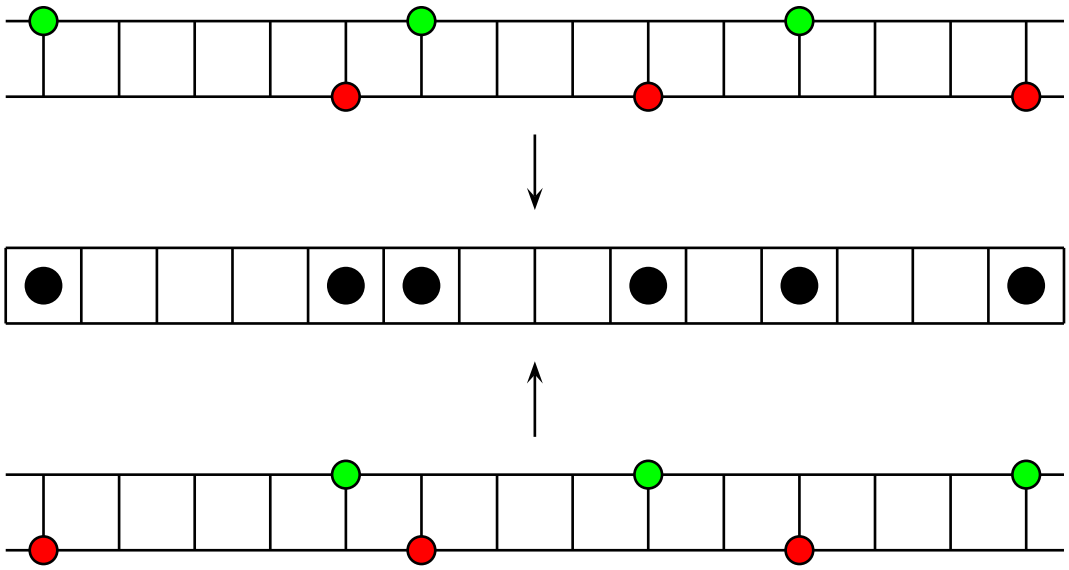

Figure 7.55: Mapping the staggered configurations of spinless fermions with infinite nearest-neighbor repulsion on a two-legged ladder to a configuration of noninteracting spinless fermions on a chain.

the factor of $\frac{1}{2}$ appears generically, as a consequence of the two-to-one nature of the map. This relation between ladder and chain expectations is analogous to the one we derived in (7.4.97), when we map from a nearest-neighbor excluded chain to a nearest-neighbor included chain. We use the subscripts 'ladder' and 'chain' just this once to distinguish between ladder and chain expectations. This notation is cumbersome, so we will not use it again in the rest of this chapter. Whether an expectation is a ladder expectation or a chain expectation will be clear from the context.

Here, let us warn that care must be exercised in identifying the chain observable O_{chain} corresponding to the ladder observable O_{ladder}. We illustrate this with the following example of $P = 4$ particles on a ladder of length $L = 6$ subject to closed shell boundary conditions. For this system, we find six $q = 0$ Bloch states, generated by the configurations shown in Table 7.11. Denoting by A_1, A_3 and A_5 the three independent

Table 7.11: The six Bloch states, their generating configurations, and ground-state amplitudes for $P = 4$ particles on a ladder of length $L = 6$ subject to periodic boundary conditions.

Bloch state	generating configuration	Bloch-state amplitude
$\|1\rangle$	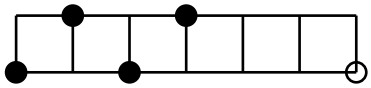	$\frac{1}{\sqrt{2}} A_1$
$\|2\rangle$	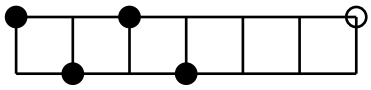	$\frac{1}{\sqrt{2}} A_1$
$\|3\rangle$	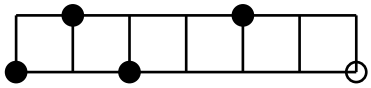	$\frac{1}{\sqrt{2}} A_3$
$\|4\rangle$	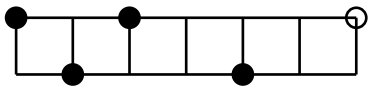	$\frac{1}{\sqrt{2}} A_3$
$\|5\rangle$	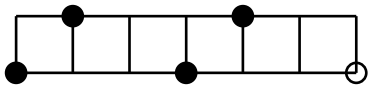	$\frac{1}{\sqrt{2}} A_5$
$\|6\rangle$	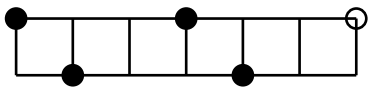	$\frac{1}{\sqrt{2}} A_5$

amplitudes, we can write the symmetric ladder-ground-state wave function as

$$|\Psi_+\rangle = \tfrac{1}{\sqrt{2}} A_1 |1\rangle + \tfrac{1}{\sqrt{2}} A_1 |2\rangle + \tfrac{1}{\sqrt{2}} A_3 |3\rangle + \tfrac{1}{\sqrt{2}} A_3 |4\rangle + \tfrac{1}{\sqrt{2}} A_5 |5\rangle + \tfrac{1}{\sqrt{2}} A_5 |6\rangle . \quad (7.6.5)$$

We map staggered ground states on this ladder to a chain of $P = 4$ particles of a chain of length $L = 6$, which has only three $q' = 0$ Bloch states, and whose ground state is

$$|\Psi'\rangle = A_1 |1'\rangle + A_3 |3'\rangle + A_5 |5'\rangle . \quad (7.6.6)$$

This tells us that we have a one-to-one Bloch-state-to-Bloch-state mapping between the ladder and the chain, if we rewrite the symmetric ladder ground state as

$$|\Psi_+\rangle = A_1 |1, +\rangle + A_3 |3, +\rangle + A_5 |5, +\rangle , \quad (7.6.7)$$

where

$$|1, +\rangle = \tfrac{1}{\sqrt{2}}(|1\rangle + |2\rangle), \quad |3, +\rangle = \tfrac{1}{\sqrt{2}}(|3\rangle + |4\rangle), \quad |5, +\rangle = \tfrac{1}{\sqrt{2}}(|5\rangle + |6\rangle) \quad (7.6.8)$$

are the symmetric ladder Bloch states that get mapped to the chain Bloch states $|1'\rangle$, $|3'\rangle$ and $|5'\rangle$ respectively. The ladder Bloch states $|1, +\rangle$, $|3, +\rangle$, and $|5, +\rangle$ consist of 12, 12, and 6 configurations respectively, while the chain Bloch states $|1'\rangle$, $|3'\rangle$, and $|5'\rangle$ consist of 6, 6, and 3 configurations respectively. Here, let us also introduce the notation

$$\begin{gathered} |1, +\rangle^* , \quad |3, +\rangle^* , \quad |5, +\rangle^* ; \\ |1'\rangle^* , \quad |3'\rangle^* , \quad |5'\rangle^* \end{gathered} \quad (7.6.9)$$

to denote the unnormalized versions of $|1, +\rangle$, $|3, +\rangle$, $|5, +\rangle$, and $|1'\rangle$, $|3'\rangle$, $|5'\rangle$ respectively.

We start by considering the identity operator on the ladder, $O = \mathbb{1}$, which is diagonal in the basis of ladder Bloch states. Its matrix elements between the unnormalized Bloch states are

$$\begin{aligned} {}^*\langle 1, +|\mathbb{1}|1, +\rangle^* &= 12, \\ {}^*\langle 3, +|\mathbb{1}|3, +\rangle^* &= 12, \\ {}^*\langle 5, +|\mathbb{1}|5, +\rangle^* &= 6. \end{aligned} \quad (7.6.10)$$

The identity operator on the chain is also diagonal in the basis of ladder Bloch states, with matrix elements

$$\begin{aligned} {}^{*}\langle 1'|\mathbb{1}|1'\rangle^{*} &= 6, \\ {}^{*}\langle 3'|\mathbb{1}|3'\rangle^{*} &= 6, \\ {}^{*}\langle 5'|\mathbb{1}|5'\rangle^{*} &= 3. \end{aligned} \tag{7.6.11}$$

By inspecting these matrix elements, we know therefore that the chain observable corresponding to the ladder identity operator is not the chain identity operator, but $O' = 2\,\mathbb{1}$. Since we have

$$\langle\Psi|\mathbb{1}|\Psi\rangle = 1 = \langle\Psi'|\mathbb{1}|\Psi'\rangle \tag{7.6.12}$$

for properly-normalized ladder and chain ground states $|\Psi\rangle$ and $|\Psi'\rangle$, we check that (7.6.4) is trivially satisfied for the assignment of corresponding observables $O = \mathbb{1} \leftrightarrow O' = 2\,\mathbb{1}$.

Next, let us consider the ladder observable

$$O = n_{1,1}. \tag{7.6.13}$$

This observable has expectation value 1 within a configuration in which the site $(1, 1)$ on the ladder is occupied, and expectation value 0 within a configuration in which the site $(1, 1)$ on the ladder is empty. Therefore, $n_{1,1}$ is diagonal in the basis formed by the three $q = 0$ symmetric ladder Bloch states, and its matrix elements between the unnormalized Bloch states are

$$\begin{aligned} {}^{*}\langle 1, +|n_{1,1}|1, +\rangle^{*} &= 4, \\ {}^{*}\langle 3, +|n_{1,1}|3, +\rangle^{*} &= 4, \\ {}^{*}\langle 5, +|n_{1,1}|5, +\rangle^{*} &= 2. \end{aligned} \tag{7.6.14}$$

If we now look at the chain observable n_1, we will find that this observable is also diagonal in the basis formed by the three $q' = 0$ chain Bloch states, with matrix elements

between unnormalized Bloch states being

$$\begin{aligned} {}^{*}\langle 1'|n_1|1'\rangle^{*} &= 4, \\ {}^{*}\langle 3'|n_1|3'\rangle^{*} &= 4, \\ {}^{*}\langle 5'|n_1|5'\rangle^{*} &= 2. \end{aligned} \tag{7.6.15}$$

Therefore, $n_{1,1}$ and n_1 form a pair of corresponding observables, based on the definition of such given in Section 7.4.6.

7.6.2 Fermi-Liquid Correlations

There are four FL correlations at range r, $\langle c^{\dagger}_{1,j} c_{j+r}\rangle$, $\langle c^{\dagger}_{1,j} c_{2,j+r}\rangle$, $\langle c^{\dagger}_{2,j} c_{1,j+r}\rangle$ and $\langle c^{\dagger}_{2,j} c_{2,j+r}\rangle$. From the staggered nature of the two degenerate ground states, we know that

$$\begin{aligned} \langle c^{\dagger}_{1,j} c_{1,j+r}\rangle &= \langle c^{\dagger}_{2,j} c_{2,j+r}\rangle\,; \\ \langle c^{\dagger}_{1,j} c_{2,j+r}\rangle &= \langle c^{\dagger}_{2,j} c_{1,j+r}\rangle \end{aligned} \tag{7.6.16}$$

in both ground states. Furthermore, we know that in the staggered ground states, two spinless fermions on the same leg must have at least one spinless fermion on the other leg somewhere between them. This means that if we annihilate a spinless fermion on leg $i = 2$, and create a spinless fermion on leg $i = 1$, for example, on the initial configuration shown in Figure 7.56, we would end up with a final configuration not found in the staggered ground state, because the spinless fermions 1 and 1′, and 1″ and 1‴, will be nearest-neighbor particles of one another. Another type of invalid final configuration we can end up with is shown in Figure 7.57, where we end up with the spinless fermions 1, 1′, and 1″ being consecutive particles on the ladder, if we annihilate a spinless fermion on leg $i = 2$, and create a spinless fermion on leg $i = 1$. Thinking through all possible cases of annihilating a spinless fermion on leg $i = 2$ and creating a spinless fermion on leg $i = 1$, we realized that we will *never* end up with a valid final staggered ground-

state configuration, starting from a valid initial staggered ground-state configuration. Therefore, the inter-leg FL correlations vanish, i.e.

$$\langle c^{\dagger}_{1,j} c_{2,j+r} \rangle = 0 = \langle c^{\dagger}_{2,j} c_{1,j+r} \rangle \,. \tag{7.6.17}$$

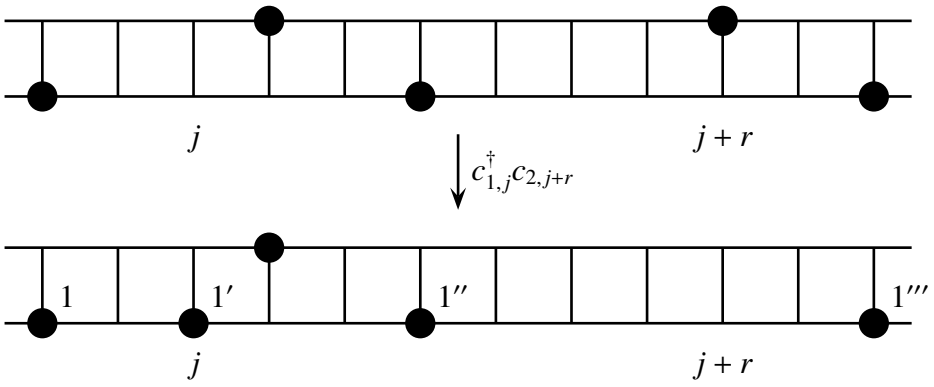

Figure 7.56: Annihilation of a spinless fermion at site $(2, j + r)$, followed by creation of a spinless fermion at site $(1, j)$, within a staggered ground-state configuration leads to a configuration not found in the ground state.

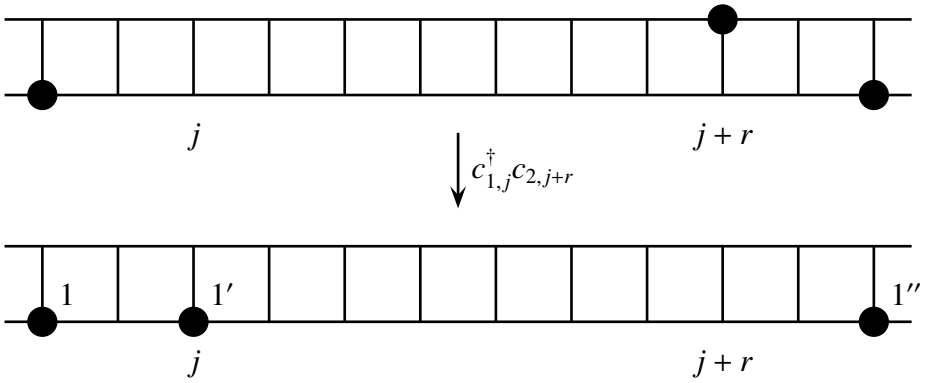

Figure 7.57: Annihilation of a spinless fermion at site $(2, j + r)$, followed by creation of a spinless fermion at site $(1, j)$, within a staggered ground-state configuration leads to a configuration not found in the ground state.

For annihilation and creation of spinless fermions on the same leg, for example, in the initial configuration shown in Figure 7.58, we find that if we annihilate the spinless

fermion at site $(1, j + r)$, and create a spinless fermion at $(1, j)$, the spinless fermions 1 and $1'$ on leg $i = 1$ would not be intervened by a spinless fermion on leg $i = 2$, while the spinless fermions 2 and $2'$ on leg $i = 2$ would also not be intervened by a spinless fermion on leg $i = 1$. This is again an invalid final configuration not found in either of the staggered ground states. The initial configuration thus contributes nothing to $\langle c^\dagger_{1,j} c_{1,j+r} \rangle$.

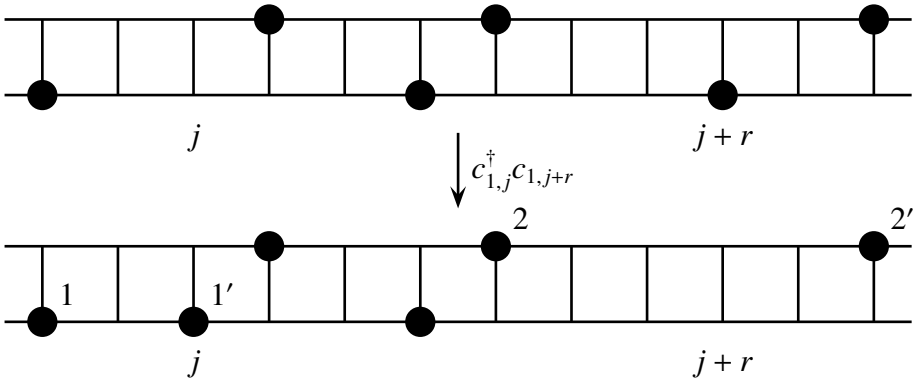

Figure 7.58: Annihilation of a spinless fermion at site $(1, j + r)$, followed by creation of a spinless fermion at site $(1, j)$, within a staggered ground-state configuration leads to a configuration not found in the ground state.

In order not to disrupt the staggered nature of the ground-state configurations, we see that the only configurations making non-zero contributions to $\langle c^\dagger_{1,j} c_{1,j+r} \rangle$ are those for which there are no intervening particles between rungs j and $j + r$. An example of one such configuration is shown in Figure 7.59. This tells us that

$$\langle c^\dagger_{1,j} c_{1,j+r} \rangle = \tfrac{1}{2} \langle c^\dagger_j (\mathbb{1} - n_{j+1}) \cdots (\mathbb{1} - n_{j+r-1}) c_{j+r} \rangle \,, \tag{7.6.18}$$

when the spinless fermions with infinite nearest-neighbor repulsion on the two-legged ladder is mapped to noninteracting spinless fermions on a chain.

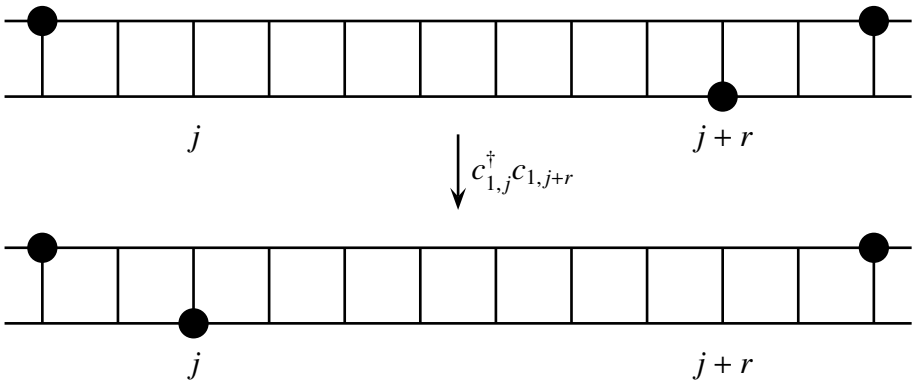

Figure 7.59: Annihilation of a spinless fermion at site $(1, j+r)$, followed by creation of a spinless fermion at site $(1, j)$, within a staggered ground-state configuration leads to a staggered ground-state configuration, when there are no intervening particles between rungs j and $j+r$.

To write (7.6.18) as a sum of minors, we first expand it as

$$\begin{aligned} 2\,\langle c^\dagger_{i,j}c_{i,j+r}\rangle = \langle c^\dagger_j c_{j+r}\rangle - \\ \langle c^\dagger_j n_{j+1}c_{j+r}\rangle - \cdots - \langle c^\dagger_j n_{j+r-1}c_{j+r}\rangle + \\ \langle c^\dagger_j n_{j+1}n_{j+2}c_{j+r}\rangle + \cdots + \langle c^\dagger_j n_{j+r-2}n_{j+r-1}c_{j+r}\rangle - \\ \langle c^\dagger_j n_{j+1}n_{j+2}n_{j+3}c_{j+r}\rangle - \cdots - \langle c^\dagger_j n_{j+r-3}n_{j+r-2}n_{j+r-1}c_{j+r}\rangle + \cdots + \\ (-1)^{r-1}\,\langle c^\dagger_j n_{j+1}\cdots n_{j+r-1}c_{j+r}\rangle\,, \end{aligned} \tag{7.6.19}$$

and note that all the terms in (7.6.19) can be written as minors of the matrix

$$\mathbf{G}(r+1) = \bar{n}\begin{bmatrix} 1 & \mathsf{g}(1) & \mathsf{g}(2) & \cdots & \mathsf{g}(r+1) \\ \mathsf{g}(1) & 1 & \mathsf{g}(1) & \cdots & \mathsf{g}(r) \\ \mathsf{g}(2) & \mathsf{g}(1) & 1 & \cdots & \mathsf{g}(r-1) \\ \vdots & \vdots & \vdots & \ddots & \vdots \\ \mathsf{g}(r+1) & \mathsf{g}(r) & \mathsf{g}(r-1) & \cdots & 1 \end{bmatrix}. \tag{7.6.20}$$

Here $\mathsf{g}(r) = g(r)$ are the values of the reduced two-point function defined in (2.3.15).

Using the relation

$$\langle c_j^\dagger n_{j+j_1-1}\cdots n_{j+j_{m-1}-1}c_{j+(r+1)-1}\rangle = (-1)^{m-1}\mathsf{G}^{1\,j_1\cdots j_{m-1}}_{j_1\cdots j_{m-1}r+1} \tag{7.6.21}$$

between $\langle c_j^\dagger n_{j+j_1-1}\cdots n_{j+j_{m-1}-1}c_{j+(r+1)-1}\rangle$ and $\mathsf{G}^{1\,j_1\cdots j_{m-1}}_{j_1\cdots j_{m-1}r+1}$, we write (7.6.19) as

$$2\,\langle c_{i,j}^\dagger c_{i,j+r}\rangle = \mathsf{G}^{1}_{r+1} + \mathsf{G}^{12}_{2(r+1)} + \cdots + \mathsf{G}^{1r}_{r(r+1)} + \mathsf{G}^{123}_{23(r+1)} + \cdots + \mathsf{G}^{1(r-1)r}_{(r-1)r(r+1)} + \cdots + \mathsf{G}^{12\cdots r}_{2\cdots r(r+1)}. \tag{7.6.22}$$

With (7.6.22), we can compute numerically the values of these two degenerate FL correlations, for separations up to $r = 20$, using an algorithm modified from the one described in Section 7.5.6, by limiting the sum to $p = 0$ intervening particles:

1. For each order $1 \le m \le r$, we run over all possible indices $1 < j_1 < j_2 < \cdots < j_{m-1} < r+1$, and construct the minors

$$\mathsf{G}^{1\,j_1\,j_2\cdots j_{m-1}}_{j_1\,j_2\cdots j_{m-1}r+1}. \tag{7.6.23}$$

2. The contribution of $\mathsf{G}^{1\,j_1\,j_2\cdots j_{m-1}}_{j_1\,j_2\cdots j_{m-1}r+1}$ to $\langle c_{i,j}^\dagger c_{i,j+r}\rangle$ is

$$\mathsf{G}^{1\,j_1\,j_2\cdots j_{m-1}}_{j_1\,j_2\cdots j_{m-1}r+1}. \tag{7.6.24}$$

From Figure 7.60, we find that the FL correlations decay exponentially with separation r. We understand this asymptotic behaviour using a constrained probabilities argument similar to that used in Section 7.5.8. To do this, let us write the FL correlation $\langle c_{i,j}^\dagger c_{i,j+r}\rangle$ as

$$\langle c_{i,j}^\dagger c_{i,j+r}\rangle = \sum_{f,i}\Psi_f^*\Psi_i = \sum_s\sum_{f_s,i_s}\Psi_{f_s}^*\Psi_{i_s}, \tag{7.6.25}$$

where i and f are all initial and final configurations making nonzero contributions to $\langle c_{i,j}^\dagger c_{i,j+r}\rangle$. We can regroup the terms in this sum over initial and final configurations, by

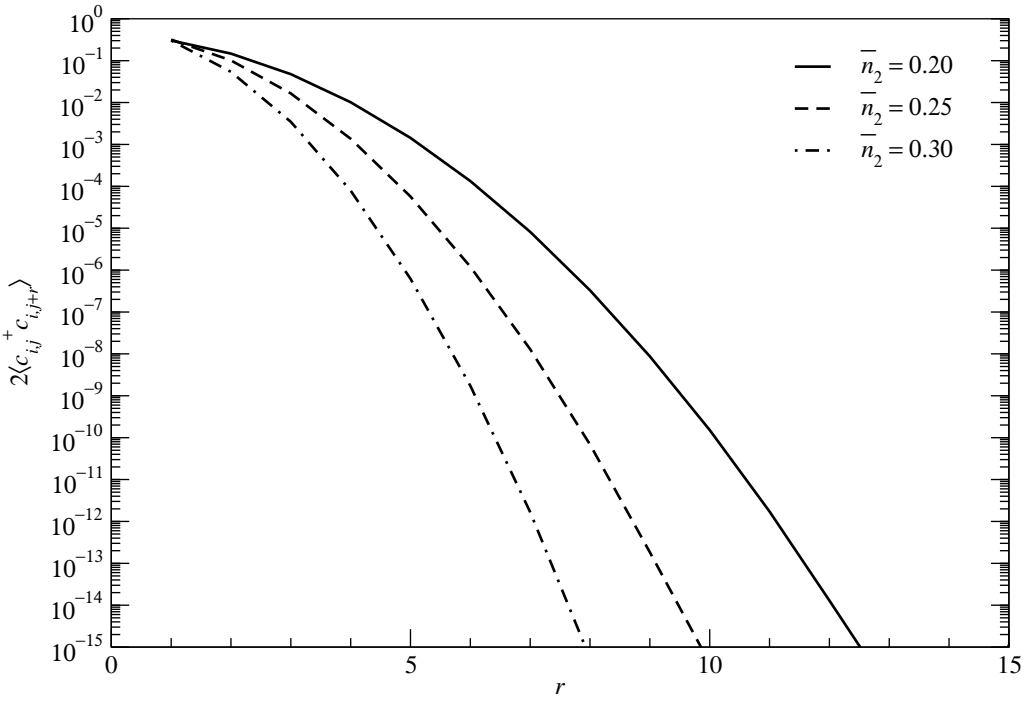

Figure 7.60: The infinite-ladder FL correlations $\langle c^{\dagger}_{i,j} c_{i,j+r} \rangle$, $i = 1, 2$, as a function of the separation $1 \leq r \leq 15$ for ladder filling fractions $\bar{n}_2 = 0.20$, 0.25 and 0.30, in the limit $t_\perp / t_\parallel = 0$, $t' = 0$.

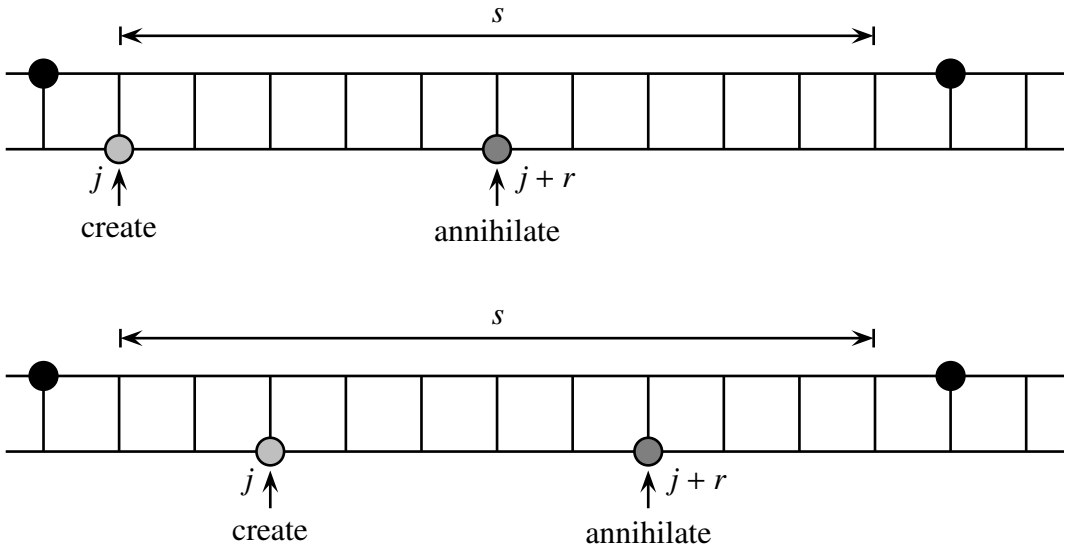

Figure 7.61: Two configurations containing a gap of length s. These two configurations make nonzero contributions to the FL correlation $\langle c^{\dagger}_{1,j} c_{1,j+r} \rangle$.

summing over each group of initial and final configurations i_s and f_s where sites j and $j+r$ reside within a gap of width s, as shown in Figure 7.61.

For a fixed gap s, there are of course a large number of initial and final configurations i_s and f_s. We can think of these configurations as the direct product of the configurations outside the gap, and the configurations (of a single spinless fermion) within the gap. The amplitudes Ψ_{i_s} and Ψ_{f_s} depends on both the configurations inside and outside the gap, but we can write these amplitudes as products $\Psi'_{i'_s}\psi(s'_i)$ and $\Psi'_{f'_s}\psi(s'_f)$. Here $\Psi'_{i'_s} = \Psi'_{f'_s}$ are the 'amplitudes' of the initial and final configurations $i'_s = f'_s$ with no spinless fermions in the gap. The 'amplitude' $\psi(s')$ of a single spinless fermion with coordinate s' in the fixed gap is the only thing that changes between the initial and final states. Therefore, we can write the fixed-gap sum of product of initial- and final-state amplitudes as

$$\sum_{f_s,i_s} \Psi^*_{f_s}\Psi_{i_s} = \sum_{s'_i,s'_f} \psi^*(s'_f)\psi(s'_i) \sum_{i'_s=f'_s} \Psi'^*_{f'_s}\Psi'_{i'_s} = \sum_{s'_i,s'_f} \psi^*(s'_f)\psi(s'_i) \sum_{i'_s} |\Psi'_{i'_s}|^2. \tag{7.6.26}$$

Here, we find that

$$P(s) = \sum_{i'_s} |\Psi'_{i'_s}|^2 \tag{7.6.27}$$

is the probability of finding a gap of width s in the ground state. With this interpretation, we can therefore write the FL correlation as

$$\langle c^\dagger_{i,j} c_{i,j+r}\rangle = \sum_s P(s) \sum_{s'_i,s'_f} \psi^*(s'_f)\psi(s'_i). \tag{7.6.28}$$

To calculate $\langle c^\dagger_{i,j} c_{i,j+r}\rangle$ exactly, we would need to know what $\psi^*(s'_f)\psi(s'_i)$ is. However, our goal is to obtain approximately the asymptotic behaviour of $\langle c^\dagger_{i,j} c_{i,j+r}\rangle$, so it suffice to note that the sum $\sum_{s'_i,s'_f} \psi^*(s'_f)\psi(s'_i)$ is generically an $O(1)$ number, which determines the fine structures (for example, even-odd alternations, or short wavelength oscillations) of the FL correlations. Therefore, the asymptotic behaviour of $\langle c^\dagger_{i,j} c_{i,j+r}\rangle$ can be obtained

from the simplified sum

$$\langle c^\dagger_{i,j} c_{i,j+r} \rangle \approx \sum_s P(s), \tag{7.6.29}$$

Now, the probability of finding a gap of width s in the ground state is also the probability of finding a contiguous cluster of s sites being completely empty in a chain of noninteracting spinless fermions. This tells us that $P(s) = w_0$ is just the zero-particle weight of the density matrix of a cluster of s sites cut out from a chain of noninteracting spinless fermions. We know from Chapters 2 and 3 that this zero-particle cluster density-matrix weight

$$w_0 = \mathscr{Q}^{-1} = \det(\mathbb{1} - G_C(s)) \tag{7.6.30}$$

is also the normalization constant of the s-site cluster density matrix.

For very large clusters, $s \gg 1$, the cluster Green-function matrix $G_C(s)$ has approximately $(1 - \bar{n}_1)s$ eigenvalues which are almost zero, and $\bar{n}_1 s$ eigenvalues which are almost one. The determinant of $\mathbb{1} - G_C(s)$ is thus essentially determined by the approximately $\bar{n}_1 s$ eigenvalues which are almost one. We made use of this fact in Section 3.5.2 to calculate the asymptotic form of $P(s) = w_0 = \mathscr{Q}^{-1}$, which we find to be

$$P(s) \approx \exp\left\{-s \int_0^{\bar{n}_1} f(1 - \bar{n}_1, x)\, dx\right\}, \tag{7.6.31}$$

where $f(\bar{n}_1, x)$ is the universaling scaling function that appears in (3.5.6).

For a gapped configuration to contribute to $\langle c^\dagger_{i,j} c_{i,j+r} \rangle$, the gap width s must be at least equal to the separation r. With the form in (7.6.31), the sum $\sum_{s=r}^{\infty} P(s)$ is a geometric series, and can thus be very simply evaluated as

$$\langle c^\dagger_{i,j} c_{i,j+r} \rangle \approx \frac{\exp\left(-r \int_0^{\bar{n}_1} f(1 - \bar{n}_1, x)\, dx\right)}{1 - \exp\left(-\int_0^{\bar{n}_1} f(1 - \bar{n}_1, x)\, dx\right)}. \tag{7.6.32}$$

This is an exponential decay in the separation r, which is what we observed numerically in Figure 7.60. We note further that as $\bar{n}_1 \to 1$ (or equivalently, $\bar{n}_2 \to \frac{1}{2}$), the FL

correlations decay fastest exponentially, whereas as $\bar{n}_1 \to 0$ (equivalent to $\bar{n}_2 \to 0$), the exponential decay is the slowest. We expect these behaviours physically, because it is more likely to find a long empty cluster when the filling fraction is low, and less likely to find a long empty cluster when the ladder is closed to half-filled.

7.6.3 Charge-Density-Wave Correlations

The four simplest CDW correlations at separation r are, taking into account their degeneracies in the staggered ground states,

$$\begin{aligned} \langle c^\dagger_{1,j} c_{1,j} c^\dagger_{1,j+r} c_{1,j+r} \rangle &= \langle c^\dagger_{2,j} c_{2,j} c^\dagger_{2,j+r} c_{2,j+r} \rangle \,, \\ \langle c^\dagger_{1,j} c_{1,j} c^\dagger_{2,j+r} c_{2,j+r} \rangle &= \langle c^\dagger_{1,j} c_{1,j} c^\dagger_{2,j+r} c_{2,j+r} \rangle \,. \end{aligned} \tag{7.6.33}$$

We can relate these to the CDW correlations in a chain of noninteracting spinless fermions, by noting that the configurations making nonzero contributions to $\langle n_{1,j} n_{1,j+r} \rangle$ are those which map to noninteracting spinless fermion configurations in which the sites j and $j + r$ are occupied, with an odd number of intervening particles between them, as shown in Figure 7.62.

Similarly, configurations making nonzero contributions to $\langle n_{1,j} n_{2,j+r} \rangle$ are those which map to noninteracting spinless fermions in which the sites j and $j + r$ are occupied, with an even number of intervening particles between them. If we add $\langle n_{1,j} n_{1,j+r} \rangle$ and $\langle n_{1,j} n_{2,j+r} \rangle$, we would pick up configurations which map to noninteracting spinless fermions in which the sites j and $j + r$ are occupied, with *any* number of intervening particles, i.e.

$$\langle n_{1,j} n_{1,j+r} \rangle + \langle n_{1,j} n_{2,j+r} \rangle = \tfrac{1}{2} \langle n_j n_{j+r} \rangle \equiv \tfrac{1}{2} \Sigma_+(r). \tag{7.6.34}$$

By the same argument, we also have

$$\langle n_{2,j} n_{1,j+r} \rangle + \langle n_{2,j} n_{2,j+r} \rangle = \tfrac{1}{2} \langle n_j n_{j+r} \rangle = \tfrac{1}{2} \Sigma_+(r). \tag{7.6.35}$$

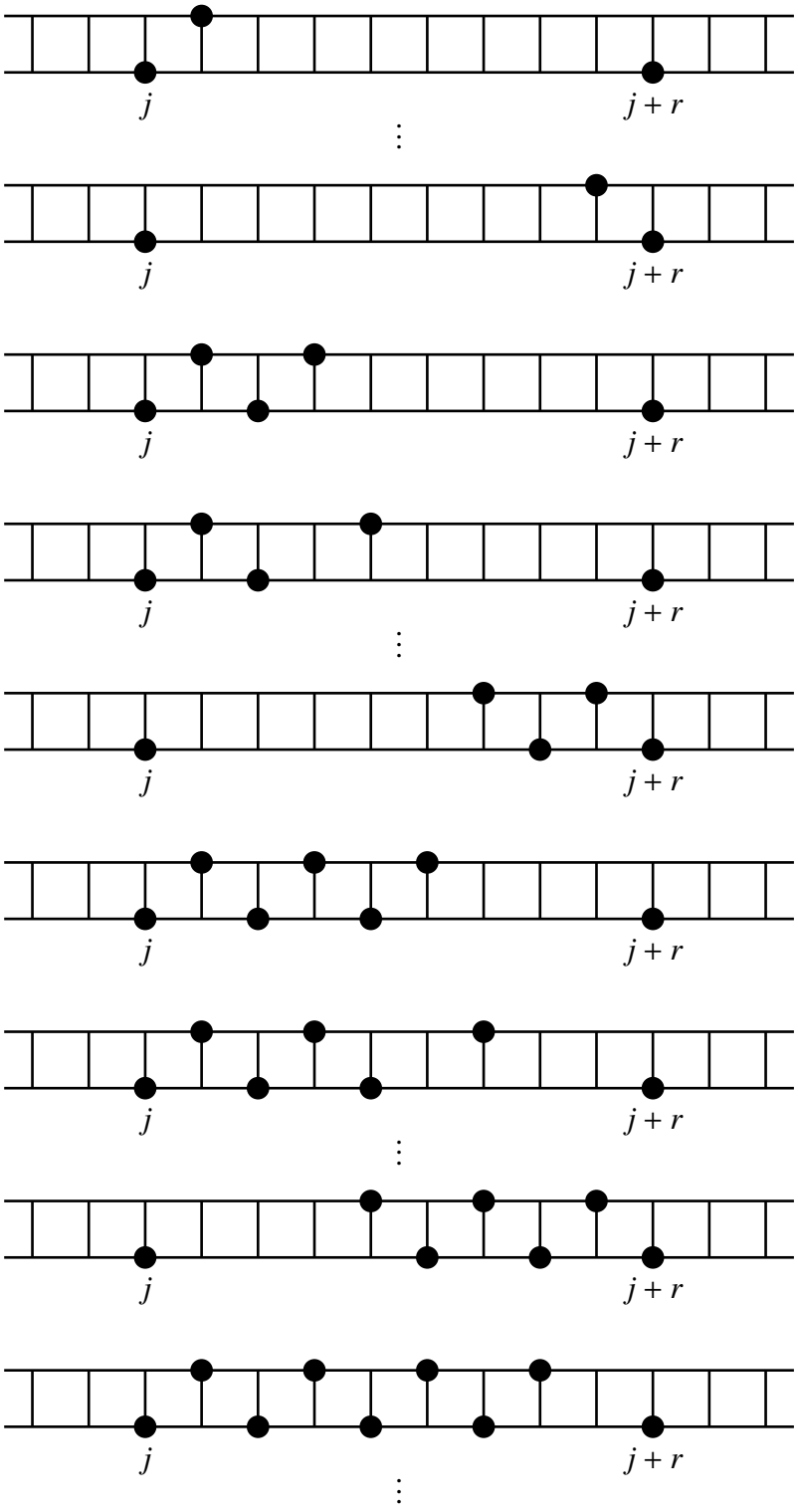

Figure 7.62: Staggered ground-state configurations making nonzero contributions to $\langle c^{\dagger}_{1,j} c_{1,j} c^{\dagger}_{1,j+r} c_{1,j+r} \rangle$.

More interestingly, if we subtract the correlations $\langle n_{1,j} n_{1,j+r} \rangle$ and $\langle n_{1,j} n_{2,j+r} \rangle$, or subtract the correlations $\langle n_{2,j} n_{2,j+r} \rangle$ and $\langle n_{2,j} n_{1,j+r} \rangle$, we would be subtracting the summed contribution of an even number of intervening particles to the noninteracting spinless fermion density-density correlation from the summed contribution of an odd number of intervening particles to the noninteracting spinless fermion density-density correlation. These correlations

$$\langle n_{1,j} n_{1,j+r} \rangle - \langle n_{1,j} n_{2,j+r} \rangle = \langle n_{2,j} n_{2,j+r} \rangle - \langle n_{2,j} n_{1,j+r} \rangle \equiv \tfrac{1}{2} \Sigma_-(r) \tag{7.6.36}$$

are also nonzero.

Ideally, we want to define a set of ladder fermion operators

$$c^\dagger_{a,j} = \cos\theta \, c^\dagger_{1,j} + \sin\theta \, c^\dagger_{2,j}, \quad c^\dagger_{b,j} = -\sin\theta \, c^\dagger_{1,j} + \cos\theta \, c^\dagger_{2,j}, \tag{7.6.37}$$

so that

$$\langle n_{a,j} n_{a,j+r} \rangle, \langle n_{b,j} n_{b,j+r} \rangle > 0; \quad \langle n_{a,j} n_{b,j+r} \rangle, \langle n_{b,j} n_{a,j+r} \rangle = 0, \tag{7.6.38}$$

i.e. $n_{a,j}$ and $n_{b,j}$ can be construed as independent density fluctuations. However, we realized that we can define no such ladder fermion operators for which the cross correlations $\langle n_{a,j} n_{b,j+r} \rangle$ and $\langle n_{b,j} n_{a,j+r} \rangle$ vanish.

Instead, the independent density fluctuations come from the linear combinations

$$n_{\pm,j} = n_{1,j} \pm n_{2,j} \tag{7.6.39}$$

of the densities $n_{1,j}$ and $n_{2,j}$. The correlation associated with $n_{+,j}$ is

$$\langle n_{+,j} n_{+,j+r} \rangle = \langle n_j n_{j+r} \rangle = \Sigma_+(r) = \bar{n}_1^2 [1 - g^2(r)], \tag{7.6.40}$$

with $\bar{n}_1$ being the chain filling fraction obtained from mapping a ladder at ladder filling fraction $\bar{n}_2$ to a chain, and $g(r)$ being the reduced two-point function defined in (2.3.15),

whereas that associated with $n_{-,j}$ is

$$\langle n_{-,j} n_{-,j+r} \rangle = 2 \Big(\langle n_{1,j} n_{1,j+r} \rangle - \langle n_{1,j} n_{2,j+r} \rangle \Big) = \Sigma_{-}(r). \tag{7.6.41}$$

The cross correlations

$$\langle n_{+,j} n_{-,j+r} \rangle = \langle n_{-,j} n_{+,j+r} \rangle \tag{7.6.42}$$

vanish identically, by virtue of (7.6.34), (7.6.35) and (7.6.36).

The forms for the independent densities $n_{+,j}$ and $n_{-,j}$ arise naturally if we think of mapping the spinless extended Hubbard ladder to a one-dimensional *t*-*J* chain of *spinful* fermions, where a spinless fermion on leg $i = 1$ gets mapped to a spin-$\downarrow$ fermion and a spinless fermion on leg $i = 2$ gets mapped to a spin-$\uparrow$ fermion. The infinite nearest-neighbor repulsion acting between spinless fermions then give rises to an infinite on-site repulsion, which prevents occupation of a chain site a spin-$\uparrow$ and spin-$\downarrow$ fermions, by as well as an infinite antiferromagnetic exchange coupling between the spins of nearest-neighbor spinful fermions. For a chain of spinful fermions, the spin-dependent densities at site j are

$$n_{j,\uparrow} = c^{\dagger}_{j,\uparrow} c_{j,\uparrow}, \quad n_{j,\downarrow} = c^{\dagger}_{j,\downarrow} c_{j,\downarrow}, \tag{7.6.43}$$

for the spin-up and spin-down fermions respectively. We see then that the densities $n_{+,j}$ and $n_{-,j}$ we constructed in (7.6.39) are mapped to the total and spin-excess densities

$$n_j = n_{j,\uparrow} + n_{j,\downarrow}, \quad \delta n_j = n_{j,\uparrow} - n_{j,\downarrow} \tag{7.6.44}$$

at site j respectively.

For a chain of noninteracting spinful fermions in the absence of any external magnetic field, the ground-state wave function is a product of the spin-up and spin-down ground-state wave functions, and so the spin-dependent CDW correlations are

$$\langle n_{j,\uparrow} n_{j+r,\uparrow} \rangle = \langle n_{j,\downarrow} n_{j+r,\downarrow} \rangle = \bar{n}^2 [1 - g^2(r)], \tag{7.6.45}$$

where $\bar{n}$ is the average number of spin-up or spin-down fermions per site, and the reduced two-point function $g(r)$ defined in (2.3.15) carries the dependence on separation r. We also have, as a result of the product nature of the ground-state wave function,

$$\begin{aligned} \langle n_{j,\uparrow} n_{j+r,\downarrow} \rangle &= \langle n_{j,\uparrow} \rangle \langle n_{j+r,\downarrow} \rangle = \bar{n}^2, \\ \langle n_{j,\downarrow} n_{j+r,\uparrow} \rangle &= \langle n_{j,\downarrow} \rangle \langle n_{j+r,\uparrow} \rangle = \bar{n}^2. \end{aligned} \tag{7.6.46}$$

The total-density-total-density correlation is therefore

$$\langle n_j n_{j+r} \rangle = \langle n_{j,\uparrow} n_{j+r,\uparrow} \rangle + \langle n_{j,\uparrow} n_{j+r,\downarrow} \rangle + \langle n_{j,\downarrow} n_{j+r,\uparrow} \rangle + \langle n_{j,\downarrow} n_{j+r,\downarrow} \rangle = 4\bar{n}^2 - 2\bar{n}^2 g^2(r), \tag{7.6.47}$$

while the spin-excess-density-spin-excess-density correlation is

$$\langle \delta n_j \delta n_{j+r} \rangle = \langle n_{j,\uparrow} n_{j+r,\uparrow} \rangle - \langle n_{j,\uparrow} n_{j+r,\downarrow} \rangle - \langle n_{j,\downarrow} n_{j+r,\uparrow} \rangle + \langle n_{j,\downarrow} n_{j+r,\downarrow} \rangle = -2\bar{n}^2 g^2(r). \tag{7.6.48}$$

As we can see, the total-density-total-density correlation asymptotes to a constant, while the spin-excess-density-spin-excess-density correlation asymptotes to zero, as $r \to \infty$, since $g(r) \to 0$ as a power law as $r \to \infty$. To look at the dependence on r specifically, one typically calculates the subtracted total-density-total-density correlation

$$\langle n_j n_{j+r} \rangle - \langle n_j \rangle \langle n_{j+r} \rangle . \tag{7.6.49}$$

For a chain of spinful fermions with $\bar{n}$ spin-up fermion per site and $\bar{n}$ spin-down fermion per site,

$$\langle n_j \rangle = \langle n_{j+r} \rangle = 2\bar{n}. \tag{7.6.50}$$

Therefore, we see that the subtracted total-density-total-density correlation

$$\langle n_j n_{j+r} \rangle - \langle n_j \rangle \langle n_{j+r} \rangle = 4\bar{n}^2 - 2\bar{n}^2 g^2(r) - 4\bar{n}^2 = -2\bar{n}^2 g^2(r), \tag{7.6.51}$$

does indeed pick out the r-dependent piece in the total-density-total-density correlation. We can also define the subtracted spin-excess-density-spin-excess-density correlation

$$\langle \delta n_j \delta n_{j+r} \rangle - \langle \delta n_j \rangle \langle \delta n_{j+r} \rangle , \tag{7.6.52}$$

but because $\langle \delta n_j \rangle = 0 = \langle \delta n_{j+r} \rangle$, this is the same as the unsubtracted spin-excess-density-spin-excess-density correlation.

For our ladder system of spinless fermions with infinite nearest-neighbor repulsion, we will define the subtracted CDW correlations to be

$$\begin{gathered} \langle n_{+,j} n_{+,j+r} \rangle - \langle n_{+,j} \rangle \langle n_{+,j+r} \rangle , \\ \langle n_{-,j} n_{-,j+r} \rangle - \langle n_{-,j} \rangle \langle n_{-,j+r} \rangle \end{gathered} \tag{7.6.53}$$

analogously. For the subtracted 'symmetric' CDW correlation, we find that the expectations $\langle n_{+,j} \rangle = \langle n_{+,j+r} \rangle$ are simply

$$\langle n_{1,j} + n_{2,j} \rangle = \langle n_{1,j} \rangle + \langle n_{2,j} \rangle = 2\bar{n}_2 = \bar{n}_1, \tag{7.6.54}$$

and thus the product of densities $\langle n_{+,j} \rangle \langle n_{+,j+r} \rangle$ is

$$\langle n_{1,j} + n_{2,j} \rangle \langle n_{1,j+r} + n_{2,j+r} \rangle = \bar{n}_1^2. \tag{7.6.55}$$

Therefore, using (7.6.40) and (7.6.55), we find the subtracted 'symmetric' CDW correlation becoming

$$\langle n_{+,j} n_{+,j+r} \rangle - \langle n_{+,j} \rangle \langle n_{+,j+r} \rangle = \bar{n}_1^2 [1 - g^2(r)] - \bar{n}_1^2 = -\bar{n}_1^2 g^2(r). \tag{7.6.56}$$

From the form of $g(r)$ in (2.3.15), we know therefore that the subtracted 'symmetric' CDW correlation decays as a power law, r^{-2}, in the separation r.

For the subtracted 'antisymmetric' CDW correlation, we find vanishing expectations of the 'antisymmetric' densities,

$$\langle n_{-,j} \rangle = \langle n_{1,j} - n_{2,j} \rangle = \langle n_{1,j} \rangle - \langle n_{2,j} \rangle = 0. \tag{7.6.57}$$

Therefore, the subtracted 'antisymmetric' CDW correlation is just equal to

$$2 \Big(\langle n_{1,j} n_{1,j+r} \rangle - \langle n_{1,j} n_{2,j+r} \rangle \Big) = \Sigma_-(r). \tag{7.6.58}$$

Computing this expectation numerically, we find that at all ladder filling fractions $\bar{n}_2$, $\Sigma_-(\bar{n}_2, r)$ oscillates about a zero average, with a decaying amplitude, and a filling-fraction-dependent wavelength, as shown in Figure 7.63. We perform nonlinear curve fitting of $\Sigma_-(\bar{n}_2, r)$ to the asymptotic form

$$Ar^{-\alpha}\cos(kr+\phi), \tag{7.6.59}$$

and the fitted parameters are shown in Table 7.12.

Table 7.12: Fitted parameters for a nonlinear curve fit of the infinite-ladder subtracted 'antisymmetric' CDW correlation $\langle n_{-,j}n_{-,j+r}\rangle - \langle n_{-,j}\rangle\langle n_{-,j+r}\rangle$, in the limit $t_\perp \ll t_\parallel$, $t' = 0$, to an asymptotic form $Ar^{-\alpha}\cos(kr+\phi)$, for ladder filling fractions $0.05 \leq \bar{n}_2 \leq 0.45$, for $r \geq 4$.

$\bar{n}_2$	A	α	k	ϕ
0.05	0.00878122	$< 1\times10^{-6}$	0.248802	−2.04297
0.10	0.0847118	0.563406	0.600169	−2.71939
0.15	0.138007	0.509542	0.929224	−2.91193
0.20	0.200888	0.483594	1.2447	−2.94563
0.25	0.297616	0.505262	1.55867	−2.95943
0.30	0.40255	0.508705	1.87704	−3.00759
0.35	0.502226	0.486091	2.1919	−3.01682
0.40	0.666241	0.483845	2.50191	−2.96897
0.45	1.00604	0.493766	2.81887	−2.96099

As expected from what we have learnt in Section 7.5.6, the effective wave vectors obtained from the nonlinear curve fit are close to $k = 2\pi\bar{n}_2 = 2k_F$, as shown in Figure 7.64. Figure 7.65 shows the fitted amplitude A as a function of the ladder filling fraction

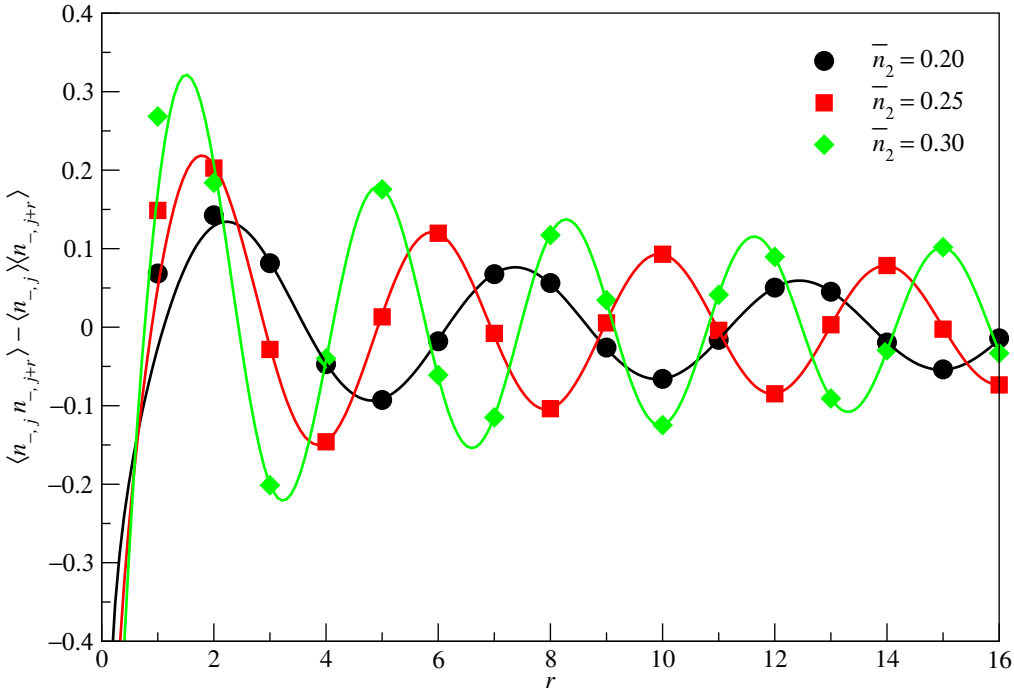

Figure 7.63: Plot of the infinite-ladder subtracted 'antisymmetric' CDW correlation $\langle n_{-,j} n_{-,j+r}\rangle - \langle n_{-,j}\rangle\langle n_{-,j+r}\rangle = \Sigma_-(\bar{n}_2, r)$ as a function of separation $1 \leq r \leq 16$ for ladder filling fractions $\bar{n}_2 = 0.20$ (black circles), 0.25 (red squares), and 0.30 (green diamonds), in the limit $t_\perp/t_\parallel = 0$, $t' = 0$. These are fitted to the form $Ar^{-\alpha}\cos(kr + \phi)$, to obtain $A = 0.200888$, $\alpha = 0.483594$, $k = 1.24470$, $\phi = -2.94563$ for $\bar{n}_2 = 0.20$ (black curve), $A = 0.297616$, $\alpha = 0.505262$, $k = 1.55867$, $\phi = -2.95943$ for $\bar{n}_2 = 0.25$ (red curve), and $A = 0.402550$, $\alpha = 0.508705$, $k = 1.87704$ and $\phi = -3.00759$ for $\bar{n}_2 = 0.30$ (green curve).

$\bar{n}_2$. As we can see, A appears to increase monotonically with $\bar{n}_2$. We find from the nonlinear curve fits that A becomes slightly larger than one near $\bar{n}_2 = \frac{1}{2}$. Again, this is a consequence of us fitting to an asymptotic form that is valid only at large separations, so we should not read too much into it. What is more interesting is the behaviour of the fitted correlation exponent α as a function of the ladder filling fraction $\bar{n}_2$: instead of a systematic variation in $\bar{n}_2$, α exhibits small fluctuations about $\frac{1}{2}$ as $\bar{n}_2$ varies. This suggests that we may in fact have a universal correlation exponent of $\alpha = \frac{1}{2}$ for the subtracted 'antisymmetric' CDW correlation.

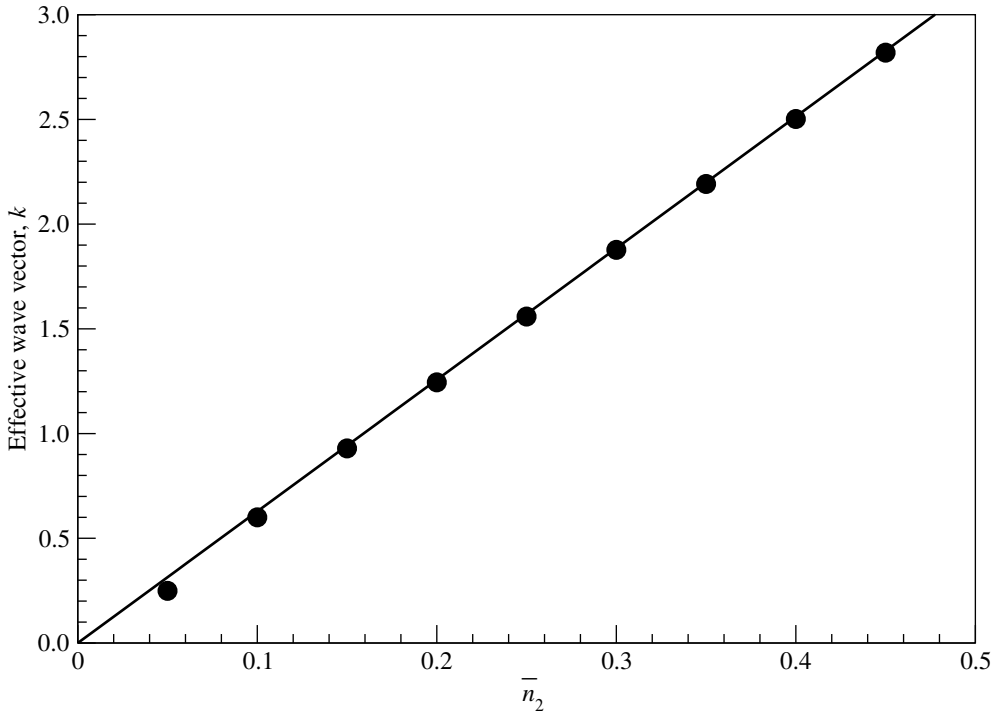

Figure 7.64: The effective wave vector k (filled circles) of the infinite-ladder subtracted 'antisymmetric' CDW correlation $\langle n_{-,j} n_{-,j+r} \rangle - \langle n_{-,j} \rangle \langle n_{-,j+r} \rangle = \Sigma_-(\bar{n}_2, r)$, in the limit $t_\perp / t_\parallel = 0$, $t' = 0$, as a function of the ladder filling fraction $\bar{n}_2$. Also shown as the solid line is the wave vector $k = 2\pi\bar{n}_2 = 2k_F$. The data points plotted here are from the four-parameter, (A, α, k, ϕ), fit to (7.6.59), shown in Table 7.12.

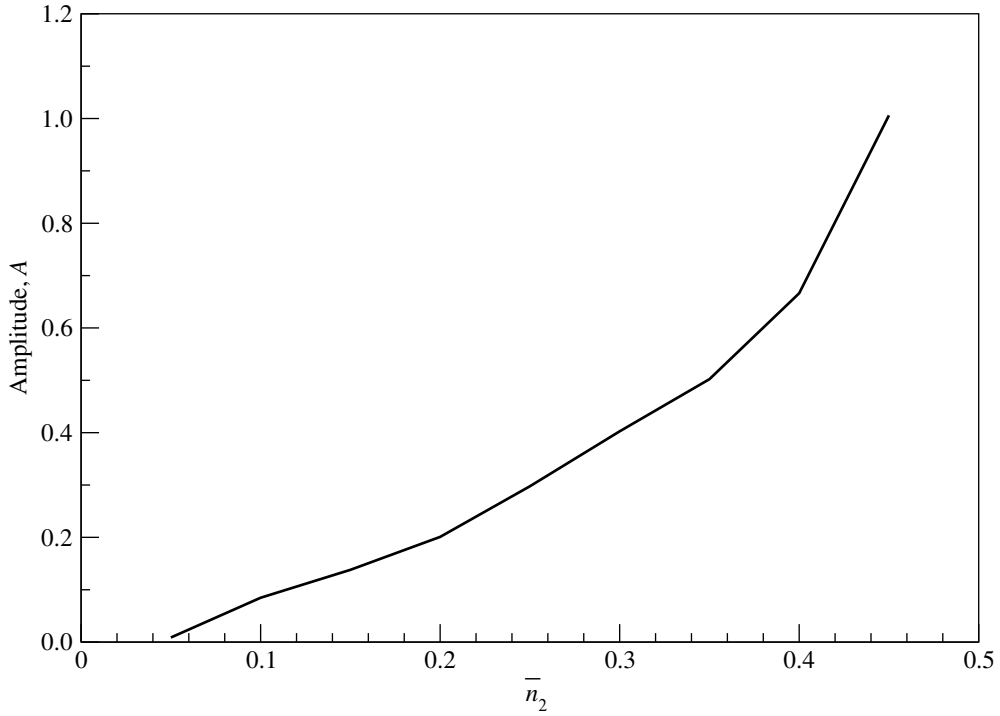

Figure 7.65: The fitted amplitude A of the infinite-ladder subtracted 'antisymmetric' CDW correlation $\langle n_{-,j} n_{-,j+r} \rangle - \langle n_{-,j} \rangle \langle n_{-,j+r} \rangle = \Sigma_-(\bar{n}_2, r)$, in the limit $t_\perp / t_\parallel = 0$, $t' = 0$, as a function of the ladder filling fraction $\bar{n}_2$. The data points plotted here are from the four-parameter, (A, α, k, ϕ), fit to (7.6.59), shown in Table 7.12.

As with the SC and CDW correlations in the strong correlated hopping limit, let us see if we can improve our confidence in the nonlinear curve fits by enforcing a strict constraint on $k = 2\pi\bar{n}_2$, and looser constraints on α and ϕ. To do this, let us assume that the leading-order correction is a power law, and fit the numerical correlations to

$$Ar^{-\alpha}\cos(2\pi\bar{n}_2 + \phi) + Br^{-\alpha'}. \tag{7.6.60}$$

We then performed five series of curve fits, by first imposing the constraints $\alpha = \frac{1}{2}$, $\phi = -\pi$, $\alpha' = 2$, and then relaxing the constraints sequentially. The fitted parameters are shown in Table 7.13.

From Table 7.13, and also the plot of the fitted amplitude A as a function of the ladder filling fraction $\bar{n}_2$ in Figure 7.66, we see that the fitted amplitude A shows good agreement across the five series of fit. We are therefore confident that we have extracted a physically meaningful quantity from the numerical correlations, apart from a small glitch at $\bar{n}_2 = 0.45$. In fact, we realize that this glitch arises when we allow both the leading-order correction amplitude B and the subdominant correlation exponent α' to vary. Frequently, we would find that when B and α' are both allowed to vary, these two parameters frequently run away to absurd values as the nonlinear curve fitting algorithm iterates. In the course of performing these five series of nonlinear curve fits, we also note visually that the qualities of the fits are sometimes very good, and always acceptable. This gives us confidence in asserting that the leading correlation exponent $\alpha = \frac{1}{2}$, and the phase shift $\phi = -\pi$, might actually be universal and independent of the filling fraction $\bar{n}_2$.

Table 7.13: Fitted parameters for five series of nonlinear curve fits of the infinite-ladder subtracted 'antisymmetric' CDW correlation $\langle n_{-,j} n_{-,j+r} \rangle - \langle n_{-,j} \rangle \langle n_{-,j+r} \rangle$, in the limit $t_\perp \ll t_\parallel$, $t' = 0$, to the asymptotic form $Ar^{-\alpha} \cos(2\pi\bar{n}_2 r + \phi) + Br^{-\alpha'}$, for ladder filling fractions $0.05 \leq \bar{n}_2 \leq 0.45$ and $r \geq 4$. We start with the constraints $\alpha = \frac{1}{2}$, $\phi = -\pi$, $\alpha' = 2$, and then relax the constraints, one at a time. When the parameter value is quoted as '-', that means that the iterations ran away for that parameter.

$\bar{n}_2$	A	α	$-\phi$	B	α'	visual
0.05	0.0218692	$\frac{1}{2}$	π	0.132019	2	very poor
	0.0235271	$\frac{1}{2}$	2.90789	0.0839567	2	good
	0.0236741	$\frac{1}{2}$	2.91084	0.0933503	2.06696	good
	0.0217220	0.463601	2.90483	0.0838472	2	good
	0.0087133	0.110763	2.75626	0.011163	0.785381	very good
0.10	0.0735304	$\frac{1}{2}$	π	0.0128967	2	not good
	0.0737714	$\frac{1}{2}$	2.98451	0.014284	2	not good
	0.0728509	$\frac{1}{2}$	3.00277	-	-	not good
	0.081333	0.543915	2.98865	−0.00213098	2	not good
	0.0806615	0.540436	2.98821	-	-	not good
0.15	0.132786	$\frac{1}{2}$	π	−0.121111	2	not good
	0.133663	$\frac{1}{2}$	3.04314	−0.061379	2	good
	0.134575	$\frac{1}{2}$	3.04859	−0.617283	3.43882	good
	0.13031	0.48775	3.04375	−0.0593088	2	good
	0.139789	0.517169	3.04905	−1.26935	3.87508	good

Table 7.13: (continued)

$\bar{n}_2$	A	α	$-\phi$	B	α'	visual
0.20	0.207111	$\frac{1}{2}$	π	−0.0964138	2	good
	0.208439	$\frac{1}{2}$	3.05502	−0.0475108	2	very good
	0.208243	$\frac{1}{2}$	3.07201	-	-	very good
	0.208292	0.499672	3.05502	−0.0476698	2	very good
	0.204522	0.491517	3.07212	-	-	very good
0.25	0.294995	$\frac{1}{2}$	π	0.0653478	2	good
	0.294644	$\frac{1}{2}$	3.07715	0.030738	2	very good
	0.294796	$\frac{1}{2}$	3.07732	0.0738726	2.54262	very good
	0.298393	0.506175	3.07735	0.0350594	2	very good
	0.302204	0.511603	3.07793	0.303116	3.28507	very good
0.30	0.389652	$\frac{1}{2}$	π	0.15048	2	good
	0.392201	$\frac{1}{2}$	3.07934	0.0727567	2	very good
	0.394401	$\frac{1}{2}$	3.09093	-	-	very good
	0.377442	0.481641	3.08081	0.0755939	2	very good
	0.395265	0.501039	3.09092	-	-	very good

Table 7.13: (continued)

$\bar{n}_2$	A	α	$-\phi$	B	α'	visual
0.35	0.522068	$\frac{1}{2}$	π	0.0336553	2	good
	0.520903	$\frac{1}{2}$	3.08163	0.0112932	2	very good
	0.518233	$\frac{1}{2}$	3.08475	-	-	very good
	0.536647	0.514249	3.08275	−0.00445497	2	very good
	0.504266	0.487687	3.08494	-	-	very good
0.40	0.683311	$\frac{1}{2}$	π	−0.193678	2	good
	0.685539	$\frac{1}{2}$	3.07797	−0.105146	2	very good
	0.691186	$\frac{1}{2}$	3.08583	-	-	very good
	0.650738	0.474146	3.07995	−0.0854691	2	very good
	0.683531	0.494772	3.08564	-	-	very good
0.45	1.00000	$\frac{1}{2}$	π	−0.39928	2	not good
	1.01739	$\frac{1}{2}$	3.02851	−0.104555	2	good
	1.01105	$\frac{1}{2}$	3.03695	-	-	good
	1.25173	0.592644	3.02756	0.0214243	2	good
	1.26143	0.595976	3.02723	0.285858	3.42786	good

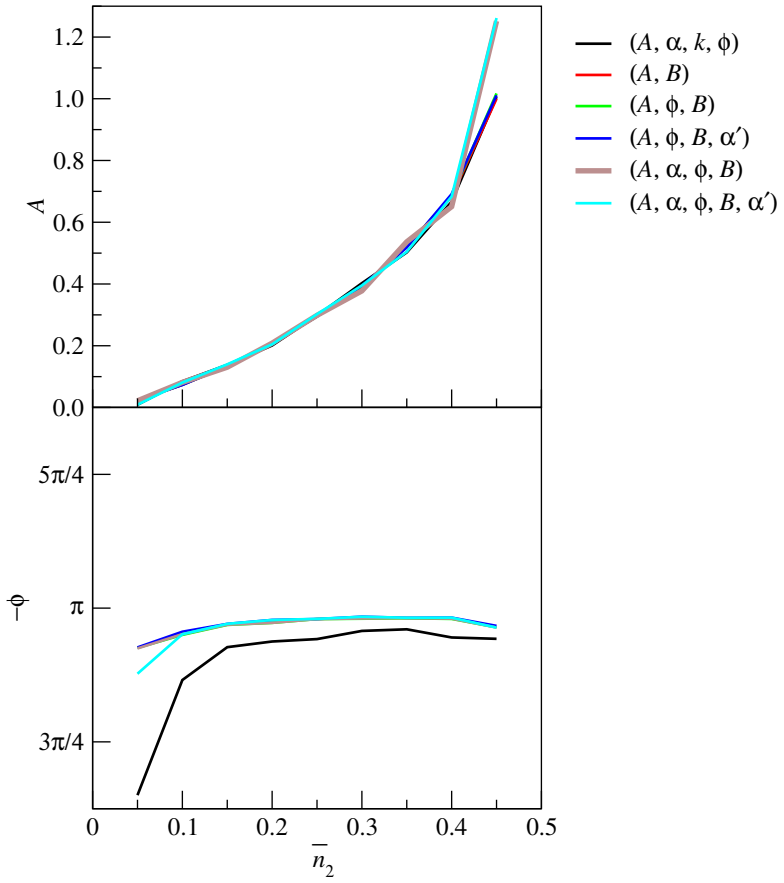

Figure 7.66: Plots of the fitted amplitude A (top) and phase shift ϕ (bottom) of the infinite-ladder subtracted 'antisymmetric' CDW correlation $\Sigma_-(\bar{n}_2, r) = \langle n_{-,j} n_{-,j+r} \rangle - \langle n_{-,j} \rangle \langle n_{-,j+r} \rangle$, in the limit $t_\perp / t_\parallel = 0$, $t' = 0$, as a function of the ladder filling fraction $\bar{n}_2$, for nonlinear curve fits to the asymptotic form (7.6.60), with and without constraints. The parameters enclosed within each parenthesis are those allowed to vary in that particular nonlinear curve fit.

7.6.4 Superconducting Correlations

Unlike the limit where $t' \gg t_{\|}, t_{\perp}$, where the spinless fermions are tightly bound into pairs, there are no bound pairs in either of the two staggered ground states in this limit of $t_{\perp} \ll t_{\|}, t' = 0$. However, within the staggered ground states there are configurations in which a spinless fermion on leg $i = 1$ and its nearest-neighbor particle on leg $i = 2$ sit on opposing corners of the same plaquette, as shown in Figure 7.67. Also shown in Figures 7.67 and 7.68 is the fact that it is possible to annihilate both of these spinless fermions, create two spinless fermions elsewhere on the ladder, and end up with a valid staggered ground-state configuration, provided certain conditions on the number of intervening particles are met.

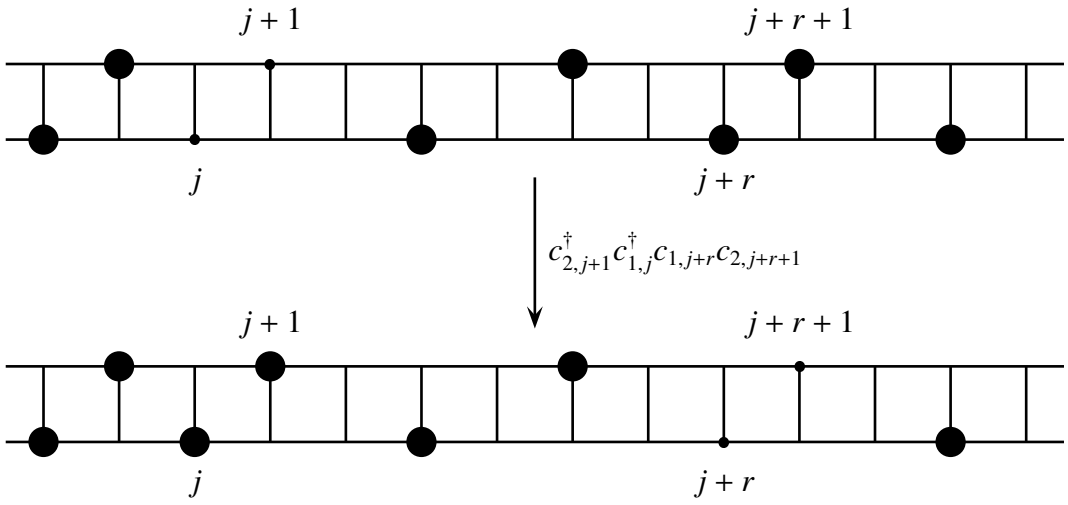

Figure 7.67: Annihilation of a pair of spinless fermions at sites $(1, j + r)$ and $(2, j + r + 1)$, followed by creation of a pair of spinless fermions at sites $(1, j)$ and $(2, j + 1)$, within a staggered ground-state configuration, leads to another staggered ground-state configuration, when there is an *even* number of intervening spinless fermions between rungs $j + 1$ and $j + r$.

For the SC correlation $\langle c^{\dagger}_{2,j+1} c^{\dagger}_{1,j} c_{1,j+r} c_{2,j+r+1} \rangle$, we see from Figure 7.67 that the only

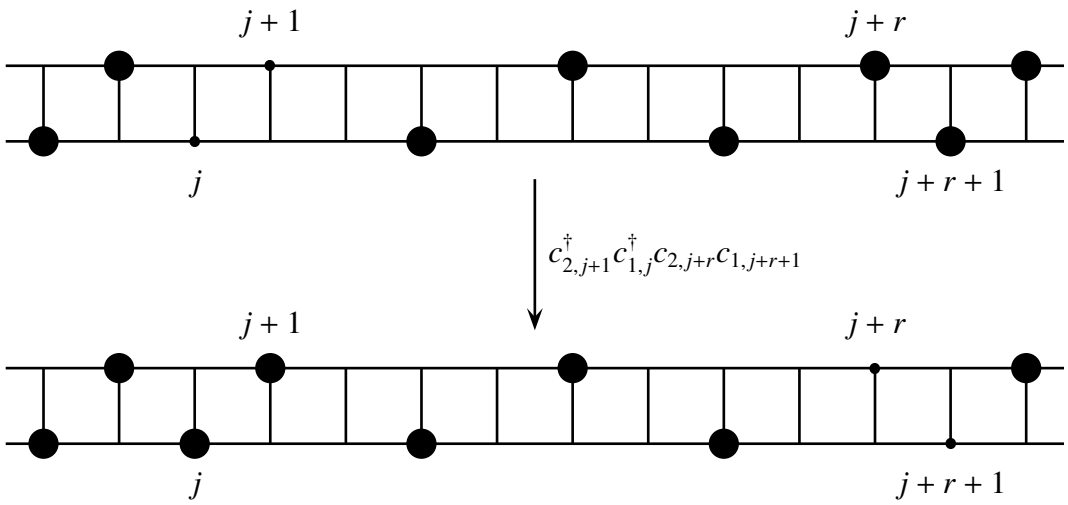

Figure 7.68: Annihilation of a pair of spinless fermions at sites $(2, j + r)$ and $(1, j + r + 1)$, followed by creation of a pair of spinless fermions at sites $(1, j)$ and $(2, j + 1)$, within a staggered ground-state configuration, leads to another staggered ground-state configuration, when there is an *odd* number of intervening spinless fermions between rungs $j + 1$ and $j + r$.

staggered ground-state configurations making nonzero contributions are those with an *even* number of intervening particles between the rungs $j+1$ and $j+r$. These of course map to noninteracting spinless fermion configurations with an even number of intervening particles between the sites $j+1$ and $j+r$, and so we have

$$\langle c^\dagger_{2,j+1} c^\dagger_{1,j} c_{1,j+r} c_{2,j+r+1} \rangle = \sum_{\substack{\text{even number} \\ \text{of intervening} \\ \text{particles}}} \tfrac{1}{2} \langle c^\dagger_{j+1} c^\dagger_j (\cdots) c_{j+r} c_{j+r+1} \rangle \,. \tag{7.6.61}$$

Similarly, for the SC correlation $\langle c^\dagger_{2,j+1} c^\dagger_{1,j} c_{2,j+r} c_{1,j+r+1} \rangle$, we see from Figure 7.68 that the only staggered ground-state configurations making nonzero contributions are those with an *odd* number of intervening particles between the rungs $j+1$ and $j+r$. These map to noninteracting spinless fermion configurations with an odd number of intervening particles between the sites $j+1$ and $j+r$, and so we have

$$\langle c^\dagger_{2,j+1} c^\dagger_{1,j} c_{2,j+r} c_{1,j+r+1} \rangle = \sum_{\substack{\text{odd number} \\ \text{of intervening} \\ \text{particles}}} \tfrac{1}{2} \langle c^\dagger_{j+1} c^\dagger_j (\cdots) c_{j+r} c_{j+r+1} \rangle \,. \tag{7.6.62}$$

Adding the two SC correlations, we therefore have

$$\langle c^\dagger_{2,j+1} c^\dagger_{1,j} c_{1,j+r} c_{2,j+r+1} \rangle + \langle c^\dagger_{2,j+1} c^\dagger_{1,j} c_{2,j+r} c_{1,j+r+1} \rangle = \tfrac{1}{2} \langle c^\dagger_{j+1} c^\dagger_j c_{j+r} c_{j+r+1} \rangle \equiv \tfrac{1}{2} \Pi_+(r), \tag{7.6.63}$$

while subtracting the two SC correlations, we have a non-vanishing, oscillatory, correlation

$$\langle c^\dagger_{2,j+1} c^\dagger_{1,j} c_{1,j+r} c_{2,j+r+1} \rangle - \langle c^\dagger_{2,j+1} c^\dagger_{1,j} c_{2,j+r} c_{1,j+r+1} \rangle \equiv \tfrac{1}{2} \Pi_-(r) \tag{7.6.64}$$

with zero mean, just like the CDW correlation $\langle n_{-,j} n_{-,j+r} \rangle$ in (7.6.41). Similarly, we find that

$$\langle c^\dagger_{1,j+1} c^\dagger_{2,j} c_{1,j+r} c_{2,j+r+1} \rangle + \langle c^\dagger_{1,j+1} c^\dagger_{2,j} c_{2,j+r} c_{1,j+r+1} \rangle = \tfrac{1}{2} \Pi_+(r), \tag{7.6.65}$$

and

$$\langle c^\dagger_{1,j+1} c^\dagger_{2,j} c_{1,j+r} c_{2,j+r+1} \rangle - \langle c^\dagger_{1,j+1} c^\dagger_{2,j} c_{2,j+r} c_{1,j+r+1} \rangle = \tfrac{1}{2} \Pi_-(r). \tag{7.6.66}$$

Defining the SC order parameters to be

$$\Delta^{\dagger}_{\pm,j} = \frac{1}{\sqrt{2}}\left(c^{\dagger}_{1,j}c^{\dagger}_{2,j+1} \pm c^{\dagger}_{1,j+1}c^{\dagger}_{2,j}\right), \tag{7.6.67}$$

we then find that

$$\begin{aligned} \langle \Delta^{\dagger}_{+,j}\Delta_{+,j+r}\rangle &= \Pi_{+}(r) \sim r^{-2}, \\ \langle \Delta^{\dagger}_{-,j}\Delta_{-,j+r}\rangle &= \Pi_{-}(r). \end{aligned} \tag{7.6.68}$$

To understand the asymptotic behaviour of $\Pi_{-}(r)$, we calculate it numerically, and find that like $\Sigma_{-}(r)$, $\Pi_{-}(r)$ oscillates about a zero average, with a decaying amplitude, and filling-fraction-dependent wavelength, as shown in Figure 7.69.

To extract the correlation exponent, and other parameters from the numerical data, we perform nonlinear curve fitting of $r^2 \langle \Delta^{\dagger}_{-,j}\Delta_{-,j+r}\rangle$ to the asymptotic form

$$Ar^{-(\beta-2)}\cos(kr+\phi), \tag{7.6.69}$$

where the pre-multiplication by r^2 is to make the curve fits more accurate. The fitted parameters are shown in Table 7.14. The first observation we make on the fitted parameters in Table 7.14 is the very obvious particle-hole symmetry: the fitted amplitudes and fitted correlation exponents for $\bar{n}_2$ and $\frac{1}{2} - \bar{n}_2$ are the same, and the phase shifts appear to satisfy

$$\phi(\bar{n}_2) + \phi(\tfrac{1}{2} - \bar{n}_2) = -2\pi. \tag{7.6.70}$$

We expect this particle-hole symmetry, since the ladder filling fractions $\bar{n}_2$ and $\frac{1}{2} - \bar{n}_2$ corresponds to the nearest-neighbor included chain filling fractions $\bar{n}_1 = 2\bar{n}_2$ and $1-\bar{n}_1 = 2(\frac{1}{2} - \bar{n}_2)$.

The effective wave vectors obtained from the nonlinear curve fits of the 'antisymmetric' SC correlation are again close to $k = 2\pi\bar{n}_2 = 2k_F$, as shown in Figure 7.70. The fitted amplitude A, as shown in Figure 7.71, has a behaviour as a function of ladder filling fraction $\bar{n}_2$ that is qualitatively different from that of the fitted amplitude of the

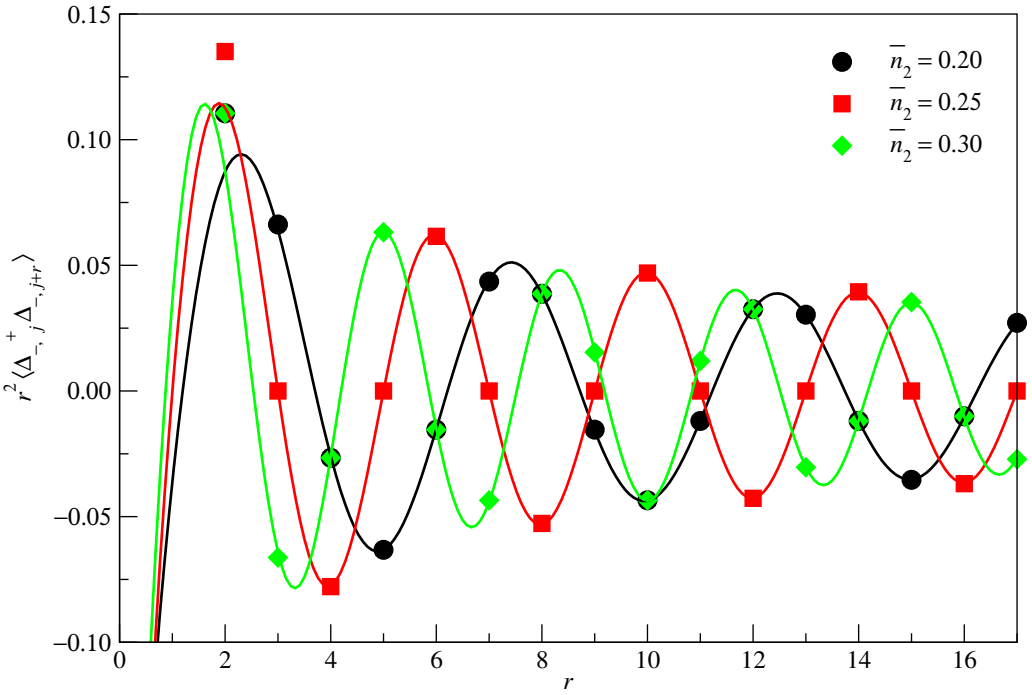

Figure 7.69: The infinite-ladder 'antisymmetric' SC correlation $r^2 \langle \Delta^\dagger_{-,j} \Delta_{-,j+r} \rangle$ as a function of separation $2 \leq r \leq 17$ for ladder filling fractions $\bar{n}_2 = 0.20$ (black circles), 0.25 (red squares), and 0.30 (green diamonds), in the limit $t_\perp / t_\parallel = 0$, $t' = 0$. These are fitted to the form $A r^{-(\beta-2)} \cos(kr + \phi)$, to obtain $A = 0.149594$, $k = 1.25231$, $\phi = -3.06667$, $\beta - 2 = 0.534336$ for $\bar{n}_2 = 0.20$ (black curve), $A = 0.164151$, $k = 1.5708$, $\phi = -3.14159$, $\beta - 2 = 0.542353$ for $\bar{n}_2 = 0.25$ (red curve), $A = 0.149594$, $k = 1.88928$, $\phi = -3.21652$, $\beta - 2 = 0.534336$ for $\bar{n}_2 = 0.30$ (green curve).

Table 7.14: Fitted parameters for a nonlinear curve fit of the infinite-ladder SC correlation $r^2 \langle \Delta^\dagger_{-,j} \Delta_{-,j+r} \rangle$, in the limit $t_\perp \ll t_\parallel$, $t' = 0$, to an asymptotic form $A r^{-(\beta-2)} \cos(kr+\phi)$, for ladder filling fractions $0.05 \leq \bar{n}_2 \leq 0.45$, for $r \geq 4$.

$\bar{n}_2$	A	$\beta - 2$	k	ϕ
0.05	0.0129802	0.187293	0.258578	−2.19433
0.10	0.0793048	0.572156	0.614113	−2.87694
0.15	0.114656	0.524555	0.934773	−2.9996
0.20	0.149594	0.534336	1.25231	−3.06667
0.25	0.164151	0.542353	1.5708	−3.14159
0.30	0.149594	0.534336	1.88928	−3.21652
0.35	0.114656	0.524555	2.20682	−3.28358
0.40	0.0793048	0.572156	2.52748	−3.40625
0.45	0.0129802	0.187293	2.88302	−4.08885

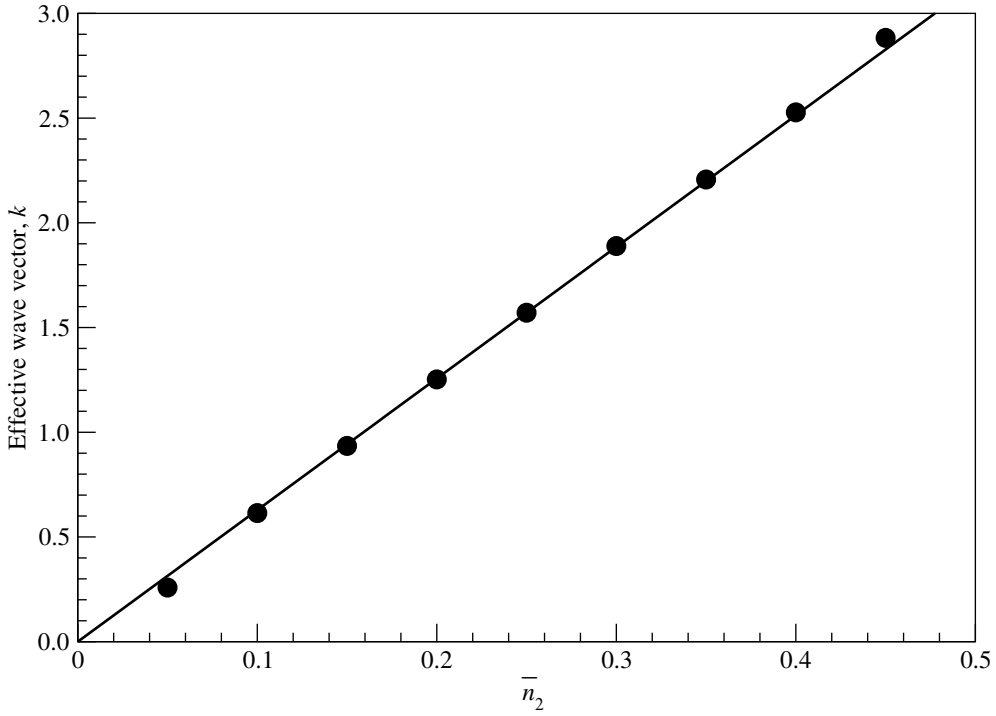

Figure 7.70: The effective wave vector k (filled circles) of the infinite-ladder 'antisymmetric' SC correlation $\langle \Delta^{\dagger}_{-,j} \Delta_{-,j+r} \rangle$, in the limit $t_{\perp} \ll t_{\parallel}$, $t' = 0$, as a function of the ladder filling fraction $\bar{n}_2$. Also shown as the solid line is the wave vector $k = 2\pi\bar{n}_2 = 2k_F$. The data points plotted here are from the four-parameter, $(A, \beta - 2, k, \phi)$ fit to (7.6.69), shown in Table 7.14.

subtracted 'antisymmetric' CDW correlation. Instead of increasing monotonically with $\bar{n}_2$, the fitted amplitude of the 'antisymmetric' SC correlation is maximum when the ladder is quarter-filled. Though it is risky business to extrapolate, we also expect from physical grounds that the amplitude vanishes at $\bar{n}_1 = 0$ and $\bar{n}_2 = \frac{1}{2}$.

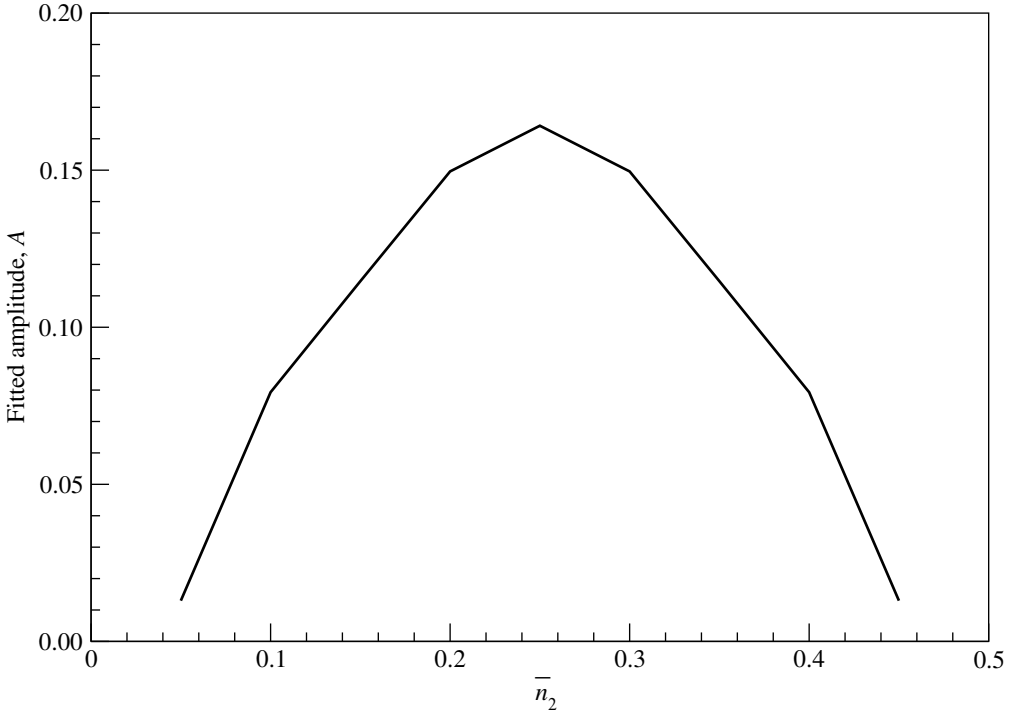

Figure 7.71: The fitted amplitude A of the infinite-ladder 'antisymmetric' SC correlation $\langle \Delta^{\dagger}_{-,j} \Delta_{-,j+r} \rangle$, in the limit $t_{\perp} \ll t_{\parallel}$, $t' = 0$, as a function of the ladder filling fraction $\bar{n}_2$. The data points plotted here are from the four-parameter, $(A, \beta - 2, k, \phi)$ fit to (7.6.69), shown in Table 7.14.

Figure 7.72 shows the fitted correlation exponent, $\beta - 2$, as a function of the ladder filling fraction $\bar{n}_2$. Unlike the fitted amplitude, $\beta(\bar{n}_2)$ appears to have additional structure as a function of $\bar{n}_2$. We suspect that this additional 'wing'-like structure is an artefact of our nonlinear curve fitting at the filling fractions $\bar{n} = 0.10$ and $\bar{n} = 0.40$. From the nonlinear curve fits over $0.05 \leq \bar{n}_2 \leq 0.45$, it also appears that $\beta \to 2$ as $\bar{n}_2 \to 0$ and

$\bar{n}_2 \to \frac{1}{2}$, which suggests noninteracting-spinless-fermion behaviour. However, we must remember that the 'antisymmetric' SC correlation $\langle \Delta^\dagger_{-,j} \Delta_{-,j+r} \rangle$ is strictly zero within a chain of noninteracting spinless fermions. In fact, performing further nonlinear curve fitting to the numerical 'antisymmetric' SC correlation for $\bar{n}_2 = 0.01$ and $\bar{n}_2 = 0.49$, we found that $\beta \approx 0$, which we know from Section 7.5.7 is not correct either. It is plausible that the structure of β as a function of $\bar{n}_2$ we see in Figure 7.72 are systematic errors incurred during the nonlinear curve fits, and $\beta \approx 2.5$ is actually an universal correlation exponent independent of $\bar{n}_2$.

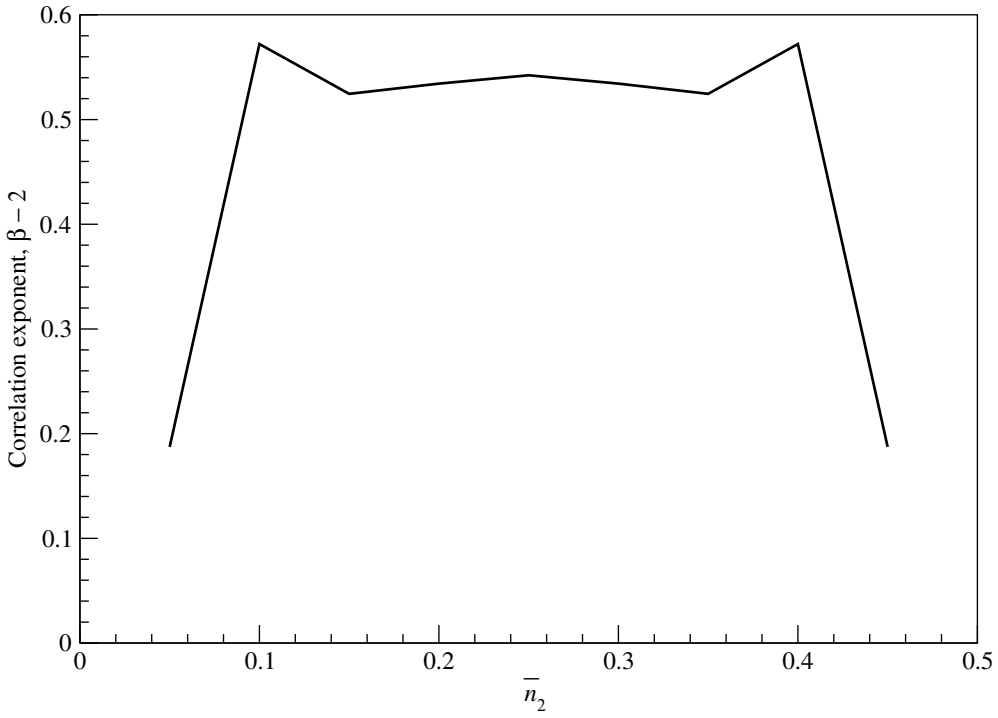

Figure 7.72: The fitted correlation exponent $\beta - 2$ of the infinite-ladder 'antisymmetric' SC correlation $\langle \Delta^\dagger_{-,j} \Delta_{-,j+r} \rangle$, in the limit $t_\perp \ll t_\parallel$, $t' = 0$, as a function of the ladder filling fraction $\bar{n}_2$. The data points plotted here are from the four-parameter, $(A, \beta - 2, k, \phi)$ fit to (7.6.69), shown in Table 7.14.

Like we do for the subtracted 'antisymmetric' CDW correlations, we perform an-

other five series of constrained nonlinear curve fits of $r^2 \langle \Delta^{\dagger}_{-,j} \Delta_{-,j+r} \rangle$ to the asymptotic form

$$Ar^{-(\beta-2)} \cos(2\pi \bar{n}_2 r + \phi) + Br^{-(\beta'-2)}, \tag{7.6.71}$$

where we assumed that the leading-order correction is a power law. Starting from the constraints $\beta - 2 = \frac{1}{2}$ and $\phi = -\pi$, which are suggested by the results of the previous nonlinear curve fit, and the arbitrary constraint $\beta' - 2 = 2$, we relax the constraints one at a time, to obtained the table of fitted parameters shown in Table 7.15.

Plotting the fitted amplitude A and phase shift ϕ in Figure 7.73, we find generally good agreement across the five series of nonlinear curve fits. From Figure 7.73, we see that the phase shift ϕ continues to exhibit the particle-hole symmetry (7.6.70) in the series of constrained nonlinear curve fits, but now appears to have such a weak dependence on the ladder filling fraction $\bar{n}_2$ that it is conceivable that, like for the subtracted 'antisymmetric' CDW correlation, the phase shift takes on a universal value of $\phi = -\pi$.

7.6.5 Discussions

Before we move on to summarize and discuss our findings in this section, let us digress a little, and talk about the physics of string operators. For example, in Section 7.4.1 we have seen how the hard-core boson two-point function $\langle b^{\dagger}_j b_{j+r} \rangle$ maps to the expectation of the string operator $c^{\dagger}_j \prod_{j'=j+1}^{j'=j+r-1} (-1)^{n_{j'}} c_{j+r}$, in the ground state of a chain of noninteracting spinless fermions. Efetov and Larkin calculated $\langle c^{\dagger}_j \prod_{j'=j+1}^{j'=j+r-1} (-1)^{n_{j'}} c_{j+r} \rangle$, and found it to decay as a power law, with exponent $\frac{1}{2}$, in the separation r between the two ends of the string operator. Since this expectation decays slower than the two-point function $\langle c^{\dagger}_j c_{j+r} \rangle \sim r^{-1}$, one might ponder why such a string operator does not play a role in determining the response functions for a chain of noninteracting spinless fermions, and why many-body theorists do not also include such string-operator expectations into

Table 7.15: Fitted parameters for five series of nonlinear curve fits of the infinite-ladder SC correlation $r^2 \langle \Delta^\dagger_{-,j} \Delta_{-,j+r} \rangle$, in the limit $t_\perp \ll t_\parallel$, $t' = 0$, to an asymptotic form $A r^{-(\beta-2)} \cos(2\pi \bar{n}_2 r + \phi) + B r^{-(\beta'-2)}$, for ladder filling fractions $0.05 \leq \bar{n}_2 \leq 0.45$, for and for separations $r \geq 4$. When the parameter value is quoted as '-', that means that the iterations ran away for that parameter.

$\bar{n}_2$	A	$\beta - 2$	$-\phi$	B	$\beta' - 2$	visual
0.05	0.0220115	$\frac{1}{2}$	π	0.128537	2	not good
	0.0232843	$\frac{1}{2}$	2.90664	0.082106	2	good
	0.0235782	$\frac{1}{2}$	2.91446	0.105524	2.15577	good
	0.0206191	0.446012	2.90488	0.0827992	2	good
	0.0096909	0.156471	2.78934	0.0149365	0.959049	good
0.10	0.0673326	$\frac{1}{2}$	π	0.0283962	2	not good
	0.0676333	$\frac{1}{2}$	3.00305	0.0293014	2	good
	0.0668403	$\frac{1}{2}$	3.02767	-	-	good
	0.077858	0.563288	3.00915	0.00750546	2	good
	0.0643958	0.483741	3.02798	-	-	good
0.15	0.108136	$\frac{1}{2}$	π	−0.0559099	2	good
	0.108618	$\frac{1}{2}$	3.075	−0.0230529	2	very good
	0.108633	$\frac{1}{2}$	3.07517	−0.0264316	2.08287	very good
	0.113579	0.521088	3.07444	−0.0264399	2	very good
	0.116464	0.531594	3.07675	−0.199456	3.21112	very good

Table 7.15: (continued)

$\bar{n}_2$	A	$\beta - 2$	$-\phi$	B	$\beta' - 2$	visual
0.20	0.138341	$\frac{1}{2}$	π	−0.042532	2	good
	0.138342	$\frac{1}{2}$	3.10555	−0.0301403	2	very good
	0.138167	$\frac{1}{2}$	3.11379	-	-	very good
	0.147022	0.527867	3.10533	−0.0206189	2	very good
	0.146358	0.525774	3.11366	-	-	very good
0.25	0.150355	$\frac{1}{2}$	π	−0.0214455	2	very good
	0.150334	$\frac{1}{2}$	3.139	−0.0222044	2	perfect
	0.148987	$\frac{1}{2}$	3.14142	-	-	perfect
	0.162504	0.537994	3.14063	−0.00798485	2	perfect
	0.164151	0.542353	3.14159	−0.000509556	-	perfect
0.30	0.139758	$\frac{1}{2}$	π	−0.0329927	2	very good
	0.139321	$\frac{1}{2}$	3.17828	−0.0163949	2	very good
	0.138678	$\frac{1}{2}$	3.16845	-	-	very good
	0.153213	0.545086	3.17639	−0.0170395	2	perfect
	0.147648	0.52935	3.16951	-	-	perfect

Table 7.15: (continued)

$\bar{n}_2$	A	$\beta - 2$	$-\phi$	B	$\beta' - 2$	visual
0.35	0.107307	$\frac{1}{2}$	π	−0.00142594	2	good
	0.108334	$\frac{1}{2}$	3.21736	0.00375022	2	very good
	0.108335	$\frac{1}{2}$	3.21735	0.00347439	1.95266	very good
	0.109996	0.507031	3.21789	0.00203508	2	very good
	0.110028	0.507149	3.21788	0.00110959	1.61539	very good
0.40	0.0681317	$\frac{1}{2}$	π	0.0449886	2	good
	0.0687036	$\frac{1}{2}$	3.26913	0.025977	2	very good
	0.0671376	$\frac{1}{2}$	3.25532	-	-	very good
	0.0777179	0.561995	3.26717	0.0196413	2	very good
	0.068302	0.507631	3.25583	-	-	very good
0.45	0.0259776	$\frac{1}{2}$	π	0.0480123	2	poor
	0.0264839	$\frac{1}{2}$	3.52099	0.021551	2	not good
	0.0268919	$\frac{1}{2}$	3.45331	-	-	not good
	0.0547479	0.832803	3.50852	0.0235339	2	not good
	0.0639897	0.891659	3.42114	-	-	not good

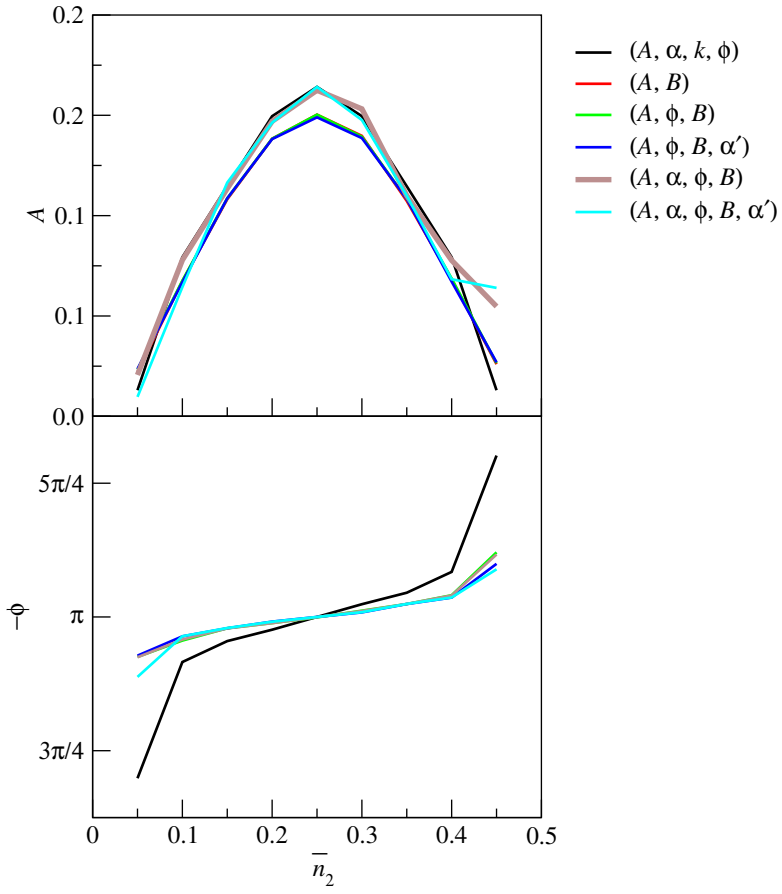

Figure 7.73: Plots of the fitted amplitude A (top) and phase shift ϕ (bottom) of the infinite-ladder subtracted 'antisymmetric' CDW correlation $\Sigma_-(\bar{n}_2, 2) = \langle n_{-,j} n_{-,j+r} \rangle - \langle n_{-,j} \rangle \langle n_{-,j+r} \rangle$, in the limit $t_\perp / t_\parallel = 0$, $t' = 0$, as a function of the ladder filling fraction $\bar{n}_2$, for nonlinear curve fits to the asymptotic form (7.6.60), with and without constraints. The parameters enclosed within each parenthesis are those allowed to vary in that particular nonlinear curve fit.

the compilation (7.2.1) of power-law decaying correlations in a Luttinger liquid.

The answer to the first question is that string operators are nonlocal observables, and we do not in general expect them to couple to local measurements. Even if we can cook up in the laboratory an experimental system that can be described by the weak inter-leg hopping ladder model, there is still no simple way to experimentally measure the string correlation functions which we have been calculating. However, we observe that when we map from this weak inter-leg hopping ladder model to another model, the string correlation functions in question may be mapped to local correlation functions. Therefore, if we can determine what that other model is, and concoct an experimental system described by this other model, we can then cheat a little, measure the local correlation functions in the second experimental system, and claim that we have measured the string correlations in the first experimental system. The answer to the second question is that the typical string correlation functions, which receive contributions only from restricted classes of configurations, typically decay exponentially with r, for the same reason why the FL correlation decays exponentially in the strong correlated hopping (Section 7.5.8) and zero inter-leg hopping (Section 7.6.2). Only in special cases, where the correlation lengths of the string correlation functions diverge, do we start seeing them decay as power laws.

In the zero inter-leg hopping limit we study in this section, the staggered ground state has long-range order, in that if we know the pth particle is on leg $i = 1$, then we know for certain that the $(p + 2s)$th particle is on leg $i = 1$, and the $(p + 2s + 1)$th particle is on leg $i = 2$, even as $s \to \infty$, and even though we have no idea where these particles are on the ladder. This long-range order is therefore not the usual kind of long-range order, which can be written in terms of the correlation between local order parameters, but is a long-range *string* order. The map from the nearest-neighbor included chain ground

state to the staggered ladder ground state, which is the inverse of the one constructed in Section 7.6.1, implicitly involves string operators, in that if we take the pth particle in the nearest-neighbor included ground state configuration, we will know whether to map it to a particle on leg $i = 1$ or leg $i = 2$, *after* we know which legs the preceding particles are on. Also, while it is deceptively simple to describe what the string operator in this inverse map does, which is to project out any combination of more than or equal to two consecutive particles on the same leg of the ladder, we know of no compact way to write down the string operator, even in this simple limit, unlike for the case of the Jordan-Wigner string.

What we do know, drawing parallels from the Jordan-Wigner map from hard-core bosons on nearest-neighbor included chains to noninteracting spinless fermions, is that a string map from one model to another will also map some products of local operators to string operators, for example, the hard-core boson $b_j^\dagger b_{j+r}$ to the spinless fermion $c_j^\dagger \prod_{j'=j+1}^{j'=j+r-1}(-1)^{n_{j'}} c_{j+r}$, and some products of local operators to products of local operators, for example, the hard-core boson $n_j n_{j+r}$ to the spinless fermion $n_j n_{j+r}$, as we have seen in Section 7.5.7. Having understood this, we realized that the 'symmetric' CDW and SC correlations in the staggered ground state get mapped to the the correlation of local operators, because the string operators involved in the map multiply and cancel each other. On the other hand, when we map the 'antisymmetric' CDW and SC staggered ground-state correlations to correlations of a chain of noninteracting spinless fermions, the string operators involved in the map do not cancel each other, and thus the resulting nearest-neighbor included chain spinless-fermion correlations are string correlations.

In Sections 7.6.3 and 7.6.4, we calculated the 'antisymmetric' CDW and SC staggered ground-state correlations using the intervening-particle expansion. This tells us that we should think of the intervening-particle expansion, with its sum over condi-

tional expectations, as defining the string correlations. In Section 7.5.6, we have in fact seen this particular aspect of the intervening-particle expansion in action for the Jordan-Wigner string, when we calculated the SC correlation in the strong correlated hopping limit. In the final stage of the analytical calculation, we mapped conditional nearest-neighbor included hard-core boson expectations to conditional nearest-neighbor included spinless-fermion expectations. These conditional nearest-neighbor included hard-core boson expectations came from the intervening-particle expansion of the nearest-neighbor excluded hard-core boson expectation, so we did not realize then that we would *still* need to use the intervening-particle expansion to calculate a nearest-neighbor included hard-core boson expectation.

Returning to our results obtained in this limit, it now becomes clear, that the 'symmetric' CDW and SC correlations map to correlations of local observables. Furthermore, seeing that their correlations are precisely those of a chain of noninteracting spinless fermions, we realized that we must indeed be dealing with a Fermi liquid, with $K_\rho = K_\sigma = 1$. We shall now argue how the behaviours of the other correlations we have calculated in this section is consistent with this observation.

First of all, we calculated in Section 7.6.2 that the ladder FL correlation $\langle c^\dagger_{i,j} c_{i,j+r} \rangle$ decays exponentially with separation r, using the argument that this correlation receives contributions only from clusters of r or more empty rungs. Based on our discussions on string operators in general, and on the inverse map from a nearest-neighbor included chain to the staggered ground states in particular, we now understand that the ladder FL correlation gets mapped to a string correlation, and realized that the restricted probability argument we used is in actual fact an intervening-particle expansion, but one in which only one term, the $p = 0$ term, is retained. Again, we can easily describe the action of the string operator in question — to ensure that the sites between j and $j + r$ on the

nearest-neighbor included chain are empty, but not write it down in a compact form.

We then noted above that the 'antisymmetric' CDW correlation, which we calculated in Section 7.6.3, actually gets mapped to a string correlation. This is despite the fact that the 'antisymmetric' CDW correlation is completely analogous to the SDW of a chain of noninteracting spinfull fermions, if we map a spinless fermion on leg $i = 1$ to a spin-$\downarrow$ fermion, and a spinless fermion on leg $i = 2$ to a spin-$\uparrow$ fermion. The noninteracting-spinfull-fermion SDW decays as a power law with exponent $\alpha = 2$, but by nonlinear curve fitting the numerical correlations to the expected asymptotic form $Ar^{-\alpha}\cos(2\pi\bar{n}_2+\phi)$, we determined that the 'antisymmetric' CDW has a power-law decay with a very convincingly universal correlation exponent $\alpha = \frac{1}{2}$. Once the nature of the nearest-neighbor included chain string observable is understood, for example, by examining the intervening-particle expansion, to be one which assigns opposite signs to chain spinless fermions mapped from opposite legs of the ladder, the universal string correlation exponent of $\alpha = \frac{1}{2}$ can be shown using a bosonization calculation to follow automatically from the universal Fermi liquid parameters $K_\rho = K_\sigma = 1$ [380].

Finally, in Section 7.6.4, we calculated numerically the 'antisymmetric' ladder SC correlation with the aid of the intervening-particle expansion. By performing nonlinear curve fitting to the numerical correlations, we then find this correlation decaying with separation as a power law, with a correlation exponent that appears to be also universal, and having value $\beta = \frac{5}{2}$. Examining the intervening-particle expansion, we find the string operator in question to be significantly more complicated. While the bosonized form of this string correlation is also not known, it is conceivable that the numerically observed correlation exponent comes from the combination

$$2K_\rho + \frac{1}{2K_\rho} = \frac{5}{2} \tag{7.6.72}$$

of the universal Fermi liquid parameter $K_\rho = 1$ [380].

7.7 Very Strong Inter-Leg Hopping

In the limit of $t_\parallel = 1$, $t' = 0$ and $t_\perp$ becoming very large, particles on the ladder will become increasingly localized onto the rungs they are on, and hop along the leg to the neighboring rung with a vanishingly small amplitude. With this in mind, we discuss the structure and properties of the resulting ground state in Section 7.7.1. Then, in Sections 7.7.2, 7.7.3 and 7.7.4, we shall make use of the intervening-particle expansion described in Section 7.4.7 to calculate the FL, CDW and SC correlations respectively. As with the strong correlated hopping limit, where the intervening-particle expansion sums over noninteracting-spinless-fermion expectations involving different separations, we calculate the infinite-ladder correlations numerically for various nearest-neighbor excluded filling fractions. We then perform nonlinear curve fitting of these numerical correlations to expected asymptotic forms to extract the correlation exponents.

7.7.1 Structure of Ground State

To understand the structure of the ground state in the limit of nearly vanishing $t_\parallel/t_\perp$, let us develop a path-integral picture, as shown in Figure 7.74. Following the time evolution for a single spinless fermion, we find that most of the time, the spinless fermion hops back and forth along a rung, and only very rarely hops along the leg to an adjacent rung, where it will spend a lot of time hopping back and forth, before hopping along the leg again. Because of this long dwell time on a rung, the spinless fermion is very nearly in the rung ground state

$$|+, j\rangle = \tfrac{1}{\sqrt{2}} \left(c^\dagger_{1,j} + c^\dagger_{2,j} \right) |0\rangle = C^\dagger_j |0\rangle \,. \tag{7.7.1}$$

Let us call a spinless fermion in the rung ground state a *rung-ground-state spinless fermion*, or a *rung fermion* in short. Rung-fermions inherit the infinite nearest-neighbor

repulsion of the bare spinless fermions, and therefore two rung-fermions in adjacent rungs experience infinite nearest-neighbor repulsion as well. With this insight, we find that the full many-body problem of spinless fermions with infinite nearest-neighbor repulsion on the two-legged ladder reduces to a one-dimensional problem of spinless rung-fermions with infinite nearest-neighbor repulsion.

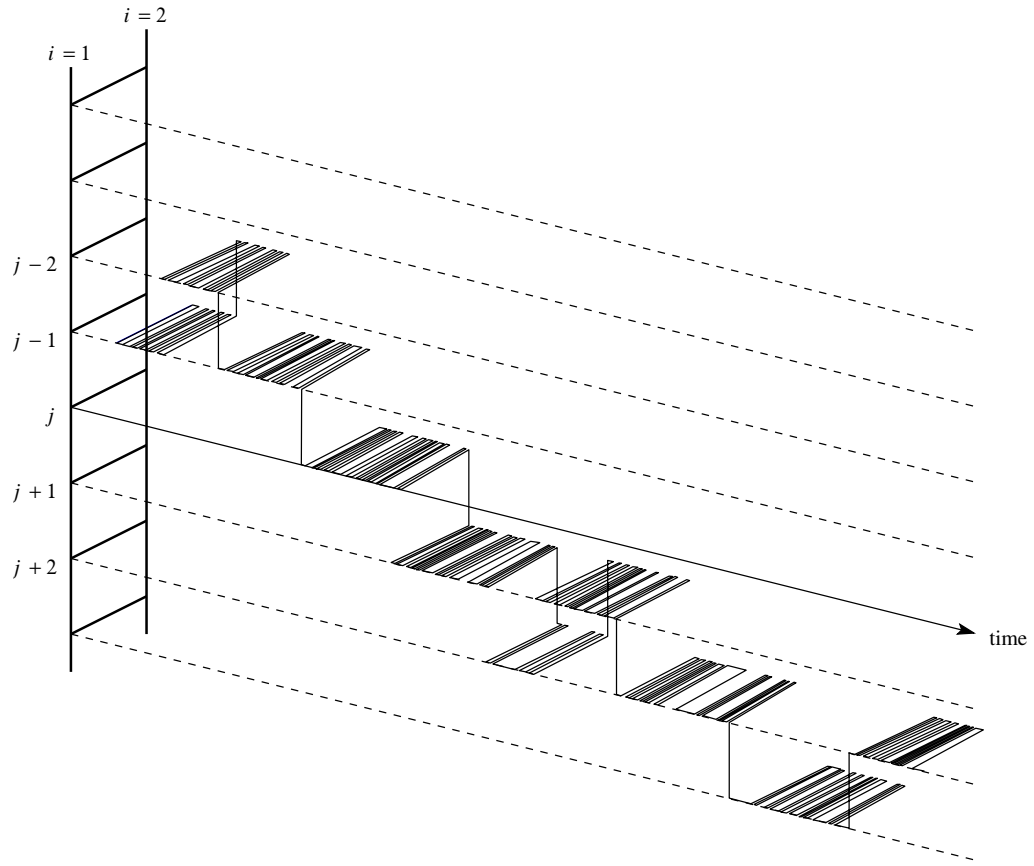

Figure 7.74: A path of a spinless fermion on a two-legged ladder with $t_{\parallel} \ll t_{\perp}$.

Using the Bloch-state-to-Bloch-state mapping described in Section 7.4.4, we can map the chain of rung-fermions with infinite nearest-neighbor repulsion to a chain of noninteracting spinless fermions. As we have explained in Sections 7.4.3, 7.4.4, and 7.4.5, there are three components to the Bloch-state-to-Bloch-state map, the first being

a map

$$c^\dagger_{j_1} c^\dagger_{j_2} \cdots c^\dagger_{j_P} |0\rangle \mapsto C^\dagger_{j_1} C^\dagger_{j_2+1} \cdots C^\dagger_{j_P+P-1} |0\rangle \tag{7.7.2}$$

between nearest-neighbor included configurations and nearest-neighbor excluded configurations, the second being a relation between the Bloch-state amplitudes, and the third being a relation between the total momentum wave vectors on the nearest-neighbor included, and nearest-neighbor excluded chains.

In Section 7.4.4, we explained how one would write the Fermi-sea ground state of a chain of noninteracting spinless fermions in terms of the nearest-neighbor included Bloch states as

$$|\Psi_F\rangle = \sum_{r_2>0} \cdots \sum_{r_P>0} \Psi_F(k_1, \ldots, k_P; r_2, \ldots, r_P) \, |q'; r_2, \ldots, r_P\rangle_{\text{chain}} \,, \tag{7.7.3}$$

where

$$|q'; r_2, \ldots, r_P\rangle_{\text{chain}} \propto \sum_{j_1} e^{-\mathrm{i}\, q' j_1} \, c^\dagger_{j_1} c^\dagger_{j_1+r_2} \cdots c^\dagger_{j_1+r_2+\cdots+r_P} |0\rangle \tag{7.7.4}$$

are the normalized nearest-neighbor included Bloch states. Using (7.7.2), we then construct the normalized rung-fermion Bloch states as

$$|q; r_2, \ldots, r_P\rangle_{\text{rung}} \propto \sum_{j_1} e^{-\mathrm{i}\, q j_1} \, C^\dagger_{j_1} C^\dagger_{j_1+r_2+1} \cdots C^\dagger_{j_1+r_2+\cdots+r_P+P-1} |0\rangle \,, \tag{7.7.5}$$

so that the nondegenerate many-rung-fermion ground state, with $q = 0 = q'$, is given by

$$|\Psi\rangle = \sum_{r_2>0} \cdots \sum_{r_P>0} \Psi_F(k_1, \ldots, k_P; r_2, \ldots, r_P) \, |q = 0; r_2, \ldots, r_P\rangle_{\text{rung}} \,. \tag{7.7.6}$$

The detailed effect of infinite nearest-neighbor repulsion is buried within the configurations of the rung-ground-state spinless fermion Bloch state $|q; r_2, \ldots, r_P\rangle_{\text{rung}}$.

As in Section 7.5.5, the use of an excluded nearest-neighbor map means that the eventual nearest-neighbor included chain filling fraction $\bar{n}_1$ is not a simple multiple of the ladder filling fraction $\bar{n}_2$. For P spinless fermions on a ladder of length L, the ladder

filling fraction is $\bar{n}_2 = P/2L$. This ladder of length L maps to a nearest-neighbor included chain of length $L' = L - P$. With P spinless fermions on it, the nearest-neighbor included chain filling fraction is

$$\bar{n}_1 = \frac{P}{L'} = \frac{P}{L-P} = \frac{\bar{n}_2}{\frac{1}{2} - \bar{n}_2}. \tag{7.7.7}$$

Since we are only dealing with effectively one-dimensional rung-fermions, the more appropriate filling fraction describing the system is the rung-fermion filling fraction $\bar{N}_1 = 2\bar{n}_2$, which is related to the eventual chain filling fraction $\bar{n}_1$ by

$$\bar{n}_1 = \frac{\bar{N}_1}{1 - \bar{N}_1}. \tag{7.7.8}$$

The ratio $\bar{N}_1/\bar{n}_1$ is the one that relates the nearest-neighbor excluded, and nearest-neighbor included expectations in (7.4.97).

In the special case of quarter-filling, $\bar{n}_2 = \frac{1}{4}$, spinless fermions occupy alternate rungs in the two degenerate ground states (either odd rungs occupied, or even rungs occupied). These are free to hop along the rungs that they reside on, but cannot hop along the legs, for non-vanishing values of $t_\parallel/t_\perp$. Even virtual processes in which a spinless fermion on rung j hops along the leg to an adjacent rung and back are essentially forbidden by the infinite nearest-neighbor repulsion, because such virtual processes, which has a time scale of $O(1/t_\parallel)$, would not be complete when the spinless fermion on the next-nearest-neighbor rung hops across the rung, which occurs on a time scale of $O(1/t_\perp)$. Virtual processes such as these only become energetically feasible when the two time scales become comparable, i.e. when $t_\parallel \lesssim t_\perp$. Therefore, over a wide range of anisotropies $t_\parallel/t_\perp$, the spinless fermions in the quarter-filled ladder with $t' = 0$ can hop back and forth along the rungs they are on, but cannot hop to the neighboring rungs. This gives rise to a symmetry breaking, where the spinless fermions are either all on the even rungs, or they are all on the odd rungs. Because translational symmetry along the ladder axis is

broken in the quarter-filled ladder ground states, we think of these as 'dynamic solids', since the constituent spinless fermions are constantly hopping back and forth along the rungs.

In this limit of $t_\perp \gg t_\parallel$, $t' = 0$, we also understand that the system phase separates for ladder filling fractions $\bar{n}_2 > \frac{1}{4}$. As shown in Figure 7.75, when the ladder is above quarter-filling, some of the spinless fermions will go into a high-density inert solid phase, where spinless fermions are arranged in a staggered array, and therefore cannot hop at all. The density of this phase is $\bar{n}_2 = \frac{1}{2}$, and since spinless fermions in this phase cannot hop, they contribute nothing to the ground-state energy. If $t_\parallel$ is comparable to $t_\perp$, the rest of the spinless fermions will go into a fluid phase, whose density is $\bar{n}_2 < \frac{1}{4}$. These spinless fermions are free to hop back and forth on the rungs they are on, and occasionally to the neighboring rungs, when permitted by nearest-neighbor exclusion. These contribute a filling-fraction-dependent total kinetic energy to the ground-state energy. The ground-state composition depends on whether the kinetic energy gained per particle, by removing a spinless fermion from the solid phase and adding it to the fluid phase, outweighs the decrease in kinetic energy per particle that results from the fluid becoming more congested.

When $t_\perp$ becomes large compared to $t_\parallel$, which is the limit we are interested in, it becomes energetically favorable, always, to remove one spinless fermion from the inert solid phase, and add it to the fluid phase, if its density is $\bar{n}_2 < \frac{1}{4}$. This is because the kinetic energy penalty to make the fluid becoming more congested, which is of $O(t_\parallel)$, is more than compensated for by the kinetic energy gain of $t_\perp$ for an extra spinless fermion freed to hop back and forth along a rung. Iterating this argument, we find then that, for $t_\perp \gg t_\parallel$, and the overall density $\bar{n}_2 > \frac{1}{4}$, the system will phase separate into an inert solid phase with density $\bar{n}_2 = \frac{1}{2}$, and a dynamic solid phase with density $\bar{n}_2 = \frac{1}{4}$. For example,

if the overall density is $\bar{n}_2 = \frac{1}{3} > \frac{1}{4}$, we will find that $\frac{1}{3}$ of the total number of spinless fermions will be in the inert solid phase, while the other $\frac{2}{3}$ of the total number of spinless fermions will be in the dynamic solid phase.

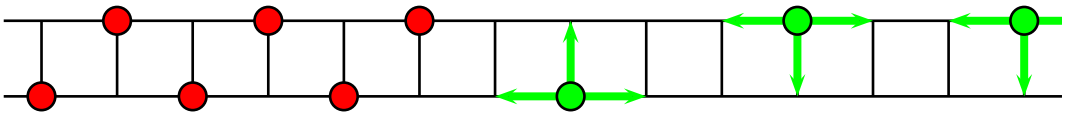

Figure 7.75: Phase separation of a greater-than-quarter-filled ladder of spinless fermions with infinite nearest-neighbor repulsion into a high-density inert solid phase (red spinless fermions) with $\bar{n}_2 = \frac{1}{2}$, and a low-density fluid phase (green spinless fermions) with $\bar{n}_2 < \frac{1}{4}$.

7.7.2 Fermi-Liquid Correlation

From the inert nature of the quarter-filled ladder ground state in the limit $t_\perp \gg t_\parallel, t' = 0$, we know that the rung-ground-state spinless fermion FL correlation is identically zero. This is because all spinless fermions are localized on every other rung of the ladder, and none of the empty rungs can be further occupied. Therefore, if we annihilate a spinless fermion on one rung, there is nowhere else on the ladder we can create another spinless fermion without violating the no-nearest-neighbor constraint.

For ladder filling fractions $\bar{n}_2 < \frac{1}{4}$, we calculate the rung-ground-state spinless fermion FL correlation $\langle C_j^\dagger C_{j+r} \rangle$ by first writing it as an intervening-particle expansion

$$\begin{aligned}\langle C_j^\dagger C_j \rangle = {} & \langle C_j^\dagger (\mathbb{1} - N_{j+1}) \cdots (\mathbb{1} - N_{j+r-1}) C_{j+r} \rangle + \\ & \langle C_j^\dagger (\mathbb{1} - N_{j+1}) N_{j+2} (\mathbb{1} - N_{j+3}) \cdots (\mathbb{1} - N_{j+r-1}) C_{j+r} \rangle + \cdots + \\ & \langle C_j^\dagger (\mathbb{1} - N_{j+1}) N_{j+2} (\mathbb{1} - N_{j+3}) N_{j+4} (\mathbb{1} - N_{j+5}) \cdots (\mathbb{1} - N_{j+r-1} C_{j+r} \rangle + \cdots ,\end{aligned} \tag{7.7.9}$$

where we have already dropped terms that would vanish by the nearest-neighbor exclusion rule described in Section 7.4.7. We then use the right-exclusion map rule described in Section 7.4.7 to map the terms in this expansion to noninteracting-spinless-fermion correlations, and the relation (7.4.97) between nearest-neighbor excluded, and nearest-neighbor included expectations, to get

$$\begin{aligned}\frac{\bar{n}_1}{\bar{N}_1}\langle C_j^\dagger C_{j+r}\rangle = \langle c_j^\dagger(\mathbb{1}-n_{j+1})\cdots(\mathbb{1}-n_{j+r-2})c_{j+r-1}\rangle + \\ \langle c_j^\dagger n_{j+1}(\mathbb{1}-n_{j+2})\cdots(\mathbb{1}-n_{j+r-3})c_{j+r-2}\rangle + \cdots + \\ \langle c_j^\dagger n_{j+1}n_{j+2}(\mathbb{1}-n_{j+3})\cdots(\mathbb{1}-n_{j+r-4})c_{j+r-3}\rangle + \cdots .\end{aligned} \tag{7.7.10}$$

The sum of noninteracting spinless fermion expectations are then evaluated numerically using the following algorithm:

1. For each $(0 \le p \le p_{\max})$-intervening-pair expectation, where $p_{\max} = \lfloor (r-2)/2 \rfloor$, we calculate the maximum separation $r_{\max} = r - p$ that can occur in the expectation, and sum over the minors that the p-intervening-pair expectation contributes order by order.

2. For each order $p+1 \le m \le r_{\max} - 1$, we run over all possible indices $1 < j_1 < j_2 < \cdots < j_{m-1} < r_{\max}$, and construct the minors

$$\mathsf{G}^{1\, j_1\, j_2 \cdots j_{m-1}}_{j_1\, j_2 \cdots j_{m-1}\, r_{\max}}. \tag{7.7.11}$$

3. The contribution of $\mathsf{G}^{1\, j_1\, j_2 \cdots j_{m-1}}_{j_1\, j_2 \cdots j_{m-1}\, r_{\max}}$ to $\langle C_j^\dagger C_{j+r}\rangle$ is

$$(-1)^p \binom{m-1}{p} \mathsf{G}^{1\, j_1\, j_2 \cdots j_{m-1}}_{j_1\, j_2 \cdots j_{m-1}\, r_{\max}}. \tag{7.7.12}$$

where $(-1)^p$ accounts for the fact that in the odd-p expansion, all the expectations $\langle c_j^\dagger n_{j_1} \ldots n_{j_{m-1}} c_{j+r_{\max}}\rangle$ are negative of their respective minors $\mathsf{G}^{1\, j_1\, j_2 \cdots j_{m-1}}_{j_1\, j_2 \cdots j_{m-1}\, r_{\max}}$. The binomial coefficient $\binom{m-1}{p}$ accounts for how many times the minor $\mathsf{G}^{1\, j_1\, j_2 \cdots j_{m-1}}_{j_1\, j_2 \cdots j_{m-1}\, r_{\max}}$

appears when we sum over all properly-ordered expectations with p intervening pairs.

4. After summing over the intervening-particle expansion, we multiply the nearest-neighbor included chain result by $\bar{N}_1/\bar{n}_1$ to get the correct numerical value for $\langle C_j^\dagger C_{j+r}\rangle$.

Figure 7.76 shows the numerically-calculated rung-fermion FL correlation $\langle C_j^\dagger C_{j+r}\rangle$ for rung-fermion filling fractions $\bar{N}_1 = 0.20, 0.30$, and 0.40. To determine the correlation exponent as a function of $\bar{N}_1$, we fit the numerical correlations to the asymptotic form $Ar^{-\nu}\cos(kr+\phi)$, over the range $0.02 \leq \bar{N}_1 \leq 0.48$. The fitted parameters are shown in Table 7.16. Figure 7.77 shows the fitted effective wave vector k as a function of the rung-fermion filling fraction $\bar{N}_1$. As expected, this agrees very well with $k = \pi\bar{N}_1 = k_F$.

The plots of the fitted amplitude A against $\bar{N}_1$, and of the correlation exponent ν against $\bar{N}_1$, are shown in Figures 7.78 and 7.79 respectively. As we can see from Figure 7.78, the fitted amplitude A has a maximum at $\bar{N}_1 \approx \frac{1}{3}$ (which corresponds to nearest-neighbor included chain filling fraction $\bar{n}_1 \approx \frac{1}{2}$). The curve fits at low and high $\bar{N}_1$ are not as reliable as those at intermediate $\bar{N}_1$, but it appears that $\lim_{\bar{N}_1\to 0} A > 0$ and $\lim_{\bar{N}_1\to\frac{1}{2}} A = 0$. In Figure 7.79, we see that ν remains close to 1 over a wide range of $\bar{N}_1$, before decreasing rapidly near $\bar{N}_1 = \frac{1}{2}$. In fact, we might be tempted to extrapolate from Figure 7.79, and say that $\lim_{\bar{N}_1\to 0}\nu = 1$ and $\lim_{\bar{N}_1\to\frac{1}{2}}\nu = 0$.

At very low filling fractions, the rung-fermions with infinite nearest-neighbor repulsion behave like noninteracting fermions. In this limit of $\bar{N}_1 \to 0$, we expect therefore that

$$\langle C_j^\dagger C_{j+r}\rangle = \frac{\sin\pi\bar{N}_1 r}{\pi r}. \tag{7.7.13}$$

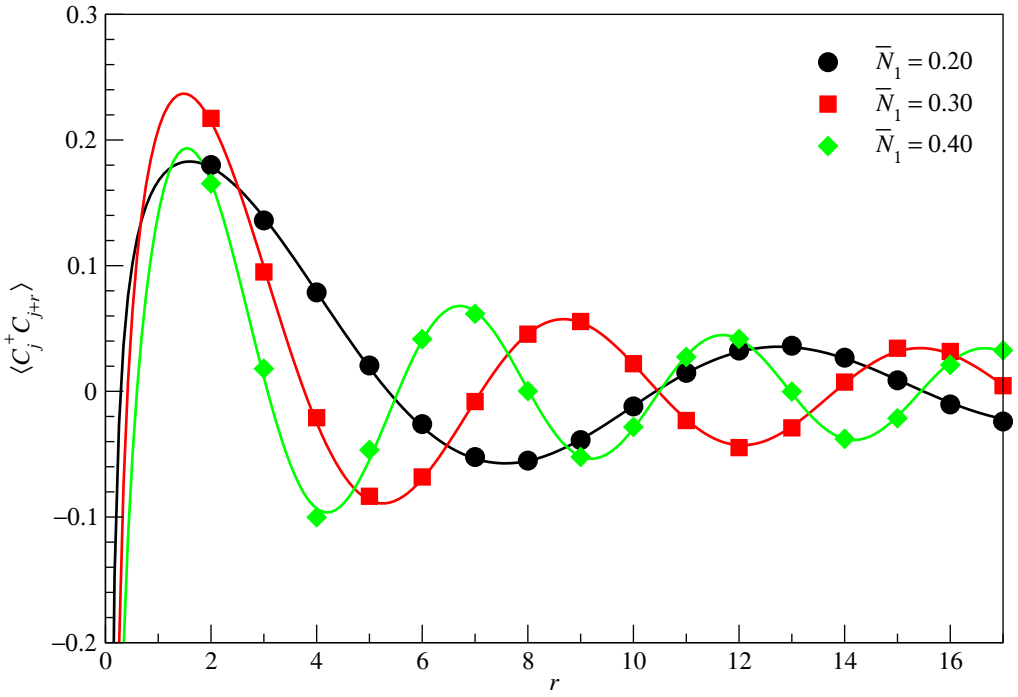

Figure 7.76: The infinite-ladder rung-ground-state spinless fermion FL correlation $\langle C_j^\dagger C_{j+r} \rangle$ as a function of separation $2 \leq r \leq 17$ for rung-fermion filling fractions $\bar{N}_1 = 0.20$ (black circles), 0.30 (red squares), and 0.40 (green diamonds), in the limit $t_\perp / t_\parallel \to \infty$, $t' = 0$. These are fitted to the form $Ar^{-\nu} \cos(kr + \phi)$, to obtain $A = 0.391249$, $k = 0.619877$, $\phi = 4.53458$ and $\nu = 0.939375$ for $\bar{N}_1 = 0.20$ (black curve), $A = 0.401282$, $k = 0.93767$, $\phi = 4.32046$ and $\nu = 0.896843$ for $\bar{N}_1 = 0.30$ (red curve), and $A = 0.287933$, $k = 1.26952$, $\phi = 3.95575$ and $\nu = 0.755978$ for $\bar{N}_1 = 0.40$ (green curve).

Table 7.16: Fitted parameters for a nonlinear curve fit of the rung-ground-state spinless fermion FL correlation to $\langle C_j^\dagger C_{j+r}\rangle = Ar^{-\nu}\cos(kr+\phi)$, for rung-fermion filling fractions over the range $0.02 \leq \bar{N}_1 \leq 0.48$.

$\bar{N}_1$	A	k	ϕ	ν
0.02	0.319872	0.0618325	4.71329	0.99161
0.04	0.310979	0.123523	4.71905	0.968294
0.06	0.304772	0.183837	4.72934	0.93987
0.08	0.313840	0.243376	4.72641	0.932523
0.10	0.336564	0.305143	4.69686	0.949641
0.12	0.355007	0.368680	4.66090	0.959674
0.14	0.364203	0.431323	4.63398	0.953151
0.16	0.372144	0.492560	4.61115	0.945784
0.18	0.383803	0.556102	4.57291	0.946507
0.20	0.391249	0.619877	4.53458	0.939375
0.22	0.396393	0.681898	4.50317	0.930298
0.24	0.402676	0.74564	4.46070	0.926759

(continued on next page)

Table 7.16: (continued)

$\bar{N}_1$	A	k	ϕ	ν
0.26	0.404930	0.810237	4.41342	0.917295
0.28	0.403959	0.873277	4.37151	0.905642
0.30	0.401282	0.93767	4.32046	0.896843
0.32	0.392486	1.00335	4.26073	0.881141
0.34	0.377738	1.06810	4.20164	0.860431
0.36	0.357205	1.13387	4.13313	0.837365
0.38	0.327558	1.20139	4.05023	0.803898
0.40	0.287933	1.26952	3.95575	0.755978
0.42	0.239326	1.33787	3.84784	0.692489
0.44	0.182711	1.40963	3.70334	0.608385
0.46	0.118029	1.48671	3.49089	0.473948
0.48	0.0491102	1.5574	3.20539	0.20731

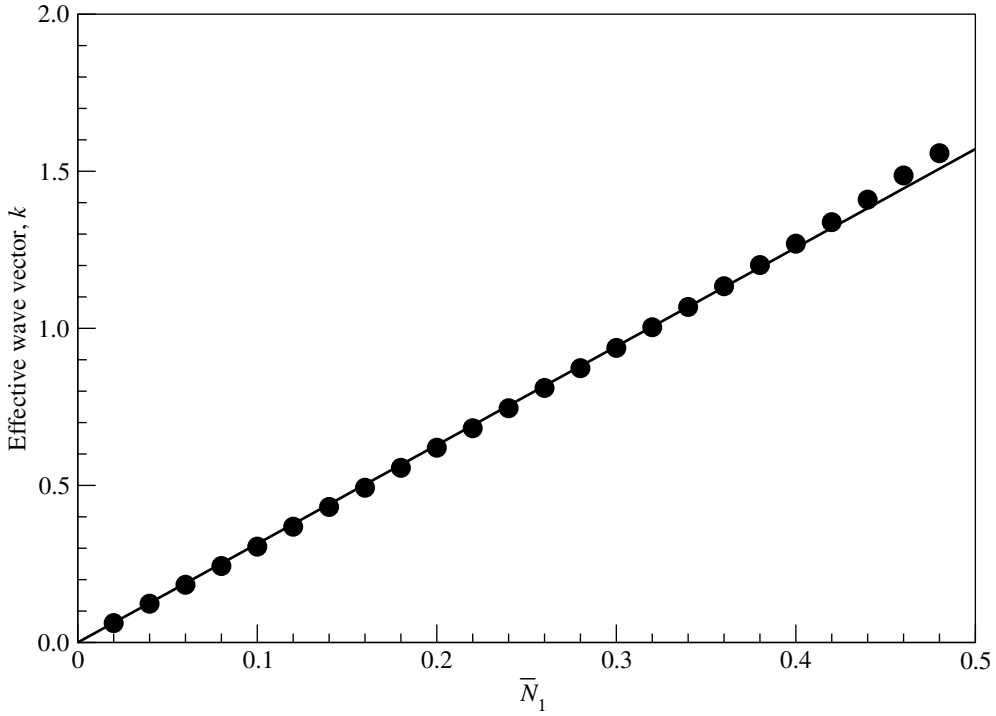

Figure 7.77: The wave vector k, governing the oscillatory behaviour of the rung-fermion FL correlation $\langle C_j^\dagger C_{j+r}\rangle$, as a function of the rung-fermion filling fraction $\bar{N}_1$. The filled circles are numerical values obtained by fitting $\langle C_j^\dagger C_{j+r}\rangle$ to the asymptotic form $Ar^{-\nu}\cos(kr+\phi)$, while the solid line is $k = \pi\bar{N}_1 = k_F$. The data points plotted here are from the four-parameter, (A, ν, k, ϕ), fit to $Ar^{-\nu}\cos(kr+\phi)$, shown in Table 7.16.

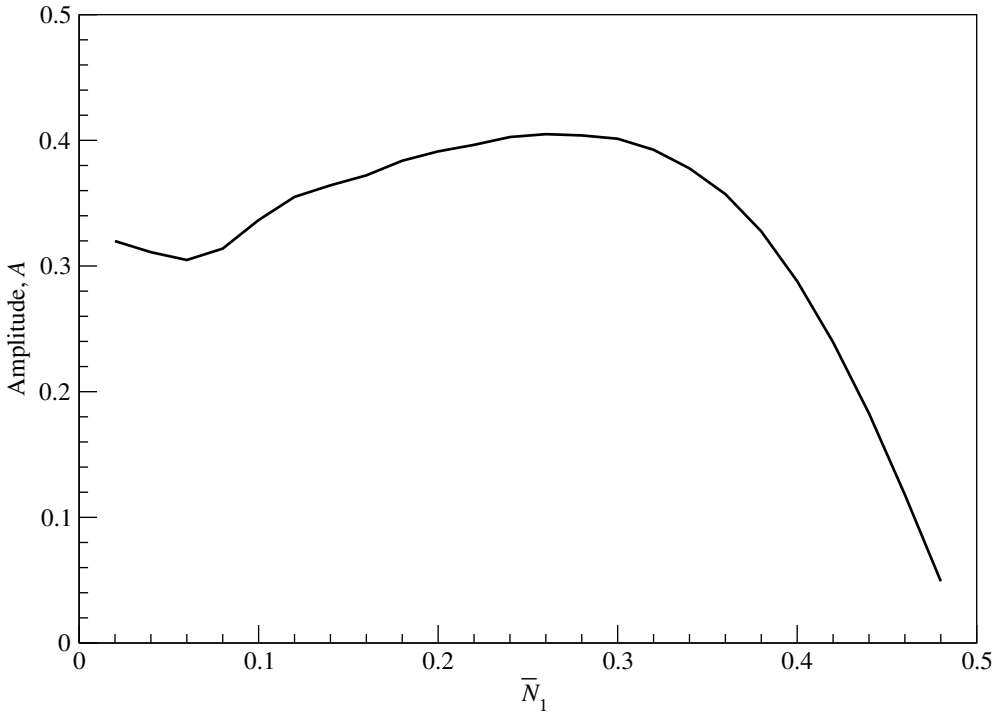

Figure 7.78: The fitted amplitude A of the rung-fermion FL correlation $\langle C_j^\dagger C_{j+r}\rangle$ as a function of the rung-fermion filling fraction $\bar{N}_1$. The data points plotted here are from the four-parameter, (A, ν, k, ϕ), fit to $Ar^{-\nu}\cos(kr+\phi)$, shown in Table 7.16.

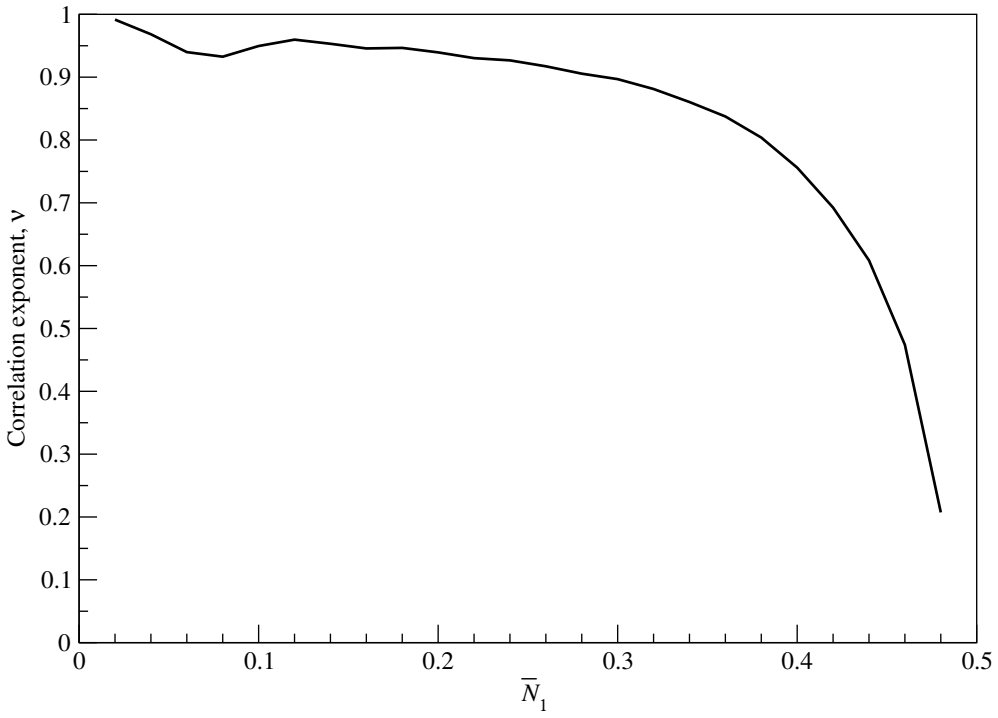

Figure 7.79: The fitted correlation exponent ν of the rung-fermion FL correlation $\langle C_j^\dagger C_{j+r}\rangle$ as a function of the rung-fermion filling fraction $\bar{N}_1$. The data points plotted here are from the four-parameter, (A, ν, k, ϕ), fit to $Ar^{-\nu}\cos(kr+\phi)$, shown in Table 7.16.

From our series of curve fits, we see that in this limit, $k = \pi\bar{N}_1 \to 0$ and $\phi \to \frac{3\pi}{2}$, so that

$$Ar^{-\nu}\cos(kr+\phi) \to Ar^{-\nu}\left[\cos kr\cos\frac{3\pi}{2} - \sin kr\sin\frac{3\pi}{2}\right] = \frac{A}{r^{\nu}}\sin kr. \qquad (7.7.14)$$

Comparing (7.7.13) and (7.7.14), we find that as $\bar{N}_1 \to 0$, we should expect A and ν to go to $\frac{1}{\pi} = 0.31831\ldots$ and 1 respectively. Indeed, from Figures 7.78 and 7.79, we see that this is indeed the case numerically.

As $\bar{N}_1 \to \frac{1}{2}$, we expect the ladder to become more and more congested, and it should therefore be increasingly difficult to annihilate a rung-ground-state fermion on some rung $j+r$, and find an empty rung at j to create a rung-ground-state fermion, without running afoul of the no-nearest-neighbor-occupation constraint. This argument tells us that the amplitude of $\langle C_j^{\dagger}C_{j+r}\rangle$ must vanish as $\bar{N}_1 \to \frac{1}{2}$, which we have indeed observed numerically in Figure 7.78, but it does not tell us whether the correlation should decay slowly or rapidly with increasing separation. In fact, very close to $\bar{N} = \frac{1}{2}$, we expect the ground-state physics of the chain of rung-fermions with infinite nearest-neighbor repulsion to be describable in terms of a low density of holes, as we have done in Section 7.5.7. Naively, we would expect from such a low-density-of-holes argument that $\langle C_j^{\dagger}C_{j+r}\rangle$ decay as r^{-1}. Instead, the nonlinear curve fits at $\bar{N}_1 \lesssim \frac{1}{2}$ tells us that $\nu < 1$, and is looking like it would extrapolate to $\lim_{\bar{N}_1\to\frac{1}{2}}\nu = 0$. Our first reaction to this observation would be that the r^{-1} power law will only become apparent over a length scale $\bar{h}^{-1}$ in terms of the hole density $\bar{h}$. This length scale diverges as $\bar{N}_1 \to \frac{1}{2}$, and consequently, in our numerical fits for $\bar{N}_1$ close to $\frac{1}{2}$, the amplitude of $\langle C_j^{\dagger}C_{j+r}\rangle$ at $r \approx 20$ will not have decayed very much compared to its maximum amplitude at $r \approx 1$, leading the nonlinear curve fitting program to conclude that the correlation exponent is $\nu \to 0$.

Thinking about this nearly-half-filled limit more carefully, we realized that what we called 'holes' are really domain walls separating a region in which the rung-fermions sit on odd rungs, from a region in which the rung-fermions sit on even rungs. The FL

correlation $\langle C_j^\dagger C_{j+r}\rangle$, which can be written as a hole-hole correlation function, then depends on how many holes there are between j and $j+r$. The idea is that, in order to annihilate a hole (create a rung-fermion) at site $j+r$ and create a hole (annihilate a rung-fermion) at site j, we must first find a configuration with a hole at $j+r$. Such a configuration will have rung-fermions at sites $j+r-2$, $j+r-4$, ..., until we encounter another hole at $j+r-2s$, and then the sequence of rung-fermions will thereafter be at sites $j+r-2s-1$, $j+r-2s-3$, dots. If r is even, $\langle C_j^\dagger C_{j+r}\rangle$ receives nonzero contributions only from those configurations with an even number of intervening holes, whereas if r is odd, $\langle C_j^\dagger C_{j+r}\rangle$ receives nonzero contributions only from those configurations with an odd number of intervening holes. This is very similar in flavor to the intervening-particle expansion of the two-point function $\langle b_j^\dagger b_{j+r}\rangle$ of a chain of nearest-neighbor included hard-core bosons, except that $\langle b_j^\dagger b_{j+r}\rangle$ receives positive contributions from configurations with an even number of intervening particles, and negative contributions from an odd number of intervening particles. Therefore, in the limit $\bar{N}_1 \to \frac{1}{2}$, we find that the FL correlation $\langle C_j^\dagger C_{j+r}\rangle$ maps to a string correlation of holes. Bosonization calculations then show that this string correlation of holes decay as a power law, with correlation exponent $\nu = \frac{1}{4}$ [380].

This prompts us to fit the numerical correlations again, this time to the mixed asymptotic form

$$\left[Ar^{-1} + Br^{-\frac{1}{4}}\right]\sin(\pi\bar{N}_1 r + \phi), \tag{7.7.15}$$

where we expect, from the discussions above, that $B \ll A = \frac{1}{\pi}$ and $\phi \to 0$ as $\bar{N}_1 \to 0$, and $B \gg A$ as $\bar{N} \to \frac{1}{2}$. From the table of fitted parameter values in Table 7.17, we find that these expectations indeed hold true. Figure 7.80 shows the fitted amplitudes A and B, and the phase shift ϕ. From Figure 7.80, we see that the fitted phase shift ϕ is indeed the expected $\phi = 0$ in the limit $\bar{N}_1 \to 0$. In the limit of $\bar{N}_1 \to \frac{1}{2}$, however, it is not clear

from Figure 7.80 whether we will have $\lim_{\bar{N}_1 \to \frac{1}{2}} \phi = \frac{\pi}{3}$ or $\lim_{\bar{N}_1 \to \frac{1}{2}} \phi = \frac{\pi}{2}$, or some value in between.

Table 7.17: Fitted parameters for a nonlinear curve fit of the rung-ground-state spinless fermion FL correlation to $\langle C_j^\dagger C_{j+r} \rangle = \left[A r^{-1} + B r^{-\frac{1}{4}} \right] \sin(\pi \bar{N}_1 r + \phi)$, for rung-fermion filling fractions over the range $0.02 \leq \bar{N}_1 \leq 0.48$.

$\bar{N}_1$	A	B	ϕ	visual
0.02	0.316752	0.00092206	0.000264712	perfect
0.04	0.309350	0.0042169	0.00373907	perfect
0.06	0.326479	0.00437132	−0.0175774	very good
0.08	0.358940	−0.000253066	−0.0561948	very good
0.10	0.363555	0.00178964	−0.0771529	very good
0.12	0.373369	0.00259193	−0.106589	very good
0.14	0.383104	0.00312688	−0.136481	very good
0.16	0.387761	0.00547859	−0.16565	very good
0.18	0.394239	0.0070759	−0.199304	very good
0.20	0.400051	0.00854717	−0.232551	very good
0.22	0.402282	0.0112083	−0.266667	very good
0.24	0.404704	0.0132795	−0.303774	very good

(continued on next page)

From Figure 7.80, we also see that the refitted particle-particle two-point function amplitude A has the same behaviour as a function of $\bar{N}_1$ as that shown in Figure 7.78 for the first fit. The hole-hole string correlation function amplitude B is always very small, but dominates over A very close to $\bar{N}_1 = \frac{1}{2}$, since $A \to 0$ in this limit. Therefore, we

Table 7.17: (continued)

$\bar{N}_1$	A	B	ϕ	visual
0.26	0.405452	0.0153261	−0.340835	very good
0.28	0.402282	0.0182126	−0.379891	very good
0.30	0.397195	0.0207073	−0.421611	very good
0.32	0.388021	0.0234571	−0.464728	very good
0.34	0.373122	0.0267653	−0.51125	very good
0.36	0.352153	0.0302453	−0.561171	very good
0.38	0.322302	0.034518	−0.615952	very good
0.40	0.283433	0.0388467	−0.676746	good
0.42	0.23084	0.0444672	−0.743953	good
0.44	0.162865	0.0508476	−0.826156	good
0.46	0.0856433	0.05388	−0.92847	good
0.48	−0.00472032	0.0534476	−1.08276	good

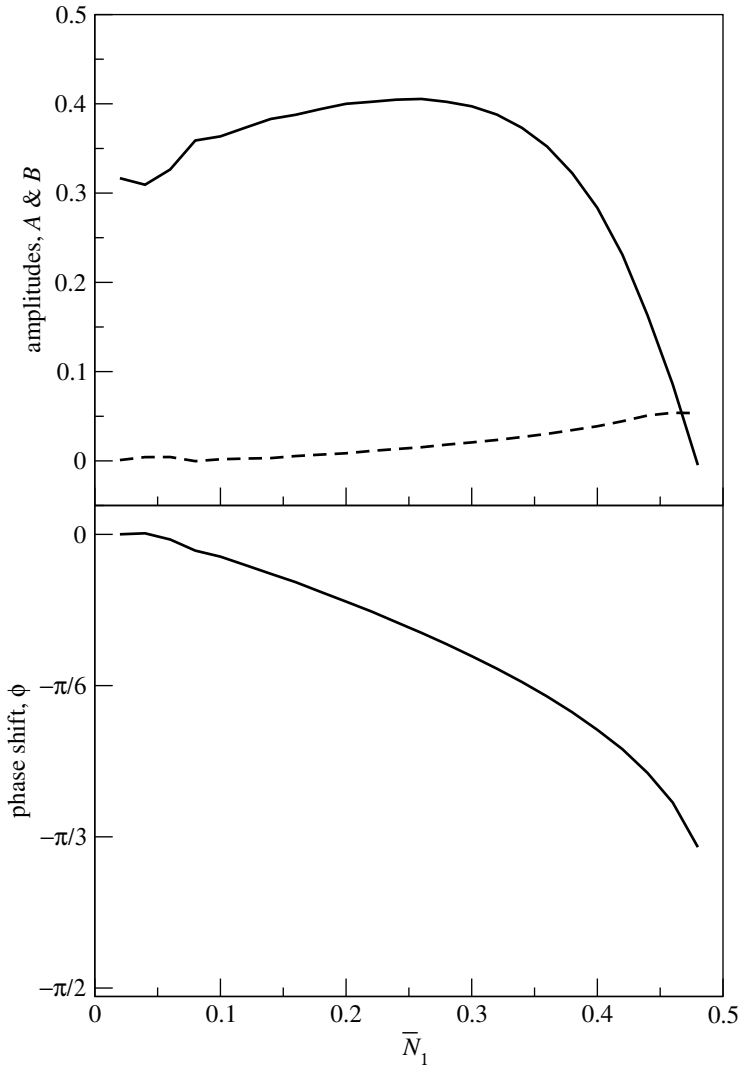

Figure 7.80: The fitted amplitudes A (solid curve, top) and B (dashed curve, top) and phase shift ϕ (black solid curve, bottom) of the rung-fermion FL correlation $\langle C_j^\dagger C_{j+r}\rangle$ as a function of the rung-fermion filling fraction $\bar{N}_1$. The data points plotted here are from the three-parameter, (A, B, ϕ), fit to (7.7.15), shown in Table 7.17.

can now explain the variable correlation exponent ν in terms of the interplay between two power laws with universal correlation exponents. In fact, the numerical correlations calculated at low filling fractions is consistent with a particle-particle two-point function exponent of $\nu = 1$, which suggests that the rung-fermion ground state is a Fermi liquid, in the strong inter-leg hopping limit.

7.7.3 Charge-Density-Wave Correlation

In the special case of a quarter-filled ladder in the limit of $t_\perp \gg t_\parallel$, $t' = 0$, the rung-fermion CDW correlation $\langle N_j N_{j+r} \rangle$ is the only non-vanishing correlation. In fact,

$$\langle N_j N_{j+r} \rangle = \begin{cases} \frac{1}{2}, & r \text{ even;} \\ 0, & r \text{ odd,} \end{cases} \tag{7.7.16}$$

is an oscillatory function with an amplitude that does not decay with separation r, i.e. there is true long-range order in the quarter-filled ladder ground state in the limit of $t_\perp \gg t_\parallel$, $t' = 0$.

Below quarter-filling, we expect no such true long-range order, and the rung-fermion CDW correlation $\langle N_j N_{j+r} \rangle$ ought to decay as a power law in r. This correlation can again be written as an intervening-particle expansion,

$$\begin{aligned} \langle N_j N_{j+r} \rangle = \langle N_j (\mathbb{1} - N_{j+1}) \cdots (\mathbb{1} - N_{j+r-1}) N_{j+r} \rangle + \\ \langle N_j (\mathbb{1} - N_{j+1}) N_{j+2} (\mathbb{1} - N_{j+3}) \cdots (\mathbb{1} - N_{j+r-1}) N_{j+r} \rangle + \cdots , \end{aligned} \tag{7.7.17}$$

and thereafter each term in the expansion can be mapped to expectations of a chain of noninteracting spinless fermions, using the rules described in Section 7.4.7, and (7.4.97),

to get

$$\frac{\bar{n}_1}{\bar{N}_1}\langle N_j N_{j+r}\rangle = \langle n_j(\mathbb{1}-n_{j+1})\cdots(\mathbb{1}-n_{j+r-2})n_{j+r-1}\rangle + \\ \langle n_j n_{j+1}(\mathbb{1}-n_{j+2})\cdots(\mathbb{1}-n_{j+r-3})n_{j+r-2}\rangle + \cdots + \\ \langle n_j n_{j+1}\cdots n_{j+p_{\max}} n_{j+r-p_{\max}-1}\rangle\,. \tag{7.7.18}$$

This sum over noninteracting-spinless-fermion expectations is then evaluated using the following algorithm:

1. For each $(0 \le p \le p_{\max})$-intervening-pair expectation, where $p_{\max} = \lfloor (r-2)/2 \rfloor$, we calculate the maximum separation $r_{\max} = r - p$ that can occur in the expectation, and sum over the minors it contribute order by order.

2. For each order $p+2 \le m \le r_{\max}$, we run over all possible indices $1 < j_1 < j_2 < \cdots < j_{m-2} < r_{\max}$, and construct the minors

$$\mathsf{G}^{1\,j_1\,j_2\cdots j_{m-2}\,r_{\max}}_{1\,j_1\,j_2\cdots j_{m-2}\,r_{\max}}. \tag{7.7.19}$$

3. The contribution of $\mathsf{G}^{1\,j_1\,j_2\cdots j_{m-2}\,r_{\max}}_{1\,j_1\,j_2\cdots j_{m-2}\,r_{\max}}$ to $\langle C_j^\dagger C_{j+r}\rangle$ is

$$(-1)^{p+m}\binom{m-2}{p}\mathsf{G}^{1\,j_1\,j_2\cdots j_{m-2}\,r_{\max}}_{1\,j_1\,j_2\cdots j_{m-2}\,r_{\max}}. \tag{7.7.20}$$

   where $(-1)^{p+m}$ accounts for the relative sign in the expansion between the noninteracting-spinless-fermion expectations $\langle c_j^\dagger n_{j_1}\ldots n_{j_{m-2}} c_{j+r_{\max}}\rangle$ and their respective minors $\mathsf{G}^{1\,j_1\,j_2\cdots j_{m-2}\,r_{\max}}_{1\,j_1\,j_2\cdots j_{m-2}\,r_{\max}}$. The binomial coefficient $\binom{m-2}{p}$ accounts for how many times the minor $\mathsf{G}^{1\,j_1\,j_2\cdots j_{m-2}\,r_{\max}}_{1\,j_1\,j_2\cdots j_{m-2}\,r_{\max}}$ appears when we sum over all properly-ordered expectations with p intervening pairs.

4. After summing over the intervening-particle expansion, we multiply the nearest-neighbor included chain result by $\bar{N}_1/\bar{n}_1$ to get the correct numerical value for $\langle N_j N_{j+r}\rangle$.

Figure 7.81 shows the numerically-calculated subtracted rung-fermion CDW correlation $\langle N_j N_{j+r}\rangle - \langle N_j\rangle \langle N_{j+r}\rangle$ for rung-fermion filling fractions $\bar{N}_1 = 0.20$, 0.30, and 0.40. To determine the correlation exponent as a function of $\bar{N}_1$, we perform a preliminary fit of the numerical correlations to the asymptotic form

$$\langle N_j N_{j+r}\rangle - \langle N_j\rangle \langle N_{j+r}\rangle = A r^{-\alpha} \cos(kr + \phi), \tag{7.7.21}$$

over the range of rung-fermion filling fractions $0.02 \leq \bar{N}_1 \leq 0.48$. The fitted parameters are shown in Table 7.18.

Table 7.18: Fitted parameters for a nonlinear curve fit of the rung-fermion subtracted CDW correlation $\langle N_j N_{j+r}\rangle - \langle N_j\rangle \langle N_{j+r}\rangle$ to the asymptotic form $A r^{-\alpha} \cos(kr + \phi)$, for rung-fermion filling fractions over the range $0.04 \leq \bar{N}_1 \leq 0.48$.

$\bar{N}_1$	A	k	ϕ	α
0.04	0.012650	0.164737	1.51703	1.12019
0.08	0.110968	0.343635	1.11765	2.07940
0.12	0.138333	0.658280	0.697320	2.16809
0.16	0.120281	0.975711	0.391302	1.93918
0.20	0.094414	1.25004	0.300512	1.55826
0.24	0.085395	1.49978	0.306820	1.25413
0.28	0.087523	1.74654	0.329155	1.02884
0.32	0.100179	1.99221	0.358140	0.871369
0.36	0.127371	2.24095	0.371215	0.772430
0.40	0.170081	2.49325	0.349978	0.686957
0.44	0.223402	2.74868	0.307780	0.579965
0.48	3.485040	3.14710	1.494010	0.094941

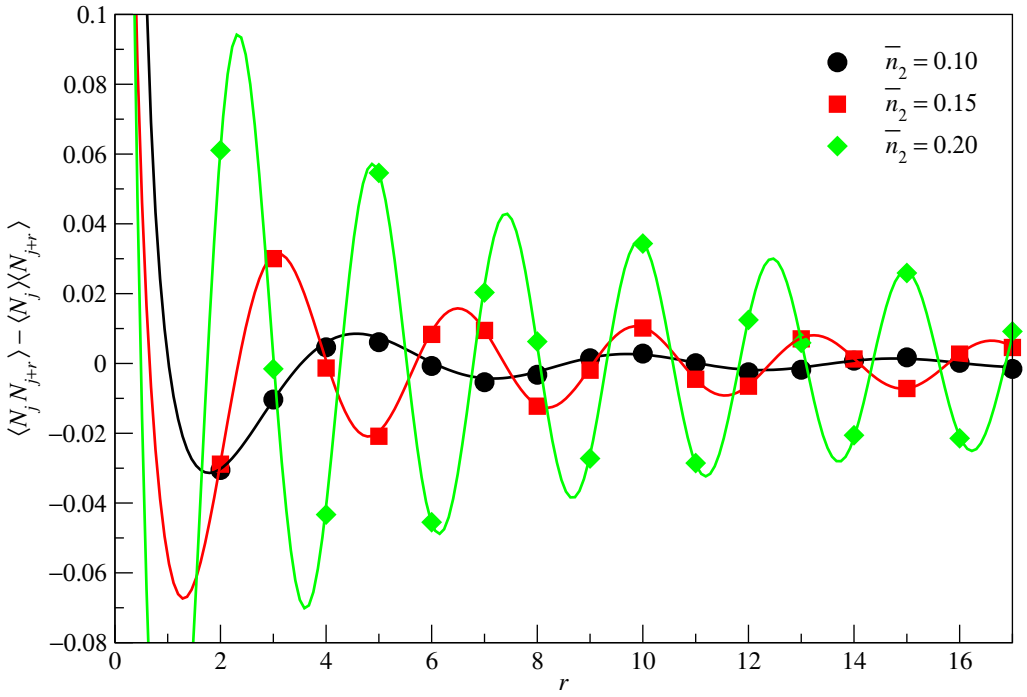

Figure 7.81: Plot of the infinite-ladder rung-fermion subtracted CDW correlation $\langle N_j N_{j+r}\rangle - \langle N_j\rangle \langle N_{j+r}\rangle$ as a function of separation $2 \leq r \leq 17$ for rung-fermion filling fractions $\bar{N}_1 = 0.20$ (black circles), 0.30 (red squares), and 0.40 (green diamonds), in the limit $t_\perp/t_\parallel \to \infty$, $t' = 0$. These are fitted to the asymptotic form $Ar^{-\alpha}\cos(kr+\phi)$, to obtain $A = 0.0944142$, $k = 1.25004$, $\phi = 0.300512$ and $\alpha = 1.55826$ for $\bar{N}_1 = 0.20$ (black curve), $A = 0.0924823$, $k = 1.86949$, $\phi = 0.343557$ and $\alpha = 0.943191$ for $\bar{N}_1 = 0.30$ (red curve), and $A = 0.170081$, $k = 2.49325$, $\phi = 0.349978$ and $\alpha = 0.686957$ for $\bar{N}_1 = 0.40$ (green curve).

While peforming this series of nonlinear curve fits, we found that compared to the fits at intermediate rung-fermion filling fractions, the fits at the lower rung-fermion filling fractions, up to around $\bar{N}_1 = 0.16$ or so, and at the highest rung-fermion filling fraction $\bar{N}_1 = 0.48$, are not as reliable. For $\bar{N}_1 = 0.48$, the fitted wave vector k converges very rapidly to the value of 3.14710, but the fitted amplitude A and fitted phase ϕ continues to run to larger and larger values, while the fitted exponent α drifts as this happens. Therefore, only the fitted wave vector k is reliable at $\bar{N}_1 = 0.48$. At the lowest rung-fermion filling fractions, the nonlinear curve fits are not reliable for a different reason. The separations of up to $r = 17$ are small compared to the effective oscillation wave length k^{-1}, and as such the asymptotic form $Ar^{-\alpha}\ \cos(kr+\phi)$ is not yet a good description of the subtracted CDW correlation $\langle N_j N_{j+r}\rangle - \langle N_j\rangle \langle N_{j+r}\rangle$. In fact, the oscillations in $\langle N_j N_{j+r}\rangle - \langle N_j\rangle \langle N_{j+r}\rangle$ are not yet strictly about a zero average. Thus, none of the fitted parameters are reliable for $\bar{N}_1 < 0.16$.

Figure 7.82 shows the expected $k = 2\pi\bar{N}_1 = 2k_F$ dependence of the effective wave vector k on rung-fermion filling fraction $\bar{N}_1$. In the Luttinger-liquid literature, the Luttinger-liquid CDW correlation is also known to contain a $4k_F$ modulation term, whose amplitude is known to be frequently much smaller than the $2k_F$ modulation term. From (7.2.1), we see that the $4k_F$-CDW correlation exponent becomes smaller than the $2k_F$-CDW correlation exponent, when $K_\rho < \frac{1}{3}$. We have not tried to fit the numerical correlations to an asymptotic form containing such a term, since the inclusion of such a term will make the nonlinear curve fitting of the CDW correlation much more difficult.

In Figure 7.83, we see that the fitted correlation exponent α decreases from a value close to $\alpha = 2$ at low rung-fermion filling fraction $\bar{N}_1$ to a value close to $\alpha = 0$ just below half-filling of rung-fermions. At very low densities, with $\bar{N}_1 \ll 1$, we expect the rung-fermions to behave like noninteracting fermions, and as such the CDW correlation

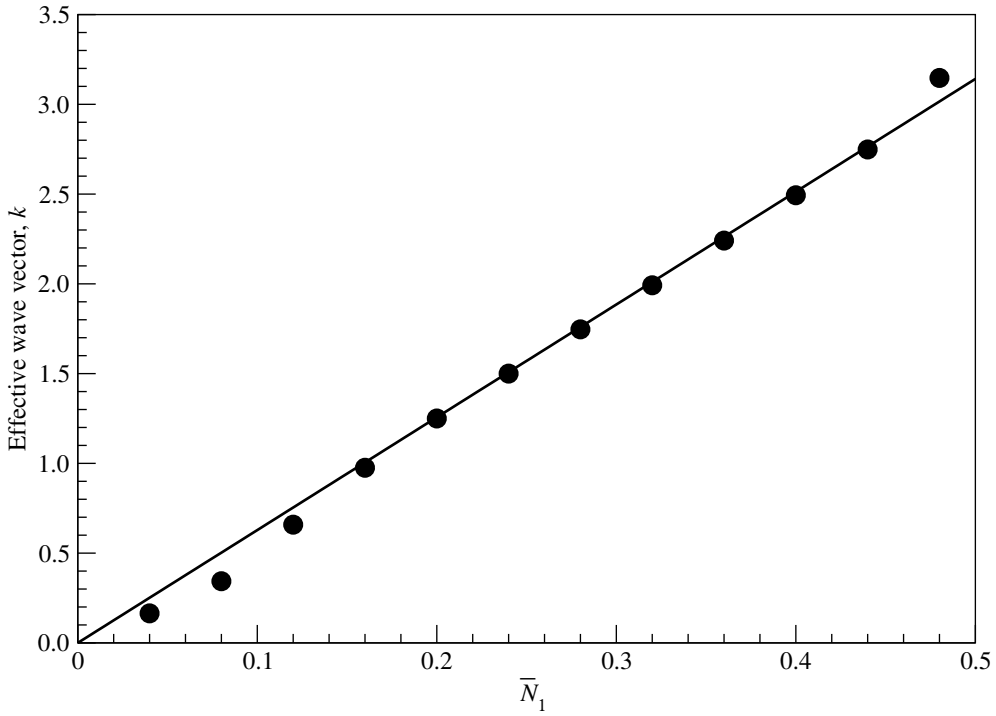

Figure 7.82: Plot of the effective wave vector k of the rung-ground-state fermion subtracted CDW correlation $\langle N_j N_{j+r}\rangle - \langle N_j\rangle \langle N_{j+r}\rangle$ as a function of the rung-fermion filling fraction $\bar{N}_1$. The filled circles are the values of k obtained from curve fits of the numerical values of $\langle N_j N_{j+r}\rangle - \langle N_j\rangle \langle N_{j+r}\rangle$ to the asymptotic form $Ar^{-\alpha}\cos(kr+\phi)$, while the solid line is $k = 2\pi\bar{N}_1 = 2k_F$. The data points plotted here are from the four-parameter, (A, α, k, ϕ), fit to $Ar^{-\alpha}\cos(kr+\phi)$ shown in Table 7.18.

exponent should be exactly $\alpha = 2$. At $\bar{N}_1 = \frac{1}{2}$, when the ladder is quarter-filled, we have true long-range CDW order, and thus the correlation exponent should be exactly $\alpha = 0$. However, we believe that this is a singular limit, in the sense that if we approach $\bar{N}_1 = \frac{1}{2}$ from below, the correlation exponent α will be nonzero, even for $\bar{N}_1$ infinitesimally smaller than $\frac{1}{2}$. Lest this argument appear to go against the behaviour of α shown in Figure 7.83, let us remind ourselves that the results in Section 7.7.2 for the FL correlation suggests strongly that the rung-fermion ground state at hand is a Fermi liquid, and thus should have universal correlation exponents.

Why then does our fitted correlation exponent α show strong $\bar{N}_1$ dependence, if the rung-fermion ground state is indeed a Fermi liquid with universal exponents? Just as for the FL correlation, we need to again think hard about the hole physics of the rung-fermion ground state very close to half-filling. In this limit, the CDW correlation $\langle N_j N_{j+r} \rangle$ can be written in terms of the hole-density-hole-density correlation $\langle P_j P_{j+r} \rangle$, where $P_j = \mathbb{1} - N_j$ is the rung-hole occupation number operator on rung j. Using an argument similar to the one used for the FL correlation $\langle C_j^\dagger C_{j+r} \rangle$ near half-filling, we realized that if r is even, $\langle P_j P_{j+r} \rangle$ receives nonzero contribution from configurations with an even number of intervening holes, whereas if r is odd, $\langle P_j P_{j+r} \rangle$ receives nonzero contribution from configurations with an odd number of intervening holes. This means that our hole-density-hole-density correlation $\langle P_j P_{j+r} \rangle$ must be mapped to a string correlation of a chain of noninteracting spinless fermions. Bosonization calculations tell us that this string correlation decays as a power law with correlation exponent $\alpha = \frac{1}{2}$ [380].

With this insight, we re-did the nonlinear curve fit of the subtracted CDW correlation, this time to the mixed asymptotic form

$$A r^{-2} + B r^{-2} \cos(2\pi \bar{N}_1 r + \phi_1) + C r^{-\frac{1}{2}} \cos(2\pi \bar{N}_1 r + \phi_2). \tag{7.7.22}$$

In the limit of $\bar{N}_1 \to 0$, we expect $C \ll |A| = B = \frac{1}{2\pi^2} = 0.050661\ldots$ and $\phi_1 = 0$,

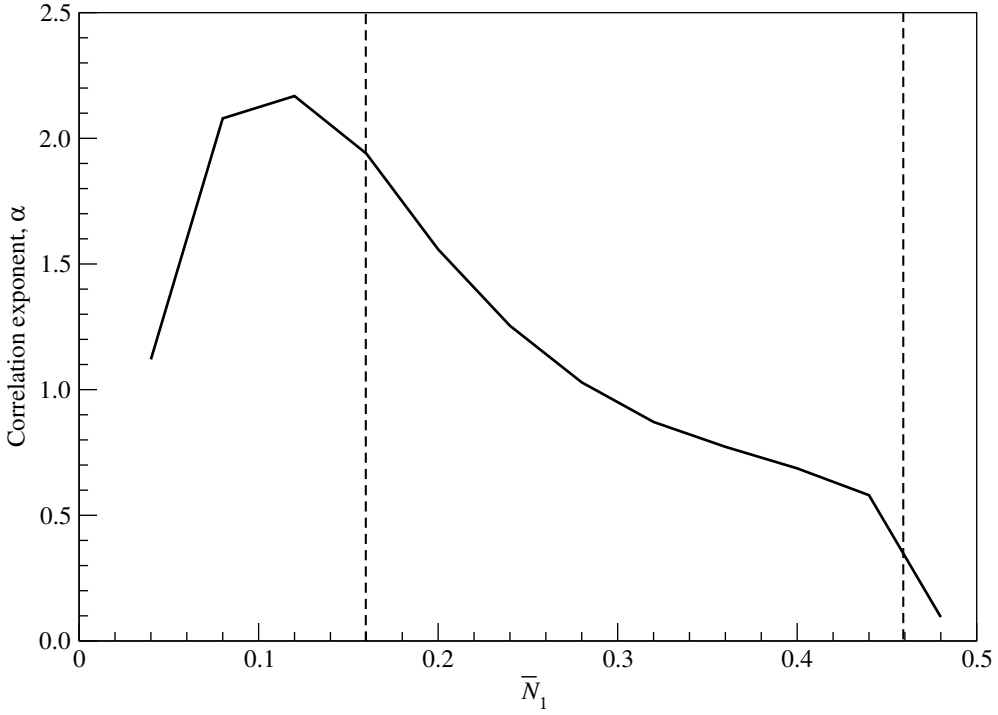

Figure 7.83: Plot of the correlation exponent α of the rung-ground-state fermion subtracted CDW correlation $\langle N_j N_{j+r}\rangle - \langle N_j\rangle \langle N_{j+r}\rangle$ as a function of the rung-fermion filling fraction $\bar{N}_1$. The black solid line connects the values of k obtained from curve fits of the numerical values of $\langle N_j N_{j+r}\rangle - \langle N_j\rangle \langle N_{j+r}\rangle$ to the asymptotic form $Ar^{-\alpha}\cos(kr+\phi)$. The correlation exponents between the two dashed lines are believed to have been obtained reliably from the nonlinear curve fits. The data points plotted here are from the four-parameter, (A, α, k, ϕ), fit to $Ar^{-\alpha}\cos(kr+\phi)$ shown in Table 7.18.

whereas in the limit of $\bar{N}_1 \to \frac{1}{2}$, we expect $C \gg A, B$, if the limit $\bar{N}_1 = \frac{1}{2}$ is not a singular limit. The fitted parameters are shown in Table 7.19. Indeed, in the limit of $\bar{N}_1 \to 0$, we find that $|A| \approx B \approx \frac{1}{2\pi^2}$, $\phi_1 \approx 0$, and $C \ll |A|, B$.

Table 7.19: Fitted parameters for a nonlinear curve fit of the rung-fermion subtracted CDW correlation $\langle N_{+,j} N_{+,j+r} \rangle - \langle N_{+,j} \rangle \langle N_{+,j+r} \rangle$ to the asymptotic form $Ar^{-2} + Br^{-2} \cos(2\pi \bar{N}_1 r + \phi_1) + Cr^{-\frac{1}{2}} \cos(2\pi \bar{N}_1 r + \phi_2)$, for rung-fermion filling fractions over the range $0.04 \leq \bar{N}_1 \leq 0.48$, and over the range of separations $4 \leq r \leq 17$.

$\bar{N}_1$	A	B	ϕ_1	C	ϕ_2	visual
0.04	−0.049770	0.050157	0.020577	0.000164	0.944409	perfect
0.08	−0.039371	0.060621	0.225813	0.000611	0.151529	perfect
0.12	−0.032928	0.070331	0.325290	0.001668	0.119271	very good
0.16	−0.031685	0.097602	0.490253	0.003345	−0.013424	very good
0.20	−0.036003	0.140777	0.422015	0.005574	0.035576	very good
0.24	−0.037089	0.161843	0.411937	0.010986	0.099372	good
0.28	−0.027037	0.221812	0.561288	0.019423	0.029246	very good
0.32	−0.011588	0.296616	0.438759	0.032219	0.075323	very good
0.36	−0.007801	0.283726	0.557881	0.058857	0.077459	very good
0.40	−0.020932	0.431791	0.816552	0.097989	0.034052	very good
0.44	−0.035278	0.374584	0.928121	0.176053	0.081982	perfect
0.48	−0.005552	0.732127	2.536600	0.408623	0.134526	perfect

Since we have true long-range order at $\bar{N}_1 = \frac{1}{2}$, we were expecting the CDW correlation $Ar^{-2} + Br^{-2} \cos(2\pi \bar{N}_1 r + \phi_1)$ to vanish, and the CDW string correlation $Cr^{-\frac{1}{2}} \cos(2\pi \bar{N}_1 r + \phi_2)$ to become large, and eventually become separation-independent

right at $\bar{N}_1 = \frac{1}{2}$. However, from the nonlinear curve fits of the numerical correlations, we find instead the amplitude A going to zero as $\bar{N}_1 \to \frac{1}{2}$, but the amplitudes B and C both becoming large. From Figure 7.84, we find the graph of B and C as functions of $\bar{N}_1$ extrapolating to

$$\lim_{\bar{N}_1 \to \frac{1}{2}} B = 1, \quad \lim_{\bar{N}_1 \to \frac{1}{2}} C = \frac{1}{2}. \tag{7.7.23}$$

We find also that ϕ_2 might be universally zero.

From Figure 7.84, we see one other rather unexpected behaviour of the amplitude B and the phase shift ϕ_1 as functions of $\bar{N}_1$: that they oscillate strongly with the rung-fermion filling fraction $\bar{N}_1$. To ascertain whether these oscillations are a numerical artefact of the nonlinear curve fitting, or results of genuine physics, we would need to compute the numerical correlations over a finer mesh of filling fractions, and perform more curve fits.

7.7.4 Superconducting Correlations

For a quarter-filled ladder in the limit $t_\perp \gg t_\parallel$, $t' = 0$, all rung-fermion SC correlations are identically zero. The argument is similar to that for FL correlations: every other rung of the ladder is occupied, and none of the empty rungs can be further occupied. Therefore, if we annihilate two rung-fermions, we can create two rung-fermions nowhere else.

Now let us calculate SC correlations $\langle \Delta_j^\dagger \Delta_{j+r} \rangle$ for ladder filling fractions $\bar{N}_1 < \frac{1}{2}$. The simplest nontrivial ladder pairing operator we can construct in this limit of $t_\perp \gg t_\parallel$, $t' = 0$, is

$$\Delta_j^\dagger = C_j^\dagger C_{j+2}^\dagger, \tag{7.7.24}$$

since it is not possible to have rung-fermions on adjacent rungs. Again, we start by writing the intervening-particle expansion of the negative of the rung-fermion SC cor-

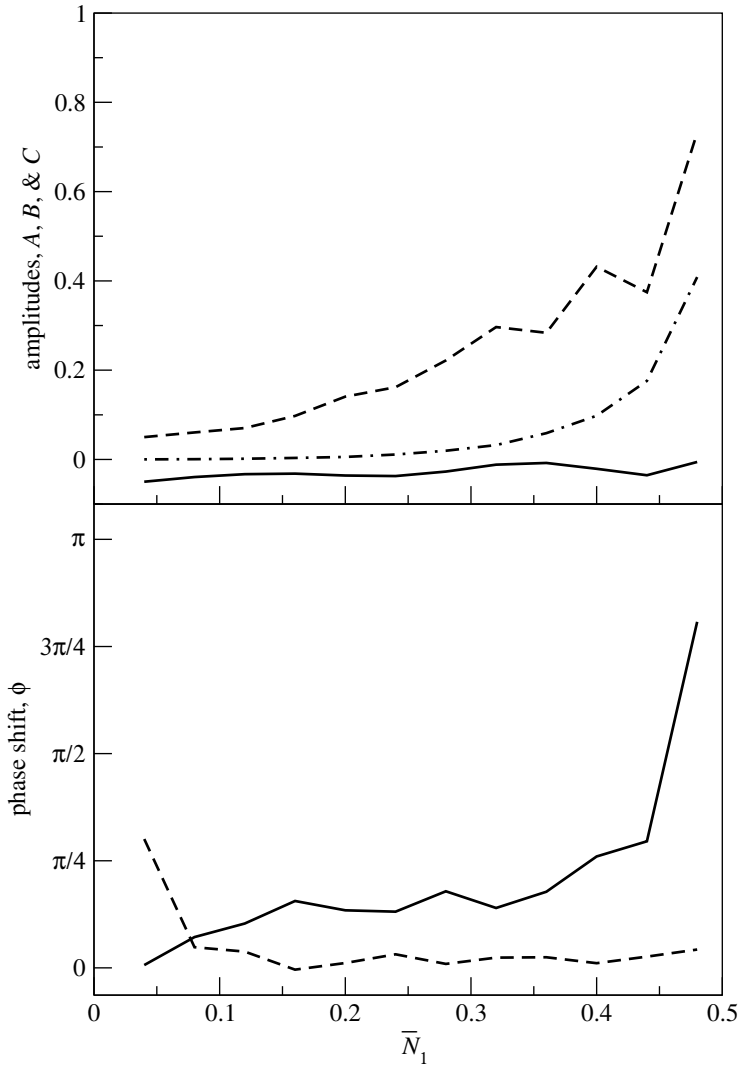

Figure 7.84: The fitted amplitudes A (solid curve, top), B (dashed curve, top) and C (dotted-dashed curve, top), and the fitted phase shifts ϕ_1 (solid curve, bottom) and ϕ_2 (dashed curve, bottom) of the rung-ground-state fermion subtracted CDW correlation $\langle N_j N_{j+r}\rangle - \langle N_j\rangle\langle N_{j+r}\rangle$ as a function of the rung-fermion filling fraction $\bar{N}_1$. The data points plotted here are from the five-parameter, $(A, B, \phi_1, C, \phi_2)$, fit to (7.7.22), shown in Table 7.19.

relation, $-\langle\Delta_j^\dagger\Delta_{j+r}\rangle = -\langle C_j^\dagger C_{j+2}^\dagger C_{j+r+2}C_{j+r}\rangle = \langle C_j^\dagger C_{j+2}^\dagger C_{j+r}C_{j+r+2}\rangle$ as an intervening-particle expansion,

$$\begin{aligned}
&\langle C_j^\dagger C_{j+2}^\dagger(\mathbb{1}-N_{j+3})\cdots(\mathbb{1}-N_{j+r-1})C_{j+r}C_{j+r+2}\rangle + \\
&\langle C_j^\dagger C_{j+2}^\dagger(\mathbb{1}-N_{j+3})N_{j+4}(\mathbb{1}-N_{j+5})\cdots(\mathbb{1}-N_{j+r-1})C_{j+r}C_{j+r+2}\rangle + \\
&\langle C_j^\dagger C_{j+2}^\dagger(\mathbb{1}-N_{j+3})\cdots N_{j+r-2}(\mathbb{1}-N_{j+r-1})C_{j+r}C_{j+r+2}\rangle + \cdots ,
\end{aligned} \tag{7.7.25}$$

and then map each term in the expansion to a corresponding noninteracting spinless fermion expectation. Using the rules described in Section 7.4.7, and (7.4.97), we find this to be

$$\begin{aligned}
-\frac{\bar{n}_1}{\bar{N}_1}\langle\Delta_j^\dagger\Delta_{j+r}\rangle = &\langle c_j^\dagger c_{j+1}^\dagger(\mathbb{1}-n_{j+2})\cdots(\mathbb{1}-n_{j+r-3})c_{j+r-2}c_{j+r-1}\rangle + \\
&\langle c_j^\dagger c_{j+1}^\dagger n_{j+2}(\mathbb{1}-n_{j+3})\cdots(\mathbb{1}-n_{j+r-3})c_{j+r-2}c_{j+r-1}\rangle + \cdots .
\end{aligned} \tag{7.7.26}$$

We calculate this sum of noninteracting-spinless-fermion expectations using the following algorithm:

1. For each $(0 \le p \le p_{\max})$-intervening-pair expectation, where $p_{\max} = \lfloor (r-3)/2 \rfloor$, we calculate the maximum separation $r_{\max} = r - p - 1$ that can occur in the expectation, and sum over the minors it contribute order by order.

2. For each order $p+2 \le m \le r_{\max}-1$, we run over all possible indices $1 < j_1 < j_2 < \cdots < j_{m-2} < r_{\max}$, and construct the minors

$$\mathsf{G}^{12 j_1 j_2 \cdots j_{m-2}}_{j_1 j_2 \cdots j_{m-2} r_{\max}(r_{\max}+1)}. \tag{7.7.27}$$

3. The contribution of $\mathsf{G}^{12 j_1 j_2 \cdots j_{m-2}}_{j_1 j_2 \cdots j_{m-2} r_{\max}(r_{\max}+1)}$ to $-\langle\Delta_j^\dagger\Delta_{j+r}\rangle$ is

$$(-1)^{p+m}\binom{m-2}{p}\mathsf{G}^{12 j_1 j_2 \cdots j_{m-2}}_{j_1 j_2 \cdots j_{m-2} r_{\max}(r_{\max}+1)}, \tag{7.7.28}$$

where $(-1)^{p+m}$ accounts for the relative sign in the expansion between the noninteracting-spinless-fermion expectations $\langle c_j^\dagger c_{j+1}^\dagger n_{j_1}\ldots n_{j_{m-2}}c_{j+r_{\max}}c_{j+r_{\max}+1}\rangle$ and their

respective minors $\mathsf{G}^{12j_1j_2\cdots j_{m-2}}_{j_1j_2\cdots j_{m-2}r_{\max}(r_{\max}+1)}$. The binomial coefficient $\binom{m-2}{p}$ accounts for how many times the minor $\mathsf{G}^{12j_1j_2\cdots j_{m-2}}_{j_1j_2\cdots j_{m-2}r_{\max}(r_{\max}+1)}$ appears when we sum over all properly-ordered expectations with p intervening pairs.

4. After summing over the intervening-particle expansion, we multiply the nearest-neighbor included chain result by $\bar{N}_1/\bar{n}_1$ to get the correct numerical value for $\langle N_j N_{j+r}\rangle$.

For a Fermi liquid, the SC correlation is

$$\langle \Delta_j^\dagger \Delta_{j+r}\rangle = \langle c_{j+1}^\dagger c_j^\dagger c_{j+r}c_{j+r+1}\rangle = -\begin{vmatrix} \langle c_{j+1}^\dagger c_{j+r}\rangle & \langle c_{j+1}^\dagger c_{j+r+1}\rangle \\ \langle c_j^\dagger c_{j+r}\rangle & \langle c_j^\dagger c_{j+r+1}\rangle \end{vmatrix}. \tag{7.7.29}$$

In the limit of large separation $r \to \infty$, this Fermi-liquid SC correlation is proportional to

$$g^2(r) = \frac{\sin^2 \bar{n}\pi r}{\bar{n}^2\pi^2 r^2} = \frac{1}{2\bar{n}^2\pi^2 r^2}\left[1 - \cos 2\bar{n}\pi r\right]. \tag{7.7.30}$$

If we write this in the form of

$$\langle \Delta_j^\dagger \Delta_{j+r}\rangle = Ar^{-\beta} + Br^{-\gamma}\cos(kr+\phi), \tag{7.7.31}$$

the exponents β and γ would both be equal to 2.

For a more general Luttinger liquid, we do not expect the two exponents to be the same. In fact, if we think of the oscillatory part of $\langle \Delta_j^\dagger \Delta_{j+r}\rangle$ to be contributed by the CDW order in the ground state, we ought to have $\gamma = \alpha$. For a Luttinger liquid, the duality between the CDW and SC correlation exponents means that $\beta = 1/\alpha$. Therefore, if the ladder ground state in this limit of $t_\perp \gg t_\parallel$, $t' = 0$, exhibits Luttinger liquid behaviour, we would expect to see the fitted values of β decreasing when the fitted values of γ are increasing, and vice versa.

Fitting the numerical values of $-\langle\Delta_j^\dagger\Delta_{j+r}\rangle$ to the asymptotic form in (7.7.31) presents two technical difficulties. Our first difficulty is that the nonlinear curve fitting functionality in xmgrace has difficulty fitting a sum of two power laws with independent amplitudes and exponents, as a result of the least square function used to perform the nonlinear curve fitting not having a well-defined minimum in the space spanned by the four power-law parameters. Our second difficulty is due to $-\langle\Delta_j^\dagger\Delta_{j+r}\rangle$ decaying too rapidly, so that its value is already very small for separations of $r \approx 10$. Therefore, the nonlinear curve fitting functionality will report a good fit even if the fitted function is not tracking the behaviour of $-\langle\Delta_j^\dagger\Delta_{j+r}\rangle$ at larger r, which is the regime of separations we are most interested in.

To overcome the second difficulty, we do what we have done in Section 7.6.4, and perform nonlinear curve fitting on $-r^2\langle\Delta_j^\dagger\Delta_{j+r}\rangle$ instead of $-\langle\Delta_j^\dagger\Delta_{j+r}\rangle$. This reweighting of the data points for larger r can be more or less justified by the argument that, if we were calculating $\langle\Delta_j^\dagger\Delta_{j+r}\rangle$ for a Fermi liquid, in which the correlation exponents are exactly $\beta = \gamma = 2$, the r^2 reweighting would be the physically correct way to fit the amplitudes and wave vector. For our extended spinless Hubbard ladder in the limit of $t_\perp \gg t_\parallel$, $t' = 0$, β and γ will both differ from 2, and we will still have to overcome the first difficulty. We do this by iteratively fitting pairs of parameters in (7.7.31), in the following sequence:

1. We first fit $-r^2\langle\Delta_j^\dagger\Delta_{j+r}\rangle$ to $A + B\cos(kr + \phi)$, to obtain an estimate for the wave vector k, the phase shift ϕ, and starting values for the amplitudes A and B.

2. Fixing the values of A, k and ϕ, we then fit $-r^2\langle\Delta_j^\dagger\Delta_{j+r}\rangle$ to $A + Br^{-(\gamma-2)}\cos(kr+\phi)$, to obtain an improved estimate for the amplitude B, as well as a first estimate for the exponent $\gamma - 2$.

3. Fixing the parameter value pairs $(B, \gamma - 2)$ and (k, ϕ), we then fit $-r^2 \langle \Delta_j^\dagger \Delta_{j+r} \rangle$ to $Ar^{-(\beta-2)} + Br^{-(\gamma-2)} \cos(kr + \phi)$, to obtain an improved estimate for the amplitude A, as well as a first estimate for the exponent $\beta - 2$.

4. Once we have an initial estimate of the parameters, we iteratively fit $-r^2 \langle \Delta_j^\dagger \Delta_{j+r} \rangle$ to the full asymptotic form $Ar^{-(\beta-2)} + Br^{-(\gamma-2)} \cos(kr + \phi)$ by:

   (a) Fix the parameter pairs $(A, \beta - 2)$ and $(B, \gamma - 2)$, and fit the parameter pair (k, ϕ);

   (b) Fix the parameter pairs (k, ϕ) and $(A, \beta - 2)$, and fit the parameter pair $(B, \gamma - 2)$.

   (c) Fix the parameter pairs $(B, \gamma - 2)$ and (k, ϕ), and fit the parameter pair $(A, \beta - 2)$;

This manner of iterative search for the minimum in a multi-parameter space, by searching within successive restricted-parameter spaces cut out certain search directions, and generally slows down the convergence. In the worst scenario, the restricted-parameter iterative search might even result in the parameters settling onto a limit cycle 'orbiting' the minimum. However, this is still infinitely better than the nonlinear curve fitting running away along some 'flat' directions in the multi-parameter space. Table 7.20 shows the typical performance of such a iterative restricted-parameter nonlinear curve fitting algorithm, while Table 7.21 show the fitted parameters obtained with such an algorithm. Figure 7.85 shows the rung-fermion SC correlations $-r^2 \langle \Delta_j^\dagger \Delta_{j+r} \rangle$ for rung-fermion filling fractions $\bar{N}_1 = 0.20$, 0.30 and 0.40.

While the fits appear to be good visually at all rung-fermion filling fractions, not all parameters are reliable at the lowest and highest rung-fermion filling fractions, judging from how slowly they converge as the curve fitting algorithm is iterated. At intermediate

Table 7.20: Convergence of the parameters in the nonlinear curve fit of $-r^2 \langle \Delta_j^\dagger \Delta_{j+r} \rangle$ to the asymptotic form $Ar^{-(\beta-2)} + Br^{-(\gamma-2)} \cos(kr + \phi)$ using a iterative restricted-parameter algorithm, for $\bar{N}_1 = 0.20$, and $7 \leq r \leq 19$. Each iteration involves restricted-parameter fits to the pair (k, ϕ), followed by fits to the pair $(B, \gamma - 2)$, and finally by fits to the pair $(A, \beta - 2)$.

iteration	A	$\beta - 2$	B	$\gamma - 2$	k	ϕ
0	0.091299	0.159515	0.004577	−0.01876	1.30116	−1.55702
1	0.100015	0.194880	0.065921	1.05248	1.26766	−0.97471
2	0.102875	0.205678	0.144057	1.36749	1.26058	−0.887271
3	0.103893	0.209441	0.186611	1.47220	1.25848	−0.862108
4	0.104268	0.210816	0.204605	1.50953	1.25770	−0.852991
5	0.104407	0.211324	0.211700	1.52336	1.25740	−0.849525
6	0.104459	0.211511	0.214406	1.52852	1.25728	−0.848243
7	0.104479	0.211587	0.215421	1.53043	1.25724	−0.847715
8	0.104486	0.211612	0.215791	1.53113	1.25723	−0.847579
9	0.104489	0.211621	0.215938	1.53141	1.25722	−0.847502
10	0.104490	0.211627	0.216017	1.53155	1.25721	−0.847434

Table 7.21: Fitted parameters for a nonlinear curve fit of the rung-fermion SC correlation $-r^2 \langle \Delta_j^\dagger \Delta_{j+r} \rangle$ to $A r^{-(\beta-2)} + B r^{-(\gamma-2)} \cos(kr + \phi)$, for ladder filling fractions over the range $0.04 \leq \bar{N}_1 \leq 0.48$, for $7 \leq r \leq 19$.

$\bar{N}_1$	A	$\beta - 2$	B	$\gamma - 2$	k	ϕ
0.04	0.0009	$< 10^{-3}$	0.0009	$< 10^{-3}$	0.14	3.3
0.08	0.010	0.064	0.07	1.7	0.48	0.37
0.12	0.030	0.15	0.73	2.4	0.69	0.41
0.16	0.0647	0.203	1.36	2.50	0.964	−0.101
0.20	0.104	0.212	0.216	1.53	1.257	−0.847
0.24	0.150	0.221	0.221	1.31	1.461	−0.535
0.28	0.193	0.227	0.576	1.49	1.720	−0.916
0.30	0.209	0.230	0.897	1.59	1.854	−1.20
0.32	0.215	0.225	0.947	1.53	2.003	−1.62
0.36	0.202	0.215	0.563	1.19	2.258	−2.01
0.40	0.144	0.184	0.489	1.07	2.507	−2.31
0.44	0.0734	0.192	0.159	0.463	3.007	0.291
0.46	0.0183	−0.300	0.0338	−0.0369	3.32	−1.87
0.48	0.000119	−1.32	0.00234	−0.30	3.06	1.80

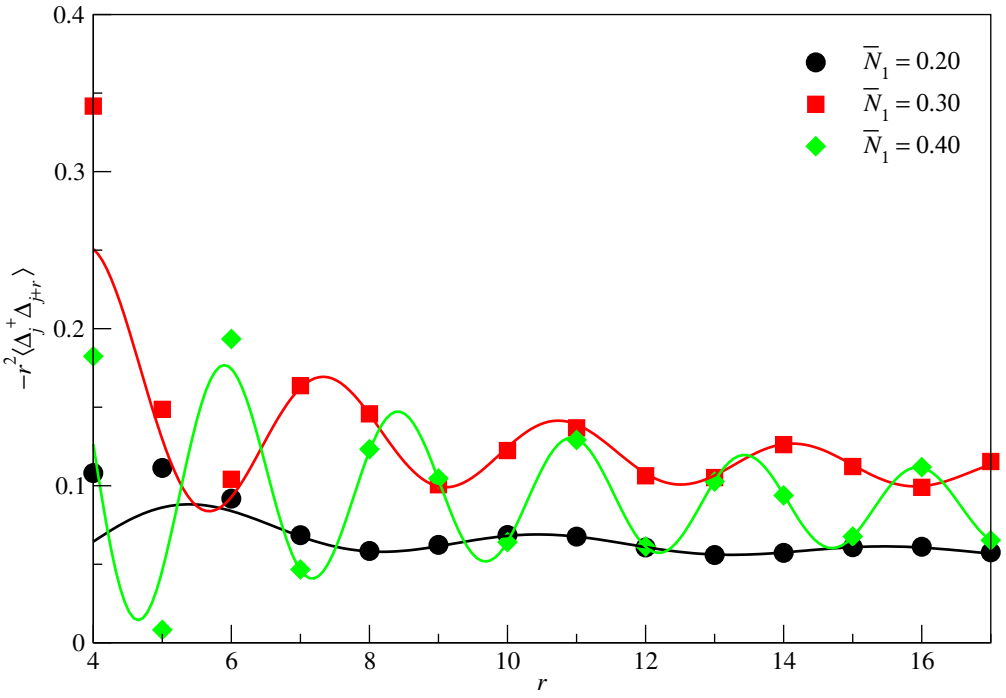

Figure 7.85: The infinite-ladder rung-fermion SC correlation $-r^2\,\langle\Delta_j^\dagger\Delta_{j+r}\rangle$ as a function of separation $4 \le r \le 17$ for ladder filling fractions $\bar{N}_1 = 0.20$ (black circles), 0.30 (red squares), and 0.40 (green diamonds), in the limit $t_\perp/t_\parallel \to \infty$, $t' = 0$. The black, red, and green solid curves are the nonlinear fits to the asymptotic form $Ar^{-(\beta-2)}+Br^{-(\gamma-2)}\cos(kr+\phi)$ for the three ladder filling fractions respectively.

rung-fermion filling fractions, the parameter pair (k, ϕ) converges the fastest, while the parameter pair $(B, \gamma - 2)$ converges the slowest. At intermediate rung-fermion filling fractions, we iterated sufficiently many times to be confident that all parameter values have converged at least up to the third significant figure. Therefore, we can say with confidence that the amplitudes A and B both exhibit maxima at a rung-fermion filling fraction of $\bar{N}_1 \approx \frac{1}{3}$, which corresponds to a nearest-neighbor included chain filling fraction of $\bar{n}_1 \approx \frac{1}{2}$. This is shown in Figure 7.86.

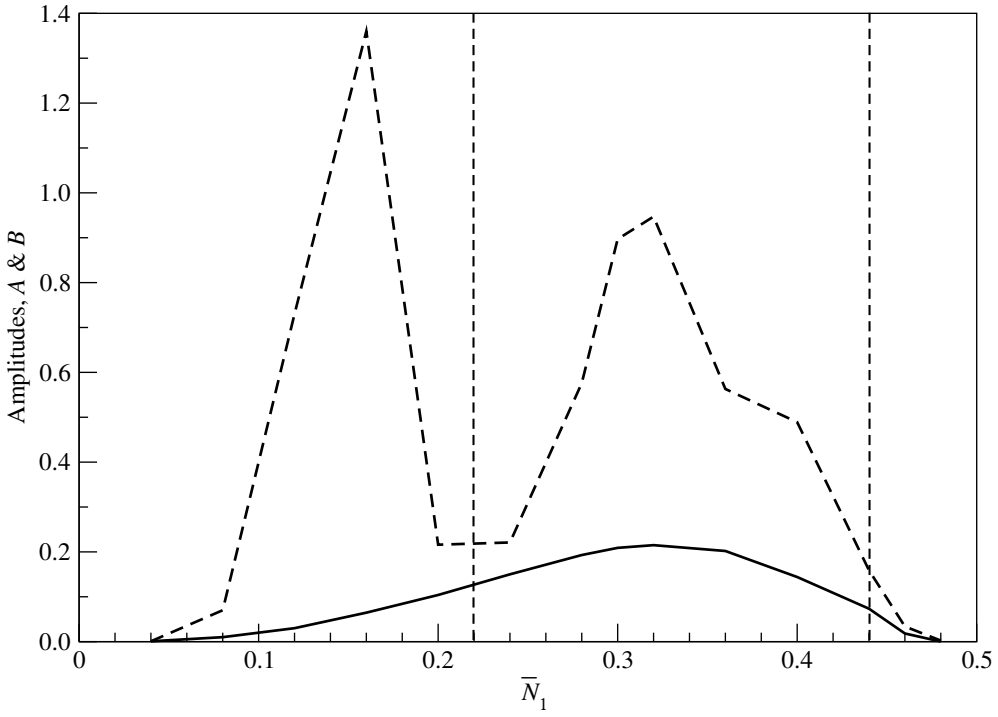

Figure 7.86: The amplitudes A (solid curve) and B (dashed curve), obtained by fitting the rung-fermion SC correlation $r^2 \langle \Delta_j^\dagger \Delta_{j+r} \rangle$ to the asymptotic form $Ar^{-(\beta-2)} + Br^{-(\gamma-2)} \cos(kr + \phi)$, as a function of the rung-fermion filling fraction $\bar{N}_1$. The fits are reliable, as far as A and B are concerned, only in the region between the dotted lines. The data points plotted here are from the six-parameter, $(A, \beta - 2, B, \gamma - 2, k, \phi)$, fit to $Ar^{-(\beta-2)} + Br^{-(\gamma-2)} \cos(kr + \phi)$, shown in Table 7.21.

From 7.21, we see that the fitted wave vectors follow the expected $k = 2\pi\bar{N}_1 = 2k_F$ behaviour. We also see that the correlation exponents β and γ take on the value $\beta = \gamma = 2$ in the very-low-density limit, which we again expect, since the rung-fermions behave very much like noninteracting fermions in the limit of vanishing rung-fermion filling fraction, $\bar{N}_1 \to 0$. As the ladder filling fraction is increased, the fitted value of the correlation exponent β increases slowly, reaching a maximum of $\beta \approx 2.2$ just before $\bar{N}_1 = \frac{1}{3}$, which corresponds to a nearest-neighbor included chain filling fraction of $\bar{n}_1 = \frac{1}{2}$, before falling off. A similar behaviour is seen in the fitted value of the correlation exponent γ, even though the fitted values are less reliable than those for β. If we disregard the fitted values for $\bar{N}_1 < 0.12$, then we see that γ attains its maximum again just before $\bar{N}_1 = \frac{1}{3}$. Thereafter, γ does not appear to fall off as fast as β.

Numerically, we find both β and γ going to zero as $\bar{N}_1 \to \frac{1}{2}$, when based on the low-density-of-holes argument presented in Section 7.7.2, we know that this should not be the case. What we do then, is to treat this series of nonlinear curve fits only as a preliminary guide to our understanding the numerical correlations. Based on the results of our refined nonlinear curve fits in Sections 7.7.2 and 7.7.3, we now have strong numerical evidence for the rung-fermion ground state being a Fermi liquid. The SC correlation exponents should therefore, also be universal, instead of varying with the rung-fermion filling fraction $\bar{N}_1$ as seen in Table 7.21.

Unlike for the FL and CDW correlations, there are no analytical bosonization calculations to help suggest values for these universal SC correlation exponents, so we simply fooled around with the exponents, and let the nonlinear curve fitting program find the appropriate amplitudes and phase shifts. Through this trial-and-error process, we find that the best fit of the numerical correlations appears to the mixed asymptotic form

$$Ar^{-\frac{1}{8}} + Br^{-\frac{1}{4}}\cos(2\pi\bar{N}_1 r + \phi_1) + Cr^{-\frac{3}{2}}\cos(2\pi\bar{N}_1 r + \phi_2) + Dr^{-\frac{7}{2}}, \tag{7.7.32}$$

whose fitted parameters are shown in Table 7.22. While varying the exponents individually, and checking the goodness of fit visually, we find the goodness of fit depending most sensitively on the leading correlation exponent. For numerical correlations fitted very well by (7.7.32), we find that the goodness of fit deteriorates significantly if we choose the leading exponent to take on values other than $\beta = \frac{1}{8}$.

Table 7.22: Fitted parameters for a nonlinear curve fit of the rung-fermion SC correlation $-r^2 \langle \Delta_j^\dagger \Delta_{j+r} \rangle$ to $Ar^{-\frac{1}{8}} + Br^{-\frac{1}{4}} \cos(2\pi \bar{N}_1 r + \phi_1) + Cr^{-\frac{3}{2}} \cos(2\pi \bar{N}_1 r + \phi_2) + Dr^{-\frac{7}{2}}$, for ladder filling fractions over the range $0.04 \leq \bar{N}_1 \leq 0.48$, and separations $7 \leq r \leq 19$.

$\bar{N}_1$	A	B	ϕ_1	C	ϕ_2	D	visual
0.04	0.00239	0.00048	−0.7732	0.02955	0.9528	−0.13531	perfect
0.08	0.01188	0.00044	−1.8207	0.04339	0.2689	−0.78260	perfect
0.12	0.02801	0.00119	−2.6643	0.09274	−0.1013	2.28557	perfect
0.16	0.05166	0.00157	−2.7081	0.14570	−0.3383	4.90195	very good
0.20	0.08170	0.00316	−2.6307	0.23855	−0.5125	7.3069	very good
0.24	0.11447	0.00415	−3.0542	0.40490	−0.8928	11.1834	very good
0.28	0.14407	0.00515	−2.4502	0.52589	−1.2234	15.1169	perfect
0.30	0.15499	0.00789	−2.4738	0.62268	−1.3346	16.2122	perfect
0.32	0.16177	0.00961	−2.4804	0.73896	−1.5086	16.1527	perfect
0.36	0.15697	0.01532	−2.4879	0.91411	−1.8760	13.3059	perfect
0.40	0.12213	0.02046	−2.4978	0.95810	−2.3331	7.25771	perfect
0.44	0.06338	0.02555	−2.1983	0.80402	−3.2469	−4.15315	very good
0.46	0.06127	0.04093	−2.5762	0.90205	−3.6848	−22.4163	very good
0.48	0.00654	0.01174	−2.3352	0.42167	−4.1534	−5.03638	not good

Looking at (7.7.32) more carefully, we might ask: what ever happened to the $A'r^{-2} + B'r^{-2}\cos 2\pi\bar{N}_1 r$ behaviour that we expect of the SC correlation in the limit of $\bar{N}_1 \to 0$? In the process of searching for the best mixed asymptotic form, we find that in general, the goodness of fit does not depend too sensitively on the non-leading exponents. We had chosen them to be $\beta' = \frac{1}{4}, \beta'' = \frac{3}{2}$, and $\beta''' = \frac{7}{2}$ to achieve the best possible fit visually, but we could equally well have chosen $\beta'' = 2 = \beta'''$ without too much loss in goodness of fit. Because of this apparent latitude in our choice for β'' and β''' (and to a lesser extent, β' as well), we should think of the term $Cr^{-\frac{3}{2}}\cos(2\pi\bar{N}_1 r + \phi_2) + Dr^{-\frac{7}{2}}$ as the sort of leading-order correction that was discussed in Section 7.5.6.2, which must be included so we can fit the leading-order asymptotic form $Ar^{-\frac{1}{8}} + Br^{-\frac{1}{4}}\cos(2\pi\bar{N}_1 r + \phi_1)$ reliably, but cannot be themselves fitted reliably (see Figure 7.87 for the fitted amplitudes A and B as functions of the rung-fermion filling fraction $\bar{N}_1$).

A more interesting question then arise: why must we hypothesize that the leading-order correction is of the form $Cr^{-\frac{3}{2}}\cos(2\pi\bar{N}_1 r+\phi_2)+Dr^{-\frac{7}{2}}$? Why would a leading-order correction of the form $Dr^{-\frac{7}{2}}$ not be sufficient to reliably fit the numerical correlation to $Ar^{-\frac{1}{8}}+Br^{-\frac{1}{4}}\cos(2\pi\bar{N}_1 r+\phi_1)$? Since the role of the leading-order correction in a nonlinear curve fit is to 'absorb' the parts of the numerical correlations that are not contributed by the leading-order asymptotic form, we speculate that a leading-order correction of the form $Dr^{-\beta'''}$ will probably be able to do a good job as well. However, since we know that the term $Cr^{-\beta'}\cos(2\pi\bar{N}_1 r + \phi_2) + Dr^{-\beta''}$, based on our argument that the chain of rung-fermions behave like a chain of noninteracting spinless fermions as $\bar{N} \to 0$, must necessarily contribute to the rung-fermion SC correlation, we might just as well use it in the curve fit. Indeed, in the course of the nonlinear curve fits, we find that the fits are never good, if we set $C = 0$ by hand, and allow only the $Dr^{-\beta'''}$ term to 'mop up' numerical correlations not contributed by the leading-order asymptotic form.

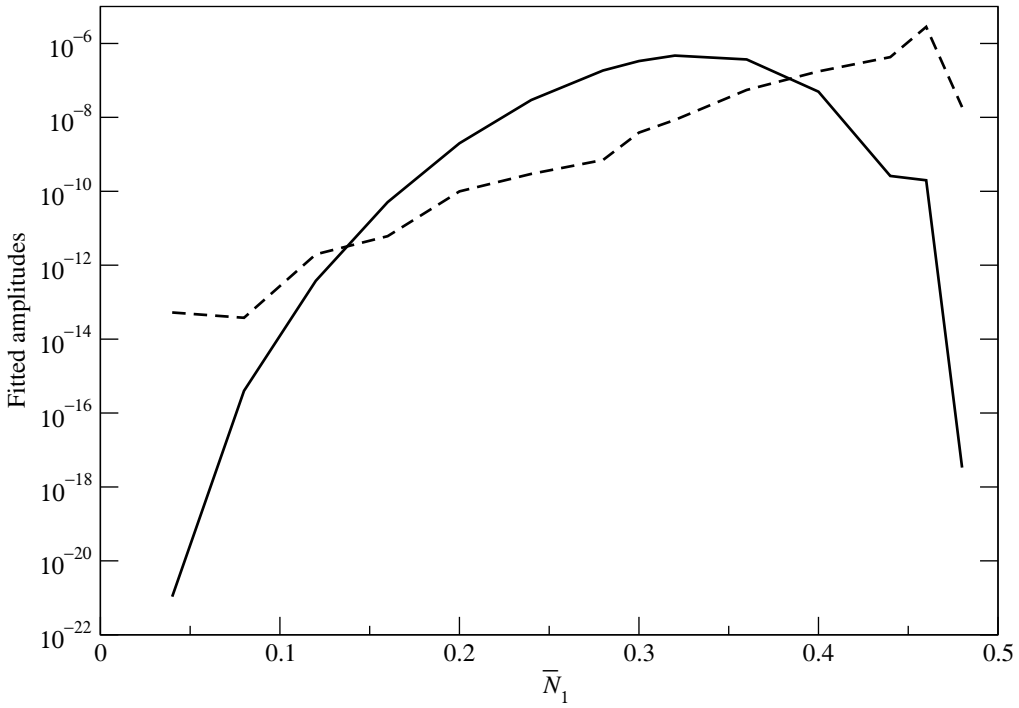

Figure 7.87: Powers A^8 (solid curve) and B^4 (dashed curve) of the amplitudes A and B, obtained by fitting the rung-fermion SC correlation $r^2 \langle \Delta_j^\dagger \Delta_{j+r} \rangle$ to the mixed asymptotic form $Ar^{-\frac{1}{8}} + Br^{-\frac{1}{4}} \cos(2\pi \bar{N}_1 r + \phi_1) + Cr^{-\frac{3}{2}} \cos(2\pi \bar{N}_1 r + \phi_2) + Dr^{-\frac{7}{2}}$, as a function of the rung-fermion filling fraction $\bar{N}_1$. These powers of the amplitudes are chosen, because they both have the unit of length, and therefore can be more sensibly compared. The data points plotted here are from the six-parameter, $(A, B, \phi_1, C, \phi_2, D)$, fit to $Ar^{-\frac{1}{8}} + Br^{-\frac{1}{4}} \cos(2\pi \bar{N}_1 r + \phi_1) + Cr^{-\frac{3}{2}} \cos(2\pi \bar{N}_1 r + \phi_2) + Dr^{-\frac{7}{2}}$, shown in Table 7.22.

CHAPTER 8

NUMERICAL STUDIES OF ORDER PARAMETERS

8.1 Chapter Preliminaries

8.1.1 A Quick Guide to Chapter 8

This chapter is the culmination of Chapters 5, 6, and 7, in which we implement computationally the operator singular value decomposition described in Chapter 6 to the correlation density matrix defined in Chapter 5, and extract order parameters for comparison against the analytical results obtained in Chapter 7.

We organize this chapter into three main parts. In the first part, which consists of Section 8.2, we discuss the computational aspects of ground-state structure analysis for exactly-diagonalized wave functions, and the operator singular value decomposition of the correlation density matrices constructed therefrom. Most importantly, we discuss how the choice of clusters affects the nature of the order parameters that we can construct, whether they pertain to CDW, FL, or SC correlations, and how we use the symmetries of the ladder Hamiltonian in (7.3.2) to classify them. We also discuss numerical difficulties in tracking the evolution of individual order parameters as a function of the cluster separation, and what we feel is the next-best manner of presenting the correlations obtained from the operator singular value decomposition.

In the second and third parts, which consists of Sections 8.3 and 8.4 respectively, we present the numerical results of our investigations into the ground-state phase diagram of the ladder Hamiltonian (7.3.2). In Section 8.3, we analyze the structure of the ED ground states for finite ladders subject to twist boundary conditions, and compare them with the infinite-ladder ground states obtained in Chapter 7. In Section 8.4, we analyze the numerical singular values obtained from the operator singular value decomposition

of the correlation density matrix, and compare the relative importance of CDW, FL, and SC correlations implied by the numerical singular values, with what we know about these correlations in the various analytical limits presented in Chapter 7.

8.1.2 Exploring the Ground-State Phase Diagram

In Figure 7.12, we gave a rough sketch of the ground-state phase diagram of the spinless extended Hubbard ladder Hamiltonian (7.3.2), based on the analytical understanding we derived from the ground states in three limiting cases. In this chapter, we wish to explore this ground-state phase diagram numerically, first by examining the structure of the ED ground-state wave functions at various points on the phase diagram, and then by operator singular value decomposing the correlation density matrix.

We do this at quarter-filling, $\bar{n}_2 = \frac{1}{4}$, which — as suggested by our analytical calculations in Chapter 7 — is special. We choose to work with the set of parameter points shown in Figure 8.1. Within this set of parameter points, some are chosen to be close to the analytical limits studied in Chapter 7, for the purpose of checking the numerical results against analytical results, while others are chosen to be far from the analytical limits, to test the operator singular value decomposition machinery over the simple analysis of the ED ground-state structures. Beyond this basic set of parameter points, other parameter points are presented where results are available.

Within this basic set of parameter points, we expect the parameter points $(t'/t_{\parallel} = 0.1, t_{\perp}/t_{\parallel} = 0)$ and $(t'/t_{\parallel} = 0, t_{\perp}/t_{\parallel} = 0.1)$ to have ground states that are very similar in structure to the zero inter-leg hopping ground state described in Section 7.6. We also expect the parameter point $(t'/t_{\parallel} = 0, t_{\perp}/t_{\parallel} = 100)$ to have a ground state very similar in structure to the strong inter-leg hopping ground state described in Section 7.7, and the parameter point $(t'/t_{\parallel} = 100, t_{\perp}/t_{\parallel} = 0)$ to have a ground state very similar in

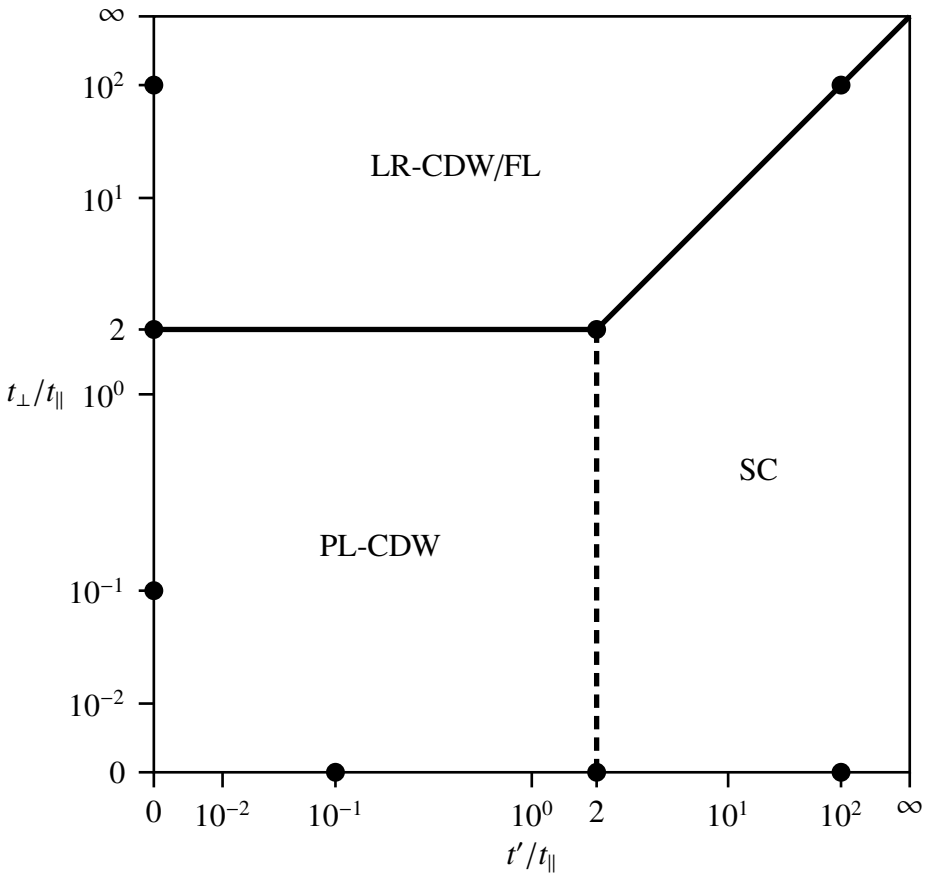

Figure 8.1: Parameter points within the phase diagram chosen for numerical study by (i) analysis of the ED ground-state structure; and (ii) operator singular value decomposition of the correlation density matrix.

structure to the infinitely-strong correlated hopping ground state described in Section 7.5. Therefore, when presenting the numerical results in Sections 8.3 and 8.4, we will present these four parameter points under a common subsection, which we shall refer to as "Known Limits".

Of the four remaining parameter points which do not lie close to the three analytical limiting cases, three lie on the zeroth-order lines of quantum phase transitions or crossover.[1] These are the parameter points $(t'/t_{\|} = 2, t_{\perp}/t_{\|} = 0)$, $(t'/t_{\|} = 0, t_{\perp}/t_{\|} = 2)$, $(t'/t_{\|} = 100, t_{\perp}/t_{\|} = 100)$, and we will present their numerical results under a common subsection which we shall refer to as " 'Phase Boundaries' ". The final parameter point, $(t'/t_{\|} = 2, t_{\perp}/t_{\|} = 2)$, is located at the intersection between the zeroth-order lines of quantum phase transitions and 'crossover', so we will present its numerical results under a subsection called " 'Tricritical Point' ", even though we cannot be sure that we have a *bona fide* quantum tricritical point.

8.2 Computational Aspects

In this section, we look at the various computational aspects of analyzing the structure of ED ground-state wave functions of finite ladders, and the operator singular value decomposition of the correlation density matrix constructed from these ED ground-state wave functions. In Section 8.2.1, we discuss some difficulties we faced when analyzing the structure of the ED ground-state wave functions. In Section 8.2.2, we look at the various order parameters that we can construct for a given choice of clusters, and how

[1] We call these lines of quantum phase transitions or crossover zeroth-order lines, because they are determined by crude balance-of-kinetic-energies arguments presented in Section 7.3.2. If we had determined their locations more precisely using first-order perturbation theory, we would call the resulting lines of quantum phase transitions or crossover first-order lines.

we can classify them based on whether they describe CDW, FL, or SC correlations, and their symmetry with respect to symmetries of the ladder Hamiltonian (7.3.2). In Section 8.2.3, we discuss the difficulties faced when analyzing the numerical singular values obtained from the operator singular value decomposition of the correlation density matrix. In Section 8.2.4, we look into the use of twist boundary conditions averaging when calculating the correlation density matrix.

8.2.1 Ground-State Structure Analysis

In Section 8.3, we adopt two different qualitative approaches to analyzing the structure of the many-body ground state. These two approaches are: (i) comparison of the many-body twisted-energy-band structure, which we will describe in Section 8.2.1.1; and (ii) comparison of the distributions of ground-state amplitudes, which we will describe in Section 8.2.1.2.

8.2.1.1 Comparison of Many-Body Twisted Energy Band Structure

When we exactly diagonalize the Hamiltonian (7.3.2) for P spinless fermions on a two-legged ladder of length L subjected to twist boundary conditions, with twist angle ϕ_x, we obtained for each wave vector $\mathbf{q}$, a set of many-body energy eigenvalues $E_n(\mathbf{q}, \phi_x)$, where $n = 1, 2, \ldots, D(\mathbf{q})$, $D(\mathbf{q})$ being the number of non-null Bloch states with wave vector $\mathbf{q}$. Since these many-body energy eigenvalues vary continuously with ϕ_x, we call them the *many-body twisted energy bands* (see also Section D.6.6).

For different parameter values in the spinless extended Hubbard ladder with correlated hops (7.3.2), the many-body twisted energy band obtained will have different structures. We can use this qualitative difference in the many-body twisted energy band structures as a means of distinguishing between two different quantum phases. For ex-

ample, if we choose a reference parameter point in the ground-state phase diagram, for which we know that the many-body ground state is in quantum phase I, and calculate its reference twisted energy band structure. We will then find, very generally, that the twisted energy band structure of another parameter point close to the reference parameter point to be very similar to the reference twisted energy band structure, whereas that for a parameter point far away, say in quantum phase II of the ground-state phase diagram, will look very different from the reference twisted band structure.

There are a few things we look out for, when we compare the many-body twisted energy band structures. First, for each twist angle ϕ_x, we look at which Bloch sector(s), labelled by the wave vector(s) $\mathbf{q}$, the ground state selected by twist boundary conditions averaging occurs in. Here, we need to worry about competing Bloch sectors, whose minimum-energy states are frequently related to each other by symmetries, as ϕ_x is varied. For example, in the reference twisted energy band structure, we may have the many-body ground state occurring in the $\mathbf{q} = (+\frac{\pi}{2}, 0)$ Bloch sector over some range of ϕ_x, and in the $\mathbf{q} = (0, -\pi)$ Bloch sector over another range of ϕ_x, and in the $\mathbf{q} = (-\frac{\pi}{2}, 0)$ Bloch sector over yet another range of ϕ_x. Let us say the $\mathbf{q} = (+\frac{\pi}{2}, 0)$ twisted minimum-energy band $E_1((+\frac{\pi}{2}, 0), \phi_x)$ crosses the $\mathbf{q} = (0, -\pi)$ twisted minimum-energy band $E_1((0, -\pi), \phi_x)$ at $\phi_x = \phi_1^*$, while the $\mathbf{q} = (0, -\pi)$ twisted minimum-energy band $E_1((0, -\pi), \phi_x)$ crosses the $\mathbf{q} = (-\frac{\pi}{2}, 0)$ twisted minimum-energy band at $\phi_x = \phi_2^*$. For a parameter point close to the reference parameter point in the same quantum phase, these crossovers may occur at different values of ϕ_x, but we should nonetheless find the $\mathbf{q} = (+\frac{\pi}{2}, 0)$, $\mathbf{q} = (0, -\pi)$, and $\mathbf{q} = (-\frac{\pi}{2}, 0)$ minimum-energy states being selected by twist boundary conditions averaging to be the ground state. However, if another parameter point has only the $\mathbf{q} = (\pm\frac{\pi}{2}, 0)$ minimum-energy states being selected by twist boundary conditions averaging, then it will not be likely that this parameter point be in the same

quantum phase as the reference parameter point.

The second thing we look out for are degeneracies between twisted energy bands in the twisted energy band structure. We believe that these degenerate twisted energy bands are important, even if they are not selected by twist boundary conditions averaging to be the ground state at any ϕ_x. Degeneracy is the clearest signature of particular symmetries in the ground state, so if the twisted energy band structure of one parameter point contains degeneracies not seen in the twisted energy band structure of another parameter point, the two parameter points cannot be in the same quantum phase.

Thirdly, we look at various global features of the twisted energy bands. These can be, for example, large gaps in the twisted energy band structure, or the relative ordering between the twisted minimum-energy bands for various Bloch sectors. For instance, in a particular quantum phase, we might have $E_1((\pm\frac{\pi}{2}, 0), \phi_x)$ being very far below the twisted energy bands of other Bloch sectors. We might also find $E_1(\mathbf{q}, \phi_x)$ always lying below $E_1(\mathbf{q}', \phi_x)$ in one quantum phase, but always lying above $E_1(\mathbf{q}', \phi_x)$ in another quantum phase.

Finally, we can also look at the qualitative character of various twisted energy bands. These need not be the overall ground state selected by twist boundary conditions averaging, at any twist angle ϕ_x. The most obvious difference in qualitative characters of a particular twisted energy band $E_1(\mathbf{q}, \phi_x)$ at two parameter points that would allow us to tell that the two parameter points represent different quantum phases, would be for $E_1(\mathbf{q}, 0)$ to a minimum at one parameter point, and a maximum at the other parameter point. We can also check whether a given twisted energy band has extrema elsewhere, whose number and locations might allow us to distinguish the quantum phases at two parameter points. Here, let us make clear that, when using the qualitative comparison between non-ground-state twisted energy bands as a means to distinguish between the

quantum phases at different parameter points, we are implicitly assuming that the many-body excited states tell us something about the character of the ground state.

8.2.1.2 Comparison of Distributions of Ground-State Amplitudes

While the comparison of twisted energy band structures can give us a visual indication whether two parameter points on the ground-state phase diagram are likely to be in two different quantum phases, no information about the structures of the ground states in the various quantum phases can be extracted from the twisted energy band structures. At the very best, we can determine the twisted energy band structures at the three analytical limits worked out in Chapter 7, and decide which analytical limit a given parameter point is closer to, through visual comparison of its twisted energy band structure with those of the three analytical limits. Our guiding principle here is: if the twisted energy band structure of a given parameter point is closest to analytical limit I, the ground state at the given parameter point will likely be close in character to the ground state in analytical limit I, and therefore the ground-state correlations at the given parameter point will also likely to be similar in behaviours to those in analytical limit I. Needless to say, this line of reasoning is very weak, and is no substitute to a direct analysis of the ground-state structure.

In Section 8.3, we analyze the structure of the ground states at different parameter points by making three type of qualitative comparisons:

1. comparing the histograms of absolute amplitudes in the minimum-energy states in different Bloch sectors, at various twist angles ϕ_x;

2. comparing the complex plots of amplitudes in the minimum-energy states in different Bloch sectors, at various twist angles ϕ_x; and

3. comparing the trajectories $\Psi_{\mathbf{n}}(\mathbf{q}, \phi_x)$, as the twist angle ϕ_x is varied, of the boundary-gauge amplitudes of selected configurations $|\mathbf{n}\rangle$ in the minimum-energy states in different Bloch sectors.

The idea behind these comparisons of ground-state amplitude distributions is similar to that behind our comparisons of twisted energy band structures: we start with the ground states in the three analytical limits, and think of these as our reference states. We determine their amplitude distributions, visualizing them either as histograms of absolute amplitudes, or as complex amplitude plots, or as trajectory plots, and use these distributions as our reference distributions. We then compare the distribution of amplitudes of the ground state at a given parameter point, visualized in one of the three ways described above, and compare it to the reference distributions. If the distribution of ground-state amplitudes at the given parameter point is qualitatively similar to one of the reference distributions, say reference distribution I for analytical limit I, we can then claim the the ground state at the given parameter point is likely to be close in character to the ground state in analytical limit I.

But what do we look out for, when making qualitative comparisons of the distributions of amplitudes? When we visualize these distribution of amplitudes as histograms of absolute amplitudes, we look out for clustering of absolute amplitudes in the histograms that would serve as signatures of this or that quantum phase. In particular, we think of each reference distribution of amplitudes as comprising a hierarchy of very structured clusters of absolute amplitudes, from the largest to the smallest. This would play the role of a 'finger print' for the reference quantum phase, the specific structure of which is expected to be qualitatively different in different reference states.

For example, Figure 8.2 shows the hierarchy of absolute amplitudes of a reference state at some hypothetical reference parameter point $(t_1, t_2 = 0)$. The pattern of clus-

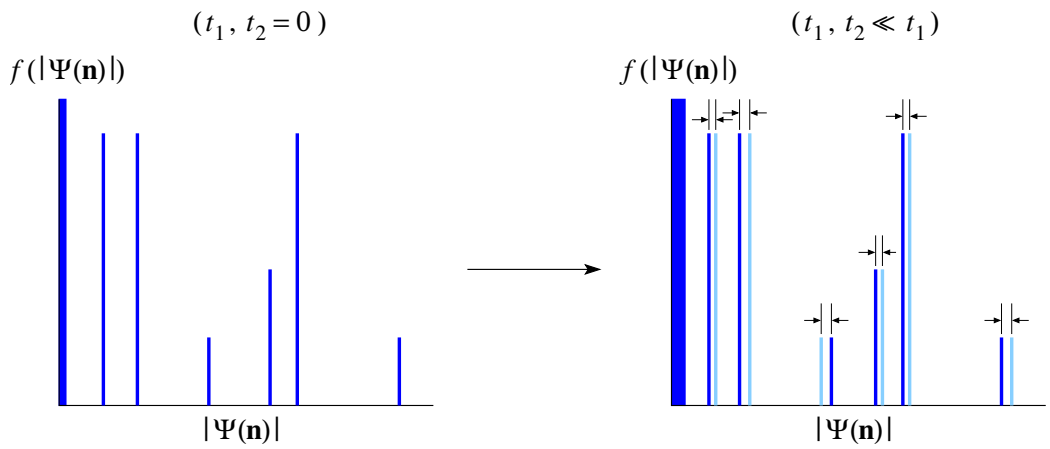

Figure 8.2: The hierarchy of absolute amplitudes of a reference state at the parameter point $(t_1, t_2 = 0)$ (left), against which the hierarchy of absolute amplitudes of the state at the parameter point $(t_1, t_2 \ll t_1)$ (right) is compared.

tering of the absolute amplitudes can be used as a 'finger print' of the reference state. When we plot the histogram of absolute amplitudes for a parameter point $(t_1, t_2 \ll t_1)$ shifted away from the reference parameter point, we find that each of the absolute amplitudes is shifted by $O(t_2/t_1)$, but otherwise the general pattern of clustering of the large to intermediate absolute amplitudes remain distinguishably similar to that of the reference state.

Apart from this robust reference-state 'finger print', which remains intact when t_2 is 'turned on', we are also interested in what happens to the absolute amplitudes which are strictly zero in the reference state. These zero absolute amplitudes are associated with configurations in excited states with different symmetries from the ground state at the reference parameter point. At the reference parameter point, these excited states would each have its own hierarchies of absolute amplitudes, furnishing 'finger prints' that are unique to each excited state. When t_2 is 'turned on', some of these reference excited states get mixed in with the reference ground state, and a whole zoo of very

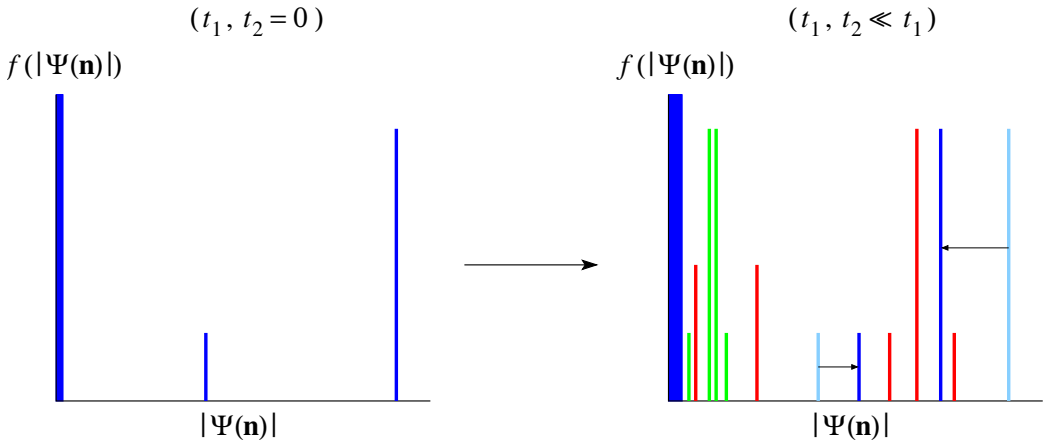

Figure 8.3: The hierarchy of small absolute amplitudes of the reference ground state at the parameter point $(t_1, t_2 = 0)$ (left), showing the two smallest non-zero absolute amplitudes (blue), and the large number of zero absolute amplitudes. When $t_2 \ll t_1$ is 'turned on', as shown on the right, these smallest non-zero absolute amplitudes get shifted by $O(t_2/t_1)$. In addition, new non-zero absolute amplitudes appear. Here we show the hierarchies of absolute amplitudes (red and green), associated with two reference excited states which get mixed in to the reference ground state when t_2 is 'turned on'. Here we illustrate the intermingling of the reference-ground-state absolute amplitudes with two hierarchies of reference-excited-state absolute amplitudes with different powers in t_2/t_1: $O(t_2/t_1)$ for the hierarchy of red absolute amplitudes, and $O(t_2/t_1)^2$ for the hierarch of green absolute amplitudes.

small absolute amplitudes appear in the histogram of absolute amplitudes at the shifted parameter point ($t_1, t_2 \ll t_1$). These new hierarchies of small absolute amplitudes can very generally be ranked, depending on the power of t_2/t_1 with which they vanish as t_2/t_1 is taken to zero.

Similarly, when we visualize the distributions of amplitudes in the form of complex amplitude plots, we also look out for clustering of complex amplitudes, which form various geometric patterns on the complex plane. But more importantly, we look out for the relative phases between the bond-gauge or boundary-gauge ground-state amplitudes. Frequently, the relative phases between the ground-state amplitudes is such that the ground-state amplitudes form various geometric patterns. For two minimum-energy states selected from the same Bloch sector by twist boundary conditions averaging to be the overall ground state, different geometric patterns formed by their respective ground-state amplitudes would then suggest that we are dealing with two different quantum phases.

Whether we plot the distributions of amplitudes as a histogram of absolute amplitudes, or as a plot of the complex amplitudes themselves, we can extract more information from the ground-state wave function, by sorting the many-body configurations according to their absolute amplitudes. In this way, we piece together the reference states and their hierarchies of absolute amplitudes, and hierarchies of many-body configurations, for use as benchmarks against which the ground-state structure at various parameter points are compared.

In some cases, we also compare the trajectories of the boundary-gauge ground-state amplitudes of specific configurations, as the twist angle ϕ_x is varied. This is chiefly to discover what effects twist boundary conditions averaging would have on the correlation density matrix, since we find that this mode of ground-state structure analysis yields very

little information on which quantum phase we are in at a given parameter point.

8.2.1.3 Problems with Indeterminate Global Phase

When we exactly diagonalize the ladder Hamiltonian matrix subject to twist boundary conditions with twist vector $\boldsymbol{\phi} = (\phi_x, 0)$ in the bond gauge, the ground state $|\Psi\rangle_{\text{bond}}$ comes with an indeterminate phase $\exp[\mathrm{i}\,\theta(\phi_x)]$. When we perform the gauge transformation (D.2.56) on the bond-gauge ground state $|\Psi\rangle_{\text{bond}}$ to obtain the boundary-gauge ground state $|\Psi\rangle_{\text{boundary}}$, this overall phase is carried over. However, when we construct the correlation density matrix from $|\Psi\rangle_{\text{boundary}}$, this indeterminate overall phase always cancels. This indeterminate overall phase is also unimportant when we plot histograms of the distribution, in the many-particle configurational basis, of absolute amplitudes in the ground-state wave functions at various twist angles ϕ_x.

We believe we can learn more about the structure of the ladder ground states by plotting either the bond-gauge or boundary-gauge complex amplitudes as a function of ϕ_x, to show the evolution of the complex amplitudes with ϕ_x. Such plots are physically meaningful if we can use the complex amplitudes *sans* the indeterminate overall phase $\exp[\mathrm{i}\,\theta(\phi_x)]$. Since the overall phase $\exp[\mathrm{i}\,\theta(\phi_x)]$ is truly indeterminate, we know of no way of pulling out the 'phase-free' complex amplitudes. Fortunately, it is not the absolute phase of each complex amplitude, but the relative phases between complex amplitudes within the ground-state wave function, that is physically important. Therefore, we can always pick a reference complex amplitude, and measure the phases of all other complex amplitudes relative to this reference complex amplitude. For convenience, we will pick the amplitude of one of the configurations with the largest absolute amplitude as the reference configuration.

Now, the ED ground-state wave functions are obtained in the bond gauge, while twist

boundary conditions averaging is performed in the boundary gauge. Therefore, we have two sets of complex amplitudes — those belonging to the bond-gauge ground-state wave functions, and those belonging to the boundary-gauge ground-state wave functions — that we can plot as functions of the twist angle ϕ_x. If we have two bond-gauge complex amplitudes with no relative phase for all ϕ_x, the corresponding boundary-gauge complex amplitudes will generically have a ϕ_x-dependent relative phase, as a consequence of the configuration-dependent gauge transformation (D.2.56). Since we understand the relative phase introduced by the gauge transformation between the complex amplitudes of two configurations, we are more interested in the intrinsic relative phase between the complex amplitudes of pairs of configurations. For this reason, we plot all relative phases in the bond gauge.

8.2.2 Choice of Clusters and Order Parameters

For spinless fermions with infinite nearest-neighbor repulsion, the smallest cluster allowing us to extract superconducting order parameters from the operator singular value decomposition of the correlation density matrix is a (2×2) cluster of sites, consisting two adjacent rungs of the two-legged ladder. However, we also perform trial numerical calculations singular value decomposing the correlation density matrix for the $(1 \times 2) + (1 \times 2)$ supercluster on two-legged ladders of various lengths. In this subsection, we discuss what order parameters can be constructed from the operator singular value decomposition of the correlation density matrices of the $(1 \times 2) + (1 \times 2)$ and $(2 \times 2) + (2 \times 2)$ superclusters, and how we classify them using the symmetries of the ladder Hamiltonian (7.3.2).

8.2.2.1 The (1 × 2) + (1 × 2) Supercluster

The smallest disconnected clusters we can pick on the two-legged ladder are one with one site on rung j, and another with one site on rung $j + r$. However, this choice of supercluster allows us to compute only the usual two-point and four-point functions. The simplest supercluster of disconnected clusters allowing us to go beyond calculating these usual correlations is the $(1 \times 2) + (1 \times 2)$ supercluster shown in Figure 8.4.

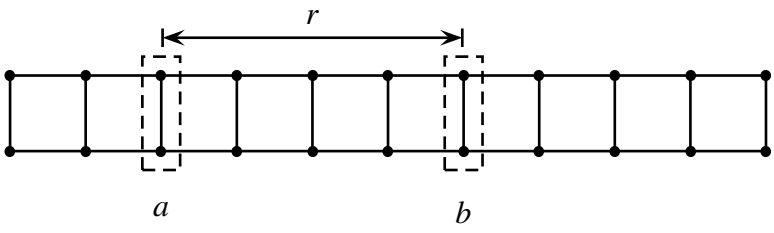

Figure 8.4: Two disconnected (1×2) clusters separated by a distance r on a two-legged ladder.

Because the model is translationally invariant, we can always choose the left cluster a to consist of the sites $(i = 1, j = 1)$ and $(i = 2, j = 1)$, so that the right cluster b consists of the sites $(i = 1, j = r + 1)$ and $(i = 2, j = r + 1)$. The supercluster ab then has a Fock-Hilbert space comprising $1 + 4 + 4 = 9$ occupation number basis states. We can then organize the matrix elements of the correlation density matrix ρ^c into a 9×9 coefficient matrix $\mathbf{K}$, on which we perform numerical singular value decomposition. The numerical singular value decomposition gives up to nine singular values and their corresponding left and right eigenvectors. To write down the operators associated with each eigenvector, we need to refer to the table of fused indices and product of referencing operators in Table 8.1.

These operators $X_{\mathbf{l}} = K^{\dagger}_{l_1} K_{l_2}$ and $Y_{\mathbf{m}} = Y^{\dagger}_{m_1} Y_{m_2}$ are classified into three types, depending on the nature of the order parameter O they pick out, when we compute expectations

Table 8.1: Fused indices $l_1 l_2$ and $m_1 m_2$ on clusters a and b respectively, and their associated products of referencing operators. Here, the label CDW is for operators which are important in charge-density-wave phases, FL is for operators which are important in Fermi liquid phases, and SF is for operators which are important in staggered-flux phases.

$l_1 l_2$	l_1	l_2	$K_{l_1}^\dagger K_{l_2}$	$m_1 m_2$	m_1	m_2	$K_{m_1}^\dagger K_{m_2}$	type
1	1	1	$(\mathbb{1} - n_{1,1})(\mathbb{1} - n_{2,1})$	1	1	1	$(\mathbb{1} - n_{1,r+1})(\mathbb{1} - n_{2,r+1})$	CDW
2	1	2	$c_{1,1}(\mathbb{1} - n_{2,1})$	2	1	2	$c_{1,r+1}(\mathbb{1} - n_{2,r+1})$	FL
3	1	3	$(\mathbb{1} - n_{1,1})c_{2,1}$	3	1	3	$(\mathbb{1} - n_{1,r+1})c_{2,r+1}$	FL
4	2	1	$(\mathbb{1} - n_{1,1})c_{2,1}^\dagger$	4	2	1	$(\mathbb{1} - n_{1,r+1})c_{2,r+1}^\dagger$	FL
5	2	2	$n_{1,1}(\mathbb{1} - n_{2,1})$	5	2	2	$n_{1,r+1}(\mathbb{1} - n_{2,r+1})$	CDW
6	2	3	$c_{1,1}^\dagger c_{2,1}$	6	2	3	$c_{1,r+1}^\dagger c_{2,r+1}$	SF
7	3	1	$(\mathbb{1} - n_{1,1})c_{2,1}^\dagger$	7	3	1	$(\mathbb{1} - n_{1,r+1})c_{2,r+1}^\dagger$	FL
8	3	2	$-c_{1,1}c_{2,1}^\dagger$	8	3	2	$-c_{1,r+1}c_{2,r+1}^\dagger$	SF
9	3	3	$(\mathbb{1} - n_{1,1})n_{2,1}$	9	3	3	$(\mathbb{1} - n_{1,r+1})n_{2,r+1}$	CDW

using the correlation density matrix

$$\langle O_{\mathbf{l}}^{\dagger} O_{\mathbf{m}} \rangle = \mathrm{Tr}\, \rho^{c} O_{\mathbf{l}}^{\dagger} O_{\mathbf{m}} = \sum_{\mathbf{l},\mathbf{m}} (\rho^{c})_{\mathbf{l},\mathbf{m}} X_{\mathbf{l}} Y_{\mathbf{m}}^{\dagger} O_{\mathbf{l}}^{\dagger} O_{\mathbf{m}}. \tag{8.2.1}$$

For example, $X = n_{1,1}(\mathbb{1} - n_{2,1})$ will yield a nonzero expectation only with the local observable $O = n_{1,1}$, which is a density operator, and so we call X a charge-density-wave-(CDW)-type operator. On the other hand, $X = c_{1,1}(\mathbb{1} - n_{2,1})$ will yield a nonzero expectation only with $O = c_{1,1}^{\dagger}$, and so we call X a Fermi-liquid-(FL)-type operator. Finally, the operator $X = c_{1,1}^{\dagger} c_{2,1}$ picks out $O = c_{1,1} c_{2,1}^{\dagger}$, which is a current operator having nonzero expectations only in staggered-flux (SF) phase, and so we classify it accordingly.

Because the ladder is symmetrical about the ladder axis, we can further classify the operators X and Y according to their symmetry about the ladder axis. For example, the CDW operator $(\mathbb{1} - n_{1,1})(\mathbb{1} - n_{2,1})$ goes to itself after reflection about the ladder axis, and so has even (+) symmetry about the ladder axis. On the other hand, the CDW operator $n_{1,1}(\mathbb{1} - n_{2,1})$ becomes $(\mathbb{1} - n_{1,1})n_{2,1}$ upon reflection about the ladder axis, and vice versa. These operators therefore do not have definite symmetry about the ladder axis, but the linear combinations $n_{1,1}(\mathbb{1} - n_{2,1}) + (\mathbb{1} - n_{1,1})n_{2,1}$ and $n_{1,1}(\mathbb{1} - n_{2,1}) - (\mathbb{1} - n_{1,1})n_{2,1}$ have even (+) and odd (−) symmetries respectively about the ladder axis. Similarly, the FL operators $c_{1,1}(\mathbb{1} - n_{2,1}) \leftrightarrow (\mathbb{1} - n_{1,1})c_{2,1}$ do not have definite symmetry about the ladder axis, but the linear combinations $c_{1,1}(\mathbb{1} - n_{2,1}) + (\mathbb{1} - n_{1,1})c_{2,1}$ and $c_{1,1}(\mathbb{1} - n_{2,1}) - (\mathbb{1} - n_{1,1})c_{2,1}$ are even (+) and odd (−) respectively. Under a reflection about the ladder axis, the SF operators $c_{1,1}^{\dagger} c_{2,1} \leftrightarrow c_{1,1} c_{2,1}^{\dagger}$. Therefore, the even and odd SF combinations are $c_{1,1}^{\dagger} c_{2,1} + c_{1,1} c_{2,1}^{\dagger}$ and $c_{1,1}^{\dagger} c_{2,1} - c_{1,1} c_{2,1}^{\dagger}$ respectively.

8.2.2.2 The (2 × 2) + (2 × 2) Supercluster

For two (2×2) clusters separated by a distance of r on a two-legged ladder, we can, by translational invariance, choose them to be $a = \{(1,1),(2,1),(1,2),(2,2)\}$ and $b = \{(1,r+1),(2,r+1),(1,r+2),(2,r+2)\}$, as shown in Figure 8.5. Each of the clusters a and b has a Fock-Hilbert space comprising $1 + 4 + 2 = 7$ states, and so the Fock-Hilbert space of the supercluster ab has $7^2 = 49$ states. The coefficient matrix $\mathbf{K}$ of the correlation density matrix ρ^c is thus 49×49, and we need the tables of fused indices and product of referencing operators, Tables 8.2 to 8.5, to help us decipher the nature of the order parameters.

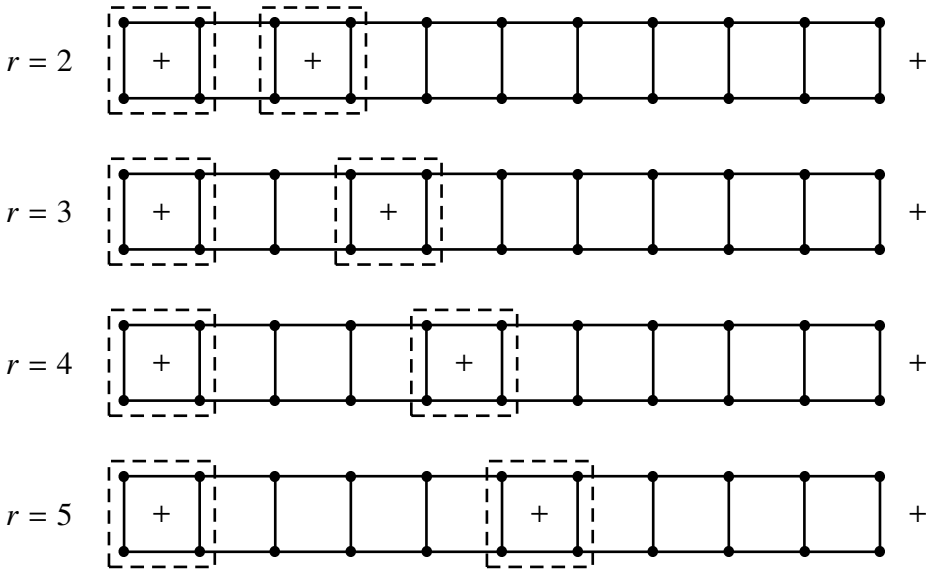

Figure 8.5: Two disconnected (2×2) clusters separated by a distance $r = 2, 3, 4, 5$ on a two-legged ladder. In this example, we have chosen a two-legged ladder of length $L = 10$ subject to periodic boundary conditions. The centers of the (2×2) clusters are marked by a '+'. The '+' on the right is the center of the repeated (2×2) cluster arising from periodic boundary conditions.

For two (2×2) clusters, there are far too many order parameters for us to keep track

Table 8.2: Fused indices $l_1 l_2$ on cluster a, and their associated CDW-type products of referencing operators. There is a corresponding set of fused indices and product of referencing operators for cluster b.

$l_1 l_2$	l_1	l_2	$K_{l_1}^{\dagger} K_{l_2}$
1	1	1	$(\mathbb{1} - n_{(0,0)})(\mathbb{1} - n_{(0,1)})(\mathbb{1} - n_{(1,0)})(\mathbb{1} - n_{(1,1)})$
9	2	2	$n_{(0,0)}(\mathbb{1} - n_{(0,1)})(\mathbb{1} - n_{(1,0)})(\mathbb{1} - n_{(1,1)})$
17	3	3	$(\mathbb{1} - n_{(0,0)})n_{(0,1)}(\mathbb{1} - n_{(1,0)})(\mathbb{1} - n_{(1,1)})$
25	4	4	$(\mathbb{1} - n_{(0,0)})(\mathbb{1} - n_{(0,1)})n_{(1,0)}(\mathbb{1} - n_{(1,1)})$
33	5	5	$(\mathbb{1} - n_{(0,0)})(\mathbb{1} - n_{(0,1)})(\mathbb{1} - n_{(1,0)})n_{(1,1)}$
41	6	6	$n_{(0,0)}(\mathbb{1} - n_{(0,1)})(\mathbb{1} - n_{(1,0)})n_{(1,1)}$
49	7	7	$(\mathbb{1} - n_{(0,0)})n_{(0,1)}n_{(1,0)}(\mathbb{1} - n_{(1,1)})$

of, as these evolve with separation r. With the aid of the ladder reflection symmetry, which induces the interchange of fused indices shown below,

$$\text{CDW}: \quad \begin{bmatrix} 1 & 9 & 25 & 41 \\ \updownarrow & \updownarrow & \updownarrow & \updownarrow \\ 1 & 17 & 33 & 49 \end{bmatrix}, \tag{8.2.2a}$$

$$\text{SF}: \quad \begin{bmatrix} 10 & 11 & 12 & 23 & 24 & 26 & 42 \\ \updownarrow & \updownarrow & \updownarrow & \updownarrow & \updownarrow & \updownarrow & \updownarrow \\ 16 & 19 & 18 & 31 & 30 & 32 & 48 \end{bmatrix}, \tag{8.2.2b}$$

$$\text{FL}: \quad \begin{bmatrix} 2 & 4 & 8 & 13 & 14 & 22 & 27 & 28 & 37 & 38 & 39 & 40 \\ \updownarrow & \updownarrow & \updownarrow & \updownarrow & \updownarrow & \updownarrow & \updownarrow & \updownarrow & \updownarrow & \updownarrow & \updownarrow & \updownarrow \\ 3 & 5 & 15 & 21 & 20 & 29 & 35 & 34 & 45 & 44 & 47 & 46 \end{bmatrix}, \tag{8.2.2c}$$

Table 8.3: Fused indices $l_1 l_2$ on cluster a, and their associated SF-type products of referencing operators. There is a corresponding set of fused indices and product of referencing operators for cluster b.

$l_1 l_2$	l_1	l_2	$K_{l_1}^\dagger K_{l_2}$
10	2	3	$c_{(0,0)}^\dagger c_{(0,1)}(\mathbb{1}-n_{(1,0)})(\mathbb{1}-n_{(1,1)})$
11	2	4	$c_{(0,0)}^\dagger(\mathbb{1}-n_{(0,1)})c_{(1,0)}(\mathbb{1}-n_{(1,1)})$
12	2	5	$c_{(0,0)}^\dagger(\mathbb{1}-n_{(0,1)})(\mathbb{1}-n_{(1,0)})c_{(1,1)}$
16	3	2	$c_{(0,0)}c_{(0,1)}^\dagger(\mathbb{1}-n_{(1,0)})(\mathbb{1}-n_{(1,1)})$
18	3	4	$(\mathbb{1}-n_{(0,0)})c_{(0,1)}^\dagger c_{(1,0)}(\mathbb{1}-n_{(1,1)})$
19	3	5	$(\mathbb{1}-n_{(0,0)})c_{(0,1)}^\dagger(\mathbb{1}-n_{(1,0)})c_{(1,1)}$
23	4	2	$c_{(0,0)}(\mathbb{1}-n_{(0,1)})c_{(1,0)}^\dagger(\mathbb{1}-n_{(1,1)})$
24	4	3	$(\mathbb{1}-n_{(0,0)})c_{(0,1)}c_{(1,0)}^\dagger(\mathbb{1}-n_{(1,1)})$
26	4	5	$(\mathbb{1}-n_{(0,0)})(\mathbb{1}-n_{(0,1)})c_{(1,0)}^\dagger c_{(1,1)}$
30	5	2	$c_{(0,0)}(\mathbb{1}-n_{(0,1)})(\mathbb{1}-n_{(1,0)})c_{(1,1)}^\dagger$
31	5	3	$(\mathbb{1}-n_{(0,0)})c_{(0,1)}(\mathbb{1}-n_{(1,0)})c_{(1,1)}^\dagger$
32	5	4	$(\mathbb{1}-n_{(0,0)})(\mathbb{1}-n_{(0,1)})c_{(1,0)}c_{(1,1)}^\dagger$
42	6	7	$c_{(0,0)}^\dagger c_{(0,1)}c_{(1,0)}c_{(1,1)}^\dagger$
48	7	6	$c_{(0,0)}c_{(0,1)}^\dagger c_{(1,0)}^\dagger c_{(1,1)}$

Table 8.4: Fused indices $l_1 l_2$ on cluster a, and their associated FL-type products of referencing operators. There is a corresponding set of fused indices and product of referencing operators for cluster b.

$l_1 l_2$	l_1	l_2	$K_{l_1}^{\dagger} K_{l_2}$
2	1	2	$c_{(0,0)}(\mathbb{1} - n_{(0,1)})(\mathbb{1} - n_{(1,0)})(\mathbb{1} - n_{(1,1)})$
3	1	3	$(\mathbb{1} - n_{(0,0)})c_{(0,1)}(\mathbb{1} - n_{(1,0)})(\mathbb{1} - n_{(1,1)})$
4	1	4	$(\mathbb{1} - n_{(0,0)})(\mathbb{1} - n_{(0,1)})c_{(1,0)}(\mathbb{1} - n_{(1,1)})$
5	1	5	$(\mathbb{1} - n_{(0,0)})(\mathbb{1} - n_{(0,1)})(\mathbb{1} - n_{(1,0)})c_{(1,1)}$
8	2	1	$c_{(0,0)}^{\dagger}(\mathbb{1} - n_{(0,1)})(\mathbb{1} - n_{(1,0)})(\mathbb{1} - n_{(1,1)})$
13	2	6	$n_{(0,0)}(\mathbb{1} - n_{(0,1)})(\mathbb{1} - n_{(1,0)})c_{(1,1)}$
14	2	7	$c_{(0,0)}^{\dagger} c_{(0,1)} c_{(1,0)}(\mathbb{1} - n_{(1,1)})$
15	3	1	$(\mathbb{1} - n_{(0,0)})c_{(0,1)}^{\dagger}(\mathbb{1} - n_{(1,0)})(\mathbb{1} - n_{(1,1)})$
20	3	6	$c_{(0,0)} c_{(0,1)}^{\dagger}(\mathbb{1} - n_{(1,0)})c_{(1,1)}$
21	3	7	$(\mathbb{1} - n_{(0,0)})n_{(0,1)}c_{(1,0)}(\mathbb{1} - n_{(1,1)})$
22	4	1	$(\mathbb{1} - n_{(0,0)})(\mathbb{1} - n_{(0,1)})c_{(1,0)}^{\dagger}(\mathbb{1} - n_{(1,1)})$
27	4	6	$c_{(0,0)}(\mathbb{1} - n_{(0,1)})c_{(1,0)}^{\dagger} c_{(1,1)}$

Table 8.4: (continued)

$l_1 l_2$	l_1	l_2	$K_{l_1}^\dagger K_{l_2}$
28	4	7	$(\mathbb{1} - n_{(0,0)})c_{(0,1)}n_{(1,0)}(\mathbb{1} - n_{(1,1)})$
29	5	1	$(\mathbb{1} - n_{(0,0)})(\mathbb{1} - n_{(0,1)})(\mathbb{1} - n_{(1,0)})c_{(1,1)}^\dagger$
34	5	6	$c_{(0,0)}(\mathbb{1} - n_{(0,1)})(\mathbb{1} - n_{(1,0)})n_{(1,1)}$
35	5	7	$(\mathbb{1} - n_{(0,0)})c_{(0,1)}c_{(1,0)}c_{(1,1)}^\dagger$
37	6	2	$n_{(0,0)}(\mathbb{1} - n_{(0,1)})(\mathbb{1} - n_{(1,0)})c_{(1,1)}^\dagger$
38	6	3	$c_{(0,0)}^\dagger c_{(0,1)}(\mathbb{1} - n_{(1,0)})c_{(1,1)}^\dagger$
39	6	4	$c_{(0,0)}^\dagger(\mathbb{1} - n_{(0,1)})c_{(1,0)}c_{(1,1)}^\dagger$
40	6	5	$c_{(0,0)}^\dagger(\mathbb{1} - n_{(0,1)})(\mathbb{1} - n_{(1,0)})n_{(1,1)}$
44	7	2	$c_{(0,0)}c_{(0,1)}^\dagger c_{(1,0)}^\dagger(\mathbb{1} - n_{(1,1)})$
45	7	3	$(\mathbb{1} - n_{(0,0)})n_{(0,1)}c_{(1,0)}^\dagger(\mathbb{1} - n_{(1,1)})$
46	7	4	$(\mathbb{1} - n_{(0,0)})c_{(0,1)}^\dagger n_{(1,0)}(\mathbb{1} - n_{(1,1)})$
47	7	5	$(\mathbb{1} - n_{(0,0)})c_{(0,1)}^\dagger c_{(1,0)}^\dagger c_{(1,1)}$

Table 8.5: Fused indices $l_1 l_2$ on cluster a, and their associated SC-type products of referencing operators. There is a corresponding set of fused indices and product of referencing operators for cluster b.

$l_1 l_2$	l_1	l_2	$K_{l_1}^\dagger K_{l_2}$
6	1	6	$c_{(0,0)}(\mathbb{1} - n_{(0,1)})(\mathbb{1} - n_{(1,0)})c_{(1,1)}$
7	1	7	$(\mathbb{1} - n_{(0,0)})c_{(0,1)}c_{(1,0)}(\mathbb{1} - n_{(1,1)})$
36	6	1	$c_{(0,0)}^\dagger(1 - n_{(0,1)})(1 - n_{(1,0)})c_{(1,1)}^\dagger$
43	7	1	$(\mathbb{1} - n_{(0,0)})c_{(0,1)}^\dagger c_{(1,0)}^\dagger(\mathbb{1} - n_{(1,1)})$

$$\text{SC}: \quad \begin{bmatrix} 6 & 36 \\ \updownarrow & \updownarrow \\ 7 & 43 \end{bmatrix}. \tag{8.2.2d}$$

we will be able to distinguish CDW+ from CDW−, SC+ from SC−, and so on, at a gross level. As with the case of the (1×2)+(1×2) clusters, there are SF order parameters which occur by themselves, but more frequently they will be mixed in with the CDW order parameters. Because of this mixing, it is not very meaningful to monitor SF as a distinct order parameter type. We will therefore not bother to classify the CDW's separately from the SF's, nor make use of the relative phase of their mixing to distinguish various CDW±'s from each other. Instead, we will monitor the maximum absolute singular value $|\sigma|$ of just six subtypes: CDW±, FL± and SC±, as a function of the separation r.

8.2.3 Singular Value Analysis

With Tables 8.2, 8.3, 8.4, and 8.5, and using the behaviour (8.2.2) of the order parameters under a reflection about the ladder axis, we can now classify the order parameters obtained from the operator singular value decomposition of the correlation density matrix. As the intercluster separation is varied, the correlation density matrix elements, and consequently the singular values, which are ground-state correlation functions, change. The structures of the eigenvectors, i.e. the amplitudes of the products of referencing operators which we used as the operator basis for operator singular value decomposition, also change with the intercluster separation.

Ideally, we would like to be able to track the evolution of each singular value and eigenvector with intercluster separation, and see for ourselves the k_F-, $2k_F$-, and $4k_F$-oscillations, and power-law or exponential decay with the intercluster separation. However, with the $(2 \times 2) + (2 \times 2)$ supercluster, we find numerous FL and CDW order

parameters of each ladder reflection symmetry (even or odd under reflection about the ladder axis). Sampling their singular values only at discrete intercluster separations, it is not possible to determine, just by looking at the amplitudes in the eigenvectors, which FL/CDW order parameter at separation r a given FL/CDW order parameter at separation $r+1$ has evolved from. Therefore, it is not possible to ascertain the signs of the FL/CDW singular values as a function of intercluster separation.

We encounter this same predicament for the SC order parameters, which come in pairs with even and odd symmetry with respect to reflection about the ladder axis, as well. When we write out the SC order parameters in the correlation density matrix, for example,

$$\rho^c = \cdots + \sigma_1 \left(\tfrac{1}{\sqrt{2}} c^\dagger_{1,1} c^\dagger_{2,2} + \tfrac{1}{\sqrt{2}} c^\dagger_{1,2} c^\dagger_{2,1}\right)\left(\tfrac{1}{\sqrt{2}} c_{1,r+1} c_{2,r+2} + \tfrac{1}{\sqrt{2}} c_{1,r+2} c_{2,r+1}\right) + \\ \sigma_2 \left(\tfrac{1}{\sqrt{2}} c_{1,1} c_{2,2} + \tfrac{1}{\sqrt{2}} c_{1,2} c_{2,1}\right)\left(\tfrac{1}{\sqrt{2}} c^\dagger_{1,r+1} c^\dagger_{2,r+2} + \tfrac{1}{\sqrt{2}} c^\dagger_{1,r+2} c^\dagger_{2,r+1}\right) + \cdots , \quad (8.2.3)$$

we see that $\sigma_2 = -\sigma_1$, because $\rho^c = (\rho^c)^\dagger$. Hence, the pair of singular values associated with the SC+ (or SC−) order parameter always come with the same magnitude, but opposite signs, as a result of the correlation density matrix being hermitian.

Given a sequence of positive and negative singular values at various intercluster separations, we can in principle fit a large number of decaying sinusoidal curves through them, and obtain a whole zoo of possible wave vectors, phase shifts, and correlation exponents. Figure 8.6 shows three hypothetical correlation functions of the same type and symmetry, having different amplitudes and different phase shifts, but are chosen for illustration purposes to have the same wave vectors and same correlation exponents. These hypothetical correlation functions are plotted, also for illustration purposes, as functions of intercluster separations not restricted to discrete values. In practice, we only have the values of these three hypothetical correlation functions at discrete inter-

cluster separations. Not able to track the evolution of individual singular values with the intercluster separation, we track instead the evolution of the *bound* of the singular values of a particular type and symmetry with the intercluster separation. This is shown in Figure 8.6 as the two black dashed lines.

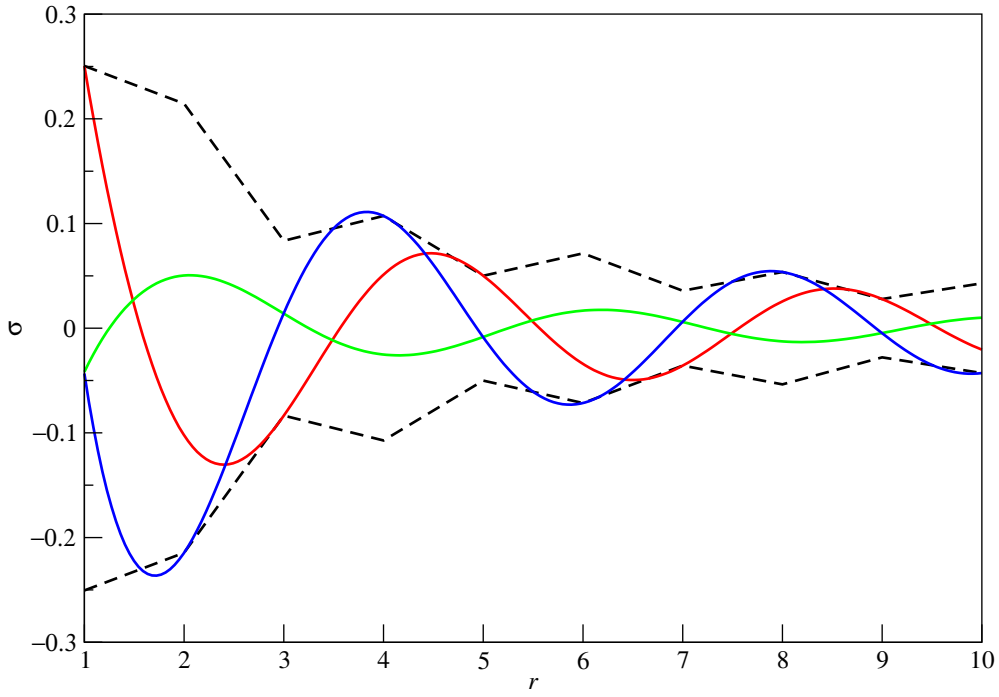

Figure 8.6: Three hypothetical singular values of the same type and symmetry, $\sigma_i = A_i r^{-\alpha_i} \cos(kr + \phi_i)$, as a function of the separation r. We have chosen $k = \pi/2$, $\alpha_1 = \alpha_2 = \alpha_3 = 1$, and $A_1 = 0.32358$, $\phi_1 = -0.88568$ (red curve); $A_2 = 0.10903$, $\phi_2 = 2.74877$ (green curve); and $A_3 = 0.43127$, $\phi_3 = 0.10055$ (blue curve). The black dashed line segments connect the maximum absolute singular values at each discrete r.

One reason why this might be a good thing to do in our numerical analysis of the singular values, is that, if eventually one, or a few, of the order parameters of a particular type and symmetry dominates at large distances, the bound that we determine from the numerical singular values would essentially be the absolute value of the dominant order parameter, or the absolute value of a linear combination of the dominant

order parameters. It is then in principle possible to determine the asymptotic amplitude and correlation exponents of the dominant order parameter or parameters by a simple nonlinear curve fit.

Now, given a symmetry-reduced subset of singular values, for example, all the CDW+ singular values, or all the FL− singular values, our procedure of picking out the maximum absolute singular value can be thought of as imposing an L_∞ norm on the symmetry-reduced subset of singular values, i.e.

$$\max_\sigma |\sigma| = \lim_{p\to\infty} \left(\sum_\sigma |\sigma|^p \right)^{1/p} . \tag{8.2.4}$$

When we think of our analysis of singular value this way, we realized that a better thing to do (but which we did not actually carry out, because it is not easy to automate and encapsulate the following calculation as a simple Octave function) would be to compute the L_2 norm

$$L_2(\{\sigma\}) = \left(\sum_\sigma |\sigma|^2 \right)^{1/2} , \tag{8.2.5}$$

of the symmetry-reduced subset of singular values, for two reasons.

First, the sum of squares of singular values is precisely the quantity that is invariant in the singular value decomposition, when we think of $M = U\Sigma V^T$ as a matrix transformation relating the matrices M and Σ. Second, we understand that each singular value in the symmetry-reduced subset are oscillatory functions of the intercluster separation. As we can see from Figure 8.6, the L_∞-norm of the symmetry-reduced subset of singular values will generally also be affected by these oscillations as a function of the intercluster separation, since at each separation r, it picks out only one of the oscillatory singular values. In contrast, the L_2-norm of the symmetry-reduced subset of singular values involve the sum of squares of the oscillatory singular values. Since we do not expect all singular values to simultaneously vanish at any intercluster separation, different singular

values in the subset must therefore be phase shifted by different amounts. We therefore expect the oscillatory behaviours of the singular values to average out each other when we sum their squares, giving us a quantity which varies more smoothly with intercluster separation.

8.2.4 Twist Boundary Conditions Averaging

To estimate the infinite-ladder correlations from the finite-ladder singular values we can obtain numerically, we need to once again rely on the method of twist boundary conditions averaging. We understood in Chapter 4 that our estimate of infinite-ladder correlations converges rather slowly with increasing number of twist vectors. To decide on how many twist vectors we must use to obtain a decent degree of convergence, we monitor in Chapter 4 the amplitude of the shell effect when the cluster density-matrix spectrum is plotted as a function of the filling fraction $\bar{n}$, and increase the number of twist vectors until the shell effect amplitude is adequately suppressed. However, building up the density-matrix spectra as a function of $\bar{n}$ is a very computationally intensive task.

For our numerical study of ladder systems, we want to expend as little computational effort as possible, and get away with just a rough gauge on the number of twist angles needed. To obtain this rough gauge, we test the method of twist boundary conditions averaging on a ladder of length $L = 6$. This is slightly longer than the shortest ladder that will fit two (1×2) clusters separated by a distance of $r = 2$. With $P = 2$ particles on the ladder, we check how quickly the singular values and eigenvectors converge with increasing number of twist angles, when the Hamiltonian parameters are $t_{\parallel} = t_{\perp} = t' = 1$.

After degeneracy averaging and twist boundary conditions averaging, we find eight nonzero singular values. Four of these corresponds to the CDW/SF order parameters, and the other four corresponds to the FL order parameters shown in Table 8.1. The four

FL order parameters come in two pairs, one with even symmetry with respect to the ladder axis (FL+), while the other with odd symmetry with respect to the ladder axis (FL−). The singular values have the same magnitude, but opposite signs within each pair. Out of the four CDW/SF order parameters, two are of even symmetry (CDW+) and two are of odd symmetry (CDW−). We find that the SF order parameters do not appear by themselves, but are mixed into some of the CDW order parameters. We can therefore use the sign of the SF contribution relative to the CDW contribution to further classify the two CDW+ and two CDW− order parameters. The convergence of these eight singular values with increasing number of unrestricted twist angles is shown in Table 8.6.

Table 8.6: Convergence of the correlation density-matrix singular values with increasing number N_ϕ of unrestricted twist angles, for $P = 2$ particles on a ladder of length $L = 6$, and $t_\parallel = t_\perp = t' = 1$.

N_ϕ	CDW+SF+	CDW+SF−	CDW−SF±	FL+	FL−
5	−0.04790337	0.00042557	−0.00430876	0.06671122	0.00110389
11	−0.04797186	0.00042516	−0.00434289	0.06742335	0.00139491
21	−0.04798948	0.00042509	−0.00435164	0.06640984	0.00148588
41	−0.04799710	0.00042506	−0.00435539	0.06865205	0.00147312
81	−0.04800058	0.00042504	−0.00435709	0.06841811	0.00149164
161	−0.04800223	0.00042504	−0.00435789	0.06899043	0.00148712
321	−0.04800292	0.00042504	−0.00435822	0.06909192	0.00148791

As we can see from Table 8.6, the singular values converge very slowly. For the rectangular integration scheme used to integrate over the twist angles, the convergence expected of a smooth function is $O(N_\phi^{-1})$. Here the convergence is clearly slower, and

we understand from Appendix D that this is the result of discontinuities in the twist surface. Worse yet, the convergences of the FL± singular values are non-monotonic, and we cannot easily improve on our estimate of the converged values by performing extrapolations. Because of this slow convergence, there is diminishing returns for using larger and larger sets of twist angles. Therefore, for the rest of our numerical studies, we select a set of 21 unrestricted twist angles $-\pi \leq \phi \leq +\pi$ for our twist boundary conditions averaging, unless specified otherwise.

8.3 Analysis of Quarter-Filled ED Ground States

In this section, we will analyze the structure of the quarter-filled ED ground states at the various parameter points on the ground-state phase diagram, and attempt to draw conclusions on what quantum phases these quarter-filled ED ground states exhibit. In Section 8.3.1, we analyze the structures of the quarter-filled ED ground states for parameter points close to the three analytical limits discussed in Chapter 7. Following this, we analyze in Section 8.3.2 the structures of the quarter-filled ED ground states for parameter points lying on the zeroth-order lines of 'quantum phase transitions' or 'crossovers' shown in Figure 8.1. Finally, in Section 8.3.3, we analyze the structre of the quarter-filled ED ground state for the parameter point lying on the zeroth-order 'quantum tricritical point', also shown in Figure 8.1.

8.3.1 Known Limits

In this subsection, we analyze the ED ground-state wave functions for parameter points close to the three analytical limits: (i) weak inter-leg hopping, (ii) strong inter-leg hopping, and (iii) strong correlated hopping, in Sections 8.3.1.1, 8.3.1.2 and 8.3.1.3 respec-

tively.

8.3.1.1 Weak Inter-Leg Hopping

In Section 7.6, we understood why the ladder ground state consists of staggered configurations, in which successive spinless fermions on the ladder occupy alternate legs. Such a staggered ground state was found to manifest strong CDW correlations, decaying as a power law with universal exponent $\alpha = \frac{1}{2}$, while the strongest SC and FL correlations were found to decay as a more rapid power law and exponentially, respectively. In this subsubsection, we examine signatures of this Luttinger-liquid physics in the ED ground-state wave functions for $P = 4$ particles on a ladder of length $L = 8$ subject to periodic boundary conditions, for parameter values $(t_\perp/t_\parallel = 0.1, t'/t_\parallel = 0)$ and $(t_\perp/t_\parallel = 0.5, t'/t_\parallel = 0)$. We then move on to study $P = 4$ particles on a ladder of length $L = 8$, subject to twist boundary conditions, for parameter values $(t_\perp/t_\parallel = 0.1, t'/t_\parallel = 0)$ and $(t_\perp/t_\parallel = 0, t'/t_\parallel = 0.1)$.

Periodic boundary conditions. For $P = 4$ particles on a ladder of length $L = 8$ subject to periodic boundary conditions, the nondegenerate ground state always occurs in the $\mathbf{q} = (0, -\pi)$ Bloch sector, for various ratios of $t_\perp/t_\parallel < 1$. The ground-state wave function consists of purely real amplitudes, and the histograms of the amplitudes are shown in Figures 8.7 and 8.8, for parameter values $(t_\perp/t_\parallel = 0.1, t'/t_\parallel = 0)$ and $(t_\perp/t_\parallel = 0.5, t'/t_\parallel = 0)$ respectively. For both parameter points, we find the same group of large absolute amplitudes, and a very similar hierarchy of intermediate to small absolute amplitudes. This hierarchy of intermediate to small absolute amplitudes is very clearly defined for the parameter point $(t_\perp/t_\parallel = 0.1, t'/t_\parallel = 0)$, and more fuzzy for the parameter point $(t_\perp/t_\parallel = 0.5, t'/t_\parallel = 0)$, especially for the small absolute amplitudes. For

both parameter points, the four staggered-ground-state configurations with the largest absolute amplitude are the same, and shown in Figure 8.9.

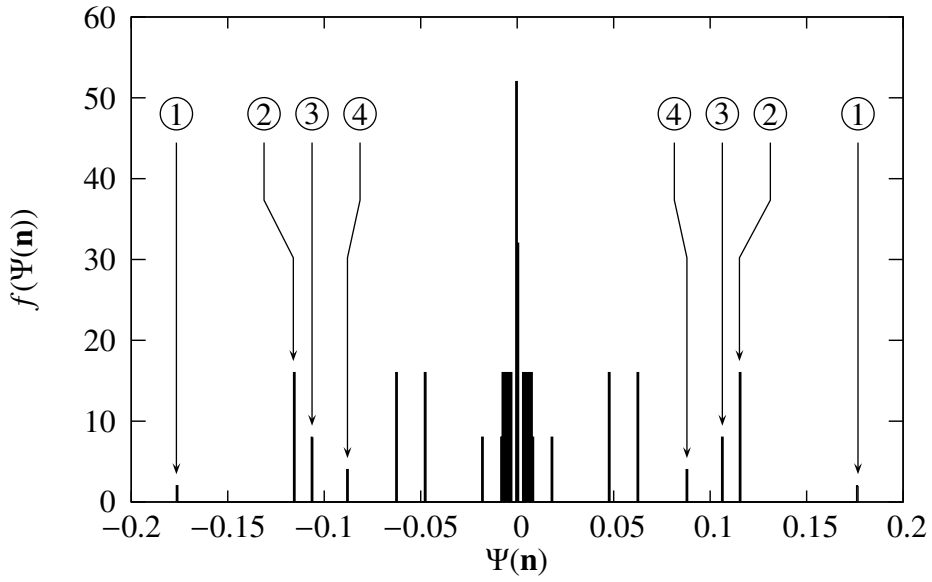

Figure 8.7: Histogram of amplitudes in the $\mathbf{q} = (0, -\pi)$ ground-state wave function of $P = 4$ particles on the spinless extended Hubbard ladder with length $L = 8$, subject to periodic boundary conditions, at the parameter point $(t_\perp/t_\parallel = 0.1, t'/t_\parallel = 0)$. The largest, second largest, third largest and fourth largest absolute amplitudes are highlighted on the histogram.

The configurations with the second largest absolute amplitude are those connected to the four largest-absolute-amplitude configurations by a single $t_\parallel$-hop. Each of the four largest-absolute-amplitude configurations admits eight independent single-particle $t_\parallel$-hops, two per particle on the ladder. Hence there are 32 staggered ground-state configurations having this second largest absolute amplitude.

There are 16 staggered ground-state configurations with the third largest absolute amplitude. These are configurations connected to the four largest-absolute-amplitude configurations by two successive particles hopping along the legs, one along the top

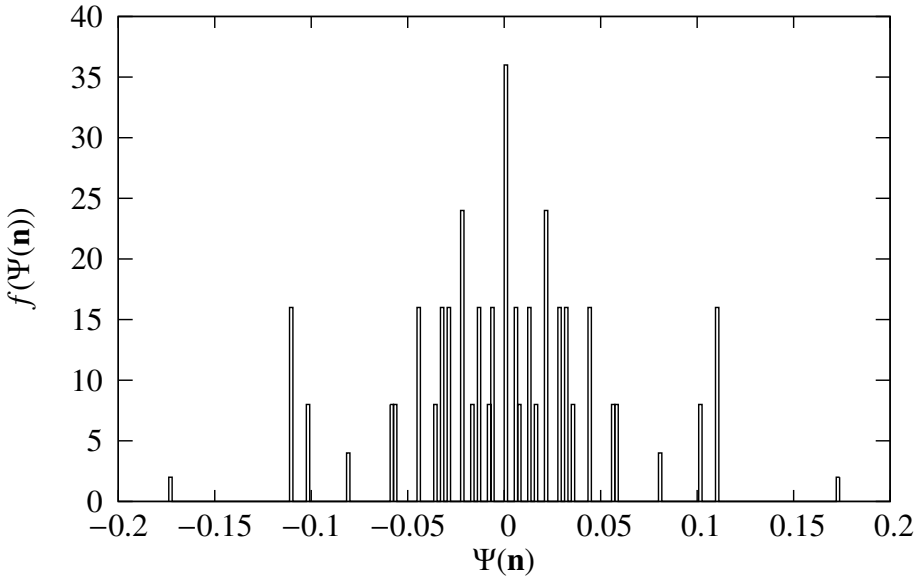

Figure 8.8: Histogram of amplitudes in the $\mathbf{q} = (0, -\pi)$ ground-state wave function of $P = 4$ particles on the spinless extended Hubbard ladder with length $L = 8$, subject to periodic boundary conditions, and with parameter values $(t_\perp/t_\parallel = 0.5, t'/t_\parallel = 0)$.

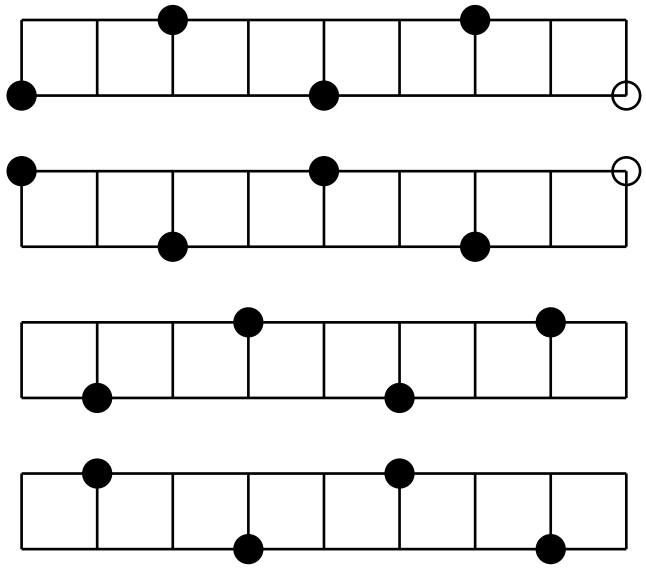

Figure 8.9: The four largest-absolute-amplitude staggered-ground-state configurations for $P = 4$ particles on the spinless extended Hubbard ladder of length $L = 8$, subject to periodic boundary conditions.

chain, and the other along the bottom chain. The two $t_{\|}$-hops are also in the same sense, i.e. if the top $t_{\|}$-hop is in the $+x$ direction, then so is the bottom $t_{\|}$-hop. One such configuration, and the largest-absolute-8.10.

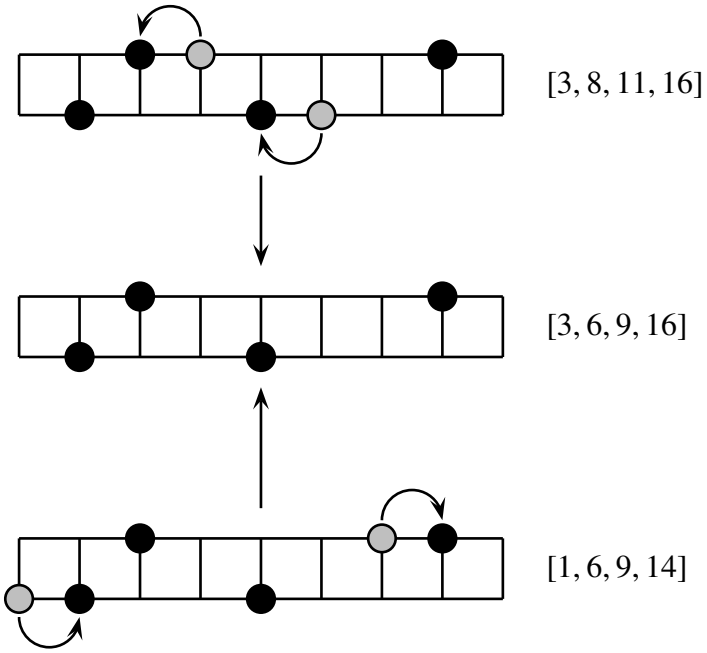

Figure 8.10: The third-largest-absolute-amplitude configuration $[3, 6, 9, 16]$ for $P = 4$ particles on a ladder of length $L = 8$ subject to periodic boundary conditions, with parameters $(t_{\perp}/t_{\|} = 0.1, t'/t_{\|} = 0)$. This configuration can be derived from two largest-absolute-amplitude configurations, $[1, 6, 9, 14]$ or $[3, 8, 11, 16]$, by two $t_{\|}$-hops.

The eight fourth-largest-absolute-amplitude staggered ground-state configurations are also derived from the largest-absolute-amplitude configurations by two $t_{\|}$-hops in the same direction. In contrast to configurations with the third largest absolute amplitude, here both hops are along the top leg or the bottom leg, and the two hopping particles are separated from one another by the stationary particles. An example configuration is shown in Figure 8.11.

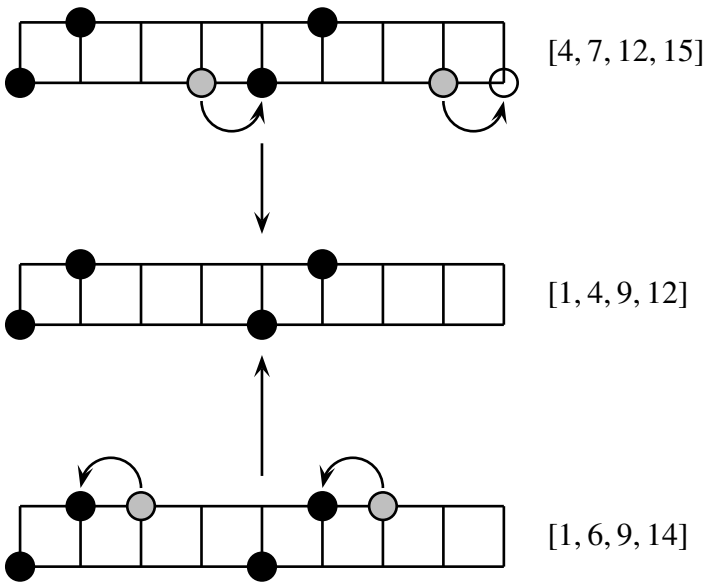

Figure 8.11: The fourth-largest-absolute-amplitude configuration $[1, 4, 9, 12]$, which can be obtained from two largest-absolute-amplitude configurations, $[4, 7, 12, 15]$ or $[1, 6, 9, 14]$, by two $t_{\|}$-hops.

Twist boundary conditions. For $P = 4$ on a ladder of length $L = 8$ subject to twist boundary conditions, with 41 twist angles $-\frac{\pi}{8} \leq \phi_x \leq +\frac{\pi}{8}$ restricted to the First Brillouin Zone, we look at the structure of the ED ground-state wave functions for two parameter points. For the parameter point $(t_\perp/t_\parallel = 0, t'/t_\parallel = 0.1)$, we see from Figure 8.12 that the nondegenerate ground state lies in the $\mathbf{q} = (+\frac{\pi}{2}, 0)$ Bloch sector for $-\frac{\pi}{8} \leq \phi_x \leq -\frac{\pi}{16}$, in the $\mathbf{q} = (0, -\pi)$ Bloch sector for $-\frac{\pi}{16} \leq \phi_x \leq +\frac{\pi}{16}$, and in the $\mathbf{q} = (-\frac{\pi}{2}, 0)$ Bloch sector for $+\frac{\pi}{16} \leq \phi_x \leq +\frac{\pi}{8}$.

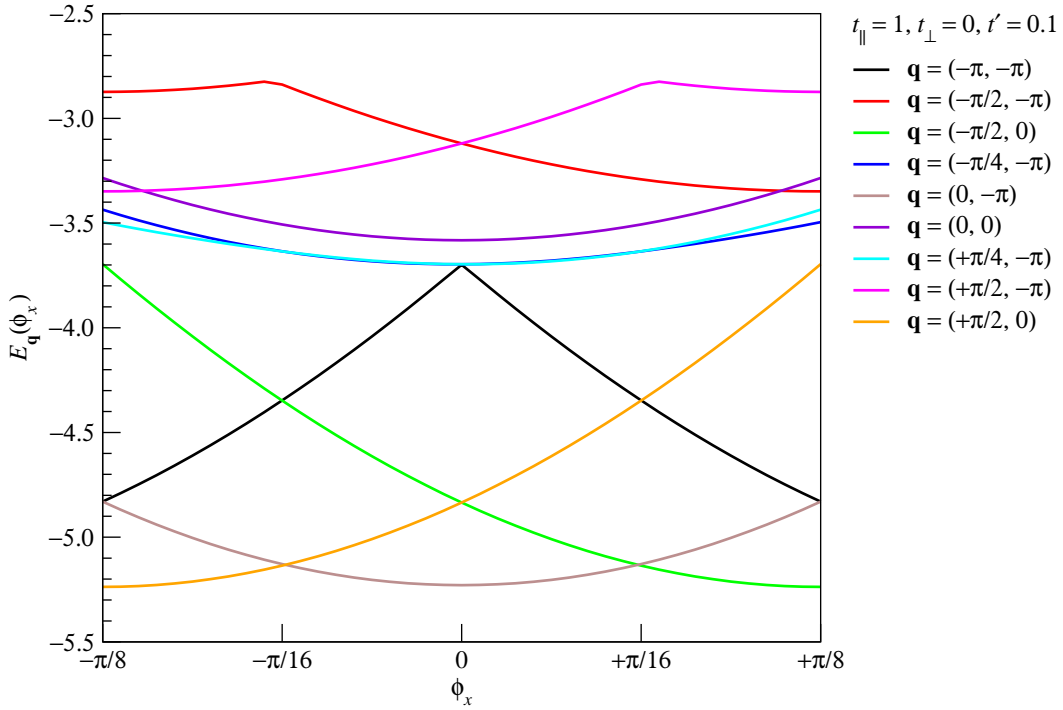

Figure 8.12: Minimum many-particle energy eigenvalues $E_{\mathbf{q}}(\phi_x)$ as a function of the twist angle ϕ_x for the Bloch sectors with wave vectors $\mathbf{q} = (-\pi, -\pi)$, $\mathbf{q} = (-\frac{\pi}{2}, -\pi)$, $\mathbf{q} = (-\frac{\pi}{4}, -\pi)$, $\mathbf{q} = (0, -\pi)$, $\mathbf{q} = (+\frac{\pi}{4}, -\pi)$, and $\mathbf{q} = (+\frac{\pi}{2}, 0)$, for $P = 4$ particles on a ladder of length $L = 8$, at the parameter point $(t_\perp/t_\parallel = 0, t'/t_\parallel = 0.1)$.

Plotting in Figure 8.13 the histograms of absolute amplitudes for the minimum-energy wave functions for the three Bloch sectors $\mathbf{q} = (-\frac{\pi}{2}, 0)$, $\mathbf{q} = (0, -\pi)$ and $\mathbf{q} =$

$(+\frac{\pi}{2}, 0)$ at twist angles $\phi_x = -\frac{\pi}{8}$, $\phi_x = -\frac{\pi}{16}$ and $\phi_x = 0$, we find the histograms of absolute amplitudes to have very similar structures: there is one group of large absolute amplitudes (the staggered ground-state configurations shown in Figure 8.9), as well as a well-defined hierarchy of intermediate absolute amplitudes. As we have understood from the case of periodic boundary conditions, the 32 configurations with the second largest absolute amplitude in all three minimum-energy wave functions are always derived from the largest-absolute-amplitude configurations by one of the particle hopping to the left or to the right along the leg it is on. All intermediate-absolute-amplitude configurations are staggered ground-state configurations, and the eight largest-absolute-amplitude configurations derived from staggered ground-state configurations by a single correlated hop has an absolute amplitude one order of magnitude smaller than the average staggered ground-state configuration absolute amplitude. This is expected, since t' is one order of magnitude smaller than $t_{\parallel}$. Other correlated-hopped configurations have even smaller absolute amplitudes.

For this parameter point of $(t_{\perp}/t_{\parallel} = 0, t'/t_{\parallel} = 0.1)$, we do not plot the evolution of the various amplitudes with the twist angle ϕ_x. While some amplitudes have absolute values which vary as ϕ_x is varied, for the large- and intermediate-absolute-amplitude configurations the magnitudes of such variations are small. Thus, the evolution of these amplitudes with ϕ_x is generally uninteresting. What we might want to note, however, is that the ground state selected at different ϕ_x might be from different Bloch sectors, and thus the relative phases between ground-state amplitudes are generically discontinous as a function of ϕ_x. For example, the bond-gauge phases of the largest-absolute-amplitude configurations [2, 5, 10, 13], [3, 8, 11, 16], and [4, 7, 12, 15] relative to [1, 6, 9, 14] in the selected ground state are shown as functions of ϕ_x in Figure 8.14.

For the parameter point $(t_{\perp}/t_{\parallel} = 0.1, t'/t_{\parallel} = 0)$, we plot the minimum energy $E_{\mathbf{q}}(\phi_x)$

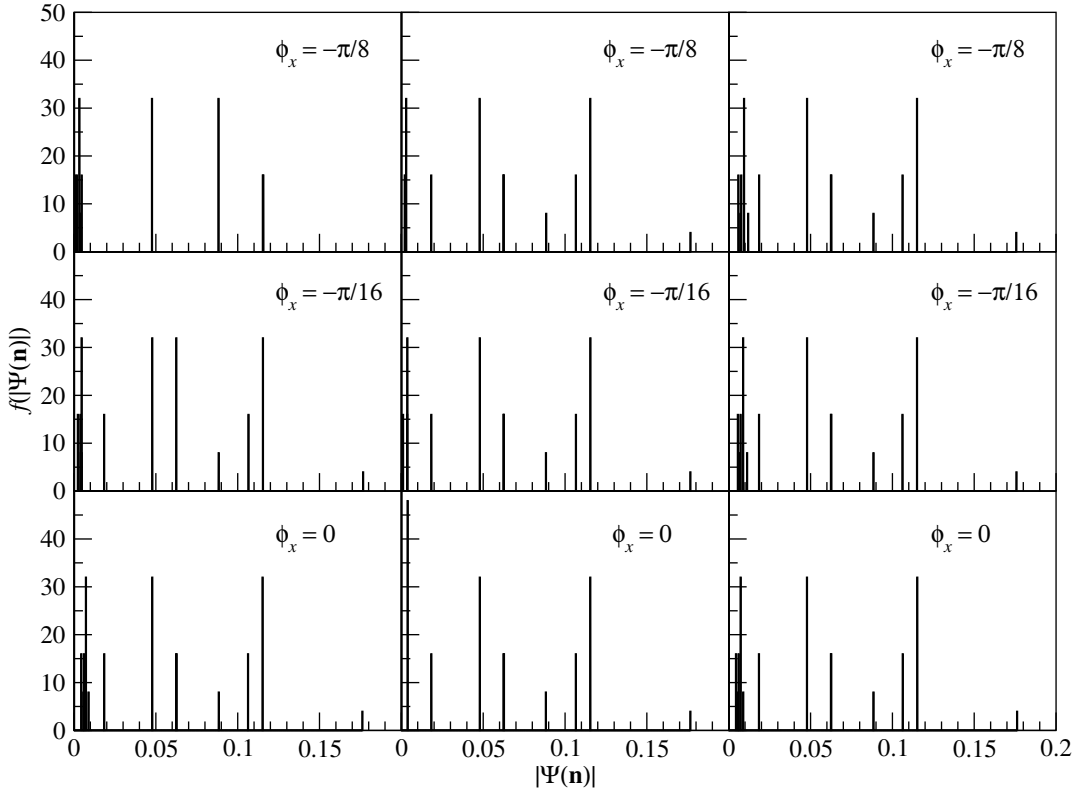

Figure 8.13: Histograms of the absolute amplitudes for minimum-energy wave functions in the $\mathbf{q} = (-\frac{\pi}{2}, 0)$ Bloch sector (left), the $\mathbf{q} = (0, -\pi)$ Bloch sector (center), and the $\mathbf{q} = (+\frac{\pi}{2}, 0)$ Bloch sector (right), for $P = 4$ particles on a ladder of length $L = 8$, at the parameter point $(t_\perp/t_\parallel = 0, t'/t_\parallel = 0.1)$, subject to twist boundary conditions with twist angles $\phi_x = -\frac{\pi}{8}$ (top), $\phi_x = -\frac{\pi}{16}$ (middle), and $\phi_x = 0$ (bottom).

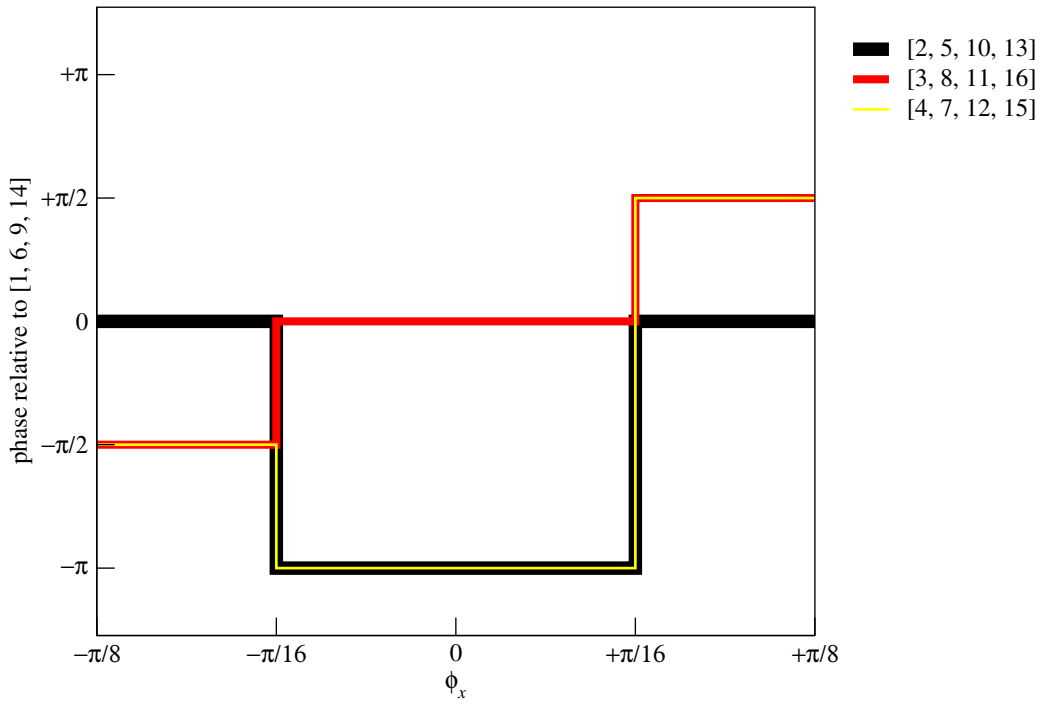

Figure 8.14: Plot of bond-gauge phases of the largest-absolute-amplitude configurations [2, 5, 10, 13] (black), [3, 8, 11, 16] (red), and [4, 7, 12, 15] (yellow) relative to the largest-absolute-amplitude configuration [1, 6, 9, 14], as a function of the twist angle ϕ_x, after ground-state selection by twist boundary conditions averaging of $P = 4$ particles on a ladder of length $L = 8$, with parameters $(t_\perp/t_\parallel = 0, t'/t_\parallel = 0.1)$.

for various Bloch sectors as functions of the twist angle ϕ_x. As shown in Figure 8.15, the behaviour of the lowest minimum energies $E_{\mathbf{q}}(\phi_x)$ for this parameter point appears to be identical to those for the parameter point $(t_\perp/t_\parallel = 0, t'/t_\parallel = 0.1)$. Ground state selection by twist boundary conditions averaging therefore picks the minimum-energy state in the $\mathbf{q} = (+\frac{\pi}{2}, 0)$ Bloch sector for $-\frac{\pi}{8} \leq \phi_x \leq -\frac{\pi}{16}$, the minimum-energy state in the $\mathbf{q} = (0, -\pi)$ Bloch sector for $-\frac{\pi}{16} \leq \phi_x \leq +\frac{\pi}{16}$, and the minimum-energy state in the $\mathbf{q} = (+\frac{\pi}{2}, 0)$ Bloch sector for $+\frac{\pi}{16} \leq \phi_x \leq +\frac{\pi}{8}$.

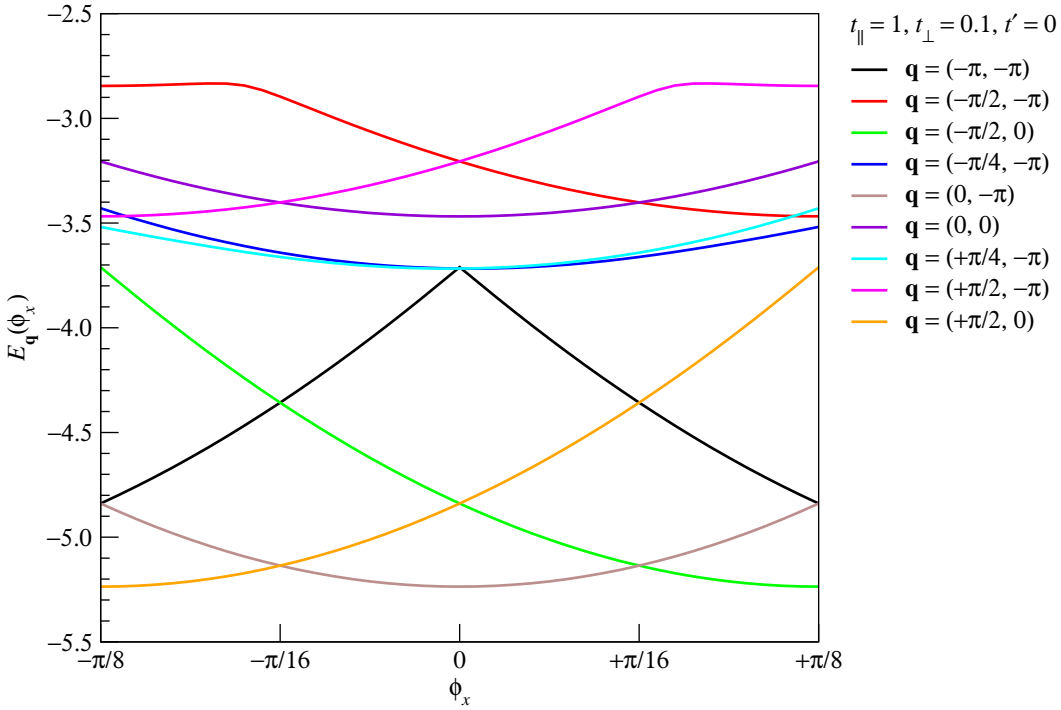

Figure 8.15: Minimum many-particle energy eigenvalues $E_{\mathbf{q}}(\phi_x)$ as a function of the twist angle ϕ_x for the Bloch sectors with wave vectors $\mathbf{q} = (-\pi, -\pi)$, $\mathbf{q} = (-\frac{\pi}{2}, -\pi)$, $\mathbf{q} = (-\frac{\pi}{4}, -\pi)$, $\mathbf{q} = (0, -\pi)$, $\mathbf{q} = (+\frac{\pi}{4}, -\pi)$, and $\mathbf{q} = (+\frac{\pi}{2}, 0)$, for $P = 4$ particles on a ladder of length $L = 8$, at the parameter point $(t_\perp/t_\parallel = 0.1, t'/t_\parallel = 0)$.

Since we are not able to discern the distinguishing features for the parameter points $(t_\perp/t_\parallel = 0.1, t'/t_\parallel = 0)$ and $(t_\perp/t_\parallel = 0, t'/t_\parallel = 0.1)$ from the lowest few minimum energies

as functions of the twist angle ϕ_x, we look at the histograms of absolute amplitudes for the minimum-energy wave functions in the $\mathbf{q} = (-\frac{\pi}{2}, 0)$, $\mathbf{q} = (0, -\pi)$ and $\mathbf{q} = (+\frac{\pi}{2}, 0)$ Bloch sectors. These are shown in Figure 8.16. Comparing Figure 8.13 and 8.16, we find that the distribution of large to intermediate absolute amplitudes appears to be same for the two parameter points, and it is the distribution of the small absolute amplitudes that set the two parameter points apart.

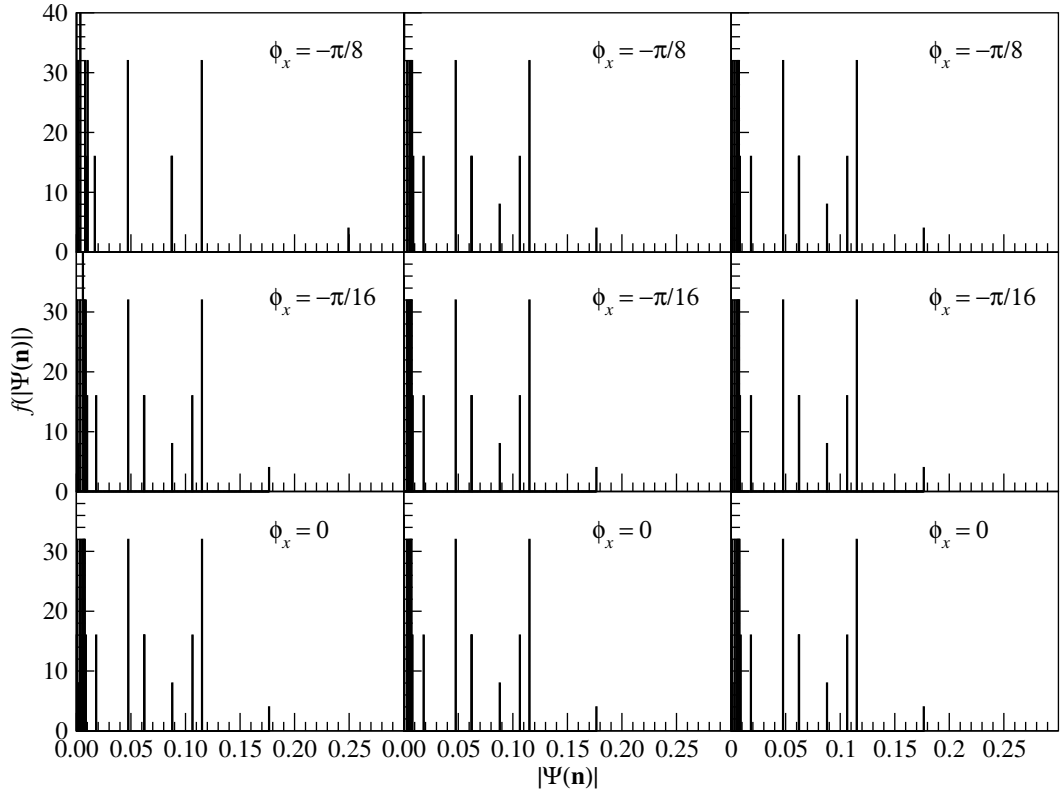

Figure 8.16: Histograms of the absolute amplitudes for minimum-energy wave functions in the $\mathbf{q} = (-\frac{\pi}{2}, 0)$ Bloch sector (left), the $\mathbf{q} = (0, -\pi)$ Bloch sector (center), and the $\mathbf{q} = (+\frac{\pi}{2}, 0)$ Bloch sector (right), for $P = 4$ particles on a ladder of length $L = 8$, at the parameter point $(t_\perp/t_\parallel = 0.1, t'/t_\parallel = 0)$, subject to twist boundary conditions with twist angles $\phi_x = -\frac{\pi}{8}$ (top), $\phi_x = -\frac{\pi}{16}$ (middle), and $\phi_x = 0$ (bottom).

The ground-state configurations with the largest absolute amplitudes are all stag-

gered-ground-state configurations. The non-staggered-ground-state configurations with the largest absolute amplitude has an absolute amplitude that is one order of magnitude smaller than the average absolute amplitude of the staggered-ground-state configurations. These 16 non-staggered-ground-state configurations are derived from the largest-absolute-amplitude staggered-ground-state configurations by a single $t_\perp$-hop.

8.3.1.2 Strong Inter-Leg Hopping

In Section 7.7, we understood how, in the limit of very strong inter-leg hopping, the ground state is that of a chain of spinless rung-fermions with infinite nearest-neighbor repulsion. When the ladder is quarter-filled, the infinite-ladder ground state is a rung-fermion solid, in which rung-fermions occupy every other rung on the ladder. Such a rung-fermion solid ground state, which is two-fold degenerate (rung-fermions occupying all the even rungs, or all the odd rungs), exhibits true long-range CDW correlations, and has vanishing FL and SC correlations. For finite ladders, we expect to see signatures of the true long-range CDW in the ED ground-state wave functions.

Periodic boundary conditions. For $P = 4$ particles on a ladder of length $L = 8$, with parameters $(t_\perp/t_\parallel = 4, t'/t_\parallel = 0)$, we find two degenerate ground states, occurring in the $\mathbf{q} = (\pm\frac{\pi}{2}, 0)$ Bloch sectors. These translation-invariant ground states corresponds to symmetric and antisymmetric combinations of the even-rung-fermion-solid and the odd-rung-fermion-solid ground states, which are not translationally invariant.

For this choice of parameters, where $t_\perp/t_\parallel$ is not very much larger than one, the $\mathbf{q} = (\pm\frac{\pi}{2}, 0)$ ground-state wave functions have rather rich structures, with 20 independent absolute amplitudes and 55 independent relative phases. Instead of just plotting histograms of absolute amplitudes, we find it more visually informative to plot the real

and imaginary parts of the amplitudes as shown in Figure 8.17, where we see three groups of large absolute amplitudes, and a cluster of small absolute amplitudes. One of the group of large absolute amplitudes (the purely real group) is common to the two ground-state wave functions, while the other two groups of purely imaginary amplitudes belong to one wave function or the other.

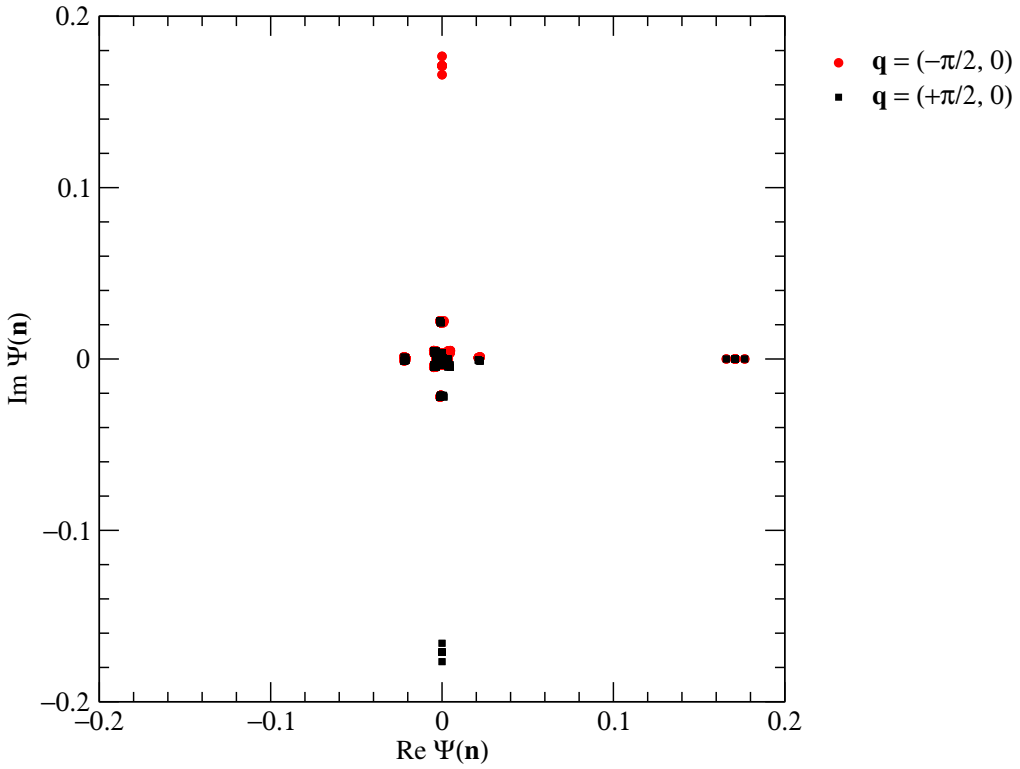

Figure 8.17: Plot of the real and imaginary parts of the amplitudes $\Psi(\mathbf{n})$ in the $\mathbf{q} = (\pm\frac{\pi}{2}, 0)$ ground-state wave functions for $P = 4$ particles on a ladder of length $L = 8$ subject to periodic boundary conditions, with parameters $(t_\perp/t_\parallel = 4, t'/t_\parallel = 0)$.

Looking at the amplitudes with small absolute values more carefully, we find the fine structure shown in Figure 8.18. We see four groups of small absolute amplitudes, each of which is shared to different degrees in the two ground-state wave functions, as well as an hyperfine structure of even smaller absolute amplitudes. From the hyperfine structure

shown in Figure 8.19, we see a central cross-shaped cluster of amplitudes common to both wave functions, and peripheral amplitudes shared to different degrees by the two wave functions.

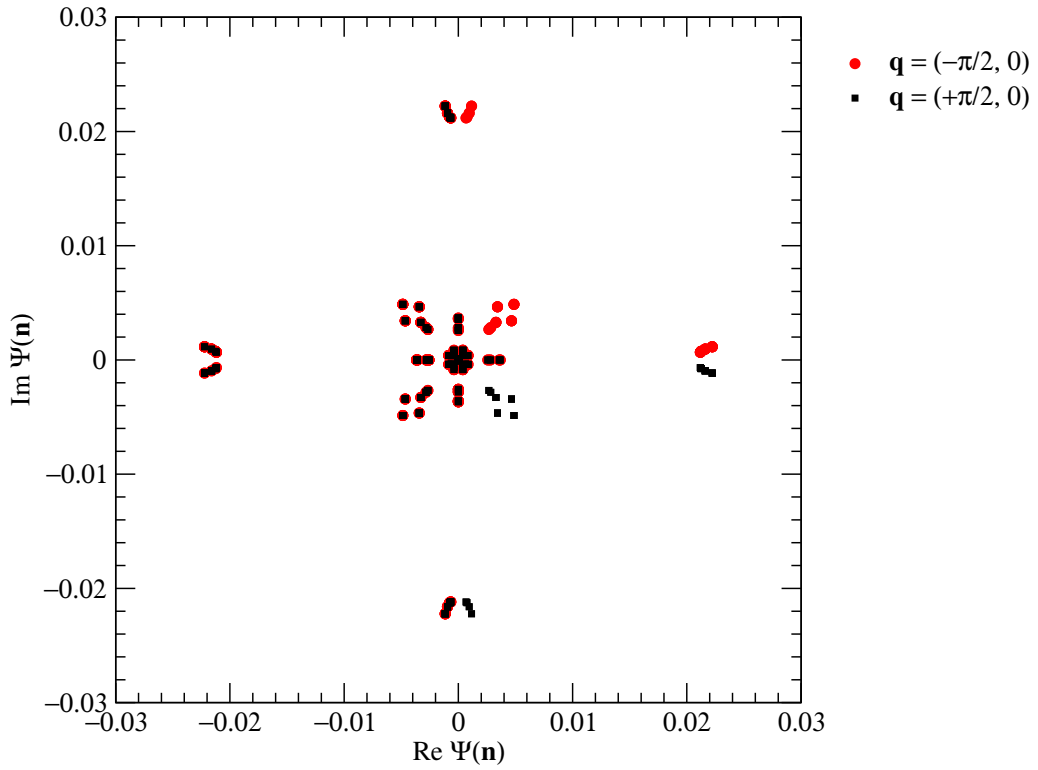

Figure 8.18: Plot of the real and imaginary parts of the amplitudes $\Psi(\mathbf{n})$ with small absolute magnitudes in the $\mathbf{q} = (\pm\frac{\pi}{2}, 0)$ ground-state wave functions for $P = 4$ particles on a ladder of length $L = 8$ subject to periodic boundary conditions, with parameters $(t_\perp/t_\parallel = 4, t'/t_\parallel = 0)$.

The purely real group of large amplitudes, which is common to both ground-state wave functions, consists of the configurations shown in Figure 8.20, with their corresponding amplitudes listed. The two purely imaginary groups (+ for $\mathbf{q} = (-\frac{\pi}{2}, 0)$ and − for $\mathbf{q} = (+\frac{\pi}{2}, 0)$) consists of the configurations shown in Figure 8.21, with their corresponding amplitudes listed. These are configurations associated with the rung-fermion

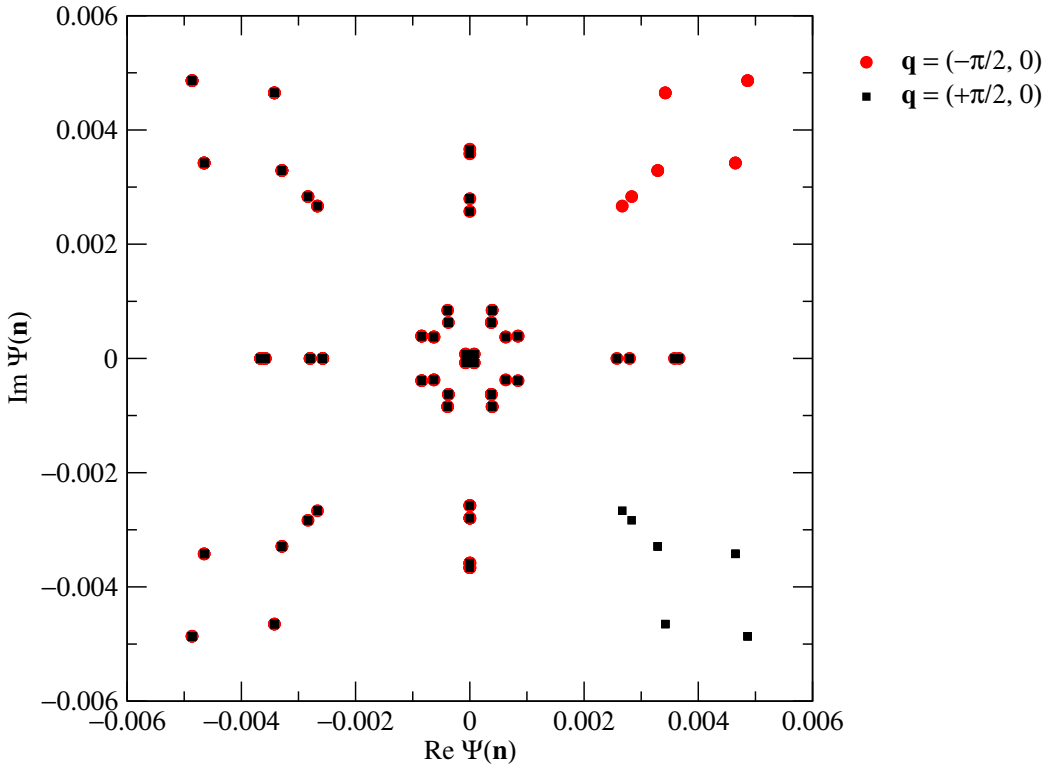

Figure 8.19: Plot of the real and imaginary parts of the amplitudes $\Psi(\mathbf{n})$ with the smallest absolute magnitudes in the $\mathbf{q} = (\pm\frac{\pi}{2}, 0)$ ground-state wave functions for $P = 4$ particles on a ladder of length $L = 8$ subject to periodic boundary conditions, with parameters $(t_\perp/t_\parallel = 4, t'/t_\parallel = 0)$.

solid ground states.

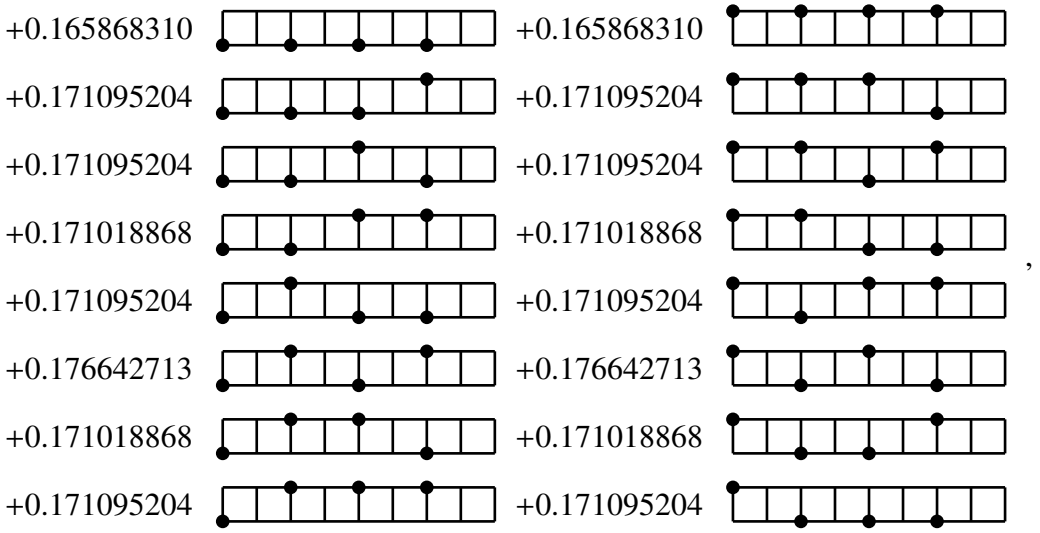

Figure 8.20: Rung-fermion-solid ground-state configurations with large, real, amplitudes for $P = 4$ particles on a ladder of length $L = 8$ subject to periodic boundary conditions, with parameters $(t_\perp/t_\parallel = 4, t'/t_\parallel = 0)$.

For the group of intermediate amplitudes, we look first at the cluster of amplitudes common to both wave functions, with real part of the amplitudes between -0.1 and -0.01. This group consists of 40 configurations, which are too many to enumerate, so we look at some examples. For example, the intermediate-amplitude configuration $[1, 5, 9, 16]$ is actually derived from the rung-fermion-solid ground-state configuration $[1, 5, 9, 14]$ by a nearest-neighbor hop along the top leg of the ladder, as shown in Figure 8.22. Also shown in Figure 8.22 is the intermediate-amplitude configuration $[2, 8, 9, 14]$, which can be obtained from the rung-fermion-solid ground-state configuration $[2, 6, 9, 14]$ by a nearest-neighbor hop along the top chain of the ladder. As expected, an intermediate-amplitude configuration derived from a large-amplitude configuration with larger absolute amplitude has a larger absolute amplitude compared to one derived from a large-amplitude configuration with smaller absolute amplitude.

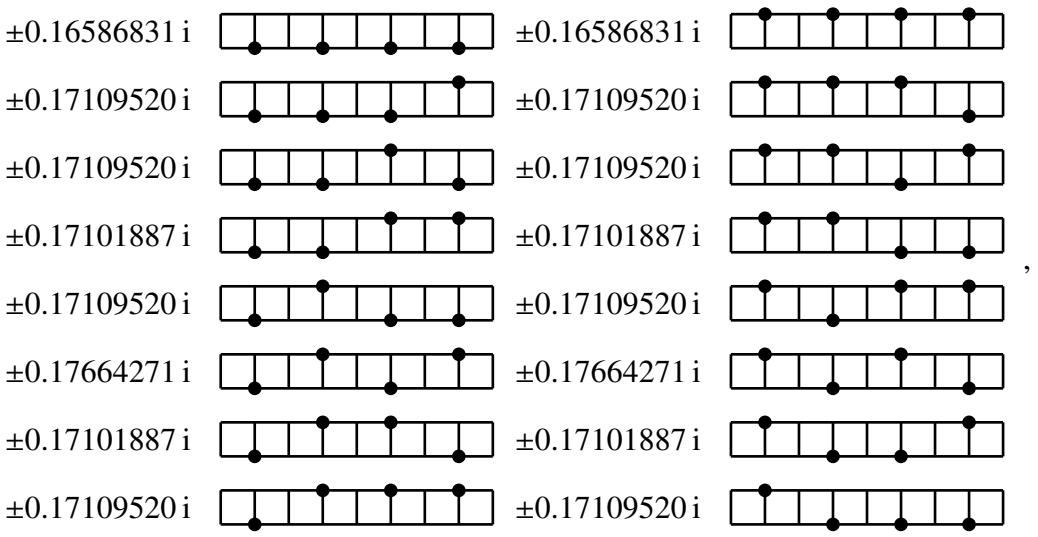

Figure 8.21: Rung-fermion-solid ground-state configurations with large, imaginary, amplitudes for $P = 4$ particles on a ladder of length $L = 8$ subject to periodic boundary conditions, with parameters $(t_\perp/t_\parallel = 4, t'/t_\parallel = 0)$.

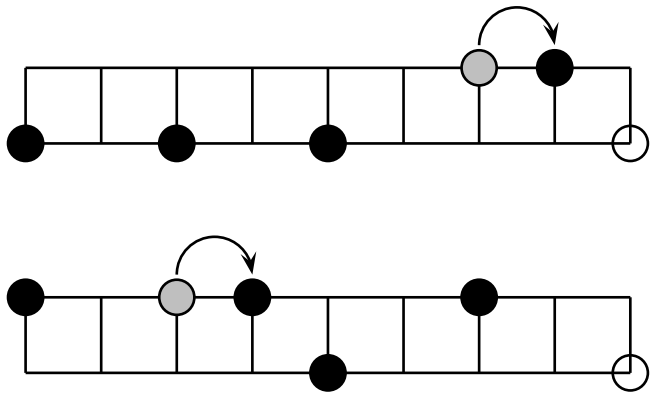

Figure 8.22: The configurations $[1, 5, 9, 16]$ (top) and $[2, 8, 9, 14]$ (bottom), which have intermediate amplitudes in the $(\pm\frac{\pi}{2}, 0)$ ground-state wave functions of $P = 4$ particles on a ladder of length $L = 8$ with $t_\perp/t_\parallel = 4$. The configuration $[1, 5, 9, 16]$ can be obtained from the large-amplitude configuration $[1, 5, 9, 14]$, while the configuration $[2, 8, 9, 14]$ can be obtained from the large-amplitude configuration $[2, 6, 9, 14]$, each by a nearest-neighbor hop as shown.

In the same way, we find that the small-amplitude configurations are derived from the intermediate-amplitude configurations by one or more nearest-neighbor hops along the chain of the ladder. For example, the small-amplitude configuration $[1, 4, 7, 13]$ is derived from either $[1, 6, 7, 13]$ or $[1, 4, 9, 13]$, which are both intermediate-amplitude configurations. We expect then that a configuration connected to the large-amplitude configuration by k nearest-neighbor hops will have an absolute amplitude that decays more or less as a power-law in k. Therefore, we expect that the dominant correlations (which are charge-density waves) in the ground state of this ladder system are contributed essentially by the large-amplitude configurations, whereas subdominant correlations receive contributions primarily from the intermediate-amplitude configurations.

Twist boundary conditions. For $P = 4$ particles on a ladder of length $L = 8$ subject to twist boundary conditions, with twist angles $-\frac{\pi}{8} \leq \phi_x \leq +\frac{\pi}{8}$ restricted to the First Brillouin Zone, at the parameter point $(t_\perp/t_\parallel = 4, t'/t_\parallel = 0)$, the lowest minimum energies are plotted in Figure 8.23 as functions of the twist angle ϕ_x. As we can see from Figure 8.23, the minimum energies in the $\mathbf{q} = (\pm\frac{\pi}{2}, 0)$ Bloch sectors are very far below those in other Bloch sectors. In Figure 8.24, we show only the minimum energies in the $\mathbf{q} = (\pm\frac{\pi}{2}, 0)$ Bloch sectors, and see that the ground state selected by twist boundary conditions averaging is in the $\mathbf{q} = (+\frac{\pi}{2}, 0)$ Bloch sector for $-\frac{\pi}{8} \leq \phi_x \leq 0$, and in the $\mathbf{q} = (-\frac{\pi}{2}, 0)$ Bloch sector for $0 \leq \phi_x \leq +\frac{\pi}{8}$.

For twist angles in the range $-\frac{\pi}{8} \leq \phi_x \leq +\frac{\pi}{8}$, the structure of the bond-gauge amplitudes in the ground state selected by twist boundary conditions averaging are always very similar to that shown in Figures 8.17, 8.18, and 8.19. Subjecting $P = 4$ particles on the ladder of length $L = 8$ to periodic boundary conditions, we saw that there is a group of large real amplitudes for both the $\mathbf{q} = (\pm\frac{\pi}{2}, 0)$ ground states. It turns out that

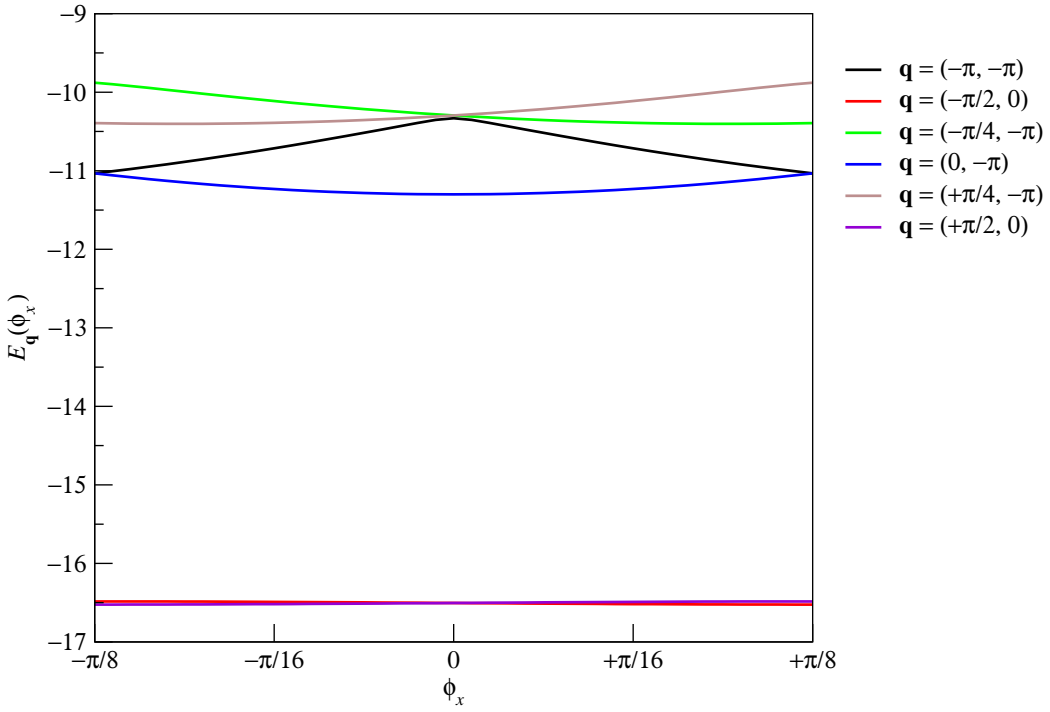

Figure 8.23: Minimum many-particle energies $E_{\mathbf{q}}(\phi_x)$ as functions of the twist angle ϕ_x for the Bloch sectors with wave vectors $\mathbf{q} = (-\pi, -\pi)$, $\mathbf{q} = (-\frac{\pi}{2}, 0)$, $\mathbf{q} = (-\frac{\pi}{4}, -\pi)$, $\mathbf{q} = (0, -\pi)$, $\mathbf{q} = (+\frac{\pi}{4}, -\pi)$, and $\mathbf{q} = (+\frac{\pi}{2}, 0)$, for $P = 4$ particles on a ladder of length $L = 8$, at the parameter point $(t_\perp/t_\parallel = 4, t'/t_\parallel = 0)$.

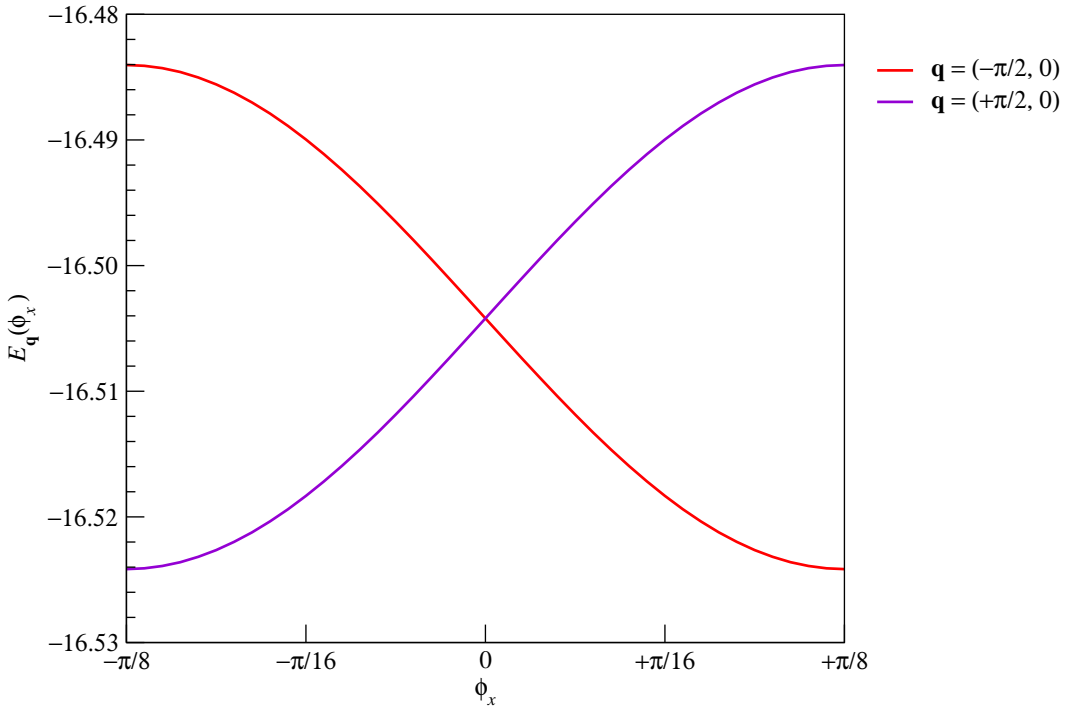

Figure 8.24: Minimum many-particle energies $E_{\mathbf{q}}(\phi_x)$ as functions of the twist angle ϕ_x for the $\mathbf{q} = (\pm\frac{\pi}{2}, 0)$ Bloch sectors, for $P = 4$ particles on a ladder of length $L = 8$, at the parameter point $(t_\perp/t_\parallel = 4, t'/t_\parallel = 0)$.

this group of amplitudes, which belongs to the rung-fermion-solid ground-state configurations shown in Figure 8.20, is always real whatever ϕ_x is in the twist boundary conditions. Therefore, we need not worry about the indeterminate overall phase discussed in Section 8.2.1, and go ahead to plot the unambiguous evolution of the boundary-gauge amplitudes as functions of the twist angle ϕ_x.

Before we do this, let us highlight the fact, presented in Appendix D, that for non-interacting spinless fermions, the amplitudes in the many-body ground-state wave function does not depend on ϕ_x in the bond gauge. In the boundary gauge, these amplitudes are periodic functions of ϕ_x. For aperiodic configurations, the boundary-gauge amplitudes have period $2\pi/L$, where L is the length of the ladder, whereas for periodic configurations, the boundary-gauge amplitudes have periods less than $2\pi/L$. For our ladder of interacting spinless fermions, we have seen so far that the ground-state amplitudes depend on ϕ_x even in the bond gauge. Therefore, after we gauge-transform these amplitudes to the boundary gauge, they do not necessarily go back to themselves after ϕ_x changes by $2\pi/L$.

In Figure 8.25, we show the evolution of one of the large-imaginary-amplitude configurations in Figure 8.21, [4, 8, 11, 15], as the twist angle is varied from $\phi_x = 0$ to $\phi_x = +\frac{\pi}{8}$. Over this range of twist angles, we find the boundary-gauge amplitude of this configuration tracing out a very nearly perfect circle. In fact, since $\boldsymbol{\phi} = (\phi_x, 0)$, only the rung indices j matters in the bond-to-boundary gauge transformation, and the group of large-imaginary-amplitude configurations all have a period of $\frac{\pi}{8}$ in ϕ_x. Another consequence of the bond-to-boundary gauge transformation depending only on the rung indices is that the large-real-amplitude configurations in Figure 8.20, have boundary-gauge amplitudes which also trace out very nearly circular trajectories as functions of ϕ_x, all have a period of $\frac{\pi}{6}$ instead of $\frac{\pi}{8}$, as shown in Figure 8.26 for one such large-real-

amplitude configuration, [1, 6, 9, 14].

Because of the modulation of absolute amplitudes observed in the intermediate bond-gauge amplitudes, we find the intermediate boundary-gauge amplitudes tracing out curves bounded between two circles. If not for the absolute amplitude modulation, the boundary-gauge amplitudes of these aperiodic intermediate-absolute-amplitude configurations would have period $\frac{\pi}{8}$ in ϕ_x. But here we find that the curves closes onto themselves only after the twist angle goes through $\Delta\phi_x = \pi$. Figure 8.27 shows the trajectory of the boundary-gauge amplitude of one such configuration, [3, 6, 9, 13], as the twist angle goes through $\Delta\phi_x = \pi$.

For the small absolute amplitudes, we have a zoo of patterns resulting from the absolute amplitude modulations coming from interactions. For example, the trajectory of the boundary-gauge amplitude of the small-absolute-amplitude configuration [1, 4, 5, 8], shown in Figure 8.28, looks like a limaçon (curve of the form $r = b + a\cos\theta$), with a period of $\Delta\phi_x = \frac{\pi}{2}$, whereas the trajectory of the boundary-gauge amplitude of the small-absolute-amplitude configuration [1, 4, 5, 11], shown in Figure 8.29, looks like a period-doubled circle, with period of $\Delta\phi_x = \pi/2$. Other boundary-gauge amplitudes are just plain crazy, like those for the small-absolute-amplitude configurations [1, 4, 5, 10] and [7, 10, 11, 15], shown in Figures 8.30 and 8.31 respectively. Both of these have a period of $\Delta\phi_x = \pi$.

Inspecting these trajectories more carefully, we find that all of them can be written as polynomials of the phase $z = \exp(\mathrm{i}\,4\phi_x)$. For example, those amplitudes tracing out a circle with period $\Delta\phi_x = \frac{\pi}{8}$ can be written as $\Psi(\mathbf{n}) \propto z^4$, while those tracing out a circle with period $\Delta\phi_x = \frac{\pi}{6}$ can be written as $\Psi(\mathbf{n}) \propto z^3$. We also fitted polynomials in z to the trajectories of the boundary-gauge amplitudes of the configurations [1, 4, 5, 8] (Figure 8.28), [1, 4, 5, 11] (Figure 8.29), and [1, 4, 5, 10] (Figure 8.30). We have not

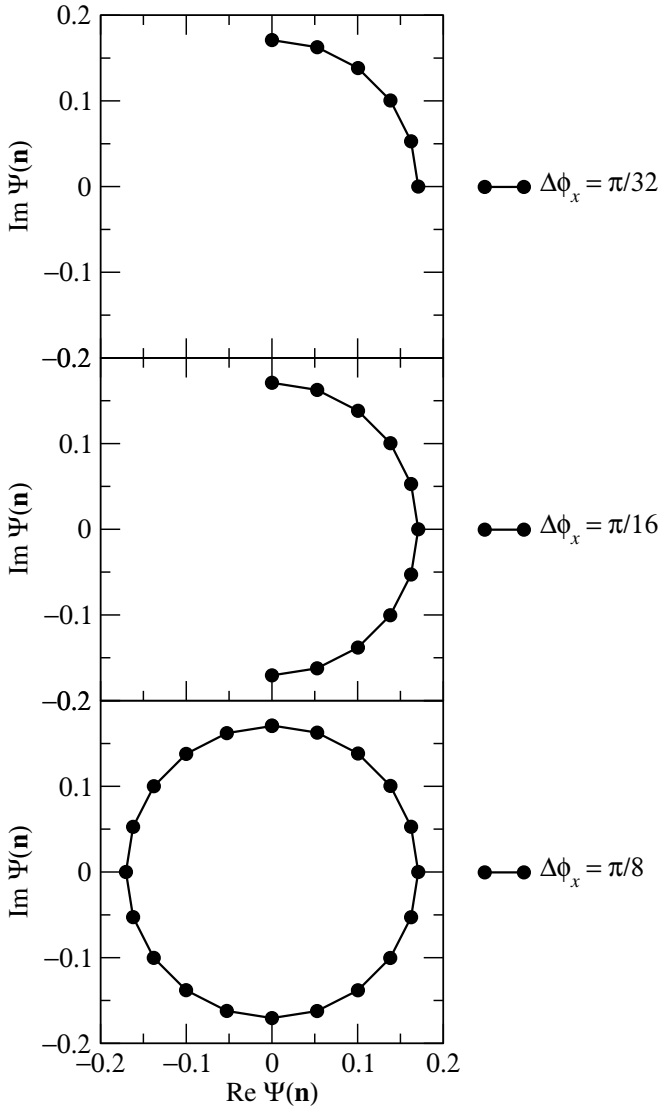

Figure 8.25: The trajectory of the boundary-gauge amplitude of the large-imaginary-amplitude configuration [4, 8, 11, 15] in the $\mathbf{q} = (-\frac{\pi}{2}, 0)$ ground-state wave function as ϕ_x changes through $\Delta\phi_x = \frac{\pi}{32}, \frac{\pi}{16}, \frac{\pi}{8}$, starting from $\phi_x = 0$ (periodic boundary conditions).

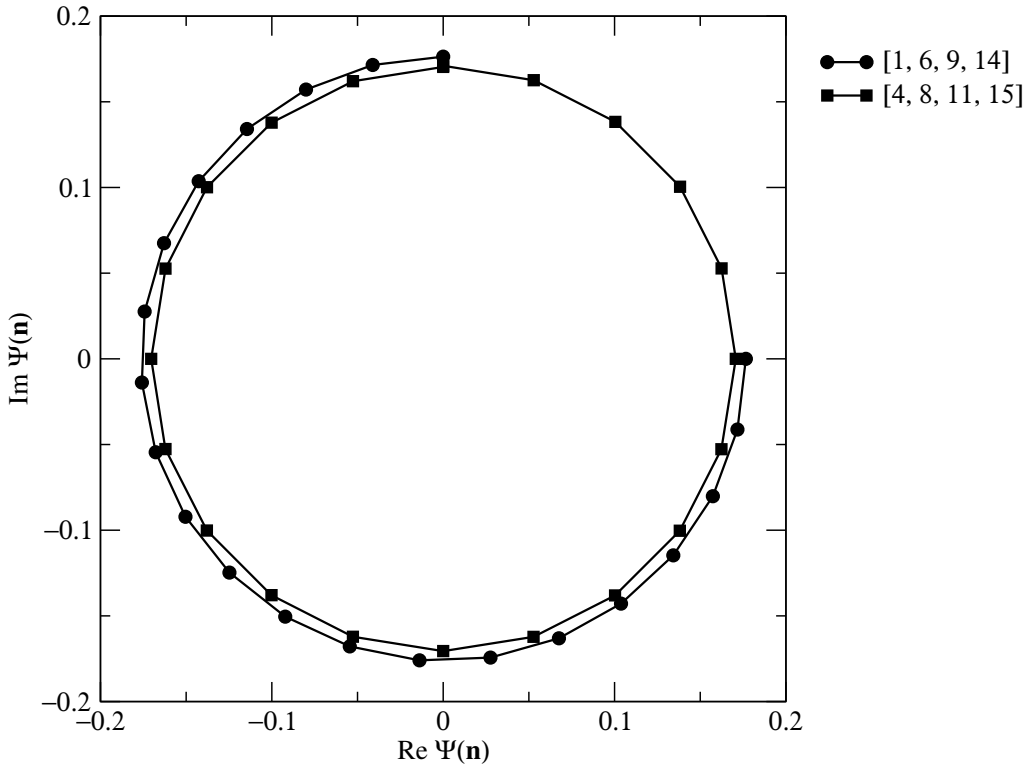

Figure 8.26: The trajectories of the boundary-gauge amplitudes of the large-real-amplitude configuration $[1, 6, 9, 14]$ and the large-imaginary-amplitude configuration $[4, 8, 11, 15]$, in the $\mathbf{q} = (-\frac{\pi}{2}, 0)$ ground-state wave function as ϕ_x changes through $\Delta\phi_x = \frac{\pi}{8}$, starting from $\phi_x = 0$ (periodic boundary conditions).

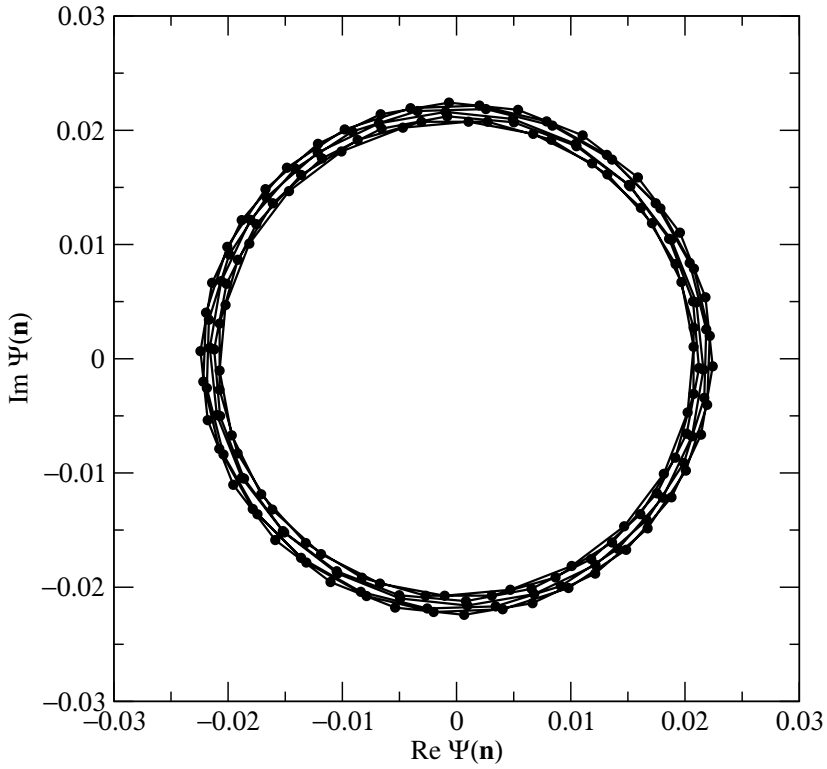

Figure 8.27: The trajectory of the boundary-gauge amplitude of the intermediate-absolute-amplitude configuration, $[3, 6, 9, 13]$, as ϕ_x changes through $\Delta\phi_x = \pi$, starting from $\phi_x = 0$ (periodic boundary conditions).

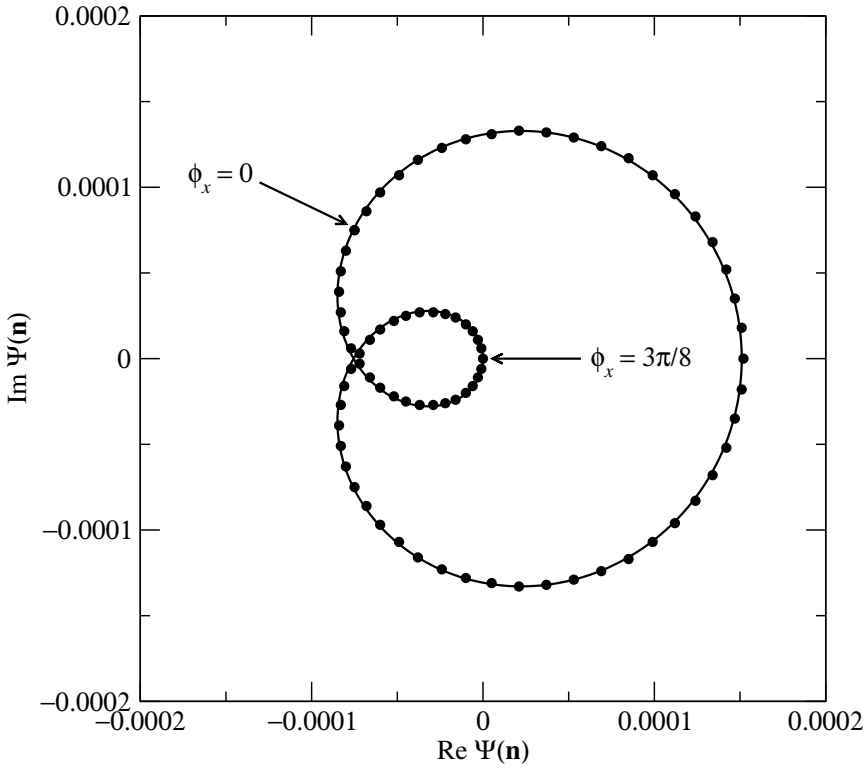

Figure 8.28: The trajectory of the boundary-gauge amplitude $\Psi([1,4,5,8])$ of the small-absolute-amplitude configuration $[1,4,5,8]$ as the twist angle ϕ_x changes through $\Delta\phi_x = \frac{\pi}{2}$, starting from $\phi_x = 0$ (periodic boundary conditions). This trajectory has been fitted to the polynomial function $\Psi([1,4,5,8]) = 7.55 \times 10^{-5}\left[\tilde{z}^* + (\tilde{z}^*)^2\right]$ (solid curve), where $\tilde{z}^* = e^{-\mathrm{i}\,4(\phi_x - \pi/8)}$. The global phase $e^{\mathrm{i}\,\pi/2}$ that get mangled with $z = e^{\mathrm{i}\,4\phi_x}$ is intrinsic to the phase relationship between the amplitude of the configuration $[1,4,5,8]$ with the large real amplitudes in the rung-fermion ground state, and has nothing to do with the indeterminate global phase coming out from numerical ED that we discussed in Section 8.2.1.3.

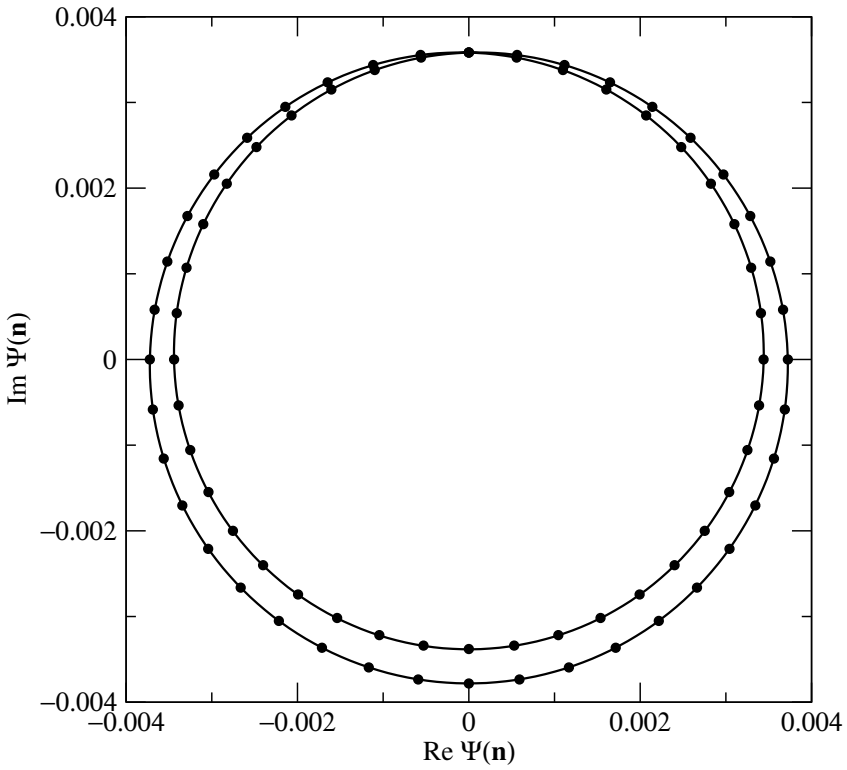

Figure 8.29: The trajectory of the boundary-gauge amplitude of the small-absolute-amplitude configuration $[1, 4, 5, 11]$ as ϕ_x changes through $\Delta\phi_x = \frac{\pi}{2}$, starting from $\phi_x = 0$ (periodic boundary conditions). This trajectory has been fitted to the polynomial function $\Psi([1, 4, 5, 11]) = 1.99 \times 10^{-4} \left(z^* + \mathrm{i}\, 18 z^{*2}\right)$ (solid curve), where $z^* = e^{-\mathrm{i}\, 4\phi_x}$ is the complex conjugate of $z = e^{\mathrm{i}\, 4\phi_x}$.

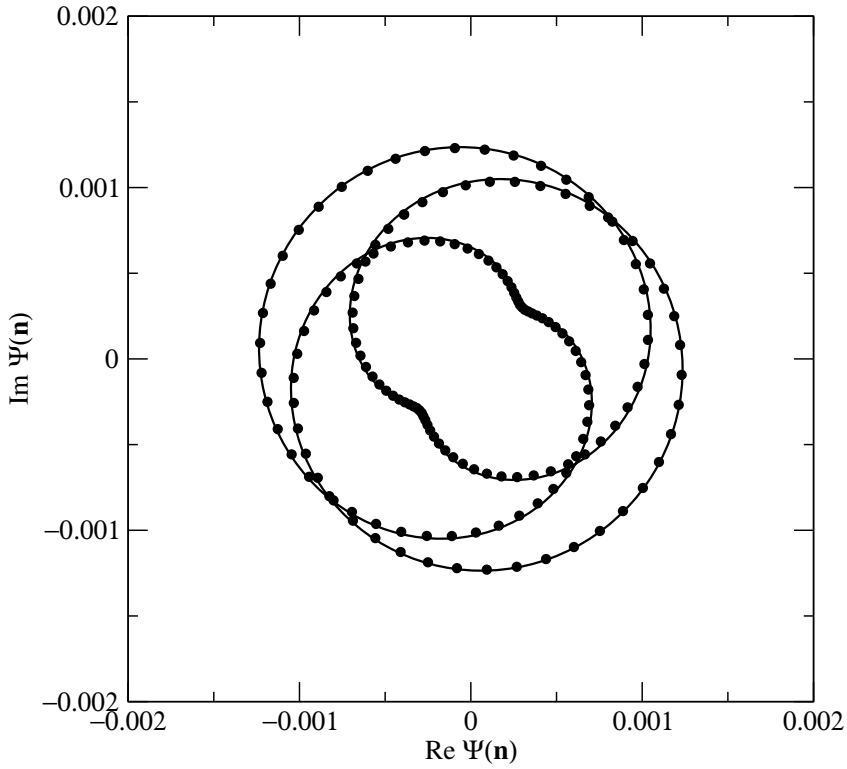

Figure 8.30: The trajectory of the boundary-gauge amplitude of the small-absolute-amplitude configuration $[1, 4, 5, 10]$ as ϕ_x changes through $\Delta\phi_x = \pi$, starting from $\phi_x = 0$ (periodic boundary conditions). This trajectory has been fitted to the function $\Psi([1, 4, 5, 10]) = 4.2 \times 10^{-4}\, e^{i\pi/4} \left(2\tilde{z}^3 - \tilde{z}^5\right)$ (solid curve), where $\tilde{z} = e^{i\,4(\phi_x - \pi/8)}$.

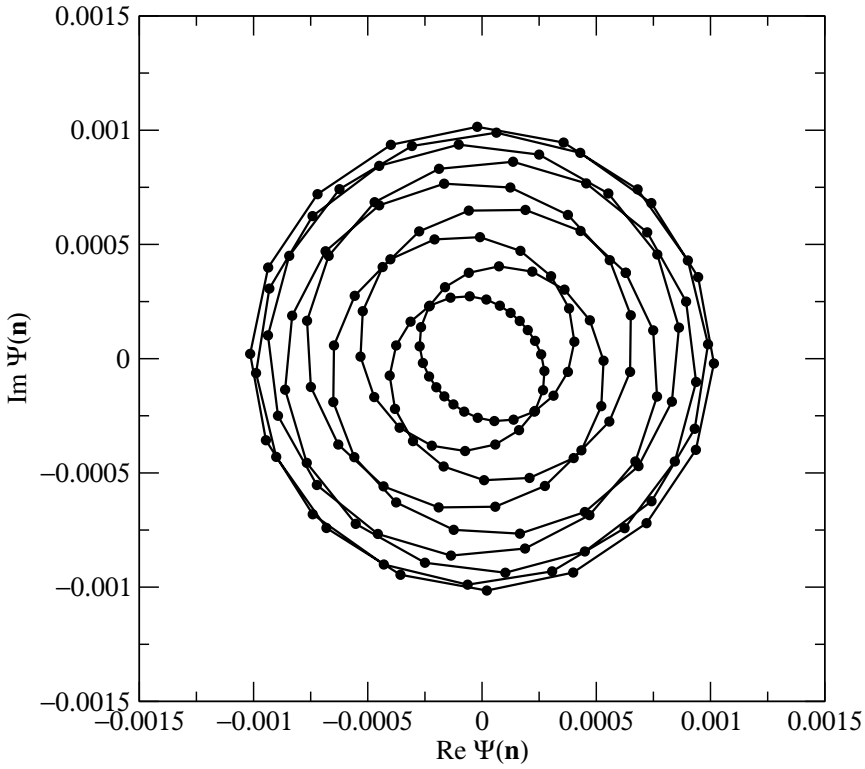

Figure 8.31: The trajectory of the boundary-gauge amplitudes of the small-absolute-amplitude configuration [7, 10, 11, 15] as ϕ_x changes through $\Delta\phi_x = \pi$, starting from $\phi_x = 0$ (periodic boundary conditions).

fitted any polynomials in z to the trajectories of the boundary-gauge amplitudes of the configurations $[3, 6, 9, 13]$ (Figure 8.27) and $[7, 10, 11, 15]$ (Figure 8.31), but from the example plots shown in Figure 8.32, it is quite likely that these can be fitted to degree-nine polynomials in z.

Twist boundary conditions averaging. For noninteracting spinless fermions, we understand from Appendix D that all amplitudes repeat themselves as functions of ϕ_x after ϕ_x goes through a change of $\Delta\phi_x = \frac{2\pi}{L}$. Therefore, it suffices to perform twist boundary conditions averaging over the set of twist angles $-\frac{\pi}{L} \leq \phi_x \leq +\frac{\pi}{L}$ restricted to the First Brillouin Zone. For our ladder of interacting spinless fermions, however, we see that there are modulations of the absolute amplitudes with periods longer than $\Delta\phi_x = \frac{2\pi}{L}$. The magnitude of these modulations are always small, and the trajectories of the large-absolute-amplitude ground-state amplitudes selected by twist boundary conditions averaging patch together almost seamlessly to yield nearly circular orbits over the range of twist angles $-\frac{\pi}{L} \leq \phi_x \leq +\frac{\pi}{L}$. Therefore, we need not worry about the absolute-amplitude modulations when twist averaging the large absolute amplitudes, i.e. averaging the large absolute amplitudes over $-\frac{\pi}{L} \leq \phi_x \leq +\frac{\pi}{L}$ is just as good as averaging them over $-\pi \leq \phi_x \leq +\pi$.

For the intermediate and small absolute amplitudes, the absolute-amplitude modulations become comparatively more important. For example, for the small-absolute-amplitude configuration $[1, 4, 5, 10]$, the absolute-amplitude modulation has a period of $\Delta\phi_x = \pi$. If we choose to twist boundary conditions average over $-\frac{\pi}{8} \leq \phi_x \leq +\frac{\pi}{8}$, as shown in Figure 8.33, we do not account for the full complexity of the evolution of $[1, 4, 5, 10]$'s boundary-gauge amplitude, shown also in Figure 8.33, as a function of the twist angle ϕ_x.

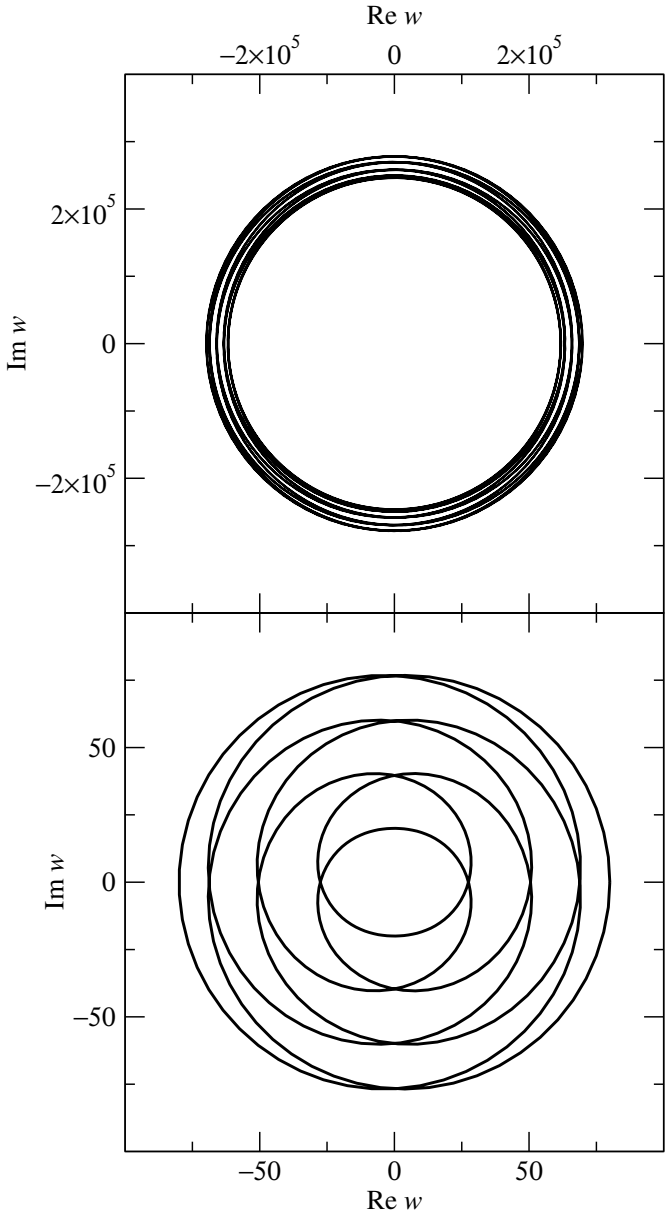

Figure 8.32: Two examples of a polynomial function w of degree nine in $z = e^{\mathrm{i}\,4\phi_x}$: $w = 4z + (4z)^3 + (4z)^5 + (4z)^7 + (4z)^9$ (top), and $w = z + z^3 + 4z^5 + 49z^7 + 25z^9$ (bottom).

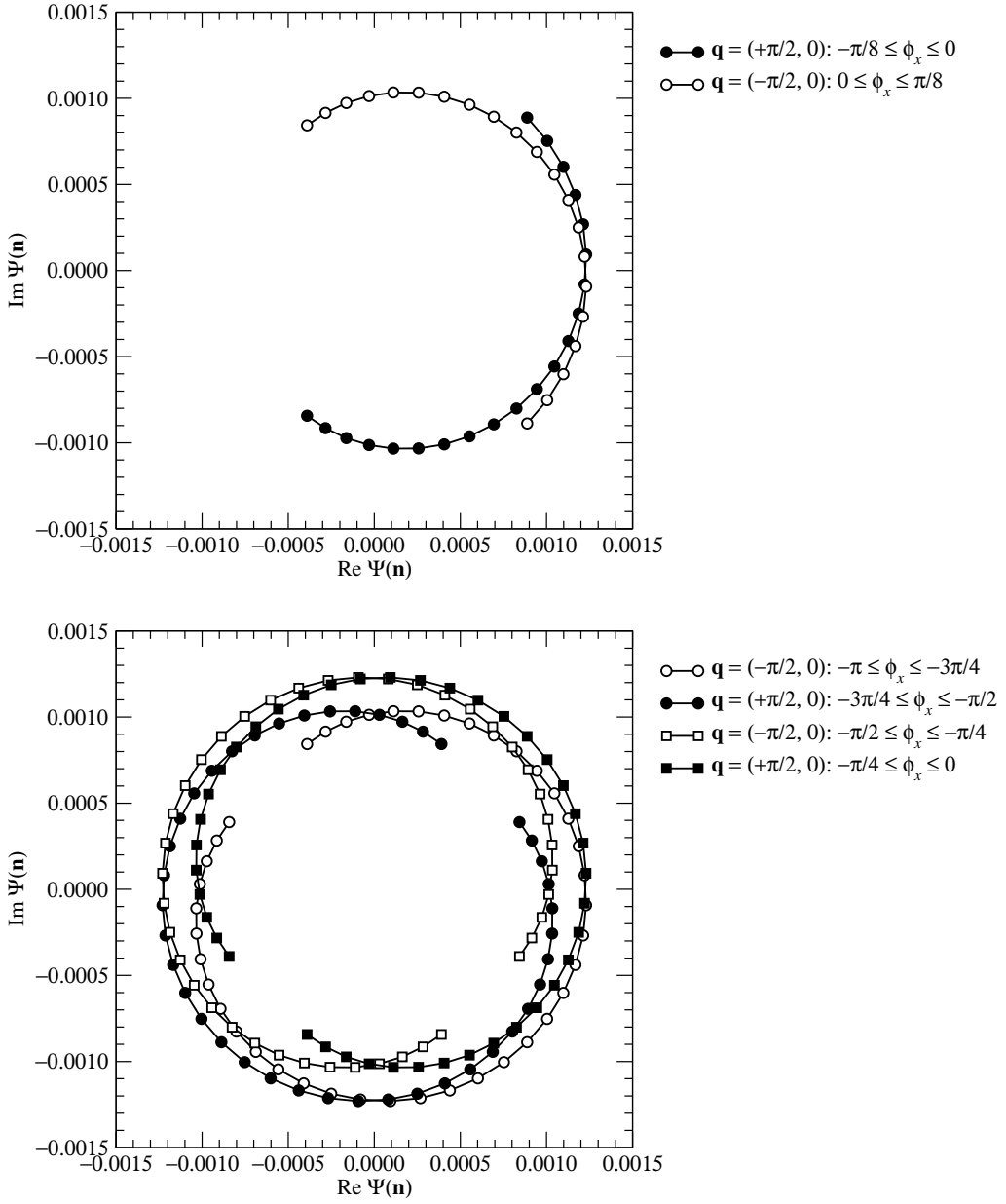

Figure 8.33: The discontinuous trajectory of the boundary-gauge ground-state amplitude of the small-absolute-amplitude configuration $[1, 4, 5, 10]$ for $P = 4$ particles on a ladder of $L = 8$ with parameter values $(t_\perp/t_\parallel = 4, t'/t_\parallel = 0)$, over the range of twist angles $-\frac{\pi}{8} \leq \phi_x \leq +\frac{\pi}{8}$ (top), and over the range of twist angles $-\pi \leq \phi_x \leq 0$ (bottom). The ground state is selected from the minimum-energy states in the $\mathbf{q} = (\pm\frac{\pi}{2}, 0)$ Bloch sectors.

While the ladder ground state already exhibits many features of the rung-fermion solid ground state at the parameter point $(t_\perp/t_\parallel = 4, t'/t_\parallel = 0)$, non-rung-fermion-solid ground-state configurations contribute sizeable amplitudes to the ground-state wave function. To get a cleaner picture, let us consider $P = 4$ particles on a ladder of length $L = 8$ subject to twist boundary conditions, at the parameter point $(t_\perp/t_\parallel = 100, t'/t_\perp = 0)$. Again, we find the minimum energies in the $\mathbf{q} = (\pm\frac{\pi}{2}, 0)$ Bloch sectors, which are $E_\mathbf{q} \approx -400$, to be very well separated from the minimum energies in the other Bloch sectors, which are $E_\mathbf{q} \approx -200$. Just as for the parameter point $(t_\perp/t_\parallel = 4, t'/t_\parallel = 0)$, the minimum-energy states in the $\mathbf{q} = (\pm\frac{\pi}{2}, 0)$ Bloch sectors are very nearly degenerate, with the ground state in the $\mathbf{q} = (+\frac{\pi}{2}, 0)$ Bloch sector for $-\frac{\pi}{8} \leq \phi_x \leq 0$, and in the $\mathbf{q} = (-\frac{\pi}{2}, 0)$ Bloch sector for $0 \leq \phi_x \leq +\frac{\pi}{8}$. The maximum difference in energy

$$\max_{-\frac{\pi}{8} \leq \phi_x \leq +\frac{\pi}{8}} \left| E_{(-\frac{\pi}{2},0)}(\phi_x) - E_{(+\frac{\pi}{2},0)}(\phi_x) \right| \tag{8.3.1}$$

between the $\mathbf{q} = (-\frac{\pi}{2}, 0)$ twisted minimum-energy band $E_{(-\frac{\pi}{2},0)}(\phi_x)$ and the $\mathbf{q} = (+\frac{\pi}{2}, 0)$ twisted minimum-energy band $E_{(+\frac{\pi}{2},0)}(\phi_x)$ is about eight orders of magnitude smaller than the ϕ_x-independent average

$$\bar{E} = \frac{1}{2}\left[E_{(-\frac{\pi}{2},0)}(\phi_x) + E_{(+\frac{\pi}{2},0)}(\phi_x) \right] \tag{8.3.2}$$

of the two twisted minimum-energy bands. We expect these two minimum-energy states to become truly degenerate as $t_\perp/t_\parallel \to \infty$.

More importantly, we are interested to know whether, the parameter point $(t_\perp/t_\parallel = 100, t'/t_\parallel)$ being closer to the infinitely-strong inter-leg hopping limit than the parameter point $(t_\perp/t_\parallel = 4, t'/t_\parallel)$, the absolute-amplitude modulations would be less pronounced. Inspecting the trajectories of the small absolute amplitudes, we find more or less the same fractional modulation of the absolute amplitudes for both parameter points. This is shown in Figure 8.34.

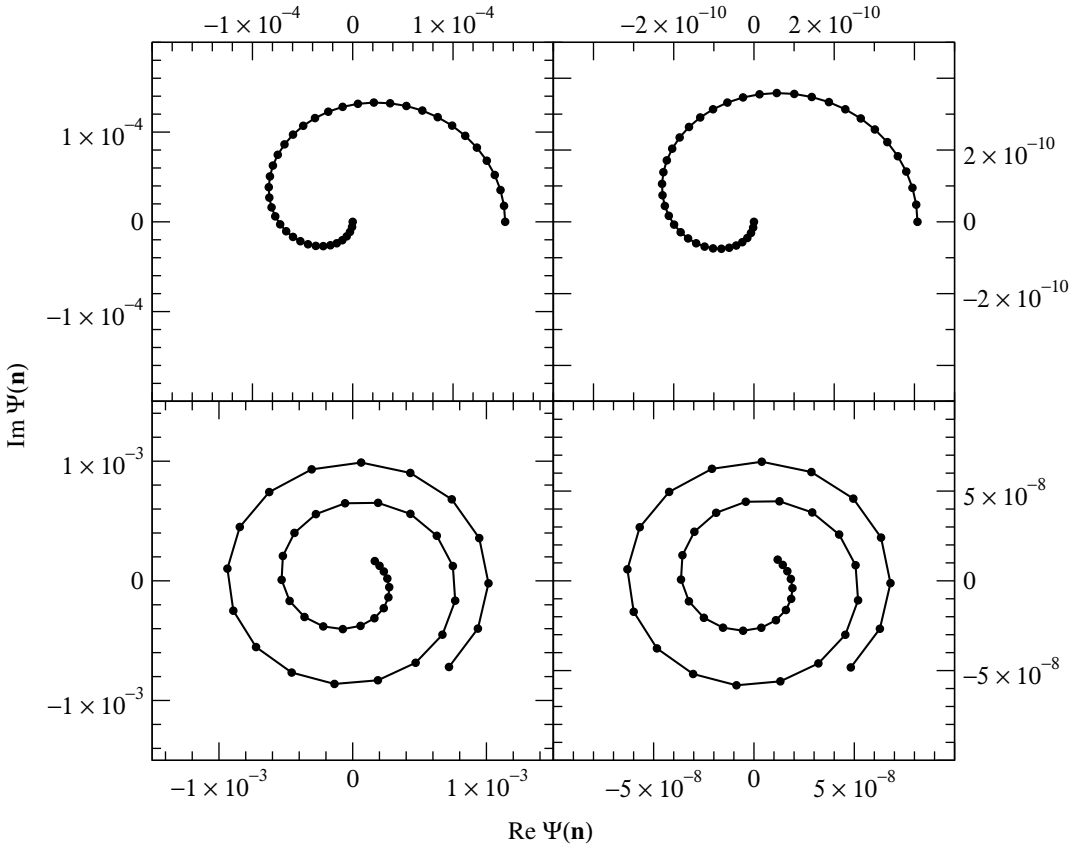

Figure 8.34: The trajectories of the boundary-gauge amplitudes of the small-absolute-amplitude configurations $[1, 4, 5, 8]$ (top) and $[7, 10, 11, 15]$ (bottom), for the parameter points $(t_\perp/t_\parallel = 4, t'/t_\parallel = 0)$ (left) and $(t_\perp/t_\parallel = 100, t'/t_\parallel = 0)$ (right), as ϕ_x changes through $\Delta\phi_x = \frac{\pi}{4}$, starting from $\phi_x = -\frac{\pi}{8}$. By comparing the plots in the left column for $t_\perp/t_\parallel = 4$ against the corresponding plots in the right column for $t_\perp/t_\parallel = 100$, we see that the absolute amplitudes of the configurations $[1, 4, 5, 8]$ and $[7, 10, 11, 15]$ apparently scales as $(t_\parallel/t_\perp)^4$.

8.3.1.3 Strong Correlated Hopping

In Section 7.5, we understood how, in the limit of infinitely-strong correlated hops, spinless fermions on the ladder form bound pairs, and the two degenerate ladder ground state consists, of solely even-flavor bound pairs in one ladder ground state, and of solely odd-flavor bound pairs in the other ladder ground state. In these ground states of bound pairs, we expect to see SC correlations dominating at large distances as a slowly-decaying power law with universal correlation exponent $\beta = \frac{1}{2}$, as well as CDW correlations which decay faster as power laws with larger exponents. The FL correlations in these ground states decay exponentially.

In this subsubsection, we look for signatures of the bound-pair ground states for $P = 4$ particles on a ladder of length $L = 8$ subject to twist boundary conditions, with twist angles between $-\frac{\pi}{8} \leq \phi_x \leq +\frac{\pi}{8}$, at the parameter point $(t_\perp/t_\parallel = 0, t'/t_\parallel = 100)$. Unlike the weak inter-leg hopping limit, where the ground state is nondegenerate, and the strong inter-leg hopping limit, where the $\mathbf{q} = (\pm\frac{\pi}{2}, 0)$ minimum-energy states are very nearly degenerate, we expect to find a truly two-fold-degenerate ground state in this strong correlated hopping limit. Indeed, as shown in Figure 8.35 we find two degenerate ground states, in the $\mathbf{q} = (-\frac{\pi}{2}, -\pi)$ and $\mathbf{q} = (+\frac{\pi}{2}, 0)$ Bloch sectors for twist angles between $-\frac{\pi}{8} \leq \phi_x \leq +\frac{\pi}{16}$, in the $\mathbf{q} = (-\pi, -\pi)$ and $\mathbf{q} = (0, 0)$ Bloch sectors for twist angles between $-\frac{\pi}{16} \leq \phi_x \leq +\frac{\pi}{16}$, and in the $\mathbf{q} = (-\frac{\pi}{2}, 0)$ and $\mathbf{q} = (+\frac{\pi}{2}, -\pi)$ Bloch sectors for twist angles between $+\frac{\pi}{16} \leq \phi_x \leq +\frac{\pi}{8}$.

In Figure 8.36, we plot the real and imaginary parts of the bond-gauge amplitudes in the minimum-energy wave functions of the $\mathbf{q} = (-\pi, -\pi)$, $\mathbf{q} = (-\frac{\pi}{2}, -\pi)$, $\mathbf{q} = (-\frac{\pi}{2}, 0)$, $\mathbf{q} = (0, 0)$, $\mathbf{q} = (+\frac{\pi}{2}, -\pi)$ and $\mathbf{q} = (+\frac{\pi}{2}, 0)$ Bloch sectors. For twist angles between $-\frac{\pi}{8} \leq \phi_x < -\frac{\pi}{16}$, the minimum-energy states of the $\mathbf{q} = (-\frac{\pi}{2}, -\pi)$ and $\mathbf{q} = (+\frac{\pi}{2}, 0)$ Bloch sectors are selected to be the ground state, and we see from Figure 8.36 that its bond-gauge

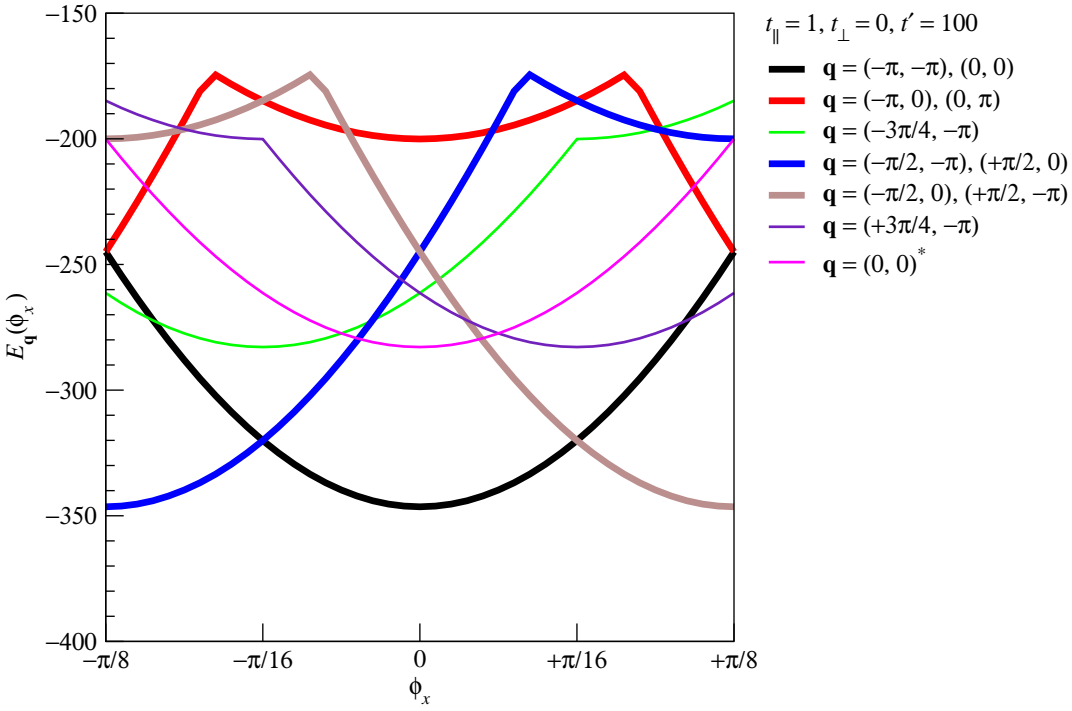

Figure 8.35: Minimum many-particle energy eigenvalues $E_{\mathbf{q}}(\phi_x)$ as a function of the twist angle ϕ_x for the Bloch sectors with wave vectors $\mathbf{q} = (-\pi, -\pi)$, $\mathbf{q} = (-\pi, 0)$, $\mathbf{q} = (-\frac{3\pi}{4}, -\pi)$, $\mathbf{q} = (-\frac{\pi}{2}, -\pi)$, $\mathbf{q} = (-\frac{\pi}{2}, 0)$, $\mathbf{q} = (0, -\pi)$, $\mathbf{q} = (0, 0)$, $\mathbf{q} = (+\frac{\pi}{2}, -\pi)$, $\mathbf{q} = (+\frac{\pi}{2}, 0)$, $\mathbf{q} = (+\frac{3\pi}{4}, -\pi)$, and the first-excited-state energy in the $\mathbf{q} = (0, 0)$ Bloch sector, for $P = 4$ particles on a ladder of length $L = 8$ subject to twist boundary conditions, at the parameter point $(t_{\perp}/t_{\parallel} = 0, t'/t_{\parallel} = 100)$.

amplitudes consist of a ring of large absolute amplitudes, a ring of intermediate absolute amplitudes, and a cluster of small absolute amplitudes. Within this same range of twist angles, we see from Figure 8.36 that the bond-gauge amplitudes in the minimum-energy wave functions of the $\mathbf{q} = (+\frac{\pi}{2}, -\pi)$ and $\mathbf{q} = (-\frac{\pi}{2}, 0)$ Bloch sectors forms a circular array of 8 unique nonzero amplitudes. It might be interesting to follow the evolution from such a circular pattern of bond-gauge amplitudes to the concentric ring of bond-gauge amplitudes for the $\mathbf{q} = (+\frac{\pi}{2}, -\pi)$ and $\mathbf{q} = (-\frac{\pi}{2}, 0)$ minimum-energy wave functions, but it is not important to do so, since the circular pattern of bond-gauge amplitudes does not occur when the minimum-energy states of the $\mathbf{q} = (+\frac{\pi}{2}, -\pi)$ and $\mathbf{q} = (-\frac{\pi}{2}, 0)$ are selected to be the ground state.

Of greater interest to us, is the fact that the bond-gauge amplitudes in the minimum-energy wave functions of the $\mathbf{q} = (-\pi, -\pi)$ and $\mathbf{q} = (0, 0)$ Bloch sectors are not all real. This is not apparent from Figure 8.36, because of the large common scale used for the imaginary part of the amplitudes. In Figure 8.37, we exaggerate the scale of the imaginary axes to show this. At this scale, the set of amplitudes in the $\mathbf{q} = (-\pi, -\pi)$ and $\mathbf{q} = (0, 0)$ minimum-energy wave functions appears to be identical, but we shall see in the discussions to follow that this is not the case for the smallest absolute amplitudes.

Two-same-flavor-bound-pair configurations. For the $\mathbf{q} = (-\pi, -\pi)$ and $\mathbf{q} = (0, 0)$ minimum-energy wave functions, the largest-absolute-amplitude configurations, over the entire range of twist angles $-\frac{\pi}{8} \leq \phi_x \leq +\frac{\pi}{8}$, are the two-same-flavor-bound-pair configurations shown in Figure 8.38. The 16 second-largest-absolute-amplitude configurations are also two-same-flavor-bound-pair configurations. These configurations, which are derived from the largest-absolute-amplitude two-same-flavor-bound-pair configurations by a single correlated hop, always have the second largest absolute amplitude in

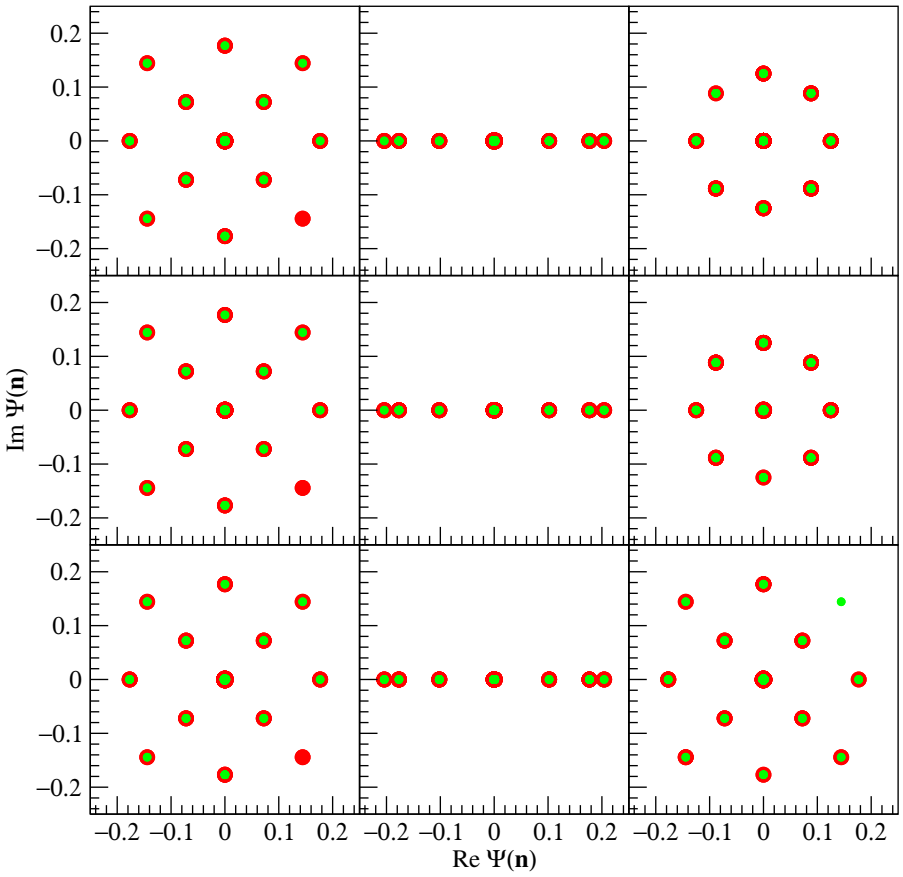

Figure 8.36: Plot of the real and imaginary parts of the amplitudes $\Psi(\mathbf{n})$ for the minimum-energy wave functions in the $\mathbf{q} = (-\frac{\pi}{2}, -\pi)$ (left, red circles), $\mathbf{q} = (+\frac{\pi}{2}, 0)$ (left, green circles), $\mathbf{q} = (-\pi, -\pi)$ (center, red circles), $\mathbf{q} = (0, 0)$ (center, green circles), $\mathbf{q} = (-\frac{\pi}{2}, 0)$ (right, red circles) and the $\mathbf{q} = (+\frac{\pi}{2}, -\pi)$ (right, green circles) Bloch sectors, for $P = 4$ particles on a ladder of length $L = 8$, at the parameter point $(t_\perp/t_\parallel = 0, t'/t_\parallel = 100)$, subject to twist boundary conditions with twist angles $\phi_x = -\pi/8$ (top), $\phi_x = -\pi/16$ (middle), and $\phi_x = 0$ (bottom).

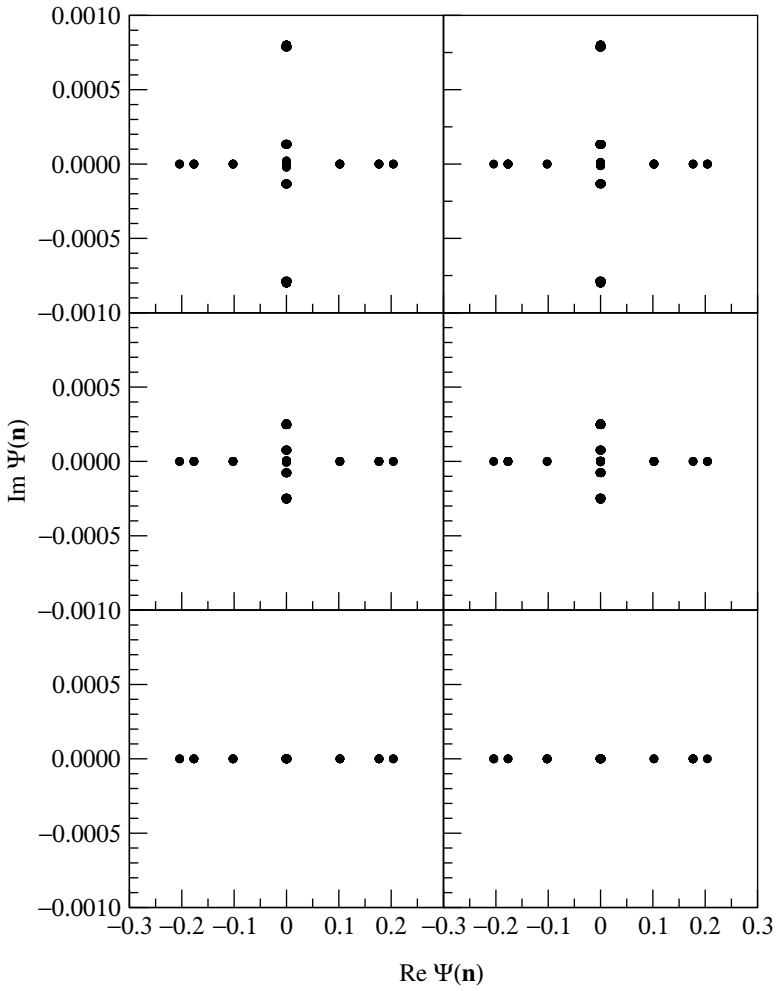

Figure 8.37: Plot of the real and imaginary parts of the amplitudes $\Psi(\mathbf{n})$ for the minimum-energy wave functions in the $\mathbf{q} = (-\pi, -\pi)$ Bloch sector (left) and $\mathbf{q} = (0, 0)$ Bloch sector (right), for $P = 4$ particles on a ladder of length $L = 8$, at the parameter point $(t_\perp/t_\parallel = 0, t'/t_\parallel = 100)$, subject to twist boundary conditions with twist angles $\phi_x = -\pi/8$ (top), $\phi_x = -\pi/16$ (middle), and $\phi_x = 0$ (bottom).

the $\mathbf{q} = (-\pi, -\pi)$ and $\mathbf{q} = (0, 0)$ minimum-energy wave functions over the entire range of twist angles $-\frac{\pi}{8} \leq \phi_x \leq +\frac{\pi}{8}$. In Figure 8.39 we show one such second-largest-absolute-amplitude two-bound-pair configuration, and the largest-absolute-amplitude two-bound-pair configuration it is derived from. The 16 third-largest-absolute-amplitude configurations are two-same-flavor-bound-pair configurations derived from the largest-absolute-amplitude configurations by two correlated hops. These configurations always have the third largest absolute amplitude in the $\mathbf{q} = (-\pi, -\pi)$ and $\mathbf{q} = (0, 0)$ minimum-energy wave functions over the entire range of twist angles $-\frac{\pi}{8} \leq \phi_x \leq +\frac{\pi}{8}$. In Figure 8.40 we show one such third-largest-absolute-amplitude two-same-flavor-bound-pair configuration, and the largest-absolute-amplitude two-same-flavor-bound-pair configuration it is derived from. The amplitudes of these bound-pair configurations are always real.

The 32 fourth-largest-absolute-amplitude configurations are more interesting, because they are not two-bound-pair configurations. Instead, they are derived from the largest-absolute-amplitude two-same-flavor-bound-pair configurations by a correlated hop, followed by a $t_{\|}$-hop which 'breaks up' one of the same-flavor bound pairs. In Figure 8.41, we show one such fourth-largest-absolute-amplitude configuration, and the largest-absolute-amplitude two-same-flavor-bound-pair configuration it is derived from. These configurations always have the fourth largest absolute amplitude in the $\mathbf{q} = (-\pi, -\pi)$ and $\mathbf{q} = (0, 0)$ minimum-energy wave functions over the entire range of twist angles $-\frac{\pi}{8} \leq \phi_x \leq +\frac{\pi}{8}$. The 32 fifth-largest-absolute-amplitude configurations are of a similar nature, but are instead derived from the largest-absolute-amplitude two-same-flavor-bound-pair configurations by a single $t_{\|}$-hop. These configurations always have the fifth largest absolute amplitude in the $\mathbf{q} = (-\pi, -\pi)$ and $\mathbf{q} = (0, 0)$ minimum-energy wave functions over the entire range of twist angles $-\frac{\pi}{8} \leq \phi_x \leq +\frac{\pi}{8}$. In Figure 8.42 we show one such fifth-largest-absolute-amplitude configuration, and the largest-

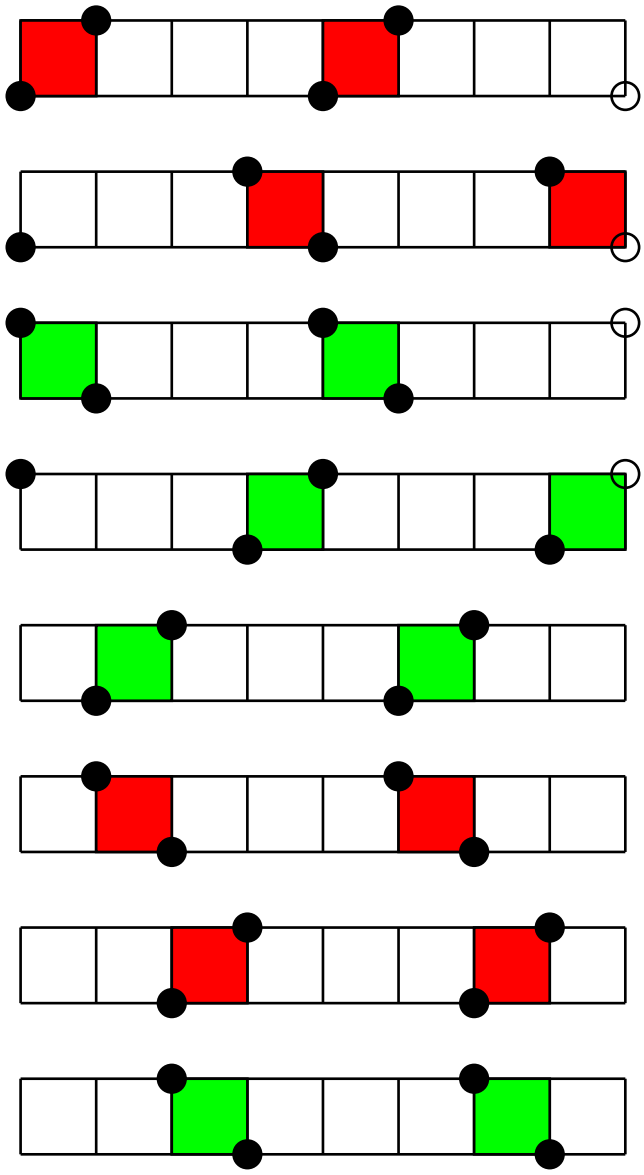

Figure 8.38: Two-same-flavor-bound-pair ground-state configurations with the largest absolute amplitude for $P = 4$ particles on a ladder of length $L = 8$ subject to twist boundary conditions, with parameters $(t_\perp/t_\parallel = 0, t'/t_\parallel = 100)$.

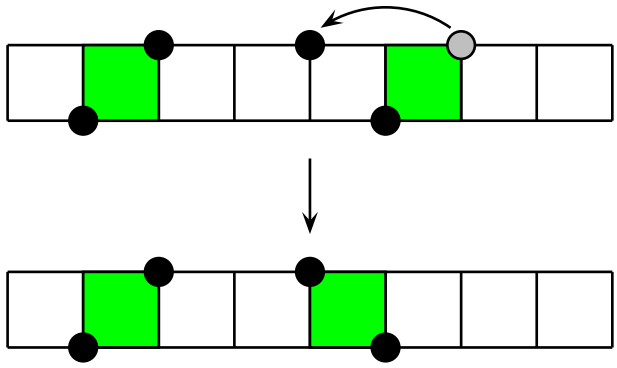

Figure 8.39: The two-same-flavor-bound-pair configuration [3, 6, 10, 11] for $P = 4$ particles on a ladder of length $L = 8$ subject to twist boundary conditions. This configuration has the second largest absolute amplitude at the parameter point $(t_\perp/t_\parallel = 0, t'/t_\parallel = 100)$, and is derived from the largest-absolute-amplitude two-same-flavor-bound-pair configuration [3, 6, 11, 14] by a single correlated hop.

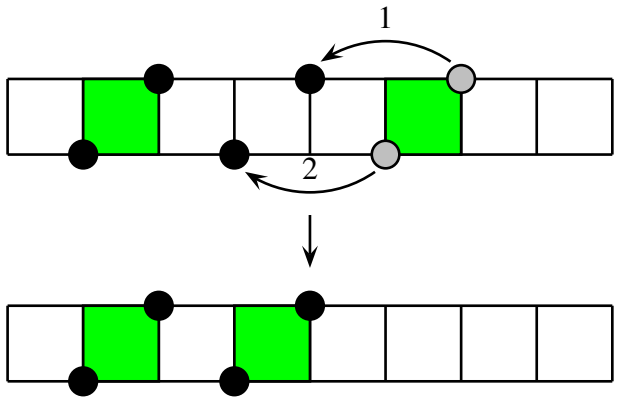

Figure 8.40: The third-largest-absolute-amplitude two-same-flavor-bound-pair configuration [3, 6, 7, 10] for $P = 4$ particles on a ladder of length $L = 8$ subject to twist boundary conditions, with parameters $(t_\perp/t_\parallel = 0, t'/t_\parallel = 100)$. This configuration is derived from the largest-absolute-amplitude two-same-flavor-bound-pair configuration [3, 6, 11, 14] by two correlated hops: the one labelled '1', followed by the one labelled '2'.

absolute-amplitude two-same-flavor-bound-pair configuration it is derived from. The 32 sixth-largest-absolute-amplitude configurations again consists of one same-flavor bound pair, and two unpaired particles. These configurations, which always have the sixth largest absolute amplitude in the $\mathbf{q} = (-\pi, -\pi)$ and $\mathbf{q} = (0, 0)$ minimum-energy wave functions over the entire range of twist angles $-\frac{\pi}{8} \leq \phi_x \leq +\frac{\pi}{8}$, are derived from the largest-absolute-amplitude two-bound-pair configurations by two correlated hops followed by a $t_{\|}$-hop that 'breaks up' the hopping same-flavor bound pair. In Figure 8.43 we show one such sixth-largest-absolute-amplitude configuration, and the largest-absolute-amplitude two-same-flavor-bound-pair configuration it is derived from. The amplitudes of these configurations, unlike the two-same-flavor-bound-pair configurations, have imaginary components comparable in magnitude to their real components, as shown in Figure 8.44.

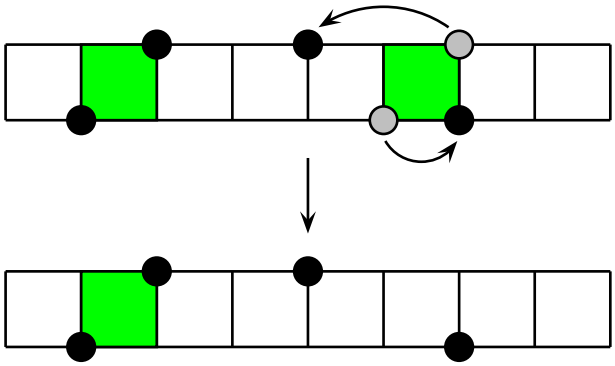

Figure 8.41: The configuration $[3, 6, 10, 13]$ for $P = 4$ particles on a ladder of length $L = 8$ subject to twist boundary conditions. This configuration has the fourth largest absolute amplitude at the parameter point $(t_{\perp}/t_{\|} = 0, t'/t_{\|} = 100)$, and is derived from the largest-absolute-amplitude two-same-flavor-bound-pair configuration $[3, 6, 11, 14]$ by a correlated hop, followed by a $t_{\|}$-hop.

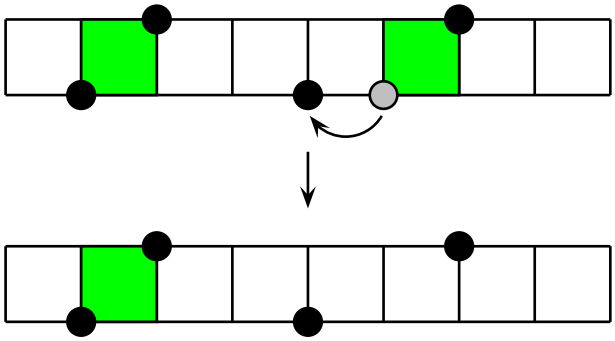

Figure 8.42: The fifth-largest-absolute-amplitude configuration $[3, 6, 9, 14]$ for $P = 4$ particles on a ladder of length $L = 8$ subject to twist boundary conditions, with parameters $(t_\perp/t_\parallel = 0, t'/t_\parallel = 100)$. This configuration is derived from the largest-absolute-amplitude two-same-flavor-bound-pair configuration $[3, 6, 11, 14]$ by a single $t_\parallel$-hop.

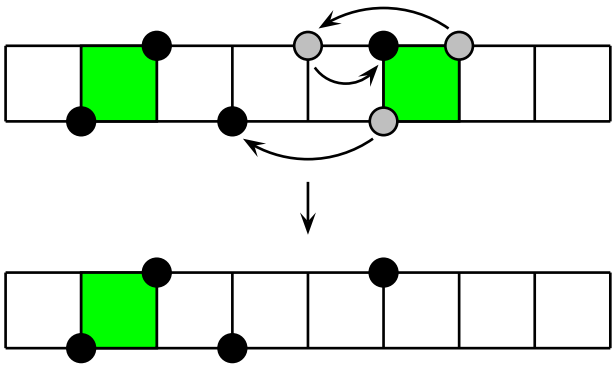

Figure 8.43: The sixth-largest-absolute-amplitude configuration $[3, 6, 7, 12]$ for $P = 4$ particles on a ladder of length $L = 8$ subject to twist boundary conditions, with parameters $(t_\perp/t_\parallel = 0, t'/t_\parallel = 100)$. This configuration is derived from the largest-absolute-amplitude two-same-flavor-bound-pair configuration $[3, 6, 11, 14]$ by two correlated hops, followed by a $t_\parallel$-hop.

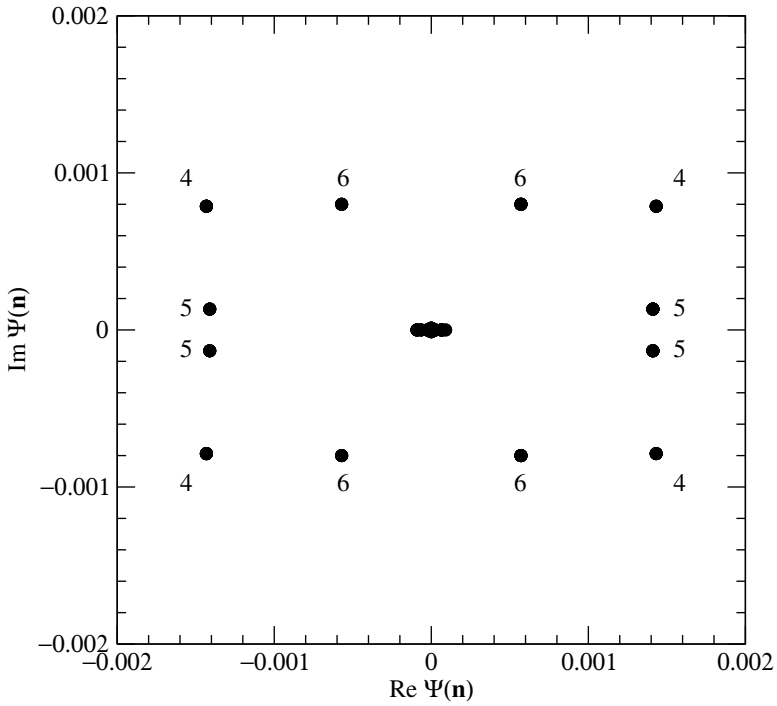

Figure 8.44: Plot of the real and imaginary parts of the amplitude $\Psi(\mathbf{n})$ for the minimum-energy wave function in the $\mathbf{q} = (0, 0)$ Bloch sector, for $P = 4$ particles on a ladder of length $L = 8$ subject to twist boundary conditions with twist angle $\phi_x = -\pi/8$. The scale of the real and imaginary axes has been chosen to emphasize the fourth, fifth, and sixth largest absolute amplitudes, which are associated with configurations with one intact same-flavor bound pair and one dissociated pair.

Two-different-flavor-bound-pair configurations. More interestingly, if we zoom in on the very small absolute amplitudes in the real-versus-imaginary plot of the amplitudes, we find a pattern of amplitudes that has a similar hierarchy to that seen for the large absolute amplitudes. This is shown in Figure 8.45 for the $\mathbf{q} = (0, 0)$ minimum-energy wave function at twist angle $\phi_x = -\frac{\pi}{8}$, and Figure 8.46 for the $\mathbf{q} = (-\pi, -\pi)$ minimum-energy wave function at twist angle $\phi_x = -\frac{\pi}{16}$. These hierarchies of amplitudes are associated with configurations having two bound pairs with different flavors, and configurations derived therefrom. In the top plot of Figure 8.45 for the $\mathbf{q} = (0, 0)$ minimum-energy wave function, the amplitudes labelled '7' and '8' are associated with two-different-flavor-bound-pair configurations. In the bottom plot of Figure 8.45 for the $\mathbf{q} = (0, 0)$ minimum-energy wave function, the amplitudes labelled '9' and '10' are associated with configurations derived from the two-different-flavor-bound-pair configurations, whereby one or both of the bound pairs dissociate as a result of two $t_{\|}$-hops. The amplitudes labelled 'a' compete with the amplitudes labelled 'b' to be the eleventh largest absolute amplitude when ϕ_x is close to $\pm\frac{\pi}{8}$. These are also associated with configurations derived from the largest-absolute-amplitude two-different-flavor-bound-pair configurations.

In the $\mathbf{q} = (-\pi, -\pi)$ minimum-energy wave function, the hierarchy of amplitudes associated with of two-different-flavor-bound-pair configurations, and configurations derived therefrom, is different. As we can see from Figure 8.46, the distribution of amplitudes is simpler, but there is more variations of the absolute amplitudes with twist angle ϕ_x, particularly for the amplitudes labelled 'c', 'd', and 'e'. We plot these three absolute amplitudes as functions of ϕ_x in Figure 8.47. None of the configurations associated with the amplitudes shown in Figure 8.47 contain two intact different-flavor bound pairs.

Let us now look at these two-different-flavor-bound-pair and derivative amplitudes

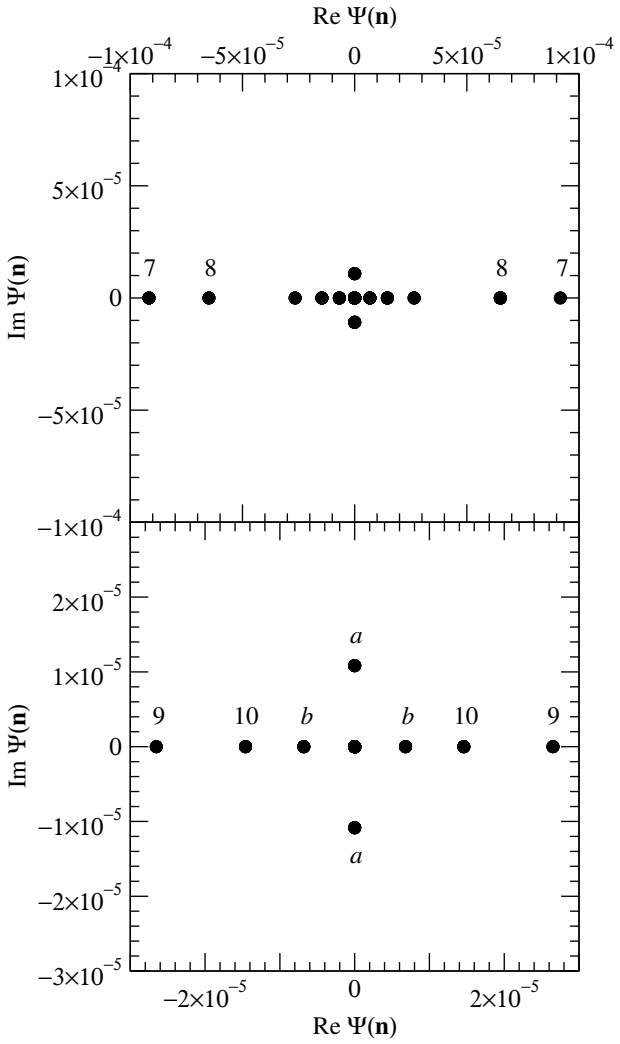

Figure 8.45: Plots of the real and imaginary parts of the amplitude $\Psi(\mathbf{n})$ for the minimum-energy wave function in the $\mathbf{q} = (0, 0)$ Bloch sector, for $P = 4$ particles on a ladder of length $L = 8$ subject to twist boundary conditions with twist angle $\phi_x = -\pi/8$. The scale of the real and imaginary axes has been chosen to emphasize the amplitudes associated with, and derived from, the two-different-flavor-bound-pair configurations.

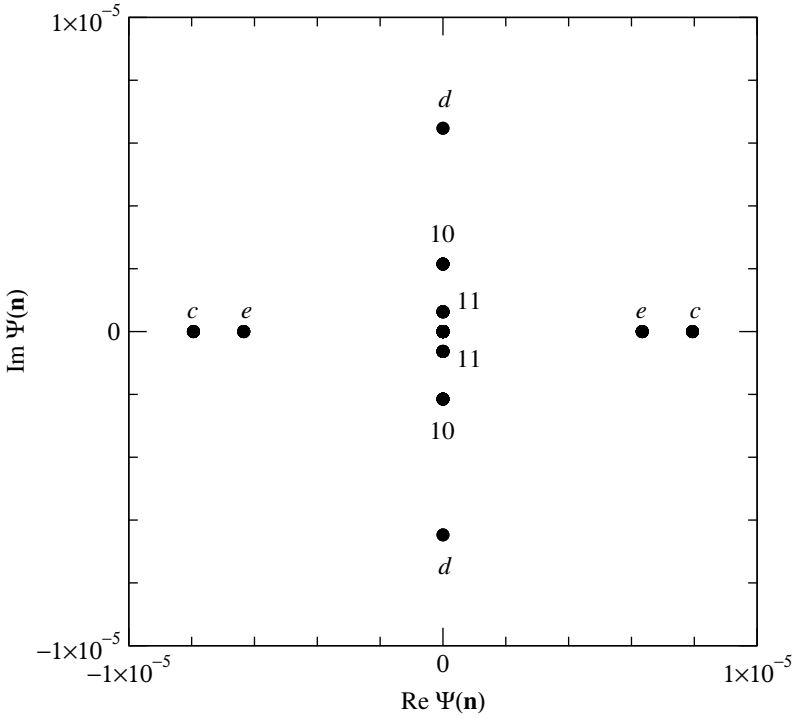

Figure 8.46: Plots of the real and imaginary parts of the amplitude $\Psi(\mathbf{n})$ for the minimum-energy wave function in the $\mathbf{q} = (0, 0)$ Bloch sector, for $P = 4$ particles on a ladder of length $L = 8$ subject to twist boundary conditions with twist angle $\phi_x = -\pi/16$. The scale of the real and imaginary axes has been chosen to emphasize the amplitudes associated with, and derived from, the two-different-flavor-bound-pair configurations.

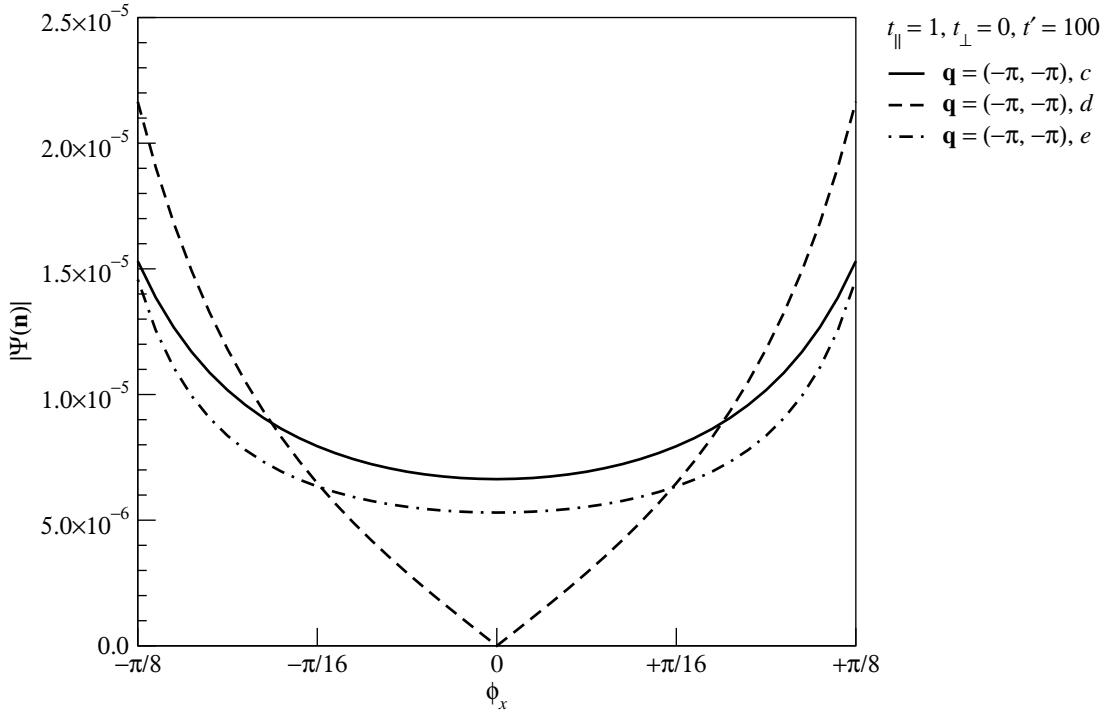

Figure 8.47: The absolute amplitudes of the 'c', 'd', and 'e' configurations in the $\mathbf{q} = (-\pi, -\pi)$ minimum-energy wave function as functions of the twist angle $-\frac{\pi}{8} \leq \phi_x \leq +\frac{\pi}{8}$, for $P = 4$ particles on a ladder of length $L = 8$ subject to twist boundary conditions, at the parameter point $(t_\perp/t_\parallel = 0, t'/t_\parallel = 100)$.

more closely. In the $\mathbf{q} = (0, 0)$ minimum-energy wave function, the two-different-flavor-bound-pair configurations shown in Figure 8.48 always have the seventh largest absolute amplitude, over the range of twist angles $-\frac{\pi}{8} \leq \phi_x \leq +\frac{\pi}{8}$. In this minimum-energy wave function, the eighth-largest-absolute-amplitude configurations are also two-different-flavor-bound-pair configurations. These configurations, derived from the largest-absolute-amplitude two-different-flavor-bound-pair configurations by a single correlated hop, always have the eighth largest absolute amplitude in the $\mathbf{q} = (0, 0)$ minimum-energy wave function over the range of twist angles $-\frac{\pi}{8} \leq \phi_x \leq +\frac{\pi}{8}$. One such configuration, and the largest-absolute-amplitude two-different-flavor-bound-pair configuration it is derived from, is shown in Figure 8.49.

In the $\mathbf{q} = (0, 0)$ minimum-energy wave function, the ninth- and tenth-largest-absolute-amplitude configurations contain no, and one, different-flavor bound pair respectively. The ninth-largest-absolute-amplitude configurations, which have the ninth largest absolute amplitude over the range of twist angles $-\frac{\pi}{8} \leq \phi_x \leq +\frac{\pi}{8}$, are derived from the two-different-flavor-bound-pair configurations by two $t_{\|}$-hops, one each by a particle from each bound pair, leading to the dissociation of both different-flavor bound pairs. In Figure 8.50, we show one such configuration, and the two-different-flavor-bound-pair configuration it is derived from. The tenth-largest-absolute-amplitude configurations, which have the tenth largest absolute amplitude over the range of twist angles $-\frac{\pi}{8} \leq \phi_x \leq +\frac{\pi}{8}$, are derived from the two-different-flavor-bound-pair configurations by two $t_{\|}$-hops, in which one bound pair remains intact, while the two particles in the dissociating bound pair hops in opposite directions. In Figure 8.51, we show one such configuration, and the two-different-flavor-bound-pair configuration it is derived from.

In the $\mathbf{q} = (0, 0)$ minimum-energy wave function, the 'b' configurations are derived from the two-*same*-flavor-bound-pair configurations by two $t_{\|}$-hops, analogous to

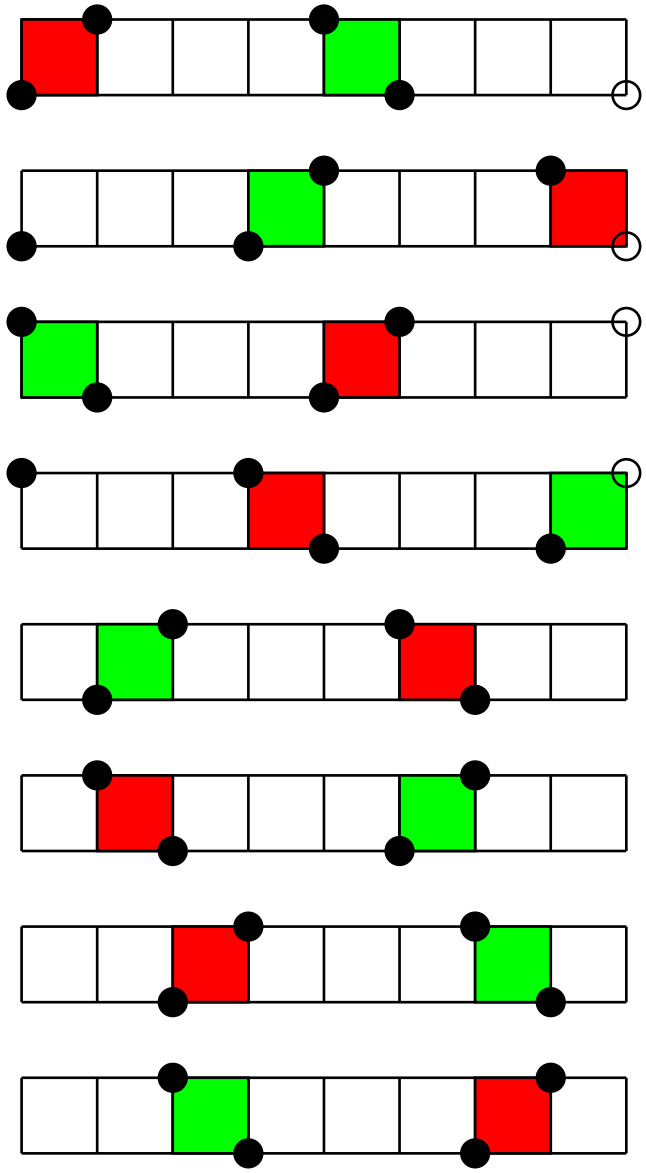

Figure 8.48: Two-bound-pair configurations with the seventh largest absolute amplitude in the $\mathbf{q} = (0, 0)$ minimum-energy wave function for $P = 4$ particles on a ladder of length $L = 8$ subject to twist boundary conditions, with parameters $(t_\perp/t_\parallel = 0, t'/t_\parallel = 100)$. These two-bound-pair configurations consist of bound pairs of different flavors.

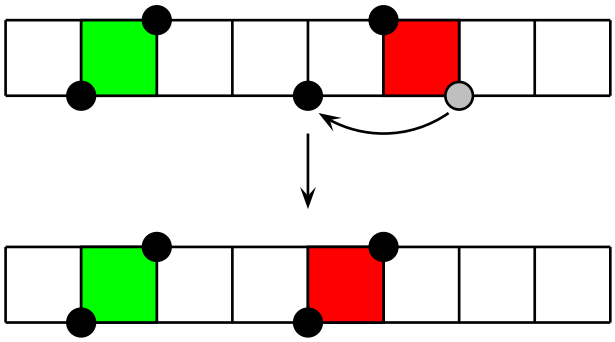

Figure 8.49: The second-largest-absolute-amplitude two-different-flavor-bound-pair configuration $[3, 6, 9, 12]$ for $P = 4$ particles on a ladder of length $L = 8$ subject to twist boundary conditions, with parameters $(t_\perp/t_\parallel = 0, t'/t_\parallel = 100)$. This configuration is derived from the largest-absolute-amplitude two-different-flavor-bound-pair configuration $[3, 6, 12, 13]$ by a single correlated hop.

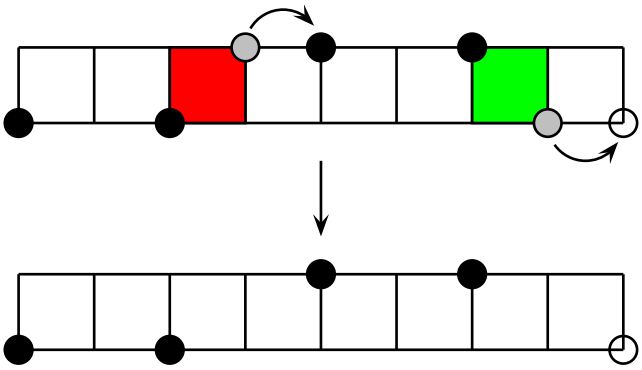

Figure 8.50: The ninth-largest-absolute-amplitude configuration $[1, 5, 10, 14]$, with no bound pairs, for $P = 4$ particles on a ladder of length $L = 8$ subject to twist boundary conditions, with parameters $(t_\perp/t_\parallel = 0, t'/t_\parallel = 100)$. This configuration is derived from the largest-absolute-amplitude two-different-flavor-bound-pair configuration $[5, 8, 14, 15]$ by two $t_\parallel$-hops.

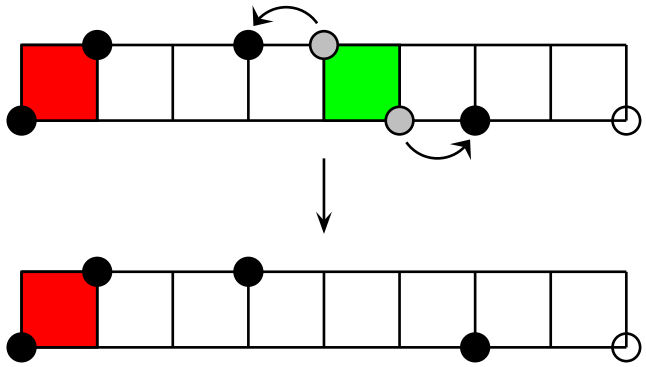

Figure 8.51: The configuration $[1, 4, 8, 13]$, with one bound pair, for $P = 4$ particles on a ladder of length $L = 8$ subject to twist boundary conditions. This configuration has the tenth largest absolute amplitude at the parameter point $(t_\perp/t_\parallel = 0, t'/t_\parallel = 100)$, and is derived from the largest-absolute-amplitude two-different-flavor-bound-pair configuration $[1, 4, 10, 11]$ by two $t_\parallel$-hops.

that in Figure 8.51. These amplitudes are therefore part of the hierarchy of amplitudes associated with two-same-flavor-bound-pair configurations, and configurations derived therefrom. In Figure 8.52, we show on such 'b' configuration, and the two-same-flavor-bound-pair configuration it is derived from. The 'a' amplitudes, on the other hand, are part of the hierarchy of amplitudes associated with two-different-flavor-bound-pair configurations, and configurations derived therefrom. The configurations associated with these amplitudes are derived from the two-different-flavor-bound-pair configurations with the second largest absolute amplitude, whereby one of the bound pairs dissociate through its particles each performing a $t_\parallel$-hop in opposite directions. In Figure 8.53, we show one such 'a' configuration, and the second-largest-absolute-amplitude two-different-flavor-bound-pair configuration it is derived from.

In the $\mathbf{q} = (-\pi, -\pi)$ minimum-energy wave function, the 'c' configurations (which are the same as the 'b' configurations in the $\mathbf{q} = (0, 0)$ minimum-energy wave function) and 'd' configurations are both derived from two-same-flavor-bound-pair configurations

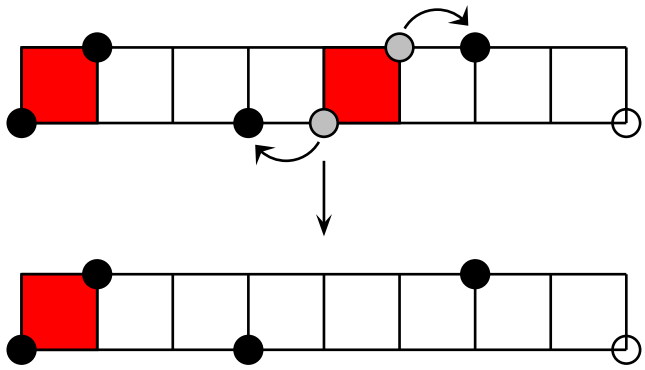

Figure 8.52: The 'b' configuration $[1, 4, 7, 14]$, with one bound pair, for $P = 4$ particles on a ladder of length $L = 8$ subject to twist boundary conditions, with parameters $(t_\perp/t_\parallel = 0, t'/t_\parallel = 100)$. This configuration is derived from the largest-absolute-amplitude two-same-flavor-bound-pair configuration $[1, 4, 9, 12]$ by two $t_\parallel$-hops.

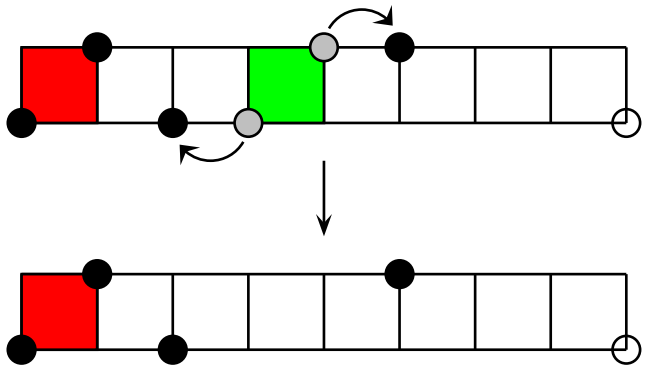

Figure 8.53: The 'a' configuration $[1, 4, 5, 12]$, with one bound pair, for $P = 4$ particles on a ladder of length $L = 8$ subject to twist boundary conditions, with parameters $(t_\perp/t_\parallel = 0, t'/t_\parallel = 100)$. This configuration is derived from the second-largest-absolute-amplitude two-different-flavor-bound-pair configuration $[1, 4, 7, 10]$ by two $t_\parallel$-hops.

by An example 'c' configuration, in which the two $t_{\|}$-hops are in opposite directions, and the two-same-flavor-bound-pair configuration it is derived from, is shown in Figure 8.52, whereas an example 'd' configuration, in which the two $t_{\|}$-hops are in the same direction, and the two-same-flavor-bound-pair configuration it is derived from, is shown in Figure 8.54.

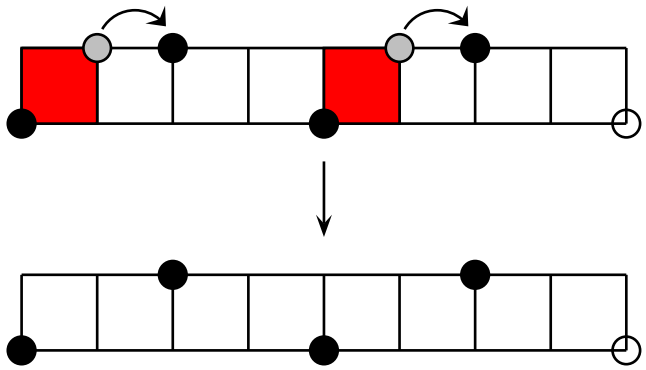

Figure 8.54: The 'd' configuration $[1, 6, 9, 14]$, with no bound pairs, for $P = 4$ particles on a ladder of length $L = 8$ subject to twist boundary conditions, with parameters $(t_{\perp}/t_{\|} = 0, t'/t_{\|} = 100)$. This configuration is derived from the largest-absolute-amplitude two-same-flavor-bound-pair configuration $[1, 4, 9, 12]$ by two $t_{\|}$-hops.

The 'e' configurations in the $\mathbf{q} = (-\pi, -\pi)$ minimum-energy wave function are derived from largest-absolute-amplitude two-different-flavor-bound-pair configurations shown in Figure 8.48 by two opposite $t_{\|}$-hops by the particles in a dissociating bound pair. We show one such configuration, and the largest-absolute-amplitude two-different-flavor-bound-pair configuration it is derived from, in Figure 8.51. The configurations whose amplitudes are labelled '10' and '11' on Figure 8.47 always have the tenth, and eleventh largest absolute amplitudes over the entire range of twist angles $-\frac{\pi}{8} \leq \phi_x \leq +\frac{\pi}{8}$. The tenth-largest-absolute-amplitude configurations are derived from the second-largest-absolute-amplitude two-different-flavor-bound-pair configurations, by the two particles in a dissociating pair $t_{\|}$-hopping in opposite directions. In Figure 8.53, we

show one tenth-largest-absolute-amplitude configuration, as well as the second-largest-absolute-amplitude two-different-flavor-bound-pair configuration it is derived from. The eleventh-largest-absolute-amplitude configurations are none other than the second-largest-absolute-amplitude two-different-flavor-bound-pair configurations. These are of course derived from the largest-absolute-amplitude two-different-flavor-bound-pair configurations by a single correlated hop. We show one such configuration in 8.49.

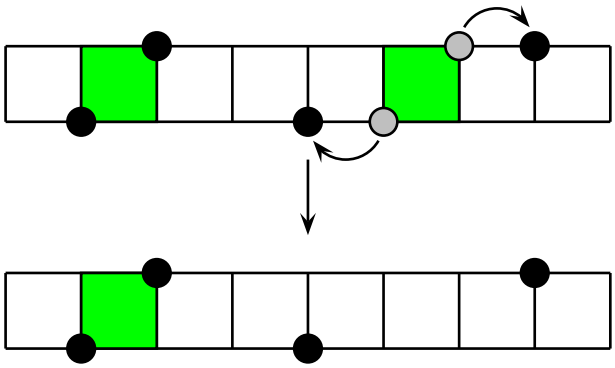

Figure 8.55: The configuration $[3, 6, 9, 16]$ for $P = 4$ particles on a ladder of length $L = 8$ subject to twist boundary conditions. This configuration has the seventh largest absolute amplitude at the parameter point $(t_\perp/t_\parallel = 0, t'/t_\parallel = 100)$, and is derived from the largest-absolute-amplitude two-bound-pair configuration $[3, 6, 11, 14]$ by two $t_\parallel$-hops.

These hierarchies of amplitudes are repeated in the minimum-energy wave functions in the $\mathbf{q} = (-\frac{\pi}{2}, -\pi)$ and $\mathbf{q} = (+\frac{\pi}{2}, 0)$ Bloch sectors, and the minimum-energy wave functions in the $\mathbf{q} = (+\frac{\pi}{2}, -\pi)$ and $\mathbf{q} = (-\frac{\pi}{2}, 0)$ Bloch sectors, which are selected as the two degenerate ground states over the ranges of twist angles $-\frac{\pi}{8} \leq \phi_x - \frac{\pi}{16}$ and $+\frac{\pi}{16} \leq \phi_x \leq +\frac{\pi}{8}$ respectively.

8.3.2 'Phase Boundaries'

In this subsection we investigate the structure of the ED ground-state wave functions at the following three points in parameter space: (i) $(t_\perp/t_\parallel = 2, t'/t_\parallel = 0)$ (Section

8.3.2.2), which lies on the zeroth-order 'phase boundary' between the LR-CDW and the PL-CDW regions of the ground-state phase diagram; (ii) $(t_\perp/t_\parallel = 0, t'/t_\parallel = 2)$ (Section 8.3.2.1), which lies on the zeroth-order 'crossover' between the PL-CDW and SC regions of the ground-state phase diagram; and (iii) $(t_\perp/t_\parallel = 100, t'/t_\parallel = 100)$ (Section 8.3.2.3), which lies on the zeroth-order 'phase boundary' between the LR-CDW and SC regions of the ground-state phase diagram.

8.3.2.1 PL-CDW and SC 'Crossover'

For $P = 4$ particles on a ladder of length $L = 8$ subject to twist boundary conditions, at the parameter point $(t_\perp/t_\parallel = 0, t'/t_\parallel = 2)$, we see from Figure 8.56 that the nondegenerate ground state occurs in the $\mathbf{q} = (+\frac{\pi}{2}, 0)$ Bloch sector for $-\frac{\pi}{8} \leq \phi_x \leq -0.145802$, in the $\mathbf{q} = (0, 0)$ Bloch sector for $-0.145802 \leq \phi_x \leq +0.145802$, and in the $\mathbf{q} = (-\frac{\pi}{2}, 0)$ Bloch sector for $+0.145802 \leq \phi_x \leq +\frac{\pi}{8}$.

At this zeroth order 'crossover' between the SC and PL-CDW phases, we expect the twisted energy bands to exhibit characteristics intermediate between those at the strong correlated hopping and weak inter-leg hopping limits. Comparing the twisted energy bands in Figure 8.56 with those in Figure 8.35 for the strong correlated hopping limit and Figure 8.12 for the weak inter-leg hopping limit, we find that the twisted energy band structure for the parameter point $(t_\perp/t_\parallel = 0, t'/t_\parallel = 2)$ resembles that of the strong correlated hopping limit more than that of the weak inter-leg hopping limit.

Now, as the ground state crosses over from the strong correlated hopping limit to the weak inter-leg hopping limit, the two-fold degeneracies between the $\mathbf{q} = (-\frac{\pi}{2}, -\pi)$ and $\mathbf{q} = (+\frac{\pi}{2}, 0)$ minimum-energy states, between the $\mathbf{q} = (-\pi, -\pi)$ and $\mathbf{q} = (0, 0)$ minimum-energy states, and between the $\mathbf{q} = (+\frac{\pi}{2}, -\pi)$ and $\mathbf{q} = (-\frac{\pi}{2}, 0)$ must be lifted. In addition, we need the twisted energy bands of the $\mathbf{q} = (-\pi, -\pi)$, $\mathbf{q} = (0, 0)$, $\mathbf{q} = (-\frac{\pi}{2}, -\pi)$ and

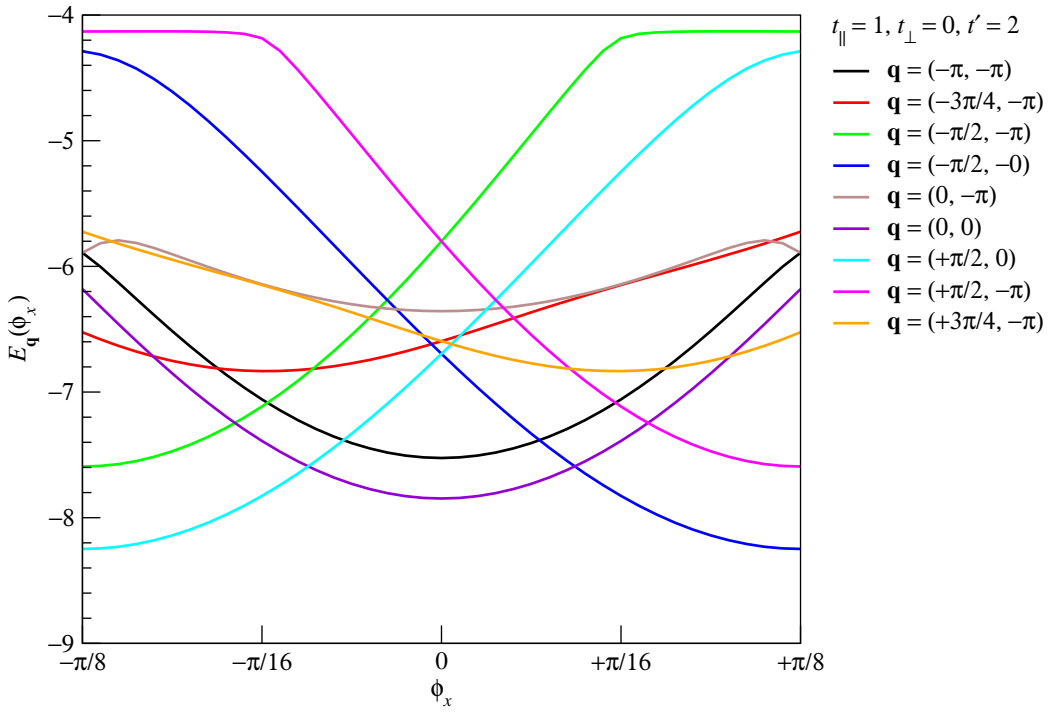

Figure 8.56: Minimum many-particle energy eigenvalues $E_{\mathbf{q}}(\phi_x)$ as a function of the twist angle ϕ_x for the Bloch sectors with wave vectors $\mathbf{q} = (-\pi, -\pi)$, $\mathbf{q} = (-\frac{3\pi}{4}, -\pi)$, $\mathbf{q} = (-\frac{\pi}{2}, -\pi)$, $\mathbf{q} = (-\frac{\pi}{2}, 0)$, $\mathbf{q} = (0, -\pi)$, $\mathbf{q} = (0, 0)$, $\mathbf{q} = (+\frac{\pi}{2}, 0)$, $\mathbf{q} = (+\frac{\pi}{2}, -\pi)$ and $\mathbf{q} = (+\frac{3\pi}{4}, -\pi)$, for $P = 4$ particles on a ladder of length $L = 8$ subject to twist boundary conditions, with parameter values $(t_{\perp}/t_{\|} = 0, t'/t_{\|} = 2)$.

$\mathbf{q} = (+\frac{\pi}{2}, -\pi)$ minimum-energy states to be raised, and the twisted energy band of the $\mathbf{q} = (0, -\pi)$ minimum-energy state to be lowered, relative to the $\mathbf{q} = (\pm\frac{\pi}{2}, 0)$ minimum energies. From Figure 8.56, we see that this is indeed happening.

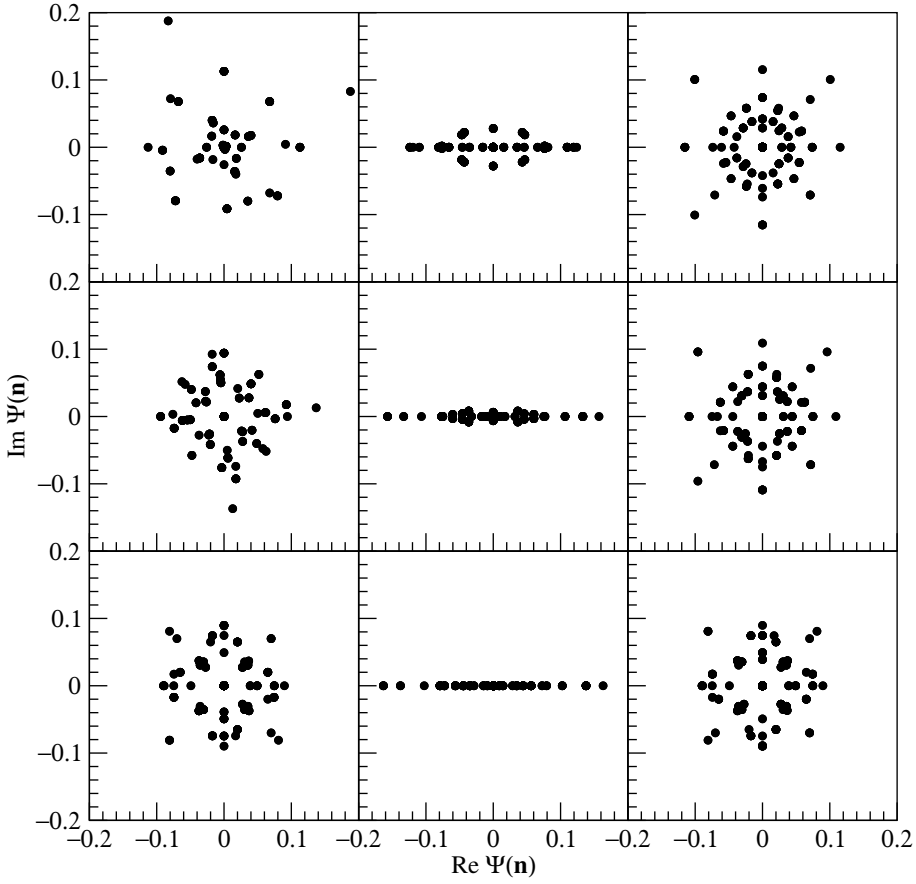

Figure 8.57: Plot of the real and imaginary parts of the amplitudes $\Psi(\mathbf{n})$ for the minimum-energy wave functions in the $\mathbf{q} = (-\frac{\pi}{2}, 0)$ Bloch sector (left), $\mathbf{q} = (0, 0)$ Bloch sector (center), and the $\mathbf{q} = (+\frac{\pi}{2}, 0)$ Bloch sector (right), for $P = 4$ particles on a ladder of length $L = 8$, at the parameter point $(t_\perp/t_\parallel = 0, t'/t_\parallel = 2)$, subject to twist boundary conditions with twist angles $\phi_x = -\frac{\pi}{8}$ (top), $\phi_x = -\frac{\pi}{16}$ (middle), and $\phi_x = 0$ (bottom).

We also expect the amplitude distribution at this parameter point $(t_\perp/t_\parallel = 0, t'/t_\parallel = 2)$ to have features intermediate between the amplitude distributions in the strong correlated hopping and weak inter-leg hopping limits. In Figure 8.57, we plot the real and imagi-

nary parts of the bond-gauge amplitudes of the $\mathbf{q} = (-\frac{\pi}{2}, 0)$, $\mathbf{q} = (0, 0)$, and $\mathbf{q} = (+\frac{\pi}{2}, 0)$ minimum-energy wave functions for the parameter point $(t_\perp/t_\parallel = 0, t'/t_\parallel = 2)$. Comparing the minimum-energy state amplitudes in the $\mathbf{q} = (+\frac{\pi}{2}, 0)$ Bloch sector for both parameter points in Figure 8.57 and Figure 8.36, we identify the group of largest absolute amplitudes for $(t_\perp/t_\parallel = 0, t'/t_\parallel = 2)$ with the group of largest absolute amplitudes for $(t_\perp/t_\parallel = 0, t'/t_\parallel = 100)$. These are the two-same-flavor-bound-pair configurations shown in Figure 8.38. These configurations always have the largest absolute amplitude over the range of twist angles $-\frac{\pi}{8} \leq \phi_x \leq +\frac{\pi}{8}$, in the ground state selected by twist boundary conditions averaging. The second-largest-absolute-amplitude configurations are also two-same-flavor-bound-pair configurations, derived from the largest-absolute-amplitude two-same-flavor-bound-pair configurations by a single correlated hop. These configurations always have the second largest absolute amplitude over the range of twist angles $-\frac{\pi}{8} \leq \phi_x \leq +\frac{\pi}{8}$, in the ground state selected by twist boundary conditions averaging. In Figure 8.39, we show one such second-largest-absolute-amplitude two-same-flavor-bound-pair configuration, and the largest-absolute-amplitude two-same-flavor-bound-pair configuration it is derived from.

Going on to the third-largest-absolute-amplitude configurations, we find that these are the two-different-flavor-configurations shown in Figure 8.48. These configurations always have the third largest absolute amplitude over the range of twist angles $-\frac{\pi}{8} \leq \phi_x \leq +\frac{\pi}{8}$, in the ground state selected by twist boundary conditions averaging. The absolute-amplitude picture then becomes complicated from this point on. The two-same-flavor-bound-pair configurations with two bound pairs of the same flavor separated center-to-center by two lattice spacings (Figure 8.40 shows one such configuration), and the two-different-flavor-bound-pair configurations with two bound pairs of different flavors separated center-to-center by three lattice spacings (Figure 8.49 shows one such config-

uration) compete to have the larger absolute amplitude. In the $\mathbf{q} = (0, 0)$ Bloch sector, the former has the larger absolute amplitude, whereas in the $\mathbf{q} = (\pm\frac{\pi}{2}, 0)$, the latter has the larger absolute amplitude. At this absolute amplitude level, which is about one half of the largest absolute amplitude, we also find the staggered ground-state configurations, an example of which is shown in Figure 8.54.

To decide where the 'crossover' occurs, we want to know how much of the two-bound-pair ground state for the strong correlated hopping limit and the staggered ground state for the weak inter-leg hopping limit are mixed into the ground state at the parameter point $(t_\perp/t_\parallel = 0, t'/t_\parallel = 2)$. However, such an analysis is complicated by the fact that some of the two-bound-pair configurations are also staggered ground-state configurations. These receive amplitude contributions from both the two-bound-pair and staggered ground states, and there is no simple way to find out what these individual contributions are.

8.3.2.2 LR-CDW and PL-CDW 'Phase Boundary'

For $P = 4$ particles on a ladder of length $L = 8$ subject to twist boundary conditions, at the parameter point $t_\perp/t_\parallel = 2, t'/t_\parallel = 0)$, we see from Figure 8.58 that the nondegenerate ground state occurs in the $\mathbf{q} = (+\frac{\pi}{2}, 0)$ Bloch sector for $-\frac{\pi}{8} \leq \phi_x \leq 0$, and in the $\mathbf{q} = (-\frac{\pi}{2}, 0)$ Bloch sector for $0 \leq \phi_x \leq +\frac{\pi}{8}$.

At this zeroth order 'phase boundary' between the LR-CDW and the PL-CDW phases, we expect the twisted energy bands to exhibit characteristics intermediate between those at strong inter-leg hopping and weak inter-leg hopping limits. Comparing the twisted energy bands in Figure 8.58 with those in Figure 8.23 for the strong inter-leg hopping limit and Figure 8.15 for the weak inter-leg hopping limit, we find that the twisted energy band structure for the parameter point $(t_\perp/t_\parallel = 2, t'/t_\parallel = 0)$ resembles

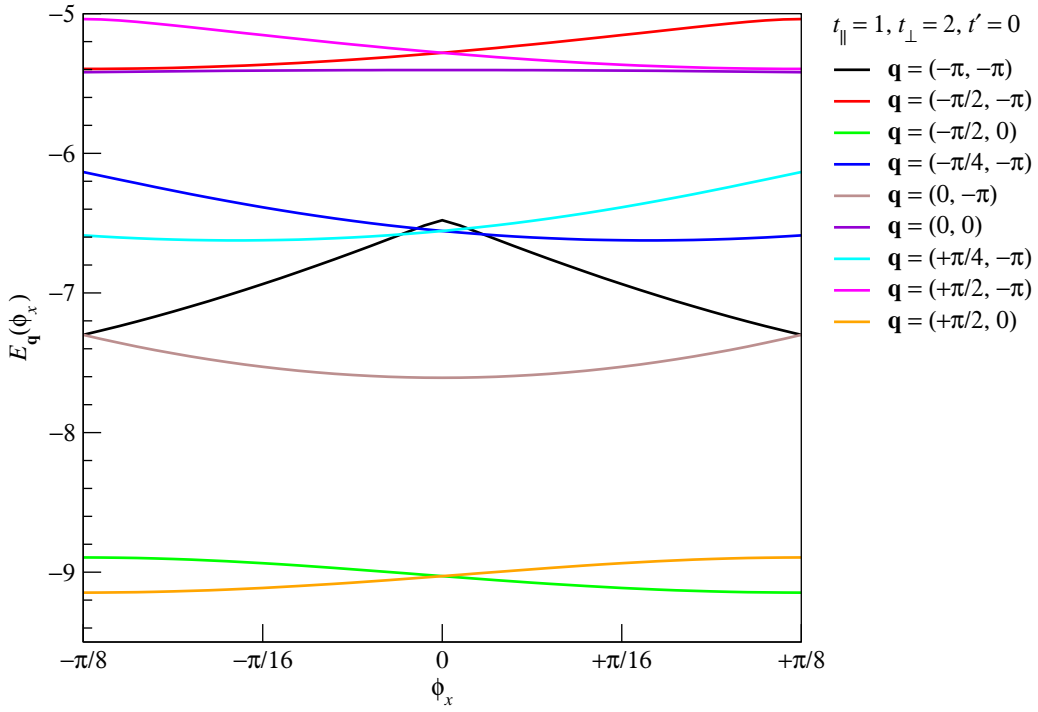

Figure 8.58: Minimum many-particle energy eigenvalues $E_{\mathbf{q}}(\phi_x)$ as a function of the twist angle ϕ_x for the Bloch sectors with wave vectors $\mathbf{q} = (-\pi, -\pi)$, $\mathbf{q} = (-\frac{\pi}{2}, -\pi)$, $\mathbf{q} = (-\frac{\pi}{2}, 0)$, $\mathbf{q} = (-\frac{\pi}{4}, -\pi)$, $\mathbf{q} = (0, -\pi)$, $\mathbf{q} = (0, 0)$, $\mathbf{q} = (+\frac{\pi}{4}, -\pi)$, $\mathbf{q} = (+\frac{\pi}{2}, -\pi)$, and $\mathbf{q} = (+\frac{\pi}{2}, 0)$, for $P = 4$ particles on a ladder of length $L = 8$ subject to twist boundary conditions, with parameter values $(t_{\perp}/t_{\|} = 2, t'/t_{\|} = 0)$.

that of the strong inter-leg hopping limit more than that of the weak inter-leg hopping limit.

Now, as the ground state goes across the 'phase boundary' between the LR-CDW and PL-CDW phases, the twisted energy bands in the LR-CDW phase has the same qualitative shapes as those in the PL-CDW phase, but where the $\mathbf{q} = (\pm\frac{\pi}{2}, 0)$ twisted energy bands cluster together with the rest of twisted energy bands in the PL-CDW phase, and look essentially like shifted copies of the twisted energy band of the $\mathbf{q} = (0, -\pi)$ minimum-energy state, the $\mathbf{q} = (\pm\frac{\pi}{2}, 0)$ twisted energy bands in the LR-CDW phase is lowered relative to the rest of the twisted energy bands. In the twisted energy band structure of the parameter point $(t_\perp/t_\parallel = 2, t'/t_\parallel = 0)$, we find that the $\mathbf{q} = (\pm\frac{\pi}{2}, 0)$ twisted energy bands have already separated cleanly from the $\mathbf{q} = (0, -\pi)$ twisted energy band.

In Figure 8.59 we plot the real and imaginary parts of the $\mathbf{q} = (\pm\frac{\pi}{2}, 0)$ minimum-energy wave functions at $\phi_x = 0$ for the parameter point $(t_\perp/t_\parallel = 2, t'/t_\parallel = 0)$. Comparing Figure 8.59 with Figures 8.17, 8.18 and 8.19, we find that the distributions of amplitudes at the parameter points $(t_\perp/t_\parallel = 2, t'/t_\parallel = 0)$ and $(t_\perp/t_\parallel = 4)$ are very similar. This suggests that the ground-state amplitudes associated with each of the groups of configurations discussed in Section 8.3.1.2 changes smoothly with $t_\perp/t_\parallel$, which follows from the fact the most important staggered ground-state configurations are also rung-fermion ground-state configurations. Consequently, correlation functions calculated from the amplitudes of finite ladders will also vary smoothly with $t_\perp/t_\parallel$, which means that unless we perform elaborate finite-size scaling analyses, we will not likely be able to extract signatures of the quantum phase transition between the PL-CDW and LR-CDW phases in the infinite ladder.

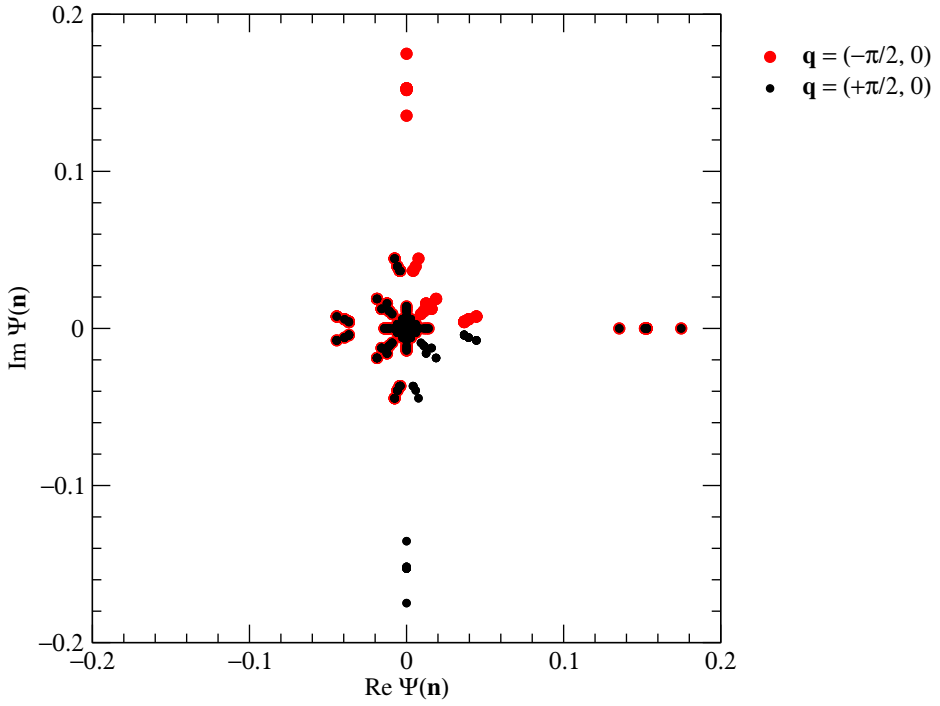

Figure 8.59: Plot of the real and imaginary parts of the amplitudes $\Psi(\mathbf{n})$ for the minimum-energy wave functions in the $\mathbf{q} = (-\frac{\pi}{2}, 0)$ (red circles) and $\mathbf{q} = (+\frac{\pi}{2}, 0)$ (black circles) Bloch sectors, for $P = 4$ particles on a ladder of length $L = 8$, at the parameter point $(t_\perp/t_\parallel = 2, t'/t_\parallel = 0)$, subject to periodic boundary conditions.

8.3.2.3 LR-CDW and SC 'Phase Boundary'

For $P = 4$ particles on a ladder of length $L = 8$ subject to twist boundary conditions, at the parameter point $(t_\perp/t_\parallel = 100, t'/t_\parallel = 100)$, we see from Figure 8.60 that the $\mathbf{q} = (\pm\frac{\pi}{2}, 0)$ minimum-energy states, which in energy are very far below the rest of the minimum-energy states for other Bloch sectors, are very nearly degenerate, even for general twist angles. The ground state selected by twist boundary conditions averaging is in the $\mathbf{q} = (+\frac{\pi}{2}, 0)$ Bloch sector for $-\frac{\pi}{8} \leq \phi_x \leq 0$ and in the $\mathbf{q} = (-\frac{\pi}{2}, 0)$ Bloch sector for $0 \leq \phi_x \leq +\frac{\pi}{8}$), but the maximum energy difference between these two nearly-degenerate minimum-energy states is only two parts in one billion.

At this zeroth order 'phase boundary' between the LR-CDW and SC phases, we expect the twisted energy bands to exhibit characteristics intermediate between those of the strong inter-leg hopping and strong correlated hopping limits. Indeed, comparing Figure 8.60 with Figures 8.23 and 8.35, we find that the twisted energy band structure for the parameter point $(t_\perp/t_\parallel = 100, t'/t_\parallel = 100)$ exhibits features of both of the twisted energy band structures in the strong inter-leg hopping and strong correlated hopping limits. Just as in the strong inter-leg hopping limit, the minimum energies of the $\mathbf{q} = (\pm\frac{\pi}{2}, 0)$ Bloch sectors are very far below the minimum energies in the rest of the Bloch sectors. Also, just as in the strong correlated hopping limit, the twisted minimum-energy bands of the $\mathbf{q} = (-\pi, -\pi)$ and $\mathbf{q} = (0, 0)$ Bloch sectors, and the twisted minimum-energy bands of the $\mathbf{q} = (-\pi, 0)$ and $\mathbf{q} = (0, -\pi)$ Bloch sectors, are degenerate.

In Figure 8.61 we plot the real and imaginary parts of the amplitudes in the $\mathbf{q} = (\pm\frac{\pi}{2}, 0)$ minimum-energy wave functions at $\phi_x = 0$ for the parameter point $(t_\perp/t_\parallel = 100, t'/t_\parallel = 100)$. Comparing Figure 8.61 with Figure 8.17, we see, not surprisingly, that the amplitude distribution at the parameter point $(t_\perp/t_\parallel = 100, t'/t_\parallel = 100)$ is practically identical to that of the strong inter-leg hopping limit at the gross level. Zooming in

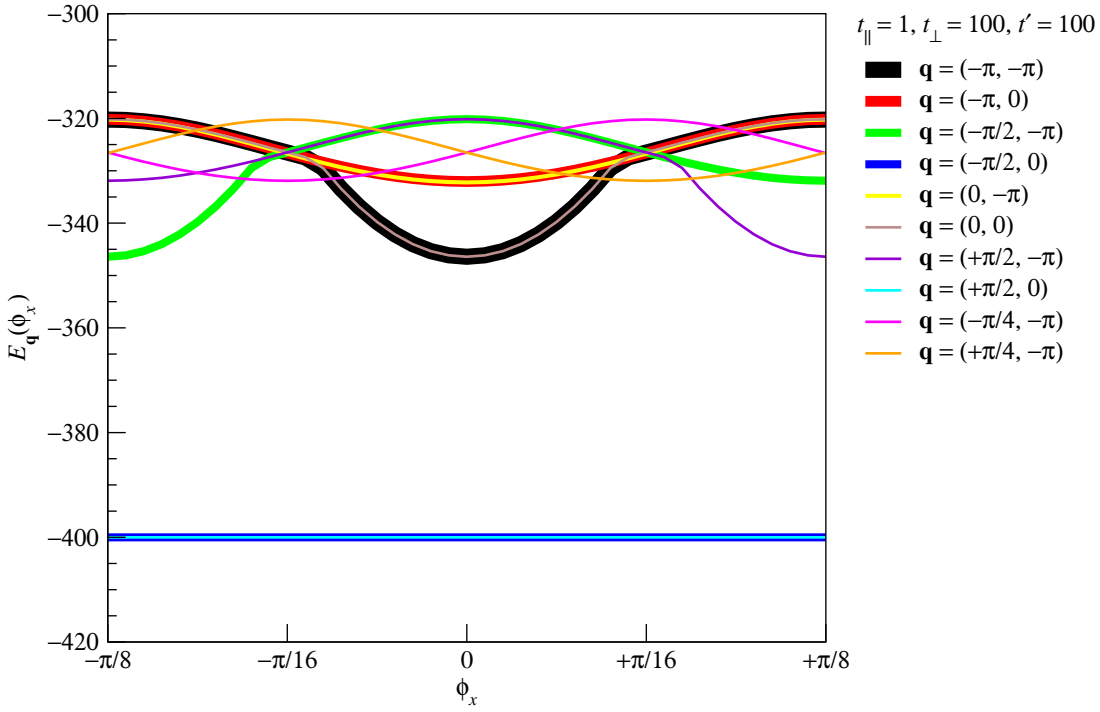

Figure 8.60: Minimum many-particle energy eigenvalues $E_{\mathbf{q}}(\phi_x)$ as a function of the twist angle ϕ_x for the Bloch sectors with wave vectors $\mathbf{q} = (-\pi, -\pi)$, $\mathbf{q} = (-\pi, 0)$, $\mathbf{q} = (-\frac{\pi}{2}, -\pi)$, $\mathbf{q} = (-\frac{\pi}{2}, 0)$, $\mathbf{q} = (-\frac{\pi}{4}, -\pi)$, $\mathbf{q} = (0, -\pi)$, $\mathbf{q} = (0, 0)$, $\mathbf{q} = (+\frac{\pi}{4}, -\pi)$, $\mathbf{q} = (+\frac{\pi}{2}, -\pi)$, and $\mathbf{q} = (+\frac{\pi}{2}, 0)$, for $P = 4$ particles on a ladder of length $L = 8$ subject to twist boundary conditions, with parameter values $(t_{\perp}/t_{\|} = 100, t'/t_{\|} = 100)$.

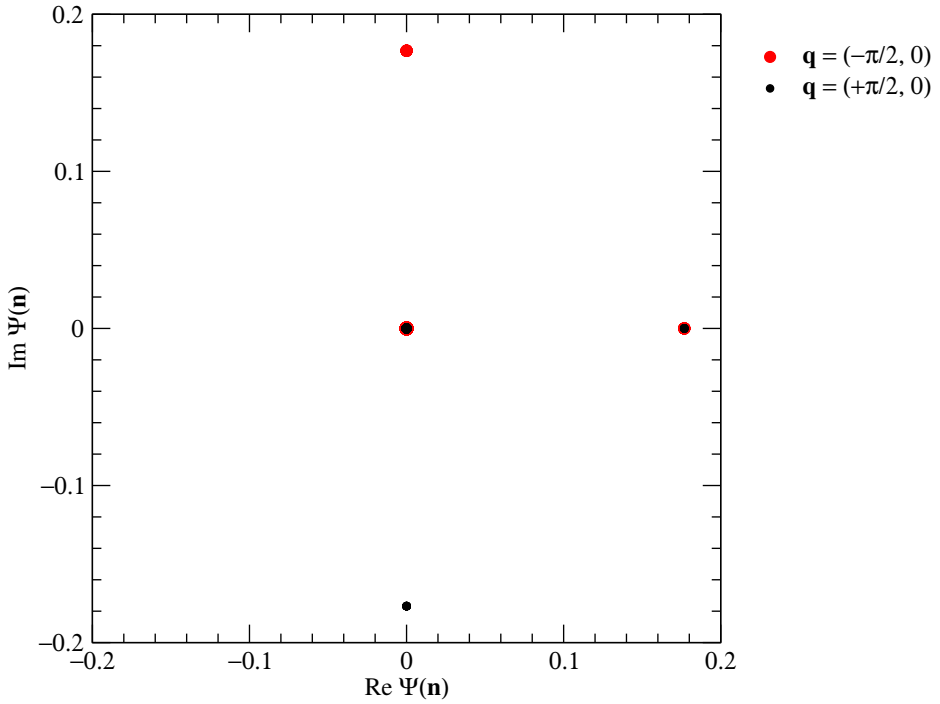

Figure 8.61: Plot of the real and imaginary parts of the amplitudes $\Psi(\mathbf{n})$ for the minimum-energy wave functions in the $\mathbf{q} = (-\frac{\pi}{2}, 0)$ (red circles) and $\mathbf{q} = (+\frac{\pi}{2}, 0)$ (black circles) Bloch sectors, for $P = 4$ particles on a ladder of length $L = 8$, at the parameter point $(t_\perp/t_\parallel = 100, t'/t_\parallel = 100)$, subject to periodic boundary conditions.

on the distribution of small absolute amplitudes in Figure 8.62, and comparing with Figures 8.18, 8.36, and 8.37, we see in the distribution of small absolute amplitudes for the parameter point $(t_\perp/t_\parallel = 100, t'/t_\parallel = 100)$ some features of that for the strong inter-leg hopping limit, and other features of that for the strong correlated hopping limit. However, as with the case of the phase boundary between the LR-CDW and PL-CDW phases, we cannot expect to see clean signatures of the LR-CDW-to-SC quantum phase transition in our numerical studies of finite ladders.

8.3.3 'Tricritical Point'

For $P = 4$ particles on a ladder of length $L = 8$ subject to twist boundary conditions, at the parameter point $(t_\perp/t_\parallel = 2, t'/t_\parallel = 2)$, we see from Figure 8.63 that the ground state selected by twist boundary conditions averaging is nondegenerate over the range of twist angles $-\frac{\pi}{8} < \phi_x < +\frac{\pi}{8}$, and occurs in the $\mathbf{q} = (0, -\pi)$ Bloch sector.

Since this parameter point is supposedly the 'quantum tricritical point', we expect the twisted energy band structure to exhibit characteristics of the twisted energy band structures of all three analytical limits. Comparing Figure 8.63 with Figures 8.12, 8.15, 8.23, and 8.35, we find that the $\mathbf{q} = (0, -\pi)$ ground-state twisted energy band at the parameter point $(t_\perp/t_\parallel = 2, t'/t_\parallel = 2)$ looks most like the $\mathbf{q} = (0, -\pi)$ twisted minimum-energy band in the weak inter-leg hopping and the strong inter-leg hopping limits, even though in the strong inter-leg hopping limit, the $\mathbf{q} = (0, -\pi)$ minimum-energy state is never selected as the ground state by twist boundary conditions averaging.

The $\mathbf{q} = (\pm\frac{\pi}{2}, 0)$ minimum-energy states, which are selected as ground states over some ranges of twist angles ϕ_x for both the weak and strong inter-leg hopping limits, are never selected as the ground states at this zeroth-order 'quantum tricritical point'. This notwithstanding, we can, as discussed in Section 8.2.1.1, still use qualitative com-

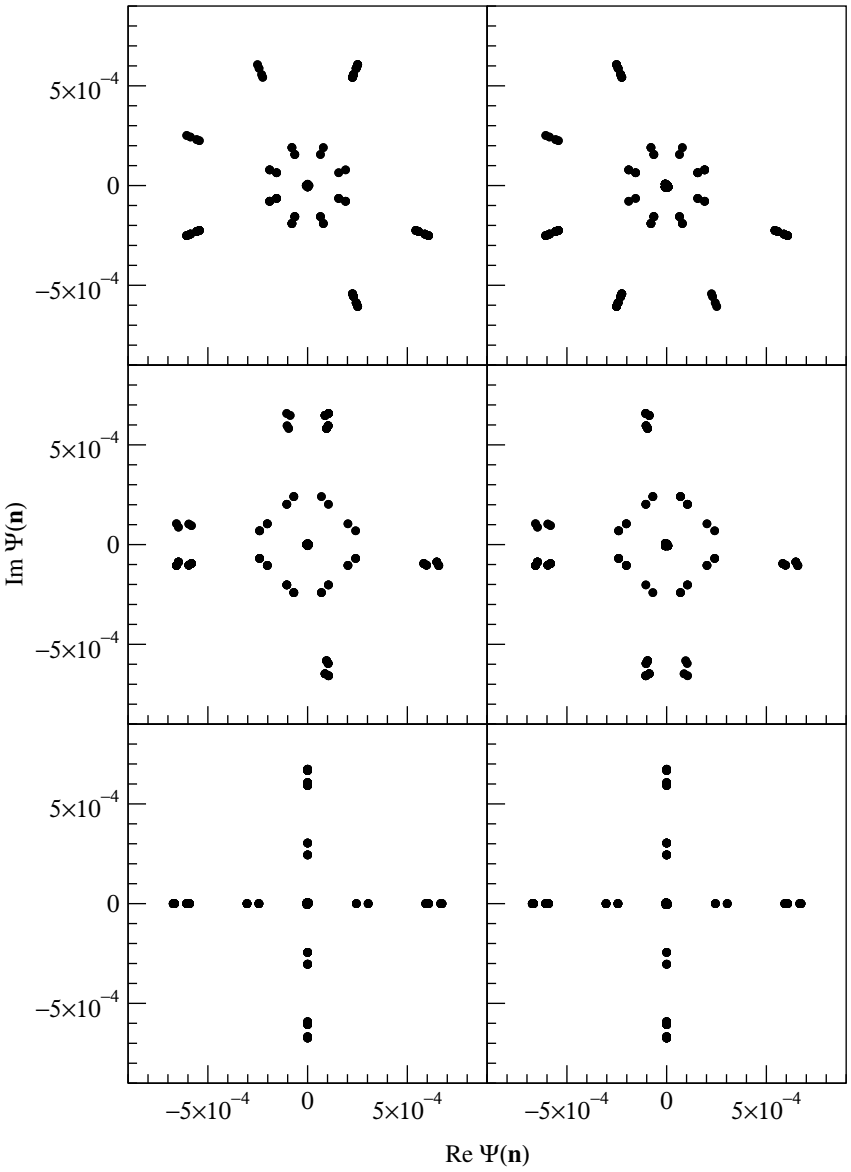

Figure 8.62: Plot of the real and imaginary parts of the amplitudes $\Psi(\mathbf{n})$ for the minimum-energy wave functions in the $\mathbf{q} = (-\frac{\pi}{2}, 0)$ (left) and $\mathbf{q} = (+\frac{\pi}{2}, 0)$ (right) Bloch sectors, for $P = 4$ particles on a ladder of length $L = 8$, at the parameter point $(t_\perp/t_\parallel = 100, t'/t_\parallel = 100)$, subject to twist boundary conditions, with twist angles $\phi_x = -\frac{\pi}{8}$ (top), $\phi_x = -\frac{\pi}{16}$ (middle), and $\phi_x = 0$ (bottom).

parisons between the $\mathbf{q} = (\pm\frac{\pi}{2}, 0)$ twisted minimum-energy bands as a means to set the three analytical limits apart. The feature that we focus on, is the common bandwidth ΔE of the $\mathbf{q} = (\pm\frac{\pi}{2}, 0)$ twisted minimum-energy bands. In the weak inter-leg hopping limit, $\Delta E \approx 2t_{\parallel}$, whereas in the strong correlated hopping limit, $\Delta E \approx 2t'$. In the strong inter-leg hopping limit, we expect from second-order perturbation theory that $\Delta E \approx t_{\parallel}/t_{\perp}^2$, which is very small in this limit. On our finite ladder of length $L = 8$, we find, looking at the $\mathbf{q} = (\pm\frac{\pi}{2}, 0)$ twisted minimum-energy bands in Figure 8.63, that their common bandwidth is on the order of $\Delta E \approx t_{\parallel}/t_{\perp}^2$. Therefore, the characters of the $\mathbf{q} = (\pm\frac{\pi}{2}, 0)$ twisted minimum-energy bands are closer to that in the strong inter-leg hopping limit.

Apart from these three twisted minimum-energy bands, the $\mathbf{q} = (-\pi, -\pi)$ and $\mathbf{q} = (0, 0)$ twisted minimum-energy bands also help define the distinguishing features of the twisted energy band structures in the three analytical limits. Looking at the $\mathbf{q} = (-\pi, -\pi)$ twisted minimum-energy band in Figure 8.63, we find that it resembles most closely that of the weak and strong inter-leg hopping limits. But instead of a kink at $\phi_x = 0$, the $\mathbf{q} = (-\pi, -\pi)$ twisted minimum-energy band at the parameter point $(t_{\perp}/t_{\parallel} = 2, t'/t_{\parallel} = 2)$ has a nonzero curvature. Comparing the behaviour of this twisted energy band as a function of the twist angle in Figures 8.12, 8.15, 8.23, 8.35, 8.56, 8.58, and 8.60 at the various parameter points, we surmised that the curvature of the $\mathbf{q} = (-\pi, -\pi)$ twisted minimum-energy band at $\phi_x = 0$ is essentially determined by the ratio $t'/t_{\perp}$, such that the shape of this twisted energy band changes with $t'/t_{\perp}$ as shown in Figure 8.64.

In fact, we see from the series of plots on the twisted energy band structures that something similar is happening to the $\mathbf{q} = (0, 0)$ twisted minimum-energy band, although we find that the $\mathbf{q} = (0, 0)$ twisted minimum-energy band is flat, instead of having a kink like the $\mathbf{q} = (-\pi, -\pi)$ twisted minimum-energy band in the limit $t'/t_{\perp} = 0$. At the parameter point $(t_{\perp}/t_{\parallel} = 2, t'/t_{\parallel} = 2)$, we find that the $\mathbf{q} = (0, 0)$ twisted minimum-

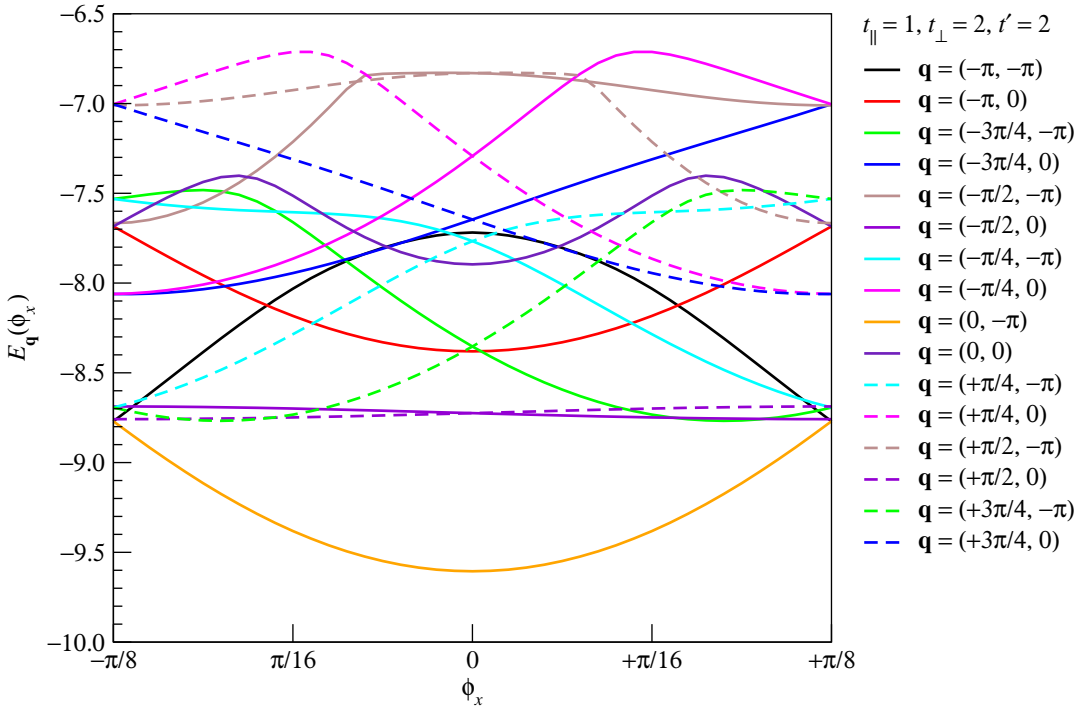

Figure 8.63: Minimum many-particle energy eigenvalues $E_{\mathbf{q}}(\phi_x)$ as a function of the twist angle ϕ_x for the Bloch sectors with wave vectors $\mathbf{q} = (-\pi, -\pi)$, $\mathbf{q} = (-\pi, 0)$, $\mathbf{q} = (-\frac{3\pi}{4}, -\pi)$, $\mathbf{q} = (-\frac{3\pi}{4}, 0)$, $\mathbf{q} = (-\frac{\pi}{2}, -\pi)$, $\mathbf{q} = (-\frac{\pi}{2}, 0)$, $\mathbf{q} = (-\frac{\pi}{4}, -\pi)$, $\mathbf{q} = (-\frac{\pi}{4}, 0)$, $\mathbf{q} = (0, -\pi)$, $\mathbf{q} = (0, 0)$, $\mathbf{q} = (+\frac{\pi}{4}, -\pi)$, $\mathbf{q} = (+\frac{\pi}{4}, 0)$, $\mathbf{q} = (+\frac{\pi}{2}, -\pi)$, $\mathbf{q} = (+\frac{\pi}{2}, 0)$, $\mathbf{q} = (+\frac{3\pi}{4}, -\pi)$, and $\mathbf{q} = (+\frac{3\pi}{4}, 0)$, for $P = 4$ particles on a ladder of length $L = 8$, with parameter values $(t_{\perp}/t_{\|} = 2, t'/t_{\|} = 2)$.

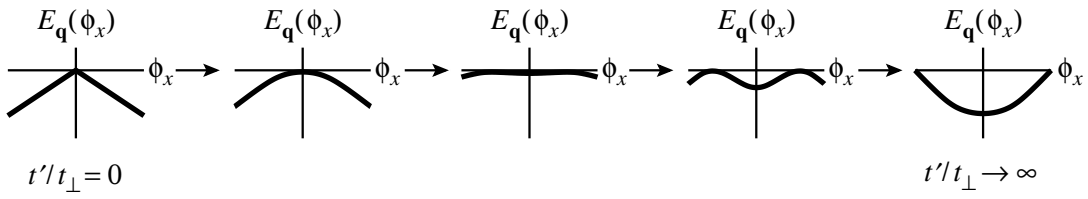

Figure 8.64: Change in character of the $\mathbf{q} = (-\pi, -\pi)$ twisted minimum-energy band $E_{\mathbf{q}}(\phi_x)$ as the ratio $t'/t_{\perp}$ is increased from $t'/t_{\perp} = 0$ to $t'/t_{\perp} \to \infty$.

energy band is still in an intermediate stage of evolution from its $(t'/t_\perp = 0)$-limit shape to its $(t'/t_\perp \to \infty)$-limit shape.

Overall, we find the twisted energy band structure at the parameter point $(t_\perp/t_\parallel = 2, t'/t_\parallel = 2)$ to exhibit features intermediate between that in the weak and strong inter-leg hopping limits, but bear very little resemblance to the twisted energy band structure in the strong correlated hopping limit. This is especially true with respect to the pairs of twisted energy bands, in the $\mathbf{q} = (-\pi, -\pi)$ and $\mathbf{q} = (0, 0)$, the $\mathbf{q} = (-\frac{\pi}{2}, -\pi)$ and $\mathbf{q} = (+\frac{\pi}{2}, 0)$, and the $\mathbf{q} = (+\frac{\pi}{2}, -\pi)$ and $\mathbf{q} = (-\frac{\pi}{2}, 0)$ Bloch sectors, that are degenerate in the strong correlated hopping limit. In Figure 8.63, we see that these pairs of twisted energy bands are far from being degenerate.

This confusing twisted-energy-band picture of which of the three analytical limits the the 'quantum 'tricritical point" ground state resembles is mirrored by the picture depicted by the amplitudes. In fact, we find that for the largest-absolute-amplitude configuration $[1, 6, 9, 14]$ (shown in Figure 8.9), the phase $e^{\mathrm{i}\theta}$ of the amplitude determined by the diagonalization routine in Octave frequently changes abruptly as we go from one twist angle to the next. This is shown in Figure 8.65. Presumably, the phase $e^{\mathrm{i}\theta}$ is a numerical artefact having nothing to do with the twist boundary conditions, and we can remove this overall phase from the ED ground-state wave functions, before plotting the real and imaginary parts of the ground-state amplitudes in Figure 8.66.

Comparing the distribution of amplitudes in Figure 8.66 for the parameter point $(t_\perp/t_\parallel = 2, t'/t_\parallel = 2)$ with the known distributions of amplitudes shown in Figures 8.17, 8.18, 8.19, and 8.36 of the analytical limits, we find that the distribution of amplitudes for the parameter point $(t_\perp/t_\parallel = 2, t'/t_\parallel = 2)$ bears no resemblance to those of the analytical limits. Therefore, we analyze the grouping of the absolute amplitudes, starting from configurations with the largest absolute amplitude. As it turns out, these are the

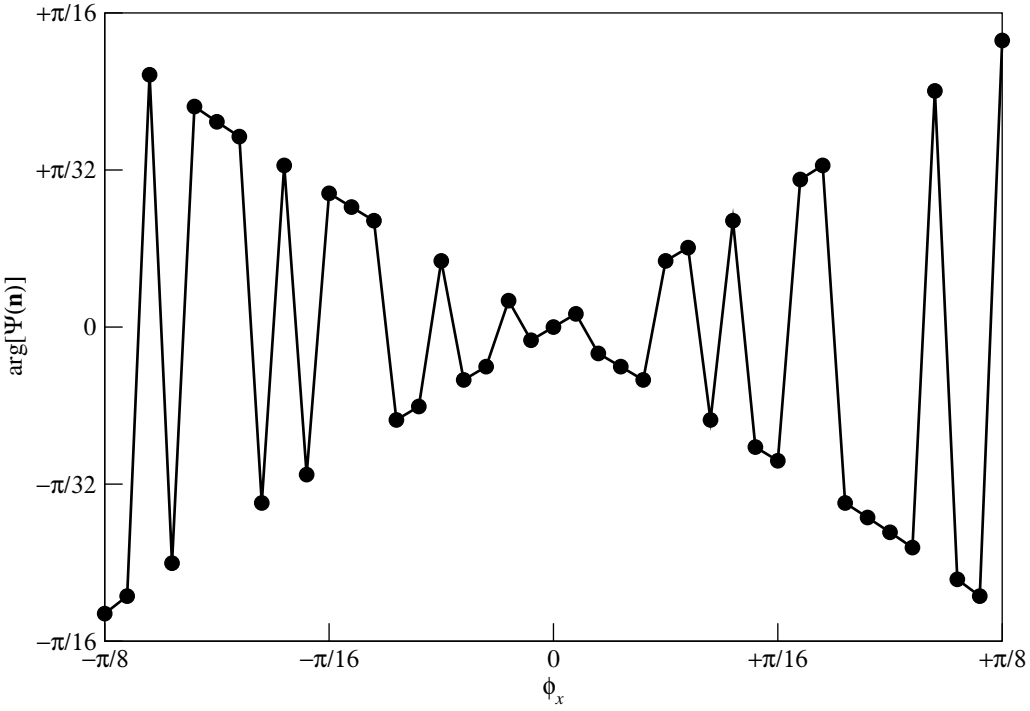

Figure 8.65: The complex argument of the $\mathbf{q} = (0, -\pi)$ ground-state amplitude of the configuration $[1, 6, 9, 14]$ for $P = 4$ particles on a ladder of $L = 8$ subject to twist boundary conditions with twist angle ϕ_x.

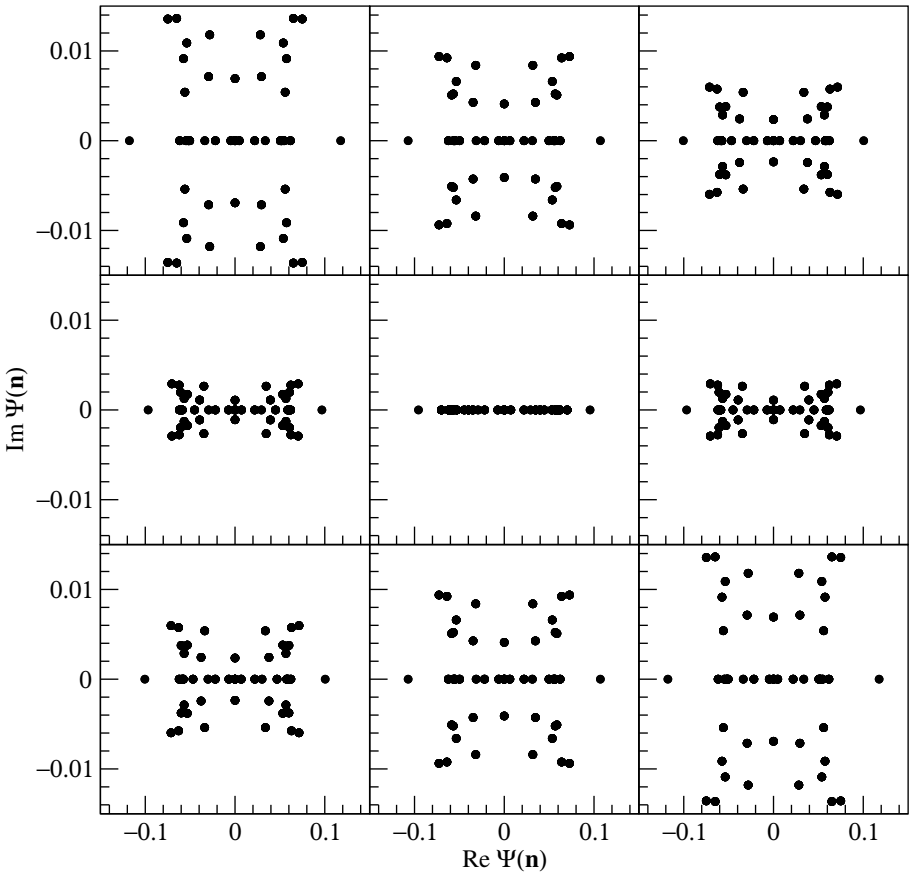

Figure 8.66: Plot of the real and imaginary parts of the amplitudes $\Psi(\mathbf{n})$ in the $\mathbf{q} = (0, -\pi)$ ground-state wave function, for $P = 4$ particles on a ladder of length $L = 8$, at the parameter point $(t_\perp/t_\parallel = 2, t'/t_\parallel = 2)$, subject to twist boundary conditions. The amplitudes are plotted for twist angles $\phi_x = -\frac{\pi}{8}$ (top left), $\phi_x = -\frac{3\pi}{32}$ (top center), $\phi_x = -\frac{\pi}{16}$ (top right), $\phi_x = -\frac{\pi}{32}$ (middle left), $\phi_x = 0$ (middle center), $\phi_x = +\frac{\pi}{32}$ (middle right), $\phi_x = +\frac{\pi}{16}$ (bottom left), $\phi_x = +\frac{3\pi}{32}$ (bottom center), and $\phi_x = +\frac{\pi}{8}$ (bottom right).

staggered configurations shown in Figure 8.9, which are the most important configurations of both the staggered ground state in the weak inter-leg hopping limit, as well as the rung-fermion ground state in the strong inter-leg hopping limit.

Since the largest-absolute-amplitude configurations in the staggered ground state (weak inter-leg hopping limit) and the rung-fermion ground state (strong inter-leg hopping limit) are the same, we must look at the structure of the second-largest-absolute-amplitude configurations, in order to decide whether our 'quantum tricritical point' ground state resembles more the staggered ground state in the weak inter-leg hopping limit, or the rung-fermion ground state in the strong inter-leg hopping limit. There are 32 such second-largest-absolute-amplitude configurations, and they turn out to be the second-largest-absolute-amplitude staggered ground state configurations, in which one particle in the staggered configuration hops to the left or right along the leg. We show eight such configurations in Figure 8.67. Since these configurations are not part of the rung-fermion ground state in the strong inter-leg hopping limit, we understand that the dominant hierarchy of amplitudes, in the ground-state wave function at the parameter point $(t_\perp/t_\parallel = 2, t'/t_\parallel = 2)$ is that of the staggered ground state in the weak inter-leg hopping limit. In this hierarchy, the next largest staggered ground-state absolute amplitude is the fourth largest overall. This group of amplitudes is associated with 16 staggered ground-state configurations, derived from the largest-absolute-amplitude staggered ground-state configurations by two successive spinless fermions (on different legs) hopping one step along the leg they are on in the same direction. One such configuration is shown in Figure 8.68.

The 32 configurations with the third largest absolute amplitude are also not rung-fermion ground-state configurations. Instead, these are derived from the 32 second-largest-absolute-amplitude configurations, in which the adjacent spinless fermion that

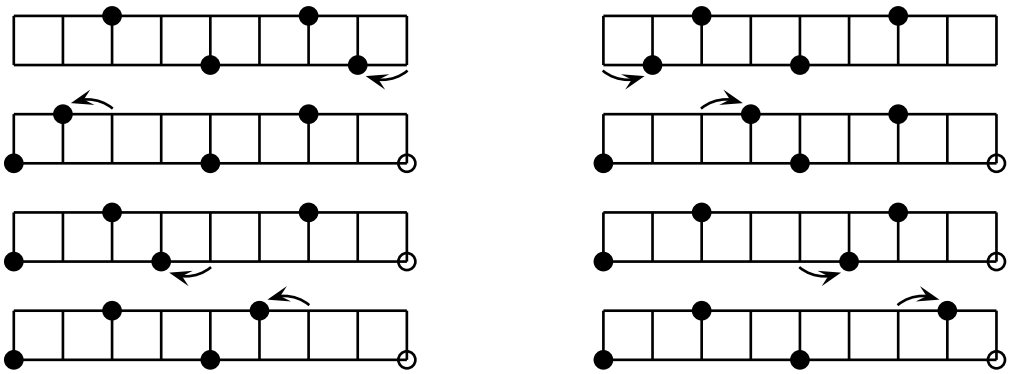

Figure 8.67: The eight staggered-ground-state configurations with the second largest absolute amplitude. These are derived from the largest-absolute-amplitude staggered ground-state configuration $[1, 6, 9, 14]$, in which one spinless fermion hops one site along the leg it is on to the left or to the right.

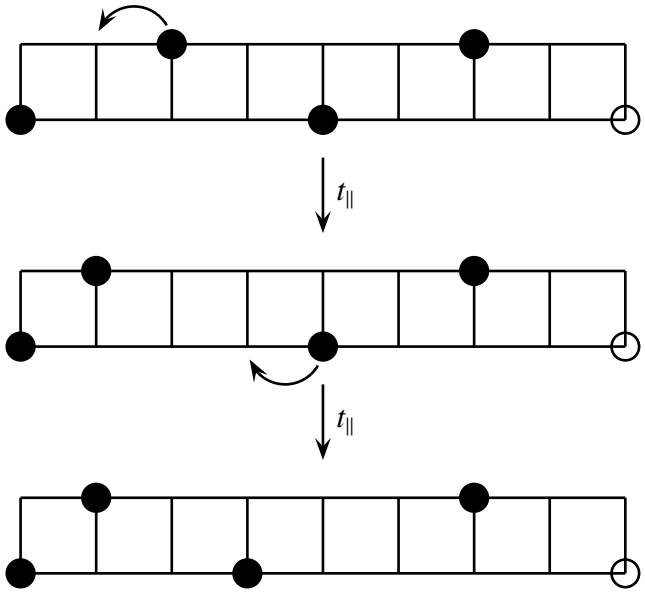

Figure 8.68: A fourth-largest-absolute-amplitude staggered ground-state configuration, $[1, 4, 7, 14]$, derived from the largest-absolute-amplitude staggered ground-state configuration $[1, 6, 9, 14]$ by one $t_{\|}$ hops each by a pair of successive spinless fermions.

the leg-hopping spinless fermion has hopped away from now hops across the rung. One of these configurations is shown in Figure 8.69. It is difficult to fit most of the remaining configurations with intermediate absolute amplitudes into the various hierarchies of staggered ground-state, rung-fermion ground-state, and two-bound-pair ground-state amplitudes, because they can frequently be obtained from the largest-absolute-amplitude and second-largest-absolute amplitude configurations by a combination of $t_{\parallel}$ hops, $t_{\perp}$ hops, as well as correlated hops.

Nevertheless, we checked that the configurations which have the largest absolute amplitude in the rung-fermion ground state (apart from the ones shown in Figure 8.9, which are also staggered ground-state configurations) have zero amplitudes in the $\mathbf{q} = (0, -\pi)$ ground-state wave function at the parameter point $(t_{\perp}/t_{\parallel} = 2, t'/t_{\parallel} = 2)$. We also checked that the two-same-flavor-bound-pair configurations, which have the second largest absolute amplitude in the two-bound-pair ground state, has an absolute amplitude that is two orders of magnitude smaller than the largest staggered ground-state absolute amplitude. This tells us that, in some sense, the parameter point $(t_{\perp}/t_{\parallel} = 2, t'/t_{\parallel} = 2)$, which is supposedly our zeroth-order 'quantum 'tricritical point", has a finite-ladder ground state that is closest to that of the weak inter-leg hopping limit, and next closest to that of the strong correlated hopping limit, but far away from that of the strong inter-leg hopping limit.

8.4 Analysis of Singular Values

As we have seen in Section 8.3, exploring the ground-state phase diagram by analyzing the structure of the ground-state wave function is extremely laborious. In Section 8.3, we also have the benefit of knowing the analytical structure of the ground state in three limiting cases, so that elsewhere on the ground-state phase diagram, we can always

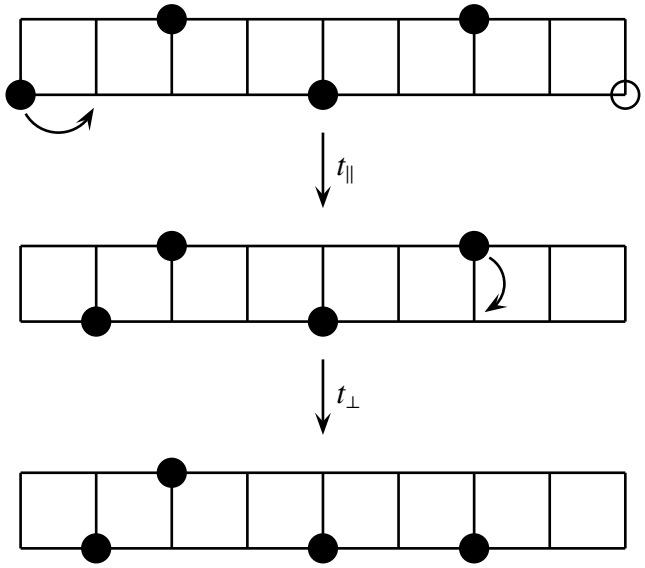

Figure 8.69: A third-largest-absolute-amplitude configuration, [3, 6, 9, 13], derived from the largest-absolute-amplitude staggered ground-state configuration [1, 6, 9, 14] by a $t_{\|}$ hop, followed by a $t_{\perp}$ hop.

figure out which hierarchy or hierarchies of amplitudes dominate in the ground state at an arbitrary parameter point $(t_{\perp}/t_{\|}, t'/t_{\|})$. Based on our discussions in Section 8.2.1, we assume that, once we figured out which reference state(s) the ED ground state resembles the most, we will have an idea of which ground-state correlations are the most important at large distances. Again, this is because we know what the important correlations are in the analytical limits.

For a general model, we will not have such luxuries. This is why extracting important ground-state correlations from ED remains an art rather than a science, and why the development of a systematic machinery to extract and sort ground-state correlations will greatly enhance the value of ED in exploring and constructing the ground-state phase diagram. In Chapters 5 and 6, we outline the main ideas behind one such systematic method, viz. the operator singular value decomposition of the correlation density matrix. In this section, we will repeat the analysis of the various parameters points selected

in Figure 8.1, by looking at the largest absolute singular values that comes out from the operator singular value decomposition of the correlation density matrix, for various intercluster separations and each order parameter type.

We will first look at the use of this numerical machinery on the $(1 \times 2) + (1 \times 2)$ supercluster in Section 8.4.1, and discuss the limitations of this simplest nontrivial supercluster. In the remaining subsections, we will work with the $(2 \times 2) + (2 \times 2)$ supercluster exclusively, and discuss what signatures we expect to find of each limiting ground state, from the relative magnitudes of the various absolute singular values.

8.4.1 The $(1 \times 2) + (1 \times 2)$ Supercluster

To get a feel of the numerics, we looked at the correlation density-matrix singular values, for various intercluster separations, for $P = 2$ particles on a ladder of length $L = 6$ subject to twist boundary conditions. We choose arbitrarily to do this at parameter point $(t_\perp/t_\parallel = 1, t'/t_\parallel = 1)$, which lies in the interior of the PL-CDW phase, according to the zeroth-order phase diagram in Figure 7.12.

For a ladder of this length, it only makes sense to go up to a intercluster separation of $r = 3$. At each intercluster separation r, we twist boundary conditions average the correlation density matrix over 21 twist angles, and thereafter plot the six independent singular values as functions of r in Figure 8.70. In this plot, we keep track of the signs of the singular values, to monitor oscillations as a function of separation. However, we find that such a linear-linear plot is not very informative, because the scale of the graph, determined essentially by the large absolute singular values, obscures the detailed behaviours of the small absolute singular values, whose absolute values are frequently three or more orders of magnitude down from the largest absolute singular value at each separation. Therefore, we plot instead the absolute singular values against separation on

the linear-logarithmic graph, as shown in Figure 8.71.

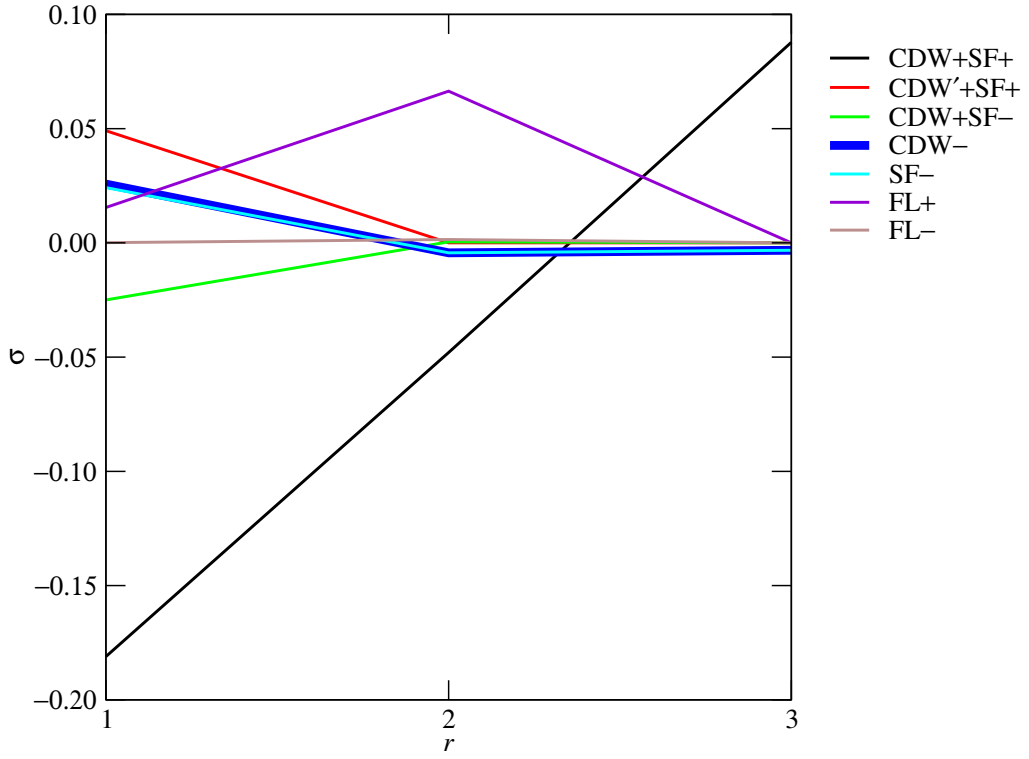

Figure 8.70: Correlation density-matrix singular values as functions of the separation r between two (1×2) clusters for $P = 2$ particles on a ladder of length $L = 6$ subject to twist boundary conditions, at the parameter point $(t_\perp/t_\parallel = 1, t'/t_\parallel = 1)$.

From Figure 8.71, we find that we can roughly distinguish between two groups of absolute singular values: the group CDW+SF+, CDW−, and SF−, which decays slowly with separation, and the group CDW′+SF+, CDW+SF−, FL+ and FL−, which decays very rapidly with separation. The rapid decay of the FL correlations agree with the results obtain in Section 7.6, where we found the FL correlations decaying exponentially in the PL-CDW phase. While we will not be able to extract correlation exponents, or even distinguish between power-law decay and exponential decay, because of the small range of separations that we are constrained to work with, we will continue to use such linear-logarithmic plots to extract the qualitative behaviours of the correlation density-

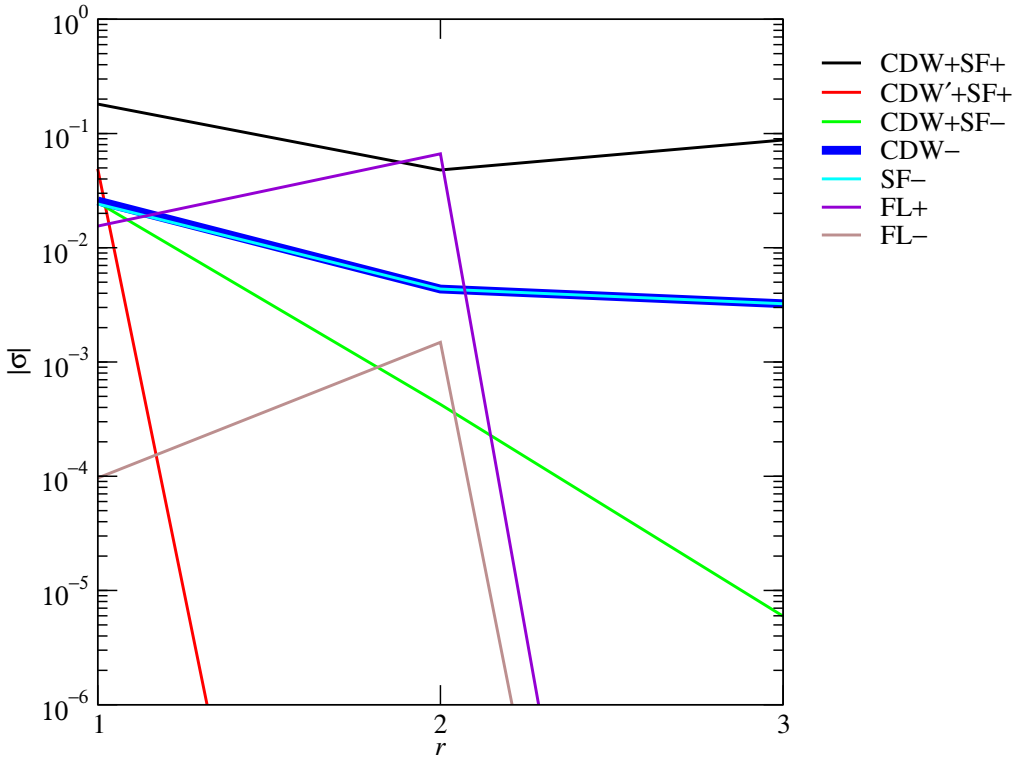

Figure 8.71: Correlation density-matrix absolute singular values as functions of the separation r between two (1×2) clusters for $P = 2$ particles on a ladder of length $L = 6$ subject to twist boundary conditions, at the parameter point $(t_\perp/t_\parallel = 1, t'/t_\parallel = 1)$.

matrix singular values.

Before moving on to a longer ladder system, let us note that the spinless extended Hubbard ladder model with infinite-nearest-neighbor repulsion and correlated hops, given by (7.3.2), has the largest Hilbert space when it is nearly quarter-filled. At this filling fraction, the largest system we can realistically handle, on a 2.0-GHz workstation with up to 1 GB of RAM, is a ladder of length $L = 16$. We can manage longer ladders, if the filling fraction is reduced from $\bar{n} \approx \frac{1}{4}$, but the whole process of exact diagonalization followed by correlation density matrix calculation would incur far too much computation time. This computation time constraint is especially severe, when we consider the fact that we would have to do twist boundary conditions averaging with 21 twist angles. A calculation that would take 10 days of computation time to complete, will take up to 200 days when we factor in twist boundary conditions averaging.

Because we hope to liberally explore the ground-state phase diagram, the maximum computation time for each parameter point, with twist boundary conditions averaging over 21 twist angles, must be limited to no more than a week. For this reason, we are constrained to work mostly with ladders of length $L = 10$, for which we have meaningful intercluster separations up to $r = 5$. We also choose to work mostly with $P = 4$ particles, because it gives two — the smallest non-trivial number of — interacting bound pairs in the strong correlated hopping limit of $t'/t_{\parallel} \to \infty$.

More importantly, because of the infinite nearest-neighbor repulsion in our model, we cannot have double occupation within the (1×2) clusters, and thus cannot construct superconducting order parameters. To be able to construct superconducting order parameters, we will need to move on to consider (2×2) clusters. Before we do so, it is a good idea to check what qualitative differences we expect between the absolute singular values in two limiting cases, the weak inter-leg hopping limit with $(t_{\perp}/t_{\parallel} = 1, t'/t_{\parallel} = 0)$

(Figure 8.72) and the strong correlated hopping limit with ($t_\perp/t_\parallel = 1, t'/t_\parallel \to \infty$) (Figure 8.73).

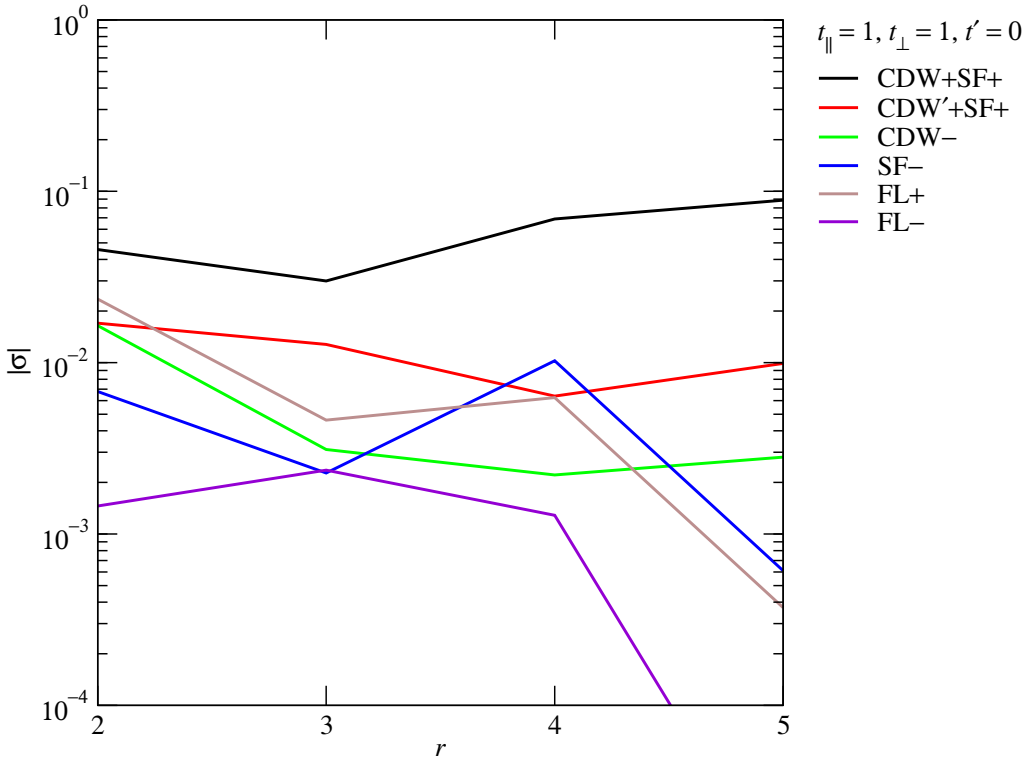

Figure 8.72: Correlation density-matrix absolute singular values as functions of the separation r between two (1×2) clusters for $P = 4$ particles on a ladder of length $L = 10$ subject to twist boundary conditions, at the parameter point $t_\perp/t_\parallel = 1, t'/t_\parallel = 0$).

From Figures 8.72 and 8.73, we can see that the singular values for the two limiting cases have very different qualitive behaviours as a function of intercluster separation r. However, there is not much we can say about them, unless we can fit the singular values to power-law or exponential decaying functions of r modulated by an oscillatory cosine function of r to extract the amplitude, correlation exponent, and the wave vector, as we have done in Chapter 7. With a maximum intercluster separation of $r_{\max} = 5$, this is not feasible, and we have to do our best to make sense of the semilogarithmic plots of absolute singular values, as we move on to work with the $(2 \times 2) + (2 \times 2)$ supercluster.

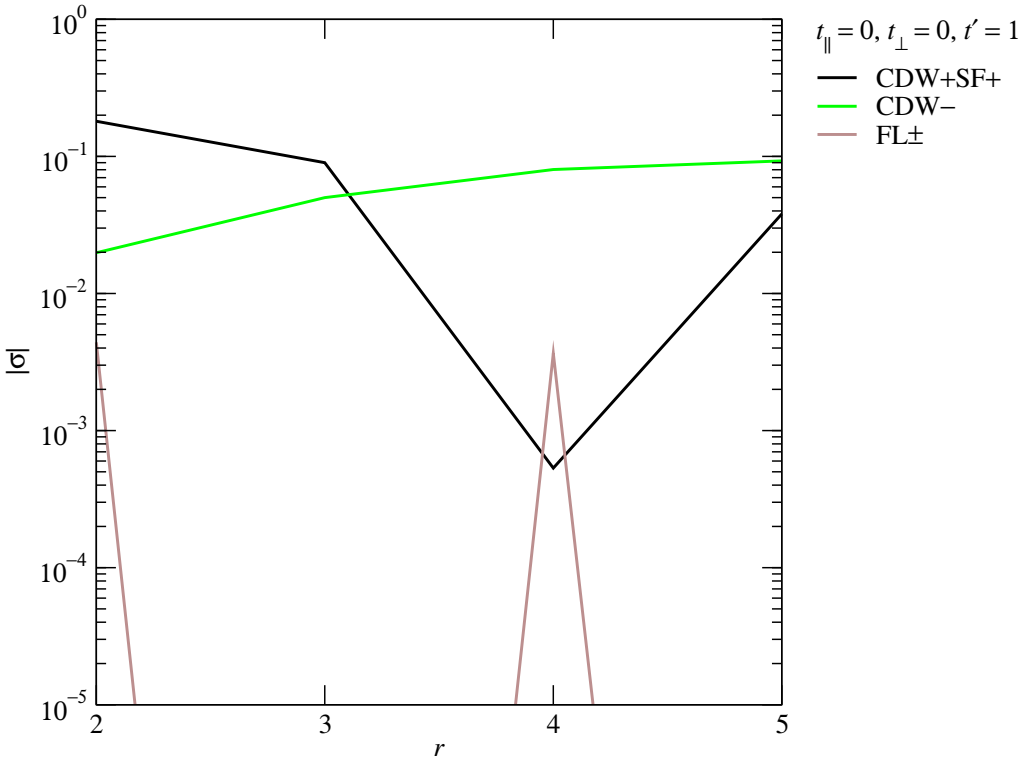

Figure 8.73: Correlation density-matrix absolute singular values as functions of the separation r between two (1×2) clusters for $P = 4$ particles on a ladder of length $L = 10$ subject to twist boundary conditions, at the parameter point $t_{\perp}/t_{\|} = 1, t'/t_{\|} \to \infty$).

8.4.2 Known Limits

In this subsection, we look at the absolute singular values obtained from the operator singular value decomposition of the correlation density matrix for parameter points close to the three analytical limits: (i) weak inter-leg hopping, (ii) strong inter-leg hopping, and (iii) strong correlated hopping, in Sections 8.4.2.1, 8.4.2.2 and 8.4.2.3.

8.4.2.1 Weak Inter-Leg Hopping

As shown in Figure 7.12, we have chosen two parameter points close to the weak inter-leg hopping limit, $(t_\perp/t_\parallel = 0.1, t'/t_\parallel = 0)$ and $(t_\perp/t_\parallel = 0, t'/t_\parallel = 0.1)$. For $P = 4$ particles on a ladder of length $L = 8$ subject to twist boundary conditions averaging over 41 twist angles restricted to the First Brillouin Zone $-\frac{\pi}{8} \leq \phi_x \leq +\frac{\pi}{8}$, the absolute singular values obtained from the operator singular value decomposition of the correlation density matrix are shown in Figures 8.74 and 8.75 respectively.

As with our analysis of the ED ground-state structure, we take advantage of our analytical understanding of the ground state in the weak inter-leg hopping limit, and ask what signatures in these plots of the absolute singular values agree with what we know analytically about the ground-state correlations in this limiting case. First of all, from the staggered nature of the infinite-ladder ground state, we know that the two-point functions $\langle c^\dagger_{1,j} c_{1,j+r} \rangle$ and $\langle c^\dagger_{2,j} c_{2,j+r} \rangle$ have identical values at all r, and we say that they are 'degenerate' correlations. In fact, for every FL observable we can write down on leg $i = 1$, we can write down a corresponding FL observable on leg $i = 2$ with the same ground-state expectation. This tells us that all infinite-ladder FL order parameters come in 'degenerate' pairs, and our method of operator singular value decomposition of the correlation density matrix always picks out the symmetric (+) and antisymmetric (−) combinations of these 'degenerate' pairs of FL order parameters. Indeed, from Figures

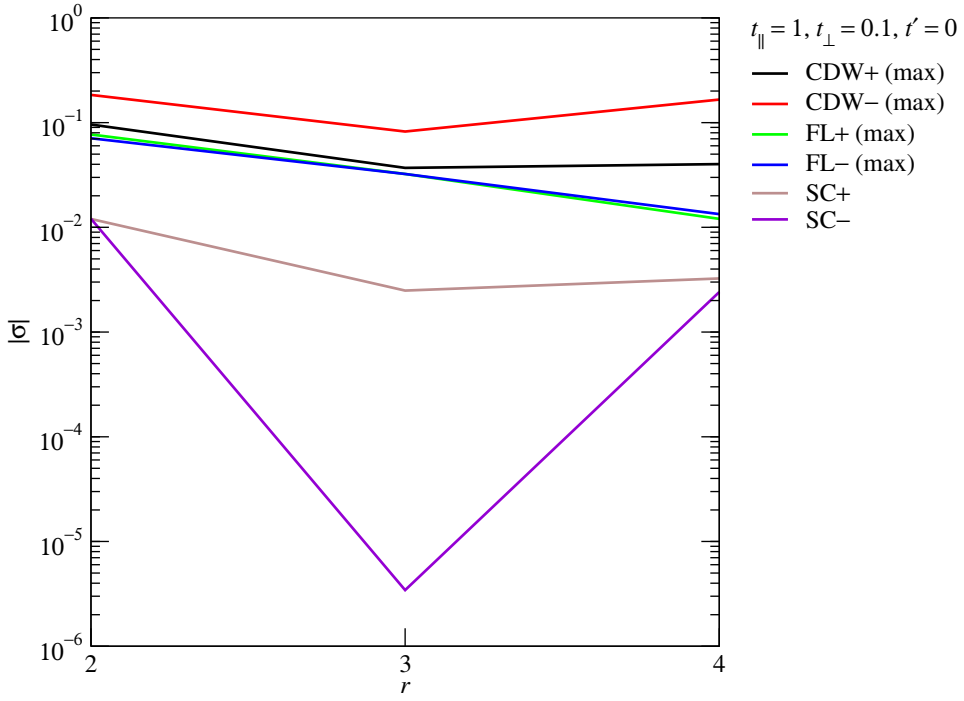

Figure 8.74: Correlation density-matrix absolute singular values $|\sigma|$ as functions of the separation r between two (2×2) clusters for $P = 4$ particles on a ladder of length $L = 8$ subject to twist boundary conditions averaging over 41 twist angles restricted to the First Brillouin Zone $-\frac{\pi}{8} \leq \phi_x \leq +\frac{\pi}{8}$, at the parameter point $(t_\perp/t_\parallel = 0.1, t'/t_\parallel = 0)$.

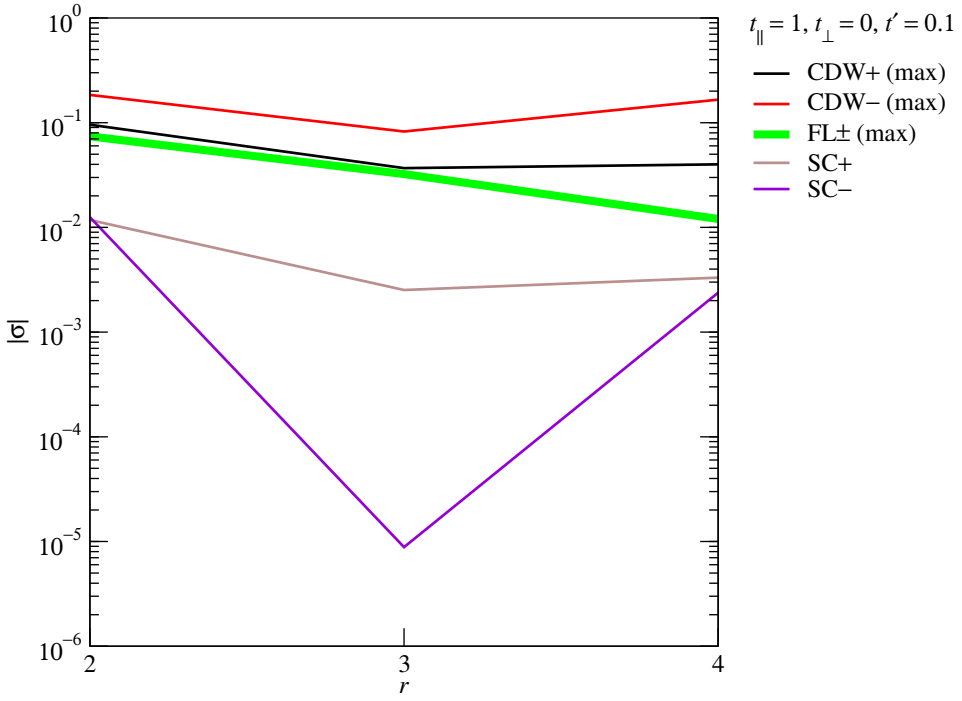

Figure 8.75: Correlation density-matrix absolute singular values $|\sigma|$ as functions of the separation r between two (2×2) clusters for $P = 4$ particles on a ladder of length $L = 8$ subject to twist boundary conditions averaging over 41 twist angles restricted to the First Brillouin Zone $-\frac{\pi}{8} \leq \phi_x \leq +\frac{\pi}{8}$, at the parameter point $(t_{\perp}/t_{\parallel} = 0, t'/t_{\parallel} = 0.1)$.

8.74 and 8.75, we find that the maximum symmetric and antisymmetric FL absolute singular values are very nearly degenerate.

Secondly, we know that in the staggered ground state, the two-point function, which is the simplest of FL correlations, decay exponentially with separation. From Figure 7.60, we see that at quarter-filling, the infinite-ladder two-point function decays slowly at first, starting from a value of about 10^{-1} at $r = 1$, but nevertheless goes down to 10^{-3} by $r = 4$. In contrast, from Figures 8.74 and 8.75, we see that the maximum FL absolute singular value decays slower, starting from a value of about 10^{-1} at $r = 2$, and going down to a value of about 10^{-2} at $r = 4$. Apart from finite size effects, which we know cannot be eliminated completely with twist boundary conditions averaging, we can think of another reason why the maximum FL absolute singular value, even if it is determined from an infinite-ladder ground state, will decay slower than the infinite-ladder two-point function. Working with (2×2) clusters whose centers are a distance r apart, we understand from Figure 8.76 that the supercluster correlation density matrix will receive contributions from $\langle c^{\dagger}_{i,j} c_{i,j+r-1} \rangle$, $\langle c^{\dagger}_{i,j} c_{i,j+r} \rangle$ and $\langle c^{\dagger}_{i,j} c_{i,j+r+1} \rangle$, and therefore, the value of the maximum FL absolute singular value at $r = 4$ is essentially determined by the two-point function at $r = 3$.

Thirdly, we learnt in Section 7.6.3 that the dominant CDW correlation in the staggered ground state decays with correlation exponent $\alpha = \frac{1}{2}$, and is antisymmetric with respect to reflection about the ladder axis. With the small intercluster separations that we have access to numerically, and having no measure of how much of the finite size effects remain after twist boundary conditions averaging, we have no reliable means to determine any correlation exponents, for comparison with those known analytically. However, from Figures 8.74 and 8.75 that the maximum CDW$-$ absolute singular value is indeed the largest, for the small range of separations we investigated. In Section 7.6.3,

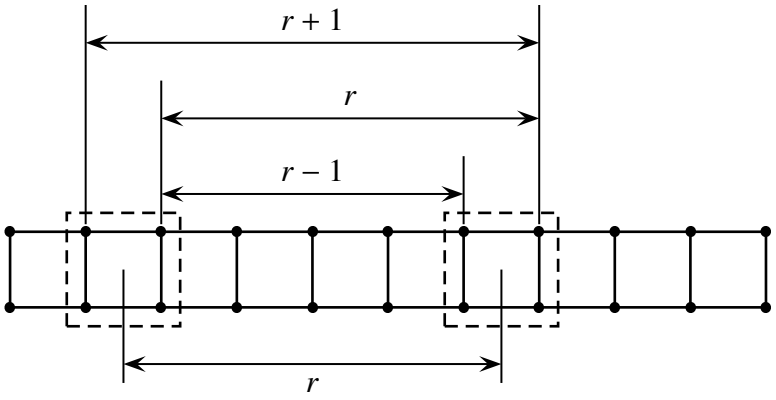

Figure 8.76: For two (2×2) clusters whose centers are a distance r apart, there are three possible intercluster two-point separations: $r-1$, r and $r+1$.

we also determined the symmetric CDW correlation exponent to be $\alpha = 2$. In Figures 8.74 and 8.75, we find that the maximum CDW+ absolute singular value does not appear to decay any faster with separation than the maximum CDW− absolute singular value. Though unlikely, it might be possible that there exists other slower-decaying symmetric infinite-ladder CDW correlations which we have not calculated in Section 7.6.3.

Finally, we learnt from Section 7.6.4 that the two simplest infinite-ladder symmetric and antisymmetric SC correlations we know how to calculate have correlation exponents of $\beta = 2$ and $\beta = 2.5$ respectively. From Figure 7.69 we also see that the infinite-ladder antisymmetric SC correlation is one order of magnitude smaller in amplitude than the infinite-ladder antisymmetric CDW correlation. From Figures 8.74 and 8.75, we see that this ratio of amplitudes seems more or less correct, but we again have no handle on the correlation exponent β.

Hoping to learn more about the nature of the dominant ground-state correlations, at least at the short ranges that we can work with numerically, we look at the structure of the order parameters coming out from the operator singular value decomposition of the correlation density matrix. Examining the eigenvectors associated with the maximum

CDW+ absolute singular value, we find that at $r = 2$, the operator components in the left eigenvector $X_{\text{CDW+}}$ having the largest absolute amplitude are

$$\begin{aligned} &(\mathbb{1} - n_{1,j})(\mathbb{1} - n_{2,j})n_{1,j+1}(\mathbb{1} - n_{2,j+1}), \\ &(\mathbb{1} - n_{1,j})(\mathbb{1} - n_{2,j})(\mathbb{1} - n_{1,j+1})n_{2,j+1}, \end{aligned} \tag{8.4.1}$$

while those in the right eigenvector $Y_{\text{CDW+}}$ having the largest absolute amplitude are

$$\begin{aligned} &c^{\dagger}_{1,j+r}(\mathbb{1} - n_{2,j+r})c_{1,j+r+1}(\mathbb{1} - n_{2,j+r+1}), \\ &(\mathbb{1} - n_{1,j+r})c^{\dagger}_{2,j+r}(\mathbb{1} - n_{1,j+r+1})c_{2,j+r+1}, \\ &c_{1,j+r}(\mathbb{1} - n_{2,j+r})c^{\dagger}_{1,j+r+1}(\mathbb{1} - n_{2,j+r+1}), \\ &(\mathbb{1} - n_{1,j+r})c_{2,j+r}(\mathbb{1} - n_{1,j+r+1})c^{\dagger}_{2,j+r+1}. \end{aligned} \tag{8.4.2}$$

This tells us that at $r = 2$, the order parameters that $X_{\text{CDW+}}$ and $Y_{\text{CDW+}}$ project out receive their largest contributions, though not overwhelmingly, from the operator components

$$\begin{aligned} &n_{1,j+1} + n_{2,j+1}, \\ &c^{\dagger}_{1,j+r}c_{1,j+r+1} + c^{\dagger}_{2,j+r}c_{2,j+r+1} + c_{1,j+r}c^{\dagger}_{1,j+r+1} + c_{2,j+r}c^{\dagger}_{2,j+r+1} \end{aligned} \tag{8.4.3}$$

respectively.

As the separation r is varied, the relative ordering of the absolute amplitudes also changes. However, the observables

$$\begin{aligned} O_{X_1} &= n_{1,j+1} + n_{2,j+1}, \\ O_{X_2} &= c^{\dagger}_{1,j}c_{1,j+1} + c^{\dagger}_{2,j}c_{2,j+1} + c_{1,j}c^{\dagger}_{1,j+1} + c_{2,j}c^{\dagger}_{2,j+1}; \\ O_{Y_1} &= n_{1,j+1} + n_{2,j+1}, \\ O_{Y_2} &= c^{\dagger}_{1,j+r}c_{1,j+r+1} + c^{\dagger}_{2,j+r}c_{2,j+r+1} + c_{1,j+r}c^{\dagger}_{1,j+r+1} + c_{2,j+r}c^{\dagger}_{2,j+r+1}, \end{aligned} \tag{8.4.4}$$

are always projected out by the operator components have the largest, second-largest, or third-largest absolute amplitudes in $X_{\text{CDW+}}$ and $Y_{\text{CDW+}}$. Since the absolute amplitudes,

of the operator components

$$\begin{aligned} X_1 &= (\mathbb{1} - n_{1,j})(\mathbb{1} - n_{2,j})n_{1,j+1}(\mathbb{1} - n_{2,j+1}) + \\ &\quad (\mathbb{1} - n_{1,j})(\mathbb{1} - n_{2,j})(\mathbb{1} - n_{1,j+1})n_{2,j+1}, \\ X_2 &= c^\dagger_{1,j+r}(\mathbb{1} - n_{2,j+r})c_{1,j+r+1}(\mathbb{1} - n_{2,j+r+1}) + \\ &\quad c_{1,j+r}(\mathbb{1} - n_{2,j+r})c^\dagger_{1,j+r+1}(\mathbb{1} - n_{2,j+r+1}) + \\ &\quad (\mathbb{1} - n_{1,j+r})c^\dagger_{2,j+r}(\mathbb{1} - n_{1,j+r+1})c_{2,j+r+1} + \\ &\quad (\mathbb{1} - n_{1,j+r})c_{2,j+r}(\mathbb{1} - n_{1,j+r+1})c^\dagger_{2,j+r+1}. \end{aligned} \tag{8.4.5}$$

and that of the operator components Y_1 and Y_2 (defined analogously as X_1 and X_2, with $j \to j + r$), are always comparable, we should think of

$$O_X = \alpha(r)O_{X_1} + \beta(r)O_{X_2}, \quad O_Y = \gamma(r)O_{Y_1} + \delta(r)O_{Y_2}, \tag{8.4.6}$$

as the approximate order parameters. In Section 7.6.3, it had not occurred to us that we should calculate the expectation $\langle O_X O_Y \rangle$, which is a product of sums of density-like and current-like operators. We think of this as a plus point of our method of operator singular value decomposition of the correlation density matrix, because it identified a form of observables that we would not have imagined to be important.

Similarly, examining the eigenvectors associated with the maximum CDW− absolute singular value over the various separations, we find that we should think of the approximate order parameters O_X and O_Y as linear combinations of the observables

$$\begin{aligned} O_{X_1} &= n_{1,j} - n_{2,j}, \\ O_{X_2} &= n_{1,j+1} - n_{2,j+1}, \\ O_{X_3} &= c^\dagger_{1,j}c_{1,j+1} - c^\dagger_{2,j}c_{2,j+1} + c_{1,j}c^\dagger_{1,j+1} - c_{2,j}c^\dagger_{2,j+1}, \\ O_{X_4} &= n_{1,j}n_{2,j+1} - n_{2,j}n_{1,j+1}, \end{aligned} \tag{8.4.7}$$

and

$$\begin{aligned} O_{Y_1} &= n_{1,j+r} - n_{2,j+r}, \\ O_{Y_2} &= n_{1,j+r+1} - n_{2,j+r+1}, \\ O_{Y_3} &= c^\dagger_{1,j+r} c_{1,j+r+1} - c^\dagger_{2,j+r} c_{2,j+r+1} + c_{1,j+r} c^\dagger_{1,j+r+1} - c_{2,j+r} c^\dagger_{2,j+r+1}, \\ O_{Y_4} &= n_{1,j+r} n_{2,j+r+1} - n_{2,j+r} n_{1,j+r+1}, \end{aligned} \tag{8.4.8}$$

respectively.

In Section 7.6.3, we calculated the CDW− correlation $\langle O_{X_1} O_{Y_1} \rangle$ (and $\langle O_{X_1} O_{Y_2} \rangle$, $\langle O_{X_2} O_{Y_1} \rangle$ and $\langle O_{X_2} O_{Y_2} \rangle$ as well, since these are of the same nature as $\langle O_{X_1} O_{Y_1} \rangle$), but not anything involving O_{X_3}, O_{X_4}, O_{Y_3} and O_{Y_4}. In this same section, we have also seen that the expectation of products of these operators will eventually map onto noninteracting-spinless-fermion expectations. Since O_{X_4} and O_{Y_4} consist of sums of the product of two creation and two annihilation operators, any expectation involving them will involve more powers of the noninteracting-spinless-fermion two-point functions, and consequently decay faster as power laws of the separation r between the clusters a and b. It is therefore plausible that, as r becomes large, O_{X_4} and O_{Y_4} will drop out of the linear combinations for O_X and O_Y respectively.

However, this power-counting argument does not work on O_{X_3} and O_{Y_3}, which consist of sums of products of one creation and annihilation operators. Unless we know through other means that the correlation of O_{X_3} and O_{Y_3} decays faster, either as a power law, or exponentially, we expect them to remain in the linear combinations for O_X and O_Y even as r becomes large. Again, without input *a priori*, we would not have included O_{X_3} and O_{Y_3} into the approximate order parameters O_X and O_Y whose correlation dominates at large distances. In this sense, the method of operator singular value decomposition of the correlation density matrix provide valuable input in identifying unexpected observables whose ground-state correlations are of comparable magnitude to those observables

whose ground-state correlations we expect to dominate at large distances.

Unlike in the maximum-absolute-singular-value CDW± eigenvectors, where we find a cluster of large absolute amplitudes, followed by absolute amplitudes which are one or more orders of magnitude smaller, the amplitudes in the maximum-absolute-singular-value FL eigenvectors exhibit no clustering. Naively, we would expect the FL operator components

$$\begin{aligned} X_5 &= (\mathbb{1} - n_{1,j})(\mathbb{1} - n_{2,j})c^\dagger_{1,j+1}(\mathbb{1} - n_{2,j+1}), \\ X_6 &= (\mathbb{1} - n_{1,j})(\mathbb{1} - n_{2,j})(\mathbb{1} - n_{1,j+1})c^\dagger_{2,j+1}, \end{aligned} \tag{8.4.9}$$

and

$$\begin{aligned} Y_5 &= c_{1,j+r}(\mathbb{1} - n_{2,j+r})(\mathbb{1} - n_{1,j+r+1})(\mathbb{1} - n_{2,j+r+1}), \\ Y_6 &= (\mathbb{1} - n_{1,j+r})c_{2,j+r}(\mathbb{1} - n_{1,j+r+1})(\mathbb{1} - n_{2,j+r+1}), \end{aligned} \tag{8.4.10}$$

to have the largest amplitudes within the maximum-absolute-singular-value FL eigenvectors, since these project out the usual two-point functions

$$\langle O_X O_Y \rangle = \langle c^\dagger_{1,j+1} c_{1,j+r} \rangle , \quad \langle c^\dagger_{1,j+1} c_{2,j+r} \rangle , \quad \langle c^\dagger_{2,j+1} c_{1,j+r} \rangle , \quad \langle c^\dagger_{2,j+1} c_{2,j+r} \rangle , \tag{8.4.11}$$

with the smallest separation within the (2×2) clusters.

Indeed, we find these FL operator components having large absolute amplitudes in the maximum-absolute-singular-value FL eigenvectors at $r = 2$ and $r = 3$, but we also find FL operator components like

$$\begin{aligned} X_7 &= c^\dagger_{1,j}(\mathbb{1} - n_{2,j})c_{1,j+1}c^\dagger_{2,j+1}, \\ X_8 &= (\mathbb{1} - n_{1,j})c^\dagger_{2,j}c^\dagger_{1,j+1}c_{2,j+1}, \end{aligned} \tag{8.4.12}$$

and

$$\begin{aligned} Y_7 &= (\mathbb{1} - n_{1,j+r})c_{2,j+r}n_{1,j+r+1}(\mathbb{1} - n_{2,j+r+1}), \\ Y_8 &= c_{1,j+r}(\mathbb{1} - n_{2,j+r})(\mathbb{1} - n_{1,j+r+1})n_{2,j+r+1}, \end{aligned} \tag{8.4.13}$$

to have large absolute amplitudes within maximum-absolute-singular-value FL eigenvectors. It may be that as r becomes larger, the absolute amplitudes of these unusual FL

operator components X_7, X_8 and Y_7, Y_8 may become small, and the maximum-absolute-singular-value FL eigenvectors look more and more like the usual FL operator components X_5, X_6 and Y_5, Y_6, but we cannot tell for sure with the small intercluster separations we have access to numerically.

Finally, the structure of the SC eigenvectors are determined essentially by symmetry with respect to reflection about the ladder axis, and we learn nothing more by examining the amplitudes in these eigenvectors.

8.4.2.2 Strong Inter-Leg Hopping

For $P = 4$ particles on a ladder of length $L = 8$ subject to twist boundary conditions averaging over 41 twist angles restricted to the First Brillouin Zone $-\frac{\pi}{8} \leq \phi_x \leq +\frac{\pi}{8}$, we show in Figure 8.77 the absolute singular values obtained from the operator singular value decomposition of the correlation density matrix at the parameter point $(t_\perp/t_\parallel = 100, t'/t_\parallel = 0)$.

In Sections 7.7.2, 7.7.3, and 7.7.4, we found the infinite-ladder symmetric CDW correlation to exhibit true long-range order, while the infinite-ladder FL and SC correlations vanish identically. From Figure 8.77, we find that indeed, the CDW+ absolute singular value does appear to not decay with increasing separation. We also find very small SC absolute singular values, on the order of 10^{-15} or smaller, which agrees with SC correlations vanishing on the infinite ladder. However, instead of having vanishingly small values, we find the FL absolute singular values decaying very rapidly with separation, starting from rather large initial values. We believe this to be due to finite size effects.

For a quarter-filled rung-fermion ground state, we can find at most one rung-fermion in any (2×2) cluster on the ladder. This means that in the maximum-absolute-singular-

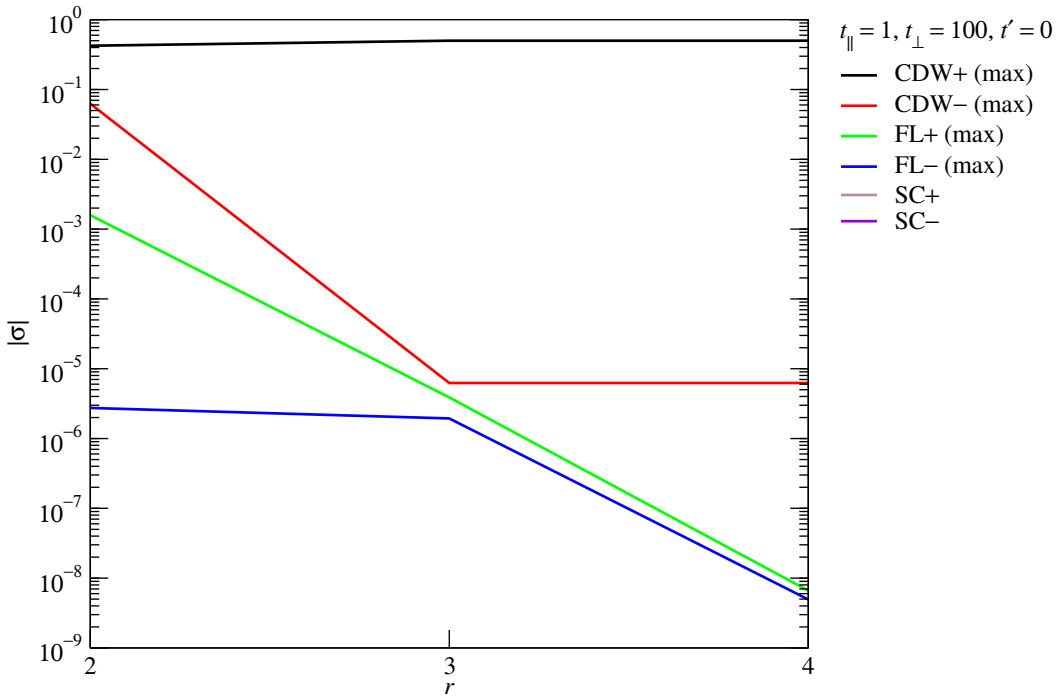

Figure 8.77: Correlation density-matrix absolute singular values $|\sigma|$ as functions of the separation r between two (2×2) clusters for $P = 4$ particles on a ladder of length $L = 8$ subject to twist boundary conditions averaging over 41 twist angles restricted to the First Brillouin Zone $-\frac{\pi}{8} \leq \phi_x \leq +\frac{\pi}{8}$, at the parameter point $(t_{\perp}/t_{\parallel} = 100, t'/t_{\parallel} = 0)$. The SC± absolute singular values have magnitudes less than 10^{-15} and thus do not appear on the scale of the plot.

value CDW+ eigenvectors, CDW operator components such as

$$n_{1,j}(\mathbb{1}-n_{2,j})(\mathbb{1}-n_{1,j+1})n_{2,j+1}, \quad (\mathbb{1}-n_{1,j})n_{2,j}n_{1,j+1}(\mathbb{1}-n_{2,j+1}), \tag{8.4.14}$$

must have zero (or very small, since $t_{\parallel}/t_{\perp} > 0$) amplitudes, even though they are allowed by the no-nearest-neighbor-occupation constraint. Examining the maximum-absolute-singular-value CDW+ eigenvectors $X_{\mathrm{CDW+}}$ and $Y_{\mathrm{CDW+}}$, we find indeed that these operator components, which project out doubly-occupied cluster states, have very small absolute amplitudes.

Also, because the immobile rung-fermions must be two lattice spacings apart in the quarter-filled rung-fermion ground state, we expect that if the separation r is even, then if in the left eigenvector $X_{\mathrm{CDW+}}$ the 'outer-rung' operator components

$$\begin{gathered} n_{1,j}(\mathbb{1}-n_{2,j})(\mathbb{1}-n_{1,j+1})(\mathbb{1}-n_{2,j+1}), \\ (\mathbb{1}-n_{1,j})n_{2,j}(\mathbb{1}-n_{1,j+1})(\mathbb{1}-n_{2,j+1}) \end{gathered} \tag{8.4.15}$$

have large absolute amplitudes, the 'inner-rung' operator components

$$\begin{gathered} n_{1,j+r}(\mathbb{1}-n_{2,j+r})(\mathbb{1}-n_{1,j+r+1})(\mathbb{1}-n_{2,j+r+1}), \\ (\mathbb{1}-n_{1,j+r})n_{2,j+r}(\mathbb{1}-n_{1,j+r+1})(\mathbb{1}-n_{2,j+r+1}) \end{gathered} \tag{8.4.16}$$

will have large absolute amplitudes in the right eigenvector $Y_{\mathrm{CDW+}}$. On the other hand, if r is odd, then if in the left eigenvector $X_{\mathrm{CDW+}}$ the 'outer-rung' operator components

$$\begin{gathered} n_{1,j}(\mathbb{1}-n_{2,j})(\mathbb{1}-n_{1,j+1})(\mathbb{1}-n_{2,j+1}), \\ (\mathbb{1}-n_{1,j})n_{2,j}(\mathbb{1}-n_{1,j+1})(\mathbb{1}-n_{2,j+1}) \end{gathered} \tag{8.4.17}$$

have large absolute amplitudes, the 'outer-rung' operator components

$$\begin{gathered} (\mathbb{1}-n_{1,j+r})(\mathbb{1}-n_{2,j+r})n_{1,j+r+1}(\mathbb{1}-n_{2,j+r+1}), \\ (\mathbb{1}-n_{1,j+r})(\mathbb{1}-n_{2,j+r})(\mathbb{1}-n_{1,j+r+1})n_{2,j+r+1} \end{gathered} \tag{8.4.18}$$

will have large absolute amplitudes in the right eigenvector $Y_{\mathrm{CDW+}}$. In Table 8.7, we show the large-absolute-amplitude cluster of CDW operator components in the maximum-absolute-singular-value CDW+ eigenvectors. Unfortunately, we find that both the 'outer-rung' and 'inner-rung' operator components have large absolute amplitudes in the right and left eigenvectors $X_{\mathrm{CDW+}}$ and $Y_{\mathrm{CDW+}}$. Thus, this every-other-rung-occupied nature of the ground state is not readily discernible from the maximum-absolute-singular-value CDW+ eigenvectors.

We initially suspected that there might actually be a *pair* of degenerate, or nearly-degenerate CDW+ singular values, one having eigenvectors in which the 'outer-rung' operator components have large absolute amplitude, while the other having eigenvectors in which the 'inner-rung' operator components have large absolute amplitudes. If this is the case, we might be able to explain our observation in terms of a mixing of these two sets of eigenvectors by the singular value decomposition program. However, a quick check showed that the second largest CDW+ absolute singular value is always very much smaller than the largest CDW+ absolute singular value. We can try to salvage the degenerate-pair-of-singular-values argument by arguing that both absolute singular values are oscillatory functions of the intercluster separation, such that when one absolute singular value goes to a maximum, the other goes close to zero, and vice versa. However, this line of argument is problematic, as we know that the singular value decomposition function we used in Octave will *not* mix such a pair of out-of-phase oscillatory absolute singular values. Our numerical observation that both 'outer-rung' and 'inner-rung' CDW operator components in the maximum-absolute-singular-value CDW+ eigenvectors have large absolute amplitudes remains a mystery.

Examining the structures of the maximum-absolute-singular-value CDW− eigenvectors, we find the large-absolute-amplitude cluster of CDW operator components shown

Table 8.7: Large-absolute-amplitude cluster of CDW-type operator components in the maximum-absolute-singular-value CDW+ left and right eigenvectors, $X_{\mathrm{CDW+}}$ and $Y_{\mathrm{CDW+}}$, for intercluster separations $r = 2, 3, 4$, obtained from the operator singular value decomposition of the correlation density matrix at the parameter point $(t_\perp/t_\parallel = 100, t'/t_\parallel = 0)$.

operator components of $X_{\mathrm{CDW+}}$	operator components of $Y_{\mathrm{CDW+}}$
$n_{1,j}(\mathbb{1} - n_{2,j})(\mathbb{1} - n_{1,j+1})(\mathbb{1} - n_{2,j+1})$	$n_{1,j+r}(\mathbb{1} - n_{2,j+r})(\mathbb{1} - n_{1,j+r+1})(\mathbb{1} - n_{2,j+r+1})$
$(\mathbb{1} - n_{1,j})n_{2,j}(\mathbb{1} - n_{1,j+1})(\mathbb{1} - n_{2,j+1})$	$(\mathbb{1} - n_{1,j+r})n_{2,j+r}(\mathbb{1} - n_{1,j+r+1})(\mathbb{1} - n_{2,j+r+1})$
$c^\dagger_{1,j}c_{2,j}(\mathbb{1} - n_{1,j+1})(\mathbb{1} - n_{2,j+1})$	$c^\dagger_{1,j+r}c_{2,j+r}(\mathbb{1} - n_{1,j+r+1})(\mathbb{1} - n_{2,j+r+1})$
$c_{1,j}c^\dagger_{2,j}(\mathbb{1} - n_{1,j+1})(\mathbb{1} - n_{2,j+1})$	$c_{1,j+r}c^\dagger_{2,j+r}(\mathbb{1} - n_{1,j+r+1})(\mathbb{1} - n_{2,j+r+1})$
$(\mathbb{1} - n_{1,j})(\mathbb{1} - n_{2,j})c^\dagger_{1,j+1}c_{2,j+1}$	$(\mathbb{1} - n_{1,j+r})(\mathbb{1} - n_{2,j+r})c^\dagger_{1,j+r+1}c_{2,j+r+1}$
$(\mathbb{1} - n_{1,j})(\mathbb{1} - n_{2,j})c_{1,j+1}c^\dagger_{2,j+1}$	$(\mathbb{1} - n_{1,j+r})(\mathbb{1} - n_{2,j+r})c_{1,j+r+1}c^\dagger_{2,j+r+1}$
$(\mathbb{1} - n_{1,j})(\mathbb{1} - n_{2,j})n_{1,j+1}(\mathbb{1} - n_{2,j+1})$	$(\mathbb{1} - n_{1,j+r})(\mathbb{1} - n_{2,j+r})n_{1,j+r+1}(\mathbb{1} - n_{2,j+r+1})$
$(\mathbb{1} - n_{1,j})(\mathbb{1} - n_{2,j})(\mathbb{1} - n_{1,j+1})n_{2,j+1}$	$(\mathbb{1} - n_{1,j+r})(\mathbb{1} - n_{2,j+r})(\mathbb{1} - n_{1,j+r+1})n_{2,j+r+1}$

in Table 8.8. These either are the only ones with nonzero amplitudes, or have absolute amplitudes two or more orders of magnitude larger than the rest of the CDW operator components. As we can see from Table 8.8, the characters of the CDW operator components in the large-absolute-amplitude cluster keep changing with separation.

Table 8.8: Large-absolute-amplitude cluster of CDW-type operator components in the maximum-absolute-singular-value CDW− left and right eigenvectors, $X_{\mathrm{CDW}-}$ and $Y_{\mathrm{CDW}-}$, for intercluster separations $r = 2, 3, 4$, obtained from the operator singular value decomposition of the correlation density matrix at the parameter point $(t_\perp/t_\parallel = 100, t'/t_\parallel = 0)$.

r	operator components of $X_{\mathrm{CDW}-}$	operator components of $Y_{\mathrm{CDW}-}$
2	$(\mathbb{1}-n_{1,j})(\mathbb{1}-n_{2,j})n_{1,j+1}(\mathbb{1}-n_{2,j+1})$	$n_{1,j+r}(\mathbb{1}-n_{2,j+r})(\mathbb{1}-n_{1,j+r+1})(\mathbb{1}-n_{2,j+r+1})$
	$(\mathbb{1}-n_{1,j})(\mathbb{1}-n_{2,j})(\mathbb{1}-n_{1,j+1})n_{2,j+1}$	$(\mathbb{1}-n_{1,j+r})n_{2,j+r}(\mathbb{1}-n_{1,j+r+1})(\mathbb{1}-n_{2,j+r+1})$
3	$(\mathbb{1}-n_{1,j})(\mathbb{1}-n_{2,j})c^\dagger_{1,j+1}c_{2,j+1}$	$c^\dagger_{1,j+r}c_{2,j+r}(\mathbb{1}-n_{1,j+r+1})(\mathbb{1}-n_{2,j+r+1})$
	$(\mathbb{1}-n_{1,j})(\mathbb{1}-n_{2,j})c_{1,j+1}c^\dagger_{2,j+1}$	$c_{1,j+r}c^\dagger_{2,j+r}(\mathbb{1}-n_{1,j+r+1})(\mathbb{1}-n_{2,j+r+1})$
4	$c^\dagger_{1,j}(\mathbb{1}-n_{2,j})(\mathbb{1}-n_{1,j+1})c_{2,j+1}$	$c^\dagger_{1,j+r}(\mathbb{1}-n_{2,j+r})(\mathbb{1}-n_{1,j+r+1})c_{2,j+r+1}$
	$(\mathbb{1}-n_{1,j})c^\dagger_{2,j}c_{1,j+1}(\mathbb{1}-n_{2,j+1})$	$(\mathbb{1}-n_{1,j+r})c^\dagger_{2,j+r}c_{1,j+r+1}(\mathbb{1}-n_{2,j+r+1})$
	$(\mathbb{1}-n_{1,j})c_{2,j}c^\dagger_{1,j+1}(\mathbb{1}-n_{2,j+1})$	$(\mathbb{1}-n_{1,j+r})c_{2,j+r}c^\dagger_{1,j+r+1}(\mathbb{1}-n_{2,j+r+1})$
	$c_{1,j}(\mathbb{1}-n_{2,j})(\mathbb{1}-n_{1,j+1})c^\dagger_{2,j+1}$	$c_{1,j+r}(\mathbb{1}-n_{2,j+r})(\mathbb{1}-n_{1,j+r+1})c^\dagger_{2,j+r+1}$
	$c^\dagger_{1,j}(\mathbb{1}-n_{2,j})c_{1,j+1}(\mathbb{1}-n_{2,j+1})$	$c^\dagger_{1,j+r}(\mathbb{1}-n_{2,j+r})c_{1,j+r+1}(\mathbb{1}-n_{2,j+r+1})$
	$(\mathbb{1}-n_{1,j})c^\dagger_{2,j}(\mathbb{1}-n_{1,j+1})c_{2,j+1}$	$(\mathbb{1}-n_{1,j+r})c^\dagger_{2,j+r}(\mathbb{1}-n_{1,j+r+1})c_{2,j+r+1}$
	$c_{1,j}(\mathbb{1}-n_{2,j})c^\dagger_{1,j+1}(\mathbb{1}-n_{2,j+1})$	$c_{1,j+r}(\mathbb{1}-n_{2,j+r})c^\dagger_{1,j+r+1}(\mathbb{1}-n_{2,j+r+1})$
	$(\mathbb{1}-n_{1,j})c_{2,j}(\mathbb{1}-n_{1,j+1})c^\dagger_{2,j+1}$	$(\mathbb{1}-n_{1,j+r})c_{2,j+r}(\mathbb{1}-n_{1,j+r+1})c^\dagger_{2,j+r+1}$

Moving on to the maximum-absolute-singular-value FL+ eigenvectors, we find that unlike the maximum-absolute-singular-value FL± eigenvectors in the limit of weak

inter-leg hopping, where we find no clustering of the FL-operator-component amplitudes, here we find very clear-cut cluster of the FL-operator-component amplitudes. The large-absolute-amplitude cluster of FL operator components are shown in Table 8.9. These have absolute amplitudes one or more orders of magnitude larger than the rest of the FL operator components. Again, we see from Table 8.9 that the characters of the FL operator components in the large-absolute-amplitude cluster change with separation r.

Table 8.9: Large-absolute-amplitude cluster of FL-type operator components in the maximum-absolute-singular-value FL+ left and right eigenvectors, $X_{\mathrm{FL+}}$ and $Y_{\mathrm{FL+}}$, for intercluster separations $r = 2, 3, 4$, obtained from the operator singular value decomposition of the correlation density matrix at the parameter point $(t_\perp/t_\parallel = 100, t'/t_\parallel = 0)$.

r	operator components of $X_{\mathrm{FL+}}$	operator components of $Y_{\mathrm{FL+}}$
2	$n_{1,j}(\mathbb{1}-n_{2,j})(\mathbb{1}-n_{1,j+1})c^\dagger_{2,j+1}$	$c_{1,j+r}(\mathbb{1}-n_{2,j+r})(\mathbb{1}-n_{1,j+r+1})(\mathbb{1}-n_{2,j+r+1})$
	$(\mathbb{1}-n_{1,j})n_{2,j}c^\dagger_{1,j+1})(\mathbb{1}-n_{2,j+1})$	$(\mathbb{1}-n_{1,j+r})c_{2,j+r}(\mathbb{1}-n_{1,j+r+1})(\mathbb{1}-n_{2,j+r+1})$
	$c^\dagger_{1,j}c_{2,j}(\mathbb{1}-n_{1,j+1})c^\dagger_{2,j+1}$	$(\mathbb{1}-n_{1,j+r})(\mathbb{1}-n_{2,j+r})c_{1,j+r+1}(\mathbb{1}-n_{2,j+r+1})$
	$c_{1,j}c^\dagger_{2,j}c^\dagger_{1,j+1}(\mathbb{1}-n_{2,j+1})$	$(\mathbb{1}-n_{1,j+r})(\mathbb{1}-n_{2,j+r})(\mathbb{1}-n_{1,j+r+1})c_{2,j+r+1}$
3	$c^\dagger_{1,j}c_{2,j}c_{1,j+1}(\mathbb{1}-n_{2,j+1})$	$c^\dagger_{1,j+r}(\mathbb{1}-n_{2,j+r})(\mathbb{1}-n_{1,j+r+1})n_{2,j+r+1}$
	$c_{1,j}c^\dagger_{2,j}(\mathbb{1}-n_{1,j+1})c_{2,j+1}$	$(\mathbb{1}-n_{1,j+r})c^\dagger_{2,j+r}n_{1,j+r+1}(\mathbb{1}-n_{2,j+r+1})$
	$n_{1,j}(\mathbb{1}-n_{2,j})(\mathbb{1}-n_{1,j+1})c_{2,j+1}$	$c^\dagger_{1,j+r}(\mathbb{1}-n_{2,j+r})c_{1,j+r+1}c^\dagger_{2,j+r+1}$
	$(\mathbb{1}-n_{1,j})n_{2,j}c_{1,j+1}(\mathbb{1}-n_{2,j+1})$	$(\mathbb{1}-n_{1,j+r})c^\dagger_{2,j+r}c^\dagger_{1,j+r+1}c_{2,j+r+1}$
4	$c^\dagger_{1,j}(\mathbb{1}-n_{2,j})(\mathbb{1}-n_{1,j+1})(\mathbb{1}-n_{2,j+1})$	$c^\dagger_{1,j+r}c_{2,j+r})c_{1,j+r+1})(\mathbb{1}-n_{2,j+r+1})$
	$(\mathbb{1}-n_{1,j})c^\dagger_{2,j}(\mathbb{1}-n_{1,j+1})(\mathbb{1}-n_{2,j+1})$	$c_{1,j+r}c^\dagger_{2,j+r}(\mathbb{1}-n_{1,j+r+1})c_{2,j+r+1})$
	$c_{1,j}(\mathbb{1}-n_{2,j})(\mathbb{1}-n_{1,j+1})(\mathbb{1}-n_{2,j+1})$	$c_{1,j+r}c_{2,j+r})(\mathbb{1}-n_{1,j+r+1})c_{2,j+r+1}$
	$(\mathbb{1}-n_{1,j})c_{2,j}(\mathbb{1}-n_{1,j+1})(\mathbb{1}-n_{2,j+1})$	$(\mathbb{1}-n_{1,j+r})n_{2,j+r}c_{1,j+r+1})(\mathbb{1}-n_{2,j+r+1})$

For the maximum-absolute-singular value FL− eigenvectors, we again find cluster-

ing of the absolute FL-operator-component amplitudes. The large-absolute-amplitude cluster of FL operator components are shown in Table 8.10. These have absolute amplitudes two to three orders of magnitude larger than the rest of the FL operator components. Again, as we can see from Table 8.10, the characters of the FL operator components in the large-absolute-amplitude cluster change with separation r.

Table 8.10: Large-absolute-amplitude cluster of FL-type operator components in the maximum-absolute-singular-value FL− left and right eigenvectors, $X_{\mathrm{FL}-}$ and $Y_{\mathrm{FL}-}$, for intercluster separations $r = 2, 3, 4$, obtained from the operator singular value decomposition of the correlation density matrix at the parameter point $(t_\perp/t_\parallel = 100, t'/t_\parallel = 0)$.

r	operator components of $X_{\mathrm{FL}-}$	operator components of $Y_{\mathrm{FL}-}$
2	$(\mathbb{1} - n_{1,j})(\mathbb{1} - n_{2,j})c^\dagger_{1,j+1}(\mathbb{1} - n_{2,j+1})$	$c^\dagger_{1,j+r}c_{2,j+r}c_{1,j+r+1}(\mathbb{1} - n_{2,j+r+1})$
	$(\mathbb{1} - n_{1,j})(\mathbb{1} - n_{2,j})(\mathbb{1} - n_{1,j+1})c^\dagger_{2,j+1})$	$c_{1,j+r}c^\dagger_{2,j+r}(\mathbb{1} - n_{1,j+r+1})c_{2,j+r+1}$
	$(\mathbb{1} - n_{1,j})(\mathbb{1} - n_{2,j})c_{1,j+1}(\mathbb{1} - n_{2,j+1})$	$n_{1,j+r}(\mathbb{1} - n_{2,j+r})(\mathbb{1} - n_{1,j+r+1})c_{2,j+r+1}$
	$(\mathbb{1} - n_{1,j})(\mathbb{1} - n_{2,j})(\mathbb{1} - n_{1,j+1})c_{2,j+1}$	$(\mathbb{1} - n_{1,j+r})n_{2,j+r}c_{1,j+r+1}(\mathbb{1} - n_{2,j+r+1})$
		$c^\dagger_{1,j+r}c_{2,j+r}(\mathbb{1} - n_{1,j+r+1})c^\dagger_{2,j+r+1}$
		$c_{1,j+r}c^\dagger_{2,j+r}c^\dagger_{1,j+r+1}(\mathbb{1} - n_{2,j+r+1})$
		$n_{1,j+r}(\mathbb{1} - n_{2,j+r})(\mathbb{1} - n_{1,j+r+1})c^\dagger_{2,j+r+1}$
		$(\mathbb{1} - n_{1,j+r})n_{2,j+r}c^\dagger_{1,j+r+1}(\mathbb{1} - n_{2,j+r+1})$
3	$(\mathbb{1} - n_{1,j})(\mathbb{1} - n_{2,j})c^\dagger_{1,j+1}(\mathbb{1} - n_{2,j+1})$	$c_{1,j+r}(\mathbb{1} - n_{2,j+r})(\mathbb{1} - n_{1,j+r+1})(\mathbb{1} - n_{2,j+r+1})$
	$(\mathbb{1} - n_{1,j})(\mathbb{1} - n_{2,j})(\mathbb{1} - n_{1,j+1})c^\dagger_{2,j+1})$	$(\mathbb{1} - n_{1,j+r})c_{2,j+r}(\mathbb{1} - n_{1,j+r+1})(\mathbb{1} - n_{2,j+r+1})$
	$(\mathbb{1} - n_{1,j})(\mathbb{1} - n_{2,j})c_{1,j+1}(\mathbb{1} - n_{2,j+1})$	$c^\dagger_{1,j+r}(\mathbb{1} - n_{2,j+r})(\mathbb{1} - n_{1,j+r+1})(\mathbb{1} - n_{2,j+r+1})$
	$(\mathbb{1} - n_{1,j})(\mathbb{1} - n_{2,j})(\mathbb{1} - n_{1,j+1})c_{2,j+1}$	$(\mathbb{1} - n_{1,j+r})c^\dagger_{2,j+r}(\mathbb{1} - n_{1,j+r+1})(\mathbb{1} - n_{2,j+r+1})$

Table 8.10: (continued)

r	operator components of $X_{\mathrm{FL}-}$	operator components of $Y_{\mathrm{FL}-}$
4	$c^{\dagger}_{1,j}(\mathbb{1}-n_{2,j})(\mathbb{1}-n_{1,j+1})(\mathbb{1}-n_{2,j+1})$	$(\mathbb{1}-n_{1,j+r})(\mathbb{1}-n_{2,j+r})c_{1,j+r+1})(\mathbb{1}-n_{2,j+r+1})$
	$(\mathbb{1}-n_{1,j})c^{\dagger}_{2,j}(\mathbb{1}-n_{1,j+1})(\mathbb{1}-n_{2,j+1})$	$(\mathbb{1}-n_{1,j+r})(\mathbb{1}-n_{2,j+r})(\mathbb{1}-n_{1,j+r+1})c_{2,j+r+1})$
	$c^{\dagger}_{1,j}(\mathbb{1}-n_{2,j})c_{1,j+1}c^{\dagger}_{2,j+1}$	$c_{1,j+r}c_{2,j+r}c_{1,j+r+1}(\mathbb{1}-n_{2,j+r+1})$
	$(\mathbb{1}-n_{1,j})c^{\dagger}_{2,j}c^{\dagger}_{1,j+1}c_{2,j+1}$	$c_{1,j+r}c^{\dagger}_{2,j+r}(\mathbb{1}-n_{1,j+r+1})c_{2,j+r+1}$
	$c^{\dagger}_{1,j}(\mathbb{1}-n_{2,j})(\mathbb{1}-n_{1,j+1})n_{2,j+1}$	$n_{1,j+r}(\mathbb{1}-n_{2,j+r})(\mathbb{1}-n_{1,j+r+1})c_{2,j+r+1}$
	$(\mathbb{1}-n_{1,j})c^{\dagger}_{2,j}n_{1,j+1}(\mathbb{1}-n_{2,j+1})$	$(\mathbb{1}-n_{1,j+r})n_{2,j+r}c_{1,j+r+1}(\mathbb{1}-n_{2,j+r+1})$
	$c_{1,j}(\mathbb{1}-n_{2,j})(\mathbb{1}-n_{1,j+1})(\mathbb{1}-n_{2,j+1})$	$(\mathbb{1}-n_{1,j+r})(\mathbb{1}-n_{2,j+r})c^{\dagger}_{1,j+r+1}(\mathbb{1}-n_{2,j+r+1})$
	$c_{1,j}(\mathbb{1}-n_{2,j})c^{\dagger}_{1,j+1}c_{2,j+1}$	$c^{\dagger}_{1,j+r}c_{2,j+r}(\mathbb{1}-n_{1,j+r+1})c^{\dagger}_{2,j+r+1}$
	$(\mathbb{1}-n_{1,j})c_{2,j}c_{1,j+1}c^{\dagger}_{2,j+1}$	$c_{1,j+r}c^{\dagger}_{2,j+r}c^{\dagger}_{1,j+r+1}(\mathbb{1}-n_{2,j+r+1})$
	$(\mathbb{1}-n_{1,j})c_{2,j}n_{1,j+1}(\mathbb{1}-n_{2,j+1})$	$n_{1,j+r}(\mathbb{1}-n_{2,j+r})(\mathbb{1}-n_{1,j+r})c^{\dagger}_{2,j+r+1}$
	$c_{1,j}(\mathbb{1}-n_{2,j})(\mathbb{1}-n_{1,j+1})n_{2,j+1}$	$(\mathbb{1}-n_{1,j+r})n_{2,j+r}c^{\dagger}_{1,j+r+1}(\mathbb{1}-n_{2,j+r+1})$

8.4.2.3 Strong Correlated Hopping

For $P = 4$ particles on a ladder of length $L = 8$ subject to twist boundary conditions averaging over 41 twist angles restricted to the First Brillouin Zone $-\frac{\pi}{8} \leq \phi_x \leq +\frac{\pi}{8}$, we show in Figure 8.78 the absolute singular values obtained from the operator singular value decomposition of the correlation density matrix at the parameter point $(t_\perp/t_\parallel = 0, t'/t_\parallel = 100)$. the maximum FL± correlations are degenerate. And the SC± correlations are very nearly degenerate.

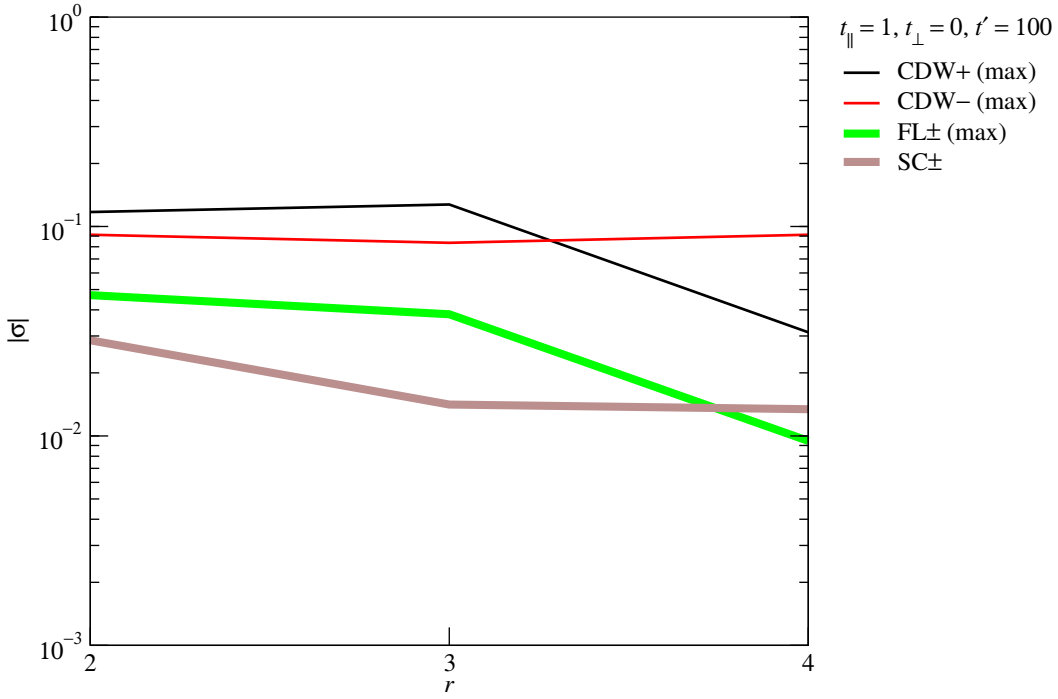

Figure 8.78: Correlation density-matrix absolute singular values $|\sigma|$ as functions of the separation r between two (2×2) clusters for $P = 4$ particles on a ladder of length $L = 8$ subject to twist boundary conditions averaging over 41 twist angles restricted to the First Brillouin Zone $-\frac{\pi}{8} \leq \phi_x \leq +\frac{\pi}{8}$, at the parameter point $(t_\perp/t_\parallel = 0, t'/t_\parallel = 100)$.

In Section 7.5.6, we found that the infinite-ladder symmetric and antisymmetric SC correlations are degenerate, and decays with separation as a power law with correlation

exponent $\beta = \frac{1}{2}$. In Section 7.5.7, we calculated the infinite-ladder subtracted CDW-π correlation, and found that it apparently decays as a power law with correlation exponent $0.6 < \alpha < 1.7$ that is filling fraction dependent. Using a restricted-probability argument, we showed also in Section 7.5.8 that the degenerate pair of two-point functions, which is the simplest FL correlations we can construct, decays exponentially with increasing separation. From Figure 8.78, we find indeed that the FL+ and FL− absolute singular values are very nearly-degenerate with each other, while the SC+ and SC− absolute singular values are very nearly-degenerate with each other. Because of the small separations we have access to numerically, we cannot know for sure that FL absolute singular values decay exponentially, or that the CDW absolute singular values decay as power laws. From Figure 8.78, we find that both CDW± absolute singular values start off with larger amplitudes than the SC± absolute singular values, which we know will dominate at large distances.

According to Matthias Troyer [381], numerical studies completed thus far have shown that the amplitudes of the SC correlations are small compared to those of CDW correlations, and the consensus amongst the computational many-body community is that in a hard-core boson system (which is effectively what we have in the strong correlated hopping limit) we would need to go to a system size that is beyond the capabilities of ED, QMC and DMRG to see SC correlations dominating CDW ones. Looking at Figures 7.40 and 7.47, we find the amplitude of the infinite-ladder SC correlations larger than that of the infinite-ladder subtracted CDW-π correlations. However, we had not calculated the infinite-ladder subtracted CDW-σ correlations in Section 7.5.5, so we have no analytical guide as to how large the amplitude of the infinite-ladder subtracted CDW-σ correlations would be relative to that of the infinite-ladder SC correlations. So one of the goals in this subsubsection would be obtained numerically from our operator

singular value decomposition of the correlation density matrix some sense of how large the amplitudes of the CDW-σ correlations would be compared to the amplitudes of the SC correlations.

Moving on to perform clustering analysis of the absolute amplitudes in the eigenvectors, we find the large-absolute-amplitude cluster of CDW operator components shown in Table 8.11, for the maximum-absolute-singular-value CDW+ eigenvectors. These have absolute amplitudes three or more orders of magnitude larger than the rest of the CDW operator components. For the ground state at this parameter point, there is practically no change in the characters of the large-absolute-amplitude CDW operator components as the separation is increased, apart from some CDW operator components dropping out of the large-absolute-amplitude cluster.

From Table 8.11, we see that at intercluster separations $r = 2$ and $r = 3$, both CDW-σ-type operator components,

$$\begin{aligned} &n_{1,j}(\mathbb{1} - n_{2,j})(\mathbb{1} - n_{1,j+1})(\mathbb{1} - n_{2,j+1}), \\ &(\mathbb{1} - n_{1,j})n_{2,j}(\mathbb{1} - n_{1,j+1})(\mathbb{1} - n_{2,j+1}), \\ &(\mathbb{1} - n_{1,j})(\mathbb{1} - n_{2,j})n_{1,j+1}(\mathbb{1} - n_{2,j+1}), \\ &(\mathbb{1} - n_{1,j})(\mathbb{1} - n_{2,j})(\mathbb{1} - n_{1,j+1})n_{2,j+1}, \end{aligned} \tag{8.4.19}$$

and CDW-π-type operator components,

$$n_{1,j}(\mathbb{1} - n_{2,j})(\mathbb{1} - n_{1,j+1}))n_{2,j+1}, \quad (\mathbb{1} - n_{1,j})n_{2,j}n_{1,j+1}(\mathbb{1} - n_{2,j+1}), \tag{8.4.20}$$

have large absolute amplitudes in the maximum-absolute-singular-value CDW+ eigenvectors $X_{\text{CDW+}}$ and $Y_{\text{CDW+}}$. At the intercluster separation $r = 4$, we find that only the CDW-σ-type operator components have large absolute amplitudes in $X_{\text{CDW+}}$ and $Y_{\text{CDW+}}$.

One plausible explanation for this observation would be that CDW-π-type operator components drop out of $X_{\text{CDW+}}$ and $Y_{\text{CDW+}}$, as r becomes large, so that as $r \to \infty$,

$X_{\mathrm{CDW}+}$ and $Y_{\mathrm{CDW}+}$ become essentially the dominant CDW-σ+ order parameters. Another plausible explanation for this observation is that the CDW-σ-type and CDW-π-type operator components have absolute amplitudes that oscillate with different wave vectors, so that for some separations $r \geq 4$, the CDW-π-type operator components will have small absolute amplitudes, and *then*, for another range of separations $r > 4$, the absolute amplitudes of the CDW-σ-type operator components will become small, and the absolute amplitudes of the CDW-π-type operator components become large. Both hypotheses will, unfortunately, require us to check numerically the maximum-absolute-singular-value CDW+ eigenvectors for longer ladders. In particular, to rule out the second hypothesis in favor of the first, we would need a minimum ladder length of $L \approx 16$, which is close the upper limit of system size that we can work with using the present computing resources (2.0-GHz processors and 1 GB of RAM).

Examining the structure of the maximum-absolute-singular-value CDW− eigenvectors, we find the large-absolute-amplitude cluster of CDW operator components shown in Table 8.12. These have absolute amplitudes one or more orders of magnitude larger than the rest of the CDW operator components. In contrast to the maximum-absolute-singular-value CDW+ eigenvectors, here we find only the CDW-σ-type operator components having large absolute amplitudes in $X_{\mathrm{CDW}-}$ and $Y_{\mathrm{CDW}-}$ at an intercluster separation of $r = 2$. The absolute amplitudes of the CDW-π-type operator components only became comparable to those of the CDW-σ-type operator components for $r \geq 3$. Again, with only numerical results from a short ladder of length $L = 8$, we are left to ponder whether the CDW-σ-type operator components would drop out of $X_{\mathrm{CDW}-}$ and $Y_{\mathrm{CDW}-}$ as $r \to \infty$, so that $X_{\mathrm{CDW}-}$ and $Y_{\mathrm{CDW}-}$ become essentially the dominant CDW-$\pi-$ order parameters in this asymptotic limit (agreeing with our conclusion in Section 7.5.7 that the antisymmetric CDW-π correlation decays with a slower power law than

Table 8.11: Large-absolute-amplitude cluster of CDW-type operator components in the maximum-absolute-singular-value CDW+ left eigenvector $X_{\mathrm{CDW+}}$ for intercluster separations $r = 2, 3, 4$, at the parameter point $(t_\perp/t_\parallel = 0, t'/t_\parallel = 100)$. The large-absolute-amplitude cluster of CDW operator components in the right eigenvector $Y_{\mathrm{CDW+}}$ are analogs of those in the left eigenvector $X_{\mathrm{CDW+}}$ for the respective separations.

r	operator components of $X_{\mathrm{CDW+}}$
2	$(\mathbb{1} - n_{1,j})(\mathbb{1} - n_{2,j})(\mathbb{1} - n_{1,j+1})(\mathbb{1} - n_{2,j+1})$
	$n_{1,j}(\mathbb{1} - n_{2,j})(\mathbb{1} - n_{1,j+1})(\mathbb{1} - n_{2,j+1})$
	$(\mathbb{1} - n_{1,j})n_{2,j}(\mathbb{1} - n_{1,j+1})(\mathbb{1} - n_{2,j+1})$
	$(\mathbb{1} - n_{1,j})(\mathbb{1} - n_{2,j})n_{1,j+1}(\mathbb{1} - n_{2,j+1})$
	$(\mathbb{1} - n_{1,j})(\mathbb{1} - n_{2,j})(\mathbb{1} - n_{1,j+1})n_{2,j+1}$
	$n_{1,j}(\mathbb{1} - n_{2,j})(\mathbb{1} - n_{1,j+1})n_{2,j+1}$
	$(\mathbb{1} - n_{1,j})n_{2,j}n_{1,j+1}(\mathbb{1} - n_{2,j+1})$
3	$(\mathbb{1} - n_{1,j})(\mathbb{1} - n_{2,j})(\mathbb{1} - n_{1,j+1})(\mathbb{1} - n_{2,j+1})$
	$n_{1,j}(\mathbb{1} - n_{2,j})(\mathbb{1} - n_{1,j+1})(\mathbb{1} - n_{2,j+1})$
	$(\mathbb{1} - n_{1,j})n_{2,j}(\mathbb{1} - n_{1,j+1})(\mathbb{1} - n_{2,j+1})$
	$(\mathbb{1} - n_{1,j})(\mathbb{1} - n_{2,j})n_{1,j+1}(\mathbb{1} - n_{2,j+1})$
	$(\mathbb{1} - n_{1,j})(\mathbb{1} - n_{2,j})(\mathbb{1} - n_{1,j+1})n_{2,j+1}$
	$n_{1,j}(\mathbb{1} - n_{2,j})(\mathbb{1} - n_{1,j+1})n_{2,j+1}$
	$(\mathbb{1} - n_{1,j})n_{2,j}n_{1,j+1}(\mathbb{1} - n_{2,j+1})$
4	$n_{1,j}(\mathbb{1} - n_{2,j})(\mathbb{1} - n_{1,j+1})(\mathbb{1} - n_{2,j+1})$
	$(\mathbb{1} - n_{1,j})n_{2,j}(\mathbb{1} - n_{1,j+1})(\mathbb{1} - n_{2,j+1})$
	$(\mathbb{1} - n_{1,j})(\mathbb{1} - n_{2,j})n_{1,j+1}(\mathbb{1} - n_{2,j+1})$
	$(\mathbb{1} - n_{1,j})(\mathbb{1} - n_{2,j})(\mathbb{1} - n_{1,j+1})n_{2,j+1}$

the symmetric CDW-π correlation), or that the absolute amplitudes of the CDW-σ-type and CDW-π-type operator components in $X_{\mathrm{CDW}-}$ and $Y_{\mathrm{CDW}-}$ are oscillatory functions of the intercluster separation r.

Moving on to the maximum-absolute-singular-value FL± eigenvectors, we find that because the maximum FL± absolute singular values are degenerate, symmetric and antisymmetric eigenvectors are mixed, and it makes no sense to perform clustering analysis of absolute amplitudes in the FL eigenvectors coming out from the operator singular value decomposition of the correlation density matrix. We can, of course, construct linear combinations of these maximum-absolute-singular-value FL eigenvectors with indefinite ladder reflection symmetry to obtain a set of maximum-absolute-singular-value FL eigenvectors with definite ladder reflection symmetry. However, we reckoned that this is too much work in exchange for the tiny amount of extra insight we expect to get, so this is not done. In fact, even the work we put in to analyze the absolute-amplitude clustering structure of the eigenvectors in general gets us very little extra insight in return. Therefore, for the rest of this section, we expend only the little work analyzing the absolute singular values, which suffices for us to paint a rough picture of the dominant phase at short separations.

8.4.3 'Phase Boundaries'

In this subsection we investigate the relative ordering of the absolute singular values obtained from the operator singular value decomposition of the correlation density matrix at three parameter points, $(t_\perp/t_\parallel = 0, t'/t_\parallel = 2)$ (Section 8.4.3.1), which lies on zeroth-order 'crossover' between the PL-CDW and SC regions of the ground-state phase diagram, $(t_\perp/t_\parallel = 2, t'/t_\parallel = 0)$ (Section 8.4.3.2), which lies on the zeroth-order 'phase boundary' between the LR-CDW and PL-CDW regions of the ground-state phase dia-

Table 8.12: Large-absolute-amplitude cluster of CDW-type operator components in the maximum-absolute-singular-value CDW− left and right eigenvectors, $X_{\mathrm{CDW}-}$ and $Y_{\mathrm{CDW}-}$, for intercluster separations $r = 2, 3, 4$, obtained from the operator singular value decomposition of the correlation density matrix at the parameter point $(t_\perp/t_\parallel = 0, t'/t_\parallel = 100)$.

r	operator components of $X_{\mathrm{CDW}-}$	operator components of $Y_{\mathrm{CDW}-}$
2	$(\mathbb{1}-n_{1,j})(\mathbb{1}-n_{2,j})n_{1,j+1}(\mathbb{1}-n_{2,j+1})$	$n_{1,j+r}(\mathbb{1}-n_{2,j+r})(\mathbb{1}-n_{1,j+r+1})(\mathbb{1}-n_{2,j+r+1})$
	$(\mathbb{1}-n_{1,j})(\mathbb{1}-n_{2,j})(\mathbb{1}-n_{1,j+1})n_{2,j+1}$	$(\mathbb{1}-n_{1,j+r})n_{2,j+r}(\mathbb{1}-n_{1,j+r+1})(\mathbb{1}-n_{2,j+r+1})$
3	$n_{1,j}(\mathbb{1}-n_{2,j})(\mathbb{1}-n_{1,j+1})(\mathbb{1}-n_{2,j+1})$	$n_{1,j+r}(\mathbb{1}-n_{2,j+r})(\mathbb{1}-n_{1,j+r+1})(\mathbb{1}-n_{2,j+r+1})$
	$(\mathbb{1}-n_{1,j})n_{2,j}(\mathbb{1}-n_{1,j+1})(\mathbb{1}-n_{2,j+1})$	$(\mathbb{1}-n_{1,j+r})n_{2,j+r}(\mathbb{1}-n_{1,j+r+1})(\mathbb{1}-n_{2,j+r+1})$
	$(\mathbb{1}-n_{1,j})(\mathbb{1}-n_{2,j})n_{1,j+1}(\mathbb{1}-n_{2,j+1})$	$(\mathbb{1}-n_{1,j+r})(\mathbb{1}-n_{2,j+r})n_{1,j+r+1}(\mathbb{1}-n_{2,j+r+1})$
	$(\mathbb{1}-n_{1,j})(\mathbb{1}-n_{2,j})(\mathbb{1}-n_{1,j+1})n_{2,j+1}$	$(\mathbb{1}-n_{1,j+r})(\mathbb{1}-n_{2,j+r})(\mathbb{1}-n_{1,j+r+1})n_{2,j+r+1}$
	$n_{1,j}(\mathbb{1}-n_{2,j})(\mathbb{1}-n_{1,j+1})n_{2,j+1}$	$n_{1,j+r}(\mathbb{1}-n_{2,j+r})(\mathbb{1}-n_{1,j+r+1})n_{2,j+r+1}$
	$(\mathbb{1}-n_{1,j})n_{2,j}n_{1,j+1}(\mathbb{1}-n_{2,j+1})$	$(\mathbb{1}-n_{1,j+r})n_{2,j+r}n_{1,j+r+1}(\mathbb{1}-n_{2,j+r+1})$
4	$n_{1,j}(\mathbb{1}-n_{2,j})(\mathbb{1}-n_{1,j+1})(\mathbb{1}-n_{2,j+1})$	$n_{1,j+r}(\mathbb{1}-n_{2,j+r})(\mathbb{1}-n_{1,j+r+1})(\mathbb{1}-n_{2,j+r+1})$
	$(\mathbb{1}-n_{1,j})n_{2,j}(\mathbb{1}-n_{1,j+1})(\mathbb{1}-n_{2,j+1})$	$(\mathbb{1}-n_{1,j+r})n_{2,j+r}(\mathbb{1}-n_{1,j+r+1})(\mathbb{1}-n_{2,j+r+1})$
	$(\mathbb{1}-n_{1,j})(\mathbb{1}-n_{2,j})n_{1,j+1}(\mathbb{1}-n_{2,j+1})$	$(\mathbb{1}-n_{1,j+r})(\mathbb{1}-n_{2,j+r})n_{1,j+r+1}(\mathbb{1}-n_{2,j+r+1})$
	$(\mathbb{1}-n_{1,j})(\mathbb{1}-n_{2,j})(\mathbb{1}-n_{1,j+1})n_{2,j+1}$	$(\mathbb{1}-n_{1,j+r})(\mathbb{1}-n_{2,j+r})(\mathbb{1}-n_{1,j+r+1})n_{2,j+r+1}$
	$n_{1,j}(\mathbb{1}-n_{2,j})(\mathbb{1}-n_{1,j+1})n_{2,j+1}$	$n_{1,j+r}(\mathbb{1}-n_{2,j+r})(\mathbb{1}-n_{1,j+r+1})n_{2,j+r+1}$
	$(\mathbb{1}-n_{1,j})n_{2,j}n_{1,j+1}(\mathbb{1}-n_{2,j+1})$	$(\mathbb{1}-n_{1,j+r})n_{2,j+r}n_{1,j+r+1}(\mathbb{1}-n_{2,j+r+1})$

gram, and ($t_\perp/t_\parallel = 100, t'/t_\parallel = 100$) (Section 8.4.3.3), which lies on the zeroth-order 'phase boundary' between the LR-CDW and SC regions of the ground-state phase diagram.

Just as in Section 8.3.2, our goal here is not to refine the zeroth-order lines of 'phase transitions' or 'crossovers', but rather, to get a sense of what signatures in the spectrum of correlation density-matrix singular values to look out for, when the parameter point we are working at is close to a line of quantum phase transition or crossover. Having abandoned the clustering analysis of the absolute amplitude of component operators in the various maximum-absolute-singular-value eigenvectors, we perform qualitative comparisons of the spectra of maximum absolute singular values instead. In particular, we look out for changes in the relative ordering between different maximum absolute singular values, and also degeneracy (or near-degeneracy) of pairs of maximum absolute singular values. This is similar in spirit to our qualitative comparisons of the twisted minimum-energy bands in Section 8.3, but in our qualitative comparisons of the spectra of maximum absolute singular values, we also know what correlations are dominant over the range of intercluster separations accessible numerically.

8.4.3.1 PL-CDW and SC 'Crossover'

For $P = 4$ particles on a ladder of length $L = 8$ subject to twist boundary conditions averaging over 41 twist angles restricted to the First Brillouin Zone $-\frac{\pi}{8} \leq \phi_x \leq +\frac{\pi}{8}$, at the parameter point ($t_\perp/t_\parallel = 0, t'/t_\parallel = 2$), the absolute singular values obtained from the operator singular value decomposition of the correlation density matrix is shown in Figure 8.79.

At this zeroth-order cross over between the SC and PL-CDW phases, we expect features exhibited by the absolute singular values as functions of the intercluster separation

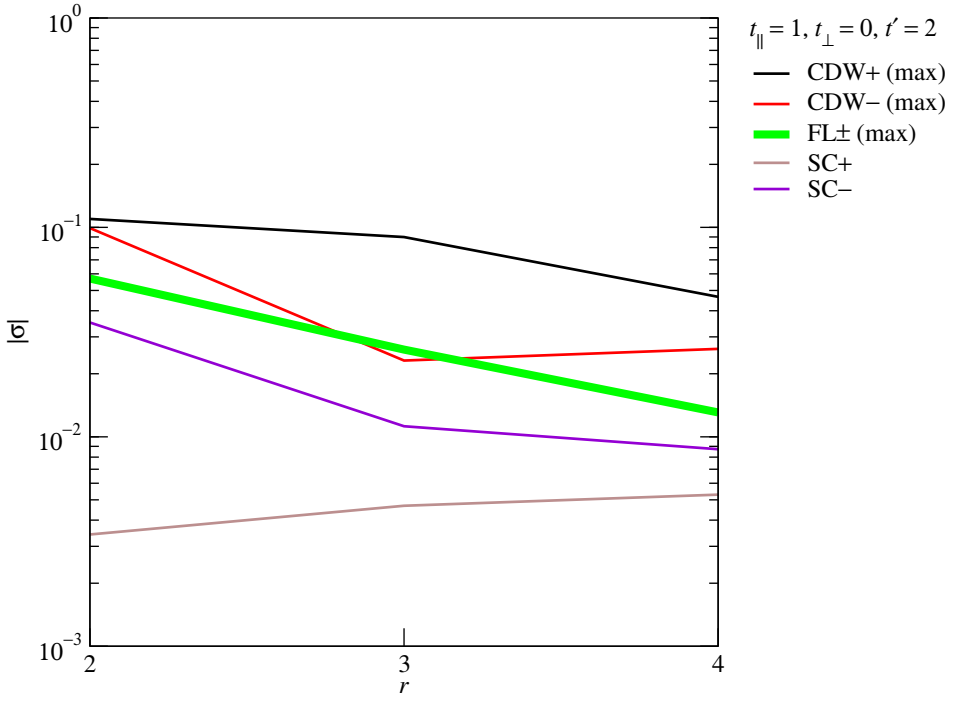

Figure 8.79: Correlation density-matrix absolute singular values $|\sigma|$ as functions of the separation r between two (2×2) clusters for $P = 4$ particles on a ladder of length $L = 8$ subject to twist boundary conditions averaging over 41 twist angles restricted to the First Brillouin Zone $-\frac{\pi}{8} \leq \phi_x \leq +\frac{\pi}{8}$, at the parameter point $(t_\perp/t_\parallel = 0, t'/t_\parallel = 2)$.

r to be intermediate between those at the strong correlated hopping and weak inter-leg hopping limits. Indeed, comparing Figure 8.79 with Figures 8.75 and 8.78, we find the SC− absolute singular value lying close to the maximum FL± absolute singular values, which is a feature we observe in the strong correlated hopping limit. We also find the maximum CDW+ absolute singular value larger than the maximum CDW− absolute singular value, which is the case for the strong correlated hopping limit, but in contrast to the weak inter-leg hopping limit, where we find the maximum CDW− absolute singular value larger than the maximum CDW+ absolute singular value instead. Therefore, by comparing the behaviour of the absolute singular values, we find the ground-state correlations at the parameter point $(t_\perp/t_\parallel = 0, t'/t_\parallel = 2)$ to be closer in nature to those in the strong correlated hopping limit. This same conclusion was reached in Section 8.3.2.1, through the analysis of the ground-state structure.

The most important qualitative difference between the absolute singular values at this parameter point $(t_\perp/t_\parallel = 0, t'/t_\parallel = 2)$ and at the strong correlated hopping limit, is the SC+ absolute singular value. From Figure 8.75, we find that in the weak inter-leg hopping limit, the nondegenerate SC+ and SC− absolute singular values are one or more orders of magnitude smaller than the FL absolute singular values. As we increase $t'/t_\parallel$ from $t'/t_\parallel = 0$ to $t'/t_\parallel \to \infty$, both SC+ and SC− absolute singular values must increase by roughly one order of magnitude, and also become degenerate in the strong correlated hopping limit shown in Figure 8.78. From Figure 8.79, we see that the SC− absolute singular values have more or less reached the strong correlated limit magnitudes, while the SC+ absolute singular value has not changed very much from its weak inter-leg hopping limit magnitudes. It would be interesting to check whether the SC± absolute singular values do increase at different rates as $t'/t_\parallel$ is increased for an infinite ladder, but along the line $t_\perp/t_\parallel$ in the ground-state phase diagram, we can neither calculate these

correlations analytically, nor compute them numerically on very long ladders.

8.4.3.2 LR-CDW and PL-CDW 'Phase Boundary'

For $P = 4$ particles on a ladder of length $L = 8$ subject to twist boundary conditions averaging over 41 twist angles restricted to the First Brillouin Zone $-\frac{\pi}{8} \leq \phi_x \leq +\frac{\pi}{8}$, at the parameter point $(t_\perp/t_\parallel = 2, t'/t_\parallel = 0)$, the absolute singular values obtained from the operator singular value decomposition of the correlation density matrix is shown in Figure 8.80.

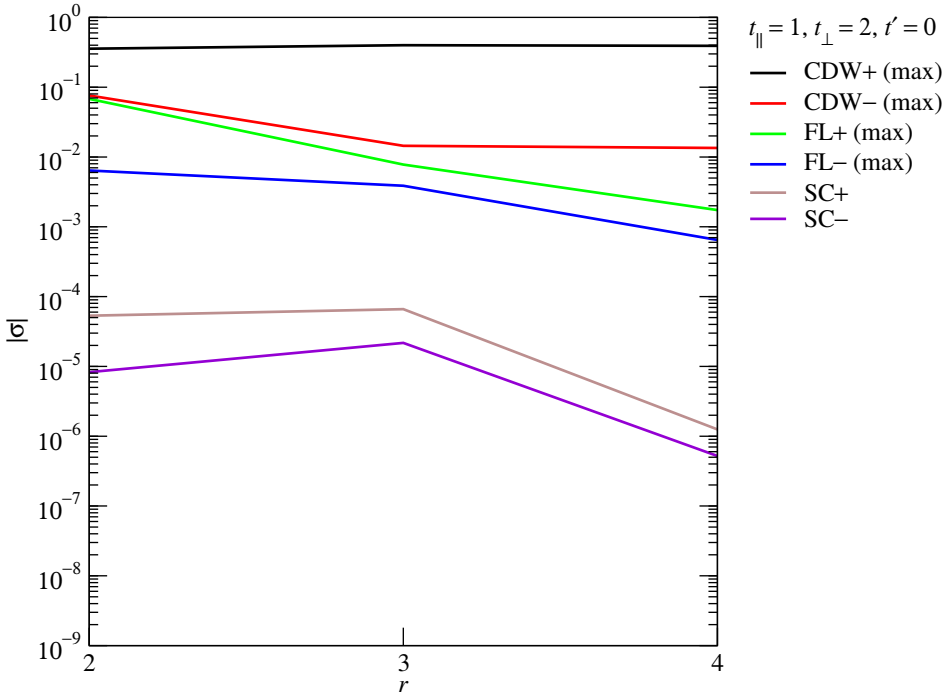

Figure 8.80: Correlation density-matrix absolute singular values $|\sigma|$ as functions of the separation r between two (2×2) clusters for $P = 4$ particles on a ladder of length $L = 8$ subject to twist boundary conditions averaging over 41 twist angles restricted to the First Brillouin Zone $-\frac{\pi}{8} \leq \phi_x \leq +\frac{\pi}{8}$, at the parameter point $(t_\perp/t_\parallel = 2, t'/t_\parallel = 0)$.

At this zeroth-order 'phase boundary' between the LR-CDW and PL-CDW phases, we expect features exhibited by the absolute singular values as functions of the inter-

cluster separation r to be intermediate between those at the weak inter-leg hopping and strong inter-leg hopping limits. Comparing the spectrum of maximum absolute singular values at this parameter point with those at the weak inter-leg hopping and strong inter-leg hopping limits, we find that Figure 8.80 appears to resemble Figure 8.77, but not Figure 8.74, in that the maximum CDW+ absolute singular value appears not to decay with increasing separation, and that the maximum FL+ and FL− absolute singular values appear to be nondegenerate. We also find the SC+ and SC− absolute singular values to have amplitudes four to five orders of magnitude below that of the maximum CDW+ absolute singular value. These are all features seen in the absolute singular values of the strong inter-leg hopping limit. Therefore, by comparing the behaviour of the absolute singular values, we find the ground-state correlations at the parameter point $(t_\perp/t_\parallel = 2, t'/t_\parallel = 0)$ to be closer in nature to those in the strong inter-leg hopping limit, the only qualitative differences being the larger amplitudes of the SC± absolute singular values, and the slower rate of decay with separation r of the FL± absolute singular values. This same conclusion was reached in Section 8.3.2.2, through the analysis of the ground-state structure.

8.4.3.3 LR-CDW and SC 'Phase Boundary'

For $P = 4$ particles on a ladder of length $L = 8$ subject to twist boundary conditions averaging over 41 twist angles restricted to the First Brillouin Zone $-\frac{\pi}{8} \leq \phi_x \leq +\frac{\pi}{8}$, at the parameter point $(t_\perp/t_\parallel = 100, t'/t_\parallel = 100)$, the absolute singular values obtained from the operator singular value decomposition of the correlation density matrix are shown in Figure 8.81.

At this zeroth-order 'phase boundary' between the LR-CDW and SC phases, we expect features exhibited by the absolute singular values as functions of the intercluster

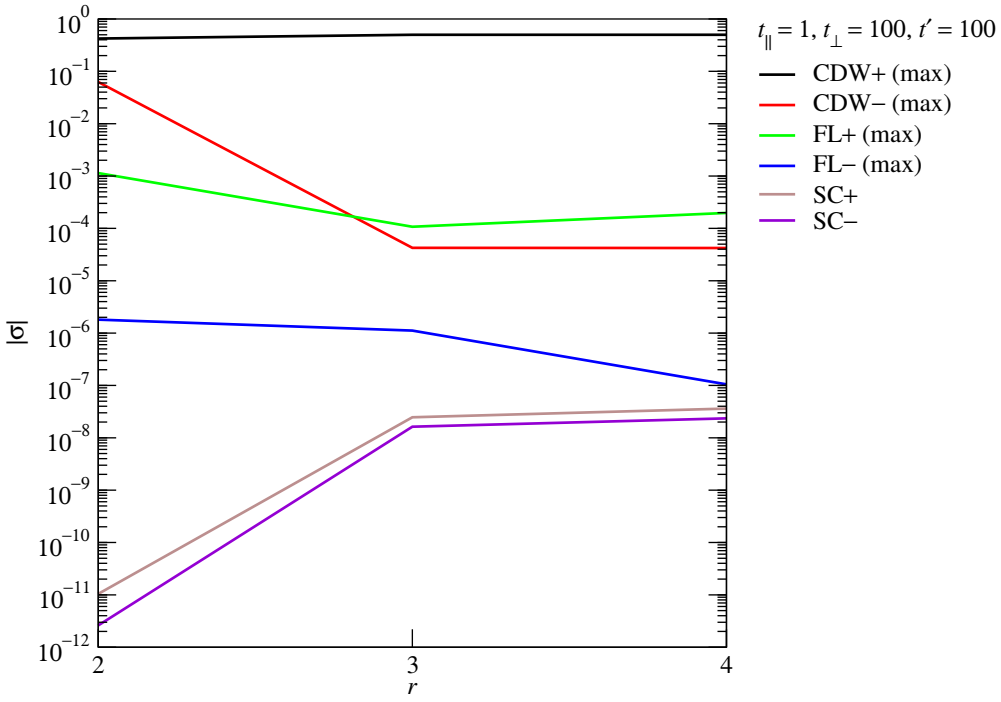

Figure 8.81: Correlation density-matrix absolute singular values $|\sigma|$ as functions of the separation r between two (2×2) clusters for $P = 4$ particles on a ladder of length $L = 8$ subject to twist boundary conditions averaging over 41 twist angles restricted to the First Brillouin Zone $-\frac{\pi}{8} \leq \phi_x \leq +\frac{\pi}{8}$, at the parameter point $(t_\perp/t_\parallel = 100, t'/t_\parallel = 100)$.

separation r to be intermediate between those at the strong inter-leg hopping and strong correlated hopping limits. Comparing Figure 8.81 with Figures 8.77 and 8.78, we find that the maximum CDW+ absolute singular value does not appear to decay with increasing separation, and neither the maximum FL± and SC± absolute singular values form degenerate pairs. More importantly, the SC+ and SC− absolute singular values have amplitudes eight or more orders of magnitude below that of the maximum CDW+ absolute singular value. These suggest that the ground-state correlations at the parameter point $(t_\perp/t_\parallel = 100, t'/t_\parallel = 100)$ are closer in nature to those in the strong inter-leg hopping limit than the strong correlated hopping limit. This agrees partially with the comparison made in Section 8.3.2.2, through the analysis of the ground-state structure.

8.4.4 'Tricritical Point'

For $P = 4$ particles on a ladder of length $L = 8$ subject to twist boundary conditions averaging over 41 twist angles restricted to the First Brillouin Zone $-\frac{\pi}{8} \leq \phi_x \leq +\frac{\pi}{8}$, at the parameter point $(t_\perp/t_\parallel = 2, t'/t_\parallel = 2)$, the absolute singular values obtained from the operator singular value decomposition of the correlation density matrix is shown in Figure 8.82.

Since this parameter point is supposedly the 'quantum 'tricritical point", we expect the absolute singular values to exhibit features from all three analytical limits. Comparing Figure 8.82 with Figures 8.74, 8.75, 8.77, and 8.78, we find that the maximum CDW+ absolute singular value is always larger than the maximum CDW− absolute singular value, which is the case in the strong inter-leg hopping limit, but appears to be decaying with separation, wherein the strong inter-leg hopping limit, it would be separation-independent. Just as in the strong inter-leg hopping limit, the maximum FL± and SC± absolute singular values do not form degenerate pairs, wherein the strong cor-

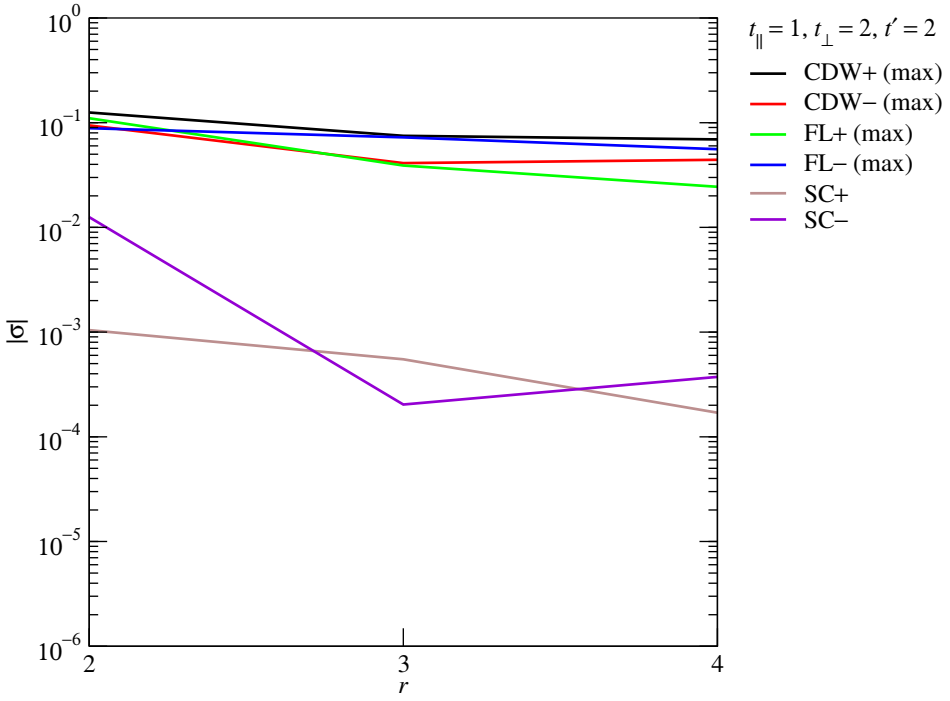

Figure 8.82: Correlation density-matrix absolute singular values $|\sigma|$ as functions of the separation r between two (2×2) clusters for $P = 4$ particles on a ladder of length $L = 8$ subject to twist boundary conditions averaging over 41 twist angles restricted to the First Brillouin Zone $-\frac{\pi}{8} \leq \phi_x \leq +\frac{\pi}{8}$, at the parameter point $(t_{\perp}/t_{\|} = 2, t'/t_{\|} = 2)$.

related hopping limit, these absolute singular values would form degenerate pairs, and wherein the weak inter-leg hopping limit, the maximum FL± absolute singular values would be degenerate, while the SC± absolute singular values would be nondegenerate. The SC± absolute singular values at this 'quantum tricritical point' are suppressed relative to the strong correlated hopping limit, but are enhanced relative to the strong inter-leg hopping limit. All things considered, we find that the ground-state correlations at this parameter point ($t_\perp/t_\parallel = 2, t'/t_\parallel = 2$) to be closest in nature to those in the strong inter-leg hopping limit. This same conclusion was reached in Section 8.3.3, through the analysis of the ground-state structure.

MANY-BODY FERMION DENSITY MATRICES

VOLUME III

A Dissertation

Presented to the Faculty of the Graduate School

of Cornell University

in Partial Fulfillment of the Requirements for the Degree of

Doctor of Philosophy

by

Siew-Ann Cheong

May 2006

CHAPTER 9

CONCLUSIONS

9.1 Overview

As we have described in Chapter 1, the work reported in this thesis consists of three main thrusts:

1. to understand the analytical and numerical structure of reduced density matrices of systems of noninteracting spinless fermions (Chapters 2, 3 and 4);

2. to understand the numerical structure of reduced density matrices of systems of interacting spinless fermions (Chapter 4); and

3. to develop a machinery, based on the correlation density matrix, to systematically extract various correlations from a numerical ground state (Chapters 5, 6 and 8).

Two major supporting calculations are also reported in this thesis:

1. a critical study of the method of twist boundary conditions averaging (Appendix D); and

2. analytical calculations of various correlation functions, for interacting spinless fermions on a two-legged ladder, in three limiting cases (Chapter 7).

In this conclusions chapter, we will summarize our main results on the reduced density matrices of noninteracting and interacting spinless fermions in Sections 9.2 and 9.3 respectively. In Section 9.4, we will summarize the chief insights we have gained developing the operator singular value decomposition of the correlation density matrix as a systematic means to extract ground-state correlations. Finally, we summarize our findings on the capabilities and limitations of the method of twist boundary conditions

averaging in Section 9.5, before moving on in Section 9.6 to describe our principal analytical results calculating the ground state wave function and various ground-state correlations of a ladder of interacting spinless fermions in three limiting cases.

Unlike in Chapter 1, the organization of this chapter will not be tied in rigidly with the organization of the chapters. Instead, we will provide a summary of the results in line with the logical units outlined above. Proper referencing to the specific chapters and sections will be provided.

9.2 Reduced Density Matrices of Noninteracting Spinless Fermions

In this part of the thesis work, we studied a system of noninteracting spinless fermions in d dimensions described by the Hamiltonian

$$H_t = -t \sum_{\langle \mathbf{r},\mathbf{r}' \rangle} \left[c^\dagger_{\mathbf{r}} c_{\mathbf{r}'} + c^\dagger_{\mathbf{r}'} c_{\mathbf{r}} \right], \tag{2.1.1}$$

where $c_{\mathbf{r}}$ and $c^\dagger_{\mathbf{r}'}$ are spinless fermion annihilation and creation operators at sites $\mathbf{r}$ and $\mathbf{r}'$ respectively, and the notation $\langle \mathbf{r}, \mathbf{r}' \rangle$ indicates that the sum is restricted to only those pairs of sites $\mathbf{r}$ and $\mathbf{r}'$ which are nearest neighbors of each other.

Reiterating what is said in Chapter 1, we choose a trivial model as our starting point for two reasons. Firstly, we have the benefit of being guided at every step of our way, knowing what the exact ground state, the Fermi sea $|\Psi_F\rangle$, of noninteracting spinless fermions looks like. Secondly, we hope to eventually develop a renormalization-group method capable of discovering that a strongly-interacting system is ultimately a Fermi liquid. Such a renormalization-group method must first pass the test on a noninteracting Fermi liquid. These two reasons motivate our investigations into the analytical and numerical structure of the density matrix of a finite cluster of sites cut out from a large, possibly infinite, system of noninteracting spinless fermions.

9.2.1 Method of Referencing Operators

In the literature, the standard way to calculate the reduced density matrix of a small subsystem within a larger system is to take the ground-state wave function, and trace out degrees of freedom outside of the small subsystem. For a finite cluster of N_C sites in an infinite system, the environment of the cluster is also infinite, and thus contains an infinite number of degrees of freedom. In Section 2.3, we show, by writing the cluster density-matrix element

$$\langle \mathbf{l}'|\rho_C|\mathbf{l}\rangle = \langle e_{\mathbf{l}}|e_{\mathbf{l}'}\rangle \tag{2.3.3}$$

between occupation number basis states $|\mathbf{l}\rangle$ and $|\mathbf{l}'\rangle$ of the cluster as the overlap between their associated environmental states, that it is also possible to write the cluster density-matrix element $\langle \mathbf{l}'|\rho_C|\mathbf{l}\rangle$ as the ground-state expectation of the product of two projection-operator-like operators. We call these projection-operator-like operators referencing operators.

For every cluster occupation number basis state

$$|\mathbf{l}\rangle = |n_1^{\mathbf{l}} n_2^{\mathbf{l}} \cdots n_{N_C}^{\mathbf{l}}\rangle\,, \tag{2.3.4}$$

the corresponding referencing operator is

$$K_{\mathbf{l}} = \prod_{j=1}^{N_C} \left[n_j^{\mathbf{l}} c_j + (1 - n_j^{\mathbf{l}}) c_j c_j^\dagger \right], \tag{2.3.5}$$

where c_j and $c_j^\dagger$ are spinless fermion operators local to the cluster. In terms of the operators $K_{\mathbf{l}}$ and their conjugates $K_{\mathbf{l}}^\dagger$, the cluster density-matrix elements can then be written as

$$\langle \mathbf{l}'|\rho_C|\mathbf{l}\rangle = \langle e_{\mathbf{l}}|e_{\mathbf{l}'}\rangle = \left\langle \Psi_F \middle| K_{\mathbf{l}}^\dagger K_{\mathbf{l}'} \middle| \Psi_F \right\rangle = \langle K_{\mathbf{l}}^\dagger K_{\mathbf{l}'}\rangle. \tag{2.3.8}$$

When written in this manner, it becomes clear that the cluster density matrix is real and symmetric, and its nonzero elements occur in $(N_C + 1)$ diagonal blocks. We call the

P_C diagonal block matrix the P_C-particle sector ρ_{C,P_C} of the cluster density matrix, or simply the P_C-particle cluster density matrix.

In the $N_C \times N_C$ one-particle cluster density matrix, the matrix element $\langle \mathbf{l}'|\rho_C|\mathbf{l}\rangle$ are between cluster occupation number basis states $|\mathbf{l}\rangle$ and $|\mathbf{l}'\rangle$ with sites j and i occupied respectively. Therefore, such a matrix element can also be written as

$$\langle \mathbf{l}'|\rho_C|\mathbf{l}\rangle = (\rho_{C,1})_{ij}. \tag{9.2.1}$$

From (2.3.8) we see that these one-particle cluster density-matrix elements are all sums of $2n$-point functions $\langle c^\dagger_{i_1} \cdots c^\dagger_{i_n} c_{j_1} \cdots c_{j_n}\rangle$. Because $2n$-point functions Wick factorizes into products of two-point functions $G_{ij} = \langle c^\dagger_i c_j\rangle$ (which can be organized into a $N_C \times N_C$ cluster Green-function matrix G_C), we find the one-particle cluster density-matrix elements to be polynomial functions of the two-point functions. Inspecting the index structure of the two-point functions $G_{i'j'}$ appearing in the expression for $(\rho_{C,1})_{ij}$, for clusters of up to $N_C = 5$ sites, we are led to conjecture that the one-particle cluster density matrix $\rho_{C,1}$ is related to the cluster Green-function matrix G_C by the closed-form formula

$$\rho_{C,1} = G_C(\mathbb{1} - G_C)^{-1} \det(\mathbb{1} - G_C). \tag{2.3.77}$$

9.2.2 Exact Formula

In Section 2.4, we prove this conjecture by adapting the the technique used by Chung and Peschel to calculate the half-chain density matrix of a chain of spinless Bogoliubov fermions. Introducing an overcomplete basis of fermionic coherent states

$$|\boldsymbol{\xi}\rangle = |\xi_1 \xi_2 \cdots \xi_N\rangle = \exp\left(-\textstyle\sum_{i=1}^N \xi_i c^\dagger_i\right)|0\rangle\,, \tag{2.4.10}$$

and using the formula

$$\langle \boldsymbol{\xi}| \exp\left(\textstyle\sum_{i,j} \Gamma_{ij} c^\dagger_i c_j\right)|\boldsymbol{\xi}'\rangle = \exp\left[\textstyle\sum_{i,j} (e^\Gamma)_{ij} \xi^*_i \xi'_j\right] \tag{2.4.11}$$

giving the matrix elements of the exponentiated bilinear operator $\exp\left(\sum_{i,j}\Gamma_{ij}c_i^\dagger c_j\right)$ between fermionic coherent states $|\boldsymbol{\xi}\rangle$ and $|\boldsymbol{\xi}'\rangle$, where e^Γ is the exponential of the matrix Γ; the formula

$$\mathrm{Tr}(A) = \int \prod_i d\xi_i^*\, d\xi_i\, e^{-\sum_i \xi_i^* \xi_i}\, \langle -\boldsymbol{\xi}|A|\boldsymbol{\xi}\rangle \tag{2.4.12}$$

for the trace of an operator A as a Grassmann integral over its coherent state matrix elements; and the formula

$$\int \prod_i d\xi_i^*\, d\xi_i\, e^{\sum_{j,k}\xi_j^* A_{jk}\xi_k} = \det A \tag{2.4.13}$$

for a Gaussian integral over Grassmann variables, we derived a closed-form formula

$$\rho_C = \det(\mathbb{1} - G_C)\, \exp\left\{\sum_{ij}\left[\log G_C(\mathbb{1} - G_C)^{-1}\right]_{ij} c_i^\dagger c_j\right\} \tag{2.4.30}$$

relating the cluster density matrix ρ_C and the cluster Green-function matrix G_C. The relation (2.3.77) that we introduced in Section 2.3 is then a corollary of (2.4.30).

9.2.3 Structure, Properties and Statistical Mechanics Analogy

In Section 2.5 (and partially reviewed in Sections 3.3.1 and 3.3.2), we looked at the implications of (2.4.30) on the structure and properties of the cluster density matrix. First, we noted that, in a suitable basis $\{f_l^\dagger|0\rangle\}$ diagonalizing the cluster Green-function matrix, we can also write the cluster density matrix in the thermodynamic form

$$\rho_C = \det(\mathbb{1} - G_C)\exp\left[-\sum_l \varphi_l f_l^\dagger f_l\right] = \mathcal{Q}^{-1}\exp[-\tilde{H}], \tag{2.5.1}$$

where the pseudo-Hamiltonian

$$\tilde{H} = \sum_l \varphi_l f_l^\dagger f_l \tag{2.5.2}$$

has a spectrum generated by the independent pseudo-fermion operators $f_l^\dagger$ and $f_{l'}^\dagger$, satisfying the anticommutation relation $\{f_l^\dagger, f_{l'}\} = \delta_{ll'}\,\mathbb{1}$.

From (2.5.2) we see that pseudo-fermions appearing in the pseudo-Hamiltonian has a dispersion relation given by the single-particle pseudo-energies

$$\varphi_l = -(\log G_C(\mathbb{1} - G_C)^{-1})_{ll} = -\log \frac{\lambda_l}{1-\lambda_l}, \tag{2.5.3}$$

for $l = 1, \ldots, N_C$, where λ_l are the eigenvalues of the cluster Green-function matrix G_C. In terms of λ_l and φ_l, we found that the normalization constant $\mathscr{Q}^{-1}$, which plays the role of the reciprocal of the thermodynamic partition function, can be written as

$$\mathscr{Q}^{-1} = \det(\mathbb{1} - G_C) = \prod_l (1 - \lambda_l), \tag{2.5.4}$$

while the one-particle cluster density-matrix weights can be written as

$$w_l = \mathscr{Q}^{-1} \exp(-\varphi_l) \tag{2.5.5}$$

respectively.

In RG calculations, it is highly desirable to ensure that the truncation scheme preserves the symmetries of the target state. To understand how this can be done in general for interacting systems, we look at the specific example of particle-hole symmetry in a noninteracting system of spinless fermions. In Section 2.5.2 we derived conditions particle-hole symmetry imposes on the eigenvalues λ_l of G_C and the one-particle pseudo-energies φ_l. We find, however, that particle-hole symmetry is partly obscured in the one-particle density-matrix weights w_l, which are exponentials of φ_l. In fact, under charge conjugation, the half-filled ground state $|\Psi_F\rangle$ goes (up to a phase) back to itself. Within the cluster, this global symmetry transformation brings the mixed state of the cluster back to the same mixed state. This stringent condition imposed on the mixed state of the cluster means that particle-hole symmetry is not merely a relation between the P_C-particle cluster density matrix and the $(N_C - P_C)$-particle cluster density matrix. Instead, particle-hole symmetry imposes strict conditions on what eigenvalues can appear in the P'_C-particle cluster density matrix, if we know the eigenvalues that appear

in the P_C-particle cluster density matrix, for all P_C and P'_C. Therefore, it is dangerous to base symmetry-preserving truncation schemes on the cluster density matrix ρ_C and its eigenvalues alone, and is not a simple matter of ensuring that we keep a $(N_C - P_C)$-particle eigenstate if the P_C-particle eigenstate related to it by particle-hole symmetry is kept.

For the purpose of formulating truncation schemes, we also note that (2.5.1) implies that the cluster density-matrix spectrum is completely determined by the cluster Green-function matrix. We need therefore determine only the one-particle eigenvalues λ_l and φ_l, as well as the pseudo-fermion operators $f_l^\dagger$, and use them to systematically generate the P_C-particle cluster density-matrix eigenstates

$$|\chi_L\rangle = \prod_{p=1}^{P_C} f_{l_p}^\dagger |0\rangle \,, \tag{3.3.1}$$

and eigenvalues

$$w_L = \mathscr{Q}^{-1} \exp\left[-\sum_{l=1}^{N_C} n_l \varphi_l \right], \tag{3.3.2}$$

where we think of the quantity

$$\Phi = \sum_l n_l \varphi_l \tag{3.3.3}$$

as the total many-particle pseudo-energy. The fact that the many-particle cluster density-matrix eigenstates and eigenvalues can be built up from the one-particle cluster density-matrix eigenstates and eigenvalues is evident in Ref. 176, but its significance was not emphasized.

In Section 3.3.1, we developed a statistical mechanics analogy between the many-particle cluster density-matrix eigenstates and the many-particle energy eigenstates of a system of noninteracting spinless fermions. Within this statistical mechanics picture, the many-particle cluster density-matrix weights w_L are the statistical weights of the many-pseudo-fermion states $|\chi_L\rangle$ in the grand canonical ensemble, *as though* the cluster

is at a finite temperature, and we can apply intuitions learnt from the statistical mechanics of real fermionic systems, to talk about the filling of single-particle pseudo-energy levels as dictated by the Fermi-Dirac distribution. We explained how the cluster density-matrix eigenstate with the maximum weight has the structure of a Fermi sea, with single-particle pseudo-energy levels filled from the lowest single-particle pseudo-energy up to the pseudo-Fermi level $\varphi_F = 0$, and how we can view cluster density-matrix eigenstates with large weights as excitations about this Fermi sea.

We proceeded to make this statistical-mechanical picture more precise, by noting that the eigenvalues λ_l of G, related to the single-particle pseudo-energies φ_l by

$$\lambda_l = \frac{1}{\exp \varphi_l + 1}, \tag{3.3.7}$$

being the average pseudo-occupation numbers of the single-particle pseudo-energy levels, are mostly close to zero or one. Just like in a Fermi sea at finite temperature, only the pseudo-occupation numbers for a small band of single-particle pseudo-energy levels are significantly different from zero or one. Therefore, the statistical mechanics of real fermionic systems tells us that, at finite temperature, the physically important many-body states are those low-energy particle-hole excitations involving single-particle energy levels within $k_B T$ of the Fermi level. Single-particle energy levels far away from the Fermi level contribute negligibly to the thermodynamic properties of the fermionic system, and are precisely the degrees of freedom to be truncated in a renormalization group analysis.

9.2.4 Operator-Based Density-Matrix Truncation Scheme

We capitalize on this insight in Section 3.3.3, and describe a recipe for an operator-based density-matrix truncation scheme based on the statistical mechanics analogy. By

demanding that single-particle pseudo-energy levels below a cutoff φ^* of the pseudo-Fermi level be always occupied, while those above cutoff φ^* of the pseudo-Fermi level be always empty, we retain as degrees of freedom only those pseudo-fermion associated with single-particle pseudo-energies $\varphi_F - \varphi^* < \varphi_l < \varphi_F + \varphi^*$. Within this operator-based truncation scheme, the effective pseudo-Hamiltonian acting on the truncated Hilbert space can be made to have the same form as the original pseudo-Hamiltonian, in the same spirit of renormalization group transformations in statistical mechanics or quantum field theory. The set of many-particle cluster density-matrix eigenstates retained are then generated by allowing all possible combinations of occupations of the single-particle pseudo-energy levels within this cutoff of the pseudo-Fermi level.

As with any newly proposed computational scheme, it is important to make a comparison with the existing state-of-the-art scheme. In the most commonly used density-matrix truncation scheme, which is used, amongst others, by the DMRG, one first calculates the density-matrix weights, rank them in descending order, and retain m many-particle density-matrix eigenstates with the largest weights. We call such a truncation scheme the *weight-ranked density-matrix truncation scheme*. It is difficult to directly compare our operator-based density-matrix truncation scheme with the weight-ranked density-matrix truncation scheme used by the DMRG, because the latter is an incremental method. Instead of obtaining the density matrix of a large cluster all at once, each iteration of the DMRG takes an approximate density matrix for a cluster of N_C sites and produces an approximate density matrix for a cluster of $(N_C + 1)$ sites. The fraction of weight kept, which is taken as the figure of merit, refers to the small truncation in each iteration. The cumulative DMRG truncation might be more appropriate to compare with our results for rather large clusters.

Nevertheless, let us note that operator-based truncation can be applied independent

of whether we calculate the cluster density matrix incrementally, or in one fell swoop. In particular, operator-based truncation could be used in a test run to apply DMRG to a noninteracting Fermi chain. One is given a truncated list of $l_{\max}$ operators $\{f_l\}$ where $l = (N_C - l_{\max} + 1)/2, \ldots, (N_C + l_{\max} - 1)/2$ for the original cluster, and a Hamiltonian projected onto it. One augments this list with the bare creation operators $c^\dagger_{N_C+1}$ on a new site that will be added, and defines the new Hamiltonian by adding the hopping to the new site. In light of the derivation in Section 2.4, we anticipate that the ground-state density matrix of the augmented system must have the same quadratic form, with new operators $\{f'_l\}$, which could presumably be obtained merely by diagonalizing the single-particle sector. One simply deletes the least important member of this list to obtain a new truncated list, which is no longer than the original one.

This difficulty notwithstanding, we carried out in Section 3.6.4 a naive comparison of the performance of the operator-based density-matrix truncation scheme against the traditional weight-ranked density-matrix truncation scheme used in the DMRG, using the ability to exhaust the sum rule

$$\sum_L w_L = 1 \tag{3.6.1}$$

for a given total numer $L_{\max}$ of density matrix eigenstates retained as a criterion. The conclusion: while the operator-based density-matrix truncation scheme does not exhaust the sum rule (3.6.1) as rapidly as the weight-ranked density-matrix truncation scheme, the truncated weight

$$W_t = \sum_{L \leq L_{\max}} w_L \leq 1 \tag{3.6.2}$$

is still of $O(1)$, i.e. the significant parts of the total density matrix weight are 'captured' by the operator-based density-matrix truncation scheme.

However, we believe it is more important to check how well a truncation scheme does by calculating physical quantities, rather than to rely solely on the truncated weight

W_t as a performance indicator. To this end, we calculated in Section 3.9 the dispersion relation of elementary excitations within the operator-based density-matrix truncation scheme (an easy thing to do), and found that the error incurred decays exponentially as $l_{\max}$, the number of single-particle pseudo-energy levels retained when $l_{\max} \ll N_C$. This error is much smaller than $O(\epsilon)$, which is expected from a naive analysis based on the discarded weight $\epsilon = 1 - W_t$. Here, there is a subtle worry that possibly, the truncation works especially well because our chosen hopping Hamiltonian (2.1.1) is so local. A Hamiltonian with longer range hopping would have the same Fermi sea and hence the same density matrix, but the truncation errors might be worse.

It would be desirable to also calculate the dispersion relation within the weight-ranked density-matrix truncation scheme, and compare the results to those obtained within the operator-based density-matrix truncation scheme. However, in the latter case it is problematic even to define the question, since each retained density matrix eigenstate would be a many-particle state. The new truncated Hamiltonian might be conveniently expressed in terms of the pseudo-creation operators $\{f_l\}$, but many combinations of occupations would not exist. The situation would be somewhat analogous to taking a simple, noninteracting hopping Hamiltonian for spinfull fermions, and imposing a Gutzwiller projection (no doubly occupied sites). In effect, the projection made a non-interacting model into an interacting one. Similarly a weight-ranked truncation must introduce spurious interactions. Hence, even if a system containing several clusters were to be exactly diagonalized (using the truncated basis) we could not immediately identify the elementary excitations. One would need, for example, to numerically compute a spectral function $S(q, \omega)$, where $(\hbar q, \hbar\omega)$ are momentum and energy, and then locate peaks as a function of $\hbar\omega$. On the other hand, a system which is truncated using the operator-based truncation scheme can still be represented by a set of creation and

annihilation operators.

Following this, we argued, based on the real-space structure of the one-particle density matrix eigenfunctions shown in Section 3.8, that an operator-based truncation scheme can also be defined naturally using the basis formed by single-particle plane wave states on the cluster of N_C sites. The dispersion relation was calculated within this operator-based plane-wave truncation scheme, and compared to that calculated within the operator-based density-matrix truncation scheme. We find that, other than getting the dispersion exactly right at the zone center of the reduced Brillouin zone, the operator-based plane-wave truncation scheme is generally inferior to the operator-based density-matrix truncation. Instead of decaying exponentially as $l_{\max}$, the error in the dispersion relation calculated within the operator-based plane-wave truncation scheme decays as a power law $l_{\max}^{-1}$, which means that more single-particle basis states need to be retained in the operator-based plane-wave truncation scheme as compared to the operator-based density-matrix truncation scheme.

9.2.5 Scaling of Density-Matrix Weights and Eigenfunctions

Having laid out the basic principles behind our operator-based density-matrix truncation scheme, we proceeded in Section 3.5 to look more closely into the distribution of single-particle pseudo-energies φ_l, and how these scale with the cluster size N_C. There are two related questions that provide the motivation for doing this: (1) the statistical mechanics of real fermionic systems suggests that single-particle energy levels within $\beta^{-1} = k_B T$ of the Fermi level are the physically relevant degrees of freedom — what then is the effective temperature $\tilde{\beta}^{-1}$ that we should use as the natural cutoff when performing operator-based truncation on $\{f_l\}_{l=1}^{N_C}$? (2) although we have associated the pseudo-dispersion relation φ_l with the dispersion relation $\epsilon(k)$ of a real fermionic system of non-

interacting spinless fermions, the wavevector k enumerating $\epsilon(k)$ is an *intensive* quantity whereas the ordinal number l enumerating φ_l is an *extensive* quantity — what would the intensive analog of l that more closely parallels the wavevector k, and how would the pseudo-dispersion relation look like in terms of this intensive label?

The natural answer to the second question would be to write the pseudo-dispersion relation φ_l as a function of l/N_C, totally analogous with how the wavevector k is enumerated as $2\pi m/N$ for a chain of N sites satisfying the Born-von Karman boundary condition. In fact, we find strong numerical evidence that suggests that the single-particle pseudo-energies, for various cluster sizes and fillings, satisfy a scaling relation of the form

$$\varphi(l, N_C, \bar{n}) \cong N_C f(\bar{n}, x), \tag{3.5.6}$$

where the scaling function $f(\bar{n}, x)$ is the proper analog of the dispersion relation $\epsilon(k)$, and the scaling variable

$$x \equiv (l - l_F)/N_C, \quad l_F = \bar{n}N_C + \tfrac{1}{2} \tag{3.5.7}$$

is the proper analog of the wavevector k. From

$$\lambda_l = \frac{1}{\exp(N_C f) + 1}, \tag{3.5.12}$$

we see indeed that the cluster size N_C plays the role of inverse temperature. We later derived, from analyzing the entanglement entropy

$$S = -\operatorname{Tr} \rho_C \log_2 \rho_C \tag{3.7.1}$$

in Section 3.7, an improved scaling formula

$$\varphi(l, N_C, \bar{n}) \approx \frac{\alpha N_C}{\kappa + \log N_C} \tilde{f}(\bar{n}, x) \tag{3.7.33}$$

for the single-particle pseudo-energies.

Associated with the second question of eigenvalue scaling is whether there are scaling relations for the one-particle cluster density-matrix eigenfunctions. We investigated this in Section 3.8, for the single-particle pseudo-Fermi eigenfunction $\chi_F(j, N_C)$, whose one-particle pseudo-energy is right at the pseudo-Fermi level. For all odd cluster sizes, we find generically that the amplitude of the pseudo-Fermi eigenfunction is strongly enhanced near the boundaries of the cluster. This feature was first observed by White in DMRG calculations [15], and explained by Gaite as a consequence of the angular quantization of the density matrix [192]. Our numerical scaling analysis then showed that the pseudo-Fermi probability density can be put into the scaling form

$$|\chi_F(j, N_C)|^2 \cong N(N_C) g(y) \frac{\frac{1}{2}[1 - (-1)^j]}{\sin^2 \pi y}, \tag{3.8.3}$$

where

$$y \equiv (j - \frac{1}{2})/N_C \tag{3.8.4}$$

is the rescaled coordinate on the cluster, and $g(y)$ is the scaling function shown in Figure 3.20, while the reciprocal of the normalization scales as

$$N^{-1}(N_C) = 0.249 N_C \log N_C + 0.668 N_C. \tag{3.8.8}$$

Our scaling results in Section 3.5 indicate that the density matrix eigenvalues behave, as the cluster size N_C is increased, very much as energy eigenstates and eigenvalues do when the system size is increased. In the latter case, we have a dispersion relation and are more or less sampling it at different wavevectors. It is not quite that simple in the density matrix case, since the scaling function (3.5.6) — our analog of the energy dispersion relation — depends on the filling $\bar{n}$. We only note that this analogy still lacks an analytical foundation. A more penetrating analysis is called for of the relation of G_C to ρ_C (or equivalently, the effect on its eigenvalues of restricting G_C to sites on a cluster). Incidentally, we noted that our equation relating G_C to ρ_C was valid at any temperature,

but we assumed zero temperature throughout Chapter 2. We expect a nonzero temperature T to become a second scaling variable. Since $T > 0$ has similar effects on the Green function $G(r)$ as does the gap introduced in (3.6.5), we expect the scaling also behaves similarly and did not investigate it.

In a real application, we are unlikely to project Hamiltonians directly onto large clusters (meaning clusters with more than 16 sites). What then is the practical value of extracting scaling forms, if they are unambiguously seen only in clusters of 100 or more sites? One answer is that, even though it is an oversimplified cartoon for the non-asymptotic situations in which it usually gets applied, a scaling law is easier to grasp than brute numerical or graphical facts. The scaling relation (3.5.6) is also a powerful tool that we can use to derive deeper understanding concerning the structure of the cluster density matrix, as well as various aspects of truncation. But in itself, the scaling relation provides only a partial answer to our first question, which is about how much of the Hilbert space of many-body states on the cluster of N_C sites we can truncate.

To answer this question more completely, we looked at the three density matrix eigenstates $|F\rangle$, $|F-1\rangle$ and $|F+1\rangle$ with the largest weights in Section 3.6.1. Using the scaling relation (3.5.6), we find that the ratios $w_{F\pm1}/w_F$ of their weights (w_F being the largest density matrix weight) approach a constant,

$$\frac{w_{F+1}}{w_F} = \frac{w_{F-1}}{w_F} \approx \exp(-f'(0)), \tag{3.6.4}$$

for a gapless system of noninteracting spinless fermions, as $N_C \to \infty$. The same result was also found for a gapped system of noninteracting spinless fermions, for which we found scaling relations governed by gap-dependent scaling functions. Furthermore, the scaling relation (3.5.6) allowed us to conclude in Section 3.6.3 that as $N_C \to \infty$, the

largest cluster density-matrix weight w_F approaches a constant,

$$w_{F,\infty} = \exp\left[-\frac{2}{1-\exp(-f'(0))}\right], \tag{3.6.23}$$

and derive approximately the dependence on the number $l_{\max}$ of single-particle pseudo-energy levels retained of the truncated weight W_t in the operator-based DM truncation scheme.

9.2.6 Finite Two-Dimensional Systems

Up till this point, our formulations have been for noninteracting spinless fermions in arbitrary dimensions, but our numerical results have been for noninteracting spinless fermions in one dimension. The formulations — the relations (2.4.30) and (2.5.1) between ρ_C and G_C, and the operator-based density-matrix truncation scheme — are also valid for finite clusters within finite systems, even though we have thus far been working exclusively with an infinite chain. Since our goal is to ultimately develop an ED-driven RG scheme for interacting systems in higher dimensions, we chose in Section 4.6 to do a benchmark study with a cross-shaped cluster of five sites, within a finite N-site system defined relative to an underlying square lattice, of noninteracting spinless fermions.

For a finite system defined by the lattice vectors $\mathbf{R}_1 = (R_{1x}, R_{1y})$ and $\mathbf{R}_2 = (R_{2x}, R_{2y})$ (see Figure 4.1), with $N = R_{1x}R_{2y} - R_{2x}R_{1y}$ sites and subject to periodic boundary conditions, we construct the cluster Green-function matrix

$$G_C(\mathbf{r}, \mathbf{r}') = \frac{1}{N} \sum_{\mathbf{k}\ \text{filled}} e^{\mathrm{i}\,\mathbf{k}\cdot(\mathbf{r}-\mathbf{r}')} \tag{4.6.3}$$

by summing over the P wave vectors $\mathbf{k}$ which are occupied. When there are two or more combinations of P occupied wave vectors giving the same total energy, we average over these degenerate combinations, as well as over all orientations of the $\mathbf{R}_1 \times \mathbf{R}_2$ system relative to the underlying square lattice, to obtain a cluster Green-function matrix having

the full point-group symmetry of the underlying square lattice. We then diagonalize the 5×5 cluster Green-function matrix to determine the eigenvalues $\lambda_{s,1}$, $\lambda_p = \lambda_{p,\pm}$, λ_d and $\lambda_{s,2}$, sorted in descending order, and labelled according to the symmetries of their associated eigenstates with respect to the underlying square lattice (see Section 4.4), and thereafter calculate the one-particle cluster density-matrix weights $w_{s,1}$, $w_{p,\pm}$, w_d and $w_{s,2}$ using (2.5.3).

Analyzing the cluster density-matrix spectra for various finite systems, we find the numerical spectra to be plagued by finite size effects (see Figure 4.4). By increasing the system size systematically, we find a unique and unambiguous infinite-system limit for the cluster density-matrix spectra, which is approached for finite systems with a couple of hundred sites (see Figures 4.5 and 4.6). Realizing that these are forbiddingly large system sizes on which to exactly diagonalize interacting systems, we then tested the apparatus of twist boundary conditions averaging on noninteracting finite systems with between 10 to 20 sites. We find that the twist boundary conditions-averaged weights for different systems and different filling fractions fall onto various smooth curves (see Figure 4.20). This assures us that, at least in the case of noninteracting spinless fermions, twist boundary conditions averaging practically eliminates finite size effects, so that the cluster density matrix approaches that obtained from the ground-state wave function of an infinite square lattice.

9.2.7 Relevance to Interacting Systems

Obviously, noninteracting systems do not require numerical studes, so we must clarify how our results in Chapters 3 and 4 are relevant to the problem of interacting systems in dimensions greater than one, addressing which, as we have emphasized time and again, is our ultimate goal. Firstly, many (gapless) systems of interest are in a phase

— Fermi liquid, d-wave superconductor — which are noninteracting in the low-energy, long-wavelength limit. In particular, when applied to an interacting Fermi liquid system, we expect (to the extent that the truncation has separated out the low energy modes) that any iterative renormalization scheme will converge on to the noninteracting Fermi liquid limit, and that it must behave properly in this limit to have even the hope of success. For interacting Fermi liquids, which we expect to have the same energy eigenstate structure as a noninteracting Fermi sea, in their low-energy limit and after a unitary transformation, their density matrices also should have the same structure as that of a noninteracting system. Hence, for a density matrix-based scheme, the first order of business is to study the density matrix for a noninteracting fermion ground state (as we have done in this thesis) or for a BCS ground state [176].

In Section 3.3 we saw how the analytical structure of the cluster density matrix given in (2.5.1) implied an operator-based density-matrix truncation scheme, where the effective degrees of freedom eventually retained are the pseudo-fermion operators f_l, which satisfy the usual anticommutation relations. For an interacting Fermi liquid, we expect to be able to write its cluster density matrix, approximately, in a form similar to (2.5.1). Therefore, instead of independently truncating the many-particle cluster density-matrix eigenstates in each P_C-particle sector, we should define the truncated states using the set of pseudo-fermion operators retained by the operator-based density-matrix truncation scheme. Quite likely, this set of pseudo-fermion operators will be closely related to the approximate quasiparticle operators of the interacting Fermi liquid, even though we expect that the truncated many-particle cluster density-matrix eigenstates will *not* be simple products of the truncated one-particle cluster density-matrix eigenstates (they were in the noninteracting case studied in Chapters 3 and 4). More thought will be needed as to discover the best recipe to optimize the truncation rule so as to balance the

needs of sectors with different particle numbers in a strongly interacting system.

A separate reason why our results for noninteracting fermions are relevant to the study of interacting systems, is that the scaling behaviour of the noninteracting density matrix should be a good guide to that of interacting systems, even though details may differ. This is in the same sense that mean-field theory is a good guide to the overall pattern of critical phenomena.

We worry more about other interacting models of interest which sit at quantum critical points not described by quasiparticle interactions, or possess fractionalized excitations. Since we do not presently understand the proper way to write their wavefunctions in terms of a spatially blocked basis, nor the proper renormalization step to capture the intercluster correlations in the fractionalized systems, we do not know if a plain cluster density matrix gives the proper basis for truncation of the states. Furthermore, in the absence of an analytic construction of the cluster density matrix, for example, for Laughlin's quantum Hall wave function or the one-dimensional Su-Schrieffer state, we cannot proceed to scaling studies of large clusters like those found in Chapter 3, but numerical studies of such density matrices might be an illuminating subject for future research.

9.3 Reduced Density Matrices of Interacting Spinless Fermions

Since its introduction in 1993 [15], the powerful DMRG method has become the state-of-the-art in the numerical study of one-dimensional interacting systems. This is especially true now, after inputs from the field of quantum computing shed light on how it can be used in conjunction with periodic boundary conditions [20]. The same cross-fertilization between DMRG and quantum computing has also allowed the originally one-dimensional DMRG algorithm to be generalized to higher dimensions [21]. How-

ever, such higher-dimensional DMRG schemes are still in a nascent stage of development, and remain relatively untested. Therefore, it is for higher-dimensional interacting systems where other analytical and numerical studies can make important contributions to the DMRG.

In particular, we found a simple algebraic structure for the cluster density matrix of noninteracting spinless fermions, in any dimensions, in Chapter 2, which led us to develop an operator-based truncation scheme preserving this simple algebraic structure of the cluster density matrix. This motivated the question of whether we can formulate similar structure-preserving operator-based truncation schemes based on the cluster density matrix of interacting spinless fermions. The work done in Chapter 4 on interacting spinless fermions is our attempt to answer this question.

9.3.1 The Extended Spinless Hubbard Model

In Chapter 4, besides working with a system of noninteracting spinless fermions, described by the Hamiltonian (2.1.1), on a two-dimensional square lattice, we also worked with a system of strongly-interacting spinless fermions with infinite nearest-neighbor repulsion described by the Hamiltonian

$$H_{tV} = -t \sum_{\langle \mathbf{r},\mathbf{r}' \rangle} \left[c^\dagger_{\mathbf{r}} c_{\mathbf{r}'} + c^\dagger_{\mathbf{r}'} c_{\mathbf{r}} \right] + V \sum_{\langle \mathbf{r},\mathbf{r}' \rangle} n_{\mathbf{r}} n_{\mathbf{r}'}, \tag{4.2.1}$$

with $V \to \infty$. This is essentially the spinless analog of the extended Hubbard model.

In Section 4.2, we explained that this model is chosen because it has a rich zero-temperature phase diagram [204–206], and is believed to be a Fermi liquid in most parts of the phase diagram. It was our hope that probing the cluster density-matrix spectra at different filling fractions would allow us to capture the signatures of the rich variety of structures that occur in the ground state, and guide us in designing an operator-based

truncation scheme for interacting Fermi liquids.

9.3.2 Formulation

Unlike for noninteracting spinless fermions, where knowledge of the closed-form formula (2.4.30) and of the structure of the Fermi sea ground state allows us to calculate the cluster density-matrix spectra from the spectra of the simpler cluster Green-function matrix, the cluster density matrix must be calculated from an ED ground-state wave function by tracing down degrees of freedom outside of the cluster. In the quantum mechanics literature, it has always been assumed that this can be done, and that the fermion signs that arise in the course of this trace down will pose no problem. In Section 4.3.2, we showed that a cluster density matrix consistent with the expected properties that the cluster density matrix can be obtained from the ground-state wave function by tracing over the environment,

$$\rho_C = \mathrm{Tr}_E\, \rho, \tag{4.3.8}$$

and that the cluster density matrix recovers the ground-state expectations

$$\langle \Psi | A | \Psi \rangle = \langle A \rangle = \mathrm{Tr}_C\, \rho_C A, \tag{4.3.6}$$

of all observables A local to the cluster, can indeed be defined for a system of fermions.

Writing the ED ground-state wave function

$$\begin{aligned} |\Psi\rangle &= \sum_{\mathbf{n}} \Psi_{\mathbf{n}} |\mathbf{n}\rangle \\ &= \sum_{\mathbf{n}} \Psi_{\mathbf{n}} c^\dagger_{j_1} \cdots c^\dagger_{j_P} |0\rangle \\ &= \sum_{\mathbf{l}} \sum_{\mathbf{m}} (-1)^{f(\mathbf{n};\mathbf{l},\mathbf{m})} \Psi_{\mathbf{l},\mathbf{m}} |\mathbf{l}\rangle\, |\mathbf{m}\rangle \\ &= \sum_{\mathbf{l}} \sum_{\mathbf{m}} (-1)^{f(\mathbf{n};\mathbf{l},\mathbf{m})} \Psi_{\mathbf{l},\mathbf{m}} c^\dagger_{m_1} \cdots c^\dagger_{m_{P_E}} c^\dagger_{l_1} \cdots c^\dagger_{l_{P_C}} |0\rangle\,, \end{aligned} \tag{((4.3.9)\&(4.3.10))}$$

in terms of the direct product of configuration bases of the cluster and the environment, and taking care handling the fermions while performing the trace down, we arrived at the formula

$$\langle \mathbf{l}|\rho_C|\mathbf{l}'\rangle = \sum_{\mathbf{m}} \sum_{\mathbf{m}'} (-1)^{f(\mathbf{n};\mathbf{l},\mathbf{m})+f(\mathbf{n}';\mathbf{l}',\mathbf{m}')} \Psi_{\mathbf{l},\mathbf{m}} \Psi^*_{\mathbf{l}',\mathbf{m}'} \delta_{\mathbf{m},\mathbf{m}'}. \tag{4.3.39}$$

for the cluster density-matrix elements. Here c_l and $c_l^\dagger$ are fermion annihilation and creation operators acting on site (x_l, y_l) within the cluster, and c_m and $c_m^\dagger$ are fermion annihilation and creation operators acting on site (x_m, y_m) within the environment. The amplitudes $\Psi_{\mathbf{l},\mathbf{m}} = \Psi_{\mathbf{n}}$ are determined by ED, while the factor $(-1)^{f(\mathbf{n};\mathbf{l},\mathbf{m})}$ comes from re-ordering the operator product $c_{j_1}^\dagger \cdots c_{j_P}^\dagger$ to get the operator product $c_{m_1}^\dagger \cdots c_{m_{P_E}}^\dagger c_{l_1}^\dagger \cdots c_{l_{P_C}}^\dagger$.

9.3.3 Computational Implementation

An Octave code base was developed from scratch for the purpose of exactly diagonalizing finite systems of interacting spinless fermions with infinite nearest-neighbor repulsion, and thereafter tracing down the ED ground-state wave function to compute the cluster density matrix. This code base consists of small helper functions performing short generic calculations, large core functions dedicated to performing intensive computations optimally, and small wrapper functions designed to simplify the interface with the core functions. This code base, which is organized into three code branches, to handle boson and fermion calculations, as well as statistics-independent calculations, is documented in great details in Appendix C. A computational complexity analysis of the trace-down algorithm used in the code base is also presented in Section 4.3.3.

9.3.4 Twist Boundary Conditions Averaging

Apart from degeneracy averaging and orientation averaging to restore full square-lattice symmetry in the cluster density matrix, we also average the cluster density matrix over twist boundary conditions to reduce finite size effects. Looking at the twist boundary conditions-averaged cluster density-matrix spectrum for the strongly-interacting system in Section 4.7, we find that the one-particle cluster density-matrix weights at the various discrete filling fractions do not quite fall onto a smooth curve, and when the data points from various finite systems are superimposed, there is still significant scatter. Nevertheless, this was the best that we could do, and we presented interpolated curves, averaged over various finite systems, of the one-particle cluster density-matrix weights as functions of the filling fraction in Figure 4.26.

Comparing the twist boundary conditions-averaged cluster density-matrix spectra for the noninteracting and strongly-interacting systems, we find that the zero-particle weights w_0 for the noninteracting and strongly-interacting systems have the same qualitative behaviour, except for the fact that w_0 for the strongly-interacting system falls significantly below that of the noninteracting system, for $\bar{n} > 0.1$, because of the smaller likelihood to find configurations containing a cross-shaped cluster of five empty sites as $\bar{n}$ increases when the spinless fermions repel each other. The one-particle weights w_{s_1}, w_p, w_d and w_{s_2} are qualitatively different for the two system types, even though the relative ordering $w_{s_1} > w_p > w_d > w_{s_2}$ is the same. More importantly, we find that, while the one-particle weights go down by roughly one order of magnitude each time as we go through the sequence $w_{s_1} \to w_p \to w_d \to w_{s_2}$ in the noninteracting system, this decay is much slower in the strongly-interacting system.

9.3.5 Operator-Based Density-Matrix Truncation Scheme

The implications of this observation to the operator-based density-matrix truncation scheme developed in Chapter 3 is that, for a small fixed fraction of one-particle eigenstates retained, the total cluster density-matrix weight of eigenstates retained would be much smaller for the strongly-interacting system compared to the noninteracting system. However, as shown in Section 3.9, we need to calculate other observables, such as the dispersion relation, before we can say for sure how badly the numerical accuracy of the truncation scheme is affected by the fact that the ratio of the smallest to the largest one-particle weights, w_{s_2}/w_{s_1}, is not very much smaller than one.

Another check we made in connection with the operator-based density-matrix truncation scheme is how well the many-particle eigenstates are represented by combinations of the retained one-particle cluster density-matrix eigenstates. For the two-particle cluster density-matrix eigenstates, we find far too many two-particle states generated by taking combinations of one-particle eigenstates. Most of these combinatorial two-particle states are invalid, because of the restriction imposed by (4.2.1) on nearest-neighbor occupation. This is not a debilitating problem, because we can always build restrictions into the operator-based density-matrix truncation scheme to have these invalid states removed. More importantly, based on the valid two-particle combinations, we predict that $w_{P_1} \gtrsim w_D > w_S$ for the three of the four distinct two-particle cluster density-matrix weights, which is indeed what we observe numerically, even though the predicted weights are off.

With these checks, we conclude that, if we so insist, it is possible to implement a modified operator-based density-matrix truncation scheme on a strongly-interacting Fermi-liquid system, by imposing additional restrictions on which many-particle states to retain, out of the set we built up using the retained one-particle cluster We are, how-

ever, not optimistic about the performance of such a truncation scheme, for two reasons. Firstly, the ratio of the maximum one-particle cluster density-matrix weight to the minimum one-particle cluster density-matrix weight is not large enough to justify keeping one and throwing the other away. Secondly, and more critically, the many-particle cluster density-matrix 'weights' we predict using the zero-particle cluster density-matrix weight, and the retained one-particle cluster density-matrix weights, agrees poorly with the many-particle cluster density-matrix weights we obtained numerically. This means that we are unlikely to have fine control over the computational accuracy of the observables we want to calculate within the truncation scheme, for a given computational time expenditure. This reward-to-effort ratio is an important factor in helping us decide how much compromise we need to make in terms of accuracy of the final result versus the time needed to acquire it.

9.4 Systematic Extraction of Ground-State Correlations

9.4.1 Motivation

Up till this point in the thesis, we have been studying the density matrix of a contiguous cluster of sites cut out from a larger system, even though we are not restricted to cluster of this nature by the formalisms, analytical and computational tools we have developed, which applies for any manner of clusters. In Chapters 2, 3 and 4, we chose to work with contiguous clusters because our chief interest is in developing truncation schemes for density-matrix-based QRG methods. The density matrix, however, can also be used as a diagnostic tool for deciding which correlations are the most important, and also discovering unexpected ones.

To use the density matrix in this way, we consider a supercluster, consisting of two

or more disjoint clusters, separated by distances that can be considered large compared to the sizes of the clusters. The supercluster density matrix can then be thought of as a generalized order parameter, containing information on all possible correlations between the disjoint clusters. We want to think of the total correlations encoded within the supercluster density matrix as being contributed by various independent quantum fluctuations, some of which are more important, some of which are less important. The hope is that, if we can somehow sort the supercluster density matrix into a sum of terms, each corresponding to one such independent quantum fluctuation, and sort them according to the magnitude of their correlations, we would be able to read off the dominant long-range order parameters. Our eventual goal would be to have an automatic, systematic, and unbiased machinery that would start from a choice of disjoint clusters, construct the supercluster density matrix, decompose it to extract, identify, and sort the various order parameters. This would be ideally suited to augment the ED, QMC or even DMRG studies and exploration of the ground-state phase diagram of strongly-correlated models which are not yet well understood analytically.

9.4.2 Correlation Density Matrix

In Section 5.2, we consider a supercluster of two disjoint clusters a and b and its supercluster density matrix ρ^{ab}. This entity contains all possible correlations between clusters a and b, include those which are local to each cluster, and are nonzero even when the two clusters are completely uncorrelated. Therefore, for the purpose of discovering nonlocal correlations between disjoint clusters, we work with the correlation density matrix

$$\rho^c = \rho^{ab} - \rho^a \otimes \rho^b, \tag{5.2.1}$$

which contains only correlations *between* clusters a and b. Here ρ^a is the density matrix of cluster a, ρ^b is the density matrix of cluster b, and $\rho^a \otimes \rho^b$ is the direct product of ρ^a and ρ^b.

Following this, we calculated analytically in Section 5.3 the correlation density matrix of (1 + 1) and (2 + 2) superclusters on a one-dimensional chain of noninteracting spinless fermions, whose ground state is a Fermi sea. We also calculated in Section 5.4 the supercluster density matrix for one-dimensional superconducting ground states of spinless fermions, for the (1 + 1) and (2 + 2) superclusters within a BCS ground state in Section 5.4.1, and for the (1 + 1) supercluster within a particle-number-projected BCS ground state in Section 5.4.4.

9.4.3 Operator Singular Value Decomposition

The correlation density matrix so defined in (5.2.1) is null if clusters a and b are completely uncorrelated. Otherwise, we argued that the nonzero, nonlocal, correlation between clusters a and b can be thought of as the sum of independent quantum fluctuations, each of which will involve the action of an operator X on cluster a, accompanied by the simultaneous action of an operator Y on cluster b.

In Section 6.3, we make this notion of independent quantum fluctuations mathematically rigorous by introducing the Frobenius orthonormalization

$$\mathrm{Tr}\, A_i A_j^\dagger = \delta_{ij}, \tag{6.3.8}$$

for pairs of quantum-mechanical operators A_i and A_j. This allows us to rigorously define the decomposition

$$\rho^c = \sigma_1 X_1 Y_1^\dagger + \sigma_2 X_2 Y_2^\dagger + \cdots + \sigma_m X_m Y_m^\dagger, \tag{6.3.1}$$

into independent combinations of operators X_l acting on cluster a, and Y_l acting on

cluster b, as an operator singular value decomposition. The m operators $\{X_1, \ldots, X_m\}$ and $\{Y_1, \ldots, Y_m\}$ can then be thought of as the nontrivial order parameters of the given quantum-mechanical state.

Our starting point is the collection of all products of two referencing operators

$$X_{\mathbf{ll'}} = K_{\mathbf{l}}^{\dagger} K_{\mathbf{l'}}, \quad Y_{\mathbf{mm'}} = K_{\mathbf{m}}^{\dagger} K_{\mathbf{m'}}. \tag{6.3.19}$$

The referencing operators $K_{\mathbf{l}}$ and $K_{\mathbf{m}}$, defined in Section 2.3.1, are such that each of them singles out a particular many-particle state, so that the product $X_{\mathbf{ll'}} = K_{\mathbf{l}}^{\dagger} K_{\mathbf{l'}}$ of two referencing operators, $K_{\mathbf{l}}$ and $K_{\mathbf{l}}$, has nonzero matrix element only between the many-particle states $|\mathbf{l}\rangle$ and $|\mathbf{l}\rangle$. Combinations of such two-referencing-operator-products can then be used build up arbitrary operators acting on the supercluster Fock-Hilbert space.

For the purpose of implementing this operator singular value decomposition of the correlation density matrix numerically, we note that the collection of two-referencing-operator-products $\{X_{\mathbf{ll'}}\}$ and $\{Y_{\mathbf{mm'}}\}$ constitute Frobenius-orthonormal bases of operators, such that

$$\mathrm{Tr}\, X_{\mathbf{ll'}} X_{\mathbf{l''l'''}}^{\dagger} = \delta_{\mathbf{ll'},\mathbf{l''l'''}}, \quad \mathrm{Tr}\, Y_{\mathbf{mm'}} Y_{\mathbf{m''m'''}}^{\dagger} = \delta_{\mathbf{mm'},\mathbf{m''m'''}}. \tag{6.3.20}$$

In terms of these two-referencing-operator-products, the correlation density matrix is

$$\rho^c = \sum_{n,n'} \left[(-1)^{f_{nn'}} \rho_{nn'}^{ab} - \rho_{ll'}^{a} \rho_{mm'}^{b} \right] K_{\mathbf{l}}^{\dagger} K_{\mathbf{l'}} K_{\mathbf{m}}^{\dagger} K_{\mathbf{m'}}. \tag{6.3.18}$$

We collect the expansion coefficients in (6.3.18) into the correlation-$\mathbf{K}$ matrix, whose matrix elements

$$K_{\lambda\mu} = \left[(-1)^{f_{nn'}} \rho_{nn'}^{ab} - \rho_{ll'}^{a} \rho_{mm'}^{b} \right], \tag{6.3.23}$$

are indexed by the fused indices $\lambda = ll'$ and $\mu = mm'$. We then perform a numerical matrix singular value decomposition of $\mathbf{K}$ to obtain the operator singular value decomposition of ρ^c.

With this operator singular value decomposition machinery sorted out, we went ahead in Section 6.4 to approximately operator singular value decompose by hand the $(1+1)$ and $(2+2)$ supercluster correlation density matrices in a one-dimensional Fermi-sea ground state, at certain limiting filling fractions. Then in Section 6.5 we operator singular value decompose by hand the $(1+1)$ supercluster correlation density matrix in a one-dimensional BCS ground state. We learnt from these practice calculations that the eigen-operators X_l and Y_l that emerge from the operator singular value decomposition of the correlation density matrix are not the usual order parameters O_l one would stick into an ED or DMRG program to calculate correlations from. Instead, we find that these are operators which project out the usual order parameters, satisfying the relation

$$\mathrm{Tr}\, X_{l'} Y_{l'}^{\dagger} O_l^{\dagger}(0) O_l(r) = \delta_{ll'}, \tag{6.4.19}$$

so that each operator product term in the singular value decomposition of ρ^c picks out *one and only one* of the proper ground-state order parameters. Consequently, we know that the correlations of the order parameter O_l is given by

$$\langle O_l^{\dagger}(0) O_l(r) \rangle = \sigma_l, \tag{6.4.20}$$

where r is the separation between clusters a and b.

9.4.4 Exploration of Phase Diagram

With the machinery of operator singular value decomposition of the correlation density matrix at hand, we explore in Chapter 8 the ground-state phase diagram of the extended

spinless Hubbard ladder with correlated hops, described by the Hamiltonian

$$\begin{aligned} H_{t_\parallel t_\perp t' V} = & -t_\parallel \sum_i \sum_j \left(c^\dagger_{i,j} c_{i,j+1} + c^\dagger_{i,j+1} c_{i,j} \right) - t_\perp \sum_i \sum_j \left(c^\dagger_{i,j} c_{i+1,j} + c^\dagger_{i+1,j} c_{i,j} \right) \\ & - t' \sum_i \sum_j \left(c^\dagger_{i,j} n_{i+1,j+1} c_{i,j+2} + c^\dagger_{i,j+2} n_{i+1,j+1} c_{i,j} \right) \\ & - t' \sum_i \sum_j \left(c^\dagger_{i+1,j} n_{i,j+1} c_{i+1,j+2} + c^\dagger_{i+1,j+2} n_{i,j+1} c_{i+1,j} \right) \\ & + V \sum_i \sum_j n_{i,j} n_{i,j+1} + V \sum_i \sum_j n_{i,j} n_{i+1,j}, \end{aligned} \tag{7.3.2}$$

with $V \to \infty$ nearest-neighbor repulsion, where $i = 1, 2$ runs over the two legs of the two-legged ladder, and $j = 1, \ldots, L$ runs over the L rungs of the two-legged ladder. An additional correlated hopping term, with absolute amplitude t', is added to the extended spinless Hubbard model (4.2.1) studied in Chapter 4 to favor superconducting correlations in some regime of the ground-state phase diagram.

We expect the ground-state phase diagram, shown in Figure 8.1, to consist of three regions (SC, PL-CDW and LR-CDW) with different dominant long-range correlations, when the ladder is quarter-filled. Each of these regions is in a quantum phase determined by one of the limiting cases studied in Chapter 7, and based on very crude energetic arguments, we have determined to zeroth order where the cross-over from PL-CDW to SC, the phase transition from PL-CDW to LR-CDW, and the phase transition from SC to LR-CDW would occur. For our exploration, we chose parameter points close to the three limiting cases, one parameter point each lying on the zeroth-order lines of cross-over and phase transitions, and also one parameter point at the intersection between the lines of cross-over and phase transitions. These parameter points are marked out on the phase diagram shown in Figure 8.1.

9.4.5 Analysis of Ground-State Wave Function

To illustrate the utility of the method of operator singular value decomposition of the correlation density matrix, we performed a benchmark study in Section 8.3 of the ground-state phase diagram by analyzing the structure of the ED ground-state wave function at the various parameter points, pretending that we are unaware of which correlation functions are important. We find that, through careful analysis of the distribution of amplitudes in the ED ground-state wave function, we are able to decide what reference state(s) the ED ground state is most similar to. In this way, we are able to obtain a picture of dominant order parameters that agrees qualitatively with the zeroth-order ground-state phase diagram shown in Figure 8.1. However, such an analysis relies on us having prior knowledge of the reference states, which are determined analytically at the three limiting cases. When analytical insights from limiting cases are not available, and particularly where the ED ground state features an unknown superposition of reference states, it becomes impossible to reliably follow the ED ground-state wave function across a line of cross-over or phase transition, and still have a clear picture of what is going on.

9.4.6 Analysis of Singular Values

This brings us to the analysis of the singular values and eigenvectors generated by the operator singular value decomposition of the correlation density matrix. In principle, this method is not affected by our knowledge or ignorance of any analytical limits, or some rough outline of the ground-state phase diagram. At any parameter point, the method automatically sorts the singular values, and so in the ideal case, we can not only decide — by looking at the eigenvector associated with the largest absolute singular value — which order parameter type is dominant at large distances, but also, through

following the evolution of the largest and next-largest absolute singular values as the parameters are varied, determine where and whether a cross-over or phase transition occurs.

In practice, we encountered several difficulties. The first minor difficulty we encountered is that the method implies no natural choice of clusters. In Section 8.2.2, we considered two possible choices of clusters, the $(1 \times 2) + (1 \times 2)$ and $(2 \times 2) + (2 \times 2)$ clusters, and worked out the order parameter types that can emerge from the operator singular value decomposition of the respective correlation density matrices. Finding that the $(1 \times 2) + (1 \times 2)$ supercluster will not admit SC-type order parameters, we worked with the $(2 \times 2) + (2 \times 2)$ supercluster through all parameter points. Based on the analysis of singular values in Section 8.4, we find a decent qualitative agreement between the picture of dominant correlations derived from looking at the largest absolute singular values at various parameter points, and the zeroth-order ground-state phase diagram shown in Figure 8.1.

We were also hopeful, before undertaking the numerical studies in Section 8.4, to be able to distinguish an exponentially decaying order parameter from one that decays as a power law, and perhaps even obtain estimates for the values of the correlation exponents, by performing nonlinear curve fits of the same nature as those done in Chapter 7. However, we found that, for the short ladders that we can exactly diagonalize with twist boundary conditions averaging, there was no reliable way to do this. This is due in part to the fact that we have numerical data for only a handful of separations, and more importantly, because we know of no way to track individual oscillatory singular values as functions of the intercluster separation. Therefore, in Section 8.4, we track as functions of the intercluster separation the largest absolute singular values in different symmetry sectors of different order-parameter types. It is also possible, and perhaps

more desirable, to track as functions of the intercluster separation the L_2 norm of all singular values within each symmetry sector of each order-parameter type, but we have not attempted to do this for this thesis.

9.5 Critical Study of Twist Boundary Conditions Averaging

In our numerical studies in Chapters 4 and 8, we exactly diagonalize small finite systems, for the purpose of calculating various expectations. We find deviations, collectively known as finite size effects, in the numerical values of the finite-system expectations from that of their infinite-system counterparts. In the computational many-body literature, there are two approaches to obtaining better approximations to the infinite-system expectations using numerical results coming from finite systems. The first is scaling analysis, where the same expectation is calculated from finite systems of different sizes, and the results extrapolated to infinite system size. The second is to average the values of the expectation calculated from the same finite system, but subject to a parametrized family of periodic boundary conditions. In Appendix D, we reviewed what is known in the literature about this method of twist boundary conditions averaging, and also derive new results of our own.

9.5.1 Literature

The standard exposition found in the computational many-body literature on how the method of twist boundary conditions averaging works is based on what happens to a system of noninteracting fermions when it is subjected to twist boundary conditions with twist vector $\boldsymbol{\phi}$. For a system of noninteracting fermions, the many-particle energy eigenstates are simple products of the one-particle energy eigenstates, and thus it suf-

fices to consider the effects twist boundary conditions have on the one-particle energy eigenstates.

Working in the boundary gauge defined in Section D.2.1.3, one can easily show for a finite system of N sites that the discrete set of wave vectors $\mathbf{k}(\boldsymbol{\phi})$ associated with the one-particle energy eigenstates, when the system is subjected to twist boundary conditions with twist vector $\boldsymbol{\phi}$, are related to the discrete set of wave vectors $\mathbf{k}_0$, when the system is subjected to periodic boundary conditions, by

$$\mathbf{k}(\phi) = \mathbf{k}_0 + \boldsymbol{\phi}, \tag{D.2.33}$$

while the single-particle energy eigenvalues become

$$\epsilon(\mathbf{k}(\boldsymbol{\phi})) = \epsilon(\mathbf{k}_0 + \boldsymbol{\phi}). \tag{D.2.20}$$

Therefore, by varying the twist vector $\boldsymbol{\phi}$, the First Brillouin Zone of the infinite system can be continuously sampled. This is known as wave vector sampling.

If the goal is to average, or integrate an observable over the First Brillouin Zone of the infinite system, the values of the observable can be computed, by ED or QMC, over a representative set of twist vectors $\{\boldsymbol{\phi}_i\}$, and then averaged or summed. Typically, the set of twist vectors chosen to be 'representative' is small.

9.5.2 Wave Vector Sampling and Ground State Selection

We elucidated the consequences of wave vector sampling further in Section D.3, working with a system of noninteracting spinless fermions. At each twist vector $\boldsymbol{\phi}$, we understand that the P-particle ground state must be built up by filling the P single-particle energy eigenstates $|\mathbf{k}_0 + \boldsymbol{\phi}\rangle$ with the lowest single-particle energies $\epsilon(\mathbf{k}_0 + \boldsymbol{\phi})$. We find in general that this ground state selection process is discontinuous in $\boldsymbol{\phi}$, i.e. if the P wave

vectors selected at twist vector $\boldsymbol{\phi}_1$ are $\{\mathbf{k}_1, \ldots, \mathbf{k}_P\}$, and we vary the twist vector continuously from $\boldsymbol{\phi}_1$ to $\boldsymbol{\phi}_2$, the P wave vectors selected to build up the P-particle ground state may change discontinuously to $\{\mathbf{k}'_1, \ldots, \mathbf{k}'_P\}$ at twist vector $\boldsymbol{\phi}_2$.

We understand this discontinuous ground state selection, which has important ramifications for the computation and averaging of various expectations, in terms of the single-particle twisted energy bands $\epsilon(\mathbf{k}_0 + \boldsymbol{\phi})$ and their band crossings. The band-crossing conditions

$$\epsilon(\mathbf{k}_0 + \boldsymbol{\phi}) = \epsilon(\mathbf{k}'_0 + \boldsymbol{\phi}) \tag{D.3.13}$$

define hypersurfaces in twist vector space separating regions in which the ground state selection is continuous, i.e. the P selected wave vectors $\{\mathbf{k}_1, \ldots, \mathbf{k}_P\}$ changes continuously as $\boldsymbol{\phi}$ is varied. Because each wave vector $\mathbf{k}_0 + \boldsymbol{\phi}$ samples one point in reciprocal space for each $\boldsymbol{\phi}$ within the First Brillouin Zone of the finite system (which is a subset of the First Brillouin Zone of the infinite system), we can also think of the hypersurfaces associated with the band-crossing conditions as defining a partition structure on the First Brillouin Zone of the infinite system.

Looking more closely into this BZ partition structure, we find its detailed structure depending on our choice of the finite system. In general, for a finite system of N sites in d dimensions, the BZ partition consists of a gross structure of large cells whose linear dimensions are on the order of $2\pi/N^{1/d}$. This gross structure is decorated by a fine structure of small cells, whose linear dimensions are on the order of $2\pi/N$, which is in turn decorated by a hyperfine structure consisting of very small cells whose linear dimensions are on the order of $2\pi/N^d$. This hierarchical structure of the BZ partition imposes a need to compromise between effort and fidelity when we numerically integrate over the First Brillouin Zone while performing twist boundary conditions averaging.

More importantly, we find that as we vary $\boldsymbol{\phi}$ over the entire finite-system FBZ, the

process of ground state selection picks out a subset of wave vectors $\mathbf{k}$ in the infinite-system FBZ. In the case of noninteracting spinless fermions, this subset of wave vectors, which consists of the union of various cells in the BZ partition, has a boundary that forms an approximate Fermi surface. For interacting fermions, we would be working with many-particle BZ partitions, the cells of which are labelled by the total momentum wave vector $\mathbf{q}$. We would then expect the union of many-particle ground-state selected cells in the BZ partition to give the approximate momentum distribution.

9.5.3 Twist Boundary Conditions Averaging Correlation Functions

Armed with our detailed understanding of how wave vector sampling leads to many-particle ground state selection, which implies a BZ partition structure, which in turn implies an approximate Fermi surface or momentum distribution, we went on in Section D.5 to investigate the twist boundary conditions averaging of various correlation functions, in particular, for those correlation functions which are given by the integral over the infinite-system FBZ of functions $f(\mathbf{k})$ of the wave vector $\mathbf{k}$, as well as of functions $g(\mathbf{K})$ of the momentum transfer $\mathbf{K} = \mathbf{k}' - \mathbf{k}$.

We find that for noninteracting spinless fermions in one dimension, the momentum distribution obtained by wave vector sampling and ground state selection is exact, for all filling fractions accessible to the finite system. Therefore, it is in principle possible to calculate the infinite-system FBZ average of any function $f(\mathbf{k})$ exactly through twist boundary conditions averaging. For noninteracting spinless fermions in two dimensions or higher, we find that the momentum distribution is always approximate, except at a small number of special filling fractions. The deviation of the twist boundary conditions averaged functions $f(\mathbf{k})$ from its infinite-system FBZ average then depends on how closely the approximate momentum distribution, which is determined by the size and

shape of the finite system, approaches the infinite-system momentum distribution.

For functions $g(\mathbf{K})$ of the momentum transfer $\mathbf{K}$, twist boundary conditions averaging was found to produce a poor approximation to the infinite-system FBZ average. This is because varying the twist vector $\boldsymbol{\phi}$ samples the same set of discrete $\mathbf{K}$'s as does periodic boundary conditions.

9.5.4 Numerical Integration Schemes

Since averaging an expectation over all twist vectors $\boldsymbol{\phi}$ in the finite-system FBZ is equivalent to integrating the expectation over the infinite-system FBZ, we want to know how to decide on a set of twist vectors $\{\boldsymbol{\phi}_i\}$ giving rise to a representative set of wave vectors $\{\mathbf{k}_j\}$ in the infinite-system FBZ. Thus, in Section D.6, we look into the possibility of adapting the two most popular numerical FBZ integration schemes used by the computational electronic structure community.

In Section D.6.2, we investigated the performance of the Monkhorst-Pack special point integration scheme, in integrating over the BZ partition, which features a hierarchy of gross, fine and hyperfine structures. We find that, if we work with a set of Monkhorst-Pack special points peppered uniformly over the infinite-system FBZ, the Monkhorst-Pack orders q for the special point integration scheme needed to integrate faithfully over the gross, fine and hyperfine structures are on the order of $N^{1/d}$, N and N^d respectively, working with a finite d-dimensional system with N sites. These Monkhorst-Pack orders can be reduced to the order of 1, $N^{(d-1)/d}$ and $N^{(d^2-1)/d}$, if the special points $\{\boldsymbol{\phi}_i\}$ are restricted to the finite-system FBZ.

Meanwhile, the residual finite size error, coming from the deviation of the momentum distribution sampled by twist boundary conditions averaging and the infinite-system momentum distribution, and determined predominantly by the gross structure of the BZ

partition, is on the order of N^{-1}. On the face of these order-of-magnitude estimates, it would appear profitable to increase N if we wish only to integrate faithfully gross and fine structures of the BZ partition. Of course, we should always be mindful of the $\exp(N)$ computational time expenditure needed for ED behind each special integration point.

In Section D.6.3, we investigated the performance of the tetrahedron integration scheme, which is the other integration scheme popular amongst computational electronic structure physicists for doing FBZ integration. We explained how the tetrahedron integration scheme sidesteps the problem of a proliferation of integration points needed to integrate faithfully the fine and hyperfine structures of the approximate momentum distribution sampled by twist boundary conditions averaging, by placing integration points only where they are needed. With this integration scheme, we can also capitalize on the observation, in Section D.4, that the twist surfaces of all observables are very nearly paraboloidal, by introducing quadratic-order interpolating functions (see Appendix E) to approximate the observable we are twist boundary conditions averaging.

Comparing the results of fine-structure tetrahedron integration with the results of Monkhorst-Pack special-point integration of various orders, we find that for the special-point integration scheme to have the same degree of precision as the tetrahedron integration scheme, very high Monkhorst-Pack orders must be used. However, we also acknowledged the difficulty of generating the fine-structure tetrahedron integration points, even though we described in Section D.6.6 an algorithm for doing so automatically. A coarse set of tetrahedron integration points, which can be deduced from symmetry, can also be used for tetrahedron integration, but we find that such a coarse tetrahedron integration mesh offers no advantage over low-order Monkhorst-Pack special-point integration, even with the use of quadratic-order shape functions.

9.6 Analytical Limits of Extended Spinless Hubbard Ladder

To help guide our numerical explorations in Chapter 8 of the ground-state phase diagram of the spinless extended Hubbard ladder with correlated hops (7.3.2), we undertook in Chapter 7 an ambitious program of developing a collection of analytical tools (see summary in Section 9.6.1), using which we calculate the ground-state wave function and various ground-state correlation functions in three limiting cases: (i) no inter-leg hopping (see summary in Section 9.6.2); (ii) strong inter-leg hopping (see summary in Section 9.6.3); and (iii) strong correlated hopping (see summary in Section 9.6.4).

9.6.1 Overview of Methods

In Section 7.4.3, 7.4.4 and 7.4.5, we developed a triplet of analytical maps that allowed us to write down the ground-state wave function of a nearest-neighbor excluded chain of hard-core bosons or spinless fermions in terms of the ground-state wave function of a nearest-neighbor included chain of hard-core bosons or spinless fermions.

The first of this triplet of maps, described in Section 7.4.3, is a configuration-to-configuration mapping from a nearest-neighbor excluded chain, in which nearest-neighbor occupation is not allowed, to a nearest-neighbor included chain, in which nearest-neighbor occupation is allowed. We explained how this mapping, which excludes the site to the right of every particle on the chain, turns a chain of spinless fermions with infinite nearest-neighbor repulsion into a chain of noninteracting spinless fermions, or a chain of hard-core bosons with infinite nearest-neighbor repulsion into a chain of hard-core bosons with no nearest-neighbor repulsion. We also explained how, because it is not one-to-one, this mapping alone does not allow us to write down the ground-state wave function of the nearest-neighbor excluded chain.

We then construct, in Section 7.4.4, a Bloch-state-Bloch-state mapping which is one-to-one, bringing us one step closer to our goal of writing the ground state of the nearest-neighbor excluded chain in terms of the ground state of the nearest-neighbor included chain. In this Bloch-state-to-Bloch-state map, we construct one nearest-neighbor excluded Bloch state for every nearest-neighbor included Bloch state. These two Bloch states do not contain the same number of configurations, but each configuration in the nearest-neighbor excluded Bloch state can be mapped to a configuration in the nearest-neighbor included Bloch state.

In Section 7.4.5, we described the wave-vector-to-wave-vector mapping, which is the final member of the triplet of maps. This map tells us which nearest-neighbor included chain wave vector q' is in one-to-one correspondence with a given nearest-neighbor excluded chain wave vector q. Combining the triplet of maps, we are then able to relate, one-to-one, each P-particle nearest-neighbor excluded chain energy eigenstate to a P-particle nearest-neighbor included chain energy eigenstate. A P-particle nearest-neighbor excluded chain energy eigenstate has the same energy eigenvalue, as well as the same set of normalized-Bloch-state amplitudes, as the P-particle nearest-neighbor included energy eigenstate it maps to. With these known sets of normalized-Bloch-state amplitudes, we can write down explicitly any nearest-neighbor excluded chain energy eigenstate, the ground state included.

In Sections 7.4.6 and 7.4.7, we described how one would make use of our explicit knowledge of the nearest-neighbor excluded chain ground state to calculate the various ground-state correlation functions. In Section 7.4.6, we first define the notion of corresponding observables, O on the nearest-neighbor excluded chain, and O' (which need not be of the same form as O) on the nearest-neighbor included chain, such that O and O' have the same matrix elements

$$\sum_{j_1} e^{-\mathrm{i}qj_1} \langle 0|A_{j_1+r_2+\cdots+r_P+P-1}\cdots A_{j_1}OA^\dagger_{j_1}\cdots A^\dagger_{j_1+r_2+\cdots+r_P+P-1}|0\rangle =$$

$$\sum_{j_1} e^{-\mathrm{i}q'j_1} \langle 0|a_{j_1+r_2+\cdots+r_P}\cdots a_{j_1}O'a^\dagger_{j_1}\cdots a^\dagger_{j_1+r_2+\cdots+r_P}|0\rangle\,, \quad (7.4.94)$$

where A_j and $A^\dagger_j$ are annihilation and creation operators on the nearest-neighbor excluded chain, while $a_{j'}$ and $a^\dagger_{j'}$ are annihilation and creation operators on the nearest-neighbor included chain, in the bases of unnormalized Bloch states of the nearest-neighbor excluded and nearest-neighbor included chains respectively. We then showed that the expectation $\langle O\rangle$ of O in the energy eigenstate $|\Psi(q)\rangle$ of the nearest-neighbor excluded chain and the expectation $\langle O'\rangle$ of O' in the energy eigenstate $|\Psi'(q')\rangle$ of the nearest-neighbor included chain are related by

$$\langle O\rangle = \frac{\bar{N}}{\bar{n}}\langle O'\rangle\,, \quad (7.4.97)$$

where $\bar{N}$ and $\bar{n}$ are the filling fractions on the nearest-neighbor excluded and nearest-neighbor included chains respectively, if $|\Psi(q)\rangle$ is mapped to $|\Psi'(q')\rangle$ by the triplet of maps described in Sections 7.4.3, 7.4.4 and 7.4.5.

With this essential ingredient at hand, we then developed in Section 7.4.7 the technique of intervening-particle expansion, where we first write the nearest-neighbor excluded chain expectation $\langle O_jO_{j+r}\rangle$ as a series expansion

$$\begin{aligned}\langle O_jO_{j+r}\rangle = {} & \langle O_j(\mathbb{1}-N_{j+1})\cdots(\mathbb{1}-N_{j+r-1})O_{j+r}\rangle + \\ & \langle O_jN_{j+1}\cdots(\mathbb{1}-N_{j+r-1})O_{j+r}\rangle + \cdots + \langle O_j(\mathbb{1}-N_{j+1})\cdots N_{j+r-1}O_{j+r}\rangle + \\ & \langle O_jN_{j+1}N_{j+2}\cdots(\mathbb{1}-N_{j+r-1})O_{j+r}\rangle + \cdots + \\ & \langle O_j(\mathbb{1}-N_{j+1})\cdots N_{j+r-2}N_{j+r-1}O_{j+r}\rangle + \cdots + \langle O_jN_{j+1}N_{j+2}\cdots N_{j+r-1}O_{j+r}\rangle\end{aligned} \quad (7.4.99)$$

of terms in which the sites between j and $j+r$ are conditionally filled or empty.

After sorting out which of these conditional expectations vanish due to the nearest-neighbor exclusion, we can evaluate the nonzero conditional expectations by constructing the corresponding observables and calculating the nearest-neighbor included chain ground-state conditional expectations. The expectation $\langle O_j O_{j+r} \rangle$ is recovered at the end by summing over the nearest-neighbor included chain ground-state conditional expectations. This completes the set of analytical tools we need to calculate the ground states and ground-state correlations in three limiting cases of the spinless extended Hubbard ladder with correlated hops.

9.6.2 Weak Inter-Leg Hopping Limit

In Section 7.6, we completely suppressed correlated and inter-leg hopping, so that the two legs of the ladder are coupled only by the infinite nearest-neighbor repulsion between particles. In this particularly simple limit, we argued in Section 7.6.1 that all configurations that occur in the ladder ground state are staggered, i.e. the two legs are alternately occupied. We find that two staggered configurations related to one another by a reflection about the ladder axis can be mapped to the same nearest-neighbor included chain configuration of noninteracting spinless fermions. The two-fold degenerate ground state can thus be written directly,

$$|\Psi_{\pm}\rangle = \sum_{j_1} \cdots \sum_{j_P} A(k_1, \ldots, k_P; j_1, \ldots, j_P) \times \frac{1}{\sqrt{2}} \left(c^{\dagger}_{1,j_1} c^{\dagger}_{2,j_2} \cdots c^{\dagger}_{1,j_{P-1}} c^{\dagger}_{2,j_P} \pm c^{\dagger}_{2,j_1} c^{\dagger}_{1,j_2} \cdots c^{\dagger}_{2,j_{P-1}} c^{\dagger}_{1,j_P} \right) |0\rangle \,, \quad (7.6.3)$$

in terms of the ground state

$$|\Psi_F\rangle = \sum_{j_1} \cdots \sum_{j_P} A(k_1, \ldots, k_P; j_1, \ldots, j_P)\, c^{\dagger}_{j_1} c^{\dagger}_{j_2} \cdots c^{\dagger}_{j_{P-1}} c^{\dagger}_{j_P} |0\rangle \quad (7.6.2)$$

of the nearest-neighbor included chain of noninteracting spinless fermions.

Based on the staggered nature of the ladder ground state in this limit, we explained in Section 7.6.2 why Fermi-liquid (FL) correlations of the form $\langle c^\dagger_{i,j} c_{i',j+r} \rangle$, where $i \neq i'$, vanish, and also developed a restricted probability argument explaining why FL correlations of the form $\langle c^\dagger_{i,j} c_{i',j+r} \rangle$ must decay exponentially. This restricted probability argument relies on the fact that the only configurations making nonzero contributions to the FL correlations form a restricted class with exponentially small total weight in the space of all ground-state configurations.

Then, in Sections 7.6.3 and 7.6.4 respectively, we calculated the charge-density-wave (CDW) and superconducting (SC) correlations in the staggered ground state, with the help of the intervening-particle expansion. By summing over the intervening-particle expansion numerically where necessary, we find that both CDW and SC correlations decay as power laws, with leading correlation exponents $\alpha_+ = 2$, $\alpha_- = \frac{1}{2}$, and $\beta_+ = 2$, $\beta_- = \frac{5}{2}$ respectively. Here, the + sign indicates that the order parameter is symmetric with respect to reflection about the ladder axis, and the − sign indicates that the order parameter is antisymmetric with respect to reflection about the ladder axis. Thus we find that the CDW− correlations dominate at large distances.

9.6.3 Strong Inter-Leg Hopping Limit

In Section 7.7, we continue to suppress the correlated hopping, but take the inter-leg hopping amplitude to be large compared to the intra-leg hopping amplitude. We argued in Section 7.7.1 that in this limit, the spinless fermions spend most of their time hopping back and forth along the rungs, and the ladder system can be thought of as a chain of interacting rung fermions, which live in the middle of the rungs. Using the triplet of maps described in Sections 7.4.3, 7.4.4 and 7.4.5, we mapped this chain of interacting rung fermions with infinite nearest-neighbor repulsion to a chain of noninteracting spinless

fermions, and write down the rung-fermion ground state

$$|\Psi\rangle = \sum_{r_2>0} \cdots \sum_{r_P>0} \Psi_F(k_1, \ldots, k_P; r_2, \ldots, r_P) \, |q = 0; r_2, \ldots, r_P\rangle_{\text{rung}} \, . \tag{7.7.6}$$

in terms of the ground state

$$|\Psi_F\rangle = \sum_{r_2>0} \cdots \sum_{r_P>0} \Psi_F(k_1, \ldots, k_P; r_2, \ldots, r_P) \, |q'; r_2, \ldots, r_P\rangle_{\text{chain}} \, , \tag{7.7.3}$$

of the chain of noninteracting spinless fermions. Here

$$|q'; r_2, \ldots, r_P\rangle_{\text{chain}} \propto \sum_{j_1} e^{-\mathrm{i}\, q' j_1} \, c^\dagger_{j_1} c^\dagger_{j_1+r_2} \cdots c^\dagger_{j_1+r_2+\cdots+r_P} \, |0\rangle \tag{7.7.4}$$

are the normalized nearest-neighbor included Bloch states, while

$$|q; r_2, \ldots, r_P\rangle_{\text{rung}} \propto \sum_{j_1} e^{-\mathrm{i}\, q j_1} \, C^\dagger_{j_1} C^\dagger_{j_1+r_2+1} \cdots C^\dagger_{j_1+r_2+\cdots+r_P+P-1} \, |0\rangle \tag{7.7.5}$$

are the the normalized rung-fermion Bloch states, with $c^\dagger_{j'}$ and $C^\dagger_j$ being spinless fermion and rung fermion creation operators on the nearest-neighbor included chain and ladder respectively.

We explained, based on the simple need of the rung fermions to satisfy nearest-neighbor exclusion, that at quarter-filling, every other rung will be occupied, and the rung fermions will not be able to hop along the legs of the ladder. This gives rise to a dynamic 'solid' of rung fermions, which are still free to hop along the rungs. Above quarter-filling, we argued that the system of rung fermions phase separates into a high-density inert solid phase with filling fraction $\bar{n} = \frac{1}{2}$, within which the spinless fermion are not free to hop along the rungs, and a low-density dynamic solid phase of rung fermions, with filling fraction $\bar{n} = \frac{1}{4}$.

After explaining why the FL and SC correlations vanish when the ladder is quarter-filled, and we end up with a long-range CDW order in this limit at the beginnings of Sections 7.7.2 and 7.7.4, we move on to calculate the various correlations at $\bar{n} < \frac{1}{4}$.

In Sections 7.7.2, 7.7.3 and 7.7.4, we find, using the triplet of maps described in Sections 7.4.3, 7.4.4 and 7.4.5, as well as the machineries of corresponding observables and intervening-particle expansion in Sections 7.4.6 and 7.4.7, that the simplest FL, CDW and SC correlations that we can constructed on the ladder all decay as power laws. By nonlinear curve fitting the correlations obtained by numerically summing over the intervening-particle expansion, we obtained a bewildering collection of correlation exponents, some of which we judged to be more reliable, and others we judged to be less reliable. The leading FL, CDW, and SC correlation exponents which we believed to be reliable are $\nu = \frac{1}{4}$, $\alpha = \frac{1}{2}$, and $\beta = \frac{1}{8}$. We thus discover that the SC correlations dominate at large distances.

9.6.4 Strong Correlated Hopping Limit

in Section 7.5, we make the correlated hopping amplitude large compared to the intra-leg and inter-leg hopping amplitudes. In this strong correlated hopping limit, we argued in Section 7.5.1 that the spinless fermions become tightly bound into correlated hopping pairs, and the effective degrees of freedom become these bosonic bound pairs. Each bound pair lives on a plaquette of the two-legged ladder, and because there are two ways to put two spinless fermions at the four corners of a plaquette without them being nearest neighbors of each other, we have two possible flavors of bound pairs, whose creation operators we can write as

$$B^\dagger_{j,+} = \begin{cases} c^\dagger_{1,j} c^\dagger_{2,j+1}, & j \text{ odd}; \\ c^\dagger_{1,j+1} c^\dagger_{2,j}, & j \text{ even}, \end{cases} \tag{7.5.2}$$

and

$$B^{\dagger}_{j,-} = \begin{cases} c^{\dagger}_{1,j+1} c^{\dagger}_{2,j}, & j \text{ odd}; \\ c^{\dagger}_{1,j} c^{\dagger}_{2,j+1}, & j \text{ even}. \end{cases} \tag{7.5.3}$$

The flavor of a bound pair is conserved, when one spinless fermion in the bound pair performs a correlated hop, and the bound pair moves over to the next plaquette. We can therefore map a ladder of bound pairs to a chain of hard-core bosons, which inherit the infinite nearest-neighbor repulsion from their constituent spinless fermions. As a result of this infinite nearest-neighbor repulsion, two hard-core bosons of the same flavor can approach each other to within two sites on the chain, while two hard-core bosons of different flavors can approach each other to within three sites on the chain. There are therefore two degenerate ground states, consisting of hard-core bosons of a single flavor, because each hard-core boson would then have the largest average chain length to hop along.

Using the triplet of maps described in Sections 7.4.3, 7.4.4 and 7.4.5 to map these two single-flavor nearest-neighbor excluded chain of hard-core bosons to the respective nearest-neighbor included chain of hard-core bosons, which can in turn to mapped to a chain of noninteracting spinless fermions using the Jordan-Wigner transformation described in Section 7.4.1, we can finally write the two-fold degenerate ground-state wave functions

$$|\Psi_{\pm}\rangle = \sum_{r_2>0} \cdots \sum_{r_P>0} |\Psi_F(k_1, \ldots, k_P; r_2, \ldots, r_P)| \, |q = 0; r_2, \ldots, r_P\rangle_{\pm} \,, \tag{7.5.34}$$

in terms of the ground state

$$|\Psi_F\rangle = \sum_{r_2>0} \cdots \sum_{r_P>0} \Psi_F(k_1, \ldots, k_P; r_2, \ldots, r_P) \, |q' = 0; r_2, \ldots, r_P\rangle \tag{7.7.3}$$

of the chain of noninteracting spinless fermions. Here,

$$|q'; r_2, \ldots, r_P\rangle_{\text{chain}} \propto \sum_{j_1} e^{-\mathrm{i}\, q' j_1} \, c^{\dagger}_{j_1} c^{\dagger}_{j_1+r_2} \cdots c^{\dagger}_{j_1+r_2+\cdots+r_P} |0\rangle \tag{7.7.4}$$

are the normalized nearest-neighbor included Bloch states, while

$$|q; r_2, \ldots, r_P\rangle_\pm \propto \sum_{j_1} e^{-\mathrm{i}\, q j_1}\, B^\dagger_{j_1,\pm} B^\dagger_{j_1+r_2+1,\pm} \cdots B^\dagger_{j_1+r_2+\cdots+r_P+P-1,\pm} |0\rangle \tag{7.5.35}$$

are the normalized Bloch states of the nearest-neighbor excluded chain of hard-core bosons.

In Section 7.5.8, we explained why the only infinite-ladder configurations that can contribute nontrivially to FL correlations of the form $\langle c^\dagger_{i,j} c_{i,j+r}\rangle$ are those containing a contiguous cluster of $p = r/2$ bound pairs, and therefore $\langle c^\dagger_{i,j} c_{i,j+r}\rangle$ is essentially the probability of finding contiguous clusters of p bound pairs in the ground state. Noting that this probability, after invoking the Jordan-Wigner transformation described in Section 7.4.1, is approximately the p-particle density-matrix weight of a cluster of p sites within a chain of noninteracting spinless fermions, we apply our results from Chapter 3, on how the single-particle pseudo-energies scale with p to conclude that the FL correlations decay exponentially with the number of contiguous bound pairs p, and hence also with the separation r, with a density-dependent correlation length.

In Sections 7.5.7 and 7.5.6, we calculated the bound-pair-bound-pair density-density correlation, which we called the CDW-π correlations, and the SC correlations using the intervening-particle expansion. After summing over terms in the intervening-particle expansions for various separations, and performing nonlinear curve fitting on the correlations for series of filling fractions, we find that both decay as power laws: the SC correlations with leading universal correlation exponent $\beta = \frac{1}{2}$, while the CDW-π correlations with leading non-universal correlation exponent $\alpha = \frac{1}{2} + \frac{5}{2}(\frac{1}{2} - \bar{N}_1)$, where $\bar{N}_1$ is the density of bound pairs. Therefore, in this limit of strong correlated hopping, we find that the CDW-π and SC correlations are equally important at large distances when the two-legged ladder is half-filled. Below half-filling, the SC correlations dominate at large distances.

APPENDIX A

CORRELATION FUNCTIONS IN A ONE-DIMENSIONAL FERMI SEA

In this short appendix, we calculate the two-point functions of a one-dimensional Fermi sea in Section A.1. Following this, we show in Section A.2 how the $2n$-point functions of the one-dimensional Fermi sea can be written as the $n \times n$ determinant of two-point functions.

A.1 Two-Point Functions

For spinless fermions in a one-dimensional system of N sites, the coordinate space annihilation and creation operators, c_j and $c_j^\dagger$, and the momentum space annihilation and creation operators, $\tilde{c}_k$ and $\tilde{c}_k^\dagger$, are related to each other by

$$\begin{aligned} c_j &= \frac{1}{\sqrt{N}} \sum_k e^{-\mathrm{i}kj} \tilde{c}_k, \qquad & \tilde{c}_k &= \frac{1}{\sqrt{N}} \sum_j e^{\mathrm{i}kj} c_j, \\ c_j^\dagger &= \frac{1}{\sqrt{N}} \sum_k e^{\mathrm{i}kj} \tilde{c}_k^\dagger, \qquad & \tilde{c}_k^\dagger &= \frac{1}{\sqrt{N}} \sum_j e^{-\mathrm{i}kj} c_j^\dagger. \end{aligned} \tag{A.1.1}$$

For noninteracting spinless fermions, the Hamiltonian

$$H = \sum_k \epsilon_k \tilde{c}_k^\dagger \tilde{c}_k \tag{A.1.2}$$

is diagonal in momentum space, and the ground state is a Fermi sea. For the rest of this appendix, we shall assume that ϵ_k is monotonically increasing in the FBZ, so that the occupied wave vectors form a single interval $-k_F \le k \le k_F$. For $\bar{n}$ spinless fermions per site, the Fermi wave vector is given by $k_F = \bar{n}\pi$.

The most important Fermi-sea correlations that we can calculate are the two-point functions

$$\langle c_{j_1}^\dagger c_{j_2} \rangle = \frac{1}{N} \sum_{k_1} \sum_{k_2} e^{\mathrm{i}k_1 j_1} \, e^{-\mathrm{i}k_2 j_2} \, \langle \tilde{c}_{k_1}^\dagger \tilde{c}_{k_2} \rangle \, . \tag{A.1.3}$$

Since the momentum-space expectation $\langle \tilde{c}^\dagger_{k_1} \tilde{c}_{k_2} \rangle$ is only nonzero when $k_1 = k_2$ is one of the occupied wave vectors, we have

$$\langle c^\dagger_{j_1} c_{j_2} \rangle = \frac{1}{N} \sum_{\substack{k_1 \\ \text{occupied}}} e^{\mathrm{i}\, k_1 (j_1 - j_2)} = \frac{1}{N} \sum_{|k_1| \le \bar{n}\pi} e^{\mathrm{i}\, k_1 (j_1 - j_2)}. \tag{A.1.4}$$

Replacing the sum by an integral, we find that

$$\langle c^\dagger_{j_1} c_{j_2} \rangle = \frac{1}{N} \sum_{|k_1| \le \bar{n}\pi} e^{\mathrm{i}\, k_1 (j_1 - j_2)} = \int_{-\bar{n}\pi}^{+\bar{n}\pi} \frac{dk}{2\pi}\, e^{\mathrm{i}\, k (j_1 - j_2)} = \frac{\sin \bar{n}\pi |j_1 - j_2|}{\pi |j_1 - j_2|}. \tag{A.1.5}$$

A.2 2*n*-Point Functions

In a Fermi sea, the $2n$-point functions

$$\langle c^\dagger_{i_1} \cdots c^\dagger_{i_n} c_{j_1} \cdots c_{j_n} \rangle = \frac{1}{N^n} \sum_{k_1} \cdots \sum_{k_n} \sum_{k'_1} \cdots \sum_{k'_n} \times$$
$$e^{\mathrm{i}\, k_1 i_1} \cdots e^{\mathrm{i}\, k_n i_n}\, e^{-\mathrm{i}\, k'_1 j_1} \cdots e^{-\mathrm{i}\, k'_n j_n}\, \langle \tilde{c}^\dagger_{k_1} \cdots \tilde{c}^\dagger_{k_n} \tilde{c}_{k'_1} \cdots \tilde{c}_{k'_n} \rangle \tag{A.2.1}$$

receive nonzero contributions only from those momentum-space expectations in which the list of wave vectors $\{k'_1, \ldots, k'_n\}$ is identical, up to permutations, to the list of wave vectors $\{k_1, \ldots, k_n\}$, and all wave vectors in the list $\{k_1, \ldots, k_n\}$ are occupied in the Fermi sea. For a list of n occupied wave vectors $\{k_1, \ldots, k_n\}$, there are $n!$ permutations $\{k'_1, \ldots, k'_n\}$ for which $\langle \tilde{c}^\dagger_{k_1} \cdots \tilde{c}^\dagger_{k_n} \tilde{c}_{k'_1} \cdots \tilde{c}_{k'_n} \rangle$ is nonzero.

Now, if $\{k'_1, \ldots, k'_n\}$ is an even permutation of $\{k_n, \ldots, k_1\}$, an even number of pairwise exchanges are needed to reorder the fermion operators in the expectation to give $\langle \tilde{c}^\dagger_{k_1} \cdots \tilde{c}^\dagger_{k_n} \tilde{c}_{k_n} \cdots \tilde{c}_{k_1} \rangle$. An even permutation therefore contributes $+\langle \tilde{c}^\dagger_{k_1} \cdots \tilde{c}^\dagger_{k_n} \tilde{c}_{k_n} \cdots \tilde{c}_{k_1} \rangle = +1$ to the expectation. On the other hand, if $\{k'_1, \ldots, k'_n\}$ is an odd permutation of $\{k_n, \ldots, k_1\}$, an odd number of pairwise exchanges are needed to reorder the fermion operators in the expectation to give $\langle \tilde{c}^\dagger_{k_1} \cdots \tilde{c}^\dagger_{k_n} \tilde{c}_{k_n} \cdots \tilde{c}_{k_1} \rangle$. An odd permutation therefore contributes $-\langle \tilde{c}^\dagger_{k_1} \cdots \tilde{c}^\dagger_{k_n} \tilde{c}_{k_n} \cdots \tilde{c}_{k_1} \rangle = -1$ to the expectation. Let us write the the list of

wave vectors that $\{k'_1, \ldots, k'_n\}$ reorders into as $\{k'_{\pi(1)}, k'_{\pi(2)}, \ldots, k'_{\pi(n)}\}$, in terms of the permutation π of n numbers, so that $k'_{\pi(1)} = k_1, k'_{\pi(2)} = k_2, \ldots, k'_{\pi(n)} = k_n$.

With this notation, we can write the $2n$-point function as

$$\begin{aligned}\langle c^\dagger_{i_1} \cdots c^\dagger_{i_n} c_{j_1} \cdots c_{j_n} \rangle &= \frac{1}{N^n} \sum_{\substack{k_1 \\ \text{occupied}}} \cdots \sum_{\substack{k_n \\ \text{occupied}}} \sum_{\pi} \sigma(\pi)\, e^{\mathrm{i}\, k_1 (i_1 - j_{\pi(1)})} \cdots e^{\mathrm{i}\, k_n (i_n - j_{\pi(n)})} \\ &= \sum_{\pi} \sigma(\pi) \left(\frac{1}{N} \sum_{\substack{k_1 \\ \text{occupied}}} e^{\mathrm{i}\, k_1 (i_1 - j_{\pi(1)})} \right) \cdots \left(\frac{1}{N} \sum_{\substack{k_n \\ \text{occupied}}} e^{\mathrm{i}\, k_n (i_n - j_{\pi(n)})} \right) \qquad \text{(A.2.2)} \\ &= \sum_{\pi} \sigma(\pi)\, \langle c^\dagger_{i_1} c_{j_{\pi(1)}} \rangle \cdots \langle c^\dagger_{i_n} c_{j_{\pi(n)}} \rangle ,\end{aligned}$$

which is the *Wick factorization* of the $2n$-point function $\langle c^\dagger_{i_1} \cdots c^\dagger_{i_n} c_{j_1} \cdots c_{j_n} \rangle$. Here $\sigma(\pi) = \pm 1$ is the sign associated with the permutation π.

We can write the $2n$-point function more succinctly as

$$\langle c^\dagger_{i_1} \cdots c^\dagger_{i_n} c_{j_1} \cdots c_{j_n} \rangle = (-1)^{\frac{n(n-1)}{2}} \begin{vmatrix} \langle c^\dagger_{i_1} c_{j_1} \rangle & \langle c^\dagger_{i_1} c_{j_2} \rangle & \cdots & \langle c^\dagger_{i_1} c_{j_n} \rangle \\ \langle c^\dagger_{i_2} c_{j_1} \rangle & \langle c^\dagger_{i_2} c_{j_2} \rangle & \cdots & \langle c^\dagger_{i_2} c_{j_n} \rangle \\ \vdots & \vdots & \ddots & \vdots \\ \langle c^\dagger_{i_n} c_{j_1} \rangle & \langle c^\dagger_{i_n} c_{j_2} \rangle & \cdots & \langle c^\dagger_{i_n} c_{j_n} \rangle \end{vmatrix} \qquad \text{(A.2.3)}$$

in the form of a determinant of two-point functions. The factor of $(-1)^{n(n-1)/2}$ is to ensure that the term $\langle c^\dagger_{i_1} c_{j_n} \rangle \langle c^\dagger_{i_2} c_{j_{n-1}} \rangle \cdots \langle c^\dagger_{i_n} c_{j_1} \rangle$ appears with a positive sign in the Wick factorization.

APPENDIX B

MATRIX BLOCK INVERSION FORMULA

Consider a square $N \times N$ symmetric matrix $\mathscr{M}$ written in matrix block form as

$$\mathscr{M} = \begin{bmatrix} A & B \\ B^T & C \end{bmatrix}, \tag{B.0.1}$$

where A is a square $N_1 \times N_1$ symmetric matrix, B is a $N_1 \times N_2$ non-square matrix and C is a square $N_2 \times N_2$ symmetric matrix. Here $N_1 + N_2 = N$.

If we write the inverse matrix $\mathscr{M}^{-1}$ also in the matrix block form

$$\mathscr{M}^{-1} = \begin{bmatrix} D & E \\ E^T & F \end{bmatrix}, \tag{B.0.2}$$

where D is a square $N_1 \times N_1$ symmetric matrix, E is a $N_1 \times N_2$ non-square matrix and F is a square $N_2 \times N_2$ symmetric matrix, how are D, E and F related to the matrix blocks A, B and C in $\mathscr{M}$?

Using the fact that $\mathscr{M}\mathscr{M}^{-1} = \mathbb{1}$, and thus

$$\begin{bmatrix} A & B \\ B^T & C \end{bmatrix} \begin{bmatrix} D & E \\ E^T & F \end{bmatrix} = \begin{bmatrix} \mathbb{1}_{N_1 \times N_1} & \mathbb{0}_{N_1 \times N_2} \\ \mathbb{0}_{N_2 \times N_1} & \mathbb{1}_{N_2 \times N_2} \end{bmatrix}, \tag{B.0.3}$$

(where the subscripts, which will henceforth be dropped for notational clarity, following the $\mathbb{1}$'s and $\mathbb{0}$'s indicate the shape and size of the matrices) we find the following relations between the matrix blocks of $\mathscr{M}$ and $\mathscr{M}^{-1}$:

$$AD + BE^T = \mathbb{1}, \tag{B.0.4a}$$

$$AE + BF = \mathbb{0}, \tag{B.0.4b}$$

$$B^T D + CE^T = \mathbb{0}, \tag{B.0.4c}$$

$$B^T E + CF = \mathbb{1}. \tag{B.0.4d}$$

Solving for D, E and F in terms of A, B and C, we find that

$$D = \left[A - BC^{-1}B^T\right]^{-1}, \tag{B.0.5a}$$

$$E = -A^{-1}B\left(C - B^TA^{-1}B\right)^{-1}, \tag{B.0.5b}$$

$$F = \left[C - B^TA^{-1}B\right]^{-1}. \tag{B.0.5c}$$

APPENDIX C

THE OCTAVE CODE BASE

C.1 Overview

C.1.1 A Quick Guide to Appendix C

This appendix documents the Octave code base we developed to exactly diagonalize finite strongly-interacting quantum lattice systems subject to various boundary conditions, to yield numerical ED ground-state wave functions, which we then use to:

1. compute and analyze the reduced density matrix of a contiguous cluster of sites within the finite system; and

2. compute, and operator singular value decompose the correlation density matrix of two or more disjoint clusters within the finite system.

The Octave code base has been actively developed for the extended Hubbard model of spinless fermions with infinite nearest-neighbor repulsion, but carry barely-functional provisions for also working with hard-core bosons with infinite nearest-neighbor repulsion, on a square lattice or a two-legged ladder.

Apart from the customary listing of codes, we will also, where appropriate, discuss code design choices and describe important algorithms. Where we have, as a simple of code evolution, come up with several algorithms that perform the same task, for example, constructing the P-particle Hilbert space, or computing the Hamiltonian matrix, we will also give a sense of the computational complexities for each algorithm, and make an estimate of the savings in computational time involved.

In the remainder of this section, we will briefly introduce the Octave language in Section C.1.2. Then in Section C.1.3, we will very briefly describe the strongly-

interacting hard-core boson and spinless fermion models that the code base is designed to handle. Finally, in Section C.1.4, we will describe the general design philosophy we adopt for the Octave code base, and how the code base is organized.

The documentation of the Octave code base in this appendix can be broken up into three main parts: (i) exact diagonalization (Sections C.2, C.3, C.4, C.5, and C.6); (ii) cluster density-matrix computation (Sections C.8 and C.9); and (iii) correlation density-matrix computation (Section C.11). There is also a minor part in Section C.10 documenting auxiliary codes for computing the cluster density matrix of a system of noninteracting spinless fermions.

In the first main part, we document the Octave code base intended for ED. In Section C.2, we document the functions which automatically generate:

1. the list of sites in finite systems with various shapes and sizes (Section C.2.1);

2. the list of nearest neighbors (Section C.2.2) and next-nearest neighbors (Section C.2.3) of each site in a given finite system;

3. the list of reciprocal lattice vectors in the First Brillouin Zone (Section C.2.4).

We also document in this section miscellaneous utility functions (Sections C.2.5 and C.2.6).

In Section C.3, we lay out in Section C.3.1 our conventions for the occupation number basis states that we are adopting for our ED computations, before launching into a detailed discussions on several algorithms to build up the P-particle Hilbert space in Section C.3.2. Following this, we describe in Section C.4 several algorithms to generate the Hamiltonian matrix, full or as a compact array of the nonzero elements, for hard-core bosons (Section C.4.1) or spinless fermions (Section C.4.2), described by the Hamiltonians (C.1.1) and (C.1.2) respectively, and also how to calculate the additional

nonzero matrix elements when the correlated hopping term (C.1.3) is introduced (Section C.4.5). For our numerical work in Chapter 8, the spinless fermion Hamiltonian C.1.2 must be made anisotropic, with one hopping matrix element along the x-direction, and another hopping matrix element along the y-direction. This results in the Hamiltonian (7.3.2), whose matrix must be computed from scratch, with a function described in Section C.4.5.

We then move on to describe how we can take advantage of translational symmetry in the ED in Section C.5. In Section C.5.1, we describe functions that apply any given translation on a P-particle configuration, and handle any fermion sign that is incurred. In Section C.5.2, we describe an algorithm that would partition the P-particle Hilbert space into translation-equivalence classes of P-particle configurations, and document the functions that implements this algorithm. In Section C.5.3, we then document the functions that make use of the translation-equivalence classes of P-particle configurations to construct the P-particle Bloch states for various allowed wave vectors. Finally, in Section C.6, we document the functions that construct the Bloch-reduced Hamiltonian matrices for each allowed wave vector (Sections C.6.1 and C.6.2) and perform the desired ED (Section C.7).

In the second main part, we document the code base intended for computing the cluster density matrix. In Section C.8, we describe the algorithms needed to reshape the vector array for the ED ground-state wave function into an appropriate matrix of amplitudes, for each P_C-particle sector of the cluster density matrix, so that the trace over the environment of the cluster can be implemented as a matrix-matrix multiplication. In Section C.9, we discuss various averaging schemes needed to ensure that the finite-system cluster density-matrix spectrum approximates, as best as it is possible, the infinite-system cluster density-matrix spectrum.

In the third main part, we document the code base intended for computing the correlation density matrix and operator singular value decompose it. This is done in Section C.11, where we describe how we would compute the cluster and supercluster Fock-Hilbert spaces (Section C.11.1), using which we concatenate the various P_C-particle sectors of the cluster and supercluster density matrices into one compact array (Section C.11.2), and thereafter organize the matrix elements of the correlation density matrix into a correlation-**K** matrix (Sections C.11.3 and C.11.4).

C.1.2 GNU Octave

GNU Octave [202], written by John W. Eaton *et al*, is a high-level language intended primarily for numerical computations, either within a convenient command line interface (where graphing functionalities are provided by gnuplot [382]), or as a batch script.

Octave provides an extensive set of tools that are for the most parts compatible with the proprietary Matlab for solving common numerical linear algebra problems, finding the roots of nonlinear equations, integrating ordinary functions, manipulating polynomials, and integrating ordinary differential and differential-algebraic equations. This set of functionalities can be easily extended via user-defined functions written in Octave's own language, or using dynamically loaded modules written in C++, C, Fortran, or other languages.

GNU Octave is available under the terms of the GNU General Public License (GPL), as published by the Free Software Foundation.

C.1.3 Model Hamiltonians

The Octave code base was developed primarily for two prototypical strongly interacting systems in two dimensions: (i) a system of bosons described by the Hamiltonian

$$H = -t \sum_{\langle i,j \rangle} \left(a_i^\dagger a_j + a_j^\dagger a_i \right) + U \sum_i n_i \left(n_i - 1 \right) + V \sum_{\langle i,j \rangle} n_i n_j, \tag{C.1.1}$$

where $a_i^\dagger$ and a_j are bosonic creation and annihilation operators, $n_i = a_i^\dagger a_i$ and $n_j = a_j^\dagger a_j$ are bosonic occupation number operators at sites i and j respectively; and (ii) a system of spinless fermions described by the Hamiltonian

$$H = -t \sum_{\langle i,j \rangle} \left(c_i^\dagger c_j + c_j^\dagger c_i \right) + V \sum_{\langle i,j \rangle} n_i n_j, \tag{C.1.2}$$

where $c_i^\dagger$ and c_j are fermionic creation and annihilation operators, $n_i = c_i^\dagger c_i$ and $n_j = c_j^\dagger c_j$ are fermionic occupation number operators at sites i and j respectively.

In the limit of $U \to \infty$, the bosonic occupation number at any site i cannot exceed 1, i.e. the bosons become hardcore, and in the limit of $V \to \infty$, occupied sites cannot be nearest neighbors of each other for both models. In this dual limit, the bosonic and fermionic Hilbert spaces for a system of N sites with P particles are identical. This allows the boson and fermion branches of the code base, which only deals with this dual limit of $U, V \to \infty$, to share common functions.

Apart from these two prototypical strongly interacting systems, we are also interested in a fermion model derived from (C.1.2) by augmenting the nearest neighbor repulsion term $V \sum_{\langle i,j \rangle} n_i n_j$ with a correlated hopping term

$$\tilde{V} = -t' \sum_{\langle\langle i,j,k \rangle\rangle} \left(c_i^\dagger n_j c_k + c_k^\dagger n_j c_i \right), \tag{C.1.3}$$

where sites i and k are next-nearest neighbors of site j. This is one of the many possible terms derived by Zhang and Henley from the nearest neighbor repulsion term using second-order perturbation theory in the limit of large but finite V [205].

C.1.4 Design and Organization

C.1.4.1 Design

In all software design, there is a constant tension between *extensibility* and *efficiency*. In general, to make a piece of code efficient, i.e. using the least amount of memory and accomplishing the given task in the shortest time (these two requirements may themselves conflict sometimes), the basic strategy is to invoke the least number of function calls, and for those function calls which are unavoidable, to minimize the depth of nested function calls. This is because a function call of the form `y = f(x)` breaks the local control flow to do a function lookup, incurring an overhead in computational time. The function call also creates a copy of the variable `x`, a further overhead in computational time, and also increases the memory usage of the overall program.

Time and memory overheads of this sorts can be eliminated by *inlining*, where the function body of `f(x)` is inserted at the points of the function calls. However, this practice gives rise to unwieldingly large and error-prone codes, which are a nightmare to maintain, debug, and extend. Hence the decision to sacrifice some computational efficiency for a code base that is designed from ground up to be modular.

The modularity of the code base is fine-grained into three function types, which I call helper, core, and wrapper functions. Helper function are small functions which perform a specific task, and are repetitively called by various core functions. Isolation of helper functions makes it easy for debugging and maintenance, and less efficient helper functions can be easily substituted for with more efficient helper functions if they have the same interface. Core functions are large functions which do the bulk of the time and memory consuming calculations, and these are the ones that our optimization efforts are targeted at. Wrapper functions are small functions which does nothing by themselves,

but only perform preliminary processing of the argument list, and determine which core functions to call upon.

C.1.4.2 Organization

The Octave code base described in this appendix is different from the one in Java developed by Naigong Zhang, who did a thesis involving the numerical ED studies of the models described by (C.1.1) and (C.1.2) [383]. The code base is organized into four directories, as shown in Figure C.1. The four directories are at the same level, but `Common/` contains functions common to the other directories. These essentially perform the functions of defining the system, providing system-related utilities, defining the Hilbert space, wrapper functions for tracing down a ground-state wave function to obtain a cluster density matrix, and functions effecting various averaging machineries.

`Boson/` and `Fermion/` essentially contain parallel sets of functions dedicated to bosonic and fermionic calculations, except that the fermion code base is further along in development than the boson code base. These contain functions building up the full Hamiltonian matrix of the system with various number of particles, building up many-body Bloch states to take advantage of translational symmetry, and to build up various Bloch-reduced Hamiltonian matrices for exact diagonalization, the machinery for twist boundary conditions averaging, and also the core functions for tracing down the ground-state wave function.

For the purpose of comparing numerical results for noninteracting and strongly-interacting spinless fermions, I also have a pretty much stand alone set of functions in `FreeFermion/`, which contains functions to build up the Hilbert space of noninteracting spinless fermions, calculate the Green function matrix of a cluster of sites, calculate the cluster density matrix from the exact formula (2.4.30), and also perform the various

averagings necessary for numerical computation on a finite system.

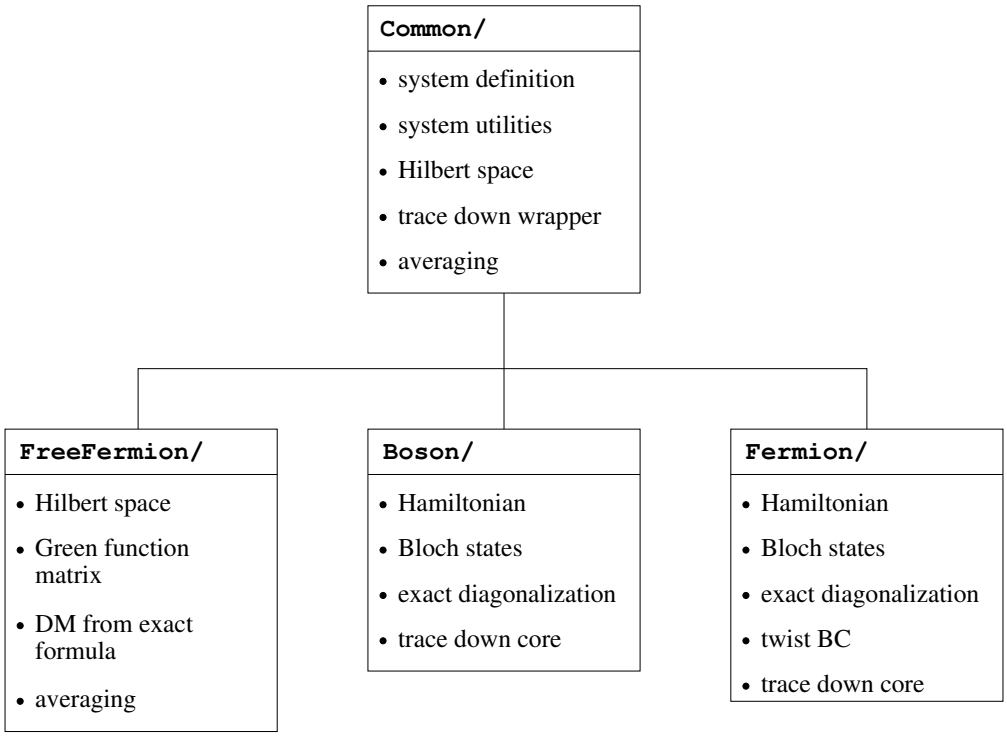

Figure C.1: Organization of code base.

C.1.4.3 Navigating Between Code Branches

Because the Octave function files are stored in separate directories, the Octave built-in variable `LOADPATH` must be modified at the start of each boson or fermion calculation. This is achieved by invoking the script `addpath` shown below. One copy of this script lies within each of the `Boson` and `Fermion` code branches. A modified version lies within the `FreeFermion` code branch, which requires access to function files in both the `Common` and `Fermion` code branches.

```
LOADPATH = sprintf("%s:. ./Common/", DEFAULT_LOADPATH);
```

C.2 System Definition and Utilities

C.2.1 Automatic Site Indexing

We define the finite system relative to an underlying infinite square lattice in terms of the lattice vectors $\mathbf{R}_1$ and $\mathbf{R}_2$, as shown in Figure C.2, such that $N = \hat{\mathbf{z}} \cdot (\mathbf{R}_1 \times \mathbf{R}_2) = R_{1x}R_{2y} - R_{2x}R_{1y} > 0$ is the number of lattice sites within the system.

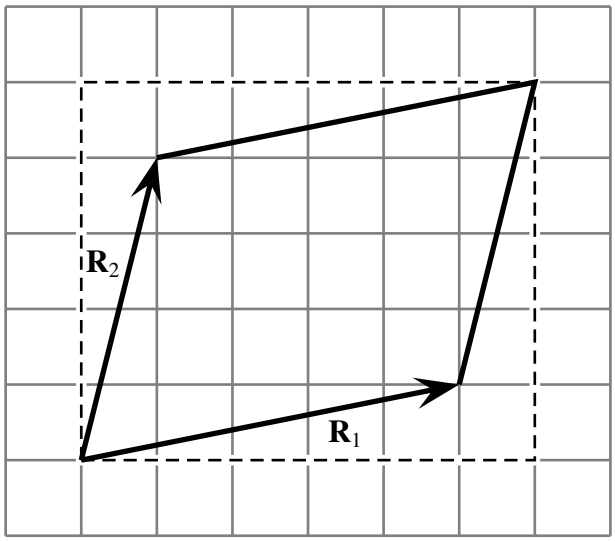

Figure C.2: Definition of system to be exactly diagonalized in terms of the lattice vectors $\mathbf{R}_1$ and $\mathbf{R}_2$. We shall denote such a system as $\mathbf{R}_1 \times \mathbf{R}_2$. In the example shown, the system is $(5, 1) \times (1, 4)$. The bounding box for this finite system, shown here as dashed lines, is calculated by the helper function `bounds`.

To automatically index the sites within such a system, we first determine the lower left and upper right coordinates of a rectangular region which bounds the system (see Figure C.2). This is done with the helper function `bounds`, whose Octave code is shown below, which takes as inputs $\mathbf{R}_1$ and $\mathbf{R}_2$, which are both 1×2 vectors.

```
function [xmin, xmax, ymin, ymax] = bounds(R1, R2)

xmin = min([0 R1(1) R2(1) R1(1) + R2(1)]);
xmax = max([0 R1(1) R2(1) R1(1) + R2(1)]);

ymin = min([0 R1(2) R2(2) R1(2) + R2(2)]);
ymax = max([0 R1(2) R2(2) R1(2) + R2(2)]);

endfunction
```

All sites lying within this bounding box are treated as candidate sites for the system, and we next need to determine whether an arbitray point $\mathbf{r} = (x, y)$, as shown in Figure C.3, is inside or outside of the system. From the figure, we see that

$$\overrightarrow{\mathrm{OA}} = \lambda\mathbf{R}_1 + \mu(\mathbf{R}_1 + \mathbf{R}_2), \quad \lambda + \mu = 1, \tag{C.2.1}$$

and

$$\overrightarrow{\mathrm{OB}} = \rho\mathbf{R}_2 + \sigma(\mathbf{R}_1 + \mathbf{R}_2), \quad \rho + \sigma = 1. \tag{C.2.2}$$

The position $\mathbf{r}$ can then be written in terms of $\overrightarrow{\mathrm{OA}}$ and $\overrightarrow{\mathrm{OB}}$ as

$$\mathbf{r} = \alpha\overrightarrow{\mathrm{OA}} = \beta\overrightarrow{\mathrm{OB}}. \tag{C.2.3}$$

For $\mathbf{r}$ to be inside the parallelogram defined by $\mathbf{R}_1$ and $\mathbf{R}_2$, which we call the *fundamental domain* of the system, we require that

$$0 \leq \alpha, \beta < 1. \tag{C.2.4}$$

To evaluate α and β given the point $\mathbf{r}$, we note from (C.2.1) and (C.2.3) that

$$\mathbf{r} = \alpha\lambda\mathbf{R}_1 + \alpha\mu(\mathbf{R}_1 + \mathbf{R}_2), \tag{C.2.5}$$

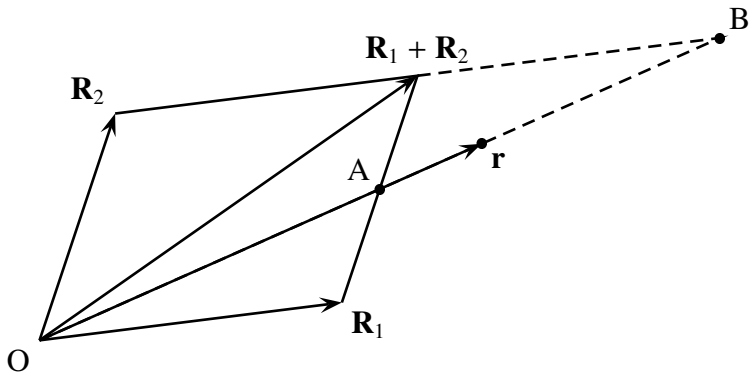

Figure C.3: Writing an arbitrary displacement vector $\mathbf{r}$ as a linear combination of the lattice vectors $\mathbf{R}_1$ and $\mathbf{R}_2$.

and by taking the dot products of $\mathbf{r}$ with $\mathbf{R}_1$ and $(\mathbf{R}_1 + \mathbf{R}_2)$, we end up with the matrix equation

$$\begin{bmatrix} |\mathbf{R}_1|^2 & |\mathbf{R}_1|^2 + \mathbf{R}_1 \cdot \mathbf{R}_2 \\ |\mathbf{R}_1|^2 + \mathbf{R}_1 \cdot \mathbf{R}_2 & |\mathbf{R}_1|^2 + |\mathbf{R}_2|^2 + 2\mathbf{R}_1 \cdot \mathbf{R}_2 \end{bmatrix} \begin{bmatrix} \alpha\lambda \\ \alpha\mu \end{bmatrix} = \begin{bmatrix} \mathbf{r} \cdot \mathbf{R}_1 \\ \mathbf{r} \cdot (\mathbf{R}_1 + \mathbf{R}_2) \end{bmatrix}, \tag{C.2.6}$$

solving which gives us $(\alpha\lambda, \alpha\mu)$. Similarly, writing

$$\mathbf{r} = \beta\rho\mathbf{R}_2 + \beta\sigma(\mathbf{R}_1 + \mathbf{R}_2) \tag{C.2.7}$$

and taking the dot products of $\mathbf{r}$ with $\mathbf{R}_2$ and $(\mathbf{R}_1 + \mathbf{R}_2)$ gives us the matrix equation

$$\begin{bmatrix} |\mathbf{R}_2|^2 & |\mathbf{R}_2|^2 + \mathbf{R}_1 \cdot \mathbf{R}_2 \\ |\mathbf{R}_2|^2 + \mathbf{R}_1 \cdot \mathbf{R}_2 & |\mathbf{R}_1|^2 + |\mathbf{R}_2|^2 + 2\mathbf{R}_1 \cdot \mathbf{R}_2 \end{bmatrix} \begin{bmatrix} \beta\rho \\ \beta\sigma \end{bmatrix} = \begin{bmatrix} \mathbf{r} \cdot \mathbf{R}_2 \\ \mathbf{r} \cdot (\mathbf{R}_1 + \mathbf{R}_2) \end{bmatrix}, \tag{C.2.8}$$

solving which gives us $(\beta\rho, \beta\sigma)$. Using the fact that $\lambda + \mu = 1 = \rho + \sigma$, we can then add the components of $(\alpha\lambda, \alpha\mu)$ to obtain α, and add the components of $(\beta\rho, \beta\sigma)$ to obtain β. Performing this computation of (α, β), the helper function `interior`, whose Octave code is shown below, determines whether a given point $\mathbf{r}$ is inside the parallelogram formed by $\mathbf{R}_1$ and $\mathbf{R}_2$. Here, all three inputs $\mathbf{r}$, $\mathbf{R}_1$ and $\mathbf{R}_2$ of `interior` are 1×2 vectors.

---

function flag = interior(r, R1, R2)

```
A = dot(R1, R1);
B = dot(R1, R2);
C = dot(R2, R2);

a = dot(r, R1);
b = dot(r, R1 + R2);
c = dot(r, R2);

Ma = [ A A + B ; A + B A + 2*B + C ];
ba = [ a ; b ];

alpha = sum(Ma\ba);
if abs(alpha) < 1e-15
    alpha = 0;
endif

Mb = [ C C + B ; C + B A + 2*B + C ];
bb = [ c ; b ];

beta = sum(Mb\bb);
if abs(beta) < 1e-15
    beta = 0;
endif
```

```
if (alpha >= 0) && (alpha < 1) && (beta >= 0) && (beta < 1)
    flag = 1;
else
    flag = 0;
endif

endfunction
```

The wrapper function `makesystem`, whose Octave code is shown below, then invokes `bounds` and `interior` to produce the list of sites $\mathbf{r}$ that are within the system. This list of sites $\mathbf{r}$ is stored in an $N \times 2$ array R, so that row j corresponds to $\mathbf{r}_j = (x_j, y_j)$.

```
function R = makesystem(R1, R2)

[xmin, xmax, ymin, ymax] = bounds(R1, R2);

k = 1;

for x = xmin:xmax
    for y = ymin:ymax
        if interior([x y], R1, R2)
            % extra check
            s1 = sum(abs([x y] - R1));
            s12 = sum(abs([x y] - R1 - R2));
            s2 = sum(abs([x y] - R2));
            if (s1 > 0) && (s12 > 0) && (s2 > 0)
```

```
                R(k, 1) = x;
                R(k, 2) = y;
                k = k + 1;
            endif
        endif
    endfor
endfor

endfunction
```

C.2.2 List of Nearest Neighbors

Because both strongly interacting models (C.1.1) and (C.1.2) forbid simultaneous occupation of sites which are nearest neighbors of each other, it is useful to always store in memory a list of nearest neighbors. This nearest neighbor list can then be used generically. In this code base, it is used in building up the P-particle Hilbert space of nearest-neighbor excluded configurations, but it can also be used to build up the P-particle Hilbert space when we have more exotic nearest-neighbor constraints. The nearest neighbor list is also used in building up the matrix for our Hamiltonians (C.1.1) or (C.1.2) with nearest-neighbor hops, with position-independent hopping matrix elements. It is also possible, using the nearest neighbor list to identify final-state configurations connected to a given initial-state configuration by a nearest-neighbor hop, when the hopping matrix elements are anisotropic (see Section C.4.6) or position-dependent.

To determine whether a given pair of sites $\mathbf{r}_i$ and $\mathbf{r}_j$, subject to periodic boundary conditions, are nearest neighbors of each other, we need to consider the separation be-

tween $\mathbf{r}_i$ and the nine positions (including $\mathbf{r}_j$) shown in Figure C.4. The sites $\mathbf{r}_i$ and $\mathbf{r}_j$ are nearest neighbors if one of these nine separations is equal to $(\pm 1, 0)$ or $(0, \pm 1)$.

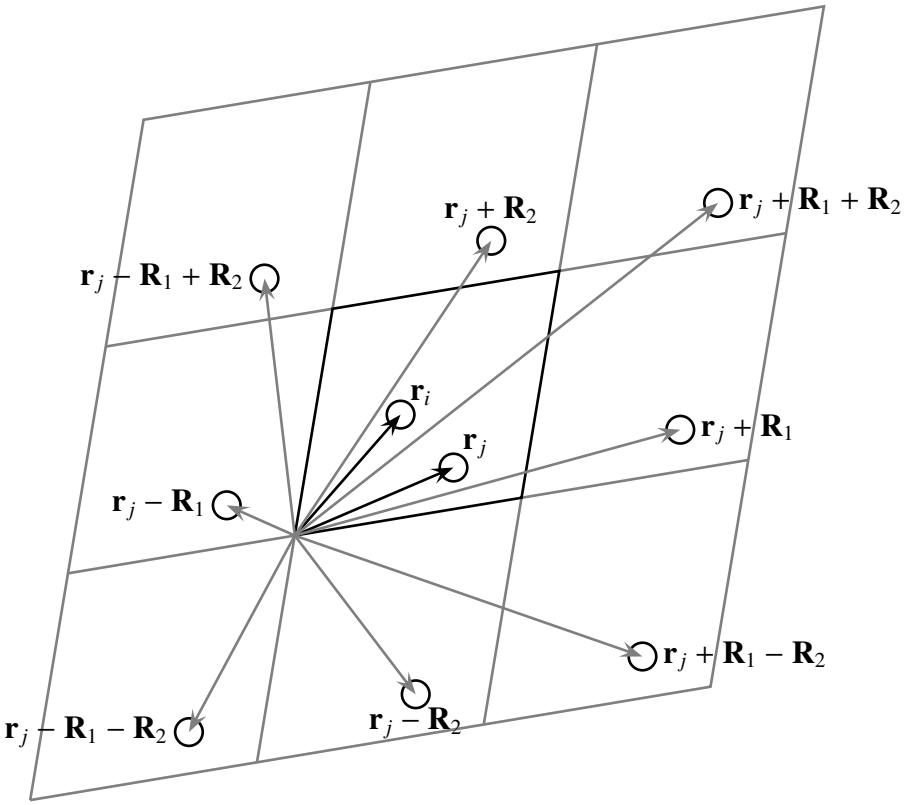

Figure C.4: Nine separations that must be taken into account to determine whether a given pair of sites, $\mathbf{r}_i$ and $\mathbf{r}_j$, subject to periodic boundary conditions, are nearest neighbors of each other.

From the topology of our underlying square lattice, we also know that each site $\mathbf{r}_i$ would have exactly four nearest neighbors, no matter what $\mathbf{R}_1$ and $\mathbf{R}_2$ are. The helper function `makeneighborlist`, whose Octave code is shown below, goes through the nine separations for every pair of sites $\mathbf{r}_i$ and $\mathbf{r}_j$, to build up a list of nearest neighbors for each of the N sites in the system. The list of nearest neighbors is organized into a $N \times 4$ array, in which the ith row gives the site indices $1 \le j_m \ne i \le N$, $m = 1, 2, 3, 4$ of the four nearest neighbors of site i.

```
function neighborlist = makeneighborlist(R, R1, R2)

N = size(R, 1);

T = [
−R1 − R2;
−R1;
−R1 + R2;
−R2;
0 0;
R2;
R1 − R2;
R1;
R1 + R2 ];

M = size(T, 1);

for i = 1:N
    r1 = R(i, :);
    l = 1;
    for j = 1:N
        r2 = R(j, :);
        for k = 1:M
            r3 = r2 + T(k, :);
```

```
            dr = r3 − r1;
            if dot(dr, dr) == 1
                neighborlist(i, l) = j;
                l = l + 1;
            endif
        endfor
    endfor
endfor

endfunction
```

C.2.3 List of Next-Nearest Neighbors

Besides storing the list of nearest neighbors in memory, it is also useful, when dealing with models in which we allow correlated hops described by (C.1.3), to also store in memory the list of next-nearest neighbors. We build up this list of next-nearest neighbors by observing that a next-nearest neighbor k (crossed circle) of site i (white circle) is simultaneously one of the nearest neighbors of *two*, j_1 and j_2 (black circles), of the nearest neighbors of site i, as shown in Figure C.5.

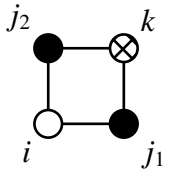

Figure C.5: Site k, a next-nearest neighbor of site i, is simultaneously a nearest neighbor of sites j_1 and j_2, which are themselves nearest neighbors of site i.

To determine all the next-nearest neighbors of site i, we go through all pairs (j_1, j_2) of

nearest neighbors of i, and determine the number of mutual nearest neighbors that they share. One of these is of course the site i, which we ignore. For large systems, each pair (j_1, j_2) will have just one common nearest neighbor apart from the site i. For small systems, in particular the two-legged ladder systems on which we calculate correlation density matrices, there will be some pairs (j_1, j_2) which have more than one common nearest neighbor apart from the site i. The helper function `makenextnearestneighborlist`, whose Octave code is shown below, takes care of this possibility, and stores the list of next-nearest neighbors as an $N \times 4$ array, in which the ith row gives the site indices $1 \leq k_m \neq i \leq N$, $m = 1, 2, 3, 4$ of the four next-nearest neighbors of site i:

```
function nnR = makenextnearestneighborlist(R, R1, R2, nR)

[N, NN] = size(nR);

for j = 1:N
    k = 1;
    for m = 1:NN-1
        nRm = nR(j, m);
        for n = m+1:NN
            nRn = nR(j, n);
            % find intersection between nR(nRm, :) and nR(nRn, :)
            nnRmn = intersection(nR(nRm, :), nR(nRn, :));
            % remove site j from this intersection
            nnRmn = complement(j, nnRmn);
            if size(nnRmn, 2) > 0
```

```
                for nn = 1:size(nnRmn, 2)
                    nnRtmp(k) = nnRmn(nn);
                    k = k + 1;
                endfor
            endif
        endfor
    endfor
    nnR(j, :) = create_set(nnRtmp);
endfor

endfunction
```

C.2.4 Reciprocal Lattice Vectors in the First Brillouin Zone

For a system defined by the lattice vectors $\mathbf{R}_1$ and $\mathbf{R}_2$, the finite-system primitive reciprocal lattice vectors $\mathbf{Q}_1$ and $\mathbf{Q}_2$ are defined such that

$$\begin{aligned} \mathbf{Q}_1 \cdot \mathbf{R}_1 &= 2\pi, \qquad \mathbf{Q}_1 \cdot \mathbf{R}_2 = 0, \\ \mathbf{Q}_2 \cdot \mathbf{R}_1 &= 0, \qquad \mathbf{Q}_2 \cdot \mathbf{R}_2 = 2\pi. \end{aligned} \tag{C.2.9}$$

As usual, these are given by

$$\mathbf{Q}_1 = 2\pi \frac{\mathbf{R}_2 \times \hat{\mathbf{z}}}{\hat{\mathbf{z}} \cdot (\mathbf{R}_1 \times \mathbf{R}_2)} = \frac{2\pi}{N} \begin{vmatrix} \hat{\mathbf{x}} & \hat{\mathbf{y}} & \hat{\mathbf{z}} \\ R_{2x} & R_{2y} & 0 \\ 0 & 0 & 1 \end{vmatrix} = \frac{2\pi}{N}(R_{2y}, -R_{2x}), \tag{C.2.10a}$$

$$\mathbf{Q}_2 = 2\pi \frac{\hat{\mathbf{z}} \times \mathbf{R}_1}{\hat{\mathbf{z}} \cdot (\mathbf{R}_1 \times \mathbf{R}_2)} = \frac{2\pi}{N} \begin{vmatrix} \hat{\mathbf{x}} & \hat{\mathbf{y}} & \hat{\mathbf{z}} \\ 0 & 0 & 1 \\ R_{1x} & R_{1y} & 0 \end{vmatrix} = \frac{2\pi}{N}(-R_{1y}, R_{1x}). \tag{C.2.10b}$$

An arbitrary reciprocal lattice vector $\mathbf{q}$ can then be written in terms of $\mathbf{Q}_1$ and $\mathbf{Q}_2$ as

$$\mathbf{q} = q_1\mathbf{Q}_1 + q_2\mathbf{Q}_2, \tag{C.2.11}$$

where q_1 and q_2 are integers. We abuse notations to write $\mathbf{q} = (q_1, q_2)$ in terms of its integer coefficients, because this representation is more convenient for numerical work.

For the purpose of recovering the full spectrum of the Hamiltonian matrix from the exact diagonalization of a set of Bloch-reduced Hamiltonian matrices, we also need the list of wave vectors $\mathbf{q}$ which lie within the First Brillouin Zone (FBZ) of the infinite square lattice (hereafter referred to as the infinite-system FBZ, as opposed to the FBZ of the fundamental domain defined by $\mathbf{R}_1 \times \mathbf{R}_2$, which will hereafter be referred to as the finite-system FBZ), which is the region in reciprocal space $-\pi \leq q_x, q_y \leq +\pi$. For example, for the $(4, 1) \times (1, 3)$ system, the finite-system primitive reciprocal lattice vectors are

$$\mathbf{Q}_1 = \frac{2\pi}{11}(3, -1), \quad \mathbf{Q}_2 = \frac{2\pi}{11}(-1, 4), \tag{C.2.12}$$

and the wave vectors $\mathbf{q} = q_1\mathbf{Q}_1 + q_2\mathbf{Q}_2$ within the infinite-system FBZ are shown below in Figure C.6. In general, for a system with N sites, there will be N wave vectors lying within the infinite-system FBZ. The Octave code for the function `makeFBZ`, which determines these N wave vectors, is shown below. The N wave vectors are stored in the $N \times 2$ array Q, the ith row of which, $(q_{1,i}, q_{2,i})$ are the integer indices of the ith wave vector $\mathbf{q}_i = q_{1,i}\mathbf{Q}_1 + q_{2,i}\mathbf{Q}_2$.

```
function Q = makeFBZ(R1, R2);

N = R1(1)*R2(2) - R2(1)*R1(2);

k = 1;
```

```
for x = −N:N
    for y = −N:N
        qx = 2∗(x∗R2(2) − y∗R1(2));
        qy = 2∗(−x∗R2(1) + y∗R1(1));
        if (qx >= −N) && (qx < N) && (qy >= −N) && (qy < N)
            Q(k, :) = [x y];
            k = k + 1;
        endif
    endfor
endfor

endfunction
```

C.2.5 Periodic Boundary Conditions

Another important helper function in the `Common` code branch is `periodicBC`, which takes a given position $\mathbf{r}$, which may or may not lie within the fundamental domain, and determines $\mathbf{r}'$ within the fundamental domain, which are related to each other by

$$\mathbf{r} = m\mathbf{R}_1 + n\mathbf{R}_2 + \mathbf{r}', \tag{C.2.13}$$

where m and n are integers. This function is used to enforce periodic boundary conditions on states generated by translations, which might bring an occupied site to a site outside the fundamental domain.

To determine m, n and $\mathbf{r}'$ for a system defined by arbitrary lattice vectors $\mathbf{R}_1$ and $\mathbf{R}_2$,

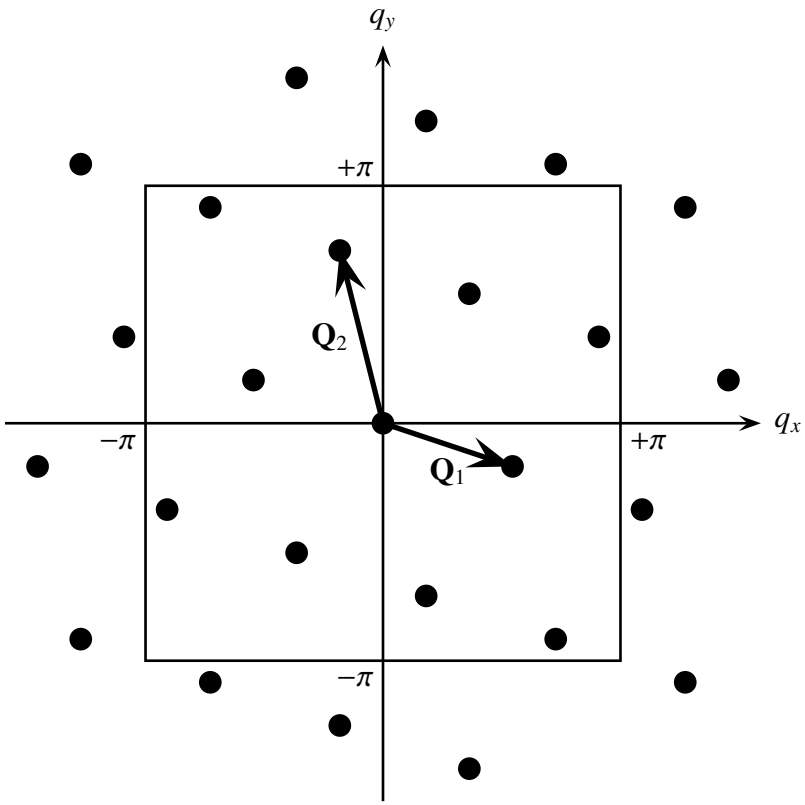

Figure C.6: The First Brillouin Zone (FBZ) of the infinite square lattice, which is the region $-\pi \leq q_x, q_y \leq +\pi$ in reciprocal space. 11 discrete reciprocal lattice vectors of the 11-site $(4,1) \times (1,3)$ system lie within the FBZ.

we recast (C.2.13) as a matrix equation

$$\begin{bmatrix} x \\ y \end{bmatrix} = \begin{bmatrix} R_{1x} & R_{2x} \\ R_{1y} & R_{2y} \end{bmatrix} \begin{bmatrix} m \\ n \end{bmatrix} + \begin{bmatrix} x' \\ y' \end{bmatrix} = \mathbf{R} \begin{bmatrix} m \\ n \end{bmatrix} + \begin{bmatrix} x' \\ y' \end{bmatrix}. \tag{C.2.14}$$

The coefficient matrix $\mathbf{R}$ in (C.2.14) is invertible, and its inverse matrix is

$$\mathbf{R}^{-1} = \frac{1}{N} \begin{bmatrix} R_{2y} & -R_{2x} \\ -R_{1y} & R_{1x} \end{bmatrix}. \tag{C.2.15}$$

Multiplying (C.2.14) by $\mathbf{R}^{-1}$, we have an equation

$$\begin{bmatrix} m \\ n \end{bmatrix} = \frac{1}{N} \begin{bmatrix} R_{2y} & -R_{2x} \\ -R_{1y} & R_{1x} \end{bmatrix} \begin{bmatrix} x \\ y \end{bmatrix} - \frac{1}{N} \begin{bmatrix} R_{2y} & -R_{2x} \\ -R_{1y} & R_{1x} \end{bmatrix} \begin{bmatrix} x' \\ y' \end{bmatrix} \tag{C.2.16}$$

for m and n.

From (C.2.10a) and (C.2.10b), we see that multiplying $\mathbf{r}'$ by the inverse matrix is like taking its inner products with the finite-system primitive reciprocal lattice vectors $\mathbf{Q}_1$ and $\mathbf{Q}_2$. Therefore, if $\mathbf{r}'$ is indeed within the fundamental domain, the elements of the resulting vector would be between -1 and 1, and so

$$\begin{aligned} m &= R_{2y}x - R_{2x}y \mod N, \\ n &= -R_{1y}x + R_{1x}y \mod N. \end{aligned} \tag{C.2.17}$$

Looking at the multiplication of $\mathbf{r}'$ by the inverse matrix more carefully,

$$\begin{bmatrix} R_{2y} & -R_{2x} \\ -R_{1y} & R_{1x} \end{bmatrix} \begin{bmatrix} x' \\ y' \end{bmatrix} = \begin{bmatrix} R_{2y}x' - R_{2x}y' \\ -R_{1y}x' + R_{1x}y' \end{bmatrix}. \tag{C.2.18}$$

we see that the first component is $\hat{\mathbf{z}}\cdot(\mathbf{r}'\times\mathbf{R}_2)$ whereas the second component is $\hat{\mathbf{z}}\cdot(\mathbf{R}_1\times\mathbf{r}')$. For $\mathbf{r}'$ within the fundamental domain, both components are positive.

However, we encounter a subtle pitfall in using the defining equation (C.2.16) in conjunction with the use of the modulo function in Matlab or Octave to solve for m and

n, because the remainder so obtained would be positive instead of negative, and we will get the wrong m and n. The correct way to solve for m and n using the Octave modulo function is to solve the negative of (C.2.16),

$$\begin{bmatrix} -m \\ -n \end{bmatrix} = \frac{1}{N} \begin{bmatrix} R_{2y} & -R_{2x} \\ -R_{1y} & R_{1x} \end{bmatrix} \begin{bmatrix} -x \\ -y \end{bmatrix} + \frac{1}{N} \begin{bmatrix} R_{2y} & -R_{2x} \\ -R_{1y} & R_{1x} \end{bmatrix} \begin{bmatrix} x' \\ y' \end{bmatrix}, \tag{C.2.19}$$

which has a positive remainder. Once we know what m and n are, we can then solve for $\mathbf{r}'$ using (C.2.13). This is implemented in a slightly different way in the function `periodicBC`, whose Octave code is shown below:

```
function y = periodicBC(r, R1, R2)

N = R1(1)*R2(2) - R1(2)*R2(1);

b = [ rem(r(1)*R2(2) - r(2)*R2(1), N); rem(r(1)*R1(2) - r(2)*R1(1), N) ];

if b(1) < 0
    b(1) = b(1) + N;
endif

if b(2) > 0
    b(2) = b(2) - N;
endif

A = [ R2(2) -R2(1); R1(2) -R1(1) ];
```

```
y = A\b;

y = y';

endfunction
```

C.2.6 Other Utility Helper Functions

There are three other utility helper functions acting at the system-level in the `Common` code branch. A pair of these, `listcoord` and `coordlist`, are transcription functions. In Section C.3, we shall see that the allowed P-particle states in the Hilbert space are organized into a $D \times P$ Hilbert space matrix. The nth row represents the nth allowed state, whose entries $[j_1, j_2, \ldots, j_P]$, where $1 \leq j_1 < j_2 < \cdots < j_P \leq N$, denote the list of the P occupied sites. The function `listcoord`, whose Octave code is shown below, takes such a list of site indices to produce a list of coordinates of the form

$$[\mathbf{r}_{j_1}, \mathbf{r}_{j_2}, \ldots, \mathbf{r}_{j_P}] = \begin{bmatrix} x_{j_1} & x_{j_2} & \cdots & x_{j_P} \\ y_{j_1} & y_{j_2} & \cdots & y_{j_P} \end{bmatrix}. \tag{C.2.20}$$

```
function s = listcoord(n, R)

P = size(n, 2);

s = R(n(1), :);

for i = 2:P
```

```
    s = [ s; R(n(i), :) ];
endfor

endfunction
```

Performing transcription the other direction is the function `coordlist`, which takes a list of coordinates $[\mathbf{r}_{j_1}, \mathbf{r}_{j_2}, \ldots, \mathbf{r}_{j_P}]$ of the form shown in (C.2.20), and produce a list of sites indices $[j_1, j_2, \ldots, j_P]$ in return. The Octave code for this function is shown below:

```
function n = coordlist(s, R)

P = size(s, 1);
N = size(R, 1);

for i = 1:P
    ni = 0;
    for j = 1:N
        if prod(s(i, :) == R(j, :)) == 1
            ni = j;
            break;
        endif
    endfor
    n(i) = ni;
endfor

endfunction
```

The third utility helper function is `translate`, which takes a list $[\mathbf{r}_{j_1}, \mathbf{r}_{j_2}, \ldots, \mathbf{r}_{j_P}]$ of P coordinates, of the form shown in (C.2.20), and translates each of the P coordinates by a translation vector $\mathbf{T}$, i.e.

$$[\mathbf{r}_{j_1}, \mathbf{r}_{j_2}, \ldots, \mathbf{r}_{j_P}] \rightarrow [\mathbf{r}_{j_1} + \mathbf{T}, \mathbf{r}_{j_2} + \mathbf{T}, \ldots, \mathbf{r}_{j_P} + \mathbf{T}], \tag{C.2.21}$$

subject to periodic boundary conditions. The Octave code for this function, whose output is another list of coordinates of the form in (C.2.20), is shown below:

```
function t = translate(s, T, R1, R2)

P = size(s, 1);

for i = 1:P
    t(i, :) = round(periodicBC(s(i, :) + T, R1, R2));
endfor

endfunction
```

C.3 Hilbert Space Definition and Utilities

C.3.1 Occupation Number Representation

In the usual occupation number representation, a P-particle state of a system of N sites is written as

$$|\mathbf{n}\rangle = |n_1 n_2 \cdots n_j \cdots n_N\rangle\,, \tag{C.3.1}$$

where $n_j = 0, 1$ is the occupation number of site j, and $\sum_{j=1}^{N} n_j = P$. If the P occupied sites are $1 \leq j_1 < j_2 < \cdots < j_P \leq N$, then we can write

$$|\mathbf{n}\rangle = a_{j_1}^{\dagger} a_{j_2}^{\dagger} \cdots a_{j_P}^{\dagger} |0\rangle \,, \tag{C.3.2}$$

where $|0\rangle$ is the vacuum. The set $\{|\mathbf{n}\rangle\}$ of all distinct P-particle occupation number states form the basis of the P-particle Hilbert space, which is the same for hardcore bosons and spinless fermions. Representing the P-particle occupation number state by the list of its occupied sites, which we call its *configuration*, i.e.

$$a_{j_1}^{\dagger} a_{j_2}^{\dagger} \cdots a_{j_P}^{\dagger} |0\rangle \mapsto [j_1, j_2, \ldots, j_P], \tag{C.3.3}$$

this basis can be organized into a $D \times P$ Hilbert space matrix V, whose rows are the D occupation number basis states. The entries $[j_1, j_2, \ldots, j_P]$, where $1 \leq j_1 < j_2 < \cdots < j_P \leq N$ in each row then denote the list of the P occupied sites.

C.3.2 Building Up the Hilbert Space Matrix

There are several ways to build up the Hilbert space matrix, and we list two schemes in this subsection. The first, more direct, scheme (Section C.3.2.1), involves sequentially stepping through all ordered lists of P distinct integers not greater than N, the number of sites in the system, and checking whether each of the ordered lists generated is admissible as a occupation number basis state under the constraint that no nearest-neighbor sites are simultaneously occupied. The P-particle Hilbert space matrix is thus generated in one fell swoop in the first scheme. The second scheme (Section C.3.2.2) makes use of the observation that all $(p-1)$-particle subconfigurations taken from the configurations of the p-particle Hilbert space matrix, are themselves configurations of the $(p-1)$-particle Hilbert space matrix. Therefore, if the $(p-1)$-particle Hilbert space matrix is given, only a small effort is needed to generate the list of all admissible configurations

of the p-particle Hilbert space matrix. In this way, we can obtain the P-particle Hilbert space matrix, by applying the second scheme recursively, starting from the one-particle Hilbert space matrix, which is trivial to construct.

If we relax the constraint on nearest-neighbor occupation, which can be done easily by modifying the function `allowstate`, the first scheme will be faster, since the second scheme incurs overhead in recursion. With the no-nearest-neighbor-occupation constraint, the first scheme is expected to be faster than the second scheme at very low filling fractions. This is because at very low filling fractions, the no-nearest-neighbor-occupation constraint excludes only a small fraction of all possible P-particle configurations, and thus the first scheme outcompetes the second scheme, with its overhead baggage of recursion. At higher filling fractions, the no-nearest-neighbor-constraint excludes a large fraction of all possible P-particle configurations. The first scheme, which generates all of these invalid configurations, along with all the valid configurations, will then be slower than the second scheme, which generates only a small number, or none, of these invalid configurations along with all the valid configurations.

For our numerical studies in this thesis, we used the second scheme exclusively. Nevertheless, we keep the function implementing the first scheme around, in case someone wants to extend the code base to work with models in which there are no constraint on nearest-neighbor occupation.

C.3.2.1 First Scheme

In this scheme, we sequentially step through all ordered lists $\{j_1, j_2, \ldots, j_P\}$ of P distinct integers, such that

$$r \leq j_r \leq N - P + r, \tag{C.3.4}$$

and check whether each of the lists so generated is an occupation number basis state admissible under the constraint of no nearest-neighbor occupation.

To sequentially step through all ordered lists $[j_1, j_2, \ldots, j_P]$ of P distinct integers satisfying (C.3.4), we invoke the recursive helper function `increment`. To see how `increment` works, let us imagine that during the recursion, we have reached a stage in which the function is called to increment the ordered list at the rth position. If $j_r + 1 \leq N-P+r$, the increment $j_r \mapsto j_r+1$ is successful, and `increment` returns the incremented ordered list. Otherwise, a 'carry' operation is necessary, and `increment` calls itself and attempt to increment the ordered list at the $(r-1)$th position.

Assuming that this 'carry' operation is successful, i.e. j_{r-1} has been incremented or set to a new minimum value possible, depending on whether a deeper-level 'carry' operation was necessary at the $(r-1)$th position, we must then set j_r to its new minimum value possible, and get `increment` to return the new ordered list. Because of the requirement that $j_r > j_{r-1}$, this new minimum value of j_r will be one more than the new value of j_{r-1}. Overall, this new value of j_r will, in a 'carry' operation effected at the rth position, be decided by the first successful increment at the $(r' < r)$th position.

By our design of the function `increment`, we will always start incrementing the ordered list from the Pth position. To step through the list of all ordered lists, we will then start from the minimal ordered list $[1, 2, \ldots, P]$, and apply `increment` repeatedly, until we obtain the maximal ordered list $[N-P+1, N-P+2, \ldots, N]$. The `increment` function, whose Octave code is shown below, is also designed to return a value of zero, if it is applied to the maximal ordered list, so that we know when to stop the recursion. In the argument list of `increment`, $n = [j_1, j_2, \ldots, j_P]$ is the ordered list to be incremented, N is the maximum value that j_P can take, and $1 \leq pos \leq P$ is the position on the ordered list to be incremented.

```
function m = increment(n, N, pos)

NC = max(size(n));

if pos > 0
    if n(pos) < N - NC + pos
        for i = 1:pos-1
            m(i) = n(i);
        endfor
        m(pos) = n(pos) + 1;
        for i = pos+1:NC
            m(i) = n(pos) + i - pos + 1;
        endfor
    else
        m = increment(n, N, pos-1);
    endif
else
    m = 0;
endif

endfunction
```

To better illustrate how `increment` works, we show below an example series of output for `increment` stepping through all ordered lists of four integers no larger than six.

```
octave:1> N = 6;
octave:2> P = 4;
octave:3> n = 1:4
n =
  1  2  3  4
octave:4> n = increment(n, N, P)
n =
  1  2  3  5
octave:5> n = increment(n, N, P)
n =
  1  2  3  6
octave:6> n = increment(n, N, P)
n =
  1  2  4  5
octave:7> n = increment(n, N, P)
n =
  1  2  4  6
octave:8> n = increment(n, N, P)
n =
  1  2  5  6
octave:9> n = increment(n, N, P)
n =
  1  3  4  5
octave:10> n = increment(n, N, P)
```

```
n =

  1  3  4  6

octave:11> n = increment(n, N, P)

n =

  1  3  5  6

octave:12> n = increment(n, N, P)

n =

  1  4  5  6

octave:13> n = increment(n, N, P)

n =

  2  3  4  5

octave:14> n = increment(n, N, P)

n =

  2  3  4  6

octave:15> n = increment(n, N, P)

n =

  2  3  5  6

octave:16> n = increment(n, N, P)

n =

  2  4  5  6

octave:17> n = increment(n, N, P)

n =

  3  4  5  6

octave:18> n = increment(n, N, P)

n = 0
```

In the example output above, when the first-level `increment` is invoked to increment the ordered list $[2, 3, 5, 6]$ at the $(P = 4)$th position, we find that j_4 has already taken up the maximum possible value of $N = 6$, and thus cannot be further incremented. The second-level `increment` is then called, from within the first-level `increment`, to increment the ordered list $[2, 3, 5, 6]$ at the $(P - 1 = 3)$rd position. However, we find that j_3 has already taken up the maximum possible value of $N - 1 = 5$, and cannot be further incremented. As such, the second-level `increment` calls the third-level `increment`, which attempts to increment the ordered list $[2, 3, 5, 6]$ at the $(P - 2 = 2)$nd position. As we can see, $j_2 = 3 < N - P + 2 = 4$, and so j_2 can be successfully incremented to its new value of $j_2 = 4$. The third-level `increment` returns control to the second-level `increment`, which must now set a new minimum value of $j_2 + 1 = 4 + 1 = 5$ for j_3, and returns control to the first-level `increment`. The first-level `increment` now set a new minimum value of $j_3 + 1 = 5 + 1 = 6$ for j_4, before returning the incremented ordered list $[2, 4, 5, 6]$. Note that as a user, we never try to increment an ordered list at any position but P. If it is necessary to perform a 'carry' operation and increment the ordered list at positions other than P, this will be done automatically by a recursive call within `increment` itself.

Apart from using the function `increment` as part of this code base, we also use it as a standalone function elsewhere. For example, in Chapter 7, the `increment` function was used in generating the list of minors that must be summed in the intervening-particle expansions of various correlations.

The second helper function `allowstate` checks whether a given ordered list $[j_1, j_2, \ldots, j_P]$ satisfying (C.3.4) constitutes an allowed occupation number basis state. To do so, we form the union of all nearest neighbors of the sites in $[j_1, j_2, \ldots, j_P]$, and check

the intersection between this ordered list and the union. If the intersection is empty, then none of the sites in $[j_1, j_2, \ldots, j_P]$ are nearest neighbors of each other, and the given ordered list constitutes an allowed occupation number basis state. The Octave code of `allowstate` is shown below. In the argument list of `allowstate`, 'state' $= [j_1, j_2, \ldots, j_P]$ is a candidate P-particle configuration whose validity we must check, and 'neighborlist' is the $N \times 4$ array of site indices of the nearest neighbors of each of the N sites within the system.

```
function flag = allowstate(state, neighborlist)

P = max(size(state));

neighbors = neighborlist(state(1), :);

for r = 2:P
    neighbors = union(neighbors, neighborlist(state(r), :));
endfor

if intersection(state, neighbors)
    flag = 0;
else
    flag = 1;
endif

endfunction
```

The core function `directhilbertspace` implementing the first scheme, and whose Octave code is shown below, invokes `increment` and `allowstate` to build up the P-particle Hilbert space in one fell swoop. This scheme can be made to work with more exotic nearest-neighbor constraints, or no constraints on nearest-neighbor occupation at all. All we need to do for this to happen is modify the helper function `allowstate`.

```
function V = directhilbertspace(P, neighborlist)

N = size(neighborlist, 1);

state = 1:P;

k = 0;

while state
    if allowstate(state, neighborlist)
        for j = 1:P
            V(k+1, j) = state(j);
        endfor
        k = k + 1;
    endif
    state = increment(state, N, P);
endwhile

if k == 0
```

```
    V = [];
endif

endfunction
```

C.3.2.2 Second Scheme

The basis for this second scheme is the fact that, if $[j_1, j_2, \ldots, j_{P-1}, j_P]$ is an allowed P-particle configuration, then $[j_1, j_2, \ldots, j_{P-1}]$ will also be an allowed $(P-1)$-particle configuration. With this observation, we can build up the P-particle Hilbert space if we are given the $(P-1)$-particle Hilbert space. In general, when a large fraction of P-particle configurations are excluded by the no-nearest-neighbor constraint, we can build up the P-particle Hilbert space matrix more quickly using the second scheme as compared to the first. This is because we generate few, or none, of the invalid P-particle configurations when applying the second scheme.

To build up the Hilbert space matrix for an arbitrary number of particles recursively, we need the core function `enlargefreehilbertspace`, whose Octave code is shown below. This core function builds up the P-particle Hilbert space matrix V_1, starting from the $(P-1)$-particle Hilbert space matrix V_0. There are two ways to do this. In the first way, we go through all configurations $[j_1, j_2, \ldots, j_{P-1}]$ taken from the $(P-1)$-particle Hilbert space matrix, form for each configuration all possible P-particle ordered lists by appending to the ordered list $[j_1, j_2, \ldots, j_{P-1}]$ the integer $j_{P-1} < j_P \leq N$, and run them through the function `allowstate`. The P-particle Hilbert space matrix then collects together all allowed P-particle configurations formed this way. This first way of implementing the second scheme will also work with generic nearest-neighbor constraints, so

long as the appropriate `allowstate` function is used.

```
function V1 = enlargehilbertspace(V0, neighborlist)

N = size(neighborlist, 1);
[D0, P0] = size(V0);

l = 0;

for j = 1:D0
    for k = V0(j, P0)+1:N
        state = [ V0(j, :) k ];
        if allowstate(state, neighborlist)
            V1(l+1, :) = state;
            l = l + 1;
        endif
    endfor
endfor

if l == 0
    V1 = [];
endif

endfunction
```

In the second way of implementing the second scheme, we observe that in the

function `enlargehilbertspace`, we have avoided the generation of most but not all ordered lists which are invalid P-particle configurations. We can do better, and not generate any invalid P-particle configurations at all, by using the function `xenlarge-hilbertspace`, whose Octave code is shown below. In `xenlargehilbertspace`, instead of appending all possible j_P in the range $[j_{P-1}+1, N]$ to the ordered list $[j_1, j_2, \ldots, j_{P-1}]$, we append only values in this range that are not nearest neighbors to any of the sites in $[j_1, j_2, \ldots, j_{P-1}]$. All P-particle ordered lists generated this way are then allowed configurations. Because the function `allowstate` is not used, and the no-nearest-neighbor-occupation constraint is hard-wired into the algorithm, the function `xenlargehilbertspace` cannot work with generic nearest-neighbor constraints. We use it exclusively in our numerical calculations, however, since we only work with the no-nearest-neighbor-occupation constraint, and because `xenlargehilbertspace` is generally the fastest in building up the P-particle Hilbert space matrix.

```
function V1 = xenlargehilbertspace(V0, neighborlist)

N = size(neighborlist, 1);
[D0, P0] = size(V0);

l = 0;

for j = 1:D0
    neighbors = V0(j, :);
    for r = 1:P0
        neighbors = union(neighbors, neighborlist(V0(j, r), :));
```

```
    endfor
    sites = complement(neighbors, [V0(j, P0)+1:N]);
    Nj = size(sites, 2);
    if Nj > 0
        for k = 1:Nj
            V1(l+1, :) = [ V0(j, :) sites(k) ];
            l = l + 1;
        endfor
    endif
endfor

if l == 0
    V1 = [];
endif

endfunction
```

The wrapper function `buildhilbertspace`, whose Octave code is shown below, then builds the trivial one-particle Hilbert space, and invokes `xenlargehilbertspace` repeatedly until the target number P of particles is reached.

```
function V = buildhilbertspace(P, neighborlist)

N = size(neighborlist, 1);

if P == 1
```

```
    V = [1:N]';
else
    V = [1:N]';
    p = 2;
    while p <= P
        V = xenlargehilbertspace(V, neighborlist);
        p = p + 1;
    endwhile
endif

endfunction
```

We show below an example output, when we use `xenlargehilbertspace` repeatedly to build up the ($P = 3$)-particle Hilbert space matrix of the $(3,1) \times (1,3)$ system with $N = 8$ sites.

```
octave:1> R1 = [ 3 1 ];
octave:2> R2 = [ 1 3 ];
octave:3> R = makesystem(R1, R2);
octave:4> N = size(R, 1)
N = 8
octave:5> nR = makeneighborlist(R, R1, R2)
nR =
  3  4  6  7
  3  4  6  7
```

```
  1  2  5  8
  1  2  5  8
  3  4  6  7
  1  2  5  8
  1  2  5  8
  3  4  6  7
octave:6> V1 = [1:N]'
V1 =
  1
  2
  3
  4
  5
  6
  7
  8
octave:7> V2 = xenlargehilbertspace(V1, nR)
V2 =
  1  2
  1  5
  1  8
  2  5
  2  8
  3  4
  3  6
```

```
   3   7
   4   6
   4   7
   5   8
   6   7
octave:8> V3 = xenlargehilbertspace(V2, nR)
V3 =
   1   2   5
   1   2   8
   1   5   8
   2   5   8
   3   4   6
   3   4   7
   3   6   7
   4   6   7
```

C.3.3 Other Utility Helper Functions

The utility helper function `listindex`, whose Octave code is shown below, gives the row index of a given configuration $[j_1, j_2, \ldots, j_P]$ (assumed to be ordered) within the P-particle Hilbert space matrix. In the argument list of `listindex`, $n = [j_1, j_2, \ldots, j_P]$ is a $1 \times P$ vector of occupied site indices, while V is the $D \times P$ Hilbert space matrix.

---

function index = listindex(n, V)

```
index = 0;
N = size(V, 1);

for i = 1:N
    if prod(n == V(i, :)) == 1
        index = i;
        break;
    endif
endfor

endfunction
```

C.4 Hamiltonian Matrix

At this point, the code base diverges into the `Boson` and `Fermion` code branches. The function names in one branch parallel those in the other, but the core functions, especially those building the Hamiltonian matrices, are necessarily different in the two code branches, because of the fermion sign that is incurred when we exchange two fermions. There are four different circumstances where we encounter fermion signs. These are described in Table C.1, along with the helper functions handling the fermion signs, and the core functions calling them. Most helper functions that are not already in the `Common` code branch are also different for the two code branches.

As far as computation of the Hamiltonian matrix is concerned, the `Boson` code branch is significantly more primitive than the `Fermion` code branch. Whereas the latter has four core functions dedicated to building up the Hamiltonian matrix, there is only

Table C.1: The various spinless fermion calculations incurring fermion signs, the `Fermion` code branch helper function designed to handle them, and the `Fermion` code branch core function making the helper function calls.

calculation	core function	helper function
Calculation of Hamiltonian matrix elements	`buildhamiltonian`	`eta`
	`buildcompacthamiltonian`	
	`quickhamiltonian`	`orderlist`
	`quickcompacthamiltonian`	
	`addcorrelatedhops`	
	`addcompactcorrelatedhops`	
	`quickcompactXYhamiltonian`	
Translate configurations to build Bloch states	`ntranslate`	`orderlist`
Trace-down calculation of cluster density matrix	`reshapepsi`	`orderlist`
Calculation of correlation density matrix	`correlationdensitymatrix`	inline calculation

one slow core function doing so in the former. This is not because it is more difficult developing code performing Hamiltonian matrix computation for bosons, nor is it because the `Boson` code branch functions need no further refinement, but simply because we have been investing essentially all our time developing the `Fermion` code branch.

In Section C.4.1, I will describe the basic algorithm behind the slow core function `buildhamiltonian` for the `Boson` code branch, and then proceed to document the analogous slow core function `buildhamiltonian` for the `Fermion` code branch in Section C.4.2. We then describe for the `Fermion` code branch, a faster core function `quickhamiltonian` for building up the Hamiltonian matrix using a different algorithm from the slow core function `buildhamiltonian`, in Section C.4.3. We use the faster core function `quickhamiltonian` exclusively for our numerical studies in Chapter 4, and its derivatives, described in Sections C.4.5 and C.4.6, for our numerical studies in Chapter 8. Though not used, we keep the slow core function `buildhamiltonian` around in the `Boson` and `Fermion` code branches to serve as a benchmark.

In our development of the `Fermion` code branch functions for Hamiltonian matrix computation, we made several important code design choices. First of all, if the size of the P-particle Hilbert space is not too large (which is the case for systems with sizes $N \lesssim 20$), and we can store the full Hamiltonian matrix in memory, we can make use of the very efficient matrix functionalities of Octave to perform matrix transformation, including the exact diagonalization of the full Hamiltonian matrix. Indeed, both our slow and fast core functions, `buildhamiltonian` and `quickhamiltonian`, build up and store the full Hamiltonian matrix. We feel that the reduction in computation time is worth the larger run-time memory footprint incurred.

For larger system sizes, the Hilbert space is so large that we can store only the nonzero elements of the Hamiltonian matrix in a compact array. We describe in Section

C.4.4 how this compact array is built up by the fast core function `quickcompacthamiltonian`, a derivative of the fast core function `quickhamiltonian`. When stored in this compact array form, full diagonalization of the Hamiltonian matrix is then no longer possible. It is still possible to perform Lanczos diagonalization with this compactly-stored Hamiltonian matrix, but the user-defined function that implements this will generally not be efficient, since it involves very slow interpreted lookups. The lookup process can be made faster, if the nonzero Hamiltonian matrix elements are stored in the same sequence as the sequence of matrix elements being referenced for matrix-vector multiplication, but the amount of work and thought that is needed to make Lanczos diagonalization of the compact-array Hamiltonian matrix more efficient cannot be justified by the slight improvement in performance.

Instead, our ED strategy is to take advantage of the the translational symmetry of our model Hamiltonians. To do this, we work with Bloch basis states, and for each wave vector, construct a Bloch-reduced Hamiltonian matrix to be exactly diagonalized. We will describe and document the functions that generate Bloch states and Bloch-reduced Hamiltonian matrices in Section C.5. Here we merely describe how they affect our design of the functions building up the Hamiltonian matrix. For the system sizes that we encounter in this thesis, the Bloch-reduced Hamiltonian matrices, or Bloch Hamiltonian matrices in short, are always small enough to fit into memory. In fact, we never encounter in the course of our numerical studies Bloch Hamiltonian matrices so large that native Octave full diagonalization is slower than Lanczos diagonalization, which we have to implement using an interpreted function script.

In the unlikely event that we make a research decision to work with systems so large that even the Bloch Hamiltonian matrices cannot fit into memory, it is always possible to calculate the Hamiltonian matrix elements on the fly. This is highly inefficient, and

even less efficient if we try to first compute the Bloch Hamiltonian matrices. We will, in this unlikely scenario, be working with the full Hilbert space, and resort to Lanczos diagonalization. Since we will not be performing matrix-vector multiplication in the usual sense, Octave is no longer the appropriate choice of language. We will most likely implement the Lanczos diagonalization in C, and later import the Lanczos wave function into Octave, to compute the cluster or correlation density matrices.

C.4.1 Hardcore Bosons

The algorithm for evaluating the matrix elements $\langle \mathbf{n}|H|\mathbf{n}'\rangle$ of the Hamiltonian given in (C.1.1) between the distinct occupation number basis states $|\mathbf{n}\rangle$ and $|\mathbf{n}'\rangle$, whose configurations are $[j_1, j_2, \ldots, j_P]$ and $[j'_1, j'_2, \ldots, j'_P]$ respectively, is as follows:

1. First determine the number of sites common to $[j_1, j_2, \ldots, j_P]$ and $[j'_1, j'_2, \ldots, j'_P]$.

2. Because the Hamiltonian in (C.1.1) can hop only one particle at a time, if the configurations $[j_1, j_2, \ldots, j_P]$ and $[j'_1, j'_2, \ldots, j'_P]$ have fewer than $P-1$ sites in common, set $\langle \mathbf{n}|H|\mathbf{n}'\rangle = 0$.

3. If the two configurations have exactly $P-1$ sites in common, i.e. they differ only in one site, find these non-common sites j (in $[j_1, j_2, \ldots, j_P]$) and j' (in $[j'_1, j'_2, \ldots, j'_P]$).

4. If j and j' are not nearest neighbors of each other, set $\langle \mathbf{n}|H|\mathbf{n}'\rangle = 0$. Else, the two configurations are connected to each other by a nearest neighbor hop. For bosons, the creation operators of different sites commute, so there is no sign problem. The matrix element is simply $\langle \mathbf{n}|H|\mathbf{n}'\rangle = -1$.

This algorithm is implemented by the function `buildhamiltonian`, whose Octave code is shown below. In the Octave code shown, V is the $D \times P$ Hilbert space ma-

trix (see Section C.3.1), 'neighborlist' is a $N \times M$ array storing the site indices of the M nearest neighbors of the N sites within the system (see Section C.2.2), and H is the $D \times D$ full Hamiltonian matrix.

```
function H = buildhamiltonian(V, neighborlist)

[D, P] = size(V);

H = zeros(D, D);

for m = 1:D
    for n = 1:D
        if size(intersection(V(m, :), V(n, :)), 2) == P - 1
            bra = complement(V(m, :), V(n, :));
            ket = complement(V(n, :), V(m, :));
            if intersection(bra, neighborlist(ket, :))
                H(m, n) = -1;
            endif
        endif
    endfor
endfor

endfunction
```

C.4.2 Spinless Fermions

For spinless fermions, the creation operators on different sites anticommute, so we need to be careful of the fermion signs associated with each of the matrix elements $\langle \mathbf{n}|H|\mathbf{n}'\rangle$, for the Hamiltonian appearing in (C.1.2). The algorithm to evaluate the matrix elements, shown below, is the same as that for hardcore bosons up till the the fourth step:

4. If j and j' are not nearest neighbors of each other, set $\langle \mathbf{n}|H|\mathbf{n}'\rangle = 0$. Else, the two configurations are connected to each other by a nearest neighbor hop. Determine the fermion phase factors $f(\mathbf{n}, j)$ and $f(\mathbf{n}', j')$ using the helper function `eta`, whose Octave code is shown below, and set $\langle \mathbf{n}|H|\mathbf{n}'\rangle = -(-1)^{f(\mathbf{n},j)+f(\mathbf{n}',j')}$.

Looking more carefully at the matrix element

$$\begin{aligned}\langle \mathbf{n}|H|\mathbf{n}'\rangle &= -\langle 0|c_{j_P}\cdots c_j\cdots c_{j_2}c_{j_1}\left(c_j^\dagger c_{j'}\right)c_{j'_1}^\dagger c_{j'_2}^\dagger\cdots c_{j'}^\dagger\cdots c_{j'_P}^\dagger|0\rangle \\ &= -(-1)^{f(\mathbf{n},j)+f(\mathbf{n}',j')}\langle 0|c_{j_P}\cdots c_{j_2}c_{j_1}c_j\left(c_j^\dagger c_{j'}\right)c_{j'}^\dagger c_{j'_1}^\dagger c_{j'_2}^\dagger\cdots c_{j'_P}^\dagger|0\rangle\,,\end{aligned} \tag{C.4.1}$$

we see that the fermion phase factor $f(\mathbf{n}, j)$ associated with the occupation number basis state $|\mathbf{n}\rangle = c_{j_1}^\dagger c_{j_2}^\dagger\cdots c_j^\dagger\cdots c_{j_P}|0\rangle$ and the site j is the number of anticommutations required to bring $c_j^\dagger$ to the front of the product of creation operators for $|\mathbf{n}\rangle$. Similarly, the fermion phase factor $f(\mathbf{n}', j')$ is the number of anticommutations required to bring $c_{j'}^\dagger$ to the front of the product of creation operators for $|\mathbf{n}'\rangle$. Because the configurations are ordered strictly according to their occupied site indices, $f(\mathbf{n}, j)$ is simply the number of sites in the configuration $[j_1, j_2, \ldots, j_P]$ whose indices are less than j, and $f(\mathbf{n}', j')$ is also simply the number of sites in the configuration $[j'_1, j'_2, \ldots, j'_P]$ whose indices are less than j'. These fermion phase factors are calculated individually using the helper function `eta`, whose Octave code is shown below. In `eta`'s argument list, 'state' = $[j_1, j_2, \ldots, j_P]$ is the $1 \times P$ vector of occupied site indices, and 'jf' is the index of the occupied site whose creation operator we must bring to the front of the product of

creation operators $c_{j_1}^{\dagger} c_{j_2}^{\dagger} \cdots c_{j_P}^{\dagger}$.

```
function fsum = eta(state, jf)

fsum = 0;

P = max(size(state));

for j = 1:P
    if jf > state(j)
        fsum = fsum + 1;
    endif
endfor

endfunction
```

The Octave code of the `Fermion` code branch's `buildhamiltonian` is shown below, where V is the $D \times P$ Hilbert space matrix, and 'neighborlist' is the $N \times M$ array storing the site indices of the M nearest neighbors of each of the N sites within the system.

```
function H = buildhamiltonian(V, neighborlist)

[D, P] = size(V);

H = zeros(D, D);
```

```
for m = 1:D
    for n = 1:D
        if size(intersection(V(m, :), V(n, :)), 2) == P - 1
            jm = complement(V(n, :), V(m, :));
            jn = complement(V(m, :), V(n, :));
            if intersection(jm, neighborlist(jn, :))
                fm = eta(V(m, :), jm);
                fn = eta(V(n, :), jn);
                if rem(fm + fn, 2) == 0
                    H(m, n) = -1;
                else
                    H(m, n) = 1;
                endif
            endif
        endif
    endfor
endfor

endfunction
```

C.4.3 Faster Algorithm for Spinless Fermions

From the Octave code above, we see the reason why this core function is slow: the algorithm is $O(D^2)$, where the dimension $D \sim e^N$ of the Hilbert space is a number that is

exponentially large in the system size N. Of the D^2 Hamiltonian matrix elements, only a very small fraction are actually nonzero, so the function `buildhamiltonian` spends most of its computational time checking pairs of configurations which are not connected to each other by a nearest neighbor hop. To arrive at a faster $O(D)$ core function, we adopt the following algorithm:

1. For each and every configuration $[j_1, j_2, \ldots, j_P]$, run through the list of occupied sites.

2. For each and every occupied site j in the configuration, run through the list of its nearest neighbors $[k_1, k_2, k_3, k_4]$. These are the sites that the particle at site j can hop to in principle.

3. For nearest neighbor k of site j, form a new list of sites by replacing j with k. This list of sites may not be properly ordered, so we order it using the function `orderlist`, whose Octave code is shown below. Besides returning a properly ordered list, `orderlist` also determines the overall fermion sign $(-1)^{f(\mathbf{n},\mathbf{n}')}$, where $|\mathbf{n}\rangle$ is the final occupation number basis state (with site k occupied), and $|\mathbf{n}'\rangle$ is the initial occupation number basis state (with site j occupied).

4. Determine the row index of the final occupation number basis state $|\mathbf{n}\rangle$ in the Hilbert space matrix using the function `listindex`. If $|\mathbf{n}\rangle$ is an invalid occupation number basis state, because pair(s) of nearest neighbors are simultaneously occupied, `listindex` will return a value of zero, in which case we do nothing. Else, with the row index of $|\mathbf{n}\rangle$, we set $\langle\mathbf{n}|H|\mathbf{n}'\rangle = -(-1)^{f(\mathbf{n},\mathbf{n}')}$.

Looking carefully at the inner product

$$\begin{aligned} &\langle 0|c_{j_P}\cdots c_{j+1}c_k c_{j-1}\cdots c_{j_2}c_{j_1}\left(c_k^\dagger c_j\right)c_{j_1}^\dagger c_{j_2}^\dagger\cdots c_{j-1}^\dagger c_j^\dagger c_{j+1}^\dagger\cdots c_{j_P}^\dagger|0\rangle \\ &= \langle 0|c_{j_P}\cdots c_{j+1}c_k c_k^\dagger c_{j-1}\cdots c_{j_2}c_{j_1}c_{j_1}^\dagger c_{j_2}^\dagger\cdots c_{j-1}^\dagger c_j c_j^\dagger c_{j+1}^\dagger\cdots c_{j_P}^\dagger|0\rangle = 1, \end{aligned} \tag{C.4.2}$$

we find that the value of the matrix element $\langle \mathbf{n}| - c_k^\dagger c_j |\mathbf{n}'\rangle$ depends only on the fermion sign incurred in properly ordering the operator product $c_{j_1}^\dagger c_{j_2}^\dagger \cdots c_{j-1}^\dagger c_k^\dagger c_{j+1}^\dagger \cdots c_{j_P}^\dagger$ to obtain the occupation number basis state $|\mathbf{n}\rangle$. This fermion sign can be computed by noting that, if $k < j-1$, then $f(\mathbf{n}, \mathbf{n}')$ is the number of sites out of the list $[j_1, j_2, \ldots, j-1]$ which are greater than k. Otherwise, if $k > j+1$, then $f(\mathbf{n}, \mathbf{n}')$ is the number of sites out of the list $[j+1, \ldots, j_P]$ which are less than k.

The helper function `orderlist` that I use to compute this fermion sign, and whose Octave code is shown below, is more generic, and does not assume that only one of the P occupied sites is out of proper order. The computational time cost of this function is bounded by P^p, where P is the total number of particles in the system, and p is the number of sites which are out of proper order. For the finite systems we studied in Chapters 4 and Chapter 8, we have $P < 10$, and $p \leq 4$, so the computational time cost is always small. We therefore need not worry about calling this helper function in the inner loops. As shown below, `orderlist` takes an improperly ordered list $n = [j_1, j_2, \ldots, j_P]$, and returns the properly ordered list $m = [j_{\pi(1)}, j_{\pi(2)}, \ldots, j_{\pi(P)}]$, along with the fermion sign f incurred in the reordering effected by the permutation $\pi : j \mapsto \pi(j)$.

```
function [m, f] = orderlist(n)

P = max(size(n));
f = 1;

i = 1;

while i < P
```

```
    % compare n(i) and n(i+1)
    if n(i) < n(i+1)
        % advance index
        i = i + 1;
    else
        % swap n(i) and n(i+1)
        tmp = n(i+1);
        n(i+1) = n(i);
        n(i) = tmp;
        % toggle sign
        f = -f;
        % reduce index, if possible, to compare new i and i-1
        if i > 1
            i = i - 1;
        % not possible to reduce index, can just advance i
        else
            i = i + 1;
        endif
    endif
endwhile

m = n;

endfunction
```

The Octave code of the function `quickhamiltonian` based on the above algorithm is shown below. Here V is the $D \times P$ Hilbert space matrix, 'neighborlist' is the $N \times M$ array of site indices of the M nearest neighbors of each of the N sites within the system, and H is the full $D \times D$ Hamiltonian matrix.

```
function H = quickhamiltonian(V, neighborlist)

[D, P] = size(V);
NBR = size(neighborlist, 2);

for m = 1:D
    for k = 1:P
        sm = V(m, :);
        for l = 1:NBR
            % for the m-th P-particle state |sm>,
            % hop the k-th particle to
            % its l-th neighboring site
            sm(k) = neighborlist(V(m, k), l);
            % reorder this state and obtain the corresponding phase
            [tmkl, fmkl] = orderlist(sm);
            % get the state index n of tmkl
            n = listindex(tmkl, V);
            % if |tmkl> is a state in V,
            % then listindex() will return a nonzero n,
            % otherwise, n = 0
            if n != 0
```

```
                H(m, n) = −fmkl;
            endif
        endfor
    endfor
endfor

endfunction
```

C.4.4 Compact Storage of Hamiltonian Matrices

Both `buildhamiltonian` and `quickhamiltonian` produce $D \times D$ Hamiltonian matrices. Most of these matrix elements are zero. When D is not too large, this is the preferred manner of storage, since we can then make use of the optimized matrix-vector manipulation capabilities of Octave. However, if D gets too large, then a trade off between computational efficiency and memory usage is necessary. The functions `buildcompacthamiltonian` and `quickcompacthamiltonian` store the row index n, column index n', and value $\langle \mathbf{n}|H|\mathbf{n}'\rangle$ of the nonzero Hamiltonian matrix elements in a $D' \times 3$ array, where D' is the total number of nonzero matrix elements, each each row is of the form

$$[n, n', \langle \mathbf{n}|H|\mathbf{n}'\rangle]. \tag{C.4.3}$$

The Octave code for the function `buildcompacthamiltonian` is shown below:

```
function Hc = buildcompacthamiltonian(V, neighborlist)

[D, P] = size(V);
```

```
p = 1;


for m = 1:D
    for n = 1:D
        if size(intersection(V(m, :), V(n, :)), 2) == P - 1
            jm = complement(V(n, :), V(m, :));
            jn = complement(V(m, :), V(n, :));
            if intersection(jm, neighborlist(jn, :))
                fm = eta(V(m, :), jm);
                fn = eta(V(n, :), jn);
                if rem(fm + fn, 2) == 0
                    Hc(p, :) = [ m n -1 ];
                    p = p + 1;
                else
                    Hc(p, :) = [ m n 1 ];
                    p = p + 1;
                endif
            endif
        endif
    endfor
endfor


endfunction
```

The Octave code for the function `quickcompacthamiltonian` is shown below:

```
function Hc = quickcompacthamiltonian(V, neighborlist)

[D, P] = size(V);
NBR = size(neighborlist, 2);

p = 1;

for m = 1:D
    for k = 1:P
        sm = V(m, :);
        for l = 1:NBR
            % for the m-th P-particle state |sm>,
            % hop the k-th particle to
            % its l-th neighboring site
            sm(k) = neighborlist(V(m, k), l);
            % reorder this state and obtain the corresponding phase
            [tmkl, fmkl] = orderlist(sm);
            % get the state index n of tmkl
            n = listindex(tmkl, V);
            % if |tmkl> is a state in V,
            % then listindex() will return a nonzero n,
            % otherwise, n = 0
            if n != 0
                % add nonzero matrix element to Hc
                Hc(p, :) = [ m n -fmkl ];
```

```
                    p = p + 1;
                endif
            endfor
        endfor
    endfor

endfunction
```

C.4.5 Adding Correlated Hops to the Hamiltonian

The functions `buildhamiltonian`, `quickhamiltonian` and their compact storage derivatives calculate only the Hamiltonian matrix for the Hamiltonians in (C.1.1) or (C.1.2), with only nearest neighbor hopping. Since they are already doing a good job, there is no need to have an analogous core function to build the Hamiltonian matrix for the model Hamiltonian in (C.1.3) with additional next-nearest neighbor correlated hopping. Instead, we will just have `buildhamiltonian` or `quickhamiltonian` (or their compact storage derivatives) build up the Hamiltonian matrix with nearest neighbor hopping, and introduce the core function `addcorrelatedhops` to add on the nonzero matrix elements coming from next-nearest neighbor correlated hopping.

There is a design issue arising from the introduction of `addcorrelatedhops`. Because we will almost certainly be performing twist boundary conditions averaging for all our cluster density matrix calculations, we need to worry about the fact that the phase twists incurred in the *bond gauge* (see Appendix D for the definition of the *bond gauge* and the *boundary gauge*) by next-nearest neighbor hops are not the same as nearest neighbor hops. There are two possible ways to account for this:

1. modify the function `addBCphase` (described in Appendix D) so that it works with both nearest and next-nearest neighbor hops; or

2. get the functions `quickhamiltonian` and `addcorrelatedhops` to return an additional array of hopping displacements, which can then be used to compute the phase twist incurred.

The second choice is conceptually cleaner, because if we decide to introduce Hamiltonians with even more exotic hops, the code can be augmented without revision of existing functions. But this choice is less easy to implement, and because of time constraints, I had to make do with the first choice. Anyone interested in extending the code base to work on more exotic Hamiltonians should definitely consider adopting the second code design.

Within the first choice for code design, the additional next-nearest neighbor hopping matrix elements are determined using the following algorithm, which uses that for `quickcompacthamiltonian` as a blueprint:

1. Run through all configurations $\{|\mathbf{n}\rangle\}$ in the Hilbert space.

2. For the configuration $|\mathbf{n}\rangle$, run through the particles from $1 \leq j \leq P$, where P is the total number of particles in the system.

3. For the jth particle selected in configuration $|\mathbf{n}\rangle = [j_1, \ldots, i, j, k, \ldots, j_P]$, whose position is given by $\mathbf{r}(\mathbf{n}, j)$, construct the configuration $|\mathbf{n}'(j)\rangle = [j_1, \ldots, i, k, \ldots, j_P]$ which does not include the jth particle.

4. Compare $|\mathbf{n}'(j)\rangle$ against the next-nearest neighbor list of the jth particle of configuration $|\mathbf{n}\rangle$, and see if any of its next-nearest neighbors are occupied.

5. If the intersection between these two lists is not empty, the jth particle in configuration $|\mathbf{n}\rangle$ is to be hopped to a site allowed by its next-nearest neighbor occupation. To do this,

   (a) pick a displacement $\mathbf{d}$ from the four possible displacements $(\pm 2, 0)$ and $(0, \pm 2)$,

   (b) determine $\mathbf{r}' = \mathbf{r}(\mathbf{n}, j) + \mathbf{d}$ subject to periodic boundary conditions,

   (c) and determine the index j' of $\mathbf{r}'$.

6. Construct the list $|\mathbf{n}'(j); j'\rangle = [j_1, \ldots, i, j', k, \ldots, j_P]$ with j' replacing j. Order this list (for fermions, determine also the fermion sign $(-1)^{f(\mathbf{n};j,j')}$ incurred in reordering the list), and determine its index in the Hilbert space matrix using the function `listindex`. If the returned value from `listindex` is nonzero, we have a candidate final state configuration $|\mathbf{n}'\rangle$.

7. Two next-nearest neighbor sites flank the correlated hop from site j to site j'. Let us call them sites k_1 and k_2. The total occupation for these two sites might be $n(\mathbf{n}; j, j') = n(k_1) + n(k_2) = 0, 1, 2$. This total occupation can be determined by taking the intersection between the lists $[k_1, k_2]$ and $[j_1, \ldots, j, \ldots, j_P]$.

8. Add the matrix element

$$\langle \mathbf{n}'|H|\mathbf{n}\rangle = -(-1)^{f(\mathbf{n};j,j')} n(\mathbf{n}; j, j')t' \tag{C.4.4}$$

   to the Hamiltonian matrix.

The Octave code for `addcorrelatedhops` is shown below, where V is the $D \times P$ Hilbert space matrix, H_0 the $D \times D$ nearest-neighbor hopping Hamiltonian matrix, R the $N \times 2$ array of coordinates of sites within the system, $\mathbf{R}_1$ and $\mathbf{R}_2$ the definining lattice

vectors of the system, *nR* the $N \times M$ array storing the site indices of the M nearest neighbors of each of the N system sites, *nnR* the $N \times M'$ array storing the site indices of the M' next-nearest neighbors of each of the N system sites, and t is the magnitude of the next-nearest neighbor correlated hopping matrix elements. The $D \times D$ correlated-hopping augmented Hamiltonian matrix is returned by `addcorrelatedhops`.

```
function H1 = addcorrelatedhops(V, H0, R, R1, R2, nR, nnR, t)

H1 = H0;

[D, P] = size(V);
N = size(R, 1);
NN = size(nR, 2);
NNN = size(nnR, 2);

T = [ 2 0; −2 0; 0 2; 0 −2 ];

for m = 1:D
    sm = V(m, :);
    for k = 1:P
        smk = complement(sm(k), sm);
        smknn = intersection(nnR(sm(k), :), smk);
        if size(smknn, 2) > 0
            for l = 1:4
                RmkT = round(periodicBC(R(sm(k), :) + T(l, :), R1, R2));
```

```
                for j = 1:N
                    if prod(RmkT == R(j, :))
                        jmkT = j;
                        break;
                    endif
                endfor
                if size(intersection(jmkT, sm), 2) == 0
                    mutualnnR = intersection(nnR(sm(k), :), nnR(jmkT, :));
                    occupiedmutualnnR = intersection(mutualnnR, sm);
                    NmkT = size(occupiedmutualnnR, 2);
                    smkT = sm;
                    smkT(k) = jmkT;
                    [tmkT, fmkT] = orderlist(smkT);
                    n = listindex(tmkT, V);
                    if n != 0
                        H1(m, n) = H1(m, n) – NmkT*fmkT*t;
                    endif
                endif
            endfor
        endif
    endfor
endfor

endfunction
```

Here let us warn that the additional correlated hopping term in (C.1.3) is only one of several correlated hopping terms derived by Zhang and Henley [205]. If we are to allow more flavors of correlated hops in (C.1.3), it is not right to have copies of `addcorrelatedhops` — one for each flavor of correlated hops — to calculate the correlated hopping matrix elements, and then simply add them afterwards. Instead, it is necessary to modify the single `addcorrelatedhops` function, so that all correlated hops that connects a given initial configuration to a given final configuration are handled consistently.

To work with systems with huge Hilbert spaces, the full Hamiltonian matrix cannot be stored in memory. The derivative function `addcompactcorrelatedhops`, whose Octave code is shown below, appends the correlated hop matrix elements to the compactified Hamiltonian array. The variables appearing in the argument list of `addcompactcorrelatedhops` are the same as those appearing in the argument list of `addcorrelatedhops`, except for H_0, which is a $D' \times 3$ compact array of the positions and values of the non-zero matrix elements of the nearest-neighbor hopping Hamiltonian. This function then returns a $D'' \times 3$ compact array of the nonzero matrix elements of the correlated-hopping augmented Hamiltonian, where $D'' > D'$.

```
function H1 = addcompactcorrelatedhops(V, H0, R, R1, R2, nR, nnR, t)

H1 = H0;

[D, P] = size(V);
N = size(R, 1);
NN = size(nR, 2);
```

```
NNN = size(nnR, 2);

T = [ 2 0; −2 0; 0 2; 0 −2 ];

p = size(H1, 1) + 1;

for m = 1:D
    sm = V(m, :);
    for k = 1:P
        smk = complement(sm(k), sm);
        smknn = intersection(nnR(sm(k), :), smk);
        if size(smknn, 2) > 0
            for l = 1:4
                RmkT = round(periodicBC(R(sm(k), :) + T(l, :), R1, R2));
                for j = 1:N
                    if prod(RmkT == R(j, :))
                        jmkT = j;
                        break;
                    endif
                endfor
                if size(intersection(jmkT, sm), 2) == 0
                    mutualnnR = intersection(nnR(sm(k), :), nnR(jmkT, :));
                    occupiedmutualnnR = intersection(mutualnnR, sm);
                    NmkT = size(occupiedmutualnnR, 2);
                    smkT = sm;
```

```
                    smkT(k) = jmkT;
                    [tmkT, fmkT] = orderlist(smkT);
                    n = listindex(tmkT, V);
                    if (n != 0) && (NmkT > 0)
                        H1(p, :) = [ m n −NmkT*fmkT*t ];
                        p = p + 1;
                    endif
                endif
            endfor
        endif
    endfor
endfor

endfunction
```

C.4.6 Anisotropic Spinless Extended Hubbard Hamiltonian

Unlike the case for the spinless extended Hubbard model with correlated hops, where we can append additional correlated hopping matrix elements to the Hamiltonian matrix produced by `quickhamiltonian` or `quickcompacthamiltonian`, the Hamiltonian matrix for the anisotropic spinless extended Hubbard model (described by the Hamiltonian in (7.3.2)) must be generated from scratch. This is accomplished by the function `quickcompactXYhamiltonian`, derived from `quickcompacthamiltonian` used for the isotropic model. The algorithm used in `quickcompactXYhamiltonian` for generating the non-zero matrix elements is the same as that used in the function

`quickcompacthamiltonian`, except for an additional check on whether the nearest-neighbor hop is along the x or y directions. The Octave code for this function is shown below, where V is the $D \times P$ Hilbert space matrix, nR the $N \times M$ array of site indices of the M nearest neighbors of each of the N system sites, R the $N \times 2$ array of coordinates of the system sites, $\mathbf{R}_1$ and $\mathbf{R}_2$ the defining lattice vectors of the system, t_x the magnitude of the nearest-neighbor hopping matrix element for hops along the x-direction, and t_y the magnitude of the nearest-neighbor hopping matrix element for hops along the y-direction.

```
function Hc = quickcompactXYhamiltonian(V, nR, R, R1, R2, tx, ty)

[D, P] = size(V);
NBR = size(nR, 2);

p = 1;

for m = 1:D
    for k = 1:P
        sm = V(m, :);
        for l = 1:NBR
            % for the m-th P-particle state |sm>,
            % hop the k-th particle to
            % its l-th neighboring site
            sm(k) = nR(V(m, k), l);
            % determine hopping vector
```

```
            dr = periodicBC(R(nR(V(m, k), l), :) − R(V(m, k), :), R1, R2);
            % reorder this state and obtain the corresponding phase
            [tmkl, fmkl] = orderlist(sm);
            % get the state index n of tmkl
            n = listindex(tmkl, V);
            % if |tmkl> is a state in V,
            % then listindex() will return a nonzero n,
            % otherwise, n = 0
            if n != 0
                % add nonzero matrix element to Hc
                % check if hop is along x- or y-direction
                if dr(1) == 0
                    Hc(p, :) = [ m n −ty*fmkl ];
                else
                    Hc(p, :) = [ m n −tx*fmkl ];
                endif
                p = p + 1;
            endif
        endfor
    endfor
endfor

endfunction
```

C.5 Translational Symmetry and Bloch States

C.5.1 Translating a Many-Particle Configuration

When we use any of the functions described in Section C.4 to build up the full Hamiltonian matrix, we have not taken into account the translational symmetry of the Hamiltonian, i.e. the Hamiltonian given by either (C.1.1) or (C.1.2) is invariant under the action of any lattice translation $T_{\mathbf{r}}$, subject to periodic boundary conditions. We expect, for example, that in the 4-particle ground state of the $(4,1)\times(1,3)$ system, the amplitudes of the configurations $[1,2,5,9]$ and $[1,4,8,11]$ shown in Figure C.7 have the same complex modulus, since the second configuration is related to the first configuration by a translation $\mathbf{T} = (2,1)$.

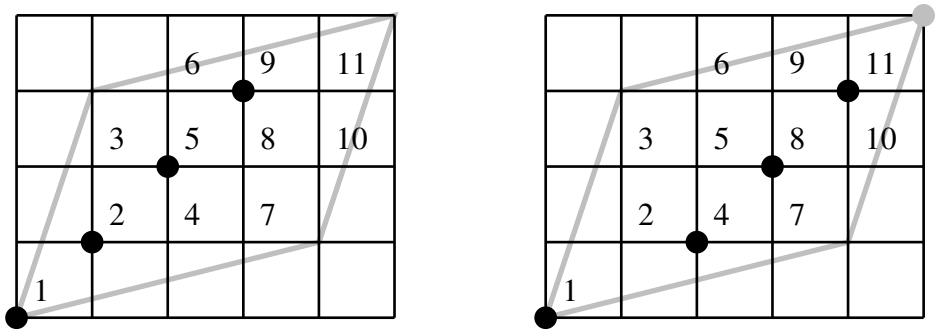

$[1,2,5,9]$ $\qquad$ $[1,4,8,11]$

Figure C.7: The configuration $[1,2,5,9]$ (left), which upon translation by the vector $\mathbf{T} = (2,1)$, becomes the configuration $[1,4,8,11]$ (right) when periodic boundary conditions are enforced upon the $(4,1)\times(1,3)$ system.

To make use of translational symmetries such as this, we want to group translationally related states together to write down a set of Bloch states

$$|\alpha,\mathbf{q}\rangle = \frac{1}{\sqrt{N}}\sum_{\mathbf{r}} e^{-\mathrm{i}\,\mathbf{q}\cdot\mathbf{r}}\,T_{\mathbf{r}}\,|\alpha\rangle\,, \tag{C.5.1}$$

where $|\alpha\rangle$ is the *generating configuration* for $|\alpha, \mathbf{q}\rangle$. For two different Bloch states $|\alpha, \mathbf{q}\rangle$ and $|\alpha', \mathbf{q}'\rangle$, their generating configurations $|\alpha\rangle$ and $|\alpha'\rangle$ are distinct configurations of P particles not related to each other by translational symmetry (but which may be related by rotational symmetry). With the usual periodic boundary conditions imposed, the allowed wave vectors $\mathbf{q}$ are such that

$$\exp(\mathrm{i}\,\mathbf{q}\cdot\mathbf{R}_1) = 1 = \exp(\mathrm{i}\,\mathbf{q}\cdot\mathbf{R}_2). \tag{C.5.2}$$

The translation operators $T_{\mathbf{r}} = T_{-\mathbf{r}}^{-1}$ appearing in (C.5.1) is defined such that

$$T_{\mathbf{r}}\,|0\rangle = |0\rangle\,, \quad T_{\mathbf{r}'} o_{\mathbf{r}}^{\dagger} T_{\mathbf{r}'}^{-1} = o_{\mathbf{r}+\mathbf{r}'}^{\dagger}. \tag{C.5.3}$$

where $o = a$ for bosons and $o = c$ for fermions.

If we write the configuration $|\alpha\rangle$ as

$$|\alpha\rangle = o_{\mathbf{r}_{j_1^\alpha}}^{\dagger} o_{\mathbf{r}_{j_2^\alpha}}^{\dagger} \cdots o_{\mathbf{r}_{j_P^\alpha}}^{\dagger} |0\rangle\,, \tag{C.5.4}$$

then the action of the translation $T_{\mathbf{r}}$ on $|\alpha\rangle$ is explicitly

$$\begin{aligned} T_{\mathbf{r}}\,|\alpha\rangle &= \left(T_{\mathbf{r}} o_{\mathbf{r}_{j_1^\alpha}}^{\dagger} T_{\mathbf{r}}^{-1}\right)\left(T_{\mathbf{r}} o_{\mathbf{r}_{j_2^\alpha}}^{\dagger} T_{\mathbf{r}}^{-1}\right)\cdots\left(T_{\mathbf{r}} o_{\mathbf{r}_{j_P^\alpha}}^{\dagger} T_{\mathbf{r}}^{-1}\right) T_{\mathbf{r}}\,|0\rangle \\ &= o_{\mathbf{r}_{j_1^\alpha}+\mathbf{r}}^{\dagger} o_{\mathbf{r}_{j_2^\alpha}+\mathbf{r}}^{\dagger} \cdots o_{\mathbf{r}_{j_P^\alpha}+\mathbf{r}}^{\dagger} |0\rangle\,. \end{aligned} \tag{C.5.5}$$

This state cannot be identified directly as

$$|\beta\rangle = o_{\mathbf{r}_{j_1^\beta}}^{\dagger} o_{\mathbf{r}_{j_2^\beta}}^{\dagger} \cdots o_{\mathbf{r}_{j_P^\beta}}^{\dagger} |0\rangle\,, \tag{C.5.6}$$

because in the occupation number basis states $|\alpha\rangle$ and $|\beta\rangle$, the creation operators are ordered according to their site indices, and the product in (C.5.5) may not have the creation operators in the proper order.

For example, in the $(4, 1) \times (1, 3)$ system, the occupation number basis states

$$[1, 2, 5, 9] = c_{(0,0)}^{\dagger} c_{(1,1)}^{\dagger} c_{(2,2)}^{\dagger} c_{(3,3)}^{\dagger} |0\rangle \tag{C.5.7}$$

and

$$[1,4,8,11] = c^{\dagger}_{(0,0)} c^{\dagger}_{(2,1)} c^{\dagger}_{(3,2)} c^{\dagger}_{(4,3)} |0\rangle \tag{C.5.8}$$

are related by a translation of $\mathbf{r} = (2,1)$. However, letting $T_{(2,1)}$ act on $[1,2,5,9]$ gives

$$\begin{aligned} T_{(2,1)}[1,2,5,9] &= c^{\dagger}_{(0,0)+(2,1)} c^{\dagger}_{(1,1)+(2,1)} c^{\dagger}_{(2,2)+(2,1)} c^{\dagger}_{(3,3)+(2,1)} |0\rangle \\ &= c^{\dagger}_{(2,1)} c^{\dagger}_{(3,2)} c^{\dagger}_{(4,3)} c^{\dagger}_{(5,4)} |0\rangle . \end{aligned} \tag{C.5.9}$$

Since $(5,4)$ lies outside the fundamental domain, it is mapped to $(0,0)$ under periodic boundary conditions by the function `periodicBC`, and so we end up with

$$T_{(2,1)}[1,2,5,9] = [4,8,11,1]. \tag{C.5.10}$$

For bosons, because the creation operators commute with one another, $[4,8,11,1] = [1,4,8,11]$. In general, if we take a configuration $[j_1, j_2, \ldots, j_P]$, use the `listcoord` function to produce a list of coordinates $[\mathbf{r}_{j_1}, \mathbf{r}_{j_2}, \ldots, \mathbf{r}_{j_P}]$, apply the `translate` function on this list of coordinates to obtain another list of coordinates $[\mathbf{r}'_{j_1}, \mathbf{r}'_{j_2}, \ldots, \mathbf{r}'_{j_P}]$, and then use the `coordlist` function to get back a list $[j'_1, j'_2, \ldots, j'_P]$, there is no guarantee that the list $[j'_1, j'_2, \ldots, j'_P]$ will be properly ordered. However, a simple `sort` function would suffice to order the list, which we can then compare with the configurations stored in the Hilbert space matrix. This sequence of operations is performed by the wrapper function `ntranslate`, whose Octave code is shown below. In the argument list of `ntranslate`, $n = [j_1, j_2, \ldots, j_P]$ is the ordered list of P occupied sites, $T = (T_x, T_y)$ the translation vector, organized as a 2×1 vector, R the $N \times 2$ array of system site coordinates, and $\mathbf{R}_1$ and $\mathbf{R}_2$ the defining lattice vectors of the system. The function `ntranslate` returns the ordered list $m = [j'_1, j'_2, \ldots, j'_P]$ of P occupied sites of the translated configuration.

---

function m = ntranslate(n, T, R1, R2, R)

```
s = listcoord(n, R);
t = translate(s, T, R1, R2);
m = sort(coordlist(t, R));
m = m';

endfunction
```

For fermions, because the creation operators anticommute with one another, we find in our little example that

$$[4, 8, 11, 1] = -[1, 4, 8, 11]. \tag{C.5.11}$$

Therefore, to translate a fermion configuration, we need also in general to keep track of the fermion signs incurred every time two fermion operators are interchanged. The wrapper function that performs this translation is also called `ntranslate`, to make the `Boson` and `Fermion` code branches parallels of each other. But instead of calling the `sort` function, the `ntranslate` function in the `Fermion` code branch, whose Octave code is shown below, calls the helper function `orderlist` to order the translated list, and also returns the fermion sign incurred by the ordering. The list of input and output variables for the `Fermion` code branch `ntranslate` function is the essentially the same as the `Boson` code branch `ntranslate` function, except that for the `Fermion` code branch, `ntranslate` also returns the fermion sign f associated with the translation.

```
function [m, f] = ntranslate(n, T, R1, R2, R)

s = listcoord(n, R);
t = translate(s, T, R1, R2);
[m, f] = orderlist(coordlist(t, R));
```

endfunction

C.5.2 Partitioning the Hilbert Space

To determine all Bloch states for a given wave vector $\mathbf{Q}$, we need to partition the Hilbert space into sectors of translationally equivalent configurations. For a system with N sites, there are N independent translations $T_{\mathbf{r}}$, each identified with a site $\mathbf{r}$ on the system. The translational symmetry sector generated by $|\alpha\rangle$ thus consists of the configurations

$$\{T_{\mathbf{r}_1}|\alpha\rangle, T_{\mathbf{r}_2}|\alpha\rangle, \ldots, T_{\mathbf{r}_N}|\alpha\rangle\}, \tag{C.5.12}$$

where $\mathbf{r}_1 = (0,0)$ to $\mathbf{r}_N$ are the position vectors of sites within the fundamental domain. This partitioning is accomplished primarily by the core function `partition`, which uses the algorithm listed below:

1. Start from the partitioned and quotient Hilbert space matrices V_P and V_Q. Here V_Q is a $D_Q \times P$ array, in which the $D_Q < D$ rows denote the P-particle configurations in the full $D \times P$ Hilbert space matrix V that are yet to be partitioned. The partitioned Hilbert space matrix V_P is a $M \times N$ array, in which each of the D_P rows consist of the indices of P-particle configurations related to each other by a translation. These M rows of V_P are thus the translational symmetry sectors for different generating configurations. All the P-particle configurations found in V are either found in V_Q or V_P, while V_P and V_Q have no P-particle configurations in common. In the case of fermions, we will also have at this starting point a $M \times N$ array of fermion signs f_P that accompany the partitioned Hilbert space matrix V_P, such that $f_P(m,n)$ is the fermion sign incurred to obtain the P-particle configuration $V_P(m,n)$ by translating the generating configuration $V_P(m,1)$.

2. Pick the first state of V_Q and call it $|\alpha\rangle$. This should be a configuration that is translationally inequivalent to any state in V_P, and will serve as the generating configuration of the translational symmetry sector that we will append to V_P.

3. Running through the set of all independent translations $\{T_{\mathbf{r}_i}\}_{i=1}^{N}$, we apply the function `ntranslate` on $|\alpha\rangle$ with translation vector $\mathbf{r}_i$, and store the index of the resulting configuration, in the order of $\mathbf{r}_i$, in a new row of V_P. In the case of fermions, `partition` will also append a new row of fermion signs incurred by ordering $T_{\mathbf{r}_i}|\alpha\rangle$ to the matrix f_P of fermion signs.

4. After updating V_P, `partition` must also 'orthogonalize' V_Q, by removing from V_Q configurations that have been added to V_P. Once this is done, `partition` can be used recursively.

The Octave code for the boson version of `partition` is shown below. This function takes a given $D_Q \times P$ quotient Hilbert space matrix V_Q, treat the first P-particle configuration in V_Q as a generating configuration, and build up the translational symmetry sector associated with this generating configuration. Abusing our variable names, we return the newly-minted translational symmetry sector as a $1 \times N$ vector of state indices, and call it V_P. The `Boson` code branch function `partition` also returns the $D'_Q \times P$ quotient Hilbert space matrix V_{PQ}, with $D'_Q < D_Q$, containing all the P-particle configurations in V_Q, less those in V_P.

```
function [VP, VPQ] = partition(V, VQ, R, R1, R2)

% prepare first state

n = VQ(1, :);
```

```
% prepare VPQ

VPQ = VQ;
NPQ = size(VPQ, 1);

% translation

N = size(R, 1);

for i = 1:N
    m = ntranslate(n, R(i, :), R1, R2, R);
    im = listindex(m, VQ);
    if im != 0
        VP(i) = listindex(m, V);
    endif
endfor

% orthogonalize VPQ

for i = 1:N
    iq = listindex(V(VP(i), :), VPQ);
    if iq != 0
        if iq == 1
            VPQ = [ VPQ(iq+1:NPQ, :) ];
```

```
            NPQ = size(VPQ, 1);
        elseif iq == NPQ
            VPQ = [ VPQ(1:iq-1, :) ];
            NPQ = size(VPQ, 1);
        else
            VPQ = [ VPQ(1:iq-1, :); VPQ(iq+1:NPQ, :) ];
            NPQ = size(VPQ, 1);
        endif
    endif
endfor

endfunction
```

The Octave code for the fermion version of `partition` is shown below. This `Fermion` code branch function returns a $1 \times N$ vector f_P of fermion signs, in addition to what the `Boson` code branch `partition` returns.

```
function [VP, VPQ, fP] = partition(V, VQ, R, R1, R2)

% prepare first state

n = VQ(1, :);

% prepare VPQ

VPQ = VQ;
```

```
NPQ = size(VPQ, 1);

% translation

N = size(R, 1);

for i = 1:N
    [m, f] = ntranslate(n, R(i, :), R1, R2, R);
    im = listindex(m, VQ);
    if im != 0
        VP(i) = listindex(m, V);
        fP(i) = f;
    endif
endfor

% orthogonalize VPQ

for i = 1:N
    iq = listindex(V(VP(i), :), VPQ);
    if iq != 0
        if iq == 1
            VPQ = [ VPQ(iq+1:NPQ, :) ];
            NPQ = size(VPQ, 1);
        elseif iq == NPQ
            VPQ = [ VPQ(1:iq−1, :) ];
```

```
            NPQ = size(VPQ, 1);
        else
            VPQ = [ VPQ(1:iq−1, :); VPQ(iq+1:NPQ, :) ];
            NPQ = size(VPQ, 1);
        endif
    endif
endfor

endfunction
```

Making use of the recursive nature of `partition`, we have a wrapper function `fullpartition` that completely partitions the Hilbert space into translation symmetry sectors. This function returns a $M \times N$ matrix V_P looking like

$$V_P = \begin{bmatrix} \text{index}\, T_{\mathbf{r}_1} |\alpha_1\rangle & \text{index}\, T_{\mathbf{r}_2} |\alpha_1\rangle & \cdots & \text{index}\, T_{\mathbf{r}_N} |\alpha_1\rangle \\ \text{index}\, T_{\mathbf{r}_1} |\alpha_2\rangle & \text{index}\, T_{\mathbf{r}_2} |\alpha_2\rangle & \cdots & \text{index}\, T_{\mathbf{r}_N} |\alpha_2\rangle \\ \vdots & \vdots & \ddots & \vdots \\ \text{index}\, T_{\mathbf{r}_1} |\alpha_M\rangle & \text{index}\, T_{\mathbf{r}_2} |\alpha_M\rangle & \cdots & \text{index}\, T_{\mathbf{r}_N} |\alpha M\rangle \end{bmatrix}, \tag{C.5.13}$$

where $\text{index}\, T_{\mathbf{r}_i} |\alpha_j\rangle$ is the index of the configuration $T_{\mathbf{r}_i} |\alpha_j\rangle$ (after proper ordering) within the Hilbert space. In the case of fermions, `fullpartition` also returns a $M \times N$ matrix f_P of fermion signs.

Note also that while there are M sectors of translationally inequivalent states, the size D of the Hilbert space is not necessarily MN. This is because for some system geometries $(\mathbf{R}_1, \mathbf{R}_2)$, we can end up with configurations $|\alpha_k\rangle$ with additional symmetries, such that

$$T_{\mathbf{r}_i} |\alpha_k\rangle = T_{\mathbf{r}_j} |\alpha_k\rangle \tag{C.5.14}$$

for $\mathbf{r}_i \neq \mathbf{r}_j$. In spite of this, we still need to keep a list of N states in the sector generated by $|\alpha_k\rangle$, because for such configurations, we would encounter special values of the reciprocal lattice vector $\mathbf{q}_l$ for which the Bloch state

$$|\alpha_k, \mathbf{q}_l\rangle = \frac{1}{\sqrt{N}} \sum_{\mathbf{r}} e^{-i\,\mathbf{q}_l\cdot\mathbf{r}} T_{\mathbf{r}} |\alpha_k\rangle \tag{C.5.15}$$

is null. We call generating configurations with the additional symmetries (C.5.14) *special configurations*, and the Bloch states they generate *special Bloch states*. It is in fact important that we end up with null special Bloch states when the wave vector $\mathbf{q}_l$ is *special*. Otherwise we would overcount the size of the Hilbert space.

The Octave code for the boson version of `fullpartition` is shown below. Here, the output V_P is the $M \times N$ fully-partitioned Hilbert space matrix.

```
function VP = fullpartition(V, R, R1, R2)

% first round

[VP, VQ] = partition(V, V, R, R1, R2);

% automate the rest

while max(size(VQ)) != 0
    [vp, VQ] = partition(V, VQ, R, R1, R2);
    VP = [ VP; vp ];
endwhile

endfunction
```

The Octave code for the fermion version of `fullpartition` is shown below. Here, the output V_P is the $M \times N$ fully-partitioned Hilbert space matrix, and f_P is the accompanying $M \times N$ matrix of fermion signs.

```
function [VP, fP] = fullpartition(V, R, R1, R2)

% first round

[VP, VQ, fP] = partition(V, V, R, R1, R2);

% automate the rest

while size(VQ, 1) != 0
    [vp, VQ, fp] = partition(V, VQ, R, R1, R2);
    VP = [ VP; vp ];
    fP = [ fP; fp ];
endwhile

endfunction
```

C.5.3 Constructing the Bloch States

To make use of (C.5.1) and the partitioned Hilbert space V_P to construct the Bloch state $|\alpha, \mathbf{q}\rangle$, we need to evaluate $\mathbf{q} \cdot \mathbf{r}$ given the integer representation of the reciprocal lattice vector $\mathbf{q} = (q_1, q_2) = q_1\mathbf{Q}_1 + q_2\mathbf{Q}_2$, for a given site $\mathbf{r} = (x, y)$ within the fundamental

domain. From (C.2.10a) and (C.2.10b), we find that this dot product can be written in terms of the components of the lattice vectors $\mathbf{R}_1$ and $\mathbf{R}_2$ as

$$\mathbf{q}\cdot\mathbf{r} = \frac{2\pi}{N}\left\{q_1\left[xR_{2y} - yR_{2x}\right] + q_2\left[R_{1x}y - R_{1y}x\right]\right\}. \tag{C.5.16}$$

The helper function `blochstate`, supplied with the translation symmetry sector generated by the configuration $|\alpha\rangle$, then constructs the properly normalized Bloch state $|\alpha, \mathbf{q}\rangle$ using (C.5.16), and returns a 0×0 null vector for those special configurations $|\alpha\rangle$ and special wave vectors $\mathbf{q}$ where $|\alpha, \mathbf{q}\rangle$ vanishes.

The Octave code of the boson version of `blochstate` is shown below, where we again abuse variable names, and refer to the $1 \times N$ translation symmetry sector of state indices by V_P. In the rest of the argument list, R is the $N \times 2$ array of system site coordinates, $\mathbf{R}_1$ and $\mathbf{R}_2$ the defining lattice vectors of the system, D the size of the Hilbert space, and (q_1, q_2) are the integer multipliers in the wave vector $\mathbf{q} = q_1\mathbf{Q}_1 + q_2\mathbf{Q}_2$, selected from the $N \times 2$ list of 'reciprocal lattice vectors' within the infinite-system FBZ generated by the `makeFBZ`. The function `blochstate` returns the $1 \times D$ vector of amplitudes for the Bloch state $|\alpha, \mathbf{q}\rangle$.

```
function a = blochstate(VP, R, R1, R2, D, q1, q2)

N = R1(1)*R2(2) - R1(2)*R2(1);

a = zeros(1, D);

for j = 1:N
    a(VP(j)) = a(VP(j)) + exp(-i*2*pi*(q1*(R(j, 1)*R2(2) - R(j, 2)*R2(1)) +\
    q2*(R1(1)*R(j, 2) - R1(2)*R(j, 1)))/N);
```

```
endfor

Na = norm(a);

if Na*D < 1
    a = [];
else
    a = a/Na;
endif

endfunction
```

The Octave code of the fermion version of `blochstate` is shown below. The list of arguments and output variable are essentially the same as the `Boson` code branch `blochstate`, except that the `Fermion` code branch `blochstate` requires an additional argument, the $1 \times N$ vector of fermion signs associated with the $1 \times N$ translational symmetry sector V_P.

```
function a = blochstate(VP, fP, R, R1, R2, D, q1, q2)

N = R1(1)*R2(2) - R1(2)*R2(1);

Q1 = 2*pi*[ R2(2) -R2(1) ]/N;
Q2 = 2*pi*[ -R1(2) R1(1) ]/N;
Q = q1*Q1 + q2*Q2;
```

```
a = zeros(1, D);

for j = 1:N
    a(VP(j)) = a(VP(j)) + fP(j)*exp(−i*dot(Q, R(j, :)));
endfor

Na = norm(a);

if Na*D < 1
    a = [];
else
    a = a/Na;
endif

endfunction
```

As can be seen from the codes above, the $1 \times D$ vector of amplitudes for the Bloch state $|\alpha, \mathbf{q}\rangle$ contains at most $N \ll D$ nonzero entries. We find this *inflated* representation of the Bloch states useful later on, when we generate the Bloch-reduced Hamiltonian matrix from the full Hamiltonian matrix. For non-null Bloch states, the product of the norm of the unnormalized Bloch state vector with D is typically $O(D)$, whereas for those special Bloch states which are nominally null, we find numerically that this product is a very small number. Therefore we adopt the criterion that, if this product is less than one, `blochstate` will return a null vector.

Also, we see from the fermion code for `blochstate` that the fermion signs asso-

ciated with each $T_{\mathbf{r}}|\alpha\rangle$ are built into the amplitudes of the N configurations within a translation symmetry sector. This frees us from the burden of tracking fermion signs later in the process of constructing the Bloch-reduced Hamiltonian matrices and performing exact diagonalization.

The wrapper function `allblochstates` then takes the partitioned Hilbert space matrix V_P (and the fermion sign matrix f_P too, if we are dealing with fermions), and calls on `blochstate` to construct all Bloch states with a given wave vector $\mathbf{q}$. The Octave code for the boson version of this wrapper function is shown below. Here, all input variables have the same form as those in the argument list of `blochstate`, except for V_P, which is now the $M \times N$ fully-partitioned Hilbert space matrix generated by `fullpartition`. The output variable a, instead of being a $1 \times D$ vector of amplitudes, is now a $M' \times D$ matrix of amplitudes, whose rows are in one-to-one correspondence with the translational symmetry sectors in V_P.

```
function a = allblochstates(VP, R, R1, R2, D, q1, q2)

M = size(VP, 1);

k = 1;

for i = 1:M
    b = blochstate(VP(i, :), R, R1, R2, D, q1, q2);
    if max(size(b)) > 0
        a(k, :) = b;
        k = k + 1;
```

```
    endif
endfor

endfunction
```

The Octave code for the fermion version of `allblochstates` is shown below, where f_P is now the full $M \times N$ matrix of fermion signs associated with the fully-partitioned $M \times N$ Hilbert space matrix V_P:

```
function a = allblochstates(VP, fP, R, R1, R2, D, q1, q2)

M = size(VP, 1);

k = 1;

for i = 1:M
    b = blochstate(VP(i, :), fP(i, :), R, R1, R2, D, q1, q2);
    if max(size(b)) > 0
        a(k, :) = b;
        k = k + 1;
    endif
endfor

endfunction
```

We note here that the number of rows M' in the output variable a of `allbloch-`

`states` is usually M, the number of distinct translational symmetry sectors. However, at special wave vector values, some of these M translational symmetry sectors give rise to null Bloch states. By construction, in the inflated representation, a contains only the non-null Bloch states, and at these special wave vectors, $M' < M$.

C.5.4 Compact Storage of Bloch States

When we use the compact array form for the Hamiltonian, there is no point storing the Bloch states as $1 \times D$ vectors, when only N of the D entries in each Bloch state can actually take on nonzero values, since we cannot take advantage of the matrix-vector multiplication functionality of Octave. We therefore have an alternate set of functions, `compactblochstate` and `allcompactblochstates`, which have been developed for the `Fermion` code branch only, to construct Bloch states and return them as $1 \times N$ vectors storing only the nonzero entries.

The Octave code for the fermion version of `compactblochstate` is shown below. The input variables in the argument list of `compactblochstate` have the same forms as those in `blochstate`, but the output variable a is now a $1 \times N$ vector of amplitudes which can actually be nonzero. We call this the *deflated* representation of the Bloch states, within which the amplitudes are organized, such that $a(1, n)$ is the amplitude of the P-particle configuration $V_P(1, n)$ in the given translational symmetry sector.

```
function a = compactblochstate(VP, fP, R, R1, R2, D, q1, q2)

N = size(R, 1);

Q1 = 2*pi*[ R2(2) -R2(1) ]/N;
```

```
Q2 = 2*pi*[ -R1(2) R1(1) ]/N;
Q = q1*Q1 + q2*Q2;

for j = 1:N
    a(j) = fP(j)*exp(-i*dot(Q, R(j, :)));
endfor

% check whether VP is a special Bloch sector, and normalize appropriately

M = size(create_set(VP), 2);

if M < N
    a = a*(M/N)/sqrt(M);
else
    a = a/sqrt(M);
endif

endfunction
```

The Octave code for the fermion version of `allcompactblochstates` is shown below. Here all input variables in the argument list of `allcompactblochstates` have the same forms as those in `allblochstates`, but the output variable a is now a $M \times N$ matrix of amplitudes which can actually be nonzero.

```
function a = allcompactblochstates(VP, fP, R, R1, R2, D, q1, q2)
```

```
M = size(VP, 1);

for i = 1:M
    b = compactblochstate(VP(i, :), fP(i, :), R, R1, R2, D, q1, q2);
    a(i, :) = b;
endfor

endfunction
```

In the inflated representation, we can easily tell whether a special Bloch state is null by checking the product of its norm with the size of the Hilbert space. If the special Bloch state is null, it is then excluded by `allblochstates` from the matrix a of all non-null Bloch states. In the deflated representation, however, the amplitudes which would have cancelled are stored in different columns of the vector, and there is no simple criterion we can implement within the present `compactblochstate` for deciding whether the deflated Bloch state we are constructing will ultimately be null. If we were industrious, we could write a helper function, called from within `compactblochstate`, which would check whether the Bloch state is special, based on the information available in V_P, and thereafter compute the appropriate sum of amplitudes to check whether the special Bloch state is null. We have not done this.

To illustrate this problem of null special Bloch states, let us look at the example of a two-legged ladder system with $\mathbf{R}_1 = (6, 0)$ and $\mathbf{R}_2 = (0, 2)$, which has $N = 12$ sites. For $P = 3$ particles within the system, the ($D = 76$)-dimensional Hilbert space partitions

into seven translational symmetry sectors,

$$V_{3P} = \begin{bmatrix} 1 & 20 & 39 & 52 & 65 & 70 & 75 & 76 & 19 & 38 & 25 & 6 \\ 2 & 22 & 40 & 54 & 66 & 72 & 15 & 36 & 50 & 64 & 29 & 14 \\ 3 & 21 & 41 & 53 & 67 & 71 & 34 & 17 & 63 & 51 & 33 & 10 \\ 4 & 24 & 42 & 56 & 7 & 30 & 44 & 60 & 68 & 74 & 35 & 18 \\ 5 & 23 & 43 & 55 & 26 & 11 & 57 & 47 & 73 & 69 & 37 & 16 \\ 8 & 32 & 45 & 62 & 8 & 32 & 45 & 62 & 8 & 32 & 45 & 62 \\ 9 & 31 & 46 & 61 & 27 & 13 & 58 & 49 & 12 & 28 & 48 & 59 \end{bmatrix}. \qquad \text{(C.5.17)}$$

The sixth translational symmetry sector, which is special, consists of the configurations

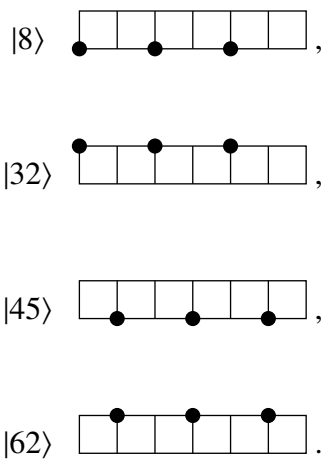

(C.5.18)

The Bloch state for this special translational symmetry sector vanishes at the wave vector $\mathbf{q} = (\frac{\pi}{3}, 0)$, because the sums of amplitudes for each configuration vanish, as shown in Table C.2.

Therefore, for $\mathbf{q} = (\frac{\pi}{3}, 0)$, the function `allblochstates` yields only six Bloch states, giving thus a 6×6 Bloch-reduced Hamiltonian matrix. Each of these six non-null Bloch states are represented within Octave as $1 \times D$ vectors with N nonzero entries. For example, for the non-null Bloch state associated with the first translational-symmetry sector, the nonzero entries are the $n = 1, 6, 19, 20, 25, 38, 39, 52, 65, 70, 75, 76$ entries of

Table C.2: Amplitude contributions and sums for the high-symmetry configurations $|8\rangle$, $|32\rangle$, $|45\rangle$, and $|62\rangle$ for the $(6,0) \times (0,2)$ ladder system, subject to periodic boundary conditions, in the $\mathbf{q} = (\frac{\pi}{3}, 0)$ Bloch sector.

	$\|8\rangle$	$\|32\rangle$	$\|45\rangle$	$\|62\rangle$
	$1,$	$1,$	$e^{-i\pi/3},$	$e^{-i\pi/3},$
contributions	$e^{-i2\pi/3},$	$e^{-i2\pi/3},$	$-1,$	$-1,$
	$e^{-i4\pi/3}$	$e^{-i4\pi/3}$	$e^{-i5\pi/3}$	$e^{-i5\pi/3}$
sum	0	0	0	0

the $1 \times D$ vector (see (C.5.17)).

After diagonalizing the Bloch-reduced Hamiltonian, we get a 6×1 ground state vector $|\psi\rangle$ in the basis of the non-vanishing Bloch states. From the 6×1 Bloch-reduced ground-state vector $|\psi\rangle$ we can reconstruct the $D \times 1$ full ground-state vector $|\Psi\rangle$ in the configurational basis very simply by performing a weighted sum

$$|\Psi\rangle = \sum_m \psi_m \, |\alpha_m\rangle \tag{C.5.19}$$

over the inflated $1 \times D$ Bloch states $|\alpha_m\rangle$, as is done in the function `blocheig` discussed in Section C.7.

In the deflated representation, I made use of the fact that each translational symmetry sector contains at most N configurations, and designed the function `compactblochstate` to return a dense $1 \times N$ vector instead of a sparse $1 \times D$ vector. Applying `compactblochstate` to the sixth Bloch sector, we find that the function returns the vector

$$|a_6\rangle = \frac{1}{\sqrt{12}}(1, 1, e^{-i\pi/3}, e^{-i\pi/3}, e^{-i2\pi/3}, e^{-i2\pi/3}, -1, -1, e^{-i4\pi/3}, e^{-i4\pi/3}, e^{-i5\pi/3}, e^{-i5\pi/3}), \tag{C.5.20}$$

when the Bloch state should have been explicitly zero, as shown in Table C.2. The only effect of retaining this deflated Bloch state in the basis for Bloch-reducing the Hamiltonian matrix would be to introduce an extraneous zero energy eigenvalue in the spectrum of the Bloch-reduced Hamiltonian matrix.

In all of the models we have studied numerically, the ground-state energy is negative. Therefore, the ED function `blochcompacteig` (described in Section C.6), which works with the deflated representation for the Bloch states, will encounter no difficulty identifying the 'physical' ED ground state, and return it accordingly as the output minimum-energy eigenstate for a given Bloch sector. In models where the ground-state energy is zero or positive, the extraneous zero energy eigenvalue introduced by keeping the null Bloch states will mean `blochcompacteig` returning a totally random wave function as the 'minimum-energy eigenfunction' some or all of the time. To deal with this properly, one would then need to refine `compactblochstate` so that it returns a null vector when the special Bloch state is null. Otherwise, a quick trick would be to shift the diagonal elements of the Hamiltonian matrix (and append them to the compact array of nonzero matrix elements, if these are not already stored in the first place), so that the lowest 'physical' ED energy eigenvalue become negative. Because they result from the null inner product between null Bloch states and the Hamiltonian matrix, the extraneous, 'non-physical', zero energy eigenvalues will not be affected by the shift.

C.6 Bloch-Reduced Hamiltonian

Because of the translational invariance of the Hamiltonian in (C.1.1) or (C.1.2), its matrix element between Bloch states of different wave vectors $\mathbf{q}$ and $\mathbf{q}'$ vanishes. The Hamiltonian, however, connects Bloch states $|\alpha, \mathbf{q}\rangle$ and $|\beta, \mathbf{q}\rangle$ with the same wave vector

q, and we can organize the matrix elements

$$H_{\alpha,\beta}(\mathbf{q}) = \langle \alpha, \mathbf{q}|H|\beta, \mathbf{q}\rangle \tag{C.6.1}$$

into a *Bloch-reduced Hamiltonian* matrix $H(\mathbf{q})$. This $M' \times M'$ matrix, where $M' \leq M$ is the number of non-null Bloch states, and $M \lesssim D/N$ is the number of translation symmetry sectors, can be constructed in two ways: (i) by the core function `blochhamiltonian` from the full Hamiltonian matrix produced either by the slow `buildhamiltonian` function or the fast `quickhamiltonian` function; or (ii) by the core function `blochcompacthamiltonian` from the compact array of nonzero Hamiltonian matrix elements produced by `quickcompacthamiltonian` or derivatives. We document the core function `blochhamiltonian` in Section C.6.1, and the core function `blochcompacthamiltonian` in Section C.6.2.

C.6.1 Construction from Full Hamiltonian Matrix

When the full $D \times D$ Hamiltonian matrix and the inflated Bloch states are available, i.e. stored in memory, we can make use of the native matrix-vector multiplication functionality of Octave to compute the Bloch-reduced Hamiltonian matrix, using the function `blochhamiltonian`. The Octave code for the `Boson` code branch version of `blochhamiltonian` is shown below, where V is the $D \times P$ Hilbert space matrix, R the $N \times 2$ array of system site coordinates, $\mathbf{R}_1$ and $\mathbf{R}_2$ the defining lattice vectors for the system, H the $D \times D$ Hamiltonian matrix, and (q_1, q_2) the integer multipliers in the wave vector $\mathbf{q} = q_1\mathbf{Q}_1 + q_2\mathbf{Q}_2$ selected from the $N \times 2$ list of 'reciprocal lattice vectors' within the infinite-system FBZ generated by `makeFBZ`. The function returns the $M' \times M'$ Bloch-reduced Hamiltonian matrix h with wave vector **q**.

---

function h = blochhamiltonian(V, R, R1, R2, H, q1, q2)

```
D = size(V, 1);

VP = fullpartition(V, R, R1, R2);

a = allblochstates(VP, R, R1, R2, D, q1, q2);

h = a*H*a';

endfunction
```

The `Fermion` code branch version of `blochhamiltonian` has been modified to make it run faster in conjunction with twist boundary conditions averaging (see Appendix D). Its Octave code is shown below, with V_P and f_P being the fully-partitioned $M \times N$ Hilbert space matrix and the $M \times N$ matrix of fermion signs respectively.

```
function h = blochhamiltonian(V, VP, fP, R, R1, R2, H, q1, q2)

D = size(V, 1);

% This is a slow function, but since it is a twist-independent operation,
% we can do it once outside of blochhamiltonian, and supply the results
% to blochhamiltonian for computation at each phi
%
% [VP, fP] = fullpartition(V, R, R1, R2);
```

```
a = allblochstates(VP, fP, R, R1, R2, D, q1, q2);

h = a*H*a';

endfunction
```

C.6.2 Construction from Compact Hamiltonian Array

When we store only the compact $D' \times 3$ array of nonzero Hamiltonian matrix elements, and the $M \times N$ array of nonzero Bloch-state amplitudes, we can no longer take advantage of the native matrix-vector multiplication functionalities of Octave to construct the $M \times M$ Bloch-reduced Hamiltonian matrix. Instead, we must handle the 'matrix-vector multiplication' of the Hamiltonian and the Bloch states, both in compact array form, ourselves. Writing the function `blochcompacthamiltonian` to do so, requires some thought.

Consider the nonzero matrix element $\langle \mathbf{n}|H|\mathbf{n}'\rangle$ stored in the compact Hamiltonian array. In most situations, the configurations $|\mathbf{n}\rangle$ and $|\mathbf{n}'\rangle$ each appears only once in a particular row of the fully-partitioned Hilbert space matrix V_P, say $|\mathbf{n}\rangle$ in row k and column l, and $|\mathbf{n}'\rangle$ in row k' and column l'. We know then that $\langle \mathbf{n}|H|\mathbf{n}'\rangle$ contributes only to the (k, k') matrix element of $H(\mathbf{q})$, with appropriate contributions from the lth and l'th entries of the kth and k'th Bloch states respectively.

On some rare occasions, the configuration $|\mathbf{n}\rangle$ or $|\mathbf{n}'\rangle$ may be special configurations, and therefore appears more than once in their respective rows, say $|\mathbf{n}\rangle$ appearing in the (k, l_1), (k, l_2), ..., (k, l_{M_k}) entries of V_P, and $|\mathbf{n}'\rangle$ appearing in the (k', l'_1), (k', l'_2), ..., $(k', l'_{M'_{k'}})$ entries of V_P. In such cases, the amplitudes of the l_1th, l_2th, ..., l_{M_k}th entries

in the kth Bloch state, and the l'_1th, l'_2th, dots, $l'_{M'_{k'}}$ th entries in the k'th Bloch state have to be summed before we take the product of their sums with $\langle \mathbf{n}|H|\mathbf{n}'\rangle$ to figure out the latter's contribution to the (k, k') matrix element of $H(\mathbf{q})$.

The Octave code for `blochcompacthamiltonian` in the `Fermion` code branch, and which has no parallel in the `Boson` code branch, is shown below. Here all the input variables have the same forms as those in the argument list of `blochhamiltonian`, except for H, which is a $D' \times 3$ compact array of the nonzero Hamiltonian matrix elements. The output variable h of `blochcompacthamiltonian` is always an $M \times M$ matrix.

```
function h = blochcompacthamiltonian(V, VP, fP, R, R1, R2, H, q1, q2)

[D, P] = size(V);
[DP, NP] = size(VP);
DC = size(H, 1);

% this can be moved outside of this function as well, since it does
% not depend on the phase angle phi, but it is a fast operation, so
% forget it for the time being

a = allcompactblochstates(VP, fP, R, R1, R2, D, q1, q2);

% H = [ { m, n, H(m, n) } ]
% |m> = V(m, :) and |n> = V(n, :)
% in most situations, |m> and |n> each appears only once in a
% particular row of VP, say |m> appears in VP(k1, :) and |n>
```

```
% appears in VP(k2, :), say |m> = VP(k1, lm) and |n> = VP(k2, ln)
% then (m, n, H(m, n)) contributes only to h(k1, k2)
% however, some states |m> and/or |n> may appear multiple
% times in a particular row of VP, and need to be handled with care
% let's say |m> = VP(k1, lm1), VP(k1, lm2), ..., VP(k1, lmM), and
% |n> = VP(k2, ln1), VP(k2, ln2), ..., VP(k2, lnN), then
% am = a(k1, lm1) + a(k1, lm2) + ... + a(k1, lmM) and
% an = a(k2, ln1) + a(k2, ln2) + ... + a(k2, lnN), so that
% h(k1, k2) = h(k1, k2) + am * H(p, 3) * an

h = zeros(DP);

for p = 1:DC
    % find (k1, lm1), (k1, lm2), ..., (k1, lmM) and accumulate into am
    % find (k2, ln1), (k2, ln2), ..., (k2, lnN) and accumulate into an
    % set k1 = k2 = 0. These should be nonzero at the end of the
    % following for loop
    k1 = k2 = 0;
    % set am = an = 0. These may be zero at the end of the for loop
    am = an = 0;
    for l = 1:DP
        if intersection(H(p, 1), VP(l, :))
            % |m> is in VP(l, :)
            k1 = l;
            for lp = 1:NP
```

```
                if H(p, 1) == VP(l, lp)
                    am = am + a(k1, lp);
                endif
            endfor
        endif
        if intersection(H(p, 2), VP(l, :))
            % |n> is in VP(l, :)
            k2 = l;
            for lp = 1:NP
                if H(p, 2) == VP(l, lp)
                    an = an + a(k2, lp);
                endif
            endfor
        endif
    endfor
    % debug
    if (k1 == 0) | (k2 == 0)
        printf('something wrong! k1 = 0 or k2 = 0!\n');
        break;
    endif
    h(k1, k2) = h(k1, k2) + am*H(p, 3)*an';
endfor

endfunction
```

C.7 Exact Diagonalizing the Bloch-Reduced Hamiltonian Matrix

Depending on whether it is obtained from `blochhamiltonian` or from `blochcompacthamiltonian`, the Bloch-reduced Hamiltonian matrix $H(\mathbf{q})$ is $M' \times M'$, with $M' \leq M$, or $M \times M$, respectively. To avoid having to keep qualifying whether $H(\mathbf{q})$ is $M' \times M'$ or $M \times M$, we shall from here on always refer to the size of $H(\mathbf{q})$ as $M' \times M'$, bearing in mind that $M' \leq M$ if we obtain $H(\mathbf{q})$ from `blochhamiltonian` and $M' = M$ if we obtain it from `blochcompacthamiltonian`. For the system sizes that we worked with, $H(\mathbf{q})$ is always small enough to fit into memory, and it becomes trivial to perform full ED on it, using the very efficient native Octave functionalities.

The eigenvectors obtained using the built-in `eig` function are all $M \times 1$ column vectors, whose components are the amplitudes of the M Bloch states with wave vector $\mathbf{q}$. A reverse transcription is therefore necessary, if we want the eigenvectors to be $D \times 1$ column vectors, whose components are amplitudes of the D occupation number basis states. For this purpose, we introduce two wrapper functions: (i) `blocheig`, which constructs the $M' \times M'$ Bloch-reduced Hamiltonian matrix $H(\mathbf{q})$ for a given wave vector $\mathbf{q}$ from the full $D \times D$ Hamiltonian matrix and the $M \times D$ matrix of inflated Bloch states, diagonalize it, and returns the $D \times 1$ wave function *Psi* associated with the lowest energy eigenvalue E; and (ii) `blochcompacteig`, which constructs the $M' \times M'$ Bloch-reduced Hamiltonian matrix $H(\mathbf{q})$ for a given wave vector $\mathbf{q}$ from the compact $D' \times 3$ Hamiltonian array and the $M \times N$ matrix of deflated Bloch states, diagonalize it, and returns the $D \times 1$ wave function *Psi* associated with the lowest energy eigenvalue E.

The Octave code for the boson version of `blocheig` is shown below:

```
function [Psi, E] = blocheig(V, R, R1, R2, H, q1, q2)
```

```
% form bloch hamiltonian

h = blochhamiltonian(V, R, R1, R2, H, q1, q2);

% diagonalize h

[v, d] = eig(h);

% d should be real, but without the symmetrization of h, it is complex
% with very small imaginary parts. Strip d into a vector, apply sort
% on its real part to find the ground state

for n = 1:size(d,1)
    D(n) = d(n,n);
endfor

[S, I] = sort(real(D));

E = S(1);
psi = v(:, I(1));

M = max(size(psi));

% psi is expressed in terms of the basis vectors of this bloch sector,
% to express it in terms of the complete basis (important for tracing
```

```
% down), we need the bloch basis

D = size(V, 1);

VP = fullpartition(V, R, R1, R2);

a = allblochstates(VP, R, R1, R2, D, q1, q2);
MR = size(a, 1);

Psi = zeros(D, 1);

for n = 1:MR
    Psi = Psi + psi(n)*a(n, :)';
endfor

endfunction
```

The Octave code for the fermion version of `blocheig` is shown below:

```
function [Psi, E] = blocheig(V, VP, fP, R, R1, R2, H, q1, q2)

% form bloch hamiltonian

h = blochhamiltonian(V, VP, fP, R, R1, R2, H, q1, q2);

% diagonalize h
```

```
[v, d] = eig(h);

% d should be real, but without the symmetrization of h, it is complex
% with very small imaginary parts. Strip d into a vector, apply sort
% on its real part to find the ground state

for n = 1:size(d,1)
    D(n) = d(n,n);
endfor

[S, I] = sort(real(D));

E = S(1);
psi = v(:, I(1));

% psi is expressed in terms of the basis vectors of this bloch sector,
% to express it in terms of the complete basis (important for tracing
% down), we need the bloch basis

D = size(V, 1);

a = allblochstates(VP, fP, R, R1, R2, D, q1, q2);
M = size(a, 1);
```

```
Psi = zeros(1, D);

for n = 1:M
    Psi = Psi + psi(n)*a(n, :);
endfor

% Because the Bloch states are stored as row vectors with the correct
% phases, Psi is a row vector. Reshape it as a column vector

Psi = reshape(Psi, size(Psi, 2), size(Psi, 1));

endfunction
```

The Octave code for the function `blochcompacteig`, which exists only in the `Fermion` code branch, is shown below:

```
function [Psi, E] = blochcompacteig(V, VP, fP, R, R1, R2, H, q1, q2)

% form bloch hamiltonian

h = blochcompacthamiltonian(V, VP, fP, R, R1, R2, H, q1, q2);

% diagonalize h

[v, d] = eig(h);
```

```
% d should be real, but without the symmetrization of h, it is complex
% with very small imaginary parts. Strip d into a vector, apply sort
% on its real part to find the ground state

for n = 1:size(d,1)
    D(n) = d(n,n);
endfor

[S, I] = sort(real(D));

E = S(1);
psi = v(:, I(1));

% psi is expressed in terms of the basis vectors of this bloch sector,
% to express it in terms of the complete basis (important for tracing
% down), we need the bloch basis

[D, P] = size(V);

a = allcompactblochstates(VP, fP, R, R1, R2, D, q1, q2);
[M, N] = size(a);

Psi = zeros(D, 1);

for m = 1:M
```

```
    for n = 1:N
        Psi(VP(m, n)) = Psi(VP(m, n)) + psi(m)*a(m, n);
    endfor
endfor

endfunction
```

C.8 Cluster Density Matrix

C.8.1 Cluster Occupation Partitioning

From (4.3.38), and knowing that we are dealing with ground states with a fixed number of particles P, we see that if $|\mathbf{l}\rangle$ and $|\mathbf{l}'\rangle$ do not contain the same number of particles P_C, then it is not possible for their environments $|\mathbf{m}\rangle$ and $|\mathbf{m}'\rangle$ to be common. This means that ρ_C is block-diagonal in the basis of occupation number states on the cluster, where each non-zero block corresponds to one particular P_C. We can therefore generate each of these diagonal blocks of ρ_C one at a time.

Suppose we want to generate the P_C-sector of ρ_C. Then the first thing that we must do is to gather all configurations $|\mathbf{n}\rangle$ containing P_C particles within the cluster. We can do this by going through the Hilbert space matrix, each time we want to calculate a sector of ρ_C, and pull out the relevant configurations. This is an $O(D)$ operation, so we want to avoid doing it frequently as far as possible. Hence, we expend an $O(D)$ effort once to partition the Hilbert space matrix into sectors with different numbers of particles within the cluster (as opposed to partitioning the Hilbert space matrix into translational symmetry sectors, which we discussed in Section C.5.2). Once this is done, we can access only the P_C sector of the Hilbert space, which contains fewer configurations,

when we wish to generate the P_C-sector of ρ_C.

The `Common` code branch core function `occupationpartition`, whose Octave code is shown below, accomplishes this cluster occupation partitioning of the Hilbert space matrix. Because the number of configurations in each P_C-sector of the Hilbert space varies with P_C and the choice of our cluster, `occupationpartition` also returns a list containing the number of configurations for each P_C. In the argument list of `occupationpartition`, V is the $D \times P$ Hilbert space matrix, and 'cluster' is the $1 \times N_C$ vector of indices of the N_C sites within the cluster. The output variables of `occupationpartition` are the occupation-partition Hilbert space matrix V_{PC} and the list D_{PC} of numbers of configurations for each number of particles within the cluster. D_{PC} is a $(N_C + 1) \times 1$ vector, such that its P_Cth element $D_{PC}(P_C)$ is the number of P-particle configurations in V having P_C particles within the cluster. $D_{PC,\max}$ is the maximum of this list of $(N_C + 1)$ numbers. V_{PC} is a $(N_C + 1) \times D_{PC,\max}$ array of the indices of P-particle configurations in V, such that $V_{PC}(P_C, n)$, where $1 \leq n \leq D_{PC}(P_C)$, is the index of the a P-particle configuration having P_C particles within the cluster.

```
function [VPC, DPC] = occupationpartition(V, cluster)

[D, P] = size(V);
NC = max(size(cluster));

DPC = zeros(NC+1, 1);

for n = 1:D
    sc = intersection(cluster, V(n, :));
```

```
    psc = size(sc, 2);
    VPC(psc+1, DPC(psc+1)+1) = n;
    DPC(psc+1) = DPC(psc+1) + 1;
endfor

endfunction
```

To calculate the P_C-sector of ρ_C, we will also need access only to those components of the ground-state wave function $|\Psi\rangle$ whose configurations contain P_C particles within the cluster. Just as we did for the Hilbert space matrix, we can partition the wave function into sectors with different number of particles within the cluster, using information available from the occupation-partition Hilbert space matrix V_{PC} (and the list D_{PC} of number of configurations), and save ourselves the computational expenditure of searching through the $D \times 1$ wave function 'Psi' repeatedly. The `Common` code branch core function `partitionpsi`, whose Octave code is shown below, is given this task. The output of `partitionpsi` is a $(N_C + 1) \times D_{PC,\max}$ matrix of amplitudes 'PsiPC'.

```
function PsiPC = partitionpsi(VPC, DPC, Psi)

DP = size(VPC, 1);

for p = 1:DP
    for q = 1:DPC(p)
        PsiPC(p, q) = Psi(VPC(p, q));
    endfor
endfor
```

endfunction

C.8.2 Fock-Hilbert Space on a Cluster

Before we can proceed to calculate the density matrix of a cluster of sites within the system, we also need to generate the Fock-Hilbert space of states on the cluster. To begin, let us note that while all configurations in the Hilbert space of the system contain P particles, not all configurations in the Fock-Hilbert space of the cluster will contain the same number P_C of particles. However, for a wave function with fixed particle number, we know from (4.3.38) that there is no cluster density matrix element between cluster configurations with different number of particles within the cluster. We can therefore generate the various P_C-sectors of the cluster Hilbert space separately, whenever they are needed for computing the P_C-sector of ρ_C. The `Common` code branch function `clusterhilbertspace`, whose Octave code is shown below, uses an algorithm very similar to that of `directhilbertspace`:

```
% this function should never be called with PC = 0 and PC > P

function VCF = clusterhilbertspace(cluster, PC, neighborlist)

VCF = [];

NC = max(size(cluster));

k = 1;
```

```
if PC > 0
    nc = 1:PC;
    while nc
        for i = 1:PC
            state(1, i) = cluster(nc(i));
        endfor
        flag = 1;
        for j = 1:PC
            if intersection(state, neighborlist(state(j), :))
                flag = 0;
            endif
        endfor
        if flag == 1
            VCF(k, :) = state;
            k = k + 1;
        endif
        nc = increment(nc, NC, PC);
    endwhile
endif

endfunction
```

On the other hand, when we calculate the correlation density matrix and singular value decompose it (see Section C.11), the full Fock-Hilbert spaces of the disconnected

clusters and their supercluster are needed. To be able to store all basis states of varying number of particles within the cluster in a single cluster Fock-Hilbert space matrix, we switch from storing configuration representations, as in the system Hilbert space matrix and each P_C-sector of the cluster Hilbert space matrix, to storing occupation number representations in the full cluster Fock-Hilbert space matrix. The `Common` code branch function `fullclusterhilbertspace`, whose Octave code is shown below, runs through the number $0 \leq P_C \leq N_C$ of particles within the cluster, calls `clusterhilbertspace` for each P_C, performs a transcription from configuration representation to occupation number representation, and concatenates the states to the full cluster Fock-Hilbert space matrix.

```
function VC = fullclusterhilbertspace(cluster, neighborlist)

% make cluster into a column vector

[NC1, NC2] = size(cluster);

if NC2 > NC1
    cluster = cluster';
    NC = NC2;
else
    NC = NC1;
endif

% PC = 0
```

```
VC = zeros(1, NC);


for PC = 1:NC
    VCP = clusterhilbertspace(cluster, PC, neighborlist);
    DCP = size(VCP, 1);
    for n = 1:DCP
        s = zeros(1, NC);
        for p = 1:PC
            s(listindex(VCP(n, p), cluster)) = 1;
        endfor
        VC = [ VC; s ];
    endfor
endfor


endfunction
```

C.8.3 Calculating a Cluster Density Matrix Sector

C.8.3.1 Reshaping the Wave Function Sector

From (4.3.39), we see that the matrix element

$$\langle \mathbf{l}|\rho_C|\mathbf{l}'\rangle = \sum_{\mathbf{m}''} \left[(-1)^{f(\mathbf{l},\mathbf{m}'')}\Psi_{\mathbf{l},\mathbf{m}''}\right]\left[(-1)^{f(\mathbf{l}',\mathbf{m}'')}\Psi^*_{\mathbf{l}',\mathbf{m}''}\right] \tag{C.8.1}$$

in the P_C-sector of ρ_C can be manipulated to look like the dot product between two complex vectors. In fact, if we define the nonsquare matrix $\tilde{\mathbf{\Psi}}_{P_C}$ such that its matrix elements are

$$(\tilde{\mathbf{\Psi}}_{P_C})_{\mathbf{l},\mathbf{m}} = (-1)^{f(\mathbf{l},\mathbf{m})}\Psi_{\mathbf{l},\mathbf{m}}, \tag{C.8.2}$$

then the matrix for the P_C-sector of ρ_C becomes

$$\boldsymbol{\rho}_{C,P_C} = \tilde{\boldsymbol{\Psi}}_{P_C} \tilde{\boldsymbol{\Psi}}^{\dagger}_{P_C}. \tag{C.8.3}$$

To take advantage of this fact, the function `reshapepsi` runs through all the amplitudes in the P_C-sector of $|\Psi\rangle$, and organizes them, after multiplying by the appropriate fermion signs, into the matrix $\tilde{\boldsymbol{\Psi}}$.

The Octave code of the fermion version of `reshapepsi` is shown below. In the argument list of `reshapepsi`, 'PsiP0' is the $1 \times D_{PC,\max}$ P_C-sector of the occupation-partitioned wave function 'PsiPC', 'VP' is the $1 \times D_{PC,\max}$ P_C-sector of the occupation-partitioned Hilbert space matrix V_{PC}, 'DP' is the number of P-particle configurations having P_C particles within the cluster, V the $D \times P$ Hilbert space matrix, 'VCP' the $D_{P_C} \times P_C$ P_C-particle cluster Hilbert space matrix generated by `clusterhilbertspace`, 'VEP' the $D_{P_E} \times (P - P_C)$ $(P - P_C)$-particle environment Hilbert space matrix generated by `clusterhilbertspace`. and 'cluster' is the $1 \times N_C$ vector of indices of sites within the cluster. The output variable returned by `reshapepsi` is $D_{P_C} \times D_{P_E}$ matrix of amplitudes 'PsiPC1', where 'PsiPC1'(l, m) is the amplitude of the P-particle configuration, whose partial configuration on the cluster is $|\mathbf{l}\rangle$, and whose partial configuration on the environment is $|\mathbf{m}\rangle$.

```
function PsiP1 = reshapepsi(PsiP0, VP, DP, V, VCP, VEP, cluster)

DC = size(VCP, 1);
DE = size(VEP, 1);

PsiP1 = zeros(DC, DE);
```

```
for n = 1:DP
    sc = sort(intersection(cluster, V(VP(n), :)));
    se = sort(complement(cluster, V(VP(n), :)));
    ls = listindex(sc, VCP);
    ms = listindex(se, VEP);
    % to find the fermion sign associated with
    % this decomposition, we observe that the
    % sign factor associated with the
    % rearrangement [ s ] -> [ sc se ] is the
    % same as that associated with the
    % rearrangement [ sc se ] -> [ s ]
    [sn, fn] = orderlist([sc se]);
    % CAUTION: the complex conjugation is needed in conjugation
    % fastclusterdensitymatrix, which needs an exterior
    % product without complex conjugation, but octave
    % always transpose with complex conjugation
    PsiP1(ls, ms) = fn*PsiP0(n)';
    % after incorporating this fermion sign
    % we can just trace down PsiP1 straightaway
endfor

endfunction
```

There is no analogous function in the `Boson` code branch, because code development has not progressed this far. Instead, this code branch uses a very much slower scheme

of tracing down the ground-state wave function to obtain the cluster density matrix. I shall not describe this scheme.

C.8.3.2 Tracing Down the Environment

The `Common` code branch wrapper function `fastclusterdensitymatrix`, whose Octave code is shown below, supplied with the cluster-occupation-partitioned Fock-Hilbert space and cluster-occupation-partitioned wave function, invokes `reshapepsi` where necessary to compute the P_C-sector of the cluster density matrix. When $P_C = 0$ or $P_C = P$, the P_C-sector of ρ_C is a 1×1 matrix, and there is no need to invoke `reshapepsi`. Here in the argument list of `fasterclusterdensitymatrix`, 'cluster' is the $1\times N_C$ vector of indices of sites within the cluster, P_C is the number of particles within the cluster, 'neighborlist' is the $N \times 4$ array of site indices of the four nearest neighbors of each of the N sites within the system, V the $D\times P$ Hilbert space matrix, 'VPC' is the $(N_C+1)\times D_{PC,\max}$ cluster occupation-partitioned Hilbert space matrix, 'DPC' is the $(N_C+1)\times 1$ list of number of configurations with each P_C-sectors of the cluster occupation-partitioned Hilbert space matrix 'VPC', and 'PsiPC' the $(N_C + 1) \times D_{PC,\max}$ cluster occupation-partition wave function. The output variable 'rho' returned by `fastclusterdensitymatrix` is the $D_{PC}(P_C) \times D_{PC}(P_C)$ P_C-sector of the cluster density matrix ρ_C.

```
function rho = fastclusterdensitymatrix(      cluster,\
                                              PC, neighborlist, V,\
                                              VPC, DPC, PsiPC)


P = size(V, 2);
```

```
if PC == 0
    rho = PsiPC(1, :)*PsiPC(1, :)';
elseif PC == P
    rho = PsiPC(P+1, 1:DPC(P+1))'*PsiPC(P+1, 1:DPC(P+1));
else
    VCP = clusterhilbertspace(cluster, PC, neighborlist);
    VEP = clusterhilbertspace(    complement(cluster, [1:size(neighborlist,1)]),\
                                  P - PC, neighborlist);
    PsiC = reshapepsi( PsiPC(PC+1, :), VPC(PC+1, :), DPC(PC+1, :),\
                       V, VCP, VEP, cluster);
    % use matrix multiplication to effect the tracing down
    rho = PsiC*PsiC';
endif

% rho generated by this function agrees with rho generated
% by clusterdensitymatrix

endfunction
```

C.9 Averaging

C.9.1 Ground-State Degeneracy

Because the Hamiltonian, given either in (C.1.1) or (C.1.2), is translationally invariant, we expect the cluster density matrix ρ_C to also be translationally invariant, i.e. for example, in the $(4, 1)\times(1, 4)$ system, the cluster density matrices for the three equivalent

clusters shown in Figure C.8 ought to have exactly the same matrix elements, if their cluster bases are chosen in an analogous sense.

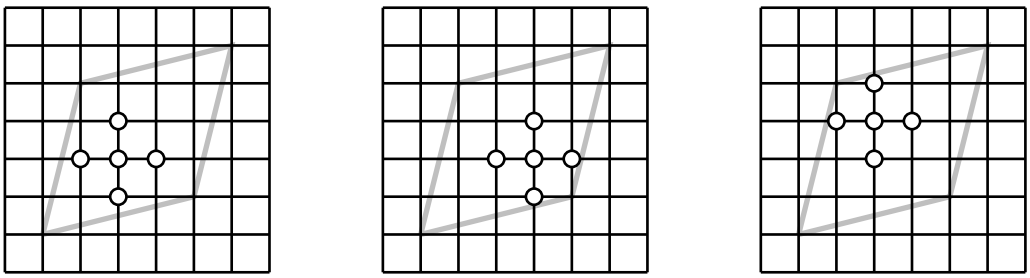

Figure C.8: Three equivalent five-site clusters in the $(4,1)\times(1,4)$ system, with 15 sites: $\mathbf{r}_1 = (0,0)$, $\mathbf{r}_2 = (1,1)$, $\mathbf{r}_3 = (1,2)$, $\mathbf{r}_4 = (1,3)$, $\mathbf{r}_5 = (2,1)$, $\mathbf{r}_6 = (2,2)$, $\mathbf{r}_7 = (2,3)$, $\mathbf{r}_8 = (2,4)$, $\mathbf{r}_9 = (3,1)$, $\mathbf{r}_{10} = (3,2)$, $\mathbf{r}_{11} = (3,3)$, $\mathbf{r}_{12} = (3,4)$, $\mathbf{r}_{13} = (4,2)$, $\mathbf{r}_{14} = (4,3)$ and $\mathbf{r}_{15} = (4,4)$. The first cluster (a) consists of the sites $\{3,5,6,7,10\}$, the the second cluster (b) consists of the sites $\{6,9,10,11,13\}$, and the third cluster (c) consists of the sites $\{4,6,7,8,11\}$. Let us call the corresponding cluster density matrices $\rho_{(a)}$, $\rho_{(b)}$ and $\rho_{(c)}$.

For $P = 3$ particles in the system, the ground state is nondegenerate, and we find indeed that $\rho_{(a)} = \rho_{(b)} = \rho_{(c)}$. For $P = 4$ particles in the system, on the other hand, the ground state is two-fold degenerate. If we use as the ground state one of the two degenerate wave functions, then we find that $\rho_{(a)} \neq \rho_{(b)} = \rho_{(c)}$. In fact, the problem is worse.

The $(4,1)\times(1,4)$ system is invariant, up to translations of the underlying infinite square lattice, under reflections about $y = x$ and $y = -x$. Let us call these two reflections σ_{y-x} and σ_{y+x} respectively. Along with the identity transformation, and a rotation through π, these two reflections form the point symmetry group

$$G = \{E, C_2, \sigma_{y-x}, \sigma_{y+x}\} \tag{C.9.1}$$

of the $(4,1)\times(1,4)$ system. In general, the point symmetry group G of a $\mathbf{R}_1\times\mathbf{R}_2$ finite system is a subgroup of

$$\mathscr{G} = \{E, i, C_4, C_2, \sigma_y, \sigma_x, \sigma_{y-x}, \sigma_{y+x}\}, \tag{C.9.2}$$

which is the point symmetry group of the infinite square lattice. Here i is an inversion about the origin, C_4 a rotation counterclockwise by $\frac{\pi}{2}$, C_2 a rotation by π, σ_y is a reflection about the x-axis, and σ_x is a reflection about the y-axis.

Denoting by U_g the unitary transformation induced by the symmetry transformation $g\in G$, we find that for $P=3$ on the $(4,1)\times(1,4)$ system, when the ground state is nondegenerate,

$$U_g\rho_C U_g^{-1} = \rho_C \tag{C.9.3}$$

for all clusters (a), (b) and (c), and for all g in G. On the other hand, if we had picked one of the two degenerate wave functions as the ground state for $P=4$, we find that

$$\begin{aligned}
&U_{\sigma_{y-x}}\rho_{(\mathrm{a})}U_{\sigma_{y-x}}^{-1} = \rho_{(\mathrm{a})}, \quad U_{\sigma_{y+x}}\rho_{(\mathrm{a})}U_{\sigma_{y+x}}^{-1} \neq \rho_{(\mathrm{a})};\\
&U_{\sigma_{y-x}}\rho_{(\mathrm{b})}U_{\sigma_{y-x}}^{-1} \neq \rho_{(\mathrm{b})}, \quad U_{\sigma_{y+x}}\rho_{(\mathrm{b})}U_{\sigma_{y+x}}^{-1} = \rho_{(\mathrm{b})};\\
&U_{\sigma_{y-x}}\rho_{(\mathrm{c})}U_{\sigma_{y-x}}^{-1} \neq \rho_{(\mathrm{c})}, \quad U_{\sigma_{y+x}}\rho_{(\mathrm{c})}U_{\sigma_{y+x}}^{-1} = \rho_{(\mathrm{c})}.
\end{aligned} \tag{C.9.4}$$

We can understand this G-symmetry breaking using a cartoon of noninteracting spinless fermions on a chain of length L. When the chain is subjected to periodic boundary conditions, the allowed single-particle wave vectors are $k_n = 2n\pi/L$, where n takes on integer values. For an odd number $P=2p+1$ of particles on the chain, the single-particle wave vectors k_{-p}, k_{-p+1}, …, k_0, …, k_{p-1}, k_p are occupied, and the total momentum of the non-degenerate many-particle ground state is

$$\hbar(k_{-p} + k_{-p+1} + \cdots k_0 + \cdots + k_{p-1} + k_p) = 0, \tag{C.9.5}$$

whereas for an even number $P=2p$ of particles on the chain, the $P=2p$ single-particle wave vectors that are occupied can either be $k_{-p}, k_{-p+1}, \ldots, k_0, \ldots, k_{p-1}$, or $k_{-p+1}, \ldots, k_0$,

$\ldots, k_{p-1}, k_p$. Both sets of single-particle wave-vector occupations lead to the same total energy. Therefore, the many-particle ground state is two-fold degenerate, one having total momentum $-\hbar k_p$, and the other having total momentum $+\hbar k_p$. For noninteracting spinless fermions in higher dimensions, the pattern of ground-state degeneracy is more complex, but we have essentially the same conclusion: when a many-particle ground state is nondegenerate, its total momentum is zero, whereas if it is m-fold degenerate, the many-particle ground states are associated with m nonzero total momenta, all having the same magnitude. This argument holds even when we go from noninteracting to interacting spinless fermions.

For a finite system with point symmetry group G, the set of all possible discrete total-momentum wave vectors is invariant under G. Except for the zero total-momentum wave vector, however, none of the discrete total-momentum wave vectors are individually invariant when acted upon by elements g of G. *Some* non-zero total-momentum wave vectors, nonetheless, will remain invariant under the action of *some* elements of G. The ground state wave function must have the same transformation properties as its total-momentum wave vector. Thus, this tells us that G-symmetry will not be broken in a nondegenerate ground state with zero total momentum, and also which point symmetries of our finite system are broken, in those degenerate ground states with non-zero total momenta.

Now, coming back to our example of $P = 4$ particles on the $(4, 1) \times (1, 4)$ system subject to periodic boundary conditions, we find the two symmetry-broken ground states having the same energy, so there is no reason to favor one over the other. Indeed, if we imagine that the finite $(4, 1) \times (1, 4)$ system is coupled to a heat bath at inverse temperature $\beta = 1/k_B T$, then at thermal equilibrium, the state of the system would be

described by the canonical ensemble density matrix

$$\rho_C(\beta) = Z^{-1}(\beta) \sum_i e^{-\beta E_i} \rho_{C,i}, \tag{C.9.6}$$

where $Z(\beta) = \sum_i e^{-\beta E_i}$ is the canonical partition function, and $\rho_{C,i}$ are the pure state density matrices associated with energy eigenvalues E_i. States within a degenerate manifold have the same energy, and therefore contribute equally to the thermodynamic density matrix $\rho_C(\beta)$. In the limit of $\beta \to \infty$, the usual thermodynamic argument is that pure states decouple from one another, and we treat their respective density matrices independently, except for those states which are degenerate. Because they appear with the same Boltzmann weight whatever the inverse temperature is, we should still treat the uniform combination instead of the individual density matrices in the limit of $\beta \to \infty$. In some situations, there might be physical reasons for us to calculate the cluster density matrix from a symmetry-broken ground state, but raw ED will likely pick a random linear combination of the desired symmetry-broken ground state with other equivalent symmetry-broken ground states, instead of getting the one of interest.

Because the uniform combination of all cluster density matrices calculated from the degenerate ground-state manifold is in effect an *averaged* ground-state cluster density matrix, we call this procedure *degeneracy averaging*. The Octave code of the `Common` code branch wrapper function `fastdegenav`, which calculates the degeneracy-averaged cluster density matrix, is shown below.

```
function rhopc = fastdegenav(V, VP, fP, R, R1, R2, H, cluster, neighborlist, PC)

D = size(V, 1);

% find ground state energy
```

```
% this is always faster if H can be stored in memory

E = eig(H);
Eg = E(1);

% initialize

if PC == 0
    rhopc = 0;
else
    VC = clusterhilbertspace(cluster, PC, neighborlist);
    DC = size(VC, 1);
    rhopc = zeros(DC);
endif

d = 0;

% generate list of anti-aliased Bloch wave vectors

Q = makeFBZ(R1, R2);

% perform occupation partition of the Hilbert space

[VPC, DPC] = occupationpartition(V, cluster);
```

```
% run through all Bloch wave vectors

for k = 1:size(R, 1)
    % this is the slowest function call in the for loop
    [Psi, Ek] = blocheig(V, VP, fP, R, R1, R2, H, Q(k,1), Q(k,2));
    if abs((Ek - Eg)/Eg) < 1/D
        PsiPC = partitionpsi(VPC, DPC, Psi);
        rpc = fastclusterdensitymatrix(     cluster, PC, neighborlist,\
                                            V, VPC, DPC, PsiPC);
        rhopc = rhopc + rpc;
        d = d + 1;
    endif
endfor

rhopc = rhopc/d;

endfunction
```

Although G-symmetry is broken in each of the states within the degenerate ground-state manifold, the uniform combination of the cluster density matrices of all such states should be invariant under G. Indeed, we find the degeneracy-averaged cluster density matrices $\bar{\rho}_{(a)}$, $\bar{\rho}_{(b)}$, and $\bar{\rho}_{(c)}$ to be identical to one another, i.e. translational symmetry has been restored. More importantly, we have the intended effect that

$$U_{\sigma_{y-x}}\bar{\rho}_C U^{-1}_{\sigma_{y-x}} = \bar{\rho}_C = U_{\sigma_{y+x}}\bar{\rho}_C U^{-1}_{\sigma_{y+x}}, \tag{C.9.7}$$

for C = (a), (b), and (c).

Further checks show that G-symmetry is also restored to a degenerate excited-state manifold by degeneracy averaging as well.

C.9.2 Alternative Argument for Degeneracy Averaging

From elementary quantum mechanics, we know that if the ground state is two-fold degenerate (say), then there exists an observable $A = A^\dagger$ which commutes with the Hamiltonian H, i.e. $[H, A] = 0$. The ground-state wave functions can then be chosen to be simultaneous eigenstates of H and A, i.e. if we call the ground-state wave functions $|\Psi_1\rangle$ and $|\Psi_2\rangle$, then

$$\begin{aligned} H|\Psi_1\rangle &= E|\Psi_1\rangle\,, \quad H|\Psi_2\rangle = E|\Psi_2\rangle\,; \\ A|\Psi_1\rangle &= a_1|\Psi_1\rangle\,, \quad A|\Psi_2\rangle = a_2|\Psi_2\rangle\,. \end{aligned} \tag{C.9.8}$$

We can then construct the cluster density matrices

$$\rho_1 = \mathrm{Tr}_E\,|\Psi_1\rangle\langle\Psi_1|\,, \quad \rho_2 = \mathrm{Tr}_E\,|\Psi_2\rangle\langle\Psi_2| \tag{C.9.9}$$

by tracing over the environment, such that

$$U_A(\theta)\rho_1 U_A^\dagger(\theta) = \rho_1, \quad U_A(\theta)\rho_2 U_A^\dagger(\theta) = \rho_2, \tag{C.9.10}$$

where

$$U_A(\theta) = \exp(i\theta A) \tag{C.9.11}$$

is a symmetry transformation generated by A.

However, the numerical diagonalization routine in Matlab or Octave tends to mix degenerate states. If this happens to $|\Psi_1\rangle$ and $|\Psi_2\rangle$, and Octave returns

$$|\Psi_1'\rangle = \cos\phi\,|\Psi_1\rangle + \sin\phi\,|\Psi_2\rangle \quad \text{and} \quad |\Psi_2'\rangle = -\sin\phi\,|\Psi_1\rangle + \cos\phi\,|\Psi_2\rangle\,, \tag{C.9.12}$$

then the cluster density matrices

$$\rho_1' = \mathrm{Tr}_E\,|\Psi_1'\rangle\langle\Psi_1'| \quad \text{and} \quad \rho_2' = \mathrm{Tr}_E\,|\Psi_2'\rangle\langle\Psi_2'| \tag{C.9.13}$$

will not be invariant under $U_A(\theta)$. This is bad, especially if the degenerate manifold of states on a whole exhibit a particular symmetry that we are interested in or keen to discover. But when the states returned by Octave do not individually preserve this symmetry, we will not be able to extract it from the cluster density matrices.

One way to overcome this problem is not to deal with the density matrices ρ'_1 and ρ'_2 separately, but with an 'invariant combination'

$$\bar{\rho}' = \tfrac{1}{2}(\rho'_1 + \rho'_2) = \tfrac{1}{2}(\rho_1 + \rho_2) = \bar{\rho}, \tag{C.9.14}$$

which is something we can calculate without knowing what mixing angle θ is. This 'invariant' cluster density matrix has the property that

$$U_A(\theta)\bar{\rho}_C U_A^\dagger(\theta) = \bar{\rho}_C, \tag{C.9.15}$$

if A is a symmetry of this degenerate manifold of states, but

$$U_B(\phi)\bar{\rho}_C U_B^\dagger(\phi) \neq \bar{\rho}_C, \tag{C.9.16}$$

if B is not a symmetry of this degenerate manifold of states. In this way, we can characterize all the symmetries of the degenerate manifold, without making *a priori* guesses as to what they might be. This is especially useful when one obtains the states through numerical means, as demonstrated very recently by Furukawa *et al* [28].

C.9.3 Orientation of System

We chose to study the cross-shaped cluster because it has the same point symmetry $\mathscr{G}$ as the underlying infinite square lattice. However, the finite system we chose has as its point symmetries the subgroup $G \subset \mathscr{G}$, so the cluster density matrix will at most be G-symmetric, after degeneracy averaging. Ultimately, our goal is to approximate from finite system calculations the cluster density matrix obtained from the true ground-state

wave function of the infinite square lattice. If the infinite-system ground state is non-degenerate, then such a cluster density matrix will necessarily be $\mathscr{G}$-symmetric. If the infinite-system ground state is degenerate, then we will invoke the same thermodynamic argument used in Section C.9.1 to imagine calculating the uniform combination of the ground-state cluster density matrices, which will be $\mathscr{G}$-symmetric.

Whether or not this is a realistic goal, the first step to take is to restore $\mathscr{G}$-symmetry to the cluster density matrix, using calculations based on the $\mathbf{R}_1 \times \mathbf{R}_2$ system. For a given set of lattice vectors $\mathbf{R}_1$ and $\mathbf{R}_2$, we can actually construct four symmetry-related systems,

$$\begin{aligned} &(R_{1x}, R_{1y}) \times (R_{2x}, R_{2y}), \\ &(R_{2y}, R_{2x}) \times (R_{1y}, R_{1x}), \\ &(R_{1x}, -R_{1y}) \times (-R_{2x}, R_{2y}), \\ &(R_{2y}, -R_{2x}) \times (-R_{1y}, R_{1x}), \end{aligned} \tag{C.9.17}$$

shown in Figure C.9. All four systems share the same point symmetry group G, since they differ from one another only in orientation. However, after degeneracy averaging to restore G-symmetry, we find that the cluster density matrices of the four systems are not all identical, because some of them are obtained from the prototypical $\mathbf{R}_1 \times \mathbf{R}_2$ system by transformations g which are in $\mathscr{G}$ but not in G.

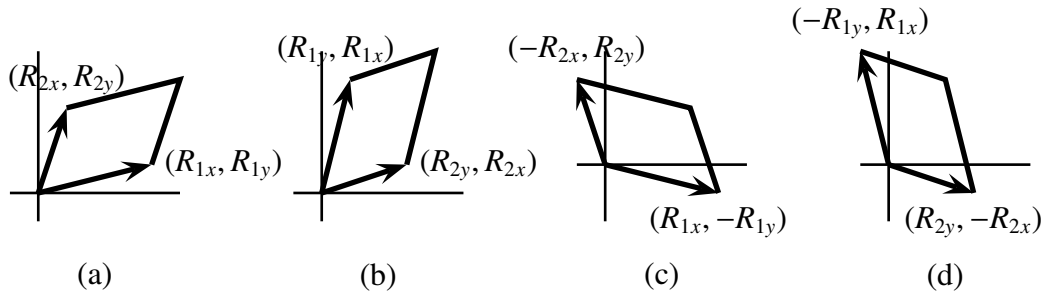

Figure C.9: The family of four symmetry-related systems, based on the $\mathbf{R}_1 \times \mathbf{R}_2$ system.

There is no reason to believe that the cluster density matrice calculated from any

one of these systems (a), (b), (c), (d), is any better than that calculated from another as an approximation for the infinite-system cluster density matrix, since the latter is $\mathscr{G}$-symmetric, while the former is only G-symmetric. However, the equally-weighted average of the four cluster density matrices

$$\bar{\bar{\rho}}_C = \tfrac{1}{4}\left(\bar{\rho}_{(a)} + \bar{\rho}_{(b)} + \bar{\rho}_{(c)} + \bar{\rho}_{(d)}\right) \tag{C.9.18}$$

is $\mathscr{G}$-symmetric, and by this virtue should be a better approximation to the infinite-system cluster density matrix. We call this procedure *orientation averaging*.

The Octave code of the `Common` code branch wrapper function `shapeav` which performs orientation averaging is shown below.

```
function rhopc = shapeav(Q1, Q2, cluster, P, PC)

% prototype system

R1 = Q1;
R2 = Q2;
R = makesystem(R1, R2);
s = listcoord(cluster, R);
neighborlist = makeneighborlist(R, R1, R2);
V = buildhilbertspace(P, neighborlist);
H = buildhamiltonian(V, neighborlist);
rpca = degenav(V, R, R1, R2, H, cluster, neighborlist, PC);

% reflected about y - x = 0
```

```
R1 = [ Q2(2) Q2(1) ];
R2 = [ Q1(2) Q1(1) ];
R = makesystem(R1, R2);
neighborlist = makeneighborlist(R, R1, R2);
V = buildhilbertspace(P, neighborlist);
H = buildhamiltonian(V, neighborlist);
for ic = 1:max(size(cluster))
    t(ic, 1) = s(ic, 2);
    t(ic, 2) = s(ic, 1);
endfor
c = sort(coordlist(t, R));
rpcb = degenav(V, R, R1, R2, H, c, neighborlist, PC);

% reflected about y

R1 = [ Q1(1) −Q1(2) ];
R2 = [ −Q2(1) Q2(2) ];
R = makesystem(R1, R2);
neighborlist = makeneighborlist(R, R1, R2);
V = buildhilbertspace(P, neighborlist);
H = buildhamiltonian(V, neighborlist);
for ic = 1:max(size(cluster))
    t(ic, 1) = R1(1) − s(ic, 1);
    t(ic, 2) = R1(2) + s(ic, 2);
endfor
```

```
c = sort(coordlist(t, R));
rpcc = degenav(V, R, R1, R2, H, c, neighborlist, PC);

% reflected about y - x = 0 followed by reflection about y

R1 = [ Q2(2) −Q2(1) ];
R2 = [ −Q1(2) Q1(1) ];
R = makesystem(R1, R2);
neighborlist = makeneighborlist(R, R1, R2);
V = buildhilbertspace(P, neighborlist);
H = buildhamiltonian(V, neighborlist);
for ic = 1:max(size(cluster))
    t(ic, 1) = R1(1) − s(ic, 2);
    t(ic, 2) = R1(2) + s(ic, 1);
endfor
c = sort(coordlist(t, R));
rpcd = degenav(V, R, R1, R2, H, c, neighborlist, PC);

rhopc = 0.25*(rpca + rpcb + rpcc + rpcd);

endfunction
```

With the cross-shaped cluster, which has full $\mathscr{G}$-symmetry, this orientation averaging can also be done without computing $\bar{\rho}_{(b)}$, $\bar{\rho}_{(c)}$ and $\bar{\rho}_{(d)}$. Instead, we can find the

orientation-averaged cluster density matrix as

$$\bar{\bar{\rho}}_C = \frac{1}{D(\mathscr{G})} \sum_{g \in \mathscr{G}} U_g \bar{\rho}_C U_g^{-1}, \tag{C.9.19}$$

where $g \in G$ is a point group transformation of the square lattice, $D(\mathscr{G})$ is the order of the group $\mathscr{G}$, and U_g is the unitary transformation of the cluster Hilbert space associated with g.

C.9.3.1 Example: The (4, 1) × (1, 3) System

For the $(4,1) \times (1,3)$ system, the four inequivalent orientations are (a) $= (4,1) \times (1,3)$, (b) $= (3,1) \times (1,4)$, (c) $= (4,-1) \times (-1,3)$, and (d) $= (3,-1) \times (1,-4)$. For $P = 4$ particles, we find for the a nondegenerate lowest energy state in the $\mathbf{q} = (0,0)$ Bloch sector. No degeneracy averaging is required, and after orientation averaging, the $P_C = 0$ to $P_C = 4$ sectors of the cluster density matrix is, in the many-body cluster basis defined in Chapter 4,

$$\rho_{C,0} = 0, \tag{C.9.20a}$$

$$\rho_{C,1} = \frac{1}{22} \begin{bmatrix} 1 & 0 & -1 & 0 & 0 \\ 0 & 1 & -1 & 0 & 0 \\ -1 & -1 & 8 & -1 & -1 \\ 0 & 0 & -1 & 1 & 0 \\ 0 & 0 & -1 & 0 & 1 \end{bmatrix}, \tag{C.9.20b}$$

$$\rho_{C,2} = \frac{1}{22}\begin{bmatrix} 1 & 0 & 0 & 0 & 0 & 0 \\ 0 & 1 & 0 & 0 & 0 & 0 \\ 0 & 0 & 0 & 0 & 0 & 0 \\ 0 & 0 & 0 & 0 & 0 & 0 \\ 0 & 0 & 0 & 0 & 1 & 0 \\ 0 & 0 & 0 & 0 & 0 & 1 \end{bmatrix}, \tag{C.9.20c}$$

$$\rho_{C,3} = \frac{1}{22}\begin{bmatrix} 1 & 0 & 0 & 0 \\ 0 & 1 & 0 & 0 \\ 0 & 0 & 1 & 0 \\ 0 & 0 & 0 & 1 \end{bmatrix}, \tag{C.9.20d}$$

$$\rho_{C,4} = \frac{1}{11}. \tag{C.9.20e}$$

The eigenvalues and eigenvectors in the zero-, two-, three- and four-particle sectors of ρ_C are trivial. In the one-particle sector, the eigenvalues and eigenvectors are obtained using xmaxima, the freely distributed Maple clone, and shown in Table C.3.

Table C.3: The one-particle eigenvalues and (unnormalized) eigenstates for the density matrix of a five-site, cross-shaped cluster in the $(4, 1) \times (1, 3)$ system with $N = 11$ sites and $P = 4$ particles.

$w_{1,l}$	$\lvert w_{1,l}\rangle$
$\frac{1}{44}(9 + \sqrt{65})$	$(1, 1, -\frac{\sqrt{65}+7}{2}, 1, 1)$
$\frac{1}{22}$	$(1, 0, 0, 0, -1)$
$\frac{1}{22}$	$(0, 1, 0, 0, -1)$
$\frac{1}{22}$	$(0, 0, 0, 1, -1)$
$\frac{1}{44}(9 - \sqrt{65})$	$(1, 1, \frac{\sqrt{65}-7}{2}, 1, 1)$

C.9.3.2 Example: The (4, 1) × (1, 4) System

For the (4, 1)×(1, 4) system, which has a higher degree of symmetry than the (4, 1)×(1, 3) system, we need only average over the orientations (a) = (4, 1)×(1, 4) and (c) = (4, −1)×(−1, 4). For $P = 4$ particles in this system, the nondegenerate ground state occurs in the $\mathbf{q} = (0, 0)$ Bloch sector. After orientation averaging, we find the $P_C = 0$ to $P_C = 4$ sectors of the cluster density matrix to be

$$\rho_{C,0} = \frac{1}{10}, \tag{C.9.21}$$

$$\rho_{C,1} = \frac{1}{540}\begin{bmatrix} 39 & 3 & 18\sqrt{3} & 3 & 0 \\ 3 & 39 & 18\sqrt{3} & 0 & 3 \\ 18\sqrt{3} & 18\sqrt{3} & 144 & 18\sqrt{3} & 18\sqrt{3} \\ 3 & 0 & 18\sqrt{3} & 39 & 3 \\ 0 & 3 & 18\sqrt{3} & 3 & 39 \end{bmatrix}, \tag{C.9.22}$$

$$\rho_{C,2} = \frac{1}{540}\begin{bmatrix} 18 & 0 & 3 & -3 & 0 & 0 \\ 0 & 18 & 3 & 3 & 0 & 0 \\ 3 & 3 & 33 & 0 & 3 & 3 \\ -3 & 3 & 0 & 33 & 3 & -3 \\ 0 & 0 & 3 & 3 & 18 & 0 \\ 0 & 0 & 3 & -3 & 0 & 18 \end{bmatrix}, \tag{C.9.23}$$

$$\rho_{C,3} = \frac{1}{1080}\begin{bmatrix} 24 & 9 & -9 & 0 \\ 9 & 24 & 0 & -9 \\ -9 & 0 & 24 & 9 \\ 0 & -9 & 9 & 24 \end{bmatrix}, \tag{C.9.24}$$

$$\rho_{C,4} = 0. \tag{C.9.25}$$

In the one-, two-, and three-particle sectors, the eigenvalues and eigenstates obtained

using xmaxima are shown in Tables C.4, C.5 and C.6.

Table C.4: The one-particle eigenvalues and (unnormalized) eigenstates for the density matrix of a five-site, cross-shaped cluster in the $(4,1)\times(1,4)$ system with $N = 15$ sites and $P = 4$ particles.

$w_{1,l}$	$\|w_{1,l}\rangle$
$\frac{1}{1080}(189 + 9\sqrt{313})$	$(1, 1, \frac{\sqrt{3}}{12}(\sqrt{313} + 11), 1, 1)$
$\frac{13}{180}$	$(1, 0, 0, 0, -1)$
$\frac{13}{180}$	$(0, 1, 0, -1, 0)$
$\frac{11}{180}$	$(1, -1, 0, -1, 1)$
$\frac{1}{1080}(189 - 9\sqrt{313})$	$(1, 1, -\frac{\sqrt{3}}{12}(\sqrt{313} - 11), 1, 1)$

C.9.4 Twist Boundary Conditions

There is a third averaging device we need to employ to better approximate the infinite-system cluster density matrix. This involves averaging over the twist vector incurred as a particle goes around the boundaries of the system. We call this procedure *twist boundary conditions averaging*, and the theoretical formulation and additional Octave codes will be discussed in greater details in Appendix D.

C.10 Noninteracting Spinless Fermions

For cluster density matrix calculations involving noninteracting spinless fermions, we use functions in the `FreeFermion` code branch. This is a pretty much standalone code branch, apart from a few `Common` code branch functions that it need access to. For noninteracting spinless fermions, we take advantage of the relation (2.4.30) between the

Table C.5: The two-particle eigenvalues and (unnormalized) eigenstates for the density matrix of a five-site, cross-shaped cluster in the $(4,1)\times(1,4)$ system with $N = 15$ sites and $P = 4$ particles.

$w_{2,l}$	$\lvert w_{2,l}\rangle$
$\frac{1}{1080}(51+3\sqrt{41})$	$(0, 1, \frac{1}{4}(\sqrt{41}+5), \frac{1}{4}(\sqrt{41}+5), 1, 0)$
$\frac{1}{1080}(51+3\sqrt{41})$	$(1, 0, \frac{1}{4}(\sqrt{41}+5), -\frac{1}{4}(\sqrt{41}+5), 0, 1)$
$\frac{1}{30}$	$(1, 0, 0, 0, 0, -1)$
$\frac{1}{30}$	$(0, 1, 0, 0, -1, 0)$
$\frac{1}{1080}(51-3\sqrt{41})$	$(1, 0, -\frac{1}{4}(\sqrt{41}-5), \frac{1}{4}(\sqrt{41}-5), 0, 1)$
$\frac{1}{1080}(51-3\sqrt{41})$	$(0, 1, -\frac{1}{4}(\sqrt{41}-5), -\frac{1}{4}(\sqrt{41}-5), 1, 0)$

Table C.6: The three-particle eigenvalues and (unnormalized) eigenstates for the density matrix of a five-site, cross-shaped cluster in the $(4,1)\times(1,4)$ system with $N = 15$ sites and $P = 4$ particles.

$w_{3,l}$	$\lvert\chi_{3,l}\rangle$
$\frac{7}{180}$	$(1, 1, -1, -1)$
$\frac{1}{45}$	$(1, 0, 0, 1)$
$\frac{1}{45}$	$(0, 1, 1, 0)$
$\frac{1}{180}$	$(1, -1, 1, -1)$

cluster density matrix ρ_C and the cluster Green function matrix G_C, and use (2.3.77) to calculate the one-particle cluster density matrix weights and eigenvectors.

In principle, we can calculate the infinite-system cluster density matrix for noninteracting spinless fermions using these relations in any dimensions. All we need is the Fermi surface for whatever filling $\bar{n}$ we are interested in to be able to calculate, by numerical integration if need be, the two-point functions $\langle\Psi|c_i^\dagger c_j|\Psi\rangle$ which are the cluster Green function matrix elements. In practice, for all but the simplest dispersion relations, the Fermi surface is difficult to explicitly specify. The Fermi surface can always be specified implicitly, but computation of two-point functions would typically become expensive. Also, the purpose of calculating the cluster density matrix for noninteracting spinless fermions is so that we have something to compare against, when we start calculating the cluster density matrix of strongly interacting spinless fermions. Since we can only work with finite systems of the latter, it is more reasonable that we also work with finite systems of the former.

C.10.1 Ground State

For a finite $\mathbf{R}_1 \times \mathbf{R}_2$ system with N sites, the N allowed Bloch wave vectors $\mathbf{q}$ are discrete. The ground state of $P \leq N$ noninteracting spinless fermions occupying such a system would involve the occupation of P wave vectors $\mathbf{q}_1, \ldots, \mathbf{q}_P$ with the lowest single-particle energies $\epsilon(\mathbf{q}_1), \ldots, \epsilon(\mathbf{q}_P)$. For noninteracting spinless fermions on a square lattice with dispersion relation

$$\epsilon(\mathbf{q}) = -2\left(\cos q_x + \cos q_y\right), \tag{C.10.1}$$

the helper function `filledk` returns a list of wave vectors $\mathbf{q}$ that are filled. The Octave code for `filledk` is shown below.

```
function kfEknk = filledk(R1, R2, P)

N = R1(1)*R2(2) - R1(2)*R2(1);
Q1 = 2*pi*[R2(2) -R2(1)]/N;
Q2 = 2*pi*[-R1(2) R1(1)]/N;

q = makeFBZ(R1, R2);
Nq = size(q, 1);

for n = 1:Nq
    k(n, :) = q(n, 1)*Q1 + q(n, 2)*Q2;
    Eq(n) = -2*(cos(k(n, 1)) + cos(k(n, 2)));
endfor

Eqd = create_set(Eq)';
Nqd = max(size(Eqd));

m = 1;
nqd = 1;
nk = 1;

while m <= P
    Dqd = 0;
    for n = 1:Nq
        if Eq(n) == Eqd(nqd)
```

```
            Dqd = Dqd + 1;
        endif
    endfor
    if m + Dqd − 1 > P
        nk = (P − m + 1)/Dqd;
    endif
    for n = 1:Nq
        if Eq(n) == Eqd(nqd)
            kfEknk(m, :) = [ k(n, :) Eq(n) nk ];
            m = m + 1;
        endif
    endfor
    nqd = nqd + 1;
endwhile

endfunction
```

The function `filledk` also returns the single-particle energies $\epsilon(\mathbf{q})$ for the filled wave vectors (for debugging purposes only), as well as the occupation number $n_{\mathbf{q}}$, which we allow to take on fractional values whenever the 'Fermi energy' ϵ_F is degenerate, so as to ensure that there is no artificial symmetry breaking for any value of P chosen.

C.10.2 Cluster Green Function Matrix

For a finite system, the two-point function is given by (4.6.3) as a sum over the occupied wave vectors supplied by `filledk`. For a given cluster of sites within the finite system,

the cluster Green function matrix G_C is computed by the function `makeG`, whose Octave code is shown below.

```
function G = makeG(R1, R2, cluster, P)

N = R1(1)*R2(2) - R1(2)*R2(1);
R = makesystem(R1, R2);

kfEknk = filledk(R1, R2, P);
Nkf = size(kfEknk, 1);
Nc = max(size(cluster));

for m = 1:Nc
    for n = 1:Nc
        G(m, n) = 0;
        r = R(cluster(m), :) - R(cluster(n), :);
        for l = 1:Nkf
            G(m, n) = G(m, n) +\
                kfEknk(l,4)*exp(i*(kfEknk(l,1)*r(1) + kfEknk(l,2)*r(2)));
        endfor
    endfor
endfor

G = G/N;

endfunction
```

C.10.3 Averaging

Because of the way we introduce fractional occupation of the wave vectors at the 'Fermi energy' in Section C.10.1, for a finite system with point symmetry group G (see Section C.9), the cluster Green function matrix G_C is fully invariant under the action of G, and is also fully translational invariant within the finite system. However, for most lattice vectors $\mathbf{R}_1$ and $\mathbf{R}_2$, the finite-system ground-state wave function does not have the full point group symmetry of the square lattice. To make the finite-system ground-state wave function fully invariant under the action of the point symmetry group $\mathscr{G}$ of the infinite square lattice (see Section C.9), orientation averaging is necessary. This is done in analogy with (C.9.19),

$$\bar{G}_C = \frac{1}{D(\mathscr{G})} \sum_{g \in \mathscr{G}} U_{g,1} G_C U_{g,1}^{-1}, \tag{C.10.2}$$

where $g \in \mathscr{G}$ is a point symmetry group transformation of the square lattice, $D(\mathscr{G})$ is the order of the point symmetry group $\mathscr{G}$, and $U_{g,1}$ is the unitary transformation acting on the one-particle sector of the cluster Hilbert space associated with g. The Octave code for the function `shapeav` which implements this orientation averaging is shown below.

```
function G = shapeav(R1, R2, cluster, P);

G0 = makeG(R1, R2, cluster, P);

load Data/symmetry.mat;

G = 0.25*(U1x*G0*U1x' + U1y*G0*U1y' +\
```

```
U1ymx*G0*U1ymx' + U1ypx*G0*U1ypx');

endfunction
```

C.11 Correlation Density Matrix

The starting point for calculating the correlation density matrix is (6.3.18), giving the matrix elements of the correlation-$\mathbf{K}$ matrix as

$$K_{\mathbf{ll'},\mathbf{mm'}} = (-1)^{f(\mathbf{n})+f(\mathbf{n'})}\rho^{ab}_{\mathbf{n},\mathbf{n'}} - \rho^{a}_{\mathbf{l},\mathbf{l'}}\rho^{b}_{\mathbf{mm'}}, \tag{C.11.1}$$

in terms of the matrix elements of ρ^a and ρ^b, the density matrices of the clusters a and b respectively, and ρ^{ab}, the density matrix of the supercluster ab. Here $|\mathbf{l}\rangle$ and $|\mathbf{l'}\rangle$ are the final and initial configurations of the cluster a, $|\mathbf{m}\rangle$ and $|\mathbf{m'}\rangle$ are the final and initial configurations of the cluster b, and $|\mathbf{n}\rangle$ and $|\mathbf{n'}\rangle$ are the final and initial configurations of the supercluster ab. The fermion signs $(-1)^{f(\mathbf{n})+f(\mathbf{n'})}$ arise when we reorder the referencing operators

$$K^{\dagger}_{\mathbf{m}}K^{\dagger}_{\mathbf{l}}K_{\mathbf{l'}}K_{\mathbf{m'}} = (-1)^{f(\mathbf{n})+f(\mathbf{n'})}K^{\dagger}_{\mathbf{l}}K_{\mathbf{l'}}K^{\dagger}_{\mathbf{m}}K_{\mathbf{m'}} \tag{C.11.2}$$

in the supercluster density matrix.

C.11.1 Cluster and Supercluster Fock-Hilbert Spaces

Even when particle number is conserved in the ground state, the particle number of cluster a (or b) need not be, so long as the *increase* in the particle number of cluster a (or b) is compensated for by a *decrease* of the same magnitude in the particle number of cluster b (or a). The correlation density matrix does break up into sectors, since

the total number of particles in both clusters is still conserved between initial and final supercluster states for which the correlation density-matrix element is nonzero.

Since it is harder to keep track of such supercluster-particle-number sectors in the correlation density matrix, than to keep track of the cluster-particle-number sectors in the cluster density matrix (see Section C.11.2), we do not bother. To construct the correlation-**K** matrix, we work with the full product cluster Fock-Hilbert space $V_C^{a,b} \times V_C^{a,b}$, which has a dimension of $[D_C^{a,b}]^2$, where $V_C^{a,b}$ is the $D_C^{a,b}$-dimensional Fock-Hilbert space of clusters a or b, containing configurations with $0 \leq P_C \leq N_C$ particles within the cluster. The correlation-**K** matrix is then $[D_C^a]^2 \times [D_C^b]^2$.

Therefore, the first step towards constructing the correlation-**K** matrix is to first build up the Fock-Hilbert spaces of the clusters and supercluster, and store the basis states within an array that will make our job of writing out the left- and right-eigenvectors X and Y convenient. To this end, we abandon the configuration representation for the basis states used thus far in the code base for exact diagonalization and for calculating the cluster density matrices, and switch to the occupation number representation instead, i.e. each basis state in the cluster Fock-Hilbert space is represented by a string of $N_C^{a,b,ab}$ integers $[n_1, n_2, \ldots, n_{N_C^{a,b,ab}}]$, each of which can take on the values $n_i = 0, 1$. Using this representation as a means of storing basis states, the Fock-Hilbert space can be generated by calling the `Common` code branch core function `clusterhilbertspace` to generate the basis states with a fixed particle number within the cluster, transcribing these basis states from the configuration representation to the occupation number representation, and taking the union of all fixed-particle-number cluster Hilbert spaces. The Octave code of the `Common` code branch wrapper function `fullclusterhilbertspace` that does this is shown below.

---

function VC = fullclusterhilbertspace(cluster, neighborlist)

```
% make cluster into a column vector

[NC1, NC2] = size(cluster);

if NC2 > NC1
    cluster = cluster';
    NC = NC2;
else
    NC = NC1;
endif

% PC = 0

VC = zeros(1, NC);

for PC = 1:NC
    VCP = clusterhilbertspace(cluster, PC, neighborlist);
    DCP = size(VCP, 1);
    for n = 1:DCP
        s = zeros(1, NC);
        for p = 1:PC
            s(listindex(VCP(n, p), cluster)) = 1;
        endfor
        VC = [ VC; s ];
```

```
    endfor
endfor

endfunction
```

C.11.2 Compactifying the Cluster Density Matrix

The matrix elements of the correlation-**K** matrix can be computed directly from (C.11.1) by repeatedly calling the `Common` code branch core function `fastclusterdensitymatrix`. However, the cluster density matrices ρ^a, ρ^b and ρ^{ab} would then not be stored, and this is sometimes inconvenient, especially when there is a need for debugging.

Instead of storing the P_C-sectors of a cluster density matrix separately, we store the full cluster density matrix in a compactified array of the form

$$\rho_C = \{[P_C, \mathbf{n}, \mathbf{n}', \langle \mathbf{n}|\rho_C(P_C)|\mathbf{n}'\rangle]\}, \tag{C.11.3}$$

where the first column stores the particle number P_C within the cluster, the second and third columns store the indices of the final and initial configurations within the P_C-particle cluster Hilbert space, and the four column stores the matrix element itself.

The Octave code for the `Common` code branch function `compactifyclusterdensitymatrix` that peforms this compactification is shown below.

```
function [r, lrPC] = compactifyclusterdensitymatrix(cluster, neighborlist, V, Psi)

[VPC, DPC] = occupationpartition(V, cluster);
PsiPC = partitionpsi(VPC, DPC, Psi);
```

```
r0 = fastclusterdensitymatrix(cluster, 0, neighborlist, V, VPC, DPC, PsiPC);


r = [ 0 1 1 r0 ];
lrPC = [ 1 ];


k = 2;


for PC = 1:max(size(cluster))
    if clusterhilbertspace(cluster, PC, neighborlist)
        lrPC(PC+1) = k;
        rPC = fastclusterdensitymatrix(    cluster, PC, neighborlist,\
                                           V, VPC, DPC, PsiPC);
        for m = 1:size(rPC, 1)
            for n = 1:size(rPC, 2)
                r(k, :) = [ PC m n rPC(m, n) ];
                k = k + 1;
            endfor
        endfor
    endif
endfor


endfunction
```

As can be seen from the code above, `compactifyclusterdensitymatrix` also returns a list of ranks for the various P_C-particle sectors of the cluster density matrix to

facilitate access to the matrix elements stored in the compactified array.

C.11.3 Correlation Density Matrix

To reduce code clutter in the `Fermion` code branch function `correlationKmatrix` that ultimately calculates the correlation-**K** matrix, I added an intermediate `Fermion` code branch function `correlationdensitymatrix` to first calculate the correlation density matrix elements, using (C.11.1), starting from the compactified cluster density matrices. To handle the fermion sign $(-1)^{f(\mathbf{n})+f(\mathbf{n}')}$, we note that the referencing operators have the form

$$K = c_{j_1}\cdots c_{j_{P_C}}(1-n_1)\cdots(1-n_{j_1-1})(1-n_{j_1+1})\cdots\times \\ (1-n_{j_{P_C}-1)})(1-n_{j_{P_C}+1})\cdots(1-n_{N_C}), \quad \text{(C.11.4)}$$

where P_C is the number of occupied sites in the cluster configuration $[j_1,\ldots,j_{P_C}]$ the referencing operator K is associated with. Therefore, if we bring $K^\dagger$ through K', where the two referencing operators have no sites in common (since one would be associated with cluster a and the other for cluster b), we pick up a nontrivial fermion sign of -1 only when we try to bring an odd number P_C of creation operators in $K^\dagger$ through an odd number P'_C of annihilation operators in K', i.e. the fermion incurred is $(-1)^{P_C P'_C}$. In (C.11.2), we bring $K^\dagger_{\mathbf{m}}$ through $K^\dagger_{\mathbf{l}}$ and $K_{\mathbf{l}'}$, hence the fermion sign incurred is $(-1)^{[P_C(\mathbf{l})+P_C(\mathbf{l}')]P_C(\mathbf{m})}$.

The Octave code for `correlationdensitymatrix` is shown below.

```
function rc = correlationdensitymatrix( rab, ra, rb, lrab, lra, lrb,\
                                        PAB, cab, ca, cb, nR)

if PAB == 0
```

```
        rc = rab(1, 4) − ra(1, 4)*rb(1, 4);
    else
        VAB = clusterhilbertspace(cab, PAB, nR);
        DAB = size(VAB, 1);
        rc = zeros(DAB);
        for n1 = 1:DAB
            l1 = intersection(ca, VAB(n1, :));
            r1 = intersection(cb, VAB(n1, :));
            for n2 = 1:DAB
                l2 = intersection(ca, VAB(n2, :));
                r2 = intersection(cb, VAB(n2, :));
                % calculate fermion sign
                if rem((size(l1, 2) + size(l2, 2))*size(r1, 2), 2) == 0
                    fn1n2 = 1;
                else
                    fn1n2 = −1;
                endif
                % calculate correlation matrix elements
                if size(l1, 2) == size(l2, 2)    % contribution from (rA x rB)
                    PA = size(l1, 2);
                    PB = size(r1, 2);
                    if PA == 0                   % then PB != 0
                        VB = clusterhilbertspace(cb, PB, nR);
                        DB = size(VB, 1);
                        ir1 = listindex(r1, VB);
```

```
        ir2 = listindex(r2, VB);
        rc(n1, n2) = fn1n2*\
            rab(lrab(PAB+1) + DAB*(n1 - 1) + n2 - 1, 4) -\
            ra(1, 4)*rb(lrb(PB+1) + DB*(ir1 - 1) + ir2 - 1, 4);
    elseif PB == 0              % then PA != 0
        VA = clusterhilbertspace(ca, PA, nR);
        DA = size(VA, 1);
        il1 = listindex(l1, VA);
        il2 = listindex(l2, VA);
        rc(n1, n2) = fn1n2*\
            rab(lrab(PAB+1) + DAB*(n1 - 1) + n2 - 1, 4) -\
            ra(lra(PA+1) + DA*(il1 - 1) + il2 - 1, 4)*rb(1, 4);
    else
        VA = clusterhilbertspace(ca, PA, nR);
        VB = clusterhilbertspace(cb, PB, nR);
        DA = size(VA, 1);
        DB = size(VB, 1);
        il1 = listindex(l1, VA);
        il2 = listindex(l2, VA);
        ir1 = listindex(r1, VB);
        ir2 = listindex(r2, VB);
        rc(n1, n2) = fn1n2*\
            rab(lrab(PAB+1) + DAB*(n1 - 1) + n2 - 1, 4) -\
            ra(lra(PA+1) + DA*(il1 - 1) + il2 - 1, 4)*\
            rb(lrb(PB+1) + DB*(ir1 - 1) + ir2 - 1, 4);
```

```
            endif
        else                                % no contribution from (rA x rB)
            rc(n1, n2) = fn1n2*\
                rab(lrab(PAB+1) + DAB*(n1 - 1) + n2 - 1, 4);
        endif
    endfor
endfor
endif

endfunction
```

C.11.4 Correlation-K Matrix

To reorganize the compactified correlation density matrix ρ^c into the correlation-**K** matrix, we need to work with the fused indices $\lambda = (\mathbf{l}, \mathbf{l}')$ for cluster a, and $\mu = (\mathbf{m}, \mathbf{m}')$ for cluster b. If the indices of the configurations $|\mathbf{l}\rangle$ and $|\mathbf{l}'\rangle$ in the Fock-Hilbert space of cluster a are l and l', while the indices of the configurations $|\mathbf{m}\rangle$ and $|\mathbf{m}'\rangle$ in the Fock-Hilbert space of cluster b are m and m', then we use the mapping

$$\lambda = (l-1)D_C^a + l', \quad \mu = (m-1)D_C^b + m', \tag{C.11.5}$$

to obtain the fused indices λ and μ.

The `Fermion` code branch wrapper function `correlationKmatrix`, whose Octave code is shown below, then perform a lookup on the compactified correlation density matrix to determine the indices l, l', m, m', compute the fused indices λ and μ, and assign the corresponding correlation density matrix element to the appropriate location in the correlation-**K** matrix.

```
function K = correlationKmatrix( rab, ra, rb, lrab, lra, lrb, cab, ca, cb,\
                                 VABf, VAf, VBf, neighborlist)

% ensure that all clusters are column vectors

if size(cab, 2) > size(cab, 1)
    cab = cab';
endif
NAB = size(cab, 1);

if size(ca, 2) > size(ca, 1)
    ca = ca';
endif
NA = size(ca, 1);

if size(cb, 2) > size(cb, 1)
    cb = cb';
endif
NB = size(cb, 1);

lD2P = size(VAf, 1);
rD2P = size(VBf, 1);

K = zeros(lD2P^2, rD2P^2);
```

```
PNmax = sum(VABf(size(VABf, 1), :));

% PN = 0

K(1, 1) = rab(1, 4) − ra(1, 4)*rb(1, 4);

% PN > 0

for PN = 1:PNmax
    rc = correlationdensitymatrix(rab, ra, rb, lrab, lra, lrb,\
        PN, cab, ca, cb, neighborlist);
    VAB = clusterhilbertspace(cab, PN, neighborlist);
    for n1 = 1:size(rc, 1)
        sl1 = intersection(ca, VAB(n1, :));
        s = zeros(1, NA);
        for p = 1:size(sl1, 2)
            s(listindex(sl1(p), ca)) = 1;
        endfor
        l1 = listindex(s, VAf);
        sr1 = intersection(cb, VAB(n1, :));
        s = zeros(1, NB);
        for p = 1:size(sr1, 2)
            s(listindex(sr1(p), cb)) = 1;
        endfor
```

```
            r1 = listindex(s, VBf);
            for n2 = 1:size(rc, 2)
                sl2 = intersection(ca, VAB(n2, :));
                s = zeros(1, NA);
                for p = 1:size(sl2, 2)
                    s(listindex(sl2(p), ca)) = 1;
                endfor
                l2 = listindex(s, VAf);
                sr2 = intersection(cb, VAB(n2, :));
                s = zeros(1, NB);
                for p = 1:size(sr2, 2)
                    s(listindex(sr2(p), cb)) = 1;
                endfor
                r2 = listindex(s, VBf);
                % compute the composite indices L and R
                L = lD2P*(l1 - 1) + l2;
                R = rD2P*(r1 - 1) + r2;
                % assign matrix elements of K
                K(L, R) = rc(n1, n2);
            endfor
        endfor
    endfor

endfunction
```

APPENDIX D

TWIST BOUNDARY CONDITIONS AVERAGING

D.1 Introduction

Numerical methods like ED and QMC are becoming increasingly indispensable tools for understanding quantum many-body systems. However, a major shortcoming of resorting to numerical solutions is that we are forced to restrict ourselves to the study of a finite system, even though it is properties of the infinite system that we are interested in. In so doing, we introduce systematic deviations, which we shall hereafter refer to as *finite size effects*, from the infinite-system value of these properties. If the quantity we seek is intensive in nature, for example, the ground state energy per particle, then a commonly used 'remedy' for the finite size effects is to calculate the desired quantity for a sequence of systems with increasing size, and then perform an extrapolation to get the infinite-system limit. Whatever amount of computing power we have at our disposal, extrapolation has to be done prudently, lest we be led to the wrong answer.

A truly infinite system has no boundaries, but when we study a finite system, we will invariably need to impose some sort of boundary conditions, [1] with open and periodic

[1] As a note of interest, let us imagine cutting the infinite system up into two parts: a finite target subsystem and an (infinite) environmental subsystem. Instead of solving the quantum many-body problem on the infinite system, we can then think of solving an equivalent quantum many-body problem on the finite target subsystem, subjected to the influence of the environmental subsystem. In principle, if we can set up the boundary conditions to mimick the effects of the environmental subsystem, then numerical results obtained from the finite target system would not 'contaminated' by finite size effects. Nguyen *et al* realizes this in Ref. 384, and attempts to draw a connection between energy eigenstates obtained under different boundary conditions and terms in the expansion of the density matrix of the finite target system. Their goal is to replace the infinite-system expectation of an observable, obtained by tracing over the density matrix, with an approximate weighted sum of its expectations over such energy eigenstates. We know, from our own studies [184, 198] that their premise is unattainable even for a system of noninteracting spinless fermions. This is because in the infinite-system

boundary conditions being the most commonly used. While preserving full lattice translational invariance, imposing periodic boundary conditions on a finite system means that we end up with a discrete set of wave vectors $\{\mathbf{k}_n\}$. Depending on how representative this discrete set of wave vectors are of the continuous set of wave vectors $\mathbf{k}$ that contribute to the infinite-system ground state, we do better at approaching the infinite-system limit of a given property when performing numerical calculations at some system sizes, and poorer at other system sizes. The result is a nonmonotonic convergence to the infinite-system limit, as the size of the finite system is increased, which makes extrapolation unreliable.

Spronken *et al* first noted in 1981 that the use of alternating periodic and antiperiodic boundary conditions for small one-dimensional systems of even lengths can yield, for the results obtained from ED, a sequence of values which varies monotonically with increasing system size [385]. This allows them to more confidently extrapolate the numerical results from the small systems to the infinite-system limit. Since then, there have been several works that utilize this manner of extrapolation [61, 386–389], which is partially justified by the analytical results of Ogata and Shiba [241] and Shastry and Sutherland [390]. While they did not take full advantage of it, Spronken *et al* realized that one can define a family of boundary, parametrized by a set of twist angles $\boldsymbol{\phi} = (\phi_1, \phi_2, \ldots, \phi_d)$, where d is the dimensionality of the system, which interpolates between the usual periodic and antiperiodic boundary conditions. This has come to be known as the *modified periodic boundary conditions* [385], or the *twist boundary conditions* [391], following Kohn, who liken the boundary conditions to a phase twist incurred by a quantum-mechanical particle moving on the surface of a d-dimensional torus in the

ground state, energy eigenstates of the finite target system have quantum-mechanical correlations which cannot be deduced *unless* we already know what the infinite-system ground state looks like.

presence of a magnetic flux [392].

As first pointed out by Spronken *et al*, the effect of imposing twist boundary conditions with twist angles $\boldsymbol{\phi}$ is to sample the discrete set of wave vectors $\{\mathbf{k}_n + \boldsymbol{\phi}\}$. By varying $\boldsymbol{\phi}$ in the twist boundary conditions, we are able to continuously sample the wave vectors $\mathbf{k}$ of the infinite system. This allows us to go beyond the limitations of a discrete set of wave vectors for a finite system, to map out excitation spectra [393] and dispersion relations [391, 394–396]. The next level of sophistication involving the use of twist boundary conditions is their application to calculating correlation and response functions. These, and calculations of ground state energy per particle or binding energy, typically involves an integration (or equivalently, an average) over the infinite-system wave vectors. Because it is computationally expensive to average such observables over a fine mesh of points covering the Brillouin zone [384, 397–402], some workers in the ED and QMC community average over only a few wave vectors sampled using twist boundary conditions [403–409]. Kawakami and Yang calculated the conductivity and transport mass of the one-dimensional *t*-*J* model using the original formulation by Kohn, and later refined by Shastry and Sutherland [410].

When people in the business of numerical solutions of small systems started exploring the use of twist boundary conditions, there was no serious effort to understand how twist boundary conditions reduce or eliminate finite size effects, apart from the wave vector sampling argument in one-dimension. They merely noted that using twist boundary conditions with extrapolation allows a faster convergence to the infinite-system limit [398, 399]. In 1993, Gammel, Campbell and Loh gave a perturbative argument, based on the Bloch Theorem, on how the use of twist boundary conditions on finite system yields some sort of mean-field like approximation to the infinite-system ground state properties [401]. Then in 1996, Gros presented his method of *grand-canonical*

integration over boundary conditions [400]. Starting from the premise of wave vector sampling through the use of twist boundary conditions, Gros showed that his method recovers exactly the thermodynamic average energy of the infinite system of noninteracting spinfull fermions in any dimensions. By comparing numerical results obtained using this method for small interacting systems against analytical results obtained using the Bethe ansatz, he also observed that finite size effects are small. More recently, Lin, Zong and Ceperley contributed further insight on the use of twist boundary conditions to control finite size effects, with a comprehensive analysis of the effects of imposing twist boundary conditions on a system of two-dimensional noninteracting fermions [411].

In this Appendix, I shall present how twist boundary conditions averaging works in pedagogical details, drawing from the existing treatments by Poilblanc [398, 399], Gros [400] and Lin *et al* [411]. In trying to apply the method of twist boundary conditions averaging ourselves, we also realized that some important questions on how the method works are not answered in the literature. These questions are:

1. what observables will the method work well on to reduce or eliminate finite size effects, and what observables will the method not work well on?

2. for a given observable, is it possible to specify how close we can get with this method, *sans* extrapolation, to the infinite-system limit?

3. if the answer to question 2 is yes, how large must the set of twist angles be to achieve a given precision?

In asking the first question, the worry at the back of our minds is whether we can make a bad choice of problems to tackle with a perfectly good technique. If there are classes of observables for which twist boundary conditions averaging will not lead us to the infinite-system limit, surely we want to know about them. As for the second and third

questions, the common concern is on the degree of control the method affords. For example, if our desired precision of ϵ is achieved with twist boundary conditions averaging on a 10-site system, we do not want to slog unnecessarily implementing a similar calculation on a 16-site system. Also, if we can get away with sampling six set of twist angles to achieve a given precision and a given system size, why work with a set of 10×10 twist angles?

To address these questions, we organize this Appendix as follows: in Section D.2.1, we will review how twist boundary conditions averaging works for a one-dimensional system of noninteracting spinless fermions, based on what is already known in the literature, and supplementing the exposition with our own findings. Undertaking this seemingly silly exercise for finite chains, we discover that twist boundary conditions averaging reproduces exactly the infinite-system limit of certain observables without the need for extrapolation, as noted in the literature. On other observables, we find that twist boundary conditions averaging does not significantly reduce finite size errors. We shall discuss why this is so, before moving on to Section D.2.2 to look at what happens when we perform twist boundary conditions averaging on a two-dimensional system of noninteracting spinless fermions on a square lattice. Here we shall see that for any given finite system, finite size effects are not eliminated for most expectations, except under very special circumstances.

Equipped with improved understanding of what twist boundary conditions averaging does and does not do, we discuss in Section D.6 attempts to milk the method dry, and get as close to the infinite-system limit as we possibly can. Noting, as Lin *et al* did [411], the similarity between twist boundary conditions averaging and Brillouin zone integration, we apply the special-point method [412–417] for the latter onto the former and analyze the results. We then move on to the next level of sophistication to discuss the

application of an equivalent of the tetrahedron integration method [418–420] in Brillouin zone integration to twist boundary conditions averaging, and its practical limitations when used in the numerical solution of quantum many-body problems.

D.2 Twist Boundary Conditions

There are two easy ways to implement twist boundary conditions. The first, and more common in the literature, is to introduce a phase twist only when a particle hops across a boundary. We call this the *boundary gauge*. The second, less common in literature, is to introduce an incremental phase twist when the particle hops along every bond. We call this the *bond gauge*. The second can be obtained from the first by performing a simple gauge transformation.

In this section, we look at the effect that twist boundary conditions have on the energy eigenvalues and eigenstates of one- and two-dimensional systems of noninteracting spinless fermions, when these are calculated in the bond and boundary gauges.

D.2.1 One-Dimensional Noninteracting Spinless Fermions

D.2.1.1 No Phase Twist

When we introduce no phase twist at all, the Hamiltonian for a N-site chain of noninteracting spinless fermions is

$$H(0) = -\sum_{j} \left(c_j^\dagger c_{j+1} + c_{j+1}^\dagger c_j \right), \tag{D.2.1}$$

where c_j and $c_j^\dagger$ are real-space fermion operators annihilating and creating a particle at site j respectively, and we have set the hopping matrix element to $t = 1$ for simplicity.

Under periodic boundary conditions, we have

$$c_{j+N} = c_j. \tag{D.2.2}$$

Introducing the momentum-space fermion operators

$$\tilde{c}_k = \frac{1}{\sqrt{N}} \sum_j e^{\mathrm{i}kj} c_j, \quad \tilde{c}_k^\dagger = \frac{1}{\sqrt{N}} \sum_j e^{-\mathrm{i}kj} c_j^\dagger, \tag{D.2.3}$$

for which we have the inverse relations

$$c_j = \frac{1}{\sqrt{N}} \sum_k e^{-\mathrm{i}kj} \tilde{c}_k, \quad c_j^\dagger = \frac{1}{\sqrt{N}} \sum_k e^{\mathrm{i}kj} \tilde{c}_k^\dagger \tag{D.2.4}$$

relating the real-space and momentum-space fermion operators, we can diagonalize the Hamiltonian explicitly as

$$\begin{aligned} H(0) &= -\sum_j \frac{1}{N} \sum_k \sum_{k'} e^{\mathrm{i}kj}\, e^{-\mathrm{i}k'(j+1)}\, \tilde{c}_k^\dagger \tilde{c}_{k'} - \sum_j \frac{1}{N} \sum_k \sum_{k'} e^{\mathrm{i}k(j+1)}\, e^{-\mathrm{i}k'j}\, \tilde{c}_k^\dagger \tilde{c}_{k'} \\ &= -\sum_k \sum_{k'} e^{-\mathrm{i}k'}\, \tilde{c}_k^\dagger \tilde{c}_{k'} \frac{1}{N} \sum_j e^{\mathrm{i}(k-k')j} - \sum_k \sum_{k'} e^{\mathrm{i}k}\, \tilde{c}_k^\dagger \tilde{c}_{k'} \frac{1}{N} \sum_j e^{\mathrm{i}(k-k')j} \\ &= -\sum_k \sum_{k'} e^{-\mathrm{i}k'}\, \tilde{c}_k^\dagger \tilde{c}_{k'}\, \delta_{k,k'} - \sum_k \sum_{k'} e^{\mathrm{i}k}\, \tilde{c}_k^\dagger \tilde{c}_{k'}\, \delta_{k,k'} \\ &= -\sum_k \left(e^{-\mathrm{i}k} + e^{\mathrm{i}k} \right) \tilde{c}_k^\dagger \tilde{c}_k = \sum_k \epsilon_k \tilde{c}_k^\dagger \tilde{c}_k, \end{aligned} \tag{D.2.5}$$

where the dispersion relation is

$$\epsilon_k = -\left(e^{-\mathrm{i}k} + e^{\mathrm{i}k} \right) = -2\cos k. \tag{D.2.6}$$

For an infinite chain, the wave vector k can take on any value between $-\pi \le k \le \pi$. For the finite chain with N sites, periodic boundary conditions imposed as (D.2.2) tells us that

$$\begin{aligned} \tilde{c}_k &= \frac{1}{\sqrt{N}} \sum_j e^{\mathrm{i}kj} c_j = \frac{1}{\sqrt{N}} \sum_{j'} e^{\mathrm{i}k(j'+N)} c_{j'+N} \\ &= e^{\mathrm{i}kN} \left(\frac{1}{\sqrt{N}} \sum_{j'} e^{\mathrm{i}kj'} c_{j'} \right) = e^{\mathrm{i}kN} \tilde{c}_k, \end{aligned} \tag{D.2.7}$$

i.e. we must have

$$k = \frac{2\pi n}{N}. \tag{D.2.8}$$

In the First Brillouin Zone (FBZ), the integers n are

$$n = -\left\lfloor \frac{N}{2} \right\rfloor, -\left\lfloor \frac{N}{2} \right\rfloor + 1, \ldots, \left\lfloor \frac{N}{2} \right\rfloor - 1, \tag{D.2.9}$$

where $\lfloor x \rfloor$ is the greatest integer less than x. Let me denote wave vectors given by (D.2.8) as k_0.

In the occupation number basis $\{c_j^\dagger |0\rangle\}_{j=1}^N$ for a single spinless fermion, the eigenvectors of $H(0)$ are of the form

$$|k_0\rangle = \frac{1}{\sqrt{N}} \sum_j e^{-\mathrm{i}\, k_0 j} c_j^\dagger |0\rangle . \tag{D.2.10}$$

We can check that these are simultaneous eigenvectors of the translation operators $T_{j'}$, whose actions on the fermion operators are given by

$$T_{j'} c_j T_{j'}^{-1} = c_{j+j'}, \quad T_{j'} c_j^\dagger T_{j'}^{-1} = c_{j+j'}^\dagger, \tag{D.2.11}$$

and whose actions on the vacuum are

$$T_{j'} |0\rangle = |0\rangle , \tag{D.2.12}$$

i.e. their actions on the occupation number basis states are

$$T_{j'} c_j^\dagger |0\rangle = \left(T_{j'} c_j^\dagger T_{j'}^\dagger \right) T_{j'} |0\rangle = c_{j+j'}^\dagger |0\rangle . \tag{D.2.13}$$

Letting $T_{j'}$ act on $|k_0\rangle$, we find that

$$T_{j'} |k_0\rangle = \frac{1}{\sqrt{N}} \sum_j e^{-\mathrm{i}\, k_0 j} c_{j+j'}^\dagger |0\rangle = \frac{1}{\sqrt{N}} \sum_{j''} e^{-\mathrm{i}\, k_0 (j''-j')} c_{j''}^\dagger |0\rangle = e^{\mathrm{i}\, k_0 j'} |k_0\rangle , \tag{D.2.14}$$

i.e. $|k_0\rangle$ is an eigenvector of $T_{j'}$ with eigenvalue $e^{\mathrm{i}\, k_0 j'}$.

D.2.1.2 Phase Twist in the Bond Gauge

When a phase twist is introduced into the twist boundary conditions in the bond gauge, we incur a phase twist of $e^{+\mathrm{i}\phi}$ for hopping across one bond in the $+x$-direction, and $e^{-\mathrm{i}\phi}$ for hopping across one bond in the $-x$-direction. The Hamiltonian for the one-dimensional system of noninteracting spinless fermions becomes

$$H(\phi) = -\sum_j \left(e^{-\mathrm{i}\phi}\, c_j^\dagger c_{j+1} + e^{\mathrm{i}\phi}\, c_{j+1}^\dagger c_j \right). \tag{D.2.15}$$

Following Lin, Zong and Ceperley, we will call ϕ the *twist angle* [411], even though our definition for this parameter is different from theirs.[2] In this gauge, we continue to demand that

$$c_{j+N} = c_j. \tag{D.2.16}$$

Using the relations (D.2.3) and (D.2.4) between the real-space and momentum-space fermion operators, we can diagonalize the Hamiltonian in (D.2.15) as

$$\begin{aligned} H(\phi) &= -\sum_j e^{-\mathrm{i}\phi} \frac{1}{N} \sum_k \sum_{k'} e^{\mathrm{i}kj}\, e^{-\mathrm{i}k'(j+1)}\, \tilde{c}_k^\dagger \tilde{c}_{k'} \\ &\quad - \sum_j e^{\mathrm{i}\phi} \frac{1}{N} \sum_k \sum_{k'} e^{\mathrm{i}k(j+1)}\, e^{\mathrm{i}k'j}\, \tilde{c}_k^\dagger \tilde{c}_{k'} \\ &= -\sum_k \sum_{k'} \Big(e^{-\mathrm{i}\phi}\, e^{-\mathrm{i}k'} \frac{1}{N} \sum_j e^{\mathrm{i}(k-k')j} + e^{\mathrm{i}\phi}\, e^{\mathrm{i}k} \frac{1}{N} \sum_j e^{\mathrm{i}(k-k')j} \Big) \tilde{c}_k^\dagger \tilde{c}_{k'}, \end{aligned} \tag{D.2.17}$$

Using the fact that

$$\frac{1}{N} \sum_j e^{\mathrm{i}(k-k')j} = \delta_{k,k'}, \tag{D.2.18}$$

we find that

$$H(\phi) = -\sum_k \left(e^{-\mathrm{i}(k+\phi)} + e^{\mathrm{i}(k+\phi)} \right) \tilde{c}_k^\dagger \tilde{c}_k = \sum_k \epsilon_k \tilde{c}_k^\dagger \tilde{c}_k, \tag{D.2.19}$$

[2] Lin, Zong and Ceperley worked in the boundary gauge, in which a particle picks up a phase twist of $e^{\mathrm{i}\theta}$ when it hops across the boundary [411]. The entity they called the twist angle is θ, which is equal to N times of our twist angle ϕ, N being the length of the chain.

with a modified dispersion relation

$$\epsilon_k = -2\cos(k+\phi). \tag{D.2.20}$$

For a finite chain of N sites, the wave vectors k satisfying the periodic boundary conditions are still the wave vectors k_0 in (D.2.10). Working with the occupation number basis $\{c_j^\dagger|0\rangle\}_{j=1}^N$, we verified numerically that the single-particle eigenstates of $H(\phi)$ are identical to those of $H(0)$. They merely correspond to different energy eigenvalues.

Another way to think about this diagonalization is to introduce the fermion operators

$$d_j = e^{-\mathrm{i}\phi j}c_j, \quad d_j^\dagger = e^{\mathrm{i}\phi j}c_j^\dagger, \tag{D.2.21}$$

and write the Hamiltonian as

$$\begin{aligned} H(\phi) &= -\sum_j \left(e^{\mathrm{i}\phi j}c_j^\dagger e^{-\mathrm{i}\phi(j+1)}c_{j+1} + e^{\mathrm{i}\phi(j+1)}c_{j+1}^\dagger e^{-i\phi j}c_j\right) \\ &= -\sum_j \left(d_j^\dagger d_{j+1} + d_{j+1}^\dagger d_j\right). \end{aligned} \tag{D.2.22}$$

Diagonalization then proceeds in the usual way, with the introduction of the momentum-space fermion operators

$$\tilde{d}_k = \frac{1}{\sqrt{N}}\sum_j e^{\mathrm{i}kj}d_j, \quad \tilde{d}_k^\dagger = \frac{1}{\sqrt{N}}\sum_j e^{-\mathrm{i}kj}d_j^\dagger, \tag{D.2.23}$$

in terms of which the Hamiltonian can be written as

$$H(\phi) = \sum_k \epsilon_k \tilde{d}_k^\dagger \tilde{d}_k, \tag{D.2.24}$$

where

$$\epsilon_k = -2\cos k. \tag{D.2.25}$$

For this set of fermion operators, the periodic boundary conditions which we should impose are

$$d_{j+N} = e^{-\mathrm{i}\phi(j+N)}c_{j+N} = e^{-\mathrm{i}\phi N}e^{-\mathrm{i}\phi j}c_j = e^{-\mathrm{i}\phi N}d_j. \tag{D.2.26}$$

This means that

$$\begin{aligned}\tilde{d}_k &= \frac{1}{\sqrt{N}}\sum_j e^{\mathrm{i}\,kj} d_j = \frac{1}{\sqrt{N}}\sum_{j'} e^{\mathrm{i}\,k(j'+N)} d_{j'+N} \\ &= e^{\mathrm{i}\,kN} e^{-i\phi N}\left(\frac{1}{\sqrt{N}}\sum_{j'} e^{\mathrm{i}\,kj'} d_{j'}\right) = e^{\mathrm{i}(k-\phi)N}\tilde{d}_k,\end{aligned} \tag{D.2.27}$$

and so, the set of allowed wave vectors are

$$k = \frac{2\pi n}{N} + \phi = k_0 + \phi. \tag{D.2.28}$$

The dispersion relation $\epsilon_k = -2\cos(k_0 + \phi)$ therefore agrees with the previous diagonalization. As for the eigenvectors, we know that for a Hamiltonian of the form (D.2.24), these must take the form

$$\begin{aligned}|k\rangle = \tilde{d}_k^\dagger |0\rangle &= \frac{1}{\sqrt{N}}\sum_j e^{-\mathrm{i}\,kj} d_j^\dagger |0\rangle \\ &= \frac{1}{\sqrt{N}}\sum_j e^{-\mathrm{i}(k_0+\phi)j} e^{\mathrm{i}\,\phi j} c_j^\dagger |0\rangle = \frac{1}{\sqrt{N}}\sum_j e^{-\mathrm{i}\,k_0 j} c_j^\dagger |0\rangle\,,\end{aligned} \tag{D.2.29}$$

i.e. these are the same eigenvectors as those of $H(0)$.

D.2.1.3 Phase Twist in the Boundary Gauge

In the boundary gauge, the phase twist incurred from the twist boundary conditions applies to a particle only when it hops across a boundary. In this gauge, the Hamiltonian is then the same as for the case of no phase twist, but the boundary conditions on the fermion operators must be modified to read

$$c_{j+N} = e^{-\mathrm{i}\,N\phi} c_j. \tag{D.2.30}$$

Note that in the literature, the phase twist across the boundary is commonly defined to be $e^{-\mathrm{i}\,\phi}$. I use a phase twist of $e^{-\mathrm{i}\,N\phi}$ instead of $e^{\mathrm{i}\,\phi}$, so that we have a consistent compounded phase twist in both the bond and boundary gauges.

In the boundary gauge, we still use (D.2.3) and (D.2.4) to diagonalize the Hamiltonian, and obtain the dispersion relation

$$\epsilon_k = -2\cos k, \tag{D.2.31}$$

but the modified boundary conditions now demand that

$$\begin{aligned}\tilde{c}_k &= \frac{1}{\sqrt{N}}\sum_j e^{\mathrm{i}\,kj}c_j = \frac{1}{\sqrt{N}}\sum_{j'} e^{\mathrm{i}\,k(j'+N)}c_{j'+N} \\ &= e^{\mathrm{i}(k-\phi)N}\left(\frac{1}{\sqrt{N}}\sum_{j'} e^{\mathrm{i}\,kj'}c_{j'}\right) = e^{\mathrm{i}(k-\phi)N}\tilde{c}_k,\end{aligned} \tag{D.2.32}$$

so that the allowed wave vectors are

$$k = \frac{2\pi n}{N} + \phi = k_0 + \phi, \tag{D.2.33}$$

i.e. the energy eigenvalues are the same in both the bond and boundary gauges, which it must be.

For numerical implementation, we note that the matrix element $\langle 0|c_1 H c_N^\dagger|0\rangle$ is

$$e^{\mathrm{i}\,N\phi}\langle 0|c_{N+1}Hc_N^\dagger|0\rangle = -e^{\mathrm{i}\,N\phi}, \tag{D.2.34}$$

if we make use of (D.2.30), and take

$$\langle 0|c_{N+1}Hc_N^\dagger|0\rangle = -1, \tag{D.2.35}$$

as would all hoppings to nearest neighbors. Similarly, we have

$$\langle 0|c_N Hc_1^\dagger|0\rangle = -e^{-\mathrm{i}\,N\phi}. \tag{D.2.36}$$

I checked numerically that the eigenvectors of such a Hamiltonian matrix are indeed given by

$$|k\rangle = \frac{1}{\sqrt{N}}\sum_j e^{-\mathrm{i}(k_0+\phi)j}c_j^\dagger|0\rangle\,. \tag{D.2.37}$$

D.2.2 Two-Dimensional Noninteracting Spinless Fermions

For a two-dimensional system of noninteracting spinless fermions on a $L \times L$ square lattice subject to twist boundary conditions, we have the bond-gauge Hamiltonian

$$H(\boldsymbol{\phi}) = -\sum_{\langle \mathbf{r},\mathbf{r}' \rangle} \left(e^{\mathrm{i}\,\boldsymbol{\phi}\cdot(\mathbf{r}'-\mathbf{r})} c^\dagger_{\mathbf{r}'} c_{\mathbf{r}} + \text{h.c.} \right), \tag{D.2.38}$$

where $c_{\mathbf{r}}$ is the real-space fermion operator which annihilates a particle at site $\mathbf{r}$, $c^\dagger_{\mathbf{r}}$ is the real-space fermion operator which creates a particle at site $\mathbf{r}$, and the sum is over nearest neighbors pairs only. Here we introduce the *twist vector*

$$\boldsymbol{\phi} = (\phi_x, \phi_y), \tag{D.2.39}$$

where ϕ_x and ϕ_y are independent phases for hops in the $+x$-direction and the $+y$-direction respectively.

Again, by introducing the momentum-space operators

$$\tilde{c}_{\mathbf{k}} = \frac{1}{L} \sum_{\mathbf{r}} e^{\mathrm{i}\,\mathbf{k}\cdot\mathbf{r}}\, c_{\mathbf{r}}, \tag{D.2.40}$$

in terms of which we can write the real-space fermion operators as

$$c_{\mathbf{r}} = \frac{1}{L} \sum_{\mathbf{k}} e^{-\mathrm{i}\,\mathbf{k}\cdot\mathbf{r}}\, \tilde{c}_{\mathbf{k}}, \tag{D.2.41}$$

we find that

$$H(\boldsymbol{\phi}) = -\sum_{\langle \mathbf{r},\mathbf{r}' \rangle} e^{\mathrm{i}\,\boldsymbol{\phi}\cdot(\mathbf{r}'-\mathbf{r})} \frac{1}{L^2} \sum_{\mathbf{k}} \sum_{\mathbf{k}'} e^{\mathrm{i}\,\mathbf{k}\cdot\mathbf{r}'}\, e^{-\mathrm{i}\,\mathbf{k}'\cdot\mathbf{r}}\, \tilde{c}^\dagger_{\mathbf{k}} \tilde{c}_{\mathbf{k}'} + \text{h.c.} \tag{D.2.42}$$

Rewriting the sum over nearest neighbors $\mathbf{r}$ and $\mathbf{r}'$ as a sum over $\mathbf{r}$ and $\boldsymbol{\rho} = \mathbf{r}' - \mathbf{r}$, where $\boldsymbol{\rho} = (\pm 1, 0)$ or $(0, \pm 1)$, we then find that

$$\begin{aligned} H &= -\sum_{\mathbf{k}} \sum_{\mathbf{k}'} \sum_{\boldsymbol{\rho}} e^{\mathrm{i}\,\boldsymbol{\phi}\cdot\boldsymbol{\rho}}\, e^{\mathrm{i}\,\mathbf{k}\cdot\boldsymbol{\rho}} \frac{1}{L^2} \sum_{\mathbf{r}} e^{\mathrm{i}(\mathbf{k}-\mathbf{k}')\cdot\mathbf{r}}\, \tilde{c}^\dagger_{\mathbf{k}} \tilde{c}_{\mathbf{k}'} \\ &= \sum_{\mathbf{k}} \epsilon_{\mathbf{k}} \tilde{c}^\dagger_{\mathbf{k}} \tilde{c}_{\mathbf{k}}, \end{aligned} \tag{D.2.43}$$

after using the fact that

$$\frac{1}{L^2}\sum_{\mathbf{r}} e^{\mathrm{i}(\mathbf{k}-\mathbf{k}')\cdot\mathbf{r}} = \delta_{\mathbf{k},\mathbf{k}'}, \tag{D.2.44}$$

where the dispersion relation is

$$\epsilon_{\mathbf{k}} = -\sum_{\rho} e^{\mathrm{i}(\mathbf{k}+\boldsymbol{\phi})\cdot\rho} = -2\left[\cos(k_x+\phi_1)+\cos(k_y+\phi_2)\right]. \tag{D.2.45}$$

For the finite square lattice, the set of allowed wave vectors, given periodic boundary conditions, is still

$$\mathbf{k}_{0\mathbf{n}} = \frac{2\pi\mathbf{n}}{L} = \frac{2\pi(n_x,n_y)}{L}, \tag{D.2.46}$$

i.e. the same as those subject to the usual periodic boundary conditions.

D.2.3 Implications for Twist Boundary Conditions Averaging

D.2.3.1 Covariant Calculation of Expectations

The goal of using twist boundary conditions averaging when calculating correlation or response functions numerically from a finite system is to approximate their infinite-system limits. To understand how this can be done properly for noninteracting spinless fermions, let us imagine two calculations being done in parallel, one for a finite system subject to twist boundary conditions, and one for an infinite system. Let us assume for simplicity that the infinite system of spinless fermions is not subjected to an external magnetic field (if it is, it is easy to generalize the arguments to follow).

Now, for a zero external magntic field $\mathbf{B} = \mathbf{0}$, there are many vector potentials $\mathbf{A}$, including the trivial one, we can write down, such that $\mathbf{B} = \nabla\times\mathbf{A} = \mathbf{0}$. Each of these vector potentials $\mathbf{A}$ corresponds to a choice of gauge for the infinite system, all of which are good for doing calculations in. As usual, we pick one particular gauge, which we call the *target gauge*, to work in. In this target gauge for the infinite system, the spinless

fermion operators $e^{-i\theta(\mathbf{r})}c^\dagger_{\mathbf{r}}$ and $e^{i\theta(\mathbf{r}')}c_{\mathbf{r}'}$ each carry an infinite-system phase determined by the gauge. Barring exceptional circumstances, we always make the implicit choice of the trivial gauge, with $\mathbf{A} = \mathbf{0}$, to be the target gauge of our infinite system of noninteracting spinless fermions, for calculating the infinite-system expectations $\langle O \rangle$ of various observables O.

In the method of twist boundary conditions averaging, our goal is to approximate these infinite-system expectations $\langle O \rangle$, using expectations calculated from a finite system subjected to twist boundary conditions over a range of twist vectors $\boldsymbol{\phi}$. Because we have already made an implicit choice of a target gauge in the infinite system, we must make an explicit choice of a target gauge in the finite system. This target finite-system gauge must be such that all observables O that we can construct in the finite system — there are clearly some infinite-system observables that we cannot construct on a finite system — carry the same gauge phases as the corresponding observables in the infinite system.

However, to formally make such a choice of target finite-system gauge, we have to deal with a problem peculiar to finite periodic systems. For example, let us say we are interested in approximating the infinite-system expectation of the observable $O = c^\dagger_1 c_2$ for a one-dimensional system of noninteracting spinless fermions. On the infinite chain, the fermion operators $c^\dagger_1$ and c_2 are separated by a distance of $r = 1$. On a finite periodic chain of length N, as shown in Figure D.1, we can interpret $c^\dagger_1$ and c_2 as not straddling the boundary of the system, and are thus separated a distance of $r = 1$, or as straddling the boundary of the system, in which case the two fermion operators are separated by a distance of $r = N - 1$. In higher dimensions, there will a large of number of paths connecting two local operators, each corresponding to a different separation.

Clearly, for a nonzero phase twist $\boldsymbol{\phi} \neq \mathbf{0}$ in the finite-system boundary conditions, the

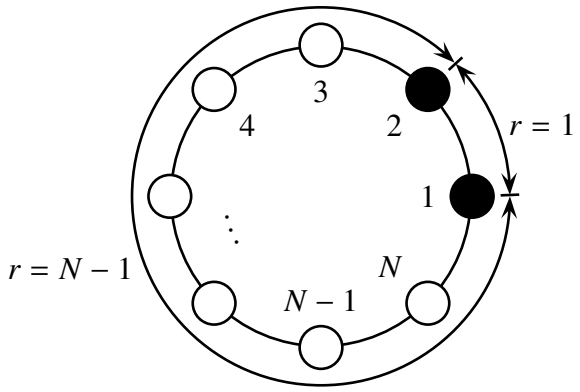

Figure D.1: The observable $c_1^\dagger c_2$ can be construed as not straddling the boundary of the N-site chain subject to periodic boundary conditions, in which case the operators involved are separated by a distance of $r = 1$, or as straddling the boundary, in which case the operators involved are separated by a distance $r = N - 1$.

finite-system gauge phases for O will in general be different for different paths, some of which straddles the boundaries, some of which do not. It is not possible to find a finite-system target gauge that would make these different finite-system gauge phases — which are path-dependent — of O, all equal to the infinite-system gauge phase of O in the infinite-system target gauge. However, it is possible to find a finite-system target gauge to make the finite-system gauge phase of O for one of the paths equal to the infinite-system gauge phase of O in the infinite-system target gauge. For the trivial target gauge we have chosen for the infinite system, we can make the finite-system gauge phase associated with the shortest paths that do not straddle the finite-system boundaries equal to the infinite-system phase, for a reasonably large class of observables. The target finite-system gauge that makes this happen is the boundary gauge described in Section D.2.1.3. We therefore perform all our twist boundary conditions averaging in the boundary gauge.

Here, let us note that, if we so wish, we can also perform twist boundary conditions

averaging in other finite-system gauges. However, for us to claim that we are approximating the infinite-system expectation of the observable O in the target infinite-system gauge, we must evaluate the finite-system expectation not of the observable O, but a covariant version of it. We do this by constructing the gauge transformation U from the boundary gauge to the finite-system gauge we wish to work in, and then transform $O \to UOU^\dagger$ appropriately. As always, the gauge transformation U is the exponential of a sum of local operators in real space (the gauge transformation, from the bond gauge to the boundary gauge, we write down in Section D.2.3.2, for example, has this form). Therefore, we know that all operators diagonal in occupation number representation will not be affected by gauge transformation.

D.2.3.2 Gauge Transformation

For an infinite system of noninteracting spinless fermions not subjected to an external magnetic field, we mimick the translational-invariance of its ground state in a finite system by imposing twist boundary conditions. However, because of the way the phase twist is implemented in the boundary gauge, the finite-system Hamiltonian matrix is not manifestly translationally invariant. This means that we have to do a little extra work, as shown in Section D.2.1.3, to take advantage of the implicit translational invariance when using the Bloch states defined in (C.5.1) to block-diagonalize the Hamiltonian matrix. On the other hand, the Hamiltonian matrix is manifestly translationally invariant in the bond gauge. We therefore perform the ED in the bond gauge, even though expectations will be calculated in the boundary gauge. For this reason, we must find the gauge transformation that maps the bond-gauge ground-state wave function to the boundary-gauge ground-state wave function.

Because such a gauge transformation is model-independent, we will attempt in this

subsection to deduce it from the many-body ground-state wave functions of noninteracting spinless fermions in the bond and boundary gauges. For a single particle, the bond-gauge and boundary-gauge ground-state wave functions are

$$|k_0\rangle = \frac{1}{\sqrt{N}} \sum_j e^{-\mathrm{i}\, k_0 j} c_j^\dagger |0\rangle \tag{D.2.47}$$

and

$$|k_0 + \phi\rangle = \frac{1}{\sqrt{N}} \sum_j e^{-\mathrm{i}(k_0+\phi) j} c_j^\dagger |0\rangle \tag{D.2.48}$$

respectively. The bond-to-boundary gauge transformation can be read off simply as

$$\varphi : c_j \to e^{\mathrm{i}\,\phi j} c_j. \tag{D.2.49}$$

We now check whether this simple substitution will work for $P \geq 2$ nointeracting particles. For $P = 2$, the bond-gauge ground-state wave function is

$$|\Psi(0)\rangle = \left(\frac{1}{\sqrt{N}} \sum_{j_1} e^{-\mathrm{i}\, k_{0,1} j_1} c_{j_1}^\dagger \right) \left(\frac{1}{\sqrt{N}} \sum_{j_2} e^{-\mathrm{i}\, k_{0,2} j_2} c_{j_2}^\dagger \right) |0\rangle \,, \tag{D.2.50}$$

where $k_{0,1}$ and $k_{0,2}$ are the two occupied single-particle wave vectors. This state can be obtained numerically by diagonalizing either $H(0)$ or $H(\phi)$ in the bond gauge. Applying the single-particle gauge transformation in (D.2.49) to the ground-state wave function in (D.2.50), we obtain the wave function

$$|\Psi(\phi)\rangle = \left(\frac{1}{\sqrt{N}} \sum_{j_1} e^{-\mathrm{i}(k_{0,1}+\phi) j_1} c_{j_1}^\dagger \right) \left(\frac{1}{\sqrt{N}} \sum_{j_2} e^{-\mathrm{i}(k_{0,2}+\phi) j_2} c_{j_2}^\dagger \right) |0\rangle \tag{D.2.51}$$

in the boundary gauge, which can be rewritten as

$$|\Psi(\phi)\rangle = \frac{1}{N^{P/2}} \sum_{j_1} \sum_{j_2} e^{-i[k_{0,1} j_1 + k_{0,2} j_2 + \phi(j_1+j_2)]} c_{j_1}^\dagger c_{j_2}^\dagger |0\rangle \,. \tag{D.2.52}$$

To check whether (D.2.52) is indeed the ground-state wave function for $P = 2$ noninteracting particles in the boundary gauge, we look numerically at a chain with $N = 5$

sites. For such a chain, the two-particle Hilbert space is

$$V_2 = \left\{ \begin{matrix} |1,2\rangle, & |1,3\rangle, & |1,4\rangle, & |1,5\rangle, & |2,3\rangle, \\ |2,4\rangle, & |2,5\rangle, & |3,4\rangle, & |3,5\rangle, & |4,5\rangle \end{matrix} \right\}, \tag{D.2.53}$$

and the Hamiltonian matrix is

$$H_2(\phi) = \begin{bmatrix} 0 & -e^{-i\phi} & 0 & 0 & 0 & 0 & +e^{+i\phi} & 0 & 0 & 0 \\ -e^{+i\phi} & 0 & -e^{-i\phi} & 0 & -e^{-i\phi} & 0 & 0 & 0 & +e^{+i\phi} & 0 \\ 0 & -e^{+i\phi} & 0 & -e^{-i\phi} & 0 & -e^{-i\phi} & 0 & 0 & 0 & +e^{+i\phi} \\ 0 & 0 & -e^{+i\phi} & 0 & 0 & 0 & -e^{-i\phi} & 0 & 0 & 0 \\ 0 & -e^{+i\phi} & 0 & 0 & 0 & -e^{-i\phi} & 0 & 0 & 0 & 0 \\ 0 & 0 & -e^{+i\phi} & 0 & -e^{+i\phi} & 0 & -e^{-i\phi} & -e^{-i\phi} & 0 & 0 \\ +e^{-i\phi} & 0 & 0 & -e^{+i\phi} & 0 & -e^{+i\phi} & 0 & 0 & -e^{-i\phi} & 0 \\ 0 & 0 & 0 & 0 & 0 & -e^{+i\phi} & 0 & 0 & -e^{-i\phi} & 0 \\ 0 & +e^{-i\phi} & 0 & 0 & 0 & 0 & -e^{+i\phi} & -e^{+i\phi} & 0 & -e^{-i\phi} \\ 0 & 0 & +e^{-i\phi} & 0 & 0 & 0 & 0 & 0 & -e^{+i\phi} & 0 \end{bmatrix}$$

in the bond gauge, and

$$H_2(\phi) = \begin{bmatrix} 0 & -1 & 0 & 0 & 0 & 0 & +e^{+i5\phi} & 0 & 0 & 0 \\ -1 & 0 & -1 & 0 & -1 & 0 & 0 & 0 & +e^{+i5\phi} & 0 \\ 0 & -1 & 0 & -1 & 0 & -1 & 0 & 0 & 0 & +e^{+i5\phi} \\ 0 & 0 & -1 & 0 & 0 & 0 & -1 & 0 & 0 & 0 \\ 0 & -1 & 0 & 0 & 0 & -1 & 0 & 0 & 0 & 0 \\ 0 & 0 & -1 & 0 & -1 & 0 & -1 & -1 & 0 & 0 \\ +e^{-i5\phi} & 0 & 0 & -1 & 0 & -1 & 0 & 0 & -1 & 0 \\ 0 & 0 & 0 & 0 & 0 & -1 & 0 & 0 & -1 & 0 \\ 0 & +e^{-i5\phi} & 0 & 0 & 0 & 0 & -1 & -1 & 0 & -1 \\ 0 & 0 & +e^{-i5\phi} & 0 & 0 & 0 & 0 & 0 & -1 & 0 \end{bmatrix}$$

in the boundary gauge.

A quick numerical check shows that the bond-gauge ground state is indeed given by (D.2.50). In this ground-state wave function, the amplitude for the term $c^\dagger_{j_1} c^\dagger_{j_2}$ is the antisymmetrized sum

$$e^{-\mathrm{i}(k_{0,1} j_1 + k_{0,2} j_2)} - e^{-\mathrm{i}(k_{0,1} j_2 + k_{0,2} j_1)}. \tag{D.2.54}$$

The amplitude of this same term, after gauge transformation, should then be

$$\begin{aligned} & e^{-i[k_{0,1} j_1 + k_{0,2} j_2 + \phi(j_1 + j_2)]} - e^{-i[k_{0,1} j_2 + k_{0,2} j_1 + \phi(j_2 + j_1)]} \\ &= e^{-i\phi(j_1 + j_2)} \left[e^{-\mathrm{i}(k_{0,1} j_1 + k_{0,2} j_2)} - e^{-\mathrm{i}(k_{0,1} j_2 + k_{0,2} j_1)} \right]. \end{aligned} \tag{D.2.55}$$

Because the phase acquired by each many-body basis state depends only on the configuration, it is easy to generate the full list of amplitudes for comparison with those obtained by exactly diagonalizing the boundary-gauge Hamiltonian. I find numerically that (D.2.52) is indeed the boundary-gauge ground-state wave function. From (D.2.55), we also deduced that the bond-to-boundary gauge transformation for a many-body occupation-number basis state $|\mathbf{n}\rangle$ is [421]

$$\varphi : |\mathbf{n}\rangle \to e^{-i\phi \sum_j n_j j} |\mathbf{n}\rangle . \tag{D.2.56}$$

Will this gauge transformation also work for interacting systems? I checked this numerically for $P = 2$ strongly-interacting spinless fermions described by the Hamiltonian

$$H_{tV} = -t \sum_j \left(c^\dagger_j c_{j+1} + c^\dagger_{j+1} c_j \right) + V \sum_j n_j n_{j+1} \tag{D.2.57}$$

with $V \to \infty$, on a chain with $N = 5$ sites. This system is highly congested, and the Hilbert space consists of the two-particle states

$$V_2 = \Big\{ [1,3], \quad [1,4], \quad [2,4], \quad [2,5], \quad [3,5] \Big\}. \tag{D.2.58}$$

The Hamiltonian matrices are

$$H_2(\phi) = \begin{bmatrix} 0 & -e^{-i\phi} & 0 & 0 & +e^{\mathrm{i}\,\phi} \\ -e^{\mathrm{i}\,\phi} & 0 & -e^{-i\phi} & 0 & 0 \\ 0 & -e^{\mathrm{i}\,\phi} & 0 & -e^{-i\phi} & 0 \\ 0 & 0 & -e^{\mathrm{i}\,\phi} & 0 & -e^{-i\phi} \\ +e^{-i\phi} & 0 & 0 & -e^{\mathrm{i}\,\phi} & 0 \end{bmatrix} \tag{D.2.59}$$

in the bond gauge, and

$$H_2(\phi) = \begin{bmatrix} 0 & -1 & 0 & 0 & +e^{\mathrm{i}\,5\phi} \\ -1 & 0 & -1 & 0 & 0 \\ 0 & -1 & 0 & -1 & 0 \\ 0 & 0 & -1 & 0 & -1 \\ +e^{-i5\phi} & 0 & 0 & -1 & 0 \end{bmatrix} \tag{D.2.60}$$

in the boundary gauge.

Diagonalizing the two Hamiltonians for various twist angles ϕ within $(-\pi/5, \pi/5)$, we find that the bond- and boundary-gauge ground-state wave functions are indeed related by the gauge transformation given in (D.2.56), which act on the two-particle states as

$$\begin{Bmatrix} |1,3\rangle \\ |1,4\rangle \\ |2,4\rangle \\ |2,5\rangle \\ |3,5\rangle \end{Bmatrix} \xrightarrow{\varphi} \begin{Bmatrix} e^{-i4\phi}\,|1,3\rangle \\ e^{-i5\phi}\,|1,4\rangle \\ e^{-i6\phi}\,|2,4\rangle \\ e^{-i7\phi}\,|2,5\rangle \\ e^{-i8\phi}\,|3,5\rangle \end{Bmatrix}. \tag{D.2.61}$$

D.3 Wave Vector Sampling and Ground-State Selection

In this section, we look at the relation between wave vector sampling, effected by varying the twist vector $\boldsymbol{\phi}$ in the twist boundary conditions, and the actual many-particle

ground state selected. In Section D.3.1, we illustrate the basic idea behind ground-state selection, using the example of noninteracting spinless fermions in one dimension. Here we introduce the notion of *single-particle twisted energy bands*, and distinguish them from the *single-particle ED energy bands* that comes out from numerical ED calculations.

Moving on to the example of noninteracting spinless fermions in two dimensions in Section D.3.2, we explain how the ground-state selection can be best understood in terms of a *Brillouin Zone (BZ) partition structure*, generated by the *crossings of single-particle twisted energy bands*. Working through numerous example BZ partition structures of finite square and nonsquare systems, we illustrate how wave vector sampling and ground-state selection combine to give us an *approximate momentum distribution*, which in the case of noninteracting spinless fermions, is bounded by an *approximate Fermi surface*. We understand that in general, this approximate Fermi surface deviates from the infinite-system Fermi surface, and thus why we would encounter remnant finite size effects in our numerical results after applying twist boundary conditions averaging.

Finally, in Section D.3.3, we discuss how we would restrict the range of twist vectors used in our twist boundary conditions, so as to sample the wave vectors in the infinite-system FBZ just once.

D.3.1 One-Dimensional Noninteracting Spinless Fermions

As we can see from (D.2.33), by varying ϕ continuously in the boundary gauge, we can sample all the wave vectors k of the infinite system [61, 386, 398, 399, 407]. This allows us, in principle, to map out any function $f(k)$ of the wave vectors for the infinite system, by performing repeated calculations of $f(k_n)$, if it is computationally cheap to do so, on the finite system with different values of ϕ. However, practically all observables are

computationally expensive to calculate, and so we cannot afford to map them out as functions of ϕ. It is therefore important to know if we can determine the value of a given observable accurately using a small set of twist angles. To check whether this is possible, let us look at what happens when we set a dumb ED program to work on the one-dimensional system of noninteracting spinless fermions.

Let us consider a chain of length $N = 4$ to make our discussions simple. In this case, there are four allowed wave vectors k_{0n},

$$k_{0,1} = -\pi, \quad k_{0,2} = -\tfrac{\pi}{2}, \quad k_{0,3} = 0, \quad k_{0,4} = +\tfrac{\pi}{2}, \tag{D.3.1}$$

and we can think of (D.2.31) and (D.2.33) as defining four energy bands $\epsilon(k_{0n} + \phi)$,

$$\begin{aligned} \epsilon_1 &= -2\cos\left(-\pi + \phi\right), \\ \epsilon_2 &= -2\cos\left(-\tfrac{\pi}{2} + \phi\right), \\ \epsilon_3 &= -2\cos\phi, \\ \epsilon_4 &= -2\cos\left(\tfrac{\pi}{2} + \phi\right), \end{aligned} \tag{D.3.2}$$

as shown in Figure D.2. We call these the *twisted energy bands*.

If we put $P = 1$ particle into this system, corresponding to a filling of $\bar{n} = \frac{1}{4}$ in the infinite system, then our dumb ED program will put this particle into the twisted energy band with the lowest single-particle energy eigenvalue. From Figure D.2, we find the wave vector of the sole occupied single-particle state to be

$$k = \begin{cases} -\pi + \phi, & -\pi \le \phi \le -3\pi/4; \\ \frac{\pi}{2} + \phi, & -3\pi/4 \le \phi \le -\pi/4; \\ \phi, & -\pi/4 \le \phi \le +\pi/4; \\ -\frac{\pi}{2} + \phi, & +\pi/4 \le \phi \le +3\pi/4; \\ -\pi + \phi, & +3\pi/4 \le \phi < +\pi. \end{cases} \tag{D.3.3}$$

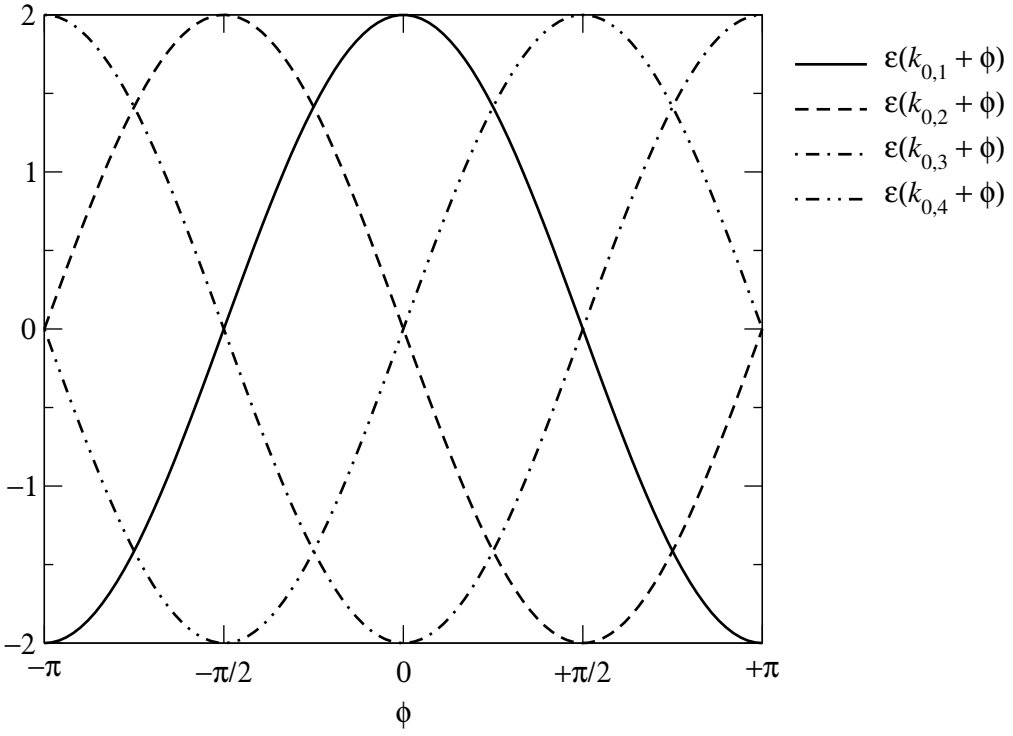

Figure D.2: The single-particle energy eigenvalues of noninteracting spinless fermions on a chain of $N = 4$ sites subject to twist boundary conditions, plotted as a function of the twist angle ϕ. We think of $\epsilon_n = \epsilon(k_{0n} + \phi)$ as energy bands (which we call *twisted energy bands*) of the pseudo-wave vector ϕ.

As we can see from Figure D.3, k changes discontinuously even as ϵ_k changes continuously but nondifferentiably. For an infinite system with $\bar{n} = \frac{1}{4}$, the occupied wave vectors ranges from $-\bar{n}\pi = -\pi/4$ to $+\bar{n}\pi = +\pi/4$. We see that by varying ϕ, we have correctly sampled these occupied wave vectors, and hence determined the correct band minimum of $\epsilon_0 = -2$ and Fermi energy $\epsilon_F = -\sqrt{2}$ for an infinite chain with $\bar{n} = \frac{1}{4}$.

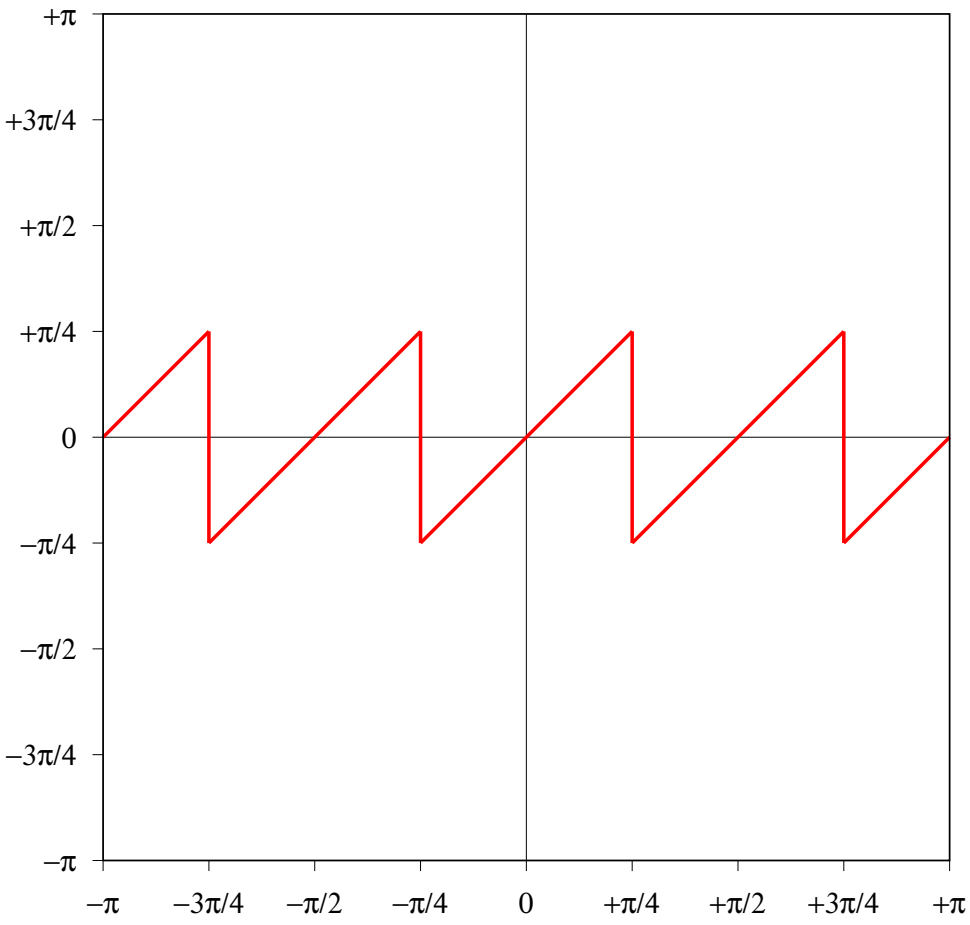

Figure D.3: The infinite-system wave vectors k sampled by a dumb ED program, for $P = 1$ noninteracting spinless fermions on a chain of $N = 4$ sites subject to twist boundary conditions, as the twist angle ϕ is varied.

If we put $P = 2$ particles into this system, corresponding to a filling of $\bar{n} = \frac{1}{2}$ in the infinite system, then our dumb ED program will put these into the two energy bands with

the lowest single-particle energy eigenvalues, as shown in Figure D.4. As with the case of $P = 1$, we find, by comparing Figure D.2 and Figure D.4, that the pair of filled-band indices depends on the twist angle ϕ. From this pair of filled-band indices, we can then determine the infinite-system wave vectors sampled, as shown in Figure D.5. Here we see that by varying ϕ over the range $(-\pi, +\pi)$, the set of wave vectors $k \in (-\pi/2, +\pi/2)$ which are occupied in the infinite system is sampled exactly $N = 4$ times.

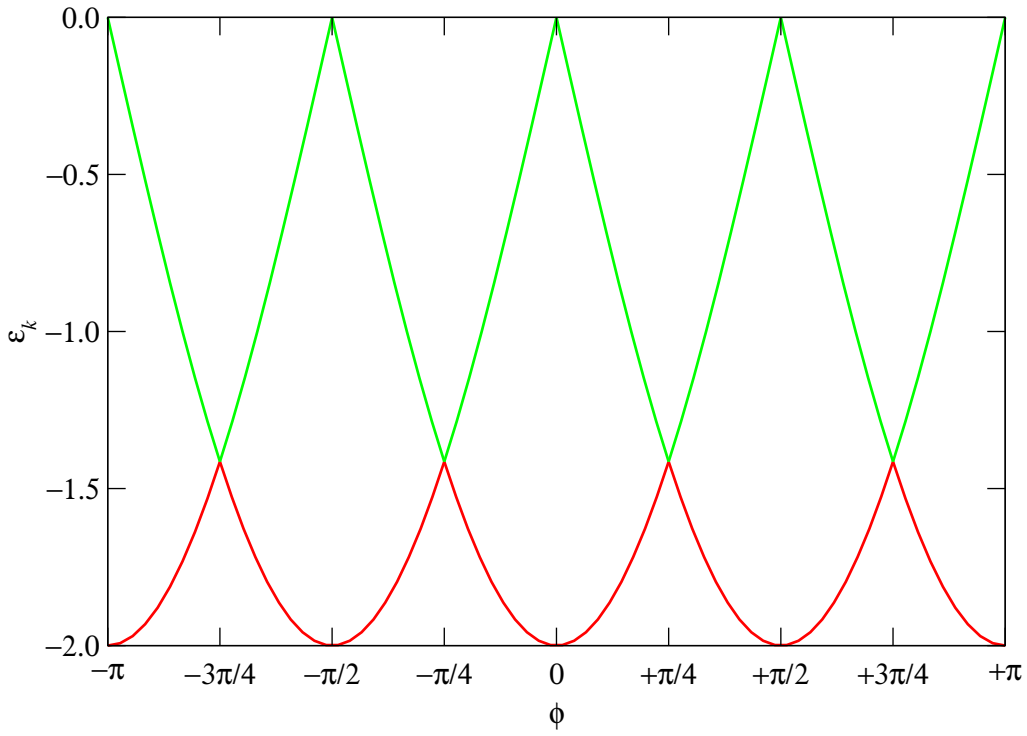

Figure D.4: The two lowest single-particle energy eigenvalues, selected by a dumb ED program, of noninteracting spinless fermions on a chain of $N = 4$ sites subject to twist boundary conditions, plotted as a function of twist angle ϕ.

From this simple example, we discover that the basic principles of twist boundary conditions averaging are:

1. for each single-particle twisted energy band $\epsilon(k_{0n} + \phi)$, all wave vectors $k = k_{0n} + \phi$ within the infinite-system FBZ can be sampled by varying the twist angle ϕ;

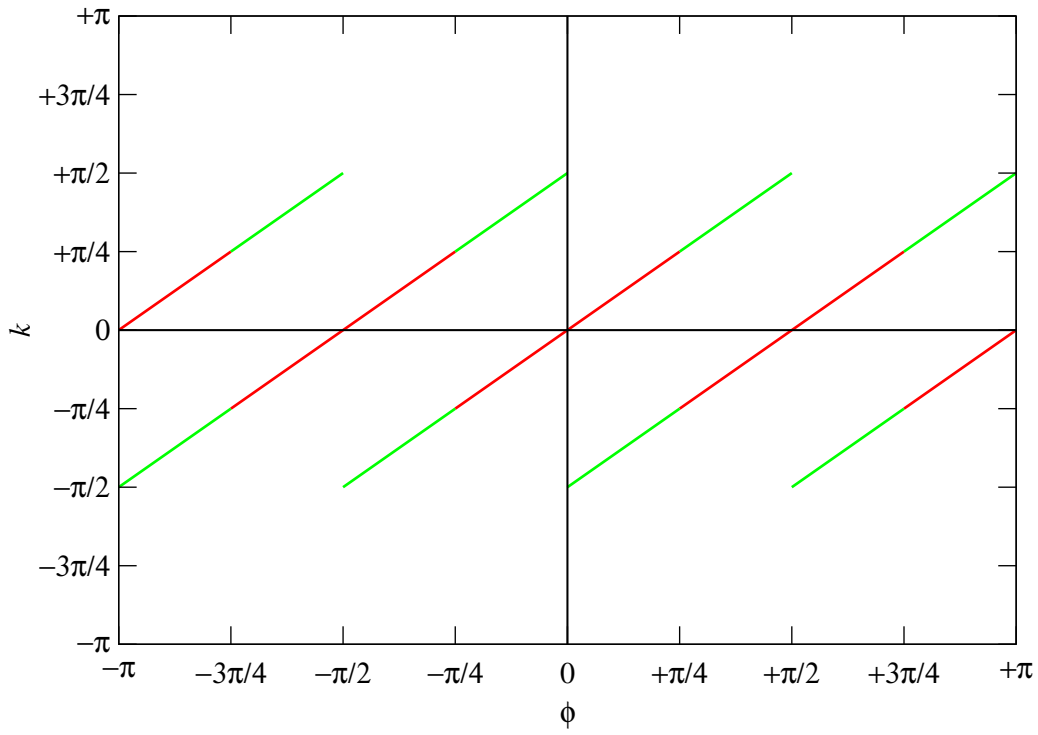

Figure D.5: The infinite-system wave vectors k sampled by a dumb ED program, for $P = 2$ noninteracting spinless fermions on a chain of $N = 4$ sites subject to twist boundary conditions, as the twist angle ϕ is varied.

2. at each twist angle ϕ, the many-particle energy eigenstate is selected. For a one-dimensional system of P noninteracting spinless fermions, this is equivalent to selecting the P single-particle twisted energy bands with the lowest single-particle energies;

3. as the twist angle is varied over the range $-\pi \leq \phi \leq +\pi$, the quantum numbers $\{k_{0n}\}$ of the selected many-particle ground state changes discontinously. As a result, the set of wave vectors $k = k_{0n} + \phi$ selected forms a 'compact' subset of the infinite-system FBZ.

We now move on to the example of a system of noninteracting spinless fermions in two dimensions, and see if we can add anything else to this list of basic principles.

D.3.2 Two-Dimensional Noninteracting Spinless Fermions

D.3.2.1 Brillouin Zone Partition Structure and Wave Vector Sampling

As with the one-dimensional system of noninteracting system, let us think of the single-particle energies $\epsilon_{\mathbf{n}}(\boldsymbol{\phi}) = \epsilon(\mathbf{k}_{0\mathbf{n}} + \boldsymbol{\phi})$ as energy bands dependent on the 'pseudo-wave vector' $\boldsymbol{\phi}$. For a $\mathbf{R}_1 \times \mathbf{R}_2$ system, there are a total of $N = R_{1x}R_{2y} - R_{2x}R_{1y}$ such bands. At a given $\boldsymbol{\phi}$, we put one particle in each band, starting with the lowest band until we have P particles in the system. For the one-dimensional system, we saw how this manner of constructing the many-body ground state samples the occupied infinite-system wave vectors k exactly for each filling $\bar{n}$ accessible to the finite system. To see whether this is true as well for the two-dimensional system, we first consider square finite systems of the form $(L, 0) \times (0, L)$.

Square systems. For $(L, 0) \times (0, L) = (2, 0) \times (0, 2)$, we have a total of $N = L^2 = 4$ sites. In the absence of a phase twist in the periodic boundary conditions, the allowed wave vectors in the FBZ are

$$\mathbf{k}_{0,1} = (-\pi, -\pi), \quad \mathbf{k}_{0,2} = (-\pi, 0), \quad \mathbf{k}_{0,3} = (0, -\pi), \quad \mathbf{k}_{0,4} = (0, 0). \tag{D.3.4}$$

When a phase twist of $\boldsymbol{\phi}$ is introduced into the periodic boundary conditions, the wave vectors are shifted by $\boldsymbol{\phi} = (\phi_x, \phi_y)$ in the boundary gauge, defining the twisted energy bands

$$\begin{aligned}
\epsilon_{\mathbf{k}_{0,1}} &= -2\cos(-\pi + \phi_x) - 2\cos(-\pi + \phi_y), \\
\epsilon_{\mathbf{k}_{0,2}} &= -2\cos(-\pi + \phi_x) - 2\cos\phi_y, \\
\epsilon_{\mathbf{k}_{0,3}} &= -2\cos\phi_x - 2\cos(-\pi + \phi_y), \\
\epsilon_{\mathbf{k}_{0,4}} &= -2\cos\phi_x - 2\cos\phi_y.
\end{aligned} \tag{D.3.5}$$

If we put $P = 1$ particle into this system, corresponding to a filling of $\bar{n} = \frac{1}{4}$ in the infinite system, then our dumb ED program will put this particle into the *first ED band* $\epsilon_{\mathbf{k}_a}$, which is the twisted energy band with the lowest energy. However, as we vary $\boldsymbol{\phi}$, the twisted energy band with the lowest energy also changes, just as we have seen happened in one dimension. To demarcate the regions in the (ϕ_x, ϕ_y) plane where each of the twisted energy bands are the minimum, we solve the equations

$$\begin{aligned}
\epsilon_{\mathbf{k}_{0,1}} &= \epsilon_{\mathbf{k}_{0,2}}, \\
\epsilon_{\mathbf{k}_{0,1}} &= \epsilon_{\mathbf{k}_{0,3}}, \\
\epsilon_{\mathbf{k}_{0,1}} &= \epsilon_{\mathbf{k}_{0,4}}, \\
\epsilon_{\mathbf{k}_{0,2}} &= \epsilon_{\mathbf{k}_{0,3}}, \\
\epsilon_{\mathbf{k}_{0,2}} &= \epsilon_{\mathbf{k}_{0,4}}, \\
\epsilon_{\mathbf{k}_{0,3}} &= \epsilon_{\mathbf{k}_{0,4}},
\end{aligned} \tag{D.3.6}$$

to find where the twisted energy bands cross each other. Solving these equations, which we call the *crossing conditions*, we find the *partition lines*

$$\begin{aligned}
\phi_y &= \pm\frac{\pi}{2}, \\
\phi_x &= \pm\frac{\pi}{2}, \\
\phi_y &= \pm\pi \pm \phi_1, \\
\phi_y &= \pm\phi_1, \\
\phi_x &= \pm\frac{\pi}{2}, \\
\phi_y &= \pm\frac{\pi}{2},
\end{aligned} \tag{D.3.7}$$

which partitions the domain of twist angles $(-\pi \leq \phi_x \leq +\pi) \times (-\pi \leq \phi_y \leq +\pi)$ into regions with different twisted band indices $\mathbf{k}_{0\mathbf{n}}$. Since the domain of twist angles will eventually map onto the First Brillouin Zone (FBZ) of the two-dimensional system, we call such a partition the *Brillouin zone partition* associated with the first ED band, or in short, the first *BZ partition*.

For the $(2,0) \times (0,2)$ system, the first BZ partition is shown in Figure D.6. As we vary $\boldsymbol{\phi}$, we find that the ground-state energy varies continuously but not differentiably. Plotting in Figure D.7 the ground-state energy as a function of $\boldsymbol{\phi}$ along the high symmetry directions ΓX, XK and ΓK, we find that there are kinks along $\phi_x = \pm\frac{\pi}{2}$ and $\phi_y = \pm\frac{\pi}{2}$, where $\epsilon = -2$. As we can see from Figure D.7, the ED band minimum and band maximum are $\epsilon_{\text{min}} = -4$ and $\epsilon_{\text{max}} = 0$ respectively.

Treating the ED band maximum $\epsilon_{\text{max}} = 0$, which is the highest occupied single-particle energy sampled by varying over twist boundary conditions, as the approximate Fermi energy, we find that we have overestimated the Fermi energy, whose value in an infinite square lattice with filling fraction $\bar{n} = \frac{1}{4}$ is $\epsilon_F \approx -1.48$, which we obtained by

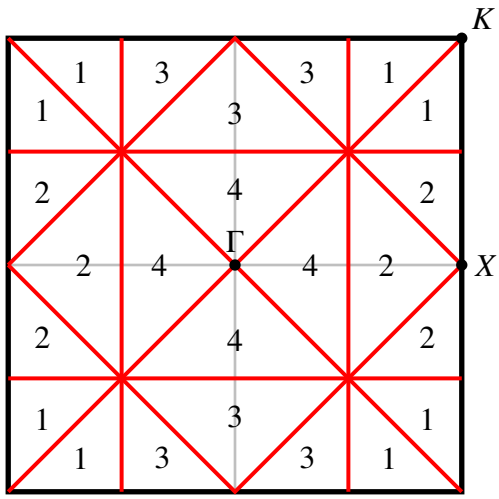

Figure D.6: First BZ partition of the $(2,0) \times (0,2)$ system subject to twist boundary conditions. The square for the BZ partition represents the twist angle domain $(-\pi \leq \phi_x \leq +\pi) \times (-\pi \leq \phi_y \leq +\pi)$, while the indices shown within the BZ partitions are the twist band indices, where $\mathbf{k}_{0,1} = (-\pi, -\pi)$, $\mathbf{k}_{0,2} = (-\pi, 0)$, $\mathbf{k}_{0,3} = (0, -\pi)$, and $\mathbf{k}_{0,4} = (0, 0)$.

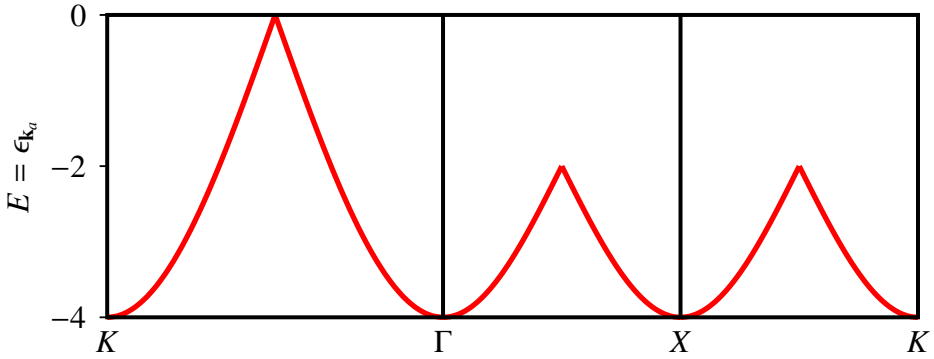

Figure D.7: Ground-state energy E, which is essentially the first ED band energy $\epsilon_{\mathbf{k}_a}$, as a function of twist vector $\boldsymbol{\phi}$ along the high-symmetry directions ΓX, XK and ΓK, for $P = 1$ noninteracting spinless fermion on a $(2, 0) \times (0, 2)$ square lattice. We see that the ground-state energy as a function of $\boldsymbol{\phi}$ is a function periodic over a cell half the size of the infinite-system FBZ. This property of twist-boundary-conditions sampled functions of $\boldsymbol{\phi}$ will be discussed in Section D.3.3.

numerically integrating the energy density of states

$$g(\epsilon) = \frac{1}{(2\pi)^2} \int d^2\mathbf{k}\, \delta(\epsilon - \epsilon(\mathbf{k})) \tag{D.3.8}$$

associated with the infinite-system dispersion relation

$$\epsilon(\mathbf{k}) = -2\left(\cos k_x + \cos k_y\right). \tag{D.3.9}$$

However, the Fermi energy is not an averaged quantity, so we do not expect to approximate it well by simplying varying the twist boundary conditions. To be more rigorous, we should compare a quantity averaged by varying the twist boundary conditions, to its infinite-system FBZ-average. To make such a comparison, we need to look at the set of wave vectors actually sampled by varying the twist vector $\boldsymbol{\phi}$.

Looking at Figure D.6, we find that in the region marked '4', we have $k_x = \phi_x$, and $k_y = \phi_y$. Therefore, varying $\boldsymbol{\phi}$ in this region gives us the range of wave vectors with

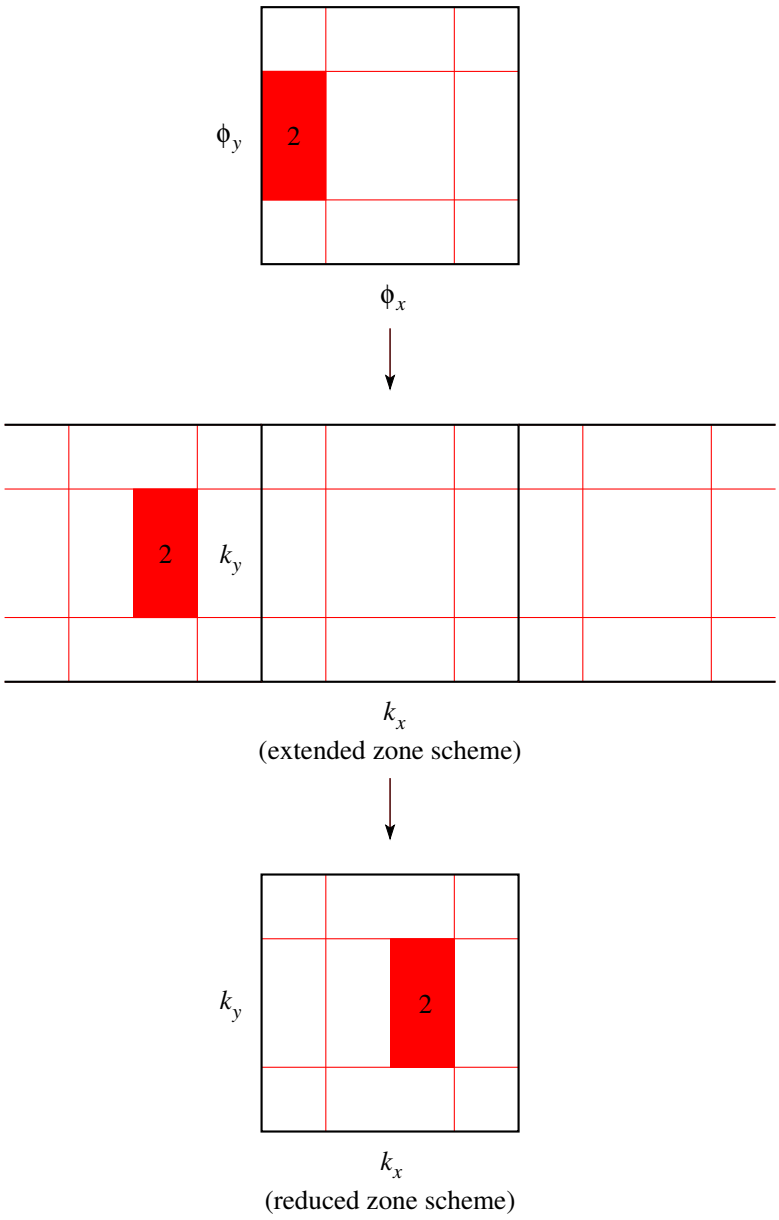

Figure D.8: The wave vectors $\mathbf{k} = (k_x, k_y)$ in the extended zone scheme (middle) and reduced zone scheme (bottom) sampled by one of the regions marked '2' (top) in the first BZ partition, of the $(2,0) \times (0,2)$ system subject to twist boundary conditions. The square for the BZ partition represents the twist angle domain $(-\pi \leq \phi_x \leq +\pi) \times (-\pi \leq \phi_y \leq +\pi)$, while the square for the sampled wave vectors represents the infinite-system FBZ $(-\pi \leq k_x \leq +\pi) \times (-\pi \leq k_y \leq +\pi)$.

$-\frac{\pi}{2} \leq k_x \leq \frac{\pi}{2}$, and $-\frac{\pi}{2} \leq k_y \leq \frac{\pi}{2}$. In the regions marked '2', the relation between (k_x, k_y) and (ϕ_x, ϕ_y) is

$$(k_x, k_y) = (-\pi + \phi_x, \phi_y). \tag{D.3.10}$$

One of the regions marked '2' has $-\pi \leq \phi_x \leq -\frac{\pi}{2}$ and $-\frac{\pi}{2} \leq \phi_y \leq \frac{\pi}{2}$, we find therefore that the wave vectors picked out by this region fall within the range $-2\pi \leq k_x \leq -\frac{3\pi}{2}$ and $-\frac{\pi}{2} \leq k_y \leq \frac{\pi}{2}$. These wave vectors fall outside the FBZ, so we bring it back into the FBZ by adding 2π to k_x, so that within the FBZ, the wave vectors sampled by varying $\boldsymbol{\phi}$ has $0 \leq k_x \leq \frac{\pi}{2}$. We show this in Figure D.8.

Similarly, the wave vectors sampled by varying $\boldsymbol{\phi}$ in the other region marked '2' also fall outside the FBZ, and we need to subtract 2π from k_x to bring them back within the FBZ. Doing so, we find that the wave vectors sampled by the two regions combine to give the range of wave vectors $-\frac{\pi}{2} \leq k_x \leq \frac{\pi}{2}$ and $-\frac{\pi}{2} \leq k_y \leq \frac{\pi}{2}$ in the FBZ, which is the same as those sampled by the region marked '4'. Repeating this wave vector sampling analysis, we find that the regions marked '1' and '3' in the first BZ partition sample this same range of wave vectors. This N-fold sampling of occupied wave vectors was observed for the one-dimensional case as well.

Comparing this region of selected wave vectors to the occupied wave vectors in the infinite-system limit, as shown in Figure D.9, we find that we are not reproducing the correct shape for the Fermi surface. If we treat the boundary of the set of selected wave vectors as an approximate Fermi surface, we can evaluate the ground-state energy per particle, by integrating over the wave vectors bounded by the approximate Fermi surface. In principle, we would perform this integration over the approximate Fermi surface numerically by setting up a mesh of M twist vectors $\{\boldsymbol{\phi}_i\}_{i=1}^{M}$, do a numerical ED at each $\boldsymbol{\phi}_i$ to obtain the total energies $\{E_i\}_{i=1}^{M}$, and then calculating the average total

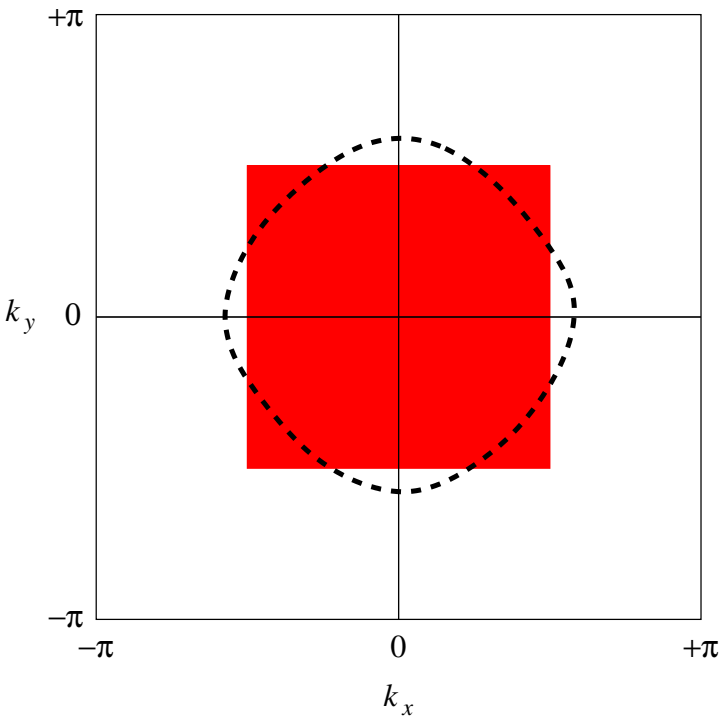

Figure D.9: The wave vectors in the FBZ sampled by twist boundary conditions for $P = 1$ noninteracting spinless fermion in the $(2, 0) \times (0, 2)$ system (red shaded region), compared to the Fermi surface (black dashed curve) of the infinite square lattice with $\bar{n} = \frac{1}{4}$, obtained by numerically integrating the energy density of states $g(\epsilon)$ in (D.3.8) associated with the infinite-system dispersion $\epsilon(\mathbf{k})$ in (D.3.9).

energy per particle as

$$\frac{E}{P} = \frac{1}{M} \sum_{i=1}^{M} \frac{E_i}{P}. \tag{D.3.11}$$

Using (D.3.11) to calculate the ground-state energy per particle, we will never need to know that $E_i = \epsilon_{\mathbf{k}_a}(\boldsymbol{\phi}_i)$, and that $\epsilon_{\mathbf{k}_a}(\boldsymbol{\phi}_i)$ is sampled from the infinite-system dispersion relation (D.3.9). But until we are ready to discuss the numerical implementations of twist boundary conditions averaging, let us cheat a little: (i) in the limit of $M \to \infty$, the sum over the twist vectors $\boldsymbol{\phi}_i$ can be converted into an integral over $\boldsymbol{\phi}$; (ii) the integral over $\boldsymbol{\phi}$ can be converted into an integral over the sampled wave vectors $\mathbf{k}$, a result that we will discuss in greater details in Section D.5; and (iii) the total energy $E(\mathbf{k})$ for just $P = 1$ particle in the system is the single-particle energy in (D.3.9). This means that the twist-boundary-conditions-averaged total energy per particle is

$$\begin{aligned} \frac{E}{P} &= \frac{1}{\pi^2} \int_{-\pi/2}^{+\pi/2} dk_x \int_{-\pi/2}^{+\pi/2} dk_y \left[-2 \left(\cos k_x + \cos k_y \right) \right] \\ &= -\frac{8}{\pi} = -2.546479089\ldots, \end{aligned} \tag{D.3.12}$$

which compares favorably with the $\bar{n} = \frac{1}{4}$ infinite-system ground-state energy per particle $E/P \approx -2.62$, obtained by numerically integrating the energy density of states $g(\epsilon)$ in (D.3.8) associated with the infinite-system dispersion relation $\epsilon(\mathbf{k})$ in (D.3.9). We shall later see in Section D.5 that two-point functions of noninteracting spinless fermions computed from the twist-boundary-conditions-sampled set of wave vectors reproduces their infinite-system values exactly in one dimension, but in general only approximately in two dimensions, as a result of the deviation of the twist-boundary-conditions-sampled Fermi surface from the infinite-system Fermi surface.

For the special filling fraction of $\bar{n} = \frac{1}{2}$, which corresponds to $P = 2$ particles in this four-site system, the twist-boundary-conditions-sampled Fermi surface matches that of infinite system exactly. We see how this can be so as follows. When we have $P = 2$

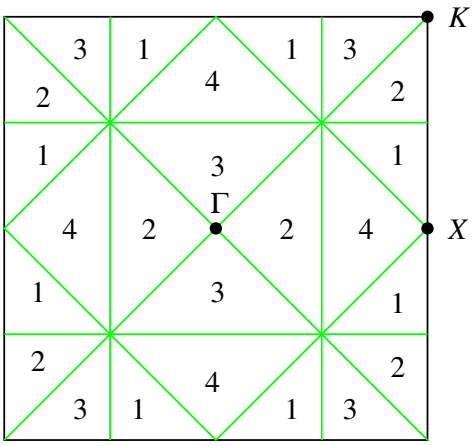

Figure D.10: Second BZ partition of the $(2,0)\times(0,2)$ system subject to twist boundary conditions. The square for the BZ partition represents the twist angle domain $(-\pi \le \phi_x \le +\pi)\times(-\pi \le \phi_y \le +\pi)$, which the indices shown within the BZ partitions are the twist band indices, where $\mathbf{k}_{0,1} = (-\pi,-\pi)$, $\mathbf{k}_{0,2} = (-\pi,0)$, $\mathbf{k}_{0,3} = (0,-\pi)$, and $\mathbf{k}_{0,4} = (0,0)$.

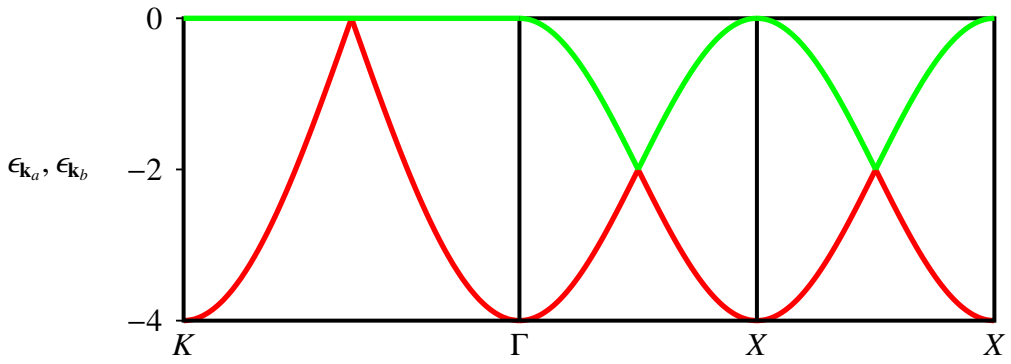

Figure D.11: Single-particle energies of the two lowest-lying ED bands $\epsilon_{\mathbf{k}_a}$ and $\epsilon_{\mathbf{k}_b}$, as functions of twist vector $\boldsymbol{\phi}$ along the high-symmetry directions ΓX, XK and ΓK, for $P = 2$ noninteracting spinless fermion on a $(2,0)\times(0,2)$ square lattice.

particles in the four-site system, our dumb ED program will put the first particle into the first ED band $\epsilon_{\mathbf{k}_a}$, which we have already studied in detail, and the second particle in the second ED band $\epsilon_{\mathbf{k}_b}$. The second BZ partition is shown in Figure D.10, and the single-particle energies of the two ED bands, plotted along the high-symmetry directions ΓX, XK and ΓK, are shown in Figure D.11. As we can see from Figure D.11, the range of single-particle energies goes from $\epsilon_{\text{min}} = -4$ to $\epsilon_{\text{max}} = 0$, which agrees with that of the infinite square lattice at half-filling.

For the infinite square lattice at half-filling, the Fermi surface is just a rotated square with vertices at the four X points in the FBZ. To see how well we approximate this Fermi surface, we look at the set of wave vectors sampled by the second BZ partition. As shown in Figure D.12, we see that the region marked '1a' on the twist angle domain samples wave vectors lying outside the FBZ, while the region marked '1b' samples wave vectors lying within the FBZ. Therefore, we must add 2π to k_x of the wave vectors sampled by the region marked '1a' to bring it back into the FBZ. Repeating this analysis for the other regions marked '1' on the twist angle domain, and adding appropriate multiples of $(2\pi, 0)$ and $(0, 2\pi)$ to those sampled wave vectors lying outside the FBZ, we find the sampled wave vectors in the reduced zone scheme as shown in Figure D.13.

Similarly, as shown in Figure D.14, the regions marked '2a' and '2b' on the twist angle domain sample wave vectors lying outside the FBZ. We must then add $(2\pi, 0)$ to both sets of sampled wave vectors to bring them back within the FBZ. Repeating this analysis for the other regions marked '2' on the twist angle domain, and adding appropriate multiples of $(2\pi, 0)$ and $(0, 2\pi)$ to those sampled wave vectors lying outside the FBZ, we find the wave vectors in the reduced zone scheme as shown in Figure D.15. As we can see, the FBZ wave vectors sampled by the twist angle regions marked '2' are identical to those sampled by the twist angle regions marked '1'. Pushing the

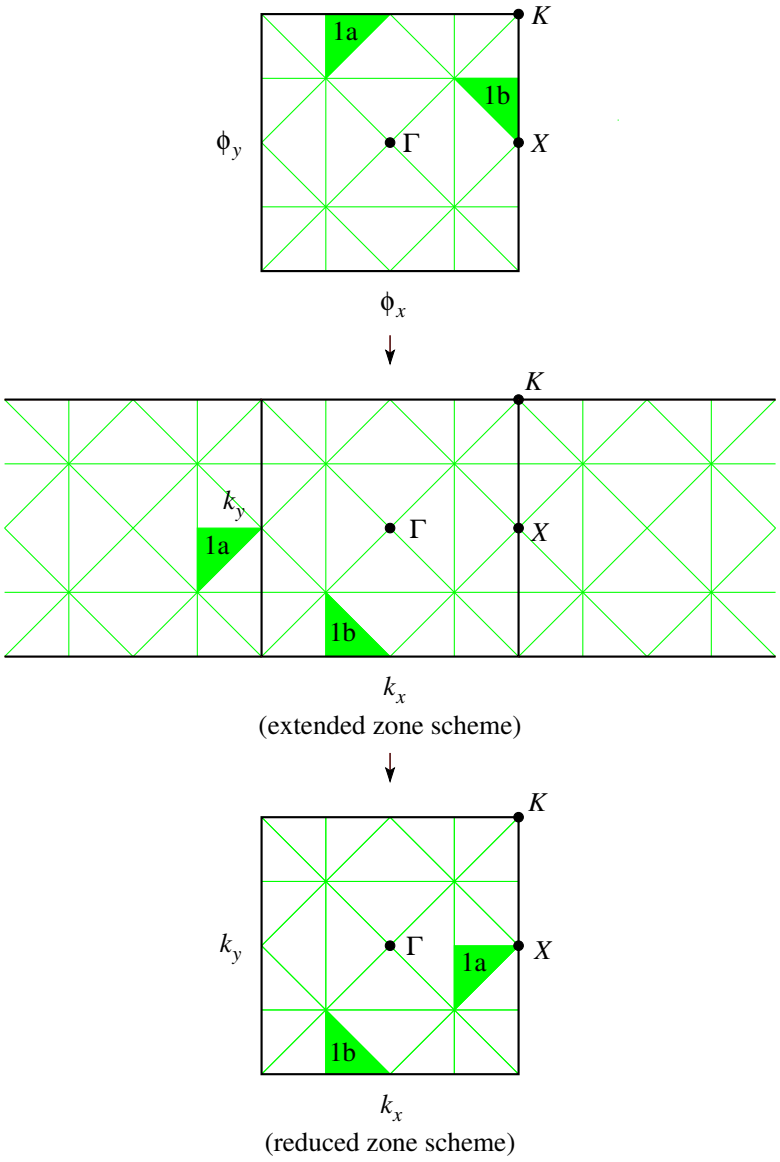

Figure D.12: The wave vectors $\mathbf{k} = (k_x, k_y)$ in the extended zone scheme (middle) and reduced zone scheme (bottom) sampled by the regions marked '1a' and '1b' (top) in the second BZ partition, of the $(2,0) \times (0,2)$ system subject to twist boundary conditions. The square for the BZ partition represents the twist angle domain $(-\pi \leq \phi_x \leq +\pi) \times (-\pi \leq \phi_y \leq +\pi)$, while the square for the sampled wave vectors represents the infinite-system FBZ $(-\pi \leq k_x \leq +\pi) \times (-\pi \leq k_y \leq +\pi)$.

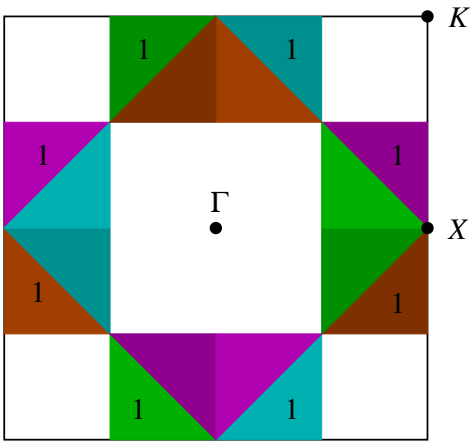

Figure D.13: Superimposed twist angle domain and the infinite-system FBZ, showing regions of the twist angle domain marked ‘1’ in the second BZ partition, and the wave vectors they sample in the FBZ. For example, the twist angles in the light turquoise region marked ‘1’ sample the FBZ wave vectors in the unmarked light turquoise region, while the twist angles in the light magenta region marked ‘1’ sample the FBZ wave vectors in the unmarked light magenta region.

analysis through for the twist angle regions marked '3' and '4', we find that we are just sampling the same set of FBZ wave vectors four times. Since we are varying $\boldsymbol{\phi}$ over the entire twist angle domain, for both the first and second BZ partitions in the case of $P = 2$ particles in the four-site system, the single-particle wave vectors sampled by twist boundary conditions is simply the union of the set of wave vectors in the infinite-system FBZ sampled by the first BZ partition, and those sampled by the second BZ partition. As shown in Figure D.16, the infinite-system momentum distribution, and thus the Fermi surface, at half-filling is reproduced exactly.

For the case of $P = 3$ particles in this 4-site system, the third BZ partition is shown in Figure D.17. Going through the same analysis as was done for $P = 1$ and $P = 2$, we find the FBZ wave vectors sampled by the third BZ partition shaded in blue in Figure D.18. As we can see from Figure D.18, the boundaries of the union of wave vectors in the infinite-system FBZ sampled by the first, second, and third BZ partitions do not approximate very well the Fermi surface of the infinite square lattice with $\bar{n} = \frac{3}{4}$.

After working through the $(2, 0) \times (0, 2)$ system in great details, we realized that for a two-dimensional system of noninteracting spinless fermions subject to twist boundary conditions, naive ground-state selection at each twist vector $\boldsymbol{\phi}$ puts P particles into the P single-particle ED energy bands with the lowest single-particle energies $\epsilon_\alpha(\boldsymbol{\phi})$. Each single-particle ED band is a patchwork of single-particle twisted energy bands, whose index $\mathbf{k}_{0\mathbf{n}}$ changes as we vary the twist vector $\boldsymbol{\phi}$. These index changes from $\mathbf{k}_{0\mathbf{n}}$ to $\mathbf{k}_{0\mathbf{n}'}$ where the single-particle twisted energy bands cross, determined by the crossing conditions

$$\epsilon_{\mathbf{n}}(\boldsymbol{\phi}) = \epsilon_{\mathbf{n}'}(\boldsymbol{\phi}). \tag{D.3.13}$$

The partition curves $\phi_y^{\mathbf{n}\mathbf{n}'}(\phi_x)$ which are the solutions to (D.3.13) define a (single-particle) partition structure for the FBZ. For a system with N sites, there are a total of N BZ

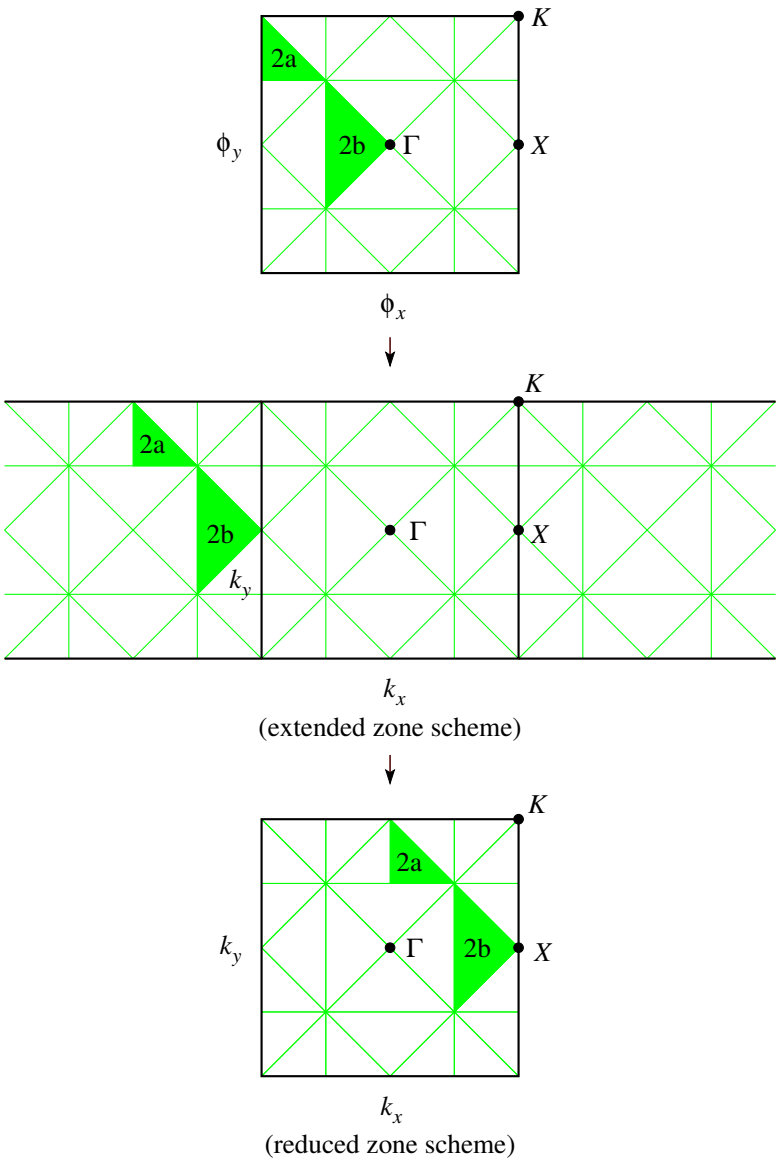

Figure D.14: The wave vectors $\mathbf{k} = (k_x, k_y)$ in the extended zone scheme (middle) and reduced zone scheme (bottom) sampled by the regions marked '2a' and '2b' (top) in the second BZ partition, of the $(2,0) \times (0,2)$ system subject to twist boundary conditions. The square for the BZ partition represents the twist angle domain $(-\pi \leq \phi_x \leq +\pi) \times (-\pi \leq \phi_y \leq +\pi)$, while the square for the sampled wave vectors represents the infinite-system FBZ $(-\pi \leq k_x \leq +\pi) \times (-\pi \leq k_y \leq +\pi)$.

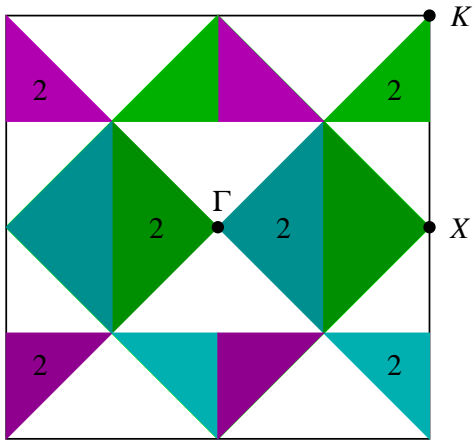

Figure D.15: Superimposed twist angle domain and the infinite-system FBZ, showing regions of the twist angle domain marked '2' in the second BZ partition, and the wave vectors they sample in the FBZ.

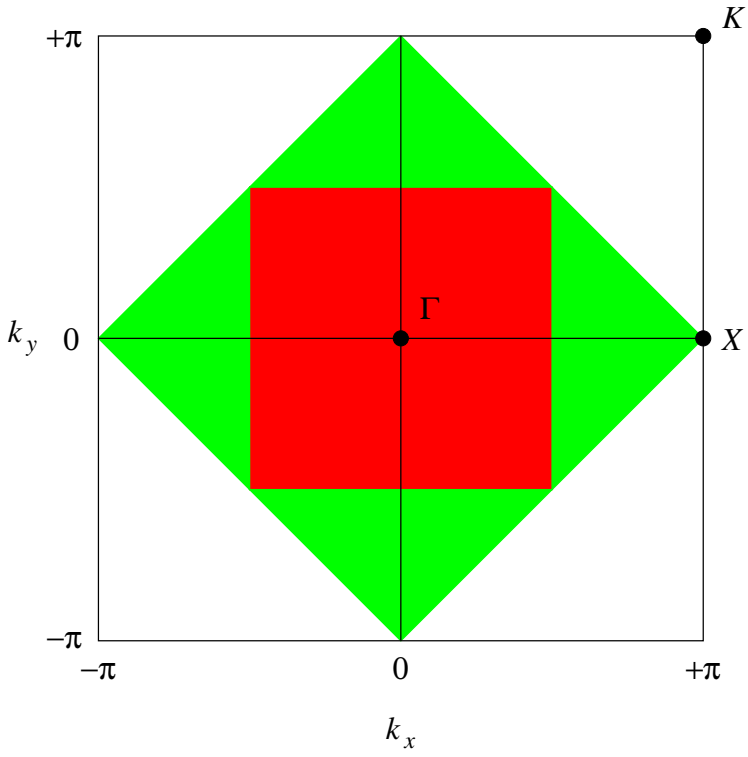

Figure D.16: The wave vectors in the FBZ sampled by twist boundary conditions for $P = 2$ noninteracting spinless fermion in the $(2,0)\times(0,2)$ system (red and green regions sampled by the first and second BZ partitions respectively).

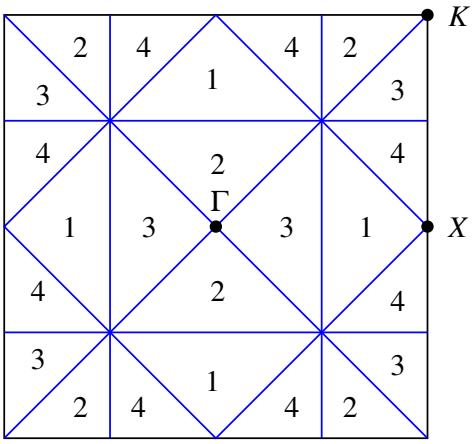

Figure D.17: Third BZ partition of the $(2,0) \times (0,2)$ system subject to twist boundary conditions. The square for the BZ partition represents the twist angle domain $(-\pi \leq \phi_x \leq +\pi) \times (-\pi \leq \phi_y \leq +\pi)$, which the indices shown within the BZ partitions are the twist band indices, where $\mathbf{k}_{0,1} = (-\pi, -\pi)$, $\mathbf{k}_{0,2} = (-\pi, 0)$, $\mathbf{k}_{0,3} = (0, -\pi)$, and $\mathbf{k}_{0,4} = (0, 0)$.

partitions, one for each ED band. For our example $(2,0) \times (0,2)$ system, the four BZ partitions are shown in Figure D.19. Partition structures such as these were known to Poilblanc [398, 399], and the relevance of the BZ partitions to many-body ground state selection by a dumb ED or QMC program was first discussed by Lin *et al* [411], where they mapped out the first through the 13th partitions for free fermions confined to a square box.

Because there are $N = L^2$ BZ partitions, we know that each infinite-system wave vector $\mathbf{k}$ in the FBZ is sampled N times. Moreover, using the higher-dimensional analog of (D.2.33), we determine the infinite-system wave vectors sampled by each partition, and find that the BZ partitions sample non-overlapping regions of the FBZ (Figure D.5 for the one-dimensional case). For the $(2,0) \times (0,2)$ system, the four non-overlapping regions (with the same total area in momentum space) of the FBZ are shown in Figure D.20.

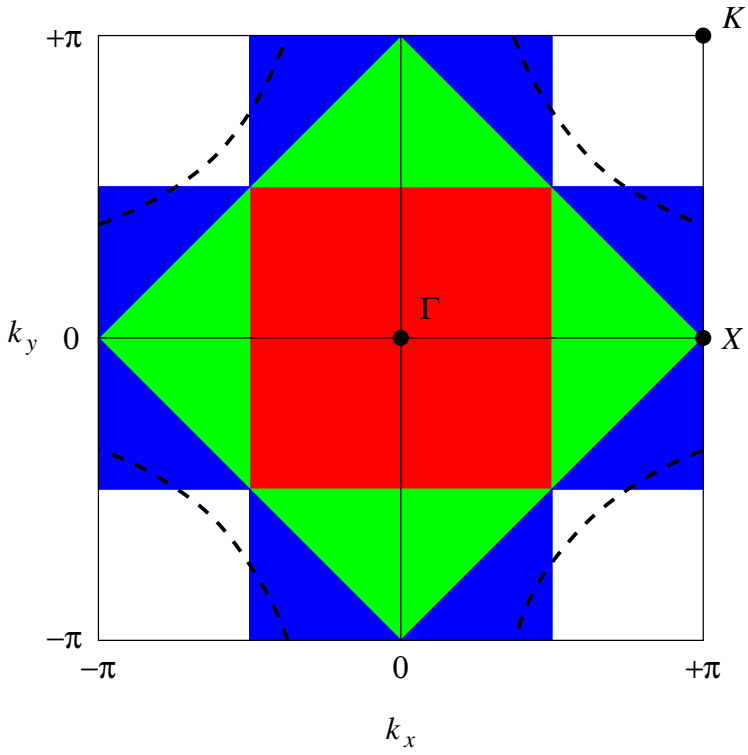

Figure D.18: The wave vectors in the FBZ sampled by twist boundary conditions for $P = 3$ noninteracting spinless fermion in the $(2, 0) \times (0, 2)$ system (red, green, and blue regions sampled by the first, second, and third BZ partitions respectively), compared to the Fermi surface (black dashed curve) of the infinite square lattice with $\bar{n} = \frac{3}{4}$, obtained by numerically integrating the energy density of states $g(\epsilon)$ in (D.3.8) associated with the infinite-system dispersion $\epsilon(\mathbf{k})$ in (D.3.9).

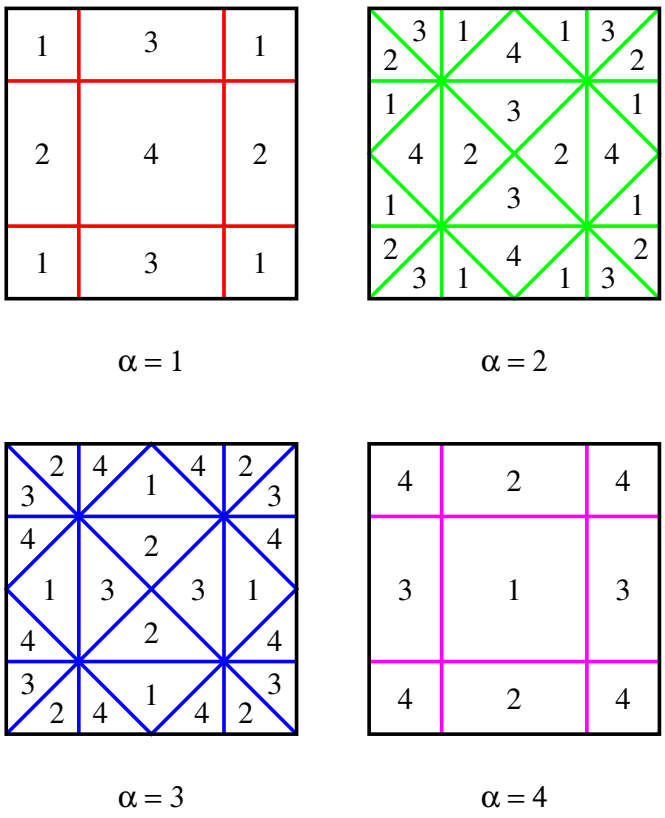

Figure D.19: BZ partition structure of the $(2,0)\times(0,2)$ system subject to twist boundary conditions, for ED band indices $\alpha = 1,2,3,4$. The square for each BZ partition represents the region of twist angle space $(-\pi \leq \phi_x \leq +\pi) \times (-\pi \leq \phi_y \leq +\pi)$, while the indices shown within the BZ partitions are the twisted band indices, where $\mathbf{k}_{\mathbf{n}_1} = (-\pi, -\pi)$, $\mathbf{k}_{\mathbf{n}_2} = (-\pi, 0)$, $\mathbf{k}_{\mathbf{n}_3} = (0, -\pi)$ and $\mathbf{k}_{\mathbf{n}_4} = (0, 0)$.

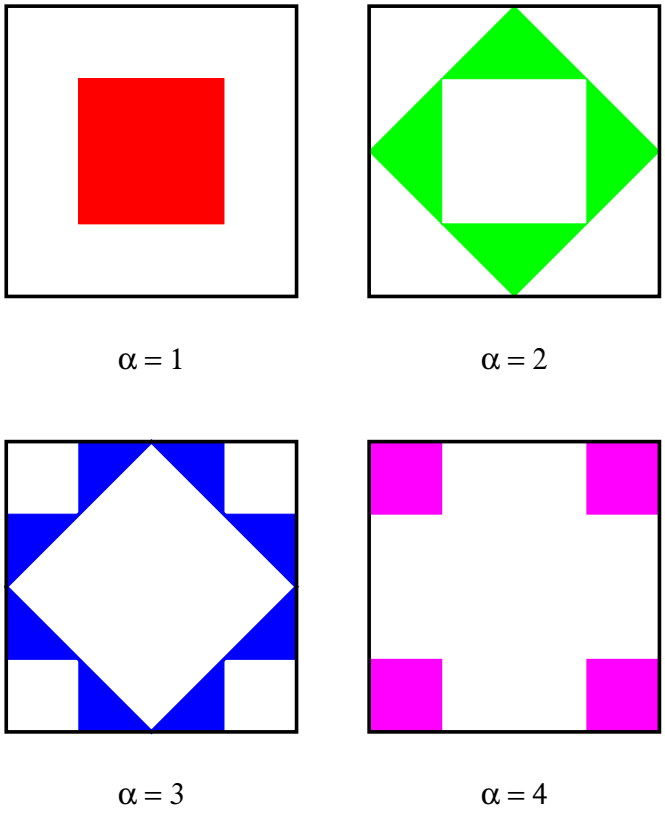

Figure D.20: Regions of the FBZ sampled by each BZ partition of the $(2,0) \times (0,2)$ system subject to twist boundary conditions, for ED band indices $\alpha = 1, 2, 3, 4$.

Before we move on to consider non-square systems, let us look at a larger square system, the $(4,0)\times(0,4)$ system with $N = 16$ sites, whose allowed wave vectors in the absence of phase twist are

$$\begin{aligned}
&\mathbf{k}_1 = (-\pi,-\pi), \quad \mathbf{k}_2 = (-\pi,-\tfrac{\pi}{2}), \quad \mathbf{k}_3 = (-\pi,0), \quad \mathbf{k}_4 = (-\pi,\tfrac{\pi}{2}),\\
&\mathbf{k}_5 = (-\tfrac{\pi}{2},-\pi), \quad \mathbf{k}_6 = (-\tfrac{\pi}{2},-\tfrac{\pi}{2}), \quad \mathbf{k}_7 = (-\tfrac{\pi}{2},0), \quad \mathbf{k}_8 = (-\tfrac{\pi}{2},\tfrac{\pi}{2}),\\
&\mathbf{k}_9 = (0,-\pi), \quad \mathbf{k}_{10} = (0,-\tfrac{\pi}{2}), \quad \mathbf{k}_{11} = (0,0), \quad \mathbf{k}_{12} = (0,\tfrac{\pi}{2}),\\
&\mathbf{k}_{13} = (\tfrac{\pi}{2},-\pi), \quad \mathbf{k}_{14} = (\tfrac{\pi}{2},-\tfrac{\pi}{2}), \quad \mathbf{k}_{15} = (\tfrac{\pi}{2},0), \quad \mathbf{k}_{16} = (\tfrac{\pi}{2},\tfrac{\pi}{2}).
\end{aligned} \tag{D.3.14}$$

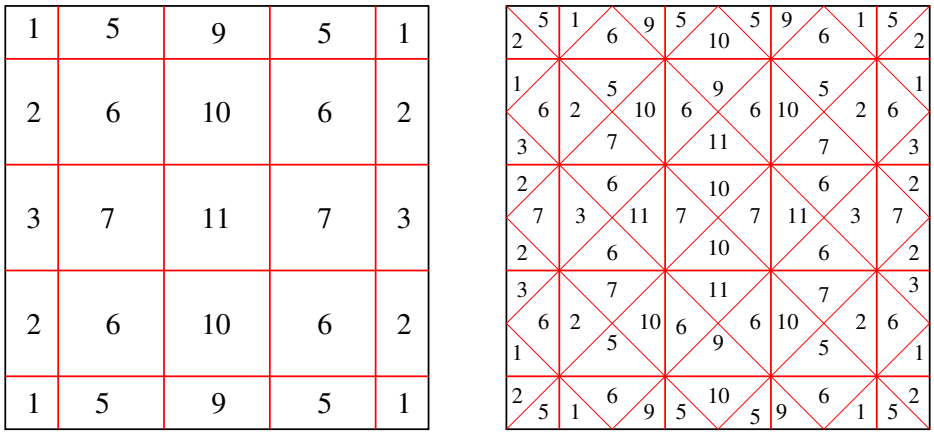

Figure D.21: First (left) and second (right) BZ partitions of the $(4,0)\times(0,4)$ system subject to twist boundary conditions. The square for each BZ partition represents the region of twist angle space $(-\pi \le \phi_x \le +\pi)\times(-\pi \le \phi_y \le +\pi)$, while the indices shown within the BZ partitions are the twisted band indices, where $\mathbf{k}_1 = (-\pi,-\pi)$, $\mathbf{k}_2 = (-\pi,-\frac{\pi}{2})$, $\mathbf{k}_3 = (-\pi,0)$, $\mathbf{k}_4 = (-\pi,\frac{\pi}{2})$, $\mathbf{k}_5 = (-\frac{\pi}{2},-\pi)$, $\mathbf{k}_6 = (-\frac{\pi}{2},-\frac{\pi}{2})$, $\mathbf{k}_7 = (-\frac{\pi}{2},0)$, $\mathbf{k}_8 = (-\frac{\pi}{2},\frac{\pi}{2})$, $\mathbf{k}_9 = (0,-\pi)$, $\mathbf{k}_{10} = (0,-\frac{\pi}{2})$, $\mathbf{k}_{11} = (0,0)$, $\mathbf{k}_{12} = (0,\frac{\pi}{2})$, $\mathbf{k}_{13} = (\frac{\pi}{2},-\pi)$, $\mathbf{k}_{14} = (\frac{\pi}{2},-\frac{\pi}{2})$, $\mathbf{k}_{15} = (\frac{\pi}{2},0)$, and $\mathbf{k}_{16} = (\frac{\pi}{2},\frac{\pi}{2})$.

The first and second BZ partitions are shown in Figure D.21, while third and fourth BZ partitions are too tedious to work out. Based on what we have learnt about wave vector sampling for the $(2,0)\times(0,2)$ system, we realized that to form the approximate

Fermi surface at $\bar{n} = \frac{1}{4}$, which corresponds to $P = 4$ particles in this 16-site system, we need to determine the regions of the infinite-system FBZ sampled by the first through the fourth BZ partition, and take their union. Do determine these regions, we do not really need the detailed structure of the BZ partitions, but only the regions marked '11' in all four BZ partitions. This is because in these regions, the twist vector $\boldsymbol{\phi}$ is related to the sampled wave vector $\mathbf{k}(\boldsymbol{\phi})$ trivially, and we know from our study of the $(2, 0) \times (0, 2)$ system that the other regions in the twist angle domain merely sample this set of infinite-system FBZ wave vectors over and over again.

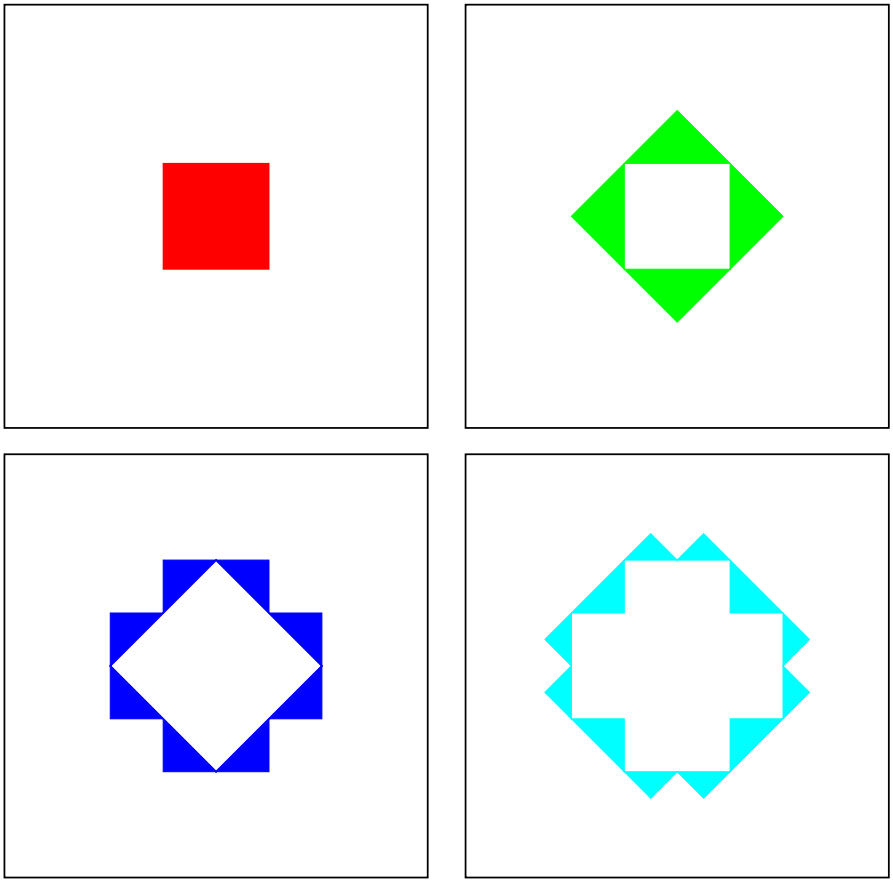

Figure D.22: Regions of the FBZ sampled by the first (top left), second (top right), third (bottom left) and fourth (bottom right) BZ partitions of the $(4, 0) \times (0, 4)$ system subject to twist boundary conditions.

With this shortcut, we then find the wave vectors sampled by the third and fourth BZ partitions, shown in Figure D.22, along with those sampled by the first and second BZ partitions. In Figure D.23, we show the union of the sets of wave vectors in the infinite-system FBZ sampled by the first through fourth BZ partitions. The approximate Fermi surface generated by twist boundary conditions is then the boundaries of this combined set of sampled wave vectors. As we can see in Figure D.23, the approximate Fermi surface agrees rather well with the infinite-system Fermi surface at $\bar{n} = \frac{1}{4}$, obtained by numerically integrating the energy density of states $g(\epsilon)$ in (D.3.8) associated with the infinite-system dispersion relation $\epsilon(\mathbf{k})$ in (D.3.9).

Non-square systems. If we choose finite systems that are also squares on the infinite square lattice, we would be dealing with a sequence of system sizes which would grow as L^2. The Hilbert space of this sequence of systems, before reduction in size with the use of symmetries, would grow as e^{L^2}. Between $L = 4$ ($N = 16$) and $L = 5$ ($N = 25$), the computational requirements would have grown by a hundred-thousand-fold for a system of spinless fermions. This rapid growth in size of the Hilbert space can be kept in check by defining square systems which are rotated relative to the infinite square lattice, or non-square systems defined by the lattice vectors $\mathbf{R}_1$ and $\mathbf{R}_2$.

One chief concern in using non-square systems is that we lose some or all of the point group symmetries of the underlying infinite square lattice. In the remainder of this section, we shall learn more about the partition structure of the general $\mathbf{R}_1 \times \mathbf{R}_2$ system, before looking at two of the simplest non-square systems, $(2, 1)\times(1, 2)$ and $(2, 1)\times(0, 2)$, which has three sites and four sites respectively. In particular, we want to see how the performance of our dumb ED program using twist boundary conditions averaging would be affected by the loss in symmetry.

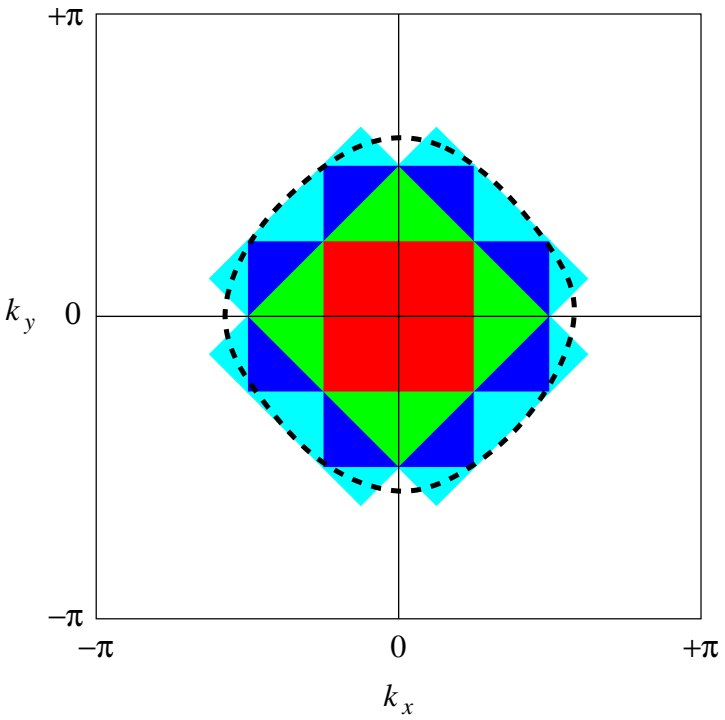

Figure D.23: The wave vectors in the FBZ sampled by twist boundary conditions for $P = 4$ noninteracting spinless fermion in the $(4, 0) \times (0, 4)$ system (red, green, blue, and cyan regions sampled by the first, second, third and fourth BZ partitions respectively), compared to the Fermi surface (black dashed curve) of the infinite square lattice with $\bar{n} = \frac{1}{4}$, obtained by numerically integrating the energy density of states $g(\epsilon)$ in (D.3.8) associated with the infinite-system dispersion relation $\epsilon(\mathbf{k})$ in (D.3.9).

D.3.2.2 Partition Structure of $\mathbf{R_1} \times \mathbf{R_2}$ System

For the $\mathbf{R}_1 \times \mathbf{R}_2$ system of noninteracting spinless fermions with dispersion relation given by (D.2.45), the crossing conditions (D.3.13) are

$$\cos(k_{0,1x} + \phi_x) + \cos(k_{0,1y} + \phi_y) = \cos(k_{0,2x} + \phi_x) + \cos(k_{0,2y} + \phi_y). \tag{D.3.15}$$

Rearranging this, we get

$$\begin{gathered}\cos(k_{0,1x} + \phi_x) - \cos(k_{0,2x} + \phi_x) = \cos(k_{0,2y} + \phi_y) - \cos(k_{0,1y} + \phi_y) \\ -2 \sin \frac{k_{0,1x} - k_{0,2x}}{2} \sin\left(\phi_x + \frac{k_{0,1x} + k_{0,2x}}{2}\right) = -2 \sin \frac{k_{0,2y} - k_{0,1y}}{2} \sin\left(\phi_y + \frac{k_{0,1y} + k_{0,2y}}{2}\right),\end{gathered} \tag{D.3.16}$$

which is of the form

$$\sin u = A \sin v. \tag{D.3.17}$$

For the square $(2, 0) \times (0, 2)$ system investigated earlier, the ratio of coefficients A is such that the solutions (u, v) are all straight lines. The solutions (u, v) are also all straight lines for non-square systems that retain specific point group symmetries of the infinite square lattice, for example, in the case of the $(2, 1) \times (1, 2)$ system to be discussed. In general, for asymmetric non-square systems, or for square system rotated relative to the underlying square lattice by an angle incompatible with the symmetry of the dispersion relation $\epsilon(\mathbf{k})$, for example, the $(2, -1) \times (1, 2)$ system which we will not discuss, the solutions (u, v) are all curves.

D.3.2.3 The $(2, 1) \times (1, 2)$ System

Brillouin zone partition structure. For this simple nonsquare system with three sites, the allowed wave vectors in the absence of a phase twist are

$$\mathbf{k}_{0,1} = \frac{2\pi}{3}(-1, -1), \quad \mathbf{k}_{0,2} = (0, 0), \quad \mathbf{k}_{0,3} = \frac{2\pi}{3}(1, 1). \tag{D.3.18}$$

The crossing conditions we need to solve are

$$\epsilon_{\mathbf{k}_{0,1}} = \epsilon_{\mathbf{k}_{0,2}} : \qquad \sin\tfrac{\pi}{3}\sin\left(\phi_x - \tfrac{\pi}{3}\right) = -\sin\tfrac{\pi}{3}\sin\left(\phi_y - \tfrac{\pi}{3}\right), \tag{D.3.19a}$$

$$\epsilon_{\mathbf{k}_{0,1}} = \epsilon_{\mathbf{k}_{0,3}} : \qquad \sin\tfrac{2\pi}{3}\sin\phi_x = -\sin\tfrac{2\pi}{3}\sin\phi_y, \tag{D.3.19b}$$

$$\epsilon_{\mathbf{k}_{0,2}} = \epsilon_{\mathbf{k}_{0,3}} : \qquad \sin\tfrac{\pi}{3}\sin\left(\phi_x + \tfrac{\pi}{3}\right) = -\sin\tfrac{\pi}{3}\sin\left(\phi_y + \tfrac{\pi}{3}\right). \tag{D.3.19c}$$

Because of the neat coefficients, this system of equations simplify to

$$\epsilon_{\mathbf{k}_{0,1}} = \epsilon_{\mathbf{k}_{0,2}} : \qquad \sin\left(\phi_x - \tfrac{\pi}{3}\right) = -\sin\left(\phi_y - \tfrac{\pi}{3}\right), \tag{D.3.20a}$$

$$\epsilon_{\mathbf{k}_{0,1}} = \epsilon_{\mathbf{k}_{0,3}} : \qquad \sin\phi_x = -\sin\phi_y, \tag{D.3.20b}$$

$$\epsilon_{\mathbf{k}_{0,2}} = \epsilon_{\mathbf{k}_{0,3}} : \qquad \sin\left(\phi_x + \tfrac{\pi}{3}\right) = -\sin\left(\phi_y + \tfrac{\pi}{3}\right), \tag{D.3.20c}$$

whose solutions are

$$\begin{aligned}
&\phi_y = -\phi_x + \tfrac{2\pi}{3} + 2n\pi, \qquad && \phi_y = \pi + \phi_x + 2n\pi; \\
&\phi_y = -\phi_x + 2n\pi, && \phi_y = \pi + \phi_x + 2n\pi; \\
&\phi_y = -\phi_x - \tfrac{2\pi}{3} + 2n\pi, && \phi_y = \pi + \phi_x + 2n\pi,
\end{aligned} \tag{D.3.21}$$

where n is an integer.

If we plot these partition lines within the twist angle domain, as shown in Figure D.24, we find a complicated partition structure which does not have the full point symmetries of the square lattice, because the finite system chosen does not. The three BZ partitions, and the regions of the infinite-system FBZ they sample are shown in Figure D.25. The accessible fillings for this system are $\bar{n} = \frac{1}{3}, \frac{2}{3}$ and 1, corresponding to $P = 1, 2$, and 3 particles in the three-site system. At these three filling fractions, the approximate Fermi surfaces are the boundaries of the infinite-system FBZ wave vectors sampled by the first BZ partition, the boundaries of the union of the infinite-system FBZ wave vectors sampled by the first and second BZ partitions, and the boundaries of the union of the infinite-system FBZ wave vectors sampled by the first, second, and third BZ

partitions. This is shown in Figure D.26. As we can see from Figure D.26, the approximate Fermi surfaces for the incomplete fillings compare terribly with the infinite-system Fermi surfaces.

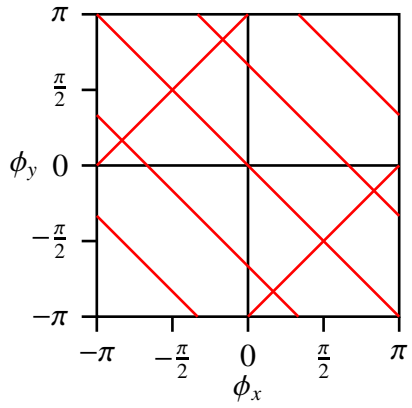

Figure D.24: Partition lines of the $(2,1)\times(1,2)$ system subject to twist boundary conditions.

Orientation averaging. To improve the resemblance of the approximate Fermi surfaces to the infinte-system ones, another averaging device, which we call *orientation averaging*, is needed. The idea is simple: instead of performing ED with twist boundary conditions on just the $\mathbf{R}_1 \times \mathbf{R}_2 = (R_{1x}, R_{1y}) \times (R_{2x}, R_{2y})$ system, we should also exactly diagonalize with twist boundary conditions three other systems: $(R_{2y}, R_{2x}) \times (R_{1y}, R_{1x})$, $(R_{1x}, -R_{1y}) \times (-R_{2x}, R_{2y})$ and $(R_{2y}, -R_{2x}) \times (-R_{1y}, R_{1x})$. These four systems have exactly the same shape, but different orientations relative to the underlying square lattice, and so we should take results from all four systems, and compute the average.

After orientation averaging, the orientation-averaged partition structure is shown in Figure D.27. In this system, if we fill in just $P = 1$ particle, the Fermi surface would enclose an area of $4\pi^2/3$. Without orientation averaging, we would have filled in the rotated rectangle centered at $(0,0)$ in the FBZ, as shown in Figure D.25. With orientation

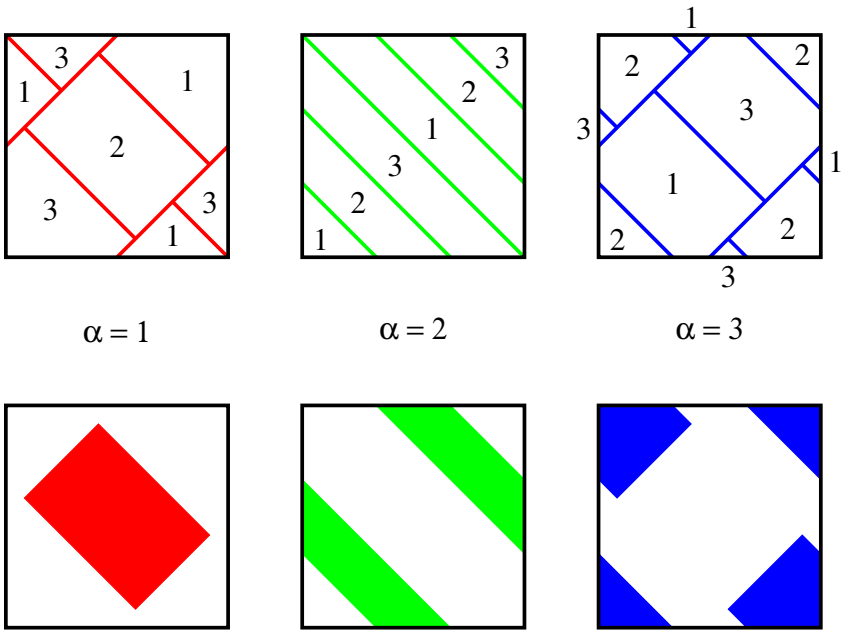

Figure D.25: BZ partition structure (top) and the regions of the infinite-system FBZ sampled by each BZ partition (bottom), of the $(2,1) \times (1,2)$ system subject to twist boundary conditions, for ED band indices $\alpha = 1, 2, 3$. The square for each BZ partition (top) represents the region of twist angle space $(-\pi \leq \phi_x \leq +\pi) \times (-\pi \leq \phi_y \leq +\pi)$, while the indices shown within or adjacent to the BZ partitions are the twisted band indices, where $\mathbf{k}_{\mathbf{n}_1} = (-\frac{2\pi}{3}, -\frac{2\pi}{3})$, $\mathbf{k}_{\mathbf{n}_2} = (0,0)$, $\mathbf{k}_{\mathbf{n}_3} = (\frac{2\pi}{3}, \frac{2\pi}{3})$. The squares for each region of sampled wave vectors (bottom) represent the infinite-system FBZ $(-\pi \leq k_x \leq +\pi) \times (-\pi \leq k_y \leq +\pi)$.

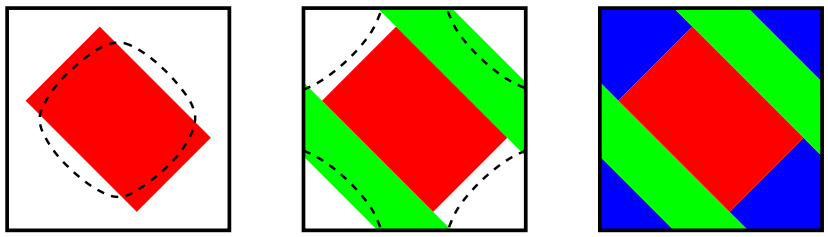

Figure D.26: The approximate momentum distributions sampled by twist boundary conditions averaging at filling fractions $\bar{n} = \frac{1}{3}$ (left), $\bar{n} = \frac{2}{3}$ (center), and $\bar{n} = 1$ (right). The regions colored red, green, and blue are the infinite-system FBZ wave vectors sampled by the first, second and third BZ partitions respectively. The approximate Fermi surfaces, which bound the sampled wave vectors, are compared to the infinite-system Fermi surfaces (black dashed curves), obtained by numerically integrating the energy density of states $g(\epsilon)$ in (D.3.8) associated with the infinite-system dispersion relation $\epsilon(\mathbf{k})$ in (D.3.9), at these filling fractions. The square for each filling fraction represents the infinite-system FBZ, $(-\pi \le k_x \le +\pi) \times (-\pi \le k_y \le +\pi)$.

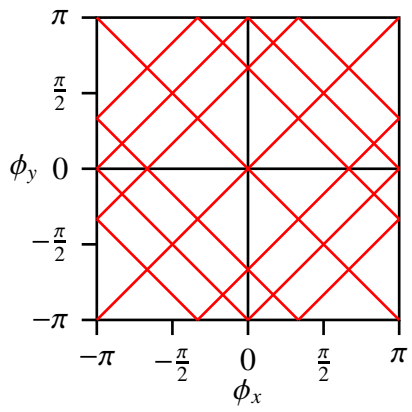

Figure D.27: Partition lines of the $(2, 1) \times (1, 2)$ system subject to twist boundary conditions, after orientation averaging.

averaging, we would be averaging the occupation between a rotated rectangle with its long axis along $\phi_y = -\phi_x$ and one with its long axis along $\phi_y = +\phi_x$. Because of this, the area that is common between the two rectangles would continue to have unit occupation, but the areas that belong to one rectangle but not the other would now have an occupation of $\frac{1}{2}$. We find that this is necessary, so that the total area occupied in momentum space remains as $4\pi^2/3$. As shown in Figure D.28, the rotated square in the middle of the partition that is completely filled has edge $2\sqrt{2}\pi/3$, and hence an area of $8\pi^2/9$. There are four rotated rectangles surrounding this central rotated square, and each has a length of $2\sqrt{2}\pi/3$ and width $\sqrt{2}\pi/6$, and thus an area of $2\pi^2/9$. The total area of these four rectangles would then be $8\pi^2/9$. If these rectangles have unit occupation, then the area of the square and rectangles would exceed $4\pi^2/3$, whereas if the rectangles have an occupation of $1/2$, the total occupied area would be

$$\frac{8\pi^2}{9} + \frac{1}{2} \cdot \frac{8\pi^2}{9} = \frac{4\pi^2}{3}. \tag{D.3.22}$$

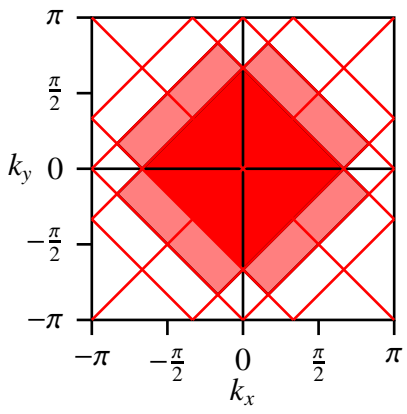

Figure D.28: The wave vectors in the FBZ sampled by twist boundary conditions for $P = 1$ noninteracting spinless fermions in the $(2,1) \times (1,2)$ system. Solid fill in this figure indicates unit filling, whereas halftone fill indicates half-filling.

We can redo the analysis for the second and third orientation-averaged BZ partitions,

to come up with Figure D.29 showing the infinite-system FBZ wave vectors sampled. The effect orientation averaging has on the wave vector sampling is to introduce fractional occupation of wave vectors in the infinite-system FBZ. Thus, instead of a harsh approximation of the momentum distributions by unions of squares and triangles with unit occupation, the jagged edges of the twist-boundary-conditions-sampled momentum distributions are smoothed out by fractional occupation of wave vectors, as shown in Figure D.30. In addition, full point group symmetry of the underlying square lattice is restored in the approximate momentum distributions, which look much better than those before orientation averaging in Figure D.26. There is a price to pay, however: with fractional occupation of the approximate momentum distribution in some regions of the infinite-system FBZ, we can no longer unambiguously define an approximate Fermi surface. This difficulty notwithstanding, we shall continue to refer to the notion of an approximate Fermi surface, as a form of mental shorthand, when discussing the technical aspects of twist boundary conditions averaging. Where orientation averaging is necessary, we shall understand the invocation of an 'approximate Fermi surface' as referring to the approximate momentum distribution, with its unit and fractional fillings.

D.3.2.4 The $(2, 1) \times (0, 2)$ System

In a sense, the $(2, 1) \times (1, 2)$ system is not too terrible a distortion of the square lattice, because it retains part of the point group symmetry of the square lattice. There are a great number of non-square systems which we can define that retains none of the point group symmetries of the square lattice. A simple non-trivial example is the $(2, 1) \times (0, 2)$ system, which has four sites. For this asymmetric system, the allowed wave vectors in the absence of a phase twist are

$$\mathbf{k}_{0,1} = \frac{\pi}{2}(-1, -2), \quad \mathbf{k}_{0,2} = \frac{\pi}{2}(-2, 0), \quad \mathbf{k}_{0,3} = \frac{\pi}{2}(1, -2), \quad \mathbf{k}_{0,4} = (0, 0). \tag{D.3.23}$$

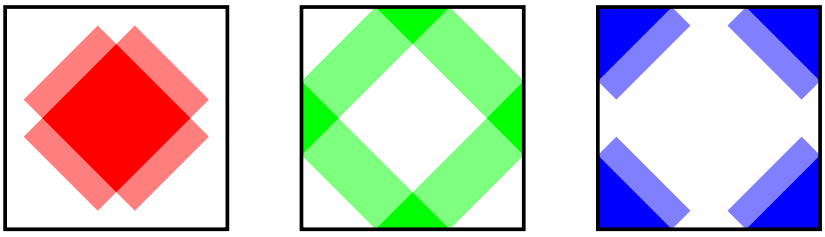

$\alpha = 1$ $\alpha = 2$ $\alpha = 3$

Figure D.29: Regions of the FBZ sampled by each BZ partition, after orientation averaging, of the $(2,1) \times (1,2)$ system subject to twist boundary conditions, for ED band indices $\alpha = 1, 2, 3$. Solid fill in this figure indicates unit filling, whereas halftone fill indicates half-filling.

The crossing conditions we need to solve, with dispersion relation given in (D.2.45), are

$$\begin{aligned}
\epsilon_{\mathbf{k}_{0,1}} = \epsilon_{\mathbf{k}_{0,2}} : &\quad -\sin\tfrac{\pi}{4}\sin\left(\phi_x - \tfrac{3\pi}{4}\right) = -\sin\tfrac{\pi}{2}\sin\left(\phi_y - \tfrac{\pi}{2}\right), \\
\epsilon_{\mathbf{k}_{0,1}} = \epsilon_{\mathbf{k}_{0,3}} : &\quad \sin\tfrac{\pi}{2}\sin\phi_x = -\sin 0 \sin\left(\phi_y - \pi\right), \\
\epsilon_{\mathbf{k}_{0,1}} = \epsilon_{\mathbf{k}_{0,4}} : &\quad \sin\tfrac{\pi}{4}\sin\left(\phi_x - \tfrac{\pi}{4}\right) = -\sin\tfrac{\pi}{2}\sin\left(\phi_y - \tfrac{\pi}{2}\right), \\
\epsilon_{\mathbf{k}_{0,2}} = \epsilon_{\mathbf{k}_{0,3}} : &\quad \sin\tfrac{3\pi}{4}\sin\left(\phi_x - \tfrac{\pi}{4}\right) = \sin\tfrac{\pi}{2}\sin\left(\phi_y - \tfrac{\pi}{2}\right), \\
\epsilon_{\mathbf{k}_{0,2}} = \epsilon_{\mathbf{k}_{0,4}} : &\quad -\sin\tfrac{\pi}{2}\sin\left(\phi_x - \tfrac{\pi}{2}\right) = \sin 0 \sin\phi_y, \\
\epsilon_{\mathbf{k}_{0,3}} = \epsilon_{\mathbf{k}_{0,4}} : &\quad -\sin\tfrac{\pi}{4}\sin\left(\phi_x + \tfrac{\pi}{4}\right) = -\sin\tfrac{\pi}{2}\sin\left(\phi_y - \tfrac{\pi}{2}\right),
\end{aligned} \tag{D.3.24}$$

which simplifies to

$$\begin{aligned}
\epsilon_{\mathbf{k}_{0,1}} = \epsilon_{\mathbf{k}_{0,2}} : &\quad \sin\tfrac{\pi}{4}\sin\left(\phi_x - \tfrac{3\pi}{4}\right) = \sin\left(\phi_y - \tfrac{\pi}{2}\right), \\
\epsilon_{\mathbf{k}_{0,1}} = \epsilon_{\mathbf{k}_{0,3}} : &\quad \sin\phi_x = 0, \\
\epsilon_{\mathbf{k}_{0,1}} = \epsilon_{\mathbf{k}_{0,4}} : &\quad \sin\tfrac{\pi}{4}\sin\left(\phi_x - \tfrac{\pi}{4}\right) = -\sin\left(\phi_y - \tfrac{\pi}{2}\right), \\
\epsilon_{\mathbf{k}_{0,2}} = \epsilon_{\mathbf{k}_{0,3}} : &\quad \sin\tfrac{3\pi}{4}\sin\left(\phi_x - \tfrac{\pi}{4}\right) = \sin\left(\phi_y - \tfrac{\pi}{2}\right), \\
\epsilon_{\mathbf{k}_{0,2}} = \epsilon_{\mathbf{k}_{0,4}} : &\quad -\sin\left(\phi_x - \tfrac{\pi}{2}\right) = 0, \\
\epsilon_{\mathbf{k}_{0,3}} = \epsilon_{\mathbf{k}_{0,4}} : &\quad \sin\tfrac{\pi}{4}\sin\left(\phi_x + \tfrac{\pi}{4}\right) = \sin\left(\phi_y - \tfrac{\pi}{2}\right).
\end{aligned} \tag{D.3.25}$$

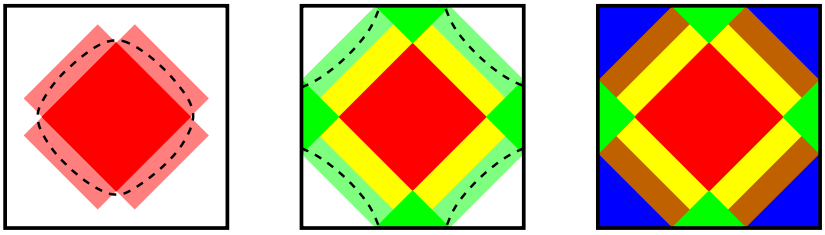

$\bar{n} = \frac{1}{3}$ $\bar{n} = \frac{2}{3}$ $\bar{n} = 1$

Figure D.30: The approximate momentum distributions sampled by twist boundary conditions averaging, after orientation averaging, at filling fractions $\bar{n} = \frac{1}{3}$ (left), $\bar{n} = \frac{2}{3}$ (center), and $\bar{n} = 1$ (right). The color scheme used is as follows: the infinite-system FBZ wave vectors sampled by the orientation-averaged first, second, and third BZ partitions with unit/half occupations, are shown in red/halftone red, green/halftone green, and blue/halftone blue respectively. Where the half-occupied wave vectors of the first and second BZ partitions (halftone red and halftone green respectively) overlap to give unit occupation, we show them in yellow; where the half-occupied wave vectors of the second and third BZ partitions (halftone green and halftone blue respectively) overlap to give unit occupation, we show them in brown. As described in the main text, we cannot define unambiguous approximate Fermi surfaces because of the fractional occupations, but we can nonetheless compare the twist-boundary-conditions-sampled momentum distributions to those bound by the infinite-system Fermi surfaces (black dashed curves), obtained by numerically integrating the energy density of states $g(\epsilon)$ in (D.3.8) associated with the infinite-system dispersion relation $\epsilon(\mathbf{k})$ in (D.3.9), at these filling fractions. The square for each filling fraction represents the infinite-system FBZ, $(-\pi \leq k_x \leq +\pi) \times (-\pi \leq k_y \leq +\pi)$.

These have solutions

$$
\begin{aligned}
\phi_y &= \sin^{-1}\left[\sin\tfrac{\pi}{4}\sin\left(\phi_x - \tfrac{3\pi}{4}\right)\right] + \tfrac{\pi}{2} + 2n\pi, \\
\phi_y &= \pi - \sin^{-1}\left[\sin\tfrac{\pi}{4}\sin\left(\phi_x - \tfrac{3\pi}{4}\right)\right] + \tfrac{\pi}{2} + 2n\pi; \\
\phi_x &= n\pi; \\
\phi_y &= \sin^{-1}\left[-\sin\tfrac{\pi}{4}\sin\left(\phi_x - \tfrac{\pi}{4}\right)\right] + \tfrac{\pi}{2} + 2n\pi, \\
\phi_y &= \pi - \sin^{-1}\left[-\sin\tfrac{\pi}{4}\sin\left(\phi_x - \tfrac{\pi}{4}\right)\right] + \tfrac{\pi}{2} + 2n\pi; \\
\phi_y &= \sin^{-1}\left[\sin\tfrac{3\pi}{4}\sin\left(\phi_x - \tfrac{\pi}{4}\right)\right] + \tfrac{\pi}{2} + 2n\pi, \\
\phi_y &= \pi - \sin^{-1}\left[\sin\tfrac{3\pi}{4}\sin\left(\phi_x - \tfrac{\pi}{4}\right)\right] + \tfrac{\pi}{2} + 2n\pi; \\
\phi_x &= \tfrac{\pi}{2} + n\pi; \\
\phi_y &= \sin^{-1}\left[\sin\tfrac{\pi}{4}\sin\left(\phi_x + \tfrac{\pi}{4}\right)\right] + \tfrac{\pi}{2} + 2n\pi, \\
\phi_y &= \pi - \sin^{-1}\left[\sin\tfrac{\pi}{4}\sin\left(\phi_x + \tfrac{\pi}{4}\right)\right] + \tfrac{\pi}{2} + 2n\pi,
\end{aligned}
\tag{D.3.26}
$$

where n is an integer.

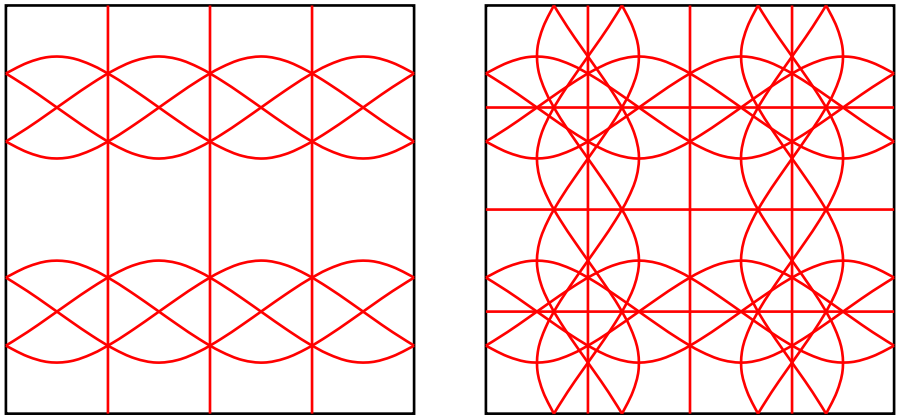

Figure D.31: The set of all partition curves of the $(2,1)\times(0,2)$ system subject to twist boundary conditions before orientation averaging (left), and the set of all partition curves after orientation averaging (right).

The BZ partition structure for the $(2,1)\times(0,2)$ system before and after orientation

averaging, is shown in Figure D.31. If we put $P = 1$ particle into the system, then the region of FBZ sampled by twist boundary conditions, before and after orientation averaging, is shown in Figure D.32. More work will be needed to figure out the orientation-averaged second BZ partition, and the FBZ wave vectors it samples, but we can already tell from the partition structure that, unlike the $(2, 0) \times (0, 2)$ case, we will not get the Fermi surface for $\bar{n} = \frac{1}{2}$ exactly right in this case.

From this simple example, we can see that the BZ partition structure of a non-square system, except for the simplest dispersion relations, and especially after orientation averaging to recover the full point group symmetry of the underlying square lattice, is immensely complicated. We shall see in Section D.4 that twist boundary conditions averaging an observable O involves integrating over the twist surface of O. This twist surface of O, which we will define in Section D.4, is generally a patchwork of piecewise continuous surfaces, which gets more complex as the BZ partition structure gets more complex. For non-square systems with such a complicated BZ partition structure, it would therefore be a herculean task to integrate over the twist surface faithfully even if the twist surface consists only of piecewise continuous paraboloids.

D.3.3 Restricting Wave Vector Sampling to the FBZ

In the preceding subsections, we have seen that by varying ϕ over the twist-angle interval $(-\pi, +\pi)$ for one-dimensional systems, and varying $\boldsymbol{\phi} = (\phi_x, \phi_y)$ over the twist-angle domain $(-\pi, +\pi) \times (-\pi, +\pi)$ for two-dimensional systems, we sampled the same set of occupied wave vectors over and over again. In fact, for a system with N sites, the set of occupied wave vectors is sampled N times. This is silly, since sampling the set of occupied wave vectors once is just as good as sampling it N times, and especially so when the computational effort involved with each twist angle ϕ or twist vector $\boldsymbol{\phi}$ is

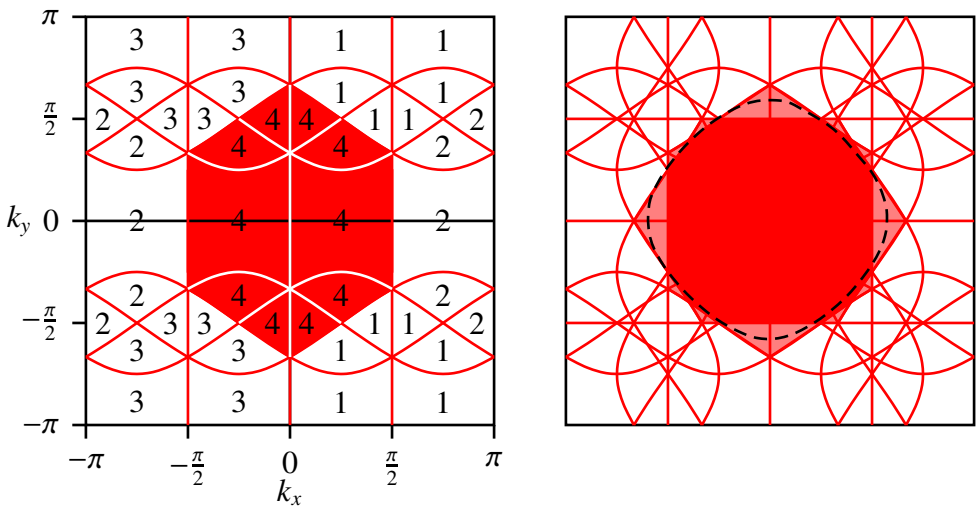

Figure D.32: Region of the FBZ sampled by the first orientation-averaged BZ partition of the $(2,1) \times (0,2)$ system subject to twist boundary conditions, before (left) and after (right) orientation averaging. Solid fill indicates unit filling, and halftone fill indicates half-filling. Also shown as a dashed curve is the infinite-system Fermi surface, obtained by numerically integrating the energy density of states $g(\epsilon)$ in (D.3.8) associated with the infinite-system dispersion relation $\epsilon(\mathbf{k})$ in (D.3.9), at a filling fraction of $\bar{n} = \frac{1}{4}$.

substantial.

For one-dimensional systems, we saw from Figures D.3 and D.5 that the occupied set of wave vectors is sampled once when we vary ϕ over the interval $(-\frac{\pi}{N}, +\frac{\pi}{N}) = (-\frac{\pi}{4}, +\frac{\pi}{4})$, which is precisely the FBZ of the finite chain we are working with. For rectangular two-dimensional systems $(L_x, 0) \times (L_y, 0)$, the FBZ is the rectangular domain $(-\frac{\pi}{L_x}, +\frac{\pi}{L_x}) \times (-\frac{\pi}{L_y}, +\frac{\pi}{L_y})$. If we restrict $\boldsymbol{\phi} = (\phi_x, \phi_y)$ to this domain, we find that we will sample the set of occupied wave vectors only once, as is evident from the $(2, 0) \times (0, 2)$ system.

It is also possible to restrict our wave vector sampling to within the FBZ for non-square systems $\mathbf{R}_1 \times \mathbf{R}_2$. To see how this can be done, let us reconsider how we arrived at the ranges $-\frac{\pi}{L_x} \leq \phi_x < +\frac{\pi}{L_x}$ and $-\frac{\pi}{L_y} \leq \phi_y < +\frac{\pi}{L_y}$ for the rectangular $(L_x, 0) \times (0, L_y)$ system, by comparing what happens in the bond and boundary gauges. In the bond gauge, a particle picks up a phase of $e^{\mathrm{i}\,\phi_x}$ if it hops across a bond in the $+x$-direction, and a phase of $e^{\mathrm{i}\,\phi_y}$ if it hops across a bond in the $+y$-direction. As shown in Figure D.33, after the particle hops from site $\mathbf{r}$ to site $\mathbf{r} + \mathbf{R}_1$, the net phase twist it incurs in the bond gauge would be $e^{\mathrm{i}\,\phi_x L_x} = e^{\mathrm{i}\,\boldsymbol{\phi}\cdot\mathbf{R}_1}$, whereas after it hops from site $\mathbf{r}$ to site $\mathbf{r} + \mathbf{R}_2$, the net phase twist it incurs in the bond gauge is $e^{\mathrm{i}\,\phi_y L_y} = e^{\mathrm{i}\,\boldsymbol{\phi}\cdot\mathbf{R}_2}$. In the boundary gauge, let us denote by $e^{i\phi_1}$ and $e^{i\phi_2}$ the phase twists incurred by a particle hopping across the x- and y-boundaries respectively.

We have chosen in Section D to have the net phase twist incurred by a particle crossing the boundaries to be the same in both gauges. Therefore,

$$e^{\mathrm{i}\,\boldsymbol{\phi}\cdot\mathbf{R}_1} = e^{\mathrm{i}\,\phi_1}, \quad e^{\mathrm{i}\,\boldsymbol{\phi}\cdot\mathbf{R}_2} = e^{\mathrm{i}\,\phi_2}, \tag{D.3.27}$$

which tells us that

$$\phi_x = \frac{\phi_1}{L_x}, \quad \phi_y = \frac{\phi_2}{L_y}. \tag{D.3.28}$$

It is easy to see in the boundary gauge that we can independently vary ϕ_1 and ϕ_2 over the interval $(-\pi, +\pi)$ to sample once over the wave vectors $\mathbf{k}$ in the FBZ. Hence, the ranges

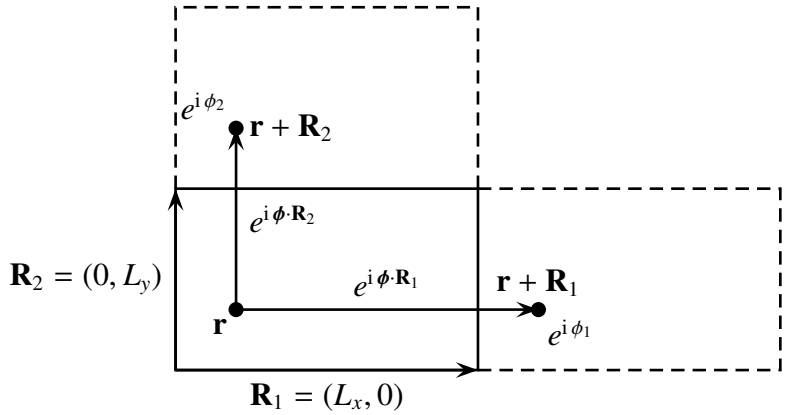

Figure D.33: Phase twists incurred when a particle hops from a site $\mathbf{r}$, across the rectangular system boundaries, to the equivalent sites $\mathbf{r} + (L_x, 0)$ and $\mathbf{r} + (0, L_y)$.

of ϕ_x and ϕ_y must be restricted to the intervals $(-\frac{\pi}{L_x}, +\frac{\pi}{L_x})$ and $(-\frac{\pi}{L_y}, +\frac{\pi}{L_y})$ respectively, to sample the FBZ once.

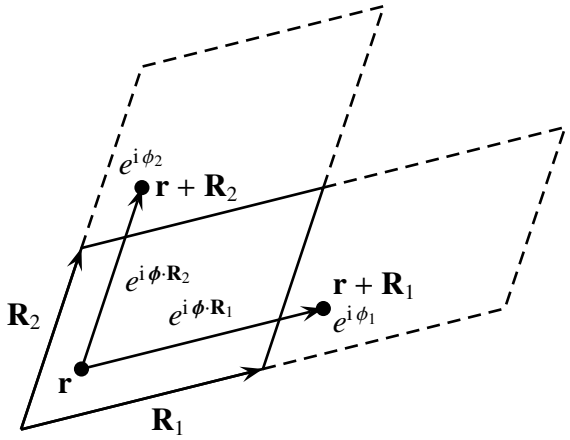

Figure D.34: Phase twists incurred when a particle hops from a site $\mathbf{r}$, across the non-square system boundaries, to the equivalent sites $\mathbf{r} + (L_x, 0)$ and $\mathbf{r} + (0, L_y)$.

For a non-square system, as shown in Figure D.34, ϕ_1 and ϕ_2 continue to be the twist angles we can independently vary over the interval $(-\pi, +\pi)$ to sample the FBZ. We can continue to hold the relation (D.3.27) as valid for the non-square system. However, the

relations between ϕ_x, ϕ_y and ϕ_1, ϕ_2 are now, when written in matrix form,

$$\begin{bmatrix} R_{1x} & R_{1y} \\ R_{2x} & R_{2y} \end{bmatrix} \begin{bmatrix} \phi_x \\ \phi_y \end{bmatrix} = \begin{bmatrix} \phi_1 \\ \phi_2 \end{bmatrix}. \tag{D.3.29}$$

This can be solved to give

$$\begin{bmatrix} \phi_x \\ \phi_y \end{bmatrix} = \frac{1}{N} \begin{bmatrix} R_{2y} & -R_{1y} \\ -R_{2x} & R_{1x} \end{bmatrix} \begin{bmatrix} \phi_1 \\ \phi_2 \end{bmatrix} = \frac{\phi_1}{2\pi} \mathbf{Q}_1 + \frac{\phi_2}{2\pi} \mathbf{Q}_2, \tag{D.3.30}$$

where $\mathbf{Q}_1$ and $\mathbf{Q}_2$ are the primitive reciprocal lattice vectors given in (C.2.10). Therefore, to sample once over the wave vectors in the FBZ, we restrict our choice of twist angles ϕ_1 and ϕ_2 to within the square domain $(-\pi, +\pi) \times (-\pi, +\pi)$, and calculate $\boldsymbol{\phi} = (\phi_x, \phi_y)$ using (D.3.30).

D.4 Twist Surfaces

For an observable A which we can calculate from a finite system, it is possible to map out its value as a function of $\boldsymbol{\phi}$. This gives a surface (or hypersurface in dimensions greater than two) which we shall call the *twist surface* of A. Zotos *et al* [391] and Poilblanc [398, 399] did a minimalist mapping of the twist surface of the ground-state energy of interacting models by tracing along a line in (ϕ_x, ϕ_y). Both noted the occurence of cusps on the twist surface as a result of the crossing of twisted energy bands. Zotos *et al* explained previous confusions in the literature in the light of these band crossings, while Poilblanc observed that the ground-state energy twist surface for a noninteracting system is piecewise paraboloidal.

Because the BZ partition structure is defined by ground-state energy selection of intersecting twisted energy bands, cusps along some of these band crossings are unavoidable on the twist surfaces of all observables. By construction, the ground-state

energy twist surface is guaranteed to be continuous, but for observables other than the ground-state energy, we sometimes find cuts along some of the band crossings. In Figure D.35 we show the twist surfaces of the many-body ground-state energy $E(\boldsymbol{\phi})$ and the two-point function $\langle\Psi(\boldsymbol{\phi})|c^\dagger_{(0,0)}c_{(1,1)}|\Psi(\boldsymbol{\phi})\rangle$ of the $(4,0)\times(0,4)$ system with $N = 4$ particles, subject to twist boundary conditions. As we can see, the twist surface of $E(\boldsymbol{\phi})$ appears to be piecewise paraboloidal, with cusps occurring along the partition lines, while the twist surface of $\langle\Psi(\boldsymbol{\phi})|c^\dagger_{(0,0)}c_{(1,1)}|\Psi(\boldsymbol{\phi})\rangle$ also has discontinuous cuts along some partition lines. We will have more to say about the impact of these twist-surface cusps and cuts on twist boundary conditions averaging in Section D.6.

For a system of noninteracting spinless fermions, all $2n$-point functions can be written as sums of products of two-point functions. Therefore, if the twist surfaces of generic two-point functions are discontinuous, the twist surfaces of the cluster density-matrix elements, as well as as the cluster density-matrix eigenvalues, which are functions of $2n$-point functions, will generally also be discontinuous. This is true for interacting systems as well. As an example, we show the twist surface of the ground-state energy of a $(4,1)\times(1,3)$ system of spinless fermions with infinite nearest-neighbor repulsion, described by the Hamiltonian (4.2.1), in Figure D.36, and the one-particle cluster density-matrix weights in Figures D.37 and D.38.

D.4.1 Phase Shifts and Occupations

The cusps and cuts on twist surfaces appear for both square and non-square systems, and their origin lies with the fact that the exactly diagonalized system is finite, no matter how hard we fudge with twist boundary conditions. To understand these twist-surface singularities, we look at the FBZ of the $(4,0)\times(0,4)$ system. For $P = 5$ particles, the set of filled wave vectors has the topology shown in Figure D.39 when there is no phase

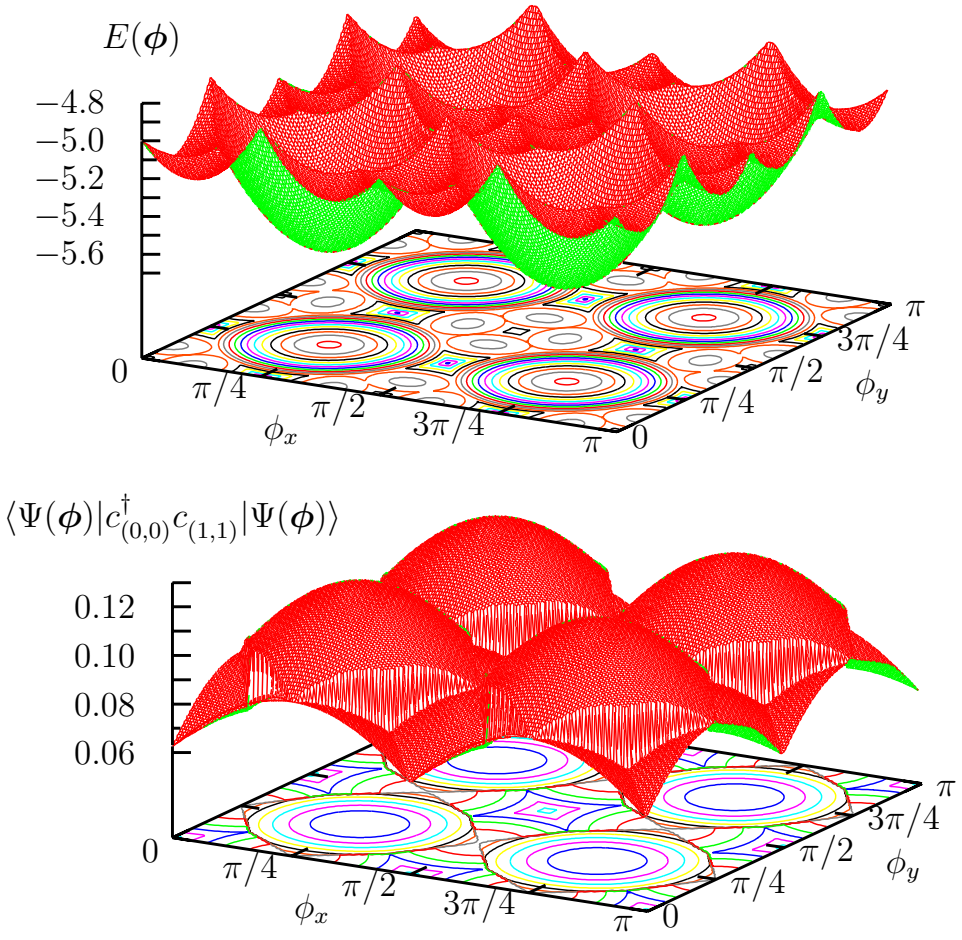

Figure D.35: Twist surfaces for the many-body ground-state energy $E(\boldsymbol{\phi})$ (top) and the two-point function $\langle\Psi(\boldsymbol{\phi})|c^\dagger_{(0,0)}c_{(1,1)}|\Psi(\boldsymbol{\phi})\rangle$ (bottom), for the $(4,0)\times(0,4)$ system with $P = 4$ noninteracting spinless fermions ($\bar{n} = \frac{1}{4}$), subject to twist boundary conditions.

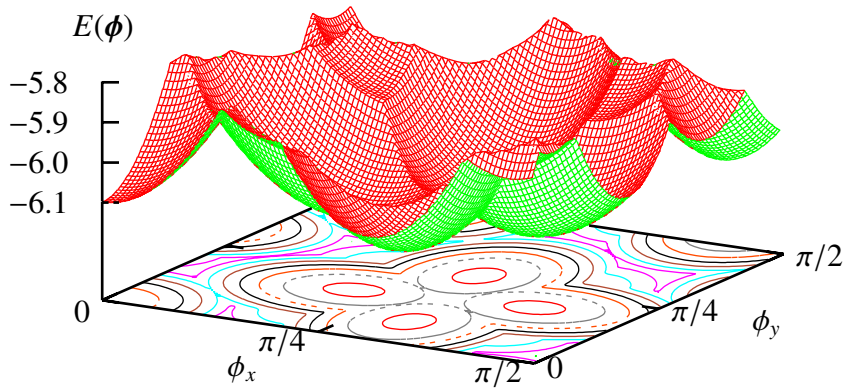

Figure D.36: Twist surface for the many-body ground-state energy $E(\boldsymbol{\phi})$ of the $(4, 1) \times (1, 3)$ system with $P = 3$ spinless fermions with infinite nearest-neighbor repulsion, subject to twist boundary conditions.

shift.

This topology remains intact for small phase shifts (ϕ_x, ϕ_y) of the grid of wave vectors. When we keep $\phi_y = 0$, and start increasing ϕ_x, the single-particle energy of $\mathbf{k}_1$ increases, and the single-particle energy of $\mathbf{k}_2$ decreases. These two single-particle energies become equal when $\mathbf{k}_1$ moved about halfway towards the edge of the FBZ, after-which the single-particle energy of $\mathbf{k}_1$ becomes higher than that of $\mathbf{k}_2$. From this point onwards, we fill $\mathbf{k}_2$ instead of $\mathbf{k}_1$. Because there are two equivalent $\mathbf{k}_2$ wave vectors, we assign an occupation of $\frac{1}{2}$ to each in our implementation to automate this filling process.

With this manner of assigning occupation as ϕ_x is increased from zero, the center-of-mass of the occupied wave vectors (or, equivalently, of the finite-system 'Fermi surface') moves along with the central wave vector $\mathbf{k}_0$, until $\mathbf{k}_1$ is energetically unfavorable to fill. When the two $\mathbf{k}_2$ wave vectors are filled, with occupation of $\frac{1}{2}$ each, the center-of-mass of the occupied wave vectors changes discontinuously from being exactly at $\mathbf{k}_0$ to a point left of $\mathbf{k}_0$. To see how this produces a discontinuous cut in the twist surface, we

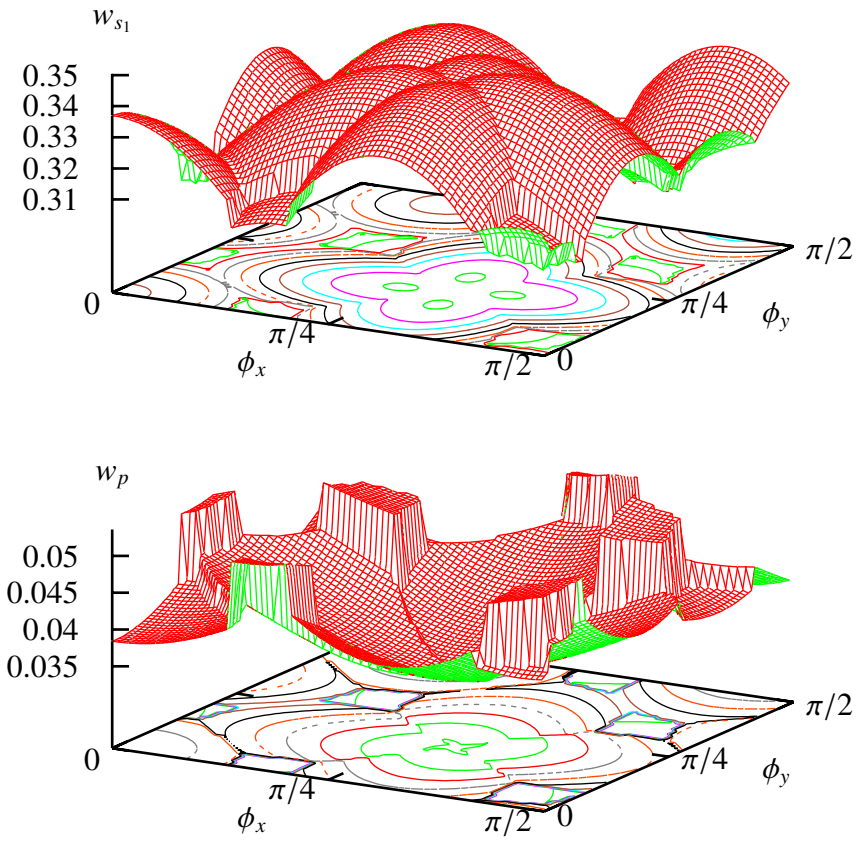

Figure D.37: Twist surfaces for the one-particle cluster density matrix weights w_{s_1} (top) and w_p (bottom) of the $(4, 1) \times (1, 3)$ system with $P = 3$ spinless fermions with infinite nearest-neighbor repulsion, subject to twist boundary conditions.

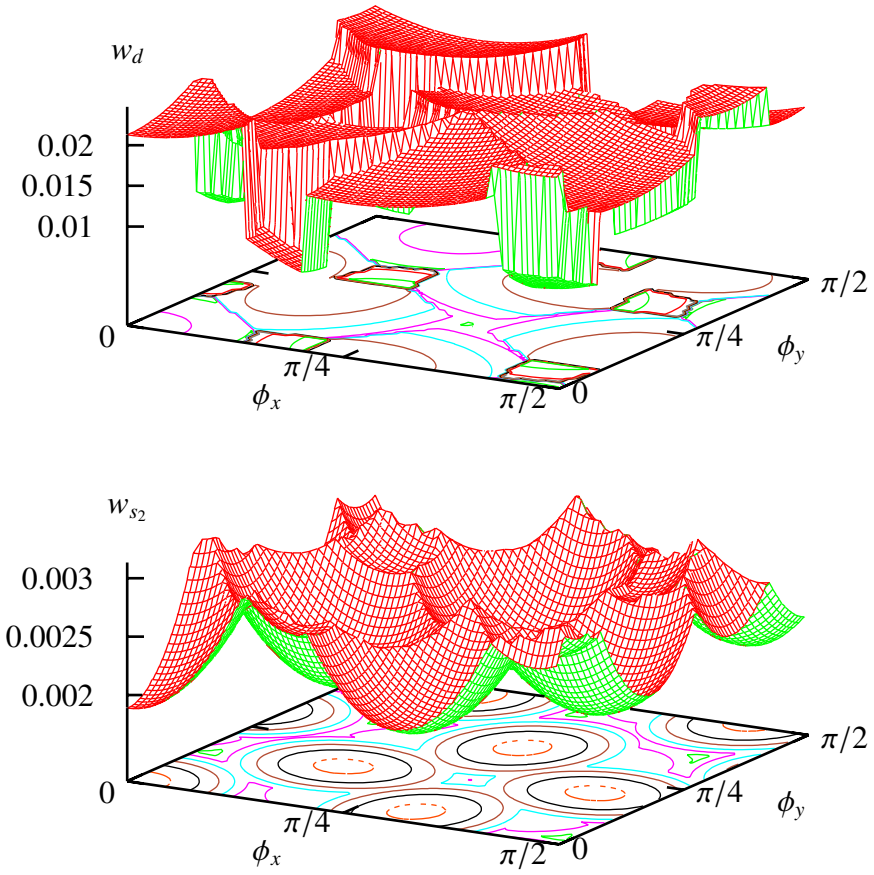

Figure D.38: Twist surfaces for the one-particle cluster density matrix weights w_d (top) and w_{s_2} (bottom) of the $(4,1) \times (1,3)$ system with $P = 3$ spinless fermions with infinite nearest-neighbor repulsion, subject to twist boundary conditions.

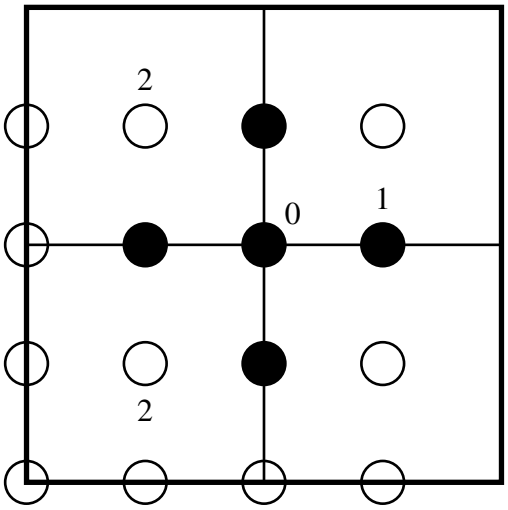

Figure D.39: Allowed wave vectors (circles) for the $(4,0) \times (0,4)$ system subject to periodic boundary conditions. For $P = 5$ particles in the system, the filled wave vectors are the filled circles.

consider the two-point function

$$G(\mathbf{r}, \boldsymbol{\phi}) = \langle \Psi(\boldsymbol{\phi}) | c^{\dagger}_{\mathbf{r}'} c_{\mathbf{r}'+\mathbf{r}} | \Psi(\boldsymbol{\phi}) \rangle = \frac{1}{N} \sum_{\mathbf{k}(\boldsymbol{\phi}) \text{ filled}} e^{\mathrm{i}\,\mathbf{k}\cdot\mathbf{r}} \tag{D.4.1}$$

of two sites separated by a displacement of $\mathbf{r} = (1,0)$. If we keep $\mathbf{k}_1$ occupied through the whole range of ϕ_x, we would have obtained the two-point function element

$$G_1(\mathbf{r}, \boldsymbol{\phi}) = \tilde{G}(\mathbf{r}, \boldsymbol{\phi}) + \frac{1}{16}\, e^{\mathrm{i}(\frac{\pi}{2}+\phi_x)}, \tag{D.4.2}$$

where

$$\tilde{G}(\mathbf{r}, \boldsymbol{\phi}) = \frac{1}{16}\left[e^{\mathrm{i}(-\frac{\pi}{2}+\phi_x)} + e^{\mathrm{i}\,\phi_x} + e^{\mathrm{i}\,\phi_x} + e^{\mathrm{i}\,\phi_x} \right] \tag{D.4.3}$$

is the contribution from the three common occupied wave vectors $(-\frac{\pi}{2}+\phi_x, 0)$, $(\phi_x, -\frac{\pi}{2})$, $(\phi_x, 0)$, and $(\phi_x, +\frac{\pi}{2})$. On the other hand, if we keep $\mathbf{k}_2$ occupied through the whole range of ϕ_x, we would have obtained the two-point function

$$G_2(\mathbf{r}, \boldsymbol{\phi}) = \tilde{G}(\mathbf{r}, \boldsymbol{\phi}) + e^{\mathrm{i}(-\frac{\pi}{2}+\phi_x)}. \tag{D.4.4}$$

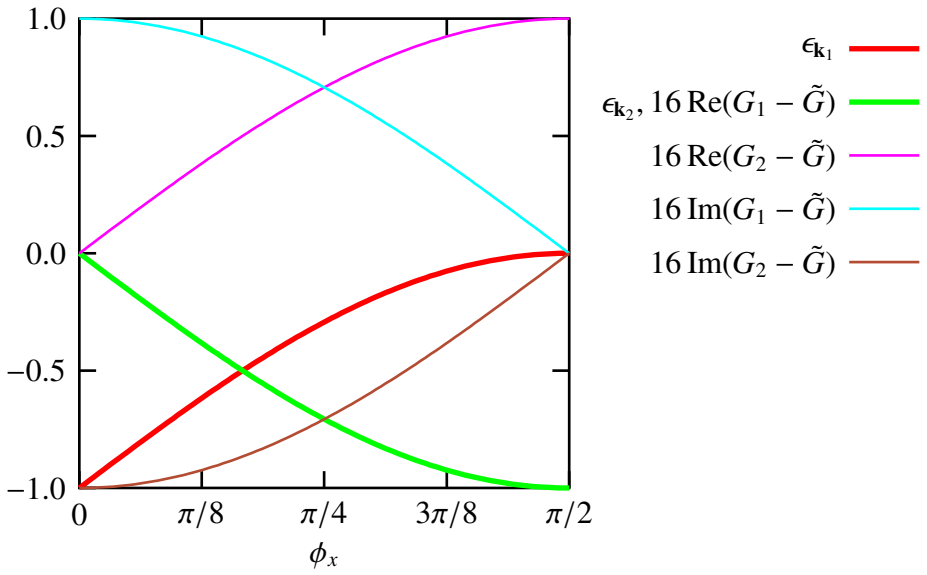

Figure D.40: Plot of the single-particle energies $\epsilon_{\mathbf{k}_1}$ and $\epsilon_{\mathbf{k}_2}$ for the wave vectors $\mathbf{k}_1 = (+\frac{\pi}{2} + \phi_x, 0)$ and $\mathbf{k}_2 = (-\frac{\pi}{2} + \phi_x, \pm\frac{\pi}{2})$, as well as the real and imaginary parts of their contributions to the two-point function between two sites separated by a displacement of $\mathbf{r} = (1, 0)$.

As we can see from Figure D.40, as we switch from filling $\mathbf{k}_1$ to filling $\mathbf{k}_2$, which occurs, for this phase twist path, somewhere between $\phi_x = \pi/8$ and $\phi_x = \pi/4$, the two-point function $G(\mathbf{r}, \boldsymbol{\phi})$ changes discontinuously from $G_1(\mathbf{r}, \boldsymbol{\phi})$ to $G_2(\mathbf{r}, \boldsymbol{\phi})$. In Section D.3.2, we have how twist boundary conditions averaging produces a decent ground-state energy per particle for a two-dimensional system of noninteracting spinless fermions, even though the approximate Fermi surface differs significantly from the true Fermi surface. We shall investigate in the next section how well twist boundary conditions averaging reproduces various correlations functions, given the presence of kinks and cuts in their twist surfaces.

D.5 Correlation Functions

D.5.1 Twist Boundary Conditions and FBZ Averaging

To understand the relationship between an average over twist boundary conditions and an average over the infinite-system FBZ, let us work first in one dimension, and consider the site-averaged value $F(\phi)$ of an arbitrary function $f(k)$ of a single wave vector, i.e.

$$F(\phi) = \frac{1}{N} \sum_{k_n(\phi) \text{ filled}} f(k_n(\phi)). \tag{D.5.1}$$

Formally, if we proceed to average $F(\phi)$ over the twist angles, we obtain the doubly-averaged value

$$\bar{F} = \frac{1}{2\pi} \int_{-\pi}^{+\pi} d\phi \, F(\phi) = \frac{1}{2\pi} \int_{-\pi}^{+\pi} d\phi \, \frac{1}{N} \sum_{k_n(\phi) \text{ filled}} f(k_n(\phi)). \tag{D.5.2}$$

From Section D.3.1, we know that as we vary the twist angle ϕ over the unrestricted range $(-\pi, +\pi)$, $k_n(\phi)$ samples the occupied wave vectors $-k_F \leq k \leq +k_F$ of the infinite system N times. This means that an integral over $-\pi \leq \phi \leq +\pi$ of the sum of $k_n(\phi)$ can

be replaced simply by N times the integral over $-k_F \leq k \leq +k_F$, i.e. the twist boundary conditions averaged value can be written as

$$\bar{F} = \frac{1}{2\pi} \int_{-k_F}^{+k_F} dk\, f(k), \tag{D.5.3}$$

which is the infinite-system limit of the average of $f(k)$.

We get this same result if we use only twist angles ϕ in the restricted range $(-\frac{\pi}{N}, +\frac{\pi}{N})$. In this restricted range of twist angles, the average of the site-averaged value $F(\phi)$ of the function $f(k)$ is

$$\begin{aligned} \bar{F} &= \frac{N}{2\pi} \int_{-\pi/N}^{+\pi/N} d\phi\, F(\phi) \\ &= \frac{N}{2\pi} \int_{-\pi/N}^{+\pi/N} d\phi\, \frac{1}{N} \sum_{k_n(\phi) \text{ filled}} f(k_n(\phi)) \\ &= \frac{1}{2\pi} \int_{-k_F}^{+k_F} dk\, f(k), \end{aligned} \tag{D.5.4}$$

since the restricted range of twist angles samples only once over the occupied wave vectors $-k_F \leq k \leq +k_F$ in the FBZ.

In two dimensions, our site-averaged value $F(\boldsymbol{\phi})$ of an arbitrary function $f(\mathbf{k})$ of the wave vector $\mathbf{k}$ is

$$F(\boldsymbol{\phi}) = \frac{1}{N} \sum_{\mathbf{k}_\alpha(\boldsymbol{\phi}) \text{ filled}} f(\mathbf{k}_\alpha(\boldsymbol{\phi})) = \frac{1}{N} \left[f(\mathbf{k}_1(\boldsymbol{\phi})) + f(\mathbf{k}_2(\boldsymbol{\phi})) + \cdots + f(\mathbf{k}_P(\boldsymbol{\phi})) \right], \tag{D.5.5}$$

where $P = \bar{n}N$ is the number of particles we put into the system. From Section D.3.2, we know that as $\boldsymbol{\phi}$ varies in the unrestricted twist angle domain, $\mathbf{k}_1(\boldsymbol{\phi})$ fills in the region of wave vectors sampled by the first BZ partition, $\mathbf{k}_2(\boldsymbol{\phi})$ wanders around the region of wave vectors sampled by the second BZ partition, and so on and so forth.

Also, as we vary $\boldsymbol{\phi}$ over the entire range $-\pi \leq \phi_x \leq \pi$ and $-\pi \leq \phi_y \leq \pi$, each wave vector in the infinite-system FBZ region Π_α sampled by the αth BZ partition is sampled exactly N times. This means that

$$\int d^2\boldsymbol{\phi}\, f(\mathbf{k}_\alpha(\boldsymbol{\phi})) = N \int_{\Pi_\alpha} d^2\mathbf{k}\, f(\mathbf{k}). \tag{D.5.6}$$

With this, we find that

$$\int d^2\boldsymbol{\phi}\, F(\boldsymbol{\phi}) = \frac{1}{N}\left[N\int_{\Pi_1} d^2\mathbf{k}\, f(\mathbf{k}) + \cdots + N\int_{\Pi_P} d^2\mathbf{k}\, f(\mathbf{k})\right]. \tag{D.5.7}$$

When we do not perform orientation averaging, the wave vectors sampled by different BZ partitions do not overlap with each other, and (D.5.7) simplifies to

$$\int d^2\boldsymbol{\phi}\, F(\boldsymbol{\phi}) = \int_{\cup_\alpha \Pi_\alpha} d^2\mathbf{k}\, f(\mathbf{k}), \tag{D.5.8}$$

where the boundaries of the approximate momentum distribution $\cup_\alpha \Pi_\alpha$ gives us the approximate Fermi surface. With this, the twist-boundary-conditions average of $f(\mathbf{k})$ can be written as

$$\bar{f} = \frac{1}{4\pi^2}\int d^2\boldsymbol{\phi}\, F(\boldsymbol{\phi}) = \frac{1}{4\pi^2}\int_{\cup_\alpha \Pi_\alpha} d^2\mathbf{k}\, f(\mathbf{k}). \tag{D.5.9}$$

When we do perform orientation averaging, we introduce fractional occupation of the wave vectors sampled by different BZ partitions, and we must modify (D.5.7) to read as

$$\int d^2\boldsymbol{\phi}\, F(\boldsymbol{\phi}) = \frac{1}{N}\left[N\int_{\Pi_1} d^2\mathbf{k}\, n_1(\mathbf{k})\, f(\mathbf{k}) + \cdots + N\int_{\Pi_P} d^2\mathbf{k}\, n_P(\mathbf{k})\, f(\mathbf{k})\right], \tag{D.5.10}$$

where $n_\alpha(\mathbf{k})$ is the occupation number of wave vector $\mathbf{k}$ in the region Π_α of the infinite-system FBZ sampled by the αth BZ partition. These regions now overlap with one another, but we have seen in Sections D.3.2.3 and D.3.2.4 that in the interior of the combined region, the fractional occupations in the overlapping regions add to give unit occupation, leading fractional occupation along the boundaries of the combined momentum distribution. The twist-boundary-conditions average of $f(\mathbf{k})$ can therefore be written as

$$\bar{f} = \frac{1}{4\pi^2}\int d^2\boldsymbol{\phi}\, F(\boldsymbol{\phi}) = \frac{1}{4\pi^2}\int_{\cup_\alpha \Pi_\alpha} d^2\mathbf{k}\, n_{\cup_\alpha \Pi_\alpha}(\mathbf{k})\, f(\mathbf{k}), \tag{D.5.11}$$

where $n_{\cup_\alpha \Pi_\alpha}(\mathbf{k})$ is the occupation of wave vector $\mathbf{k}$ in the combined region $\cup_\alpha \Pi_\alpha$, with overlaps between the various Π_α and Π_β accounted for.

D.5.2 Two-Point Functions in One Dimension

In Section D.3.1, we saw that by varying the twist angle ϕ over the range $(-\pi, +\pi)$, we sample exactly the range of wave vectors that are occupied in the infinite one-dimensional noninteracting system. This allows us to recover the infinite-system limit of the ground-state energy per particle exactly. In this section, let us look at how well twist boundary conditions averaging does in reproducing infinite-system correlations such as the two-point function

$$G_{ij} = \langle \Psi | c_i^\dagger c_j | \Psi \rangle = \frac{1}{2\pi} \int_{-k_F}^{+k_F} dk \, e^{\mathrm{i}\, k(i-j)} = \frac{1}{2\pi} \int_{-\bar{n}\pi}^{+\bar{n}\pi} dk \, e^{\mathrm{i}\, k(i-j)}. \tag{D.5.12}$$

For a finite chain of noninteracting spinless fermions and subject to twist boundary conditions with phase twist ϕ, the two-point function evaluated directly from the finite-chain ground-state wave function is

$$G_{ij}(\phi) = \langle \Psi(\phi) | c_i^\dagger c_j | \Psi(\phi) \rangle = \frac{1}{N} \sum_{k(\phi) \text{ filled}} e^{\mathrm{i}\, k(i-j)}, \tag{D.5.13}$$

where N is the number of sites in the finite system. Using the results obtained in Section D.5.1, we find that the twist-boundary-conditions-averaged two point function

$$\bar{G}_{ij} = \frac{1}{2\pi} \int_{-\pi}^{\pi} d\phi \, G_{ij}(\phi) = \frac{1}{2\pi} \int_{-\bar{n}\pi}^{+\bar{n}\pi} dk \, e^{\mathrm{i}\, k(i-j)} \tag{D.5.14}$$

is none other than the infinite-system two-point function. Therefore, it is clear that twist boundary conditions averaging the finite-system two-point function reproduces its infinite-system limit exactly.

D.5.3 $2n$-Point Functions in One Dimension

In their investigation on the effectiveness of twist boundary conditions averaging for reducing finite size effects in correlation functions of the one-dimensional Hubbard model,

Nguyen *et al* noted that the method does not perform well for charge-charge correlation functions [384]. We look into this problem from the perspective of a noninteracting system, and consider the four-point function

$$\langle\Psi(\phi)|n_0 n_r|\Psi(\phi)\rangle = \frac{1}{N^2}\sum_{k_1}\sum_{k_2}\sum_{k_3}\sum_{k_4} e^{\mathrm{i}(k_3-k_4)r}\,\langle\Psi(\phi)|\tilde{c}^\dagger_{k_1}\tilde{c}_{k_2}\tilde{c}^\dagger_{k_3}\tilde{c}_{k_4}|\Psi(\phi)\rangle\,. \tag{D.5.15}$$

For the chain with $N = 4$ sites, let us denote by $\epsilon_a(\phi)$, $\epsilon_b(\phi)$, $\epsilon_c(\phi)$ and $\epsilon_d(\phi)$ the four ED bands single-particle energy bands. If we have $P = 2$ particles in this system, then the two filled bands $\epsilon_a(\phi)$ (red) and $\epsilon_b(\phi)$ (green) are shown in Figure D.4. For this 'many'-body ground state, the four-point function is simply

$$\begin{aligned}
\langle\Psi(\phi)|n_0 n_r|\Psi(\phi)\rangle = \frac{1}{16}\Big[&e^{\mathrm{i}\,k_a r}\,e^{-\mathrm{i}\,k_b r}\,\langle\Psi(\phi)|\tilde{c}^\dagger_{k_a}\tilde{c}^\dagger_{k_b}\tilde{c}_{k_a}\tilde{c}_{k_b}|\Psi(\phi)\rangle \\
&+ e^{\mathrm{i}\,k_a r}\,e^{-\mathrm{i}\,k_a r}\,\langle\Psi(\phi)|\tilde{c}^\dagger_{k_a}\tilde{c}^\dagger_{k_b}\tilde{c}_{k_b}\tilde{c}_{k_a}|\Psi(\phi)\rangle \\
&+ e^{\mathrm{i}\,k_b r}\,e^{-\mathrm{i}\,k_b r}\,\langle\Psi(\phi)|\tilde{c}^\dagger_{k_b}\tilde{c}^\dagger_{k_a}\tilde{c}_{k_a}\tilde{c}_{k_b}|\Psi(\phi)\rangle \\
&+ e^{\mathrm{i}\,k_b r}\,e^{-\mathrm{i}\,k_a r}\,\langle\Psi(\phi)|\tilde{c}^\dagger_{k_b}\tilde{c}^\dagger_{k_a}\tilde{c}_{k_b}\tilde{c}_{k_a}|\Psi(\phi)\rangle\Big] \\
= \frac{1}{16}\Big[&-e^{\mathrm{i}(k_a-k_b)r} + 1 + 1 - e^{-\mathrm{i}(k_a-k_b)r}\Big] \\
= \frac{1}{16}&\left[2 - 2\cos(k_a - k_b)r\right] = \frac{1}{4}\sin^2\tfrac{1}{2}(k_a - k_b)r,
\end{aligned} \tag{D.5.16}$$

where $k_a(\phi)$ and $k_b(\phi)$ are the wave vectors selected for $\epsilon_a(\phi)$ and $\epsilon_b(\phi)$ respectively.

Here we see the problem with twist boundary condition averaging four-point functions: for an infinite system, four-point functions can be reduced to a sum of integrals over the momentum transfer $K = k_a - k_b$, where k_a and k_b are free to take on values within the occupied range $(-k_F, k_F)$ *independently*. In the finite-system calculations, as we can see from Figure D.5, $k_a(\phi)$ and $k_b(\phi)$ cannot vary independently. In fact, for the $N = 4$ chain with $P = 2$ particles, $k_a(\phi) - k_b(\phi) = \pm\frac{\pi}{2}$, which means that the four-point function calculated from ED of such a system does not actually depend on the twist angle!

In general, for a chain with N sites and P particles, the four-point correlation function calculated at a particular twist angle would be

$$\langle\Psi(\phi)|n_0 n_r|\Psi(\phi)\rangle = \frac{1}{N^2}\sum_{\substack{k_a,k_b\\ \text{filled}}}\{1-\cos[(k_a-k_b)r]\}\,, \tag{D.5.17}$$

where the differences $(k_a - k_b)$ do not depend on ϕ, but changes from one region in the BZ partition to another. For $N = 4$ and $P = 2$, which corresponds to $\bar{n} = \frac{1}{2}$ in the infinite-system limit, $k_a - k_b = \pm\frac{\pi}{2}$, so that looking very specifically at the case of $r = 1$, we find that

$$\langle\Psi(\phi)|n_0 n_1|\Psi(\phi)\rangle = \frac{1}{4}\sin^2\tfrac{1}{2}(k_a-k_b) = \frac{1}{4}\sin^2\left(\pm\frac{\pi}{4}\right) = \frac{1}{8} = 0.125. \tag{D.5.18}$$

To get the infinite-system filling of $\bar{n} = \frac{1}{2}$, we can also work with $N = 6$ and $P = 3$, in which case we find the four-point function to be

$$\langle\Psi(\phi)|n_0 n_1|\Psi(\phi)\rangle = \frac{1}{36}\left[6-2\cos(k_a-k_b)-2\cos(k_a-k_c)-2\cos(k_b-k_c)\right], \tag{D.5.19}$$

where k_a, k_b and k_c are the three occupied ED band wave vectors. For this set of occupied wave vectors, the possible momentum transfers are

$$k_a - k_b = \pm\frac{\pi}{3}, \quad k_a - k_c = \pm\frac{2\pi}{3}, \quad k_b - k_c = \pm\frac{\pi}{3}. \tag{D.5.20}$$

Hence the four-point function works out to be

$$\begin{aligned}\langle\Psi(\phi)|n_0 n_1|\Psi(\phi)\rangle &= \frac{1}{36}\left[6-2\cos\left(\pm\frac{\pi}{3}\right)-2\cos\left(\pm\frac{2\pi}{3}\right)-2\cos\left(\pm\frac{\pi}{3}\right)\right]\\ &= \frac{1}{36}\left[6-1+1-1\right] = 0.138888\ldots.\end{aligned} \tag{D.5.21}$$

For $N = 8$ and $P = 4$, it is easy to show that

$$\begin{aligned}\langle\Psi(\phi)|n_0 n_1|\Psi(\phi)\rangle &= \frac{1}{64}\Big[12-2\cos\left(\pm\frac{\pi}{4}\right)-2\cos\left(\pm\frac{\pi}{2}\right)-2\cos\left(\pm\frac{3\pi}{4}\right)\\ &\qquad -2\cos\left(\pm\frac{\pi}{4}\right)-2\cos\left(\pm\frac{\pi}{2}\right)-2\cos\left(\pm\frac{\pi}{4}\right)\Big]\\ &= \frac{1}{64}\left[12-\sqrt{2}-0+\sqrt{2}-\sqrt{2}-0-\sqrt{2}\right]\\ &= 0.143305\ldots.\end{aligned} \tag{D.5.22}$$

Compared to the infinite-system limit of this four-point function at half-filling,

$$\langle\Psi|n_0 n_1|\Psi\rangle = \langle c_0^\dagger c_0\rangle\langle c_1^\dagger c_1\rangle - \langle c_0^\dagger c_1\rangle\langle c_1^\dagger c_0\rangle = \frac{1}{4} - \frac{1}{\pi^2} = 0.148678\ldots, \tag{D.5.23}$$

we find that we get better agreement as we go to larger systems. However, at a fixed finite system size, we obtain no improvement by varying ϕ, because none of the finite-system momentum transfers depends on ϕ. Therefore, we can argue generally that averaging over twist boundary conditions for a one-dimensional system does not help to bring $2n$-point functions, for $n > 1$, closer to the infinite-system limit.

D.5.4 $2n$-Point Functions in Two Dimensions

For a two-dimensional system of noninteracting spinless fermions, we saw based on our discussions in Section D.3.2 that the approximate Fermi surface formed by the twist-boundary-conditions-sampled infinite-system FBZ wave vectors exhibits finite size deviations from the infinite-system Fermi surface, *except* for the special filling fractions $\bar{n} = \frac{1}{2}, 1$, where the approximate and infinite-system Fermi surfaces agree. The goal of this subsection is to understand what effect(s) these finite size deviations have when we perform twist boundary conditions averaging on arbitrary functions $f(\mathbf{k})$ and $g(\mathbf{K})$, of the wave vector $\mathbf{k}$ and momentum transfer $\mathbf{K}$ respectively. We shall continue to think of the two-point function

$$G(\mathbf{r}_i, \mathbf{r}_j) = \frac{1}{4\pi^2}\int_{\text{occupied}} d^2\mathbf{k}\, e^{-\mathrm{i}\,\mathbf{k}\cdot(\mathbf{r}_i - \mathbf{r}_j)} \tag{D.5.24}$$

and the four-point function

$$\langle n_{\mathbf{r}_i} n_{\mathbf{r}_j}\rangle = \frac{1}{16\pi^4}\iint_{\text{occupied}} d^2\mathbf{k}\, d^2\mathbf{k}'\, \left\{1 - \cos\left[(\mathbf{k}' - \mathbf{k})\cdot(\mathbf{r}_i - \mathbf{r}_j)\right]\right\} \tag{D.5.25}$$

as examples of infinite-system FBZ-averages of functions

$$f(\mathbf{k}) = \exp\left[-\mathrm{i}\,\mathbf{k}\cdot(\mathbf{r}_i - \mathbf{r}_j)\right] \tag{D.5.26}$$

of the wave vector $\mathbf{k}$, and

$$g(\mathbf{K}) = 1 - \cos\left[\mathbf{K} \cdot (\mathbf{r}_i - \mathbf{r}_j)\right] \tag{D.5.27}$$

of the momentum transfer $\mathbf{K} = \mathbf{k}' - \mathbf{k}$, which we are attempting to approximate, by performing twist boundary conditions averaging on $f(\mathbf{k})$ and $g(\mathbf{K})$ respectively.

In the case of twist boundary conditions averaging $f(\mathbf{k})$ over the twist vector domain $(-\pi \leq \phi_x \leq +\pi) \times (-\pi \leq \phi_y \leq +\pi)$, we understand from Section D.3.2 that we are effectively averaging $f(\mathbf{k})$ over the region of the infinite-system FBZ bounded by the approximate Fermi surface. Since the approximate Fermi surface is not exact in two dimensions, except at the special filling fractions of $\bar{n} = \frac{1}{2}, 1$, we realized, without the need to go through the actual calculations, that unlike the case in one-dimension, finite size effects will not be completely eliminated.

Next, let us look at the twist boundary conditions averaging of $g(\mathbf{K})$ over the twist vector domain $(-\pi \leq \phi_x \leq +\pi) \times (-\pi \leq \phi_y \leq +\pi)$. From exactly diagonalizing a finite system of noninteracting spinless fermions at twist vector $\boldsymbol{\phi}$, the momentum transfer is rightfully $\mathbf{K}(\boldsymbol{\phi}) = \mathbf{k}_\alpha(\boldsymbol{\phi}) - \mathbf{k}_\beta(\boldsymbol{\phi})$, where α and β denote filled single-particle ED bands. As is the case for one-dimensional systems, we find from (D.2.46) that twist boundary conditions averaging samples a discrete set of momentum transfers. In two dimensions, these form 'shells' with sharp corners in the (K_x, K_y)-space. For example, for the $(3, 0) \times (0, 3)$ system subject to twist boundary conditions with twist vector $\boldsymbol{\phi} = (\phi_x, \phi_y)$, the discrete set of momentum transfers are illustrated in Figure D.41.

For $P = 5$ particles in the nine-site system, the single-particle wave vectors $\mathbf{k}_2$, $\mathbf{k}_4$, $\mathbf{k}_5$, $\mathbf{k}_6$ and $\mathbf{k}_8$ are occupied at the given twist vector $\boldsymbol{\phi}$. The set of momentum transfers we can obtain from these five occupied wave vectors is shown in Table D.1. From Table D.1, we see that the momentum transfers $\mathbf{K}_1$, $\mathbf{K}_3$, $\mathbf{K}_6$ and $\mathbf{K}_8$ are sampled twice, while the momentum transfers $\mathbf{K}_2$, $\mathbf{K}_4$, $\mathbf{K}_5$ and $\mathbf{K}_7$ are sampled three times. Therefore, if we

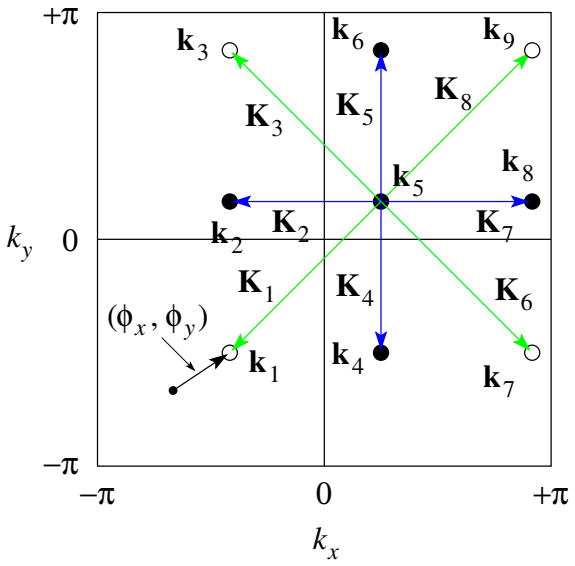

Figure D.41: The nine allowed wave vectors for the $(3,0)\times(0,3)$ system subject to twist boundary conditions with twist vector $\boldsymbol{\phi} = (\phi_x, \phi_y)$, and the eight momentum transfers that can be constructed from pairs of the nine allowed wave vectors. Blue momentum transfers have weight $w_{\mathbf{K}} = 3$, while green momentum transfers have weight $w_{\mathbf{K}} = 2$ (see text).

Table D.1: The set of momentum transfers $\mathbf{K}$ that can be obtained from the difference $\mathbf{k}_\alpha - \mathbf{k}_\beta$ of two, $\mathbf{k}_\alpha$ and $\mathbf{k}_\beta$, out of five occupied single-particle wave vectors, $\mathbf{k}_2$, $\mathbf{k}_4$, $\mathbf{k}_5$, $\mathbf{k}_6$ and $\mathbf{k}_8$. When $\mathbf{K}$ extends out of the infinite-system FBZ, we have what is known in solid-state physics as an Umklapp term. We add appropriate multiples of 2π to each component of $\mathbf{K}$ to determine its equivalent within the FBZ.

$\mathbf{k}_\alpha$	$\mathbf{k}_\beta$	$\mathbf{K}$	remark
$\mathbf{k}_2$	$\mathbf{k}_4$	$\mathbf{K}_3$	
$\mathbf{k}_2$	$\mathbf{k}_5$	$\mathbf{K}_2$	
$\mathbf{k}_2$	$\mathbf{k}_6$	$\mathbf{K}_1$	
$\mathbf{k}_2$	$\mathbf{k}_8$	$\mathbf{K}_7$	Umklapp
$\mathbf{k}_4$	$\mathbf{k}_2$	$\mathbf{K}_6$	
$\mathbf{k}_4$	$\mathbf{k}_5$	$\mathbf{K}_4$	
$\mathbf{k}_4$	$\mathbf{k}_6$	$\mathbf{K}_5$	Umklapp
$\mathbf{k}_4$	$\mathbf{k}_8$	$\mathbf{K}_1$	
$\mathbf{k}_5$	$\mathbf{k}_2$	$\mathbf{K}_7$	
$\mathbf{k}_5$	$\mathbf{k}_4$	$\mathbf{K}_5$	
$\mathbf{k}_5$	$\mathbf{k}_6$	$\mathbf{K}_4$	
$\mathbf{k}_5$	$\mathbf{k}_8$	$\mathbf{K}_2$	
$\mathbf{k}_6$	$\mathbf{k}_2$	$\mathbf{K}_8$	
$\mathbf{k}_6$	$\mathbf{k}_4$	$\mathbf{K}_4$	Umklapp
$\mathbf{k}_6$	$\mathbf{k}_5$	$\mathbf{K}_5$	
$\mathbf{k}_6$	$\mathbf{k}_8$	$\mathbf{K}_3$	
$\mathbf{k}_8$	$\mathbf{k}_2$	$\mathbf{K}_2$	Umklapp
$\mathbf{k}_8$	$\mathbf{k}_4$	$\mathbf{K}_8$	
$\mathbf{k}_8$	$\mathbf{k}_5$	$\mathbf{K}_7$	
$\mathbf{k}_8$	$\mathbf{k}_6$	$\mathbf{K}_6$	

convert the average

$$\frac{1}{N^2}\sum_{\substack{\mathbf{k}_\alpha,\mathbf{k}_\beta\\ \text{filled}}} g(\mathbf{k}_\alpha - \mathbf{k}_\beta) = \frac{1}{N^2}\sum_{\mathbf{K}} w_{\mathbf{K}} g(\mathbf{K}) \tag{D.5.28}$$

of $g(\mathbf{K}) = g(\mathbf{k}_\alpha - \mathbf{k}_\beta)$ from a double sum over the occupied single-particle wave vectors $\mathbf{k}_\alpha$ and $\mathbf{k}_\beta$ to a weighted sum over distinct values of $\mathbf{K}$, we obtain the list of weights

$$\begin{aligned} &w_{\mathbf{K}_1} = 2, \quad w_{\mathbf{K}_2} = 3, \quad w_{\mathbf{K}_3} = 2, \quad w_{\mathbf{K}_4} = 3, \\ &w_{\mathbf{K}_5} = 3, \quad w_{\mathbf{K}_6} = 2, \quad w_{\mathbf{K}_7} = 3, \quad w_{\mathbf{K}_8} = 2. \end{aligned} \tag{D.5.29}$$

When we vary the twist vector $\boldsymbol{\phi}$ over the twist angle domain $(-\pi \leq \phi_x \leq +\pi)\times(-\pi \leq \phi_y \leq +\pi)$, the set of occupied single-particle wave vectors $\{\mathbf{k}_\alpha\}$ changes, and consequently so does the set of momentum transfers, as shown in Figure D.42, for example. As a result, the sum over distinct momentum transfers $\mathbf{K}$ involve different sets of weights $w_{\mathbf{K}}$ at different twist vectors $\boldsymbol{\phi}$. Based on Figures D.41 and D.42, and Table D.1, we understand thus that the effect of averaging over all twist boundary conditions, is to average the weights $w_{\mathbf{K}}$. In Figure D.43, we show the twist-boundary-conditions-averaged weights for the $(3,0)\times(0,3)$ system with $P = 5$ particles, and compare them with the weights when the system is subject to plain periodic boundary conditions. As Figure D.43 illustrates, the effect of averaging over twist boundary conditions is to 'soften' the corners of the 'shells' of discrete momentum transfers.

In one dimension, we have seen that twist boundary conditions averaging is ineffective at reducing finite size effects in functions $g(\mathbf{K})$ of momentum transfer when $g(\mathbf{K})$ are calculated from a finite system. In two dimensions, we saw that the corners of the 'shells' of discrete momentum transfers are 'softened', but the magnitude of this 'softening' is small. To see whether this 'softened' set of weights will result in an averaged $g(\mathbf{K})$ that approximates the infinite-system FBZ-average better than the 'hard' set of weights, we return to the example of the $(3,0)\times(0,3)$ system, to calculate the

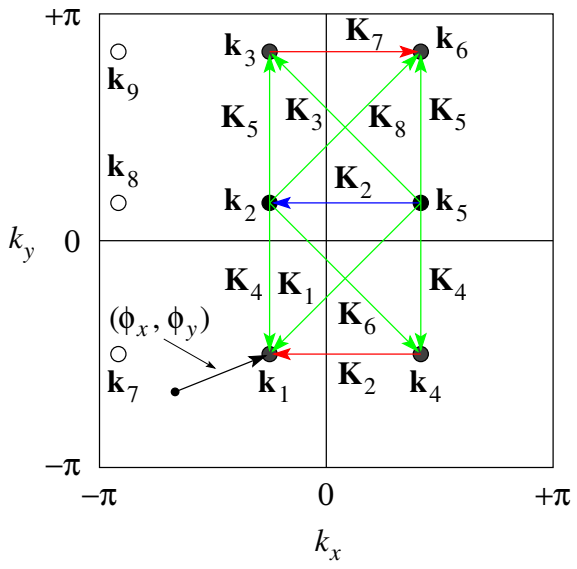

Figure D.42: The nine allowed wave vectors for the $(3,0)\times(0,3)$ system subject to twist boundary conditions with twist vector $\boldsymbol{\phi} = (\phi_x, \phi_y)$, and some momentum transfers that can be constructed from pairs of the occupied wave vectors. For $P = 5$ particles in the nine-site system, the wave vectors $\mathbf{k}_2$ and $\mathbf{k}_5$, which are shown as black solid circles, have unit filling, while the wave vectors $\mathbf{k}_1$, $\mathbf{k}_3$, $\mathbf{k}_4$ and $\mathbf{k}_6$, which are shown as gray circles, are three-quarter filled. Momentum transfers with different weights are shown in different colors.

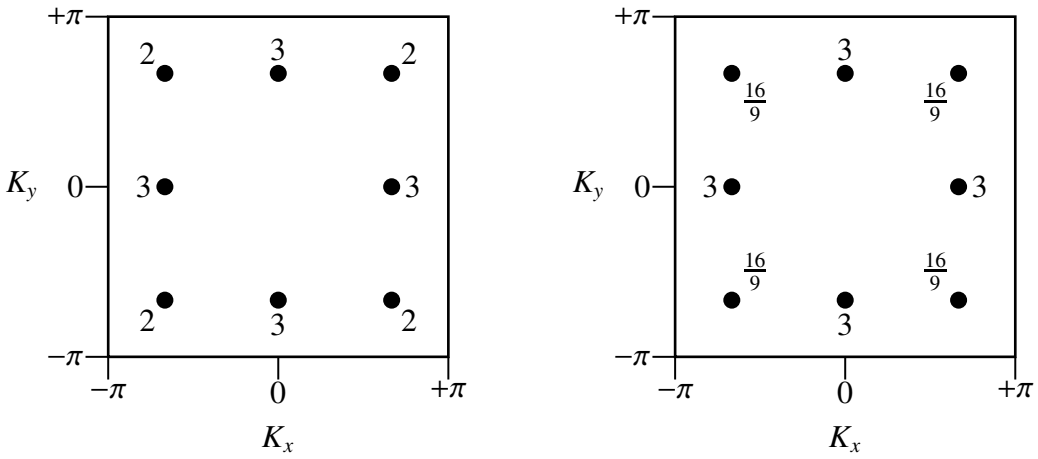

Figure D.43: Distinct momentum transfers $\mathbf{K}$ and their respective weights $w_{\mathbf{K}}$ for the $(3,0)\times(0,3)$ system with $N = 5$ particles, subject to (a) periodic boundary conditions, and (b) twist boundary conditions averaging.

four-point function $\langle n_{(0,0)} n_{(1,0)} \rangle$. We find that, when subjected to plain periodic boundary conditions, this four-point function evaluates to

$$\begin{aligned}\frac{1}{N^2}\sum_{\mathbf{K}} w_{\mathbf{K}}\,(1-\cos K_x) = \tfrac{1}{81}\Big[&2(1-\cos\tfrac{2\pi}{3}) + 3(1-\cos\tfrac{2\pi}{3}) + 2(1-\cos\tfrac{2\pi}{3}) + \\ &3(1-\cos 0) + 3(1-\cos 0) + \\ &2(1-\cos\tfrac{2\pi}{3}) + 3(1-\cos\tfrac{2\pi}{3}) + 2(1-\cos\tfrac{2\pi}{3})\Big] \\ = \tfrac{14}{81}(1-\cos\tfrac{2\pi}{3}) &= 0.259259\ldots,\end{aligned} \tag{D.5.30}$$

whereas with twist boundary conditions averaging, $\langle n_{(0,0)} n_{(1,0)} \rangle$ evaluates to

$$\begin{aligned}\frac{1}{N^2}\sum_{\mathbf{K}} w_{\mathbf{K}}\,(1-\cos K_x) = \tfrac{1}{81}\Big[&\tfrac{16}{9}(1-\cos\tfrac{2\pi}{3}) + 3(1-\cos\tfrac{2\pi}{3}) + \\ &\tfrac{16}{9}(1-\cos\tfrac{2\pi}{3}) + 3(1-\cos 0) + 3(1-\cos 0) + \\ &\tfrac{16}{9}(1-\cos\tfrac{2\pi}{3}) + 3(1-\cos\tfrac{2\pi}{3}) + \tfrac{16}{9}(1-\cos\tfrac{2\pi}{3})\Big] \\ = \tfrac{118}{729}(1-\cos\tfrac{2\pi}{3}) &= 0.242798\ldots.\end{aligned} \tag{D.5.31}$$

By evaluating the sum

$$\frac{1}{N^2}\sum_{\substack{\mathbf{k},\mathbf{k}'\\ \text{filled}}}[1-\cos(k'_x-k_x)] \tag{D.5.32}$$

numerically for a large system with $N \approx 10^4$, we find the infinite-system limit of the four-point function to be

$$\langle n_{(0,0)}n_{(1,0)}\rangle = 0.26827. \tag{D.5.33}$$

We see therefore that the value of $\langle n_{(0,0)}n_{(1,0)}\rangle$ evaluated from the $(3,0)\times(0,3)$ system subject to plain periodic boundary conditions to be a poor approximation of the infinite-system value of $\langle n_{(0,0)}n_{(1,0)}\rangle$. When we twist boundary conditions average the $(3,0)\times(0,3)$ system, the agreement between the twist-boundary-conditions averaged value of $\langle n_{(0,0)}n_{(1,0)}\rangle$ and the infinite-system value of $\langle n_{(0,0)}n_{(1,0)}\rangle$ became worst. We believe that this degradation in the quality of the approximation is not generic, and the generic situation is that, just as in the one-dimensional case, twist boundary conditions averaging does no better than plain periodic boundary conditions, at reducing finite size effects and approximating the infinite-system limits of four-, and higher $2n$-point functions.

For an interacting Fermi liquid, the ground state is a complicated beast, but its low-energy excitation spectrum has the same structure as that of a noninteracting Fermi liquid. Therefore, if we think of the two-point function $\langle\Psi|c^\dagger_{\mathbf{r}}c_{\mathbf{r}'}|\Psi\rangle$ as the overlap between the excited states $c_{\mathbf{r}}|\Psi\rangle = N^{-1/2}\sum_{\mathbf{k}} e^{-i\mathbf{k}\cdot\mathbf{r}}\,\tilde{c}_{\mathbf{k}}|\Psi\rangle$ and $c_{\mathbf{r}'}|\Psi\rangle = N^{-1/2}\sum_{\mathbf{k}} e^{-i\mathbf{k}\cdot\mathbf{r}'}\,\tilde{c}_{\mathbf{k}}|\Psi\rangle$, we can make use of the fact that the bare operators $\tilde{c}_{\mathbf{k}}$ are related to the quasiparticle operators $\tilde{C}_{\mathbf{k}}$ by a unitary transformation, and write the two excited states properly as a sum over the action on $|\Psi\rangle$ by the quasiparticle operators. Since the unitary transformation relating $\tilde{c}_{\mathbf{k}}$ and $\tilde{C}_{\mathbf{k}}$ gives $\tilde{c}_{\mathbf{k}}$ as a sum of terms, starting from $\tilde{C}_{\mathbf{k}}$, but also involving

$\tilde{C}_{\mathbf{k}}\tilde{C}^{\dagger}_{\mathbf{k}'}\tilde{C}_{\mathbf{k}}$, $\tilde{C}_{\mathbf{k}}\tilde{C}^{\dagger}_{\mathbf{k}'}\tilde{C}_{\mathbf{k}'}\tilde{C}^{\dagger}_{\mathbf{k}''}\tilde{C}_{\mathbf{k}''}$, and higher powers of $\tilde{C}_{\mathbf{k}}$, we find that the two-point function

$$\langle\Psi|c_i^{\dagger}c_j|\Psi\rangle = \frac{1}{N}\sum_{\mathbf{k}} f_1(\mathbf{k}) + \frac{1}{N^2}\sum_{\mathbf{k},\mathbf{k}'} f_2(\mathbf{k},\mathbf{k}') + \frac{1}{N^3}\sum_{\mathbf{k},\mathbf{k}',\mathbf{k}''} f_3(\mathbf{k},\mathbf{k}',\mathbf{k}'') + \cdots \quad \text{(D.5.34)}$$

is not the infinite-system FBZ average of a function $f_1(\mathbf{k})$ of a single wave vector $\mathbf{k}$, but also involves terms which are the infinite-system FBZ averages of the functions $f_2(\mathbf{k},\mathbf{k}')$ of two wave vectors $\mathbf{k}$ and $\mathbf{k}'$, $f_3(\mathbf{k},\mathbf{k}',\mathbf{k}'')$ of three wave vectors $\mathbf{k}$, $\mathbf{k}'$ and $\mathbf{k}'$, and even higher-order terms involving more wave vectors.

From our discussions earlier in this section, we know that the method of twist boundary conditions averaging approximates the infinite-system FBZ average of functions $f(\mathbf{k})$ of a single wave vector $\mathbf{k}$ well, because the occupied wave vectors $\mathbf{k}$ in the infinite-system FBZ can be sampled continuously by varying $\boldsymbol{\phi}$. On the other hand, the method of twist boundary conditions averaging does a poor job approximating the infinite-system FBZ average of functions $g(\mathbf{k},\mathbf{k}')$ of two wave vectors $\mathbf{k}$ and $\mathbf{k}'$, because the sum of the two wave vectors $\mathbf{k}'+\mathbf{k}$ can be sampled continuously by varying $\boldsymbol{\phi}$, but not the difference of the two wave vectors $\mathbf{k}'-\mathbf{k}$. Similarly, for $n \geq 3$ wave vectors, there will be one linear combination of wave vectors that cannot be sampled continuously by varying $\boldsymbol{\phi}$. For this reason, the twist-boundary-conditions-averaged functions of $\mathbf{k}'-\mathbf{k}$, and other ineffectively sampled linear combinations of three or more wave vectors, will continue to be plagued by finite size effects. We expect thus that the method of twist boundary conditions averaging produces a poorer estimate of the infinite-system limit of all correlations, of an interacting Fermi liquid in particular, and of other interacting systems in general.

D.6 Twist Boundary Conditions Averaging and Brillouin Zone Integration

In Section D.5.4, we saw that twist boundary conditions averaging will not eliminate finite size effects when we use it to calculate two-point functions, because of the approximate nature of the Fermi surface formed by the set of FBZ wave vectors sampled. For higher $2n$-point functions, twist boundary conditions averaging offers no improvement over the results obtained with only periodic boundary conditions. For the expectation of a typical observable, which can always be written as a sum of products of $2n$-point functions, we will most likely find ourselves stuck with some remnant finite size effects that cannot be gotten rid of even with the most industrious application of twist boundary conditions averaging.

While this sounds depressing, to say the least, it is the best we can do, if we are constrained to work with one particular small finite system, and not a sequence of finite systems. In the latter case, we can improve upon the results from twist boundary conditions by performing a further extrapolation. With this in mind, we ask ourselves a question on the technical implementation of twist boundary conditions averaging: should we be aiming for a faithful integration of the twist surface, by taking into account its piecewise continuous nature as defined by the set of all partition curves? After all, Poilblanc shifted integrations points off the partition lines to avoid cusps and cuts, and obtained rather decent-looking results [398, 399]. In other words, should we care about incurring a 1% error whilst integrating over the twist surface, when the converged numerical integration over the approximate Fermi surface leads us to an answer that deviates from the infinite-system limit by 5%?

D.6.1 Brillouin Zone Integration

Here we shall argue that, in the absence of *a priori* knowledge of the momentum distribution, which is the case for interacting systems, performing a faithful integration of the twist surface is the best that we can do. Having said this, we need to take into account the possibility that each integration point might be computationally expensive to obtain — which it is, for the cluster density matrix elements of a system of spinless fermions with infinite nearest-neighbor repulsion. Moreover, we know of the presence of cusps and cuts in the twist surface, and where they are if we are handed the dispersion relations, as is the case for noninteracting spinless fermions, but such information will not come to us easily for an interacting system. In response to such a challenge, and understanding how the problem of integrating over $\boldsymbol{\phi}$ is very much like the problem of integrating $\mathbf{k}$ in the FBZ, we learn from the computational electronic structure community, where the problem of integrating the band structure over the FBZ is frequently encountered. Two integration schemes are commonly in use, the special-point scheme [412–417] and the tetrahedron scheme [418–420, 422–428].

The reason we find two instead of one popular method of FBZ integration in the literature is, according to Blöchl [429], their complementary nature: the special-point scheme is good for semiconductors and insulators, using information from a small set of sampling wave vectors, but not good for metals, whereas the tetrehedron integration scheme is designed for the partially filled bands of metals, although accuracy is achieved at the expense of a larger set of sampling wave vectors. Of course, there are exceptions to this general characterization. Enders points out that the special-point scheme fails in semiconductors for certain band structures [430], while Pickard and Payne identifies band crossing as one problem that impairs both the tetrahedron integration scheme and the special-point scheme [431]. The special-point scheme has also been made to work

on metals through the use of smearing techniques to smooth out discontinuities in the momentum distribution, the most successful being the one by Methfessel and Paxton [432].

D.6.2 Special-Point Integration Scheme

D.6.2.1 Historical Background

We look first at the special-point integration scheme [412–417], which is suggested by Lin, Zong and Ceperley [411] for twist boundary conditions averaging because it typically requires only a few integration points. The special-point integration scheme is, in essence, an approximation scheme that seeks to replace an integration over the FBZ by a weighted sum over a set of special wave vectors,

$$\frac{1}{V_{\mathrm{FBZ}}} \int d^3\mathbf{k}\, f(\mathbf{k}) \approx \sum_i w_i f(\mathbf{k}_i), \tag{D.6.1}$$

where $\{\mathbf{k}_i\}$ is the set of special points, and $\{w_i\}$ are their corresponding weights. The idea that this can be done for a function $f(\mathbf{k})$ which is reasonably smoothly varying over the FBZ is first put forth by Baldereschi, who approximated the FBZ average using a single special point, called the *mean value point* or the *Baldereschi point* [412]. Motivated by this result, Chadi and Cohen first extended Baldereschi's analysis to an integration scheme with three special points at Γ, X and L [413], before explaining in a subsequent paper the theoretical basis for the special-point integration scheme [414].

Given a periodic function $f(\mathbf{k})$ which has the complete symmetry of the lattice, we can always write it as

$$f(\mathbf{k}) = f_0 + \sum_{m=1}^{\infty} f_m A_m(\mathbf{k}), \tag{D.6.2}$$

where

$$A_m(\mathbf{k}) = \sum_{|\mathbf{r}|=C_m} e^{\mathrm{i}\,\mathbf{k}\cdot\mathbf{r}}, \tag{D.6.3}$$

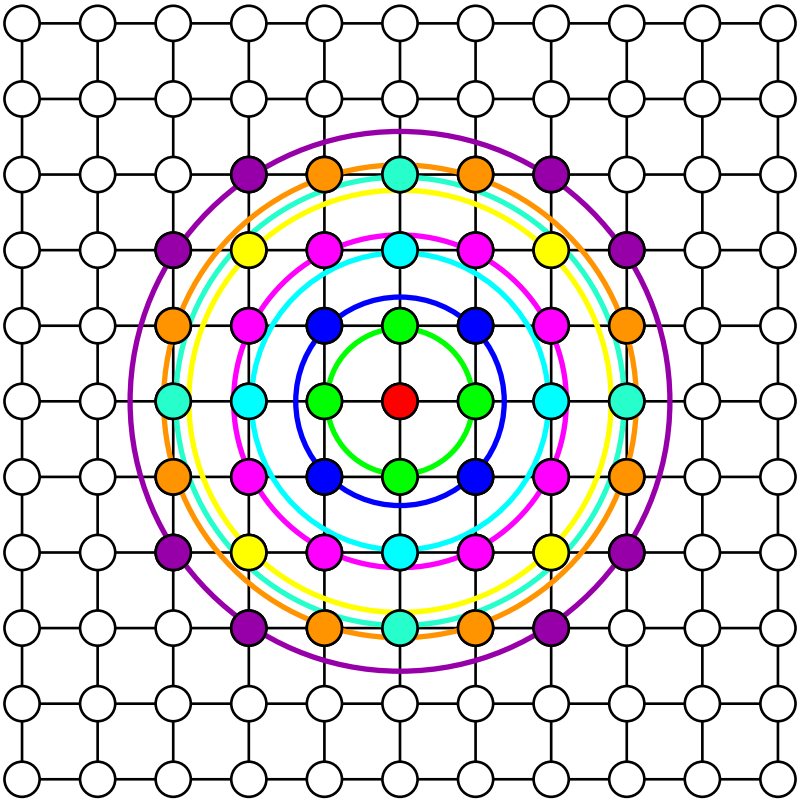

Figure D.44: The first nine shells of the square lattice.

is the plane wave symmetrized over the mth *star* or *shell* of sites $\mathbf{r}$ related to each other by point group symmetries of the lattice. For example, the first few shells of sites of the square lattice is shown in Figure D.44. When we integrate over the FBZ, the average value of $f(\mathbf{k})$ is simply given by f_0. Therefore, if it is possible to find a set of special points $\{\mathbf{k}_i\}$ for which $A_m(\mathbf{k}_i) = 0$ for all m, evaluation of the integral of $f(\mathbf{k})$ would be equivalent to evaluation of $f(\mathbf{k})$ at any of these special points.

Of course, the real world is not so rosy, and such special points do not in fact exist, so Chadi and Cohen shot for the next best thing: because for a smoothly varying function, the coefficients f_m decay rapidly with m, we can truncate the Fourier series (D.6.2), and write

$$f(\mathbf{k}) \approx f_0 + \sum_{m=1}^{N} f_m A_m(\mathbf{k}). \tag{D.6.4}$$

For this finite set of symmetrized plane waves, it is then possible to find a set of n special points $\{\mathbf{k}_i\}$ and weights $\{w_i\}$, such that

$$\begin{gathered} \sum_{i=1}^{n} w_i A_m(\mathbf{k}_i) = 0, \quad m = 1, \ldots, N; \\ \sum_{i=1}^{n} w_i = 1. \end{gathered} \tag{D.6.5}$$

It can then be shown, using the fact that the symmetrized plane waves are orthogonal functions over the FBZ, that

$$f_0 \approx \sum_{i=1}^{n} w_i f(\mathbf{k}_i). \tag{D.6.6}$$

Chadi and Cohen then proved that one can recursively refine the above approximation by augmenting the existing set of special points. After developing the method, they calculated the first few lower order special point sets for the SC, BCC, FCC, and HCP lattices. Following this, Cunningham applied Chadi and Cohen's method to work out the special point sets for various 2-dimensional lattices [433], while Macot and Frank,

and later Rogan and Lagos, worked out in greater detail formulas for the Chadi-Cohen method [434, 435].

The next major development came when Monkhorst and Pack realized that the symmetrized plane waves with $m = 1, \ldots, N(q)$ form a set of orthonormal functions over the discrete set of wave vectors

$$\mathbf{k}_{prs} = u_p \, \mathbf{b}_1 + u_r \, \mathbf{b}_2 + u_s \, \mathbf{b}_3, \tag{D.6.7}$$

where $\mathbf{b}_i$ are the primitive reciprocal lattice vectors, and

$$u_r = \frac{2r - q - 1}{2q}, \quad r = 1, 2, \ldots, q, \tag{D.6.8}$$

is a set of q fractional indices, which generates a uniform mesh over the FBZ. This became a catalyst for the popularity of the special-point scheme because of the ease in generating increasingly refined sets of special points, without the need to solve (D.6.5) or recursion. Moreno and Soler later explained that the special-point scheme is just a fancy way to put a uniform mesh of $\mathbf{k}$-points onto the FBZ, which can done more transparently by choosing a cutoff length in real space, compute the corresponding Δk, and then mesh the FBZ, or just the irreducible part of the FBZ (IBZ) [436]. Hama and Watanabe explained that the special-point scheme is an open-type Lagrange quadrature of lowest order, and derived more formulas for constructing sets of special points and their weights, apart from those given by the Monkhorst-Pack formula (D.6.8) [437].

D.6.2.2 Performance

Seeing that twist boundary conditions averaging samples the filled infinite-system wave vectors exactly for the one-dimensional noninteracting system, we expect the integration using special points generated by the Monkhorst-Pack scheme to converge onto the exact infinite-system limit for observables such as ground-state energy per particle. Indeed,

Table D.2: The Monkhorst-Pack sampling wave vectors $\mathbf{k}_{pr}$, and their associated weights w_{pr} in the IBZ, of order $q = 1$ to $q = 5$ for a two-dimensional square lattice. Here u_r are the fractional indices given by (D.6.8), and $N(q)$ the number of sampling wave vectors within the IBZ. If we had chose to integrate over the entire FBZ, there would be q^2 sampling wave vectors for order q, having equal weights $1/q^2$.

q	u_r	$\mathbf{k}_{pr}$	w_{pr}	$N(q)$
1	0	$(0,0)$	1	1
2	$-\frac{1}{4}, \frac{1}{4}$	$\pi(\frac{1}{2}, \frac{1}{2})$	1	1
3	$-\frac{1}{3}, 0, \frac{1}{3}$	$(0,0)$	$\frac{1}{9}$	3
		$\pi(\frac{2}{3}, 0)$	$\frac{4}{9}$	
		$\pi(\frac{2}{3}, \frac{2}{3})$	$\frac{4}{9}$	
4	$-\frac{3}{8}, -\frac{1}{8}, \frac{1}{8}, \frac{3}{8}$	$\pi(\frac{1}{4}, \frac{1}{4})$	$\frac{1}{4}$	3
		$\pi(\frac{3}{4}, \frac{1}{4})$	$\frac{1}{2}$	
		$\pi(\frac{3}{4}, \frac{3}{4})$	$\frac{1}{4}$	
5	$-\frac{2}{5}, -\frac{1}{5}, 0,$	$(0,0)$	$\frac{1}{25}$	6
	$\frac{1}{5}, \frac{2}{5}$	$\pi(\frac{2}{5}, 0)$	$\frac{4}{25}$	
		$\pi(\frac{2}{5}, \frac{2}{5})$	$\frac{4}{25}$	
		$\pi(\frac{4}{5}, 0)$	$\frac{4}{25}$	
		$\pi(\frac{4}{5}, \frac{2}{5})$	$\frac{8}{25}$	
		$\pi(\frac{4}{5}, \frac{4}{5})$	$\frac{4}{25}$	

Table D.3: The Monkhorst-Pack sampling wave vectors $\mathbf{k}_{pr}$, and their associated weights w_{pr} in the IBZ, of order $q = 6$ to $q = 7$ for a two-dimensional square lattice. Here u_r are the fractional indices given by (D.6.8), and $N(q)$ the number of sampling wave vectors within the IBZ. If we had chose to integrate over the entire FBZ, there would be q^2 sampling wave vectors for order q, having equal weights $1/q^2$.

q	u_r	$\mathbf{k}_{pr}$	w_{pr}	$N(q)$
6	$-\frac{5}{12}, -\frac{3}{12}, -\frac{1}{12},$	$\pi(\frac{1}{6}, \frac{1}{6})$	$\frac{1}{9}$	6
	$\frac{1}{12}, \frac{3}{12}, \frac{5}{12}$	$\pi(\frac{1}{2}, \frac{1}{6})$	$\frac{2}{9}$	
		$\pi(\frac{1}{2}, \frac{1}{2})$	$\frac{1}{9}$	
		$\pi(\frac{5}{6}, \frac{1}{6})$	$\frac{2}{9}$	
		$\pi(\frac{5}{6}, \frac{1}{2})$	$\frac{2}{9}$	
		$\pi(\frac{5}{6}, \frac{5}{6})$	$\frac{1}{9}$	
7	$-\frac{3}{7}, -\frac{2}{7},$	$(0, 0)$	$\frac{1}{49}$	10
	$-\frac{1}{7}, 0, \frac{1}{7}$	$\pi(\frac{1}{4}, 0)$	$\frac{4}{49}$	
	$\frac{2}{7}, \frac{3}{7}$	$\pi(\frac{1}{4}, \frac{1}{4})$	$\frac{4}{49}$	
		$\pi(\frac{1}{2}, 0)$	$\frac{4}{49}$	
		$\pi(\frac{1}{2}, \frac{1}{4})$	$\frac{8}{49}$	
		$\pi(\frac{1}{2}, \frac{1}{2})$	$\frac{4}{49}$	
		$\pi(\frac{3}{4}, 0)$	$\frac{4}{49}$	
		$\pi(\frac{3}{4}, \frac{1}{4})$	$\frac{8}{49}$	
		$\pi(\frac{3}{4}, \frac{1}{2})$	$\frac{8}{49}$	
		$\pi(\frac{3}{4}, \frac{3}{4})$	$\frac{4}{49}$	

Table D.4: The Monkhorst-Pack sampling wave vectors $\mathbf{k}_{pr}$, and their associated weights w_{pr} in the IBZ, of order $q = 8$ for a two-dimensional square lattice. These sampling wave vectors were also derived by Cunningham using the Chadi-Cohen method (see reference in text). Here u_r are the fractional indices given by (D.6.8), and $N(q)$ the number of sampling wave vectors within the IBZ. If we had chose to integrate over the entire FBZ, there would be q^2 sampling wave vectors for order q, having equal weights $1/q^2$.

q	u_r	$\mathbf{k}_{pr}$	w_{pr}	$N(q)$
8	$-\frac{7}{16}, -\frac{5}{16},$	$\pi(\frac{1}{8}, \frac{1}{8})$	$\frac{1}{16}$	10
	$-\frac{3}{16}, -\frac{1}{16},$	$\pi(\frac{3}{8}, \frac{1}{8})$	$\frac{1}{8}$	
	$\frac{1}{16}, \frac{3}{16},$	$\pi(\frac{3}{8}, \frac{3}{8})$	$\frac{1}{16}$	
	$\frac{5}{16}, \frac{7}{16}$	$\pi(\frac{5}{8}, \frac{1}{8})$	$\frac{1}{8}$	
		$\pi(\frac{5}{8}, \frac{3}{8})$	$\frac{1}{8}$	
		$\pi(\frac{5}{8}, \frac{5}{8})$	$\frac{1}{16}$	
		$\pi(\frac{7}{8}, \frac{1}{8})$	$\frac{1}{8}$	
		$\pi(\frac{7}{8}, \frac{3}{8})$	$\frac{1}{8}$	
		$\pi(\frac{7}{8}, \frac{5}{8})$	$\frac{1}{8}$	
		$\pi(\frac{7}{8}, \frac{7}{8})$	$\frac{1}{16}$	

for $N = 3$ and $\bar{n} = \frac{2}{3}$, whose infinite-system ground-state energy per particle is $E/P = -3\sqrt{3}/2\pi = -0.826993\ldots$, the Monkhorst-Pack integration scheme does approach this value as the order q of the integration scheme is increased (see Tables D.2 to D.4 for the sampling wave vectors, generated using (D.6.8), associated with order q). This is shown in Figure D.45. We observe that the even q's converge onto the infinite-system limit from below, while the odd q's converge onto the infinite-system limit from above. For comparable q's, the performance with even q is slightly better than for odd q.

For two-dimensional noninteracting systems, we first examine the performance of the Monkhorst-Pack scheme for the $(2,0) \times (0,2)$ system, which is square. For this system, we know that the Fermi surface sampled by twist boundary conditions averaging agrees with the infinite-system Fermi surface at $\bar{n} = \frac{1}{2}$. Figure D.46 shows the infinite-system wave vectors sampled by the $q = 3$ Monkhorst-Pack integration points over the unrestricted twist angle domain $(-\pi, +\pi) \times (-\pi, +\pi)$, while Figure D.47 shows the expected convergence, as the order q of the integration scheme is increased, of the ground-state energy per particle E/P and the two-point function $\langle\Psi|c^{\dagger}_{(0,0)}c_{(1,0)}|\Psi\rangle$, onto their respective infinite-system limits.

We then investigate the performance of the Monkhorst-Pack scheme for the $(2,1) \times (1,2)$ system with $\bar{n} = \frac{1}{3}$ and $\bar{n} = \frac{2}{3}$, integrating over the restricted twist angle domain. This is shown in Figure D.48. As we can see, for the ground-state energy per particle E/P, the special-point scheme converges fairly rapidly, by $q \approx 5$, onto the twist boundary conditions averaged values, which are the values of E/P calculated by analytically integrating over the approximate Fermi surfaces. The twist boundary conditions averaged values of E/P for $\bar{n} = \frac{1}{3}$ and $\bar{n} = \frac{2}{3}$ are then found to be close to their respective infinite-system limits. For the two-point function $\langle\Psi|c^{\dagger}_{(0,0)}c_{(1,0)}|\Psi\rangle$, the special-point scheme converges slower, particularly for $\bar{n} = \frac{2}{3}$, but otherwise the limiting values as

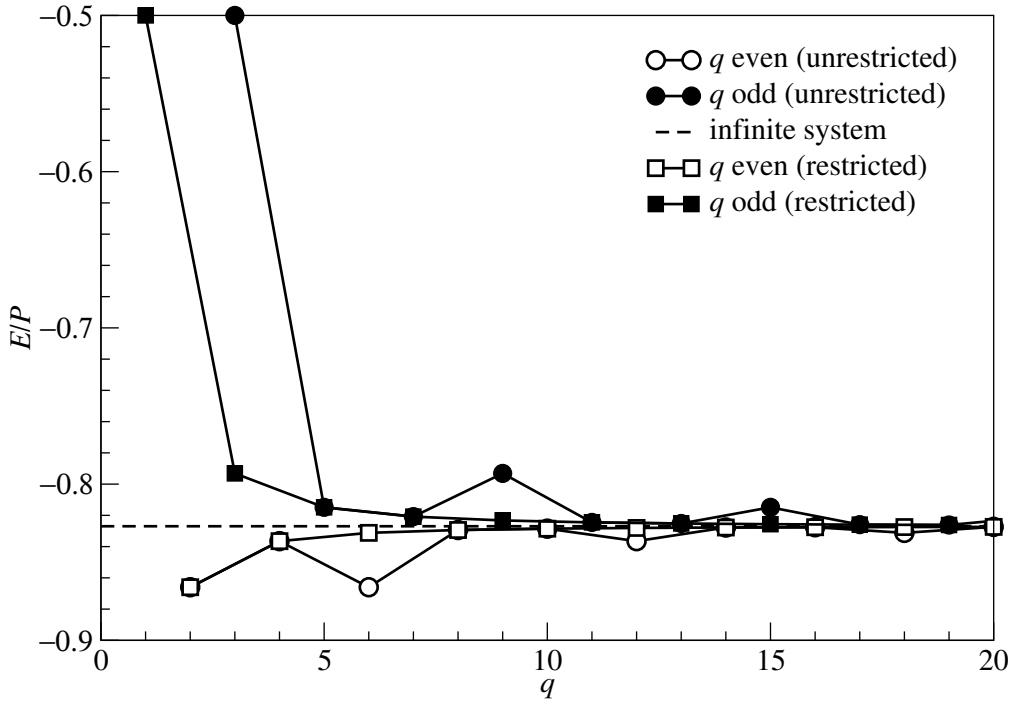

Figure D.45: Performance of the Monkhorst-Pack special-point integration scheme in twist boundary-conditions-averaging, over the unrestricted and restricted range of twist angles, the ground-state energy per particle E/P of the one-dimensional system of non-interacting spinless fermions with $N = 3$ and $\bar{n} = \frac{2}{3}$. Convergence to the infinite-system limit, shown as the dashed line, is fairly rapid whether we used the unrestricted or restricted range. For Monkhorst-Pack special-point integration over the restricted range of twist angles $-\frac{\pi}{3} \leq \phi < +\frac{\pi}{3}$, convergence is effectively achieved at $q \approx 8$, whereas over the unrestricted range $-\pi \leq \phi < +\pi$, convergence is effectively achieved at $q \approx 16$. Comparing the convergence of the special-point integration scheme over the restricted and unrestricted range of twist angles, we find the integration over the restricted range of twist angles converging monotonically with q, and the integration over the unrestricted range of twist angles converging non-monotonically with q.

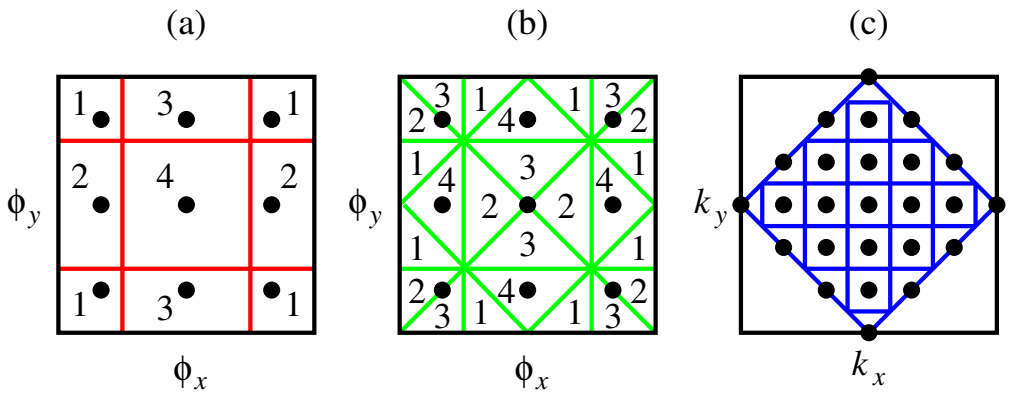

Figure D.46: Monkhorst-Pack special points of order $q = 3$, in relation to (a) the $\alpha = 1$ BZ partition, and (b) the $\alpha = 2$ BZ partition of the $(2,0) \times (0,2)$ system with $P = 2$ particles subject to twist boundary conditions. The combined set of infinite-system wave vectors sampled by these special points from the $\alpha = 1, 2$ BZ partitions is shown in (c). Looking at the weight associated with each sampled infinite-system wave vector, we find that the special-point integration scheme is equivalent to a rectangular integration scheme, illustrated schematically in (c).

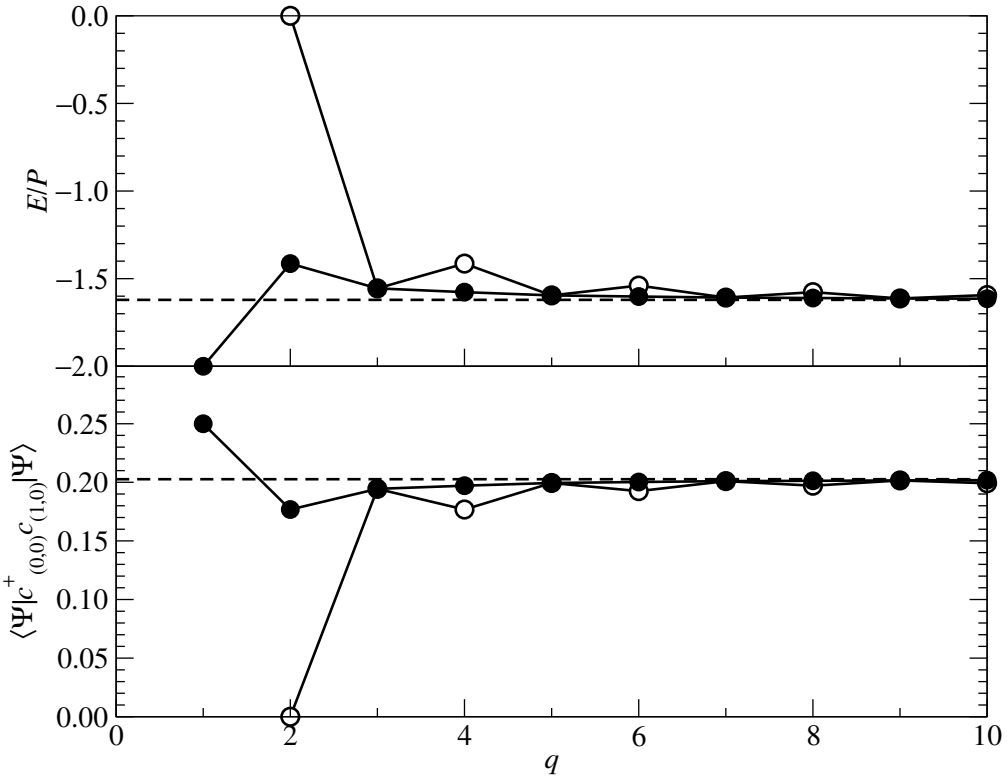

Figure D.47: Performance of the Monkhorst-Pack special-point integration scheme in twist boundary conditions averaging, over the unrestricted (open circles) and restricted (filled circles) twist angle domains, the ground-state energy per particle E/N (top) and two-point function $\langle\Psi|c^{\dagger}_{(0,0)}c_{(1,0)}|\Psi\rangle$ (bottom) of the $(2,0)\times(0,2)$ system of $P = 2$ noninteracting spinless fermions. The infinite-system limit of these two quantities are shown as dashed lines in the respective plots.

$q \to \infty$ are close to the infinite-system limits.

As we can see, the special-point integration scheme performs rather well, as far as convergence to the faithful integration over the approximate Fermi surface is concerned. The convergence is not onto the infinite-system limit, but this can be attributed to the fact that the Fermi surface generated by twist boundary conditions averaging (and orientation averaging, if necessary) does not approximate the infinite-system Fermi surface well enough. In any case, we see that while the special-point method was conceived to handle smooth functions $f(\mathbf{k})$ whose symmetrized Fourier coefficients fall off rapidly, it handles functions with cusps and cuts reasonably well with a small number of special points, so long as their symmetrized Fourier coefficients fall off sufficiently fast.

D.6.2.3 Minimum Monkhorst-Pack Special-Point Integration Order

In fact, having understood that the special-point integration scheme over the twist angle domain is essentially equivalent to a rectangular integration scheme over the approximate momentum distribution in the infinite-system FBZ, we can make a rough estimate for the minimum Monkhorst-Pack order q needed to special-point integrate a two-dimensional surface to a prescribed precision. Based on our understanding of the gross structure of the BZ partition, we know that for a N-site system, the unrestricted twist angle domain $(-\pi \leq \phi_x \leq +\pi) \times (-\pi \leq \phi_y \leq +\pi)$ is partitioned into many regions, each labelled by the quantum number n of a wave vector $\mathbf{k}_{0n}$ allowed by periodic boundary conditions. There are N such allowed wave vectors, $n = 1, \ldots, N$, and the combined area of the regions labelled by quantum number n is $4\pi^2/N$. We call the union of the regions labelled by quantum number n the *twist angle region covered by the quantum number n*, and note that twist angle regions covered by each of the N quantum numbers have the same area.

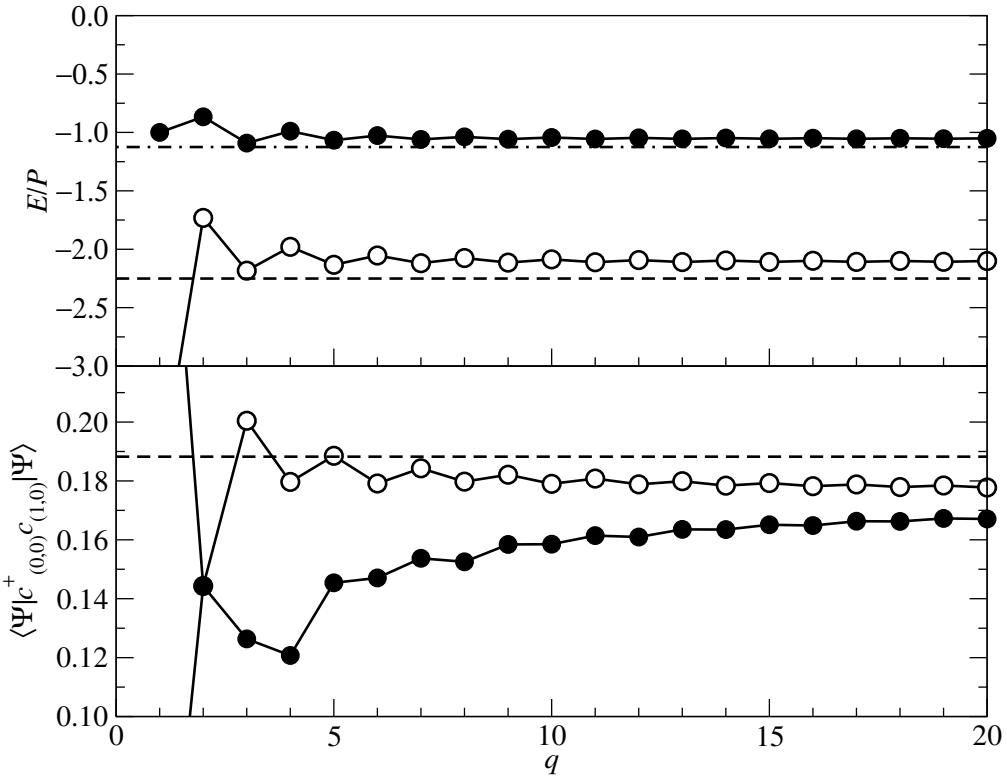

Figure D.48: Performance of the Monkhorst-Pack special-point integration scheme in twist boundary conditions averaging, over the restricted twist angle domain, the ground-state energy per particle E/P (top) and two-point function $\langle\Psi|c^{\dagger}_{(0,0)}c_{(1,0)}|\Psi\rangle$ (bottom) of the $(2,1)\times(1,2)$ system of $P = 1, 2$ noninteracting spinless fermions. We see that E/P for $\bar{n} = \frac{1}{3}$ (○) and $\bar{n} = \frac{2}{3}$ (●) converge at more or less the same rate to values close to their respective infinite-system limits (dashed line for $\bar{n} = \frac{1}{3}$ and dot-dashed line for $\bar{n} = \frac{2}{3}$ in the top plot), while $\langle\Psi|c^{\dagger}_{(0,0)}c_{(1,0)}|\Psi\rangle$ for $\bar{n} = \frac{1}{3}$ (○) converges faster than that for $\bar{n} = \frac{2}{3}$ (●) to values close to their common infinite-system limit (dashed line in bottom plot).

Now, if we generate an order-q Monkhorst-Pack mesh of integration points, we would have q^2 integration points $\{\boldsymbol{\phi}_i\}$ uniformly distributed over the unrestricted twist angle domain. There would thus be q^2/N integration points within each twist angle region. From Section D.3.2.1, we know that each BZ partition samples the same set of infinite-system FBZ wave vectors N times, if we vary the twist vector $\boldsymbol{\phi}$ over the unrestricted twist angle domain. We also know that the set of wave vectors sampled by each BZ partition occupies an area of $4\pi^2/N$ in the infinite-system FBZ. We find two different cases: (i) if the Monkhorst-Pack order q is *commensurate* with the finite system shape and size, the integration points $\{\boldsymbol{\phi}_i\}$ in all the N twist angle regions, for different quantum numbers n, sample the same q^2/N infinite-system FBZ wave vectors $\{\mathbf{k}_i\}$; or (ii) if the Monkhorst-Pack order q is *incommensurate* with the finite system shape and size, the integration points $\{\boldsymbol{\phi}_i\}$ in different twist angle regions sample different infinite-system FBZ wave vectors $\{\mathbf{k}_i\}$.

In the commensurate case, we therefore end up with q^2/N $\mathbf{k}$-integration points within an area of $4\pi^2/N$, and so the density of $\mathbf{k}$-integration points is

$$\frac{q^2/N}{4\pi^2/N} = \frac{q^2}{4\pi^2}. \tag{D.6.9}$$

Let us call ϵ the *precision* of the integration scheme, if it is a target quantity we seek to achieve, and call ϵ the *integration error* of the integration scheme, if we are interested in how it converges with the fineness of the integration grid. Since the rectangular integration scheme is $O(h)$, we know that the precision ϵ of the special-point integration scheme is directly proportional to the size h of the integration grid. This means that for a given precision ϵ, we need $h = 2\pi/q$ equal to a constant, and thus the commensurate Monkhorst-Pack order q needed to special-point integrate the gross structure of a twist surface to a given precision is independent of the system size.

In the incommensurate case, on the other hand, because the $\boldsymbol{\phi}$-integration points

in each twist angle region samples different **k**-integration points, we end up with $N \times q^2/N = q^2$ **k**-integration points uniformly distributed within an area of $4\pi^2/N$. The density of **k**-integration points is thus

$$\frac{q^2}{4\pi^2/N} = \frac{Nq^2}{4\pi^2}, \tag{D.6.10}$$

and consequently, $h = 2\pi/q\sqrt{N}$. For a fixed precision ϵ, we want h to be a constant, which in turn means that the incommensurate Monkhorst-Pack order q needed to special-point integrate the gross structure of a twist surface to a given precision is

$$q = \frac{C_0}{\sqrt{N}}, \tag{D.6.11}$$

for some constant C_0. It follows that for a given system size N and a given precision ϵ, it is always better to work with an incommensurate Monkhorst-Pack order q. In anticipation of our discussions on the fine and hyperfine BZ partition structures, let us state this result for the incommensurate case in another way. Since unrestricted twist vectors in an area of $4\pi^2$ samples infinite-system FBZ wave vectors in an area of $4\pi^2/N$, if we have q $\boldsymbol{\phi}$-integration points every 2π, we will end up with $q\sqrt{N}$ **k**-integration points every 2π. For a fixed precision, we want a fixed number of **k**-integration points every 2π, and thus the Monkhorst-Pack order q must depend on the system size as $1/\sqrt{N}$ in (D.6.11).

In the above analysis, we obtained a dependence of $q \sim 1/\sqrt{N}$ by assuming that the twist surface is smooth over gross partition elements with a linear dimension of $2\pi/\sqrt{N}$. If the twist surface is devoid of fine and hyperfine structures, the integration error will decrease monotonically as $O(q^{-1})$ as we increase q. However, when the twist surface contains fine structures, whose linear dimensions are on the order of $2\pi/N$, we will find the integration error decreasing initially as $O(q^{-1})$, plateaus off for a while, before resuming its monotonic decreasing behaviour as q is further increased.

We understand the plateau in the integration error as a function of q as follows. The fine structure regions on the twist surface are small compared to the gross structure regions, and therefore makes only a small contribution δI to the overall integral I over the twist surface. When q is small, the integration error ϵ_0 over the gross structure is much larger than δI, and so the overall integration error $\epsilon = \epsilon_0 + \delta I$ is essentially dominated by ϵ_0, which decreases with increasing q as q^{-1}. After increasing q for a while, the integration mesh would be fine enough that it covers the gross structure very well, but not the fine structure. When we reach this stage, the gross structure integration error ϵ_0 becomes smaller than δI, and the overall integration error $\epsilon = \epsilon_0 + \delta I$ becomes dominated by δI, which does not depend on q. Only when the integration mesh becomes fine enough to properly cover the fine structure regions, will we be integrating out the contribution δI by these regions. If we call the integration error incurred over the fine structure regions as ϵ_1, we would find the overall integration error to be $\epsilon = \epsilon_0 + \epsilon_1$. Since both ϵ_0 and ϵ_1 decreases with q as q^{-1}, with different prefactors, we find the overall integration error ϵ decreasing with increasing q as q^{-1} again.

In the ϵ_1-dominated regime, let us pick a target precision $\epsilon \approx \epsilon_1$. This must be proportional to the $\mathbf{k}$-integration grid size h, which we know to be

$$\frac{2\pi}{q\sqrt{N}}. \tag{D.6.12}$$

Demanding that this grid size be a constant determined by ϵ will again give us the dependence

$$q = \frac{C_1}{\sqrt{N}} \tag{D.6.13}$$

of the Monkhorst-Pack order q on the system size N, for some constant C_1.

Finally, if our twist surface to be integrated contains hyperfine structures, whose linear dimension is $2\pi/N^2$, as well as fine structures, the integration error ϵ, when plotted

as a function of the Monkhorst-Pack order q, will have two plateaus. The first is of course the cross-over from ϵ being dominated by the integration error ϵ_0 over the gross structures to ϵ being dominated by the integration error ϵ_1 over the fine structures. The second plateau is then the cross-over from ϵ being dominated by the integration error ϵ_1 over the fine structures to ϵ being dominated by the integration error over the hyperfine structures. When ϵ is dominated by ϵ_2, we will again find that

$$q = \frac{C_2}{\sqrt{N}}, \tag{D.6.14}$$

for some constant C_2.

The $q \sim 1/\sqrt{N}$ behaviour of q at fixed precisions in (D.6.11), (D.6.13) and (D.6.14) is not very useful to us, because the constants C_0, C_1 and C_2 changes with q. What we want instead, is what minimum value q_1 must take, if we are interested in integrating the twist surface down to its fine structures, and what minimum value q_2 must take, if we are interested in integrating the twist surface down to its hyperfine structures. There is no objective criterion to use here, so let us say that we 'start' integrating the fine structures of the twist surface, when we have a minimum of two **k**-integration points straddling each of the fine structure regions. For order-q Monkhorst-Pack special-point integration, the linear spacing between **k**-integration points is $2\pi/q\sqrt{N}$, and so this requirement of two **k**-integration points straddling a fine structure region with linear dimension $2\pi/N$ tells us that

$$\frac{2\pi/N}{2\pi/q\sqrt{N}} = 2, \tag{D.6.15}$$

i.e. the minimum Monkhorst-Pack order q_1 we need to integrate the twist surface down to its fine structures is

$$q_1 = 2\sqrt{N}. \tag{D.6.16}$$

Similarly, to have two **k**-integration points straddling a hyperfine structure region

with linear dimension $2\pi/N^2$, we must have

$$\frac{2\pi/N^2}{2\pi/q\sqrt{N}} = 2, \tag{D.6.17}$$

i.e. the minimum Monkhorst-Pack order q_2 we need to integrate the twist surface down to its hyperfine structures is

$$q_2 = 2N^{3/2}. \tag{D.6.18}$$

By requiring that we have

$$\frac{2\pi/\sqrt{N}}{2\pi/q\sqrt{N}} = 2 \tag{D.6.19}$$

k-integration points straddling a gross structure region with linear dimension $2\pi/\sqrt{N}$, we can define a similar 'minimum' Monkhorst-Pack order

$$q_0 = 2 \tag{D.6.20}$$

needed to integrate the twist surface 'down' to its gross structures.

When we generate order-q Monkhorst-Pack $\boldsymbol{\phi}$-special-integration points within the restricted twist angle domain (see Section D.3.3), by generating the q^2 $\boldsymbol{\phi}$-integration points in (ϕ_1, ϕ_2) space, we have a density of

$$\frac{q^2}{4\pi^2/N} = \frac{Nq^2}{4\pi^2} \tag{D.6.21}$$

of $\boldsymbol{\phi}$-integration points. Each $\boldsymbol{\phi}$-integration point then samples just one **k**-integration point within the infinite-system FBZ, and so the density of **k**-integration points is again

$$\frac{Nq^2}{4\pi^2}. \tag{D.6.22}$$

For a given precision, the density of **k**-integration points is fixed, and we find, just as we did for special-point integration over the unrestricted twist angle domain, that

$$q \sim \frac{1}{\sqrt{N}}. \tag{D.6.23}$$

Since the density of **k**-integration points in (D.6.22) is identical to that in (D.6.10), our estimates for the minimum orders q_0, q_1 and q_2 to 'start' integrating over the gross, fine, and hyperfine structures will continue to be given by (D.6.20), (D.6.16) and (D.6.18) respectively.

Of course, the results of special-point integration with orders q_0, q_1 or q_2, are far from converging onto the twist-surface integrals over the gross, fine, and hyperfine structures. We see in Figures D.47 and D.48, for $(2,0)\times(0,2)$ and $(2,1)\times(1,2)$ systems, that we need to go to $q \approx 7$ to get good convergence onto the twist-surface integrals of the gross structures. For the $(2,0)\times(0,2)$ system, and the $(2,1)\times(1,2)$ system without orientation averaging, there are no fine and hyperfine features in the BZ partition structure. From Figure D.47, however, the larger integration errors at even q, which are commensurate with the $(2,0)\times(0,2)$ system, and the smaller integration errors at odd q, which are incommensurate with the $(2,0)\times(0,2)$ system, are clear.

In Figure D.49, I show the restricted special-point integration of the ground-state energy per particle E/P and the two-point function $\langle\Psi|c^{\dagger}_{(0,0)}c_{(1,0)}|\Psi\rangle$ for the asymmetric $(3,-1)\times(0,3)$ system, which has $N = 9$ sites. The BZ partition structure of this system consists of a hierarchy of gross, fine and hyperfine structures. From Figure D.49, we see that the ground-state energy per particle for the $(3,-1)\times(0,3)$ system has more or less converged at the Monkhorst-Pack order of $q \approx 7$, just as it did for the $(2,0)\times(0,2)$ and $(2,1)\times(1,2)$ systems. This agrees with our estimate of a fixed order of convergence for observables whose twist surfaces have no cuts, so that fine and hyperfine BZ partition structures do not affect the numerical integration significantly. In contrast, the two-point function converges very slowly with increasing q, because of cuts along the hyperfine structure on its twist surface. For this $(3,-1)\times(0,3)$ system, with $N = 9$ sites, we need to go to $q_2 = 2N^{3/2} = 54$ to 'start' integrating over the hyperfine structures, and as we

can see from Figure D.49 that the two-point function has not quite converged at $q = 200$.

Here we see the need for some sort of compromise. If the system size N is small, then we need only a small number of special points to perform integration over the twist surface, down to the hyperfine structures. However, for small systems, the finite size effects remaining after twist boundary conditions averaging may be unacceptably large. On the other hand, if the system size N is larger, then we would have much smaller finite size effects after twist boundary conditions averaging, but the number of special points needed to integrate down to the hyperfine structures will become too large for the twist surface integration to be computationally feasible. The other thing we note when undertaking special-point integration over twist boundary conditions, is that the contributions δI from the fine structures and $\delta^2 I$ from the hyperfine structures to the overall integral I are not equally important for different system sizes. In particular, the linear dimension of the hyperfine structure goes as N^{-2}, but from the few examples that we have investigated in Section D.3.2, the number of hyperfine structure regions in the BZ partition does not grow quite as fast as N^2. This means that $\delta^2 I$ will become less and less important as we go to larger and larger systems. The optimum system size to perform twist boundary conditions averaging on, would then one decided by the trade-off between integrating the fine structures fast (smaller system), and obtaining accurate estimates of the infinite-system limit (larger system).

D.6.3 Tetrahedron Integration Scheme

An important feature of special-point integration schemes is the use of a uniform grid of integration points. This turns out to be its chief shortcoming when we try to apply it onto a BZ partition consisting of a non-uniform hierarchy of gross, fine and hyperfine structures. If we want to account for twist-surface cuts which occur at the boundaries of

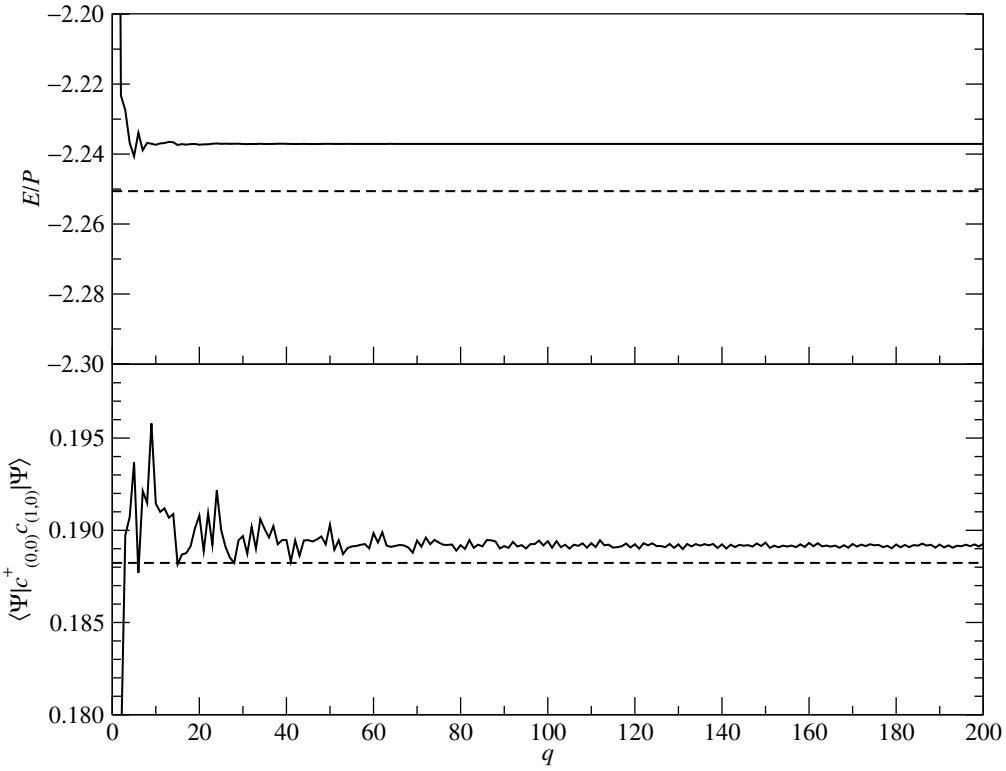

Figure D.49: Performance of the Monkhorst-Pack special-point integration scheme in twist boundary conditions averaging, over the restricted twist angle domain, the ground-state energy per particle E/P (top) and two-point function $\langle\Psi|c^{\dagger}_{(0,0)}c_{(1,0)}|\Psi\rangle$ (bottom) of the $(3,-1)\times(0,3)$ system of $P=3$ noninteracting spinless fermions, equivalent to a filling fraction of $\bar{n}=\frac{1}{3}$. We see that E/P converges to a value close to the infinite-system limit (dashed line) at an order of $q\approx 8$, while $\langle\Psi|c^{\dagger}_{(0,0)}c_{(1,0)}|\Psi\rangle$ converges to a value close to the infinite-system limit (dashed line) only very slowly. By visual inspection, this seems to be happening around $q\approx 100$.

the hyperfine structures, we would then be forced to use a very fine mesh, so as to have the two to four integration points within the small partition elements. In larger partition elements, such a fine mesh would be an overkill — we would be using a large number of integration points to integrate a smooth function.

In contrast, the tetrahedron integration scheme [418–420] does not require uniform meshes, and one is free to place integration points whereever appropriate. Because the integration over the twist surface is done analytically piecewise, the error incurred by this scheme depends on how well the set of interpolation functions approximate the twist surface within each element of the BZ partition. In this Section, I will illustrate the use of quadratic-order interpolating functions to take advantage of the nearly piecewise quadratic nature of the twist surface, tetrahedron integrating the $(2,0)\times(0,2)$ and $(4,0)\times(0,4)$ system as an example by hand in Sections D.6.3.1 and D.6.3.2. To automate the tetrahedron integration scheme, the quadratic function interpolating each piecewise continuous fragment of the twist surface must be determined automatically. Here we rely on a wealth of existing technology on interpolation functions, also called *shape functions*, accumulated by the finite elements method community [438–440], which we can directly apply when using quadratic-order tetrahedron integration in Section D.6.4.

At first glance, it appears that this integration scheme requires prior knowledge of the BZ partition structure, so that we know where to locate our integration points. If this is the case, then the tetrahedron integration scheme would be unusable for interacting systems with twist boundary conditions averaging. Fortunately, we observe that in the BZ partition structure, there is a hierarchy of element sizes. Refined elements usually do not occur near high-symmetry points in the FBZ, so unless the twist surface is strongly discontinuous at these refined elements, we can ignore them with only a slight loss in fidelity. The coarse-grained elements obtained by absorbing refined elements into the

larger elements can probably be deduced from symmetry, and so the integration mesh can be defined without detailed knowledge of the BZ partition structure.

I shall illustrate this approximate location of integration points in the tetrahedron integration of the two-point function $\langle\Psi|c^\dagger_{(0,0)}c_{(1,0)}|\Psi\rangle$, using as examples the $(4,0)\times(0,4)$ and the $(2,1)\times(0,2)$ systems, both at $\bar{n} = \frac{1}{4}$. The $(4,0)\times(0,4)$ system, which has a uniform BZ partition structure without hyperfine structure, would require a minimum order of $q_{\min} \approx 2\sqrt{N} = 8$ (64 integration points without symmetry reduction) over the restricted twist domain in the special-point integration scheme to handle just the fine structures. The $(2,1)\times(0,2)$ system, on the other hand, has a nonuniform BZ partition structure with hyperfine structure. If we want only to integrate faithfully the BZ partition fine structures, we need to go to $q \approx 4$ (16 integration points without symmetry reduction) over the restricted twist angle domain in the special-point integration scheme. If we want to integrate faithfully the BZ partition hyperfine structures, we will need to go to $q \approx 16$ (64 integration points without symmetry reduction) over the restricted twist angle domain.

D.6.3.1 Tetrahedron Integrating the $(2,0)\times(0,2)$ System By Hand

For the $(2,0)\times(0,2)$ system at quarter-filling, the basic pattern of the twist surface determined completely by the first BZ partition, shown shifted by $(-\frac{\pi}{2},-\frac{\pi}{2})$ in Figure D.50. Cusps and cuts will only occur at $\phi_x,\phi_y = \pm\frac{\pi}{2},\pm\frac{3\pi}{2}$, and within each fragment, the twist surface will be nearly paraboloidal. To take advantage of this in, say the twist surface fragment labeled '4', we evaluate the observable being twist boundary conditions averaged at five twist points, and use these values to fit a quadratic function to the twist surface. For example, we can pick the twist points $(-\frac{\pi}{2},-\frac{\pi}{2})$, $(-\frac{\pi}{2},\frac{\pi}{2})$, $(\frac{\pi}{2},-\frac{\pi}{2})$, $(\frac{\pi}{2},\frac{\pi}{2})$ and $(0,0)$, fit a quadratic function based on the values of the observable at these five points,

and then integrate the quadratic function to perform the averaging.

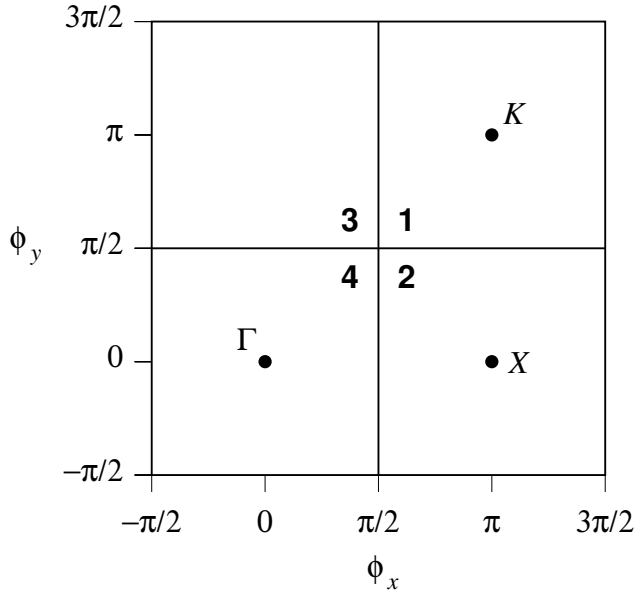

Figure D.50: The first BZ partition of the $(2,0)\times(0,2)$ system subject to twist boundary conditions, shifted by $(-\frac{\pi}{2},-\frac{\pi}{2})$.

Based on the results of Section D.5.1, we know that the two-point function of a finite two-dimensional system of noninteracting spinless fermions is, after twist boundary conditions averaging,

$$\bar{G}(\mathbf{r}) = \frac{1}{4\pi^2}\int d^2\boldsymbol{\phi}\, G(\mathbf{r},\boldsymbol{\phi}) = \frac{1}{4\pi^2}\int_{\cup_\alpha \Pi_\alpha} d^2\mathbf{k}\, g(\mathbf{k},\mathbf{r}), \tag{D.6.24}$$

where we denote the plane wave by

$$g(\mathbf{k},\mathbf{r}) \equiv e^{\mathrm{i}\,\mathbf{k}\cdot\mathbf{r}}. \tag{D.6.25}$$

For $\mathbf{r} = (0,0)$, $\bar{G}(\mathbf{r})$ is given by the area bounded by the approximate Fermi surface divided by $4\pi^2$. But this area is the same as that bounded by the true Fermi surface, and so twist boundary conditions averaging will always give us the correct answer for $\bar{G}(\mathbf{R}) = \text{area bounded by Fermi surface}/4\pi^2 = \bar{n}$. Thus, no approximate integration of the twist surface is required.

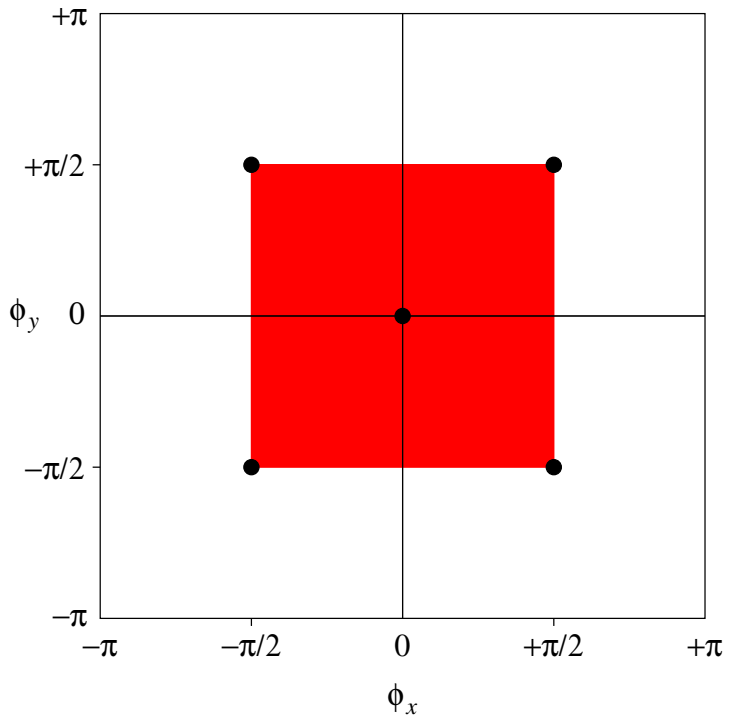

Figure D.51: The fragment of the twist surface labeled ‘4’, of the $(2,0) \times (0,2)$ system with $P = 1$ noninteracting spinless fermions, and the five sampling points used to fit a quartic function.

For $\mathbf{r} = (1, 0)$, let us choose the sampling points to be

$$\mathbf{q}_1 = (-\tfrac{\pi}{2}, -\tfrac{\pi}{2}), \quad \mathbf{q}_2 = (-\tfrac{\pi}{2}, \tfrac{\pi}{2}), \quad \mathbf{q}_3 = (0, 0), \quad \mathbf{q}_4 = (\tfrac{\pi}{2}, -\tfrac{\pi}{2}), \quad \mathbf{q}_5 = (\tfrac{\pi}{2}, \tfrac{\pi}{2}). \quad \text{(D.6.26)}$$

At these five sampling points, shown in Figure D.51, we have

$$g(\mathbf{q}_1, \mathbf{r}) = -\,\mathrm{i}, \quad g(\mathbf{q}_2, \mathbf{r}) = -\,\mathrm{i}, \quad g(\mathbf{q}_3, \mathbf{r}) = 1, \quad g(\mathbf{q}_4, \mathbf{r}) = \mathrm{i}, \quad g(\mathbf{q}_5, \mathbf{r}) = \mathrm{i}\,. \quad \text{(D.6.27)}$$

We can thus fit the plane-wave function to the quartic function

$$g(\mathbf{k}, \mathbf{r}) \approx \frac{16}{\pi^4}\left(\tfrac{\pi}{2} - k_x\right)\left(\tfrac{\pi}{2} + k_x\right)\left(\tfrac{\pi}{2} - k_y\right)\left(\tfrac{\pi}{2} + k_y\right) + \frac{2\,\mathrm{i}}{\pi}\,k_x \quad \text{(D.6.28)}$$

within the fragment. Using this quartic approximation, we evaluate the twist-boundary-conditions-averaged two-point function to be

$$\begin{aligned} \bar{G}(\mathbf{r}) &= \frac{1}{4\pi^2}\int_{-\pi/2}^{\pi/2} dk_x \int_{-\pi/2}^{\pi/2} dk_y \times \\ &\qquad \left[\frac{16}{\pi^4}\left(\tfrac{\pi}{2} - k_x\right)\left(\tfrac{\pi}{2} + k_x\right)\left(\tfrac{\pi}{2} - k_y\right)\left(\tfrac{\pi}{2} + k_y\right) + \frac{2\,\mathrm{i}}{\pi}\,k_x\right] \\ &= \frac{1}{4\pi^2}\frac{4\pi^2}{9} = \frac{1}{9} = 0.111111\ldots. \end{aligned} \quad \text{(D.6.29)}$$

This compares rather poorly with $G(\mathbf{r}) \approx 0.164$ for an infinite square lattice at $\bar{n} = \frac{1}{4}$. Since we cannot calculate $G(\mathbf{r})$ analytically at $\bar{n} = \frac{1}{4}$ for an infinite square lattice analytically, I compute the infinite system G_{01} by summing over the occupied wave vectors for a very large system, up to $N \sim 10^4$.

D.6.3.2 Tetrahedron Integrating the (4, 0) × (0, 4) System By Hand

For the $(4, 0) \times (0, 4)$ system with $P = 4$ particles, the approximate $\bar{n} = \frac{1}{4}$ Fermi surface has the funny shape shown in Figure D.23. We cut this up into five pieces, and use the

17 sampling points shown in Figure D.52. These sampling points are

$$\begin{gathered}
\mathbf{q}_0 = (0,0), \\
\mathbf{q}_1 = (\tfrac{\pi}{2},0), \quad \mathbf{q}_2 = (0,\tfrac{\pi}{2}), \quad \mathbf{q}_3 = (-\tfrac{\pi}{2},0), \quad \mathbf{q}_4 = (0,-\tfrac{\pi}{2}), \\
\mathbf{q}_5 = (\tfrac{5\pi}{16},-\tfrac{5\pi}{16}), \quad \mathbf{q}_6 = (\tfrac{5\pi}{16},\tfrac{5\pi}{16}), \quad \mathbf{q}_7 = (-\tfrac{5\pi}{16},\tfrac{5\pi}{16}), \quad \mathbf{q}_8 = (-\tfrac{5\pi}{16},-\tfrac{5\pi}{16}), \\
\mathbf{q}_9 = (-\tfrac{\pi}{8},-\tfrac{5\pi}{8}), \quad \mathbf{q}_{10} = (\tfrac{\pi}{8},-\tfrac{5\pi}{8}), \quad \mathbf{q}_{11} = (\tfrac{5\pi}{8},-\tfrac{\pi}{8}), \quad \mathbf{q}_{12} = (\tfrac{5\pi}{8},\tfrac{\pi}{8}), \\
\mathbf{q}_{13} = (\tfrac{\pi}{8},\tfrac{5\pi}{8}), \quad \mathbf{q}_{14} = (-\tfrac{\pi}{8},\tfrac{5\pi}{8}), \quad \mathbf{q}_{15} = (-\tfrac{5\pi}{8},\tfrac{\pi}{8}), \quad \mathbf{q}_{16} = (-\tfrac{5\pi}{8},-\tfrac{\pi}{8}).
\end{gathered} \tag{D.6.30}$$

The total area bounded by this approximate Fermi surface is of course

$$A = \left(\frac{\pi}{\sqrt{2}}\right)^2 + 4\left(\frac{\pi}{\sqrt{2}}\right)\left(\frac{\pi}{4\sqrt{2}}\right) = \frac{\pi^2}{2} + \frac{\pi^2}{2} = \pi^2, \tag{D.6.31}$$

which is $\frac{1}{4}$ of the total area of the FBZ.

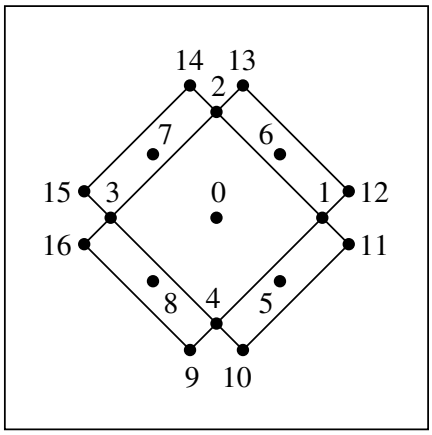

Figure D.52: Approximate Fermi surface of the $(4,0) \times (0,4)$ system with $P = 4$ non-interacting spinless fermions subject to twist boundary conditions, and the 17 sampling points used for quadratic tetrahedron integration.

Again, we calculate the twist-boundary-conditions-averaged two-point function for $\mathbf{r} = (1,0)$. For the region centered at $\mathbf{q}_0$, we have

$$g(\mathbf{q}_0,\mathbf{r}) = 1, \quad g(\mathbf{q}_1,\mathbf{r}) = \mathrm{i}, \quad g(\mathbf{q}_2,\mathbf{r}) = 1, \quad g(\mathbf{q}_3,\mathbf{r}) = -\mathrm{i}, \quad g(\mathbf{q}_4,\mathbf{r}) = 1. \tag{D.6.32}$$

By inspection, the quadratic fit to these values is

$$g(\mathbf{k}, \mathbf{r}) = \frac{4}{\pi^2}(\tfrac{\pi}{2} - k_x)(\tfrac{\pi}{2} + k_x) + \frac{2\,\mathrm{i}}{\pi}\,k_x. \tag{D.6.33}$$

Integrating this gives

$$\int d^2\mathbf{k}\, g(\mathbf{k}, \mathbf{r}) = \frac{5\pi^2}{12}. \tag{D.6.34}$$

By writing the integrals for the remaining four regions explicitly, we can check easily that the sum of the integrals for the four regions is four times the real part of the integral of any one region. For the region centered at $\mathbf{q}_6$, we have

$$\begin{gathered} g(\mathbf{q}_6, \mathbf{r}) = e^{5\,\mathrm{i}\pi/16}, \quad g(\mathbf{q}_1, \mathbf{r}) = \mathrm{i}, \quad g(\mathbf{q}_2, \mathbf{r}) = 1, \\ g(\mathbf{q}_{13}, \mathbf{r}) = e^{\mathrm{i}\pi/8}, \quad g(\mathbf{q}_{12}, \mathbf{r}) = e^{5\,\mathrm{i}\pi/8}. \end{gathered} \tag{D.6.35}$$

We do not know what the quadratic fit to these values is by inspection, so we have to consider a general quadratic function of k_x and k_y, which has the form

$$Ak_x^2 + Bk_y^2 + Ck_xk_y + Dk_x + Ek_y + F. \tag{D.6.36}$$

This has six parameters, so in general we will need one more sampling point. For the sake of convenience, let us choose this sixth sampling point within this region to be the midpoint of $\mathbf{q}_1$ and $\mathbf{q}_2$, and call it $\mathbf{q}_{17} = (\frac{\pi}{4}, \frac{\pi}{4})$, so that $g(\mathbf{q}_{17}, \mathbf{r}) = e^{\mathrm{i}\pi/4}$. With this additional point, the set of sampling points no longer have the symmetry of the region centered about $\mathbf{q}_6$. This is not important, since the tetrahedron integration by hand in this example calculation is only intended as a demonstration. If we ever need to do tetrahedron integration properly, we will be using the finite-elements machinery described in Section D.6.4. There we will find the finite-element set of quadratic-order integration points preserves the symmetry of the quadrilateral region we are integrating.

Coming back our integration of the region centered about $\mathbf{q}_6$, we find a matrix equa-

tion

$$\begin{bmatrix} \frac{25\pi^2}{256} & \frac{25\pi^2}{256} & \frac{25\pi^2}{256} & \frac{5\pi}{16} & \frac{5\pi}{16} & 1 \\ \frac{\pi^2}{4} & 0 & 0 & \frac{\pi}{2} & 0 & 1 \\ 0 & \frac{\pi^2}{4} & 0 & 0 & \frac{\pi}{2} & 1 \\ \frac{\pi^2}{64} & \frac{25\pi^2}{64} & \frac{5\pi^2}{64} & \frac{\pi}{8} & \frac{5\pi}{8} & 1 \\ \frac{25\pi^2}{64} & \frac{\pi^2}{64} & \frac{5\pi^2}{64} & \frac{5\pi}{8} & \frac{\pi}{8} & 1 \\ \frac{\pi^2}{16} & \frac{\pi^2}{16} & \frac{\pi^2}{16} & \frac{\pi}{4} & \frac{\pi}{4} & 1 \end{bmatrix} \begin{bmatrix} A \\ B \\ C \\ D \\ E \\ F \end{bmatrix} = \begin{bmatrix} e^{5\,\mathrm{i}\,\pi/16} \\ \mathrm{i} \\ 1 \\ e^{\mathrm{i}\,\pi/8} \\ e^{5\,\mathrm{i}\,\pi/8} \\ e^{\mathrm{i}\,\pi/4} \end{bmatrix}, \tag{D.6.37}$$

which we need to solve to determine the coefficients A, B, C, D, E and F. The solution, as given by *Mathematica*, is

$$A = \frac{-10 + 12\cos\frac{\pi}{8} + 60\cos\frac{\pi}{4} - 64\cos\frac{5\pi}{16} + 20\cos\frac{5\pi}{8}}{\pi^2} + \mathrm{i}\,\frac{-18 + 12\sin\frac{\pi}{8} + 60\sin\frac{\pi}{4} - 64\sin\frac{5\pi}{16} + 20\sin\frac{5\pi}{8}}{\pi^2}, \tag{D.6.38a}$$

$$B = \frac{-18 + 20\cos\frac{\pi}{8} + 60\cos\frac{\pi}{4} - 64\cos\frac{5\pi}{16} + 12\cos\frac{5\pi}{8}}{\pi^2} + \mathrm{i}\,\frac{-10 + 20\sin\frac{\pi}{8} + 60\sin\frac{\pi}{4} - 64\sin\frac{5\pi}{16} + 12\sin\frac{5\pi}{8}}{\pi^2}, \tag{D.6.38b}$$

$$C = \frac{-36 + 32\cos\frac{\pi}{8} + 136\cos\frac{\pi}{4} - 128\cos\frac{5\pi}{16} + 32\cos\frac{5\pi}{8}}{\pi^2} + \mathrm{i}\,\frac{-36 + 32\sin\frac{\pi}{8} + 136\sin\frac{\pi}{4} - 128\sin\frac{5\pi}{16} + 32\sin\frac{5\pi}{8}}{\pi^2}, \tag{D.6.38c}$$

$$D = \frac{15 - 16\cos\frac{\pi}{8} - 80\cos\frac{\pi}{4} + 80\cos\frac{5\pi}{16} - 20\cos\frac{5\pi}{8}}{\pi} + \mathrm{i}\,\frac{21 - 16\sin\frac{\pi}{8} - 80\sin\frac{\pi}{4} + 80\sin\frac{5\pi}{16} - 20\sin\frac{5\pi}{8}}{\pi}, \tag{D.6.38d}$$

$$E = \frac{21 - 20\cos\frac{\pi}{8} - 80\cos\frac{\pi}{4} + 80\cos\frac{5\pi}{16} - 16\cos\frac{5\pi}{8}}{\pi} + \mathrm{i}\,\frac{15 - 20\sin\frac{\pi}{8} - 80\sin\frac{\pi}{4} + 80\sin\frac{5\pi}{16} - 16\sin\frac{5\pi}{8}}{\pi}, \tag{D.6.38e}$$

$$F = \left[-5 + 5\cos\frac{\pi}{8} + 25\cos\frac{\pi}{4} - 24\cos\frac{5\pi}{16} + 5\cos\frac{5\pi}{8}\right] + \mathrm{i}\left[-5 + 5\sin\frac{\pi}{8} + 25\sin\frac{\pi}{4} - 24\sin\frac{5\pi}{16} + 5\sin\frac{5\pi}{8}\right]. \tag{D.6.38f}$$

Letting *Mathematica* do the integration over this region centered at $\mathbf{q}_6$, we obtain

$$\begin{aligned}
&A\left[\frac{\pi^4}{8192}+\frac{21\pi^4}{2048}+\frac{113\pi^4}{24576}\right]+B\left[\frac{97\pi^4}{24576}+\frac{11\pi^4}{1024}+\frac{7\pi^4}{24576}\right]\\
&+C\left[\frac{\pi^4}{1536}+\frac{33\pi^4}{4096}+\frac{13\pi^4}{12288}\right]+D\left[\frac{\pi^3}{768}+\frac{15\pi^3}{512}+\frac{13\pi^3}{1536}\right]\\
&+E\left[\frac{\pi^3}{128}+\frac{15\pi^3}{512}+\frac{\pi^3}{512}\right]+F\left[\frac{\pi^2}{64}+\frac{3\pi^2}{32}+\frac{\pi^2}{64}\right]\\
&=\frac{23\pi^4}{1536}A+\frac{23\pi^4}{1536}B+\frac{5\pi^4}{512}C+\frac{5\pi^3}{128}D+\frac{5\pi^3}{128}E+\frac{\pi^2}{8}F\\
&=\frac{\pi^2}{96}\left(1+\cos\frac{\pi}{8}+8\cos\frac{5\pi}{16}+\cos\frac{5\pi}{8}\right)\\
&\quad+\mathrm{i}\,\frac{\pi^2}{96}\left(1+\sin\frac{\pi}{8}+8\sin\frac{5\pi}{16}+\sin\frac{5\pi}{8}\right).
\end{aligned} \tag{D.6.39}$$

The integral of $g(\mathbf{k},\mathbf{r})$ over all four regions, being four times the real part of (D.6.39), is thus

$$\int d^2\mathbf{k}\, g(\mathbf{k},\mathbf{r}) = \frac{5\pi^2}{12}+\frac{\pi^2}{24}\left(1+\cos\frac{\pi}{8}+8\cos\frac{5\pi}{16}+\cos\frac{5\pi}{8}\right). \tag{D.6.40}$$

Combining the results in (D.6.34) and (D.6.40), we then find the twist-boundary-conditions-averaged two-point function to be

$$\begin{aligned}
\bar{G}_{01} &= \frac{1}{4\pi^2}\int_{\cup_i \Pi_i} d^2\mathbf{k}\, g(\mathbf{k},\mathbf{r})\\
&= \frac{5}{48}+\frac{1}{96}\left(1+\cos\frac{\pi}{8}+8\cos\frac{5\pi}{16}+\cos\frac{5\pi}{8}\right) = 0.166518\ldots.
\end{aligned} \tag{D.6.41}$$

This is not quite the infinite-system limit, but it is a lot closer to the infinite-system limit than for the $(2,0)\times(0,2)$ system.

D.6.4 Finite-Element Tetrahedron Integration

From the two examples above, we find that the shape of the approximate Fermi surface plays a very important role in determining how close we come to the infinite system limit when calculating various physical quantities. The approximate Fermi surface is formed by the tessellation of triangles whose total area is equal to the momentum-space

area bounded by the true Fermi surface. The size of these tessellation triangles decreases as the system size is increased, so as we go to a larger and larger finite system, we can approximate the Fermi surface better and better. With quadratic interpolation over the tessellated area, we can evaluate twist-boundary-conditions-averaged observables with relatively few sampling wave vectors, but we run into the following technical difficulties in implementing such an approximate integration scheme:

1. In the example calculations shown above, I have determined the integration points by hand. We see that even for a system as small as $(4,0)\times(0,4)$, the approximate Fermi surface has quite a complicated shape. Visually inspecting this approximate surface and deciding the optimal sampling points is easy, but automating this process is likely to be a programming nightmare;

2. Given a user defined set of sampling points (obtained by visual inspection or symmetry considerations), it would be a computationally straightforward task to construct the sampling matrix (the 6×6 matrix in (D.6.37)) and the sampling vector (the vector of values of $g(\mathbf{k},\mathbf{r})$ if we are computing the two-point function, and in general the vector of values of the observable we intend to average over twist boundary conditions), and therefrom obtain the coefficients A through F for the generalized quadratic fit of the twist surface for our observable of interest.

   In our example calculation, we had *Mathematica* integrate the resulting quadratic function in the various regions, where the integrands and limits are simple enough that we can input them into *Mathematica* manually. For more complex approximate Fermi surfaces, cut up into a large number of triangles and rectangles having various orientations, we can no longer rely on interacting with *Mathematica* to get through the calculations. Ultimately, all these calculations, from constructing the

quadratic approximating functions, to integrating them over various triangles and rectangles, must be automated.

Fortunately for us, the second problem has already been solved by engineers, who have developed a mature technology of finite element analysis of various polynomial orders, the important ingredients of which are compiled in Appendix E. The first problem remains daunting, but we will look at various approaches to automate the selection of sampling points as we move along. At the very worst, if we really need to have the precise positions of these sampling points, we might be able to implement line search algorithms to find where the cusps and cuts are, and subsequently to figure out where these cusps and cuts meet.

D.6.4.1 Indiscriminate Finite-Element Integration of the $(2,0)\times(0,2)$ System

Returning to the $(2,0)\times(0,2)$ system, we can simply pick the entire approximate Fermi surface as one finite element, with area $A = \pi^2$. Choosing the integration nodes of the square element as in (D.6.26), using the values of $g(\mathbf{k},\mathbf{r})$ in (D.6.27), and the weights α_i from (E.1.5), we then find from (E.3.3) and (E.3.4) that

$$\begin{aligned}\iint dk_x\, dk_y\, g(\mathbf{k},\mathbf{r}) &= \frac{\pi^2}{4}\sum_i \alpha_i g_i \\ &= \frac{\pi^2}{4}\left[1\cdot\frac{8}{3} - \mathrm{i}\cdot\frac{1}{3} - \mathrm{i}\cdot\frac{1}{3} + \mathrm{i}\cdot\frac{1}{3} + \mathrm{i}\cdot\frac{1}{3}\right] = \frac{2\pi^2}{3}.\end{aligned} \tag{D.6.42}$$

Hence the twist-boundary-conditions-averaged two-point function is

$$\bar{G}(\mathbf{r}) = \frac{1}{4\pi^2}\iint dk_x\, dk_y\, g(\mathbf{k},\mathbf{r}) = \frac{1}{4\pi^2}\frac{2\pi^2}{3} = \frac{1}{6} = 0.1666\ldots, \tag{D.6.43}$$

which is different from the answer that we obtained in Section D.6.3.1, when we tetrahedron integrated the approximate Fermi surface of the $(2,0)\times(0,2)$ system by hand using a quartic fit. The quadratic-order tetrahedron integration of the approximate Fermi sur-

face of the $(2,0)\times(0,2)$ system with $P=1$ noninteracting spinless fermions is actually quite close to the quarter-filled infinite-system limit of $0.16410\ldots$.

D.6.4.2 Indiscriminate Finite-Element Integration of the $(4,0)\times(0,4)$ System

For the 16-site $(4,0)\times(0,4)$ system at $\bar{n}=\frac{1}{4}$, let us break the area bounded by the approximate Fermi surface into five pieces (elements) for finite-element integration, shown in Figure D.52. For the central square element, which has an area of $A=\pi^2/2$, we have the nodal values

$$g_0=1,\quad g_1=\mathrm{i},\quad g_2=1,\quad g_3=-\mathrm{i},\quad g_4=1, \tag{D.6.44}$$

and so

$$\begin{aligned}\iint dk_x\,dk_y\,g(\mathbf{k},\mathbf{R}) &= \frac{\pi^2}{8}\sum_i \alpha_i g_i \\ &= \frac{\pi^2}{8}\left[1\cdot\frac{8}{3}+\mathrm{i}\cdot\frac{1}{3}+1\cdot\frac{1}{3}-\mathrm{i}\cdot\frac{1}{3}+1\cdot\frac{1}{3}\right] \\ &= \frac{\pi^2}{8}\frac{10}{3}=\frac{5\pi^2}{12}.\end{aligned} \tag{D.6.45}$$

This is the same answer as that obtained through the more clumsy way in Section D.6.3.2.

For the top right rectangular element in Figure D.52, with integration nodes $\mathbf{q}_1$, $\mathbf{q}_2$, $\mathbf{q}_6$, $\mathbf{q}_{12}$ and $\mathbf{q}_{13}$, and whose area is $\frac{\pi^2}{8}$, we have

$$g_6=e^{5\,\mathrm{i}\pi/16},\quad g_1=\mathrm{i},\quad g_{12}=e^{5\,\mathrm{i}\pi/8},\quad g_{13}=e^{\mathrm{i}\pi/8},\quad g_2=1, \tag{D.6.46}$$

and so

$$\begin{aligned}\iint dk_x\, dk_y\, g(\mathbf{k},\mathbf{r}) &= \frac{\pi^2}{32}\sum_i \alpha_i g_i \\ &= \frac{\pi^2}{8}\left[e^{5\,\mathrm{i}\,\pi/16}\cdot\frac{8}{3}+\mathrm{i}\cdot\frac{1}{3}+e^{5\,\mathrm{i}\,\pi/8}\cdot\frac{1}{3}+e^{\mathrm{i}\,\pi/8}\cdot\frac{1}{3}+1\cdot\frac{1}{3}\right] \\ &= \frac{\pi^2}{96}\Bigg[\left(1+\cos\frac{\pi}{8}+\cos\frac{5\pi}{16}+\cos\frac{5\pi}{8}\right) \\ &\quad +\mathrm{i}\left(1+\sin\frac{\pi}{8}+\sin\frac{5\pi}{16}+\sin\frac{5\pi}{8}\right)\Bigg],\end{aligned} \tag{D.6.47}$$

which is the same as that obtained in Section D.6.3.2. This is expected, since in Section D.6.3.2 we were essentially doing by hand all the finite-element calculations that we have done here, *without* the benefit of the finite elements analysis shown in Appendix E. Combining (D.6.45) and (D.6.47), we find the same approximate answer for the averaged two-point function as in (D.6.41).

D.6.4.3 Discriminate Finite-Element Integration of the $(4,0)\times(0,4)$

So far I have ignored the information provided by the BZ partitioning, and cut up the approximate Fermi surface myself. Would integrating one partition at a time give an answer even closer to the infinite system limit? We check by integrating the sets of wave vectors sampled by the four BZ partitions of the $(4,0)\times(0,4)$ system with $P=4$ particles, shown in Figure D.53, one at a time.

The first BZ partition samples a square region of FBZ wave vectors centered at $\mathbf{q}_0=(0,0)$ and vertices at $\mathbf{q}_1=(-\frac{\pi}{4},-\frac{\pi}{4})$, $\mathbf{q}_2=(\frac{\pi}{4},-\frac{\pi}{4})$, $\mathbf{q}_3=(\frac{\pi}{4},\frac{\pi}{4})$, and $\mathbf{q}_4=(-\frac{\pi}{4},\frac{\pi}{4})$. This element has an area of $A=\pi^2/4$, and nodal values

$$g_0=1,\quad g_1=e^{-\mathrm{i}\,\pi/4},\quad g_2=e^{\mathrm{i}\,\pi/4},\quad g_3=e^{\mathrm{i}\,\pi/4},\quad g_4=e^{-\mathrm{i}\,\pi/4}. \tag{D.6.48}$$

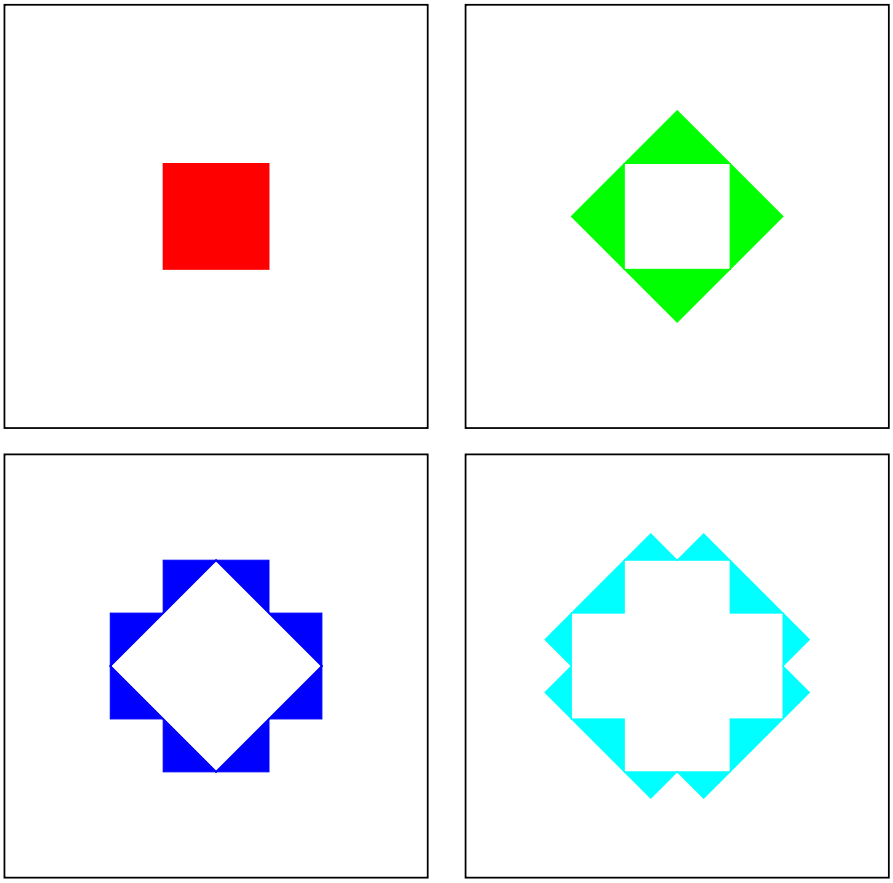

Figure D.53: Regions of the infinite-system FBZ sampled by the first (top left), second (top right), third (bottom left) and fourth (bottom right) BZ partitions of the $(4,0)\times(0,4)$ system with $P = 4$ particles subject to twist boundary conditions. This is the same figure as Figure D.22, reproduced here for easy reference.

The integral over this first partition is therefore

$$\begin{aligned}\iint_{\Pi_1} dk_x\, dk_y\, g(\mathbf{k},\mathbf{R}) &= \frac{\pi^2}{16}\left[1\cdot\frac{8}{3}+e^{-\mathrm{i}\pi/4}\cdot\frac{1}{3}+e^{\mathrm{i}\pi/4}\cdot\frac{1}{3}+e^{\mathrm{i}\pi/4}\cdot\frac{1}{3}+e^{-\mathrm{i}\pi/4}\cdot\frac{1}{3}\right]\\ &= \frac{\pi^2}{12}\left(2+\cos\frac{\pi}{4}\right).\end{aligned} \tag{D.6.49}$$

The second BZ partition samples four triangular region of FBZ wave vectors, also with total area $A = \pi^2/4$. For the right triangular element shown in Figure D.54, which has area $A_1 = \pi^2/16$, and the integration nodes chosen, we have integration-nodal values

$$g_0 = e^{\mathrm{i}\pi/3}, \quad g_1 = e^{\mathrm{i}\pi/4}, \quad g_2 = e^{\mathrm{i}\pi/4}, \quad g_3 = e^{\mathrm{i}\pi/2}. \tag{D.6.50}$$

Using finite-element results on the standard quadratic triangular element found in Appendix E.2, the approximate integral of the plane wave $g(\mathbf{k},\mathbf{r})$ within this triangular element is found to be

$$\begin{aligned}\iint dk_x\, dk_y\, g(\mathbf{k},\mathbf{r}) &\approx \frac{\pi^2}{12\sqrt{3}}\left[e^{\mathrm{i}\pi/3}\cdot\frac{9\sqrt{3}}{16}+e^{\mathrm{i}\pi/4}\cdot\frac{\sqrt{3}}{16}+e^{\mathrm{i}\pi/4}\cdot\frac{\sqrt{3}}{16}+e^{\mathrm{i}\pi/2}\cdot\frac{\sqrt{3}}{16}\right]\\ &= \frac{\pi^2}{192}\left[\left(9\cos\frac{\pi}{3}+2\cos\frac{\pi}{4}\right)+i\left(9\sin\frac{\pi}{3}+2\sin\frac{\pi}{4}+1\right)\right].\end{aligned} \tag{D.6.51}$$

We can easily check that the right and left triangular elements together give twice the real part of this expression.

For the top triangular element, and chosen integration nodes as shown in Figure D.54, we have the integration-nodal values

$$g_{0'} = 1, \quad g_{1'} = e^{-\mathrm{i}\pi/4}, \quad g_{2'} = e^{\mathrm{i}\pi/4}, \quad g_{3'} = 1. \tag{D.6.52}$$

The approximate integral of $g(\mathbf{k},\mathbf{r})$ within this triangular element is therefore

$$\begin{aligned}\iint dk_x\, dk_y\, g(\mathbf{k},\mathbf{r}) &\approx \frac{\pi^2}{12\sqrt{3}}\left[1\cdot\frac{9\sqrt{3}}{16}+e^{-i\pi/4}\cdot\frac{\sqrt{3}}{16}+e^{\mathrm{i}\pi/4}\cdot\frac{\sqrt{3}}{16}+1\cdot\frac{\sqrt{3}}{16}\right]\\ &= \frac{\pi^2}{192}\left[10+2\cos\frac{\pi}{4}\right].\end{aligned} \tag{D.6.53}$$

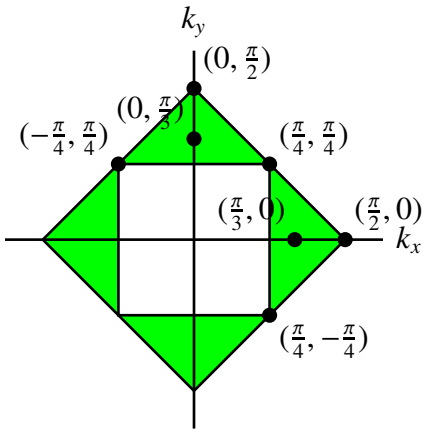

Figure D.54: Region of the infinite-system FBZ, which consists of four triangular elements, sampled by the second BZ partition of the $(4, 0) \times (0, 4)$ system. The integration nodes chosen for finite-element integration of the right triangular element are $\mathbf{q}_0 = (\frac{\pi}{3}, 0)$, $\mathbf{q}_1 = (\frac{\pi}{4}, \frac{\pi}{4})$, $\mathbf{q}_2 = (\frac{\pi}{4}, -\frac{\pi}{4})$, and $\mathbf{q}_3 = (\frac{\pi}{2}, 0)$, while the integration nodes chosen for finite-element integration of the top triangular element are $\mathbf{q}_{0'} = (0, \frac{\pi}{3})$, $\mathbf{q}_{1'} = (-\frac{\pi}{4}, \frac{\pi}{4})$, $\mathbf{q}_{2'} = (\frac{\pi}{4}, \frac{\pi}{4})$ and $\mathbf{q}_{3'} = (0, \frac{\pi}{2})$.

Again, we can easily check that the top and bottom triangular elements together give twice this expression.

Therefore, all in all, we find the integral of the plane wave $g(\mathbf{k}, \mathbf{r})$ over the infinite-system FBZ wave vectors sampled by the second BZ partition to be

$$\begin{aligned}\iint_{\Pi_2} dk_x\, dk_y\, g(\mathbf{k}, \mathbf{r}) &\approx \frac{\pi^2}{96}\left[9\cos\frac{\pi}{3} + 2\cos\frac{\pi}{4}\right] + \frac{\pi^2}{96}\left[10 + 2\cos\frac{\pi}{4}\right] \\ &= \frac{\pi^2}{96}\left[10 + 4\cos\frac{\pi}{4} + 9\cos\frac{\pi}{3}\right].\end{aligned} \tag{D.6.54}$$

Moving on to infinite-system FBZ wave vectors sampled by the third BZ partition, we find eight triangular elements each with area $\pi^2/32$. For the integration nodes chosen for the NNE triangle shown in Figure D.55, the integration-nodal values are

$$g_0 = e^{5\,\mathrm{i}\pi/12}, \quad g_1 = e^{\mathrm{i}\pi/4}, \quad g_2 = e^{\mathrm{i}\pi/2}, \quad g_3 = e^{\mathrm{i}\pi/2}. \tag{D.6.55}$$

The approximate integral of $g(\mathbf{k}, \mathbf{r})$ within this triangular element is therefore

$$\begin{aligned}\iint dk_x\, dk_y\, g(\mathbf{k}, \mathbf{r}) &\approx \frac{\pi^2}{24\sqrt{3}}\left[e^{5\,\mathrm{i}\pi/12}\cdot\frac{9\sqrt{3}}{16} + e^{\mathrm{i}\pi/4}\cdot\frac{\sqrt{3}}{16} + e^{\mathrm{i}\pi/2}\cdot\frac{\sqrt{3}}{16} + e^{\mathrm{i}\pi/2}\cdot\frac{\sqrt{3}}{16}\right] \\ &= \frac{\pi^2}{384}\left[\left(9\cos\frac{5\pi}{12} + \cos\frac{\pi}{4}\right) + \mathrm{i}\left(2 + 9\sin\frac{5\pi}{12} + \sin\frac{\pi}{4}\right)\right].\end{aligned} \tag{D.6.56}$$

We can check that the NNE and NNW triangles together give twice the real part of (D.6.56), which is also what the SSE and SSW triangles would give together. So all in all, we have four times the real part of (D.6.56).

For the ENE triangular elements, with chosen integration nodes shown in Figure D.55, we have the integration-nodal values

$$g_{0'} = e^{\mathrm{i}\pi/6}, \quad g_{1'} = 1, \quad g_{2'} = e^{\mathrm{i}\pi/4}, \quad g_{3'} = e^{\mathrm{i}\pi/4}. \tag{D.6.57}$$

The approximate integral of $g(\mathbf{k}, \mathbf{r})$ within this triangular element is therefore

$$\begin{aligned}\iint dk_x\, dk_y\, g(\mathbf{k}, \mathbf{R}) &\approx \frac{\pi^2}{24\sqrt{3}}\left[e^{\mathrm{i}\pi/6}\cdot\frac{9\sqrt{3}}{16} + 1\cdot\frac{\sqrt{3}}{16} + e^{\mathrm{i}\pi/4}\cdot\frac{\sqrt{3}}{16} + e^{\mathrm{i}\pi/4}\cdot\frac{\sqrt{3}}{16}\right] \\ &= \frac{\pi^2}{384}\left[\left(9\cos\frac{\pi}{6} + 1 + 2\cos\frac{\pi}{4}\right) + \mathrm{i}\left(9\sin\frac{\pi}{6} + 2\sin\frac{\pi}{4}\right)\right].\end{aligned} \tag{D.6.58}$$

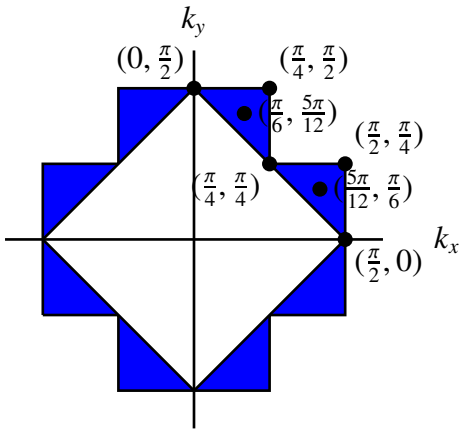

Figure D.55: Region of the infinite-system FBZ, which consists of eight triangular elements, sampled by the third BZ partition of the $(4, 0) \times (0, 4)$ system. We shall refer to these eight triangular elements using the cardinal directions, clockwise from the top, as the NNE, ENE, ESE, SSE, SSW, WSW, WNW, and NNW triangles. The integration nodes chosen for finite-element integration of the NNE triangular element are $\mathbf{q}_0 = (\frac{5\pi}{12}, \frac{\pi}{6})$, $\mathbf{q}_1 = (\frac{\pi}{4}, \frac{\pi}{4})$, $\mathbf{q}_2 = (\frac{\pi}{2}, 0)$, and $\mathbf{q}_3 = (\frac{\pi}{2}, \frac{\pi}{4})$, while the integration nodes chosen for finite-element integration of the ENE triangular element are $\mathbf{q}_{0'} = (\frac{\pi}{6}, \frac{5\pi}{12})$, $\mathbf{q}_{1'} = (0, \frac{\pi}{2})$, $\mathbf{q}_{2'} = (\frac{\pi}{4}, \frac{\pi}{4})$ and $\mathbf{q}_{3'} = (\frac{\pi}{4}, \frac{\pi}{2})$.

We can check that the ENE and WNW triangles together give twice the real part of (D.6.58), which is also what the ESE and WSW triangles would give together. So all in all, we have four times the real part of (D.6.58). Adding all the contributions, we find that

$$\begin{aligned}\iint_{\Pi_3} dk_x\, dk_y\, g(\mathbf{k},\mathbf{r}) &\approx \frac{\pi^2}{96}\left[\left(9\cos\frac{5\pi}{12}+\cos\frac{\pi}{4}\right)+\left(9\cos\frac{\pi}{6}+1+2\cos\frac{\pi}{4}\right)\right]\\ &= \frac{\pi^2}{96}\left[1+9\cos\frac{\pi}{6}+3\cos\frac{\pi}{4}+9\cos\frac{5\pi}{12}\right].\end{aligned} \tag{D.6.59}$$

Finally, we look at the set of infinite-system FBZ wave vectors sampled by the fourth BZ partition, which consists of four larger triangular elements of area $\pi^2/32$, and eight smaller triangular elements of area $\pi^2/64$. Let us first look at one of the larger triangular elements, the NE triangular element with integration nodes shown in Figure D.56. The integration-nodal values are

$$g_0 = e^{\mathrm{i}\,\pi/3}, \quad g_1 = e^{\mathrm{i}\,\pi/4}, \quad g_2 = e^{\mathrm{i}\,\pi/2}, \quad g_3 = e^{\mathrm{i}\,\pi/4}, \tag{D.6.60}$$

and the approximate integral of $g(\mathbf{k},\mathbf{r})$ within this triangular element is thus

$$\begin{aligned}\iint dk_x\, dk_y\, g(\mathbf{k},\mathbf{r}) &\approx \frac{\pi^2}{24\sqrt{3}}\left[e^{\mathrm{i}\,\pi/3}\cdot\frac{9\sqrt{3}}{16}+e^{\mathrm{i}\,\pi/4}\cdot\frac{\sqrt{3}}{16}+e^{\mathrm{i}\,\pi/2}\cdot\frac{\sqrt{3}}{16}+e^{\mathrm{i}\,\pi/4}\cdot\frac{\sqrt{3}}{16}\right]\\ &= \frac{\pi^2}{384}\left[\left(9\cos\frac{\pi}{3}+2\cos\frac{\pi}{4}\right)+\mathrm{i}\left(9\sin\frac{\pi}{3}+1+2\sin\frac{\pi}{4}\right)\right].\end{aligned} \tag{D.6.61}$$

We can check that the NE and NW triangular elements together give twice the real part of (D.6.61), which is also what the SE and SW triangles would give together. So all in all, we have four times the real part of (D.6.61).

For the small ENE triangular element, we choose the integration nodes as shown in Figure D.56. For this triangular element, the integration-nodal values are

$$g_{0'} = e^{13\,\mathrm{i}\,\pi/24}, \quad g_{1'} = \mathrm{i}, \quad g_{2'} = e^{5i\pi/8}, \quad g_{3'} = \mathrm{i}\,. \tag{D.6.62}$$

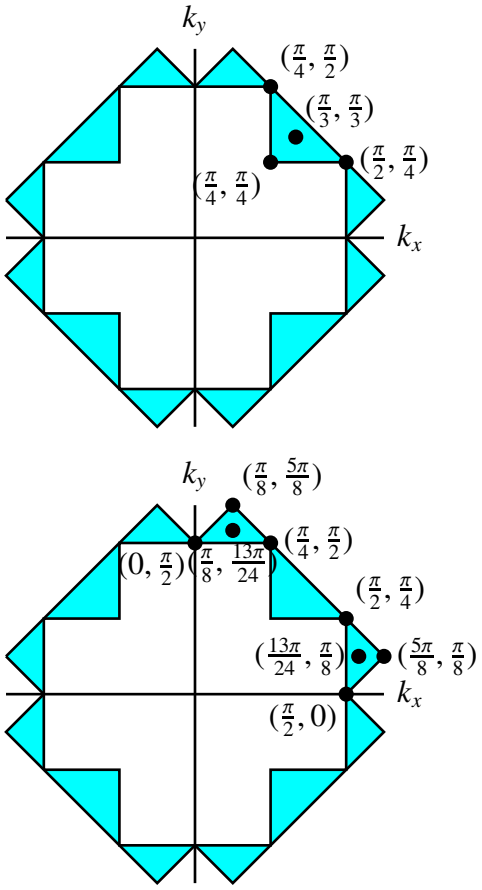

Figure D.56: Region of the infinite-system FBZ, which consists of four large and eight small triangular elements, sampled by the fourth BZ partition of the $(4, 0)\times(0, 4)$ system. We shall refer to these 12 triangular elements using the cardinal directions. The four large triangular elements are, clockwise from top, the NE, SE, SW and NW triangles, while the eight small triangular elements are, clockwise from top, the NNE, ENE, ESE, SSE, SSW, WSW, WNW, and NNW triangles. The integration nodes chosen for finite-element integration of the large NE triangular element are $\mathbf{q}_0 = (\frac{\pi}{3}, \frac{\pi}{3})$, $\mathbf{q}_1 = (\frac{\pi}{4}, \frac{\pi}{4})$, $\mathbf{q}_2 = (\frac{\pi}{2}, \frac{\pi}{4})$, and $\mathbf{q}_3 = (\frac{\pi}{4}, \frac{\pi}{2})$, those chosen for finite-element integration of the small ENE triangular element are $\mathbf{q}_{0'} = (\frac{13\pi}{24}, \frac{\pi}{8})$, $\mathbf{q}_{1'} = (\frac{\pi}{2}, 0)$, $\mathbf{q}_{2'} = (\frac{5\pi}{8}, \frac{\pi}{8})$, and $\mathbf{q}_{3'} = (\frac{\pi}{2}, \frac{\pi}{4})$, and those chosen for finite-element integration of the small NNE triangular element are $\mathbf{q}_{0''} = (\frac{\pi}{8}, \frac{13\pi}{24})$, $\mathbf{q}_{1''} = (0, \frac{\pi}{2})$, $\mathbf{q}_{2''} = (\frac{\pi}{4}, \frac{\pi}{2})$ and $\mathbf{q}_{3''} = (\frac{\pi}{8}, \frac{5\pi}{8})$.

The approximate integral of the phase within this triangular element is therefore

$$\begin{aligned}\iint dk_x\, dk_y\, g(\mathbf{k},\mathbf{R}) &\approx \frac{\pi^2}{48\sqrt{3}}\left[e^{13i\pi/24}\cdot\frac{9\sqrt{3}}{16}+i\cdot\frac{\sqrt{3}}{16}+e^{5i\pi/8}\cdot\frac{\sqrt{3}}{16}+i\cdot\frac{\sqrt{3}}{16}\right]\\ &=\frac{\pi^2}{768}\left[\left(9\cos\frac{13\pi}{24}+\cos\frac{5\pi}{8}\right)+i\left(9\sin\frac{13\pi}{24}+2+\sin\frac{5\pi}{8}\right)\right].\end{aligned} \tag{D.6.63}$$

We can check that the ENE and WNW triangles together give twice the real part of (D.6.63), which is also what the ESE and WSW triangles would give together. So all in all, we have four times the real part of the (D.6.63).

For the small NNE triangular element, we choose the integration nodes as shown in Figure D.56. The integration-nodal values are

$$g_{0''}=e^{\mathrm{i}\pi/8},\quad g_{1''}=1,\quad g_{2''}=e^{\mathrm{i}\pi/4},\quad g_{3''}=e^{\mathrm{i}\pi/8}, \tag{D.6.64}$$

and the approximate integral of $g(\mathbf{k},\mathbf{r})$ within this triangular element is

$$\begin{aligned}\iint dk_x\, dk_y\, g(\mathbf{k},\mathbf{R}) &\approx \frac{\pi^2}{48\sqrt{3}}\left[e^{\mathrm{i}\pi/8}\cdot\frac{9\sqrt{3}}{16}+1\cdot\frac{\sqrt{3}}{16}+e^{\mathrm{i}\pi/4}\cdot\frac{\sqrt{3}}{16}+e^{\mathrm{i}\pi/8}\cdot\frac{\sqrt{3}}{16}\right]\\ &=\frac{\pi^2}{768}\left[\left(10\cos\frac{\pi}{8}+1+\cos\frac{\pi}{4}\right)+\mathrm{i}\left(10\sin\frac{\pi}{8}+\sin\frac{\pi}{4}\right)\right].\end{aligned} \tag{D.6.65}$$

We can check that the NNE and NNW triangles together give twice the real part of (D.6.65), which is also what the SSE and SSW triangles would give together. So all in all, we have four times the real part of the (D.6.65). Adding all the contributions from the fourth BZ partition, we find that

$$\begin{aligned}\iint_{\Pi_4} dk_x\, dk_y\, g(\mathbf{k},\mathbf{r}) \approx{}& \frac{\pi^2}{192}\Big[2\left(9\cos\frac{\pi}{3}+2\cos\frac{\pi}{4}\right)\\ &+\left(9\cos\frac{13\pi}{24}+\cos\frac{5\pi}{8}\right)\\ &+\left(10\cos\frac{\pi}{8}+1+\cos\frac{\pi}{4}\right)\Big]\\ ={}&\frac{\pi^2}{192}\Big[1+10\cos\frac{\pi}{8}+5\cos\frac{\pi}{4}\\ &+18\cos\frac{\pi}{3}+9\cos\frac{13\pi}{24}+\cos\frac{5\pi}{8}\Big].\end{aligned} \tag{D.6.66}$$

Summing up the contributions from all four BZ partitions, we then obtain

$$\iint dk_x\, dk_y\, g(\mathbf{k},\mathbf{r}) \approx \frac{\pi^2}{192}\Big[55 + 9\cos\frac{13\pi}{24} + 18\cos\frac{5\pi}{12} + \cos\frac{5\pi}{8} + 36\cos\frac{\pi}{3} + 35\cos\frac{\pi}{4} + 18\cos\frac{\pi}{6} + 10\cos\frac{\pi}{8}\Big] \tag{D.6.67}$$

for the integral of $g(\mathbf{k},\mathbf{r})$, and thus the twist-boundary-conditions-averaged two-point function is

$$\bar{G}(\mathbf{r}) \approx \frac{1}{768}\Big[55 + 9\cos\frac{13\pi}{24} + 18\cos\frac{5\pi}{12} + \cos\frac{5\pi}{8} + 36\cos\frac{\pi}{3} + 35\cos\frac{\pi}{4} + 18\cos\frac{\pi}{6} + 10\cos\frac{\pi}{8}\Big] = 0.16364\ldots, \tag{D.6.68}$$

which is closer to the infinite system limit compared to the indiscriminate way of cutting up the approximate Fermi surface in Section D.6.4.2.

D.6.5 Automatic Coarse Mesh Generation

As we can see, the integration over the finite elements are easy to do by hand, and also easy to implement computationally, provided the mesh is given. In the previous example calculation for the $(4,0)\times(0,4)$ system at $\bar{n} = \frac{1}{4}$, the $\mathbf{k}$-integration mesh $\{\mathbf{k}_i\}$ was hand-picked, based on the approximate Fermi surface that twist boundary conditions averaging generates in the infinite-system FBZ. It turns out that there is no $\boldsymbol{\phi}$-integration mesh $\{\boldsymbol{\phi}_j\}$ which we can place on the restricted or unrestricted twist angle domain, so that the set of $\boldsymbol{\phi}$-integration points $\{\boldsymbol{\phi}_j\}$ sample only infinite-system FBZ wave vectors within the set of $\mathbf{k}$-integration points. The best that we can hope to do, is to choose a $\boldsymbol{\phi}$-integration mesh $\{\boldsymbol{\phi}_j\}$ over the twist angle domain, which samples a superset of the desired $\mathbf{k}$-integration mesh $\{\mathbf{k}_i\}$. We can then cheat, and pick out the $\mathbf{k}$-integration points that we need visually, or devise an algorithm to pick out the desired $\mathbf{k}$-integration points from the superset sampled by the $\boldsymbol{\phi}$-integration points $\{\boldsymbol{\phi}_j\}$. In Figure D.57, we show a nonuniform mesh of 640 unrestricted $\boldsymbol{\phi}$-integration points $\{\boldsymbol{\phi}_j\}$ which samples a superset

of **k**-integration points containing the chosen quadratic-order **k**-integration mesh of 49 distinct infinite-system FBZ wave vectors.

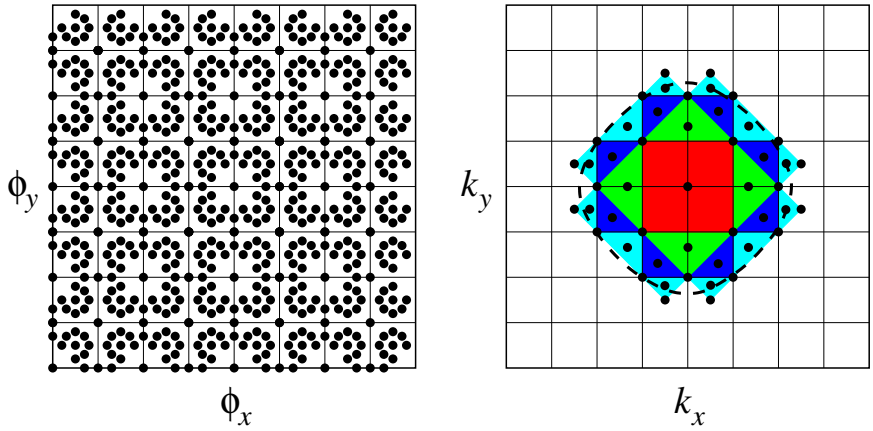

Figure D.57: For the $(4,0) \times (0,4)$ system at $\bar{n} = \frac{1}{4}$ and subject to twist boundary conditions averaging, a $\boldsymbol{\phi}$-integration mesh of 640 unrestricted integration points $\{\boldsymbol{\phi}_j\}$ will sample a superset of the 49 **k**-integration points needed to tetrahedron-integrate the fine structures of the approximate Fermi surface (right) at the quadratic level of approximation. Also shown as a dashed curve is the infinite-system Fermi surface at $\bar{n} = \frac{1}{4}$, obtained by numerically integrating the energy density of states $g(\epsilon)$ in (D.3.8) associated with the infinite-system dispersion relation $\epsilon(\mathbf{k})$ in (D.3.9).

While we noted that in Section D.6.4.3 that such a fine BZ-partition-based integration mesh has superior performance to one where we indiscriminately cut up the approximate Fermi surface in Section D.6.4.2, we must confess that we cannot generate such a mesh automatically, unless we already know the BZ partition structure. For a noninteracting system, the BZ partition structure is known to us, but not so for an interacting system. Therefore, we consider a smaller set of 128 unrestricted $\boldsymbol{\phi}$-integration points $\{\boldsymbol{\phi}_j\}$, shown in Figure D.58, needed to sample a superset of 17 quadratic-order **k**-integration nodes in the infinite-system FBZ. This high-symmetry set of **k**-integration points define triangular elements which adequately accounts for the coarse-grained structure of the

approximate Fermi surface.

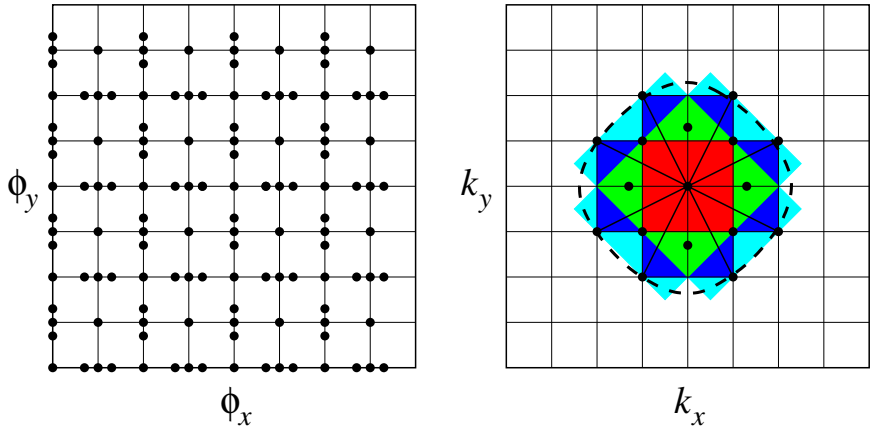

Figure D.58: For the $(4,0)\times(0,4)$ system at $\bar{n}=\frac{1}{4}$ and subject to twist boundary conditions averaging, a coarse-grained integration mesh of 128 unrestricted $\boldsymbol{\phi}$-integration points $\{\boldsymbol{\phi}_j\}$ (left) will sample a superset of $\mathbf{k}$-integration points containing the high-symmetry set of 17 $\mathbf{k}$-integration points accounting for the gross features of the approximate Fermi surface (right). Also shown as a dashed curve is the infinite-system Fermi surface at $\bar{n}=\frac{1}{4}$, obtained by numerically integrating the energy density of states $g(\epsilon)$ in (D.3.8) associated with the infinite-system dispersion relation $\epsilon(\mathbf{k})$ in (D.3.9).

D.6.5.1 Tetrahedron and Special-Point Integration of the $(4,0)\times(0,4)$ System

In Table D.5, we compare the performance of the unrestricted fine and coarse tetrahedron integration schemes with unrestricted special-point integration schemes of various orders q, in evaluating the twist-boundary-conditions-averaged two-point function $\langle\Psi|c^{\dagger}_{(0,0)}c_{(1,0)}|\Psi\rangle$. As we can see, the full tetrahedron integration scheme (640 integration points) approaches the infinite-system limit better than the $q=32$ special-point integration scheme (1024 integration points). This is expected from the fact that we are using quadratic-order interpolation in the tetrahedron integration scheme, whereas

the special-point integration scheme is equivalent to integration with zeroth-order interpolation. The accuracy of the full quadratic-order tetrahedron integration with 640 $\boldsymbol{\phi}$-integration points is only matched by special-point integration when we go to an order of $q = 128$, which uses a total of 16384 $\boldsymbol{\phi}$-integration points.

However, we need to be aware that the mesh for the full tetrahedron integration scheme was designed with full knowledge of how the approximate Fermi surface looks like. If the mesh was to be designed utilizing only the square lattice symmetry, and perhaps the filling $\bar{n}$, then the only reasonable mesh we can come up with is the coarse-grained integration mesh shown in Figure D.58. The performance of tetrahedron integration with such a coarse mesh, which has 128 $\boldsymbol{\phi}$-integration points, is expectedly inferior to the full tetrahedron integration, but comparable to the $q = 8$ special-point integration, which uses 64 $\boldsymbol{\phi}$-integration points. We see that there is no incentive to use coarse-grained tetrahedron integration, since $q = 8$ special-point integration does just as well with half the number of $\boldsymbol{\phi}$-integration points, and is simpler to implement.

D.6.5.2 Tetrahedron and Special-Point Integration of the $(2, 1) \times (0, 2)$ System

For this nonsquare system, about 300 unrestricted $\boldsymbol{\phi}$-integration points would be required to perform full quadratic-order tetrahedron integration. Compared to the $(4, 0) \times (0, 4)$ system, we encounter additional difficulties. Firstly, we find that the location of most of the integration points depend sensitively on the details of the dispersion relation $\epsilon_{\mathbf{k}}$. Secondly, the BZ partitions consists of curvilinear elements, whose edges are curves, determined to a great extent by $\epsilon_{\mathbf{k}}$, instead of straight lines. Because these curves are where cusps and cuts on the twist surface occur, the elemental domain of integration ought be restricted to the area bounded by these curves, if the full tetrahedron integration of a given observable is to faithfully reproduce the twist-surface integral of the

Table D.5: Comparison between the infinite-system value of the two-point function $\langle\Psi|c^{\dagger}_{(0,0)}c_{(1,0)}|\Psi\rangle$, and the values coming from twist boundary conditions averaging of the $(4,0)\times(0,4)$ system, calculated using unrestricted full tetrahedron integration (TI), unrestricted coarse-grained TI, and unrestricted q-special-point integration (SPI).

	$\langle\Psi\|c^{\dagger}_{(0,0)}c_{(1,0)}\|\Psi\rangle$	deviation
infinite-system	0.16428	-
full TI	0.16364	−0.00064
coarsed-grained TI	0.15115	−0.01313
SPI, $q = 8$	0.17970	+0.01542
SPI, $q = 16$	0.17090	+0.00662
SPI, $q = 32$	0.16721	+0.00293
SPI, $q = 64$	0.16573	+0.00145
SPI, $q = 128$	0.16458	+0.00030
SPI, $q = 256$	0.16413	−0.00015

observable.

Accepting in this case that full tetrahedron integration is not feasible, we check whether a coarse-grained tetrahedron integration might offer an advantage over special-point integration. With the high-symmetry set of sampled infinite-system FBZ wave vectors shown in Figure D.59, we find that coarse-grained tetrahedron integration gives $\langle\Psi|c^{\dagger}_{(0,0)}c_{(1,0)}|\Psi\rangle = 0.15115$ for the $(2,1)\times(0,2)$ system, which is the same as that obtained for the $(4,0)\times(0,4)$ system. For special-point integration with $q = 8$ (a total of 64 integration points before symmetry reduction), the value of this two-point function is $\langle\Psi|c^{\dagger}_{(0,0)}c_{(1,0)}|\Psi\rangle = 0.16332$ (which is unexpectedly close to the infinite-system limit), even though the special-point integrated value eventually converges onto $\langle\Psi|c^{\dagger}_{(0,0)}c_{(1,0)}|\Psi\rangle = 0.17403$ as $q \to \infty$. Again, we find that there is no advantage to using coarse-grained tetrahedron integration over low-order special-point integration.

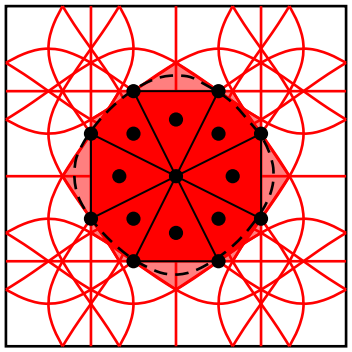

Figure D.59: A high-symmetry set of 17 coarse **k**-integration points in the infinite-system FBZ of the $(2,1)\times(0,2)$ system subject to twist boundary conditions. Solid fill indicates integral filling, and halftone fill indicates half-filling. The infinite-system Fermi surface, obtained by obtained by numerically integrating the energy density of states $g(\epsilon)$ in (D.3.8) associated with the infinite-system dispersion relation $\epsilon(\mathbf{k})$ in (D.3.9), is shown as a dashed curve.

D.6.6 Automatic Fine Mesh Generation

Because of the high computational cost to integrate the twist surface with a fine mesh, we will mostly be doing either coarse mesh tetrahedron integration, or special-point integration of an equivalent low order. However, as an academic exercise, we want to know how to automatically generate a fine mesh for finite-element tetrahedron integration, should it become absolutely crucial to do so.

To begin with, let us keep the discussion general, so that the algorithm works for both noninteracting and interacting systems. For a finite system with N sites and P particles, we have N allowed wave vectors $\mathbf{k}_{0,n}$ under ordinary periodic boundary conditions. For translationally invariant interacting systems, the wave vectors $\{\mathbf{k}_n\}$ remain valid quantum numbers, and they will continue to sample the infinite-system wave vectors $\mathbf{k}$ in the same way as for noninteracting systems, according to (D.2.46). Using the Bloch states (C.5.1) constructed from these allowed wave vectors as a basis, the Hamiltonian matrix can be reduced to N diagonal blocks, called the Bloch-reduced Hamiltonians, each characterized by an allowed wave vector $\mathbf{k}_{0,n}$. These Bloch-reduced Hamiltonians have sizes that are on the order of $(D/N) \times (D/N)$, where D is the dimension of the system Hilbert space. Diagonalizing the Bloch-reduced Hamiltonian $H(\mathbf{k}_{0,n})$ associated with the allowed vector $\mathbf{k}_{0,n}$, we will obtain $\sim(D/N)$ many-body energy eigenvalues and eigenstates, which we will label as $E_l(\mathbf{k}_{0,n})$ and $|E_l(\mathbf{k}_{0,n})\rangle$ respectively, where the index $l = 1, \ldots, \sim(D/N)$. When we impose twist boundary conditions, and vary the twist vector continuously, the many-body energy eigenvalues and eigenstates also vary continuously. For twist vector $\boldsymbol{\phi}$, we write them as $E_l(\mathbf{k}_n(\boldsymbol{\phi}))$ and $|E_{nl}(\boldsymbol{\phi})\rangle$ respectively. Just like we called $\epsilon_{\mathbf{k}_{0,n}}(\boldsymbol{\phi})$ the (single-particle) twist energy bands, let us call $E_l(\mathbf{k}_n(\boldsymbol{\phi}))$ the *many-body twisted energy bands*.

Selecting the many-body state with the lowest energy as the ground state then picks

out a pair of indices (n, l) at every $\boldsymbol{\phi}$. Based on our analysis of noninteracting spinless fermions, we expect this many-body ground state selection to define a many-body ground-state BZ partition structure, in which the unrestricted twist angle domain $(-\pi \leq \phi_x \leq +\pi) \times (-\pi \leq \phi_y \leq +\pi)$ is cut up into elements of constant (n, l). The boundaries between the BZ partition elements with quantum numbers (n, l) and the BZ partition elements with quantum numbers (n', l') are determined by the many-body crossing condition

$$E_l(\mathbf{k}_n(\boldsymbol{\phi})) = E_{l'}(\mathbf{k}_{n'}(\boldsymbol{\phi})). \tag{D.6.69}$$

It is also possible to think about the BZ partition structure of excited states, but we will for the most part be interested only in the ground-state BZ partition structure. For the ground-state BZ partition structure, let us denote by $\pi_{nl;n'l'}$ the partition curve along which the (n, l) many-body twisted energy band crosses the (n', l') many-body twisted energy band. Twist surfaces have cusps and cuts only along such partition curves. For non-square systems, we need to perform orientation averaging. This produces an enlarged set of partition curves invariant under square-lattice point group symmetry transformations.

The integration points we seek are the intersection between pairs of orientation-averaged partition curves. Each partition curve carries two pairs of indices (n, l) and (n', l'), so each integration point carry four pairs of indices (n, l), (n', l'), (n'', l'') and (n''', l'''). At such an integration point, $E_l(\mathbf{k}_n(\boldsymbol{\phi})) = E_{l'}(\mathbf{k}_{n'}(\boldsymbol{\phi}))$ and $E_{l''}(\mathbf{k}_{n''}(\boldsymbol{\phi})) = E_{l'''}(\mathbf{k}_{n'''}(\boldsymbol{\phi}))$, but we do not necessarily have $E_l(\mathbf{k}_n(\boldsymbol{\phi})) = E_{l''}(\mathbf{k}_{n''}(\boldsymbol{\phi}))$. We therefore write the integration point as $\boldsymbol{\phi}_{nln'l'}^{n''l''n'''l'''}$, with the understanding that

$$\boldsymbol{\phi}_{nln'l'}^{n''l''n'''l'''} = \boldsymbol{\phi}_{n'l'nl}^{n''l''n'''l'''} = \boldsymbol{\phi}_{nln'l'}^{n'''l'''n''l''} = \boldsymbol{\phi}_{n'l'nl}^{n'''l'''n''l''}, \tag{D.6.70}$$

i.e. interchange of the pairs of indices strictly within the subscript or strictly within the superscript refers to the same integration point, but interchange of pairs of indices

between the subscript and superscript, for example,

$$\boldsymbol{\phi}_{nln'l'}^{n''l''n'''l'''} \neq \boldsymbol{\phi}_{n''l''n'l'}^{nln'''l'''}, \tag{D.6.71}$$

refers to different integration points.

For interacting spinless fermions in an asymmetric system, or one whose symmetry is incompatible with the symmetry of many-particle twisted energy bands (for example, a square system rotated relative to the underlying infinite square lattice by an angle that is not a multiple of $\frac{\pi}{4}$), these integration points must be solved numerically. If we run through all $n = 1, \ldots, N$, and $l = 1, \ldots, \sim D/N$, we would have a total of D many-body twisted energy bands to monitor. This is far too many, especially when most of the (n, l) many-body energy eigenstates will never be selected as the ground state. Therefore, we will simply monitor the N minimum-energy eigenstates in the N Bloch sectors, and not worry about the quantum number l, which might change as we vary $\boldsymbol{\phi}$. We can use the following algorithm:

1. For a non-square system $\mathbf{R}_1 \times \mathbf{R}_2 = (R_{1x}, R_{1y}) \times (R_{2x}, R_{2y})$, orientation averaging requires us to work with the partition curves coming from all four systems in (C.9.17) with the same shape. From these four systems, we pick one with orientation a, and one with orientation b. The orientation indices run from $a, b = 1, \ldots, 4$.

2. For the system with orientation a, we pick a pair of indices (n, n') such that $n \neq n'$, while for the system with orientation b, we pick a pair of indices (n'', n''') such that $n'' \neq n'''$. The twist band indices run from $n, n', n'', n''' = 1, \ldots, N$.

3. To find the integration node $\boldsymbol{\phi}_{nn'}^{n''n'''}(a, b)$, we need to solve the simultaneous nonlinear equations

$$\begin{aligned} E(\mathbf{k}_n^a(\boldsymbol{\phi})) - E(\mathbf{k}_{\mathbf{n}'}^a(\boldsymbol{\phi})) = 0, \\ E(\mathbf{k}_{n''}^b(\boldsymbol{\phi})) - E(\mathbf{k}_{n'''}^b(\boldsymbol{\phi}) = 0, \end{aligned} \tag{D.6.72}$$

where $\mathbf{k}_n^a(\boldsymbol{\phi}) = \mathbf{k}_{0,n}^a + \boldsymbol{\phi}$ is the nth allowed wave vector in the system with orientation a.

4. We then randomly pick, and store, an initial twist vector $\boldsymbol{\phi}$. Starting from this initial value of $\boldsymbol{\phi}$, we can use any of the many iterative nonlinear root finding algorithms (see for example, in Chapter 9 of Ref. 441) to solve for $\boldsymbol{\phi}_{nn'}^{n''n'''}(a,b)$. If a converged $\boldsymbol{\phi}$-integration point $\boldsymbol{\phi}_{nn'}^{n''n'''}(a,b)$ is found, we will store it in a masterlist of $\boldsymbol{\phi}$-integration points. Else, if the root-finding algorithm fails to converge after `MAXITER` steps, there is unlikely to be a solution in the vicinity of our initial guess $\boldsymbol{\phi}$, and we stop the iterations.

5. We restart the nonlinear root finding with another random $\boldsymbol{\phi}$, which we will also store. If a converged $\boldsymbol{\phi}$-integration point is found, we compare it to the masterlist of $\boldsymbol{\phi}$-integration points. If the newly acquired $\boldsymbol{\phi}$-integration point is new, it is appended to the masterlist. Otherwise, it is discarded. If the root-finding algorithm fails to converge after `MAXITER` steps, we stop the iterations.

6. We stop finding more $\boldsymbol{\phi}$-integration points for the pairs of indices (n,n') and (n'',n'''), if we have already generated more than N^2 random initial guesses $\boldsymbol{\phi}$, *and* the average separation between the $\boldsymbol{\phi}$'s is less than $2\pi/N$. We should be confident that we have found most of the $\boldsymbol{\phi}$-integration points necessary to tetrahedron-integrate the twist-surface fine structures associated with (n,n')-(n'',n''') faithfully. We can change this stopping criteria to greater than N^4 initial random guesses *and* an average separation of less than $2\pi/N^2$ between the initial random guesses, if we want to tetrahedron-integrate the twist-surface hyperfine structures.

7. We repeat steps 4 to 6 for the next pair of indices (n'',n''') for the system with orientation b, before going on to the next pair of indices (n,n') for the system with

orientation a.

8. We repeat steps 2 to 7 for the next orientation index b, before going on to the next orientation index a.

9. Up till this point, we have integration points in the interior of the twist angle domain. We will also need to determine the integration points on the boundaries of the twist angle domain, if performing unrestricted integration, or on the boundaries of the FBZ, if performing restricted integration. On the boundaries, the integration points need not be the intersection between two partition curves. Therefore, we need only apply one-dimensional root finding algorithms on the nonlinear equations (D.6.72) separately. On the boundaries of the twist angle domain, the single variable would either be ϕ_x or ϕ_y, whereas on the boundaries of the FBZ, the single variable would either be ϕ_1 or ϕ_2.

Once we have a masterlist of unique integration points, which we relabel with a running index m, we can tessellate the twist surface. This is done by calculating an adjacency matrix $\mathbf{A}$ for the masterlist of integration points, such that its matrix elements are

$$\mathbf{A}(m,m') = \begin{cases} 1, & \text{if } \boldsymbol{\phi}_m \text{ and } \boldsymbol{\phi}_{m'} \text{ are adjacent integration points;} \\ 0, & \text{otherwise.} \end{cases} \tag{D.6.73}$$

Two integration points $\boldsymbol{\phi}_m$ and $\boldsymbol{\phi}_{m'}$ are considered to be adjacent if they (i) lie on the same partition curve $\pi_{nl;n'l'}$; and (ii) there are no integration point $\boldsymbol{\phi}_{m''}$ lying on $\pi_{nl;n'l'}$ between $\boldsymbol{\phi}_m$ and $\boldsymbol{\phi}_{m'}$. To make the integration over the finite elements efficient, we can also ensure that we are only integrating over triangular elements. The mesh generated by adjacency meshing can be refined, by breaking up quadrilateral elements into triangular elements.

Finally, if we wish to perform quadratic-order integration over curvilinear triangular elements, the coefficients ξ_{12}, ξ_{23} and ξ_{31} will be needed for the three edges of the curvilinear triangular element (see Appendix E.4). To get these, we need to iterate over the list of triangular elements. For each edge of the triangular element, which is a segment of a partition curve, we determine the orientation a of the system, as well as the twisted band indices n and n' the partition curve is derived from. We then run another one-dimensional root finding algorithm on

$$E(\mathbf{k}_n^a(\boldsymbol{\phi})) - E(\mathbf{k}_{n'}^a(\boldsymbol{\phi})) = 0, \tag{D.6.74}$$

using as $v + w$ as the independent variable, at $u = 0$, where u, v, w are the standard edge variables shown in Appendix E.4. The root $(v + w)_0$ found can then be fitted to (E.4.2) to back out the parameter ξ for this edge. Once all the curvilinear coefficients ξ_{12}, ξ_{23} and ξ_{31} are found, the corresponding curvilinear weights $\beta(\xi)$ can be determined using (E.4.7), and the quadratic-order finite-element integral of the curvilinear triangular element calculated using (E.4.9).

D.6.7 Improving Upon the FBZ Integration

For either the special-point or tetrahedron integration schemes, the residual finite size error, when twist boundary conditions averaging the function $f(\mathbf{k})$ in two dimensions, is proportional to

$$\overline{f(k_F)}\,|\Delta\mathbf{k}|^2, \tag{D.6.75}$$

where $\overline{f(k_F)}$ is the average value of the function around the approximate Fermi surface. Summing up the contributions from the gross structure, the fine structure, and the hyperfine structure of the twist surface to the finite size error, we can write $|\Delta\mathbf{k}|^2$ as

$$|\Delta\mathbf{k}|^2 \approx \frac{a_0}{N} + \frac{a_1}{N^2} + \frac{a_2}{N^4}, \tag{D.6.76}$$

where a_0, a_1 and a_2 are coefficients dependent on the shape of the system. For a given filling, it is possible to choose a sequence of finite systems (for example, the $(2,0) \times (0,2)$ system with $P = 1$ particle, and the $(4,0) \times (0,4)$ system with $P = 2$ particles) of increasing size where the approximate Fermi surfaces do not change appreciably, i.e. $\overline{f(k_F)}$ will remain more or less constant across the sequence of finite systems. If we get results from more than three such systems, we can then fit the results to a cubic polynomial in $1/N$, and extrapolate to $1/N \to 0$ to obtain the infinite-system limit. If we have results from three or fewer such systems, we can fit the results to a polynomial of lower order, dropping terms in (D.6.76) with the highest order in $1/N$.

Another shortcoming of investigating a finite system numerically is that we can only access a sparse set of filling fractions $\bar{n}$. In Ref. 400, Gros describes how to perform twist boundary conditions averaging in a grand-canonical ensemble of finite systems with N sites. By adjusting the chemical potential parameter in the machinery, the filling fraction of the finite system can be varied continuously. After learning about the BZ partition structure generated by twist boundary conditions averaging, I suspect that we can fake an approximate Fermi surface corresponding to filling fractions between P/N and $(P+1)/N$ by interpolating between the BZ partition structure of the P-particle ground state, and the BZ partition structure of the $(P+1)$-particle ground state. For a noninteracting system, we know that the single-particle twisted energy bands are independent of the number of particles we put into the system. Therefore, this BZ partition structure interpolation is equivalent to an interpolation between the Pth single-particle twisted energy band, and the $(P+1)$th single-particle twisted energy band.

From our critical study of how the method of twist boundary conditions averaging works for noninteracting systems, we know that in going from occupying the Pth single-particle twisted energy band to occupying the $(P+1)$th single-particle twisted energy

band, we are sampling additional fragments of the FBZ, which may require an additional ΔM integration points to integrate over. We use the (possibly) larger set of integration points of the $(P+1)$th BZ partition structure to integrate over both BZ partitions, and define the interpolated value

$$\overline{\langle O\rangle}(\lambda) = \lambda\overline{\langle O\rangle}_P + (1-\lambda)\overline{\langle O\rangle}_{P+1}, \tag{D.6.77}$$

for the observable O. Here $\overline{\langle O\rangle}_P$ and $\overline{\langle O\rangle}_{P+1}$ are the twist-boundary-conditions-averaged values for the expectation of O in the P- and $(P+1)$-particle ground states of the finite system, and the interpolated filling fraction is

$$\bar{n} = \lambda\,\frac{P}{N} + (1-\lambda)\,\frac{P+1}{N}. \tag{D.6.78}$$

Using the $(4,0)\times(0,4)$ system of noninteracting spinless fermions as an example, we see from Figure D.60 that the interpolation scheme defined in (D.6.77) essentially reweighs the wave vectors sampled when the system contains $P=2$ particles and $P=3$ particles, so as to introduce fractional occupation of the $P=3$ single-particle twisted energy band.

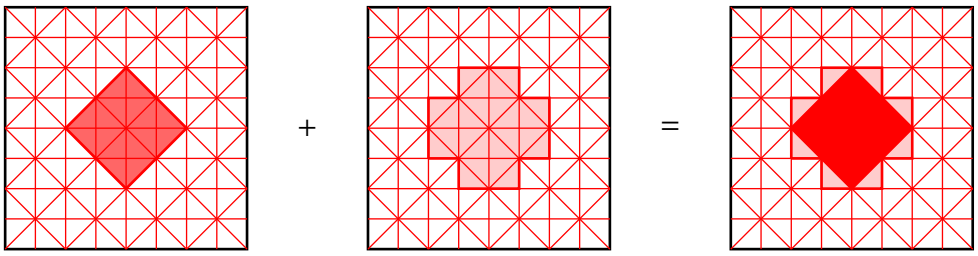

Figure D.60: Partition interpolation between the $P=2$ (left) and $P=3$ (center) BZ partition structures of the $(4,0)\times(0,4)$ system of noninteracting spinless fermions subjected to twist boundary conditions, to give an interpolated BZ partition structure (right) with fractional occupation about the Fermi surface.

D.7 Octave Functions for Twist Boundary Conditions Averaging

The Octave code base described in Appendix C is designed for ED and cluster density matrix computation for finite systems subject to periodic boundary conditions. Most of the functions are not affected by the introduction of twist boundary conditions. There are only three major omissions by the existing code base: (1) when subject to twist boundary conditions with twist vector $\boldsymbol{\phi}$, the hopping matrix element is $-\exp[\mathrm{i}\,\boldsymbol{\phi}\cdot(\mathbf{r}'-\mathbf{r})]$ from neighboring sites $\mathbf{r}$ to $\mathbf{r}'$ instead of -1 in the bond gauge, where we do our EDs; (2) we need some means of getting the boundary-gauge ground-state wave function from the bond-gauge ground-state wave function; and (3) utility functions that would implement the twist boundary conditions averaging.

In Section D.7.1, we look at the function `addBCphase` and its compact analog `addcompactBCphase`, which multiplies the appropriate phase to each nonzero Hamiltonian matrix element. In Section D.7.2, we look at how to implement the gauge transformation of the ground-state wave function from the bond gauge to the boundary gauge. In Section D.7.3 we look at the various modifications that must be made to the existing averaging functions to accomodate twist boundary conditions averaging. Then, we describe in Section D.7.4 the additional functions needed for twist boundary conditions averaging noninteracting spinless fermions.

D.7.1 Hamiltonian Matrix Elements

For the spinless extended Hubbard model, we only have hops between nearest neighors. But we also want to be able to handle correlated hops to next-next-nearest-neighbor sites, which involves a displacement of two lattice spacings. The function `addBCphase`, whose algorithm is patterned after the function `buildhamiltonian` (rarely used, be-

cause the function `quickhamiltonian` is generally faster), and whose Octave code is shown below, handles both types of displacements.

```
function H1 = addBCphase(H0, V, R, R1, R2, phi)

[D P] = size(V);

T = [
−R1 − R2;
−R1;
−R1 + R2;
−R2;
0 0;
R2;
R1 − R2;
R1;
R1 + R2 ];

M = size(T, 1);

H1 = zeros(D, D);

for m = 1:D
    for n = 1:D
        % should be okay even in the presence of a potential
```

```
        if abs(H0(m, n))
            jm = complement(V(n, :), V(m, :));
            jn = complement(V(m, :), V(n, :));
            for k = 1:M
                if norm(R(jn, :) + T(k, :) - R(jm, :)) == 1
                    dR = R(jn, :) + T(k, :) - R(jm, :);
                elseif norm(R(jn, :) + T(k, :) - R(jm, :)) == 2
                    dR = R(jn, :) + T(k, :) - R(jm, :);
                endif
            endfor
            H1(m, n) = H0(m, n)*exp(-i*(dR(1)*phi(1)+dR(2)*phi(2)));
        endif
    endfor
endfor

endfunction
```

This function is slow, because of the nested $O(D^2)$ for loops, which has to be used when the Hamiltonian matrix is not compactly stored. For compactified Hamiltonian matrices, the much faster function `addcompactBCphase`, whose Octave code is shown below, should be used.

```
function H1 = addcompactBCphase(H0, V, R, R1, R2, phi)

T = [
-R1 - R2;
```

```
−R1;
−R1 + R2;
−R2;
0 0;
R2;
R1 − R2;
R1;
R1 + R2 ];

M = size(T, 1);

for p = 1:size(H0, 1)
    % should be okay even in the presence of a potential
    jm = complement(V(H0(p, 2), :), V(H0(p, 1), :));
    jn = complement(V(H0(p, 1), :), V(H0(p, 2), :));
    for k = 1:M
        if norm(R(jn, :) + T(k, :) − R(jm, :)) == 1
            dR = R(jn, :) + T(k, :) − R(jm, :);
        elseif norm(R(jn, :) + T(k, :) − R(jm, :)) == 2
            dR = R(jn, :) + T(k, :) − R(jm, :);
        endif
    endfor
    H1(p, :) = [ H0(p, 1) H0(p, 2) H0(p, 3)*exp(i*(dR(1)*phi(1)+dR(2)*phi(2))) ];
endfor
```

```
endfunction
```

D.7.2 Bond-to-Boundary Gauge Transformation

The bond-to-boundary gauge transformation introduced in (D.2.56) applies to both bosons and fermions, so we put the function `bondtoboundary` in the `Common` code branch. The Octave code of this small function is shown below.

```
function Psi1 = bondtoboundary(V, R, Psi0, phi)

[D, P] = size(V);

for n = 1:D
    Phi = 0;
    for p = 1:P
        Phi = Phi + dot(phi, R(V(n, p), :));
    endfor
    Psi1(n, 1) = Psi0(n, 1)*exp(-i*Phi);
endfor

endfunction
```

D.7.3 Degeneracy and Shape Averaging

To perform twist boundary conditions averaging over a set of M twist vectors $\boldsymbol{\phi}$ for a system of a given orientation, we need to perform N ED of the Bloch-reduced Hamiltonian

matrices for each $\boldsymbol{\phi}$. For each $\boldsymbol{\phi}$, we therefore end up with one or more degenerate bond-gauge ground-state wave functions. These must be gauge transformed to the boundary gauge before we calculate the cluster density matrices within the ground-state manifold to perform degeneracy averaging. After degeneracy averaging, we will also need to average over the orientations of our finite system relative to the cluster. All this must be done at a fixed twist vector, to give a degeneracy-averaged, orientation-averaged cluster density matrix, before we can move on to the next twist vector. Because of this requirement, we need analogs of the functions `fastdegenav` and `shapeav`. The `Common` code branch function `fastdegenavphase`, whose Octave code is shown below, is practically just a copy of `fastdegenav`, differing only in the line of code where we perform bond-to-boundary gauge transformation.

```
function rhopc = fastdegenavphase(V, VP, fP, R, R1, R2, H,\
                                  cluster, neighborlist, PC, phi)

D = size(V, 1);

% find ground state energy
% this is always faster if H can be stored in memory

E = eig(H);
Eg = E(1);

% initialize
```

```
if PC == 0
    rhopc = 0;
else
    VC = clusterhilbertspace(cluster, PC, neighborlist);
    DC = size(VC, 1);
    rhopc = zeros(DC);
endif

d = 0;

% generate list of anti-aliased Bloch wave vectors

Q = makeFBZ(R1, R2);

% perform occupation partition of the Hilbert space

[VPC, DPC] = occupationpartition(V, cluster);

% run through all Bloch wave vectors

for k = 1:size(R, 1)
    % this is the slowest function call in the for loop
    [Psi, Ek] = blocheig(V, VP, fP, R, R1, R2, H, Q(k,1), Q(k,2));
    if abs((Ek - Eg)/Eg) < 1/D
        % gauge transform ground-state wave function
```

```
        % this is the only point where the phase phi is needed
        Psi = bondtoboundary(V, R, Psi, phi);
        PsiPC = partitionpsi(VPC, DPC, Psi);
        rpc = fastclusterdensitymatrix(cluster, PC,\
                                neighborlist, V, VPC, DPC, PsiPC);
        rhopc = rhopc + rpc;
        d = d + 1;
    endif
endfor

rhopc = rhopc/d;

endfunction
```

For our cross-shaped cluster, which has the same point group symmetry as the underlying square lattice, we can calculate the orientation-averaged cluster density matrix using (C.9.19), so I have not bothered to implement a version of `shapeav` incorporating twist boundary conditions. Ideally, we should have an automated machinery that would compute the symmetry-group transformation matrices g for a given cluster, and a given number of particles within the cluster. But we never managed to move beyond the cross-shaped cluster, so I have adopted quick-fix coding to implement the shape-averaging at the script level. In fact, there is also a quick-fix version of `fastdegenavphase`, which is called `quickfixdegenavphase`, which performs ED on the full Hamiltonian matrix, whenever it fits into memory. The Octave for this function, which runs faster by a factor of four to five without all the overheads, is shown below.

```
function rhopc = quickfixdegenavphase(V, R, R1, R2, H,\
                                      cluster, neighborlist, PC, phi)

D = size(V, 1);

% diagonalize the full hamiltonian H to find all eigenvalues and eigenvectors
% this is the fastest possible route, provided H can be stored in memory

[PsiH, dH] = eig(H);

for n = 1:D
    E(n) = real(dH(n, n));
endfor

Eg = min(E);

% initialize

if PC == 0
    rhopc = 0;
else
    VC = clusterhilbertspace(cluster, PC, neighborlist);
    DC = size(VC, 1);
    rhopc = zeros(DC);
endif
```

```
d = 0;

% perform occupation partition of the Hilbert space

[VPC, DPC] = occupationpartition(V, cluster);

% run through all energy eigenvalues to count degeneracy

if abs(Eg) > 0
    for n = 1:D
        if abs((E(n) - Eg)/Eg) < 1/D
            % gauge transform ground-state wave function
            Psi = bondtoboundary(V, R, PsiH(:, n), phi);
            PsiPC = partitionpsi(VPC, DPC, Psi);
            rpc = fastclusterdensitymatrix(cluster, PC, neighborlist,\
                    V, VPC, DPC, PsiPC);
            rhopc = rhopc + rpc;
            d = d + 1;
        endif
    endfor
else
    for n = 1:D
        if abs(E(n)) < 1/D
            % gauge transform ground-state wave function
```

```
            Psi = bondtoboundary(V, R, PsiH(:, n), phi);
            PsiPC = partitionpsi(VPC, DPC, Psi);
            rpc = fastclusterdensitymatrix(cluster, PC, neighborlist,\
                    V, VPC, DPC, PsiPC);
            rhopc = rhopc + rpc;
            d = d + 1;
        endif
    endfor
endif

rhopc = rhopc/d;

endfunction
```

D.7.4 Noninteracting Spinless Fermions

For noninteracting spinless fermions, the cluster density matrix ρ_C is calculated from the cluster Green-function matrix G_C using the exact formula (2.4.30). Based on what we understand twist boundary conditions does to the single-particle occupations, this formula continues to hold true for arbitrary twist vectors $\boldsymbol{\phi}$. However, the function `filledk`, which fills P noninteracting particles into the P (out of N in total) lowest energy single-particle energy bands, does not account for the shift in energy of the single-particle bands with nonzero $\boldsymbol{\phi}$. Therefore, we add a modified copy of this function, called `filledkphase`, into the `FreeFermion` code branch. The Octave code of `filledkphase` is shown below.

```
function kfEknk = filledkphase(R1, R2, P, phi)

N = R1(1)*R2(2) - R1(2)*R2(1);
Q1 = 2*pi*[R2(2) -R2(1)]/N;
Q2 = 2*pi*[-R1(2) R1(1)]/N;

q = makeFBZ(R1, R2);
Nq = size(q, 1);

for n = 1:Nq
    k(n, :) = q(n, 1)*Q1 + q(n, 2)*Q2 + phi;
    Eq(n) = -(cos(k(n, 1)) + cos(k(n, 2)));
endfor

Eqd = create_set(Eq)';
Nqd = max(size(Eqd));

m = 1;
nqd = 1;
nk = 1;

while m <= P
    Dqd = 0;
    for n = 1:Nq
        if Eq(n) == Eqd(nqd)
```

```
            Dqd = Dqd + 1;
        endif
    endfor
    if m + Dqd − 1 > P
        nk = (P − m + 1)/Dqd;
    endif
    for n = 1:Nq
        if Eq(n) == Eqd(nqd)
            kfEknk(m, :) = [ k(n, :) Eq(n) nk ];
            m = m + 1;
        endif
    endfor
    nqd = nqd + 1;
endwhile

endfunction
```

Using the list of wave vectors generated by `filledkphase`, the cluster Green-function matrix can then be calculated using (4.6.3). This is done by the function `makeGphase`, which is an analog of `makeG` taking into account the twist vector $\boldsymbol{\phi}$ in the boundary conditions. The Octave code of `makeGphase` is shown below.

```
function G = makeGphase(R1, R2, cluster, P, phi)

N = R1(1)*R2(2) − R1(2)*R2(1);
R = makesystem(R1, R2);
```

```
kfEknk = filledkphase(R1, R2, P, phi);
Nkf = size(kfEknk, 1);
Nc = max(size(cluster));

for m = 1:Nc
    for n = 1:Nc
        G(m, n) = 0;
        r = R(cluster(m), :) - R(cluster(n), :);
        for l = 1:Nkf
            G(m, n) = G(m, n) + kfEknk(l,4)*exp(i*(kfEknk(l,1)*r(1) +\
                kfEknk(l,2)*r(2)));
        endfor
    endfor
endfor

G = G/N;

endfunction
```

For noninteracting spinless fermions, there is no need to perform degeneracy averaging. This has been taken care of by `filledkphase` whilst generating the occupied wave vectors, by allowing wave vectors with degenerate single-particle energies at the Fermi surface to have fractional occupation. However, we still need to average over the orientation of the finite system relative to the cluster. This is performed by the func-

tion `shapeavphase`, whose Octave code is shown below. Note that this is a quick-fix function intended to work only with the cross-shaped cluster.

```
function G = shapeavphase(R1, R2, cluster, P, phi);

G0 = makeGphase(R1, R2, cluster, P, phi);

load Data/symmetry.mat;

G = 0.25*(U1x*G0*U1x' + U1y*G0*U1y' +\
        U1ymx*G0*U1ymx' + U1ypx*G0*U1ypx');

endfunction
```

APPENDIX E

FINITE ELEMENT ANALYSIS

In Appendix D, we made use of some results on finite element analysis tetrahedron-integrating over the First Brillouin Zone of twist vectors, while performing twist boundary conditions averaging of the many-particle ground-state energy and $2n$-point functions of finite non-square systems of noninteracting spinless fermions. In this appendix, we provide some necessary background on finite element analysis, and derive the results used in Appendix D. In particular, we introduce quadratic-order shape functions, and evaluate their integrals, on the standard square and triangular finite elements, in Sections E.1 and E.2 respectively. We then show in Section E.3 how to write the shape-function integrals of nonstandard triangular and quadrilateral finite elements in terms of those of the standard triangular and square finite elements. Finally, we discuss briefly the integration analysis of curvilinear finite elements in Section E.4.

E.1 Standard Quadratic-Order Square Finite Element

In the finite elements literature, the "industry standard" quadratic-order square finite element is the unit square with corners at $(0,0)$, $(1,0)$, $(0,1)$ and $(1,1)$, with integration nodes at these four corners, the midpoints of the four edges, as well as at the center of the unit square. We choose instead the square shown in Figure E.1 as our standard quadratic-order square element. We do not use the "industry standard" quadratic-order square finite element, because it requires the determination of nine integration-nodal values, as oppose to five integration-nodal values for the square element shown in Figure E.1. We remind readers that each integration-nodal value (of the total energy for example, if we are integrating over the total energy twist surface) is obtained through an exact diagonalization of an interacting Hamiltonian, which is the essential constraint in our

numerical work, and our primary computation time concern forces us to introduce as few integration nodes as possible.

In finite element analysis, one introduces *interpolating functions*, or *shape functions*, with the property

$$u_i(\mathbf{r}_j) = \delta_{ij}, \tag{E.1.1}$$

where $\mathbf{r}_j$ is the position of the jth integration node, $u_i(\mathbf{r})$ is the shape function associated with the ith integration node, such that

$$\tilde{f}_4(\mathbf{r}) = \sum_{i=0}^{i=4} f_i u_i(\mathbf{r}) \tag{E.1.2}$$

approximates the function $f(\mathbf{r})$ over the finite element, $f_i \equiv f(\mathbf{r}_i)$ being the value of $f(\mathbf{r})$ at the ith integration node. Shape functions of various polynomial orders for the "industry standard" square element are well-studied, and frequently tabulated [438–440].

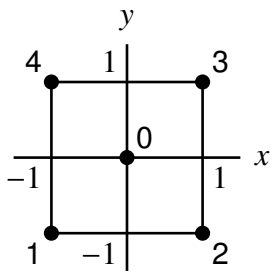

Figure E.1: Our standard five-integration-node, quadratic-order, square finite element, whose area is $A_4 = 4$.

For the five-integration-node square finite element shown in Figure E.1 that we chose to work with, we have to work out the shape functions ourselves. These shape functions,

$$u_0(x, y) = 1 - \tfrac{1}{2}(x^2 + y^2), \tag{E.1.3a}$$

$$u_1(x, y) = \tfrac{1}{8}(x^2 + y^2 + 2xy - 2x - 2y), \tag{E.1.3b}$$

$$u_2(x, y) = \tfrac{1}{8}(x^2 + y^2 - 2xy + 2x - 2y), \tag{E.1.3c}$$

$$u_3(x,y) = \tfrac{1}{8}(x^2 + y^2 + 2xy + 2x + 2y), \tag{E.1.3d}$$

$$u_4(x,y) = \tfrac{1}{8}(x^2 + y^2 - 2xy - 2x + 2y). \tag{E.1.3e}$$

are the simplest quadratic-order polynomials of $\mathbf{r}$ satisfying (E.1.1). We graph the behaviour of these shape functions along the lines 12, 23 and 103 in Figure E.2.

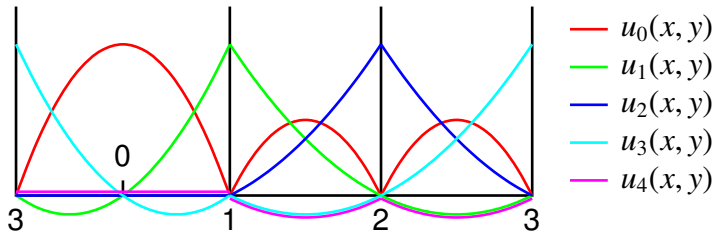

Figure E.2: Shape functions of the standard, five-integration-node, quadratic-order, square finite element. The sections of the shape functions are taken along the lines 12, 23 and 103 (see Figure E.1).

If we know the values of $f(x,y)$ at the integration nodes (x_i, y_i), $i = 0, 1, 2, 3, 4$, we can approximate the integral of $f(x,y)$ over the square finite element, using (E.1.2), as

$$\iint dx\,dy\, f(x,y) \approx \sum_{i=0}^{i=4} f_i \iint dx\,dy\, u_i(x,y) = \sum_{i=0}^{i=4} \alpha_i f_i. \tag{E.1.4}$$

Furthermore, if we tile the two-dimensional domain we wish to integrate $f(x,y)$ over with copies of the standard, five-integration-node, quadratic-order, square finite element, we realize that while the integration-nodal values f_i vary from finite element to finite element, the weights

$$\alpha_0 = \int_{-1}^{1} dx \int_{-1}^{1} dy\, u_0(x,y) = \frac{8}{3}, \tag{E.1.5a}$$

$$\alpha_1 = \int_{-1}^{1} dx \int_{-1}^{1} dy\, u_1(x,y) = \frac{1}{3}, \tag{E.1.5b}$$

$$\alpha_2 = \int_{-1}^{1} dx \int_{-1}^{1} dy\, u_2(x,y) = \frac{1}{3}, \tag{E.1.5c}$$

$$\alpha_3 = \int_{-1}^{1} dx \int_{-1}^{1} dy\, u_3(x,y) = \frac{1}{3}, \tag{E.1.5d}$$

$$\alpha_4 = \int_{-1}^{1} dx \int_{-1}^{1} dy\, u_4(x,y) = \frac{1}{3}, \tag{E.1.5e}$$

are always the same. Therefore, we can evaluate them once, and store them in a look-up table.

E.2 Standard Triangular Element

As with the quadratic-order square finite element, we choose to work with a four-integration-node, quadratic-order, triangular finite element, shown in Figure E.3, that is different from the "industry standard" triangular finite element, which has more nodes. For this standard four-integration-node, quadratic-order, triangular finite element, we define the shape functions to be

$$u_0(x,y) = 1 - (x^2 + y^2), \tag{E.2.1a}$$

$$u_1(x,y) = \frac{2}{\sqrt{3}} x \left(\frac{x}{\sqrt{3}} + y \right), \tag{E.2.1b}$$

$$u_2(x,y) = \frac{2}{\sqrt{3}} x \left(\frac{x}{\sqrt{3}} - y \right), \tag{E.2.1c}$$

$$u_3(x,y) = -\frac{1}{3} x^2 + y^2, \tag{E.2.1d}$$

so that they satisfy the property

$$u_i(\mathbf{r}_j) = \delta_{ij}, \tag{E.2.2}$$

where $\mathbf{r}_j$ is the position of the jth integration node, and $i, j = 0, 1, 2, 3$.

In terms of the shape functions defined in (E.2.1), a continuous function $f(x,y)$ defined within the domain of the standard triangular element can be approximated at the quadratic level as

$$f(x,y) \approx \tilde{f}_3(x,y) = \sum_{i=0}^{i=3} f_i\, u_i(x,y). \tag{E.2.3}$$

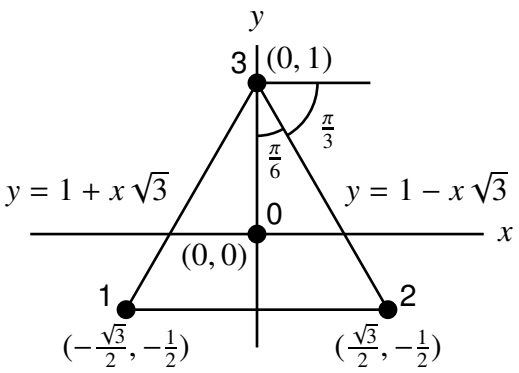

Figure E.3: Our standard four-integration-node, quadratic-order, triangular finite element, whose area is $A_3 = 3\sqrt{3}/4$.

The integral of $f(x, y)$ over the domain of the standard triangular element can then be approximated as

$$\iint dx\, dy\, f(x, y) \approx \sum_{i=0}^{i=3} \alpha_i f_i, \tag{E.2.4}$$

where the integrals α_i of the shape functions can be evaluated to be

$$\alpha_0 = \iint dx\, dy\, u_0(x, y) = \frac{9\sqrt{3}}{16}, \tag{E.2.5a}$$

$$\alpha_1 = \iint dx\, dy\, u_1(x, y) = \frac{\sqrt{3}}{16}, \tag{E.2.5b}$$

$$\alpha_2 = \iint dx\, dy\, u_2(x, y) = \frac{\sqrt{3}}{16}, \tag{E.2.5c}$$

$$\alpha_3 = \iint dx\, dy\, u_3(x, y) = \frac{\sqrt{3}}{16}. \tag{E.2.5d}$$

E.3 Nonstandard Finite Elements

In general, it is impossible to tile a given two-dimensional domain with only the standard triangular and square finite elements shown in Figures E.1 and E.3. For two-dimensional domains with curve edges, we would need to use triangular and quadrilateral finite elements of various shapes and sizes to produce a good approximate mesh. In this section, we learn how to deal with such nonstandard finite elements, which we can think of as

derivable from the standard finite elements by linear transformations and translations.

To begin with, let us note that the approximate form (E.1.4) or (E.2.4) of the integral of $f(x, y)$ over the finite element remains unchanged if the finite element is translated, or rotated. Under a scaling transformation, where $x \to ax$ and $y \to by$, however, the integrals of the shape functions get scaled by ab, and thus we find the integral of $f(x, y)$ to be approximately

$$\iint dx\, dy\, f(x, y) \approx ab \sum_i \alpha_i f_i, \tag{E.3.1}$$

for a rectangular finite element whose length is $2a$ and whose width is $2b$.

In general, if we have a nonstandard finite element (in the primed coordinates) which can be transformed into the standard finite element (in the unprimed coordinates) by the linear transformation

$$\mathbf{r}' = \mathbf{M}\mathbf{r}, \tag{E.3.2}$$

we can show that

$$\iint dx'\, dy'\, f(x', y') = \det \mathbf{M} \iint dx\, dy\, f(x, y) \approx \det \mathbf{M} \sum_i \alpha_i f_i. \tag{E.3.3}$$

The good thing about (E.3.3) is that we do not need to know what the matrix $\mathbf{M}$ is to compute $\det \mathbf{M}$, since this is just the ratio of the area of the nonstandard finite element to the area of the standard finite element. If the area of the nonstandard element is A', then

$$\det \mathbf{M} = \frac{A'}{A_k}, \tag{E.3.4}$$

where $k = 4$ and $A_k = 4$ if we are transforming a nonstandard quadrilateral finite element to our standard square finite element, and $k = 3$ and $A_k = 3\sqrt{3}/4$ if we are transforming a nonstandard triangular finite element to our standard triangular finite element.

E.4 Curvilinear Finite Elements

In Appendix D, we saw that for non-square systems, the approximate twist surface integration after orientation averaging must be carried out over a domain bounded by curves rather than by straight lines. To faithfully integrate over the domain (see Figure E.4), we can either refine the finite element mesh in the vicinity of the curved boundaries, or we can tile the domain boundaries with curvilinear finite elements. The latter option is preferred, because the former necessarily introduce a large number of finite element nodes — something we cannot afford, since the computational time cost is determined essentially by the exact diagonalization we have to do at each node. Also, since a quadrilateral finite element can always be cut up into two triangular finite elements, at the cost of introducing one more finite element node, we will deal exclusively with curvilinear triangular finite elements in this section.

To integrate a continuous function $f(x, y)$ faithfully over the curvilinear finite element, whose domain we denote as Ω, we want to modify the weights α_i appropriately, so that the expression

$$\int_\Omega dx\, dy\, f(x, y) \approx \sum_i \alpha_i f_i, \tag{E.4.1}$$

continues to be a good approximation of the desired integral. To do this, we first ensure, at the expense of introducing a small number of additional finite elements and integration nodes, that the curvature of the curved edges do not change sign within any given finite element. We call such edges *uniformly curved*.

Since the functional forms of these uniformly curved edges are not known to us in general, we approximate each curved edge with the parametric function

$$y = \frac{\sqrt{3}}{\pi} \sin^{-1}(\xi \cos \pi x), \quad -\frac{1}{2} \le x \le \frac{1}{2}, \tag{E.4.2}$$

i.e. all three edges of a curvilinear triangular finite element will be described by (E.4.2),

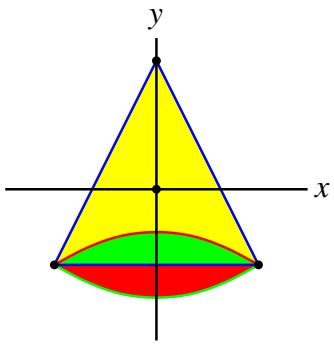

Figure E.4: A curvilinear triangular finite element with one curved edge. If the curved edge is concave, the integration domain is shaded in yellow, and we would over-integrate such a finite element by the region shaded green if we apply (E.2.4), meant for a linear triangular element, directly. On the other hand, if the curved edge is convex, the integration domain is the union of the regions shaded yellow, green and red, and we would under-integrate such a finite element by the region shaded red if we apply (E.2.4), meant for a linear triangular element, directly.

each with its own value of $\xi \in (-1, 1)$ ($\xi = 0$ will then give a straight edge). We chose this parametric function because it is the precise form the curved edges will take in the BZ partition structure of a two-dimensional non-square system of noninteracting spinless fermions. We show the family of such curves with $\xi > 0$ in Figure E.5.

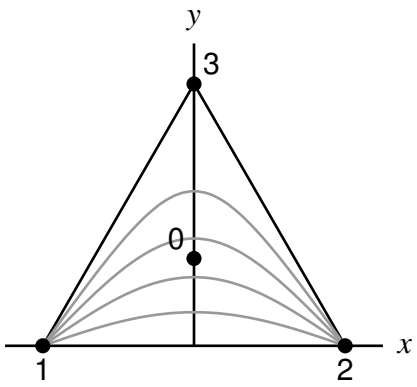

Figure E.5: The one-parameter family of curved edges defined by (E.4.2) for a curvilinear triangular finite element, for $\xi > 0$.

For the purpose of deriving the modified weights, let us shift the standard triangular finite element in Figure E.3 such that the base of the triangular element is along the x axis. The shape functions for this shifted triangular element are thus

$$u_0(x, y) = 1 - 3\left[x^2 + (y - \tfrac{1}{2\sqrt{3}})^2\right], \tag{E.4.3a}$$

$$u_1(x, y) = 2\sqrt{3}\, x\left[\frac{x}{\sqrt{3}} + (y - \tfrac{1}{2\sqrt{3}})\right], \tag{E.4.3b}$$

$$u_2(x, y) = 2\sqrt{3}\, x\left[\frac{x}{\sqrt{3}} - (y - \tfrac{1}{2\sqrt{3}})\right], \tag{E.4.3c}$$

$$u_3(x, y) = -x^2 + 3(y - \tfrac{1}{2\sqrt{3}})^2. \tag{E.4.3d}$$

To calculate the modified weights

$$\alpha_i(\xi) = \int_{-1/2}^{0} dx \int_{\frac{\sqrt{3}}{\sin}^{-1}(\xi\cos\pi x)}^{\frac{\sqrt{3}}{2}+\sqrt{3}x} dy\, u_i(x, y) + \int_{0}^{1/2} dx \int_{\frac{\sqrt{3}}{\pi}\sin^{-1}(\xi\cos\pi x)}^{\frac{\sqrt{3}}{2}-\sqrt{3}x} dy\, u_i(x, y), \tag{E.4.4}$$

which do not depend on the origin of the triangular finite element, we write (E.4.4) as

$$\alpha_i(\xi) = \alpha_i(0) - \beta_i(\xi), \tag{E.4.5}$$

where $\alpha_i(0)$ are the linear triangular finite element weights given in (E.2.5), while the *differential weights* $\beta_i(\xi)$ are defined by

$$\beta_i(\xi) = \int_{-1/2}^{1/2} dx \int_0^{\frac{\sqrt{3}}{\pi}\sin^{-1}(\xi\cos\pi x)} dy\, u_i(x,y). \tag{E.4.6}$$

Not knowing how to evaluate $\beta_i(\xi)$ analytically, we resort to evaluating them numerically over the range of parameters $-1 \le \xi \le 1$, and then fit polynomial functions to the data sets obtained. These data points, and the corresponding polynomial fits,

$$\begin{aligned}
\beta_0(\xi) &= 0.20835\,\xi + 0.16480\,\xi^2 + 0.042874\,\xi^3 - \\
&\quad 0.29529\,\xi^4 - 0.41887\,\xi^5 + 1.1211\,\xi^6 + \\
&\quad 0.65682\,\xi^7 - 1.4907\,\xi^8 - 0.37965\,\xi^9 + 0.71594\,\xi^{10}, && \text{(E.4.7a)}\\
\beta_1(\xi) &= 0.033253\,\xi + 0.0017604\,\xi^3 + 0.0013972\,\xi^5 - \\
&\quad 0.0016081\,\xi^7 + 0.0012821\,\xi^9, && \text{(E.4.7b)}\\
\beta_2(\xi) &= 0.033253\,\xi + 0.0017604\,\xi^3 + 0.0013972\,\xi^5 - \\
&\quad 0.0016081\,\xi^7 + 0.0012821\,\xi^9, && \text{(E.4.7c)}\\
\beta_3(\xi) &= 0.080566\,\xi - 0.16234\,\xi^2 - 0.08379\,\xi^3 + \\
&\quad 0.27096\,\xi^4 + 0.77292\,\xi^5 - 1.0389\,\xi^6 - \\
&\quad 1.2053\,\xi^7 + 1.3802\,\xi^8 + 0.68574\,\xi^9 - 0.66585\,\xi^{10}, && \text{(E.4.7d)}
\end{aligned}$$

are shown in Figure E.6. Having obtain the polynomial fits (E.4.7), we will use them to evaluate $\beta_i(\xi)$ for any given ξ, and not have to evaluate $\beta_i(\xi)$ by time-consuming numerical integrations each and every time.

In general, a curvilinear triangular finite element may have more than one curved edge. Let us denote by ξ_{ij} the parameter associated with the curve edge between finite element nodes i and j. In terms of the standard weights $\alpha_i(0)$, and the differential weights $\beta_i(\xi)$, the integral of $f(x,y)$ over the domain of a curvilinear triangular finite element,

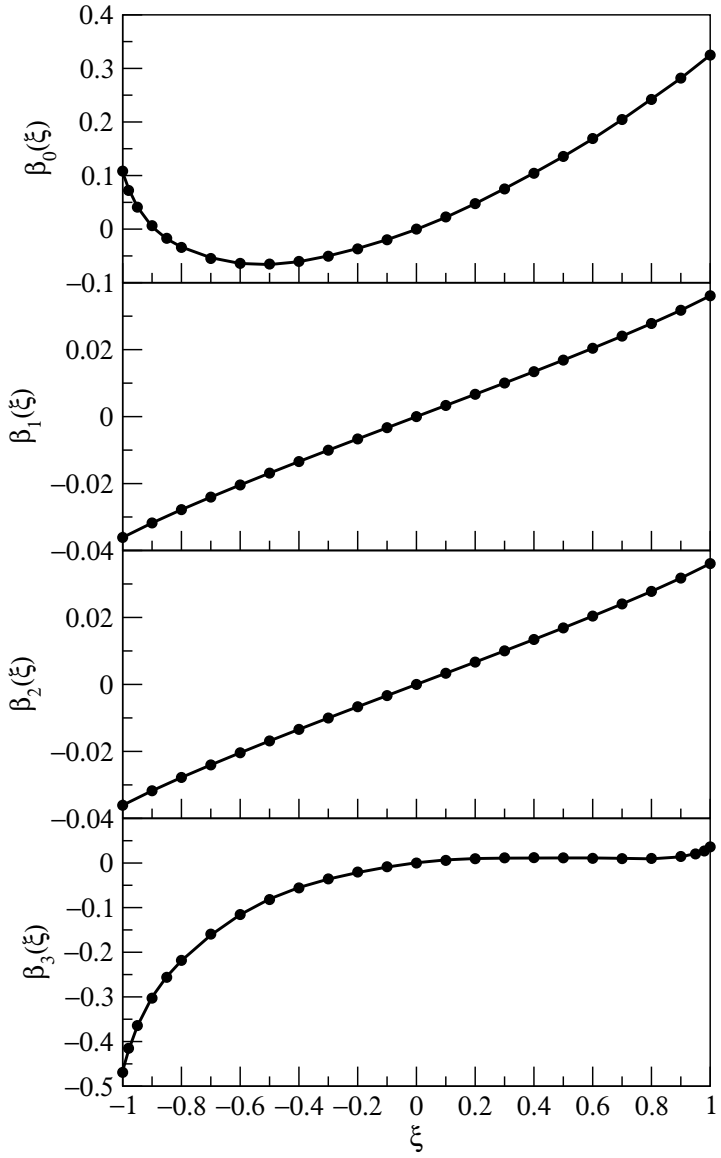

Figure E.6: The differential weights $\beta_i(\xi)$ (black circles), over the range of parameters $-1 \leq \xi \leq 1$, for $i = 0, 1, 2, 3$, for a curvilinear triangular finite element with straight sides, and a curved base given by (E.4.2). The red curves are high-order polynomial fits to the numerical differential weights given in (E.4.7).

derived from the standard triangular finite element and having parameters $(\xi_{12}, \xi_{23}, \xi_{31})$, can be approximated as

$$\iint_{\Omega} dx\, dy\, f(x,y) \approx \sum_{i=0}^{i=3} \left[\alpha_i - \beta_i(\xi_{12}) - \beta_i(\xi_{23}) - \beta_i(\xi_{31})\right] f_i. \tag{E.4.8}$$

For a curvilinear triangular finite element, derived from a nonstandard triangular finite element and having parameters $(\xi_{12}, \xi_{23}, \xi_{31})$, we have

$$\iint_{\Omega'} dx'\, dy'\, f(x',y') \approx \det \mathbf{M} \sum_{i=0}^{i=3} \left[\alpha_i - \beta_i(\xi_{12}) - \beta_i(\xi_{23}) - \beta_i(\xi_{31})\right] f_i, \tag{E.4.9}$$

where the Jacobian $\det \mathbf{M}$ is the ratio of areas of the nonstandard *linear* triangular finite element to the standard *linear* triangular finite element.

The final hurdle we have to overcome, to be able to use (E.4.9), is determining the curvilinear parameters $(\xi_{12}, \xi_{23}, \xi_{31})$. From (E.4.2), we see that these parameters are most readily determined from the value of y at the midpoint of the edges, but we can also determine them from other points along the edge. Depending on how the many-body crossing conditions (D.6.69) are solved to provide the finite element mesh, this parameter determination may or may not involve more exact diagonalizations.

BIBLIOGRAPHY

[1] R. J. Baxter. *Exactly Solved Models in Statistical Mechanics*. Academic Press (London), 1982.

[2] D. C. Mattis (editor). *The Many-Body Problem: An Encyclopedia of Exactly Solved Models in One Dimension*. World Scientific (Singapore), 1992.

[3] V. E. Korepin and F. H. L. Essler (editors). *Exactly Solvable Models of Strongly Correlated Electrons*. World Scientific (Singapore), 1994.

[4] B. Sutherland. *Beautiful Models: 70 Years of Exactly Solved Quantum Many-Body Problems*. World Scientific (Singapore), 2004.

[5] T. W. Burkhardt and J. M. J. van Leeuwen, editors. *Real-Space Renormalization*. Springer-Verlag (Berlin), 1982.

[6] T. P. Živković, B. L. Sandleback, T. G. Schmalz, and D. J. Klein. "Heisenberg Model for the Square-Planar Lattice and Fragments". *Phys. Rev. B*, 41(4):2249–2256, 1990.

[7] V. O. Cheranovski, T. G. Schmalz, and D. J. Klein. "Real-Space Renormalization for Heisenberg Models on Two-Dimensional Lattices". *J. Chem. Phys.*, 101(7):5841–5846, 1994.

[8] J.-P. Malrieu and N. Guihéry. "Real-Space Renormalization Group with Effective Interactions". *Phys. Rev. B*, 63(8):085110, 2001.

[9] M.-B. Lepetit and E. Manousakis. "Real-Space Renormalization-Group Studies of Low-Dimensional Quantum Antiferromagnets". *Phys. Rev. B*, 48(2):1028–1035, 1993.

[10] P. Monthoux and E. Manousakis. "Low-Lying Excitation Spectrum of Quantum Many-Body Systems". *Phys. Rev. B*, 54(21):15101–15108, 1996.

[11] P. Monthoux. "Block-Spin Approach to Electron Correlations". *Phys. Rev. B*, 56:11653–11658, 1997.

[12] A. Degenhard. "A Nonperturbative Real-Space Renormalization Group Scheme". *J. Phys. A: Math. Gen.*, 33:6173–6185, 2000.

[13] R. J. Bursill. "Density-Matrix Renormalization-Group Algorithm for Quantum Lattice Systems With a Large Number of States Per Site". *Phys. Rev. B*, 60:1643–1649, 1999.

[14] S. R. White. "Density Matrix Formulation for Quantum Renormalization Groups". *Phys. Rev. Lett.*, 69:2863–2866, 1992.

[15] S. R. White. "Density-Matrix Algorithms for Quantum Renormalization Groups". *Phys. Rev. B*, 48:10345–10356, 1993.

[16] S. Östlund and S. Rommer. "Thermodynamic Limit of Density Matrix Renormalization". *Phys. Rev. Lett.*, 75:3537–3540, 1995.

[17] S. R. White. "Strongly Correlated Electron Systems and the Density Matrix Renormalization Group". *Phys. Rep.*, 301:187–204, 1998.

[18] R. M. Noack, S. R. White, and D. J. Scalapino. "The Density-Matrix Renormalization Group for Fermion Systems". In David P. Landau, Kin-Keung Mon, and Heinz-Bernd Schüttler, editors, *Computer Simulation Studies in Condensed Matter Physics VII (Proceedings of the Seventh Workshop, Athens, GA, USA, 28 February – 4 March 1994)*, pages 85–98, Athens, Georgia, USA, 1994.

[19] S. Liang and H. Pang. "Approximate Diagonalization Using the Density-Matrix Renormalization-Group Method: A Two-Dimensional-System Perspective". *Phys. Rev. B*, 49:9214–9217, 1994.

[20] F. Verstraete, D. Porras, and J. I. Cirac. "Density Matrix Renormalization Group and Periodic Boundary Conditions: A Quantum Information Perspective". *Phys. Rev. Lett.*, 93(22):227205, 2004.

[21] F. Verstraete and J. I. Cirac. "Renormalization Algorithms for Quantum-Many Body Systems in Two and Higher Dimensions". *www.arXiv.org preprint*, cond-mat/0407066, 2004.

[22] C. J. Morningstar and M. Weinstein. "Contractor Renormalization-Group Method — A New Computational Technique for Lattice Systems". *Phys. Rev. Lett.*, 73(14):1873–1877, 1994.

[23] C. Morningstar and M. Weinstein. "Contractor Renormalization Group Technology and Exact Hamiltonian Real-Space Renormalization Group Transformations". *Phys. Rev. D*, 54(6):4131–4151, 1996.

[24] E. Altman and A. Auerbach. "Plaquette Boson-Fermion Model of Cuprates". *Phys. Rev. B*, 65(10):104508, 2002.

[25] E. Berg, E. Altman, and A. Auerbach. "Singlet Excitations in Pyrochlore: A Study of Quantum Frustration". *Phys. Rev. Lett*, 90(14):147204, 2003.

[26] R. Budnik and A. Auerbach. "Low-Energy Singlets in the Heisenberg Antiferromagnet on the Kagome Lattice". *Phys. Rev. Lett.*, 93(18):187205, 2004.

[27] S. Capponi, A. Läuchli, and M. Mambrini. "Numerical Contractor Renormalization Method for Quantum Spin Models". *Phys. Rev. B*, 70(10):104424, 2004.

[28] S. Furukawa, G. Misguich, and M. Oshikawa. "Detection of Exotic Order Parameters of Quantum Antiferromagnets through Reduced Density Matrices". *Prog. Theor. Phys. Suppl.*, 159:143–147, 2005. See also "Systematic Derivation of Order Parameters Through Reduced Density Matrices", cond-mat/0508469.

[29] G. H. Golub and C. F. van Loan. *Matrix Computations*. Johns Hopkins Studies in Mathematical Sciences. John Hopkins University Press, 3rd edition, 1996.

[30] Z. Bai, J. Demmel, J. Dongarra, A. Ruhe, and H. van der Vorst (editors). *Templates for the Solution of Algebraic Eigenvalue Problems: A Practical Guide*. Society for Industrial and Applied Mathematics (Philadelphia), 2000.

[31] LAPACK — Linear Algebra PACKage. `http://www.netlib.org/lapack/`.

[32] Z. Bai, C. Bischof, L. S. Blackford, J. Demmel, J. Dongarra, J. Du Croz, A. Greenhaum, S. Hammarling, A. McKenney, D. Sorensen, and E. Anderson (editors). *LAPACK Users' Guide*. Society for Industrial and Applied Mathematics (Philadelphia), 3rd edition, 2000.

[33] LAPACK95 — Fortran95 interface to LAPACK. `http://www.netlib.org/lapack95/`.

[34] L. S. Blackford, J. Dongarra, J. Du Croz, S. Hammarling, M. Marinova, J. Wasniewsk, P. Yalamov, and V. A. Barker (editors). *LAPACK95 Users' Guide*. Society for Industrial and Applied Mathematics (Philadelphia), 2001.

[35] H. Q. Lin and J. E. Gubernatis. "Exact Diagonalization Methods for Quantum Systems". *Comp. Phys.*, 7(4):400–407, 1993.

[36] A. Booten and H. van der Vorst. "Cracking Large-Scale Eigenvalue Problems, Part I: Algorithms". *Comp. Phys.*, 10(3):239–242, 1996.

[37] A. Booten and H. van der Vorst. "Cracking Large-Scale Eigenvalue Problems, Part II: Implementations". *Comp. Phys.*, 10(4):331–334, 1996.

[38] E. Dagotto. "Numerical Studies of Strongly Correlated Electronic Models". *Int. J. Mod. Phys. B*, 5(1–2):77–111, 1991.

[39] E. Dagotto. "Correlated Electrons in High-Temperature Superconductors". *Rev. Mod. Phys*, 66(3):763–840, 1994.

[40] A. Laüchli. "Quantum Lattice Models and Introduction to Exact Diagonalization". `http://www.comp-phys.org:16080/lugano04/Talks/QLM_ED.pdf`. First ALPS User Workshop on Computational Methods for Strongly Correlated Systems and Nanomagnetics, September 26 to October 1, 2004, Lugano, Switzerland.

[41] D. Poilblanc. "Advanced Exact Diagonalization". http://www.comp-phys.org:16080/lugano04/Talks/QLM_ED.pdf. First ALPS User Workshop on Computational Methods for Strongly Correlated Systems and Nanomagnetics, September 26 to October 1, 2004, Lugano, Switzerland.

[42] H. Shiba and P. A. Pincus. "Thermodynamic Properties of the One-Dimensional Half-Filled-Band Hubbard Model". *Phys. Rev. B*, 5(5):1966–1980, 1972.

[43] H. Shiba. "Thermodynamics Properties of the One-Dimensional Half-Filled-Band Hubbard Model. II.". *Prog. Theor. Phys.*, 48(6B):2171–2186, 1972.

[44] K.-H. Heinig and J. Monecke. "Specific Heat of the Four-Point Hubbard Model". *Phys. Status Solidi (b)*, 49(2):K139–K140, 1972.

[45] K.-H. Heinig and J. Monecke. "Magnetic Properties of the Four-Point Hubbard Model". *Phys. Status Solidi (b)*, 49(2):K141–K143, 1972.

[46] A. Reich and L. M. Falicov. "Calculation of Fluctuations and Photoemission Properties in a Tetrahedral-Cluster Model for an Intermediate-Valence System". *Phys. Rev. B*, 34(10):6752–6758, 1986.

[47] J. C. Parlebas, R. H. Victora, and L. M. Falicov. "Four-site crystal model for an intermediate-valence system". *J. Magn. Magn. Mater.*, 54–57:405–406 Part 1, 1986.

[48] J. C. Parlebas, R. H. Victora, and L. M. Falicov. "Exact Solution of a 4-Site Crystal Model for an Intermediate-Valence System". *J. Phys. (France)*, 47(6):1029–1034, 1986.

[49] J. Callaway, D. P. Chen, and R. Tang. "The Hubbard-Model for Small Clusters". *Z. Phys. D*, 3(1):91–96, 1986.

[50] J. Callaway. "Numerical Simulation of the Resonant Valence-Bond State". *Phys. Rev. B*, 35(16):8723–8725, 1987.

[51] J. Callaway, D. P. Chen, and R. Tang. "Ground-State and Thermodynamic Properties of the Hubbard Model Applied to Small Clusters". *Phys. Rev. B*, 35(8):3705–3714, 1987.

[52] J. Callaway, D. P. Chen, and Y. Zhang. "Hubbard Model for a Cubic Cluster". *Phys. Rev. B*, 36(4):2084–2091, 1987.

[53] P. K. Misra, D. G. Kanhere, and J. Callaway. "Periodic Anderson Model for Four-Site Clusters". *Phys. Rev. B*, 35(10):5013–5024, 1987.

[54] J. Callaway, D. P. Chen, D. G. Kanhere, and P. K. Misra. "Cluster Simulation of the Lattice Anderson Model". *Phys. Rev. B*, 38(4):2583–2595, 1988.

[55] H. Q. Lin, J. E. Hirsch, and D. J. Scalapino. "Pairing in the Two-Dimensional Hubbard Model: An Exact Diagonalization Study". *Phys. Rev. B*, 37(13):7359–7367, 1988.

[56] D. P. Chen and J. Callaway. "Ground State of the Periodic Anderson Model: Comparison of Exact Diagonalization and Monte Carlo Results". *Phys. Rev. B*, 38(16):11869–11870, 1988.

[57] C. Lanczos. "Iteration Method for Solution of Eigenvalue Problem of Linear Differential and Integral Operators". *United States Bureau of Standards Journal of Research*, 45(4):255–282, 1950.

[58] C. Lanczos. "Iterative Solution of Large-Scale Linear Systems". *J. Soc. Indust. Appl. Math.*, 6(1):91–109, 1958.

[59] J. C. Bonner and M. E. Fisher. "Linear Magnetic Chains with Anisotropic Coupling". *Phys. Rev.*, 135(3A):A640–A658, 1964.

[60] J. Oitmaa and D. D. Betts. "Ground-State of 2 Quantum Models of Magnetism". *Can. J. Phys.*, 56(7):897–901, 1978.

[61] R. Jullien and R. M. Martin. "Ground-State and Low-Lying Excitations of the Periodic Anderson Hamiltonian in One Dimension from Finite Cell Calculations". *Phys. Rev. B*, 26(11):6173–6185, 1982.

[62] H. Fehske, M. Kinateder, G. Wellein, and A. R. Bishop. "Quantum Lattice Effects in Mixed-Valence Transition-Metal Chain Complexes". *Phys. Rev. B*, 63(24):245121, 2001.

[63] H. Fehske, A. Weiße, and G. Wellein. "Exact Diagonalization Results for Strongly Correlated Electron-Phonon Systems". In H. Rollnik and D. Wolf, editors, *NIC Symposium 2001, 5–6 December 2001, Jülich, Germany*, pages 259–269. John von Neumann Institut für Computing, 2002.

[64] M. Cini, G. Stefanucci, E. Perfetto, and A. Callegari. " 'Spin-Disentangled' Exact Diagonalization of Repulsive Hubbard Systems: Superconducting Pair Propagation". *J. Phys: Condens. Matter*, 14(43):L709–L714, 2002.

[65] H. de Raedt and W. von der Linden. "Monte Carlo Diagonalization of Many-Body Problems: Application to Fermion Systems". *Phys. Rev. B*, 45(15):8787–8790, 1992.

[66] H. De Raedt and M. Frick. "Stochastic Diagonalization". *Phys. Rep.*, 231(3):107–149, 1993.

[67] T. Mizusaki, M. Honma, and T. Otsuka. "Quantum Monte Carlo Diagonalization with Angular Momentum Projection". *Phys. Rev. C*, 53(6):2786–2793, 1996.

[68] L. Visscher, H. De Raedt, and W. C. Nieuwpoort. "A New Configuration Selection Method for Configuration-Interaction Calculations". *Chem. Phys. Lett.*, 227(3):327–336, 1994.

[69] K. Michielsen and H. De Raedt. Off-diagonal long-range order in generalized hubbard models. *Int. J. Mod. Phys. B*, 11(11):1311–1335, 1997.

[70] T. Husslein, W. Fettes, and I. Morgenstern. "Comparison of Calculations for the Hubbard Model Obtained with Quantum-Monte-Carlo, Exact, and Stochastic diagonalization". *Int. J. Mod. Phys. C*, 8(2):397–415, 1997.

[71] W. Fettes, I. Morgenstern, and T. Husslein. "Application of the SD Technique for Solving a BCS-Reduced Hubbard Like Hamiltonian". *Int. J. Mod. Phys. C*, 8(5):1037–1061, 1997.

[72] W. Fettes and I. Morgenstern. "Finite Size Scaling in the tt'-Hubbard Model and in BCS-Reduced Hubbard Models". *Int. J. Mod. Phys. C*, 9(7):943–985, 1998.

[73] S. Nandy, P. Chaudhury, and S. P. Bhattacharyya. "Stochastic Diagonalization of Hamiltonian: A Genetic Algorithm-Based Approach". *Int. J. Quant. Chem.*, 90(1):188–194, 2002.

[74] W. Fettes and I. Morgenstern. "Limitations of the Stochastic Diagonalization and the Projector QMC in the 2D Hubbard Model". *Comp. Phys. Comms.*, 124(1–3):148–168, 2000.

[75] D. P. Landau and K. Binder. *A Guide to Monte Carlo Simulations in Statistical Physics*. Cambridge University Press (Cambridge, UK), 2000.

[76] M. E. J. Newman and G. T. Barkema. *Monte Carlo Methods in Statistical Physics*. Oxford University Press (Oxford, UK), 1999.

[77] N. Metropolis. "Phase Shifts – Middle Squares – Wave Equation". In Herbert A. Meyer, editor, *Symposium on Monte Carlo Methods*, pages 29–36. John Wiley & Sons (New York), 1956.

[78] J. M. Thijssen. *Computational Physics*. Cambridge University Press (Cambridge, UK), 1999.

[79] J. B. Anderson. "A Random-Walk Simulation of the Schrödinger Equation: H_3^+". *J. Chem. Phys.*, 63(4):1499–1503, 1975.

[80] J. B. Anderson. "Quantum Chemistry by Random Walk. H ^2P, H_3^+ D_{3h} $^1A_1'$, H_2 $^3\Sigma_g^+$, Be ^1S". *J. Chem. Phys.*, 65(10):4121–4127, 1976.

[81] J. B. Anderson. "Quantum Chemistry By Random Walk: Higher Accuracy". *J. Chem. Phys.*, 73(8):3897–3899, 1980.

[82] W. L. McMillan. "Ground State of Liquid He^4". *Phys. Rev.*, 138(2A):A442–A451, 1965.

[83] D. M. Ceperley, G. V. Chester, and M. H. Kalos. "Monte Carlo Simulation of a Many-Fermion Study". *Phys. Rev. B*, 16(7):3081–3099, 1977.

[84] D. M. Ceperley. "Ground State of the Fermion One-Component Plasma: A Monte Carlo Study in Two and Three Dimensions". *Phys. Rev. B*, 18(7):3126–3138, 1978.

[85] M. H. Kalos. "Monte Carlo Calculations of the Ground State of Three- and Four-Body Nuclei". *Phys. Rev.*, 128(4):1791–1795, 1962.

[86] M. H. Kalos. "Energy of a Boson Fluid With Lennard-Jones Potentials". *Phys. Rev. A*, 2(1):250–255, 1970.

[87] J.-P. Hansen, D. Levesque, and D. Schiff. "Fluid-Solid Phase Transition of a Hard-Sphere Bose System". *Phys. Rev. A*, 3(2):776–780, 1971.

[88] K. S. Liu, M. H. Kalos, and G. V. Chester. "Quantum Hard Spheres in a Channel". *Phys. Rev. A*, 10(1):303–308, 1974.

[89] M. H. Kalos, D. Levesque, and L. Verlet. "Helium at Zero Temperature with Hard-Sphere and Other Forces". *Phys. Rev. A*, 9(5):2178–2195, 1974.

[90] P. A. Whitlock, D. M. Ceperley, G. V. Chester, and M. H. Kalos. "Properties of Liquid and Solid ^{4}He". *Phys. Rev. B*, 19(11):5598–5633, 1979.

[91] D. M. Ceperley, G. V. Chester, and M. H. Kalos. "Exact Calculations of the Ground State of Model Neutron Matter". *Phys. Rev. D*, 13(12):3208–3213, 1976.

[92] D. M. Ceperley, G. V. Chester, and M. H. Kalos. "Monte Carlo Study of the Ground State of Bosons Interacting With Yukawa Potentials". *Phys. Rev. B*, 17(3):1070–1081, 1978.

[93] D. M. Ceperley and M. H. Kalos. "Quantum Many-Body Problems". In K. Binder, editor, *Monte Carlo Methods in Statistical Physics*, pages 145–194. Springer-Verlag (Berlin), 1979.

[94] H. F. Fosdick and L. D. Jordan. "Path-Integral Calculation of the Two-Particle Slater Sum for ^{4}He". *Phys. Rev.*, 143(1):58–66, 1966.

[95] L. D. Jordan and H. F. Fosdick. "Three-Particle Effects in the Pair Distribution Function of He^4 Gas". *Phys. Rev.*, 171(1):128–149, 1968.

[96] S. G. Brush. "Functional Integrals and Statistical Physics". *Rev. Mod. Phys.*, 33(1):79–92, 1961.

[97] J. D. Reger and A. P. Young. "Monte Carlo Simulations of the Spin-$\frac{1}{2}$ Heisenberg Antiferromagnet on a Square Lattice". *Phys. Rev. B*, 37(10):5978–5981, 1988.

[98] M. Gross, E. Sánchez-Velasco, and E. Siggia. "Ground State Properties of the Two-Dimensional Antiferromagnetic Heisenberg Model". *Phys. Rev. B*, 39(4):2484–2493, 1989.

[99] K. E. Schmidt and D. M. Ceperley. "Monte Carlo Techniques for Quantum Fluids, Solids and Droplets". In K. Binder, editor, *The Monte Carlo Method in Condensed Matter Physics*, pages 205–248. Springer-Verlag (Berlin), 1995.

[100] G. J. Tawa, J. W. Moskowitz, P. A. Whitlock, and K. E. Schmidt. "Accurate 1st Principles Calculation of Many-Body Interactions". *Int. J. Supercomp. Appl. High Performance Comp.*, 5(1):57–71, 1991.

[101] S. A. Vitiello and K. E. Schmidt. "Optimization of ^{4}He Wave Functions for the Liquid and Solid Phases". *Phys. Rev. B*, 46(9):5442–5447, 1992.

[102] E. A. Kolganova, A. K. Motovilov, and S. A. Sofianos. "Three-Body Configuration Space Calculations with Hard-Core Potentials". *J. Phys. B*, 31(6):1279–1302, 1998.

[103] M. Boninsegni and E. Manousakis. "Quasihole Excitation in a Quantum Antiferromagnet: Variational Monte Carlo Calculation". *Phys. Rev. B*, 43(13):10353–10363, 1991.

[104] Y. K. Kwon, D. M. Ceperley, and R. M. Martin. "Effects of Three-Body and Backflow Correlations in the Two-Dimensional Electron Gas". *Phys. Rev. B*, 48(16):12037–12046, 1993.

[105] Y. K. Kwon, D. M. Ceperley, and R. M. Martin. "Transient-Estimate Monte Carlo in the Two-Dimensional Electron Gas". *Phys. Rev. B*, 53(11):7376–7382, 1996.

[106] Y. K. Kwon, D. M. Ceperley, and R. M. Martin. "Effects of Backflow Correlation in the Three-Dimensional Electron Gas: Quantum Monte Carlo Study". *Phys. Rev. B*, 58(11):6800–6806, 1998.

[107] L. Reatto and G. L. Masserini. "Shadow Wave Function for Many-Boson Systems". *Phys. Rev. B*, 38(7):4516–4522, 1988.

[108] S. Vitiello, K. Runge, and M. H. Kalos. "Variational Calculations for Solid and Liquid ^{4}He With a "Shadow" Wave Function". *Phys. Rev. Lett.*, 60(19):1970–1972, 1988.

[109] S. A. Vitiello, K. J. Runge, G. V. Chester, and M. H. Chester. "Shadow Wave-Function Variational Calculations of Crystalline and Liquid-Phases of He-4". *Phys. Rev. B*, 42(1):228–239, 1990.

[110] F. Pederiva, A. Ferrante, S. Fantoni, and L. Reatto. "Quantum Theory of Solid-Liquid Coexistence and Interface in ^{4}He". *Phys. Rev. Lett.*, 72(16):2589–2592, 1994.

[111] N. Trivedi and D. M. Ceperley. "Ground-State Correlations of Quantum Antiferromagnets: A Green-Function Monte Carlo Study". *Phys. Rev. B*, 41(7):4552–4569, 1990.

[112] D. J. Klein and H. M. Pickett. "Nodal Hypersurfaces and Anderson's Random-Walk Simulation of the Schrödinger Equation". *J. Chem. Phys.*, 64(11):4811–4812, 1976.

[113] M. S. L. du Croo de Jongh, J. M. J. van Leeuwen, and W. van Saarloos. "Incorporation of Density-Matrix Wave Functions in Monte Carlo Simulations: Application to the Frustrated Heisenberg Model". *Phys. Rev. B*, 62(22):14844–14854, 2000.

[114] G. An and J. M. J. van Leeuwen. "Fixed-Node Monte Carlo Study of the Two-Dimensional Hubbard Model". *Phys. Rev. B*, 44(17):9410–9417, 1991.

[115] S. Liang. "Monte Carlo Calculations of the Correlation Functions for Heisenberg Spin Chains at $T = 0$". *Phys. Rev. Lett.*, 64(13):1597–1600, 1990.

[116] S. Liang. "Existence of Néel Order at $T = 0$ in the Spin-$\frac{1}{2}$ Antiferromagnetic Heisenberg Model on a Square Lattice". *Phys. Rev. B*, 42(10):6555–6560, 1990.

[117] Y. C. Chen and T. K. Lee. "New Phase in the One-Dimensional *t*-*J* Model". *Phys. Rev. B*, 47(17):11548–11551, 1993.

[118] Y. C. Chen and T. K. Lee. "*t*-*J* Model Studied by the Power Lanczos Method". *Phys. Rev. B*, 51(10):6723–6726, 1995.

[119] D. M. Ceperley and B. J. Alder. "Ground State of the Electron Gas by a Stochastic Method". *Phys. Rev. Lett.*, 45(7):566–569, 1980.

[120] N. Trivedi and D. M. Ceperley. "Green-Function Monte Carlo Study of Quantum Antiferromagnets". *Phys. Rev. B*, 40(4):2737–2740, 1989.

[121] H. F. Trotter. "On the Product of Semi-Groups of Operators". *Proc. Am. Math. Soc.*, 10(4):545–551, 1959.

[122] M. Suzuki. "Relationship Between d-Dimensional Quantal Spin Systems and $(d + 1)$-Dimensional Ising Systems — Equivalence, Critical Exponents and Systematic Approximants of Partition-Function and Spin Correlations". *Prog. Theor. Phys.*, 56(5):1454–1469, 1976.

[123] J. A. Barker. "A Quantum-Statistical Monte Carlo Method; Path Integrals with Boundary Conditions". *J. Chem. Phys.*, 70(6):2914–2918, 1979.

[124] J. E. Hirsch, D. J. Scalapino, R. L. Sugar, and R. Blankenbecler. "Efficient Monte Carlo Procedure for Systems with Fermions". *Phys. Rev. Lett.*, 47(22):1628–1631, 1981.

[125] J. E. Hirsch, R. L. Sugar, D. J. Scalapino, and R. Blankenbecler. "Monte Carlo Simulations of One-Dimensional Fermion Systems". *Phys. Rev. B*, 29(9):5033–5055, 1982.

[126] J. E. Hirsch and D. J. Scalapino. "$2p_F$ and $4p_F$ Instabilities in a One-Quarter-Filled-Band Hubbard Model". *Phys. Rev. B*, 27(12):7169–7185, 1983.

[127] T. Barnes, D. Kotchan, and E. S. Swanson. "Evidence for a Phase Transition in the Zero-Temperature Anisotropic Two-Dimensional Heisenberg Antiferromagnet". *Phys. Rev. B*, 39(7):4357–4362, 1989.

[128] J. Carlson. "Ground-State and Low-Lying Excitations of the Heisenberg Antiferromagnet". *Phys. Rev. B*, 40(1):846–849, 1989.

[129] H. J. M. van Bemmel, D. F. B. ten Haaf, W. van Saarloos, J. M. J. van Leeuwen, and G. An. "Fixed-Node Quantum Monte Carlo Method for Lattice Fermions". *Phys. Rev. Lett.*, 72(15):2442–2445, 1994.

[130] D. F. B. ten Haaf, J. M. J. van Leeuwen H. J. M. van Bemmel, W. van Saarloos, and D. M. Ceperley. "Proof for an Upper Bound in Fixed-Node Monte Carlo for Lattice Fermions". *Phys. Rev. B*, 51(19):13039–13045, 1995.

[131] H. de Raedt and W. von der Linden. "Quantum Lattice Problems". In K. Binder, editor, *The Monte Carlo Method in Condensed Matter Physics*, pages 249–284. Springer-Verlag (Berlin), 1995.

[132] M. F. Herman, E. J. Bruskin, and B. J. Berne. "On Path Integral Monte Carlo Simulations". *J. Chem. Phys.*, 76(10):5150–5155, 1982.

[133] D. Thirumalai, Randall W. Hall, and B. J. Berne. "A Path Integral Monte Carlo Study of Liquid Neon and the Quantum Effective Pair Potential". *J. Chem. Phys.*, 81(6):2523–2527, 1984.

[134] E. L. Pollock and D. M. Ceperley. "Simulation of Quantum Many-Body Systems by Path-Integral Methods". *Phys. Rev. B*, 30(5):2555–2568, 1984.

[135] P. G. Wolynes. "Imaginary Time Path Integral Monte Carlo Route to Rate Coefficients for Nonadiabatic Barrier Crossing". *J. Chem. Phys.*, 87(11):6559–6561, 1987.

[136] A. Kuki. "Electronic Tunneling Paths in Proteins". *Structure and Bonding*, 75:49–81, 1991.

[137] D. Marx, P. Nielaba, and K. Binder. "Path-Integral Monte Carlo Study of a Model Adsorbate with Internal Quantum States". *Phys. Rev. B*, 47(13):7788–7804, 1993.

[138] R. Martonák and E. Tosatti. "Path-Integral Monte Carlo Study of a Model Two-Dimensional Quantum Paraelectric". *Phys. Rev. B*, 49(18):12596–12613, 1994.

[139] C. P. Herrero. "Thermally Assisted Tunneling of Hydrogen in Silicon: A Path-Integral Monte Carlo Study". *Phys. Rev. B*, 55(15):9235–9238, 1997.

[140] K. Yamaguchi, S. Yamanaka, M. Nishino, Y. Takano, Y. Kitagawa, H. Nagao, and Y. Yoshioka. "Symmetry and Broken Symmetries in Molecular Orbital Descriptions of Unstable Molecules II. Alignment, Frustration and Tunneling of Spins in Mesoscopic Molecular Magnets". *Theor. Chem. Acc.*, 102:328–345, 1999.

[141] E. Sim, G. Krilov, and B. J. Berne. "Quantum Rate Constants From Short-Time Dynamics: An Analytic Continuation Approach". *J. Phys. Chem. A*, 105(12):2824–2833, 2001.

[142] W. Janke and T. Sauer. "Path Integral Monte Carlo Using Multigrid Techniques". *Chem. Phys. Lett.*, 201(5–6):499–505, 1993.

[143] J. Shumway and D. M. Ceperley. "Path Integral Monte Carlo Simulations for Fermion Systems: Pairing in the Electron-Hole Plasma". *J. Phys. IV*, 10(P5):3–16, 2000.

[144] F. F. Assaad and D. Würtz. "Charge and Spin Structures in the One-Dimensional *t-J* Model". *Phys. Rev. B*, 44(6):2681–2696, 1991.

[145] M. A. Lee, K. A. Motakabbir, and K. E. Schmidt. "Ground State of the Extended One-Dimensional Hubbard Model: A Green's Function Monte Carlo Algorithm". *Phys. Rev. Lett.*, 53(12):1191–1194, 1984.

[146] J. E. Hirsch. "Two-Dimensional Hubbard Model: Numerical Simulation Study". *Phys. Rev. B*, 31(7):4403–4419, 1985.

[147] M. A. Lee, K. E. Schmidt, M. H. Kalos, and G. V. Chester. "Green's Function Monte Carlo Method for Liquid ^{3}He". *Phys. Rev. Lett.*, 46(11):728–731, 1981.

[148] D. M. Arnow, M. H. Kalos, M. A. Lee, and K. E. Schmidt. "Green's Function Monte Carlo for Few Fermions Problems". *J. Chem. Phys.*, 77(11):5562–5572, 1982.

[149] N. Furukawa and M. Imada. "Minus Sign Problem in the Monte Carlo Simulation of Lattice Fermion Systems". *J. Phys. Soc. Jpn.*, 60(3):810–824, 1991.

[150] Jr. E. Y. Loh, J. E. Gubernatis, R. T. Scalettar, S. R. White, D. J. Scalapino, and R. L. Sugar. "Sign Problem in the Numerical Simulation of Many-Electron Systems". *Phys. Rev. B*, 41(13):9301–9307, 1990.

[151] S. Fahy and D. R. Hamann. "Diffusive Behavior of States in the Hubbard-Stratonovich Transformation". *Phys. Rev. B*, 43(1):765–779, 1991.

[152] S. Sorella. "Green Function Monte Carlo With Stochastic Reconfiguration". *Phys. Rev. Lett.*, 80(20):4558–4561, 1998.

[153] S. Sorella and L. Capriotti. "Green Function Monte Carlo With Stochastic Reconfiguration: An Effective Remedy for the Sign Problem". *Phys. Rev. B*, 61(4):2599–2612, 2000.

[154] C. H. Mak, R. Egger, and H. Weber-Gottschick. "Multilevel Blocking Approach to the Fermion Sign Problem in Path-Integral Monte Carlo Simulations". *Phys. Rev. Lett.*, 81(21):4533–4536, 1998.

[155] C. H. Mak and R. Egger. "A Multilevel Blocking Approach to the Sign Problem in Real-Time Quantum Monte Carlo Simulations". *J. Chem. Phys.*, 110(1):12–14, 1999.

[156] R. Egger, L. Mühlbacher, and C. H. Mak. "Path-integral Monte Carlo Simulations Without the Sign Problem: Multilevel Blocking Approach for Effective Actions". *Phys. Rev. E*, 61(5):5961–5966, 2000.

[157] M. V. Dikovsky and C. H. Mak. "Analysis of the Multilevel Blocking Approach to the Fermion Sign Problem: Accuracy, Errors, and Practice". *Phys. Rev. B*, 63(23):235105, 2001.

[158] F. Alet, P. Dayal, A. Grzesik, A. Honecker, M. Körner, A. Läuchli, S. R. Manmana, I. P. McCulloch, F. Michel, R. M. Noack, G. Schmid, U. Schollwöck, F. Stöckli, S. Todo, S. Trebst, M. Troyer, P. Werner, and S. Wessel (ALPS collaboration). "The ALPS Project: Open Source Software for Strongly Correlated Systems". *J. Phys. Soc. Jpn.*, 74 Suppl.:30–35, 2005.

[159] Algorithms and Libraries for Physics Simulations (ALPS). `http://alps.comp-phys.org/`.

[160] Ö. Legeza and G. Fáth. "Accuracy of the Density-Matrix Renormalization-Group Method". *Phys. Rev. B*, 53(21):14349–14358, 1996.

[161] I. Peschel, X. Wang, M. Kaulke, and K. Hallberg (editors). *"Density-Matrix Renormalization: A New Numerical Method In Physics"*. Springer-Verlag (Berlin), 1999.

[162] N. Shibata. "Application of the Density Matrix Renormalization Group Method to Finite Temperatures and Two-Dimensional Systems". *J. Phys. A: Math. Gen.*, 36(37):R381–R410, 2003.

[163] K. Hallberg. "Density Matrix Renormalization: A Review of the Method and Its Applications". In D. Sénéchal, A.-M. Tremblay, and C. Bourbonnais (editors), editors, *Theoretical Methods for Strongly Correlated Electrons*. Springer (New York), 2004.

[164] A. Degenhard, J. Rodríguez-Laguna, and S. N. Santalla. "Density Matrix Renormalization Group Approach to Nonequilibrium Phenomena". *Multiscale Modeling & Simulation*, 3(1):89–105, 2004.

[165] J. Dukelsky and S. Pittel. "The Density Matrix Renormalization Group for Finite Fermi Systems". *Rep. Prog. Phys.*, 67:513–552, 2004.

[166] U. Schollwöck. "The Density-Matrix Renormalization Group". *Rev. Mod. Phys.*, 77(1):259–315, 2005.

[167] S. D. Drell, M. Weinstein, and S. Yankielowicz. "Quantum Field Theories on a Lattice: Variational Methods for Arbitrary Coupling Strengths and the Ising Model in a Transverse Magnetic Field". *Phys. Rev. D*, 16(6):1769–1781, 1977.

[168] J. N. Fields, H. W. J. Blöte, and J. C. Bonner. "Renormalization Group and Other Calculations for the One-Dimensional Spin-1/2 Dimerized Heisenberg Antiferromagnet". *J. Appl. Phys.*, 50(B3):1807–1809, 1979.

[169] H. W. J. Blöte, J. C. Bonner, and J. N. Fields. "Zero Temperature Quantum Renormalization Group". *J. Magn. Magn. Mater.*, 15–18(1):405–406, 1980.

[170] J. E. Hirsch. "Renormalization-Group Study of the Hubbard Model". *Phys. Rev. B*, 22(11):5259–5266, 1980.

[171] C. Y. Pan and X. Chen. "Renormalization-Group Study of High-Spin Heisenberg Antiferromagnets". *Phys. Rev. B*, 36(16):8600–8606, 1987.

[172] H. Q. Lin and C. Y. Pan. "Renormalization Group Study of the Anistropic and Alternating Heisenberg Antiferromagnets". *J. Phys. (France)*, 49(C–8):1415–1416, 1988.

[173] D. C. Mattis and R. Schilling. "Failure of Renormalization-Group Method in Semi-Classical Limit". *J. Phys. C*, 14(24):L729–L732, 1981.

[174] D. C. Mattis and C. Y. Pan. "Ground-State Energy of Heisenberg Antiferromagnet for Spins $s = \frac{1}{2}$ and $s = 1$ in $d = 1$ and 2 Dimensions". *Phys. Rev. Lett.*, 61(4):463–466, 1988.

[175] D. C. Mattis and C. Y. Pan. "Mattis and Pan Reply". *Phys. Rev. Lett.*, 61(19):2279, 1988.

[176] M. C. Chung and I. Peschel. "Density-Matrix Spectra of Solvable Fermionic Systems". *Phys. Rev. B*, 64:064412, 2001.

[177] I. Peschel, M. Kaulke, and Ö. Legeza. "Density-Matrix Spectra for Integrable Models". *Ann. Phys. (Leipzig)*, 8:153–164, 1999.

[178] I. Peschel and M.-C. Chung. "Density Matrices for a Chain of Oscillators". *J. Phys. A: Math. Gen.*, 32:8419–8428, 1999.

[179] R. P. Feynman. *Statistical Mechanics: A Set of Lectures*. Addison-Wesley (Reading, Massachussets), 1972.

[180] B. d'Espagnat. *Conceptual Foundations of Quantum Mechanics*. Addison-Wesley (Reading, Massachussets), 2nd edition, 1989.

[181] L. E. Ballentine. *Quantum Mechanics: A Modern Development*. World Scientific (Singapore), 1998.

[182] J. W. Negele and H. Orland. *Quantum Many-Particle Systems*. Perseus (Cambridge, Massachussets), 1998.

[183] I. Peschel. "Calculation of Reduced Density Matrices From Correlation Functions". *J. Phys. A: Math. Gen.*, 36(14):L205–L208, 2003.

[184] S.-A. Cheong and C. L. Henley. "Many-Body Density Matrices for Free Fermions". *Phys. Rev. B*, 69(7):075111, 2004.

[185] R. K. Pathria. *Statistical Mechanics*. Butterworth-Heinemann (Oxford), 2nd edition, 1996.

[186] E. R. Davidson and L. L. Jones. "Natural Expansion of Exact Wavefunctions. II. The Hydrogen-Molecule Ground State". *J. Chem. Phys.*, 37:2966–2971, 1962.

[187] C. F. Bender and E. R. Davidson. "A Natural Orbital Based Energy Calculation for Helium Hydride and Lithium Hydride". *J. Phys. Chem.*, 70:2675–2685, 1966.

[188] F. Jensen. *Introduction to Computational Chemistry*. John Wiley & Sons (Chichester), 1999.

[189] P. W. Anderson. "Poor Man's Derivation of Scaling Laws for Kondo Problem". *J. Phys. C*, 3:2436–2441, 1970.

[190] T. Xiang. "Density-Matrix Renormalization Group Method in Momentum Space". *Phys. Rev. B*, 53:R10445–R10448, 1996.

[191] J. Dukelsky and G. Sierra. "Density Matrix Renormalization Group Study of Ultrasmall Superconducting Grains". *Phys. Rev. Lett.*, 83:172–175, 1999.

[192] J. Gaite. "Angular Quantization and the Density Matrix Renormalization Group". *Mod. Phys. Lett.*, A16:1109–1116, 2001.

[193] K. Okunishi, Y. Hieida, and Y. Akutsu. "Universal Asymptotic Eigenvalue Distribution of Density Matrices and Corner Transfer Matrices in the Thermodynamic Limit". *Phys. Rev. E*, 59:R6227–R6230, 1999.

[194] M.-C. Chung and I. Peschel. "Density-Matrix Spectra for Two-Dimensional Systems". *Phys. Rev. B*, 62(7):4191–4193, 2000.

[195] W. Feller. *An Introduction to Probability Theory and Its Applications*, volume I. John Wiley (New York), 3rd edition, 1968.

[196] E. W. Weisstein. Lindeberg-Feller Central Limit Theorem. `http://mathworld.wolfram.com/Lindeberg-FellerCentralLimitTheorem.html`. From *MathWorld* — A Wolfram Web Resource.

[197] F. Gebhard, K. Bott, M. Scheidler, P. Thomas, and S. W. Koch. "Optical Absorption of Non-Interacting Tight-Binding Electrons in a Peierls-Distorted Chain at Half Band-Filling". *Phil. Mag. B*, 75:1–12, 1997.

[198] S.-A. Cheong and C. L. Henley. "Operator-Based Truncation Scheme Based on the Many-Body Fermion Density Matrix". *Phys. Rev. B*, 69(7):075112, 2004.

[199] G. Vidal, J. I. Latorre, E. Rico, and A. Kitaev. "Entanglement in Quantum Critical Phenomena". *Phys. Rev. Lett.*, 90(22):227902, 2003.

[200] J. I. Latorre, E. Rico, and G. Vidal. "Ground State Entanglement in Quantum Spin Chains". *Quant. Info. Comp.*, 4(1):48–92, 2004.

[201] B.-Q. Jin and V. E. Korepin. "Quantum Spin Chain, Toeplitz Determinants and the Fisher-Hartwig Conjecture". *J. Stat. Phys.*, 116(1–4):79–95, 2004.

[202] Octave. `http://www.octave.org/`.

[203] I. Peschel. "On the Reduced Density Matrix for a Chain of Free Electrons". *J. Stat. Mech.: Theor. Exp.*, June:P06004, 2004.

[204] C. L. Henley and N. G. Zhang. "Spinless Fermions and Charged Stripes at the Strong-Coupling Limit". *Phys. Rev. B*, 63(23):233107, 2001.

[205] N. G. Zhang and C. L. Henley. "Stripes and Holes in a Two-Dimensional Model of Spinless Fermions or Hardcore Bosons". *Phys. Rev. B*, 68(1):014506, 2003.

[206] N. G. Zhang and C. L. Henley. "Dilute Limit of a Strongly-Interacting Model of Spinless Fermions and Hardcore Bosons on the Square Lattice". *Eur. Phys. J. B*, 38(3):409–430, 2004.

[207] E. W. Weisstein. Dihedral Group D_4. `http://mathworld.wolfram.com/DihedralGroupD4.html`. From *MathWorld* — A Wolfram Web Resource.

[208] J. M. Hollas. *Modern Spectroscopy*. John Wiley & Sons (Chichester), 3rd edition, 1996.

[209] M. Lax. *Symmetry Principles in Solid State and Molecular Physics*. Dover (Mineola, New York), 2001.

[210] M. Abramowitz and I. A. Stegun. *Handbook of Mathematical Functions*. Dover (New York), 1965.

[211] S.-A. Cheong and C. L. Henley. "Many-Body Density Matrices On a Two-Dimensional Square Lattice: Noninteracting and Strongly Interacting Spinless Fermions". *www.arXiv.org preprint*, cond-mat/0508750, 2005.

[212] Modified Bessel Function. `http://www.efunda.com/math/bessel/modifiedbessel.cfm`.

[213] B. F. Bayman. "A Derivation of the Pairing-Correlation Method". *Nucl. Phys.*, 15(1):33–38, 1960.

[214] K. Dietrich, H. J. Mang, and J. H. Pradal. "Conservation of Particle Number in the Nuclear Pairing Model". *Phys. Rev.*, 135(1B):B22–B34, 1964.

[215] N. Ullah. "Projection of Angular Momentum and Fixed Particle Number from BCS Wave Function". *Phys. Rev. C*, 5(1):285–287, 1972.

[216] M. Fellah, T. F. Hammann, and D. E. Medjadi. "Fixed Particle Number and Angular Momentum Double-Projected BCS Wave Functions". *Phys. Rev. C*, 8(5):1585–1592, 1973.

[217] C. W. Ma and J. O. Rasmussen. "Microscopic Calculations of High-Spin Rotational States". *Phys. Rev. C*, 16(3):1179–1195, 1977.

[218] M. Kyotoku. "Analytical Number-Projected BCS Nuclear Model". *Phys. Rev. C*, 37(5):2242–2244, 1988.

[219] H. Flocard and N. Onishi. "On the Restoration of Symmetry in Paired Fermion Systems". *Ann. Phys.*, 254:275–327, 1997.

[220] J. A. Sheikh, P. Ring, E. Lopes, and R. Rossignoli. "Pairing Correlations and Particle-Number Projection Methods". *Phys. Rev. C*, 66(4):044318, 2002.

[221] F. Braun and J. von Delft. "Fixed-N Superconductivity: The Crossover from the Bulk to the Few-Electron Limit". *Phys. Rev. Lett.*, 81(21):4712–4715, 1998.

[222] K. Tanaka and F. Marsiglio. "Even-Odd and Super-Even Effects in the Attractive Hubbard Model". *Phys. Rev. B*, 60(5):3508–3526, 1999.

[223] K. Tanaka and F. Marsiglio. "Possible Electronic Shell Structure of Nanoscale Superconductors". *Phys. Lett. A*, 265:133–138, 2000.

[224] K. Tanaka and F. Marsiglio. "Fixed Number and Quantum Size Effects in Nanoscale Superconductors". *Physica C*, 341–348:277–278, 2000.

[225] S. Tomonaga. "Remarks on Blochs Method of Sound Waves Applied to Many-Fermion Problems". *Prog. Theor. Phys.*, 5(4):544–569, 1950.

[226] J. M. Luttinger. "An Exactly Soluble Model of a Many-Fermion System". *J. Math. Phys.*, 4(9):1154–1162, 1963.

[227] A. Luther and V. J. Emery. "Backward Scattering in the One-Dimensional Electron Gas". *Phys. Rev. Lett.*, 33(10):589–592, 1974.

[228] V. J. Emery. "Theory of the One-Dimensional Electron Gas". In J. T. Devreese, R. P. Evrard, and V. E. van Doren, editors, *Highly Conducting One-Dimensional Solids*, pages 247–303. Plenum Press (New York), 1979.

[229] J. Sólyom. "The Fermi Gas Model of One-Dimensional Conductors". *Adv. Phys.*, 28(2):201–303, 1979.

[230] J. Voit. "Phase Diagram and Correlation Functions of the Half-Filled Extended Hubbard Model in One Dimension". *Phys. Rev. B*, 45(8):4027–4042, 1992.

[231] J. Voit. "One-Dimensional Fermi Liquids". *Rep. Prog. Phys.*, 58(9):977–1116, 1995.

[232] A. Luther and I. Peschel. "Calculation of Critical Exponents in Two Dimensions From Quantum Field Theory in One Dimension". *Phys. Rev. B*, 12(9):3908–3917, 1975.

[233] T. Giamarchi and H. J. Schulz. "Correlation Functions of One-Dimensional Quantum Systems". *Phys. Rev. B*, 39(7):4620–4629, 1989.

[234] H. J. Schulz. "Correlated Fermions in One Dimension". *Int. J. Mod. Phys. B*, 5(1–2):57–74, 1991.

[235] C. N. Yang. "Some Exact Results for the Many-Body Problem in One Dimension With Repulsive Delta-Function Interaction". *Phys. Rev. Lett.*, 19(23):1312–1315, 1967.

[236] E. H. Lieb and F. Y. Wu. "Absence of Mott Transition in an Exact Solution of the Short-Range, One-Band Model in One Dimension". *Phys. Rev. Lett.*, 20(25):1445–1448, 1968.

[237] B. S. Shastry. "Decorated Star-Triangle Relations and Exact Integrability of the One-Dimensional Hubbard Model". *J. Stat. Phys.*, 50(1–2):57–79, 1988.

[238] A. Parola and S. Sorella. "Asymptotic Spin-Spin Correlations of the $U \rightarrow \infty$ One-Dimensional Hubbard Model". *Phys. Rev. Lett.*, 64(15):1831–1834, 1990.

[239] Z. Y. Weng, D. N. Sheng, C. S. Ting, and Z. B. Su. "One-Dimensional Large-U Hubbard Model: An Analytical Approach". *Phys. Rev. Lett.*, 67(23):3318–3321, 1991.

[240] M. Imada and Y. Hatsugai. "Numerical Studies on the Hubbard Model and the t-J Model in One- and Two-Dimensions". *J. Phys. Soc. Jpn.*, 58(10):3752–3780, 1989.

[241] M. Ogata and H. Shiba. "Bethe-Ansatz Wave Function, Momentum Distribution, and Spin Correlation in the One-Dimensional Strongly Correlated Hubbard Model". *Phys. Rev. B*, 41(4):2326–2338, 1990.

[242] S. Sorella, A. Parola, M. Parrinello, and E. Tosatti. "Non-Fermi-Liquid Exponents of the One-Dimensional Hubbard Model". *Europhys. Lett.*, 12(8):721–726, 1990.

[243] J. H. Xu and J. Yu. "Correlation Functions and Dynamical Properties of the One-Dimensional Hubbard Model". *Phys. Rev. B*, 45(12):6931–6934, 1992.

[244] A. A. Belavin, A. M. Polyakov, and A. B. Zamolodchikov. "Infinite Conformal Symmetry in Two-Dimensional Quantum Field Fheory". *Nucl. Phys. B*, 241(2):333–380, 1984.

[245] H. W. J. Blöte, J. L. Cardy, and M. P. Nightingale. "Conformal Invariance, the Central Charge, and Universal Finite-Size Amplitudes at Criticality". *Phys. Rev. Lett.*, 56(7):742–745, 1986.

[246] J. L. Cardy. "Operator Content of Two-Dimensional Conformally Invariant Theories". *Nucl. Phys. B*, 270:186–204, 1986.

[247] F. Woynarovich. "Finite-Size Effects in a Non-Half-Filled Hubbard Chain". *J. Phys. A: Math. Gen.*, 22:4243–4256, 1989.

[248] H. Frahm and V. E. Korepin. "Critical Exponents for the One-Dimensional Hubbard Model". *Phys. Rev. B*, 42(16):10553–10565, 1990.

[249] H. Frahm and V. E. Korepin. "Correlation Functions of the One-Dimensional Hubbard Model in a Magnetic Field". *Phys. Rev. B*, 43(7):5653–5662, 1991.

[250] N. Kawakami and S.-K. Yang. "Luttinger anomaly exponent of momentum distribution in the Hubbard Chain". *Phys. Lett. A*, 148(6–7):359–362, 1990.

[251] H. Frahm and V. E. Korepin. "Critical Exponents in the One-Dimensional Hubbard Model". *Int. J. Mod. Phys. B*, 8(4):403–415, 1994.

[252] H. J. Schulz. "Correlation Exponents and the Metal-Insulator Transition in the One-Dimensional Hubbard Model". *Phys. Rev. Lett.*, 64(23):2831–2834, 1990.

[253] M. Imada, N. Furukawa, and T. M. Rice. "Crossover of Spin Correlations in the One-Dimensional Hubbard Model". *J. Phys. Soc. Jpn.*, 61(11):3861–3864, 1992.

[254] H. de Raedt and A. Lagendijk. "Monte Carlo Calculation of the Thermodynamic Properties of a Quantum Model: A One-Dimensional Fermion Lattice Model". *Phys. Rev. Lett.*, 46(2):77–80, 1981.

[255] J. E. Hirsch and D. J. Scalapino. "$2p_F$ and $4p_F$ Instabilities in the One-Dimensional Electron Gas". *Phys. Rev. Lett.*, 50(15):1168–1171, 1983.

[256] J. E. Hirsch and D. J. Scalapino. "$2p_F$ and $4p_F$ Instabilities in the One-Dimensional Hubbard Model". *Phys. Rev. B*, 29(10):5554–5561, 1984.

[257] M. Tsuchiizu and A. Furusaki. "Ground-State Phase Diagram of the One-Dimensional Half-Filled Extended Hubbard Model". *Phys. Rev. B*, 69(3):035103, 2004.

[258] C. K. Lai. "Lattice Gas With Nearest-Neighbor Interaction in One Dimension With Arbitrary Statistics". *J. Math. Phys.*, 15(10):1675–1676, 1974.

[259] B. Sutherland. "Model for a Multi-Component Quantum System". *Phys. Rev. B*, 12(9):3795–3805, 1975.

[260] P. Schlottmann. "Integrable Narrow-Band Model With Possible Relevance to Heavy-Fermion Systems". *Phys. Rev. B*, 36(10):5177–5185, 1987.

[261] P. A. Bares and G. Blatter. "Supersymmetric *t-J* Model in One Dimension: Separation of Spin and Charge". *Phys. Rev. Lett.*, 64(21):2567–2570, 1990.

[262] P.-A. Bares, G. Blatter, and M. Ogata. "Exact Solution of the *t-J* Model in One Dimension at $2t = \pm J$: Ground State and Excitation Spectrum". *Phys. Rev. B*, 44(1):130–154, 1991.

[263] S. Sarkar. "Bethe-Ansatz Solution of the *t-J* Model". *J. Phys. A: Math. Gen.*, 23:L409–414, 1990.

[264] N. Kawakami and S.-K. Yang. "Correlation Functions in the One-Dimensional *t-J* Model". *Phys. Rev. Lett.*, 65(18):2309–2311, 1990.

[265] N. Kawakami and S.-K. Yang. "Luttinger Liquid Properties of Highly Correlated Electron Systems in One Dimension". *J. Phys: Condens. Matter*, 3:5983–6008, 1991.

[266] N. Kawakami and S.-K. Yang. "Application of Conformal Field Theory to Electron Systems". *Prog. Theor. Phys. Suppl.*, 106:157–165, 1991.

[267] N. Kawakami and S.-K. Yang. "Conformal Field Theory Approach to One-Dimensional Quantum Liquids". *Prog. Theor. Phys. Suppl.*, 107:59–75, 1992.

[268] M. Imada. "Superconducting Correlation of the One-Dimensional *t-J* Model". *J. Phys. Soc. Jpn.*, 59(11):4121–4128, 1990.

[269] K. J. von Szczepanski, P. Horsch, W. Stephan, and M. Ziegler. "Single-Particle Excitations in a Quantum Antiferromagnet". *Phys. Rev. B*, 41(4):2017–2029, 1990.

[270] M. Ogata, M. U. Luchini, S. Sorella, and F. F. Assaad. "Phase Diagram of the One-Dimensional *t-J* Model". *Phys. Rev. Lett.*, 66(18):2388–2391, 1991.

[271] M. Luchini, M. Ogata, W. Putikka, and T. M. Rice. "Phase Diagram of the *t-J* Model". *Physica C*, 185–189:141–146, 1991.

[272] T. Pruschke and H. Shiba. "Pairing Correlations for the 1-Dimensional *t-J* Model". *Physica C*, 185–189:1573–1574, 1991.

[273] K. Sano and K. Takano. "Numerical Study on Spin and Charge Degrees of Freedom in One-Dimensional *t-J* Model". *Physica C*, 185–189:1725–1726, 1991.

[274] E. Dagotto, J. Riera, and D. J. Scalapino. "Superconductivity in Ladders and Coupled Planes". *Phys. Rev. B*, 45(10):5744–5747, 1992.

[275] T. Pruschke and H. Shiba. "Superconducting Correlations in the One-Dimensional *t-J* Model". *Phys. Rev. B*, 46(1):356–365, 1992.

[276] K. J. von Szczepanski, P. Horsch, W. Stephan, and M. Ziegler. "Erratum: Single-Particle Excitations in a Quantum Antiferromagnet[Phys. Rev. B 41, 2017 (1990)]". *Phys. Rev. B*, 45(9):5118, 1992.

[277] M. Troyer, H. Tsunetsugu, T. M. Rice, J. Riera, and E. Dagotto. "Spin Gap and Superconductivity in the One-Dimensional *t-J* Model With Coulomb Repulsion". *Phys. Rev. B*, 48(6):4002–4013, 1993.

[278] B. Ammon, M. Troyer, and H. Tsunetsugu. "Effect of the Three-Site Hopping Term on the *t-J* Model". *Phys. Rev. B*, 52(1):629–636, 1995.

[279] L. Chen and S. Moukouri. "Numerical Renormalization-Group Study of the One-Dimensional *t-J* Model". *Phys. Rev. B*, 53(4):1866–1870, 1996.

[280] C. S. Hellberg and E. J. Mele. "Phase Diagram of the One-Dimensional *t-J* Model From Variational Theory". *Phys. Rev. Lett.*, 67(15):2080–2083, 1991.

[281] H. Yokoyama and M. Ogata. "Variational Wave Functions and Ground-State Properties in the One-Dimensional *t-J* Model". *Phys. Rev. Lett.*, 67(25):3610–3613, 1991.

[282] T. Xiang and N. d'Ambrumenil. "Charge-Spin Separation and the Ground-State Wave Function of the One-Dimensional *t-J* Model". *Phys. Rev. B*, 45(14):8150–8153, 1992.

[283] C. S. Hellberg and E. J. Mele. "Luttinger-Liquid Instability in the One-Dimensional *t-J* Model". *Phys. Rev. B*, 48(1):646–649, 1993.

[284] M. Marder, N. Papanicolaou, and G. C. Psaltakis. "Phase Separation in a *t-J* Model". *Phys. Rev. B*, 41(10):6920–6932, 1990.

[285] M. Imada. "Spin-Dimer State Model and Spin-Phonon Coupling Model of Superconductivity". *J. Phys. Soc. Jpn.*, 60(6):1877–1880, 1991.

[286] V. J. Emery, S. A. Kivelson, and H. Q. Lin. "Phase Separation in the *t-J* Model". *Phys. Rev. Lett.*, 64(4):475–478, 1990.

[287] S. A. Kivelson, V. J. Emery, and H. Q. Lin. "Doped Antiferromagnets in the Weak-Hopping Limit". *Phys. Rev. B*, 42(10):6523–6530, 1990.

[288] M. Ogata, M. U. Luchini, and T. M. Rice. "Spin Gap in a Generalized One-Dimensional *t-J* Model". *Phys. Rev. B*, 44(21):12083–12085, 1991.

[289] E. Dagotto and J. Riera. "Superconductivity in the Two-Dimensional *t-J* Model". *Phys. Rev. B*, 46(18):12084–12087, 1992.

[290] H. Frahm and A. Schadschneider. "Critical Exponents of the Degenerate Hubbard Model". *J. Phys. A: Math. Gen.*, 26:1463–1480, 1993.

[291] K. A. Muttalib and V. J. Emery. "Solvable Two-Band Model of Fermions". *Phys. Rev. Lett.*, 57(11):1370–1373, 1986.

[292] K. Kuroki and H. Aoki. "Realization of Negative-*U* Superconductivity in a Class of Purely Repulsive Systems: Interacting Carrier and Insulating bands". *Phys. Rev. Lett.*, 69(26):3820–3823, 1992.

[293] M. Fabrizio and A. Parola. "Spin-Charge Separation in a Model of Two Coupled Chains". *Phys. Rev. Lett.*, 70(2):226–229, 1993.

[294] K. Kuroki and H. Aoki. "Superconductivity in Metal-Insulator Composite Bands: A Realization of Negative-*U* Pairing in Purely Repulsive Systems". *Phys. Rev. B*, 48(10):7598–7617, 1993.

[295] A. M. Finkel'stein and A. I. Larkin. "Two Coupled Chains With Tomonaga-Luttinger Interactions". *Phys. Rev. B*, 47(16):10461–10473, 1993.

[296] D. G. Clarke, S. P. Strong, and P. W. Anderson. "Incoherence of Single Particle Hopping Between Luttinger Liquids". *Phys. Rev. Lett.*, 72(20):3218–3221, 1994.

[297] K. Kuroki and H. Aoki. "Superconductivity in a Repulsively Interacting Two-Band Fermi Gas". *Phys. Rev. Lett.*, 72(18):2947–2950, 1994.

[298] N. Nagaosa. "Bipolaron Picture of Spin Gap State in Double-Chain Systems". *Sol. State Comm.*, 94(7):495–498, 1995.

[299] H. J. Schulz. "Coupled Luttinger Liquids". In T. Martin, G. Montambaux, and J. Tran Thanh Van, editors, *Correlated Fermions and Transport in Mesoscopic Systems (Proceedings of the XXXI Rencontres de Moriond conference on Correlated Fermions and Transport in Mesoscopic Systems, Les Arcs, France, January 1996)*, page 81, Gif–sur–Yvette, France, 1996. Editions Frontieres.

[300] H. J. Schulz. "Phases of Two Coupled Luttinger Liquids". *Phys. Rev. B*, 53(6):R2959–R2962, 1996.

[301] H. J. Schulz. "Phase Diagrams and Correlation Exponents for Quantum Spin Chains of Arbitrary Spin Quantum Number". *Phys. Rev. B*, 34(9):6372–6385, 1986.

[302] E. Dagotto and A. Moreo. "Zero-Temperature Properties of the Two-Dimensional Heisenberg Antiferromagnet: A Numerical Study". *Phys. Rev. B*, 38(7):5087–5090, 1988.

[303] S. P. Strong and A. J. Millis. "Competition Between Singlet Formation and Magnetic Ordering in One-Dimensional Spin Systems". *Phys. Rev. Lett.*, 69(16):2419–2422, 1992.

[304] T. Barnes, E. Dagotto, J. Riera, and E. S. Swanson. "Excitation Spectrum of Heisenberg Spin Ladders". *Phys. Rev. B*, 47(6):3196–3203, 1993.

[305] A. Parola, S. Sorella, and Q. F. Zhong. "Realization of a Spin Liquid in a Two Dimensional Quantum Antiferromagnet". *Phys. Rev. Lett.*, 71(26):4393–4396, 1993.

[306] M. Azzouz, L. Chen, and S. Moukouri. "Calculation of the Singlet-Triplet Gap of the Antiferromagnetic Heisenberg Model on a Ladder". *Phys. Rev. B*, 50(9):6233–6237, 1994.

[307] T. Barnes and J. Riera. "Susceptibility and Excitation Spectrum of $(VO)_2P_2O_7$ in Ladder and Dimer-Chain Models". *Phys. Rev. B*, 50(10):6817–6822, 1994.

[308] S. Gopalan, T. M. Rice, and M. Sigrist. "Spin Ladders With Spin Gaps: A Description of a Class of Cuprates". *Phys. Rev. B*, 49(13):8901–8910, 1994.

[309] S. P. Strong and A. J. Millis. "Competition Between Singlet Formation and Magnetic Ordering in One-Dimensional Spin Systems". *Phys. Rev. B*, 50(14):9911–9923, 1994.

[310] M. Troyer, H. Tsunetsugu, and D. Würtz. "Thermodynamics and Spin Gap of the Heisenberg Ladder Calculated By the Look-Ahead Lanczos Algorithm". *Phys. Rev. B*, 50(18):13515–13527, 1994.

[311] S. R. White, R. M. Noack, and D. J. Scalapino. "Resonating Valence Bond Theory of Coupled Heisenberg Chains". *Phys. Rev. Lett.*, 73(6):886–889, 1994.

[312] S. R. White, R. M. Noack, and D. J. Scalapino. "Density Matrix Renormalization Group Calculations for Doped Hubbard Ladders". *J. Low Temp. Phys.*, 99(3–4):593–598, 1995.

[313] B. Frischmuth, B. Ammon, and M. Troyer. "Susceptibility and Low-Temperature Thermodynamics of Spin-$\frac{1}{2}$ Heisenberg Ladders". *Phys. Rev. B*, 54(6):R3714–R3717, 1996.

[314] E. Dagotto and T. M. Rice. "Surprises on the Way from One- to Two-Dimensional Quantum Magnets: The Ladder Materials". *Science*, 271(5249):618–623, 1996.

[315] M. Azuma, Z. Hiroi, M. Takano, K. Ishida, and Y. Kitaoka. "Observation of a Spin Gap in $SrCu_2O_3$ Comprising Spin-$\frac{1}{2}$ Quasi-1D Two-Leg Ladders". *Phys. Rev. Lett.*, 73(25):3463–3466, 1994.

[316] R. S. Eccleston, T. Barnes, J. Brody, and J. W. Johnson. "Inelastic Neutron Scattering From the Spin Ladder Compound $(VO)_2P_2O_7$". *Phys. Rev. Lett.*, 73(19):2626–2629, 1994.

[317] J. C. Bonner, S. A. Friedberg, H. Kobayashi, D. L. Meier, and W. J. Blöte. "Alternating Linear-Chain Antiferromagnetism in Copper Nitrate $Cu(NO_3)_2 \cdot 2.5\ H_2O$". *Phys. Rev. B*, 27(1):248–260, 1983.

[318] D. C. Johnston, J. W. Johnson, D. P. Goshorn, and A. J. Jacobson. "Magnetic Susceptibility of $(VO)_2P_2O_7$: A One-Dimensional Spin-$\frac{1}{2}$ Heisenberg Antiferromagnet With a Ladder Spin Configuration and a Singlet Ground State". *Phys. Rev. B*, 35(1):219–222, 1987.

[319] Z. Hiroi, M. Takano, M. Azuma, Y. Takeda, and Y. Bando. "A New Superconducting Cupric Oxide Found in the Sr-Cu-O System". *Physica C*, 185–189:521–524, 1991.

[320] Z. Hiroi and M. Takano. "Absence of Superconductivity in the Doped Antiferromagnetic Spin Ladder Compound $(La,Sr)CuO_{2.5}$". *Nature*, 377(6544):41–43, 1995.

[321] L. Balents and M. P. A. Fisher. "Weak-Coupling Phase Diagram of the Two-Chain Hubbard Model". *Phys. Rev. B*, 53(18):12133–12141, 1996.

[322] M. Fabrizio, A. Parola, and E. Tosatti. "Strong-Coupling Phases of Two Hubbard Chains With Interchain Hopping". *Phys. Rev. B*, 46(5):3159–3162, 1992.

[323] M. Fabrizio. "Role of Transverse Hopping in a Two-Coupled-Chains Model". *Phys. Rev. B*, 48(21):15838–15860, 1993.

[324] D. V. Khveshchenko and T. M. Rice. "Spin-Gap Fixed Points in the Double-Chain Problem". *Phys. Rev. B*, 50(1):252–257, 1994.

[325] T. Kimura, K. Kuroki, and H. Aoki. "Correlation Functions in the Three-Chain Hubbard Ladder". *Phys. Rev. B*, 54(14):R9608–R9611, 1996.

[326] E. Orignac and T. Giamarchi. "Effects of Weak Disorder on Two Coupled Hubbard Chains". *Phys. Rev. B*, 53(16):R10453–R10456, 1996.

[327] H.-H. Lin, L. Balents, and M. P. A. Fisher. "*N*-Chain Hubbard Model in Weak Coupling". *Phys. Rev. B*, 56(11):6569–6593, 1997.

[328] T. Kimura, K. Kuroki, and H. Aoki. "Pairing Correlation in the Three-Leg Hubbard Ladder — Renormalization Group and Quantum Monte Carlo Studies". *J. Phys. Soc. Jpn.*, 67(4):1377–1390, 1998.

[329] H.-H. Lin, L. Balents, and M. P. A. Fisher. "Exact SO(8) Symmetry in the Weakly-Interacting Two-Leg Ladder". *Phys. Rev. B*, 58(4):1794–1825, 1998.

[330] E. Orignac and Y. Suzumura. "Competition of Disorder and Interchain Hopping in a Two-Chain Hubbard Model". *Eur. Phys. J. B*, 23:57–67, 2001.

[331] R. M. Noack, S. R. White, and D. J. Scalapino. "Correlations in a Two-Chain Hubbard Model". *Phys. Rev. Lett.*, 73(6):882–885, 1994.

[332] R. M. Noack, S. R. White, and D. J. Scalapino. "The Doped Two-Chain Hubbard Model". *Europhys. Lett.*, 30(3):163–168, 1995.

[333] R. M. Noack, S. R. White, and D. J. Scalapino. "The Ground State of the Two-Leg Hubbard Ladder: A Density-Matrix Renormalization Group Study". *Physica C*, 270:281–296, 1996.

[334] R. M. Noack, D. J. Scalapino, and S. R. White. "Ground-State Properties of the Two-Chain Hubbard Ladder". *Phil. Mag. B*, 74(5):485–496, 1996.

[335] D. Poilblanc, D. J. Scalapino, and W. Hanke. "Spin and Charge Modes of the *t*-*J* Ladder". *Phys. Rev. B*, 52(9):6796–6800, 1995.

[336] D. J. Scalapino. "Numerical Studies of the 2-Leg Hubbard Ladder". *Physica C*, 282–287:157–161, 1997.

[337] T. M. Rice, S. Gopalan, and M. Sigrist. "Superconductivity, Spin Gaps and Luttinger Liquids in a Class of Cuprates". *Europhys. Lett.*, 23(6):445–449, 1993.

[338] J. Sólyom and J. Timonen. "Anisotropic Heisenberg Chain With Composite Spin". *Phys. Rev. B*, 34(1):487–489, 1986.

[339] K. Yamaji, K. Harigaya, T. Yanagisawa, and Y. Shimoi. "Superconducting Phase Diagram of the Two-Band Model Investigated by the Exact Diagonalization Method". *J. Phys. Soc. Jpn.*, 61(10):3689–3698, 1992.

[340] K. Yamaji and Y. Shimoi. "Superconducting Transition of the Two-Chain Hubbard Model Indicated by Diagonalization Calculations". *Physica C*, 222:349–360, 1994.

[341] K. Yamaji, Y. Shimoi, and T. Yanagisawa. "Superconductivity Indications of the Two-Chain Hubbard Model Due to the Two-Band Effect". *Physica C*, 235–240:2221–2222, 1994.

[342] D. J. Scalapino, R. L. Sugar, R. M. Noack, S. R. White, R. T. Scalettar, M. Vekic, and J. W. Cannon. "Insulating States of Correlated Electrons". *J. Low Temp. Phys.*, 99(3–4):487–498, 1995.

[343] Y. Shimoi, K. Yamaji, and T. Yanagisawa. "Superconductivity Due to the Two-Band Mechanism in the Two-Chain and Two-Dimensional Hubbard Model". *Synth. Met.*, 70:1017–1018, 1995.

[344] T. Yanagisawa, Y. Shimoi, and K. Yamaji. "Superconducting Phase of a Two-Chain Hubbard Model". *Phys. Rev. B*, 52(6):R3860–R3863, 1995.

[345] K. Kuroki, T. Kimura, and H. Aoki. "Quantum Monte Carlo Study of the Pairing Correlation in the Hubbard Ladder". *Phys. Rev. B*, 54(22):R15641–R15644, 1996.

[346] T. Kimura, K. Kuroki, and H. Aoki. "Superconductivity in the Three-Leg Hubbard Ladder: A Quantum Monte Carlo Study". *J. Phys. Soc. Jpn.*, 66(6):1599–1602, 1997.

[347] Y. Asai. "Superconducting, Magnetic, and Charge Correlations in the Doped Two-Chain Hubbard Model". *Phys. Rev. B*, 52(14):10390–10394, 1995.

[348] H. Endres, R. M. Noack, W. Hanke, D. Poilblanc, and D. J. Scalapino. "Dynamical Properties of Two Coupled Hubbard Chains at Half-Filling". *Phys. Rev. B*, 53(9):5530–5540, 1996.

[349] H. Endres, R. M. Noack, W. Ziegler, and W. Hanke. "Dynamical Properties of Doped Strongly Coupled Hubbard Chains". *Physica B*, 230–232:811–815, 1997.

[350] R. M. Noack, N. Bulut, D. J. Scalapino, and M. G. Zacher. "Enhanced $d_{x^2-y^2}$ Pairing Correlations in the Two-Leg Hubbard Ladder". *Phys. Rev. B*, 56(12):7162–7166, 1997.

[351] K. Penc, H. Shiba, F. Mila, and T. Tsukagoshi. "Ferromagnetism in Multiband Hubbard Models: From Weak to Strong Coulomb Repulsion". *Phys. Rev. B*, 54(6):4056–4067, 1996.

[352] T. Munehisa and Y. Munehisa. "Quantum Monte Carlo Study of An Extended Hubbard Model on a Two-Leg Ladder". *J. Phys. Soc. Jpn*, 66(12):3876–3880, 1997.

[353] P. Donohue, M. Tsuchiizu, T. Giamarchi, and Y. Suzumura. "Spinless Femion Ladders at Half Filling". *Phys. Rev. B*, 63(4):045121, 2001.

[354] M. Tsuchiizu and A. Furusaki. "Generalized Two-Leg Hubbard Ladder at Half Filling: Phase Diagram and Quantum Criticalities". *Phys. Rev. B*, 66(24):245106, 2002.

[355] E. Orignac and R. Citro. "Charge Density Waves and Bond Order Waves in a Quarter Filled Extended Hubbard Ladder". *Eur. Phys. J. B*, 33:419–438, 2003.

[356] R. Citro and E. Orignac. "Quantum Phase Transitions in a Quarter-Filled Hubbard Ladder". *Physica C*, 408–410:290–291, 2004.

[357] K. Takano and K. Sano. "Dimer States in the One-Dimensional t-J-J' Model". *Phys. Rev. B*, 48(13):9831–9834, 1993.

[358] M. Sigrist, T. M. Rice, and F. C. Zhang. "Superconductivity in a Quasi-One-Dimensional Spin Liquid". *Phys. Rev. B*, 49(17):12058–12061, 1994.

[359] D. V. Khveshchenko. "Singlet Pairing in the Double-Chain t-J Model". *Phys. Rev. B*, 50(1):380–384, 1994.

[360] H. Tsunetsugu, M. Troyer, and T. M. Rice. "Pairing and Excitation Spectrum in Doped t-J Ladders". *Phys. Rev. B*, 49(22):16078–16081, 1994.

[361] M. Imada. "Spin-Gap State and Superconducting Correlations in One-Dimensional Dimerized t-J Model". *Phys. Rev. B*, 48(1):550–556, 1993.

[362] C. A. Hayward, D. Poilblanc, R. M. Noack, D. J. Scalapino, and W. Hanke. "Evidence for a Superfluid Density in t-J Ladders". *Phys. Rev. Lett.*, 75(5):926–929, 1995.

[363] H. Tsunetsugu, M. Troyer, and T. M. Rice. "Singlet Stripe Phases in the Planar t-J Model". *Phys. Rev. B*, 51(22):16456–16459, 1995.

[364] C. A. Hayward and D. Poilblanc. "Luttinger-Liquid Behavior and Superconducting Correlations in t-J Ladders". *Phys. Rev. B*, 53(17):11721–11728, 1996.

[365] M. Troyer, H. Tsunetsugu, and T. M. Rice. "Properties of Lightly Doped t-J Two-Leg Ladders". *Phys. Rev. B*, 53(1):251–267, 1996.

[366] K. B. Efetov and A. I. Larkin. "Correlation Functions in One-Dimensional Systems With a Strong Interaction". *Sov. Phys. JETP*, 42(2):390–396, 1976.

[367] P. Jordan and E. Wigner. "Pauli's Equivalence Prohibition". *Z. Phys.*, 47(9–10):631–651, 1928.

[368] P. Fendley, B. Nienhuis, and K. Schoutens. "Lattice Fermion Models with Supersymmetry". *J. Phys. A: Math. Gen.*, 36(50):12399–12424, 2003.

[369] Inverse Symbolic Calculator. http://oldweb.cecm.sfu.ca/projects/ISC/ISCmain.html.

[370] M. Girardeau. "Relationship Between Systems of Impenetrable Bosons and Fermions in One Dimension". *J. Math. Phys.*, 1(6):516–523, 1960.

[371] M. A. Cazalilla. "Differences Between the Tonks Regimes in the Continuum and on the Lattice". *Phys. Rev. A*, 70(4):041604(R), 2004.

[372] Grace. http://plasma-gate.weizmann.ac.il/Grace/.

[373] Levenberg-marquardt method. http://www-fp.mcs.anl.gov/otc/Guide/OptWeb/continuous/unconstrained/non%linearls/section2_1_2.html.

[374] J. M. Luttinger. "Fermi Surface and Some Simple Equilibrium Properties of a System of Interacting Fermions". *Phys. Rev.*, 119(4):1153–1163, 1960.

[375] M. Oshikawa. "Topological Approach to Luttinger's Theorem and the Fermi Surface of a Kondo Lattice". *Phys. Rev. Lett.*, 84(15):3370–3373, 2000.

[376] I. Dzyaloshinskii. "Some Consequences of the Luttinger Theorem: The Luttinger Surfaces in Non-Fermi Liquids and Mott Insulators". *Phys. Rev. B*, 68(8):085113, 2003.

[377] M. M. Korshunov and S. G. Ovchinnikov. "Generalization of Luttinger's Theorem for Strongly Correlated Electron Systems". *Physics of the Solid State*, 45(8):1415–1422, 2003.

[378] A. Paramekanti and A. Vishwanath. "Extending Luttinger's Theorem to Z_2 Fractionalized Phases of Matter". *Phys. Rev. B*, 70(24):245118, 2004.

[379] Y.-L. Liu. "Luttinger Theorem and Nonlinear Response of Quantum Many-Particle Systems". *Phys. Rev. B*, 72(15):155104, 2005.

[380] C. L. Henley. Private communications.

[381] M. Troyer. Private communications.

[382] Gnuplot. http://www.gnuplot.info/.

[383] N. G. Zhang. *Strongly-Interacting Spinless Fermions and Hardcore Bosons on the Square Lattice*. PhD thesis, Cornell University, January 2002.

[384] M. C. Nguyen, P. Santini, and P. Erdös. "Numerical Calculation of Correlation Functions by Boundary Condition Averaging: Test on the One-Dimensional Hubbard Model". *Comp. Phys. Comms.*, 92:16–20, 1995.

[385] G. Spronken, R. Jullien, and M. Avignon. "Real-Space Scaling Methods Applied to An Interacting Fermion Hamiltonian". *Phys. Rev. B*, 24(9):5356–5362, 1981.

[386] R. Jullien and R. M. Martin. "Properties of the Periodic Anderson Hamiltonian: Calculations on Finite Cells". *J. Appl. Phys.*, 53(3):2137–2139, 1982.

[387] V. Waas, H. Büttner, and J. Voit. "Finite-size Studies of Phases and Dimerization in One-Dimensional Extended Peierls-Hubbard Models". *Phys. Rev. B*, 41(13):9366–9376, 1990.

[388] H. Tsunetsugu, Y. Hatsugai, K. Ueda, and M. Sigrist. "Spin-Liquid Ground State of the Half-Filled Kondo Lattice in One Dimension". *Phys. Rev. B*, 46(5):3175–3178, 1992.

[389] T. Nishino and K. Ueda. "Spin- and Charge-Excitation Gaps in the One-Dimensional Periodic Anderson Model". *Phys. Rev. B*, 47(19):12451–12458, 1993.

[390] B. S. Shastry and B. Sutherland. "Twisted Boundary Conditions and Effective Mass in Heisenberg-Ising and Hubbard Rings". *Phys. Rev. Lett.*, 65(2):243–246, 1990.

[391] X. Zotos, P. Prelovšek, and I. Sega. "Single-Hole Effective Masses in the *t-J* Model". *Phys. Rev. B*, 42(13):8445–8450, 1990.

[392] W. Kohn. "Theory of the Insulating State". *Phys. Rev.*, 133(1A):A171–A181, 1964.

[393] A. M. Oleś, G. Tréglia, D. Spanjaard, and R. Jullien. "One-Hole Excitation Spectra of the One-Dimensional Hubbard Model". *Phys. Rev. B*, 32(4):2167–2177, 1985.

[394] X. Zotos and F. Pelzer. "Exact and Numerical Study of the Effective Hopping of a Particle Interacting With a Fermionic Bath in One Dimension". *Phys. Rev. B*, 37(10):5045–5049, 1988.

[395] P. Prelovšek, A. Ramšak, and I. Sega. "Ferromagnetic Polarons in a One-Dimensional *t-J* Model With Next-Nearest-Neighbor Hopping". *Phys. Rev. B*, 44(21):11795–11801, 1991.

[396] K. Tsutsui, Y. Ohta, R. Eder, S. Maekawa, E. Dagotto, and J. A. Riera. "Heavy Quasiparticles in the Anderson Lattice Model". *Phys. Rev. Lett.*, 76(2):279–282, 1996.

[397] E. Y. Loh, Jr. and D. K. Campbell. "Optical-Absorption in Extended Peierls-Hubbard Models". *Synth. Met.*, 27(1–2):A499–A508, 1988.

[398] D. Poilblanc and E. Dagotto. "Optical Mass in the *t*-*J* Model". *Phys. Rev. B*, 44:R466–R469, 1991.

[399] D. Poilblanc. "Twisted Boundary Conditions in Cluster Calculations of the Optical Conductivity in Two-Dimensional Lattice Models". *Phys. Rev. B*, 44(17):9562–9581, 1991.

[400] C. Gros. "The Boundary-Condition Integration Technique — Results for the Hubbard-Model in 1D and 2D". *Z. Phys. B – Condensed Matter*, 86(3):359–365, 1992.

[401] J. T. Gammel, D. K. Campbell, and E. Y. Loh, Jr. "Extracting Infinite System Properties From Finite-Size Clusters — Phase Randomization Boundary-Condition Averaging". *Synth. Met.*, 55–57(2–3):4437–4442, 1993.

[402] C. Gros. "Control of the Finite-Size Corrections in Exact Diagonalization Studies". *Phys. Rev. B*, 53(11):6865–6868, 1996.

[403] J. A. Riera and A. P. Young. "Ferromagnetism in the One-Band Hubbard Model". *Phys. Rev. B*, 40(7):5285–5288, 1989.

[404] R. M. Fye. "Quantum Monte Carlo Study of the One-Dimensional Symmetric Anderson Lattice". *Phys. Rev. B*, 41(4):2490–2509, 1990.

[405] A. Moreo, E. Dagotto, T. Jolicoeur, and J. Riera. "Incommensurate Correlations in the *t*-*J* and Frustrated spin-$\frac{1}{2}$ Heisenberg Models". *Phys. Rev. B*, 42(10):6283–6293, 1990.

[406] J. A. Riera. "Binding of Holes in Two-Dimensional Lattices With Different Boundary Conditions". *Phys. Rev. B*, 43(4):3681–3683, 1991.

[407] R. Valentí, C. Gros, P. J. Hirschfeld, and W. Stephan. "Rigorous Bounds for Ground-State Properties of Correlated Fermi Systems". *Phys. Rev. B*, 44(24):13203–13212, 1991.

[408] P. Santini, L. C. Andreani, and H. Beck. "Magnetic Correlations in the Anderson Lattice: An Exact-Diagonalization Study". *Phys. Rev. B*, 47(2):1130–1133, 1993.

[409] W. M. C. Foulkes, L. Mitas, R. J. Needs, and G. Rajagopal. "Quantum Monte Carlo Simulations of Solids". *Rev. Mod. Phys.*, 73(1):33–83, 2001 and references therein.

[410] N. Kawakami and S.-K. Yang. "Conductivity and Transport Mass in the 1D *t*-*J* Model at $t = J$". *Physica C*, 185–189:1429–1430, 1991.

[411] C. Lin, F. H. Zong, and D. M. Ceperley. "Twist-Averaged Boundary Conditions in Continuum Quantum Monte Carlo Algorithms". *Phys. Rev. E*, 64:016702, 2001.

[412] A. Baldereschi. "Mean-Value Point in the Brillouin Zone". *Phys. Rev. B*, 7(12):5212–5215, 1973.

[413] D. J. Chadi and M. L. Cohen. "Electronic Structure of $Hg_{1-x}Cd_xTe$ Alloys and Charge-Density Calculations Using Representative k Points". *Phys. Rev. B*, 7(2):692–699, 1973.

[414] D. J. Chadi and M. L. Cohen. "Special Points in the Brillouin Zone". *Phys. Rev. B*, 8(12):5747–5753, 1973.

[415] H. J. Monkhorst and J. D. Pack. "Special Points for Brillouin-Zone Integration". *Phys. Rev. B*, 13(12):5188–5192, 1976.

[416] D. J. Chadi. "Special Points for Brillouin-Zone Integration". *Phys. Rev. B*, 16(4):1746–1747, 1977.

[417] J. D. Pack and H. J. Monkhorst. "Special Points for Brillouin-Zone Integrations — A Reply". *Phys. Rev. B*, 16(4):1748–1749, 1977.

[418] L. Kleinman and J. C. Phillips. "Crystal Potential and Energy Bands of Semiconductors. I. Self-Consistent Calculations for Diamond". *Phys. Rev.*, 116(4):880–884, 1959.

[419] G. Gilat and L. J. Raubenheimer. "Accurate Numerical Method for Calculating Frequency-Distribution Functions in Solids". *Phys. Rev.*, 144(2):390–395, 1966.

[420] G. Lehmann and M. Taut. "Numerical Calculations of Density of States and Related Properties". *Phys. Stat. Solidi B*, 54(2):469–477, 1972.

[421] M. Yamanaka, M. Oshikawa, and I. Affleck. "Nonperturbative Approach to Luttinger's Theorem in One Dimension". *Phys. Rev. Lett.*, 79(6):1110–1113, 1997.

[422] A.-B. Chen. "Simple Brillouin-Zone Schem for the Spectral Properties of Solids". *Phys. Rev. B*, 16(8):3291–3302, 1977.

[423] L. Kleinman. "Error in the Tetrahedron Integration Scheme". *Phys. Rev. B*, 28(2):1139–1141, 1983.

[424] O. Jespen and G. K. Andersen. "No Error in the Tetrahedron Integration Scheme". *Phys. Rev. B*, 29(10):5965, 1984.

[425] J. Oriade. "Warped Linear Analytic Tetrahedral Scheme for Brillouin-Zone Integrations". *Int. J. Quant. Chem.*, 27(1):97–101, 1985.

[426] S. Kaprzyk and P. E. Mijnarends. "A Simple Linear Analytic Method for Brillouin Zone Integration of Spectral Functions in the Complex Energy Plane". *J. Phys. C: Solid State Phys.*, 19:1283–1292, 1986.

[427] G. Wiesenekker and E. J. Baerends. "Quadratic Integration Over the Three-Dimensional Brillouin Zone". *J. Phys: Condens. Matter*, 3:6721–6742, 1991.

[428] O. Pulci, B. Adolph, U. Grossner, and F. Bechstedt. "*Ab Initio* Calculation of the Reflectance Anisotropy of Surfaces: The Triangle Method". *Phys. Rev. B*, 58(8):4721–4727, 1998.

[429] O. Jespen P. E. Blöchl and O. K. Andersen. "Improved Tetrahedron Method for Brillouin-Zone Integrations". *Phys. Rev. B*, 49(23):16223–16233, 1994.

[430] P. Enders. "Special-Lines Approximation to Brillouin Zone Integration". *Semicond. Sci. Technol.*, 11:187–189, 1996.

[431] C. J. Pickard and M. C. Payne. "Extrapolative Approaches to Brillouin-Zone Integration". *Phys. Rev. B*, 59(7):4685–4693, 1999.

[432] M. Methfessel and A. T. Paxton. "High-Precision Sampling for Brillouin-Zone Integration in Metals". *Phys. Rev. B*, 40:3616–3621, 1989.

[433] S. L. Cunningham. "Special Points in the Two-Dimensional Brillouin Zone". *Phys. Rev. B*, 10:4988–4994, 1974.

[434] L. Macot and B. Frank. "Formulas for the Chadi-Cohen Process". *Phys. Rev. B*, 41(7):4469–4474, 1990.

[435] J. Rogan and M. Lagos. "Non-Recursive Chadi-Cohen Integration Over the Brillouin Zone of Cubic Crystals". *Phil. Mag. B*, 81(6):551–559, 2001.

[436] J. Moreno and J. M. Soler. "Optimal Meshes for Integrals in Real- and Reciprocal-Space Unit Cells". *Phys. Rev. B*, 45(24):13891–13898, 1992.

[437] J. Hama and M. Watanabe. "General Formulae for the Special Points and Their Weighting Factors in k-Space Integration". *J. Phys: Condens. Matter*, 4:4583–4594, 1992.

[438] A. J. Davies. *The Finite Element Method: A First Approach*. Oxford University Press (New York), 1980.

[439] J. N. Reddy. *An Introduction to the Finite Element Method*. McGraw-Hill (New York), 1984.

[440] O. C. Zienkiewicz and R. L. Taylor. *The Finite Element Method*, volume 1: The Basis. Butterworth-Heinemann (Oxford), 5th edition, 2000.

[441] W. H. Press, S. A. Teukolsky, W. T. Vetterling, and B. P. Flannery. *Numerical Recipes in C: The Art of Scientific Computing*. Cambridge University Press (New York), 2nd edition, 1992.